Jason S. Lewis
Albert D. Windhorst
Brian M. Zeglis
Editors

Radiopharmaceutical Chemistry

Springer

Radiopharmaceutical Chemistry

Jason S. Lewis • Albert D. Windhorst • Brian M. Zeglis
Editors

Radiopharmaceutical Chemistry

Springer

Editors
Jason S. Lewis
Department of Radiology
Memorial Sloan Kettering Cancer Center
New York, NY
USA

Brian M. Zeglis
Department of Chemistry
Hunter College
City University of New York
New York, NY
USA

Albert D. Windhorst
Department of Radiology and
Nuclear Medicine
VU University Medical Center
Amsterdam
The Netherlands

ISBN 978-3-319-98946-4 ISBN 978-3-319-98947-1 (eBook)
https://doi.org/10.1007/978-3-319-98947-1

Library of Congress Control Number: 2018965920

This Springer imprint is published by the registered company Springer Nature Switzerland AG
The registered company address is: Gewerbestrasse 11, 6330 Cham, Switzerland

Foreword

In the second volume of his journals, Ralph Waldo Emerson wrote, "Chemistry began by saying it would change the baser metals into gold. By not doing that, it has done much greater things." As I sat down to write this Foreword, Emerson's words came to mind for two reasons. First, perhaps more than any other branch of science, radiopharmaceutical chemistry depends on the transmutation of one element into another. And second, while Emerson was, of course, talking about chemistry as a whole, it is hard to deny that the remarkable story of radiopharmaceutical chemistry over the last half century provides a particularly fine example of the "greater things" of which he speaks.

The clinical efficacy of radiopharmaceuticals – particularly radiopharmaceuticals for imaging – is predicated on the *tracer principle*, the notion that radiolabeled compounds are administered in such small molar amounts that they do not significantly perturb the biological systems with which they interact. This is critical both with respect to the integrity of the biological assays they provide and in the context of side effects for patients. To illustrate the latter, there have been ~50 million clinical PET imaging studies without a reported complication from the radiotracer. The benefits of the tracer principle are clear. However, working with such small amounts of radionuclides creates both opportunities and a challenging scenario for radiochemists: many of the principles of stoichiometry and mass action in chemical reactions are not applicable at the "tracer scale." Yet this is not the only way in which radiopharmaceutical chemistry is unique. The short-lived nature of many radionuclides means that time is of the essence during the synthesis of radiopharmaceuticals, an issue that prioritizes the incorporation of radionuclides at late stages in the synthesis of a tracer. This, in turn, has led to the advent of novel automated systems for radiosynthetic processes and, because of the minute masses involved, has more recently fueled the development of small microsynthesizers as well. Ultimately, while radiopharmaceutical chemistry is based on many general principles of chemistry, these key differences have forced the field to undergo an evolution all its own.

In this textbook, Professors Lewis, Windhorst, and Zeglis have – arguably for the first time – created a comprehensive educational framework for radiopharmaceutical chemistry. Each chapter has been thoughtfully crafted by leading experts from around the world, and the trio of editors has merged these contributions into a cohesive and accessible book that will undoubtedly become an indispensable guide for students and radiochemists at all levels of education and experience. The interdisciplinary and specialized nature of radiopharmaceutical chemistry has had two important implications for the training of radiochemists. First, radiochemistry and radiopharmaceutical chemistry are seldom taught during the undergraduate years. And second, aspiring radiochemists often come to the field after years of training in other disciplines, including organic, medicinal, inorganic, and materials chemistry. While the latter has provided a pipeline of diverse talent, it has also created an educational gap: for years, aspiring radiochemists – whether undergraduates, graduate students, postdoctoral fellows, or experienced chemists – have not had the benefit of a single, authoritative resource to help them transition into the field of radiopharmaceutical chemistry. This is even more important now due to the ever-growing importance of molecular imaging in transferring knowledge from the *in vitro* biological sciences to *in vivo* animal models of disease and to clinical research and practice, along with the integration of molecular imaging diagnostics with molecular and

cell-based therapies. This textbook *emphatically* closes that gap and, in doing so, will play a critical role in the education of the next generations of radiopharmaceutical chemists worldwide.

I have had the good fortune to be involved in one branch of radiopharmaceutical chemistry – PET imaging – since the very beginning, starting with my invention of the PET scanner with my postdoctoral fellow at the time, Dr. Edward Hoffman. This journey has given me an acute appreciation for the interdisciplinary nature of the field of nuclear imaging. Indeed, the origin and advancement of nuclear medicine have their foundation in the collaboration and cooperation of physicists, engineers, physicians, and (of course) radiochemists. The three parts of this textbook – First Principles, Radiochemistry, and Special Topics – reflect this interdisciplinary approach. An extraordinarily wide array of topics is covered, ranging from the fundamentals of the production and decay of radionuclides to electrophilic radiofluorinations and the coordination of radiometals. The book also addresses the integration of radiotracers with therapy in theranostics as well as the translation of radiopharmaceuticals to clinical practice to improve the care of patients.

Finally, on a personal note, I have spent my entire professional career working with a wide array of radiochemists, many of whom are contributors to this book. Over the years, they have displayed an inspiring passion for this field, and it has been a pleasure spending so much time as teachers and students of each other and – most importantly – building lifelong friendships with them.

Michael E. Phelps
Department of Molecular and Medical Pharmacology
Crump Institute for Molecular Imaging
David Geffen School of Medicine at UCLA
Los Angeles, CA, USA

Preface

From the naming of "radioactivity" in 1897 by Marie Curie to the first intravenous injection of radium in 1913 to the installation of the first PET/MRI in 2008, the use of radiolabeled compounds has become fully integrated into medical care. The stunning clinical successes of nuclear imaging and targeted radiotherapy have resulted in rapid growth in the field of radiopharmaceutical chemistry. Without question, this growth will ultimately prove extremely beneficial to the field (and, by extension, nuclear medicine). However, at this point, interest in the field outpaces the academic and educational infrastructure needed to train new radiopharmaceutical chemists. The aim of this book is to help bridge this educational gap at a time when an increasing number of young scientists are interested in radiopharmaceutical chemistry.

When conceiving and developing this book (over a number of beers), we requested that the authors of each chapter regard their contribution not as a review but rather as a piece of a larger educational framework meant for undergraduate students, postgraduate students, and postdocs. We also asked that the chapters include "tricks of the trade," methods that are vital for success but are often not discussed in the primary literature. Ultimately, we hope that this book can fill an important niche in the educational landscape of radiochemistry and thus prove vital to the training of the next generation of radiopharmaceutical chemists.

The book is divided into three overarching parts: First Principles, Radiochemistry, and Special Topics. The first ten chapters seek to offer "bird's-eye view" discussions that cover fundamental and broad issues in the field. The second part is the "meat" of the book and delves much deeper, covering both well-established and state-of-the-art techniques in radiopharmaceutical chemistry. This part has been divided according to radionuclide and includes chapters on radiolabeling methods using both common and emerging medical isotopes. Finally, the third part of the book is dedicated to chapters that – frankly – do not fit elsewhere in the work yet still contain important information for young radiochemists.

The three of us have dedicated our careers to radiochemistry, and this book is the manifestation of our desire to grow the field we love. This work would not have been possible without extraordinary contributions – following occasional arm-twisting on our part – from our dear friends and colleagues. Their efforts and work are very much appreciated. We would also like to thank Katherine Kreilkamp (Developmental Editor, Springer Nature) for her incredible hard work, persistence, and ability to keep us on our toes, as well as Margaret Moore (Editor, Clinical Medicine, Springer) for signing on to this idea at the very beginning. Finally, we would like to thank our better halves, Mikel Ross, Monique Bolland, and Emily Zeglis, for their patience and understanding while this work developed and, in particular, for wrangling some very active 2-year-olds (Elliott Zeglis, Grace Lewis, and Evan Lewis).

New York, NY, USA — Jason S. Lewis
Amsterdam, The Netherlands — Albert D. Windhorst
New York, NY, USA — Brian M. Zeglis

Contents

Part I First Principles

Why Nuclear Imaging and Radiotherapy? 3
David Mankoff

A Short History of Nuclear Medicine 11
Carolyn J. Anderson, Xiaoxi Ling, David J. Schlyer, and Cathy S. Cutler

The Basics of Nuclear Chemistry and Radiochemistry: An Introduction to Nuclear Transformations and Radioactive Emissions 27
Frank Rösch

Methods for the Production of Radionuclides for Medicine 63
Lauren L. Radford and Suzanne E. Lapi

An Overview of Targeted Radiotherapy 85
Michal Grzmil, Alexander Meisel, Martin Behé, and Roger Schibli

An Overview of Nuclear Imaging 101
Pat Zanzonico

Small Molecules as Radiopharmaceutical Vectors 119
Antony D. Gee, Salvatore Bongarzone, and Alan A. Wilson

Peptides as Radiopharmaceutical Vectors 137
Ryan A. Davis, Sven H. Hausner, and Julie L. Sutcliffe

Immunoglobulins as Radiopharmaceutical Vectors 163
Danielle J. Vugts and Guus A. M. S. van Dongen

Nanoparticles as Radiopharmaceutical Vectors 181
Anyanee Kamkaew, Emily B. Ehlerding, and Weibo Cai

Part II Radiochemistry

The Radiopharmaceutical Chemistry of Carbon-11: Basic Principles 207
Gunnar Antoni

The Radiopharmaceutical Chemistry of Carbon-11: Tracers and Applications 221
Verena Pichler, Neydher Berroterán-Infante, Marius Ozenil, Sarah Pfaff, Cécile Philippe, and Wolfgang Wadsak

The Radiopharmaceutical Chemistry of Nitrogen-13 and Oxygen-15 237
Vanessa Gómez-Vallejo, Luka Rejc, Fernando López-Gallego, and Jordi Llop

The Radiopharmaceutical Chemistry of the Radionuclides of Gallium and Indium 255
Julia E. Blower, Maggie S. Cooper, Cinzia Imberti, Michelle T. Ma, Christopher Marshall, Jennifer D. Young, and Philip J. Blower

The Radiopharmaceutical Chemistry of Fluorine-18: Nucleophilic Fluorinations 273
Johannes Ermert and Bernd Neumaier

The Radiopharmaceutical Chemistry of Fluorine-18: Electrophilic Fluorinations 285
Michael Wagner and Frank Wuest

The Radiopharmaceutical Chemistry of Fluorine-18: Next-Generation Fluorinations 297
Anu J. Airaksinen

The Radiopharmaceutical Chemistry of Technetium-99m 311
Stephanie M. Rathmann, Zainab Ahmad, Samantha Slikboer, Holly A. Bilton, Denis P. Snider, and John F. Valliant

The Radiopharmaceutical Chemistry of the Radioisotopes of Copper 335
Xiaoxi Ling, Cathy S. Cutler, and Carolyn J. Anderson

The Radiopharmaceutical Chemistry of the Radioisotopes of Lutetium and Yttrium 359
Elaheh Khozeimeh Sarbisheh and Eric W. Price

The Radiopharmaceutical Chemistry of Zirconium-89 371
Bernadette V. Marquez-Nostra and Nerissa Viola

The Radiopharmaceutical Chemistry of the Radioisotopes of Iodine 391
Ganesan Vaidyanathan and Michael R. Zalutsky

The Radiopharmaceutical Chemistry of Alpha-Emitting Radionuclides 409
D. Scott Wilbur

The Radiopharmaceutical Chemistry of Seldom-Used Radionuclides in Nuclear Medicine 425
Jason P. Holland

Part III Special Topics

Bioconjugation Methods for Radiopharmaceutical Chemistry 449
Jens Cardinale, Carolina Giammei, Nedra Jouini, and Thomas L. Mindt

Click Chemistry in Radiopharmaceutical Chemistry 467
James C. Knight and Bart Cornelissen

Equipment and Instrumentation for Radiopharmaceutical Chemistry 481
Stephen Thompson and Peter J. H. Scott

Kinetic Modeling of Radiotracers 501
Mark Lubberink and Kerstin Heurling

An Introduction to Radiation Protection 515
Brian Serencsits, Brian M. Quinn, and Lawrence T. Dauer

An Introduction to Biostatistics 531
Kristen M. Cunanan and Mithat Gönen

Choosing a Target for Nuclear Imaging or Targeted Radiotherapy 541
Andrew M. Scott, Yit Wooi Goh, Sze Ting Lee, and Salvatore U. Berlangieri

Target Identification, Lead Discovery, and Optimization 555
Julien Dimastromatteo and Kimberly A. Kelly

Preclinical Experimentation in Oncology 569
Sridhar Nimmagadda, Sagar Shelake, and Martin G. Pomper

Preclinical Experimentation in Neurology 583
Kristina Herfert, Sabina Marciano, Laura Kuebler, Sabrina Buss, Natalie Landeck, Julia G. Mannheim, and Hanna Napieczynska

The Clinical Translation Process in Europe 607
Iván Peñuelas and Philip H. Elsinga

The Clinical Translation Process in the United States 619
Sonia Sequeira and Serge K. Lyashchenko

Setting Up a Successful Radiopharmaceutical Production Facility 627
Ashley Mishoe and Phillip DeNoble

Index 635

Editors and Contributors

Editors

Jason S. Lewis, PhD Department of Radiology, Memorial Sloan Kettering Cancer Center, New York, NY, USA

Albert D. Windhorst, PhD Department of Radiology and Nuclear Medicine, VU University Medical Center, Amsterdam, The Netherlands

Brian M. Zeglis, PhD Department of Chemistry, Hunter College, City University of New York, New York, NY, USA

Contributors

Zainab Ahmad, HBSc Department of Chemistry and Chemical Biology, McMaster University, Hamilton, ON, Canada

Anu J. Airaksinen, PhD Department of Chemistry – Radiochemistry, University of Helsinki, Helsinki, Finland

Carolyn J. Anderson, PhD Department of Medicine, University of Pittsburgh, Pittsburgh, PA, USA

Gunnar Antoni, PhD PET Centre, Uppsala University Hospital, Uppsala, Sweden

Martin Behé, PhD Center for Radiopharmaceutical Sciences ETH-PSI-USZ, Paul Scherrer Institute, Villigen-PSI, Switzerland

Salvatore U. Berlangieri, MB BS (Hons) Department of Molecular Imaging and Therapy, Austin Hospital, Heidelberg, VIC, Australia

Neydher Berroterán-Infante, Dipl-Chem Department of Biomedical Imaging and Image-guided Therapy, Division of Nuclear Medicine, Medical University of Vienna, Vienna, Austria

Holly A. Bilton, HBSc Department of Chemistry and Chemical Biology, McMaster University, Hamilton, ON, Canada

Julia E. Blower, MChem, MRes, PhD School of Biomedical Engineering & Imaging Sciences, King's College London, St. Thomas' Hospital, London, UK

Philip J. Blower, BA Dphil School of Biomedical Engineering & Imaging Sciences, King's College London, St. Thomas' Hospital, London, UK

Salvatore Bongarzone, PhD Imaging Chemistry & Biology, King's College London, London, UK

Sabrina Buss, MSc Department of Preclinical Imaging and Radiopharmacy, University of Tübingen, Tübingen, Germany

Weibo Cai, PhD Department of Radiology, University of Wisconsin – Madison, Madison, WI, USA

Jens Cardinale, PhD Ludwig Boltzmann Institute Applied Diagnostics, General Hospital Vienna (AKH), Vienna, Austria

Maggie S. Cooper, PhD School of Biomedical Engineering & Imaging Sciences, King's College London, St. Thomas' Hospital, London, UK

Bart Cornelissen, PhD CRUK/MRC Oxford Institute for Radiation Oncology, Radiobiology Research Institute, Churchill Hospital (Headington), Department of Oncology, University of Oxford, Oxford, UK

Kristen M. Cunanan, PhD Department of Epidemiology and Biostatistics, Memorial Sloan Kettering Cancer Center, New York, NY, USA

Cathy S. Cutler, PhD Medical Isotope Research & Production (MIRP) Program, Collider Accelerator Department, Brookhaven National Laboratory, Upton, NY, USA

Lawrence T. Dauer, PhD Department of Medical Physics, Memorial Sloan Kettering Cancer Center, New York, NY, USA

Ryan A. Davis, PhD Department of Internal Medicine, University of California Davis, Sacramento, CA, USA

Phillip DeNoble, PharmD Department of Radiology, Memorial Sloan Kettering Cancer Center, New York, NY, USA

Julien Dimastromatteo, PhD Department of Biomedical Engineering, School of Medicine, University of Virginia, Charlottesville, VA, USA

Emily B. Ehlerding, MS Department of Medical Physics, University of Wisconsin – Madison, Madison, WI, USA

Philip H. Elsinga, PhD Department of Nuclear Medicine and Molecular Imaging, University Medical Center Groningen, University of Groningen, Groningen, The Netherlands

Faculty of Medical Sciences, University of Groningen, Groningen, The Netherlands

Johannes Ermert, PhD Institute of Neuroscience and Medicine, Nuclear Chemistry, Forschungszentrum Jülich GmbH, Jülich, Germany

Antony D. Gee, PhD Imaging Chemistry & Biology, King's College London, London, UK

Carolina Giammei, MSc Ludwig Boltzmann Institute Applied Diagnostics, General Hospital Vienna (AKH), Vienna, Austria

Yit Wooi Goh, PhD Tumor Targeting Laboratory, Olivia Newton-John Cancer Research Institute, Melbourne, VIC, Australia

Vanessa Gómez-Vallejo, PhD Radiochemistry Platform, Center for Cooperative Research in Biomaterials, CIC biomaGUNE, San Sebastián, Guipúzcoa, Spain

Mithat Gönen, PhD Department of Epidemiology and Biostatistics, Memorial Sloan Kettering Cancer Center, New York, NY, USA

Michal Grzmil, PhD Center for Radiopharmaceutical Sciences ETH-PSI-USZ, Paul Scherrer Institute, Villigen-PSI, Switzerland

Sven H. Hausner, PhD Department of Internal Medicine, University of California Davis, Sacramento, CA, USA

Kristina Herfert, PhD Department of Preclinical Imaging and Radiopharmacy, University of Tübingen, Tübingen, Germany

Kerstin Heurling, PhD Wallenberg Centre for Molecular and Translational Medicine and the Institute of Neuroscience and Physiology, University of Gothenburg, Gotenburg, Sweden

Jason P. Holland, DPhil Department of Chemistry, University of Zurich, Zurich, Switzerland

Cinzia Imberti, MRes, MSc School of Biomedical Engineering & Imaging Sciences, King's College London, St. Thomas' Hospital, London, UK

Nedra Jouini, MSc Ludwig Boltzmann Institute Applied Diagnostics, General Hospital Vienna (AKH), Vienna, Austria

Anyanee Kamkaew, PhD School of Chemistry, Institute of Science, Suranaree University of Technology, Nakhon Ratchasima, Thailand

Kimberly A. Kelly, PhD Department of Biomedical Engineering, School of Medicine, University of Virginia, Charlottesville, VA, USA

Elaheh Khozeimeh Sarbisheh, PhD Department of Chemistry, University of Saskatchewan, Saskatoon, SK, Canada

James C. Knight, PhD CRUK/MRC Oxford Institute for Radiation Oncology, Radiobiology Research Institute, Churchill Hospital (Headington), Department of Oncology, University of Oxford, Oxford, UK

Laura Kuebler, MSc Department of Preclinical Imaging and Radiopharmacy, University of Tübingen, Tübingen, Germany

Natalie Landeck, PhD Department of Experimental Medical Science, Lund University, Lund, Skane, Sweden

Suzanne E. Lapi, PhD Department of Radiology, University of Alabama at Birmingham, Birmingham, AL, USA

Sze Ting Lee, MBBS, PhD Department of Molecular Imaging and Therapy, Austin Hospital, Heidelberg, VIC, Australia

Xiaoxi Ling, PhD Department of Medicine, University of Pittsburgh, Pittsburgh, PA, USA

Jordi Llop, PhD Radiochemistry and Nuclear Imaging, Center for Cooperative Research in Biomaterials, CIC biomaGUNE, San Sebastián, Guipúzcoa, Spain

Fernando López-Gallego, PhD Institute of Synthetic Chemistry and Catalysis (IQSCH), University of Zaragoza, Zaragoza, Spain

Fundacion ARAID, Zaragoza, Spain

Mark Lubberink, PhD Department of Surgical Sciences – Radiology & Nuclear Medicine, Uppsala University and Medical Physics, Uppsala University Hospital, Uppsala, Sweden

Serge K. Lyashchenko, PharmD Department of Radiology, Memorial Sloan Kettering Cancer Center, New York, NY, USA

Michelle T. Ma, PhD, BSc School of Biomedical Engineering & Imaging Sciences, King's College London, St. Thomas' Hospital, London, UK

David Mankoff, MD, PhD Department of Radiology, Hospital of the University of Pennsylvania, University of Pennsylvania School of Medicine, Philadelphia, PA, USA

Julia G. Mannheim, PhD Department of Preclinical Imaging and Radiopharmacy, University of Tübingen, Tübingen, Germany

Sabina Marciano, MSc Department of Preclinical Imaging and Radiopharmacy, University of Tübingen, Tübingen, Germany

Bernadette V. Marquez-Nostra, PhD Department of Radiology and Biomedical Imaging, PET Center, Yale University, New Haven, CT, USA

Christopher Marshall, MSc, PhD Wales Research and Diagnostic PET Imaging Centre, University Hospital of Wales, School of Medicine, Cardiff University, Cardiff, UK

Alexander Meisel, MD Department of Nuclear Medicine, University Hospital of Zurich, Zurich, Switzerland

Department of Internal Medicine—Oncology & Hematology, Stadtspital Waid, Zurich, Switzerland

Institute of Pharmaceutical Sciences, Department of Chemistry and Applied Biosciences ETH Zurich, Zurich, Switzerland

Thomas L. Mindt, PhD Ludwig Boltzmann Institute Applied Diagnostics, General Hospital Vienna (AKH), Vienna, Austria

Ashley Mishoe, PharmD Department of Radiology and Biomedical Imaging, University of California San Francisco, San Francisco, CA, USA

Hanna Napieczynska, MSc Department of Animal Phenotyping, Max Delbrück Center for Molecular Medicine, Berlin, Germany

Bernd Neumaier, PhD Institute of Neuroscience and Medicine, Nuclear Chemistry, Forschungszentrum Jülich GmbH, Jülich, Germany

Sridhar Nimmagadda, PhD Russell H. Morgan Department of Radiology and Radiological Science, Johns Hopkins University School of Medicine, Baltimore, MD, USA

Marius Ozenil, MSc Department of Biomedical Imaging and Image-guided Therapy, Division of Nuclear Medicine, Medical University of Vienna, Vienna, Austria

Iván Peñuelas, PhD Unidad de Radiofarmacia, Clinica Universidad de Navarra, Pamplona, Spain

Sarah Pfaff, MSc Department of Biomedical Imaging and Image-guided Therapy, Division of Nuclear Medicine, Medical University of Vienna, Vienna, Austria

Cécile Philippe, Mag Dr Department of Biomedical Imaging and Image-guided Therapy, Division of Nuclear Medicine, Medical University of Vienna, Vienna, Austria

Verena Pichler, Mag Dr Department of Biomedical Imaging and Image-guided Therapy, Division of Nuclear Medicine, Medical University of Vienna, Vienna, Austria

Martin G. Pomper, MD, PhD Russell H. Morgan Department of Radiology and Radiological Science, Johns Hopkins University School of Medicine, Baltimore, MD, USA

Eric W. Price, PhD Department of Chemistry, University of Saskatchewan, Saskatoon, SK, Canada

Brian M. Quinn, MS Department of Medical Physics, Memorial Sloan Kettering Cancer Center, New York, NY, USA

Lauren L. Radford, PhD Department of Radiology, University of Alabama at Birmingham, Birmingham, AL, USA

Stephanie M. Rathmann, MSc, HBSc Department of Chemistry and Chemical Biology, McMaster University, Hamilton, ON, Canada

Luka Rejc, PhD Radiochemistry and Nuclear Imaging, Center for Cooperative Research in Biomaterials, CIC biomaGUNE, San Sebastián, Guipúzcoa, Spain

Frank Rösch, PhD Institute of Nuclear Chemistry, Johannes Gutenberg-Universität Mainz, Mainz, Germany

Roger Schibli, PhD Center for Radiopharmaceutical Sciences ETH-PSI-USZ, Paul Scherrer Institute, Villigen-PSI, Switzerland

David J. Schlyer, PhD Department of Biology, Brookhaven National Laboratory, Upton, NY, USA

Andrew M. Scott, MB BS (Hons), MD Department of Molecular Imaging and Therapy, Austin Hospital, Heidelberg, VIC, Australia

Peter J. H. Scott, PhD Department of Radiology, University of Michigan, Ann Arbor, MI, USA

Sonia Sequeira, PhD Department of Research and Technology Management, Memorial Sloan Kettering Cancer Center, New York, NY, USA

Brian Serencsits, MHP Department of Medical Physics, Memorial Sloan Kettering Cancer Center, New York, NY, USA

Sagar Shelake, B Pharm, PhD Russell H. Morgan Department of Radiology and Radiological Science, Johns Hopkins University School of Medicine, Baltimore, MD, USA

Samantha Slikboer, BSc Department of Chemistry and Chemical Biology, McMaster University, Hamilton, ON, Canada

Denis P. Snider, PhD Department of Chemistry and Chemical Biology, McMaster University, Hamilton, ON, Canada

Julie L. Sutcliffe, PhD Department of Internal Medicine and Department of Biomedical Engineering, University of California Davis, Sacramento, CA, USA

Stephen Thompson, PhD Department of Radiology, University of Michigan, Ann Arbor, MI, USA

Ganesan Vaidyanathan, PhD Department of Radiology, Duke University Medical Center, Durham, NC, USA

John F. Valliant, PhD Department of Chemistry and Chemical Biology, McMaster University, Hamilton, ON, Canada

Guus A. M. S. van Dongen, PhD Department of Radiology & Nuclear Medicine, VU University Medical Center, Amsterdam, The Netherlands

Nerissa Viola, PhD Department of Oncology, Karmanos Cancer Institute, Wayne State University, Detroit, MI, USA

Danielle J. Vugts, PhD Department of Radiology & Nuclear Medicine, VU University Medical Center, Amsterdam, The Netherlands

Wolfgang Wadsak, MSc, PhD Department of Biomedical Imaging and Image-guided Therapy, Division of Nuclear Medicine, Medical University of Vienna, Vienna, Austria

Michael Wagner, PhD Department of Oncology, University of Alberta, Edmonton, AB, Canada

D. Scott Wilbur, PhD Department of Radiation Oncology, University of Washington, Seattle, WA, USA

Alan A. Wilson, PhD Imaging and Pre-Clinical Research, Centre for Addiction and Mental Health, Toronto, ON, Canada

Frank Wuest, PhD Department of Oncology, University of Alberta, Edmonton, AB, Canada

Jennifer D. Young, MChem, MRes School of Biomedical Engineering & Imaging Sciences, King's College London, St. Thomas' Hospital, London, UK

Michael R. Zalutsky, PhD Departments of Radiology, Radiation Oncology, Pathology, and Biomedical Engineering, Duke University Medical Center, Durham, NC, USA

Pat Zanzonico, PhD, DABR Department of Medical Physics, Memorial Sloan Kettering Cancer Center, New York, NY, USA

Part I

First Principles

Why Nuclear Imaging and Radiotherapy?

David Mankoff

Fundamentals

What Is Nuclear Medicine?

Nuclear medicine is classically defined as the application of radionuclides to medicine [1]. Nuclear medicine takes advantage of the unique properties of radioactive elements, which have significantly different physical properties compared to stable elements but identical chemical behavior. More specifically, radionuclides decay at a characteristic rate (*i.e.* half-life) via the emission of particles or electromagnetic radiation (*e.g.* positrons, gamma rays, *etc.*). These emissions can be harnessed to facilitate the imaging or therapy of disease. Radiolabeled molecules, termed "radiopharmaceuticals," are an essential element in the medical subspecialty of nuclear medicine [2]. As such, radiopharmaceutical chemistry—the branch of chemistry dedicated to the synthesis, characterization, and evaluation of radiopharmaceuticals—is a fundamental and critical component of nuclear medicine.

Why Nuclear Imaging?

Nuclear imaging is predicated on the fact that essentially none of the biomolecules within the body are radioactive. As a result, radiopharmaceuticals can be distinguished easily from native molecules, providing nearly infinite contrast for imaging. This represents a dramatic departure from other imaging modalities—such as computer tomography (CT)—in which *all* tissues produce a signal and differences in the intensity of the signal between different tissues provide image contrast. In principle, every molecule of a diagnostic radiopharmaceutical can be detected over its lifetime, providing extraordinary sensitivity for imaging [3, 4]. In practice, however, several factors—including the limits of detection devices, the absorption of emissions before they leave the body (attenuation), and the need to limit radiation exposure to patients—all impose limits on imaging the emissions from a radiopharmaceutical. That said, it is possible to generate high-quality images using radioactivity doses as low as 30–600 MBq, values which correspond to as little as nanomoles of the compound or less, depending upon the half-life of the radionuclide [5–7] (see Table 1 for a representative calculation). This unique property allows radiopharmaceuticals to behave as true molecular tracers without perturbing the native biochemistry of the system, following the tracer principle of De Hevesy [2].

Why Nuclear Radiotherapy?

Nuclear radiotherapy (also called radionuclide therapy) is predicated on the use of radiopharmaceuticals to deliver therapeutic radiation to a target within the body [8–10]. For example, diphosphonates—which are commonly labeled with the gamma-emitting radionuclide ^{99m}Tc to enable the imaging of bone mineralization——can also be labeled with a beta particle-emitting radionuclide such as ^{153}Sm to deliver therapeutic radiation to sites of new bone formation, most typically for the treatment of cancer metastases [11]. Nuclear radiotherapy offers some significant advantages over traditional systemic therapy with nonradioactive drugs (*e.g.* chemotherapy) and external beam radiotherapy. Unlike traditional chemotherapeutics, radiopharmaceuticals can deliver potent therapeutic doses that are not limited by the biochemical action of the drug on the target. Radiopharmaceuticals are administered at low molecular doses and therefore do not generate the nonspecific off-target biochemical effects that can be seen at higher doses of chemotherapeutics. Compared to external beam radiotherapy, molecularly targeted radiopharmaceuticals are typically able to deliver radiation to tissues more selectively than

D. Mankoff (✉)
Department of Radiology, Hospital of the University of Pennsylvania, University of Pennsylvania School of Medicine, Philadelphia, PA, USA
e-mail: david.mankoff@uphs.upenn.edu

J. S. Lewis et al. (eds.), *Radiopharmaceutical Chemistry*, https://doi.org/10.1007/978-3-319-98947-1_1

Table 1 Example of the nuclear medicine tracer principle based on radiopharmaceutical radioactivity dose and theoretical mass limits

The following illustrates the tracer principle of nuclear imaging in the case of the radiopharmaceutical [^{18}F]fluoroestradiol (FES), an analog of estradiol used for the visualization of the regional expression of the estrogen receptor (ER) in breast cancer [5, 6]
Calculation of the molecular quantity of FES needed to image regional ER expression
Radioactivity needed to generate an image, balancing radiation dose and imaging quality: 185 MBq (5 mCi)
Typical specific activity of FES at the time of injection: 37 GBq/μmol (1 Ci/μmole)
The molar dose associated with this dose of radioactivity: 5 nmol
Expected peak concentration after the infusion of FES for a typical 5 L distribution volume: 1 nM
Physiologic range for the concentration of circulating estradiol: as low as 1 nM in menopausal patients
Thus—at transient peak concentrations—the molecular concentration of FES is at or below the lower limits of physiologic concentrations of estradiol, permitting PET imaging of FES-ER binding without perturbing the biology of native estrogen

spatially-targeted external beam radiotherapy. For example, nuclear radiotherapy of thyroid cancer with Na^{131}I can deliver up to 10–15 Gy to thyroid cancer cells without disturbing most adjacent neck tissues. In contrast, only 5–7 Gy can be deposited in the thyroid cancer cells during external beam radiotherapy due to concerns surrounding the toxicity to normal tissues [12]. Yet nuclear radiotherapy is not perfect, of course. Indeed, nuclear radiotherapy is limited by the specificity of the probe for the targeted disease—typically cancer or endocrine disorders—and by the toxicity to organs involved in the absorption, transport, and clearance of the radiopharmaceuticals.

Why Nuclear Medicine Vis-a-Vis Alternatives?

Nuclear imaging and radiotherapy gain their principal advantages over competing approaches from the "tracer principle." The essence of "tracer principle" is that radiopharmaceuticals are administered at such low molar masses that they can create high-contrast images or deliver therapeutic doses without perturbing native biochemistry whatsoever. As such, nuclear medicine approaches hold their greatest advantages over other forms of imaging and therapy in molecularly sensitive processes—*i.e.* those that are most readily affected by low doses of exogenous molecules—including metabolism, receptor binding, and cellular transport [2, 13, 14]. More specifically, glucose metabolism [13, 15], binding to neuroendocrine and steroid receptors [5], and amino acid transport [16, 17] are three clinically important examples of biologic processes that are well served by radiopharmaceutical-based strategies. Nonetheless, nuclear medicine approaches inevitably have some disadvantages compared to other imaging and therapeutic modalities:

- Nuclear medicine offers limited spatial resolution compared to modalities such as X-ray or CT.
- Nuclear medicine involves exposure to radiation, unlike modalities such as MRI or ultrasound.
- Nuclear medicine requires patient-specific radiation safety precautions for treatments, unlike chemotherapy and external beam radiotherapy.

Ultimately, the advantages of nuclear approaches outweigh their disadvantages when applied to diseases associated with molecular targets that can be targeted by diagnostic or therapeutic radiopharmaceuticals. This has led to the considerable use of radiopharmaceuticals in both clinical practice and clinical research for oncology, endocrinology, neuropsychiatry, cardiology, and several other diseases, as outlined later in the chapter.

Details

Clinical Applications for Nuclear Imaging

Nuclear imaging is a key tool for clinical diagnosis that is used thousands of time each day around the world. It is most commonly used to detect and quantify organ function and/or abnormal physiology and molecular biochemistry in a variety of disorders [1]. The need to trace a particular physiologic process or molecular pathway is a common trait of many current clinical applications. Below is a non-exhaustive list of common clinical situations in which nuclear imaging is applied, in rough order of frequency. One or more examples of radiopharmaceuticals used for each application are provided as well.

- *To detect cancer and/or document its spread:*
  - By imaging aberrant glucose metabolism using [^{18}F]fluorodeoxyglucose (FDG) [15] (Fig. 1)
  - By imaging abnormal amino acid transport using [^{18}F]fluciclovine [16, 17] (FACBC)
  - By imaging the expression of cancer-specific biomarkers using ^{18}F- and ^{68}Ga-labeled small-molecule ligands that target prostate-specific membrane antigen [18]
  - By imaging new bone formation associated with cancer metastases using [^{99m}Tc]methylene diphosphonate (MDP) or [^{18}F]NaF [19] (Fig. 2)
- *To identify and quantify endocrine disorders:*
  - By characterizing and quantifying the basis of hyperthyroidism indicated by the uptake and retention of iodine using [^{123}I]NaI [20]
  - By localizing abnormal catecholamine-producing tumors such as pheochromocytomas and neuroblastomas using [^{123}I]metaiodobenzylguanidine (mIBG) [21]

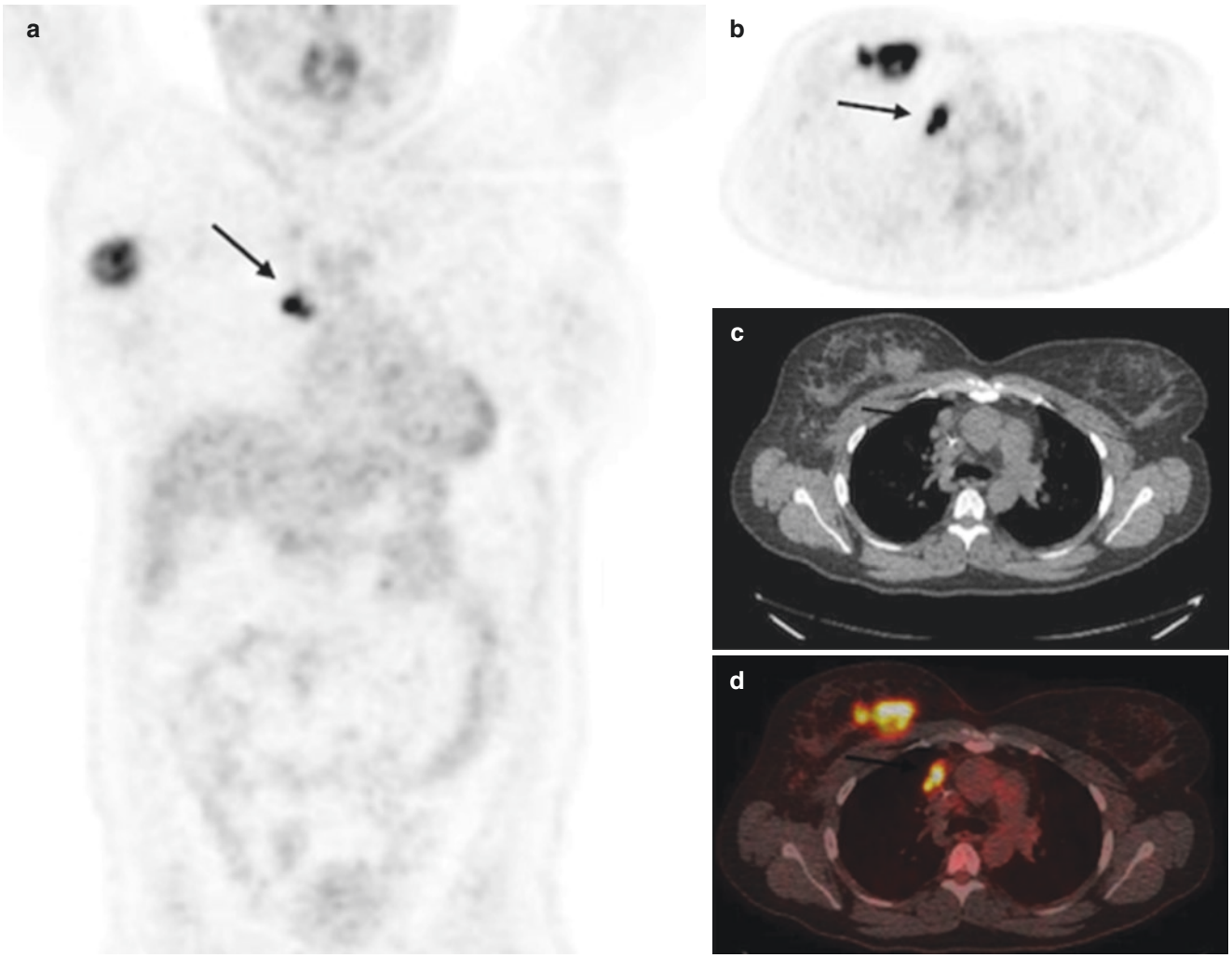

Fig. 1 [^{18}F]fluorodeoxyglucose ([^{18}F]FDG) PET/CT of breast cancer demonstrates the spread of the disease to small mediastinal nodes that are not detected by CT (*arrows*). Image **a** is a coronal PET image of the regional retention of FDG; on the right, axial PET images (**b**) have been combined with CT in the images (**c**) to yield fused images overlaying PET and CT images (**d**)

  - By localizing neuroendocrine tumors on the basis of somatostatin receptor expression using [^{111}In]pentetreotide or [^{68}Ga]-DOTATATE [21] (Fig. 3)
- *To detect and monitor cardiovascular disease:*
  - By identifying significant coronary artery disease on the basis of the delivery of perfusion agents retained in myocardium using [^{99m}Tc]sestamibi or [^{82}Rb]RbCl [22, 23]
  - By measuring aberrant presynaptic cardiac innervation in heart failure and arrhythmias using [^{123}I]mIBG [24]
- *To identify patterns associated with specific neurologic and psychiatric diseases:*
  - By identifying seizure foci on the basis of aberrant perfusion and/or glucose metabolism using [^{99m}Tc]ECD or [^{18}F]FDG, respectively [25]
  - By diagnosing Alzheimer's dementia on the basis of the deposition of amyloid in neural plaques using [^{11}C] Pittsburgh compound B (PIB) or ^{18}F-labeled analogs [26] (Fig. 4)
- *To document normal and abnormal function of excretory organs:*
  - By determining the causes of renal dysfunction by tracing the clearance of renal substrates using [^{99m}Tc] MAG3 [27]
  - By documenting cholecystitis and biliary dyskinesia by tracking biliary excretion using [^{99m}Tc]mebrofenin [28]
- *To identify regional tissue damage due to infection, trauma, etc.:*
  - By localizing bone trauma and infection on the basis reactive new bone formation using [^{99m}Tc]MDP [19]
  - By localizing infection using white blood cells (WBCs) labeled using [^{111}In]oxime [29]

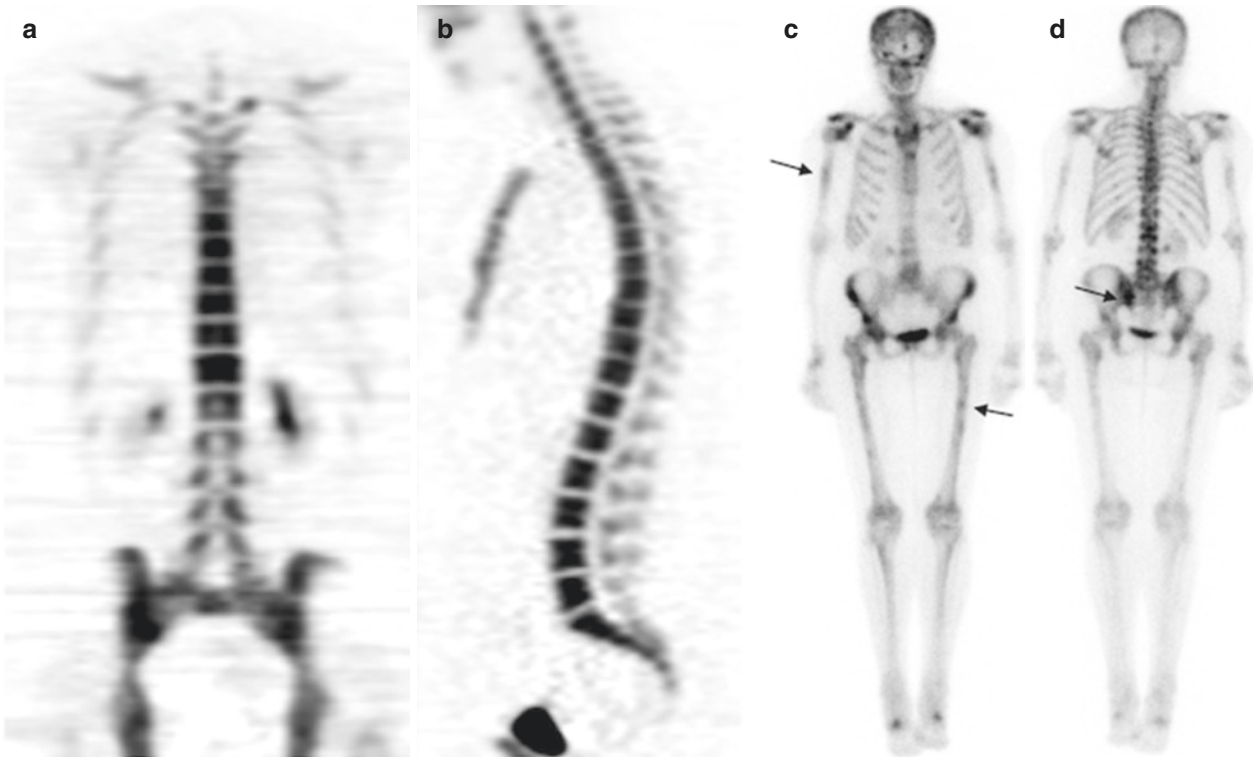

Fig. 2 Bone imaging using [^{18}F]NaF (PET imaging, **a** and **b**) [^{99m}Tc] methylene diphosphonate (MDP, single-photon imaging, **c** and **d**). The FDG PET scan shows the normal distribution of the tracer from the skull base to the pelvis in coronal (**a**) and sagittal tomographic views (**b**). The MDP bone scan shows anterior (**c**) and posterior (**d**) planar images that demonstrate multiple bone metastases, including sites in the left femur, right humerus, and left sacrum (*arrows*)

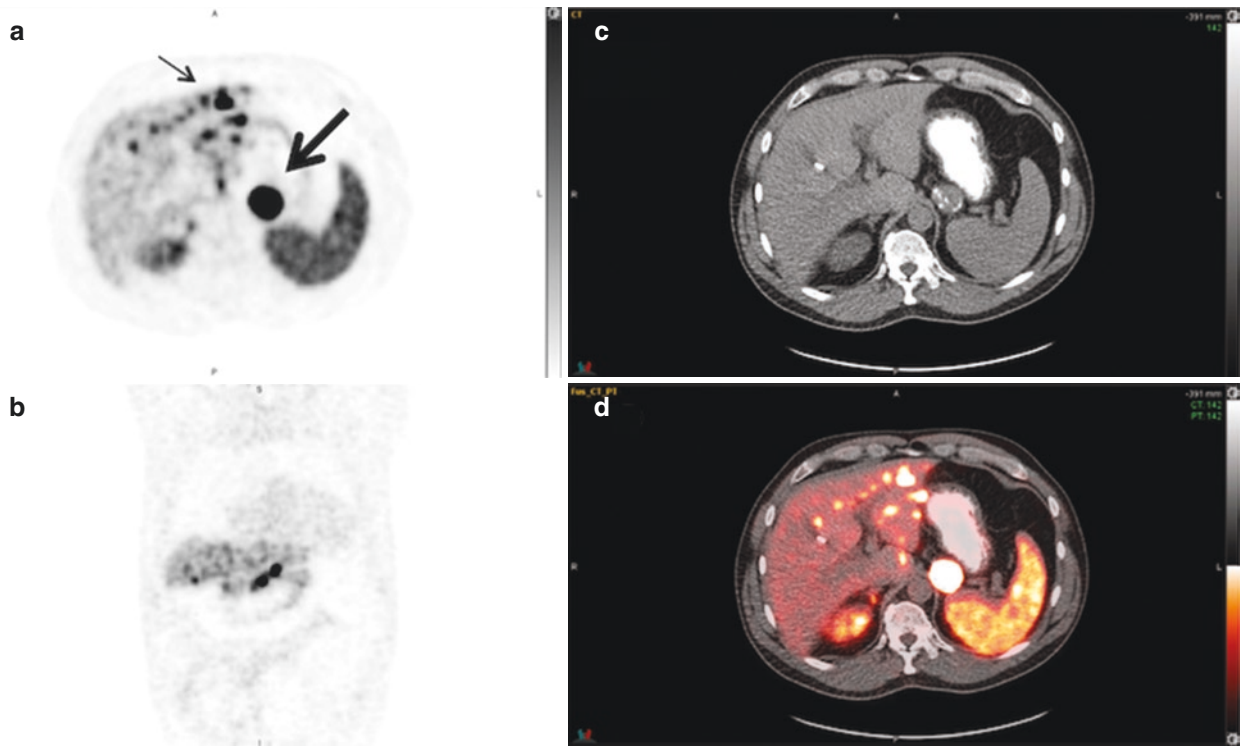

Fig. 3 The staging of neuroendocrine tumors using [^{68}Ga]DOTATE PET/CT. These images demonstrate the feasibility of imaging somatostatin receptor-expressing carcinoid tumor deposits on the emission PET scans (axial view, **a**, coronal view, **b**) and relate the localization of sites of radiopharmaceutical uptake to anatomic sites indicated by the accompanying CT (**c**) and depicted on fused PET and CT images (**d**). Images depict a low-grade neuroendocrine tumor presenting as a perigastric mass (thick arrow) with numerous liver metastases (*thin arrow*)

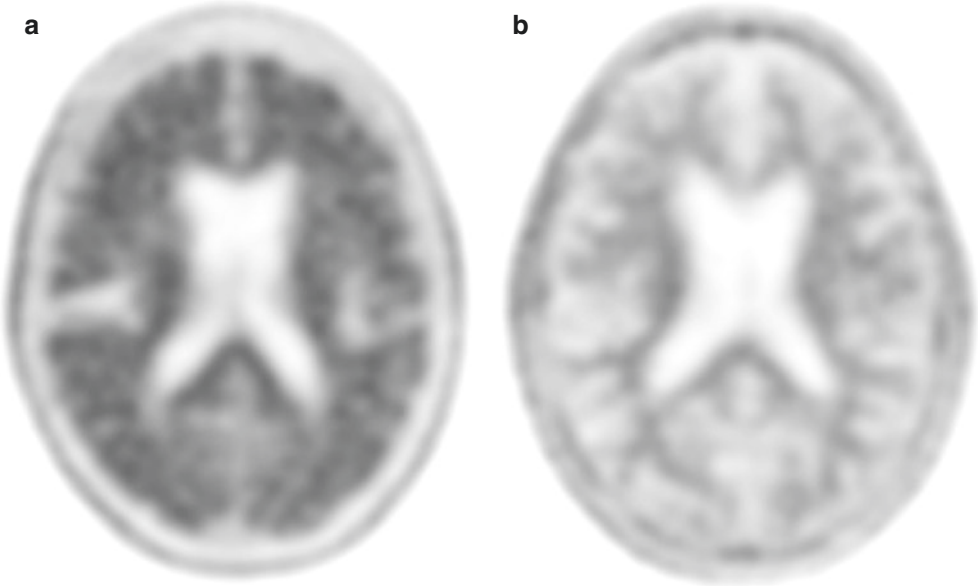

Fig. 4 Imaging amyloid deposition in Alzheimer's dementia neural plaques using [^{18}F]florbetapir. [^{18}F] florbetapir PET images from an Alzheimer's disease patient (**a**) and a normal control subject (**b**) are shown. The prominent cortical tracer binding in (**a**) indicates the presence of moderate amyloid plaques, as compared to absence of cortical binding in a negative scan (**b**). Nonspecific white matter binding is present in both the positive and negative [^{18}F] florbetapir scans

A common thread that runs through all of these applications is the need to localize and measure specific physiologic and molecular processes associated with either normal organ function or tissue dysfunction. In recent years, fundamental research in biology has led to the identification of new targets, and radiopharmaceutical chemists have leveraged this information for the creation of novel radiopharmaceuticals. This has increased the specificity of clinical diagnostic tasks through the use of imaging agents based on receptor-targeted ligands, substrates for specific transporters, and metabolic substrates specific to certain disease and tissue repair processes [14, 30, 31].

Clinical Applications of Nuclear Radiotherapy

Nuclear radiotherapy, while certainly an important clinical tool, is somewhat less commonly used than nuclear imaging. The first—and still most common—use of nuclear radiotherapy is the treatment of hyperthyroidism caused by Graves' disease and toxic nodular goiter. In this approach, modest doses of [^{131}I]NaI provide a safe and highly effective therapeutic alternative to more risky and/or toxic alternatives such as surgery or antithyroid medications. Specifically, in Graves' disease and toxic nodular goiter—in which a large fraction of ingested iodine (typically, well in excess of 30%) goes to the thyroid—thyroid tissue can be ablated by targeted radiotherapy with minimal radiation exposure to the rest of the body [32, 33].

The remaining applications of nuclear therapy largely focus on treating cancer, in which the small risk of modest radiation exposure to some normal tissues is offset by the potential for considerable therapeutic efficacy in otherwise often refractory disorders [8, 34]. The established therapeutic radiopharmaceuticals rely upon targeting either transport phenomena, metabolic pathways, or characteristic tumor biomarkers. Some examples of the established roles of nuclear radiotherapy in the treatment of cancer include:

- Thyroid cancer, using [^{131}I]NaI (typically higher doses than those needed in hyperthyroid treatments) [12] (Fig. 5)
- Painful bone metastases, using bone-targeting agents such as [^{89}Sr]$SrCl_2$, [^{223}Ra]$RaCl_2$, and [^{153}Sm]EDMP [11]
- Catecholamine-producing cancers (*i.e.* neuroblastoma and malignant pheochromocytoma), using the catecholamine transporter substrate [^{131}I]mIBG [21, 35]
- Neuroendocrine tumors, using ^{177}Lu or ^{90}Y-labeled analogs of somatostatin receptor-targeted peptides [21]

An additional type of nuclear radiotherapy is termed "radioimmunotherapy" and takes advantage of the specificity and affinity of monoclonal antibodies for molecular markers of disease. Radioimmunotherapy is predicated on the use of therapeutic radioimmunoconjugates, most commonly labeled with beta particle-emitting radionuclides such as ^{131}I or ^{90}Y [36, 37]. The application of radioimmunotherapy to B-cell lymphoma generated considerable excitement and resulted in two FDA-approved agents—Bexxar and Zevalin—which are based on anti-CD20 antibodies labeled with ^{131}I and ^{90}Y, respectively [37]. Though these were popular at the time of their introduction, advances in the application of non-labeled anti-CD20 antibodies (*e.g.* rituximab) and other drugs limited the more widespread use of these agents.

There has been considerable recent excitement over the future of nuclear radiotherapy [34]. This optimism has been driven by two recent trends in radiopharmaceutical research:

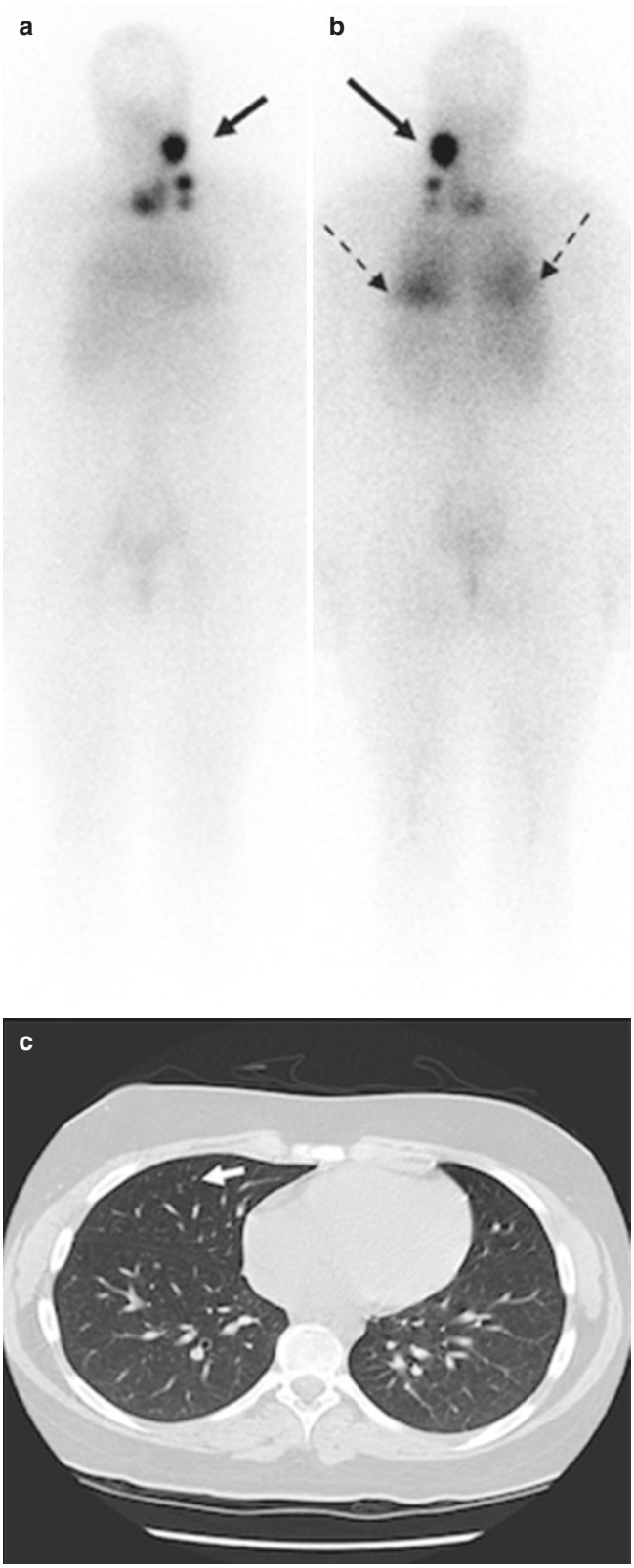

Fig. 5 Imaging with [^{123}I]NaI or low-dose [^{131}I]NaI provides a highly sensitive and specific way to detect the metastatic spread of thyroid cancer to sites of disease outside of the neck. In this case, anterior (**a**) and posterior (**b**) planar whole-body images taken 7 days after a therapeutic dose of [^{131}I]NaI demonstrate regional lymph node metastases in the neck (*solid arrow*) and distant metastatic spread to the small nodules in the lung bases (*dashed arrows*). Lung metastases were not as easily seen by CT (**c**, arrow indicates a single small nodule) but were readily apparent in the radioiodine images

1. The increased success in generating highly targeted small molecules and peptides that have high uptake and retention in cancerous tissues (*e.g.* PSMA-targeted therapeutics for prostate cancer) [18].
2. The increased potency and efficacy for therapeutic radiopharmaceuticals labeled with alpha-emitting radionuclides. For example, the recent approval of the alpha-emitting radiotherapeutic [^{223}Ra]$RaCl_2$ was heralded in clinical trials for demonstrating both highly effective pain palliation and improved survival [9]. This represents a notable departure from many years of experience with beta-emitting therapeutics which provided effective pain palliation but did not improve survival [11].

Tricks of the Trade

What Tools Do We Need?

The current and future success of nuclear imaging and therapy depends on several key technical issues:

- *Imaging instrumentation*: Over 50 years ago, the specialty of nuclear medicine was brought into the mainstream by the advent of the gamma camera, which enabled the practical collection of high-quality single-photon emitting radiopharmaceutical images in the clinic. In the 1990s and early 2000s, the advent of clinically practical positron emission tomography (PET) and PET/CT enabled clinical PET imaging to become an important and rapidly advancing part of nuclear medicine. Advances in the design of detectors and imaging systems have played a large role in the advancement of nuclear medicine [38] and have enabled the acquisition of high-quality, quantitative images with lower and lower doses of radiopharmaceuticals. Further advances in the design of hybrid imaging platforms and novel imaging devices will likely add significantly to our current capabilities [3, 4].
- *Image computing and analytics*: Advances in computational capability—enabled by advances in computing hardware and algorithms—have led to improved imaging quality at low tracer doses though sophisticated image reconstruction and post-reconstruction processing [39]. Further advances in image analysis and advanced analytics (such as machine learning-based feature extraction) will continue to maximize our ability to draw meaningful diagnostic information from nuclear imaging and guide the safer and more effective dosing in nuclear radiotherapy.

However, while instrumentation and analytics have set the pace of discovery and advancement in nuclear medicine for many years, the future of the specialty will increasingly be determined by radiopharmaceutical research and development.

Rapid advances in our understanding of the molecular biology of health and disease underlie an increasing trend toward precision medicine using treatments guided by molecular diagnostics [14, 30, 31, 40]. As such, advances in nuclear medicine will increasingly be driven by the development of new and improved radiopharmaceuticals to guide precision medicine. The creation of paired nuclear diagnostic and therapeutic agents—known as "theranostics"—will be particularly important, as theranostics provide unparalleled opportunities with regard to the selection of patients for treatment as well as the monitoring of ongoing therapies [34]. There is therefore much reason to believe that radiopharmaceutical chemistry will increase in importance as a discipline in nuclear medicine specifically and biomedical research in general.

Controversial Issues

Will Other Imaging and Therapeutic Approaches Replace Nuclear Approaches?

The need to administer radioisotopes—and the inherent practical difficulties and need for radiation exposure—has been seen as a disadvantage of nuclear medicine since its creation. This has led many to predict the demise of the specialty over the years, especially in light of the advent of new imaging modalities such as CT and MRI. In addition, the recent development of nonnuclear probes with molecular capability—*e.g.* agents for ultrasound, optical imaging, and hyperpolarized MR—has created concerns about incremental threats to the field. Some of these concerns have been realized. For example, the use of CT to detect liver metastases replaced the nuclear liver spleen scan in the 1980s.

However, nuclear imaging procedures continue to retain significant advantages over other approaches, especially when the application is focused upon the molecular basis of the disease. For example, the aberrant glycolysis of malignant tissues compared to normal tissues reintroduced nuclear imaging as a key component of the detection of liver metastasis using [^{18}F]FDG PET/CT and now PET/MR [41]. The ongoing discovery of disease-specific biomarkers will provide an increasing basis for the use of molecular tracers for the diagnosis and treatment of disease [40]. As a result, the ongoing application of nuclear medicine for diagnosis and treatment will depend critically on radiochemistry.

The Future

What Does the Future of Nuclear Medicine Look Like?

The future of nuclear medicine will continue to exploit the unique properties of radiopharmaceuticals to exploit the tracer principle for diagnosis and treatment. Several issues within the field of radiochemistry will help drive the future of nuclear medicine [14, 30, 31]:

- *The development of precision diagnostics for precision medicine*
- *The creation of improved targeted therapeutics for cancer and other diseases*
- *The advent of paired diagnostics and therapeutics*, with nuclear imaging paired with both nuclear and non-nuclear therapeutics

The Bottom Line

- Nuclear medicine is the application of radioactive elements to medicine.
- Radiopharmaceuticals operate on the "tracer principle," namely, that radioactive tracers are administered at such low molar doses that they do not perturb the native biology of the system into which they are introduced.
- Nuclear imaging radiopharmaceuticals provide high sensitivity and molecular specificity.
- Radionuclide therapy provides a highly targeted treatment modality based upon the physical impact of radiation. It is similar to external beam radiotherapy but much more targeted.
- Radiopharmaceuticals provide a key link between basic biology and clinical practice. The future of nuclear medicine depends upon the ability of radiopharmaceutical chemists to leverage advances in molecular biology into new approaches to clinical imaging and therapy.

Acknowledgment The author wishes to thank Drs. Katrina Korhonen, Austin Pantel, Yin Jie Chen, and Ilya Nasrallah of the University of Pennsylvania for their help with the images for this chapter.

References

1. Frey KA, Royal HD, Di Carli MF, Dillehay GL, Gordon L, Mankoff DA, et al. ABNM position statement: nuclear medicine professional competency and scope of practice. J Nucl Med. 2011;52(6):994–7.
2. Mankoff DA. A definition of molecular imaging. J Nucl Med. 2007;48(6):18N. 21N
3. Cherry SR, Badawi RD, Karp JS, Moses WW, Price P, Jones T. Total-body imaging: transforming the role of positron emission tomography. Sci Transl Med. 2017;9(381):pii: eaaf6169.
4. Surti S. Update on time-of-flight PET imaging. J Nucl Med. 2015;56(1):98–105.
5. Mankoff DA, Link JM, Linden HM, Sundararajan L, Krohn KA. Tumor receptor imaging. J Nucl Med. 2008;9(Suppl 2):149S–63S.
6. Peterson LM, Kurland BF, Link JM, Schubert EK, Stekhova S, Linden HM, et al. Factors influencing the uptake of

[18]F-fluoroestradiol in patients with estrogen receptor positive breast cancer. Nucl Med Biol. 2011;38(7):969–78.
7. Tu Z, Mach RH. C-11 radiochemistry in cancer imaging applications. Curr Top Med Chem. 2010;10(11):1060–95.
8. Jhanwar YS, Divgi C. Current status of therapy of solid tumors. J Nucl Med. 2005;46(Suppl 1):141S–50S.
9. Parker C, Nilsson S, Heinrich D, Helle SI, O'Sullivan JM, Fossa SD, et al. Alpha emitter radium-223 and survival in metastatic prostate cancer. N Engl J Med. 2013;369(3):213–23.
10. Schmidt M, Baum RP, Simon T, Howman-Giles R. Therapeutic nuclear medicine in pediatric malignancy. Q J Nucl Med Mol Imaging. 2010;54(4):411–28.
11. Pandit-Taskar N, Batraki M, Divgi CR. Radiopharmaceutical therapy for palliation of bone pain from osseous metastases. J Nucl Med. 2004;45(8):1358–65.
12. Pryma DA, Mandel SJ. Radioiodine therapy for thyroid cancer in the era of risk stratification and alternative targeted therapies. J Nucl Med. 2014;55(9):1485–91.
13. Cutler CS, Lewis JS, Anderson CJ. Utilization of metabolic, transport and receptor-mediated processes to deliver agents for cancer diagnosis. Adv Drug Deliv Rev. 1999;37(1–3):189–211.
14. O'Connor JP, Aboagye EO, Adams JE, Aerts HJ, Barrington SF, Beer AJ, et al. Imaging biomarker roadmap for cancer studies. Nat Rev Clin Oncol. 2017;14(3):169–86.
15. Mankoff DA, Eary JF, Link JM, Muzi M, Rajendran JG, Spence AM, et al. Tumor-specific positron emission tomography imaging in patients: [18F] fluorodeoxyglucose and beyond. Clin Cancer Res. 2007;13(12):3460–9.
16. Huang C, McConathy J. Radiolabeled amino acids for oncologic imaging. J Nucl Med. 2013;54(7):1007–10.
17. Schuster DM, Nanni C, Fanti S. Evaluation of prostate cancer with radiolabeled amino acid analogs. J Nucl Med. 2016;57(Suppl 3):61S–6S.
18. Schwarzenboeck SM, Rauscher I, Bluemel C, Fendler WP, Rowe SP, Pomper MG, et al. PSMA ligands for PET imaging of prostate cancer. J Nucl Med. 2017;58(10):1545–52.
19. Even-Sapir E. Imaging of malignant bone involvement by morphologic, scintigraphic, and hybrid modalities. J Nucl Med. 2005;46(8):1356–67.
20. Meller J, Becker W. The continuing importance of thyroid scintigraphy in the era of high-resolution ultrasound. Eur J Nucl Med Mol Imaging. 2002;29(Suppl 2):S425–38.
21. Baum RP, Kulkarni HR, Carreras C. Peptides and receptors in image-guided therapy: theranostics for neuroendocrine neoplasms. Sem Nucl Med. 2012;42(3):190–207.
22. Bravo PE, Di Carli MF, Dorbala S. Role of PET to evaluate coronary microvascular dysfunction in non-ischemic cardiomyopathies. Heart Fail Rev. 2017;22(4):455–64.
23. Dorbala S, Di Carli MF. Cardiac PET perfusion: prognosis, risk stratification, and clinical management. Sem Nucl Med. 2014;44(5):344–57.
24. Jamali HK, Waqar F, Gerson MC. Cardiac autonomic innervation. J Nucl Cardiol. 2017;24(5):1558–70.
25. Mountz JM, Patterson CM, Tamber MS. Pediatric epilepsy: neurology, functional imaging, and neurosurgery. Sem Nucl Med. 2017;47(2):170–87.
26. Nasrallah IM, Wolk DA. Multimodality imaging of Alzheimer disease and other neurodegenerative dementias. J Nucl Med. 2014;55(12):2003–11.
27. Taylor AT. Radionuclides in nephrourology, Part 2: pitfalls and diagnostic applications. J Nucl Med. 2014;55(5):786–98.
28. Ziessman HA. Hepatobiliary scintigraphy in 2014. J Nucl Med. 2014;55(6):967–75.
29. Palestro CJ. Radionuclide imaging of musculoskeletal infection: a review. J Nucl Med. 2016;57(9):1406–12.
30. Aboagye EO, Kraeber-Bodere F. Highlights lecture EANM 2016: "Embracing molecular imaging and multi-modal imaging: a smart move for nuclear medicine towards personalized medicine". Eur J Nucl Med Mol Imaging. 2017;44(9):1559–74.
31. Jaffee EM, Dang CV, Agus DB, Alexander BM, Anderson KC, Ashworth A, et al. Future cancer research priorities in the USA: a Lancet Oncology Commission. Lancet Oncol. 2017;18(11):e653–706.
32. Biersack HJ, Hotze A. The clinician and the thyroid. Eur J Nucl Med. 1991;18(9):761–78.
33. Smith TJ, Hegedus L. Graves' disease. N Engl J Med. 2016;375(16):1552–65.
34. Yordanova A, Eppard E, Kurpig S, Bundschuh RA, Schonberger S, Gonzalez-Carmona M, et al. Theranostics in nuclear medicine practice. Onco Targets Ther. 2017;10:4821–8.
35. Divgi C. Targeted systemic radiotherapy of pheochromocytoma and medullary thyroid cancer. Sem Nucl Med. 2011;41(5):369–73.
36. Larson SM, Carrasquillo JA, Cheung NK, Press OW. Radioimmunotherapy of human tumours. Nat Rev Cancer. 2015;15(6):347–60.
37. Pandit-Taskar N, Hamlin PA, Reyes S, Larson SM, Divgi CR. New strategies in radioimmunotherapy for lymphoma. Curr Oncol Rep. 2003;5(5):364–71.
38. Mankoff DA, Pryma DA. The contribution of physics to Nuclear Medicine: physicians' perspective on future directions. EJNMMI Phys. 2014;1(1):5.
39. Bhargava R, Madabhushi A. Emerging themes in image informatics and molecular analysis for digital pathology. Annu Rev Biomed Eng. 2016;18:387–412.
40. Mankoff DA, Farwell MD, Clark AS, Pryma DA. Making molecular imaging a clinical tool for precision oncology: a review. JAMA Oncol. 2017;3(5):695–701.
41. Khandani AH, Wahl RL. Applications of PET in liver imaging. Radiol Clin N Am. 2005;43(5):849–60, vii.

A Short History of Nuclear Medicine

Carolyn J. Anderson, Xiaoxi Ling, David J. Schlyer, and Cathy S. Cutler

The Discovery of Radiation and Radioactivity

Diagnostic *in vivo* imaging was born with the discovery of x-rays in 1895 by Wilhelm Conrad Roentgen, a German physics professor working in Wurzburg (Fig. 1a). On November 8, 1895, he was studying light emissions generated by electrical discharges in an evacuated glass Hittorf-Crookes tube that he was using to investigate cathode rays (*i.e.* electrons) (Fig. 1b). The tubes were covered in black paper and the room was dark, but he noticed that a screen across the room was glowing. Remarkably, when he blocked the beam with his hand, he could see the bones in his hand projected on the screen. Roentgen spent several weeks experimenting with the new rays, and on December 28, 1895, he gave a report entitled "*On the Use of the New Rays*" to a local physics society, during which he presented a 30-min exposure of his wife's hand on a photographic plate (Fig. 1c). By 1896, x-rays were becoming an established tool in medicine, and in 1901, Roentgen won the Nobel Prize in Physics.

Radioactivity was discovered by Antoine Henri Becquerel in Paris in 1896. Upon learning of Roentgen's discovery of x-rays, Becquerel chose to study the "mysterious rays" created when he exposed $K_2UO_2(SO_4)_2 \cdot H_2O$ to sunlight and placed it on photographic plates wrapped in black paper. When developed, the plates showed an image of the uranium crystals, and he initially believed that the sun's energy was absorbed by the uranium, which then emitted x-rays (see Fig. 2). The uranium-covered plates were returned to a drawer, and although Becquerel expected only faint images, they remained strong and clear. He later demonstrated that the radiation emitted by uranium shared certain characteristics with x-rays but—unlike x-rays—could be deflected by a magnetic field and, therefore, must consist of charged particles.

Although Becquerel was awarded the 1903 Nobel Prize in Physics for his discovery of radioactivity, the term itself was coined by Marie Sklodowska Curie. In 1897, she was looking for a topic for her doctoral thesis research. She was fascinated by the work of Becquerel and decided to systematically investigate the uranium "rays" using an electrometer based on the piezoelectric effect that was constructed by her husband Pierre and his brother Jacques. Madame Curie discovered that thorium emitted the same rays as uranium and that the strength of the rays did not depend on the chemical composition, only on the amount of uranium or thorium in the sample. She concluded that the radiation did not depend on the arrangement of the atoms in the molecule but was linked to the interior of the atoms themselves. This was a revolutionary finding that completely changed the field of physics. Madame Curie then obtained natural ore samples containing uranium and thorium from geological museums and found that pitchblende had 4–5 times the amount of radioactivity that was expected based on the amount of uranium. From this finding, she determined that the ore samples contained a new element that was more "active" than uranium. Marie and her husband Pierre (Fig. 3) then extracted the uranium from the ore and found that the residual material was indeed more "active" than the pure uranium. In addition to uranium, the ore contained the radioactive elements polonium (named for Marie's native country, Poland) and radium (from the fact that it radiated very strongly). The unit of radioactivity "Curie (Ci)" is equivalent to 1 g of radium and was named in Madame Curie's honor.

The Curies were awarded the Nobel Prize in Physics in 1903 for their work on radioactivity. Pierre Curie died sud-

C. J. Anderson (✉) · X. Ling
Departments of Medicine, Radiology, Bioengineering, and Pharmacology & Chemical Biology, University of Pittsburgh, Pittsburgh, PA, USA
e-mail: andersoncj@upmc.edu

D. J. Schlyer
Department of Biology, Brookhaven National Laboratory, Upton, NY, USA

C. S. Cutler
Medical Isotope Research & Production (MIRP) Program, Collider Accelerator Department, Brookhaven National Laboratory, Upton, NY, USA

J. S. Lewis et al. (eds.), *Radiopharmaceutical Chemistry*, https://doi.org/10.1007/978-3-319-98947-1_2

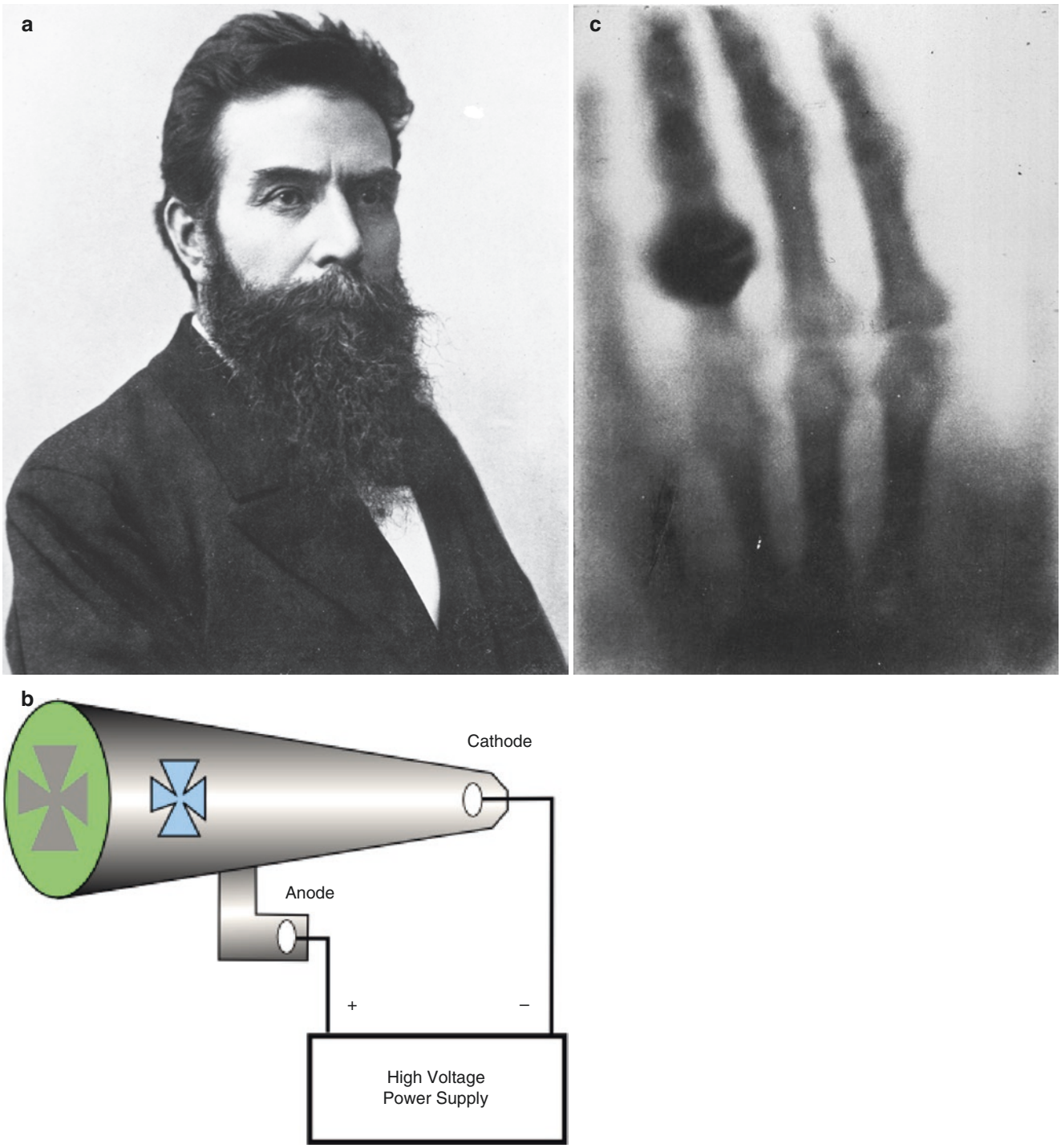

Fig. 1 (**a**) Wilhelm Conrad Roentgen (1845–1923) who discovered x-rays when working with a (**b**) Hittorf-Crookes tube to study cathode rays. (**c**) X-ray taken by Roentgen of his wife's hand and presented to the local physics society on December 28, 1895. (Images courtesy of the National Library of Medicine; Wikimedia, Public domain: by Chetvorno, rebuilt by Drondent, https://commons.wikimedia.org/wiki/File:Crookes_tube2_diagram.svg and the National Library of Medicine, respectively)

denly on April 19, 1906, when he slipped in the rain and fell under a heavy horse-drawn cart. Marie continued their work, even taking over Pierre's teaching position and thus becoming the Sorbonne's first female professor. Madame Curie was later awarded a *second* Nobel Prize in Chemistry in 1911 "in recognition of her services to the advancement of chemistry by the discovery of the elements radium and polonium, by the isolation of radium and the study of the nature and compounds of this remarkable element." She was the first person—male or female—to be awarded two Nobel Prizes.

The Discovery of the Neutron

Ernest Rutherford developed a crude model of the atom in the early twentieth century that included positively charged protons and negatively charged electrons. However, it was known at this time that the atomic mass of an element was approximately twice the atomic number (or number of protons) *and* that the mass was concentrated in the nucleus. The missing piece of the puzzle—the uncharged neutron—was not part of Rutherford's model, and many scientists set out to find the elusive particle. Rutherford went on to be the first to recognize that an element could be transformed into a different element by artificial means [1]. After bombarding nitrogen gas with alpha particles, he noticed that sometimes the alpha particle was stopped and a proton with high kinetic energy was released. This was the first production of oxygen-17 via the $^{14}N(\alpha,p)^{17}O$ nuclear reaction. In 1930, Walther Bothe and Herbert Becker bombarded Be, B, F, and Li with alpha particles emitted from polonium (Po) and showed that these reactions resulted in the emission of highly penetrating radiation. Irène and Frédéric Joliot-Curie—Marie and Pierre's daughter and son-in-law—investigated these reactions and postulated that the radiation produced was high-energy gamma rays. However, when they allowed these "gamma rays" to hit a thin piece of paraffin (rich in hydrogen atoms), very fast hydrogen nuclei were ejected from the paraffin [2]. They stuck by their original conclusion, even though gamma rays have no mass and therefore could not have ejected the hydrogen nuclei from the paraffin. James Chadwick at the Cavendish Laboratory in Cambridge also studied the reactions performed by Bothe and Becker. Chadwick repeated the experiment of bombarding ^{9}Be with alpha particles, and he found that the results were compatible with the energy and momentum conservation of the production of ^{12}C and a neutron [2]. This discovery of the neutron—with no net electric charge and a mass slightly larger than the

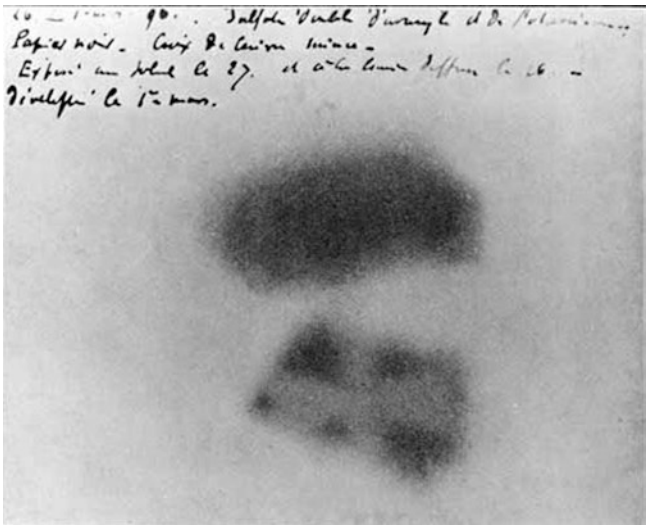

Fig. 2 A photographic plate made by Henri Becquerel illustrating the effects of exposure to radioactivity. A metal maltese cross placed between the plate and the radioactive uranium salt left a clearly visible shadow on the plate. (Wikimedia: This work is in the public domain in its country of origin and other countries and areas, where the copyright term is the author's life plus 100 years or less [70 years in the USA] https://commons.wikimedia.org/wiki/File:Becquerel_plate.jpg)

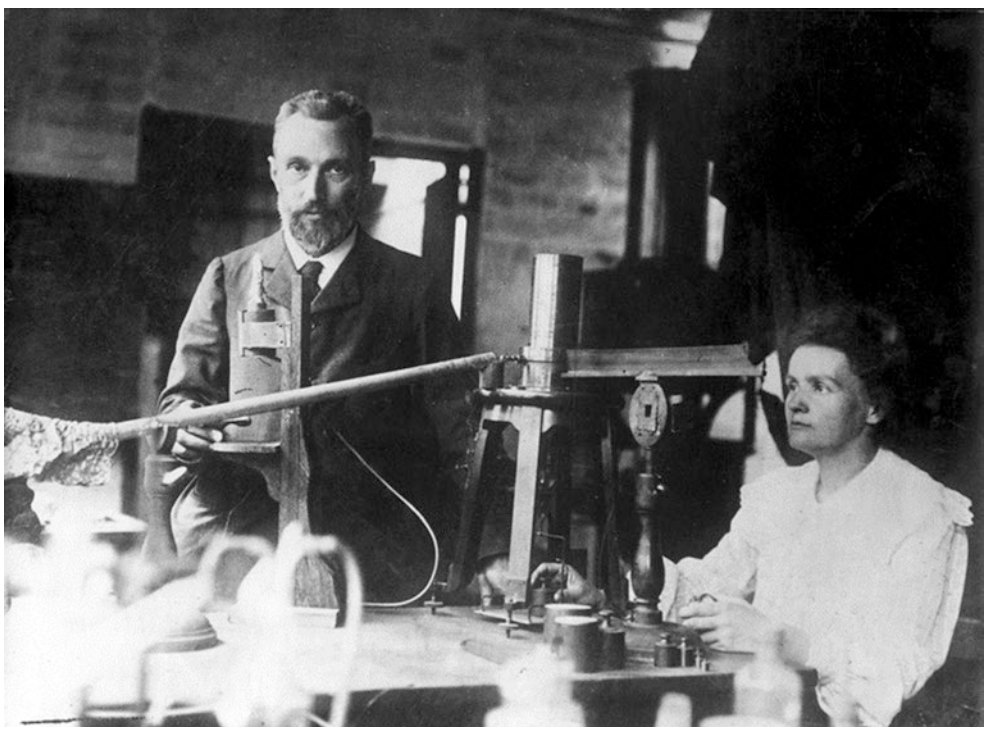

Fig. 3 Pierre and Marie Curie at work in their laboratory at the Sorbonne (Wikimedia: The copyright of this image has expired because it was published more than 70 years ago without a public claim of authorship (anonymous or pseudonymous), and no subsequent claim of authorship was made in the 70 years following its first publication. https://commons.wikimedia.org/wiki/File:Pierre_and_Marie_Curie.jpg)

proton—was central to understanding atomic structure and to the advancement of the field of radionuclide production. Indeed, neutrons are produced by nuclear fission (discovered by Otto Hahn, Fritz Strassmann, and Lise Meitner in 1938) and can be incorporated into the nuclei of elements to produce new, typically beta-emitting radionuclides.

The Discovery of Artificial Radioactivity and the Tracer Principle

In 1934, following in the footsteps of Pierre and Marie Curie, Irène and Frédéric Joliot-Curie created radioactive elements by irradiating stable nuclides with alpha particles. More specifically the Joliot-Curies bombarded a series of elements with alpha particles, including H, He, Li, B, Be, C, N, O, F, Na, Al, Ca, Mg, Ni, and Ag. Of these, only three produced artificial radioactivity. The bombardment of aluminum ($Z = 13$) by alpha particles produced from polonium decay produced radioactive phosphorus ($Z = 15$) plus a neutron.

$$^{27}_{13}Al + {}^{4}_{2}He \rightarrow {}^{30}_{15}P + {}^{1}_{0}n$$

They then observed that this phosphorus decayed to silicon, releasing a positron.

$${}^{30}_{15}P \rightarrow {}^{30}_{14}Si + {}^{0}_{1}p$$

Following a similar reaction with boron, they were able to condense the positron-emitting radionuclide nitrogen-13—which gave off radiation with a ~10-min half-life—into a separate vessel to confirm that they had in fact created a different element artificially (Fig. 4).

Due to some earlier misinterpretations of their experiments—which led to others discovering both the neutron and the positron—there was initially some doubt surrounding the Joliot-Curies' observations. Soon, however, they were able to reproduce and confirm their discovery of the production of artificial radioactivity [3]. As a result, Irène and Frédéric Joliot-Curie won the Nobel Prize in Chemistry in 1935 "in recognition of their synthesis of new radioactive elements" [4], work that laid the foundation for modern day nuclear medicine and radiopharmaceutical chemistry.

At about the same time, Ernest O. Lawrence developed the first cyclotron at the University of California at Berkeley. Interestingly, Lawrence was also producing artificial radioactivity with the cyclotron, but he failed to notice these residual emissions because the same switch that operated the cyclotron also operated the Geiger counter in the lab. This work of Lawrence's team—along with the work of the Joliot-Curies in the early 1930s—led to the discovery of iodine-131 (Glenn Seaborg and John Livingood) and technetium-99m (Emilio Segre and Glenn Seaborg) in 1938 at Berkeley and set the stage for the use of cyclotrons for the production of radionuclides for positron emission tomography (PET) and single-photon emission computed tomography (SPECT). In recognition of his work, Ernest Lawrence received the Nobel Prize in Physics in 1939 "for the invention and development of the cyclotron and for results obtained with it, especially with regard to artificial radioactive elements" [5].

George de Hevesy (Fig. 5)—who has been called the "father of nuclear medicine"—first described the radiotracer principle that underpins the use of radionuclides to investigate the behavior of stable atoms and molecules [6]. Simply

Fig. 4 Irène and Frédéric Joliot-Curie in their laboratory in 1935 (Agence de presse Meurisse. Bibliotheque national de France. Wikimedia: This work is in the public domain in its country of origin and other countries and areas where the copyright term is the author's life plus 70 years or less. https://commons.wikimedia.org/wiki/File:Ir%C3%A8ne_et_Fr%C3%A9d%C3%A9ric_Joliot-Curie_1935.jpg)

put, the tracer principle states that radiopharmaceuticals can participate in biological processes but do not alter or perturb them. In this way, radiopharmaceuticals facilitate the imaging of normal and disease processes without interfering with them. This phenomenon, of course, is predicated on the fact that minute molar amounts of radiopharmaceuticals can be detected with relative ease. The first radiotracer experiment in animals used bismuth-210 to follow the circulation of Bi-containing antisyphilitic drugs in rabbits. De Hevesy received the 1943 Nobel Prize for this discovery [7]. De Hevesy's other seminal contributions to radiochemistry include his study of reactions with neutrons. More specifically, he exposed dysprosium to a neutron stream, upon which the element became exceedingly active; this was the first demonstration of neutron activation analysis. Based on these initial experiments, he determined the relative neutron flux of various irradiation positions and activated other samples, including rhodium foils and europium samples. Neutron activation analysis is the most powerful nondestructive analytic technique for elemental analysis of solid samples.

Fig. 5 George de Hevesy received the Nobel Prize (Chemistry) for elucidating the tracer principle. (Wikimedia: This image is in the public domain because its copyright has expired and its author is anonymous. This applies those countries with a copyright term of 70 years after the work was made available to the public and the author never disclosed their identity. https://commons.wikimedia.org/wiki/File:George_de_Hevesy.jpg)

The Discovery and Use of the Radionuclides of Iodine

The effects of iodine on the thyroid were first studied only a few years after the discovery of the element in seaweed in 1811. Remarkably, iodine was first used to treat a goiter only 8 years later [8]. The Massachusetts General Hospital (MGH) Thyroid Clinic—established by J. Howard Means in 1920—began using stable iodine to treat hyperthyroid patients. In 1936, Saul Hertz, a member (and later director) of the MGH Thyroid Clinic, asked a colloquium at Harvard Medical School whether iodine could be made radioactive. Karl Compton, then president of MGH, said he would look into it [9]. The outcome was a cooperative program between MGH and the Massachusetts Institute of Technology focused on producing iodine-128 ($t_{1/2}$ = 25 min) using a neutron source and studying its uptake in rabbits [10]. A group at Berkeley led by Joe Hamilton and Mayo Soley was doing similar studies in rabbits, and Hamilton asked Glenn Seaborg in 1936 if a longer-lived isotope of iodine could be produced. Seaborg and John Livingood quickly responded by using deuterons from the Berkeley cyclotron to bombard tellurium-128 and create iodine-130 ($t_{1/2}$ = 12 h) and iodine-131 ($t_{1/2}$ = 8 days), work they published in 1938 [11] (Fig. 6). Subsequent studies with iodine-131 allowed the *in vivo* tracking of the radionuclide over long time periods [12].

Although initial studies with the radionuclides of iodine focused on treating hyperthyroid disease, a few different groups in New York were investigating treating thyroid cancer with iodine-130 starting in the early 1940s. They found that the ablation of the thyroid—which reduced the thyroid's competition for the uptake of the iodine—was necessary for the treatment of metastases [13, 14]. These seminal studies changed thyroid cancer from a death sentence to a disease with an overall survival rate of about 85% [15].

Early Studies with Radionuclides of Carbon

In the late 1930s, Ernest Lawrence's laboratory at Berkeley was producing carbon-11 (C-11; $t_{1/2}$ = 20 min) on a more or less routine basis by bombarding boron oxide with deuterons. Martin Kamen, Sam Ruben, and I.L. Chaikoff used carbon-11 to study the metabolism of carbohydrates. In these studies, ^{11}C-labeled glucose was prepared by feeding [^{11}C]CO_2 to plants, which produce radioactive glucose via photosynthesis that then could be used for the investigation of metabolism in lab rats. The photosynthesis-based method of producing ^{11}C-labeled glucose was later applied in the 1970s by both the Welch lab [16] and Raichle and colleagues [17].

Fig. 6 Glenn Seaborg (*left*) and John Livingood (*right*) with their manuscript on the production of iodine-131 (©2010 The Regents of the University of California, through the Lawrence Berkeley National Laboratory, used with permission)

Of course, carbon-11's 20-min half-life meant that the investigators at Berkeley were somewhat limited in what they could investigate. As a result, Kamen and Ruben (Fig. 7) then enthusiastically pursued the production of carbon-14. Based on calculations they knew it could be made, but they had no idea what its half-life would be, though they expected it to be longer-lived [18]. In February 1940, Kamen prepared a graphite target and bombarded it with 5700 μAmp hr of 7–8 MeV deuterons on the 60-inch cyclotron at Berkeley. Ruben analyzed the irradiated target by precipitating $CaCO_3$ and found persistent activity that could be ascribed to carbon-14 [19]. In a confirmatory experiment, they showed that bombarding of ammonium nitrate with slow neutrons produced gaseous carbon-14, which was also precipitated as $[^{14}C]CaCO_3$ [19]. Kamen and Ruben calculated a tentative half-life of 4000 years for carbon-14, a value which was fairly close to the true half-life of 5700 years that was determined many years later [20]. Ultimately, the discovery of carbon-14 is considered a seminal moment in radiochemistry due to the importance of carbon in the life sciences.

It is worth noting that Samuel Ruben—the co-discoverer of carbon-14—died tragically in 1943 from a work-related accident. In addition to being a brilliant scientist, Martin Kamen was an accomplished viola player and was close friends with many Bay Area musicians, including the famous violinist Isaac Stern. In part because of Kamen's "social life," he was held in high suspicion by the FBI and army security that surrounded the Manhattan Project. In 1945, Kamen was forced to leave Berkeley after being accused of leaking nuclear weapon secrets to Russia. After being unemployed for part of that year, Arthur Holly Compton hired him to run the cyclotron facility at Washington University in St. Louis. It took more than 10 years, but Kamen was able to clear his name, and he wrote about his fascinating scientific and accidental political life in the 1985 book, "*Radiant Science, Dark Politics: A Memoir of the Nuclear Age*" [18].

Post-World War II Nuclear Medicine

The development of the atomic bomb and its use in destroying Hiroshima and Nagasaki at the end of World War II resulted in the founding of the Atomic Energy Commission (AEC) in 1946 to promote peaceful uses of nuclear chemistry and radiochemistry. Part of the mission of the AEC was to advance the use of radionuclides for nuclear medicine imaging and therapy. In 1946, it was announced that fission-produced radionuclides, including iodine-131, were immediately available from the Manhattan Project at Oak Ridge, TN [21]. Funding from the AEC fueled several seminal discoveries related to nuclear medicine and molecular imaging, including the development of gamma scintigraphy, SPECT cameras, PET scanners, and the $^{99}Mo/^{99m}Tc$ generator, just to name a few.

The $^{99}Mo/^{99m}Tc$ Generator and ^{99m}Tc-Labeled Radiopharmaceuticals

The element technetium was discovered in Palermo, Italy, by Segre and Perrier in 1937 [22]. Segre was working at the University of California and noted that an interior deflector lip made of molybdenum had been bombarded with deuterons and may have contained the unknown element 43. He brought parts of the deflector back to Italy and worked with Perrier to develop a chemical separation strategy to isolate

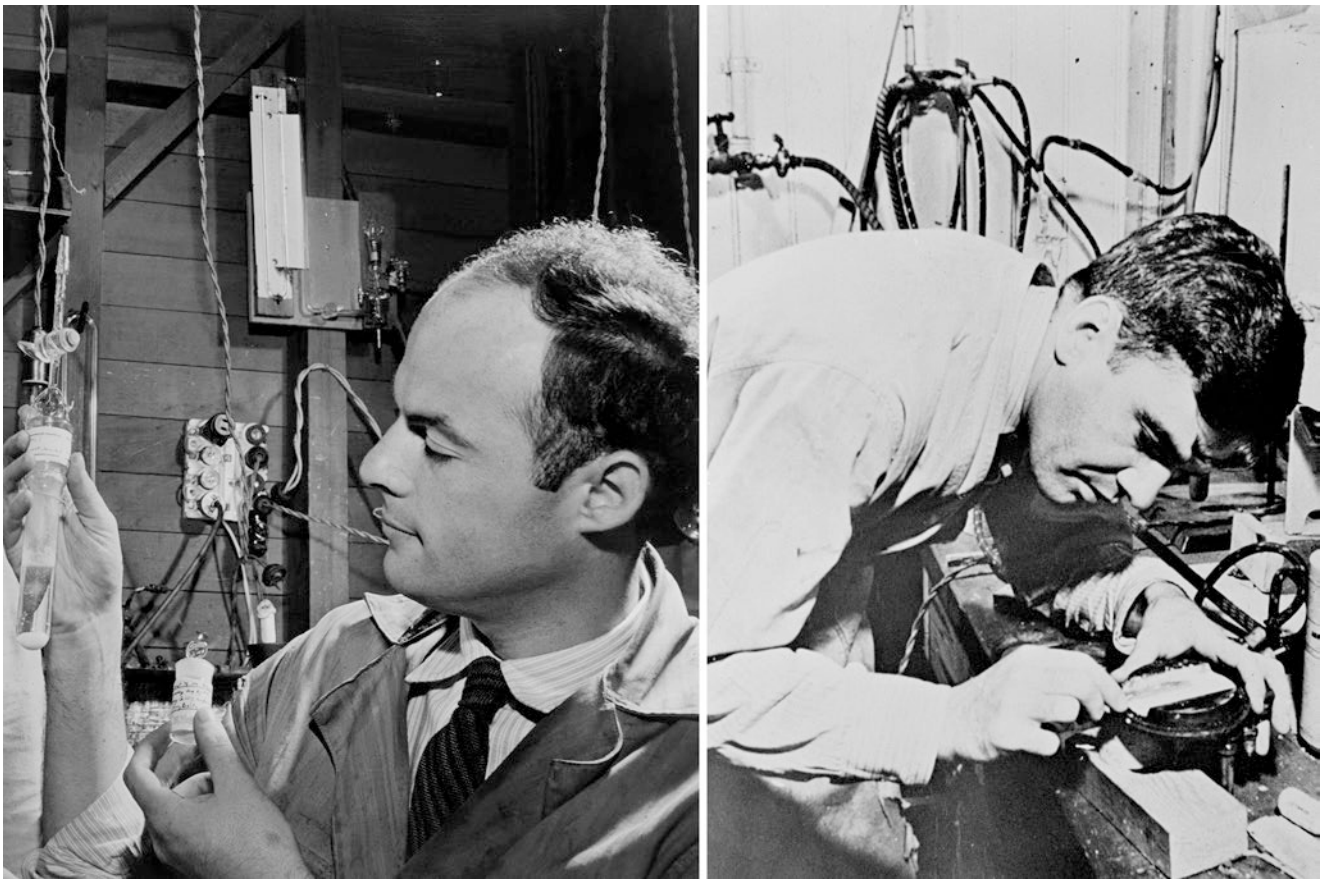

Fig. 7 Samuel Ruben (*left*) and Martin Kamen (*right*) discovered carbon-14 (©2010 The Regents of the University of California, through the Lawrence Berkeley National Laboratory, used with permission)

the element and evaluate its chemistry. Although their studies were successful, it took an additional 11 years for the element to be named. Segre returned to Berkeley to work with Seaborg to study shorter-lived radionuclides of the element, which led to the discovery of technetium-99m ($t_{1/2}$ ~ 6 h) [23]. However, nuclear isomeric states were not well understood at the time, which held up publication of the work. Its discovery was later corroborated when it was isolated from fission products, though it would take another 20 years before the medical potential of technetium-99m was realized.

The nuclear properties of technetium-99m—including its intermediate half-life, 140 keV photons, and lack of particle emissions—as well as its rich chemistry make it ideal for imaging *in vivo* function on the molecular level. As a result, the use of technetium-99m was strongly promoted by Powell Richards (Fig. 8) in the 1950s and 1960s [24, 25]. Remarkably, a patent for the medical use of technetium-99m was submitted but was rejected, as it was felt that the use of the radionuclide would never expand beyond research applications. However, during the 1960s, Beck pointed out that the optimum detection energy for sodium iodide crystals was 150 keV [26]. Paul Harper from the University of Chicago then became interested in technetium-99m and arranged to have generators shipped form Brookhaven to Chicago; he went on to demonstrate the effectiveness of technetium-99m for imaging the liver, brain, and thyroid [27]. As an aside, it is worth noting that the first generator system developed was not for the production of technetium-99m but rather iodine-132 (from tellurium-132) [28]. This tellurium-132 was derived from fission products, and fortuitously, a radioactive impurity was noted [28, 29]. It was then demonstrated that this impurity—molybdenum-99—was following the tellurium-132 through the separation process, a discovery which led to the eventual development of the Mo-99/Tc-99m generator [24, 30]. The generator has been vastly improved over the years, ultimately yielding the currently used version that is eluted with saline and produced from molybdenum-99 that is derived mostly from fission products.

Fig. 8 *Left*: Walter Tucker (*left*) and Powell Richards (*right) Right*: the first Mo-99/Tc-99m generator created in 1958 by Walter Tucker and Margaret Greene. (Courtesy of Brookhaven National Laboratory)

Development of Imaging Instrumentation

In addition to the creation of radionuclides, the development of imaging instrumentation was essential for the expansion of nuclear medicine. Initially, detection was performed using Geiger-Mueller counters that were moved manually over the target of interest to measure the uptake of the radionuclide. One of the initial evaluations was to measure the rate of iodine uptake in the thyroid gland to assess if the nodule was benign or malignant. This proved difficult, as the counters were insensitive to the high gamma emissions from iodine-131. In 1960, Benedict Cassen (Fig. 9) started evaluating metallic crystals as scintillators that could enhance sensitivity by switching out the detectors in GM counters with calcium tungstate to facilitate the enhanced detection of iodine, a development which led to the development of the scintillation counter. Later he switched to thallium-doped sodium iodide crystals, added photomultiplier tubes (resulting in increased sensitivity), and automated the system to scan over the thyroid to produce an image. The scintillation detector was quickly expanded to take nuclear images of other organs as well.

The next advance came with the development of the rectilinear scanner, which automated the positioning of the scanner and became the standard instrument used for nuclear imaging from the 1950s to the early 1970s. A major limitation of this technology was the amount of time it took to image large organs. In this regard, a breakthrough came with Hal Anger's invention of a gamma camera that incorporated

Fig. 9 Hal Anger and Benedict Cassen made key discoveries in nuclear medicine instrumentation. Left: Anger exhibiting the scintillation camera at the annual meeting of the Society of Nuclear Medicine. Right: Cassen, inventor of the rectilinear scanner in the early 1950s (From Wagner [32], with permission)

collimation to view the entire organ of interest at one time and added an array of photomultiplier tubes to improve detection efficiency (see Fig. 9) [31, 32].

In 1953, a multidetector instrument for the localization of brain tumors with positron-emitting radionuclides was developed by Brownell and Sweet [33–35]. The device worked by moving the patient with respect to the detectors and having a pen make a mark on a sheet of paper whenever there was a coincident event (Fig. 10).

In 1966, at Brookhaven National Laboratory, Yamamoto *et al.* developed the first circular array of detectors for

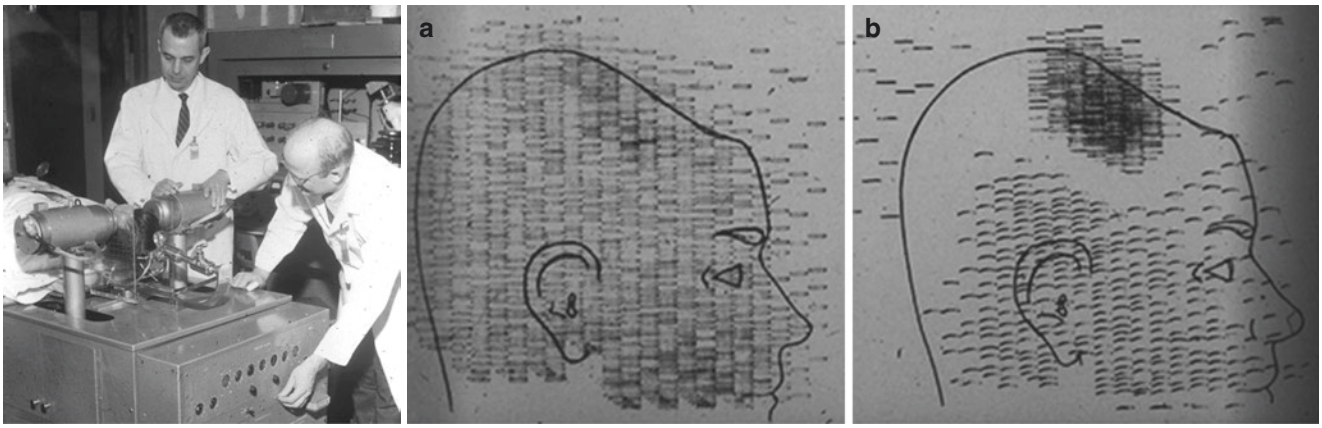

Fig. 10 *Left*: multidetector instrument for the localization of brain tumors with positron-emitting radionuclides developed by Brownell and Sweet. *Right*: images from this scanner showing the presence of a brain tumor (*image b*) (Images courtesy of Anna-Liisa Brownell)

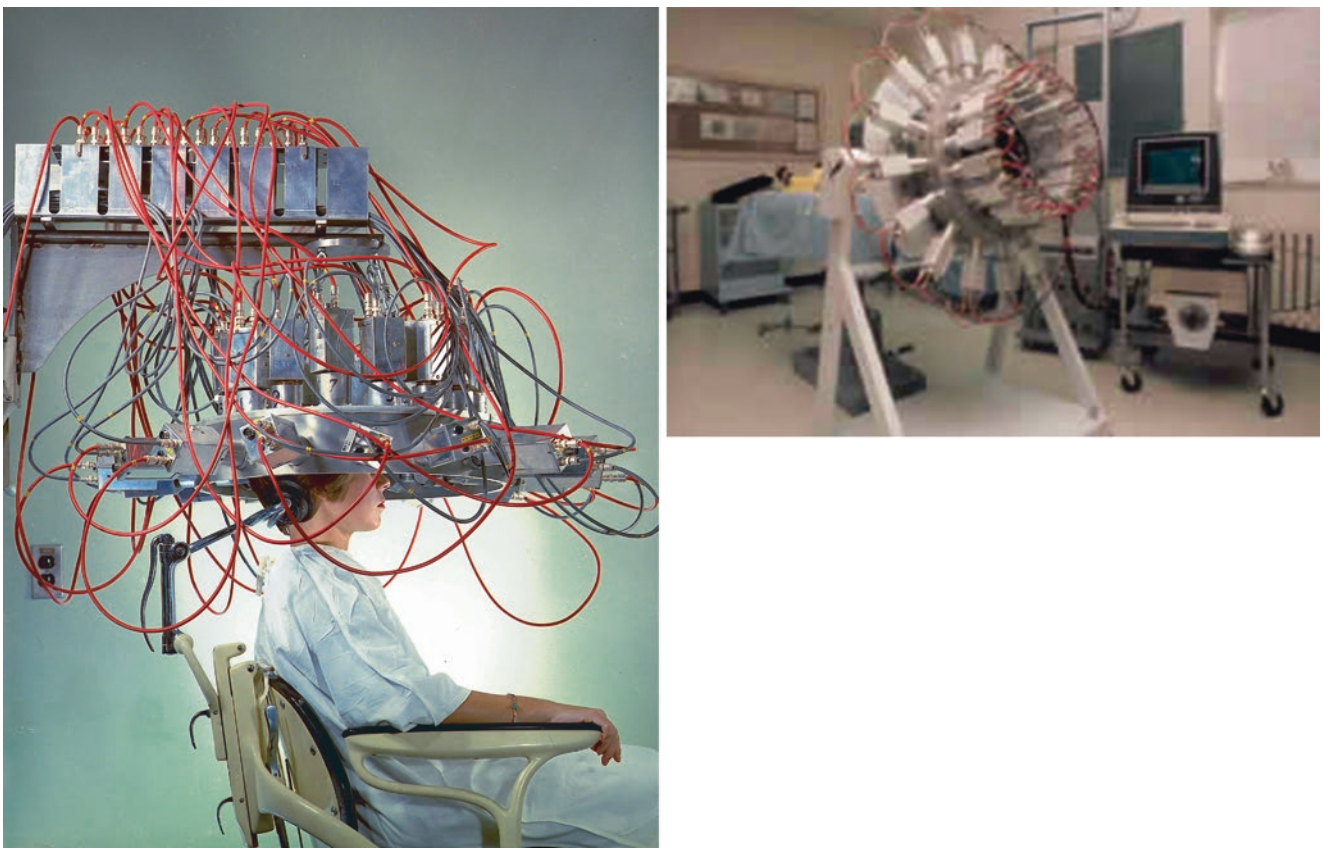

Fig. 11 *Left*: circular array of detectors used for brain imaging. *Right*: original "Positome" configuration ("positome" was the original name given to this brain PET scanner). (Courtesy of Brookhaven National Laboratory)

imaging the brain, nicknamed the "head shrinker" or "hair dryer" due to its shape (Fig. 11).

In the 1960s, David Kuhl and Roy Edwards developed a nuclear medicine tomographic imaging device and introduced the concept of longitudinal and transaxial tomography [36]. This machine was the predecessor of modern SPECT systems and demonstrated the usefulness of tomographic imaging in nuclear medicine. Godfrey Hounsfield went on to develop transverse axial tomography for radiography, which aided in the development of positron emission tomography (PET) [37, 38]. A PET instrument that employed filtered back projection was developed by Ter-Pogossian, Phelps, and Hoffman in 1975 [39, 40]. A picture of this scanner—with Henry Wagner as the research subject—is shown in Fig. 12.

Initially, tomographic reconstruction with a gamma camera was achieved by rotating the patient in front of a station-

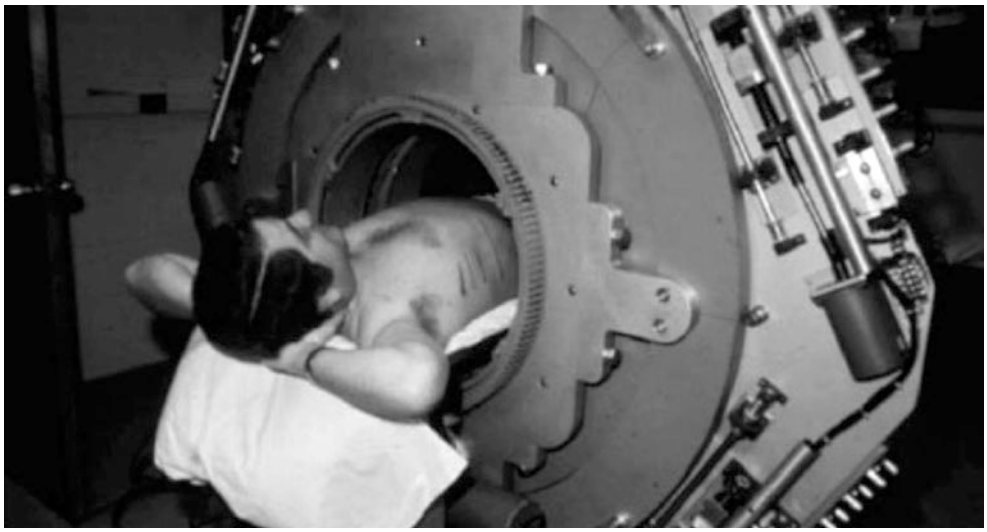

Fig. 12 Henry Wagner inside one of the early PET scanners at Washington University (Courtesy of Mallinckrodt Institute of Radiology, Washington University School of Medicine, St. Louis, Missouri)

ary camera. It wasn't until 1977 that Keyes *et al.* at the University of Michigan created the first camera that rotated around the patient [41]. This was followed up by the introduction of the cantilever system by Larsson in the 1980s [42].

The Production of Radionuclides

After the development of the cyclotron at Berkeley and the discovery of the artificial production of isotopes by Irene Curie and Frederic Joliet, the production and use of carbon-11 ($t_{1/2}$ ~ 20 min), nitrogen-13 ($t_{1/2}$ ~ 10 min), and fluorine-18 ($t_{1/2}$ ~ 120 min) in biological radiotracers began. George de Hevesy used radionuclides of lead to study transport in plants and later employed radionuclides of bismuth to study antisyphilitic drugs in humans. Lawrence's brother John, a physician, used sodium-24 as a tracer for the absorption of electrolytes, in a series of experiments designed to get funding for the further development of the cyclotron (Fig. 13).

In the 1930s, Kamen studied the uptake of carbon dioxide labeled with carbon-11 in plants [43]. Furthermore, lactic acid labeled with carbon-11 in the 1, 2, and 3 positions was used by Cramer and Kistiakowsky to study metabolic pathways [44]. Carbon-11 was first used in humans by Tobias *et al.* to study the behavior ^{11}C-labeled carbon monoxide in man [45]. The first study with nitrogen-13 was performed by Rueben *et al.* and focused on interrogating nitrogen fixation by nonlegume plants. In the early 1940s, Volker *et al.* used fluorine-18 to study the absorption of fluoride by tooth enamel and bones. However, despite these early advances, interest in these short-lived radionuclides dwindled in the 1940s and 1950s [46].

Enrico Fermi was the first to produce isotopes with neutrons in 1934. To this end, he set up his own neutron source by filling a glass tube with beryllium and 800 mCi of radon. Next, he obtained a number of elements—including chromium, silver, and iodine—and fabricated them into cylinders, which he placed around the neutron source. After some time, the neutron source was removed from the cylinders, and the radioactivity produced by the neutron bombardment was

Fig. 13 John Lawrence used sodium-24 as a tracer to track the absorption of electrolytes. (Wikimedia. This image is a work of a US Department of Energy (or predecessor organization) employee, taken or made as part of that person's official duties. As a work of the US federal government, the image is in the public domain. https://commons.wikimedia.org/wiki/File:Joseph-Hamilton-drinking-radiosodium.jpg)

measured by inserting a Geiger-Muller counter into the cylinders. Fermi demonstrated that the radionuclides derived from neutron irradiation decayed by beta emission and not positron emission. Later, he bombarded uranium with neutrons and predicted it would produce a heavier element. A German chemist, Ida Noddack, analyzed Fermi's neutron-irradiated uranium samples and demonstrated the presence of *lighter*—rather than *heavier*—elements. This was confirmed by Otto Hahn and Lise Meitner, and the theory of fission was developed. Upon reviewing Fermi's work, de Hevesy went on to irradiate sulfur with neutrons, producing phosphorus-32 to evaluate its metabolism in rats. Robley Evans, a physicist at MIT, used neutrons to produce iodine-128 to evaluate thyroid metabolism. Fermi first described moderators that could be used to regulate the chain reaction and were used to develop the nuclear reactor at the University of Chicago. This quickly led to the development of reactors at national lab facilities that were used to produce radionuclides. After the end of World War II and the secrecy surrounding their existence, many radionuclides became available from Oak Ridge, including iodine-131, gold-198, and phosphorus-32. Likely due to their longer half-lives, these radionuclides garnered more interest than those produced using cyclotrons. For example, reactor-produced carbon-14 ($t_{1/2}$ = 5,730 years), tritium ($t_{1/2}$ = 12.3 years), and phosphorous-32 ($t_{1/2}$ = 14.3 days) were used to evaluate biochemical pathways. The longer half-lives of these radionuclides also allowed them to be shipped remotely and incorporated into natural biomolecules. As we have noted above, the shorter-lived radionuclides produced by accelerators—such as carbon-11 ($t_{1/2}$ ~ 20 min)—did not have obvious immediate applications, and thus interest fell off until much later.

The production of many radionuclides was made possible in part because instrumentation that was originally designed for physics experiments was repurposed for the production of new radionuclides. For example, in the 1950s, Powers and Ter-Pogossian used the cyclotron in the physics department at Washington University to produce oxygen-15 ($t_{1/2}$ = 2.0 min) to evaluate oxygen tension in malignant neoplasms, a development which led to growth in the use of radioactive gases to evaluate repertory and cerebral metabolic studies [47, 48]. These experiments also fueled interest in other short-lived positron-emitting radionuclides and spurred the installation of cyclotrons at various academic medical centers around the world, including Hammersmith Hospital, Washington University Medical Center, the University of California Los Angeles, the University of Chicago, and Memorial Sloan Kettering Cancer Center.

The Discovery and Applications of FDG

2-Deoxy-2-[^{18}F]fluoro-D-glucose—often abbreviated [^{18}F]FDG or simply FDG—is a radiolabeled form of glucose in which a fluorine-18 atom takes the place of a hydroxyl group. FDG was developed with the specific purpose of measuring glucose metabolism in the human brain. The fact that the removal of the hydroxyl group in the 2-position prevents the hexokinase reaction was noted in 1954 by Sols and Crane (Fig. 14), who remarked "2-deoxy-glucose possesses certain advantages over glucose as a substrate for experimental studies with crude preparations of brain and other tissue hexokinases. The phosphate ester formed from 2-deoxyglucose is not inhibitory, and it is not a substrate for either phosphohexose isomerase or glucose-6-phosphate dehydrogenase. Thus, the use of 2-deoxyglucose isolates the hexokinase reaction [49]." Louis Sokoloff and Martin Reivich (Fig. 15) took this information and developed a method for using ^{14}C-labeled

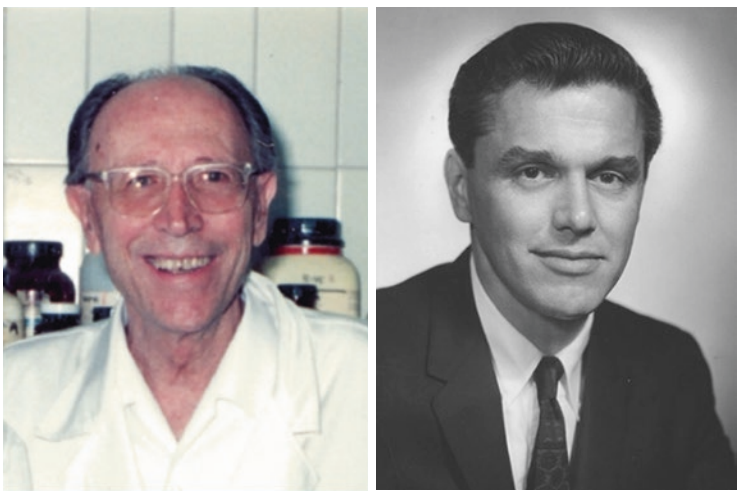

Alberto Sols Robert Crane

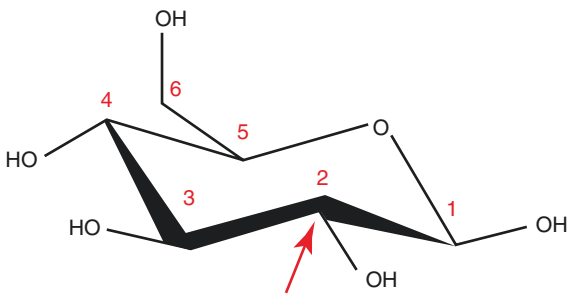

Fig. 14 *Left*: Alberto Sols and Robert Crane, who showed that removing the hydroxyl in the 2-position prevents the hexokinase reaction. *Right*: structure of glucose, with all carbons numbered; the red arrow points to the carbon labeled with carbon-14 by Sokoloff and Reivich (Courtesy of Brookhaven National Laboratory)

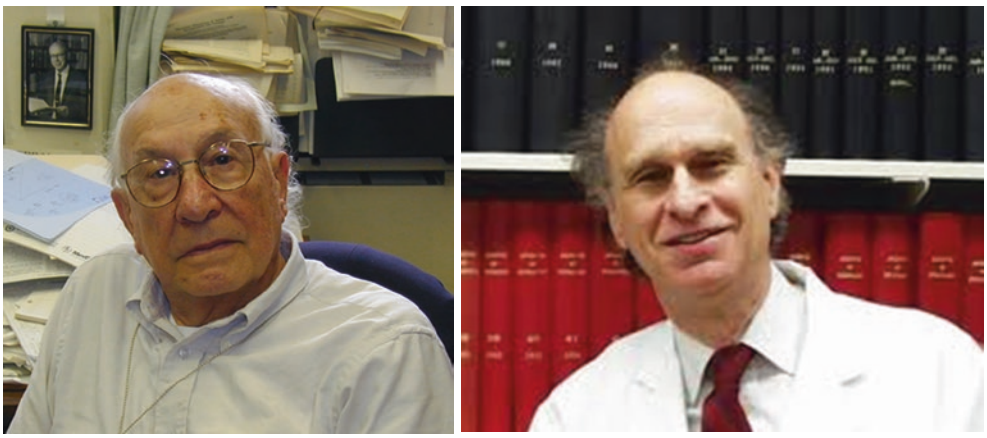

Fig. 15 Louis Sokoloff (left) and Martin Reivich (right), who developed a method to produce C-14 labeled 2-deoxyglucose and measure its metabolism in rodents (Courtesy of Brookhaven National Laboratory)

deoxyglucose to measure metabolism in animals. Their work was published in *Science* in 1975 and proved to be a very valuable tool for the study of glucose metabolism [50].

Since ^{14}C-labeled glucose could not be used in humans because of the radionuclide's long half-life and the inability to image the distribution of the radioactivity, a search for an alternative tracer ensued. The idea to use a positron-emitting radionuclide was developed by scientists at the University of Pennsylvania, who took the problem to Alfred Wolf at Brookhaven National Laboratory, where it was discussed in a 1973 meeting entitled "*Discussion of Programs of Mutual Interest with Emphasis on Labeled Carbohydrates for Brain Function Studies.*" Eventually, Al Wolf—together with David Christman and a young scientist, Joanna Fowler—came up with the idea for an ^{18}F-labeled variant of glucose. Fluorine-18 was a good choice for several reasons: (1) it is a pure positron emitter (no gammas) with a low positron endpoint energy; (2) it has a 110 minute half-life; (3) it decays to a stable product (^{18}O); and, perhaps most importantly, (4) it is chemically reactive. Al Wolf and Joanna Fowler got together with two postdoctoral fellows, Tatsuo Ido and Chung Nan Wan, to work on the problem. Richard Lambrecht and Ron Finn had developed a target to produce fluorine-18 via the ^{20}Ne(p,α)^{18}F reaction using neon gas spiked with a small amount of F_2 gas in a nickel tube. The three chemists came up with a radiosynthesis using [^{18}F]F_2 and tri-*O*-acetoxy-D-glucal (Fig. 16). The synthesis took 2 h to complete and produced FDG with an 8% yield. A page from Tatsuo Ido's notebook—shown in Fig. 16—documents the successful synthesis of [^{18}F]FDG on July 14, 1975. With ^{18}FDG, it was possible for the first time to translate the [^{14}C]2-deoxyglucose autoradiographic method developed by Louis Sokoloff to the clinic.

At the time, the closest PET scanner was in Philadelphia, so it was necessary to fly the [^{18}F]FDG from BNL to Philadelphia so that it could be imaged in a human. Not surprisingly, the logistics of this were challenging. The [^{18}F]FDG was made at Brookhaven, packaged by the health physics group, driven to the nearby local airport, put on a small four-person plane, flown to Philadelphia airport where it was met by an ambulance from the hospital, and driven to the University of Pennsylvania where it could be injected (Fig. 17) [51]. The group at the University of Pennsylvania included a number of people who were (or would become) leaders in the field, including Michael Phelps, David Kuhl, Abass Alavi, and Ed Hoffman (Fig. 18).

After this initial delivery, the clinical use of [^{18}F]FDG began to grow substantially. While [^{18}F]FDG was initially developed for brain imaging, several other preclinical studies in the late 1970s and early 1980s suggested that the radiotracer could also be useful for the imaging of myocardial metabolism and tumor metabolism [52]. A major milestone was achieved in 1986, when Kurt Hamacher developed a synthesis for FDG using [^{18}F]fluoride (Fig. 19) [53]. His synthesis was advantageous because it gave a 50% yield in 50 min, required no added fluorine-19, and was amenable to automation. This synthesis has gradually been improved over the years: today, [^{18}F]FDG is produced in high yield in less than 30 min.

As the number of applications of [^{18}F]FDG expanded and its use in cancer diagnosis became more widely recognized, the number of publications using [^{18}F]FDG grew rapidly (Fig. 20). This rapid growth led to the reimbursement of [^{18}F]FDG PET by insurance companies. These developments were key in the success of [^{18}F]FDG, and the drive for reimbursement was led by Mike Phelps and Ed Hoffman, with the Institute for Clinical PET. Ultimately, reimbursement allowed [^{18}F]FDG PET to become a routine clinical tool and increased the number of doses given in a year from a few thousand to two million in 2017.

The groundbreaking discovery of [^{18}F]FDG opened doors to the exploration of a wide range of diseases and conditions, including drug addiction, eating disorders, attention deficit hyperactivity disorder (ADHD), Alzheimer's disease, epi-

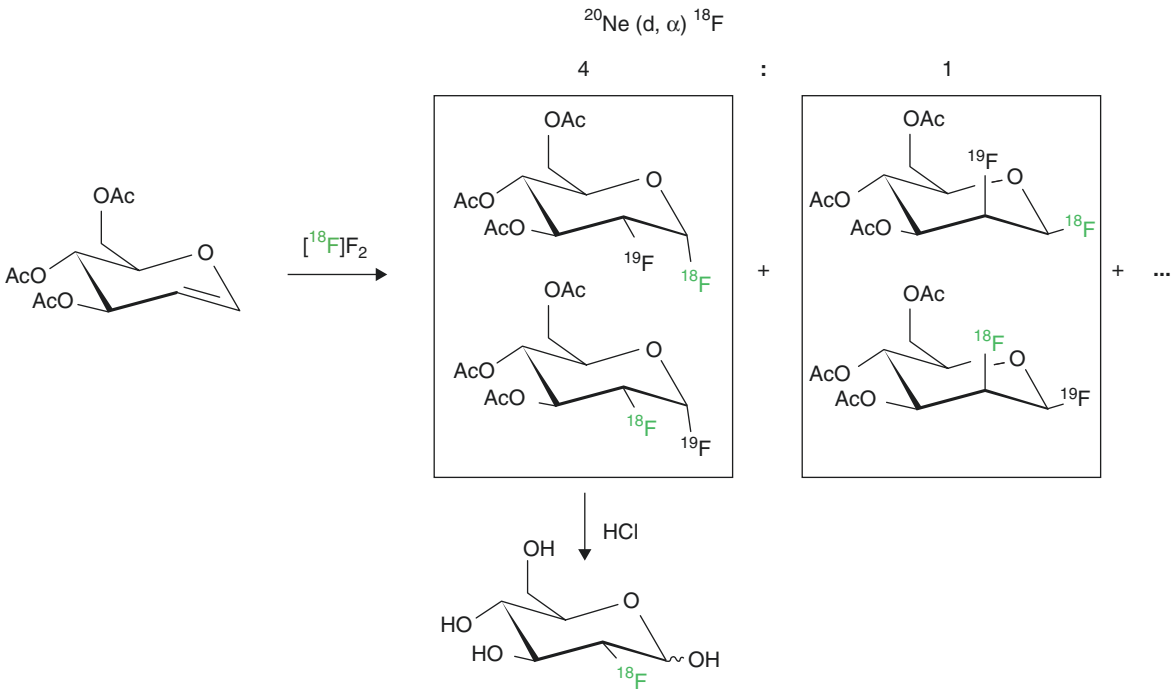

2-deoxy-2-[^{18}F]fluoro-D-glucose

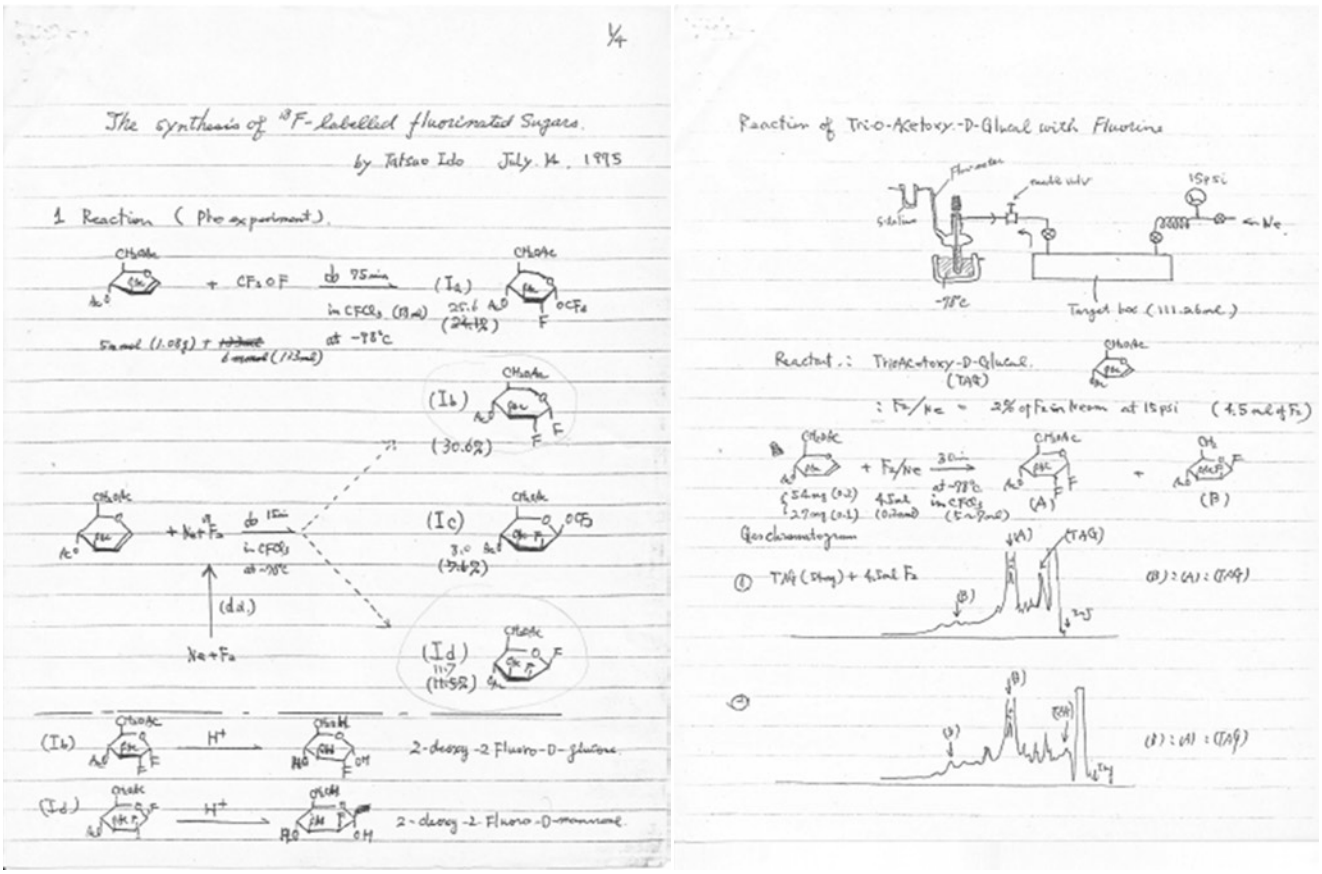

Fig. 16 *Top*: reaction scheme showing the synthesis of FDG from the reaction between [^{18}F]F_2 and tri-*O*-acetoxy-D-glucal. *Bottom*: lab notebook page describing the synthesis of [^{18}F]FDG by Tatsuo Ido (Courtesy of Brookhaven National Laboratory)

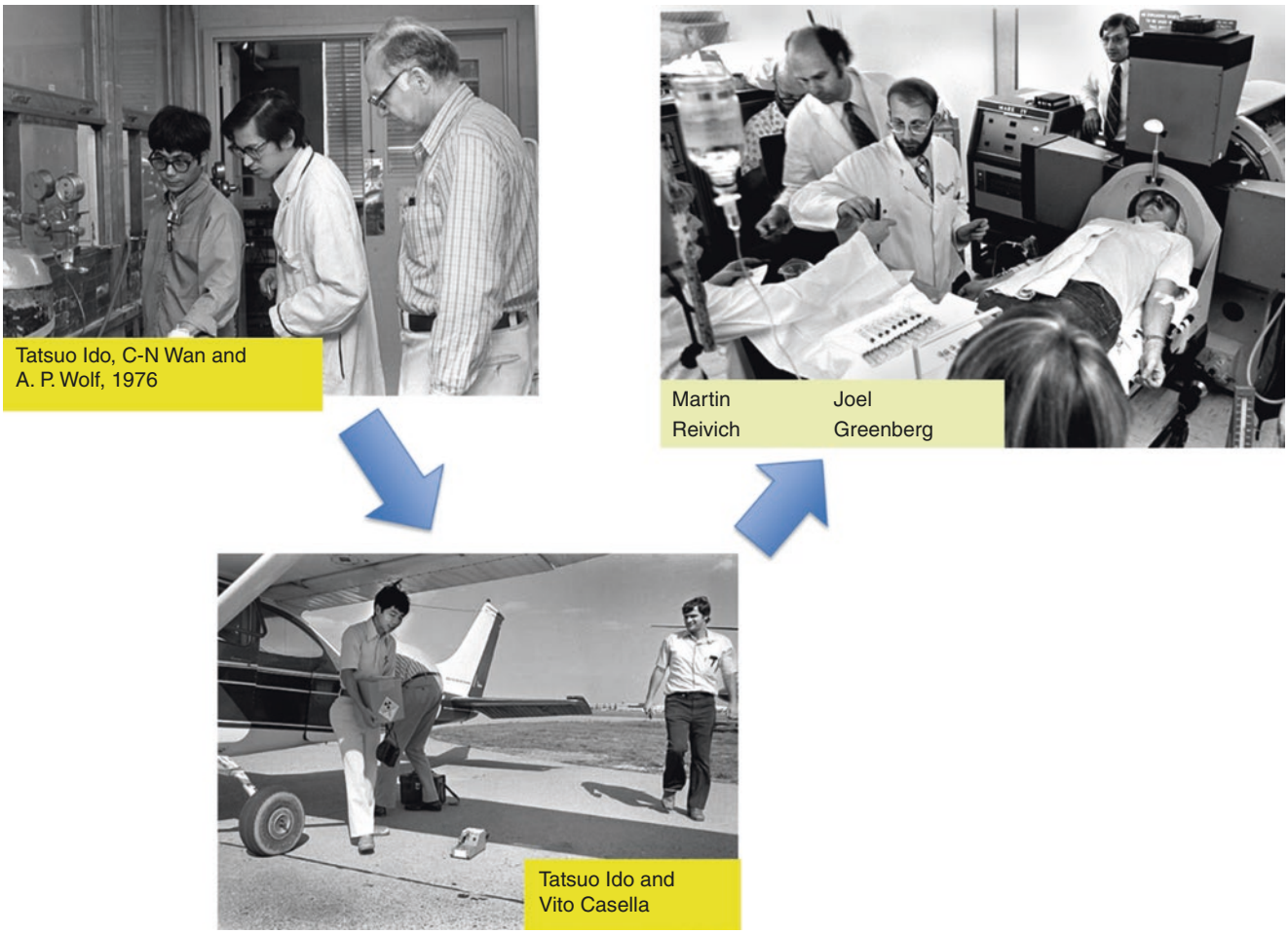

Fig. 17 *Top left*: Tatsuo Ido, Chung Nan Wan, and Alfred Wolf producing [^{18}F]FDG at BNL. *Top right*: Martin Reivich and Joel Greenberg participating in human imaging using [^{18}F]FDG at the University of Pennsylvania. *Bottom*: Tatsuo Ido and Vito Casella transporting the [^{18}F]FDG by plane (Courtesy of Brookhaven National Laboratory)

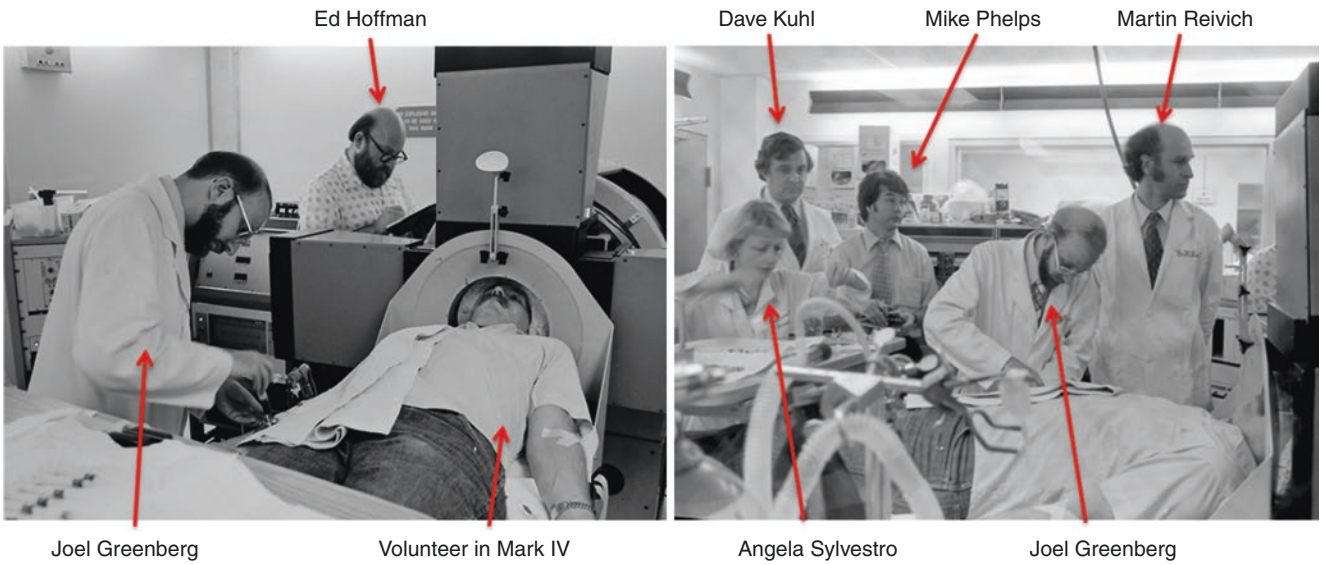

Fig. 18 *Left*: Ed Hoffman and Joel Greenberg using [^{18}F]FDG imaging with a volunteer in the Mark IV. *Right*: the team at the University of Pennsylvania: Dave Kuhl, Mike Phelps, Martin Reivich, Angela Sylvestro, and Joel Greenberg (Courtesy of Brookhaven National Laboratory)


Kurt Hamacher

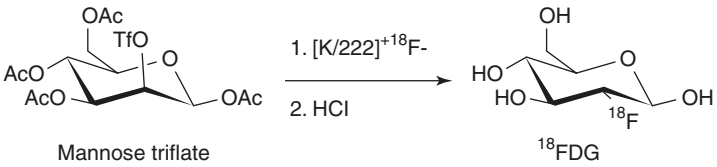

Fig. 19 *Left*: Kurt Hamacher. *Right*: scheme showing the improved synthesis of [^{18}F]FDG using [^{18}F]fluoride (Courtesy of Brookhaven National Laboratory)

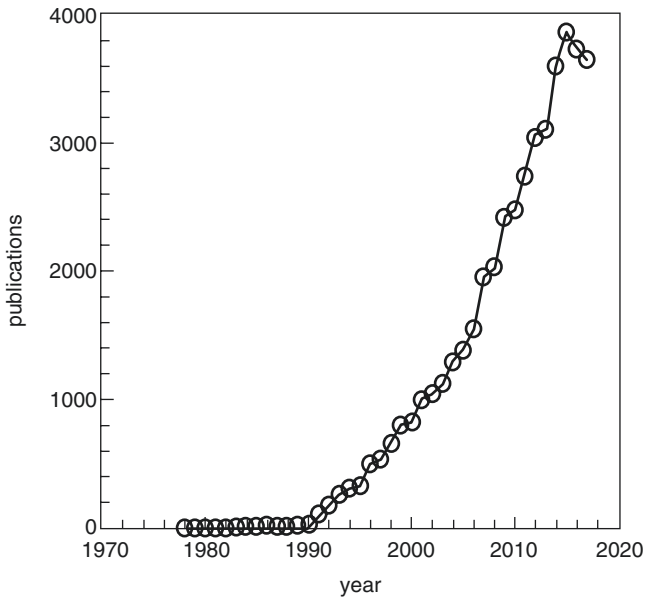

Fig. 20 Graph showing the number of publications involving [^{18}F]FDG from the late 1970s to 2017 based on searching "fluorodeoxyglucose" or "FDG" on the ISI Web of Knowledge

lepsy, and coronary artery disease. Of course, [^{18}F]FDG PET imaging has also fundamentally reshaped the diagnosis, staging, and treatment monitoring of cancer. Because tumor cells have high demand for glucose, [^{18}F]FDG PET scans can pick out these "hot spots" from surrounding healthy tissue, even before anatomical changes are detected.

The Bottom Line

- The science that formed the foundation of modern radiopharmaceutical chemistry flourished in a relatively short time frame.
- The discovery of the x-ray in 1895 was quickly exploited in clinical practice and launched the discovery of natural and artificial radioactivity, which ultimately has had an enormous impact on human health.
- Although the ultimate goal of the Manhattan Project was the development of atomic weapons, the Atomic Energy Agency (now the Department of Energy) was founded to leverage the science behind war into a means of diagnosing and treating disease. Nuclear reactors that were once used to produce weapons-grade uranium and plutonium now make beta-emitting radionuclides for targeted radionuclide therapy.
- Accelerators and cyclotrons—and the technology behind them—that were first developed in the 1930s for physics experiments are now used to produce a plethora of radionuclides for medicine.
- Major advances in organic chemistry have been applied to the rapid radiosynthesis of tracers bearing short-lived radionuclides for PET imaging.
- The science and technology behind radiopharmaceutical chemistry continues to grow, as new radiopharmaceuticals for cardiology, neurology, and oncology become approved for clinical use throughout the world.

References

1. Rutherford E. LIV. Collision of α particles with light atoms. IV. An anomalous effect in nitrogen. London Edinburgh Dublin Philos Mag J Sci. 2009;37(222):581–7. https://doi.org/10.1080/14786440608635919.
2. Nesvizhevsky V, Villain J. The discovery of the neutron and its consequences (1930–1940). Comptes Rendus Physique. 2017;18(9–10):592–600.
3. Gilmer P. Irene Joliot-Curie, a Nobel laureate in artificial radioactivity. In: Chiu MH, Gilmer PJ, Treagust DF, editors. Celebrating the 100th anniversary of Madame Marie Sklodowska Curie's Nobel prize in chemistry. Rotterdam: Sense Publishers; 2011.
4. The Nobel Prize in Chemistry 1935. Nobelprize.org. Nobel Media AB 2014. http://www.nobelprize.org/nobel_prizes/chemistry/laureates/1935/. Accessed 4 June 2018.
5. The Nobel Prize in Physics 1939. Nobelprize.org. Nobel Media AB 2014. http://www.nobelprize.org/nobel_prizes/physics/laureates/1939/. Accessed 4 June 2018.
6. Niese S. George de Hevesy (1885–1966): Founder of radioanalytical chemistry. Czech J Phys. 2006;56(Suppl D):D3–D11.
7. The Nobel Prize in Chemistry 1943. Nobelprize.org. Nobel Media AB 2014. http://www.nobelprize.org/nobel_prizes/chemistry/laureates/1943/. Accessed 4 June 2018.
8. Abraham GE. The history of iodine in medicine Part II: Thyroid fixaion and medical iodophobia. Iodine Study # 16. Optimox. http://www.optimox.com/iodine-study-16. Accessed 8 July 2018.
9. Becker DV, Sawin CT. Radioiodine and thyroid disease: the beginning. Semin Nucl Med. 1996;26(3):155–64.

10. Hertz S, Roberts A, Evans RD. Radioactive iodine as an indicator in the study of thyroid physiology. Proc Soc Exp Biol Med. 1938;38:510–3.
11. Livingood JJ, Seaborg GT. Radioactive isotopes of iodine. Phys Rev. 1938;54(10):775–82.
12. Hamilton JG, Soley MH. Studies in iodine metabolism by the use of a new radioactive isotope of iodine. Am J Phys. 1939;127:557–72
13. Keston AS, Ball RP, Frantz VK, Palmer WW. Storage of radioactive iodine in a metastasis from thyroid carcinoma. Science. 1946;95:362–3.
14. Seidlin SM, Marinelli LD, Oshry E. Radioactive iodine therapy; effect on functioning metastases of adenocarcinoma of the thyroid. J Am Med Assoc. 1946;132(14):838–47.
15. Luster M, Clarke SE, Dietlein M, Lassmann M, Lind P, Oyen WJ, et al. Guidelines for radioiodine therapy of differentiated thyroid cancer. Eur J Nucl Med Mol Imaging. 2008;35(10):1941–59.
16. Lifton JF, Welch MJ. Preparation of glucose labeled with 20-minute half-lived carbon-11. Radiat Res. 1971;45(1):35–40.
17. Raichle ME, Larson KB, Phelps ME, Grubb RL Jr, Welch MJ, Ter-Pogossian MM. In vivo measurement of brain glucose transport and metabolism employing glucose--11C. Am J Phys. 1975;228(6):1936–48.
18. Kamen MD. Radiation science, dark politics: a memoir of the nuclear age. Berkeley/Los Angeles: University of California Press, Ltd; 1985.
19. Ruben S, Kamen MD. Long-lived radioactive carbon: C14. Phys Rev. 1941;59:349–54.
20. Kamen MD. Early history of carbon-14. Science. 1963;140(3567):584–90.
21. Availability of radioactive isotopes. Science. 1946;103:697–705.
22. Perrier C, Segrè E. Radioactive isotopes of element 43. Nature. 1937;140(3535):193–4.
23. Segrè E, Seaborg GT. Nuclear isomerism in element 43. Phys Rev. 1938;54(9):772.
24. Richards P, Tucker WD, Srivastava SC. Technetium-99m: an historical perspective. Int J Appl Radiat Isot. 1982;33(10):793–9.
25. Richards P. Nuclide generators. Radioactive pharmaceuticals. Oak Ridge: US Atomic Energy Commission; 1966.
26. Beck RN. A theoretical evaluation of brain scanning systems. J Nucl Med. 1961;2:314–24.
27. Harper PV, Lathrop KA, Charleston D, Beck R. Optimization of a scanning method using Tc-99m. Nucleonics. 1964;22(1):50–4.
28. Stang LG Jr, Tucker WD, Banks HO Jr, Doering RF, Mills TH. Production of iodine-132. Nucleonics. 1954;12(8):22–4.
29. Stang LG Jr, Tucker WD, Doering RF, Weiss AJ, Greene MW, Banks HO Jr. Development of methods for the production of certain short-lived radioisotopes. Radioisotopes in Scientific Research: Proceedings of the First UNESCO International Conference held in Paris, September 9–20, 1957. New York/London: Pergamon; 1958.
30. Tucker W, Greene M, Weiss A, Murrenhoff A. Methods of preparation of some carrier-free radioisotopes involving sorption on alumina. USAEC Report BNL-3746. Brookhaven National Laboratory: Upton; 1958.
31. r4 Tapscott E. Nuclear medicine pioneer, Hal O. Anger, 1920–2005. J Nucl Med Technol. 2005;33(4):250–3.
32. Wagner HN. A personal history of nuclear medicine. London: Springer-Verlag; 2006.
33. Brownell GL. A history of positron imaging. Presentation prepared in celebration of the 50th year of services of the author to the Massachusetts General Hospital on October 15, 1999.
34. Nutt R. The history of positron emission tomography. Mol Imaging Biol. 2002;4(1):11–26.
35. Brownell GL, Sweet WH. Localization of brain tumors. Nucleonics. 1953;11:40–5.
36. Kuhl DE, Edwards RQ. Reorganizing data from transverse section scans of the brain using digital processing. Radiology. 1968;91(5):975–83.
37. Hounsfield GN. Computerized transverse axial scanning (tomography): part 1. Description of system. Description of system. 1973;46(552):1016–22.
38. Hounsfield GN, Inventor EMI Limited (Hayes, Middlesex, EN), Assignee. Method and apparatus for measuring x or γ-radiation absorption or transmission at plural angles and analyzing the data. United States 1973.
39. Phelps ME, Hoffman EJ, Mullani NA, Ter-Pogossian MM. Application of annihilation coincidence detection to transaxial reconstruction tomography. J Nucl Med. 1975;16(3):210–24.
40. Ter-Pogossian MM, Phelps ME, Hoffman EJ, Mullani NA. A positron-emission transaxial tomograph for nuclear imaging (PETT). Radiology. 1975;114(1):89–98.
41. Keyes JW Jr, Orlandea N, Heetderks WJ, Leonard PF, Rogers WL. The Humongotron—a scintillation-camera transaxial tomograph. J Nucl Med. 1977;18(4):381–7.
42. Larsson SA. Gamma camera emission tomography. Development and properties of a multi-sectional emission computed tomography system. Acta Radiol Suppl. 1980;363:1–75.
43. Kamen MD. The isotopes of carbon. In: Isotopic tracers in biology: an introduction to tracer methodology. 3rd ed. New York: Academic Press; 1957.
44. Cramer RD, Kistiakowsky GB. The synthesis of radioactive lactate acid. J Biol Chem. 1941;137:549–55.
45. Tobias CA, Lawrence JH, Roughton FJW, Root WS, Gregersen MI. The elimination of carbon monoxide from the human body with reference to the possible conversion of CO to CO2. Am J Physiol. 1945;145(2):253–63. https://doi.org/10.1152/ajplegacy.1945.145.2.253.
46. Volker JF, Hodge HC, Wilson HJ, Van Voorhis SN. The adsorption of fluorides by enamel, dentin, bone, and hydroxyapatite as shown by the radioactive isotope. J Biol Chem. 1940;134:543–8.
47. Ter-Pogossian MM, Herscovitch P. Radioactive oxygen-15 in the study of cerebral blood flow, blood volume, and oxygen metabolism. Semin Nucl Med. 1985;15(4):377–94.
48. Ter-Pogossian MM, Powers WE, editors. The use of radioactive oxygen-15 in the determination of oxygen content in malignant neoplasms. Radioisotopes in Scientific Research: Proceedings of the First UNESCO International Conference held in Paris, September 9–20, 1957. New York/London: Pergamon; 1958.
49. Sols A, Crane RK. Substrate specificity of brain hexokinase. J Biol Chem. 1954;210(2):581–95.
50. Kennedy C, Des Rosiers M, Jehle J, Reivich M, Sharpe F, Sokoloff L. Mapping of functional neural pathways by autoradiographic survey of local metabolic rate with (14C) deoxyglucose. Science. 1975;187(4179):850–3.
51. Reivich M, Kuhl D, Wolf A, Greenberg J, Phelps M, Ido T, et al. Measurement of local cerebral glucose metabolism in man with 18F-2-fluoro-2-deoxy-d-glucose. Acta Neurol Scand Suppl. 1977;64:190–1.
52. Som P, Atkins HL, Bandoypadhyay D, Fowler JS, MacGregor RR, Matsui K, et al. A fluorinated glucose analog, 2-fluoro-2-deoxy-D-glucose (F-18): nontoxic tracer for rapid tumor detection. J Nucl Med. 1980;21(7):670–5.
53. Hamacher K, Coenen HH, Stocklin G. Efficient stereospecific synthesis of no-carrier-added 2-[18F]-fluoro-2-deoxy-D-glucose using aminopolyether supported nucleophilic substitution. J Nucl Med. 1986;27(2):235–8.

The Basics of Nuclear Chemistry and Radiochemistry: An Introduction to Nuclear Transformations and Radioactive Emissions

Frank Rösch

Processes of Transformations: Overview

In order to understand the origin and character of individual radioactive emissions accompanying nuclear transformation processes, we first need to answer three questions:

- What is an unstable nucleus?
- What is its motivation to transform?
- What is the best way for it to transform?

It is important to note that the following discussion aims at describing phenomena relevant to radiopharmaceutical chemistry and nuclear medicine. See recently published texts for a comprehensive review on all aspects of nuclear chemistry related to radiopharmaceutical chemistry [1–3].

Composition and Mass of an Atomic Nucleus

The atom is composedof the nucleus and the shell. All nuclei of atoms (except for one of the isotopes of hydrogen, which contains one proton and no neutrons) are composed of two kinds of nucleons: protons and neutrons. The shell of the atom is populated by electrons. For an electrically neutral atom, the number of electrons in the shell is equal to the number of protons in the nucleus. Table 1 summarizes the characteristic parameters for these three subatomic particles. The classical properties of these particles (*i.e.* their absolute mass and charge) can be expressed in terms of real mass.

The nomenclature of nuclear chemistry and physics presents the nucleus in the following way: the number of protons (Z) and the number of neutrons (N) are displayed as lower indices to the left and right of the symbol of the chemical element, while the overall mass number (A)—*i.e.* the sum of the number of protons and neutrons—is presented to the upper left of the symbol of the chemical element. Figure 1 illustrates this for the three most relevant nuclei of the chemical element hydrogen. The three nuclei all have the same number of protons, namely, one, and all have one electron in their shell, which makes the nucleus the chemical element hydrogen. The number of neutrons, however, differs, and so does the mass number. The individual nuclei are called "isotopes", and in the case of hydrogen (and exclusively for that chemical element and no other element), the three isotopes have individual names: hydrogen, deuterium, and tritium(with *deuterium* and *tritium* reflecting the mass number).

Mass and Mass Defect

We now may believe that the mass of the nucleus is the sum of the masses of the protons and neutrons located in it. Let's use the known absolute masses of the neutron and the proton and simply sum up according to the mass number, A, to yield the absolute mass of the nucleus. However, the result we obtain differs from our expectation: the simple sum of the masses of the individual—i.e. *non-bound*—nucleons does not reflect the real mass of the nucleus containing exactly the same nucleons *bound* together. The nucleus is lighter than its individual components! This represents one of the most fundamental effects of our material world. The difference is expressed as the *mass defect*: $\Delta m^{defect} = m^{nucleus} - m^{sum\ of\ individual,\ non\text{-}bound\ nucleons}$.

Figure 2 illustrates the situation for the nucleus of the helium isotope ^{4}He. Let's calculate the masses. What we need are three values: the absolute mass of the nucleus as determined experimentally, the absolute mass of the proton, and the absolute mass of the neutron as given in Table 1 in terms of kg.

But wait a moment! Those absolute masses are extremely low and not convenient to handle. Accordingly, two other expressions of mass are preferred in nuclear sciences. One is the equivalent of mass in terms of energy according to

F. Rösch (✉)
Institute of Nuclear Chemistry, Johannes Gutenberg-Universität Mainz, Mainz, Germany
e-mail: froesch@uni-mainz.de

J. S. Lewis et al. (eds.), *Radiopharmaceutical Chemistry*, https://doi.org/10.1007/978-3-319-98947-1_3

$E = mc^2$. This yields energy values with the electron volt (eV) unit; see Table 1.

The other version is to utilize a relative mass parameter: the *atomic mass unit*. It considers the experimentally very precisely known mass of a stable isotope of a prominent atom, divides this mass by the number of nucleons, and provides a value that describes the mass an average nucleon contributes to the mass of the whole atom. The reference is the carbon isotope of mass number 12, a nice nucleus: very abundant on earth, very symmetric with 6 protons and 6 neutrons, all nucleons existing as pairs. The experimentally determined absolute mass of one single carbon-12 *atom* is $19.92648 \cdot 10^{-27}$ kg. It is divided by its mass number 12. The value resulting from $19.92648 \cdot 10^{-27}$ kg/12 is $1.66054 \cdot 10^{-27}$ kg which is called the "atomic mass unit", u. With this parameter in hand, the absolute mass of every other isotope is easily estimated by just multiplying the mass number, A, of the given isotope by the atomic mass unit, u. Also for the subatomic particles such as the electron, proton, and neutron, masses can be expressed as parts of u; see Table 1. For a systematic presentation of the individual values of atomic mass and other parameters such as mean nucleon binding energy, see the AMDC—Atomic Mass Data Center—IAEA Nuclear Data Services [4] and Atomic Mass Evaluations [5, 6]. More data compilations for 2016 can be found in references [7, 8].

Table 1 Summary of the basic properties of the three basic constituents of atoms of chemical elements: the electron, proton, and neutron

Particle	q	m		
	C	kg	u	MeV
Electron	$-1.602 \cdot 10^{-19}$	$9.109 \cdot 10^{-31}$	0.00055	0.511
Proton	$+1.602 \cdot 10^{-19}$	$1.673 \cdot 10^{-27}$	1.00728	938.272
Neutron	0	$1.675 \cdot 10^{-27}$	1.00867	939.566

The elementary charges are −1, +1, and 0 for the three particles and are given as values of the elementary charge unit C (Coulomb). The mass is given in units of kilogram and u, as well as in energy in MeV via $E = mc^2$. u = $1.66054 \cdot 10^{-27}$ kg = 931.494 MeV, 1 eV = $1.602177 \cdot 10^{-19}$ J

Let's now turn to a real example. The nucleus ^{4}He (which represents the α-particle) is composed of two protons and two neutrons. The mass of the ^{4}He nucleus *expected* by summing $2m_p$ (u) + $2m_n$ (u) is 4.03188 (u). The *experimental* value for the mass of the He *atom* is 4.00260325415 u. The corresponding value for the He *nucleus* (obtained by subtracting mass and binding energy contribution of the two electrons) results in 4.00150 u. The total mass of the nucleus is thus smaller than the sum of the four individual nucleon masses not bound together: Δm is 4.00150 u – 4.03188 u = − 0.030377 u (see Fig. 2). See Wang *et al.* for a tabulated presentation of the mass defect values for all the stable nuclei [6].

Binding Energy

Where is that mass—"the mass defect, Δm"—going? Of course, mass cannot disappear:it is translated into energy according to $\Delta E = \Delta mc^2$. What happens? Once nucleons

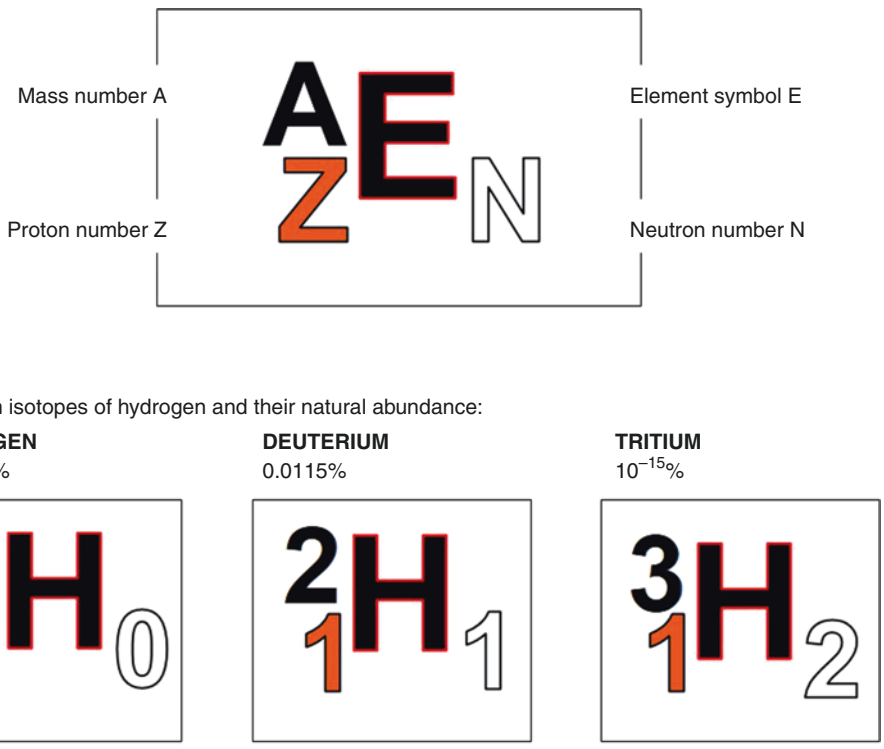

Fig. 1 Notation of nuclides in nuclear and radiochemistry and examples for three isotopes of hydrogen

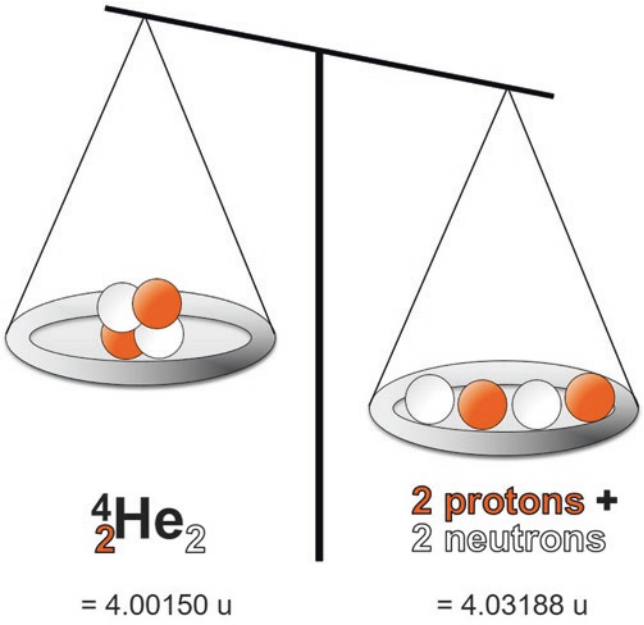

Fig. 2 Mass defect: The nucleus of an atom is lighter in mass (and, consequently, lower in energy) than the weight of the sum of its identical but non-bound components

Table 2 Experimental masses of atoms, mass excess, as well as overall and mean binding energies for ^{4}He, ^{12}C, ^{56}Fe, and ^{238}U. The nucleus ^{12}C may serve as a relative scale again and is involved in defining a *mass excess* value, indicating the relative difference in binding energy between the "reference" ^{12}C nucleus and any other nucleus

Nucleus	(Atomic) Mass	Mass excess	Binding energy	
	experiment (MeV)	Δm^{excess} (MeV)	Overall per nucleus E_B (MeV)	Mean per nucleon $\bar{E}_B$ (MeV)
^{4}He	4.002603	+2.425	28.296	7.074
^{12}C	12.000000	0	92.162	7.680
^{56}Fe	55.934937	−60.605	492.258	8.790
^{238}U	238.050788	+ 47.309	1801.689	7.570

approach a very small distance between each other (on the order of fm, *i.e.* the dimension of the atom nucleus), they are attracted to each other by the "strong force"—the strongest force known in our universe—and combine to form a nucleus. The energy all the nucleons *save* once bound together compared to their former non-bound state is called the "overall binding energy". The equivalents of Δm and ΔE thus reflect the overall binding energy, E_B, of the nucleus. Nucleon binding energies correlate with mass defect values via $E_B = \Delta E = \Delta mc^2$. Accordingly, the overall binding energy of a nucleus increases with increasing numbers of nucleons in it. Table 2 gives examples for four nuclei. However, a more interesting parameter is the "mean binding energy", which is the average binding energy contributed by an individual nucleon: $\bar{E}_B = \frac{E_B}{A}$.

Let's calculate the mean binding energies of the 4 nucleons of the helium-4 nucleus as well as the 12 nucleons within the carbon-12 nucleus. The overall binding energy of the ^{4}He nucleus is 0.03038 u = $0.05045 \cdot 10^{-27}$ kg in terms of mass and $4.53 \cdot 10^{-12}$ J or 28.295660 MeV in terms of energy. The *mean binding energy per nucleon* within the ^{4}He nucleus is $\bar{E}_B$ = 28.295660 MeV / 4 = 7.073915 MeV. For ^{12}C, it is 7.680 MeV. Compared to $\bar{E}_B(^4He)$ = 7.074 MeV, the 12 nucleons of carbon-12 are bound more strongly together within the ^{12}C nucleus. This mean binding energy increases further with the increasing mass number, reaching maximum values of ~8.8 MeV for mass numbers around 56–62 but then starting to diminish for very heavy nuclei. Table 2 lists the values of experimental atomic masses, overall and mean binding energies, and the mass excess for ^{4}He (a light nucleus), ^{12}C, ^{56}Fe (a medium mass number nucleus), and ^{238}U (a very heavy nucleus).

The maximum values for mean nucleon binding energy are $\bar{E}_B$ = 8.790 MeV for ^{56}Fe, 8.792 MeV for ^{58}Fe, and 8.794 MeV for ^{62}Ni. However, mean binding energies are quite similar compared to the strongly varying mass numbers and atomic weights, at least for most of the nuclei of A > 10. In this broad range of 10 < A < 238 for stable nuclei, average values for $\bar{E}_B$ are 8.2 ± 0.6 MeV. $\bar{E}_B$ values for the ~250 stable and more than 3000 unstable nuclei are tabulated in reference [6].

Models

A key question in the nuclear sciences is understanding the correlation between the mass number A (*i.e.* the total number of nucleons in the nucleus) and $\bar{E}_B$, the mean nucleon binding energy. There is a huge data set for the absolute masses of the ~250 stable nuclei known and their corresponding mean nucleon binding energies. The basic theory is the "liquid drop model", which is accompanied by a complementary "shell model". The "liquid drop model" (LDM) of the atomic nucleus postulates that all protons are identical, all neutrons are identical, and all nucleons are distributed homogeneously within the nucleus like H_2O molecules within a drop of liquid water.

The semiempiric mathematics quantifying these experimentally known dependencies is the so-called Weizsäcker equation. The equation may be divided into five (or more) parts for volume, surface, Coulomb forces, symmetry, and pairing. Each term of this equation has a physical rationale that describes the various ways the two different types of nucleons contribute to binding energy. For some terms, there is a dependency on mass number, A, exclusively. For others, the individual contributions caused by either protons or neutrons are reflected as well. Finally, each of the terms gets a coefficient, values that are just adjustments of a polynomial

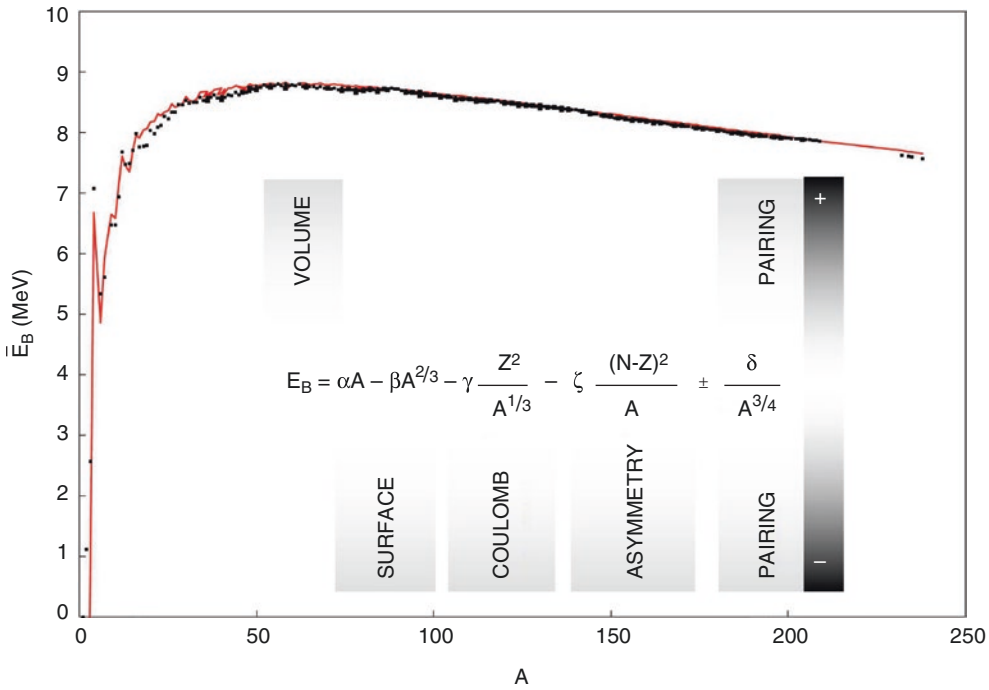

Fig. 3 Correlation of mean nucleon binding energies, $\bar{E}_B$, versus mass number. Black squares are experimental values for stable nuclei, the three uranium isotopes U-234, U-235, and U-238, and Th-232; the red line indicates the polynomial according to the Weizsäcker equation inserted

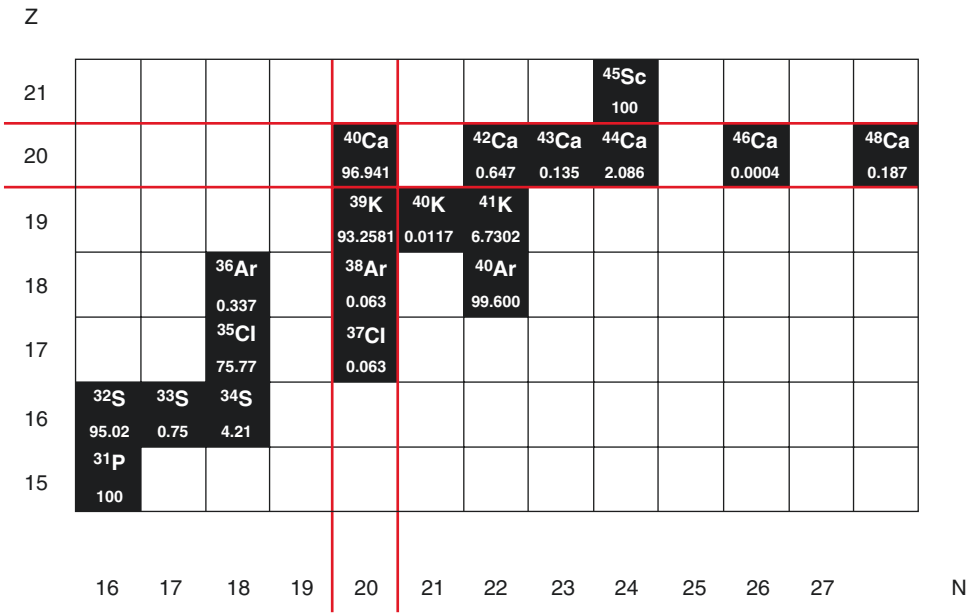

Fig. 4 The "over-expression" of stable isotopes (black boxes) of magic number 20. Excerpt of the Chart of Nuclei. There are four stable isotopes representing N = 20 but zero for N = 19 and just one for N = 21. There are six stable isotopes representing Z = 20 (the chemical element calcium) but only three for Z = 19 and just one for Z = 21. Lower numbers in the boxes indicate the natural abundance of individual stable isotopes of one element. For calcium, the most abundant isotope is ^{40}Ca, a "double-magic" nucleus (20 protons + 20 neutrons)

to the "experimental" values of mean nucleon binding energy. The equation itself is inserted into Fig. 3. The polynomial correlation obtained is also shown in Fig. 3.

Overall, the result is excellent—with some exceptions! For some mass numbers, there are extreme deviations between real values and the ones predicted by the LDM. This begs for another approach, which is reflected by the "shell model". Among the existing sets of A, Z, and N with the ~250 stable nuclei known, there is a surprising over-expression of stable nuclei that possess 2, 8, 20, 28, 50, and 82 protons or neutrons. Why? As long as the reason for that (over-expression) was not clear, those numbers were called "magic". Figure 4 shows that "over-expression" for isotopes of magic number 20.

Nuclei expressing these numbers for protons or neutrons seem to be (and are) more stable than predicted by the LDM. Consequently, another theory accompanies the liquid drop model theory: the "shell model" (SM). Similar to the orbital theory of electrons, both protons and neutrons are supposed to exist at characteristic shell levels with individual quantum numbers. This model centres on two key postulates that are dramatic departures from LDM:

(i) The nucleons are not distributed homogeneously but rather in specific "shells".
(ii) All the protons and all the neutrons are different from each other, *i.e.* having individual characteristics that make each nucleon in the nucleus unique.

A key challenge to organize the protons and neutrons of a nucleus into shell structures was to identify a system of shell arrangements, in which the balance of the nucleons involved represents "full" (or "closed") shell occupancies and reflect the "magic" numbers. This is similar to the full occupancies of the noble gases in the Periodic Table of the Elements, in which electrons are filled into all the existing vacancies of one period.

The SM also helps to understand the occurrence of both *excited* and *ground* states for a nucleus. Once there are defined shell occupancies for protons and neutrons, it is straightforward to accept the idea that a certain nucleon may (for a certain period of time) exist within a higher shell as an excited level and subsequently "de-excite" back to its ground-state level. This is analogous to the well-known behaviour of excited electrons, which of course "de-excite" to their ground-state electron shell accompanied by the emission of electromagnetic radiation. In fact, following nuclear transformations within unstable nuclei, the nucleons of the newly formed nucleus frequently do not reside within their ground-state shells but rather at higher energy shells, defining an "excited nucleus". Only when the excited nucleon "falls" to its lower energy shell can the ground-state nuclear level be achieved. This is the essence of radioactive emissions such as γ-rays (see below).

From Stable to Unstable Nuclei

Both LDM and SM were developed based on parameters (experimentally precisely determined masses) of ~ 250 stable atoms. Those nuclei are characterized by a set of proton and neutron and mass numbers Z, N, and A, respectively, which represents nuclei of maximum mean nucleon binding energy, accordingly. One can conclude that the stability of an atomic nucleus of mass A is basically a question of the right mixture between protons and neutrons for a given value of A. If "right", the nucleus owns the optimum value of the mean nucleon binding energy for that value, reflecting the correlation $\bar{E}_B = f(A)$. If that particular mixture of nucleons behind those stable nuclei deviates from the optimum value, $\bar{E}_B$ values are lower, and the nucleus of that value of A is not stable anymore. Being not stable does not mean "not existing". A suboptimal mean nucleon binding energy does guarantee stability but allows the nucleus to exist for a certain period of time. The question is: If the nucleus exists but is not stable, what is it doing?

The answer: Such an unstable nucleus tries to stabilize! Its "private" motivation is to improve the mean nucleon binding energy by optimising the existing mixture of protons and neutrons into a better, more stable mixture. *This is the essence of radioactive transformations*. The old unstable nucleus will find a way to form a new, lower mass nucleus that is characterized by increased mean nucleon binding energy. Put another way, the unstable nucleus simply obeys one of the general laws in the universe: to improve its status in terms of energy and mass. Consequently, the process itself is exothermic and spontaneous. The velocity of this transformation (we will later define this in terms of "half-life") is simply proportional to the gain in terms of $+\bar{E}_B$ and −m.

The only issue remaining is to understand how a given unstable nucleus manages this transformation. In fact, there are several pathways, and we will soon learn how clever a nucleus can be in selecting the best route.

Transformation, non "Decay"

In the literature, the behaviour of an unstable nucleus is typically expressed as if it "decays". Let's first agree on a definition. Does the unstable nucleus really "decay"? The philosophic answer is that nothing decays, it only transforms into something new. An unstable nucleus, K1, thus transforms into a more stable one by optimising its mean nucleon binding energy. The absolute mass of the transformation product nucleus, K2—which may be truly stable or simply "more stable" (but still "radioactive") and in need of another step of transformation—is less than the absolute mass of the initial unstable nucleus. This transformation thus proceeds exothermically. The difference in mass is typically expressed in terms of energy, ΔE, and is referred to as the Q value of a transformation. However, there is a third component to consider. This is the "radiation", which is released and accompanies the transformation processes. This kind of emission is generally associated with "radioactivity". At this stage, it is called "x" and subsumes the various kinds of "radiation" to be discussed later in detail (Fig. 5).

Primary Transformations Versus Secondary Transitions and Post-processes The primary goal of an unstable nucleus is to optimize its nucleon composition. "Radioactivity"—*i.e.* all of the forms of radioactive emission we observe—simply is a phenomenon accompanying the individual processes an unstable nucleus undergoes to increase its mean nucleon binding energy! In the following, let's define a hierarchy of these processes of transformation: primary processes, secondary processes, and post-processes (Fig. 6).

It all begins with a "primary" transformation: the change in the nucleon composition of the unstable nucleus:

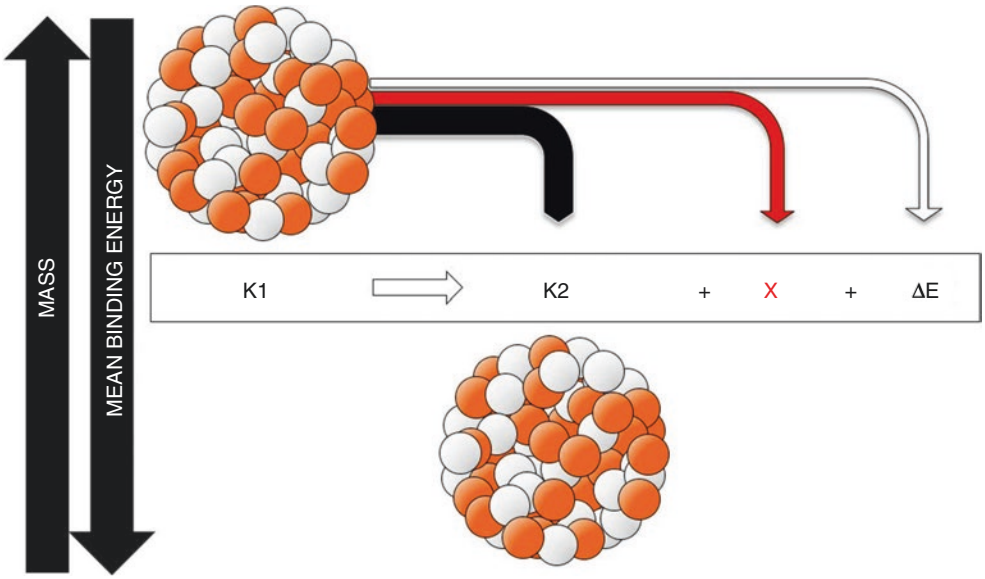

Fig. 5 Simplified scheme of primary transformation of an unstable nuclide, K1, into a more stable nuclide, K2. This "x" typically is a particle, such as a ^{4}He nucleus (the α-particle) or an electron (as in β-processes)

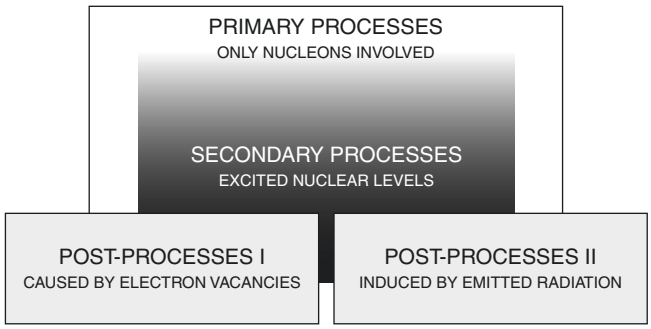

Fig. 6 Hierarchy of the primary transformation of unstable nuclei, the subsequent secondary transitions, and the parallel post-processes

K1(A_1,Z_1,N_1). This change results in the formation of a new nucleus: K2 (A_2,Z_2,N_2). The three subtypes of primary transformations are β-processes (where A remains constant with $A_2 = A_1$, only Z and N changes by one unit to $Z_2 = Z_1 \pm 1$, $N_2 = N_1 \pm 1$), α-emission (where A changes $A_2 = A_1 - 4$, $Z_2 = Z_1 - 2$ and $N_2 = N_1 - 2$), and spontaneous fission.

In some cases, the nucleons of the newly formed K2 do not directly appear at the ground-state nuclear shell levels but instead occupy higher-energy shells. This situation is termed the formation of an "excited state" nucleus, °K2, which must subsequently de-excite to create the ground-state nucleus. The excited and de-excited nuclear states all belong to the same nucleus of identical set of (A_2,Z_2,N_2). This process of de-excitation encompasses the "secondary" transitions described here.

Finally, two classes of post-processes—both of which produce their own types of radioactive emissions—must also be considered. These processes do not concern the *nucleus* itself; instead, they either occur within the electron *shell* of the transforming nucleus or *outside* the atom.

Mechanism of Primary Transformation Processes Three subtypes of primary processes differ in terms of the way that unstable nuclides convert into stable ones by changing the absolute number of nucleons (changing A) or by modifying the ratio between protons and neutron (changing the Z:N ratio for constant A). In the latter cases, an "excess" neutron "just" converts into a proton (supposing the nucleus owns an excess of neutrons over protons) or vice versa. In other cases, a nucleus releases a number of nucleons, typically as a small cluster of two neutrons and two protons (the α-particle), in order to lower its mass number, A. For a limited number of very heavy nuclides, there is a third option: spontaneously splitting the large nucleus into (usually two) fractions in a process called "spontaneous fission" (sf). The latter pathway is not relevant to molecular imaging or therapy and thus will not be discussed further (Fig. 7).

Secondary Transitions: No Change in Nucleon Composition In some cases, the rearrangement of nucleons in primary transformations directly yields the ground state of the new nucleus, K2. In many other cases, the proton and/or neutron shell occupancies of the newly formed nucleus are not identical to those of the ground state of that nucleus. Consequently, the newly formed nucleus exists—for shorter or longer periods of time—in an "excited" state. Those excited states subsequently de-excite to levels of lower energy according to the shell model of the nucleus. Secondary processes proceed within one and the same nucleus, *i.e.* at both ΔZ and $\Delta A = 0$. Those "secondary" processes are better described as "transitions" than "transformations". Again, there are three subtypes of secondary transformations: the emission of electromagnetic radiation, the formation of inner conversion electrons, and pair formation. (The first, known as γ-emission, represents the most relevant subtype for SPECT imaging).

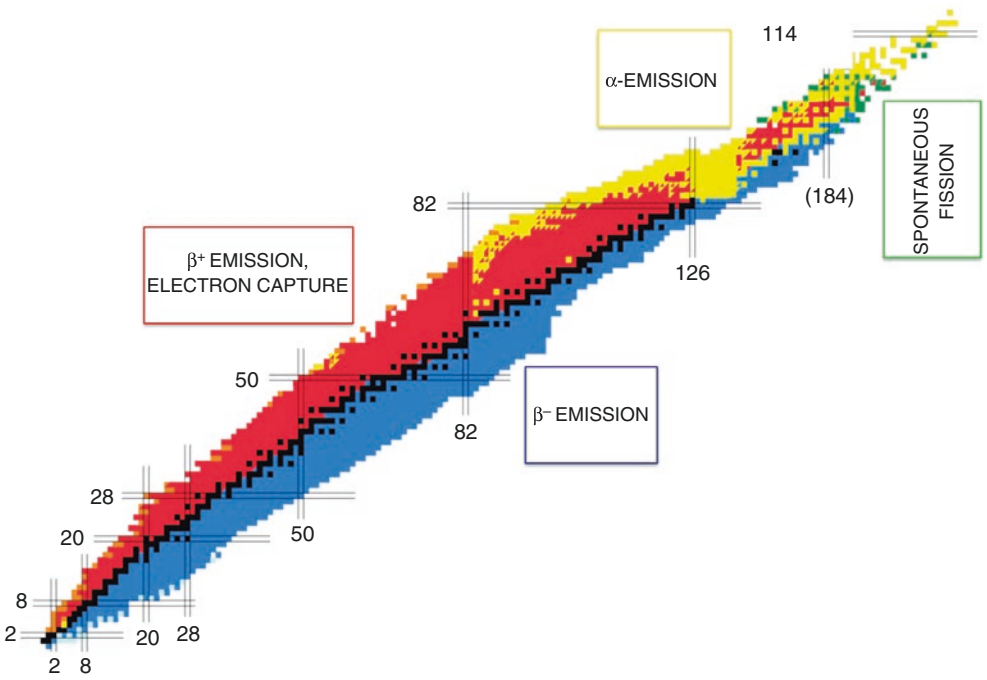

Fig. 7 Distribution of radionuclides in the Chart of Nuclides undergoing β-processes, α-emission, and spontaneous fission. According to the Karlsruhe Chart of Nuclides, β-processes are indicated either by blue (β^-) or red (β^+ or ε) colour, α-emission in yellow, and spontaneous fission in green

Post-processes Some of the primary transformation mechanisms (in particular the *electron capture* process) as well as a secondary transition pathway (namely, *inner conversion*) leave a hole within the electron shell surrounding that nucleus. While the new *nucleus*, K2, is already formed, the vacancy in the *electron shell* of the atom must be filled. The two ways to organize this are the emission of X-rays and the emission of Auger and Coster-Kronig shell electrons. These processes are categorized as "post-processes I". The most relevant emission produced by these processes is X-rays. Like γ-emission, X-rays are electromagnetic radiation. However, their origin is different: while γ-emission is created within the nucleus via the de-excitation of excited nuclear levels, X-rays are generated within the electron shell.

Independently, the particle emission "x" released in primary and secondary processes interacts with the many other, stable atoms surrounding the newly formed nuclide, K2. The effects induced by these interactions are discussed as "post-processes II". Most relevant (at least in the context of nuclear medicine) are β^+ particles—*i.e.* positrons, formed in the primary β process. Positrons interact with electrons to induce an annihilation phenomenon, which produces a pair of 511 keV γ-rays that form the basis of PET.

β-Transformations

Three Pathways: β^--Process, β^+-Process, and Electron Capture (ε)

Let's start with a neutron-rich unstable isotope. What should it do to stabilize itself? The elimination of a neutron seems to be a good idea. However, this would require sufficient energy to eliminate that nucleon from the nucleus, which is not necessarily available. (Remember, the average binding energy per nucleon is around 8 MeV!) On the other hand, it is helpful to think about an "excess" of neutrons as tantamount to a "deficit" of protons. In light of this approach, the clever unstable nucleus comes up with a brilliant idea: converting a neutron into a proton would solve the problem in an elegant way. The inverse applies to neutron-deficient (proton-rich) isotopes, which can gain stability by converting a proton into a neutron. Converting a nucleon in excess to a nucleon in deficit is the foundation of the β-process. In this manner, the mass number of the nucleus will remain constant throughout the transformation.

The conversion of a neutron into a proton results in the process ${}_ZK1 \rightarrow {}_{Z+1}K2$. This is accompanied by the emission of a *negatively charged electron* and is called a β^--process. The conversion of a proton into a neutron results in the opposite case: ${}_ZK1 \rightarrow {}_{Z-1}K2$. While there is only one approach for the ${}_ZK1 \rightarrow {}_{Z+1}K2$ conversion, there are two options for the ${}_ZK1 \rightarrow {}_{Z-1}K2$ process. The one accompanied by the emission of a *positively charged electron* is called the β^+-process. Alternatively, or in parallel, neutron-deficient nuclides may transform by the *capture of an electron* from the K electron shell. This type of β-process is named "electron capture" (ε).

From Isotopes to Isobars All β-transformations of unstable nuclides proceed at A = constant. Neutron-rich isotopes transform via the neutron → proton conversion. The new nuclide, K2, has a composition of (Z + 1, N−1) and arrives at a nuclide that is a heavier chemical element. Proton-rich nuclides utilize proton → neutron conversion and yield a new nuclide, K2, of (Z−1, N + 1) composition. K2 represents a

chemical element of lower Z. This transformation may continue in a stepwise fashion—K1 → K2 → K3, *etc.*—until the Z to N ratio reaches that of a stable nuclide.

This is illustrated in more detail in Fig. 8. An isobar line is indicated at A = 18 with ^{18}O as the stable nuclide. The β⁺- and electron capture processes approach ^{18}O coming from the proton-rich nuclides ^{18}Ne and ^{18}F, while the β⁻-processes approach ^{18}O via the ^{18}B → ^{18}C → ^{18}N cascade.

From Isobars to Parabolas The diagonal isobar line may be converted into a parabola and gives a correlation of the type $\Delta\bar{E}_B = f(Z)$ at A = constant. The blue nuclides from Fig. 8 shift to the left side of the parabola, because they are of low Z compared to the red nuclides, which are of higher Z. Each primary transformation step increases $\bar{E}_B$ values. Typically, the value of $\Delta\bar{E}_B = f(Z)$ increases exponentially. This is reflected by the exponential expression of a parabola. The maximum mean nucleon binding energy is located at the vertex of the parabola, representing the stable nuclide. This is true for a single mass number A. It holds true for the neighboured mass numbers as well. Each of the many isobar lines of the Chart of Nuclides thus owns a maximum of mean nucleon binding energy for a specific value of Z. As the various terms of the Weizsäcker equation all include a multiple of mass number A, the equation may be transformed for the value of Z which lies at the vertex of the parabola. The expression is $Z_A = f(A^{constant})$. Z_A is the proton number with optimum mean nucleon binding energy.

$$Z_A = \frac{A}{2.0 + 0.0154A^{2/3}}$$

As is characteristic for the mathematics of a parabola, the two ascents scale exponentially and thus become sharper and sharper. The x-axis, however, scales linearly with respect to Z. This indicates that the differences in mean nucleon energy between successive transformations of K1 → K2 are large at both "ends" of the parabola and become less and less pronounced the closer the transformation step is to the vertex. Simply put, the sharper the ascent, the more unstable the nuclides are.

However, those parabolas need a second look, which refers to the fact whether the number of protons or neutrons is even or odd. Let's consider the combination of protons and neutrons in the nucleus in terms of (Z, N). For (Z = even, N = odd) and (Z = odd, N = even) nuclides, the new nuclide is of the same category: (even, odd) turns into (odd, even) and *vice versa*. This is the case for all isobars of odd mass number A. In this case (A = odd), there is only one parabola, and this is exemplified in Fig. 9 for mass number *A* = 95. In contrast, an (Z = odd, N = odd) nuclide turns into an (Z = even, N = even) nuclide and an (Z = even, N = even) nuclide turns into an (Z = odd, N = odd) one. This yields two separate curves as indicated in Fig. 10 for mass number *A* = 96.

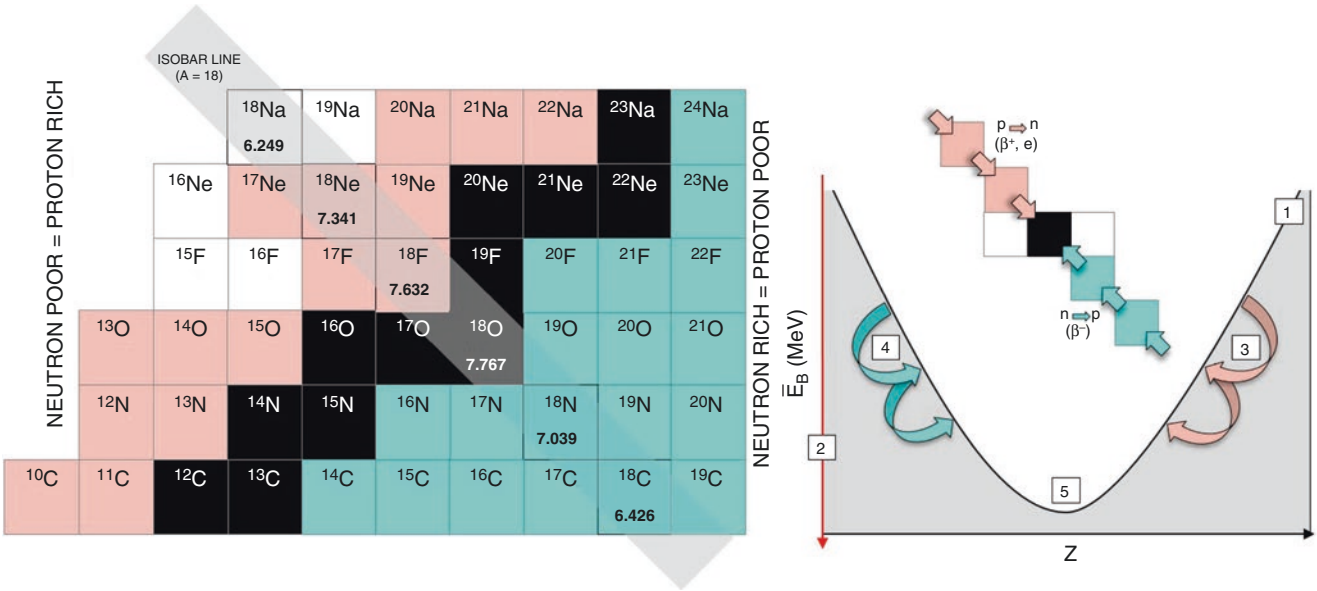

Fig. 8 *Left*: β-transformation of unstable nuclides along the *A* = 18 isobar line with $\bar{E}_B$ values in MeV. ^{18}O is the nucleus of maximum mean nucleon binding energy of this isobar line; it is stable. The β⁺ and electron capture processes approach ^{18}O coming from the proton-rich nuclides ^{18}Ne and ^{18}F; the β⁻-processes accumulate at ^{18}O via ^{18}B → ^{18}C → ^{18}N →. *Right*: A selected isobar may be turned into a parabola (**1**) using a coordinate system of type $\bar{E}_B = f(Z)^{A = constant}$. Note the direction of changes in $\bar{E}_B$. (**2**) The proton-rich unstable nuclei successively transform via β⁺ or ε on the right side. The β⁻ transformations are on the left side. With either step of the transformation, $\bar{E}_B$ increases by characteristic amounts of $\Delta\bar{E}_B$. Interestingly, the individual values of $\Delta\bar{E}_B$ become smaller for each step (**3**). Finally, both arms of the parabola approach the vertex of the parabola (**4**), where the most stable nuclide (or two stable ones) is (are) found

From Two-Dimensional Isobars and Parabolas to the Three-Dimension Valley of β-Stability There are many isobar lines across the Chart of Nuclides [9], ranging from short ones (*e.g.* A = 3 with the two nuclides ^{3}H and ^{3}He) to very long ones (*e.g.* A = 100 including 15 nuclides). Arranging these two-dimensional parabolas into a successive series of many parabolas creates a three-dimensional plot (Fig. 11). Unstable nuclides are positioned along the hillsides, stable nuclides at the bottom of the valley. The latter is called the "valley of β-stability". The direction of the valley does not correspond to a straight line (which would have been the isodiaphere of N = A) but makes a soft turn to the right side. All the stable nuclides depicted in Fig. 4 of the chart of nuclide diagram lie in that "valley".

Quarks: The Elementary Particles Behind the Nucleons

The essence of the β-processes is turning either a neutron into a proton or *vice versa*. Nucleon binding energies improve, which is best expressed by the isobar parabola of $\bar{E}_B = f(Z)$ along an isobar. However, how can one sort of nucleon simply convert into the other one? In order to get an idea of this kind of wonder, a look into the theory of *elementary particles* and *quantum physics* is needed.

Elementary Particles While proton, neutron, and electron have been classified as "subatomic", it does not necessarily mean that these particles are not further divisible. While this holds true for the electron—which therefore is classified as "elementary particle"—the proton and the neutron are composed of other sub-nucleon particles. According to the development of the "standard theory of particle physics", elementary particles (*i.e.* those which really cannot be divided further) can be arranged according to spin and electric charge. The spin of the particle may be half-integer or integer. Fermions all have half-integer spin values, while bosons have integer spin values. Fermions can be further subdivided according to charge. Fermions with integer electric charges are called "leptons", while fermions with non-integer electric charges are called "quarks". Both leptons and quarks can be subdivided further! For example, the electron is a fermion and a lepton (spin 1/2 and charge −1). There are likewise several types of bosons. The photon, for example, is a boson: spin = 1. The mediators allowing for the interactions between elementary particles are also called "field quanta".

The elementary particles are summarized in Table 3. There are quarks—defined by non-integer spin and non-integer electric charge (yielding either +2/3 or −1/3)—and leptons, defined by half-integer spin and integer electric charge (0 or −1). In contrast, mediators or field quanta are characterized by integer electric charge (0, +1, or −1) and integer spin. This group belongs to the class of bosons. Gluons are the field quanta mediating the strong interaction (strong in power, short in distance), attracting nucleons, and being responsible for the formation of nuclei of atoms. In contrast, the W and Z bosons are correlated with the weak interaction. The photon is the field quantum mediating electromagnetic interaction.

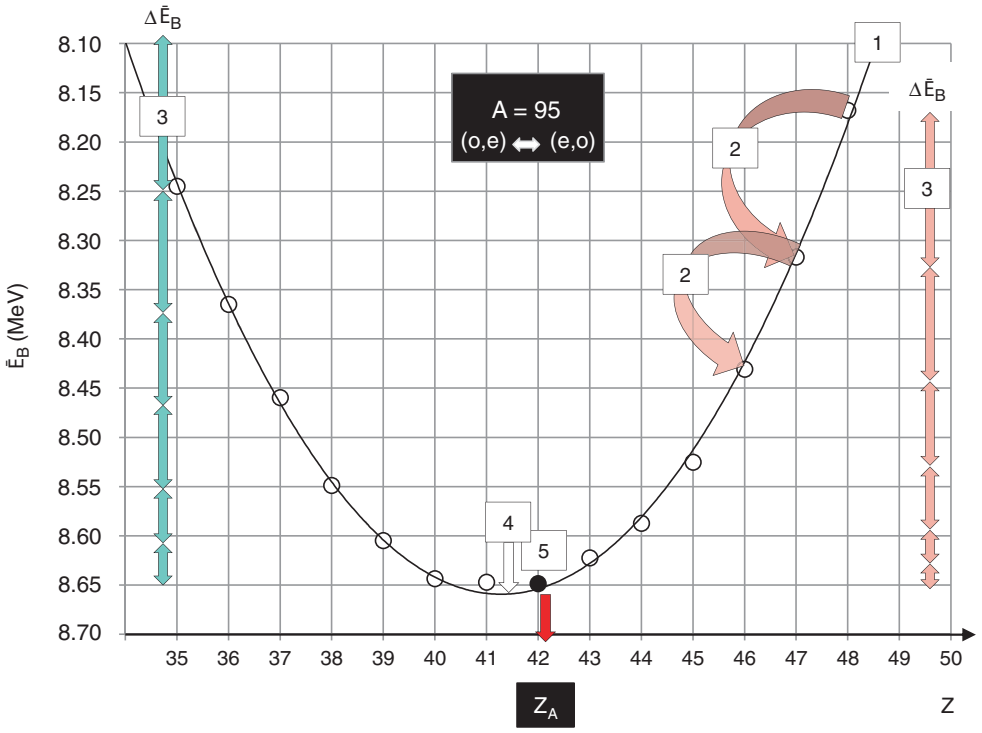

Fig. 9 β-parabola for mass number *A* = 95: Isobars of odd mass number A represent transformations of (even, odd) nuclides into (odd, even) nuclides and vice versa. (**1**) one single parabola; (**2**) successive transformations of type β^+ or ε at the right side and of type β^- at the left side; (**3**) decreasing differences in mean nucleon binding energy when approaching the vertex of the parabola; (**4**) Z_A is 40.937; (**5**) the only one stable nuclide is ^{95}Mo ($Z = 42$) with the largest value of $\bar{E}_B$

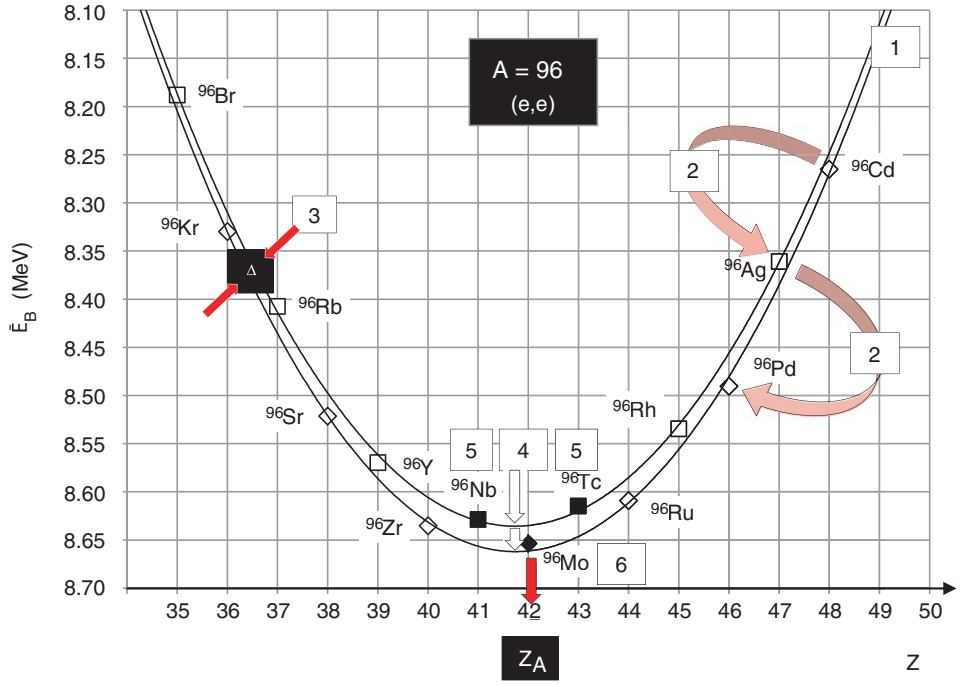

Fig. 10 β-parabolas for mass number $A = 96$: Isobars of even mass number A represent transformations of (even, even) nuclides into (odd, odd) nuclides and *vice versa*. The impact of the parity term of the Weizsäcker equation creates two parabolas with a shift of $\pm\ \delta/A^{¾}$: (**1**) two separate parabolas with the one for (even, even) nuclides "below", which is at higher values of $\bar{E}_B$; (**2**) successive transformations of type β^+ or ε at the right side and of type β^- at the left side alternating from (even, even) to (odd, odd) nuclides and so on; (**3**) the shift in energy between the two parabolas is $2\delta/A^{¾}$; (**4**) $Z_A = 41.328$; (**5**) the most stable nuclide is ^{96}Mo (largest value of nucleon binding energy). The stability of the two (odd, odd) nuclides needs to be studied in detail. In this case, ^{96}Ru is also stable, while ^{96}Zr has a half-life of $3.9 \cdot 10^{19}$ years (!)

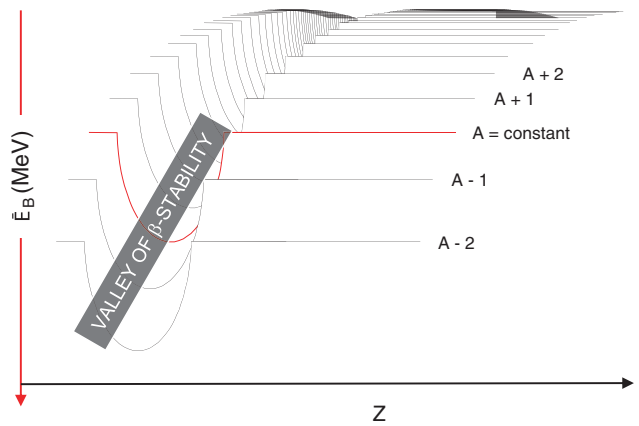

Fig. 11 β transformation processes along a coordinate system of mean nucleon binding energy $\bar{E}_B$ vs. Z at A = constant form a parabola. If many parabolas are arranged with increasing A, the illustration reflects a valley formed by two hillsides. This "valley of β-stability" is composed of all the stable nuclides known

Quarks and leptons are structured into three families, and—among other factors—arranged according to their mass (or energy) (Fig. 12).

Now we understand the composition of a nucleon. A proton is composed of two up quarks (2 times the electric charge of +2/3 makes a +4/3 charge) and one down quark (electric charge −1/3). The resulting total charge thus is +1. A neutron consists of one up quark and two down quarks, and their particular electric charges compensate to the overall charge of 0 (Fig. 13).

Antimatter Each quark and lepton has a "twin" that is identical with regard to all parameters except charge. These "twins" are called *anti*particles. The most prominent *anti*particle in the context of nuclear medicine and radiochemistry is the positron. It owns exactly all the properties of the electron (mass, spin), but its charge is +1 instead of −1. Another relevant system of elementary particle/antiparticle is the electron neutrino and its anti-electron neutrino (see below).

Table 3 Overview on the system of elementary particles showing electric charge and intrinsic spin

Elementary particle	name	symbol	el. charge	spin (ħ)	
quarks	up	u (u_R, u_G, u_B)	+⅔	½	fermions
	down	d (d_R, d_G, d_B)	-⅓	½	
	charmed	c (c_R, c_G, c_B)	+⅔	½	
	strange	s (s_R, s_G, s_B)	-⅓	½	
	top	t (t_R, t_G, t_B)	+⅔	½	
	bottom	b (b_R, b_G, b_B)	-⅓	½	
leptons	electron	e^-	-1	½	
	e⁻-neutrino	ν_e	0	½	
	muon	μ^-	-1	½	
	μ⁻-neutrino	ν_μ	0	½	
	tau	τ^-	-1	½	
	τ⁻-neutrino	ν_τ	0	½	
mediators	photon	γ	0	1	bosons
(field quanta)	bosons	W^+	+1	1	
		W^-	-1	1	
		Z^o	0	1	
	gluons	g_i (i = 1 ... 8)	0	1	

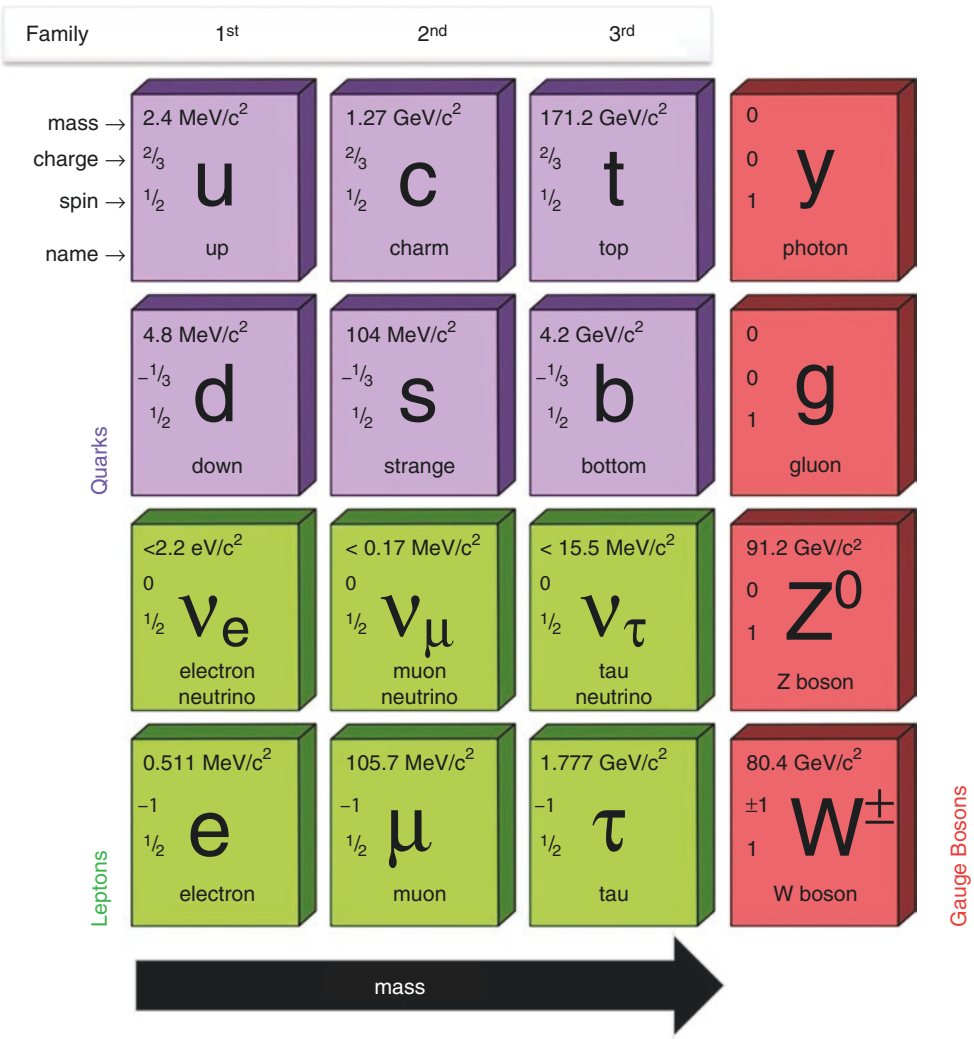

Fig. 12 Families of elementary particles and their field quanta. The first family includes the up quark and the down quark, the electron and the electron neutrino. The second family collects the charmed quark, strange quark, muon, muon neutrino, *etc*.

The First Family in the Context of β-Transformations To understand the basic features of β-transformation processes of unstable nuclides, only the first family of elementary particles is relevant: two quarks (down and up), two leptons (electron and electron neutrino), the *anti*matter version of these two leptons (positron and electron *anti*neutrino), and two field quanta (photon and gauge bosons). The essence of β^--processes is now accessible by utilising the concept of quarks. In all cases, only one of the three quarks of each nucleon is involved (the "actor"). The two other quarks just watch the others and arecalled "spectators".

β^- Process The conversion of a neutron into a proton is the metamorphosis of one d-quark into one u-quark. The initial composition of $2 \times d + 1\ u$ $\left(= 2 \times -\frac{1}{3} + 1 \times +\frac{2}{3} = 0\right)$ thus turns into $1 \times d + 2\ u$ $\left(= 1 \times -\frac{1}{3} + 2 \times +\frac{2}{3} = +1\right)$. The mechanism is illustrated for the β^--process. Figure 13 illustrates the principal changes among the quarks involved (up quark, down quark). Yet, there is one more question: why should one sort of quark turn into the other one? There is a force needed to manage this fundamental process: the mediators. The mediators relevant in β^-, β^+, and electron capture transformation processes are the W^-, W^+, and Z^o bosons, respectively. Feynman has suggested graphical presentations of this process (and many other processes in elementary particle physics). Figure 13 (*right)* shows how the W^- boson mediates the metamorphosis of the d-quark.

β^+- and EC Processes During the conversionof a proton into a neutron, the opposite occurs. A u-quark turns into a d-quark. In this case, it is the W^+ boson and the Z^o boson, respectively, mediating the metamorphosis, and the elementary particles created are the positron and the electron neutrino.

β-Transformation and Laws of Symmetry Figure 13 (*right*) indicates the appearance of the particleessential to β-transformation: the β^- electron. In addition, there is an electron neutrino. Let's understand the origin of both of these particles. The metamorphoses of one member of the first family of quarks into the other one perfectly explain the balance in quarks and perfectly explain the conversion of one sort of nucleon into the other one. However, it introduces several other questions.

The first: What about the balance in charge? For β^--processes, a neutral nucleon had changed into a +1 charged nucleon. For β^+ and EC processes, a positively charged nucleon had changed into a neutral one. Where is the missing charge *going* (for β^-- and β^+-processes) or *coming from* (for the EC process)? The answer is another elementary particle of the first family—the electron—is needed *to carry the charge.* Note that in the present context, this electron is referred to as β-particle. It is the origin of the electron which is responsible for this terminology: the β-particle electron is an electron created during these nuclear processes.

β^--Process The emission of a "normal" electron within the $n \rightarrow p$ conversion satisfies the balance of electric charge: it is $0 \rightarrow (+1) + (-1)$.

β^+-Process The $p \rightarrow n$ conversion requires the emission of the *anti*matter kind of electron, the +1 charged positron. The balance of electric charge then is $(+1) \rightarrow (0) + (+1)$.

EC Process The $p \rightarrow n$ conversion can occur through another pathway, the electron capture (ε). Here, the proton captures a "normal" electron. The balance of electric charge then is $(+1) + (-1) \rightarrow (0)$.

The second question: What about the balance in orbital momentum, the spin? The answer is that another elementary particle of the first family—the electron neutrino—is needed *to carry the spin*. Let's consider the $n \rightarrow p$ conversion of a neutron. The neutron's spin is 1/2, so the total spin of the left side of the transformation equation is non-integer. Among the transformation products discussed so far, the spin 1/2 of the proton and the spin 1/2 of the electron combine to an integer number. So here comes a problem: the overall spins of the starting particles and the product particles differ! As simply *postulated* (!) by Pauli, a third reaction product is needed to solve the problem. It should have no electric charge so as to not disturb the symmetry in electric charge and (almost) no mass, in order to not disrupt the balance in electric charge and mass achieved so far. However, it should carry a half-integer spin. The neutrino hypothesis perfectly fits with all three subtypes of the β-process (Fig. 14).

The last issue of symmetry to consider is that between the matter and antimatter, another fundamental law in physics. It requires a balance in terms of particles and antiparticles. For example, the metamorphosis of a neutron into a proton creates a β^- electron, an elementary particle. This now requires the simultaneous creation of an antiparticle. In the present case, we observe the formation of an electron antineutrino, not the electron neutrino. For the β^+-process, the opposite occurs. Changing a proton into a neutron needs the formation of a positively charged β-particle: the positron. The positron is an antimatter particle, so the electron neutrino needed for reasons of symmetry in spin must be the "real" electron neutrino.

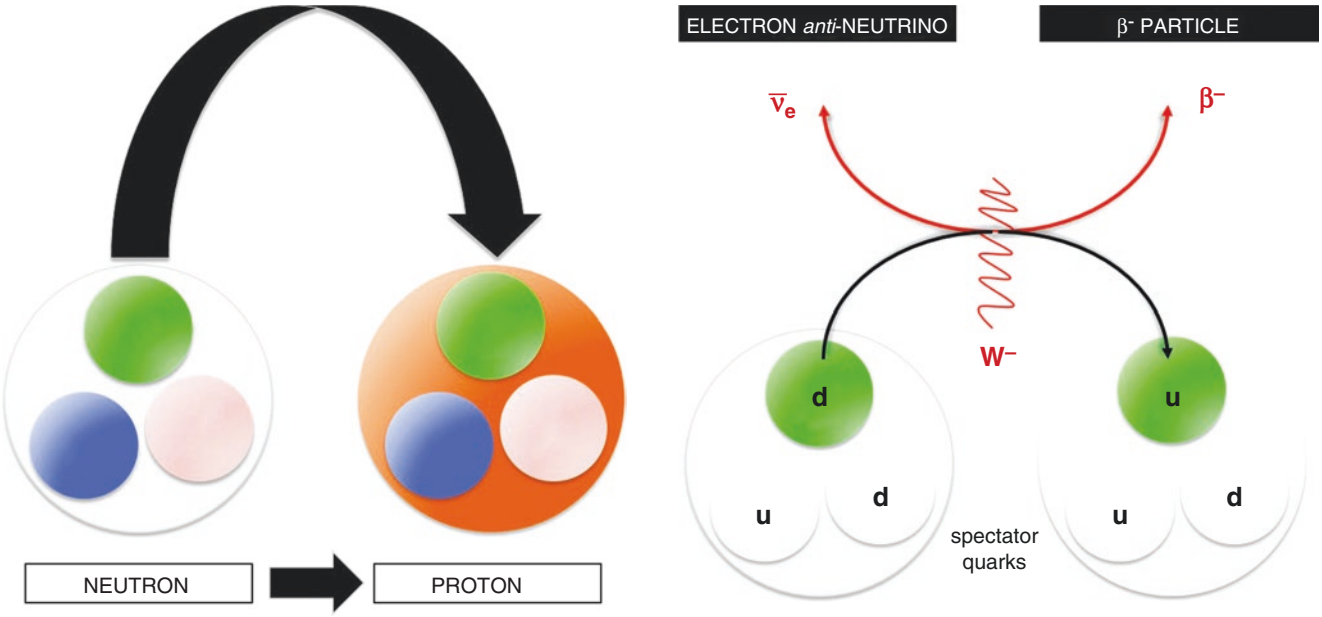

Fig. 13 *Left*: The metamorphosis of quarks (here one d-quark into a u-quark) explains the conversion of a neutron into a proton. The other down quark and the up quark of the neutron remain unchanged. *Right*: Diagram of the process, indicating the appearance of the other members of the first family responsible for the β^- transformation: the W^- boson, the electron antineutrino, the β^- particle; see further in the text

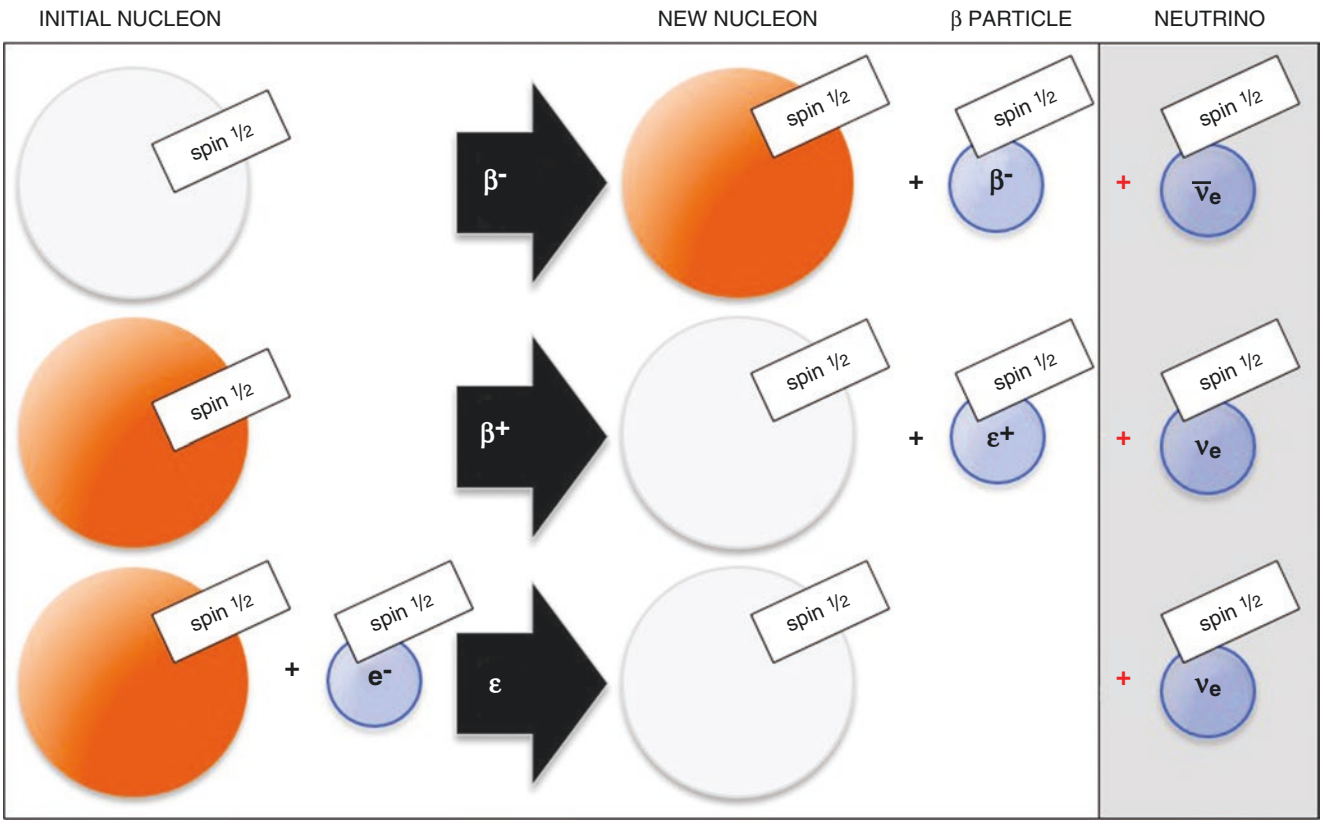

Fig. 14 Balances in electric charge and momentum for nucleon conversion representing the three subtypes of primary β-transformation. Grey and orange circles represent the neutron and the proton, respectively. In all cases, it is an electron or β-particle, respectively, which handles the balance in charge, though in different ways for the β^--process, the β^+-process, and the electron capture ε. For symmetry in momentum, in all cases an electron neutrino is emitted in the context of nucleon conversions. It guaranties the conservation of spin

Energetics of β-Transformations: Values of ΔE and Q

The Q Value The three subtypes of β-transformation all are characterized by a balance of mass between the initial unstable nuclide, K1, and the transformation product nuclide, K2. The new nuclide *must* be of lesser mass in order to guarantee an exothermic transformation. In different words, differences between the masses of the new nuclide and the old one are always positive: +Δm, which is also +ΔE. The value of mass refers to the whole nuclide (M) rather than the mass (m) of nuclei alone. If atomic mass data (in u) are used as tabulated, the mass of the nucleus is obtained by subtracting the mass of the electrons from the whole atom mass. The value of ΔE is specified as the Q value of the process. The three subtypes of transformations thus own individual values: Q_{β^-}, Q_{β^+}, and Q_{ε}. Supposing a given unstable nuclide is able to undergo two or all three subtypes of the transformation, each branch will thus be characterized by its individual amount of energy. Among the many unstable nuclei undergoing β-transformation, the range of Q values is very large. There are small Q values such as 18.55 keV for tritium and large ones such as 14.1 MeV for ^{8}B. This covers about three orders ofmagnitude.

Specific Effects for β⁺-Emission Versus Electron Capture The way the Q value is calculated—*i.e.* the difference between the masses of the nuclide formed minus the mass of the initial nuclide—is in part modified according to the role of the β-particles emitted and the electron captured, respectively. The β⁺-subtype starts from K1 and creates two components, namely K2 and the positron. The electron capture subtype starts from nuclide K1 and collects one *additional* electron on top of the initial electron shell configuration of the corresponding atom and only next forms K2. The overall masses to consider are thus the mass M of the nuclides *and* the masses of the electrons involved. For K1, the latter includes the masses of the number of shell electrons equivalent to the number of its protons (Z), *i.e.* $\{M_{K1} - Z \cdot m_e\}$, while for K2, this number of shell electrons is one fewer, *i.e.* $[M_{K2} - (Z-1) \cdot m_e]$. The masses of the electron antineutrino electron neutrino can be neglected. The resulting balances in mass are the following:

$$\Delta M\left(\beta^+\right) = \left\{\left(M_{K2} - (Z-1)m_e\right) + 1 \cdot m_e\right\} - \left\{M_{K1} - Z m_e\right\}$$
$$= \left(M_{K2} - M_{K1}\right) + 2 m_e$$

$$\Delta M(\varepsilon) = \left\{M_{K2} - (Z-1)m_e\right\} - \left\{\left(M_{K1} - Z m_e\right) + 1 m_e\right\}$$
$$= \left(M_{K2} - M_{K1}\right)$$

Accordingly, whatever the difference in mass of the two nuclides, the β⁺ transformation requires an excess of that ΔM plus $2 \cdot m_e$. The amount of energy which equals the mass of two electrons is $2 \cdot m_e \cdot c^2 = 2.\ 0.511$ MeV = 1.022 MeV. In contrast, electron capture and β⁻-processes areenergetically satisfied by "just" $M_{K2} < M_{K1}$. This discriminates the pathways of proton-rich unstable nuclides, *i.e.* β⁺ and ε-transformation. For example, the positron emitter ^{18}F transforms to stable ^{18}O. Atomic masses are 18.000937 u and 17.999160 u, Δu = 0.001777 u, and in terms of energy (1 u = 938.272 MeV), it is 1.667 MeV, i.e. >1.022 MeV. It allows to utilize both pathways, positron emission and electron capture. (In reality, it prefers positron emission 96.7% of the time.) ^{7}Be transforms into stable ^{7}Li. Atomic masses are 7.016929 u and 7.016003 u, Δu = 0.000926 u = 0.869 MeV, i.e. <1.022 MeV. As a result, ^{7}Be is unable to undergo positron emission, and electron capture is its only option.

Electron Capture? How can a proton, located in the nucleus of an atom, "capture" an electron? Didn't we learn that the electrons orbit in electron shells far away from the nucleus? This takes us to the quantum mechanics of atomic shell electron. Their orbital momentum as characterized by the set of quantum numbers defines individual spatial distributions within an atom with certain probabilities. Interestingly, for *s*-orbital electrons (because of their orbital momentum of $l = 0$ and the corresponding spherical distribution of probabilities of existence), there is a very low probability that the electron exists close to and even "inside" the nucleus! Relatively speaking, this probability is most pronounced for K-shell electrons rather than L or even M-shell electrons. The probability of electron capture increases with decreasing distance of the K-shell to the nucleus. The higher the element's proton number Z is, the higher the probability of electron capture. The distance between nucleus and K-shell follows a function of $1/Z^2$. This allowsus to draw several conclusions:

1. Unstable proton-rich nuclides that preferentially utilize β⁺ transformation are among the elements of the second period of the periodic table of the elements [*e.g.* carbon (^{11}C, $t_{½}$ = 20.38 min), nitrogen (^{13}N, $t_{½}$ = 9.96 min), oxygen (^{15}O, $t_{½}$ = 2.03 min), and fluorine (^{18}F, $t_{½}$ = 109.7 min)]. In these cases, the abundance of the β⁺-subtype is 99.76%, 99%, 99.9%, and 96.7% for ^{11}C, ^{13}N, ^{15}O, and ^{18}F, respectively. These nuclides have become key nuclides for medically important molecular imaging and diagnosis via positron emission tomography (PET) and find extensive application in radiopharmaceutical chemistry. Nevertheless, there are also unstable nuclides of elements above $Z = 20$ emitting positrons at percentages, which are relevant for practical application. Yet in these cases, the percentage of positron emission drops: ^{64}Cu = 17.9%, ^{68}Ga = 88.0%, ^{73}Se = 65.0%, ^{86}Y = 34.0%, ^{89}Zr = 23.0%, ^{90}Nb = 51.1%, and ^{124}I = 24.0%, for example.
2. Electron capture consequently dominates in the case of the unstable proton-rich nuclides of heavy elements. Many of the key radionuclides used in SPECT diagnosis

undergo electron capture as the primary transformation and continue with secondary transitions yielding γ-emissions via excited nuclear levels. Examples of these nuclides include ^{67}Ga, ^{111}In, and ^{123}I.

Kinetic Energetics of β-Transformation Products

Recoil Let's assume the β-particle is ejected from K2, *i.e.* the former K1. The impulse it takes causes a somehow opposite impulse to K2. This is referred to as the "recoil energy" of K2. It is linked with (a) the Q value of the transformation, (b) its own mass, and (c) the kinetic energy, E_β, of the emitted β-particle and the electron neutrino (or the electron neutrino exclusively in case of electron capture). In addition, it is influenced by the spatial arrangements the two elementary particles are emitted. K2 recoil energies thus lie between the theoretical maximum value and zero. The maximum kinetic energy $^{RECOIL}E_{K2}{}^{max}$ the recoil nucleus may get is

$$^{\text{RECOIL}}E_{K2}^{max} = \left(\frac{E_\beta^{max}}{2c^2} + m_{\beta^0}\right)\frac{E_\beta^{max}}{m_{K2}}$$

For example, the β^- transformation of ^{14}C into ^{14}N yields $^{RECOIL}E_{K2}{}^{max} = E^{max}(^{14}N) = 6.9$ eV. ($m_{K2} = 14$ u, $m_\beta{}^o = 0.511$ keV, $E_\beta{}^{max} = 0.156$ MeV).

The recoil energies of K2 are higher when the kinetic energy of the β-particle is high and the mass number of K2 is low. For example, at mass numbers (A) around 100 and maximum kinetic energies of the β-particle of 1 MeV, values of $^{RECOIL}E_{K2}{}^{max}$ are about 10 eV.

Distribution of Kinetic Energies: β-Particle and Electron Neutrino As the recoil nucleus just gets a very low amount of the total kinetic energy, the dominant fraction is left for the small particles emitted. In electron capture, all the remaining kinetic energy goes to the electron neutrino. Consequently, the electron neutrino gets a kinetic energy of a discrete energy value. However, in β^- and β^+ transformations this is different. β-particles and the electron neutrinos share their fraction of kinetic energy "statistically". There are cases in which the β-particle gets all the kinetic energy ($E_\beta{}^{max}$), and nothing is left for the electron neutrino—or *vice versa*.

In reality, there is a distribution between both the elementary particles, and consequently, kinetic energies observed for β-particles and for electron neutrinos show a continuous spectrum. The β-particle kinetic energies thus lie between the theoretical maximum value and zero. For example, the β^--particles emitted from ^{3}H and ^{14}C show maximum kinetic energies $E_\beta{}^{max}$ of 18.591 keV and 156.476 keV, respectively. Typical maximum energies for β^- and β^+ particles range from about 20 keV to a few MeV. However, the fraction of β-particles that reaches this maximum energy is very low. Most of the β^--particles show energies (most abundant average or mean energies ($E_\beta{}^{mean}$ or $\bar{E}_\beta$) typically are around $\frac{1}{3}$ $E_\beta{}^{max}$. The same applies to positrons emitted within the β^+-subtype of β-transformation. Figure 15 shows profiles of the continuous spectra of the positrons emitted from four relevant nuclides used in medical diagnosis (PET). The values of $E_\beta{}^{max}$ depend on the Q value of the transformation.

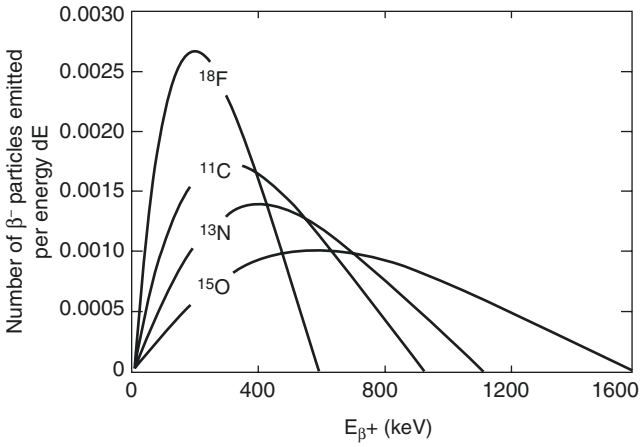

Fig. 15 Continuous spectra of positrons emitted from ^{15}O, ^{13}N, ^{11}C, and ^{18}F

Quantum Theory of β-Transformation Phenomena

The process of nucleon transformation inside the nucleus of an atom is explained by quantum physics theory. The basic terminology is called "Fermi's golden rule". It defines the probability (P_{fi}) of transition (per unit of time) between initial (*i*) and final (*f*) states from one energy eigenstate of a quantum system (here represented by the nuclide K1) into another one (the final nuclide K2). Figure 16 compares the phenomenological process and the quantum physical approach.

Several parameters are needed to quantitatively understand β-transformation, such as phase space volumes, densities of energy states, probabilities of transition, and the overlap of wave functions of the initial state and the possible final states. Each state is expressed by a density profile, *i.e.* the number n of states per unit of energy (dn/dE). With the negligible mass of the electron neutrino and very small recoil energy of K2, the densities of states are expressed in terms of overall energy, Q_β, of the transformation relative to the

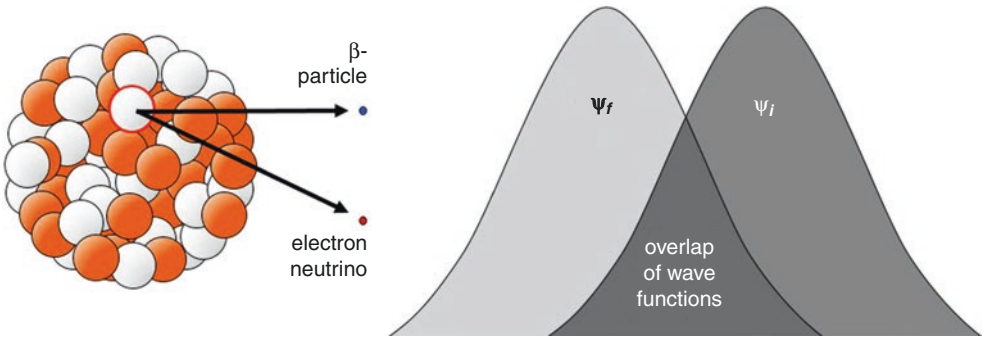

Fig. 16 Phenomenology of the β-transformation (*left*) and the principal concept in quantum theory (*right*) showing wave functions Ψ_i and Ψ_f

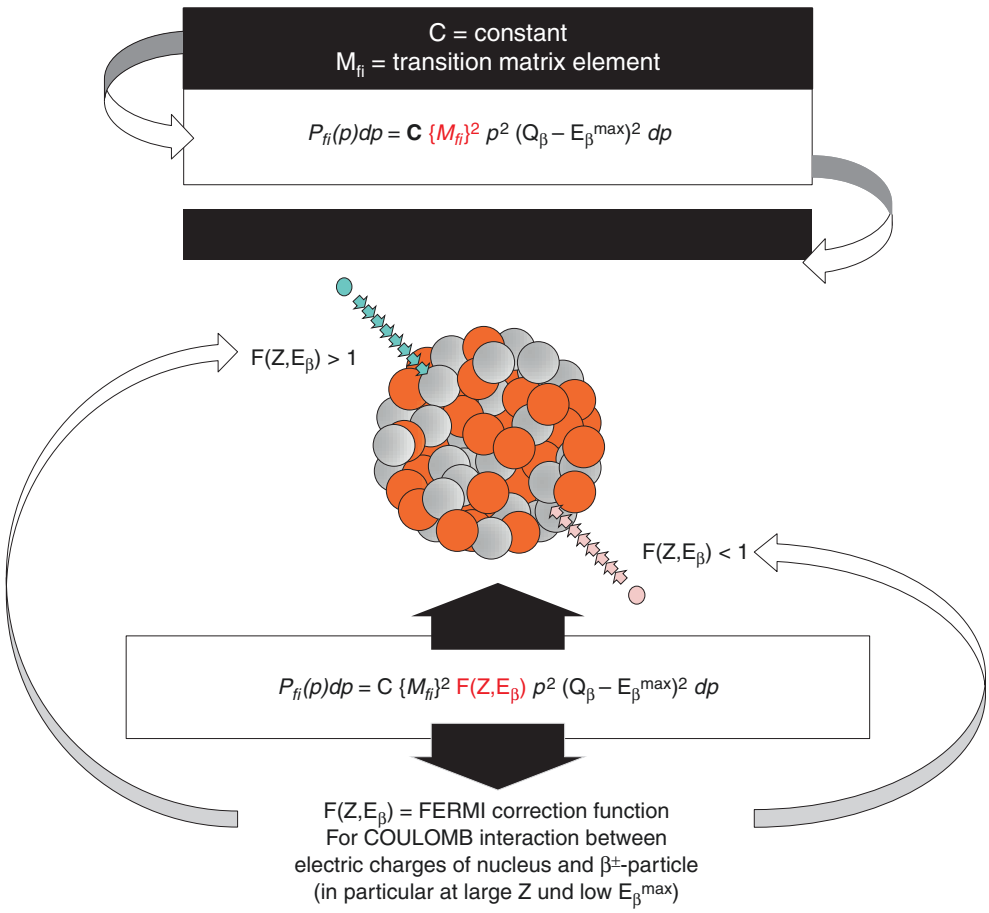

Fig. 17 Fermi's golden rule: The number of states for β-particle and electron neutrino per volume segments combines to densities of states for both elementary particles. Probabilities of transition are described by the transition matrix element, M_{fi}, while several numerical parameters are combined to a constant $C = V^2 / (2p^3\ c^3\ \hbar^7)$. This equation includes an additional factor, the Fermi correction term. It reflects the fraction of kinetic energy an electron loses after its emission from the nucleus due to Coulomb attraction and the positron gains due to Coulomb repulsion

maximum kinetic energy of the β-particle emitted. The mathematics relates the probability (P_{fi}) of transition (transition rate = transitions per unit time) to phase spaces via a matrix element $\{M_{fi}\}^2$. This matrix element considers the overlapping wave functions of the final and initial states, Ψ_f and Ψ_i, and includes the Hamilton operator $\hat{H}$ of the weak interaction. If the overlap of the wave functions is large, the probability of transition is high. The most relevant equations and their relationship are illustrated in Fig. 17.

Velocities of β-Transformations

Correlations Between Q Value and $\Delta\bar{E}_B$ with Half-Life
Q values correlate with the half-life of the transformation. For larger Q_β-values, the transformation steps proceed quickly. This perfectly fits with the β-transformation parabolas shown in Figs. 9 and 10, for example. The further the nuclides are from the vertex of the parabola, the steeper the sides of the parabola become. While the unit of the x-axis is Z±1 and is

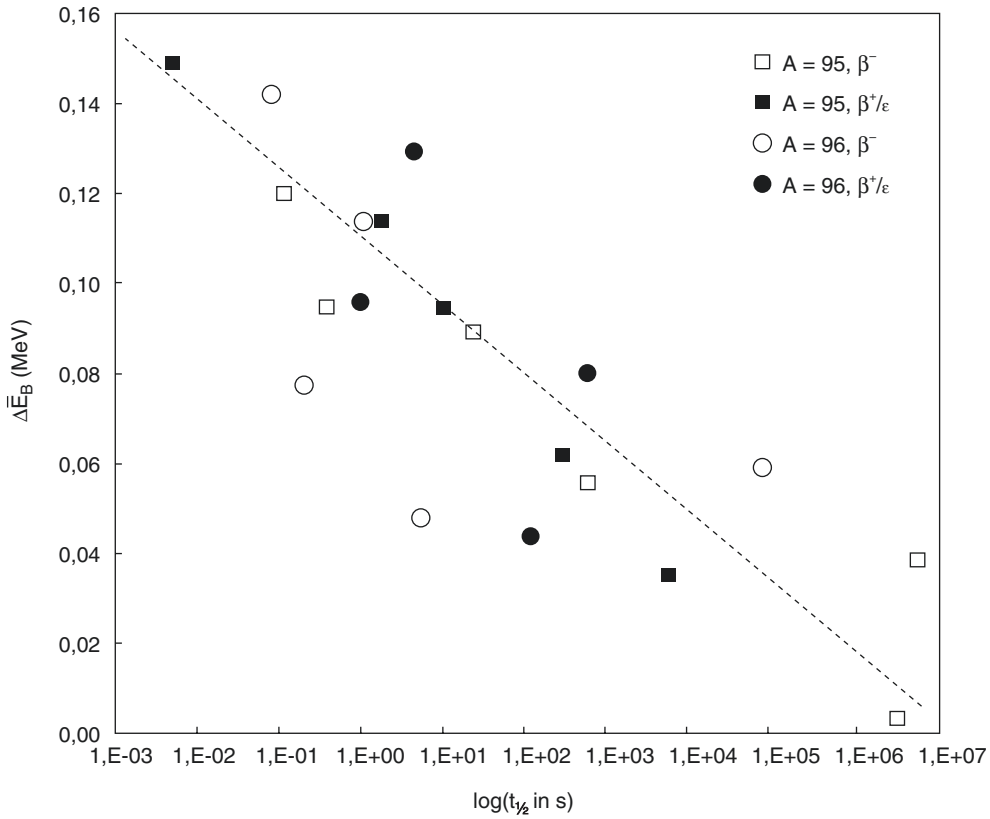

Fig. 18 Half-lives of β-transformations along parabolas for mass numbers $A = 95$ and 96 correlate with the successive gain in $\Delta\bar{E}_B$ per transformation towards the vertex of the parabola. For values of $\Delta\bar{E}_B > 0.1$ MeV, the half-lives are seconds or less. For values of $\Delta\bar{E}_B < 0.1$ MeV, half-lives approach hours, days, and even years

thus linear, the y-axis representing the mean nucleon binding energy is exponential. Figure 18 compares the "win" in mean nucleon binding energy, $\Delta\bar{E}_B$, with the corresponding half-life of this transformation for all the unstable nuclides covered by both Figs. 9 and 10, *i.e.* for all β-transformations along the isobars of mass numbers 95 and 96.

Similarly, the Q values are (in general) inversely proportional to the half-life or directly proportional to the transformation constant. The larger the value of $\Delta\bar{E}_B$, the larger the value of E_β^{max} (or Q_β) and the faster the transformations. Figure 19 illustrates the correlation between E_β^{max} and the half-life ($t_{½}$) and transformation constant (λ; $t_{½} = \ln 2 / \lambda$) for the same nuclides as shown in Fig. 18. Clearly, small changes in energy (Q_β or E_β^{max}) have an impressive impact on the half-life of the transformation.

Logft Values The correlation between nuclear transformation energetics and velocities is also addressed by quantum mechanics as introduced via the Fermi equation. The equation introduced in Fig. 17 can be modified towards a version expressing the transformation constant, λ (Fig. 20). It separates two parts and defines the integral on the left as velocity (λ), while the integral on the right is subsumed as the f-value. If velocity is expressed as half-life $t_{½} = t$, a product ft is derived. It is typically given on a logarithmic scale. The relevant message here is that low values of logft reflect high probabilities of nuclear transformation and short half-lives. The larger a logft value becomes, the lower the probability of transformation and the longer the half-life.

Selection Rules The logft concept overlaps with other systematics in nuclear transitions: selection rules. In this regard, the two relevant nuclear properties are the *overall spin* of a nuclear level and its *parity.*

Overall Nuclear Spin *J* Each nucleon in anucleus owns its characteristic individual orbital spin. The sum of all individual spins creates the overall spin, *J*, of a given nuclear state. Overall spin values thus may be different between the initial state of the unstable nuclide transforming, K1, and the ground state of the new nuclide, K2. In addition, the new nucleus formed may be the ground state of K2 or an intermediate excited nuclear state, °K2. Those different nuclear states of the same nucleus may differ in *J*. An excited nuclear level is characterized by individual nucleons populating higher-energy shell positions of quantum numbers different to the corresponding ground state of the same nucleus. Accordingly, *overall nuclear spin J* numbers may differ between excited and ground-state levels of K2.

Parity *Π* In quantum physics, parity refers to changes of physical quantities under spatial inversion within a polar coordinate system. Mathematically, parity refers to how wave

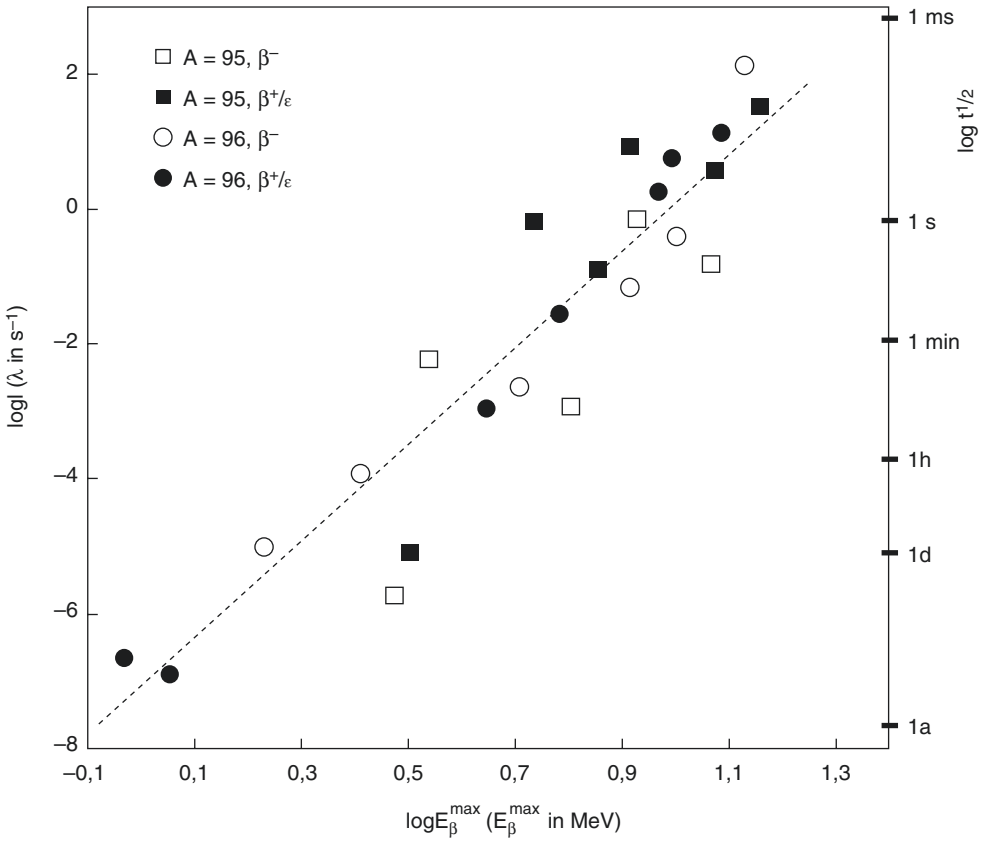

Fig. 19 Correlation of maximum kinetic energy of the emitted β-particles and the transformation constant (left) and half-life (right) of the β transformation for nuclides of mass numbers $A = 95$ and 96. For changes in E_β^{max} of one order of magnitude (*e.g.* from 1 to 10 MeV), the transformation constant/the half-life changes by seven orders of magnitude

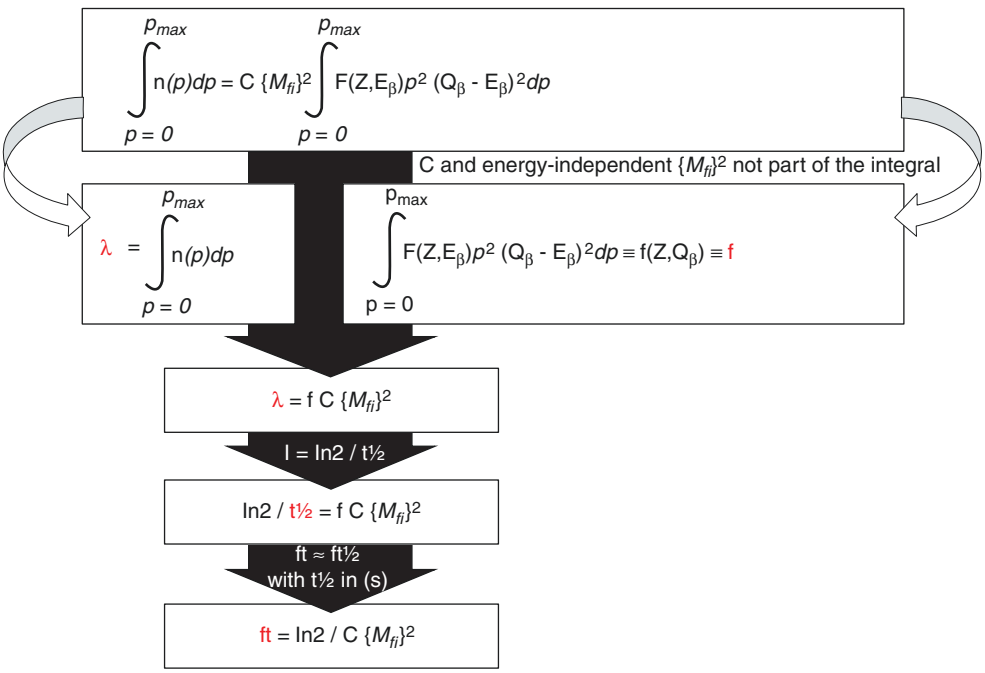

Fig. 20 Deriving a ft-parameter from the Fermi equation

functions with corresponding eigenvalues and parity operators change in the course of spatial inversion. While the three coordinates change from, *e.g.* (+x,+y,+z) to (−x, −y, −z), the quantum parameters in terms of wave functions and eigenvalues may also change or not. Parity is thus indicated as + or −.

Overall, the spin and parity of a certain nuclear level are expressed as J^Π. Now, the transformations must be discussed in terms of changes in overall spin and parity, *i.e.* ΔJ and $\Delta\Pi$: changes are $\Delta J = 0, 1, 2, 3, 4, \ldots$, and either $\Delta\Pi = +$ or $-$. The termini derived from selection rules are "allowed" and "for-

bidden" with internal gradations and reflect the dimension of the changes. Allowed transitions are either "superallowed" or just "allowed". Superallowed refers to the absence of changes in overall spin and parity, *i.e.* $\Delta J = 0$, and $\Delta \Pi = +$. They overlap with "allowed" transitions, which still remain $\Delta \Pi = +$ but may accept the lowest change in overall spin: $\Delta J = 1$.

"Forbidden": The more changes there are in J, the more the transitions become forbidden. Forbidden nuclear transitions are of much lower probability compared to less forbidden or allowed transitions: the more forbidden a transition is, the lower its velocity.

Excited States in β-Transformations

Primary transformation processes of unstable nuclides, K1, do not necessarily directly yield the ground state of the newly formed nuclide, K2. Instead, the energetically excited levels ($^{\odot i}$K2) of the new nuclide may be populated. Excited nuclear levels of a certain nucleus differ from the ground state of that nucleus simply because one or more nucleons of the nucleus exist—for a certain period of time: typically 10^{-12} s and in other cases for seconds, minutes, and years—in a higher-energy nucleon shell. (This is introduced here in the context of β-transformations but also holds true for the α-emission pathway as well.) These energetically different states all belong to the new nuclide in terms of mass number A, proton number Z, and neutron number N, but a nucleon may occupy a higher-energy nucleon shell. Accordingly, the nucleon of an excited nuclear level owns a quantum number different from the one it belongs to in its ground state. For the whole nucleus, the "overall nuclear spin" may be different compared to its ground state. Consequently, every nuclear state is defined by its characteristic set of overall spin and parity.

Figure 21 illustrates various excited levels for ^{90}Y, a β$^-$-emitting radionuclide that is medically relevant due to its role in endoradiation therapy. The ground state of ^{90}Y is 2^-, and β$^-$ transformation starts from that level. The transformation product nuclide is stable ^{90}Zr. There are two relevant individual excited nuclear states to discuss. Its highest-energy excited state ($^{\odot 2}$K2) is of 2^+. The energetically lower excited level of $^{\odot 1}$K2 is of 0^+. Next, there is a ground state, $^{\odot}$K2, which is of 0^+ again. Theoretically, there are three principle primary transformations, namely, K1 → ^{2}K2, K1 → $^{\odot 1}$K2, and K1 → ^{g}K2, with the corresponding logft values. The most probable transformations are those in which the changes in overall spin and parity are lowest. The dominating transformation is K1 → ^{g}K2, with no change in J and a change in Π. This set is true also for K1 → $^{\odot 2}$K2, but the two routes differ in their logft values: 8.1 vs. 9.4 in favour of K1 → ^{g}K2. Accordingly, the experimentally observed relative probabilities of the three possible transformations for K1 towards ^{g}K2, $^{\odot 1}$K2, and $^{\odot 2}$K2 are 99.982%, 0.017%, and < 10^{-6}%, respectively.

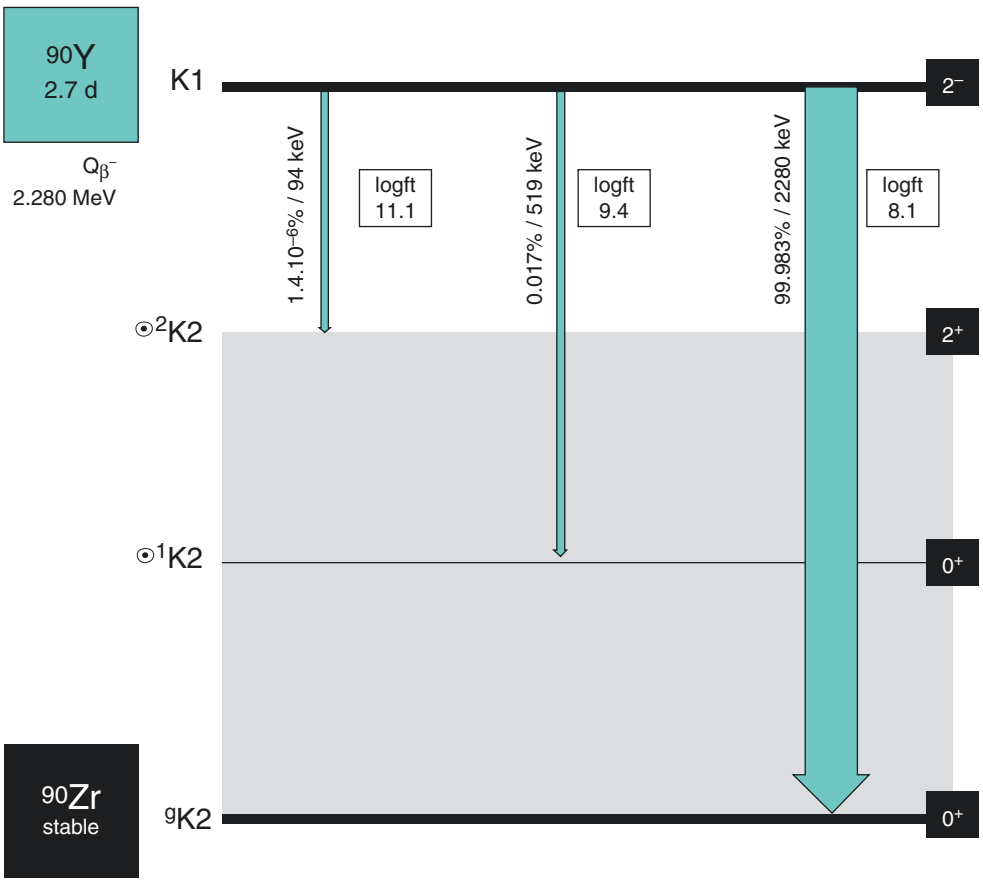

Fig. 21 β$^-$ transformation pathways of ^{90}Y towards ground-state and excited nuclear levels of stable ^{90}Zr

α-Emission

From β-Transformation to α-Emission

For all mass numbers (A) from 1 to 209, β-processes yield one definite stable nuclide or two, depending on (even, even) or (even, odd) nucleon composition (see Figs. 9 and 10). This paradigm does not continue when A > 209. As an example, let's consider the mechanism of β-transformation of the A = 226 isobar. The radium isotope 226 represents the most stable nucleon composition along this isobar. ^{226}Ra by far shows the longest half-life of this isobar at 1600 years. The neighbours at Z + i are of much lower stability, and their half-lives are in the range of hours (29 h for ^{226}Ac) and minutes (31 min and 1.8 min for ^{226}Th and ^{226}Pa, respectively) and decrease further down to milliseconds (280 ms for ^{226}U and 31 ms for ^{226}Np). For the Z-i arm of the parabola, ^{226}Fr and ^{226}Rn show half-lives of 48 s and 7.4 min, respectively. In the present case, the nuclide at the vertex of the isobar parabola of $\bar{E}_B = f(Z)$ is ^{226}Ra, yet it is not stable (Fig. 22).

Thus, β-transformation has done its best to build the most stable nuclide of the A = 226 isobar, but it has not been able to create a stable nucleon configuration. Consequently, ^{226}Ra must transform to a more stable nucleon configuration by a mode other than β-transformation. This is the moment that the unstable nuclides cannot continue following the A = constant strategy for stabilization. So, what should this unstable nuclide do? The answer lies in two classes of transformations of ^{A}K2 < ^{A}K1: cluster emission (the most relevant version is the emission of α particles) and spontaneous fission.

The emission of an α-particle immediately reduces the mass of the unstable nuclide, K1, and changes both its proton and neutron numbers: it is a primary transformation. The reason the α-particle is preferred lies in its very high "internal" stability. The mean nucleon binding energy of ^{4}He nucleus is 7.074 MeV, and the nucleus is further stabilized due to a double-magic nucleon shell configuration (Z = 2, N = 2). The α-transformation thus balances mass between the initial unstable nuclide, K1, and the transformation product nuclide, K2, in a clear way: the mass number of the new nuclide is

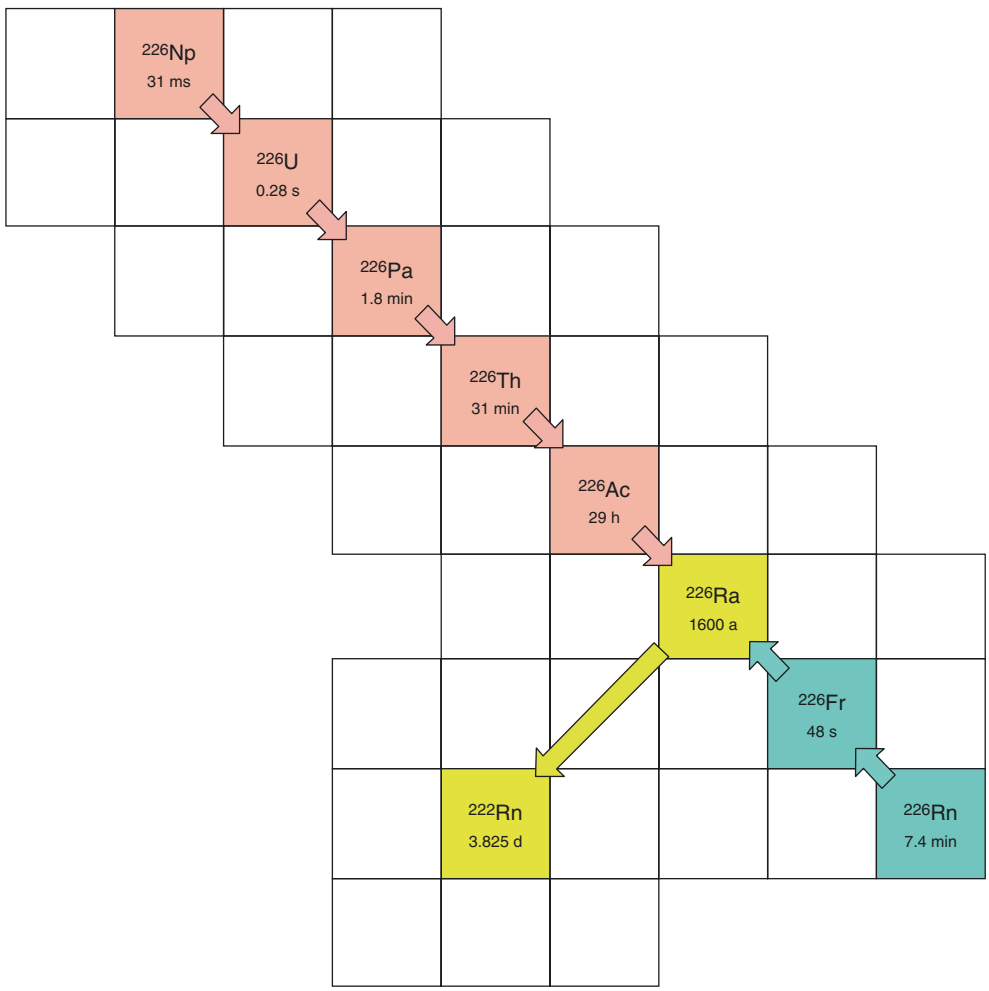

Fig. 22 β-transformation processes along the isobar *A* = 226. The most stable (but not *really* stable) and longest-lived nuclide is ^{226}Ra. This unstable nuclide of optimum mean nucleon binding energy along the isobar transforms through α-emission to ^{222}Rn, thereby switching to a new, lower isobar. In the Karlsruhe Chart of Nuclides [9], α-emitting radionuclides are indicated by yellow colour

reduced by 4. Those changes in ΔA (4) and in ΔZ (2) result in increased mean nucleon binding energies according to the LDM (Fig. 23), at least for heavy elements with A > ca. 130.

The emission of *one* α-particlemay generate a stable nucleon mixture but also may result in a nuclide that is "more stable" but not *actually* stable. This effect can be explained following the example given in Fig. 22. ^{226}Ra starts to transform by α-emission; it follows an isodiaphere line forming a product of Z-2 and N-2 composition: the transformation product is ^{222}Rn and wins mean nucleon binding energy: $\bar{E}_B$ = 7.695 MeV for ^{222}Rn vs. 7.662 MeV for ^{226}Ra. Yet, this new nuclide is not stable. The transformation may continue via another α-emission. This is exactly the case for ^{226}Ra as illustrated by the natural chain of transformations of the 4n + 2 series: ^{226}Ra originates from ^{230}Th by α-emission, and ^{226}Ra itself continues to form daughters by successive α-emission as ^{226}Ra → α → ^{222}Rn → α → ^{218}Po → α → ^{214}Pb (Fig. 24).

From α-Transformations to β-Processes

With each individual α-emission process, the nucleus increases the ratio between the number of its neutrons and protons. It is 138/88 = 1.568 for ^{226}Ra, 136/86 = 1.581 for ^{222}Rn, 134/84 = 1.595 for ^{218}Po, and 132/82 = 1.610 for ^{214}Pb. The excess of neutrons is reaching a dramatic level, and β-transformation is energetically favoured. Now, here comes the teamwork of α- and β-transformations: for ^{214}Pb, the β-process becomes the only pathway to further stabilize the nucleus. It happens along the neutron-rich arm of the isobar is parabola at A = 214 = constant until a new, local maximum of the mean nucleon binding energy for this particular isobar is reached. This new maximum of $\bar{E}_B$ could represent a stable nuclide, but this is not possible for A = 214; there is no stable nuclide. If not, a situation occurs like that explained in the beginning for transformations along the isobar *A* = 226, and another α-emission follows (Fig. 24).

Simultaneous β- and α-Emission

As indicated in Fig. 22, α- and β-transformation not only may alternate from one transformation step to the next, they may appear simultaneously for one and the same nuclide! Obviously, ΔE values may be positive for different primary transformation options. In this case, each pathway gets its individual absolute value according to the different balances in mass, for which notations are Q_α and Q_β, respectively. Figure 24 shows the routes for parallel β- and α-emission (^{214}Bi and ^{210}Pb). Another example is ^{213}Bi (Fig. 25). In addition, α-emission and electron capture may occur simultaneously as, for example, in ^{211}At. This is an example of an artificially produced radionuclide.

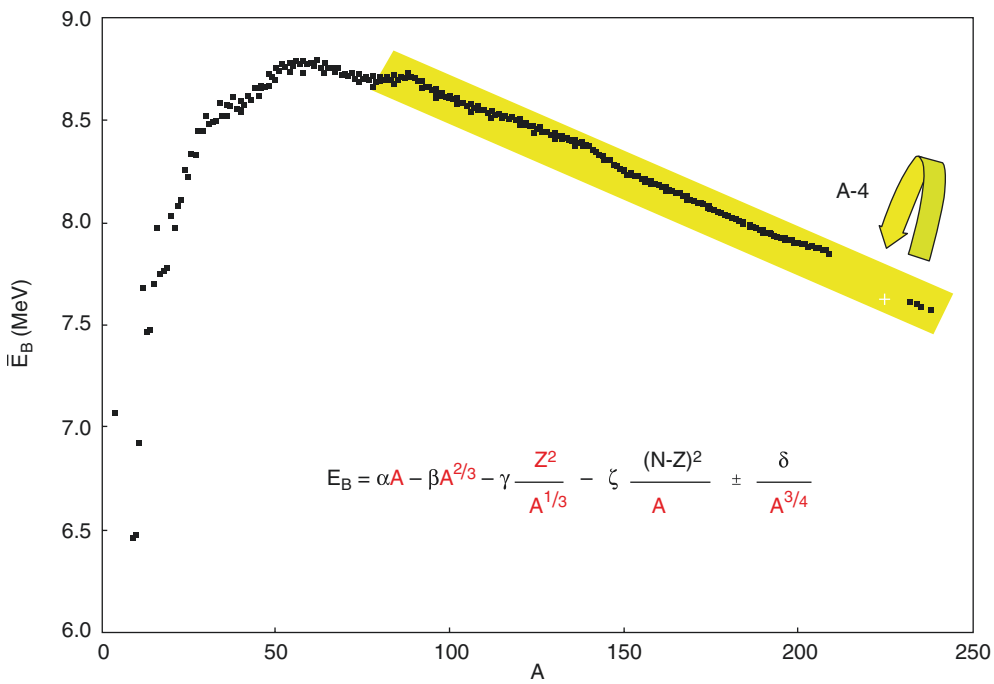

Fig. 23 Each α-emission from K1 creates a new nucleus, K2, with mass A-4, *i.e.* the new nucleus is located left to the initial one. For high mass number A (approximately above A ca. 130), this "automatically" gives a gain in mean nucleon binding energy. The corresponding values are calculated via the Weizsäcker equation, and the parameters changing between K1 and K2 are those for A, Z, and N in terms of A-4, Z-2, and N-2

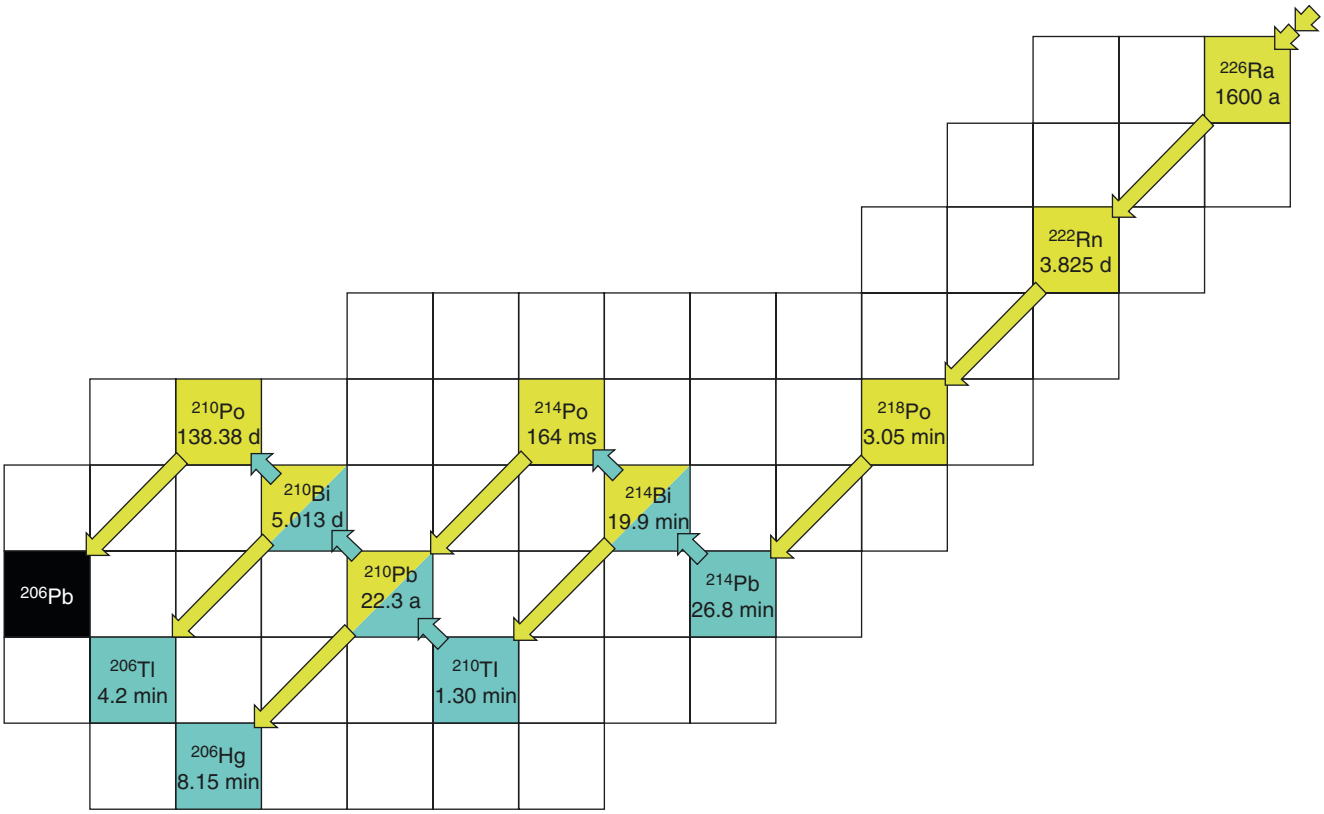

Fig. 24 Continuation of the naturally occurring ^{238}U transformation chain subsequent to the α-emissions from ^{226}Ra. The direct chain of α-emission terminates at ^{214}Pb. The next primary transformations are two β⁻-processes. At ^{214}Bi, a branched chain starts with simultaneous transformation via β⁻ and α-emission. Those individual directions finally terminate together at the stable nuclide ^{206}Pb

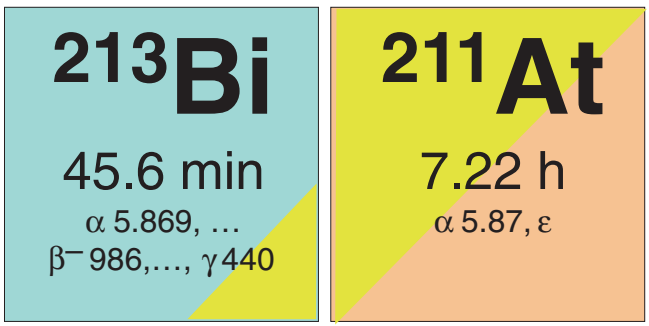

Fig. 25 Notation of parallel options of primary transformations for one and the same nuclide. ^{213}Bi: 2.1% α-emission (Q_α = 5.982 MeV, main α-energy 5.869 MeV) + 97.9% β⁻ emission (Q_β = 1.427 MeV, main maximum β⁻ energy 0.986 MeV), main γ-emission 440 keV. ^{211}At: 41.8% α-emission (Q_α = 5.982 MeV, main α-energy 5.87 MeV) + 58.2% electron capture (ε) emission (Q_ε = 785 keV). See other studies for individual numbers [4–8]. The size of the colour-coded area qualitatively indicates the proportions between the different branches of transformation

Energetics of α-Emission

Absolute Values of Q_α The α-transformation process occurs spontaneously and is nonreversible like all the other primary transformation pathways. The absolute value of Q_α basically depends on the masses of the two nuclides and their difference, accordingly, and involves the mass of the α-particle emitted. The range of Q_α values is rather small, approximately between 1 and 10 MeV.

Kinetic Energies of α-Particles and Recoil Nuclei Similar to β-transformations, the impulses ($p = m \cdot v$) and kinetic energies ($E = ½\, m \cdot v^2$) refer to the two species formed in the primary nuclear transition. This results in a balance for the α-particle emitted and K2 recoiled as $m_\alpha \cdot E_\alpha = m_{K2} \cdot E_{K2}$. The overall energy, Q_α, is allocated to the α-particle emitted and the recoil nucleus ^{RECOIL}K2 according to the following equations.

$$p_{K2} = p_\alpha$$

$$Q_\alpha = {}^{RECOIL}E_{K2} + E_\alpha$$

Kinetic energies are distributed between the α-particle and K2 directly and depend only on the mass number of K2 (the mass of the α-particle is always the same). Consequently, the kinetic energy of the α-particle is discrete. Its value is nuclide-specific and representative, like a fingerprint. Absolute values of kinetic energies of the α-particle are

Table 4 Values of Q_α and kinetic and recoil energies of the transformation products of the ^{238}U α-emission process. Mass excess data are used to determine Q_α. The kinetic energies of the α-particles are obtained by simply using mass numbers

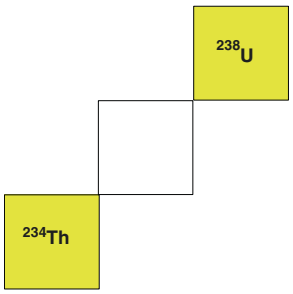

Q_α	$= \Delta E = \Delta m^{excess}{}_{*K1} - (\Delta m^{excess}{}_{K2} + \Delta m^{excess}{}_{\alpha})$ $= 47.3091 - (40.6140 + 2.4249)$ MeV $= 4.270$ MeV
E_α	$= Q_\alpha / (1 + m_\alpha / m_{K2})$ $= 4.270$ MeV $/ (1 + 4/234)$ $= 4.198$ MeV
$^{RECOIL}E(^{234}Th)$	$= Q_\alpha - E_\alpha$ $= 4.270$ MeV $- 4.198$ MeV $= 0.072$ MeV

higher in the case in which the Q_α-value is high and the mass number of the nuclide is low.

$$E_\alpha = \frac{Q_\alpha}{1 + \frac{m_\alpha}{m_{K2}}}$$

Table 4 gives the corresponding numbers for the α-emission of ^{238}U.

Velocities of Transformation

Q_α values correlate with the half-life of the radionuclide. This exactly has the same tendency as discussed for β-transformations. The larger the Q_α-value, the larger the gain in energy a nuclide "wins" in terms of mean nucleon binding energy, $\Delta\bar{E}_B$, when transforming (and the faster the transformation proceeds in terms of short half-life $t_{½}$ or large transformation constant, λ). Similar to β-transformation, α-transformations cover half-lives of milliseconds to billions of years. Figure 26 shows an experimental α-spectrum generated by the naturally occuring transformation chain of $^{228}Th \rightarrow {}^{224}Ra \rightarrow {}^{220}Rn \rightarrow {}^{216}Po$. It reflects the relationship between the energy of the α-particle and the half-life of the transformation: the higher the energy of the α-particle, the shorter the half-life.

Quantum Mechanics of α-Transformation Phenomena

The Quantum Mechanical Phenomenon of "Tunnelling" Let's consider the nucleus ^{238}U again. The protons inside induce a potential energy U^C due to coulomb forces of ≈ 28.5 MeV at a radius of 9.3 fm, the radius of the uranium nucleus. Consequently, one must expect that an α-particle leaving this nucleus should have at least 28.5 MeV energy. However, the kinetic energy of the emitted α-particle is 4.198 MeV (only!), as calculated in Table 4. It precisely corresponds to the experimentally measured kinetic energy of the α-particle as released from ^{238}U. What's wrong? Nothing! The key wording here is "tunnelling", and this phenomenon may look like the schematic drawn in Fig. 27. The α-particle has left the potential well and has "tunnelled" through the potential wall. It becomes a "free" particle. The kinetic energy of the α-particle after tunnelling through the Coulomb barrier is much lower than the height of the barrier and corresponds to the energy at which tunnelling was successful.

Mathematics of the Tunnel Effect As introduced for β-transformation, quantum mechanical models consider an initial and a final state of a transformation, with a corresponding probability, p_{fi}, of transition (per unit of time) from one energy of a quantum system (nuclide K1) into another one (nuclide K2). For α-emission, there are three particular aspects:

1. Prior to the emission, the α-particle must be preformed as such inside the homogeneous ensemble of the many individual nucleons within the large nucleus. This may happen with a given probability due to the special stability of the $Z = 2 + N = 2$ cluster of double-magic shell characteristics of the ^4He nucleus, the α-particle.
2. Suggesting the cluster was formed anywhere within the nucleus, this cluster must be present close to the surface of the nucleus. This includes an anticipated sort of "transport" or "diffusion".
3. Only following this imaginary formation and virtual transport, the tunnelling itself of the particle through the barrier is discussed.

Figure 28 illustrates this phenomenology. Although there is evidence for the processes of the preformation of an α-particle [1] and its diffusion to the surface of the nucleus [2], the mathematical model subsumes these two steps into the frequency factor, f (also called the "reduced transition probability"). This describes how often an α-cluster appears at the surface of the nucleus and "knocks on the door". Once it has appeared at the surface, it gets a chance to leave the nucleus via the tunnelling effect. The probability for this step is defined by the penetrability factor, P (also the "transition factor" or "penetrability").

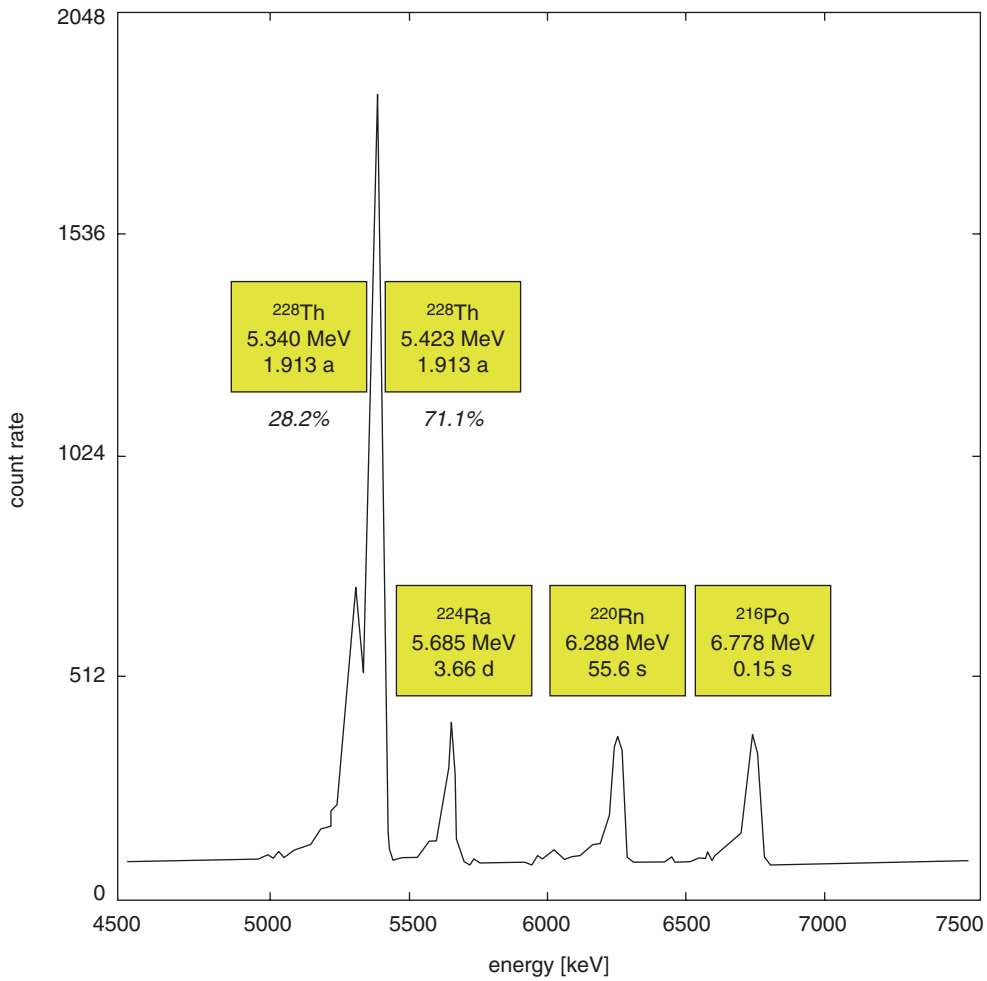

Fig. 26 Experimental α-spectrum including the four α-emitting members successively formed in the ^{232}Th chain. The higher the energy of the α-particle emitted and the Q_α values (given in MeV), the shorter the half-life. ^{228}Th (Q_α = 5.520 MeV, E_α = 5.340 and 5.423 MeV $t_{½}$ = 1.913 a), ^{224}Ra (Q_α = 5.789 MeV, E_α = 5.685 MeV, $t_{½}$ = 3.66 d), ^{220}Rn (Q_α = 6.405 MeV, E_α = 6.288 MeV, $t_{½}$ = 55.6 s) and ^{216}Po (Q_α = 6.907 MeV, E_α = 6.778 MeV, $t_{½}$ = 0.15 s)

The two components to handle this mathematically are the factors *f* and P. Both factors determine the overall efficacy, and the concept is to define the total velocity of an α-emission as a product, reflecting the velocity of the α-transformation in terms of the transformation constant $\lambda = fP$. The individual expressions for the two factors are summarized in Fig. 29.

Most of the parameters involved in the equations in Fig. 28 reflect basic properties of the atomic nucleus: E^C = energy of the potential wall (typically around 28 MeV and 30 MeV); m´ = reduced mass ($m' = m_\alpha\, m_{K2}/(m_\alpha + m_{K2})$, *i.e.* for heavy elements $m' \approx m_{K2}$); Z_{K2} = proton number of K2; Q_a = overall energy of the α-transformation; and r_{K2} = radius of K2. G is the Gamow factor and its values are on the order of *G* = 30–60. With this dimension it becomes clear that the probability of penetrating (tunnelling) a potential well is extremely low. The same is true for the frequency factor. Depending on the proton number, it is about $Z_{K2}^{-4/3}$, which makes it $1.9 \cdot 10^{-20}$ s^{-1} for Z_{K2} between 58 and 98.

Excited States in α-Transformations

As in β-transformation, α-transformations do not necessarily yield the ground state of the nuclide K2 directly but may populate energetically enriched levels of the newly formed nuclide. Figure 30 shows two α-emitting nuclides, with the α-emission producing the ground state of K2 directly and exclusively (^{212}Po) or a transformation cascade through several excited states (^{226}Ra.)

Spontaneous Fission

For unstable nuclides of increasing mass number of about A > 234, α-emission is a promising choice of transformation. However, there is another possibility, the third and final type of primary transformation process—spontaneous fission—which creates even larger differences in ΔA. This option appears at very large nuclei. Fission yields two fragments, K2 and K3, of the initial nuclide K1 with characteristic mass distributions. Spontaneous fission is not discussed further in this chapter, because it is not relevant to radiopharmaceutical chemistry and nuclear medicine. It must be mentioned, however, that induced fission, *e.g.* of ^{235}U, is indeed relevant, if only farther up the chain: it is the main source of fission products such as ^{99}Mo and ^{90}Sr, which are of the upmost importance to nuclear medicine.

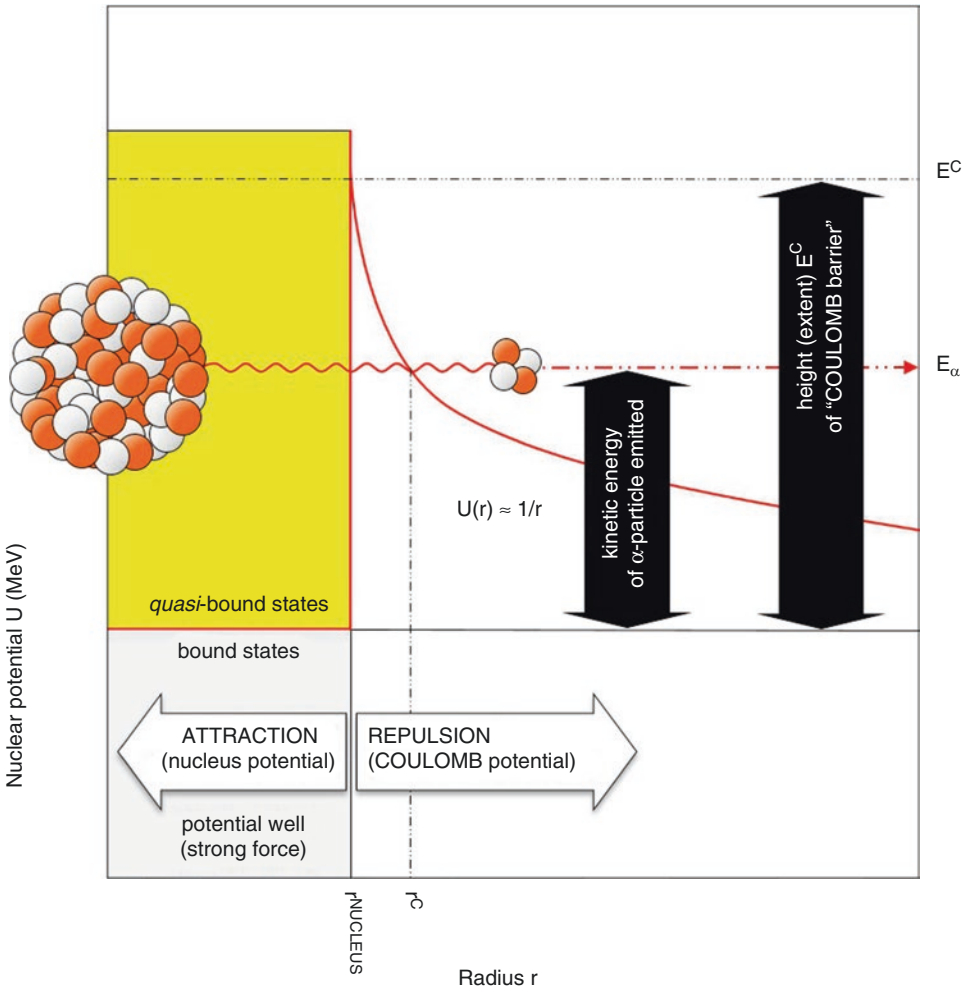

Fig. 27 Concept of the tunnelling of an α-particle through a Coulomb barrier of a nucleus. E^C gives the amount of potential energy due to the Coulomb forces, and E_α the kinetic energy of the α-particle after tunnelling at a virtual radius r^C

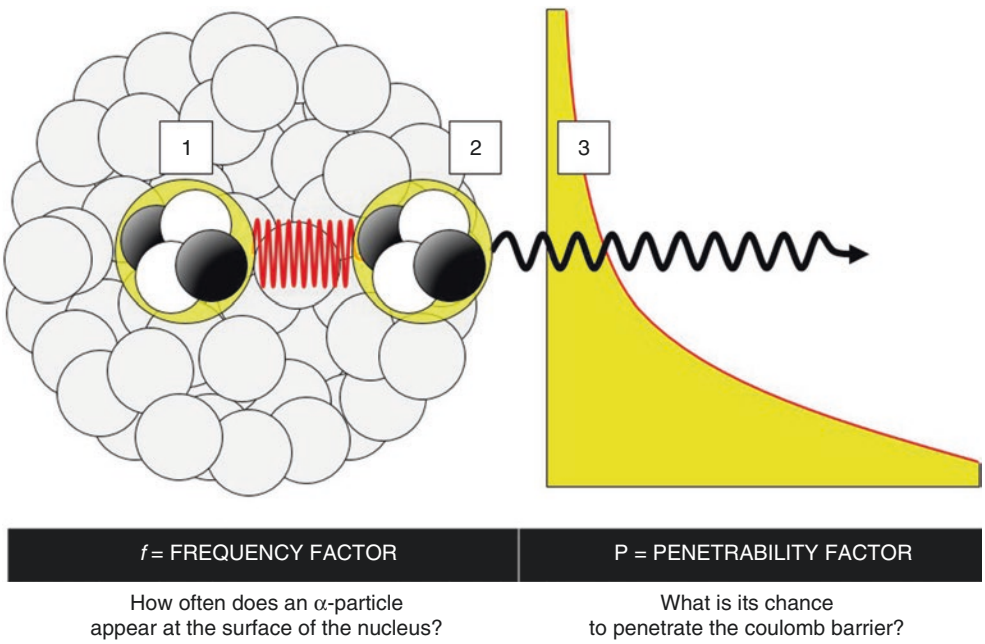

Fig. 28 Phenomenology of the α-emission process in terms of frequency factor and penetrability factor: (**1**) the *formation* of an α-particle inside the nucleus, (**2**) the delivery of this nucleon cluster towards the surface of the nucleus, (**3**) the release of the α-particle and tunnelling the Coulomb barrier of the nucleus

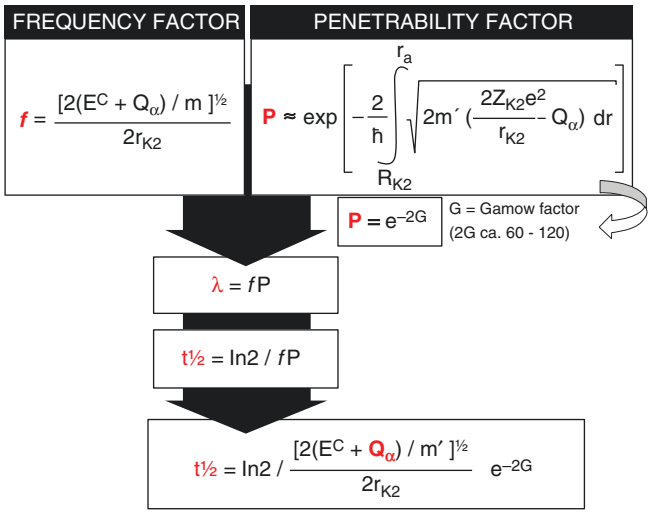

Fig. 29 Half-lives of α-emission correlated with quantum mechanical parameters: Key parameters are the frequency factor, *f*, and the penetrability factor, P. The exponent in P is called the Gamow factor, G

Secondary Transformations

From Primary to Secondary Transformations

Excited Nuclear States As already indicated in the sections on the "Post-processes of Primary Transformations and Secondary Transitions" for β- and α-processes, a primary transformation does not necessarily lead to the ground state of the new nuclide K2 formed. Instead, individual excited states, $^{\odot i}$K2, are populated. Excited nuclear levels appear when one or more individual protons or neutrons of the newly formed nucleus K2 do not immediately find themselves within the nucleon shells corresponding to the ground state of the nucleus. Instead, they occupy higher-energy shells.

Similar to excited electrons of an atomic shell, these nucleons "fall" towards lower-energy nuclear levels. The transitions from a higher-energy nuclear state may proceed to a lower-energy excited nuclear state or to the final ground

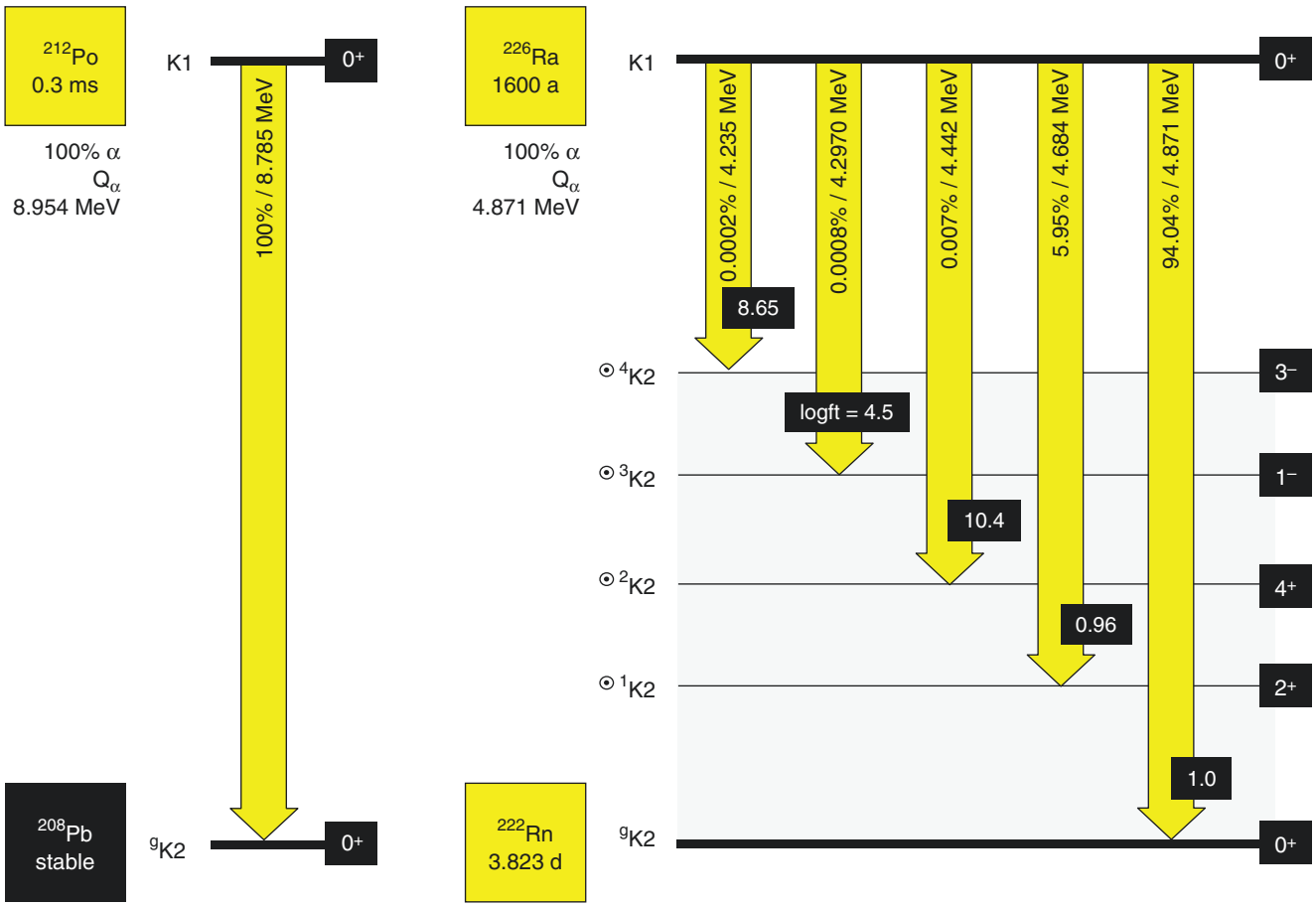

Fig. 30 *Left*: α-emission as direct transformation into the ground state of K2 (^{212}Po → ^{208}Pb). Overall spin and parity are indicated for K1 and ^{g}K2. There are no changes. *Right*: α-emissions of ^{226}Ra populating several excited states of ^{222}Rn. Symmetry parameters are indicated for K1 and ^{g}K2 and for four excited levels, $^{\odot i}$K2, of ^{222}Rn. Each arrow shows the logft value for the transformation, the corresponding abundance of the five individual α-emissions, and the corresponding energies of the α-particles emitted. Kinetic energy of the emitted α-particle is maximum for K1 → ^{g}K2 (4.871 MeV). The most probable transformation is K1 → ^{g}K2 (94.04%) because of overall spin and parity values that are identical for both nuclei

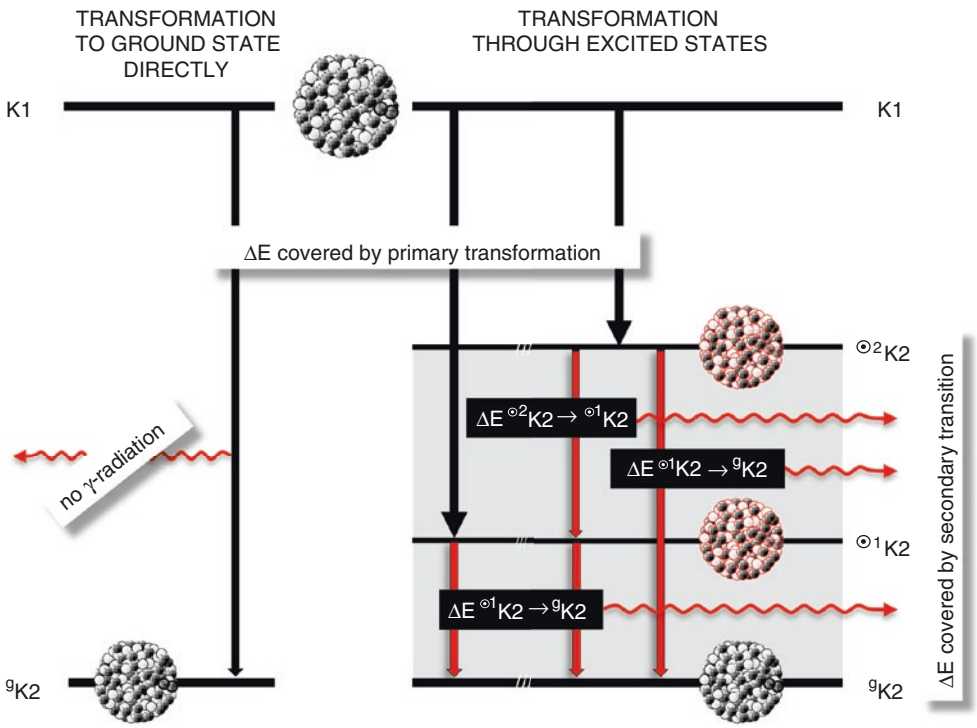

Fig. 31 Excited nuclear states of the newly formed nucleus, K2, populated in primary transformations de-excite to lower-energy nuclear levels. Each excited and ground-state level of a particular nucleus owns its set of quantum numbers (such as overall spin and parity) and a characteristic energy. Theoretically, all possible transitions may occur, such as from each excited level directly into the ground state or from each excited level to the ones of lower energy. Transitions between two levels involved address a specific amount of energy, as represented by ΔE between the two levels. The question is how that specific amount of ΔE is managed by the nucleus. As shown in this illustration, there are three options

state of the nucleus, ^{g}K2. In each case, the specific differences of ΔE between the two nuclear levels are carried away by "secondary" transitions (Fig. 31). It is the essence of secondary transformations that the numbers for Z, N, and A do not change as long as only the individual nuclear levels of the product nucleus K″ are involved. This is the reason the terminology "transition" is preferred instead of "transformation".

Metastable Nuclides/Nuclear Isomers De-excitation between individual excited states or finally from one excited state to the ground state is very fast, typically lasting only 10^{-16} to 10^{-13} s. The overall secondary transformation is thus extremely fast, even when cascades of several transitions are involved. However, individual excited states, $^{\odot i}$K2, may show half-lives much longer than the half-lives of the other excited levels of one and the same nuclide, $^{\odot}$K2.

This is often observed for very small values of $^{\odot i}$ΔE and in the context of selection rules, *i.e.* whenever the differences in overall angular momentum are large (octa-, hexa-, or higher multipole orders) or the parity is violated (see below). This excited state is not *really stable* (this is true for the ground state of ^{g}K2, exclusively) but nevertheless remains "meta"-stable for a significant period of time and is referred to as ^{m}K2. Compared to the ground state, it reflects a nucleus of identical nucleon composition in terms of A, Z, and N and is therefore also referred to as "nuclear isomer". There are many *meta*stable isomers with half-lives in the range of minutes, hours, days, and years. The Chart of Nuclides involves more than 3000 stable and unstable nucleon configurations. In addition, about 700 of these nuclides show (at least one) metastable isomers. Some of these metastable radionuclides are of interest in fundamental research; others are relevant to important practical application. Such an example is depicted in Fig. 32: the ground-state and the metastable states of technetium-99. The *meta*stable ^{99m}Tc is the most relevant radionuclide in diagnostic nuclear medicine. Its half-life is 6.0 h. Its secondary transition in terms of γ-emission releases a 141 keV energy photon of high (89%) branching.

Options for Secondary Emissions

There are three principal routes to manage the difference in energy, ΔE, between different excited levels or one exited level and the ground state of a given nucleus.

The most frequently occurring (and for the detection of radioactive transformation very valuable) sort of secondary emission consists of the release of electromagnetic radiation as γ-quanta, *i.e.* photons, with $\Delta E = E_{\gamma}$. The second option is the

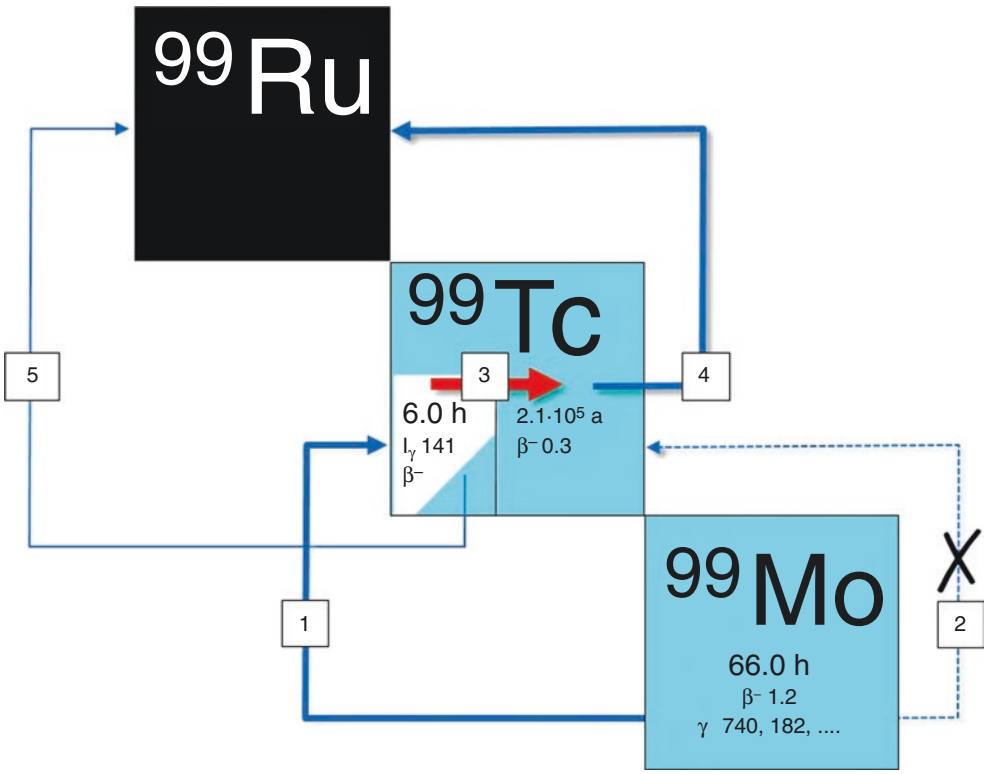

Fig. 32 Metastable nuclear isomer ^{99m}Tc and ground state ^{99g}Tc (**2**) of technetium-99 show individual half-lives. ^{99m}Tc is populated (**1**) in high abundance from ^{99}Mo in the course of its many β⁻-transformations to individual excited nuclear levels of technetium-99, while there is no direct β⁻-transformation to the ground state ^{99g}Tc (**2**). ^{99m}Tc de-excites dominantly in a secondary transition accompanied by photon emission of 141 keV energy to the ground state ^{99g}Tc (**3**). The ^{99g}Tc continues the stabilization via β⁻ transformation to the ultimate stable nuclide of the A = 99 isobar: ^{99}Ru (**4**). In parallel, yet with a much lower probability, the metastable ^{99m}Tc may transform independently via a direct β⁻-transformation to ^{99}Ru as well (**5**)

conversion of this particular amount of ΔE into the release of an already existing electron of that nuclide from its inner electron shell, creating a "conversion electron". The third option is the transformation of ΔE directly into matter according to $E = mc^2$. It creates a pair of two particles, representing matter (electron) and *anti*matter (positron). Note that the three pathways may occur simultaneously for one and the same transition.

Photon Emission According to the standard model, the photon is an elementary particle (see Table 3). It belongs to the field quanta and is the mediator of the electromagnetic force. Different from other mediators, its mass is zero. Still, it obeys the wave-particle duality of quantum mechanics. It is of no charge, and because its charge is zero, it has no *anti*-particle. Its spin is 1, and because of that, it is a boson. Its parity is −1 (Fig. 33).

The electromagnetic radiation created emitted from unstable nuclei can be divided into two subparts: γ-radiation and X-rays. Both represent photons, but the difference is not the absolute value of frequency, wavelength, and energy. Instead, it is their origin.

γ-Rays Gamma radiation here is meant to originate *from the nucleus* of a radionuclide via the de-excitation of an excited level of the nucleus. In terms of wavelength, it is approximately $<10^{-11}$ m (which is <10 pm or < 0.1 A, *i.e.*

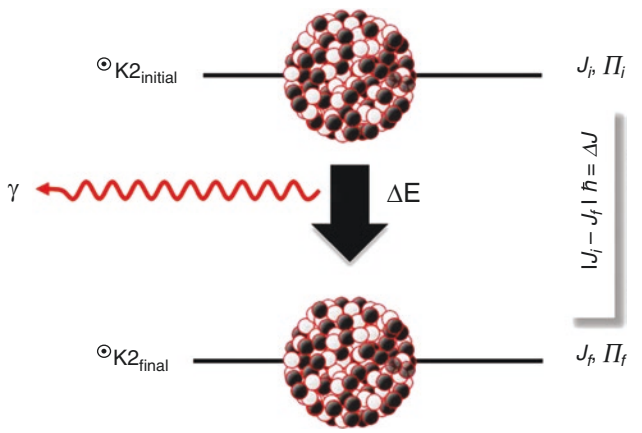

Fig. 33 De-excitation between two excited nuclear states defined by quantum physical parameters J and Π for initial and final state. Both levels are characterized by the energy differences ΔE between the two states, the orbital quantum number (l), the magnetic orbital quantum number, the spin quantum number (s) and the resulting overall orbital momentum (L), the overall angular momentum (S), and the overall momentum (J) obtained from orbital-spin coupling. The characteristic difference in energy, ΔE, is released as γ-radiation. The transition via photon emission proceeds in specific values of ΔJ, and the photon must carry away this difference in overall momentum

shorter than the diameter of the nucleus of the atom); in terms of energy, it is >0.1 MeV.

X-Rays In the framework of radioactive processes (but also in conventional X-ray spectroscopy), electromagnetic radia-

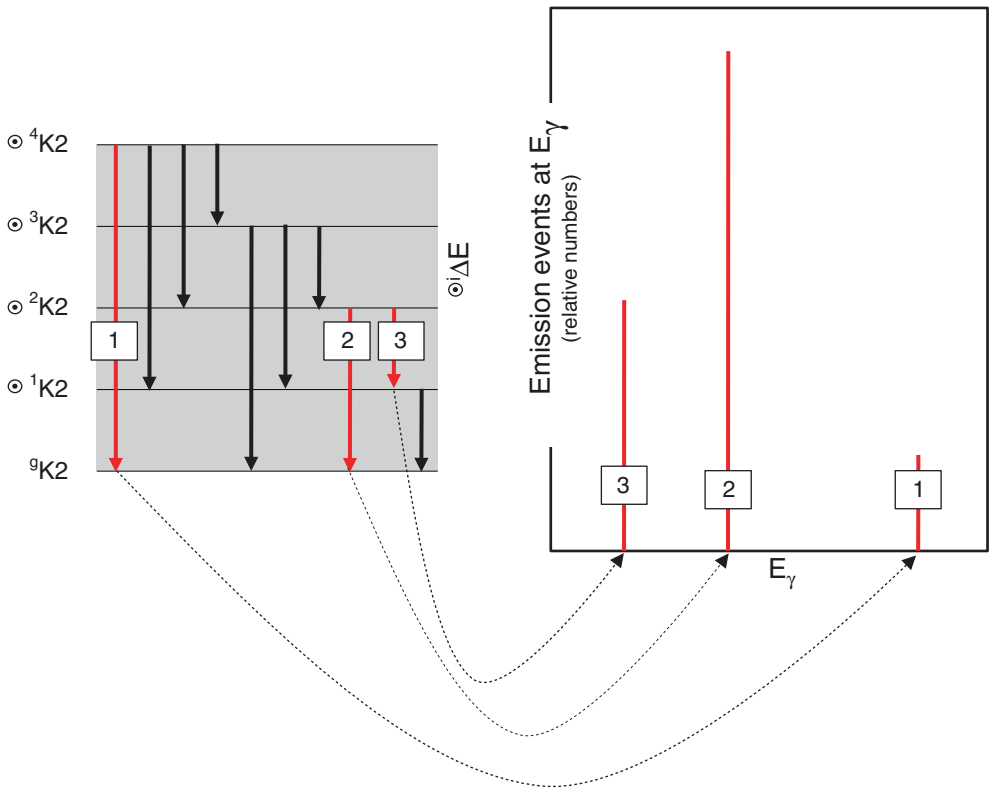

Fig. 34 Hypothetical cascade of secondary transitions for altogether three excited and one ground-state states of K2. For simplicity, three transitions are selected in red, namely $^{\odot}$K4 → ^{g}K2, $^{\odot 2}$K2 → $^{\odot 1}$K2, and $^{\odot 2}$K2 → ^{g}K2. In terms of ΔEγ, the order is $^{\odot}$K4 → ^{g}K2 > $^{\odot 2}$K2 → $^{\odot 1}$K2 > $^{\odot 2}$K2 → ^{g}K2. This is how the three photon emissions are recorded in the G-spectrum as f(ΔEγ). What about the intensity of the three lines? It is given here as Iγ = $^{\odot 2}$K2 → $^{\odot 1}$K2 > $^{\odot 2}$K2 → ^{g}K2 > $^{\odot}$K4 → ^{g}K2. The question is, how can we explain the individual branching of the three selected emissions?

tion emitted *from the shell* of the atom—*i.e.* not from the nucleus—is signified as X-radiation (the creation and properties of those X-rays is discussed later under post-processes I). Compared to γ-rays, their wavelengths are higher (ca. 0.01–10 nm), and their energies are lower (ca. 0.1 keV to ca. 0.1 MeV). Thus, the spectral domain of X-ray lies between γ-rays and UV light. In terms of energy, a further phenomenological notation relates to the penetration power of the radiation and discriminates between "soft" X-rays (energies <10 keV) and "hard" X-rays (~10–120 keV).

According to the shell model of the atomic nucleus, the quantum number (basically the spin-orbit quantum number) of a nucleon within a higher shell may differ from those within lower shells. Accordingly, the overall spin of the excited nuclear level of that nucleus may differ from the overall spin of its ground state. Those changes between individual levels have to be seen in the light of quantum physics, *e.g.* how do overall spin and parity change? Let's take an arbitrary example to identify the problem and also to understand the creation of a γ-spectrum. Figure 34 shows a hypothetical cascade of secondary transitions for altogether three states of K2: two excited ones, $^{\odot 2}$K2 and $^{\odot 1}$K2, and the ground state, ^{g}K2. Starting from K1, there are many possible transitions. The question is whether these different options proceed with identical probabilities? Or are some of the transition steps preferred and others not? If the latter is true, then why?

Indeed, all of the potential steps have an individual branching. The reason for this defined protocol takes us back to intrinsic quantum physical parameters of the nucleons and of a certain nuclear state: overall orbital momentum (spin) and parity. Similar to primary β- and α-transformations, secondary photon transitions are also defined by initial and final wave functions as well as a transition matrix element. The most relevant quantum physical parameters needed for each initial and final state are the overall momentum *J,* and the parity II.

Conservation of Orbital Momentum Whenever a secondarytransition occurs, accompanied by the emission of a photon (*i.e.* $^{\odot i}$K2 → $^{\odot(i-1)}$K2 + γ), the process must conserve quantum physical parameters. For the orbital momentum, the balance of spin is $J(^{\odot i}\mathrm{K2}) = J(^{\odot(i-1)}\mathrm{K2}) + l_{\gamma}$. The photon takes away a spin of $l = 1$. Consequently, such a transition is impossible in the case $J(^{\odot i}\mathrm{K2}) = 0$ and $J(^{\odot (i-1)}\mathrm{K2}) = 0$, *i.e.* ΔJ must be >0 to allow for the emission of a photon.

Transition Probabilities for Multipoles of Different Orders Because the nucleus represents electromagnetic multipoles of different orders (multipoles, dipoles, quadrupoles, *etc.* depending on momentum numbers), there are selection rules for the release of photons. The selection rules refer to the important impact coming from the orbital moments. Individual velocities, λ, are a measure of transition

probabilities: large values of λ (short half-lives) would indicate high probabilities and *vice versa*. Typically, those half-lives are extremely short and cover nanoseconds and picoseconds.

Conversion Electrons

"Inner conversion" or "internal conversion" (IC) represents a situation in which the difference in energy, $^{\odot i}\Delta E$, between two nuclear levels is *directly* transferred to an atomic shell electron. If that amount of energy is larger than the electron binding energy of that electron shell, $E_{B(e)}$, an electron is ejected from the atom. All of the internal conversion electrons ejected are former s-orbital electrons, and most of these electrons originate from s-orbital as "close" to the nucleus as possible. The kinetic energy, E_{IC}, of the ejected electron is equivalent to the value of $^{\odot i}\Delta E$ minus the energy, which was needed to overcompensate for the electron binding energy (Fig. 35). Internal conversion electrons thus have a discrete energy, different from β^- electrons.

$$E_{IC} = {}^{\odot i}\Delta E - E_{B(e)}$$

Internal conversion is a domain for low-energy $^{\odot i}\Delta E$ transitions and in particular for monopole modes of $0^+ \rightarrow 0^+$, for which γ-emission is not possible.

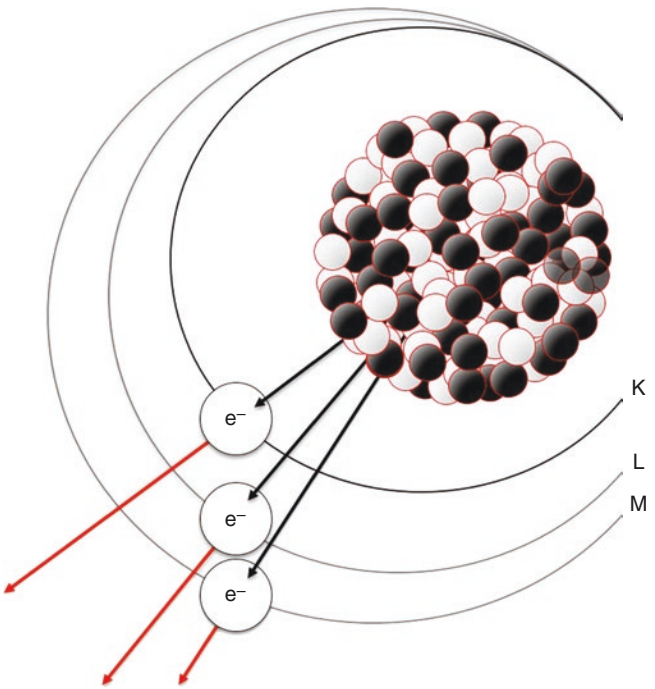

Fig. 35 Origin of internal conversion electrons from individual s-shell orbitals of individual main quantum number n, *i.e.* K-shell, L-shell, etc.

Pair Formation

The third pathway of secondary transitions is "pair formation". In this case, the equivalent of $^{\odot i}\Delta E$ is converted into real matter: an electron and its *anti*particle, the positron. The masses of both particles are 0.511 MeV (or 0.00055 u). As a result, pair formation thus exclusively emerges in cases in which $^{\odot i}\Delta E > 1.022$ MeV. Clearly, this only occurs for relatively high differences between the energy of the two nuclear levels involved.

Post-processes of Primary Transformations and Secondary Transitions

Finally, there are additional processes—termed post-processes—which inherently accompany some of the primary and secondary processes. In principle, there are two classes of post-processes. The first kind is caused by vacancies in the electron shell of the transforming atom and the pathway the atom chooses to refill those holes. The second is caused by electrons, which initially originated from primary transformations or secondary transitions, namely, beta particles (the positron or the electron) and IC electrons. It is of upmost importance to note that these two classes of post-effects in turn create *new kinds of radioactive emissions*, which are not yet seen in primary and secondary processes.

Vacancies of Shell Electrons

Remember that the primary electron capture transformation involves the capture of a shell electron to combine with a proton in the atoms nucleus. Remember also that the secondary inner conversion process is predicated on the release of a shell electron due to the de-excitation of excited nuclear levels (Fig. 36). Yet even when these two processes are done forming a new *nucleus*, the newly formed *atom* is still "not ready". It lacks an electron in its shell, *i.e.* $Z \neq e$.

Let's have a look how the new-born atom handles this vacancy in one of its shell. Electron vacancies typically appear in electron shells close to the nucleus. The K-shell is preferred, the L-shell is less affected, *etc.* (Note that only s-electrons are also involved, no matter what shell is affected.) There are two different pathways, each of which handles this vacancy promptly and induces different radiative emissions (see below).

Electron Vacancies Filled via Electromagnetic Radiation The first approach to refilling an electron vacancy proceeds through the *import* of electrons located in the higher shells of that atom. Figure 37 illustrates the pathways for filling a vacancy in the K- or L-shells. Any electron

hole is typically filled from an electron from the shell close to it. Typically, an L-shell electron fills a K-shell electron vacancy. In parallel, an electron from the N-shell may transit to the same K-shell electron vacancy, but this process is less common. Suppose the initial vacancy appeared in the L-shell, analogous electrons from the M- or N-shell may fill that hole. The transitions are named K_α or K_β for L→K or M→K and L_α or L_β for M→L or N→L, respectively. Here, K or L indicate the position of the hole to be refilled, and the Greek index indicates whether the arriving electron descended from the closest (α) or the next (β) main shell.

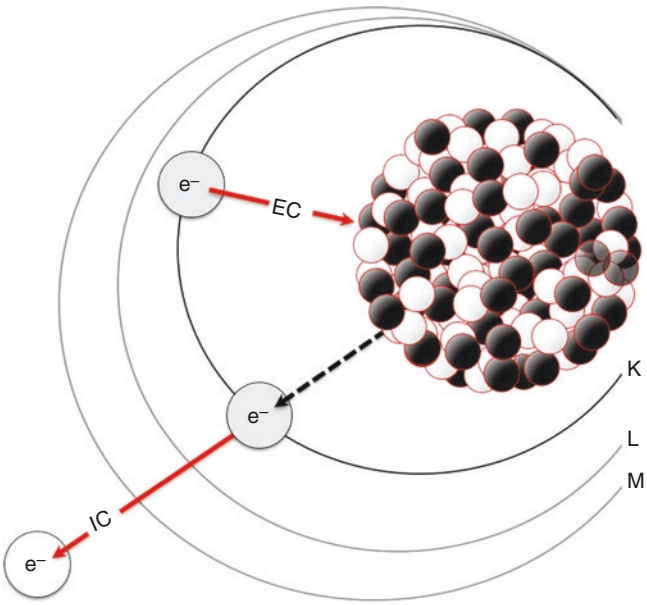

Fig. 36 Post-effects motivated by a vacancy in an electron shell of the atom. This occurs after a primary electron capture transformation of a proton-rich nuclide or after a secondary internal conversion

Characteristic X-Rays Electron energies are a function of the main quantum number: $E_{B(e)}(n) = -R_H Z^2 . 1/n^2$, R_H is the Rydberg constant, 13.6 eV. The difference in binding energies of the electron between the initial state and the final state (the original hole) is obtained as indicated in Fig. 37. Consequently, there is a characteristic difference in energy, ΔE, which is released in terms of electromagnetic radiation, depending on Z and Δn. This energy is called an X-ray (rather than a γ-ray) because of its different origin. For a given nucleus (Z), the X-rays get characteristic values, depending on the shells involved.

Electron Vacancies Filled via Electron Emissions Electron vacancies as created in Fig. 35 can also be refilled by a *radiation-free* process. The basic step remains the same: the transit of an electron from a nearby higher shell. The difference is that the amount of ΔE this time is not released as X-ray but is spent to release another electron from a higher shell. The process is referred to as a radiationless "reorganization" due to a "direct" interaction of two electrons. This particular electron is immediately ejected from the atom. In this case, no electromagnetic radiation is emitted. If electrons are emitted in the course of processes between different main shells (interstate transitions), they are called Auger (A) electrons. If the pathway involves sub-

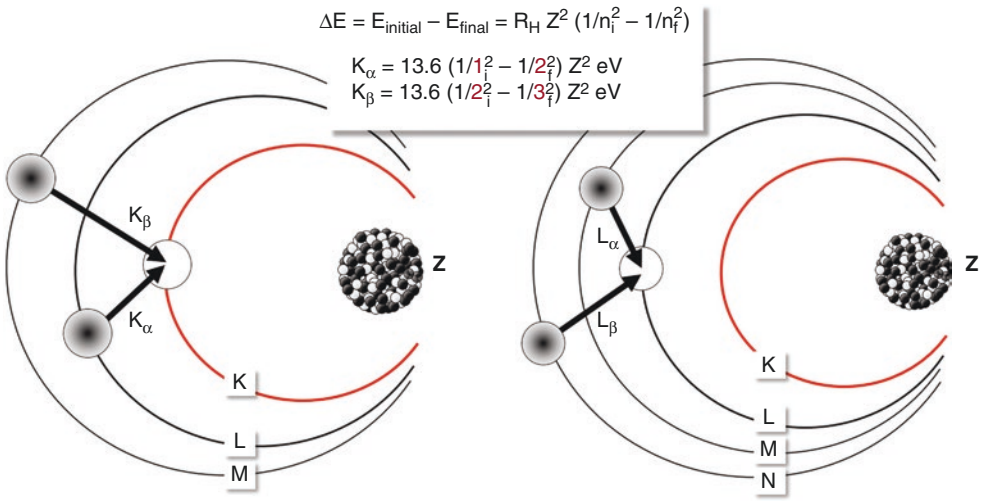

Fig. 37 Transitions of electrons from higher shells to a vacancy in a K-shell (left) or L-shell (right) and their notations. Red represents the K-shall the electron vacancy is created. The hole is filled via successive transitions of electrons from higher-energy shells (L, M, N, *etc.*) with decreasing probability. ΔE is the difference in electron binding energies between the initial shell where the transiting electron originates and the final shell where the vacancy is. R_H is the Rydberg constant, 13.6 eV. Furthermore, there are notations such as $K_{\alpha 1}$ and $K_{\alpha 2}$. This indicates electron transitions into the K-shell vacancy from two different energetic levels within the L-shell (due to the different quantum numbers $l = 0$ and 1). Their differences in ΔE are very low, and the relative abundances between values of $K_{\alpha 1}$ and $K_{\alpha 2}$ are about 2:1

shells of one and the same main shell, they are called intrastate transitions or Coster-Kronig (CK) electrons.

The overall number of electron ejected thus is larger than the number of all the shells (and subshells) of a given atom and thus is larger in the case of chemical elements of high main quantum number relative to those located in lower quantum number periods. Indeed, the overall number of A and CK electrons ejected increases with increasing Z but does not directly mirror the number of atomic electron shells in the corresponding elements. The final state after emission of all the shell electrons leaves a highly charged cation instead of a neutral atom. ^{125}I, for example, is a nuclide which primarily transforms through electron capture to an excited state of ^{125}Te, leaving a vacancy in the K-shell. In this case, the number of Auger and Coster-Kronig electrons emitted is about 25. This, of course, must cause dramatic changes in the chemical environment of that newly created atom.

The energy of the electrons emitted parallels the binding energies of the individual shells involved. Typically, A and CK electrons are within a range of approximately 20 to 500 eV. Though each electron thus gets an individual discrete energy, but the various electrons emitted within several shell cascades represent a mixture of several characteristic energies.

X-Ray Emission Versus Electron Emission Once a vacancy in an s-shell electron is handled, the radiative and radiation-less post-effects proceed in parallel yet with individual ratios between the two pathways. The fluorescence yield, $\omega_{X\text{-}ray}$ (ω_K, $\omega_{L'}$ …), gives the percentage for the filling of an electron vacancy through radiative processes. The total process of addressing the hole created by primary or secondary transformations of an unstable nuclide than is $\omega_{X\text{-}ray} + \omega_{(A)+(CK)} = 1$. The ratio between X-ray and Auger and Coster-Kronig electron emission depends on the proton number of the nucleus and thus the absolute energies of the electrons and the relative differences between individual electron shell levels. Fluorescence dominates at higher Z.

Post-Effects Caused by Emitted Electrons

The second sort of post-effects is caused by electrons which initially originate from primary or secondary transitions, namely, beta particles (positrons or electrons) and IC electrons. Post-effects here are due to the way these particles interact with the surrounding condensed matter.

The Destiny of the Positron Let's start with the positron, which itself is an *anti*matter particle. It thus is supposed to annihilate with its matter counterpart, the electron (Fig. 38, *left*). This annihilation happens whenever a positron is created. Clearly, this occurs after the primary β^+ transformation of a proton-rich nuclide. However, a positron can also be created (together with an electron) in the process of pair formation.

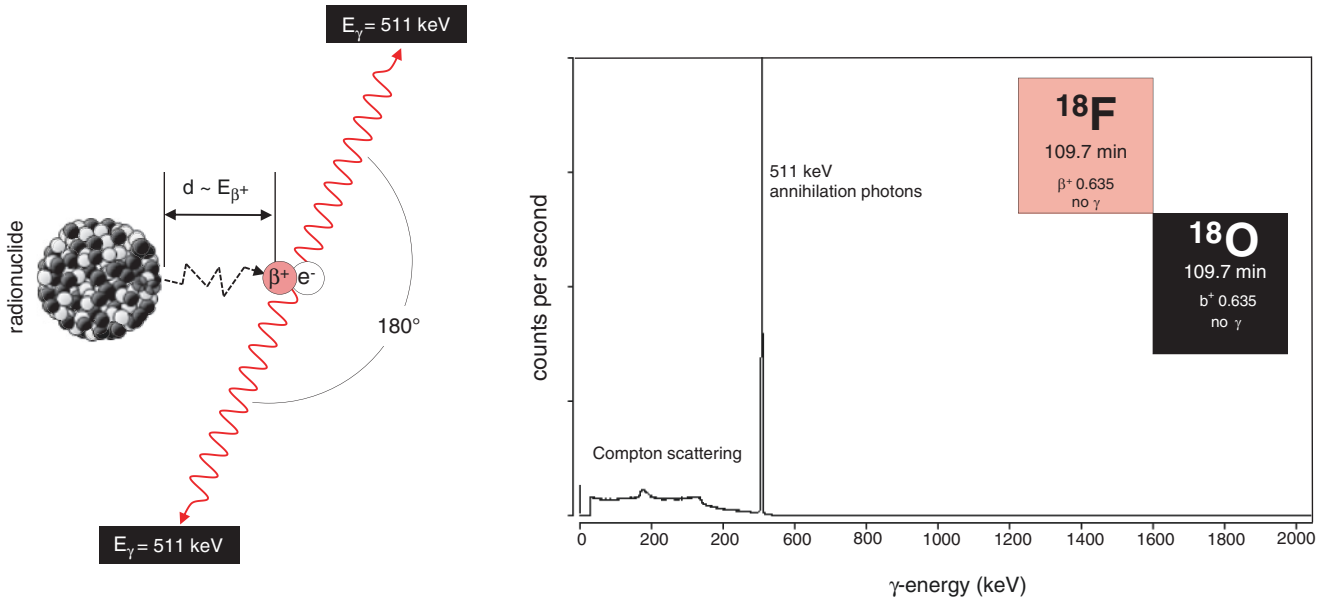

Fig. 38 Post-effects related to the appearance of a positron. Left: The positron is emitted from the transforming unstable nucleus, K1, and interacts with the surrounding condensed matter, in particular with the shell electrons of atoms and molecules. At kinetic energy close to zero, it combines with an electron. The masses of the two elementary particles convert into energy as $E = mc^2$. This energy is released as γ-radiation in terms of two photons of each 511 keV energy, which are emitted in opposite directions. Right: This electromagnetic emission is recorded in a γ-spectrum as intense 511 keV peak, as shown for emitter ^{18}F when transforming to stable ^{18}O via positron emission. Note that the γ-radiation is not created directly in the course of the transformation of the unstable nucleus

What happens with the positron? In a vacuum, the answer to this question is nothing! Of course, things change in (condensed) matter. In this case, the positron intensely interacts via inelastic and elastic scattering with the electrons located in the shells of atoms or molecules. These interactions reduce the kinetic energy of the moving positron until it is at almost zero kinetic energy: it has "thermalized". Now, the interaction of the positron with a shell electron becomes elastic and finally the positron may combine with an electron. This represents the formation of a pair of matter + *anti*matter particles and results in the annihilation of the two particles.

What is annihilation? The mass of the two particles converts into energy according to $E = m_e c^2$. With the (rest) mass of the electron of $m_e = 9.109383 \cdot 10^{-28}$ $g = 0.00054858$ u and the energy equivalent of $E_e = 510.9989$ keV (see Table 1), the overall energy is 2×510.9989 keV = 1.0219978 MeV. This energy is emitted as electromagnetic radiation composed of two photons of 510.9989 keV each, emitted in opposite directions (see Fig. 38).

Inner *Bremsstrahlung* Whenever an electron—either emitted in the course of β^- transformation or created during internal conversion—interacts with the *nuclei* of atoms or molecules representing surrounding condensed matter, it induces *bremsstrahlung* (from *bremsen* "to brake" and *Strahlung* "radiation", *i.e.* "braking radiation" or "deceleration radiation"). *Bremsstrahlung* is induced whenever an electron transits with a given kinetic energy along an atomic nucleus (Fig. 39). The interaction leads to a loss of kinetic energy, and the energy lost (ΔE) is converted into electromagnetic energy, in this case photons. This time, the electromagnetic radiation is called internal or "inner *bremsstrahlung*". This energy of these photons is lower than the energy of X-rays emitted for the same nuclide. The number of these bremsstrahlung photons per transformation is $<10^{-3}$ $(\Delta E)^2$. Obviously, its impact is greater for high Z and low E_γ.

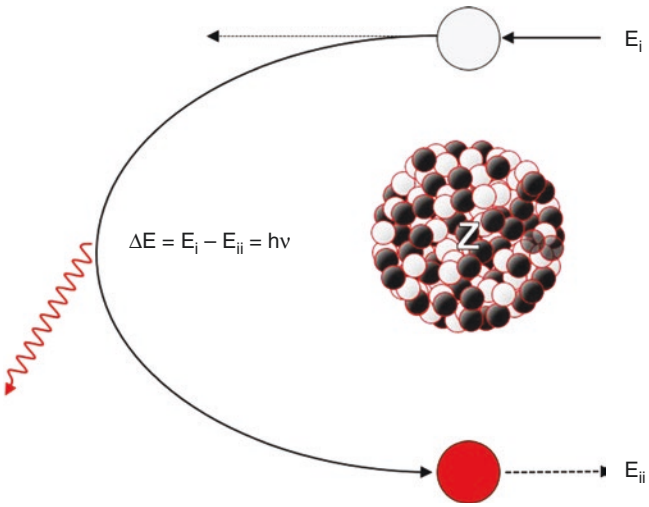

Fig. 39 The origin of inner bremsstrahlung: An electron originating from nuclear transformation processes is attenuated within the nucleus of surrounding atoms. The kinetic energy the electron loses from its initial E_i to lower values, E_{ii}, is emitted as electromagnetic radiation

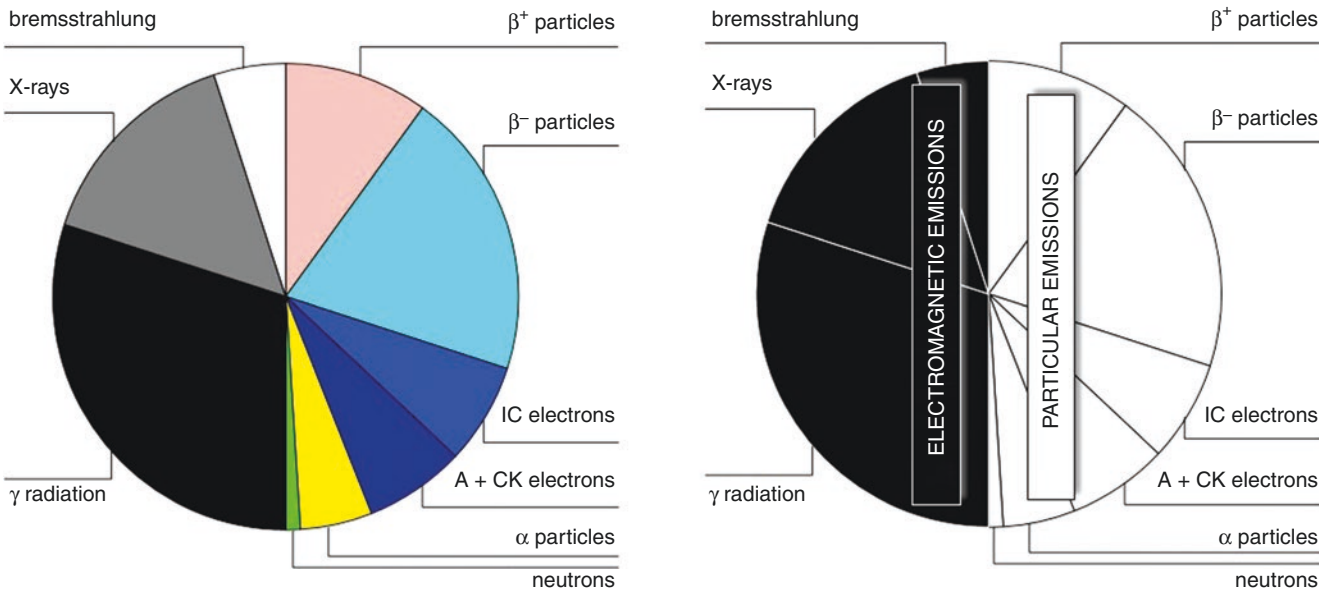

Fig. 40 The spectrum of different radiations in terms of their origin (left) as well as in terms of their character, *i.e.* particulate or electromagnetic (right). A + CK means Auger and Coster-Kronig electrons

Summary

An unstable nucleus, K1, transforms in order to improve the mean nucleon binding energy of its nucleons in a product nucleus, K2. This is managed by three principal kinds of primary transformation. In many cases, a primary transformation process populates energetically excited nuclear levels of K2, which de-excite via three options of secondary transitions. In parallel, several kinds of post-processes are induced. For most of those processes, we do not observe the fate of the transforming nucleus directly. However, the basic signals we observe are related to the radioactive emissions, which accompany those nuclear transformations and transitions.

This chapter has tried to describe the individual radiations and their corresponding sources. The emissions originating from primary transformations are β^- electrons, β^+ electrons, (*i.e.* positrons), and α-particles. All three are extremely relevant to radiopharmaceutical chemistry and nuclear medicine. (The electron neutrinos also emitted cannot be recorded easily, and thus they are not relevant to radiopharmaceutical chemistry and nuclear medicine.)

The emissions originating from secondary transitions are the single γ-photons (extremely relevant to radiopharmaceutical chemistry and nuclear medicine, in particular for SPECT), conversion electrons (discussed as potential particles for therapy), and the products of pair formation.

Those emissions originating from post-effects are the 511 keV annihilation photons (extremely relevant to radiopharmaceutical chemistry and nuclear medicine, in particular for PET), X-ray photons, and Auger-type electrons.

In reality, several of those radiations can be observed for the same unstable nuclide simultaneously. Figure 40 summarizes the different radiations in terms of their origin as well as their character, *i.e.* particulate or electromagnetic.

This broad spectrum of radioactive emissions is a gift of nature, in particular to scientists and physicians working in the field of radiopharmaceutical chemistry and nuclear medicine. Some isotopes can be selected for diagnostic purposes simply because they offer photon radiations—*i.e.* electromagnetic emissions—which are not (or only weakly) absorbed when penetrating the human body. This allows for the quantitative determination of absolute activities, which is a feature of PET tracers. Furthermore, it avoids critical radiation doses to the patient. In contrast, if a high but locally focused radiation dose is preferred for therapeutic purposes, there are particle-emitting radionuclides available as well! The particles considered routinely these days—α-particles and β-electrons—are emitted from unstable nuclei in the course of primary α- and β-transformations, though electrons emitted during secondary and post-processes (*e.g.* IC or Auger electrons) can be therapeutically relevant as well.

It is important to remember that for a given radionuclide, the desired radioactive emission is often accompanied by other parallel emissions. Some of them can be ignored (*e.g.* electron neutrinos), while others are negligible if they appear in low abundance. For example, ^{18}F is not a "pure" positron emitter. About 4 of 100 nuclei of ^{18}F transform via electron capture. As a consequence, there are emissions caused by refilling the vacancy created in the K-shell of the atom: X-rays, Auger electrons, and Coster-Kronig electrons. However, these emissions are rare enough such that they do not matter in terms of radiation detection and radiation dose. But what about ^{64}Cu, a radionuclide typically used for PET imaging? Its positron branching is only 17.9% and is accompanied by 43.1% of EC and 39% of β-emission. In this case, these parallel emissions may require further consideration.

And what if the primary positron emission pathway involves excited nuclear states? High-energy photons of high abundance originating from the de-excitation of those excited nuclear levels may complicate the quantitative registration of the 511 keV annihilation radiation of that "positron emitter". This is an issue in particular for the positron-emitter ^{86}Y [10]. On the other hand, primary electron capture makes ^{111}In a typical SPECT isotope because the excited nuclear levels produce low-energy photons via secondary processes. But what about the post-processes? The electrons released in the course of refilling the hole in the electron shell (as created by the initial EC process) may be (and indeed are) of "therapeutic" interest (see, *e.g.* the "therapeutic" studies of ^{111}In-labeled octreotide tracers [11]). And finally, one more example: even if there is a neutron-reach radionuclide defined as a 100% β^- emitter, the emitted electron will definitely induce bremsstrahlung. This may be considered a risk, as it causes additional radiation dose. However, in other cases cases—for example, the therapeutic use of ^{90}Y-labeled radiopharmaceuticals—the bremsstrahlung emissions actually represent a benefit, as they allow for imaging.

In conclusion, the primary interest of radiopharmaceutical chemists is often in the use of a given radionuclide's "ideal" radioactive emission. However, it is nonetheless essential to identify and to understand the fully transformation pathway of each candidate. Once these things have been considered and a "best" candidate for a certain application has been identified, another set of questions arises: How can this particular radionuclide be produced in high yield, ideal radionuclidic purity, and chemical identity? These questions will be addressed in the following chapters.

References

1. Vértes A, Nagy S, Klencsár Z, Lovas RG, Rösch F, editors. Handbook of nuclear chemistry, 6 vol., 2nd ed. Berlin-Heidelberg: Springer; 2011.
2. Rösch F, editor. Nuclear- and radiochemistry. Vol. I: Introduction. Berlin/Boston: Walter de Gruyter; 2014.
3. Rösch F, editor. Nuclear- and radiochemistry. Vol. II: Modern applications. Berlin/Boston: Walter de Gruyter; 2016.

4. International Atomic Energy Agency. Nuclear Data Services. AMDC – Atomic Mass Data Center. https://www-nds.iaea.org/amdc/. Last Updated: 9 Nov 2017 Accessed 8 Jan 2018.
5. Huang WJ, Audi G, Wang M, Kondev FG, Naimi S, Xu X. The AME2016 atomic mass evaluation (I). Evaluation of input data; and adjustment procedures. Chin Phys C. 2017;41(3):030002.
6. Wang M, Audi G, Kondev FG, Huang WJ, Naimi S, Xu X. The AME2016 atomic mass evaluation (II). Tables, graphs and references. Chin Phys C. 2017;41(3):030003.
7. National Nuclear Data Center, Brookhaven National Laboratory. Interactive chart of nuclides. (Masses and reaction data for all nuclides across the periodic table, based on ENSDF and the Nuclear Wallet Cards). www.nndc.bnl.gov/chart. Accessed 8 Jan 2018.
8. Wieser ME, Berglund M. Weight of natural elements. Pure Appl Chem. 2009;81(11):2131–56.
9. Magill J. Chart of nuclides, nuclear data in Nucleonica, Karslruhe. 2010. https://www.nucleonica.com/.../8/8a/NuTRoNS-2-ChartofNuclides.pdf. Accessed 8 Jan 2018.
10. Rösch F, Herzog H, Qaim SM. The beginning and development of the theranostic approach in nuclear medicine, as exemplified by the radionuclide pair 86Y and 90Y. Pharmaceuticals (Basel). 2017;10(2):56. https://doi.org/10.3390/ph10020056.
11. Krenning EP, Kooij PP, Bakker WH, Breeman WAP, Postema PTE, Kwekkeboom DJ, et al. Radiotherapy with a radiolabeled somatostatin analogue, [^{111}In-DTPA-D-Phe^{1}]-octreotide: a case history. Ann N Y Acad Sci. 1994;733:496–506.

Methods for the Production of Radionuclides for Medicine

Lauren L. Radford and Suzanne E. Lapi

Overview

The effective utilization of radionuclides in medicine has led to the continued and increased development of methods for their production and purification. While some radionuclides are produced in nature, almost none of those are used directly in nuclear medicine. Therefore, most radionuclides of interest must be produced by artificial means. The use of nuclear reactors, particle accelerators, and other means has given rise to an entire toolbox of radionuclides with different half-lives, decay modes, and chemical properties that are now available for the development of radiopharmaceuticals (Tables 1, 2, and 3). In this chapter, the basics of the production of these radionuclides as well as the energetics of nuclear reactions will be introduced.

The vast majority of radionuclides are produced using two types of instruments: nuclear reactors and accelerators. In nuclear reactors, neutrons are generated via the fission of nuclear fuel or neutron-capture reactions on stable targets. These neutrons are then used to create neutron-rich radionuclides that typically decay through beta emission and are therefore useful for targeted radiotherapy. Accelerators, in contrast, accelerate protons or other charged particles to induce nuclear reactions on target materials. These reactions can create proton-rich radionuclides that decay by positron emission and are therefore useful for imaging applications.

Nuclear generators are another way to provide a ready supply of relatively short-lived radionuclides. A long-lived parent isotope—typically produced using a cyclotron or nuclear reactor—that decays into a medically useful daughter radionuclide can be trapped onto a resin and readily shipped around the globe. As concentrations of the daughter radionuclide increase due to the decay of the parent, the former can be harvested for use. This cycle can, of course, be repeated many times, thus providing a convenient source of the shorter-lived daughter radionuclide. In addition to being convenient, generators help provide a source of radionuclides in areas where access to a cyclotron or reactor may be limited.

While there are several other methods that can be used to produce radionuclides, the ones outlined in this chapter are the most commonly encountered.

Radionuclides Found in Nature

The assortment of radionuclides found in nature falls into several categories. Some radionuclides can be formed via ongoing natural processes. For example, cosmic rays striking atmospheric nuclei induce nuclear reactions that form *cosmogenic* radionuclides. One such radionuclide is carbon-14 ($t_{1/2}$ = 5730 y), which is formed from neutrons striking atmospheric nitrogen-14. It can be found in organic materials, which is the basis of carbon dating. *Primordial* radionuclides, on the other hand, were formed billions of years ago during the formation of the earth but are so long-lived that they and their daughters are still present today. Two examples of these radionuclides are uranium-238 ($t_{1/2} = 4.47 \times 10^9$ y) and potassium-40 ($t_{1/2} = 1.26 \times 10^9$ y), the latter of which is present in glass, concrete, and many other materials (including you!). It is important to note, however, that not all radionuclides found in the environment today were produced naturally. Some are the results of nuclear weapons testing, which occurred primarily from 1945 to 1980. Indeed, the creation of these *anthropogenic* radionuclides led to increased background levels of certain radionuclides—such as tritium—all over the world.

Nuclear Reactions

All other radionuclides on earth are artificial and are produced artificially though nuclear reactions. The production of radionuclides typically involves the collision of an

L. L. Radford · S. E. Lapi (✉)
Department of Radiology, University of Alabama at Birmingham, Birmingham, AL, USA
e-mail: lapi@uab.edu

J. S. Lewis et al. (eds.), *Radiopharmaceutical Chemistry*, https://doi.org/10.1007/978-3-319-98947-1_4

Table 1 Radionuclides for positron emission tomography (PET)

Isotope	Half-life	Primary decay mode (branching ratio)	Mean β^+ energy (keV)	β^+ end-point energy (keV)	% abundance β^+	Production route	References
^{11}C	20.364 (14) min	β^+ (1)	385.70 (44)	960.4 (10)	99.7669 (25)	^{14}N(p,α)^{11}C	
^{13}N	9.965 (4) min	β^+ (1)	491.82 (12)	1198.5 (3)	99.8036 (20)	^{16}O(p,α)^{13}N	
^{15}O	122.24 (16) s	β^+ (1)	735.28 (23)	1732.0 (5)	99.9003 (10)	^{15}N(p,n)^{15}O	
						^{14}N(d,n)^{15}O	
^{18}F	109.77 (5) min	β^+ (1)	249.8 (3)	633.5 (6)	96.73 (4)	^{18}O(p,n)^{18}F	
						^{20}Ne(d,α)^{18}F	
^{34m}Cl	31.99 (3) min	ε + β^+ (0.55)	554.32	1311.78 (5)	25.6 (6)	^{34}S(p,n)^{34m}Cl	
		IT (0.45)	1098.57	2488.43 (5)	28.4 (8)	^{32}S(α,pn)^{34m}Cl	
^{38}K	7.636 (18) min	ε + β^+ (1)	1212.08 (20)	2724.4 (4)	99.92	^{38}Ar(p,n)^{38}K	
^{43}Sc	3.891 (12) h	ε + β^+ (1)	344.46 (83)	825.8 (19)	17.2 (5)	^{40}Ca(α,p)^{43}Sc	Walczak, R et al. EJNMMI Phys. 2, 2015, 33
			508.10 (85)	1198.7 (19)	70.9 (6)	^{40}Ca(α,n)^{43}Ti→^{43}Sc	
^{44}Sc	3.97 (4) h	ε + β^+ (1)	632.0 (9)	1473.5 (18)	94.27 (5)	^{47}Ti(p,α)^{44m,g}Sc	
						^{44}Ca(p,n)^{44}Sc	
						^{45}Sc(n,2n)^{44}Sc	
						^{44}Ti/^{44}Sc generator	
^{45}Ti	184.8 (5) min	ε + β^+ (1)	438.93 (22)	1040.1 (5)	84.80 (13)	^{45}Sc(p,n)^{45}Ti	
^{51}Mn	46.2 (1) min	ε + β^+ (1)	963.72 (19)	2185.5 (3)	96.89 (3)	^{50}Cr(d,n)^{51}Mn	
						^{nat}Cr(p,x)^{51}Mn	
^{52}Mn	5.591 (3) d	ε + β^+ (1)	241.59 (80)	573.3 (19)	29.4 (4)	^{nat}Cr(p,xn)^{52}Mn	
						^{52}Cr(p,n)^{52}Mn	
^{52m}Mn	21.1 (2) min	ε + β^+ (0.9825)	1174.01 (90)	2633.2 (19)	96.4 (5)	^{52}Fe/^{52m}Mn generator	
		IT (0.0175)					
^{52}Fe	8.725 (8) h	ε + β^+ (1)	2058.1 (30)	4474 (6)	99.620 (4)	^{nat}Ni(p,x)^{52}Fe	
^{55}Co	17.53 (3) h	ε + β^+ (1)	435.68 (20)	1021.3 (4)	25.6 (15)	^{58}Ni(p,α)^{55}Co	
			476.22 (00)	1113.2 (4)	4.26 (20)	^{56}Fe(p,2n)^{55}Co	
			648.98 (20)	1498.5 (4)	46 (3)	^{54}Fe(d,n)^{55}Co	
^{60}Cu	23.7 (4) min	ε + β^+ (1)	440.0 (10)	1027.4 (16)	1.17 (8)	^{60}Ni(p,n)^{60}Cu	
			804.9 (10)	1836.5 (16)	4.59 (22)		
			839.6 (10)	1911.8 (16)	11.6 (4)		
			872.0 (10)	1981.8 (16)	49.0 (23)		
			1104.2 (10)	2479.8 (16)	2.8 (3)		
			1324.9 (10)	2947.1 (16)	15.0 (12)		
			1720.1 (11)	3773.5 (16)	5 (3)		
^{61}Cu	3.339 (8) h	ε + β^+ (1)	238.45 (43)	559.5 (10)	2.6 (5)	^{61}Ni(p,n)^{60}Cu	
			398.90 (44)	932.5 (10)	5.5 (10)	^{60}Ni(d,n)^{61}Cu	
			493.83 (45)	1148.1 (10)	2.3 (4)		
			523.82 (45)	1215.5 (10)	51 (5)		
^{62}Cu	9.673 (3) min	ε + β^+ (1)	1320.7 (5)	2936.9 (5)	97.60 (3)	^{62}Zn/^{62}Cu generator	
^{64}Cu	12.701 (2) h	ε + β^+ (0.615)	278.21 (9)	653.03 (20)	17.60 (22)	^{64}Ni(p,n)^{64}Cu	
		β^- (0.385)				^{67}Zn(p,α)^{64}Cu	

Table 1 (continued)

Isotope	Half-life	Primary decay mode (branching ratio)	Mean β^+ energy (keV)	β^+ end-point energy (keV)	% abundance β^+	Production route	References
^{63}Zn	38.47 (5) min	$\varepsilon + \beta^+$ (1)	599.9 (8)	1382.4 (16)	4.9 (4)	^{63}Cu(p,n)^{63}Zn	
			732.5 (8)	1674.8 (16)	7.0 (3)		
			1042.3 (8)	2344.5 (16)	80.3 (7)		
^{66}Ga	9.49 (3) h	$\varepsilon + \beta^+$ (1)	397.1 (14)	924 (3)	3.7 (3)	^{66}Zn(p,n)^{66}Ga	
			1904.1 (15)	4153 (3)	51 (4)	^{63}Cu(α,n)^{66}Ga	
^{68}Ga	67.71 (8) min	$\varepsilon + \beta^+$ (1)	352.59 (52)	821.7 (12)	1.190 (10)	^{68}Ge/^{68}Ga generator	
			836.02 (56)	1899.1 (12)	87.72 (9)		
^{69}Ge	39.05 (10) h	$\varepsilon + \beta^+$ (1)	271.45 (22)	631.0 (5)	2.3 (3)	^{69}Ga(p,n)^{69}Ge	
			522.10 (23)	1205.1 (5)	21 (5)		
^{71}As	65.30 (7) h	$\varepsilon + \beta^+$ (1)	352.0 (18	816 (4)	27.9 (8)	^{70}Ge(p,γ)^{71}As	
^{72}As	26.0 (1) h	$\varepsilon + \beta^+$ (1)	824.3 (19)	1870 (4)	5.82 (18)	^{72}Se/^{72}As generator	
			1117.0 (19)	2500 (4)	64.2 (4)		
			1528.5 (19)	3334 (4)	16.3 (17)		
^{74}As	17.77 (2) d	$\varepsilon + \beta^+$ (0.66)	408.0 (8)	944.6 (17)	26.1 (22)	^{74}Ge(p,n)^{74}As	
		β^- (0.34)	701.1 (8)	1540.5 (17)	3.0 (20)	^{73}Ge(d,n)^{74}As	
^{73}Se	7.15 (8) h	$\varepsilon + \beta^+$ (1)	562.0 (45)	1290 (10)	64.7 (9)	^{70}Ge(α,n)^{73}Se	Blessing, G et al. Intl J Radiat Appl Instrum Part A. 43, 1992, 455–61
						^{75}As(p,3n)^{73}Se	Mushtaq, A et al. Intl J Radiat Appl Instrum Part A. 39, 1988, 1085–91
						^{75}As(d,4n)^{73}Se	
^{75}Br	96.7 (13) min	$\varepsilon + \beta^+$ (1)	498.1 (18)	1145 (4)	1.03 (11)	^{76}Se(p,2n)^{75}Br	
			514.0 (18)	1181 (4)	3.6 (4)		
			601.4 (18)	1376 (4)	3.30 (20)		
			636.5 (18)	1454 (4)	1.24 (14)		
			708.1 (19)	1612 (4)	4.9 (8)		
			772.5 (19)	1753 (4)	53 (3)		
			904.3 (19)	2040 (4)	4 (4)		
^{76}Br	16.2 (2) h	$\varepsilon + \beta^+$ (1)	336 (7)	781 (9)	1.44 (13)	^{76}Se(p,n)^{76}Br	
			375 (7)	871 (9)	6.3 (6)	^{75}As(α,3n)^{76}Br	
			427 (7)	990 (9)	5.2 (4)		
			551 (7)	1271 (9)	1.24 (13)		
			953 (7)	2153 (9)	1.0 (4)		
			1221 (7)	2725 (9)	2.8 (13)		
			1265 (7)	2819 (9)	2.1 (7)		
			1532 (8)	3383 (9)	25.8 (19)		
			1800 (8)	3941 (9)	6.0 (10)		
^{82}Rb	1.2575 (2) min	$\varepsilon + \beta^+$ (1)	1167.6 (33)	2601 (7)	13.13 (14)	^{82}Sr/^{82}Rb generator	
			1534.6 (34)	3378 (7)	81.76 (17)		
^{82m}Rb	6.472 (6) h	$\varepsilon + \beta^+$ (1)	353 (11)	798 (7)	19.7 (16)	^{82}Kr(p,n)^{82m}Rb	
^{83}Sr	32.41 (3) h	$\varepsilon + \beta^+$ (1)	361.4 (27)	827 (6)	3.2 (3)	^{85}Rb(p,3n)^{83}Sr	Kastleiner, S *et al.* Appl Radiat Isot. 56, 2002, 685–95
			529.3 (27)	1209 (6)	11 (3)	^{82}Kr(^{3}He,2n)^{83}Sr	
			548.1 (27)	1251 (6)	12.4 (11)		

(continued)

Table 1 (continued)

Isotope	Half-life	Primary decay mode (branching ratio)	Mean β^+ energy (keV)	β^+ end-point energy (keV)	% abundance β^+	Production route	References
^{86}Y	14.74 (2) h	ε + β^+ (1)	394.1 (62)	900 (14)	1.10 (20)	^{86}Sr(p,n)^{86}Y	
			452.2 (62)	1033 (14)	1.9 (4)		
			509.4 (63)	1162 (14)	1.33 (11)		
			535.4 (63)	1221 (14)	11.9 (5)		
			681.1 (64)	1545 (14)	5.6 (5)		
			767.8 (64)	1736 (14)	1.7 (10)		
			883.3 (65)	1988 (14)	3.6 (9)		
			1436.8 (66)	3141 (14)	2.0 (11)		
^{89}Zr	78.41 (12) h	ε + β^+ (1)	395.5 (11)	902 (3)	22.74 (24)	^{89}Y(p,n)^{89}Zr	
^{90}Nb	14.60 (5) h	ε + β^+ (1)	662.2 (18)	1500 (4)	51.1 (18)	^{90}Zr(p,n)^{90}Nb	
^{94m}Tc	52.0 (10) min	ε + β^+ (1)	1094.20	2439 (5)	67.6 (4)	^{94}Mo(p,n)^{94m}Tc	
^{110m}In	69.1 (5) min	ε + β^+ (1)	1014.7 (56)	2260 (12)	60.7 (4)	^{110}Sn/^{110m}In generator	
						^{110}Cd(p,n)^{110m}In	
						^{111}Cd(p,2n)^{110m}In	
^{118}Sb	3.6 (1) min	ε + β^+ (1)	1188.6 (14)	2635 (3)	73.2 (3)	^{118}Te/^{118}Sb generator	
^{120}I	81.6 (2) min	ε + β^+ (1)	960.1 (69)	2137 (15)	2.13 (14)	^{122}Te(p,3n)^{120}I	
			1131.4 (70)	2510 (15)	6.2 (5)		
			1386.0 (70)	3058 (15)	1.93 (18)		
			1542.4 (71)	3392 (15)	2.7 (5)		
			1845.0 (72)	4033 (15)	29.3 (7)		
			2099.3 (70)	4593 (15)	19.0 (17)		
^{122}I	3.63 (6) min	ε + β^+ (1)	1195.3 (24)	2648 (5)	10 (3)	^{122}Xe/^{122}I generator	
			1458.1 (24)	3212 (5)	67 (5)		
^{124}I	4.1760 (3) d	ε + β^+ (1)	687.04 (86)	1534.9 (19)	11.7 (10)	^{124}Te(p,n)^{124}I	
			974.74 (85)	2137.6 (19)	10.7 (9)		
^{152}Tb	17.5 (1) h	ε + β^+ (1)	920 (18)	2040 (4)	2.30 (12)	^{143}Nd(^{12}C,5n)^{152}Tb	Allen, BJ et al. Appl Radiat Isot. 54, 2001 , 53–58
			1065 (18)	2340 (4)	1.20 (7)	^{144}Nd(^{12}C,4n)^{152}Tb	
			1186 (19)	2620 (4)	5.9 (8)	^{145}Nd(^{12}C,3n)^{152}Tb	
			1337 (18)	2970 (4)	8.0 (13)	Proton-induced spallation on ^{nat}Ta	Allen, BJ et al. Appl Radiat Isot. 54, 2001, 53–58

Table 2 Radionuclides for single-photon emission computed tomography (SPECT)*

Isotope	Half-life	Primary decay mode (branching ratio)	γ energy (keV)	% abundance γ	Production route	References
^{67}Ga	3.2617 (5) d	ε (1)	91.265 (5)	3.11 (4)	^{68}Zn(p,2n)^{67}Ga	
			93.310 (5)	38.81 (3)		
			184.576 (10)	21.410 (10)		
			208.950 (10)	2.460 (10)		
			300.217 (10)	16.64 (12)		
			393.527 (10)	4.56 (24)		
^{99m}Tc	6.0067 (5) h	IT (1)	140.511 (1)	89 (4)	^{99}Mo/^{99m}Tc generator	
^{111}In	2.8047 (4) d	ε (1)	171.28 (3)	90.7 (9)	^{111}Cd(p,n)^{111m,g}In	
			245.35 (4)	94.1 (10)	^{112}Cd(p,2n)^{111m,g}In	
^{123}I	13.2235 (19) h	ε (1)	158.97 (5)	83.3	^{123}Xe/^{123}I generator	
			528.96 (5)	1.39 (4)	^{124}Xe(p,pn)^{123}I	

Table 2 (continued)

Isotope	Half-life	Primary decay mode (branching ratio)	γ energy (keV)	% abundance γ	Production route	References
^{125}I	59.407 (10) d	ε (1)	35.4925 (5)	6.68 (13)	^{124}Xe(n,γ)^{125}Xe→^{125}I	
^{155}Tb	5.32 (6) d	ε (1)	60.012 (3)	1.11 (7)	Proton-induced spallation on ^{nat}Ta	Allen, BJ et al. Appl Radiat Isot. 54, 2001, 53–58
			86.55 (3)	32.0 (18)		
			105.318 (3)	25.1		
			148.64 (1)	2.65 (14)		
			161.29 (1)	2.76 (15)		
			163.28 (1)	4.44 (23)		
			180.08 (1)	7.5 (4)		
			262.27 (1)	5.3 (3)		
			340.67 (1)	1.18 (7)		
			367.36 (1)	1.48 (19)		
^{201}Tl	3.0421 (17) d	ε (1)	68.89 (XR)	22 (4)	^{203}Tl(p,3n)^{201}Pb→^{201}Tl	
			70.818 (XR)	37 (6)	^{202}Hg(p,2n)^{201}Tl	Birattari, C et al. J Labelled Compd Radiopharm. 19, 1982, 1330–32
			79.824 (XR)	4.4 (7)		
			80.225 (XR)	8.5 (14)		
			82.473 (XR)	3.1 (5)		
			135.34 (4)	2.565 (24)		
			167.43 (7)	10.00		

*While many radionuclides have gamma rays that can be imaged using SPECT, those listed in this table are used solely for SPECT imaging

Table 3 Radionuclides used for therapy

Isotope	Half-life	Primary decay mode (Branching ratio)	Mean particle energy (keV)	End-point energy (keV)	% abundance	Production route	References
^{32}P	14.268 (5) d	β$^-$ (1)	695.03	1710.66 (4)	100	^{31}P(n,γ)^{32}P	
						^{32}S(n,p)^{32}P	
^{47}Sc	3.3492 (6) d	β$^-$ (1)	142.6 (7)	440.9 (19)	68.4 (6)	^{44}Ca(α,p)^{47}Sc	
			203.9 (8)	600.3 (19)	31.6 (6)	^{48}Ti(p,2p)^{47}Sc	
						^{48}Ti(γ,p)^{47}Sc	
						^{47}Ti(n,p)^{47}Sc	
^{66}Cu	5.120 (14) min	β$^-$ (1)	628.1 (6)	1601.7 (10)	9.01 (9)	^{65}Cu(n,γ)^{66}Cu	
			1112.1 (6)	2640.9 (10)	90.77 (9)	^{66}Zn(n,p)^{66}Cu	
^{67}Cu	61.83 (12) h	β$^-$ (1)	121 (3)	377.1 (15)	57 (6)	^{67}Zn(n,p)^{67}Cu	Smith, et al. App Rad Iso 70 2012 2377–83
			154 (3)	468.4 (15)	22.0 (22)	^{68}Zn(p,2p)^{67}Cu	
			189 (3)	561.7 (15)	20.0 (20)	^{68}Zn(γ,p)^{67}Cu	
						^{70}Zn(p,α)^{67}Cu	
^{77}As	38.79 (5) h	β$^-$ (1)	228.8 (7)	683.0 (18)	97.0 (3)	^{76}Ge(n,γ)^{77}Ge→^{77}As	
^{77}Br	57.036 (6) h	ε (1)	Auger/CE			^{75}As(α,2n)^{77}Br	
						^{77}Se(p,n)^{77}Br	
^{89}Sr	50.563 (25) d	β$^-$ (1)	587.1 (11)	1500.9 (25)	99.99036 (5)	Nuclear fission	
^{90}Y	64.053 (20) h	β$^-$ (1)	933.7 (12)	2280.1 (16)	99.9885 (14)	^{90}Sr/^{90}Y generator	

(continued)

Table 3 (continued)

Isotope	Half-life	Primary decay mode (Branching ratio)	Mean particle energy (keV)	End-point energy (keV)	% abundance	Production route	References
^{105}Rh	35.36 (6)	β⁻ (1)	69.9 (10)	248 (3)	19.7 (5)	^{104}Ru(n,γ)^{105}Ru→^{105}Rh	Jia, W. et al Platinum Metals Rev 44 2000 50
			73.9 (10)	261 (3)	5.2 (4)		
			179.4 (11)	567.2 (25)	75.0 (6)		
^{103}Pd	16.991 (19)	ε (1)	Auger/CE			^{102}Pd(n,γ)^{103}Pd	
						^{103}Rh(p,n)^{103}Pd	
^{111}Ag	7.45 (1) d	β⁻ (1)	223.5 (12)	694.7 (14)	7.1 (5)	^{110}Pd(n,γ)^{111}Pd→^{111}Ag	
			278.9 (12)	791.4 (14)	1.00 (20)		
			360.4 (13)	1036.8 (14)	92 (5)		
^{117m}Sn	13.76 (4) d	IT (1)	Auger/CE			^{116}Sn(n,γ)^{117m}Sn	
						^{117}Sn(n,nγ)^{117m}Sn	
^{131}I	8.0252 (6) d	β⁻ (1)	69.36 (25)	247.9 (6)	2.08 (3)	^{130}Te(n,γ)^{131}Te→^{131}I	
			96.62 (26)	333.8 (6)	7.23 (1)	^{235}U fission	
			191.58 (30)	629.7 (6)	89.6 (8)		
^{133}Xe	5.2475 (5) d	β⁻ (1)	75.16 (75)	266.8 (24)	1.4 (6)	^{235}U fission	
			100.62 (79)	346.4 (24)	98.5 (13)		
^{149}Tb	4.118 (25) h	α^{++} (0.167)		3967 (3)	16.7	Proton-induced spallation on ^{nat}Ta	Allen, et al. App Rad Iso 54 2001 53–58
		ε (0.833)					
^{161}Tb	6.89 (2) d	β⁻ (1)	137.7 (5)	461.2 (13)	25.7 (16)	^{160}Gd(n,γ)^{161}Gd→^{161}Tb	Lehenberger S, et al. Nucl Med Biol. 2011 38 917–924
			157.4 (5)	518.4 (13)	65 (4)		
			174.6 (5)	567.3 (13)	5 (5)		
			183.7 (5)	593.0 (13)	5 (5)		
^{149}Pm	53.08 (5) h	β⁻ (1)	256.2 (15)	785 (4)	3.40 (20)	^{148}Nd(n,γ)^{149}Nd→^{149}Pm	
			369.1 (15)	1071 (4)	95.9 (3)		
^{153}Sm	46.284 (4) h	β⁻ (1)	199.5 (3)	634.7 (7)	31.3 (9)	^{152}Sm(n,γ)^{153}Sm	
			225.3 (3)	704.4 (7)	49.4 (18)		
			264.3 (3)	807.6 (7)	18.4 (17)		
^{166}Ho	26.824 (12) h	β⁻ (1)	651.33 (38)	1774.1 (9)	49.9 (12)	^{165}Ho(n,γ)^{166}Ho	
			693.96 (39)	1854.7 (9)	48.8 (12)		
^{177}Lu	6.647 (4) d	β⁻ (1)	47.66 (23)	177.0 (8)	11.61 (11)	^{176}Lu(n,γ)^{177}Lu	Dash, A et al. Nucl Med Mol Imaging 49 2015 85–107
			111.69 (26)	385.3 (8)	9.0 (5)	^{176}Yb(n,γ)^{177}Yb→^{177}Lu	
			149.35 (28)	498.3 (8)	79.4 (5)		
^{186}Re	3.7186 (5) d	β⁻ (0.925)	306.1 (4)	932.3 (9)	21.54 (14)	^{185}Re(n,γ)^{186}Re	
			359.2 (4)	1069.5 (9)	70.99 (12)	^{186}W(p,n)^{186}Re	
						^{189}Os(p,α)^{186}Re	
^{188}Re	17.003 (3) h	β⁻ (1)	527.78 (17)	1487.4 (4)	1.748 (20)	^{188}W/^{188}Re generator	
			728.88 (18)	1965.4 (4)	26.3 (5)		
			795.41 (18)	2120.4 (4)	70.0 (5)		
^{195m}Pt	4.010 (5) d	IT (1)	Auger/CE			^{194}Pt(n,γ)^{195m}Pt	
						^{195}Pt(n,n′γ)^{195m}Pt	
						^{194}Ir(n,γ)^{195m}Ir→^{195m}Pt	
						^{192}Os(α,n)^{195m}Pt	

Table 3 (continued)

Isotope	Half-life	Primary decay mode (Branching ratio)	Mean particle energy (keV)	End-point energy (keV)	% abundance	Production route	References
^{212}Bi	60.55 (6) min	β^- (0.641)	192.6 (6)	631.4 (17)	1.86 (4)	^{212}Pb/^{212}Bi generator	
			230.8 (7)	739.4 (17)	1.44 (4)		
			533.1 (7)	1524.8 (17)	4.47 (11)		
			834.2 (8)	2252.1 (17)	55.37 (11)		
		α^{++} (0.359)		6050.78 (3)	25.13 (7)		
				6089.88 (3)	9.75 (5)		
^{213}Bi	45.61 (6) min	β^- (0.978)	320.4 (19)	983 (5)	30.79 (24)	^{225}Ac/^{213}Bi generator	
			492.2 (20)	1423 (5)	65.9 (4)		
		α^{++} (0.022)		5875 (4)	1.959 (9)		
^{211}At	7.214 (7) h	α^{++} (0.418)		5869.5 (22)	41.80	^{209}Bi(α,2n)^{211}At	
		ε (0.582)					
^{212}Pb	10.64 (1) h	β^- (1)	41.1 (6)	154.6 (19)	5.08 (9)	Decay product of ^{232}Th	
			93.5 (7)	331.3 (19)	83.1 (16)		
			171.7 (7)	569.9 (19)	11.9 (16)		
^{223}Ra	11.43 (5) d	α^{++} (1)		5433.6 (5)	2.22 (20)	Decay product of ^{235}U	
				5501.6 (10)	1.00 (15)		
				5539.80 (90)	9.00 (20)		
				5606.73 (30)	25.2 (5)		
				5716.23 (29)	51.6 (13)		
				5747.0 (4)	9.00 (20)		
				5871.3 (10)	1.00 (20)		
^{225}Ac	10.0 (1) d	α^{++} (1)		5580 (3)	1.20 (10)	^{225}Ra/^{225}Ac generator	
				5609 (3)	1.10 (10)	^{229}Th/^{225}Ac generator	
				5637 (2)	4.4 (3)		
				5682 (2)	1.30 (20)		
				5724 (3)	3.1 (5)		
				5732 (2)	8.0 (5)		
				5732 (2)	1.32 (10)		
				5790.6 (22)	8.6 (9)		
				5792.5 (22)	18.1 (20)		
				5830 (2)	50.7 (15)		
^{230}U	20.8 (21) d	α^{++} (1)		5817.5 (7)	32.00 (20)	^{231}Pa(γ,n)^{230}Pa→^{230}U	Hashimoto, T et al. Rad chem and radanal lett 28 1977 385–391
				5888.4 (7)	67.4 (4)	^{231}Pa(p,2n)^{230}U	Morgenstern, A et al. Anal Chem 80 2008 8763–70

incoming particle or photon with the nucleus of a stationary target atom, thereby causing a nuclear reaction. Nuclear reactions are written very similarly to chemical reactions: an arrow separates the reactants and the products, and each side of the equation must be balanced with respect to mass number, charge, and total energy. As a general example, let's take the example of a stationary target nucleus (X) being hit with an incoming particle (a), which will produce a residual or product nucleus (Y), as well as a secondary particle (b). This can be written as:

$X + a \rightarrow Y + b$ or, in shorthand, as X(a, b)Y.

For example, ^{18}O(p, n)^{18}F indicates a proton-induced (a) reaction on an ^{18}O nucleus (X) leading to the emission of a neutron (b) and a ^{18}F residual nucleus (Y).

The Energetics of Nuclear Reactions

In any reaction, the total amount of energy must be conserved. Because we know that $E = mc^2$, the amount of energy

released or consumed in a nuclear reaction (Q) can be calculated by converting the difference in the atomic masses between the reactants and the products into energy. In other words:

$$Q = (m_{\text{reactants}} - m_{\text{products}})c^2 = [(m_X + m_a) - (m_Y + m_b)]c^2$$

In doing so, a reaction is designated as endoergic ($Q < 0$) or exoergic ($Q > 0$). For an example, consider the proton bombardment of oxygen-18 to produce radioactive fluorine-18, a common medical radionuclide. The full reaction is written as:

$$Z_A = \frac{A}{2.0 + 0.0154A^{2/3}}$$

Notice, that on each side, the mass number (A) and the proton number (Z) are balanced. Calculating Q for $^{18}O(p, n)^{18}F$ gives:

$$Q = [(17.999161 + 1.007825) - (18.000938 + 1.008665)]c^2$$
$$Q = -0.002617c^2$$

Because the mass-to-energy conversion for 1 amu = 931.5 MeV, Q can be converted to MeV. As a result, $Q = -2.44$ MeV. This value means that in order for this reaction to proceed, the kinetic energy of the projectile (E_a) must exceed 2.44 MeV. In general, $Q + E_a$ must be greater than zero for a reaction to occur, but note that this is only one of the criteria for determining whether or not a reaction can occur. Additional factors—such as the conservation of momentum and overcoming the Coulomb barrier—must also be taken into account.

In any nuclear reaction, the target nucleus (X) will necessarily gain some velocity and recoil after it is impacted by the incoming projectile due to the conservation of momentum. Therefore, not all of the projectile's kinetic energy will be available for the reaction to proceed. This kinetic energy (E_X) transfer must be taken into account when determining whether the criteria for a possible nuclear reaction are still met. This new criterion then becomes $Q + E_a - E_X > 0$, in which:

$$\Delta M\left(\beta^+\right) = \left\{\left(M_{K2} - (Z-1)m_e\right) + 1m_e\right\} - \left\{M_{K1} - Zm_e\right\}$$
$$= \left(M_{K2} - M_{K1}\right) + 2m_e$$

Thus, to calculate the new kinetic energy needed for an incident projectile (taking into account linear momentum), the equation becomes:

$$\Delta M(\varepsilon) = \left\{M_{K2} - (Z-1)m_e\right\} - \left\{\left(M_{K1} - Zm_e\right) + 1m_e\right\}$$
$$= \left(M_{K2} - M_{K1}\right)$$

$$^{\text{RECOIL}}E_{K2}^{\max} = \left(\frac{E_\beta^{\max}}{2c^2} + m_{\beta^0}\right)\frac{E_\beta^{\max}}{m_{K2}}$$

$$p_{K2} = p_\alpha$$

If we return to our example of $^{18}O(p,n)^{18}F$, the new kinetic energy required by the projectile becomes:

$$Q_\alpha = {}^{\text{RECOIL}}E_{K2} + E_\alpha$$

The contribution that the conservation of momentum makes toward calculating E_a becomes more significant when the size of the projectile and the target are closely matched.

If the projectile is a charged particle, then the electrostatic repulsion between the incoming projectile and the positively charged target nucleus must also be considered. As the incoming (charged) particle gets closer to the target nucleus, it starts to "see" the charge of the target nucleus and is repelled. The energy required to overcome these electrostatic, repelling forces is known as the Coulomb barrier. A quick equation to calculate the Coulomb barrier (V^0) in MeV is:

$$E_\alpha = \frac{Q_\alpha}{1 + \frac{m_\alpha}{m_{K2}}}$$

in which Z_x is the charge on the target nucleus, Z_a is the charge on the projectile, and R_X and R_a are the radii of the target nucleus and projectile, respectively, and can be calculated by the equation $R = 1.4A^{1/3}$ (in fm).

The amount of kinetic energy of a projectile required for a nuclear reaction to occur with some probability is called the "threshold energy." The threshold energy can be calculated by applying the momentum correction to the Q value (if negative) or to the Coulomb barrier value, whichever is higher. Going back to our example of $^{18}O(p, n)^{18}F$, the Coulomb barrier can be calculated as 2.27 MeV. In this case, because the absolute value of Q is larger than the Coulomb barrier, we should apply the conservation of momentum correction to the Q value for this reaction (as above), producing a threshold energy of 2.58 MeV.

The Fundamentals of Nuclear Reactors

High-abundance (flux) neutron sources can be obtained in a variety of ways, such as from fission or from charged-particle-induced reactions at accelerators. Our focus will be on the most abundant sources of neutrons: nuclear reactors. In nuclear reactors, neutrons are generated by nuclear fission, the splitting of a nucleus into two smaller parts with the co-emission of several neutrons. Nuclear reactors exist for a variety of applications, including the generation of electricity, research, radionuclide production, or some combination of these three. Our focus of course will be on those used for the production of radionuclides used in nuclear medicine.

In order to operate, all reactors require fuel in the form of fissile material (*e.g.* uranium-235, plutonium-239). A schematic of a pressurized water reactor core is shown in Fig. 1. Once the fission of the fuel is initiated—typically by a primary neutron source such as californium-252—more neu-

trons are released, which can in turn interact with the fuel to produce more fission events. Once this happens, the reaction becomes self-sustaining. In the case of uranium-235 (the most common fuel type), every fission event results in the release of approximately 2.44 neutrons. In order for the reaction to become self-sustaining, at least one of those neutrons must trigger another fission event (known as a chain reaction). In other words, the neutron multiplication factor (k) must be equal to one. The smallest amount of fuel needed for $k = 1$ is known as the critical mass, but reactors often operate at or slightly higher than critical mass so that $k > 1$ (supercritical mass). In this way, the self-sustaining nature of the reaction is ensured despite the presence of factors that may impair the efficiency of the reaction, such as "reactor poisons" that absorb neutrons.

If a supercritical fission reaction is allowed to continue out of control ($k > 1$), the results can be catastrophic. Indeed, generating a supercritical reaction is the guiding principle behind the creation of nuclear weapons. In a reactor, control rods are used to make certain that the chain reaction continues in a controlled manner. Control rods act as neutron "sponges" and are made out of alloys containing materials with high neutron-capture cross sections (*e.g.* B or Cd). The insertion and removal of control rods allow operators to decrease or increase the neutron flux. As the fuel is slowly consumed, the control rods are gradually extracted in order to maintain a constant neutron flux. Every 6 years or so, however, the fuel must be replaced.

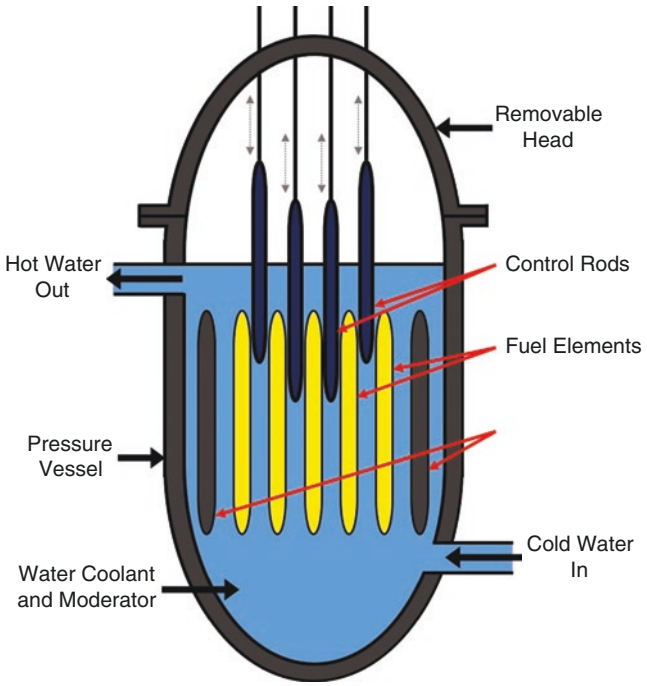

Fig. 1 A schematic of a pressurized water reactor core. The fuel elements contain fissile material and are surrounded by water, which acts as both coolant and moderator. Control rods can be inserted or removed from the top of the core between the fuel elements to either decrease or increase neutron flux

The "fast" neutrons released in the fission of uranium-235 have average energies of >1 MeV and must be slowed down to energies more favorable for neutron capture or fission. In general, the probability of a nuclear reaction with neutrons increases as the speed of the neutron decreases. To do this, moderating materials such as H_2O, D_2O, or graphite are used to slow fast neutrons to epithermal (0.025 eV–0.4 eV) and thermal (<0.025 eV) energies. Good moderating materials have low neutron-capture cross sections, so as not to decrease the neutron flux. Modern reactor designs typically use D_2O as both the coolant and moderator as an added safety measure. In the absence of heavy water, the thermal neutron flux would be lost, and fission would largely cease.

In natural uranium ores, the isotopic abundance of uranium-235 is only 0.72%, which is insufficient for generating the neutron flux required for radionuclide production. Therefore, natural uranium must be enriched to increase the percentage of uranium-235 before it can be used as nuclear fuel. The degree of enrichment depends on the type of reactor and its purpose. For instance, nuclear power reactors typically use low-enriched uranium (LEU) fuel, with enrichment levels of 2–5%. If the uranium-235 enrichment level is 20% or above, it is considered highly enriched uranium (HEU) and is carefully regulated to prevent the proliferation of nuclear weapons. Research reactors for the production of radionuclides (Fig. 2) have traditionally used HEU fuel with enrichment levels of up to 93% in order to create compact reactor cores with high neutron fluxes [1]. Today, many research reactors have converted to using LEU fuel, and there is a global push to continue this trend [2].

The Production of Radionuclides in Nuclear Reactors

Nuclear Reaction Cross Sections

Calculating the threshold energy of an incoming particle does not necessarily describe the probability of a reaction occurring, rather only that it *can* occur at all. Instead, the probability of a given nuclear reaction is termed the cross section (σ), which has units of area. Typically, area is reported in units such as cm^2; however, the probability of a reaction is extremely small, and so cross sections are typically reported in barns (b, $1\ b = 1 \times 10^{-24}\ cm^2$). The term barn was a unit defined by scientists during the Manhattan Project to describe the fission probability for uranium-235, which had a cross section "as big as a barn" [3].

In general, as the incoming neutron's energy decreases, the probability of neutron capture increases. Looking at an excitation function (a plot of cross section vs. energy) for a

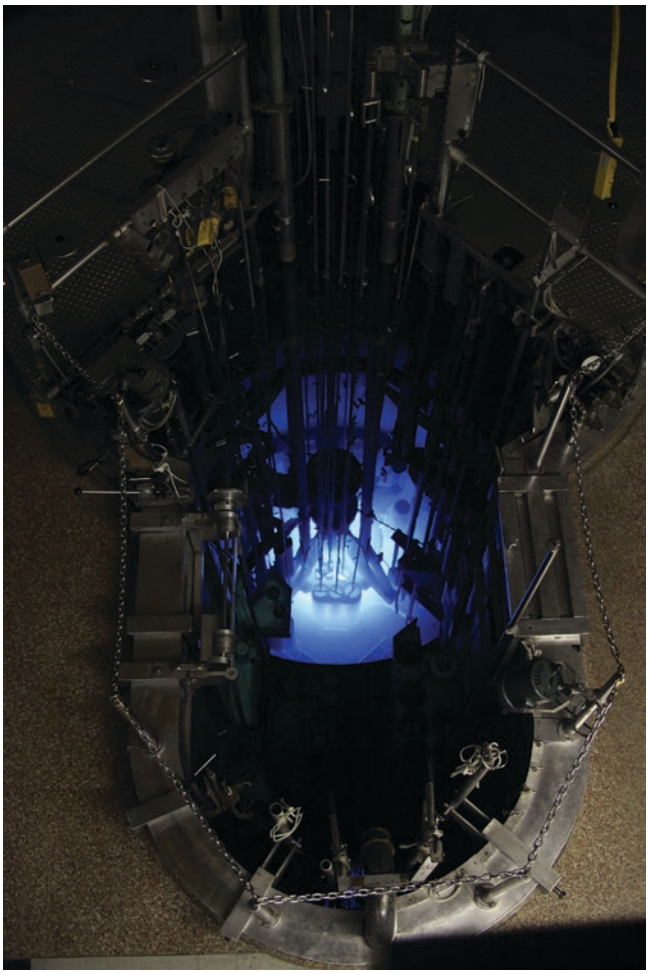

Fig. 2 The University of Missouri Research Reactor (MURR) is an example of an open pool pressurized water reactor. The reactor uses light water as both moderator and coolant. The blue glow is caused by Cherenkov radiation, which occurs when beta particles give off electromagnetic energy as they travel through the water. (Photo courtesy of the University of Missouri Research Reactor Center, with permission)

given nuclear reaction helps to illustrate this (Fig. 3) [4]. The decrease in σ is roughly $1/v_n$, where v_n is the velocity of the neutron. The feature of the graph where sharp spikes in σ suddenly appear is known as the resonance region. The resonance peaks correspond to different nuclear energy levels of the nucleus, which becomes excited by the incoming neutron.

Neutron-Capture Reactions

In a nuclear reactor, neutrons are bombarding the target from every direction, and this neutron flux (φ) is described in units of neutrons/cm^2/s. Therefore, the rate of production (R) of any product of a neutron-induced reaction is equal to $\varphi\sigma N_{tgt}$, where N_{tgt} is the number of target atoms. Often we are looking at reactions to produce radioactive nuclei, where the rate

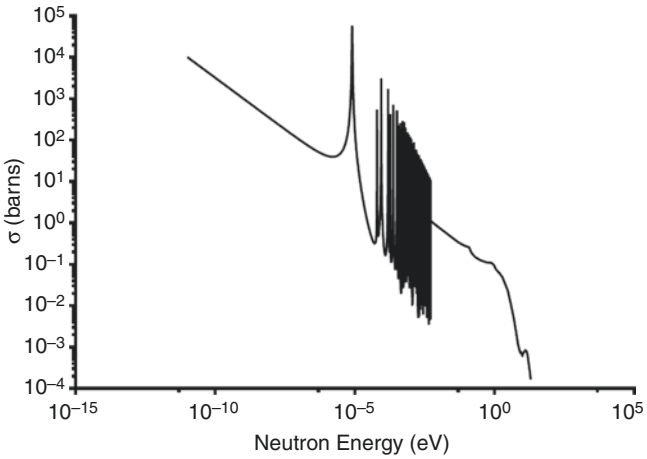

Fig. 3 An excitation function for the (n,γ) reaction on ^{152}Sm [4]

of change in the number of radioactive nuclei is equal to the production rate minus the decay rate.

$$E_{IC} = {}^{\odot i}\Delta E - E_{B(e)}$$

Knowing this, we can derive the production equation used to predict the radioactivity that will result from the bombardment:

$$\frac{dN}{dt} = \sigma\varphi N_{tgt} - \lambda N$$

Rearranging this equation gives:

$$\frac{dN}{\sigma\varphi N_{tgt} - \lambda N} = dt$$

Taking the integral of both sides gives a standard integral of the form that can be easily simplified as follows:

$$\int \frac{dN}{\sigma\varphi N_{tgt} - \lambda N} = \int dt$$

$$N = \frac{\sigma\varphi N_{tgt}}{\lambda}\left(1 - e^{-\lambda t}\right)$$

We know that radioactivity is directly related to the number of atoms by A = λN. As a result, this equation then becomes:

$$A = \sigma\varphi N_{tgt}\left(1 - e^{-\lambda t}\right)$$

where A is in units of disintegrations per second (or Becquerel) and t is the irradiation time. Notice that in order for the units to correctly cancel and for A to be in the correct units of s^{-1}, the cross-sectional parameter must be in units of cm^2. The latter part of the equation (in parentheses) is called the saturation factor. This takes into account the fact that eventually one will have a steady-state number of radionuclides in the target as the production rate equals the decay rate. The saturation factor needs to be considered when

determining how long to irradiate targets. Typically, targets are irradiated for a maximum time of several half-lives of the produced radionuclide. The graph in Fig. 4 illustrates how the saturation factor and the half-life of the produced radionuclide affect one another. The maximum amount of radioactivity that can be produced is shown in Fig. 4 by the red dotted line. After one half-life of the product radionuclide has passed, 50% of the maximum radioactivity has been reached. After two half-lives, 75% of the maximum has been reached and so forth. Thus, irradiating a target for too long starts to yield diminishing returns.

To factor in the post-bombardment time—the time the irradiated material is often allowed to "cool" prior to being handled—into the total amount of radioactivity created, the equation below can be used:

$$A = \varphi N \sigma \left(1 - e^{-\lambda t_{\text{irr}}}\right)\left(e^{-\lambda t_{\text{post}}}\right)$$

where t_{post} is the amount of time that passes after the bombardment ends.

Target Considerations

Because neutrons do not attenuate in a sample as rapidly as charged particles, targets for neutron irradiation tend to be larger than targets for accelerators. Generally, target materials are solid metal or oxide powders but can also be liquid or gas [5]. Prior to irradiation, targets are fully encapsulated in an ampoule (typically aluminum or quartz) and then placed into a special holder. The target material must be able to withstand high temperatures (as much as 1000 °C). Once the target has been prepared, it can be introduced to the neutron flux in a variety of ways. For most irradiations, the sample holder will be inserted into the reactor pool via a hydraulic system, allowing the sample to be retrieved during normal operation. Pneumatic tube systems are also commonplace at research reactors; however, these systems are generally reserved for short bombardments at a lower neutron flux and thus are not typically used for the production of radionuclides.

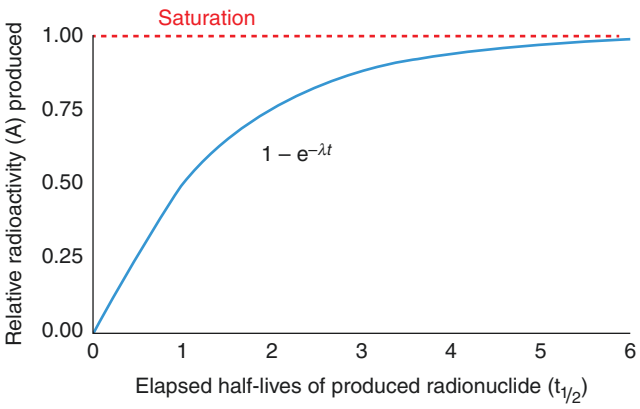

Fig. 4 The production of a radionuclide in a target as a function of irradiation time

There are several other practical considerations that must be considered during the development of targets:

1. Target burnup
2. Product burnup
3. Self-shielding

"Burnup" refers to the degradation or loss of material. "Target burnup" becomes significant if the target material is irradiated for a long period of time and has a large cross section. Eventually, enough of the target will have been converted to the desired radionuclide such that there is a significant difference between the initial and postirradiation target masses, adversely affecting further production rates. In contrast, "product burnup" must be taken into account when the produced radionuclide *also* has a large neutron-capture cross section. If the product itself undergoes neutron capture, this will again reduce the overall yield of the desired radionuclide. Lastly, "self-shielding" becomes predominant in large targets that have high absorption cross sections. Essentially, the target nuclei in the inner part of the target do not experience the desired neutron flux due to the absorption of neutrons by the outer part of the target, resulting in decreased product yield.

(n,γ) Reactions and Specific Activity

The specific activity (A_s) of a radionuclide—as it relates to production—is defined as the radioactivity of the desired radionuclide divided by the total mass of the final product, expressed as Bq/g. The (n,γ) reactions typical of reactor production result in neutron-rich radionuclides that decay by beta emission, making them useful for therapy. However the products of (n,γ) reactions are chemically identical to the target atom, making separation chemistry extremely difficult and often impossible. This means that the resulting products often have low specific activity. Examples of radionuclides made in this way include the therapeutic radionuclides samarium-153 ($t_{1/2}$ = 1.93 d) and lutetium-177 ($t_{1/2}$ = 6.65 d). In the case of lutetium-177, a reasonably high yield can still be achieved because lutetium-176 has a large neutron-capture cross section. Consider the following example: 10 mg of [^{176}Lu]Lu_2O_3 (70% enriched in ^{176}Lu; σ_{th} = 2100 b) is irradiated for 3 days in a reactor at a thermal neutron flux of 3×10^{13} n/cm^2/s. At the end of the 3 days, the theoretical

amount of lutetium-177 will be 358.3 GBq (9.68 Ci) and the A_s would be 35.83 GBq/mg (968 mCi/mg). In other words, roughly 1.4% of the lutetium-176 atoms were converted to lutetium-177.

High specific activity radionuclides can be obtained from reactors via indirect production routes in which the decay of the reactor-produced parent isotope results in the desired product. In the case of lutetium-177, an indirect production route exists via the ^{176}Yb$(n, \gamma)^{177}$Yb $\frac{E_B}{A}$ ^{177}Lu pathway, and the product can be separated from the target material. While lutetium-177 produced this way can be prepared with a much higher specific activity, the low neutron-capture cross section of ytterbium-176, the difficulty of the Yb/Lu separation, and the necessity of recycling the expensive target material all need to be taken into account before selecting this production route.

Fission Reactions

Neutron bombardment of fissile target material is another way to produce radionuclides. Fission almost always results in neutron-rich daughters that decay by beta emission. The most popular example of this is the bombardment of uranium-235 targets with thermal neutrons to produce molybdenum-99. In this case, the uranium-235 nucleus splits asymmetrically into two fission products: one with A = 80–110 and the other with A = 130–150 (Fig. 5) [6]. For the lighter fission product, mass numbers around 100 are made with highest probability, and so molybdenum-99 is produced in roughly 6.1% of fission events [7, 8]. Following the irradiation, the targets must then be processed, and the molybdenum-99 must be extracted for use. While molybdenum-99 is not used directly in nuclear medicine, its daughter, technetium-99m, is used in 70–80% of all nuclear medicine scans [9]. Other examples of fission products useful in nuclear medicine are iodine-131 and strontium-90.

(n,p) and (2n,γ) Reactions

The (n,p) and $(2n,\gamma)$ reaction pathways are less common in radionuclide production. In the case of (n,p) reactions, the product is chemically different from the target and can be separated, providing a high specific activity product. In order for an (n, p) reaction to occur, fast neutrons are needed that exceed the threshold energy for the nuclear reaction. Examples of radionuclides that can be produced this way are ^{64}Zn$(n, p)^{64}$Cu and ^{32}S$(n, p)^{32}$P. Double-neutron capture is also difficult to achieve and requires a high neutron flux. The $(2n,\gamma)$ reaction can be performed with tungsten-186 to produce tungsten-188, which decays to the therapeutic radionuclide rhenium-188.

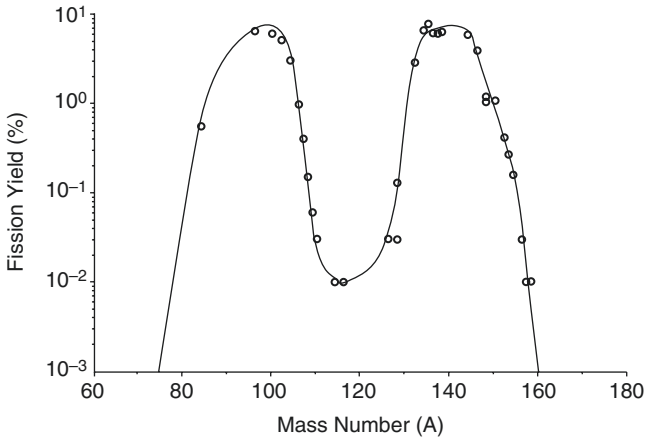

Fig. 5 Cumulative thermal neutron fission probabilities for uranium-235. The line was added to guide the eye. (Data from Koning *et al.* [6])

Fundamentals of Cyclotrons

Cyclotrons are the most common type of accelerator used to produce medical radionuclides via bombardment with charged particles. Because they accelerate charged particles in a circular fashion, cyclotrons take up less space than their linear counterparts. Several hundred cyclotrons can be found in academic centers, hospitals, and industrial production facilities worldwide. Typically, they accelerate charged particles to energies between 11 and 30 MeV, although larger machines are available. Cyclotrons can accelerate positive (*e.g.* protons, alpha particles) or negative (*e.g.* hydride ions) ions, but the majority of commercial machines manufactured today are negative ion. What follows is an overview of the fundamentals of cyclotrons; for more details, see the text *Principles of Charged Particle Acceleration* [10].

Plasma/Ion Source

The ion source of a cyclotron generates the charged particles. To do this, the ion source requires a "feed gas," the type of which depends on the desired ion. For example, $[^1H]H_2$ is used to generate protons or hydride ions, while $[^2H]H_2$ or He is used to generate deuterons or alpha particles, respectively. A plasma is typically generated by the emission of electrons from a filament (*e.g.* tungsten) held at high current which generates a cloud of ions that are often confined by a magnetic field inside the source. The ions are extracted from the source into the center region of cyclotron vacuum via an extraction electrode maintained at a high voltage with a charge opposite that of the ions being extracted.

Acceleration and Constraining Forces

The acceleration of the ions in a cyclotron occurs in a high-vacuum environment to avoid molecular collisions that can cause the loss of ions (from neutralization), changes in the trajectory of the ions, or the unnecessary radioactivation of components. The ions are constrained in a circular orbit by a magnetic field, and an electric potential applied repetitively to the ions is used for acceleration. The acceleration electrodes are sometimes called "dees" due to their shape in early cyclotrons. Today, however, they are commonly wedge-shaped as shown in Fig. 6.

The basic principle of cyclotron acceleration relies on the use of an alternating voltage between the "dee" electrodes with a frequency equal to the orbital frequency of the particles. Take, for example, the acceleration of a negative ion—H^-—inside the cyclotron schematic shown in the left-hand side of Fig. 6. The particle moves in a circular orbit as it is contained in a magnetic field perpendicular to the plane of the electrodes. When the particle reaches the "gap" shown in Fig. 6, the electrode ahead will have a positive charge, and the previous electrode will have a negative charge. Thus, the particle is accelerated across the gap and gains energy. The particle continues on its circular path until it reaches the gap on the other side. At this point, the electrode potentials are switched so that the electrode ahead becomes positive and the previous electrode becomes negative, and the particle again gains energy as it crosses the gap. This process is repeated for each orbit. Note that for this example, the electrode polarity actually changes twice during the particle orbit. As the particle gains energy, it travels with a higher velocity and in an orbit with a larger radius in a path that essentially spirals out from the center. It is important to note that the time to complete an orbit is always the same, thus the cyclotron is accelerating many batches of particles at once. The magnet both confines the particles to a circular path and also helps to focus the particles and correct for the relativistic mass increase as the particles approach the speed of light.

Equations of the Motion of Particles

As previously described, most cyclotrons used for the production of medical radionuclides are called isochronous cyclotrons, meaning that the particle arrives at the accelerating gap at the exact same time that the voltage between the electrodes oscillates. Thus, the time to traverse the path between the applications of accelerating voltage must be constant. This balance is accomplished by setting the circular motion force (mv^2/r) equal to the confining magnetic force (qvB) and solving for $v = qBr/m$. Thus, the time to traverse a circle is $t = 2pr/v = 2\ pm/qB$ (period), and the frequency is $f = qB/2\ pm$. This is known as the cyclotron frequency and *is independent of the radius at which the particle is travelling*. Typically, cyclotron voltage oscillation frequencies are in the 10s of MHz range, which is known as the radio-frequency range or RF.

Extraction

When the particles reach the outermost orbits, they are extracted from the circular path and are either directed onto a target or down a beamline. The mode of extraction depends on the charge of the ions being accelerated and may involve an extraction foil (for negative ions) or a deflector (for positive ions), as illustrated in Fig. 7. Negative ions are passed through a carbon foil (sometimes

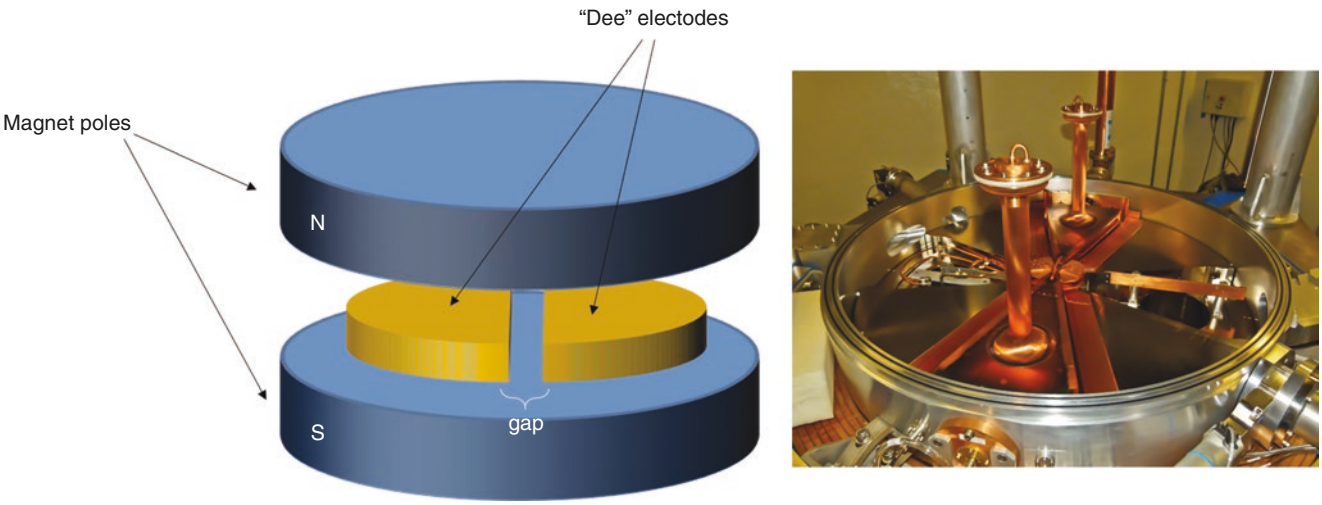

Fig. 6 (*Left*) A cyclotron schematic illustrating the confining magnet and accelerating "dee" configuration; (*right*) The cyclotron "dees" at the University of Alabama at Birmingham

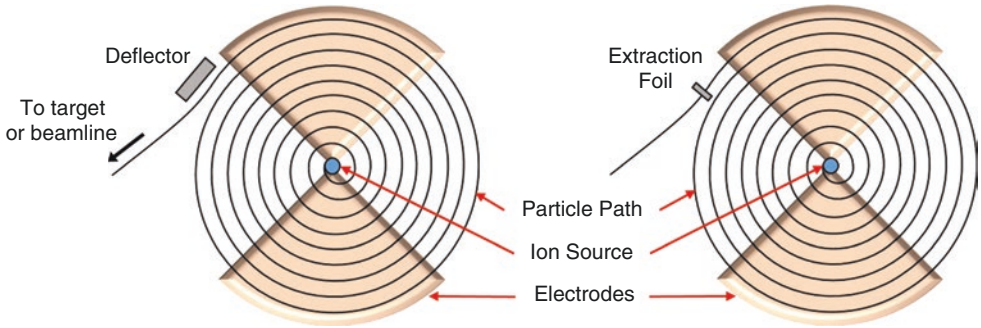

Fig. 7 Two common methods used in cyclotrons for particle beam extraction. (*Left*) A deflector is used to extract positive ions; (*right*) an extraction foil is used to strip electrons from negative ions, producing a positive ion beam

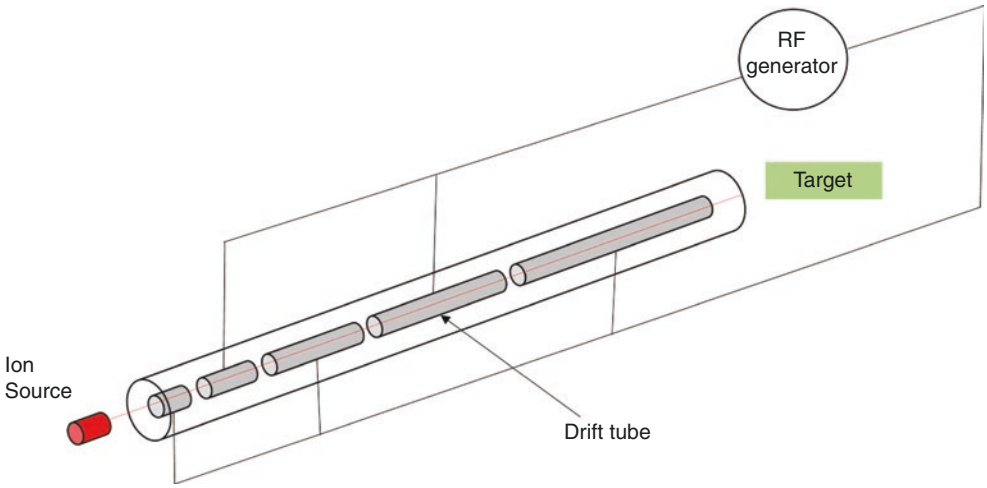

Fig. 8 Linac schematic illustrating the concept of a drift tube linac

called an extraction foil) in order to remove the electrons associated with the ions. In this manner, the ion changes from being negatively charged to positively charged and thus switches its trajectory in the magnetic field. This alteration in direction is used to direct the (now positively charged) ion into a target or down a beamline. For variable energy cyclotrons, the extraction foil may be at the end of a movable arm, which can extend to inner orbits for extraction of lower-energy particles or outer orbits for higher-energy particles. Alternatively, for positive ions, a deflector that creates an electric/magnetic perturbation in the ion's path can be used to direct the ion into a target or down a beamline.

Linear Accelerators

An alternative strategy for particle acceleration is the use of a linear accelerator (linac). As the name clearly suggests, linear accelerators accelerate particles down a linear path. The particle can still be accelerated by oppositely charged electrodes. In this case, however, the electrodes are sequential, as shown in Fig. 8 which illustrates the concept of a drift tube linac. The particles are accelerated between the gaps in the electrodes, which alternate in positive and negative charge in a similar fashion to the electrodes of a cyclotron. Due to the particle's increase in velocity as it moves down the tube, the length of each tube/electrode must increase in order to keep the time between gaps the same (similar to the longer path length due to increasing radius in a cyclotron). The drift tube linac is so named because the particles do not "feel" any force while they are inside the tubes and so are said to be "drifting."

Accelerator Targets

Targets for charged particle reactions using accelerators may be solid, liquid, or gas. The materials used to contain the target material are typically chosen based on thermal conductivity, melting point, machinability, and a low amount of "activation" (the amount of secondary radionuclides produced by particle beam interactions with the target housing material). Care must also be taken to select target bodies that do not react with the target material or the desired radioisotope. An excellent resource related to research on accelerator targetry is the proceedings of the Workshop on Targetry and Target Chemistry (WTTC) [11].

Gas Targets

The most common nuclear reaction used on a gas target is $^{14}N(p,\alpha)^{11}C$, which produces the positron-emitting radionuclide carbon-11 ($t_{1/2}$ = 20 min). The typical target shape for this reaction is cylindrical or conical with water cooling on the outside of the contained gas. A typical gas target chamber is shown in Fig. 9. The gas is typically contained inside the target chamber at high pressure and is contained via a thin isolation foil. To allow for increased heat dissipation, a helium-cooling chamber is often included in front of the gas target material, which in turn is isolated from the accelerator vacuum by another isolation foil (as shown in Fig. 9). Like all materials, gas targets are subject to heat effects in that the gas expands (and rises) when heated. The radionuclides produced can also undergo interactions with the walls of the target chamber.

The energy deposited in the target gas by the particle beam can also be used for in-target chemistry (sometimes referred to as "hot-atom" chemistry). The fact that the radionuclide is formed with some excess energy can be exploited to advance chemical reactions that include the radionuclide, converting it into a more desirable chemical form suitable for subsequent chemistry. For example, one can make $[^{11}C]CO_2$ by the addition of a small amount of O_2 to the target gas [12] or $[^{11}C]CH_4$ by the addition of H_2 to the target gas [13]. After irradiation, the gas can be easily transferred to the chemistry area via a transfer line accompanied by a helium push gas.

Liquid Targets

The most common nuclear reaction used on a liquid target is $^{18}O(p, n)^{18}F$, which produces the positron-emitting radionuclide fluorine-18 ($t_{1/2}$ = 110 min) via the bombardment of enriched $[^{18}O]H_2O$ (commonly called a "water target"). Water targets typically are 1–4 mL in volume and—similar to some gas targets—typically contain an isolation foil that contained helium-cooling window in between the water chamber and the accelerator vacuum. In some cases, a grid may be used to reinforce the window strength [14]. Due to the widespread success of the radiopharmaceutical [^{18}F]fluorodeoxyglucose ([^{18}F]FDG), there is a desire to make large quantities of fluorine-18. Hence, many different designs of these targets exist with a focus on heat/power dissipation. For example, targets using methods to allow for the reflux of the boiling target water, overpressure, and other techniques have been described in the literature [15]. Typically, the water cell is constructed of a relatively inert material that has low activation, such as niobium or tantalum. This material is carefully selected, as the $[^{18}F]F^-$ ion produced is very chemically reactive and may react with (and stick to) the target chamber if it is constructed out of another material such as aluminum.

The other main use for liquid targets is for the production of nitrogen-13 via the $^{16}O(p,n)^{13}N$ reaction. Similar to the hot-atom chemistry techniques described in the "Gas Target" section, a small amount of ethanol is typically added to the nitrogen-13 production target in order to ensure that the produced nitrogen-13 is in the desired reduced form of $[^{13}N]NH_3$.

Solid Targets

The nuclear reactions generated by the use of solid targets are much more varied than those used for gas or liquid targets. Solid target irradiations also typically require a more complex apparatus than gas or liquid targets. As a result, the irradiation of solid targets is feasible at fewer sites. Nevertheless, many groups have reported on the production of a wide range of radionuclides using solid targets with a variety of particle energies. In addition, the form of the target material can vary. Electroplated metals, pressed pow-

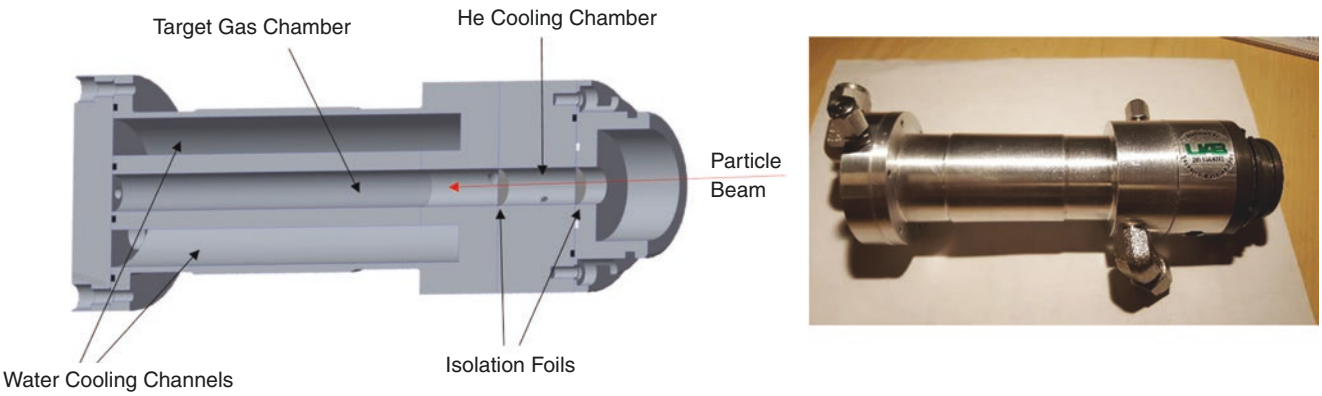

Fig. 9 (*Left*) Typical gas target configuration; (*right*) gas target at the University of Alabama at Birmingham

ders, foils, and melts have all been used to create solid targets for the production of radionuclides [16–18]. As the solid material is typically dissolved before separation chemistry, mechanisms to transport the irradiated solid target out of the irradiation area and into the chemical processing area have also been investigated by both academic groups and industry. Solid targets often make use of enriched target materials, which are relatively expensive and often need to be recycled to make using these materials economically feasible.

Lower-energy machines often use a coin target approach to solid targets as shown in Fig. 10 [19]. Target "coins" are typically inert substrates (gold, niobium, or platinum) that have been electroplated or sputtered with the desired target material. Radionuclides that can be produced via the coin target approach are copper-64 via the ^{64}Ni(p,n) reaction and zirconium-89 via the ^{89}Y(p,n) reaction [19, 20]. Several radionuclides produced at higher energies (typically at commercial facilities or national laboratories) use specially made solid targets designed to operate at high currents. For example, the commonly used isotope indium-111 is typically produced via the irradiation of Cd targets. The production of strontium-82 is also accomplished by high-power irradiations of Rb targets (either Rb or RbCl), which can withstand high energies and currents [21, 22].

Cross Sections for the Reactions of Charged Particles

All charged particle nuclear reactions have a threshold energy due to the Coulomb barrier (for neutrons this can be zero). Typically, as a function of projectile energy, cross-sectional (σ) profiles increase to a maxima and then decrease due to competing reaction channels as shown in Fig. 11 [23]. Charged particle reactions usually have a much lower σ than for neutron reactions. The production equation resembles that of Sect. 4.5.2 with some alterations.

$$A = nIx\sigma\left(1 - e^{-\lambda t}\right)$$

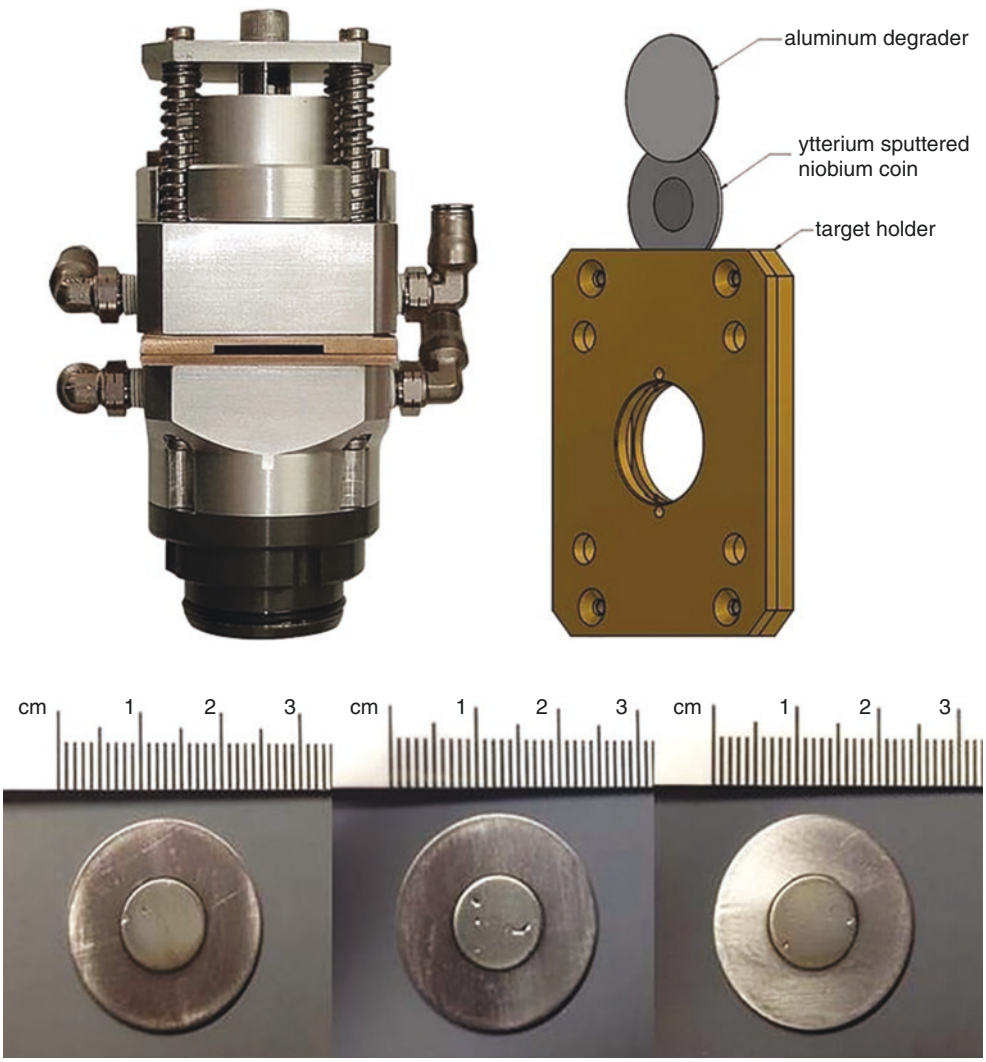

Fig. 10 Typical "coin" target configuration illustrating a sputtered Y layer on a Nb coin which is used to produce zirconium-89 via the ^{89}Y(p,n)^{89}Zr reaction (From Queern *et al.* [19], with permission)

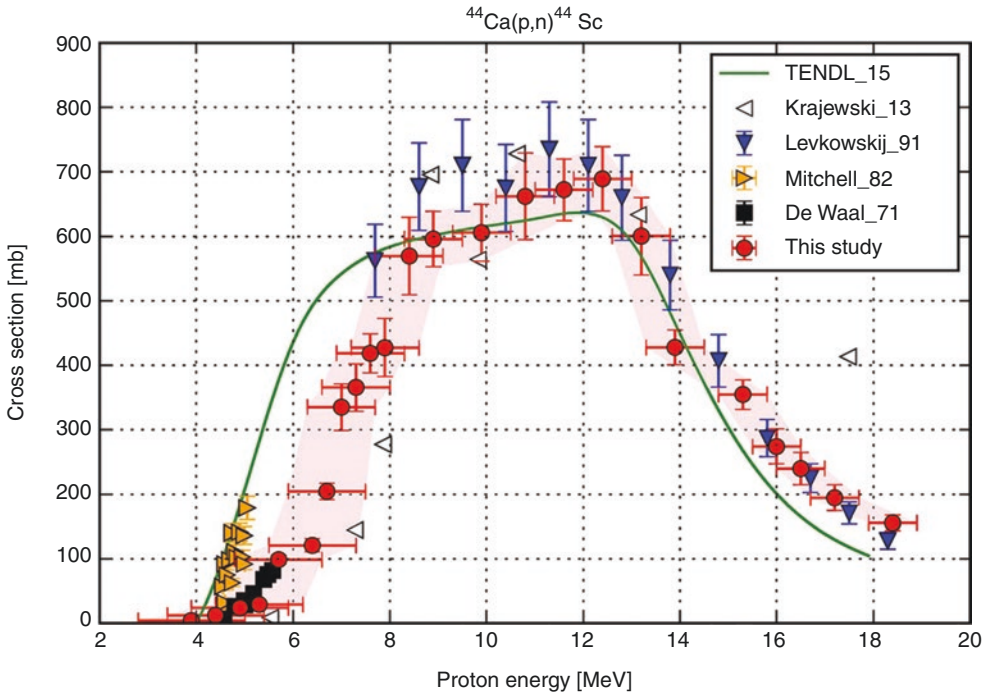

Fig. 11 Production cross sections for the $^{44}Ca(p,n)^{44}Sc$ reaction (From Carzaniga *et al.* [23], with permission)

where n = number of nuclei/cm^3 of target, I = current (particles/s), x = target thickness (cm), σ = reaction cross section (cm^2), and t = irradiation time. It is also important to note that the saturation effect discussed in the reactor production section also applies for the production of radionuclides via charged particle reactions.

Thus far, we have assumed that the target is "thin," with negligible charged particle energy loss and flux within the target. However, if we are considering thicker target material, this is not the case. Charged particle beams interact with the target material, losing both energy and flux. Neutrons interact very weakly with matter, and thus most targets for neutron irradiations can be considered thin. For the sake of simplicity, a thick target can be considered as a stack of thin targets, each subject to a different cross section, particle energy, and flux.

Radionuclide Generators

Another source of radionuclides for medical use is a device called a radionuclide generator. Essentially, in a radionuclide generator, a resin-bound, longer-lived parent radionuclide decays to chemically different daughter nuclide, which can subsequently be separated easily from the parent. Generators allow for shorter-lived radionuclides to be kept in ready supply at hospitals and research facilities, providing a consistent product for routine use. This is especially important in the clinic.

The most commonly used generator in nuclear medicine is the $^{99}Mo/^{99m}Tc$ generator. In this case, the parent radionuclide is molybdenum-99 ($t_{1/2}$ = 2.75 days), which decays to the daughter technetium-99m ($t_{1/2}$ = 6.0 h). The $[^{99}Mo][MoO_4]^{2-}$ is fixed to a solid acidic alumina support from which the technetium-99m is eluted or "milked" as $[^{99m}Tc][TcO_4]^-$, in which Tc has an oxidation state of +7. After a period of time (*e.g.* 24 h, as shown in Fig. 12), the technetium-99m builds up from the decay of molybdenum-99 and can be eluted. The amount of radioactivity of the daughter nuclide can be described by the equation:

$$A_2 = \mathrm{BR}\left(\frac{\lambda_2}{\lambda_2 - \lambda_1}\right) A_1^0 \left(e^{-\lambda_1 t} - e^{-\lambda_2 t}\right) + A_2^0 e^{-\lambda_2 t}$$

where $A_1{}^0$ is the parent activity at time zero and A_2 is the daughter activity at time t. The relationship between the activity of molybdenum-99 and technetium-99m—in which the half-life of the parent is only a few times greater than the half-life of the daughter—is known as *transient equilibrium*.

More recently, there has been a significant increase in the use of the $^{68}Ge/^{68}Ga$ generator [24]. In this case, the half-life of the parent—germanium-68 ($t_{1/2}$ = 271 d)—is much longer than the half-life of the daughter, gallium-68 ($t_{1/2}$ = 67.8 min), and thus one can assume that over short periods of time, the radioactivity of the daughter is forming at a relatively constant rate. Eventually, the radioactivity of the daughter reaches a saturation value at which the rate of the formation of the daughter equals the rate of decay of the daughter, a condition known as *secular equilibrium*.

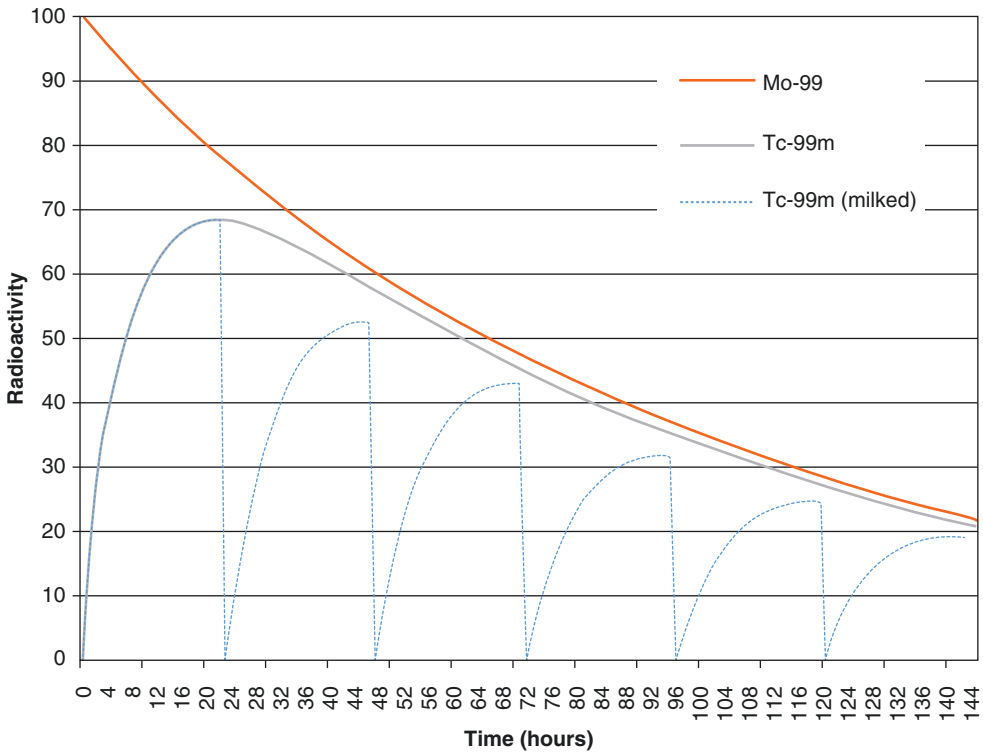

Fig. 12 Decay characteristics of a ^{99}Mo/^{99m}Tc generator

Photonuclear Isotope Production

More recently, several groups have been exploring the concept of using photonuclear reactions to produce radionuclides [25, 26]. In this technique, electrons are accelerated toward a high-Z radiator (such as tungsten) with which the electrons interact to produce a shower of photons, which in turn induce nuclear reactions—typically (γ,n) or (γ,p)—in the target material. This production route allows access to a new set of targets and product radionuclides that are currently accessible by neutron or charged particle routes. The production of useable quantities of radionuclides via this mechanism requires high-current electron accelerators. The benefits of photonuclear production include the ability to use compact, lightweight, and relatively inexpensive accelerators. The drawbacks are that the relative cross sections of photonuclear reactions are comparatively small and high-intensity photon beams of sufficient energy are difficult to produce and tend to result in significant heating of the target. Overall, the range of photons in material suggest much larger targets are required to maximize activity, which may lead to challenges for subsequent chemical processing. While this method is still in the research phase, as electron accelerator technology advances, high yields of radionuclides may be possible.

Practical Considerations for the Production of Radionuclides

As is clear from the preceding discussion, a collaborative effort from a multitalented team is required in order to produce radionuclides. This includes engineers to maintain the nuclear reactor or accelerator and chemists to process the targets.

Important considerations should also be made to weigh the pros and cons of alternative production methods if they are available. Nuclear reactors are less common than cyclotrons but allow for the irradiation of many samples at once for long irradiation times if necessary. Medical cyclotrons are more common, and for radionuclides with shorter half-lives, this is an advantage for shipping purposes. Typically, complementary sets of radionuclides can be produced via the reactor and accelerator routes.

Simulation Tools for the Production of Radionuclides

A variety of tools are available which may be of use when designing targets for the production of medical radionuclides. In particular, the freely available code *Stopping and Range of Ions in Matter* (SRIM) yields a Monte Carlo simu-

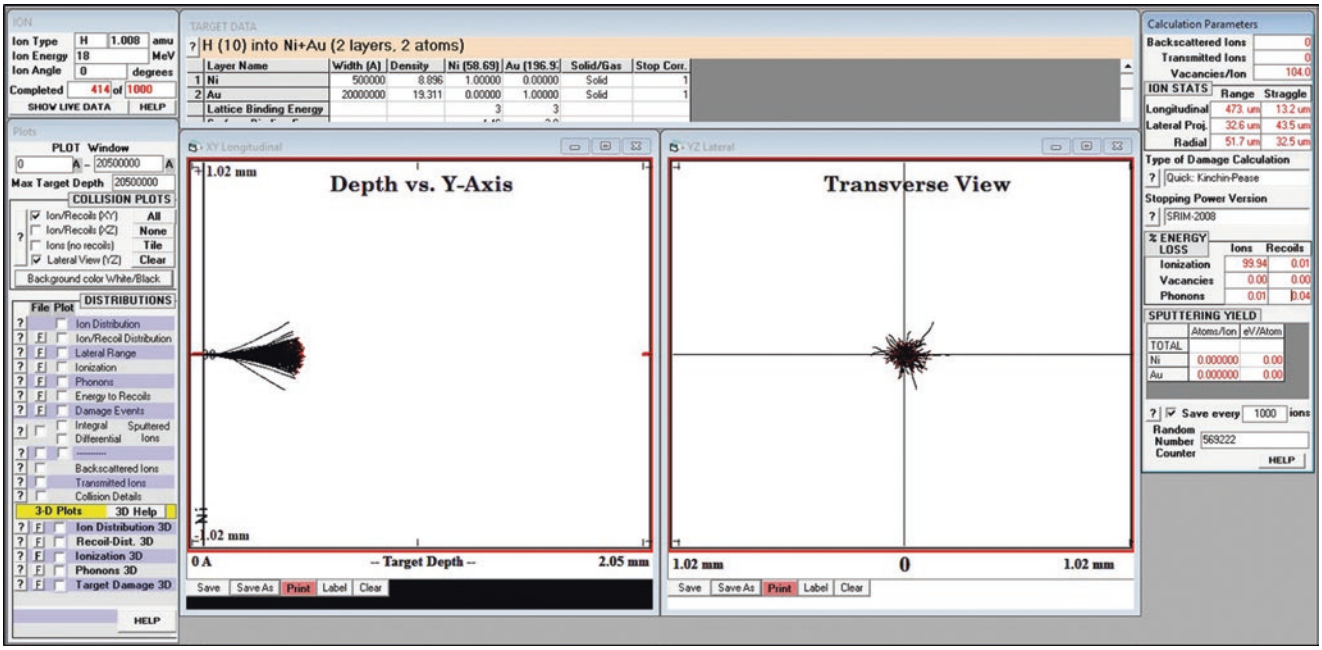

Fig. 13 Using "Stopping and Range of Ions in Matter" (SRIM) [27] to aid in the design of target materials in this simulation, 18 MeV protons are being used to bombard a target that has two layers. The first is 50 μm of Ni, and the second is 2 mm of Au. The proton beam shows minimal scatter through the Ni, but in the Au material, it quickly scatters, and most of the protons are stopped at an average depth of approximately 470 μm. (Screenshot used with the kind permission of James F. Ziegler [27])

lation of charged particles in matter and can be of great help in target design. A screenshot (Fig. 13) is provided as an example [27]. SRIM can provide information on the distance the charged particle travels in a certain material, its energy loss as it passes through the material, and the scatter of the charged particle beam. All of this information may inform changes to the thickness and/or density of the target as well as the use of degraders (which degrade the charged particle beam energy if necessary) in order to obtain the correct energy of the charged particle for the desired nuclear reaction.

Choosing a Target Material for the Production of Radionuclides

When choosing a target material, several factors should be considered, including the percentage of target atoms in the target material, the radioimpurities that can be produced via its irradiation, the chemical properties of the target (including its thermal conductivity), and the ease of the chemical processing of the target. In addition, one should consider the need for expensive enriched materials (if necessary), the cost of the target, and the possibility of recycling the target for reuse. These considerations may also be quite different for the production of radionuclides via reactor or charged particle reaction routes. A good source of nuclear decay and reaction data that may help inform these decisions is the national nuclear data center (https://www.nndc.bnl.gov/). Furthermore, the International Atomic Energy Agency (IAEA) has compiled a number of medically related cross sections at https://www-nds.iaea.org/medical/.

Innovative Targetry

Investigators have made use of innovative reaction routes or targetry to enable the production of radionuclides for medical use. For example, the "two-shoot" method for producing $[^{18}F]F_2$ was widely used for the production of electrophilic fluorine [28]. In the first phase of this method, the $[^{18}O]O_2$ gas is irradiated to produce $[^{18}F]F^-$. As $[^{18}F]F^-$ is very reactive, it adheres to the walls of the gas target chamber. The enriched $[^{18}O]O_2$ gas can then be cryotrapped and recovered for additional irradiations. The second irradiation involves the irradiation of an Ar/F_2 mixture. During this second bombardment, the environment inside the target causes the F_2 to exchange with $[^{18}F]F^-$ on the walls of target chamber, creating $[^{18}F]F_2$. It is important to note, however, that this $[^{18}F]F_2$ will have low specific activity due to the addition of nonradioactive—or "cold"—F_2.

Several groups have also reported on the concept of using targets composed of dissolved metallic salts in an attempt to overcome some of the difficulties with working

with solid target materials [29–31]. These "salty" targets allow for the omission of the dissolution step as well as the use of typical "water" targets for the development of new radionuclides. However, some of the drawbacks of this approach include the lower density of target atoms (which dramatically decreases the yield) and (in some cases) solubility issues [31].

Issues Related to the Supply of Radionuclides: HEU Reactors and Technetium-99m

Recently, there has been a lot of discussion about the future of the supply of molybdenum-99 for ^{99}Mo/^{99m}Tc generators [32]. As discussed in a previous section, until recently, the most common source of molybdenum-99 was as a fission product from HEU targets. These targets are mainly irradiated at older nuclear reactors that are nearing the end of their life spans. In fact, the Canadian NRU reactor—which up until recently supplied >50% of the US market for molybdenum-99—recently announced that they were no longer going to produce this important medical radionuclide. To compound the issue, the use of HEU is a security concern, as this material could potentially be used to make nuclear weapons. Thus, there is a substantial push to investigate alternative routes for the production of molybdenum-99 and/or technetium-99m. One method is by fissioning LEU targets, either in conventional reactors or via novel designs [33]. This method has one very significant advantage: the molybdenum-99 produced via this route is essentially identical to that produced via the HEU route and thus can be used with the same (approved) generators. In addition, the fission route can be used to simultaneously make other important radionuclides such as iodine-131. On the other hand, the yields of this approach may be much lower, and production via this route yields a significant amount of by-products. Other routes for the production of molybdenum-99 include the production of low specific activity molybdenum-99 via the ^{100}Mo(γ,n) or ^{98}Mo(n,γ) reactions [7]. While these routes are both feasible for the production of large quantities of molybdenum-99, the amount of mass required for a typical generator is much increased, and thus a new generator configuration must be developed and approved by the appropriate regulatory bodies.[1]

An alternative solution is the direct production of technetium-99m via the charged particle reaction ^{100}Mo(p,$2n$) [35]. This method bypasses the generator completely and thus overcomes some of the issues that come with a central distribution model. However, it also omits some of the conveniences that are provided by a generator model, as a local cyclotron facility would be required for the production (and distribution) of a radionuclide with a 6 h half-life. As this is an alternate route to the production of this widely used radionuclide, additional regulatory approvals would also be required before this new material could be used on a routine basis in the clinic. Several high-level documents are available which discuss the molybdenum-99 supply issue in detail [7, 33].

[1]On February 8, 2018, the FDA announced the approval of a technetium-99m generator that uses low specific activity molybdenum-99. This is the first FDA-approved generator that uses molybdenum-99 produced using a non-uranium process.

Conclusion

The production of radionuclides is an ongoing process under continuous research and refinement. Finding the most elegant route for producing a radionuclide involves not only determining the best reaction pathway but also takes into consideration every aspect of production, from the creation of target materials to the separation of the radionuclide and the recycling of the target. Production routes for new and more exotic radionuclides are vigorously being developed, leading to a well-equipped toolbox for the creation of the next generation of radiopharmaceuticals.

The Bottom Line

- Radionuclides used in nuclear medicine are almost exclusively produced using nuclear reactors and particle accelerators.
- Nuclear reactors are used to bombard targets with neutrons, while particle accelerators are used to bombard targets with a variety of charged particles (*e.g.* hydride ions, protons, deuterons, and alpha particles).
- Targets for radionuclide production can be solid, liquid, or gas.
- Therapeutic radionuclides are typically produced in reactors and have low specific activity, while diagnostic radionuclides are often produced using particle accelerators and have high specific activity.
- Radionuclide generators provide a convenient, on-site source for short-lived radionuclides.

References

1. Muranaka RG. Conversion of research reactors to low-enrichment uranium fuels. IAEA Bull. 1983;25(1):18–20.
2. National Academies of Sciences, Engineering, and Medicine. Reducing the use of highly enriched uranium in civilian research reactors. 2016. https://www.nap.edu/catalog/21818/reducing-the-use-of-highly-enriched-uranium-in-civilian-research-reactors. Accessed 31 Oct 2017.

3. Holloway MG, Baker CP. How the barn was born. Phys Today. 1972;25(7):9. http://physicstoday.scitation.org/doi/10.1063/1.3070918. Accessed 1 Nov 2017.
4. Chadwick MB, Herman M, Obložinský P, Dunn ME, Danon Y, Kahler AC, et al. ENDF/B-VII.1 nuclear data for science and technology: cross sections, covariances, fission product yields and decay data. Nuclear Data Sheets. 2011;112(12):2887–996.
5. IAEA TECDOC 1340. Manual for reactor produced radioisotopes. Vienna: International Atomic Energy Agency. http://www-pub.iaea.org/books/IAEABooks/6407/Manual-for-Reactor-Produced-Radioisotopes. Accessed 31 Oct 2017.
6. Koning A, Forrest R, Kellett M, Mills R, Henriksson H, Rugama Y, et al. The JEFF-3.1 Nuclear Data Library – JEFF Report 21. Organisation for Economic Co-Operation and Development; 2006. Report No. NEA--6190. http://inis.iaea.org/Search/search.aspx?orig_q=RN:45026295. Accessed 1 Nov 2017.
7. National Academies of Sciences, Engineering, and Medicine. Molybdenum-99 for medical imaging. 2016. https://www.nap.edu/catalog/23563/molybdenum-99-for-medical-imaging. Accessed 21 Oct 2017.
8. Bradley E. Non-HEU production technologies for Molybdenum-99 and Technetium-99m. Vienna: International Atomic Energy Agency; 2013.
9. National Research Council (US) Committee on Medical Isotope Production Without Highly Enriched URanium. Molybdenum-99/technetium-99m production and use. Washington DC: National Academies Press. 2009. https://www.ncbi.nlm.nih.gov/books/NBK215133/. Accessed 28 Oct 2017.
10. Humphries S Jr. Principles of charged particle acceleration. Mineola: Dover Publications; 2013.
11. Workshops on Targetry and Target Chemistry. Proceedings for targetry workshop 1985–2016. TRIUMF, University of British Columbia, Vancouver. http://wttc.triumf.ca/proceedings.html. Accessed 7 Apr 2018.
12. Matthews CME, Laszlo G, Campbell EJM, Kibby PM, Freedman S. Exchange of $^{11}CO_2$ in arterial blood with body CO_2 pools. Respir Physiol. 1968;6(1):29–44.
13. Buckley KR, Jivan S, Ruth TJ. Improved yields for the in situ production of [^{11}C]CH_4 using a niobium target chamber. Nucl Med Biol. 2004;31(6):825–7.
14. Nye JA, Avila-Rodriguez MA, Nickles RJ. A grid-mounted niobium body target for the production of reactive [^{18}F]fluoride. Appl Radiat Isot. 2006;64(5):536–9.
15. Peeples JL, Stokely MH, Michael Doster J. Thermal performance of batch boiling water targets for ^{18}F production. Appl Radiat Isot. 2011;69(10):1349–54.
16. Nye JA, Avila-Rodriguez MA, Nickles RJ. A new binary compound for the production of ^{124}I via the ^{124}Te(p,n)^{124}I reaction. Appl Radiat Isot. 2007;65(4):407–12.
17. Mastren T, Marquez BV, Sultan DE, Bollinger E, Eisenbeis P, Voller T, et al. Cyclotron production of high–specific activity ^{55}Co and in vivo evaluation of the stability of ^{55}Co metal-chelate-peptide complexes. Mol Imaging. 2015;14(10):7290.2015.00025.
18. Hilgers K, Coenen HH, Qaim SM. Production of the therapeutic radionuclides ^{193m}Pt and ^{195m}Pt with high specific activity via α-particle-induced reactions on ^{192}Os. Appl Radiat Isot. 2008;66(4):545–51.
19. Queern SL, Aweda TA, Massicano AVF, Clanton NA, El Sayed R, Sader JA, et al. Production of Zr-89 using sputtered yttrium coin targets. Nucl Med Biol. 2017;50(Suppl C):11–6.
20. McCarthy DW, Shefer RE, Klinkowstein RE, Bass LA, Margeneau WH, Cutler CS, et al. Efficient production of high specific activity ^{64}Cu using a biomedical cyclotron. Nucl Med Biol. 1997;24(1):35–43.
21. Fassbender ME, Ballard B, Birnbaum ER, Engle JW, John KD, Maassen JR, et al. Proton irradiation parameters and chemical separation procedure for the bulk production of high-specific-activity ^{186g}Re using WO_3 targets. Radiochim Acta. 2013;101(5):339–46.
22. Mausner LF, Prach T, Srivastava SC. Production of ^{82}Sr by proton irradiation of RbCl. Int J Rad Appl Instrum A. 1987;38(3):181–4.
23. Carzaniga TS, Auger M, Braccini S, Bunka M, Ereditato A, Nesteruk KP, et al. Measurement of ^{43}Sc and ^{44}Sc production cross-section with an 18 MeV medical PET cyclotron. Appl Radiat Isot. 2017;129:96–102.
24. Fani M, Andre JP, Maecke HR. ^{68}Ga-PET: a powerful generator-based alternative to cyclotron-based pet radiopharmaceuticals. Contrast Media Mol Imaging. 2008;3(2):53–63.
25. Mamtimin M, Harmon F, Starovoitova VN. Sc-47 production from titanium targets using electron linacs. Appl Radiat Isot. 2015 Aug;102:1–4.
26. Howard S, Starovoitova VN. Target optimization for the photonuclear production of radioisotopes. Appl Radiat Isot. 2015;96(Suppl C):162–7.
27. Ziegler JF, Biersack JP. Stopping and range of ions in matter; SRIM. www.srim.org. Accessed 7 Apr 2018.
28. Nickles RJ, Daube ME, Ruth TJ. An $^{18}O_2$ target for the production of [^{18}F]F_2. Int J Appl Radiat Isot. 1984;35(2):117–22.
29. Pandey MK, Bansal A, Engelbrecht HP, Byrne JF, Packard AB, DeGrado TR. Improved production and processing of ^{89}Zr using a solution target. Nucl Med Biol. 2016;43(1):97–100.
30. Oehlke E, Hoehr C, Hou X, Hanemaayer V, Zeisler S, Adam MJ, et al. Production of Y-86 and other radiometals for research purposes using a solution target system. Nucl Med Biol. 2015;42(11):842–9.
31. Jensen M, Clark J. Direct production of Ga-68 from proton bombardment of concentrated aqueous solutions of [Zn-68] Zinc Chloride. In Haroun S, Givskov AD, Jensen M, editors. The 13th International Workshop on Targetry and Target Chemistry Proceedings. Roskilde: Danmarks Tekniske Universitet, Risø Nationallaboratoriet for Bæredygtig Energi. 2011. pp. 288–92. (Denmark. Forskningscenter Risoe. Risoe-R; No. 1787(EN)).
32. Ruth TJ. The medical isotope crisis: how we got here and where we are going. J Nucl Med Technol. 2014;42(4):245–8.
33. Nuclear Science Advisory Committee (NSAC) ^{99}Molybdenum (^{99}Mo) Subcommittee. Annual assessment of the NNSA-material management and minimization (M^3) ^{99}Mo program. 2016, November 3. https://science.energy.gov/~/media/np/nsac/pdf/docs/2016/Mo-99_NSAC-approved-2016.pdf. Accessed 21 Oct 2017.
34. Selivanova SV, Lavallée É, Senta H, Caouette L, McEwan AJB, Guérin B, et al. Clinical trial with sodium ^{99m}Tc-pertechnetate produced by a medium-energy cyclotron: biodistribution and safety assessment in patients with abnormal thyroid function. J Nucl Med. 2017;58(5):791–8.
35. Hou X, Tanguay J, Buckley K, Schaffer P, Bénard F, Ruth TJ, et al. Molybdenum target specifications for cyclotron production of ^{99m}Tc based on patient dose estimates. Phys Med Biol. 2015;61(2):542.

An Overview of Targeted Radiotherapy

Michal Grzmil, Alexander Meisel, Martin Behé, and Roger Schibli

Introduction to Targeted Radionuclide Therapy in Oncology

Currently, half of all diagnosed cancer patients will receive radiotherapy as a standard-of-care treatment, either alone or in combination with surgery or chemotherapy. External beam radiation therapy (EBRT) has been commonly used for many decades. While some patients respond to EBRT, many others—such as glioblastoma patients—have very low response rates to the treatment [1]. During cancer progression, metastasis leads to the spread of cancer cells to surrounding tissues as well as to distant organs. In addition, a study of liquid biopsies reported circulating tumor cells (CTC)—cells shed either from the primary or secondary tumors—can remain in the bloodstream or bodily fluids after standard-of-care treatment and are associated with both resistance to therapy and fatal recurrence [2, 3]. Perhaps not surprisingly, the presence of cancer cells in various parts of the body significantly hinders therapeutic responses to EBRT. Strategies for targeted radionuclide therapy (TRT) have been developed in order to more accurately and efficiently deliver radiation to secondary cancer lesions and disseminated disease. Indeed, orally or intravenously administrated radiopharmaceuticals can target primary tumors as well as metastatic lesions from *inside* the body, and their selectivity for tumor tissue prevents injury to healthy organs.

M. Grzmil · M. Behé · R. Schibli (✉)
Center for Radiopharmaceutical Sciences ETH-PSI-USZ, Paul Scherrer Institute, Villigen-PSI, Switzerland
e-mail: roger.schibli@psi.ch

A. Meisel
Department of Nuclear Medicine, University Hospital of Zurich, Zurich, Switzerland

Department of Internal Medicine—Oncology & Hematology, Stadtspital Waid, Zurich, Switzerland

Institute of Pharmaceutical Sciences, Department of Chemistry and Applied Biosciences ETH Zurich, Zurich, Switzerland

The earliest studies focused on radionuclides that specifically accumulate in certain organs or pathological tissues in the absence of any targeting vector. In the early 1940s, radioactive iodine (RAI) treatment was successfully used for the treatment of patients with hyperthyroidism. At the same time, radioiodine also enabled the detection of previously unidentified metastatic lesions in treated patients, demonstrating its diagnostic potential at a very early stage [4]. A few years later in 1946, the Atomic Energy Act (AEA) in the United States approved the use of radionuclides in medicine. Since then, nuclear medicine—previously known as atomic medicine—has become established as an integral discipline in medicine.

Over the same period, iodine-131—or radioactive iodine, as it is sometimes known—has become a standard diagnostic and therapeutic radiopharmaceutical for thyroid cancer and hyperthyroidism. The thyroid gland absorbs circulating iodine, and thus RAI can be used for targeting tumors in the thyroid, cancerous lesions that remain after the resection of the gland, and cancer cells that spread to the lymph nodes or other parts of the body. Notably, not all types of thyroid cancer take up RAI; the most notable example of this is medullary thyroid cancer (MTC), which originates in parafollicular C-cells which do not accumulate iodine [5]. Although the clinical use of iodine-131 is effective, RAI can only be used for a very limited number of cancers, such as papillary or follicular thyroid cancers.

For the vast majority of cancers, therefore, the therapeutic radionuclide must be covalently attached to a vector capable of selectively and specifically delivering the radioactivity to the tumor tissue in question [6]. This is most often achieved by using biomolecular vectors that can bind tumor biomarkers with high affinity and specificity. The accurate and efficient targeting of tumors not only ensures the maximum possible dose of therapeutic radiation to the malignant tissue but can also reduce cytotoxic side effects to healthy organs as well as those involved in the excretion of radiopharmaceuticals. In nuclear medicine, research into optimizing the properties of therapeutic radiopharmaceuticals—including their

J. S. Lewis et al. (eds.), *Radiopharmaceutical Chemistry*, https://doi.org/10.1007/978-3-319-98947-1_5

affinity, stability, and pharmacokinetic profile—are often aimed at increasing the radiation dose delivered to cancer cells while limiting the damage to healthy tissues.

Therapeutic Radionuclides

There are a wide variety of therapeutic radionuclides with varying half-lives and types of emission. Generally speaking, the type of radionuclide used in a therapeutic radiopharmaceutical must be tailored to the specific type of cancer or even the stage of the disease being treated. As shown in Fig. 1, radionuclides that undergo α-decay produce particles composed of two neutrons and two protons, whereas radionuclides that undergo β-decay emit energetic electrons from their nuclei [7–9] (see chapter "The Basics of Nuclear Chemistry and Radiochemistry: An Introduction to Nuclear Transformations and Radioactive Emissions" for an in-depth discussion of radioactive decay). Some radionuclides can also emit Auger or conversion electrons via secondary effects. α-Particles have high linear energy transfer (LET)—approximately 80 keV/μm—and are capable of damaging DNA both directly and via the production of reactive oxygen species (ROS). β-Particles and Auger electrons, in contrast, have low LET values of 0.2–2 keV/μm or 4–26 keV/μm, respectively. Particles with both high and low LET can be useful for TRT depending on the nature of the disease. For example, the TRT of leukemia and lymphoma typically requires lower energy particles than the TRT of solid tumors.

The range of these particles in tissue represents a critical consideration when designing a therapeutic radiopharmaceutical. β-Particles have a range of a few mm in tissue, while alpha particles and Auger electrons have relatively short ranges of 40–100 μm or below 5 μm, respectively. Not surprisingly, particles with short ranges are more effective for small tumors, while particles with longer ranges are more effective against larger tumors. Interestingly, it is commonly thought that the particles with the shortest range—Auger electrons—must be *in the nucleus* to kill cells, though recent studies suggest that the cell membranes of ovarian cancer cells may be more sensitive to Auger electrons than the cytoplasm [10]. The range of a particle becomes particularly relevant in the context of tumor heterogeneity. Indeed, both the heterogeneous expression of antigens and differences in vascularization can result in the uneven spatial distribution of radiopharmaceuticals in some tumors [11]. In these cases, more complete therapeutic responses can be achieved using radionuclides which emit particles with longer ranges that can impact not only the cells to which the radiopharmaceutical is attached but also neighboring cells with lower levels of the radiopharmaceutical. This is known as the "cross-fire effect." Unfortunately, however, the cross-fire effect may also have an unwanted impact on adjacent healthy tissues.

Two other traits of a radionuclide—half-life and the creation of radioactive daughters—must also be considered. Generally speaking, the physical half-life of the radionuclide should be matched to the biological half-life of the molecular vector. In a stark departure from diagnostic nuclear medicine, radionuclides with longer half-lives—for example, yttrium-90 ($t_{1/2}$ = 2.7 d) or lutetium-177 ($t_{1/2}$ = 6.7 d)—are typically preferred for therapeutic applications. That said, the use of radionuclides with half-lives that are *too* long risks causing side effects in healthy organs. Finally, it is important to remember that the decay of a given radionuclide may produce radioactive daughters which can produce different forms of radiation and distribute elsewhere in the body, including healthy organs. For example, the alpha-emitter actinium-225 has shown promising activity in clinical trials for cancer treatment. However, its decay chain produces several daughter radionuclides—most notably bismuth-213—that are liberated from the original metal chelator. As a result, bismuth-213 and its daughter nuclide lead-209 can be released from the vector and can translocate from tumor sites to healthy organs. This increases the radiotoxicity of ^{225}Ac-based radiopharmaceuticals and limits the maximum amount of radioactivity that can be administered [12].

Radiation-Induced Cell Death

The ultimate goal of selectively delivering ionizing radiation (IR) to tumors is destroying cancer cells. This can be mediated directly via the emitted particles (in TRT) or gamma rays (in EBRT) or indirectly via the production of reactive oxygen species (ROS), which are produced from the radiolysis of water. Both radiation and ROS such as short-lived free hydroxyl radicals [$HO^{\cdot}$] can significantly damage cellular structures and organelles, including the nucleus and the DNA contained therein. Depending on the nature of the ionization radiation, radiation-mediated DNA damage can include the creation of oxidized bases, abasic sites, single-strand breaks, double-strand breaks, DNA cross-links, and complex chromosomal rearrangements [13]. Although DNA damage is believed to be the primary cause of radiation-induced cell death, it is also believed that ROS-mediated damage to the mitochondria and cell membrane contributes as well [14, 15]. The creation of unrepaired DNA lesions and cellular damage can lead to apoptosis and mitotic catastrophe, the two major mechanisms of radiation-induced cell death [16]. In the former, induced programed cell death (apoptosis) activates cysteine proteases, caspases that promote the degradation of cellular components including the proteins involved in DNA damage repair and survival. During mitotic catastrophe, delayed DNA damage induced by ionizing radiation results in the aberrant segregation of chromosomes and the formation of giant cells with multiple micronuclei which eventually undergo cell death via apoptosis, necrosis, or senescence [17].

a

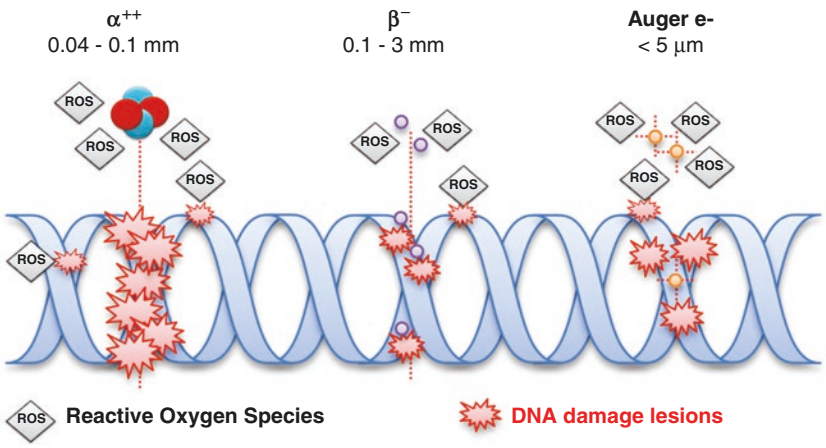

b

Nuclide	Emission	Half-life (days)	Emax (MeV)	Mean Range (mm)
Actinium-255 (Ac-225)	α, β	10.0	5.83 (α)	0.04-0.1
Astatine-211 (At-211)	α	0.33	5.87	0.04-0.1
Radium-223 (Ra-223)	α	11.4	5.78	0.04-0.1
Lutetium (Lu-177)	β, γ	6.7	0.50 (β)	0.28
Iodine-131 (I-131)	β, γ	8.0	0.81 (β)	0.40
Samarium-153 (Sm-153)	β, γ	1.9	0.80 (β)	0.53
Rhenium-186 (Re-186)	β, γ	3.8	1.10 (β)	0.92
Copper-67 (Cu-67)	β, γ	2.6	0.57 (β)	0.60
Strontium-89 (Sr-89)	β	50.5	1.46	2.40
Yttrium-90 (Y-90)	β	2.7	2.30	2.76
Terbium-161 (Tb-161)	β, Auger	6.89	0.59 (β)	0.20
Gallium-67 (Ga-67)	Auger, γ	3.3	0.009 (Auger)	0.002-2.4 µm
Iodine-125 (I-125)	Auger	60.1	0.03	0.002-0.5 µm

Fig. 1 DNA damage by different types of radioactive nuclides. (**a**) Schematic representation of the ionization density of α-particles, β-particles, and Auger electrons. α-Particles—composed of two neutrons and two protons—possess high linear energy transfer (LET) of approximately 80 keV/µm and are densely ionizing. β-Particles, with LET of 0.2-2 keV/µm, are sparsely ionizing. Auger electrons, with LET of 4–26 keV/µm, form clusters with high-density ionization. (**b**) Examples of therapeutic radionuclides

Radioresistance

While radiation-induced damage often results in cell death, in other cases, the acquired or innate radioresistance of tumors can make killing cancer cells with ionizing radiation difficult. Importantly, the radioresistance of tumors depends on many factors, including the nature of the radiation and the dose delivered as well as the type, stage, genetic background, heterogeneity, and pathomorphology of the cancer. For example, solid tumors are often hypoxic, a trait that can

inhibit the radiation-mediated formation of ROS and thus attenuate indirect damage to cellular structures [18]. Furthermore, a radiomics study—which is based on an analysis of tumor images acquired via PET or MRI and responses to external radiotherapy—indicates a correlation between intratumoral heterogeneity and radioresistance [19, 20]. Importantly, the majority of our knowledge of tumor radiobiology has emerged from studies using conventional external beam radiation, a technique which produces homogenous irradiation at relatively high absorbed dose rates. Less is known about the response of cancer cells to radiotherapy via targeted radiopharmaceuticals, which produce heterogeneous irradiation with lower absorbed doses.

On the cellular level, several pathways can promote the survival of cells in the face of IR-induced damage. Chief among these are the DNA damage response (DDR) pathways (Fig. 2). A wide variety of enzymes and mechanisms mediate the cellular response to DNA damage [21]. Shortly after the DNA is damaged, an enzyme known as poly (ADP-ribose) polymerase (PARP) binds to the DNA lesions and creates poly(ADP-ribose) chains that recruit other enzymes in the DNA damage response. Subsequently, two major proteins in the DNA damage response—ataxia-telangiectasia mutated/checkpoint kinase 2 (ATM/Chk2) and ATM- and Rad3-related/checkpoint kinase 1 (ATR/Chk1)—activate several other downstream proteins that coordinate DNA repair and cell cycle progression, including phosphatidylinositide 3-kinase (PI3K), DNA-dependent protein kinase (DNA-PK), and transcription factor p53 [22–24]. Indeed, tumor suppressor p53 plays a particularly significant role in the cellular response to ionizing radiation by regulating the transcription of several key proteins involved in the regulation of the cell cycle, DNA repair, and apoptosis. These proteins include cyclin-dependent kinase inhibitor 1 (p21), growth arrest and DNA damage (GADD45), phosphoserine binding proteins 14–3-3, and apoptosis regulator bcl-2-like protein 4 (BAX) [25]. The nonhomologous end joining (NHEJ) and homologous recombination repair (HRR) pathways are two major mechanisms of DNA repair activated in response to ionizing radiation [26]. The relative contributions of the two pathways are highly dependent on the cell cycle, though both effectively preserve the integrity of the genome.

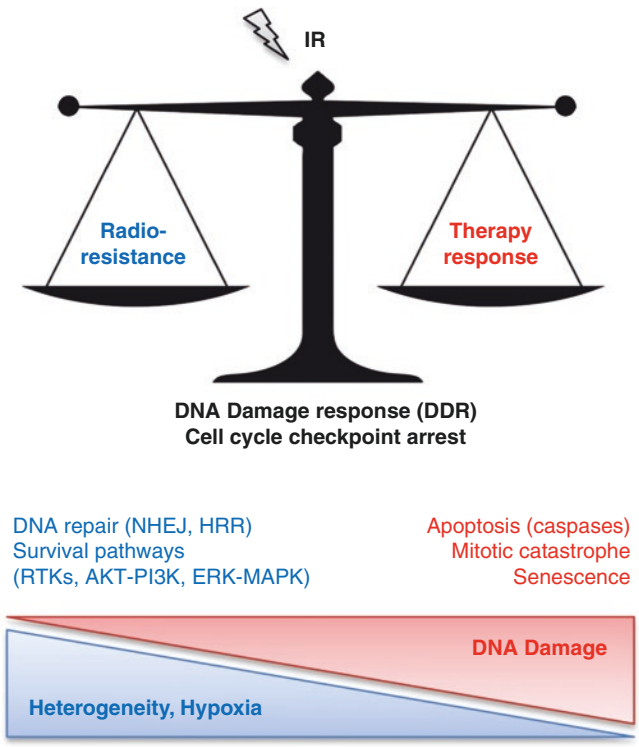

Fig. 2 The response of a cancer cell to radiotherapy. Ionizing radiation (IR) induces the DNA damage response (DDR), which leads to cell cycle arrest and promotes DNA repair or cell death via apoptosis, mitotic catastrophe, or senescence. Two major DNA repair mechanisms include nonhomologous end joining (NHEJ) and homologous recombination repair (HRR). Several other IR-activated signaling pathways support the survival of the cell

Radioresistance can also be conferred by cellular pathways other than the DNA damage response. For example, the ROS generated by ionizing radiation can interfere with several growth and survival regulators—including human epidermal growth factor receptor 2 (HER2), extracellular signal-regulated kinases 1 and 2 (ERK1/2), and serine/threonine-specific protein kinase B (PKB, also known as AKT)—whose activation prevents cancer cells from undergoing apoptosis [27]. Another important mechanism that influences the cytotoxicity of IR is autophagy: a process that maintains cellular homeostasis in the presence of cellular stress (*e.g.* during starvation) and promotes survival via the self-digestion of destroyed organelles for the generation of "building blocks" for new organelles. In various cancers, radiotherapy can induce autophagy, and several preclinical studies have shown that modulating autophagy signaling pathways can improve the efficacy of radiotherapy [27].

Molecular Targets and Radiotherapeutics

Types of Targeting

A variety of targeting mechanisms have been used to deliver therapeutic radionuclides to tumor tissue. For effective delivery, radionuclides need to be covalently bound to vectors with high affinities to cancer cells. These vectors can take on a variety of forms, including small molecules (*e.g.* steroids), peptide ligands, monoclonal antibodies, and nanoparticles. The selection of the most suitable vector requires the consideration of several factors, such as affinity, stability, and excretion routes. For example, peptides and small molecules are

often limited by their short *in vivo* half-lives, which range from minutes to a few hours due to their clearance by the renal and hepatobiliary systems. As a result, radiolabeled peptides and small molecules deposit large amounts of energy over short periods of time. In contrast, the clearance of radiolabeled antibodies requires more time, typically several days to 3 weeks. This, of course, results in the accumulation of radiation dose over a larger time period. Thus, the most suitable vector for a therapeutic application must be tailored to the specific radionuclide as well as the cancer type. In some cases, the radionuclide itself is selectively taken up by tumor tissue. As we have mentioned, sodium iodine-131 has been approved for the treatment of hyperthyroidism and differentiated thyroid cancers. Similarly, several metallic radionuclides that can bind to hydroxyapatite—an essential component of the bone matrix—have been used for the targeted therapy of bone metastases. To wit, radium-223 dichloride [^{223}Ra]$RaCl_2$—currently marketed as Xofigo®—has proven clinically effective for the treatment of patients with bone metastases from castration-resistant prostate cancers, and samarium-[^{153}Sm]Sm-lexidronam and [^{89}Sr]$SrCl_2$ have been used for the palliative care of patients suffering from bone pain due to osteoblastic and skeletal metastasis [28, 29].

In other cases, differences in the anatomy of the tumor and the host tissue provide a conduit for selective targeting. For example, selective interarterial radiation therapy (SIRT)—also known as radioembolization—is approved for the treatment of non-operative patients with hepatocellular carcinoma and liver metastases. SIRT employs ^{90}Y-labeled microspheres made of glass (*TheraSphere*®) or

a

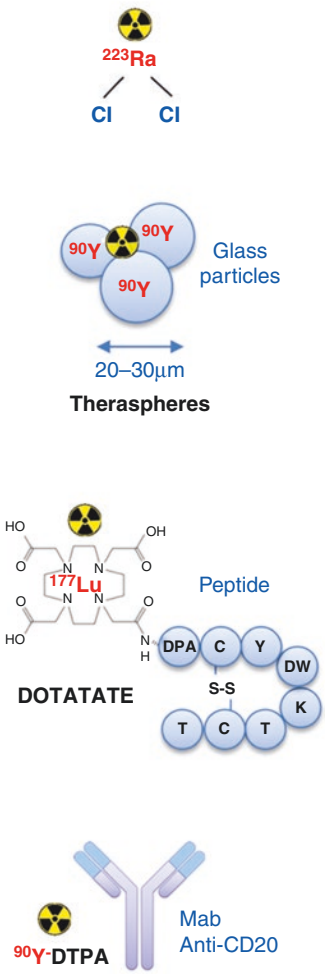

b

Radiopharmaceutical	Target	Therapeutic indication
Radionuclide therapy		
Sodium iodide (I-131)	Thyroid gland	Hyperthyroidism, differentiated thyroid cancer
Radium dichloride (Ra-223)	Bone matrix	Castration-resistant prostate cancer, symptomatic bone metastases
Samarium lexidronam (Sm-153)	Bone matrix	Relief of pain, osteoblastic metastasis
Strontium-89 chloride (Sr-89)	Bone matrix	Relief of pain, skeletal metastases
Selective interarterial radiation therapy (SIRT)		
Microspheres (Y-90) Teraspheres or SIR-spheres	Intravascular space	Hepatocellular cancer and liver metastasis
Peptide receptor radionuclide therapy (PRRT)		
DOTATATE (Lu-177)* Lutathera	Somatostatin receptor	Neuroendocrine tumors
Radioimmunotherapy (RIT)		
Ibritumomab tiuxetan, Zevalin (Y-90)	CD20 antigen	Non-Hodgkin's lymphoma (NHL)
Tositumomab, Bexxar (I-131)	CD20 antigen	Non-Hodgkin's lymphoma (NHL)

Fig. 3 Approved targeted radionuclide therapies in oncology. (**a**) Examples of radiopharmaceuticals used in clinic for internal radiotherapy. From top to bottom: schematic representations of [^{223}Ra]$RaCl_2$ (Xofigo®), yttrium-90-embedded microspheres (TheraSpheres®), ^{177}Lu-labeled DOTATATE, and the ^{90}Y-labeled monoclonal anti-CD-20 antibody (mAb) Zevalin. (**b**) Approved list of radiopharmaceuticals, their targets, and their therapeutic indications in oncology. (*Approved by the U.S. F.D.A. in 2018)

a biocompatible polymer resin (*SIR-Spheres*®) with diameters ranging from 20–30 or 20–60 μm, respectively [30]. The radioactive microspheres are administrated into the hepatic artery and are selectively distributed in the tumor microvasculature because the tumor, unlike normal liver tissue, receives the vast majority of its blood supply via the hepatic artery [31] (Fig. 3).

For most other types of tumors, however, the effective delivery of radionuclides is predicated on the use of biomolecular vectors—typically short peptides (*e.g.* octreotide) or monoclonal antibodies (*e.g.* ibritumomab)—that can target cancer biomarkers with high affinity and selectivity [32, 33]. These biomolecules can be radiolabeled with therapeutic radionuclides either directly or through the use of prosthetic groups or bifunctional chelators such as DOTA (1,4,7,10-tetraazacyclododecane-1,4,7,10-tetraacetic acid) or NODAGA (1,4,7-triazacyclononane,1-glutaric acid-4,7-acetic acid) [34, 35].

G-Protein-Coupled Receptors (GPCR)

The identification and characterization of molecular targets—most often transmembrane receptors or antigens that are either exclusively expressed or highly overexpressed by cancer cells—are critical for successful targeted radionuclide therapy. G-protein-coupled receptors (GPCR) represent promising targets since they are frequently overexpressed in human cancers and bind peptide ligands with high affinity and selectivity [36, 37]. Peptide-based radiotherapeutics that are agonists of GPCR bind to the receptor and cause rapid conformational changes. These activated GPCRs undergo desensitization via an arrestin-mediated internalization process, during which the receptors are transported either to lysosomes for degradation or to endosomes for recycling back to the cell surface [38]. Critically, this internalization process delivers the therapeutic radionuclides into the cells, where they can do even more damage. Other GPCR-binding peptides that are antagonists (and thus do not activate this internalization pathway) are also currently under evaluation for their potential in TRT [39].

The overexpression of somatostatin receptors (SSTR)—a member of this GPCR family—in neuroendocrine tumors has spurred the extensive development of peptide receptor radionuclide therapies for the disease. SSTRs exist in five different isoforms: SSTR1–5 [40]. While normal tissues express very low levels of SSTR2, almost 70% of NETs overexpress this isoform. DOTA-bearing variants of the SSTR2-targeting peptide octreotide (DOTA-TOC and DOTA-TATE) bind the receptor with high affinity and selectivity and have been used clinically for both imaging and peptide receptor radionuclide therapy (PRRT). Indeed, PET/CT with ^{68}Ga-labeled DOTA-TATE has been used in patients with NETs for diagnostic imaging as well as to predict the efficacy of PRRT with ^{177}Lu- or ^{90}Y-labeled DOTA-TOC or DOTA-TATE [41–43]. Patients treated with [^{177}Lu]Lu-DOTA-TATE (*LUTATHERA*®, US Food and Drug Administration (FDA)-approved in the United States in 2018) show improved overall survival of several years from the time of diagnosis [44].

SSTR agonists such as octreotide have certainly shown value in the clinic, but as we have noted, they are not the only possible approach to SSTR-targeted PRRT. For example, clinical studies using the SSTR *antagonist* [^{111}In]In-DOTA-BASS—which binds and inhibits SSTR but has a slow internalization rate—demonstrate that this peptide boasts favorable pharmacokinetics, higher tumor uptake, faster clearance from receptor-positive healthy tissues, and lower renal uptake compared to its agonist cousin [^{111}In]In-DTPA-octreotide [39]. The favorable pharmacokinetic profiles of antagonists have been demonstrated in other cases, as well. For example, the gastrin-releasing peptide receptor (GRPR) antagonist [^{111}In]In-RM1 has a lower affinity for its target than the agonist [^{111}In]In-AMBA but has displayed higher uptake in tumor tissue, presumably due to a threefold higher number of available binding sites for the antagonist [45].

As summarized in Fig. 2, there are only a handful of therapeutic radiopharmaceuticals that have gained FDA approval. However, the number of peptide- or antibody-based radiopharmaceuticals in clinical trials is growing. For example, high levels of the cholecystokinin B receptor (CCKBR) are expressed in medullary thyroid cancer (MTC), prompting the development of minigastrin peptides which bind with a high affinity to CCKBR [46]. Currently, lutetium-177- or indium-111-labeled variants of minigastrin have entered into pilot and phase I studies for PRRT and imaging, respectively [47].

Prostate-Specific Membrane Antigen (PSMA)

A membrane-bound glycoprotein known (somewhat anachronistically) as prostate-specific membrane antigen (PSMA) is expressed in very high levels by prostate cancer tumors as well as the neovasculature of most solid tumors. Over the last 20 years, PSMA has been the target for the development of several therapeutic radiopharmaceuticals based on both antibody (*e.g.* lutetium-177-labeled J591, a monoclonal antibody to PSMA) and small molecule vectors. For example, a ^{177}Lu-labeled variant of the small molecule PSMA ligand PSMA-617 has favorable dosimetry with low kidney uptake, and a clinical trial using this agent for the TRT of patients with metastatic castration-resistant prostate cancer showed a PSA decrease in more than half of the patients which correlated with decreases in both the number and size of lesions [48]. Another pilot clinical study using the same ligand labeled with the alpha-emitting radionuclide actinium-225—

[^{225}Ac]Ac-PSMA-617—produced reductions in PSA below measurable levels as well as complete responses without hematologic toxicity, indicating significant benefits for advanced-stage prostate cancer patients and a clear need for a trial in a larger cohort of patients [49].

Folate Receptor Alpha

Folate receptor alpha (FRα) is another important target which correlates with tumor stage and grade and is highly overexpressed in approximately 40% of malignant tumors of epithelial origin, including lung, breast, and ovarian cancer. The FRα-targeting chimeric monoclonal antibody MOv18 IgG1 was radiolabeled with iodine-131, and an early clinical study produced promising results with minimal toxicities in ovarian cancer patients [50]. Furthermore, folic acid itself has a high affinity to FRα and undergoes receptor-mediated internalization. As a result, radiolabeled variants of folic acid have been leveraged to deliver therapeutic radionuclides to FRα-expressing tumors in preclinical models of cancer, and their potential for cancer therapy is currently under investigation.

Norepinephrine Transporter

Neuroblastoma is the most common pediatric extracranial tumor, accounting for approximately 8% of childhood malignancies with poor prognosis. The norepinephrine transporter (NET)—which, as its name suggests, is responsible for shuttling norepinephrine into cells—is overexpressed in neuroblastoma and has thus become a target for the development of tumor-targeted radiotherapeutics [51]. Metaiodobenzylguanidine (MIBG) is an analogue of noradrenaline (norepinephrine) that accumulates in adrenergic nerve terminals. Radiolabeled [^{131}I]I-MIBG is an FDA-approved SPECT imaging agent for a variety of neuroendocrine tumors and has been in clinical development for the treatment of pheochromocytomas/paragangliomas (PHEO/PGL), carcinoid tumors, and neuroblastomas. Clinical studies in patients with neuroblastoma showed that treatment with [^{131}I]I-MIBG improves survival rates and prolongs stable disease. However, the responses were usually low, and the hematologic toxicity associated with the treatment may require bone marrow transplants in patients treated with high doses [52].

CD-20

CD-20 is a transmembrane calcium channel that is expressed on pre-B and mature B lymphocytes and, even more importantly, overexpressed on more than 90% of B-cell non-Hodgkin lymphomas (NHL). As a result, CD-20 has become an attractive target for the targeted radiotherapy—and, more specifically, targeted radio*immuno*therapy—of NHL [53]. The radiosensitivity of lymphomas has further fueled this work, as these diseases have among the highest response rates to TRT. Zevalin (ibritumomab tiuxetan) is a yttrium-90-labeled, CD-20-targeting monoclonal antibody that was the first approved drug for the radioimmunotherapy of resistant and recurrent forms of NHL. In patients with advanced-stage follicular lymphoma, the therapy extended the 8-year progression-free survival (PFS) of patients by 19% and improved the time to next treatment by 5.1 years [54]. A radioiodinated variant of another CD-20-targeting antibody—[^{131}I]I-tositumomab; Bexxar™—has also garnered FDA approval and proven efficacy for the treatment of NHL as well as diffuse B-cell lymphoma and multiple myeloma [55].

Other Targets for Radioimmunotherapeutics

Currently, several other radioimmunoconjugates are in clinical development for the RIT of a number of different types of cancer. For example, the results from phase I and II trials with an iodine-131-labeled chimeric monoclonal antibody that binds to the DNA-histone H1 complex (Cotara) show increased overall survival results in malignant gliomas [56]. In addition, an [^{131}I]I-labeled radioimmunoconjugate of the Hab18-/CD47-targeting monoclonal antibody metuximab (Licartin) has produced promising results in hepatocellular carcinoma (HCC) [57]. Interestingly, treatment with the anti-HAb18G/CD147 antibody alone significantly decreases the secretion of matrix metalloproteinases (MMP) and reduces the invasive potential of HCC cells; thus, its labeling with a radionuclide further potentiates its antitumoral effect [58]. Another promising radioimmunotherapeutic is [^{131}I]I-L19, a radioiodinated variant of the fully human antibody radretumab. Radretumab binds to the extradomain-B splice variant of fibronectin, which is highly expressed in various lymphoma subtypes as well as multiple myeloma derived from bone marrow. The first clinical trial of [^{131}I]I-L19 in patients with advanced relapsed lymphoma showed favorable benefit and risk profiles and revealed that the radioimmunoconjugate induced complete response in both relapsed Hodgkin lymphoma and diffuse large B-cell lymphoma patients [59].

Overcoming Obstacles in TRT

Developments in PRRT

The limitation of PRRT is very often related to the stability of the radiopharmaceuticals themselves. The *in vivo* half-lives of peptides and small proteins range from a few minutes

to a few hours due to their proteolysis and rapid clearance. In some cases, these short half-lives can prevent the delivery of a suitable amount of therapeutic radioactivity to the target tissue. This, of course, reduces the efficacy of PRRT. A number of laboratories have worked to devise strategies to circumvent this issue. For example, relatively short peptides which contain D-amino acids—rather than naturally occurring L-amino acids—maintain their affinity for their biomolecular targets but have displayed resistance to proteolytic degradation *in vivo*. To wit, reducing the number of amino acids in somatostatin ($t_{1/2}$ = a few minutes) from 14 to 8 and replacing two L-amino acids with D-analogues (creating octreotide) resulted in a dramatic increase of the peptide's metabolic half-life to 1.5 h [60]. In an alternative strategy, the co-administration of protease inhibitors alongside radiolabeled peptides can reduce the degradation of the latter and thus increase its bioavailability and accumulation at target sites. For instance, neutral endopeptidase (NEP) is an enzyme that is involved in the degradation of gastrin and cholecystokinin peptides. The co-administration of radiolabeled gastrin analogues along with the NEP inhibitor phosphoramidon (PA) significantly increased the tumoral uptake of the radiolabeled peptide in preclinical models [61].

Still others have tried to alter the clearance of radiolabeled peptides in order to increase their *in vivo* half-lives and bioavailability. Proteins and peptides with molecular weights below 60 kDa are typically cleared rapidly by the renal-urinary tract. As a result, some laboratories have worked to increase the circulation time of peptides by increasing their molecular weight and shifting their excretion pathway. For example, both PEGylating peptides and coupling them to serum albumin have been shown to extend their *in vivo* half-lives, reduce their uptake in the kidneys, and boost their uptake in the tumor [62–65]. More specifically, constructs containing both a radiolabeled (*i.e.* lutetium-177) variant of folate and a low-molecular-weight albumin-binding entity showed enhanced blood circulation time, increased tumor uptake, reduced retention in the kidneys, and—most importantly—inhibited tumor growth and prolonged survival in a mouse model of cervical cancer [66, 67]. In addition, the introduction of a short aliphatic linker between the albumin-binding moiety and the folic acid further improved tumoral uptake in preclinical models [68]. However, this strategy is not without its risks. Indeed, the coupled moieties, especially if they are large or sterically bulky, may interfere with the biological activity of the peptides [69].

Pretargeted Radioimmunotherapy

A variety of laboratories have focused on the development of approaches to "pretargeted" radioimmunotherapy (PRIT) in order to reduce the radiation dose to healthy organs created by circulating radiolabeled antibodies [70]. In these treatments, a nonradioactive, tumor-targeting antibody is first injected and given sufficient time to accumulate at the tumor and clear from healthy tissues. Subsequently, a radioactive compound is administrated which can bind the tumor-bound antibody with high affinity but will otherwise be cleared rapidly from the blood by the kidneys or liver. The sequential administration of the unlabeled antibody and the radiopharmaceutical allows PRIT to leverage the exquisite tumor targeting of antibodies while skirting the long pharmacokinetic half-lives (and high dose rates to healthy organs) of radioimmunoconjugates (Fig. 4).

The earliest approaches to PRIT were predicated on the extraordinarily strong interaction between the bacterial protein streptavidin (SA) and the small molecule biotin [71, 72]. To this end, tumor-targeting antibodies modified with SA or biotin were used in conjunction with biotin- or SA-based radioligands bearing therapeutic radionuclides. In some cases, a third compound—a "clearing agent"—was injected in between the antibody and the radionuclide to accelerate the clearance of unbound antibody from the blood. For example, in a phase I clinical study in patients with anaplastic astrocytoma and glioblastoma, a tenascin-targeted biotinylated antibody was injected followed by an avidin-based clearing agent to remove unbound antibody from the blood. Subsequently, a ^{90}Y-labeled DOTA-biotin radioligand was administrated for therapy. Stable disease was achieved in 50% of patients, whereas 25% of treated patients showed tumor regression [73]. Similarly, a PRIT phase 1 trial using an anti-CD-20-streptavidin fusion protein (B9E9FP) in conjunction with a biotin-based radioligand has shown promise in patients with B-cell non-Hodgkin lymphoma [74]. Ultimately, however, while PRIT approaches based on streptavidin and biotin have produced encouraging clinical results, problems relating to the immunogenicity of streptavidin and the endogenous expression of biotin may complicate their clinical applications.

Several other approaches to PRIT are currently being developed, including strategies based on complementary oligonucleotides and bioorthogonal click chemistry [75–77]. The most advanced strategies rely on the use of bispecific antibodies that can simultaneously bind both a cancer antigen and a radiolabeled hapten. Critically, these bispecific antibodies (bsAbs) bind their haptens reversibly, so particular attention has been paid to increasing the affinity of this interaction through the development of *bivalent* radioligands that can cross-link bsAbs on the surface of cancer cells. The earliest studies with these systems employed CEA- and cG250-targeting bsAbs that could bind [^{111}In]In-DTPA (or [$^{86/90}$Y]Y-DTPA) complexes as well [78–80]. More recently, phase I/II clinical trials using an anti-CEA bsAb with a bivalent [^{131}I]I-DTPA hapten in patients with recurrent medullary thyroid carcinoma (MTC) produced long-term disease stabilization in 53% of patients, although therapeutic responses were observed only in a few patients

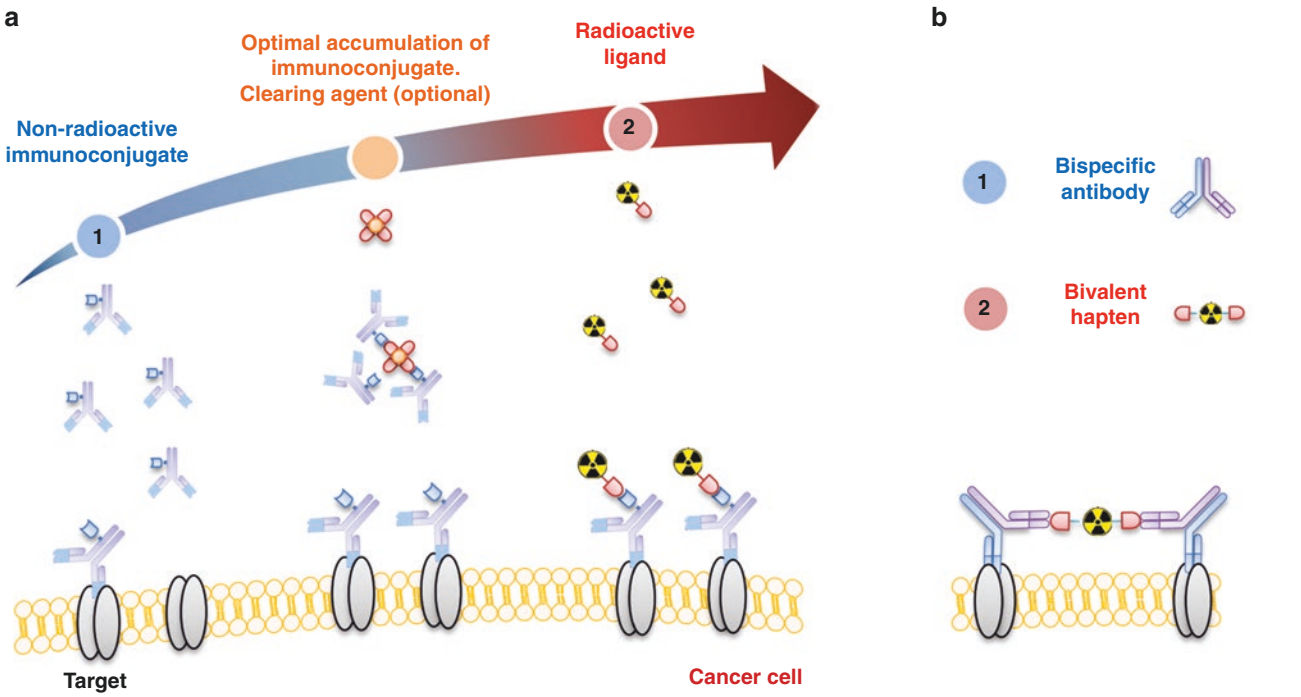

c

Clinical trial	Pretargeting method	Radioactive vector	Ref
B-cell non-Hodgkin lymphoma (NHL)	Anti-CD20-streptavidin fusion protein, clearance with biotin poly-N-acetyl-galactosamine	^{90}Y-/^{111}In-DOTA-biotin	75
Anaplastic astrocytoma and glioblastoma (GBM)	Anti-tenascin biotinylated monoclonal antibody and avidin-based agent	^{90}Y-DOTA-biotin	74
Recurrent medullary thyroid cancer (MTC)	Anti-carcinoembryonic antigen (CEA)/anti-DTPA-indium bispecific monoclonal antibody	^{131}I-DTPA bivalent hapten	83

Fig. 4 Schematic representation of pretargeting methods. (**a**) First, a nonradioactive immunoconjugate is administrated for targeting cancer cells. The optimal accumulation of the immunoconjugate is usually accomplished within 24–48 h. In some cases, a "clearing agent" is injected to accelerate the clearance of unbound circulating antibody from the blood. In the second step, a radioactive ligand is administrated that binds to the tumor-bound antibody with high affinity and is cleared rapidly by excretory organs such as the kidneys or liver. (**b**) Pretargeting with bispecific antibodies that simultaneously bind both a cancer antigen and a radiolabeled hapten. (**c**) Examples of pretargeting methods applied in clinical trials

[81]. Further clinical studies confirmed an increase in the overall survival of high-risk patients as well as durable complete response of more than 40 months and durable stable disease (more than 6 months) in 2.4 and 73.8% of patients, respectively [82]. In the end, pretargeting is clearly a promising approach to improving RIT; however, PRIT is undeniably more complex than conventional RIT, making the former a challenge from regulatory, clinical, and logistical standpoints.

Clinical Application of Targeted Radionuclide Therapy

Unfortunately, for nearly six decades, the therapeutic application of radionuclides was limited to diseases of the thyroid. Meanwhile, molecular imaging [83] and external beam radiotherapy are applied in 50% of all cancer patients [1] and have become cornerstones in the management and treatment of cancer. During this period, however, the development of

TRT never stagnated, and its clinical benefit was evident on the individual patient level or in smaller cohorts. Yet large phase III trials remained absent, a major drawback in the era of evidence-based medicine (especially if competing treatments are available). One can only speculate about the reasons, but the tremendous cost of such clinical studies and the lack of involvement of the pharmaceutical industry are likely to be at least partially responsible.

The clinical study of [^{90}Y]Y-Ibritumomab tiuxetan published in 2008 represents the first phase III trial of a therapeutic radiopharmaceutical outside of the field of thyroid diseases [84]. Patients with follicular lymphoma—stage III or IV disease and partial or complete response after first-line therapy—were randomized between the radioimmunoconjugate and no further treatment. The primary endpoint was progression-free survival (PFS). [^{90}Y]Y-Ibritumomab tiuxetan produced a significantly prolonged PFS (13.3 months vs. 36.5 months, hazard ratio (HR) [95% CI] = 0.465 [0.357–0.605], $p < 0.001$). Even though the prolonged PFS could be confirmed after a longer follow-up of 7.3 years, no improvement of overall survival (OS) could be observed. Nevertheless, an 8-year OS of 84% is impressive, and with the large number of treatment options after progression/recurrence (*e.g.* obinutuzumab, idealisib, bendamustin, or autologous stem cell transplantation), it becomes difficult to show such a difference, especially in an indolent disease. This fact should be therefore not seen as a major disadvantage for this radioimmunoconjugate.

The release of the results of the ALSYMPCA phase III trial with [^{223}Ra]$RaCl_2$ (Xofigo®) completely changed the treatment landscape of metastatic castration-resistant prostate cancer (mCRPC) [85]. This study also highlighted the immense potential of TRT when it is applied in the right disease, at the right disease stage, and at an optimal time point in the course of the disease. Xofigo® did not only improve the overall survival (14.9 vs. 11.3 months, hazard ratio (HR) [95% CI] = 0.70 [0.58–0.83], $p < 0.001$) but was also associated with significantly fewer side effects (Fig. 5). Although this can be mainly attributed to superior disease control—the lack of progression of the prostate cancer without subsequent clinical symptoms monitored as side effects—such observations are very rarely seen. Since Xofigo®'s safety profile can be considered exceptional, it received the highest score (5 of 5) on the ESMO clinical benefit scale as the only treatment option for mCRPC [86]. Additionally Xofigo® was associated with a prolonged time to the first symptomatic skeletal event (15.6 vs. 9.8 months, hazard ratio (HR) [95% CI] = 0.66 [0.52–0.83], $p < 0.001$) [85] and reduced the risk for external beam radiotherapy due to pain progression (hazard ratio (HR) [95% CI] = 0.67 [0.53–0.85], $p = 0.001$) or spinal cord compression (hazard ratio (HR) [95% CI] = 0.52 [0.29–0.93], $p = 0.010$) [87].

As we have discussed, SIRT was first described in the late 1960s, and preliminary clinical results were published as early as 1988. However, the first phase III trial has only recently been published by Guy van Hazel *et al.* in 2016, nearly 30 years later(!) [88] (Fig. 6). The original objective of the SIRFLOX trial was the investigation of the improvement of progression-free survival (PFS) when SIRT is combined with one of the standard chemotherapeutic options (FOLFOX: folinic acid, 5-fluoruracil, and oxaliplatin) in patients with metastatic colorectal cancer (mCRC) and liver predominant disease. The slow accrual of patients required an extensive amendment of the trial protocol because of the rapidly developing treatment landscape for mCRC. As a result, targeted therapies—in this case, the neutralizing VEGF-A antibody bevacizumab—had to be incorporated into the trial. Indeed, this case stands as a fine example of the difficult standing of TRT in previous years. The lack of improvement in the primary study endpoint, PFS (10.2 months for FOLFOX ± bevacizumab vs. 10.7 months for FOLFOX ± bevacizumab + SIRT, hazard ratio (HR) [95% CI] = 0.93 [0.77–1.12], $p = 0.43$), didn't necessarily improve the situation of an undefined clinical benefit. However, the efficacy of SIRT has been illustrated by the significantly prolonged PFS in the liver (12.6 months for FOLFOX ± bevacizumab vs. 20.5 months for FOLFOX ± bevacizumab + SIRT, hazard ratio (HR) [95% CI] = 0.69 [0.55–0.90], $p = 0.002$) and by the increased response rate of liver metastases (68.8% vs. 78.7%, $p = 0.042$). These data underscore that the lack of overall benefit can be attributed to the limitations associated with the local character of the treatment. The hope that SIRT could still become an important option for the first-line treatment of mCRC was rekindled after the pooled analysis of the SIRFLOX, FOXFIRE, and FOXFIRE-Global studies showed an overall survival advantage for right-sided tumors (hazard ratio (HR) [95% CI] = 0.67 [0.48–0.92]) [89] (see Fig. 5), although the other two trials (which have been conducted later) have missed their primary endpoints as well.

For primary, unresectable liver tumors like cholangiocarcinomas or hepatocellular carcinomas, SIRT is a safe, well-tolerated, and effective treatment [90, 91]. Although few would challenge the therapeutic value of SIRT in this context, the final results of several large phase III trials are still pending (*e.g.* SIRveNIB, SORAMIC, and SIR-TACE-CCC) [91]. The SARAH trial was the first phase III trial, with 459 patients. The standard of care (sorafenib) was compared to SIRT. Though the two had the same outcome in terms of overall survival (8.0 months for SIRT vs. 9.9 months for sorafenib, $p = 0.179$), SIRT was associated with a significantly improved response rate (19.0% vs. 11.6%, $p = 0.042$) and improved quality of life ($p = 0.005$) [92]. Despite the fact that the primary endpoint of an improved overall survival was not met, these results are relevant in this highly palliative setting, since tolerability and quality of life are estimated even higher than other outcome measures from a patient's perspective.

One of the biggest breakthroughs in therapeutic nuclear medicine was the publication of the NETTER phase III trial in the beginning of 2017 [93]. As we have discussed above, [^{177}Lu]

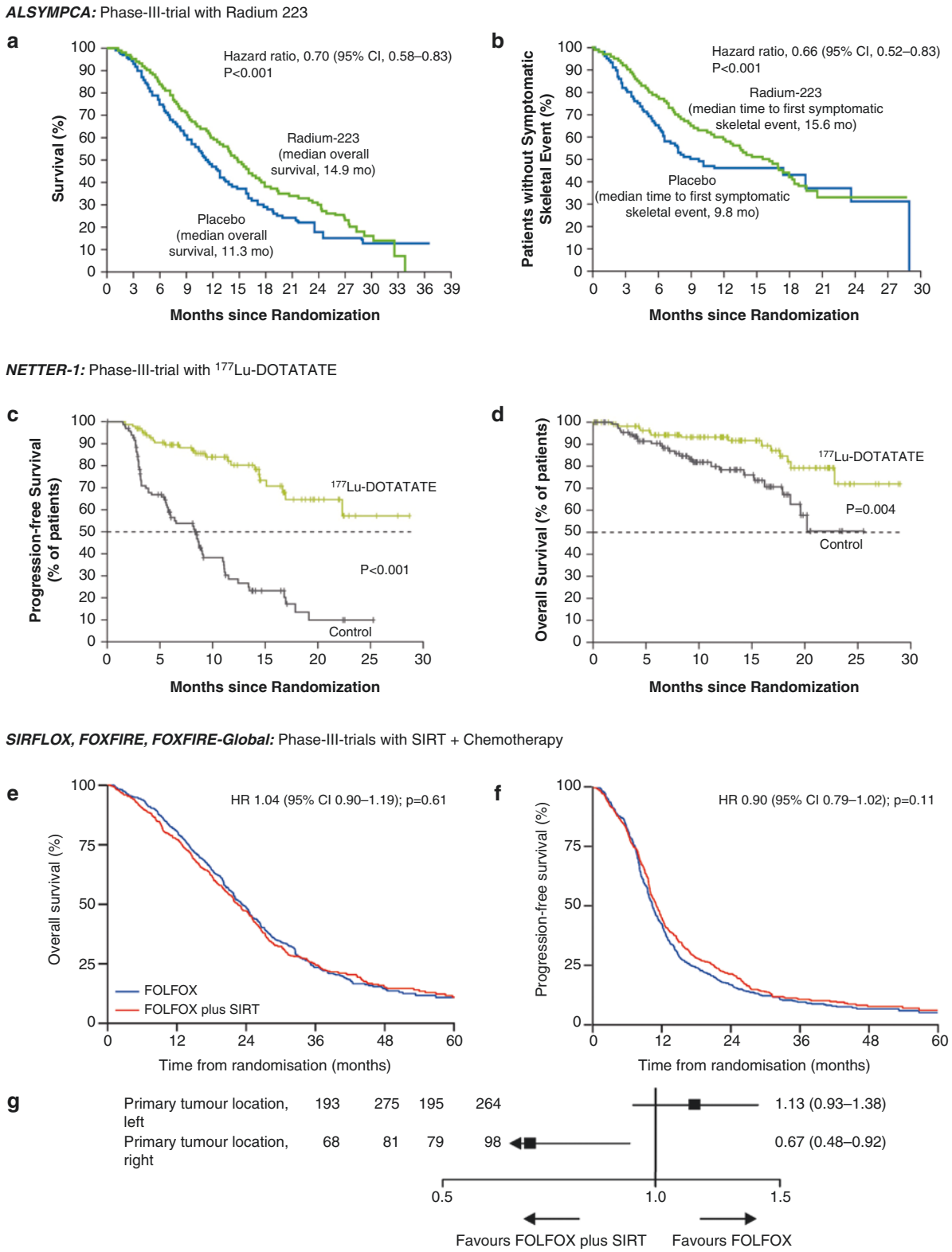

Fig. 5 Kaplan-Meier survival estimates for therapeutic radionuclides with a significant overall survival advantage or strong trend toward improved survival. The ALSYMPCA trial showed a benefit in overall survival (**a**) and a delay until the occurrence of skeletal-related events (**b**) [96]. [^{177}Lu]Lu-DOTATATE was able to improve the overall- and progression-free survival in the NETTER-1 trial (**c**) [93]. Although the early combination of SIRT and chemotherapy could not improve the survival in the SIRFLOX, FOXFIRE, and FOXFIRE-Global trials (**e** and **f**), for the overall population, a significant reduction in the probability of death was observed in a post hoc analysis of right-sided tumors (G) [89]. (**a** from Hoskin *et al.* [96] with permission; **b** from Strosberg *et al.* [93] with permission; **c** from Wasan *et al.* [89] with permission)

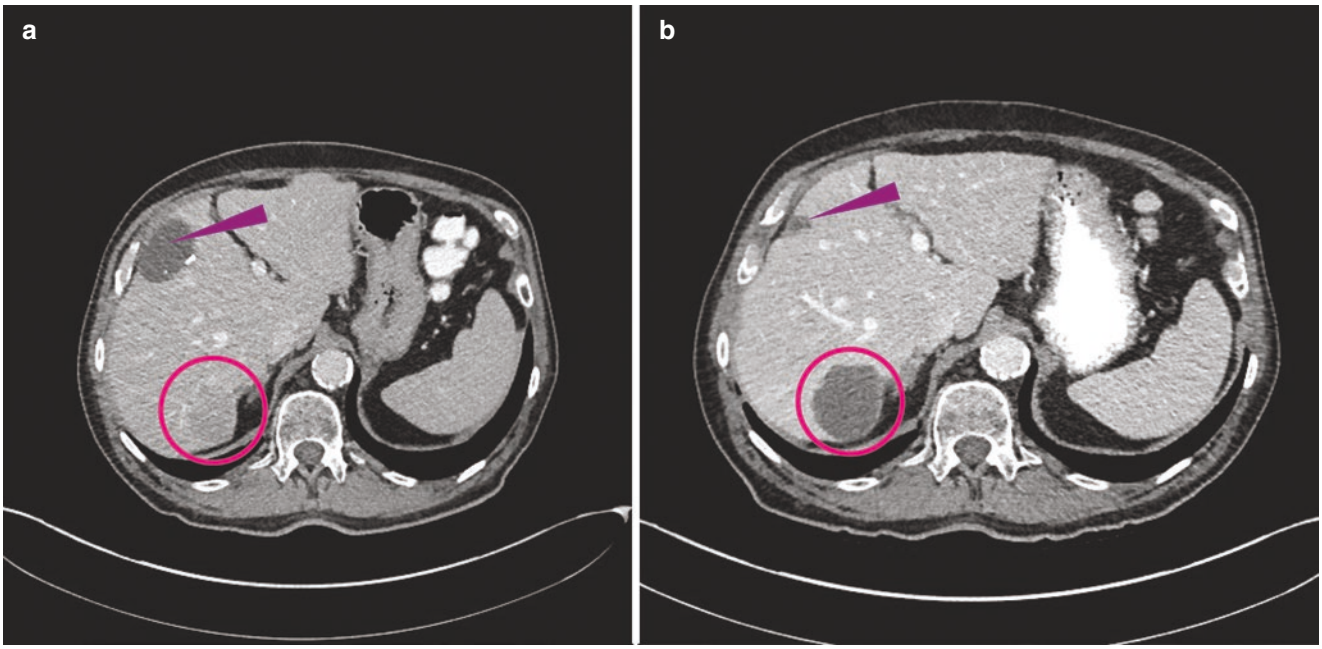

Fig. 6 Selective interarterial radiation therapy (SIRT) of a singular hepatic metastasis in a patient with colorectal cancer. The circles mark the metastasis before (**a**) and after (**b**) the intervention, illustrating complete remission. The *arrows* indicate a bilioma (collection of bile fluid) that is steadily regressing over time

Lu-DOTATATE is a somatostatin receptor-targeting radiopharmaceutical for the PRRT of well-differentiated neuroendocrine tumors which has shown promising results in smaller patient cohorts since 1992 [94]. In the NETTER trial, a PFS benefit with an impressive magnitude became evident: [^{177}Lu] Lu-DOTATATE vs. best supportive care including octreotide long-acting repeatable, PFS not reached vs. 8.4 months (HR) [95% CI] = 0.21 [0.13–0.33], $p < 0.001$. The response rate was also significantly higher in the [^{177}Lu]Lu-DOTATATE arm compared to the control arm (18% vs. 3%, $p < 0.001$). The planned interim analysis for overall survival showed 14 deaths in the [^{177}Lu]Lu-DOTATATE arm vs. 26 deaths in the control arm ($p = 0.004$). Since the predefined statistical margins were not met, the results are too immature to provide a median overall survival estimate in either group (see Fig. 5).

Taken together these results from the last 5 years reinforce the immense potential of TRT in a variety of malignancies. The high quality, appropriate size, and proper execution of these phase III trials have allowed for the implementation of these radiopharmaceuticals into clinical guidelines with the highest level of evidence.

How Does TRT Fit into Multimodal Treatment Strategies?

Since the currently approved stable of therapeutic radionuclides is generally well tolerated, they qualify for combinatorial and sequential approaches. In this regard, one of the best examples is Xofigo®. In the ALYSMPCA phase III trial, the reported rate for non-hematological ≥ grade 3 adverse events was as low as 5% (except for bone pain: 21%). But even this rate was lower than in the placebo arm. The rate of hematological ≥ grade 3 adverse events did not exceed 15%, with anemia (13%) and thrombocytopenia (6%) as the most common. Overall adverse events have been less frequently observed for Xofigo®, an outstanding finding [85]. One of the initial concerns of Xofigo® was that the radiation—even though the alpha particles only have a 100 µm range in tissue—could negatively affect the application of subsequent chemotherapies due to chronic bone marrow damage. A secondary post hoc analysis of the trial could mitigate these reservations, since it has shown a literally identical rate of subsequent chemotherapies, with no differences in the duration of the chemotherapy and no significant differences in overall hematological toxicity [95]. In addition, a gain in median overall survival could be observed irrespective of the previous use of docetaxel (previous docetaxel use hazard ratio (HR) [95% CI] = 0.70 [0.56–0.88], $p = 0.002$, 14.4 vs. 11.3 months; no previous docetaxel use hazard ratio (HR) [95% CI] = 0.69 [0.52–0.92], $p = 0.01$, 16.1 vs. 11.5 months) [96]. Therefore it can be concluded that Xofigo® is effectively independent of preceding treatments, nor does it negatively impact the application of subsequent therapies.

At the same time, a phase IIIb trialindicated an additional survival gain when Xofigo® was combined with novel antihormonal agents or the RANKL-targeting antibody denosumab (which inhibits the activity of osteoclasts). For both

combinations, the median survival was not reached at the time of data cutoff [97]. Currently a large number of clinical trials are evaluating dose escalations, novel combination therapies, and different indications. The combination therapies being investigated include the use of the immune checkpoint inhibitors pembrolizumab and atezolizumab, the microtubule inhibitor docetaxel, and VEGF inhibitors. Clear cell renal cancer, urothelial cancer, and breast cancer metastatic to the bone as well as multiple myeloma have all become subjects of trials as well. Although the latter is a hematological malignancy, it is also characterized by osteolytic bone lesions. Since osteolytic metastases have a fundamentally different biology than osteoblastic bone metastases in mCRPC, it will be exciting to see the extent to which Xofigo® effects the course of these malignancies. In light of the markedly prolonged survival of cancer patients in a growing number of diseases, rechallenging will be a crucial factor for the acceptance of this treatment, especially when it is able to produce long-lasting responses. It seems that this will be feasible for Xofigo® without observing increased toxicities [98].

The sequential application of SIRT and PRRT was also proven safe and effective in patients with progressive liver metastases of neuroendocrine tumors, respectively [99]. Although the response and overall survival rates have not been compared between the patients with (45%, 18/40 pts.) and without previous PRRT (55%, 22/40 pts.), SIRT produced a disease control rate (complete remission + partial remission + stable disease) of 94% after 3 months and 57% after 20 months.

Shifting gears briefly, surgery is an important treatment option in the management of many cancer patients. Therefore, it is interesting to contemplate whether TRT could be used in combination with surgical interventions as well. Data to answer this question has only been systematically collected for SIRT, though in this case, there were no signs that SIRT negatively impacts the outcome of liver resections or even liver transplantations.

To sum up this section, TRT can be safely combined with other treatment options, can be repetitively applied, and has no negative impact on subsequent chemotherapies or surgical procedures.

Limitations for the Use of TRT

Up to this point, we have spent a great deal of time discussing the enormous potential of targeted radiotherapy and the possibility of integrating TRT into the general treatment strategies for a variety of different cancers. In light of this promise, there must be reasons why TRT has yet to be applied widely in the clinic. One major explanation might be the enormous logistic requirements. The implementation of TRT requires a radiopharmaceutical production facility with the attendant knowledge and certifications, imaging facilities, hospital beds with radioactive protection as well as storage, and resources for the disposal of radioactive waste. Taken together, the increases in cost associated with these requirements make TRT affordable only for high-volume or academic centers. Furthermore, compared to chemo- or targeted therapy, the handling of radiopharmaceuticals for TRT is relatively complicated. Moreover, patients who receive TRT require special considerations even after death [100]. Considering these complicating circumstances, it is perhaps not surprising that TRT often becomes the second choice, especially if equally effective alternatives are available. The clinical choice between [^{90}Y]Y-Ibritumomab tiuxetan and rituximab or obinutuzumab maintenance therapy may provide an example of this phenomenon [101].

Finally, although recent experimental data indicates that cure with targeted radiotherapies might slowly become reality [102], all currently used TRTs are palliative. As survival times are becoming longer, it will be critical to find solutions for the problem of secondary malignancies, mainly hematological neoplasms like myelodysplastic syndrome (MDS) and different forms leukemia with frequencies of up to 2% [54, 93].

The Future

It is currently an exciting time for both preclinical and clinical research in TRT. Perhaps not surprisingly, a tremendous amount of preclinical research is dedicated to improving the delivery of these radiopharmaceuticals to tumor tissue. While some laboratories have focused on the development of strategies to increase the therapeutic ratio and efficacy of radiopharmaceuticals by boosting their uptake in tumor tissue and reducing their accumulation in healthy organs, others have sought to facilitate the more efficient targeting of heterogeneous cancers. Still others are exploring ways to exploit or induce radiosensitivity within tumors. For example, a recent preclinical study revealed that concomitant treatment with small molecule inhibitors (*e.g.* kinase inhibitors) diminished the activation of survival pathways and consequently sensitized cancer cells to radiolabeled peptides [103]. Clearly, deepening our understanding of the resistance mechanisms to TRT and the appropriate application of combinatory treatments holds promise for the creation of more effective approaches to internal radiotherapy. Last but not least, the development of novel therapeutic radionuclides (*e.g.* alpha-emitters) may also significantly improve the clinical efficacy of TRT. All in all, there are still many challenges ahead in the optimization and clinical deployment of TRT. Nevertheless, progress in the development of new vectors, radionuclides, combinatory treatments, and administration methods will significantly enhance the therapeutic efficacy of TRT in the future.

The Bottom Line

- Targeted radionuclide therapy (TRT) accurately and efficiently delivers radiation to tumors and metastatic lesions while reducing cytotoxic side effects to healthy organs.
- Ionizing radiation induces cancer cell death either directly via emitted particles or indirectly via reactive oxygen species produced from the radiolysis of water.
- Therapeutic radiopharmaceuticals are composed of α-, β-, or Auger electron-emitting radionuclides that are bound to vectors—such as small molecules, peptides, antibodies, or nanoparticles—with high affinity and selectivity for cancer antigens.
- A wide array of therapeutic radionuclides are available, and the physical properties of a radionuclide—such as its type of emission, half-life, and particle range in tissue—should be considered when creating a therapeutic radiopharmaceutical and must be tailored to the specific type of cancer that is being targeted.
- Although recent preclinical and clinical studies have produced promising results, the widespread clinical implementation of TRT still faces several challenges.
- A wide variety of approaches to increasing the safety and efficacy of TRT are currently being explored, including the development of new vectors and radionuclides, the optimization of the biological properties of therapeutic radiopharmaceuticals, and the modulation of the sensitivity of tumors to radiation through combinatory treatment strategies.

References

1. Begg AC, Stewart FA, Vens C. Strategies to improve radiotherapy with targeted drugs. Nat Rev Cancer. 2011;11(4):239–53.
2. Paoletti C, Hayes DF. Circulating tumor cells. Adv Exp Med Biol. 2016;882:235–58.
3. Adams DL, Adams DK, He J, Kalhor N, Zhang M, Xu T, et al. Sequential tracking of PD-L1 expression and RAD50 induction in circulating tumor and stromal cells of lung cancer patients undergoing radiotherapy. Clin Cancer Res. 2017;23(19):5948–58.
4. Verburg FA, de Keizer B, van Isselt JW. Use of radiopharmaceuticals for diagnosis, treatment, and follow-up of differentiated thyroid carcinoma. Anti Cancer Agents Med Chem. 2007;7(4):399–409.
5. Verburg FA, Brans B, Mottaghy FM. Molecular nuclear therapies for thyroid carcinoma. Methods. 2011;55(3):230–7.
6. Gudkov SV, Shilyagina NY, Vodeneev VA, Zvyagin AV. Targeted radionuclide therapy of human tumors. Int J Mol Sci. 2015;17(1):pii: E33.
7. Milenic DE, Brady ED, Brechbiel MW. Antibody-targeted radiation cancer therapy. Nat Rev Drug Discov. 2004;3(6):488–99.
8. Volkert WA, Goeckeler WF, Ehrhardt GJ, Ketring AR. Therapeutic radionuclides: production and decay property considerations. J Nucl Med. 1991;32(1):174–85.
9. Yeong CH, Cheng MH, Ng KH. Therapeutic radionuclides in nuclear medicine: current and future prospects. J Zhejiang Univ Sci B. 2014;15(10):845–63.
10. Pouget JP, Santoro L, Raymond L, Chouin N, Bardies M, Bascoul-Mollevi C, et al. Cell membrane is a more sensitive target than cytoplasm to dense ionization produced by auger electrons. Radiat Res. 2008;170(2):192–200.
11. Denison TA, Bae YH. Tumor heterogeneity and its implication for drug delivery. J Control Release. 2012;164(2):187–91.
12. Dorso L, Bigot-Corbel E, Abadie J, Diab M, Gouard S, Bruchertseifer F, et al. Long-term toxicity of ^{213}Bi-labelled BSA in mice. PLoS One. 2016;11(3):e0151330.
13. Khanna A. DNA damage in cancer therapeutics: a boon or a curse? Cancer Res. 2015;75(11):2133–8.
14. Pouget JP, Lozza C, Deshayes E, Boudousq V, Navarro-Teulon I. Introduction to radiobiology of targeted radionuclide therapy. Front Med (Lausanne). 2015;2:12.
15. Szumiel I. Ionizing radiation-induced oxidative stress, epigenetic changes and genomic instability: the pivotal role of mitochondria. Int J Radiat Biol. 2015;91(1):1–12.
16. Eriksson D, Stigbrand T. Radiation-induced cell death mechanisms. Tumour Biol. 2010;31(4):363–72.
17. Vakifahmetoglu H, Olsson M, Zhivotovsky B. Death through a tragedy: mitotic catastrophe. Cell Death Differ. 2008;15(7):1153–62.
18. Hill RP, Bristow RG, Fyles A, Koritzinsky M, Milosevic M, Wouters BG. Hypoxia and predicting radiation response. Semin Radiat Oncol. 2015;25(4):260–72.
19. O'Connor JP, Rose CJ, Waterton JC, Carano RA, Parker GJ, Jackson A. Imaging intratumor heterogeneity: role in therapy response, resistance, and clinical outcome. Clin Cancer Res. 2015;21(2):249–57.
20. Sala E, Mema E, Himoto Y, Veeraraghavan H, Brenton JD, Snyder A, et al. Unravelling tumour heterogeneity using next-generation imaging: radiomics, radiogenomics, and habitat imaging. Clin Radiol. 2017;72(1):3–10.
21. Kim BM, Hong Y, Lee S, Liu P, Lim JH, Lee YH, et al. Therapeutic implications for overcoming radiation resistance in cancer therapy. Int J Mol Sci. 2015;16(11):26880–913.
22. Jette N, Lees-Miller SP. The DNA-dependent protein kinase: a multifunctional protein kinase with roles in DNA double strand break repair and mitosis. Prog Biophys Mol Biol. 2015;117(2–3):194–205.
23. Yan S, Sorrell M, Berman Z. Functional interplay between ATM/ATR-mediated DNA damage response and DNA repair pathways in oxidative stress. Cell Mol Life Sci. 2014;71(20):3951–67.
24. Zhan M, Han ZC. Phosphatidylinositide 3-kinase/AKT in radiation responses. Histol Histopathol. 2004;19(3):915–23.
25. Bieging KT, Mello SS, Attardi LD. Unravelling mechanisms of p53-mediated tumour suppression. Nat Rev Cancer. 2014;14(5):359–70.
26. Santivasi WL, Xia F. Ionizing radiation-induced DNA damage, response, and repair. Antioxid Redox Signal. 2014;21(2):251–9.
27. Hein AL, Ouellette MM, Yan Y. Radiation-induced signaling pathways that promote cancer cell survival (review). Int J Oncol. 2014;45(5):1813–9.
28. Guerra Liberal FDC, Tavares AAS, Tavares J. Palliative treatment of metastatic bone pain with radiopharmaceuticals: a perspective beyond Strontium-89 and Samarium-153. Appl Radiat Isot. 2016;110:87–99.
29. Vogelzang NJ. Radium-223 dichloride for the treatment of castration-resistant prostate cancer with symptomatic bone metastases. Expert Rev Clin Pharmacol. 2017;10(8):809–19.
30. Memon K, Lewandowski RJ, Kulik L, Riaz A, Mulcahy MF, Salem R. Radioembolization for primary and metastatic liver cancer. Semin Radiat Oncol. 2011;21(4):294–302.
31. Favelier S, Germain T, Genson PY, Cercueil JP, Denys A, Krause D, et al. Anatomy of liver arteries for interventional radiology. Diagn Interv Imaging. 2015;96(6):537–46.
32. Chinn P, Braslawsky G, White C, Hanna N. Antibody therapy of non-Hodgkin's B-cell lymphoma. Cancer Immunol Immunother. 2003;52(5):257–80.

33. Norenberg JP, Krenning BJ, Konings IR, Kusewitt DF, Nayak TK, Anderson TL, et al. ^{213}Bi-[DOTA0, Tyr3]octreotide peptide receptor radionuclide therapy of pancreatic tumors in a preclinical animal model. Clin Cancer Res. 2006;12(3 Pt 1):897–903.
34. Brechbiel MW. Bifunctional chelates for metal nuclides. Q J Nucl Med Mol Imaging. 2008;52(2):166–73.
35. Sosabowski JK, Mather SJ. Conjugation of DOTA-like chelating agents to peptides and radiolabeling with trivalent metallic isotopes. Nat Protoc. 2006;1(2):972–6.
36. Dorsam RT, Gutkind JS. G-protein-coupled receptors and cancer. Nat Rev Cancer. 2007;7(2):79–94.
37. Lappano R, Maggiolini M. G protein-coupled receptors: novel targets for drug discovery in cancer. Nat Rev Drug Discov. 2011;10(1):47–60.
38. O'Hayre M, Degese MS, Gutkind JS. Novel insights into G protein and G protein-coupled receptor signaling in cancer. Curr Opin Cell Biol. 2014;27:126–35.
39. Wild D, Fani M, Behe M, Brink I, Rivier JE, Reubi JC, et al. First clinical evidence that imaging with somatostatin receptor antagonists is feasible. J Nucl Med. 2011;52(9):1412–7.
40. Reubi JC, Waser B, Schaer JC, Laissue JA. Somatostatin receptor sst1-sst5 expression in normal and neoplastic human tissues using receptor autoradiography with subtype-selective ligands. Eur J Nucl Med. 2001;28(7):836–46.
41. Ambrosini V, Campana D, Tomassetti P, Fanti S. ^{68}Ga-labelled peptides for diagnosis of gastroenteropancreatic NET. Eur J Nucl Med Mol Imaging. 2012;39(Suppl 1):S52–60.
42. Kwekkeboom DJ, Kam BL, van Essen M, Teunissen JJ, van Eijck CH, Valkema R, et al. Somatostatin-receptor-based imaging and therapy of gastroenteropancreatic neuroendocrine tumors. Endocr Relat Cancer. 2010;17(1):R53–73.
43. van Essen M, Krenning EP, Kam BL, de Jong M, Valkema R, Kwekkeboom DJ. Peptide-receptor radionuclide therapy for endocrine tumors. Nat Rev Endocrinol. 2009;5(7):382–93.
44. Kam BL, Teunissen JJ, Krenning EP, de Herder WW, Khan S, van Vliet EI, et al. Lutetium-labelled peptides for therapy of neuroendocrine tumours. Eur J Nucl Med Mol Imaging. 2012;39(Suppl 1):S103–12.
45. Mansi R, Wang X, Forrer F, Kneifel S, Tamma ML, Waser B, et al. Evaluation of a 1,4,7,10-tetraazacyclododecane-1,4,7,10-tetraacetic acid-conjugated bombesin-based radioantagonist for the labeling with single-photon emission computed tomography, positron emission tomography, and therapeutic radionuclides. Clin Cancer Res. 2009;15(16):5240–9.
46. Behr TM, Behe MP. Cholecystokinin-B/Gastrin receptor-targeting peptides for staging and therapy of medullary thyroid cancer and other cholecystokinin-B receptor-expressing malignancies. Semin Nucl Med. 2002;32(2):97–109.
47. Fani M, Peitl PK, Velikyan I. Current status of radiopharmaceuticals for the theranostics of neuroendocrine neoplasms. Pharmaceuticals (Basel). 2017;10(1):pii: E30.
48. Kratochwil C, Giesel FL, Stefanova M, Benesova M, Bronzel M, Afshar-Oromieh A, et al. PSMA-targeted radionuclide therapy of metastatic castration-resistant prostate cancer with ^{177}Lu-labeled PSMA-617. J Nucl Med. 2016;57(8):1170–6.
49. Kratochwil C, Bruchertseifer F, Giesel FL, Weis M, Verburg FA, Mottaghy F, et al. ^{225}Ac-PSMA-617 for PSMA-targeted alpha-radiation therapy of metastatic castration-resistant prostate cancer. J Nucl Med.2016;57(12):1941–4.
50. Cheung A, Bax HJ, Josephs DH, Ilieva KM, Pellizzari G, Opzoomer J, et al. Targeting folate receptor alpha for cancer treatment. Oncotarget. 2016;7(32):52553–74.
51. Streby KA, Shah N, Ranalli MA, Kunkler A, Cripe TP. Nothing but NET: a review of norepinephrine transporter expression and efficacy of ^{131}I-mIBG therapy. Pediatr Blood Cancer. 2015;62(1):5–11.
52. Sharp SE, Trout AT, Weiss BD, Gelfand MJ. MIBG in neuroblastoma diagnostic imaging and therapy. Radiographics. 2016;36(1):258–78.
53. Maloney DG. Anti-CD20 antibody therapy for B-cell lymphomas. N Engl J Med. 2012;366(21):2008–16.
54. Morschhauser F, Radford J, Van Hoof A, Botto B, Rohatiner AZ, Salles G, et al. ^{90}Yttrium-ibritumomab tiuxetan consolidation of first remission in advanced-stage follicular non-Hodgkin lymphoma: updated results after a median follow-up of 7.3 years from the International, Randomized, Phase III First-Line Indolent trial. J Clin Oncol. 2013;31(16):1977–83.
55. Goldsmith SJ. Radioimmunotherapy of lymphoma: Bexxar and Zevalin. Semin Nucl Med. 2010;40(2):122–35.
56. Hdeib A, Sloan A. Targeted radioimmunotherapy: the role of ^{131}I-chTNT-1/B mAb (Cotara) for treatment of high-grade gliomas. Future Oncol. 2012;8(6):659–69.
57. Chen ZN, Mi L, Xu J, Song F, Zhang Q, Zhang Z, et al. Targeting radioimmunotherapy of hepatocellular carcinoma with iodine (^{131}I) metuximab injection: clinical phase I/II trials. Int J Radiat Oncol Biol Phys. 2006;65(2):435–44.
58. Xu J, Xu HY, Zhang Q, Song F, Jiang JL, Yang XM, et al. HAb18G/CD147 functions in invasion and metastasis of hepatocellular carcinoma. Mol Cancer Res. 2007;5(6):605–14.
59. Erba PA, Sollini M, Orciuolo E, Traino C, Petrini M, Paganelli G, et al. Radioimmunotherapy with radretumab in patients with relapsed hematologic malignancies. J Nucl Med. 2012;53(6):922–7.
60. Werle M, Bernkop-Schnurch A. Strategies to improve plasma half life time of peptide and protein drugs. Amino Acids. 2006;30(4):351–67.
61. Kaloudi A, Nock BA, Krenning EP, Maina T, De Jong M. Radiolabeled gastrin/CCK analogs in tumor diagnosis: towards higher stability and improved tumor targeting. Q J Nucl Med Mol Imaging. 2015;59(3):287–302.
62. Chae SY, Chun YG, Lee S, Jin CH, Lee ES, Lee KC, et al. Pharmacokinetic and pharmacodynamic evaluation of site-specific PEGylated glucagon-like peptide-1 analogs as flexible postprandial-glucose controllers. J Pharm Sci. 2009;98(4):1556–67.
63. Chen H, Wang G, Lang L, Jacobson O, Kiesewetter DO, Liu Y, et al. Chemical conjugation of Evans blue derivative: a strategy to develop long-acting therapeutics through albumin binding. Theranostics. 2016;6(2):243–53.
64. Vegt E, van Eerd JE, Eek A, Oyen WJ, Wetzels JF, de Jong M, et al. Reducing renal uptake of radiolabeled peptides using albumin fragments. J Nucl Med. 2008;49(9):1506–11.
65. Veronese FM, Pasut G. PEGylation, successful approach to drug delivery. Drug Discov Today. 2005;10(21):1451–8.
66. Haller S, Reber J, Brandt S, Bernhardt P, Groehn V, Schibli R, et al. Folate receptor-targeted radionuclide therapy: preclinical investigation of anti-tumor effects and potential radionephropathy. Nucl Med Biol. 2015;42(10):770–9.
67. Muller C, Struthers H, Winiger C, Zhernosekov K, Schibli R. DOTA conjugate with an albumin-binding entity enables the first folic acid-targeted ^{177}Lu-radionuclide tumor therapy in mice. J Nucl Med. 2013;54(1):124–31.
68. Siwowska K, Haller S, Bortoli F, Benesova M, Groehn V, Bernhardt P, et al. Preclinical comparison of albumin-binding radiofolates: impact of linker entities on the in vitro and in vivo properties. Mol Pharm. 2017;14(2):523–32.
69. Gaberc-Porekar V, Zore I, Podobnik B, Menart V. Obstacles and pitfalls in the PEGylation of therapeutic proteins. Curr Opin Drug Discov Devel. 2008;11(2):242–50.
70. Kraeber-Bodere F, Rousseau C, Bodet-Milin C, Frampas E, Faivre-Chauvet A, Rauscher A, et al. A pretargeting system for tumor PET imaging and radioimmunotherapy. Front Pharmacol. 2015;6:54.
71. Hendrickson WA, Pahler A, Smith JL, Satow Y, Merritt EA, Phizackerley RP. Crystal structure of core streptavidin determined from multiwavelength anomalous diffraction of synchrotron radiation. Proc Natl Acad Sci U S A. 1989;86(7):2190–4.

72. Weber PC, Ohlendorf DH, Wendoloski JJ, Salemme FR. Structural origins of high-affinity biotin binding to streptavidin. Science. 1989;243(4887):85–8.
73. Paganelli G, Bartolomei M, Ferrari M, Cremonesi M, Broggi G, Maira G, et al. Pre-targeted locoregional radioimmunotherapy with Y-biotin in glioma patients: phase I study and preliminary therapeutic results. Cancer Biother Radiopharm. 2001;16(3):227–35.
74. Forero A, Weiden PL, Vose JM, Knox SJ, LoBuglio AF, Hankins J, et al. Phase 1 trial of a novel anti-CD20 fusion protein in pretargeted radioimmunotherapy for B-cell non-Hodgkin lymphoma. Blood. 2004;104(1):227–36.
75. Bos ES, Kuijpers WH, Meesters-Winters M, Pham DT, de Haan AS, van Doornmalen AM, et al. In vitro evaluation of DNA-DNA hybridization as a two-step approach in radioimmunotherapy of cancer. Cancer Res. 1994;54(13):3479–86.
76. Rossin R, Lappchen T, van den Bosch SM, Laforest R, Robillard MS. Diels-Alder reaction for tumor pretargeting: in vivo chemistry can boost tumor radiation dose compared with directly labeled antibody. J Nucl Med. 2013;54(11):1989–95.
77. Rossin R, Verkerk PR, van den Bosch SM, Vulders RC, Verel I, Lub J, et al. In vivo chemistry for pretargeted tumor imaging in live mice. Angew Chem Int Ed Engl. 2010;49(19):3375–8.
78. Boerman OC, Kranenborg MH, Oosterwijk E, Griffiths GL, McBride WJ, Oyen WJ, et al. Pretargeting of renal cell carcinoma: improved tumor targeting with a bivalent chelate. Cancer Res. 1999;59(17):4400–5.
79. Goodwin DA, Meares CF, McTigue M, Chaovapong W, Diamanti CI, Ransone CH, et al. Pretargeted immunoscintigraphy: effect of hapten valency on murine tumor uptake. J Nucl Med. 1992;33(11):2006–13.
80. Le Doussal JM, Gruaz-Guyon A, Martin M, Gautherot E, Delaage M, Barbet J. Targeting of indium-111 labeled bivalent hapten to human melanoma mediated by bispecific monoclonal antibody conjugates: imaging of tumors hosted in nude mice. Cancer Res. 1990;50(11):3445–52.
81. Kraeber-Bodere F, Rousseau C, Bodet-Milin C, Ferrer L, Faivre-Chauvet A, Campion L, et al. Targeting, toxicity, and efficacy of 2-step, pretargeted radioimmunotherapy using a chimeric bispecific antibody and ^{131}Ilabeled bivalent hapten in a phase I optimization clinical trial. J Nucl Med. 2006;47(2):247–55.
82. Chatal JF, Campion L, Kraeber-Bodere F, Bardet S, Vuillez JP, Charbonnel B, et al. Survival improvement in patients with medullary thyroid carcinoma who undergo pretargeted anti-carcinoembryonic-antigen radioimmunotherapy: a collaborative study with the French Endocrine Tumor Group. J Clin Oncol. 2006;24(11):1705–11.
83. Lambin P, Leijenaar RTH, Deist TM, Peerlings J, de Jong EEC, van Timmeren J, et al. Radiomics: the bridge between medical imaging and personalized medicine. Nat Rev Clin Oncol. 2017;14:749.
84. Morschhauser F, Radford J, Hoof AV, Vitolo U, Soubeyran P, Tilly H, et al. Phase III trial of consolidation therapy with yttrium-90–ibritumomab tiuxetan compared with no additional therapy after first remission in advanced follicular lymphoma. J Clin Oncol. 2008;26(32):5156–64.
85. Parker C, Nilsson S, Heinrich D, Helle SI, O'Sullivan JM, Fosså SD, et al. Alpha emitter radium-223 and survival in metastatic prostate cancer. N Engl J Med. 2013;369(3):213–23.
86. Oudard S, Courbon F. Controversies and consensus in the innovation access for cancer therapy in the European countries: on the subject of metastatic prostate cancer. Ann Oncol. 2017;28(2):421–6.
87. Sartor O, Coleman R, Nilsson S, Heinrich D, Helle SI, O'Sullivan JM, et al. Effect of radium-223 dichloride on symptomatic skeletal events in patients with castration-resistant prostate cancer and bone metastases: results from a phase 3, double-blind, randomised trial. Lancet Oncol. 2014;15(7):738–46.
88. Hazel GA, Heinemann V, Sharma NK, Findlay MPN, Ricke J, Peeters M, et al. SIRFLOX: randomized phase III trial comparing first-line mFOLFOX6 (plus or minus bevacizumab) versus mFOLFOX6 (plus or minus bevacizumab) plus selective internal radiation therapy in patients with metastatic colorectal cancer. J Clin Oncol. 2016;34(15):1723–31.
89. Wasan HS et al. First-line selective internal radiotherapy plus chemotherapy versus chemotherapy alone in patients with liver metastases from colorectal cancer (FOXFIRE, SIRFLOX, and FOXFIRE-Global): a combined analysis of three multicentre, randomised, phase 3 trials. Lancet Oncol. 2017; 1159–71. https://doi.org/10.1016/S1470-2045(17)30457-6.
90. Wang EA, Broadwell SR, Bellavia RJ, Stein JP. Selective internal radiation therapy with SIR-Spheres in hepatocellular carcinoma and cholangiocarcinoma. J Gastrointest Oncol. 2016;8(2):266–78.
91. Wang EA, Stein JP, Bellavia RJ, Broadwell SR. Treatment options for unresectable HCC with a focus on SIRT with yttrium-90 resin microspheres. Int J Clin Pract. 2017;71(11):e12972–n/a.
92. Bouattour M, Assenat E, Guiu B, Ilonca Alina D, Pageaux G-P, Sibert A, et al. LBA-001Efficacy, tolerability and impact on quality of life of selective internal radiation therapy (with yttrium-90 resin microspheres) or sorafenib in patients with locally advanced hepatocellular carcinoma: The SARAH trial. Ann Oncol. 2017;28(Suppl_3):mdx302-mdx.
93. Strosberg J, El-Haddad G, Wolin E, Hendifar A, Yao J, Chasen B, et al. Phase 3 trial of 177Lu-dotatate for midgut neuroendocrine tumors. N Engl J Med. 2017;376(2):125–35.
94. Smit Duijzentkunst DA, Kwekkeboom DJ, Bodei L. Somatostatin receptor 2–targeting compounds. J Nucl Med. 2017;58(Suppl 2):54S–60S.
95. Sartor O, Hoskin P, Coleman RE, Nilsson S, Vogelzang NJ, Petrenciuc O, et al. Chemotherapy following radium-223 dichloride treatment in ALSYMPCA. Prostate. 2016;76(10):905–16.
96. Hoskin P, et al. Efficacy and safety of radium-223 dichloride in patients with castration-resistant prostate cancer and symptomatic bone metastases, with or without previous docetaxel use: a prespecified subgroup analysis from the randomised, double-blind, phase 3 ALSYMPC. Lancet Oncol. 2014;15:1397–406.
97. Saad F, et al. Radium-223 and concomitant therapies in patients with metastatic castration-resistant prostate cancer: an international, early access, open-label, singlearm phase 3b trial. Lancet Oncol. 2016;17:1306–16.
98. Sartor O, Heinrich D, Mariados N, Méndez Vidal MJ, Keizman D, Thellenberg Karlsson C, et al. Re-treatment with radium-223: first experience from an international, open-label, phase I/II study in patients with castration-resistant prostate cancer and bone metastases. Ann Oncol. 2017;28(10):2464–71.
99. Barbier CE, Garske-Román U, Sandström M, Nyman R, Granberg D. Selective internal radiation therapy in patients with progressive neuroendocrine liver metastases. Eur J Nucl Med Mol Imaging. 2016;43(8):1425–31.
100. Nelson K, Vause PEJ, Koropova P. Post-mortem considerations of yttrium-90 (^{90}Y) microsphere therapy procedures. Health Phys. 2008;95(5):S156–61.
101. Marcus R, Davies A, Ando K, Klapper W, Opat S, Owen C, et al. Obinutuzumab for the first-line treatment of follicular lymphoma. N Engl J Med. 2017;377(14):1331–44.
102. Cheal SM, Fung EK, Patel M, Xu H, Guo H-F, Zanzonico PB, et al. Curative multicycle radioimmunotherapy monitored by quantitative SPECT/CT-based theranostics, using bispecific antibody pretargeting strategy in colorectal cancer. J Nucl Med. 2017;58(11):1735–42.
103. Grzmil M, Seebacher J, Hess D, Behe M, Schibli R, Moncayo G, et al. Inhibition of MNK pathways enhances cancer cell response to chemotherapy with temozolomide and targeted radionuclide therapy. Cell Signal. 2016;28(9):1412-21.

An Overview of Nuclear Imaging

Pat Zanzonico

Introduction

Nuclear imaging, including single-photon emission computed tomography (SPECT) and positron-emission tomography (PET), utilizes unsealed sources of radioactivity administered—almost always systemically and usually intravenously—in the form of radiopharmaceuticals. Diagnostic nuclear imaging of patients is part of the clinical specialty known as nuclear medicine.[1] In recent years, another term, "molecular imaging," has become firmly entrenched in the lexicon of both clinical practice and preclinical research; it is defined as "… the visualization, characterization, and measurement of biological processes at the molecular and cellular levels in humans and other living systems." [1] While it is not modality-specific, the term is often closely associated with nuclear imaging and, in particular, SPECT and PET.

Interactions of Radiation with Matter

Radiations emitted as a result of radioactive decay—such as x-rays, γ-rays and β-particles—are "ionizing" radiations. Such radiations ionize the atoms or molecules of a stopping medium and produce free negative electrons and positive ions. X-rays and γ-rays are far more penetrating than β-rays. In soft tissue, x-rays and γ-rays with energies of several hundred kilo-electron volts (keV) will typically travel 5–10 cm before interacting, while β-particles with similar energies will travel no further than approximately 1 mm. "Diagnostic" x-rays and γ-rays interact with matter by the photoelectric effect or by Compton scattering [2, 3]. In the photoelectric effect, an x-ray's or γ-ray's energy is completely transferred to an orbital electron in an atom of the stopping medium, ejecting the electron from the atom as a so-called photoelectron. The x-ray or γ-ray thus disappears in the process. In Compton scattering, only a portion of the incident x-ray's or γ-ray's energy is transferred to an orbital electron, which is ejected from the atom as a so-called recoil electron. In this case, the scattered x-ray's or γ-ray's energy is therefore less than that of the incident x-ray or γ-ray, and it travels in a different direction. Importantly, because of their change in direction, x-rays or γ-rays which are Compton-scattered in the patient's body and detected with a gamma camera or other imaging device may erroneously appear to originate from a direction different from that of the original x-ray or γ-ray. Compton scattering, which is the predominant mode of interaction of "diagnostic" x-rays and γ-rays in tissues, thus represents one of the major impediments to the accurate spatial localization and high-contrast detection of radionuclides *in vivo*. However, if the detection system has the ability to distinguish radiations of different energies, many of these Compton-scattered x-rays or γ-rays can be effectively removed based on the fact that their energy is lower than that of the original (*i.e.* unscattered) x-rays or γ-rays.

Radionuclides used for PET decay, of course, by emitting positrons (*i.e.* positive electrons). Like "ordinary" beta particles (*i.e.* negative electrons), positrons travel only ~1–2 mm or less in tissue. This distance depends on the kinetic energy of the emitted positrons, and some radionuclides emit more energetic positrons that can have a range up to ~10 mm. Once it has exhausted its kinetic energy and reached the end of its range, a positron undergoes mutual annihilation with an electron in the medium, since positrons and electrons are antiparticles of one another. As a result of the positron-electron annihilation, their rest mass energies (the energy equivalent of their respective masses) are converted to two 511-keV γ-rays emitted in opposite directions, that is, 180° apart. These back-to-back annihilation photons are utilized in coincidence detection and PET.

[1] Although nuclear medicine remains primarily a diagnostic specialty, unsealed sources of radioactivity are also used therapeutically. The therapeutic applications of nuclear medicine are beyond the scope of this chapter, however.

P. Zanzonico (✉)
Department of Medical Physics, Memorial Sloan Kettering Cancer Center, New York, NY, USA
e-mail: zanzonip@mskcc.org

J. S. Lewis et al. (eds.), *Radiopharmaceutical Chemistry*, https://doi.org/10.1007/978-3-319-98947-1_6

Advantages and Disadvantages of Nuclear Imaging

The ionizing radiations that accompany the decay of radionuclides within radiopharmaceuticals can be detected, measured, and imaged noninvasively with instruments such as gamma cameras and SPECT and PET scanners. Nuclear imaging in general—and SPECT and PET in particular—offers a number of important advantages in the context of clinical practice as well as clinical and preclinical research. First, both the specific activity (*i.e.* activity per unit mass) of radiopharmaceuticals and the detection sensitivity of nuclear imaging instruments are sufficiently high that the activity typically needed for imaging corresponds to non-pharmacologic, non-perturbing mass doses (typically in the sub-nmol range). This is in contrast to computed tomography (CT) and magnetic resonance imaging (MRI), for example, in which the mass doses of various contrast agents are far higher—typically in the μmol to mmol range—and thus may influence the system being studied. Second, radionuclide images are quantitative or at least semiquantitative, meaning that image "intensity" (*i.e.* count density) reflects the radiopharmaceutical-derived activity concentration. Routinely for PET, and increasingly for SPECT, images can be absolutely quantitative and may be parameterized, for example, in terms of activity concentration. For other imaging modalities, the relationship between the contrast agent or other analyte concentration and image intensity is typically not as direct. Third, a large number and variety of targeted radiopharmaceuticals (including receptor-binding ligands, antibodies, nanoparticles, *etc.*) have been and continue to be developed for the increasingly specific characterization of *in situ* biology.

It is important to note that despite these positive attributes, nuclear imaging is not without its drawbacks. One of these limitations is relatively coarse spatial resolution. Expressed as the full-width half-maximum (FWHM) of the system point or line spread function, the resolution of nuclear imaging modalities ranges from ~5 mm for clinical PET to ~15 mm for clinical SPECT (in both of these modalities, the spatial resolution is considerably better in preclinical systems). This is about an order of magnitude poorer than the spatial resolution of CT and MRI. Further, nuclear imaging is, of course, a radiation-based modality and thus delivers low but non-negligible radiation doses to patients or experimental animals, with effective doses typically of the order of 10 millisieverts (mSv) and maximal organ absorbed doses of up to several milligrays (mGy) per study [4]. Finally, nuclear images generally include only limited anatomic information, which may complicate their analysis and interpretation. With the increasingly widespread availability of multimodality devices (*i.e.* PET-CT, SPECT-CT, and, most recently, PET-MRI), nuclear images reflecting *in vivo* function may be accurately registered and fused with anatomic images, largely overcoming this limitation.

This chapter reviews the underlying physical principles and design and operation of gamma cameras and SPECT and PET scanners. Some fundamental principles of SPECT and PET radiopharmaceuticals are briefly reviewed as well.

Types of Nuclear Imaging

Planar versus Tomographic Imaging

In planar, or two-dimensional, nuclear imaging (also known as projection imaging), radiations emanating from activity at all depths of the subject are projected onto an imaging detector. In the first order, therefore, the image counts in a given pixel represent the ray sum, or integral, of the radiations emitted over the full-depth volume of tissue corresponding to (*i.e.* underlying) that pixel. Therefore, for a structure of interest such as a tumor, both the tumor itself and the background tissues contribute counts to the total counts in a given pixel. This degrades image contrast (expressed, for example, as the tumor-to-background counts-per-pixel ratio) and compromises the visualization and quantitation of activity in the tumor—in some instances, to the point that tumors or other tissues of interest may be completely obscured.

A "tomogram," in contrast, is literally a picture of a slice through the subject. Tomographic imaging thus eliminates or at least minimizes the counts in the image arising from activity outside the tissue of interest and thus improves both image contrast and the overall visualization of tumors and organs. Tomography may be characterized as either transmission or emission tomography depending on the origin of the radiation. In transmission tomography (*i.e.* CT), x-rays are transmitted through the subject. In emission tomography, x-rays or γ-rays are emitted by radiopharmaceuticals located within the subject. Emission tomography can be further characterized on the basis of the nature of the emitted radiation. Single photons, such as γ-rays associated with isomeric transition and x-rays associated with electron capture or internal conversion, form the basis of SPECT. The two 511-keV annihilation photons simultaneously emitted following the annihilation of positrons and electrons form the basis of PET.

The basic paradigm of tomographic imaging includes the acquisition of images from multiple angles around a patient (multiple projections), the correction of the data for nonuniform response of the imaging system and other signal-degrading factors, and the mathematical reconstruction of transverse tissue-section images. In SPECT and PET, the transverse images are essentially contiguous, with no intersection gaps. Therefore, the reconstructed three-dimensional array of volume elements, or voxels, may be rearranged at any angle relative to the longitudinal axis of the patient and thus yield coronal, sagittal, and oblique as well as transverse images. As noted, the principal advantage of

tomography lies in its improved image contrast and greater quantitative accuracy: by eliminating the count contribution from activities in tissues above and below the tissue section of interest, the target-to-background ratio and the accuracy of the image-derived activity concentrations improve. Another important advantage of emission tomography lies in its ability to visualize the three-dimensional distribution of activity *in situ*, that is, to ascertain the depths of foci of activity.

Static Versus Dynamic Imaging

Several types of nuclear imaging—static, dynamic, and whole-body—may be performed in either planar or tomographic formats. Static imaging involves the acquisition of a stable distribution of activity, a distribution that does not vary significantly over the course of the acquisition.

Dynamic imaging involves the acquisition of a temporally varying distribution of activity as a series of images (or frames). Often, several frame sets (or "segments") of different frame durations are used in a single study, with shorter-duration frames comprising the early segments (when the *in vivo* distribution of a radiopharmaceutical is changing rapidly) and progressively longer-duration frames comprising the later segments (when the radiotracer distribution changes more slowly or stabilizes). The time-varying data provided by such studies may be used to derive information on dynamic processes. In conjunction with compartmental or other types of kinetic models, such data may yield estimates of functional parameters in absolute terms. For example, ^{15}O-labeled water has been used to measure regional perfusion in milliliters per minutes per gram of tissue (mL/min/g). Gated imaging is a type of dynamic imaging particularly important in cardiology, for example, for estimating left ventricular (LV) function (ejection fraction) and assessing LV wall motion. In gated imaging, a physiological "event" (such as the R wave of the electrocardiogram) in a repeating physiological process (such as the cardiac cycle) triggers the start of acquisition of a series of frames over each repetition of the process. The corresponding frames in each repetition are summed to yield a statistically reliable sequence of images over the cyclical process.

Dynamic acquisition is typically performed in "frame mode," with the number(s) and duration(s) of frames preset prior to acquisition. Alternatively, dynamic studies may be performed in so-called list mode, with the acquisition of a list of individual counts and with each count identified by its acquisition time and position coordinates. Importantly, for list-mode data, the time binning is completely flexible and can be done and redone as often as necessary to optimize the dynamic framing. This provides great flexibility for dynamic imaging in instances where the temporal resolution required may not be known prior to the study or, in the case of gated studies, the duration of the (cardiac) cycle may vary somewhat irregular (*e.g.* due to arrhythmia). In contrast to frame-mode studies, there is really no distinction between the collection of static and dynamic images in list mode: if the acquired data are binned into a single frame, a static study results, while binning of the same data into multiple frames yields a dynamic study. Dynamic gamma camera data are generally acquired in frame mode; PET data are acquired exclusively in list mode.

Whole-Body Imaging

Whole-body imaging provides the distribution of a radiopharmaceutical throughout the entire body in a single image. An implicit assumption of this approach is that the whole-body distribution of the radiopharmaceutical is reasonably stable over the duration of the scan. For gamma camera-based whole-body imaging, either the detector(s) is(are) slowly translated over the stationary patient or the patient table is slowly translated between the stationary detectors. Scan speeds are typically 5–10 cm/min, with scans including the entire length of the body. Despite the motion of the detector(s) relative to patient, there is little to no perceptible degradation in image quality with whole-body scanning. Because a single SPECT study of a specific region of the body currently requires data acquisition over 20–30 min, whole-body SPECT scanning would require acquisition of multiple individual SPECT scans and thus could take as long as several hours, prohibitively slow for routine clinical practice.

The imaging gantries of clinical PET scanners generally span a distance of 15–25 cm in the patient's longitudinal direction. A whole-body PET scan will typically require data acquisition over several minutes at each of six to seven discrete (*i.e.* stationary) bed positions, with a seamless whole-body image formed via the subsequent merging, or "knitting," of these discrete images. With modern three-dimensional (3D) PET scanners, the images acquired at successive bed positions must overlap considerably in order to yield reasonably consistent data in terms of statistical quality over the entire length of the patient.

Basic Principles of Radiation Detection

Radiation detectors are generally characterized as either scintillation or ionization detectors [2, 3]. In scintillation detectors, visible light is produced as radiation excites atoms of a crystal, and this light is converted to an electronic signal (or pulse) and amplified by a photomultiplier tube (PMT) and its associated high (~1,000-V) voltage. In ionization

detectors, free electrons produced when radiation ionizes a stopping material are collected to produce a small electronic signal. For nuclear imaging, which is generally "count-limited," scintillation detectors are preferred because of their high sensitivity. However, devices based on solid-state ionization detectors are also available, but these remain less common in clinical practice than scintillation detector-based devices.

Scintillation Detectors

In scintillation detectors (Fig. 1) [2, 3], radiation interacts with and deposits energy in a scintillator, most commonly, a crystalline solid such as thallium-doped sodium iodide (NaI(Tl)). The radiation energy deposited is converted to visible light, with the amount of light proportional to the amount of radiation energy deposited. Because the light is emitted isotropically, the inner surface of the light-tight crystal housing is coated with a reflective material so that light emitted toward the sides and front of the crystal is reflected back toward the photomultiplier tube (PMT). This maximizes the amount of light collected and therefore the overall sensitivity of the detector and also ensures that the amount of light detected is proportional to the energy of the absorbed photons. Interposed between the back of the crystal and the entrance window of the PMT is the light guide, sometimes simply a thin layer of transparent optical gel. The light guide optically couples the crystal to the PMT and thus maximizes the transmission of the light signal from the crystal into the PMT.

The PMT consists of an evacuated glass enclosure containing a series of dynodes maintained at different voltages. Coated on the inner surface of the PMT's entrance window is the photocathode. When struck by the light from the crystal, the photocathode ejects electrons. Immediately beyond the photocathode is the focusing grid, which is maintained at a relatively low positive voltage relative to the photocathode. Once the "focused" electrons pass through the focusing grid, they are attracted by a relatively large positive voltage relative to the photocathode (~300 V) on the first of a series of small metallic elements, the dynodes. The resulting high-speed impact of each electron results in the ejection of an *average* of three electrons from the dynode surface. These ejected electrons are then attracted by the even larger positive voltage (~400 V) on the second dynode. The impact of these electrons on the second dynode surface ejects an additional three electrons on average for each incident electron. Typically, a PMT has 10–12 such dynodes (or stages), each ~100 V more positive than the preceding dynode. This configuration results in an overall electron amplification factor of 3^{10}–3^{12} for the entire PMT. At the collection anode, an output signal is generated. The irregular PMT output signal is shaped into a logic (*i.e.* square-wave) pulse that can be electronically manipulated. In the past, this was accomplished by a preamplifier; nowadays, pulse shaping, amplification, *etc.* are performed by digital electronics and computer software. The amplitudes (or "heights") of the resulting electrical pulses are proportional to the number of electrons produced at the PMT photocathode and thus the energy of the incident radiation. These pulses can then be sorted according to their respective heights by an energy discriminator (also known as a pulse-height analyzer), and those pulses with a pulse height (*i.e.* energy) within a preset photopeak energy window are counted or, in the case of an imag-

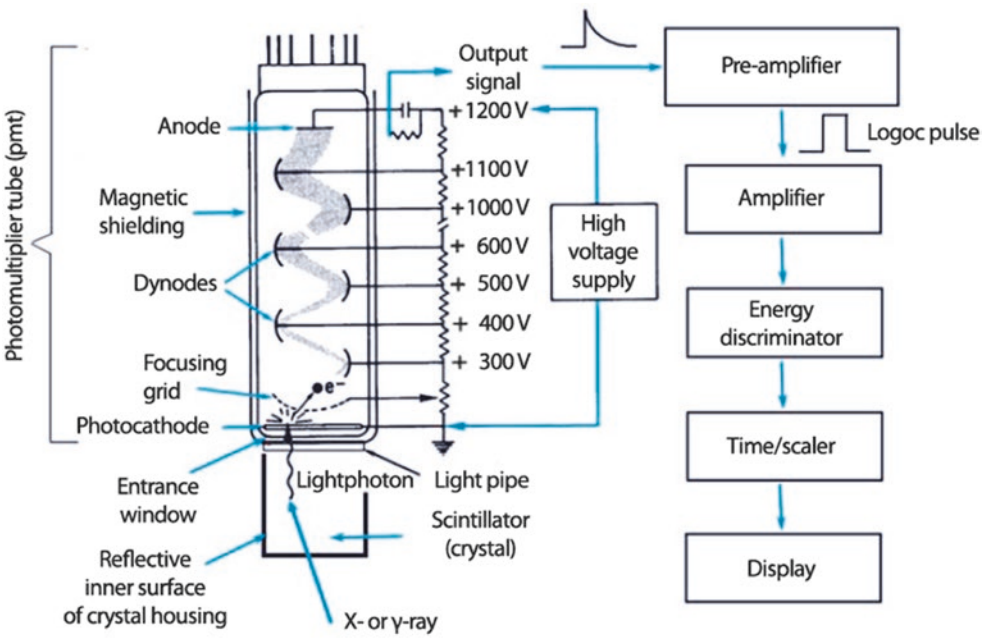

Fig. 1 Basic design and operation of a scintillation detector. Note that only two of the four pulses have heights lying within the preset pulse height range (*i.e.* correspond to photon energies within the preset photopeak energy window). Thus, only those two photons are counted (in the case of a radiation counter) or included in the image (in the case of a radiation imager). The other two photons—with pulse heights and therefore energies outside the photopeak energy window—are not counted or included in the image. (Adapted from Zanzonico and Heller [3] with permission)

ing device, included in the image. In recent years, new PMT configurations have been developed that allow enhanced approaches to position determination in gamma cameras and SPECT and PET scanners. These include the position-sensitive PMT (PSPMT), which provides two-dimensional position information across the face (*i.e.* entrance window) of the PMT.

The silicon photodiode is an alternative to the PMT for the conversion of scintillation light into electronic signals. Photodiodes typically have a gain of only one (compared to the ~10^6-fold gain of PMTs) and thus require low-noise electronics. So-called avalanche photodiodes (or APDs)—in which the number of electrons produced by the visible light is amplified—have considerably higher gains (on the order of 100–1,000) but still require low-noise readout electronics. An alternative to traditional vacuum-tube PMTs and silicon (Si) photomultipliers (or "SiPMs") are single-photon-sensitive devices built from an APD array on a Si substrate [5]. The performance parameters of SiPMs are comparable to those of traditional PMTs but with a much more compact form factor.

The scintillation detection materials most widely used in nuclear medicine—all inorganic scintillators—are bismuth germanate (BGO, $Bi_4Ge_3O_{12}$), cerium-doped gadolinium oxyorthosilicate (GSO(Ce) or GSO, Gd_2SiO_5:Ce), cerium-doped lutetium oxyorthosilicate (LSO(Ce) or LSO, Lu_2SiO_5:Ce), and cerium-doped lutetium-yttrium oxyorthosilicate (LYSO(Ce) or LYSO, Lu_2YSiO_5:Ce), as well as thallium-doped sodium iodide [NaI(Tl)] [2, 3, 6, 7]. PET scanners primarily use BGO, GSO, LSO, or LYSO, and gamma cameras NaI(Tl). The most important practical features of scintillation detectors include:

- High mass density (ρ) and effective atomic number (Z_{eff}) to maximize the photon stopping power (*i.e.* intrinsic efficiency) of the detector
- High light (scintillation) output to maximize the signal and thus minimize statistical uncertainty in the energy of the detected signal
- For PET, high speed of the output light pulse to shorten the coincidence timing window (τ) and thus minimize the number of random events without sacrificing a significant portion of the signal (see below)

As noted, higher-ρ and higher-Z_{eff} atomic materials such as BGO, GSO, LSO, and LYSO have emerged as the detectors of choice for PET because of their greater stopping power for 511-keV annihilation γ-rays. The mean free path (MFP) for 511-keV γ-rays is at least twice as long in NaI(Tl) as in BGO, GSO, or LSO. GSO, LSO, and LYSO have almost tenfold faster light output than BGO, with LSO and LYSO having a much greater (two- to threefold greater) light output than either BGO or GSO. GSO has somewhat better energy resolution[2] and, therefore, scatter rejection capability than either BGO or LSO. A notable disadvantage of LSO and LYSO is the presence of a naturally occurring long-lived radionuclide of lutetium: lutetium-176 (^{176}Lu) [6]. ^{176}Lu has an isotopic abundance of 2.6% and a half-life of ~4×10^{10} years and emits two prompt γ-rays (88% abundance) of 201 and 306 keV in energy, respectively. The summed energy of these two γ-rays is 507 keV, which falls well within the 511-keV energy windows commonly used in PET scanners. For example, the presence of ^{176}Lu results in a measured background count rate of 240 cps/cm^3 of LSO. This has a negligible effect on activities and the resulting count rates typically encountered in PET scanning, however.

Semiconductor-Based Ionization Detectors

Semiconductor radiation detectors represent the main alternative to scintillator detector-based imaging systems. Such detectors are so-called direct-conversion devices, a major advantage of which is that they minimize the random effects associated with scintillation production and the propagation and conversion of the optical signal to an electronic signal. When an x-ray or γ-ray interacts in a semiconductor detector, one or more energetic electrons are created and subsequently lose energy through ionization of atoms in the semiconductor material, among other processes. The ionization creates electron-hole (e-h) pairs, in which a hole is the positively charged electron vacancy in the valence band that remains after an electron has been raised into the conduction band. The application of a bias voltage creates an electric field that causes these two types of charge carriers to migrate in opposite directions. These moving charges induce transient currents in the detector electrodes, thereby allowing the measurement of the detector's response to an incident x-ray or γ-ray.

Semiconductor detectors offer several potential advantages over scintillator detectors [8]. By eliminating the need for bulky PMTs, semiconductor imaging systems can be made much more compact than PMT-based imaging systems. More importantly, the direct conversion of energy deposited by x-rays or γ-rays into electron-hole pairs eliminates the light-to-electrical signal transduction step and the associated loss of signal. Further, since the energy required to create an electron-hole pair in most semiconductors is small (typically 3–5 eV), each incident photon generates a large number of charge carriers. In principle, therefore, Poisson noise is considerably reduced and energy resolution considerably improved in semiconductor detectors compared to scintillation detectors. It is important to note, how-

[2]Energy resolution is a parameter which reflects the ability of radiation detectors to distinguish radiations of different energies.

ever, that defects (*i.e.* inherent irregularities in the crystal lattice) can trap electrons produced by radiation and thus reduce the total charge collected. As a result of such incomplete charge collection, the otherwise excellent energy resolution of semiconductors is degraded. Practical and reasonably economical crystal-growing techniques have been developed for cadmium telluride (CdTe), mercuric iodide (HgI_2), and cadmium zinc telluride (CdZnTe) (also known as "CZT"), all of which have been incorporated into commercial intraoperative gamma probes and gamma cameras [8, 9].

Radiation detectors may be quantitatively characterized by many different performance parameters. Among the most important of these are sensitivity (or efficiency), energy resolution, count-rate performance, and, for devices which localize (image) as well as count radiation, spatial resolution and uniformity [10].

Gamma Cameras and SPECT Scanners

The Gamma Camera

Developed in the late 1950s by Hal Anger, the gamma camera (Fig. 2)—also known as the scintillation or Anger camera—has long been the predominant imaging device in nuclear medicine [2, 3]. Its large detector area allows simultaneous and therefore rapid data acquisition over a large area of the body. Almost universally, gamma camera crystals are composed of a plate of NaI(Tl) and vary in thickness from approximately 6 to 24 mm. A 9.5-mm-thick crystal provides a reasonable balance between sensitivity and resolution and is the most widely used for general gamma camera imaging. About 95% of the 140-keV photons from ^{99m}Tc are absorbed in a 9.5-mm-thick crystal. Nowadays, clinical gamma camera crystals are most commonly rectangular in shape and ~50 × 60 cm in area for general-purpose imaging. Crystals smaller in area are used on dedicated cardiac systems.

Once the incident radiation passes through the collimator, it strikes, and may produce a scintillation within, the crystal. The resulting light signal is distributed among a two-dimensional array of PMTs backing the crystal, the light intensity varying inversely with the distance between the position of the scintillation and the respective PMT: the farther the PMT is from the scintillation, the less light it receives and the smaller its output pulse. This inverse relationship is the basis of the Anger position logic circuitry for determining the precise position of a scintillation within the crystal. In older gamma cameras, the x- and y-coordinates were calculated by analog circuitry (*i.e.* using matrices of resistors). In current systems, this is done by digitizing the output signal from each PMT and using digital electronics.

The gamma camera collimator, almost always comprised of lead, "directionalizes" the incoming radiation. Any radiation traveling at an oblique angle to the axes of the holes (apertures) will strike the lead walls (septa) between the holes and not reach the crystal (*e.g.* event 4 in Fig. 2). As a result, only radiations traveling perpendicular or nearly perpendicular to the crystal surface pass through the apertures and contribute counts to the resulting image. Otherwise, without a collimator, radiations would strike the crystal at positions unrelated to the locations of the radiation emission within the subject. A certain fraction of photons striking the septa will nonetheless pass through them and reach the crystal; this phenomenon, which degrades image quality, is known as "septal penetration." Almost all collimators used in the clinic are parallel-hole collimators, with the apertures and septa parallel to one another. In addition, single-aperture pinhole collimators—most commonly used for thyroid imaging because of their pronounced magnifying effect—are available as well. Pinhole collimators, however, suffer from low sensitivity, limited field of view, and geometric distortion. Geometric distortion refers to the variation of the magnification with both the distance between the source and aperture and the lateral position in the field of view. Therefore, pinhole collimators are rarely used for clinical imaging other than for the thyroid (normally a small, relatively flat organ). For preclinical SPECT, multi-aperture pinhole collimation is now the standard approach, since it combines the magnification effect (and improved resolution) of pinhole collimation with the greater sensitivity afforded by multiple apertures.

Gamma camera collimators are "rated" with respect to photon energy and resolution/sensitivity. Low-energy, or "technetium," collimators—including "low-energy all-purpose (LEAP)" (or "general all-purpose (GAP)"), "low-energy high-resolution" (LEHR)," and "low-energy high-sensitivity" (LEHS)" collimators—are designed to image radionuclides emitting x-rays and γ-rays less than 200 keV in energy. These include ^{99m}Tc (photopeak energy: 140 keV) as well as thallium-201 (^{201}Tl; 68–80 keV) and iodine-123 (^{123}I; 159 keV). Medium-energy, or "gallium," collimators are designed for radionuclides emitting x-rays and γ-rays 200–300 keV in energy, including gallium-67 (^{67}Ga; 93, 185, and 300 keV) as well as indium-111 (^{111}In; 172 and 247 keV). High-energy, or "iodine," collimators are designed to image radionuclides emitting x-rays and γ-rays greater than 300 keV in energy, including ^{131}I (364 keV). In progressing from low- to medium- to high-energy collimation, the collimators are made longer and the septa thicker in order to interpose more lead between the subject and the crystal. This is done in order to maintain septal penetration (*i.e.* expressed as the percent of counts in an image attributable to photons penetrating the septa) at or below an acceptably low level, typically 5%. This, in turn, reduces the overall fraction of emitted x-rays and γ-rays reaching the crystal. To compensate (at least in part) for the resulting lower sensitivity, the apertures are made wider in progressing from low- to medium- to-high-energy collimators. This, however, degrades spatial resolution by dispersing the counts

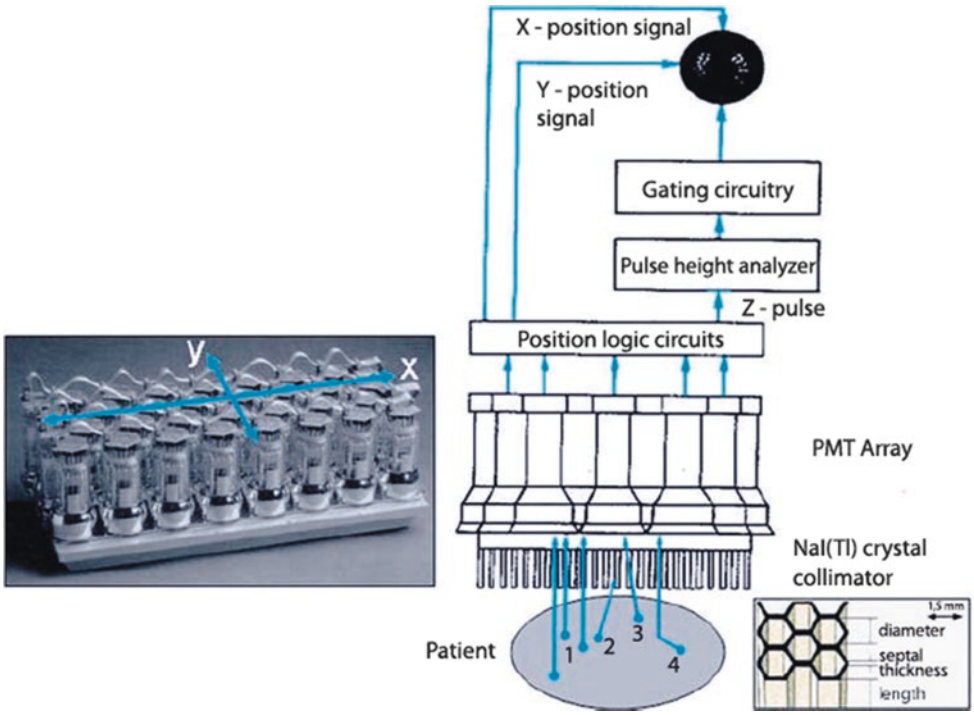

Fig. 2 Basic design of a gamma camera, consisting of a multi-hole collimator, a thin large-area NaI(Tl) crystal, a two-dimensional array of PMTs and associated electronics (high-voltage power supply, preamplifier, and amplifier), position logic circuitry, energy discriminator, and image display. Note that there are actually two position logic circuits for the determination separately of the x- and y-positions of the scintillation within the crystal. Note further that the output signal from each PMT is actually split into three parts, one (the z pulse) for the determination of the energy of the incident radiation as well as one each for the determination of its x- and y-positions. In current-day gamma cameras, the output signal from each PMT is digitized, and the position of each event is determined with computer software. The left inset shows a photograph of the two-dimensional PMT array backing the crystal in a typical rectangular field-of-view gamma camera. The right inset shows a drawing of a portion of a parallel-hole collimator, identifying the dimensions—aperture diameter, septal thickness, and septal length—of such a collimator. The "desirable" events (*arrows labeled* **1**) are unscattered (*i.e.* photopeak) photons traveling in a direction parallel or nearly parallel to the axes of the apertures and thus yielding correctly positioned counts in the gamma camera image. "Undesirable" events include scattered as well as unscattered photons that travel in a direction oblique to the axes of the apertures (**2**) and are thus eliminated by attenuation by one or more collimator septa; septal penetration (**3**), unscattered photons that travel in a direction oblique to the axes of the apertures yet pass through the septa and yield mispositioned counts; and scatter (**4**), photons that undergo Compton scattering within the patient and are either eliminated by energy discrimination or are not eliminated and yield mispositioned counts. (Adapted from Zanconico and Heller [3] with permission)

passing through each aperture over a large area of the crystal. Overall, therefore, gamma camera images are progressively poorer in quality for radionuclides emitting low-, medium-, and high-energy x and γ-rays. For each energy rating (and as indicated above for low-energy collimators), collimators may also be further rated as "general-purpose" (or "all-purpose"), "high-resolution," or "high-sensitivity." Compared to general-purpose collimators, high-resolution collimators have narrower apertures (and therefore lower sensitivity), and high-sensitivity collimators have wider apertures (and therefore coarser resolution). In instances in which a radionuclide emits multiple photons, it is the highest-energy photon that dictates the collimator to be used. For example, a medium-energy collimator must still be used to image gallium-67 (photon energies: 93, 185, and 300 keV), even if only the two lower-energy (*i.e.* the 93- and 185-keV) photons are used for imaging.

The FWHM spatial resolution, $FWHM_{system}$, of gamma cameras is determined by a combination of physical and instrumentation factors. Intrinsic resolution, $FWHM_{intrinsic}$, is the component of spatial resolution contributed by the crystal and associated electronics and is related to statistical fluctuations in pulse formation; typical values are on the order of 5 mm. These statistical fluctuations include variations in the production of light photons resulting from x-ray or γ-ray interactions in the crystal and in the number of electrons emitted by the photocathode and the series of dynodes in the PMTs. Collimator (or geometric) resolution, $FWHM_{collimator}$, represents the major contribution to system resolution and is determined by the collimator design. Collimator resolution is improved (*i.e.* lowered) by reducing the diameter of the collimator aperture, the source-to-collimator face distance, and the collimator thickness. System resolution is further degraded by the contributions of septal-penetration resolution ($FWHM_{penetration}$) and by scatter resolution ($FWHM_{scatter}$). The overall spatial resolution of a gamma camera system, $FWHM_{system}$, can be obtained by combining in quadrature the resolution of the respective components of the system [11

$$FWHM_{\text{system}} = \sqrt{FWHM\text{intrinsic}^2 + FWHM\text{collimator}^2 + FWHM\text{penetration}^2 + FWHM\text{scatter}^2} \quad (1)]:$$

SPECT Data Acquisition

Although there are many possible combinations of detector number, geometry, and motion that can acquire the necessary projection data, rotating gamma camera-based SPECT systems are by far the most common [12]. Nowadays, two-detector systems predominate clinically, and two- to four-detector systems preclinically. The basic SPECT imaging paradigm includes the acquisition of planar projection images from multiple angles around the subject, the correction of the acquired data for nonuniform scanner response and possibly other signal-degrading effects, and the mathematical reconstruction of thin (several millimeter-thick) transverse tissue-section images [12]. The raw data are acquired as a series of discrete planar images at multiple angles about the longitudinal axis of the patient (Fig. 3). The number of counts recorded in each projection image pixel represents the ray sum, or line integral, of the sampling line perpendicular to and extending from the detector through the subject. The following are typical SPECT acquisition parameters: 20–30 min for data acquisition, ~60 to ~120 projection images (corresponding to angular increment between successive projection images of 6 to 3°, respectively), and a 180 or 360° rotation for cardiac or non-cardiac studies, respectively. An angular increment in excess of 6° between successive projection images will result in prohibitive under-sampling artifacts in the reconstructed images. Because of the length of time required for a single SPECT study (20–30 min), dynamic SPECT and whole-body SPECT remain largely impractical. It should be emphasized that SPECT images can in principle be quantitative in absolute terms, with voxel values representing the local activity concentration [13–15]. However, in contrast to PET, this is often not the case in routine practice because of the confounding effects of scatter and attenuation. Accurate correction for these effects remains more challenging in SPECT than in PET [13, 14].

Although PET offers important advantages over SPECT (*i.e.* generally better spatial resolution, higher sensitivity, and more accurate activity quantitation), SPECT offers the capability of multi-radionuclide imaging. Because different SPECT radionuclides emit x-rays and γ-rays of different energies, multiple radionuclides—and therefore multiple radiopharmaceuticals—can be imaged simultaneously using distinct, radionuclide-specific photopeak energy windows. In contrast, all PET radionuclides emit positrons and, consequently, annihilation photons of the same energy, 511 keV. Therefore, PET radiotracers cannot be distinguished on the basis of energy discrimination, and multiple PET radiopharmaceuticals cannot be imaged simultaneously.

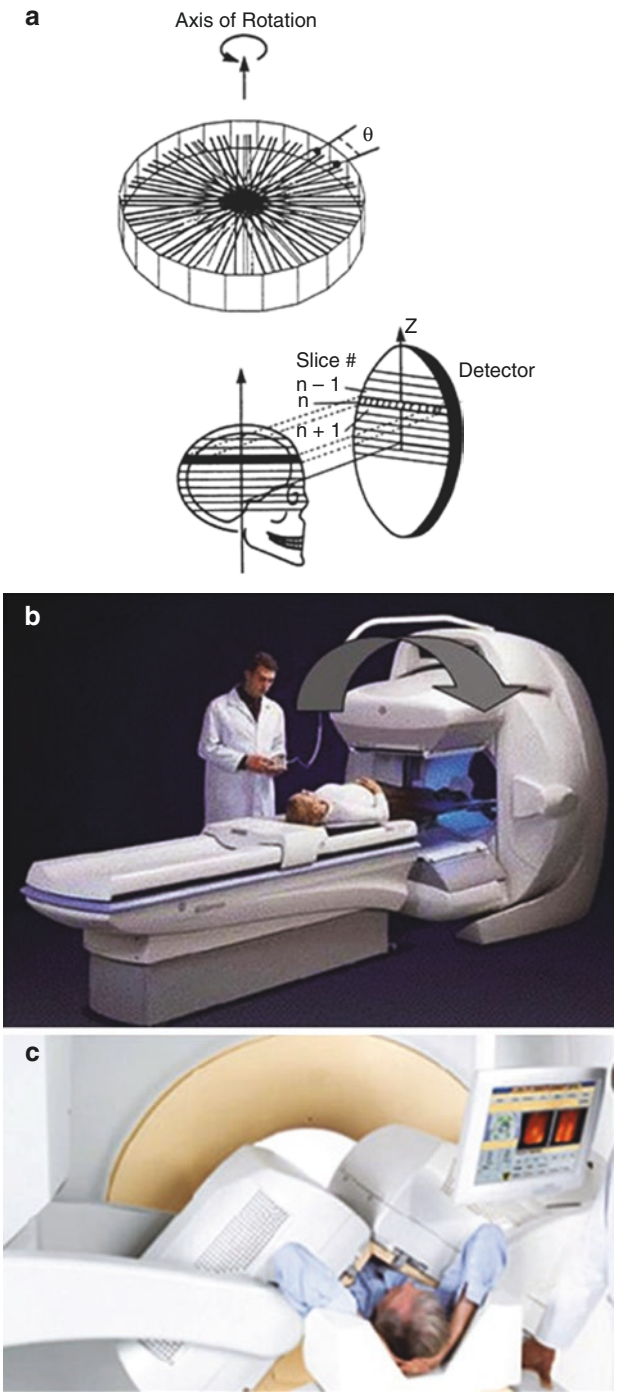

Fig. 3 (**a**) The basic data-acquisition paradigm in rotating gamma camera SPECT. Photographs of a dual-detector gamma camera, with (**b**) the two detectors in opposed positions, as routinely used for a 360° rotation and general (non-cardiac) SPECT, and (**c**) the two detectors perpendicular to each other, as routinely used for a 180° rotation and cardiac SPECT (with projection images acquired from approximately right anterior oblique to left posterior oblique). The advantage of such two-detector systems is that two projection images can be acquired simultaneously, and the acquisition time is therefore halved. (From Zanconico [12] with permission)

PET Scanners

PET is based on the coincidence detection (ACD) of the two colinear (very nearly 180° apart) 511- keV γ-rays resulting from the mutual annihilation of a positron and an electron (Fig. 4a) [2, 3, 7]. A typical PET scanner and the detector configurations used in modern scanners are shown in Fig. 4b. Each individual annihilation photon is referred to as a "single" event, and the total count rate of individual annihilation photons is called the "singles count rate." When both photons from an annihilation are detected simultaneously (in coincidence), this triggers the coincidence circuit, and a "true coincidence event" ("true") is generated. The various events associated with ACD of positron-emitting radionuclides—including trues, randoms, scatter, and spurious coincidences—are illustrated in Fig. 5 [7]. The singles count rate in PET is typically much higher than the trues count rate. The volume between the opposed coincidence detectors absorbing the two annihilation photons (the shaded area in Fig. 4a) is referred to as a "line of response (LOR)," even though it is actually a volume of response. In PET, LORs are defined electronically, and an important advantage of ACD is that absorptive collimation (as is used in gamma cameras) is not required. As a result, the sensitivity of PET is two to three orders of magnitude higher than that of gamma camera imaging. Modern PET scanners generally employ a series

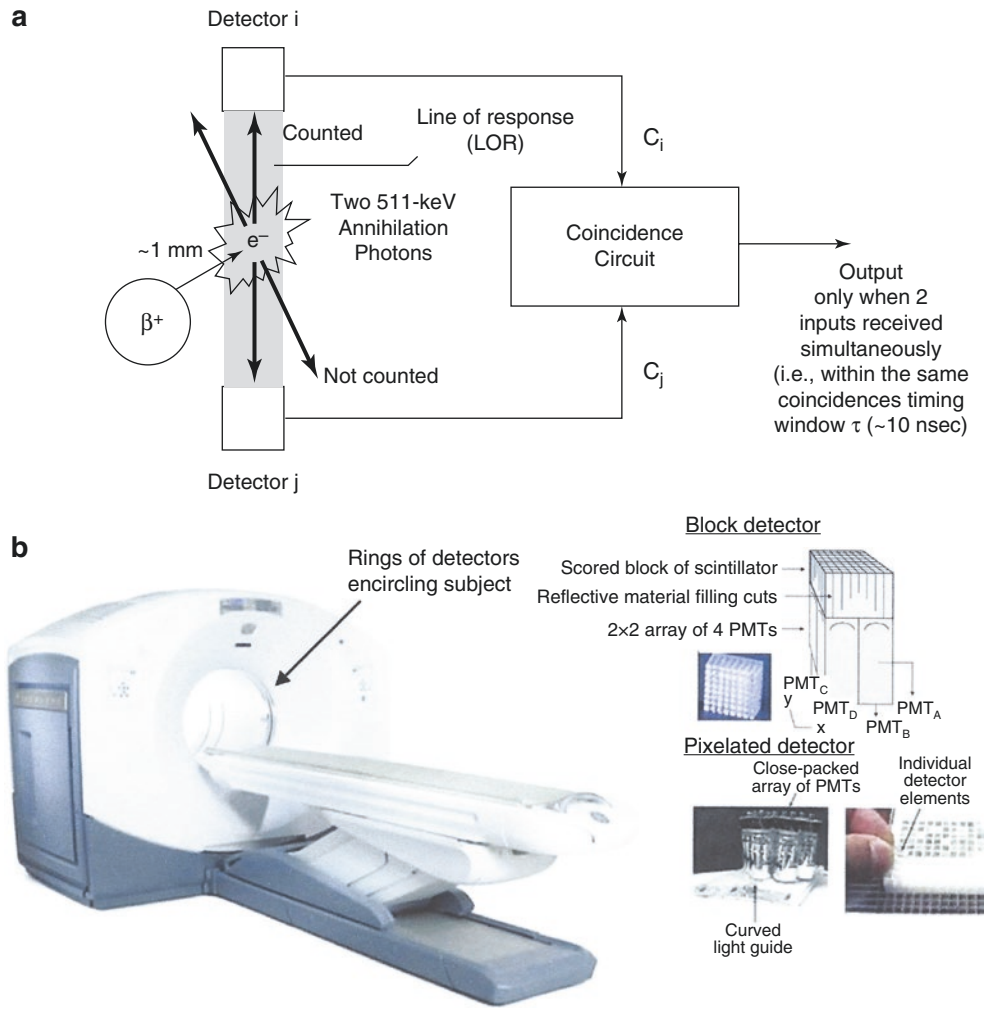

Fig. 4 (**a**) Annihilation coincidence detection (ACD) of the two opposed 511-keV γ-rays resulting from positron decay and positron-electron annihilation. Note that the true coincidence (or "trues") count rate is much less than the singles count rates, C_i and C_j. The short coincidence timing window, τ (<10 nsec), minimizes the number of random coincidence events (see Fig. 5). At the same time, however, most of the annihilation photons therefore do not produce coincidence events. (**b**) A photograph of a PET scanner (left panel). In the right panel are shown a block detector (top) and pixilated detectors (bottom) used in PET scanners. The block detector consists of a cubic piece of scintillator scored to variable depths into a two-dimensional array of detector elements, typically backed by a 2 × 2 array of PSPMTs. Pixilated detectors consist of individual scintillator detector elements backed by a continuous light guide and a close-packed array of PMTs. For both the block and pixilated detectors, the individual detector elements are typically ~2 × 2 mm in area. (Adapted from Zanzonico [7] with permission)

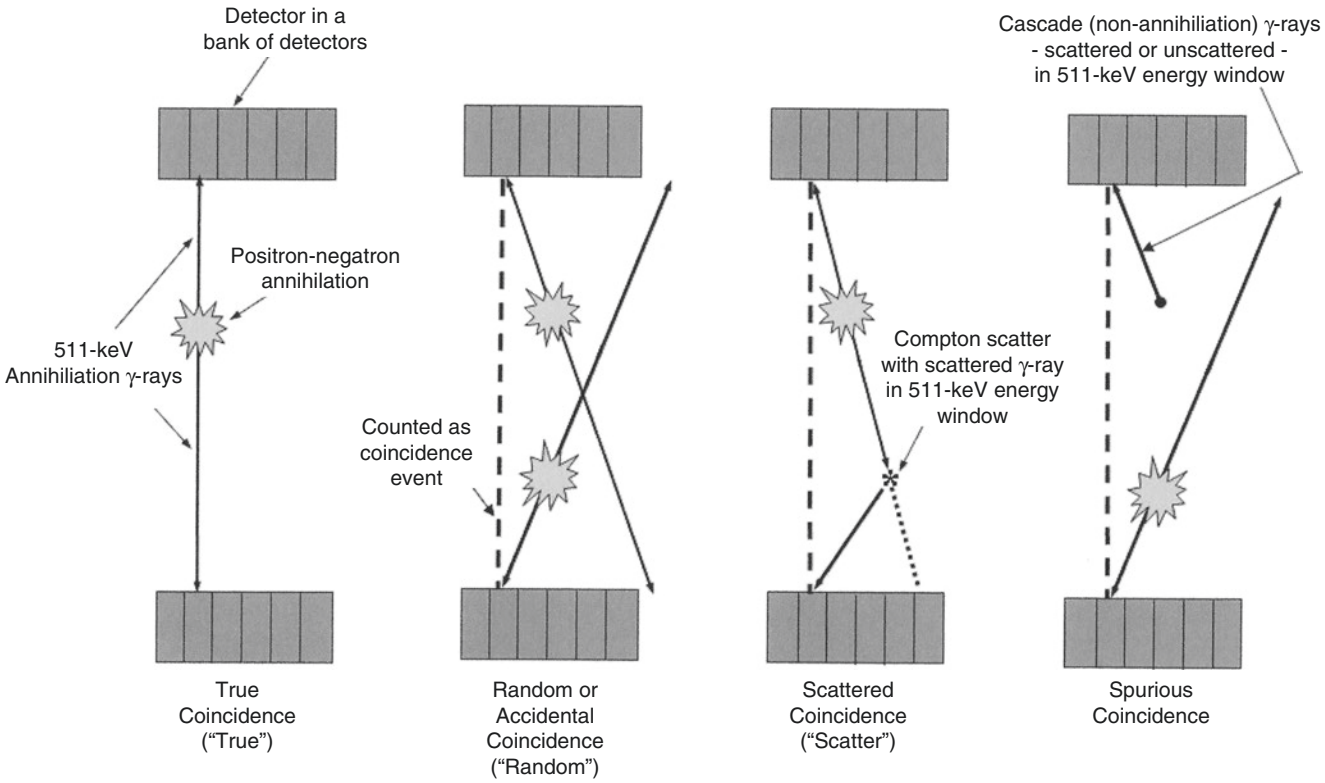

Fig. 5 The various events associated with the ACD of positron-emitting radionuclides, illustrated for two opposed banks of coincidence detectors and assuming only one opposed pair of detectors are in coincidence. A true coincidence ("true") is counted only when each of the two 511-keV annihilation γ-rays for a single positron-electron annihilation is not scattered and is detected within the timing window, τ, of the two coincidence detectors. A random or accidental coincidence ("random") is an inappropriately detected and positioned coincidence (the dashed line) that arises from two separate annihilations, with one γ-ray from each of the two annihilations detected within the timing window τ of the coincidence-detector pair. A scattered coincidence ("scatter") is a mispositioned coincidence (the dashed line) resulting from a single annihilation, with one of the γ-rays undergoing a small-angle Compton scatter but retaining sufficient energy to fall within the 511-keV energy window. A spurious coincidence is an inappropriately detected and positioned coincidence (the dashed line) that arises from an annihilation γ-ray and a cascade γ-ray that is scattered or unscattered but has sufficient energy to fall within the 511-keV energy window. Spurious coincidences occur only for radionuclides which emit both positrons and high-energy prompt cascade γ-rays, specifically γ-rays with energies (either scattered or unscattered) lying within the 511-keV energy window. (From Zanzonico [7] with permission)

of adjacent rings of discrete, small-area detectors (*i.e.* scored block detectors or pixilated detectors) encircling the subject and typically spanning a distance of 1525 cm in the patient's longitudinal direction (Fig. 4b).

PET ring scanners originally employed lead or tungsten walls, or septa, positioned between and extending radially inward from the detector blocks [7]. In this approach, known as two-dimensional (2D) PET, these inter-ring annular septa define plane-by-plane LORs and largely eliminate out-of-plane annihilation γ-rays. By eliminating most of the contribution from out-of-plane randoms and scatter, image quality is improved, especially for large-volume sources (*i.e.* as in whole-body PET). However, 2D PET eliminates most of the trues as well and thus reduces sensitivity. Removing the septa altogether and including coincidence events from all of the LORs among all the detectors significantly increase PET detector sensitivity. This is known as three-dimensional (3D) PET and is the prevailing design for state-of-the-art PET scanners [7, 16]. Sensitivity is increased up to approximately five-fold in 3D relative to 2D PET but with a considerable increase in the randoms and scatter count rates. Clinically, the scatter-to-true count rate ratios range from 0.2 (2D) to 0.5 (3D) in the brain and from 0.4 (2D) to 2 (3D) in the whole body [17].

Increasingly important, time-of-flight (TOF) PET scanners utilize the measured difference between the detection times of the two annihilation photons arising from the decay of a positron. This allows for at least the approximate spatial localization (12–18 cm) of the annihilation event along the LOR with current values, 400–600 psec, of coincidence time resolution [18, 19]. This does not improve the spatial resolution of state-of-the-art PET scanners (~5 mm = 0.5 cm) but reduces the random coincidence rate and improves the signal-to-noise ratio (SNR), especially for large subjects [20]. This is important, as conventional

(*i.e.* non-TOF) PET image quality is degraded with increasing patient size due to more pronounced attenuation, more scatter, and fewer trues.

As with gamma cameras, the overall spatial resolution of PET scanners results from a combination of physical and instrumentation factors. There are several important limitations imposed on resolution by the basic physics of positron-electron annihilation. First, for a given radionuclide, positrons are emitted over a spectrum of initial kinetic energies ranging from 0 to a characteristic maximum, or end-point, energy, E_{max}. The associated average positron energy, $\bar{E}$, is approximately one-third of its end-point energy, $\bar{E} \approx \frac{1}{3} E_{max}$. As a result, positrons will travel a finite distance from the decaying nucleus, ranging from 0 to a maximum called the extrapolated range, R_e, which corresponds to the highest-energy positrons [21]. For the positron-emitting nuclides used to date in PET, the maximum energies (E_{max}) vary from 0.58 to 3.7 mega-electron volts (MeV), and the extrapolated ranges (R_e) vary from 2 to 20 mm. Although the finite positron range acts to blur PET images (*i.e.* degrade spatial resolution), the range-related blurring, $FWHM_{range}$, is mitigated by the spectral distribution of positron energies for a given radionuclide as well as the characteristically tortuous path positrons travel [21, 22]. The positron range degrades spatial resolution by only ~0.1 mm for ^{18}F (E_{max} = 0.640 MeV) and ~0.5 mm for ^{15}O (E_{max} = 1.72 MeV) [21]; these values are actually much shorter than the respective extrapolated positron ranges.

The second physics-related limitation on PET performance is the non-colinearity of the two annihilation photons. Because a positron may have some small residual (non-zero) momentum and kinetic energy at the end of its range, the two annihilation photons are not always emitted exactly back-to-back (*i.e.* 180° apart) but rather deviate from colinearity by an average of 0.25° [23]. The non-colinearity-related blurring, $FWHM_{180°}$, varies from ~2 mm for an 90-cm diameter whole-body PET to ~0.7 mm for a 30-cm diameter brain PET to ~0.3 mm for a 12-cm diameter small-animal PET [17].

Two additional instrumentation-related determinants of overall spatial resolution are the intrinsic detector resolution and the depth-of-interaction effect. For discrete detector elements, the intrinsic resolution, $FWHM_{intrinsic}$, is determined by the detector element width (d), increasing from $\frac{d}{2}$ midway between the opposed coincidence detectors to d at the face of either detector [17].

For PET systems employing rings of discrete, small-area detectors, the thickness of the detector elements (2–3 cm) results in a degradation of spatial resolution termed the depth-of-interaction (DOI), or parallax, effect [17]. In whole-body PET scanners—with a typical detector thickness of 2–3 cm, detector width of ~4 mm, and detector ring diameter of ~80 cm—the DOI effect degrades spatial resolution by up to 50% at 10 cm from the center of the detector ring. Because the DOI effect decreases as the detector ring diameter increases, clinical PET systems have detector rings substantially larger in diameter than that needed to accommodate patients. A variety of approaches have been developed to correct for the DOI effect in small-diameter, preclinical PET scanners, where the DOI effect is more pronounced [17, 24, 25].

In a manner analogous to Eq. (1), the spatial resolution at the center of the field of view (where the DOI effect is negligible) of a PET system, $FWHM_{system}$, can be obtained by combining in quadrature the resolution of the respective components of the system:

$$FWHM_{system} = \sqrt{FWHM\text{intrinsic}^2 + FWHM\text{range}^2 + FWHM180^{\circ 2}} \quad (2)$$

Data Processing and Image Reconstruction in SPECT and PET

Data "Corrections"

Even optimally performing SPECT or PET scanners exhibit some nonuniformity of response [7, 10, 12]. This nonuniformity is measured by irradiating the imaging detectors with a uniform photon flux. The measured nonuniformity is then used to generate a correction; this is a routine component of the quality assurance program for SPECT and PET scanners.

A second correction is related to the fact that radiation detectors necessarily have a finite "dead time" and associated count losses [17]. The dead time, typically of the order of 1–10 μsec, is the interval of time required for a counting system to record an event during which additional events cannot be recorded. As a result, the measured count rate is systematically lower than the actual count rate. However, such count losses are significant only at "high" count rates (*i.e.* greater than ~100,000 counts per second (cps) per detector, which is of the order of the inverse of the dead time in seconds, for modern detectors). Dead-time count losses are generally minimal with the activities administered for diagnostic imaging with gamma cameras and SPECT systems. For PET systems, however, a real-time correction for dead time count losses is routinely applied to the measured count rates, most commonly by scaling up the measured count rate based on an empirically derived mathematical relationship between measured and true count rates. As noted, count rates encountered in PET are much higher than in SPECT—in part because of the use of electronic rather than absorptive collimation—and therefore accurate dead time correction is more critical in PET.

In rotating gamma camera SPECT, if the mechanical and electronic centers of rotation (CORs) are aligned, the pixel location of the projection of the COR onto the projection image matrix will be the same for all projection images, and for all such images, the counts in each pixel will then be projected across the appropriate row of pixels in the tomographic image matrix [10, 26, 27]. If, however, the mechanical and electronic CORs are not aligned, the pixel location of the COR will vary among the projection images, and the counts in each projection image pixel will be projected across different locations in the tomographic image matrix, resulting in blurred reconstructed images. In today's SPECT systems, the misalignment of CORs may be easily measured, and corrections can be easily created and applied. In contrast, PET scanners typically utilize fixed rings of detectors and thus do not suffer from COR misalignment.

In PET, randoms (accidental coincidences) increase the detected coincidence count rate by introducing mispositioned events and thus reduce image contrast and distort the relationship between image intensity and activity concentration [7]. Several reliable methods are available for randoms correction and are routinely applied on clinical as well as preclinical PET scanners.

Scatter results in generally diffuse background counts in reconstructed images, reducing contrast and distorting the relationship between image intensity and activity concentration [13, 28, 29]. In the case of PET, scatter counts as a portion of the total detected events are far more abundant in 3D than in 2D PET—especially for body imaging of larger (*i.e.* adult) patients—and its correction is more challenging in 3D than in 2D PET. Nonetheless, robust scatter corrections have been developed and implemented on current 3D PET scanners [28, 29]. Although not used as routinely as in PET, scatter corrections have been implemented in SPECT as well [30].

The correction for the attenuation of the γ-rays as they pass through tissue is generally the largest correction in SPECT and PET. The correction factors can range from ~2 for a ^{99m}Tc SPECT scan of the brain (roughly equivalent to a to 10-cm diameter water-equivalent cylinder) to ~15 for a PET scan of the abdomen (equivalent to a 30-cm diameter water-equivalent cylinder). The magnitude of the correction depends on the energy of the γ-rays (variable for SPECT studies and 511 keV for PET studies), the thickness of tissue(s) that the γ-rays must traverse before exiting the patient, and the attenuation characteristics of the tissue(s). One of the attractive features of PET is the relative ease of applying accurate and precise corrections for attenuation based on the fact that attenuation depends only on the *total* thickness of the attenuation medium (at least for a uniformly attenuating medium). Like scatter corrections, attenuation corrections in SPECT are not yet as well developed or as reliable as those in PET, because, for single photons, the attenuation correction factors depend on the depth of the source as well as the thickness of the attenuation medium. With the introduction and widespread availability of hybrid (*i.e.* PET-CT and SPECT-CT) devices, attenuation corrections are now routinely derived by CT imaging.

Image Reconstruction

In SPECT and PET, the raw data are essentially the same (though acquired with very different detector geometries): one-dimensional projections (sets of parallel line integrals or ray sums) of the radiations emitted from the patient. In order to convert these data into a usable form, they must be mathematically transformed and reconstructed into a set of transverse images. These may then be reformatted into coronal, sagittal, and even oblique images. (Raw PET data must undergo several reformatting steps in order to create the one-dimensional projection data for image reconstruction.)

Historically, one of the most widely used algorithms for the reconstruction of tomographic images was filtered back projection (FBP). The basic procedure is as follows. Each projection is Fourier transformed into spatial-frequency space. The projection is mathematically filtered to amplify certain spatial frequencies and to dampen or eliminate other spatial frequencies. The filtered projection is inverse Fourier transformed from frequency back to real space. The filtered projection data in real space are then uniformly distributed (or back-projected) over the reconstructed image matrix. To eliminate spatial frequencies beyond the maximum frequency imageable by the scanner (*i.e.* the Nyquist frequency, ν_N) and thereby eliminate certain artifacts as well as excessive statistical uncertainty (noise or mottle), filters (known as Hanning, Butterworth, *etc.*) with cut-off frequencies, ν_c, set equal to ν_N or some fraction thereof, are used. Although the resulting reconstructed images have somewhat degraded spatial resolution, they are far less "noisy" (mottled). The filter and the value of the cut-off frequency may be selected by the user. Care should be exercised in doing so, however, as these parameters affect the appearance and quantitative accuracy of the reconstructed images. Scanner manufacturers generally provide recommended values for the filters and filter parameters for different types of studies; in SPECT, for example, the recommended filter and cut-off frequency will depend on the radionuclide and the region of the body imaged.

In contrast to so-called analytic reconstruction methods such as FBP, iterative algorithms attempt to progressively refine estimates of the activity distribution (rather than directly calculate the distribution) by maximizing or minimizing some "target function." The solution is said to "converge" when the difference of the target function between successive estimates (iterations) of the activity distribution is less than some pre-specified value. Importantly, iterative

reconstruction algorithms allow for the incorporation of realistic modeling of the data-acquisition process (including effects of attenuation and of scatter), the modeling of statistical noise, and the inclusion of pertinent a priori information (*e.g.* only non-negative count values). Widely used iterative reconstruction algorithms include the maximum-likelihood expectation maximization (MLEM) and the ordered-subset expectation maximization (OSEM) algorithms. The OSEM algorithm, which is actually a modified version of the MLEM algorithm, converges more rapidly than MLEM and is now the most widely used iterative reconstruction method in PET as well as SPECT.

Once the PET emission data have been corrected for dead time, randoms, system response (by normalization), scatter, and attenuation, the count rate per voxel in the reconstructed tomographic images is proportional to the local activity concentration and is finally converted to activity concentration using a measured system calibration factor, $(MBq/cm^3)/(cps/voxel)$ [7]. As noted, SPECT images can be made quantitative in an analogous manner. In practice, however, the pertinent corrections (especially scatter and attenuation corrections) are currently not as reliable or routine in SPECT as in PET. A more clinically relevant expression of local activity concentration is in terms of the decay-corrected fraction or percent of the administered activity per cubic centimeter or, more commonly, in terms of the standard uptake value (SUV):

$$\mathrm{SUV} = \frac{\text{MBq / gm of tissue}}{\text{MBq injected / gm body mass}} \qquad (3)$$

Multimodality (*i.e.* Hybrid) Systems

Historically, and somewhat arbitrarily, imaging modalities have often been divided into two general categories, structural (or anatomical) and functional (or physiological). Anatomical modalities (*i.e.* depicting primarily morphology) include computed tomography (CT), magnetic resonance imaging (MRI), and ultrasound (US). Functional modalities (*i.e.* depicting primarily information related to underlying physiology and biochemistry) include PET and SPECT. Since information derived from multiple modalities is often complementary (*e.g.* localizing the site of an apparently abnormal metabolic process to a pathologic structure such as a tumor), the integration of this information can be helpful and, at times, even critical. In addition to the anatomic localization of "signal" foci, image registration and fusion provide intra- as well as inter-modality corroboration of diverse images and more accurate and reliable diagnostic and treatment-monitoring information. The problem, however, is that differences in image size and dynamic range, voxel dimensions, image orientation, subject position and posture, and information quality and quantity make it difficult to unambiguously co-locate areas of interest in multiple image sets. The objective of image registration and fusion, therefore, is (a) to appropriately modify the format, size, position, and even shape of one or both image sets to provide a point-to-point correspondence between image sets and (b) to provide a practical integrated display of the images thus aligned. This process entails spatial registration of the respective images in a common coordinate system [31]. In multimodality, or hybrid, devices, images are acquired on a single device and transparently registered and fused with the manufacturer's integrated software. These combine high-performance state-of-the-art PET and CT scanners and, more recently, SPECT and CT scanners in a single device [32–35] and provide near-perfect registration of images of *in vivo* function (PET or SPECT) and anatomy (CT). PET-CT scanners have already had a major impact on clinical practice, particularly in oncology, to the point that no "PET-only" systems are currently being marketed. The PET or SPECT and CT gantries in such devices are actually separate; the respective fields of view are separated by a distance of the order of 1 m, and the PET or SPECT and CT scans are performed sequentially. With the incorporation of 16- to 256-slice spiral CT scanners, applications in cardiology as well as oncology are growing rapidly.

The recent introduction of PET-MRI [36–39] multimodality devices will no doubt lead to new and important applications of nuclear imaging [40], as PET and MRI studies (including dynamic studies) can be performed simultaneously. This is in contrast to PET-CT, in which, as noted, there are temporal and spatial offsets between the PET and CT studies.

Radiopharmaceuticals

Over the years, a large number and variety of radiopharmaceuticals for SPECT and PET have been developed. Molecularly targeted radiotracers continue to be developed for increasingly sensitive and specific detection, staging, and monitoring of disease as well as the characterization of *in situ* biology. Although an in-depth discussion of radiochemistry and radiopharmacology is beyond the scope of this chapter, important considerations in the development of radiotracers are discussed briefly below.

Implicit in the suitability of a radionuclide for *in vivo* imaging is that it emits in sufficient abundance radiations penetrating enough to escape from the body and interact with external detectors. These emissions include γ-rays and characteristic x-rays ("single photons") used for SPECT and planar gamma camera imaging or the 511-keV annihilation γ-rays associated with positron (β^+) decay and used for PET. In addition, radionuclides for imaging ideally should emit few or no non-penetrating radiations, that is, particulate

radiations such as β-particles and electrons (excluding, of course, the positrons necessary for signal generation in PET). Such particulate radiations typically have ranges in tissue of the order of 1 mm or less and thus cannot escape from the body and be detected externally. As such, these radiations contribute to the radiation dose to tissues and organs without providing any imageable signal.[3] Further, an imaging radionuclide ideally should have a physical half-life comparable to the time required for the administered radiotracer to localize in the tissue of interest. This will provide sufficient time for it to localize in that tissue while still retaining a near-maximal imaging signal once it localizes, followed by the elimination of the radioactivity via a combination of physical decay and biological clearance. The radiation doses to patients and individuals around them and the potential problem of radioactive contamination are thereby minimized.

For planar imaging and SPECT, the ideal radionuclide emits x-rays and γ-rays with energies of 100 to 200 keV in an abundance of 100% (*i.e.* 1 x-ray or γ-ray emitted per decay) while also emitting minimal particulate radiations and higher-energy x-rays and γ-rays. With a mean free path in soft tissue of the order of 10 cm and in NaI(Tl) of less than 0.5 cm, 100- to 200-keV photons provide adequate penetrability through tissue yet are low enough in energy to be efficiently collimated and stopped in the relatively thin scintillation detectors used in gamma cameras, yielding optimum-quality images with reasonably low radiation doses to the patient. The absence of higher-energy x-rays and γ-rays (*i.e.* with energies in excess of several 100 keV) is important because such radiations cannot be efficiently collimated and detected. Yet they may undergo scatter in the patient and/or detector hardware and contribute, even with energy discrimination, mispositioned and otherwise spurious counts to the image. Based on these criteria, ^{99m}Tc is a near-ideal radionuclide for gamma camera imaging, emitting only a 140-keV γ-ray and few particulate radiations. Iodine-131 (^{131}I), on the other hand, emits a relatively high-energy, difficult-to-collimate 364-keV γ-ray as well as abundant β-particles.

For PET, a radionuclide emitting low-energy, short-range positrons with a 100% abundance (*i.e.* a 100% positron branching ratio) and no high-energy prompt γ-rays is ideal; fluorine-18, for example, is such a radionuclide. The positron range places a lower limit on spatial resolution (as discussed above), so the lower the energy and the shorter the range of the positron, the better the spatial resolution that is ultimately achievable. Some positron-emitting radionuclides also emit significant numbers of high-energy prompt γ-rays, and such γ-rays may be in cascade with each other or with the positron. These can result in spurious events that are spatially uncorrelated but are nonetheless counted as true events [41, 42]. Although such coincidences degrade overall quality and quantitative accuracy to some extent, radionuclides such as copper-62 (^{62}Cu), gallium-66 (^{66}Ga), gallium-68 (^{68}Ga), bromine-75 (^{75}Br), rubidium-82 (^{82}Rb), yttrium-86 (^{86}Y), zirconium-89 (^{89}Zr), and iodine-124 (^{124}I) have all been used effectively in PET [41, 42].

SPECT radiotracers are generally labeled with radiometals (*e.g.* ^{99m}Tc or ^{111}In) or radioiodines (*i.e.* ^{123}I or ^{131}I). PET radiotracers may utilize radionuclides of the "physiologic elements," carbon-11 (^{11}C), nitrogen-13 (^{13}N), or oxygen-15 (^{15}O), as well as fluorine-18 (^{18}F). However, the half-lives of ^{11}C, ^{13}N, and ^{15}O are generally too short for routine clinical use without an on-site cyclotron for their production. Instead, therefore, ^{18}F ($t_{1/2}$ ~ 110 min) is often covalently incorporated into organic compounds with minimal perturbation of their structure and biologic behavior. Gallium-68 (^{68}Ga) ($t_{1/2}$ ~ 68 min) is even shorter-lived but is produced from generator in which the parent radionuclide is long-lived germanium-68 (^{68}Ge) ($t_{1/2}$ ~ 270 days). ^{68}Ga is being used increasingly as a radiolabel for a variety of PET tracers without the need for an on-site cyclotron. A notable feature of PET is the number and variety of biologically important molecules that have been developed as radiotracers. For example, ^{18}F-fluoro-2-deoxyglucose (FDG), by far the most widely used PET radiotracer, has dramatically impacted patient management in oncology. It is a metabolically trapped structural analog of glucose whose uptake is related to the levels of expression of glucose transporters and of glucose metabolism (*i.e.* glycolysis).

An important property of a radiotracer—in addition to high specificity and avidity for its molecular target, of course—is its pharmacokinetics. Radiotracers should clear rapidly from the circulation and off-target tissues in order to reduce background activity and thereby enhance the target tissue-to-background concentration ratio. In this regard, small-molecule radiotracers are generally preferred because of their rapid renal clearance and elimination. On the other hand, excessively rapid clearance is undesirable: if the radiotracer is not "available" for target-tissue uptake for a sufficient length of time, its uptake in the targeted tissue may be suboptimal, and the targeted tissue may therefore be difficult or impossible to image. As discussed above, the physical half-life of the radiolabel should be comparable to that of the radiotracer's uptake half-time in the targeted tissue (assuming, for the sake of simplicity, that the clearance and the uptake kinetics follow mono-exponential models). High molecular-weight radiotracers are cleared slowly from the circulation and also localize slowly in the targeted tissue; half-times in the blood of radiolabeled antibodies are typically of the order of several days, for example. Such tracers often exhibit pronounced non-specific off-target localization in tissues of the reticuloendothelial system (RES)

[3]High-energy (> ~1-MeV) beta particles (such as those emitted by the pure beta-particle emitter yttium-90, for example) produce a small but imageable amount of *bremsstrahlung* ["brake radiation") x-rays] as they slow down in tissue. *Bremsstrahlung* imaging is not widely used, however, and produces poor quality images.

(*i.e.* liver, spleen, and bone marrow) because the "leaky" sinusoidal vasculature in such tissues facilitates their egress from the circulation into the RES. Overall, therefore, target-to-background ratios of antibodies may be suboptimal, with notably high radiation doses to the RES (including the radiosensitive hematopoietic marrow); the latter consideration is particularly important for radioimmunotherapy.

Nanoparticles are emerging as promising targeted carriers not only of drugs but also of radionuclides for imaging and, potentially, therapy based on the following advantageous properties: multivalency, multimodality signaling, and high-capacity therapeutic or imaging payloads. The surface of nanoparticles may be functionalized with multiple copies of the targeting moiety (such as a receptor-binding ligand or an antibody or antibody fragment), effectively yielding a multivalent platform with higher-affinity targeting than a monovalent agent. An additional advantage of nanoparticles is that they are amenable to multimodality imaging, for example, by incorporating radionuclides for nuclear imaging *and* fluorescent dyes for optical imaging. Such a construct could be used in a surgical or endoscopic setting, where the nuclear signal can be used for pre-surgical localization of disease and/or sentinel lymph nodes, and the optical signal for intraoperative delineation of tumor margins and thus evaluation of the completeness of tumor resection [43]. Another attractive feature of nanoparticles is that the amount of payload delivered to the targeted tissue, whether drugs or radionuclides for imaging or therapy, may be maximized by incorporating multiple copies of the payload into each particle. Small and even relatively large molecules are generally limited in this respect in that attachment of multiple copies of the payload (*i.e.* the number of molecules per particle) may alter their molecular structure to the point that their target binding and other biological properties are adversely affected or even eliminated.

Despite the unique potential advantages of nanoparticles as therapeutic or diagnostic platforms, they must be cleared from the body in a reasonably short time frame both to minimize non-specific background signal and to avoid long-term organ (*e.g.* liver) retention and toxicity. Given the generally large size and reactive surface topography, the development of rapidly clearing nanoparticles is challenging. Nonetheless, surface-functionalized nanoparticles with hydrodynamic radii of no greater than 6 nm have been shown to exhibit rapid renal clearance as well as reasonable uptake in targeted tumors in experimental animals [44, 45].

The Bottom Line

- The clinical application of radiopharmaceuticals, particularly in PET, has grown dramatically over the last several decades, with the annual number of nuclear medicine procedures increasing three-fold (from 7 million to 20 million) between 1985 and 2005 [46].
- Nuclear imaging offers a number of important advantages in the context of clinical practice as well as clinical and preclinical research, including the possibility of imaging molecular targets and/or physiological processes without perturbing them, the ability to quantify images, and the wide range of targeted radiopharmaceuticals.
- However, nuclear imaging is not without its drawbacks, including relatively coarse spatial resolution, the exposure of patients to radioactivity and therefore radiation, and the limited anatomic data provided by the scans. With regard to this last point, however, the increasingly widespread availability of multimodality devices (*i.e.* PET-CT, SPECT-CT, and, most recently, PET-MRI) is largely overcoming this limitation.
- In planar, or two-dimensional, nuclear imaging, radiations emanating from activity at all depths of the subject are projected onto an imaging detector. In contrast, tomographic imaging is predicated on the acquisition of images from multiple angles around a patient, the correction of the data for non-uniform response of the imaging system and other signal-degrading factors, and the mathematical reconstruction of transverse tissue-section images.
- Radiation detectors are generally characterized as either scintillation or ionization detectors. In scintillation detectors, visible light is produced as radiation excites atoms of a crystal, and this light is converted to an electronic signal and amplified by a photomultiplier tube and its associated high voltage. In ionization detectors, free electrons produced when radiation ionizes a stopping material are collected to produce a small electronic signal. For nuclear imaging, which is generally "count-limited," scintillation detectors are preferred because of their high sensitivity.
- Although there are many possible combinations of detector number, geometry, and motion, rotating gamma camera-based SPECT systems are by far the most common. The basic SPECT imaging paradigm includes the acquisition of planar projection images from multiple angles around the subject, the correction of the acquired data for non-uniform scanner response and possibly other signal-degrading effects, and the mathematical reconstruction of thin transverse tissue-section images.
- PET is based on the annihilation coincidence detection of the two colinear 511-keV γ-rays resulting from the mutual annihilation of a positron and an electron. When both photons from an annihilation are detected simultaneously, this triggers the coincidence circuit, and a "true coincidence event" is generated.
- Once the PET emission data have been corrected, the count rate per voxel in the reconstructed tomographic images is proportional to the local activity concentration and is finally converted to activity concentration using a

measured system calibration factor, (MBq/cm^3)/(cps/voxel). A more clinically relevant expression of local activity concentration is the standard uptake value (SUV).

- In SPECT and PET, the raw data are essentially the same: one-dimensional projections of the radiations emitted from the patient. In order to convert these data into a usable form, they must be mathematically transformed and reconstructed into a set of transverse images. These may then be reformatted into coronal, sagittal, and even oblique images.
- Although PET offers important advantages over SPECT (*i.e.* generally better spatial resolution, higher sensitivity, and more accurate activity quantitation), SPECT offers the capability of multi-radionuclide imaging.
- Although the spatial resolution of SPECT and PET is excellent by historical standards for these modalities, it remains relatively coarse compared to CT and MRI (~1 mm or better). The distinctive and important advantages of nuclear imaging will nonetheless ensure that SPECT and PET (particularly in combination with CT or MRI) will remain invaluable molecular imaging modalities in clinical practice and in clinical and preclinical research.

References

1. Mankoff DA. A definition of molecular imaging. J Nucl Med. 2007; 48:18N, 21N.
2. Zanzonico P. Principles of nuclear medicine imaging. Planar, SPECT, PET, multi-modality, and autoradiography systems. Radiat Res. 2012;177(4):349–64.
3. Zanzonico P, Heller S. Physics, instrumentation, and radiation protection. In: Biersack HJ, Freeman LM, editors. Clinical nuclear medicine. Berlin/ Heidelberg: Springer-Verlag; 2007. p. 1–33.
4. Mettler FA Jr, Huda W, Yoshizumi TT, Mahesh M. Effective doses in radiology and diagnostic nuclear medicine: a catalog. Radiology. 2008;248(1):254–63.
5. Otte N. The silicon photomultiplier – a new device for high energy physics, astroparticle physics, industrial and medical applications (0018). SNIC Symposium, 2006, April 3–6. Palo Alto: Stanford University; 2006. www.slac.stanford.edu/econf/C0604032/papers/0018.pdf Accessed 24 May 2018.
6. Humm JL, Rosenfeld A, Del Guerra A. From PET detectors to PET scanners. Eur J Nucl Med Mol Imaging. 2003;30(11):1574–97.
7. Zanzonico P. Positron emission tomography: a review of basic principles, scanner design and performance, and current systems. Semin Nucl Med. 2004;34(2):87–111.
8. Zanzonico P, Heller S. The intraoperative gamma probe: basic principles and choices available. Semin Nucl Med. 2000;30(1):33–48.
9. Heller S, Zanzonico P. Nuclear probes and intraoperative gamma cameras. Semin Nucl Med. 2011;41(3):166–81.
10. Zanzonico P. Routine quality control of clinical nuclear medicine instrumentation: a brief review. J Nucl Med. 2008;49(7):1114–31.
11. Saha GS. Physics and radiobiology of nuclear medicine. New York: Springer-Verlag; 1993. p. 107–23.
12. Zanzonico PB. Technical requirements for SPECT: equipment and quality control. In: Kramer EL, Sanger JJ, editors. Clinical applications in SPECT. New York: Raven Press; 1995. p. 7–41.
13. Frey EC, Humm JL, Ljungberg M. Accuracy and precision of radioactivity quantification in nuclear medicine images. Semin Nucl Med. 2012;42(3):208–18.
14. Tsui BM, Zhao X, Frey EC, McCartney WH. Quantitative single-photon emission computed tomography: basics and clinical considerations. Semin Nucl Med. 1994;24(1):38–65.
15. Dewaraja YK, Frey EC, Sgouros G, Brill AB, Roberson P, Zanzonico PB, Ljungberg M. MIRD pamphlet no. 23: quantitative SPECT for patient-specific 3-dimensional dosimetry in internal radionuclide therapy. J Nucl Med. 2012;53(8):1310–25.
16. Townsend DW, Bendriem B. Introduction to 3D PET. In: Bendriem B, Townsend DW, editors. The theory and practice of 3D PET, B. Dordrecht: Kluwer Academic Publishers; 1998. p. 1–10.
17. Cherry SR, Sorenson JA, Phelps ME. Physics in nuclear medicine. 3rd ed. Philadelphia: Saunders; 2003.
18. Lewellen TK. Time-of-flight PET. Semin Nucl Med. 1998;28(3):268–75.
19. Moses W. Recent advances and future advances in time-of-flight pet. Nucl Instrum Methods Phys Res A. 2007;580(2):919–24.
20. Karp JS, Surti S, Daube-Witherspoon ME, Muehllehner G. Benefit of time-of-flight in PET: experimental and clinical results. J Nucl Med. 2008;49(3):462–70.
21. Levin CS, Hoffman EJ. Calculation of positron range and its effect on the fundamental limit of positron emission tomography system spatial resolution. Phys Med Biol. 1999;44(3):781–99.
22. Derenzo SE. Mathematical removal of positron range blurring in high-resolution tomography. IEEE Trans Nucl Sci. 1986;33(1):565–9.
23. Berko S, Hereford FL. Experimental studies of positron interactions in solids and liquids. Rev Mod Phys. 1956;28(3):299–307.
24. Yang Y, Wu Y, Qi J, St James S, Du H, Dokhale PA, et al. A prototype PET scanner with DOI-encoding detectors. J Nucl Med. 2008;49(7):1132–40.
25. Mosset JB, Devroede O, Krieguer M, Rey M, Vieira JM Jung JH, et al. Development of an optimised LSO/LuYAP phoswich detector head for the ClearPET camera. IEEE Nucl Sci Sym Conf Rec. 2004:2439–2443.
26. Greer K, Jaszczak RJ, Harris C, Coleman RE. Quality control in SPECT. J Nucl Med Technol. 1985;13(2):76–85.
27. Harkness BA, Rogers WL, Clinthorne NH, Keyes JW Jr. SPECT: Quality control procedures and artifact identification. J Nucl Med Technol. 1983;11(2):55–60.
28. Meikle SR, Badawi RD. Quantitative techniques PET. In: Bailey DL, Townsend DW, Valk PE, Maisey MN, editors. Positron emission tomography: basic sciences. London: Springer-Verlag; 2005. p. 93–126.
29. Bailey DL. Quantitative procedures in 3D PET. In: Bendriem B, Townsend DW, editors. The theory and practice of 3D PET, B. Dordrecht: Kluwer Academic Publishers; 1998. p. 55–109.
30. Ogawa K, Harata Y, Ichihara T, Kubo A, Hashimoto S. A practical method for position-dependent Compton-scatter correction in single photon-emission CT. IEEE Trans Med Imaging. 1991;10(3):408–2.
31. Zanzonico PB, Nehmeh SA. Introduction to clinical and laboratory (small-animal) image registration and fusion. Conf Proc IEEE Eng Med Biol Soc. 2006;1:1580–3.
32. Beyer T, Townsend DW, Blodgett TM. Dual-modality PET/CT tomography for clinical oncology. Q J Nucl Med. 2002;46(1):24–34.
33. Israel O, Goldsmith SJ, editors. Hybrid SPECT/CT: imaging in clinical practice. Boca Raton: CRC Press/Taylor & Francis; 2006.
34. Townsend DW, Beyer T. A combined PET/CT scanner: the path to true image fusion. Br J Radiol. 2002;75 Spec No:S24–30.
35. Townsend DW, Beyer T, Blodgett TM. PET/CT scanners: a hardware approach to image fusion. Semin Nucl Med. 2003;33(3):193–204.
36. Judenhofer MS, Wehrl HF, Newport DF, Catana C, Siegel SB, Becker M, et al. Simultaneous PET-MRI: a new approach for functional and morphological imaging. Nat Med. 2008;14(4):459–65.

37. Pichler BJ, Judenhofer MS, Wehrl HF. PET/MRI hybrid imaging: devices and initial results. Eur Radiol. 2008;18(6):1077–86.
38. Pichler BJ, Kolb A, Nägele T, Schlemmer HP. PET/MRI: paving the way for the next generation of clinical multimodality imaging applications. J Nucl Med. 2010;51(3):333–6.
39. Pichler BJ, Wehrl HF, Kolb A, Judenhofer MS. Positron emission tomography/magnetic resonance imaging: the next generation of multimodality imaging? Semin Nucl Med. 2008;38(3):199–208.
40. Beyer T, Freudenberg LS, Czernin J, Townsend DW. The future of hybrid imaging-part 3: PET/MR, small-animal imaging and beyond. Insights Imaging. 2011;2(3):235–46.
41. Graham MC, Pentlow KS, Mawlawi O, Finn RD, Daghighian F, Larson SM. An investigation of the physical characteristics of 66Ga as an isotope for PET imaging and quantification. Med Phys. 1997;24(2):317–26.
42. Pentlow KS, Finn RD, Larson SM, Erdi YE, Beattie BJ, Humm JL. Quantitative imaging of yttrium-86 with PET: the occurrence and correction of anomalous apparent activity in high density regions. Clin Positron Imaging. 2000;3(3):85–90.
43. Bradbury MS, Pauliah M, Zanzonico P, Wiesner U, Patel S. Intraoperative mapping of sentinel lymph node metastases using a clinically translated ultrasmall silica nanoparticle. Wiley Interdiscip Rev Nanomed Nanobiotechnol. 2016;8(4):535–53.
44. Choi HS, Liu W, Liu F, Nasr K, Misra P, Bawendi MG, Frangioni JV. Design considerations for tumour-targeted nanoparticles. Nat Nanotechnol. 2010;5(1):42–7.
45. Phillips E, Penate-Medina O, Zanzonico PB, Carvajal RD, Mohan P, Ye Y, et al. Clinical translation of an ultrasmall inorganic optical-PET imaging nanoparticle probe. Sci Transl Med. 2014;6(260):260ra149.
46. Amis ES Jr, Butler PF, Applegate KE, Birnbaum SB, Brateman LF, Hevezi JM, et al. American College of Radiology. American College of Radiology white paper on radiation dose in medicine. J Am Coll Radiol. 2007;4(5):272–84.

Small Molecules as Radiopharmaceutical Vectors

Antony D. Gee, Salvatore Bongarzone, and Alan A. Wilson

A wide repertoire of small molecule PET radiopharmaceuticals has been successfully developed over the last 30–40 years [1]. Both the acceleration of the discovery of novel targets and advances in our understanding of pathophysiological mechanisms have created a rapidly increasing demand for new radiotracers. Alongside the traditional academic pursuit of new radiotracers, the resources of the pharmaceutical industry have been increasingly engaged in creating novel radiotracers for the development of new therapeutics and companion diagnostics.

The radiotracers used today have a wide variety of origins. Some are based on existing ^{3}H- and ^{14}C-labeled compounds. The ubiquitous 2-[^{18}F]-fluorodeoxyglucose, for example, is a descendant of 2-[^{14}C]deoxyglucose, a ^{14}C-labeled compound developed by Sokoloff *et al.* [2]. Over the years, rational approaches to the development of radiopharmaceuticals have evolved. This chapter will describe some 'tried and tested' approaches that have been used to select, design, and evaluate successful PET radiotracers. The chapter is divided into two parts: 'design parameters' and 'test criteria'.

In the first section, we will cover several critical 'design parameters' for the creation of effective small molecule radiopharmaceuticals (Table 1, top). More specifically, we will discuss an eclectic set of physicochemical and pharmacological properties, guidelines, tolerances, and 'rules of thumb' that—when considered together—can assist in the identification of molecules that are more likely to produce successful radiotracers. These criteria can be considered prior to performing any physical experiments, using data that may be gleaned from a variety of sources, including literature reports, databases, and *in silico* tools. It must be remembered, however, that some of these criteria are not 'hard and fast' rules but rather guidelines. Simply put, exceptions can and will be found. This underscores the fact that we admittedly do not yet fully understand the molecular and pharmacological requirements for radiotracers. Some examples of these exceptions are provided in the commentary.

Table 1 Design and test criterion for the discovery and development of small molecule radiotracers

Design criteria
Choosing and appropriate target
High affinity and selectivity for the target
Ease of radiosynthesis
Maximizing target accessibility while minimizing non-displaceable binding
Test Criteria
Good signal-to-noise ratio *in vivo*
Good *in vivo* pharmacokinetics
In vivo distribution and pharmacology consistent with literature reports
Low levels of radiolabeled metabolites in the region of interest
High sensitivity towards the target

In the second section, we describe a set of quantitative metrics for radiolabeled tracers that can be obtained via a series of *in vitro* and *in vivo* experiments to determine a radiotracer's potential utility (Table 1, bottom). There are many possible variations for these tests, often depending on the resources and infrastructure available. Yet if these test criteria are experimentally verified in one way or another, the chances of producing a useful radiotracer for *in vivo* imaging are greatly increased. It is important to note, however, that simple 'usefulness' is—for better or worse—not the endgame here. Indeed, even after an effective radiopharmaceutical has been created, there are further translational hurdles that must be negotiated before a radiotracer is considered suitable for *in vivo* imaging in humans. These will also be discussed.

Throughout the chapter, concepts are illustrated and reinforced graphically using a set of cartoon representations of an idealized *in vivo* environment (Fig. 1).

A. D. Gee (✉) · S. Bongarzone
Imaging Chemistry & Biology, King's College London, London, UK
e-mail: antony.gee@kcl.ac.uk

A. A. Wilson
Imaging and Pre-Clinical Research, Centre for Addiction and Mental Health, Toronto, ON, Canada
e-mail: alan.wilson@camhpet.ca

J. S. Lewis et al. (eds.), *Radiopharmaceutical Chemistry*, https://doi.org/10.1007/978-3-319-98947-1_7

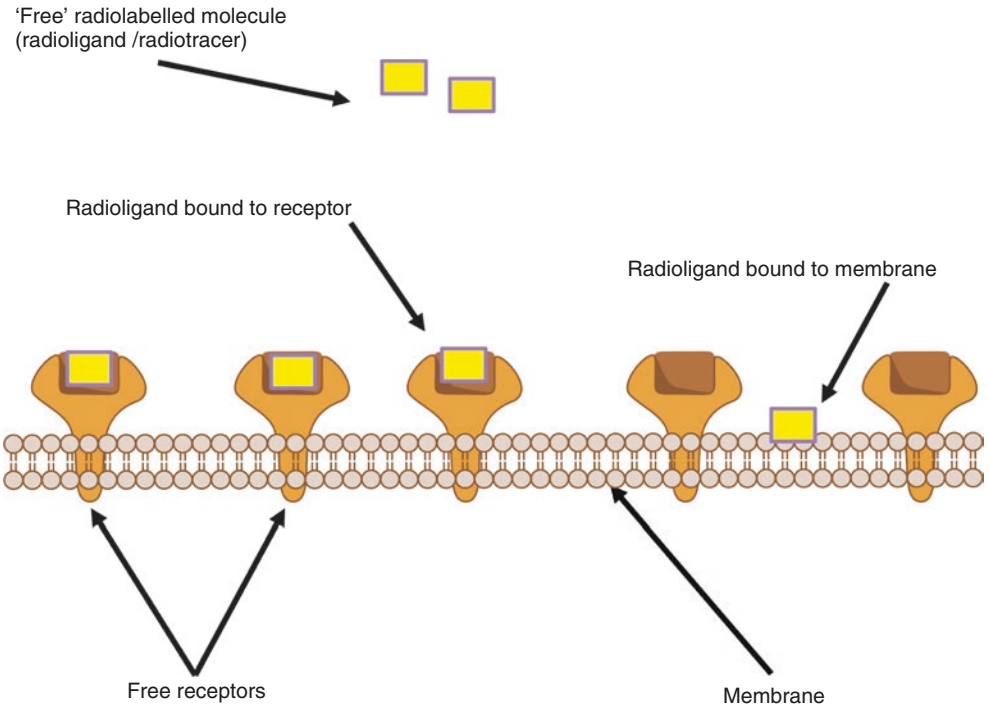

Fig. 1 Representation of some key concepts in the development of PET radiotracers

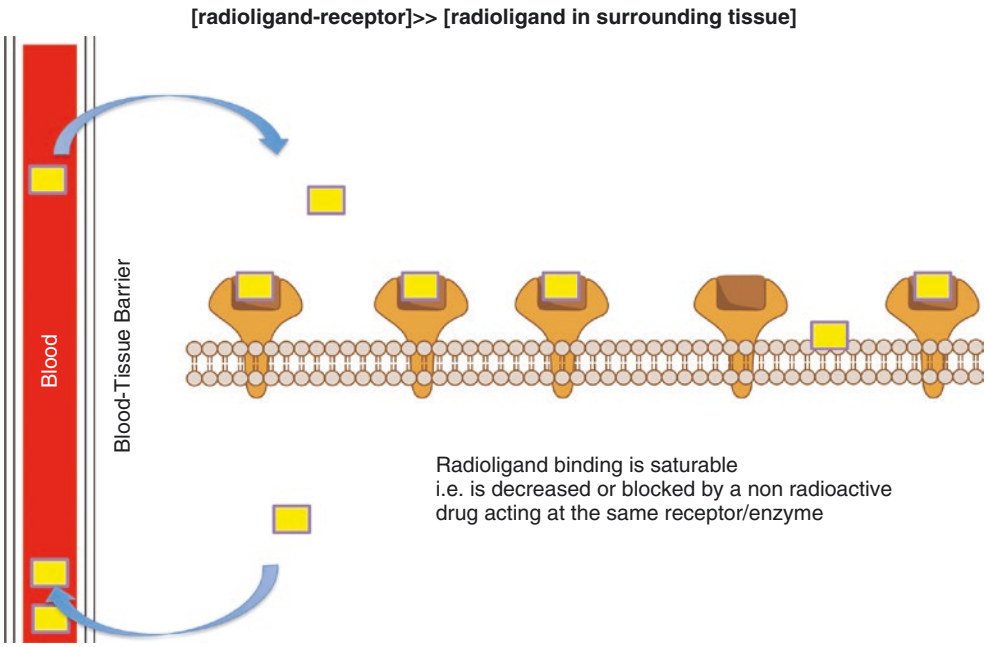

Fig. 2 Representation of the properties of an ideal CNS radiotracer: [radioligand-receptor] >> [radioligand in surrounding tissue]

An example schematic—a representation of the properties of an ideal radiotracer—is shown in Fig. 2. After the radiotracer is introduced to the blood via intravenous administration, it is able diffuse across the blood-tissue barrier, where it initially occupies the aqueous environment between cells. The radiotracer can subsequently bind to its molecular target, bind to non-target membranes or proteins, or diffuse across the blood-tissue barrier back into the bloodstream. For an ideal radiotracer (at a suitable time point after administration), there is significantly greater binding to the target than the surrounding compartments (*i.e.* [radiotracer bound to target receptors] >> ([free

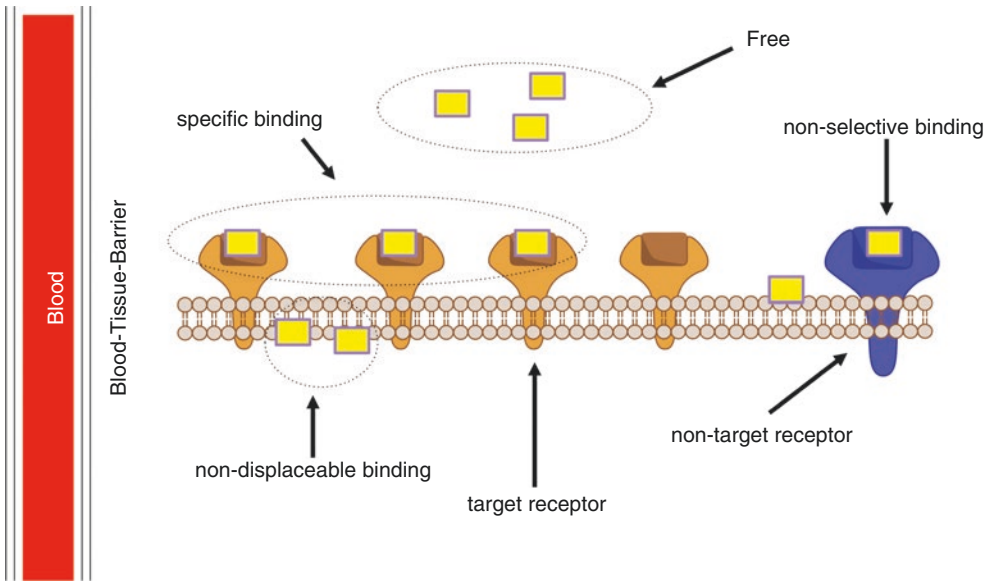

Fig. 3 Specific binding, non-selective binding, and non-displaceable binding

radiotracer] + [radiotracer bound to the membrane] + [radiotracer bound to non-target receptors])). Binding to (unwanted) non-target receptors is termed 'non-selective binding' (Fig. 3).

One brief aside before we begin in earnest: the term 'non-specific binding' is often used in the literature to describe the binding of a radiopharmaceutical to *all* non-target entities, including non-target receptors, serum proteins, membranes, *etc.* Strictly speaking, this is a misnomer. The binding of a radiopharmaceutical to non-target receptors is best described as 'non-selective binding', and the indiscriminate binding of a radiopharmaceutical to serum proteins and membranes is best described as 'non-displaceable binding'. To avoid this confusion, the terms 'non-selective binding' and 'non-displaceable binding' are recommended and are used consistently throughout this chapter.

Part 1: Design Criteria for Small Molecule Radiotracers

Requirement 1: Choosing an Appropriate Target

The first requirement when selecting an appropriate target for a radiotracer discovery program is knowing the concentration of the target protein (B_{max}) in the region of interest (ROI) (*e.g.* the tumour, thalamus, cerebellum, *etc.*). A quick poll of radiotracers developed over the past three decades shows—with only a few exceptions—that the lowest B_{max} that has been successfully imaged is around 1 nM. Target concentrations are typically expressed in units of nM, mol/g, or mol/cm^3 tissue.

Dopamine D_2 receptors (for which several radiotracers have been developed) are present in the 10–20 nM range. If the target protein is present in sub-nanomolar concentrations, very special efforts are required to develop an effective radiotracer. A pictorial representation of a tissue with a low target concentration is shown in Fig. 4. Compared to the idealized case shown in Fig. 2, the number of target proteins is too low to provide significant signal contrast. To overcome this, a radiotracer must have higher affinity for its receptor or reduced propensity for non-displaceable and non-selective binding.

The appropriateness of a target also depends on the physical size (or volume) of the ROI in which the target is located (Fig. 5) [3]. The size/volume of the ROI is typically expressed in units of micrometer, mm, mm^3, cm^3, *etc.*

In this regard, there are a number of criteria to consider, including motion correction (for moving organs such as the heart or lungs), co-registration with an anatomical atlas, and camera sensitivity and resolution. If the molecular target of interest is present in sufficient concentration and in a ROI with a volume exceeding the resolution of the scanner (*e.g.* the striatum, thalamus, cerebellum, large tumour, *etc.*), it is usually relatively easy to accurately quantify the concentration of the tracer within the target. However, ROIs that have sizes similar to or less than the resolution of the camera (*e.g.* the raphe nucleus, substantia nigra, microtumours, etc.) can appear 'blurred' or 'smeared out'. Furthermore, the radioactivity concentrations in these regions can be underestimated, making it difficult to identify and accurately quantify the binding of the radiotracer to the target.

The 'smearing out' of the tissue signal is termed the partial volume effect—the loss of apparent radioactivity concentration in small ROIs because of the limited resolution

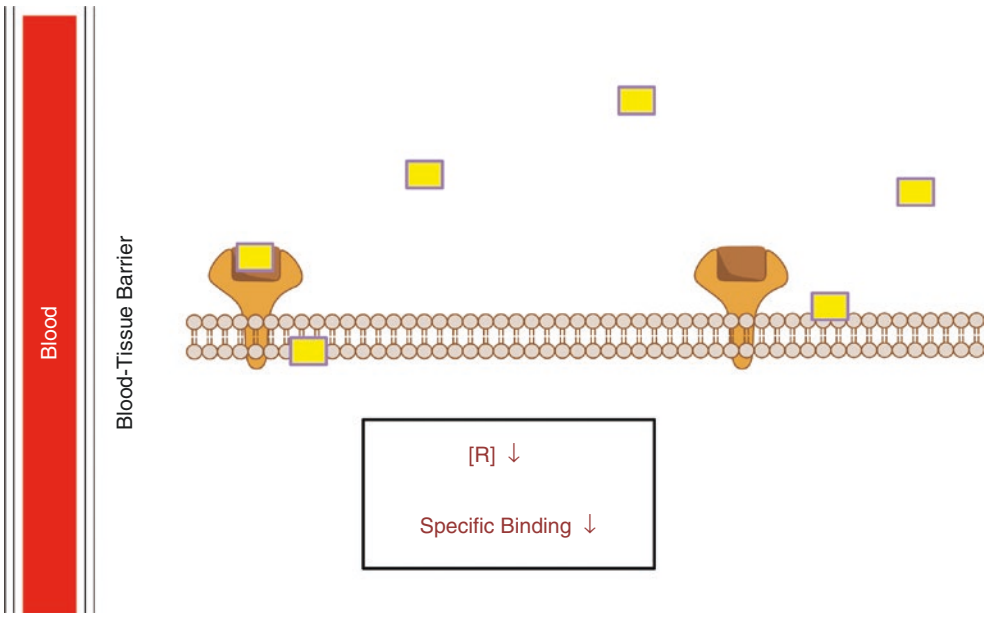

Fig. 4 Representation of a cell with low target expression

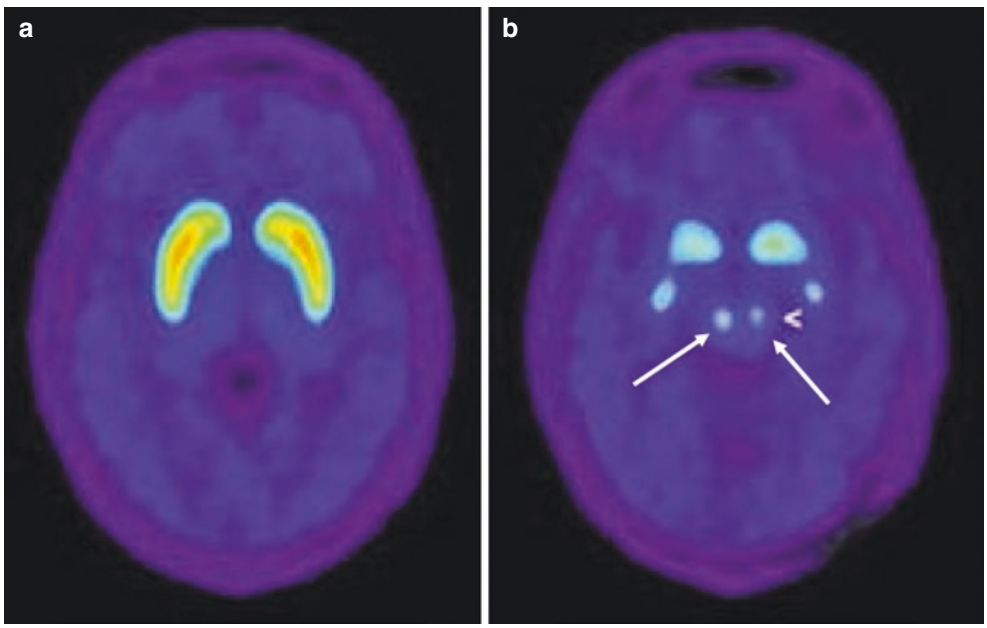

Fig. 5 Visualizing large vs. small target regions: (**a**) imaging of large target regions, the striatum; (**b**) imaging of small target regions, the substantia nigra nuclei (see arrows). (Adapted from Varrone *et al.* [3], with permission)

of the scanner. At present, the practical resolution of clinical PET scanners is typically in the range of 2–5 mm. If the ROI about the same size as the resolution of the scanner, the activity concentration of the structure appears to 'spill out' into the surrounding tissue and is thus underestimated compared to the true value (Fig. 6). If the ROI in which the target resides is very small, the radioactivity concentration is almost impossible to quantify. Great efforts are being made by the imaging community to improve the resolution and sensitivity of PET scanners. Readers are referred to reviews on this subject for in depth treatment of the subject.

Requirement 2: High Affinity and Selectivity for the Target

Affinity For a particular molecular target, the magnitude of B_{max} and the physical size of the ROI in which the target resides influence the affinity needed for an effective radiotracer. To illustrate this, let us consider the targeting of three individual monoamine transporters: the dopamine transporter (DAT), the serotonin transporter (SERT), and the norepinephrine (noradrenaline) transporter (NET). The expression levels of these proteins in the central

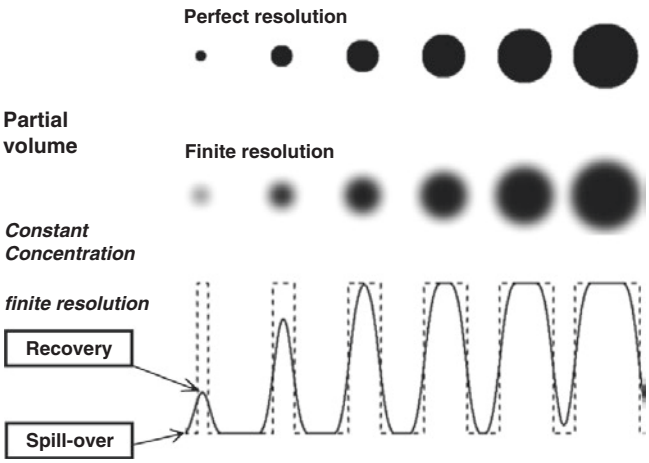

Fig. 6 Illustration of the partial volume effect

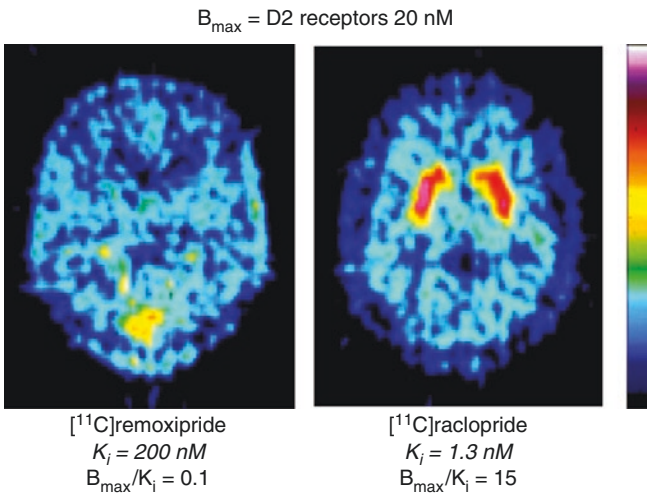

Fig. 7 PET brain scans of two dopamine D2-targeted radiotracers with different affinities. [^{11}C]Remoxipride has a lower affinity of 200 nM and does not give a noticeable PET signal in the striatum (a region rich in D2 receptors). [^{11}C]Raclopride, in contrast, has a much higher affinity (in the low nanomolar range), enabling adequate visualization of striatal D2 receptors. (Courtesy of Drs. Lars Farde and Christer Halldin, Department of Clinical Neuroscience, Karolinska University Hospital, Stockholm, Sweden)

Table 2 Required affinity for radiotracers to image DAT, SERT, and NET

Target	B_{max}	Required affinity (K_d)	Radiotracers
DAT	>100 nM	10 nM	>20 radiotracers
SERT	20 nM	2 nM	3–4 radiotracers
NET	5 nM	0.5 nM	No good radiotracer

DAT dopamine transporter, *SERT* serotonin transporter, *NET* norepinephrine (noradrenaline) transporter

nervous system (CNS) are quite different with B_{max} values DAT > SERT > NET (Table 2).

For imaging DAT, a radiotracer with an affinity (K_d) of between 10 and 100 nM is required. Producing small molecules with affinities in this range is not too challenging for modern medicinal chemistry, and several DAT radiotracers have been successfully developed. The SERT, however, is expressed at ~5 times lower concentrations than the DAT. As a result, a radiotracer with an affinity 5 times greater is required to image SERT with similar target-to-background ratios. This requirement puts greater demands on medicinal chemistry, and it is perhaps not surprising that only a few radiotracers have been developed for SERT to date. Finally, the NET is present in even *lower* concentrations than DAT and SERT, necessitating a radiotracer with a sub-nanomolar affinity for the target. Despite some decent attempts, there are currently no really effective radiotracers for NET.

More generally speaking, if the affinity of a radiotracer for its target is too low, sufficient target-to-background contrast ratios will not be achieved. This phenomenon is illustrated in Fig. 7: specific binding decreases as the affinity of the radioligand decreases.

Over the years, some researchers have developed a rule of thumb for estimating the minimum affinity required to target a certain expression level of protein (B_{max}). The binding of a radiotracer to a target is related to its affinity for the target and the target concentration. A useful way to quantify this was developed by Eckelman *et al.* [4] using a derivation of the Scatchard plot (Fig. 8) and Eq. 1 (the Scatchard equation):

$$\frac{[\text{Bound radiotracer}]}{[\text{Unbound radiotracer}]} = \frac{B_{max}}{K_d} - \frac{[\text{Bound radiotracer}]}{K_d}$$

For a radioligand to behave as a tracer, the amount bound radioligand approaches zero, and the equation reduces to the following (Eq. 2):

$$\frac{[\text{Bound radiotracer}]}{[\text{Unbound radiotracer}]} = \frac{B_{max}}{K_d}$$

Eckleman *et al.* proposed that a minimum ratio [Bound radiotracer]/[Unbound radiotracer]—or signal/noise ratio—of 10 is needed for a successful radiotracer. In other words, the ratio of the B_{max} of the target to the K_d of the radiotracer must be at least 10 in order to achieve adequate signal-to-background contrast ratios *in vivo*. If this equation is used to plot a series of isocontours representing different protein expression levels, the graph in Fig. 9 can be generated (Gee, previously unpublished data). The ratio [Bound radiotracer]/[Unbound radiotracer] is shown on the *Y* axis, and the affinity of the radiotracer (K_d) is shown on the *x*-axis. This graph clearly shows that achieving signal-to-noise ratios of 10 is contingent upon both B_{max} and K_d. For example, a target with

a B_{max} of 100 nM requires a radiotracer with a K_d of 10 nM in order to obtain a B/F ratio of 10. However, a radiotracer with a K_d of between 1 and 0.1 nM is needed to image a target with a B_{max} value in the 3 nM range.

Patel *et al.* demonstrated the correlation between B_{max}/K_d ratios and signal-to-noise ratios for a small number of radiotracers with different affinities and molecular targets at different expression levels (Table 3) [5].

As we have noted, high affinity for a target is typically a good thing. However, it is important to note that sometimes the affinity of a radiotracer can be *too* high. In this case, the distribution of the radiotracer may become dependent on blood flow and transport rather than the expression level of the target itself. Furthermore, high affinity radiotracers often exhibit 'irreversible' kinetic behaviour, making them unsuitable for reliable quantification because quantitative *in vivo* pharmacokinetic analyses typically assume 'steady-state' or 'pseudo-equilibrium' conditions.

Selectivity The selectivity of a radiotracer depends on a number of factors, including its affinity for the target, the B_{max} of the target, and the presence of 'interfering' target. The latter can be illustrated by differences in the expression of dopamine and serotonin neurons in the brain as shown in Fig. 10.

There are some regions of the brain where dopamine and serotonin neurons are co-expressed and other regions where serotonin receptors or dopamine receptors are predominant. We have already stated that the affinity needed for a radiotracer is dictated by the expression level—or B_{max}—of the target. However, if the radiotracer is 'non-selective' (*i.e.* binds to more than one target), both the location and the B_{max} of the interfering target need to be considered. For example, if our goal is to develop a radiotracer to image the SERT in

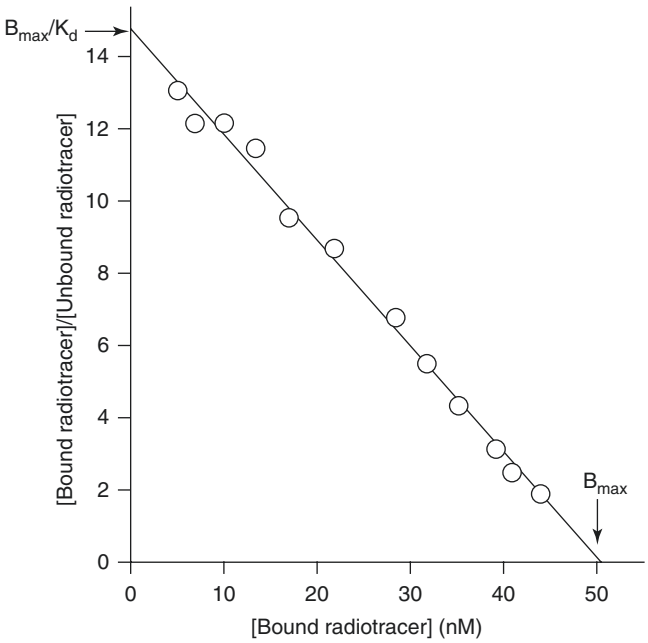

Fig. 8 The Scatchard plot. (From Patel and Gibson [5], with permission)

Table 3 B_{max}/K_d ratio of common CNS radiotracers

Target	Radiotracer	B_{max} (nM)	K_d (nM)	B_{max}/K_d
DAT	[^{11}C]cocaine	150	130	1.2
DAT	[^{18}F]β-CFT	180	11	16
D2	[^{11}C]raclopride	19	3.5	5.4
D2	[^{11}C]*N*-methylspiperone	19	0.1	190
CB1	[^{18}F]MK9470	14	0.3	47
m-AChR	[^{123}I]/[^{11}C]QNB	150	0.2	750
m-GluR5	[^{18}F]FPEB	50	0.2	250
m-GluR5	[^{18}F]PyrPEB	50	16	3

From Patel and Gibson [5], with permission
DAT dopamine transporter, B_{max} the concentration of the target protein, K_d affinity

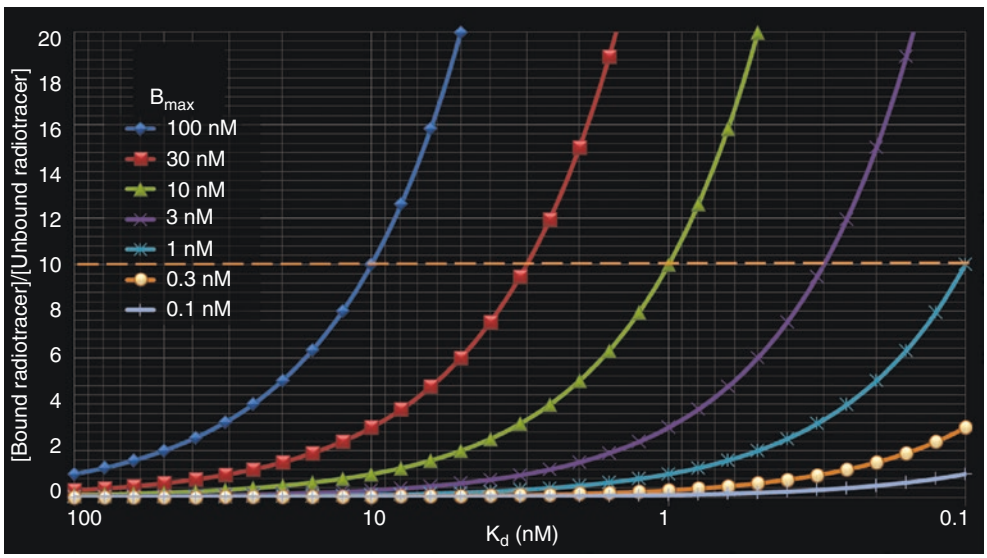

Fig. 9 'Plot' illustrating the [bound radiotracer]/[unbound radiotracer] ratio as a function of B_{max} and K_d

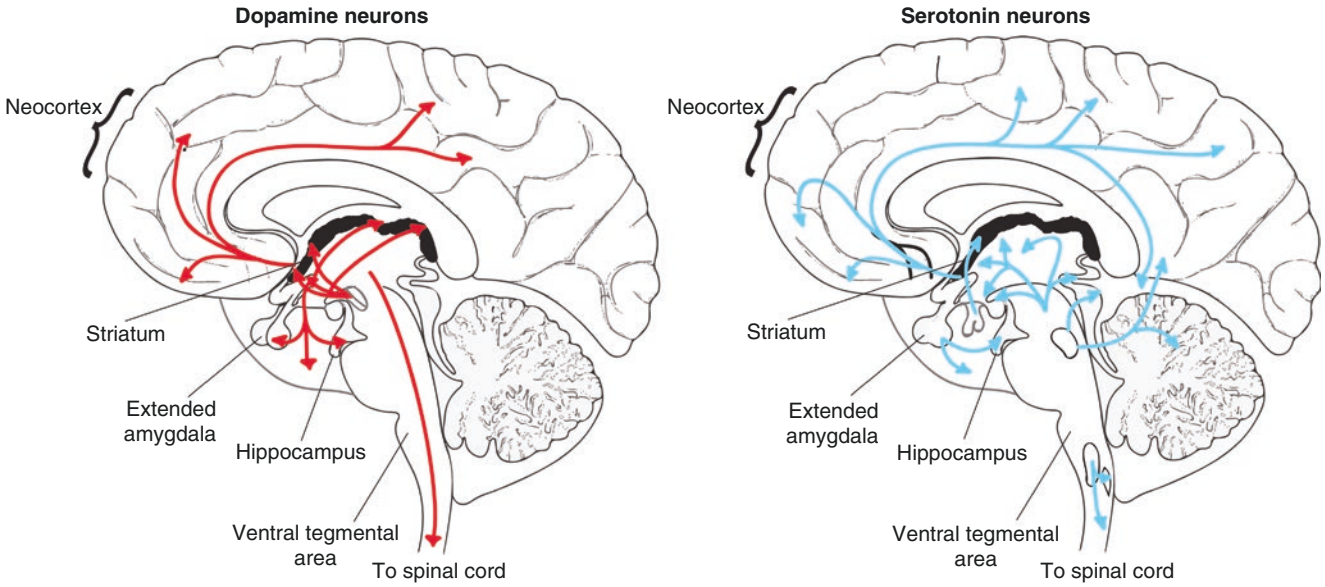

Fig. 10 The required selectivity of a radiotracer depends upon the affinity (K_d) of the radiotracer for its target, the presence of interfering targets, the B_{max} of the target, and the localization of the target. (Adapted with permission from Neuroscience & Graphic Design for the Centre for Neuroimaging Sciences at King's College London. https://neuroscience-graphicdesign.com/, courtesy of the artist Gill Brown)

the striatum, the radiotracer will require selectivity for SERT vs. DAT of ca. 100 or greater. This is because the B_{max} of DAT in the striatum is much greater than the B_{max} of SERT in the same area (see Table 1). However, if the goal is to image the DAT in the striatum, then we can live with a non-selective radiotracer, because the expression of DAT is so much higher than that of the SERT the same region.

Requirement 3: Ease of Radiosynthesis

Other chapters within this book cover methods for the radiosynthesis of tracers with radionuclides ranging from ^{11}C to ^{225}Ac. Many of these methods have proven to be robust and have been applied to a wide number of radiopharmaceuticals. Other radionuclides are used less frequently, possibly due to their complexity, their need for a narrow set of structural or synthetic criteria, or the lack of availability of appropriate labeling methods. When designing a new radiotracer, the selection of a robust approach to radiolabeling should be a priority. Accessibility is key. Even the most fantastic radiotracer can be rendered irrelevant if it can only be produced one time in ten attempts. Moreover, radiosynthetic strategies to produce radiotracers bearing short half-life radionuclides must be rapid.

That said, if a difficult-to-make radiotracer has nonetheless demonstrated the ability to address an unmet need, radiopharmaceutical chemists can develop more robust synthetic pathways. As this book demonstrates, the field of radiopharmaceutical chemistry is active and evolving, and significant progress has been made in recent years to create a wide variety of robust labeling methods.

Requirement 4: Maximizing Target Accessibility While Minimizing Non-displaceable Binding

To be able to image a target protein, a radiotracer must be able to reach that target. For most radiotracers (see exceptions below), this means having the ability to diffuse from the blood into the tissue of interest through the plasma membrane via a passive transport. The inability to access the tissue of interest is one of the most frequent reasons for radiotracers to fail. There are many factors which contribute to a radiotracer's ability to diffuse passively across a membrane. Admittedly, many of these are poorly understood; however, the lipophilicity of a molecule seems to be one of the physicochemical parameters that is significantly correlated with tissue penetration.

The most common method to measure lipophilicity is the octanol-water 'shake-flask' method. In this assay, the radiotracer is introduced into a system containing equal volumes of octanol and water, shaken vigorously, and allowed to partition between the octanol and water phases. The 'lipophilicity' is measured as the log of the partition coefficient of the non-charged molecule between the two phases (Fig. 11).

If the pH of the aqueous layer adjusted to physiological pH (7.4), the measure is termed a LogD value and accounts for the partition of both charged and non-charged species at

physiological pH. If a tracer is not sufficiently lipophilic—*i.e.* is too hydrophilic—it will not be able to diffuse across cell membranes from the blood pool in order to reach its target (Fig. 12).

Great efforts have been made to develop *a priori* rules for predicting a molecule's ability to penetrate into tissue. Lipinski's 'rule of five' is a notable example of a multiparametric *in silico* approach to predicting the tissue permeability of small molecule drug candidates. Empirical screening procedures—including assays using artificial phospholipid bilayers, cell monolayers, and even chromatographic methods—are also adopted occasionally to probe the interplay between lipophilicity and passive permeability. It is important, however, that molecules that cross membranes via active or facilitated transport (*e.g.* amino acid transporters, glucose transporters, P-glycoprotein, efflux pumps, *etc.*) are exempt from these membrane diffusion and lipophilicity discussions.

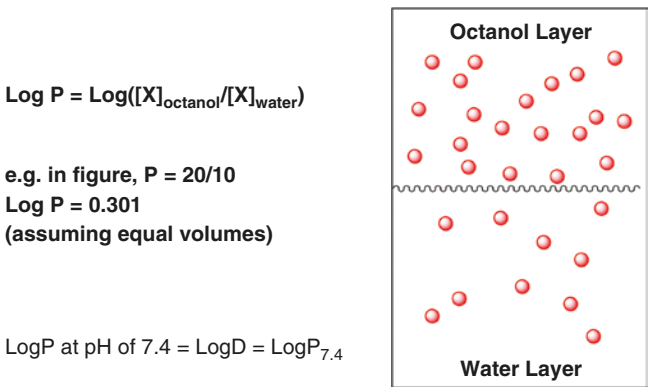

Fig. 11 Illustration of the estimation of an octanol-water partition coefficient

The importance of lipophilicity also extends to non-displaceable binding (NDB). Non-displaceable binding is the affinity of the radiotracer for all non-saturable components of tissue, such as lipids, phospholipids, membranes, *etc.* In other words, the radioligand-tissue binding cannot be displaced or blocked by macroscopic quantities of non-radioactive blocking agents. NDB is independent of the target, and it increases linearly with increasing lipophilicity of radiotracer (Fig. 13). In nuclear imaging, the NDB can be considered the 'noise' or 'background 'signal', while the specific binding is the 'contrast'. Indeed, high non-displaceable binding is probably the primary reason for the failure of many radiotracers. The correlation between NDB and the lipophilicity of a radiotracer is strong. Generally speaking, higher values of LogD produce more non-displaceable binding.

All of this leaves us with a bit of a conundrum. If the lipophilicity of a radiotracer is too low, it will not be able to access the target. However, if the lipophilicity of a radiotracer is too high, it will have high NDB. This begs the question: *what is the optimal lipophilicity for a radiotracer?*

The optimal lipophilicity value for a radiotracer is a balance between a number of parameters:

- *Target accessibility*: a degree of lipophilicity is required to help the radiotracer diffuse across cell membranes.
- *Non-displaceable binding*: High NDB is observed if the lipophilicity is too high.
- *Plasma protein binding:* The bloodstream contains numerous proteins (*e.g.* albumin). Plasma protein binding is increased with increasing molecule lipophilicity; if the plasma protein binding is too high, very little radiotracer is 'free' to find its target.

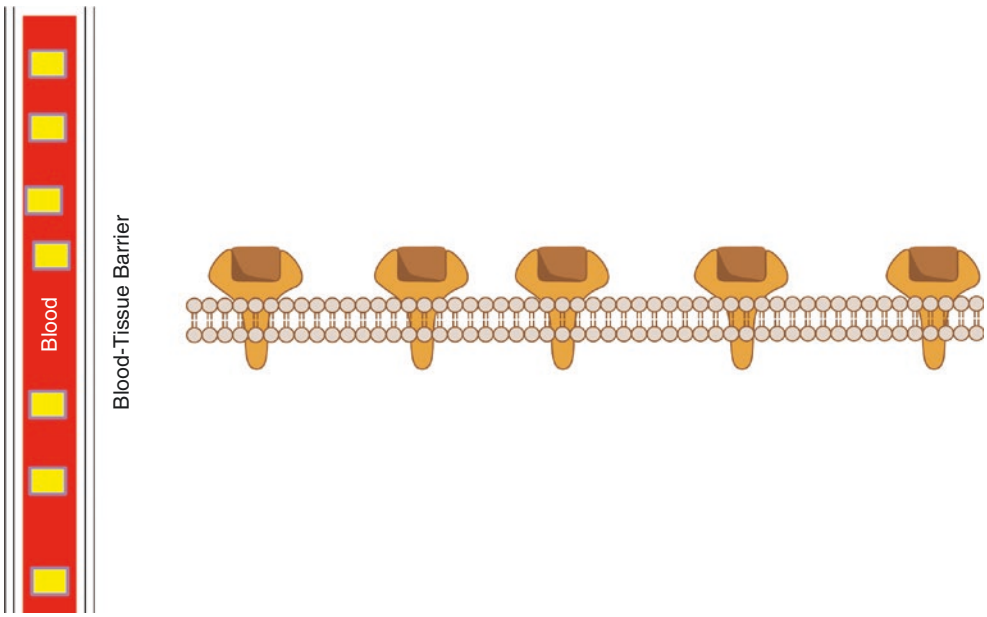

Fig. 12 Radiotracers which are not sufficiently lipophilic may struggle to cross membranes to reach their targets

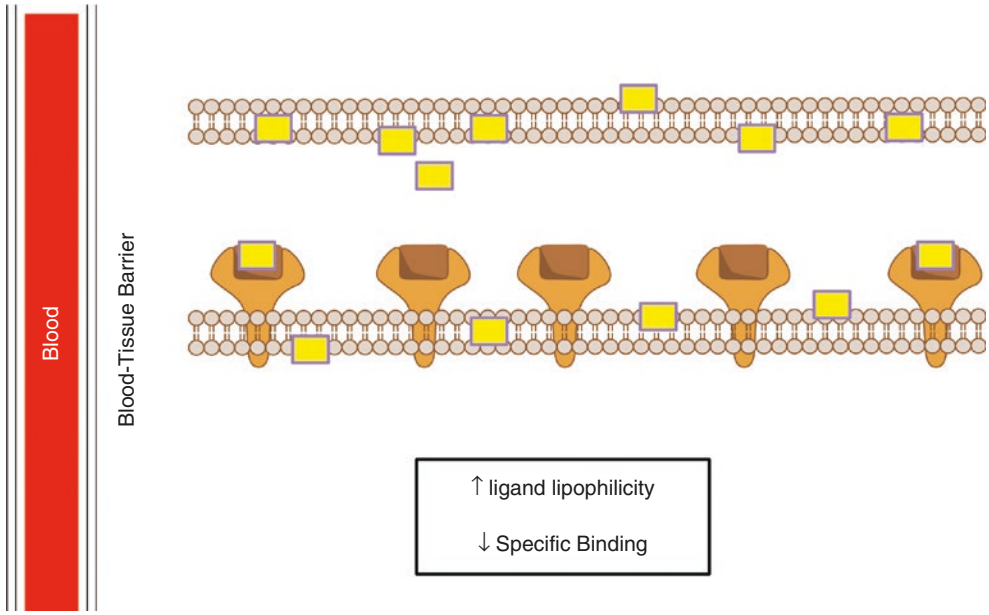

Fig. 13 High lipophilicity can result in high non-displaceable binding (NDB)

- *Affinity:* Because receptors and enzymes are themselves proteins, the binding affinity of radiotracers to many molecular recognition sites actually often increases with increased lipophilicity!

Researchers have typically found that LogD (or LogP) values of 1–3 are optimal to balance the competing factors discussed above (see Waterhouse 2004 for a discussion on this topic) [6].

The importance of properly measuring the LogD values of radiotracers was discussed by Wilson *et al.* along with a recommendation of how to accurately measure this parameter. There are also many computer programmes that can be used to calculate LogP and LogD values from structures. However, these should be treated with caution, as they are often inaccurate. While these may be useful for comparing the lipophilicity of analogues across a series of compounds, it is strongly recommended that *experimentally determined* LogD and LogP values be used whenever possible.

While the '1–3 LogP' rule is very useful, there are (inevitably) notable exceptions. For example, WAY100635 has a LogD value of 3.1, but [^{11}C]WAY100635 has negligible non-saturable binding and rapid tissue washout *in vivo* (Fig. 14). Conversely, CFT has LogD values of around 0.6 but [^{11}C]CFT exhibits high non-displaceable binding *in vivo* accompanied by slow washout from tissues.

The fact that there are many exceptions to the 'LogP 1–3' rule suggests that lipophilicity is not the only factor contributing to non-saturable binding and that the molecular basis of non-displaceable binding as a whole is poorly understood. In this regard, advances in our understanding of NDB could be very helpful in refining the selection criteria used during the discovery of radiotracers, which to

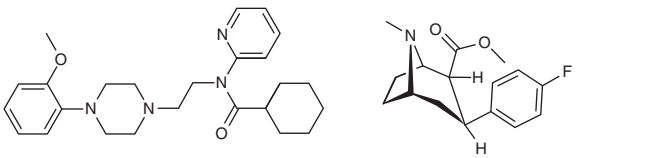

Fig. 14 Notable exceptions to the 'LogD = 1–3 rule'

date has a high attrition rate. Researchers have proposed hypotheses regarding the molecular mechanisms of non-saturable binding. Baciu *et al.*, for example, have proposed that non-displaceable binding may be linked to the ability of a molecule to hydrolyse the fatty acid chains of membrane phospholipids (1,2-dioleoyl-sn-glycero-3-phosphocholine (DOPC)) *via* an autocatalysed acid hydrolysis mechanism [7] (Fig. 15).

The investigators observed that the rate of membrane digestion caused by cationic amphiphilic drug-like (CAD) was *inversely* correlated the magnitude of its *in vivo* NDB.

According to this hypothesis, molecules—such as CAD—that rapidly hydrolyse membrane phospholipids exhibit low NDB because they are able to rapidly translocate across the membrane to reach their target (Fig. 16). The authors further hypothesized that the translocation might be facilitated by the formation of micelles around the molecule, facilitating its transport in the aqueous intracellular environment, the so-called membrane munching hypothesis of NDB. Conversely, molecules that only slowly hydrolyse the membrane—or do not do so at all—exhibit high NDB because they become 'stuck' at the polar-apolar interface of the phospholipid membrane (Fig. 17).

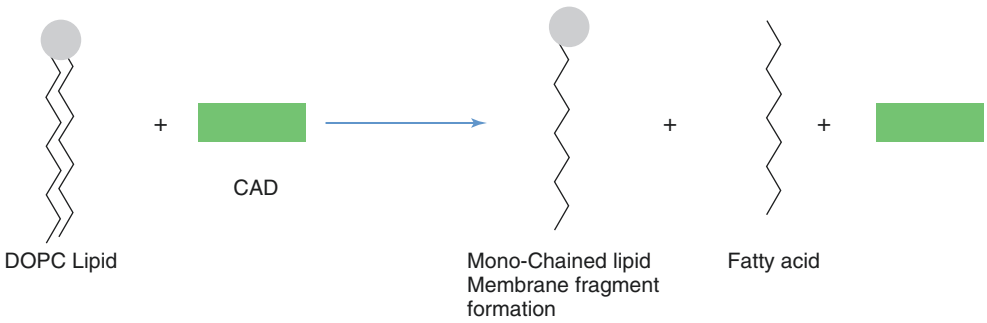

Fig. 15 Acid hydrolysis of the ester linkage of DOPC

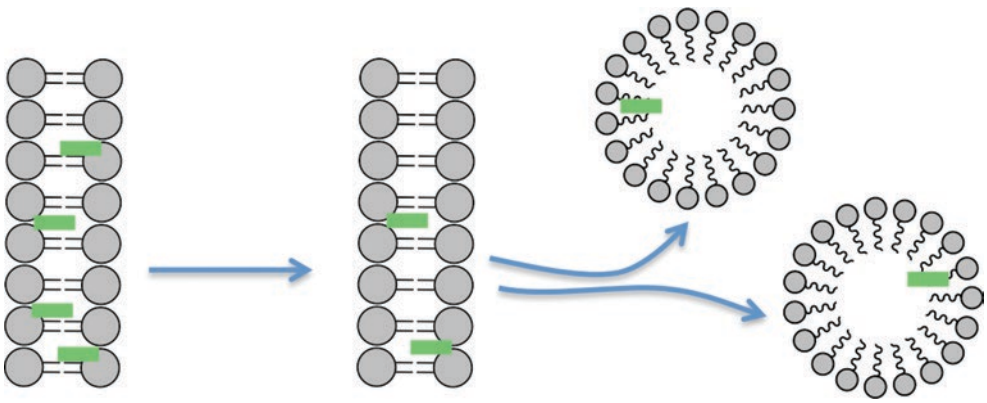

Fig. 16 Molecules (green rectangle) that rapidly hydrolyse membrane phospholipids exhibit low NDB because they are able to rapidly translocate across the membrane to reach their target

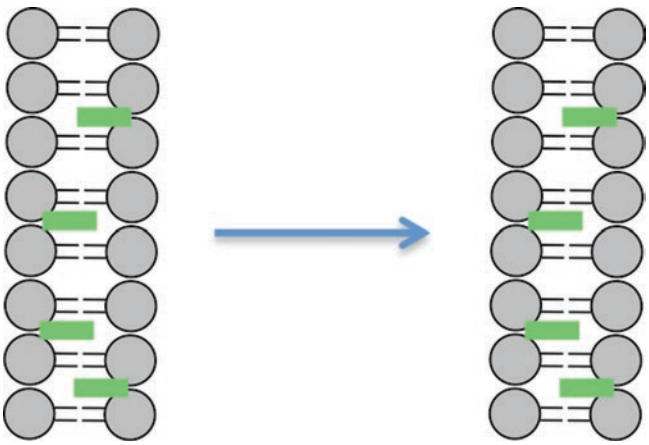

Fig. 17 Molecules (green rectangle) that only slowly hydrolyse the membrane—or do not do so at all—exhibit high NDB because they become 'stuck' at the polar-apolar interface of the phospholipid membrane

Further evidence for the insufficiency of LogP as an accurate indicator of non-displaceable binding came from ab initio quantum mechanical calculations of the interaction energy of between drugs and lipids. The interaction energy between drugs and lipids was shown to be a better predictor of *in vivo* NDB than estimates obtained from experimentally determined LogP values. Not surprisingly, calculated Log P values have even poorer correlations with the degree of *in vivo* NDB! Ultimately, further research into the molecular mechanisms of non-displaceable binding and transmembrane relocation will sharpen our understanding of these phenomena as well as our ability to design molecules that have low NDB while effectively targeting proteins of interest.

Starting Points for the Development of Novel Radiotracers

There are a several starting points that one can use when beginning the development a novel radiotracer. These include publications on structure-activity relationships, existing pharmaceuticals, and existing radiotracers (as well the patent literature). Each of these sources can contain information that will allow for at least an initial assessment of a molecule's potential to fulfil the design criteria discussed above without having to perform a single experiment. Empirical rules are also being developed—particularly by drug companies—to facilitate the identification of promising platforms for radioligands by screening compound libraries for candidates with the molecular hallmarks of successful radiotracers (Table 4).

A recurring trend within the field is the creation of 'second-generation' radiotracers following the initial report of a 'first-generation' radiotracer. The 'first-generation' tracer may be promising but suboptimal with respect to some key trait (*e.g.* kinetics, selectivity, metabolism, high non-displaceable bind-

Table 4 Minimum starting points for the development of a small molecule radiotracer

Property	Ideal situation	Minimum starting points
B_{max}	Known B_{max} and location of the target in animals and humans	Know approximate location and B_{max}—at least in an animal (model)
Affinity	Known	Known for analogues at least
Selectivity	Known	Known for analogues at least
Metabolism	Known	Rarely known
Log P	Known	Easily calculated values but inaccurate; measurable if compound or radiotracer is available
Radiosynthesis	Robust and simple radiochemistry methods for labeling Commercially available precursors/reagents Commercially available automated synthesis apparatus	Possible synthetic route to the target compound (may need significant resources for development for a new radiosynthetic route, with associated higher risk of failure)

ing, or radiolabel). In this case, this 'first-generation' radiotracer can be an inspiration for 'second-generation' iterations. There are numerous examples of this phenomenon, including radiotracers that target the DAT, TSPO, amyloid, PSMA, and somatostatin receptors.

While many of these 'second-generation' radiotracers provide useful incremental improvements (or create intellectual property), the overall process can frequently represent an unnecessary duplication of effort and resources. Furthermore, it can actually hinder the translational progress of class of agents when each group develops its 'own flavour' of a particular radiotracer. Clearly, embarking on the development of 'me-too' radiotracers should be carefully considered in order to assess if the investigation is an effective use of resources.

Other Pathways to Radiotracer Discovery

A useful starting point in the development of novel radiotracer is the use of tritium-labeled compounds. The creation of these radiopharmaceuticals does not require the use of a cyclotron, and a single batch is often sufficient to conduct many experiments. Furthermore, the evaluation of tritiated radiotracers is not constrained by the short half-lives of many radionuclides, making *in vitro* binding studies easy. More recently, techniques such as MALDI imaging and mass spectroscopy are starting to be utilized as alternatives to using radioactive compounds as starting points for the discovery of radiotracers, opening doors for even more efficient discovery efforts in the future.

Part 2: Test Criteria

Assuming the initial design parameters have been met for a candidate radiotracer and its molecular target, the next step is to evaluate a prototype radioligand against a set of test criteria to see whether or not it can be developed into a successful radiotracer. The five test criteria are as follows:

- Good signal-to-noise ratio *in vivo*
- Good *in vivo* pharmacokinetics
- *In vivo* distribution and pharmacology consistent with literature reports
- Low levels of radiolabeled metabolites in the region of interest
- High sensitivity towards the target

There are many different ways that these test criteria can be addressed. The choice of methods often comes down to the resources available, for example, the availability of instrumentation for *in vitro* studies or access to small animal PET scanners. Each set of strategies has its own set of pros and cons. Yet ultimately, irrespective of differences in the experimental approach, the same test criteria need to be addressed. The examples illustrated below are based upon the *in vivo* evaluation of radiotracers in rodents as well as the use of *ex vivo* tissue dissection and counting methods.

To illustrate the testing phase for a candidate radiotracer, a reconstruction of the test criteria used in the development of the ultimately successful SERT radiotracer, DASB, is described. The published details of this work by can be found in Wilson *et al.* [8]. The SERT is a protein expressed in the CNS which recycles the neurotransmitter serotonin after being released as a result of neuronal firing. The released serotonin is transported back into the presynaptic serotonin nerve terminals for repackaging in neurotransmitter vesicles. The SERT is the site of action for many antidepressant drugs (*e.g.* Prozac, paroxetine, fluoxetine, *etc.*).

The starting point for the SERT radiotracer development campaign (resulting in the discovery of the DASB radiotracer) was found in the patent literature, specifically a class of compounds that had not previously been explored as an imaging agent but met the design criteria described above (Fig. 18).

Encouraged by the discovery of SERT-5, Wilson et al. set out to label this lead compound via methylation with ^{11}C-methyl iodide to test whether the compound could be labeled. This was indeed found to be the case (Fig. 19) [8].

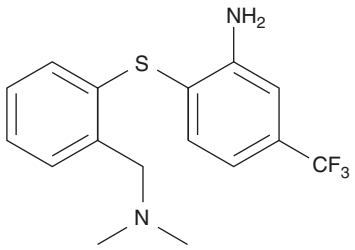

SERT-5

- Reported in patent WO 97/17325 (1996)
- IC_{50} for inhibition of reuptake of serotonin - 0.02 nM
- Claimed to be selective for SERT over DAT and NET
- Suitable site for radiolabeling with C-11

Fig. 18 SERT-5—the lead compound for serotonin transporter radiotracer development

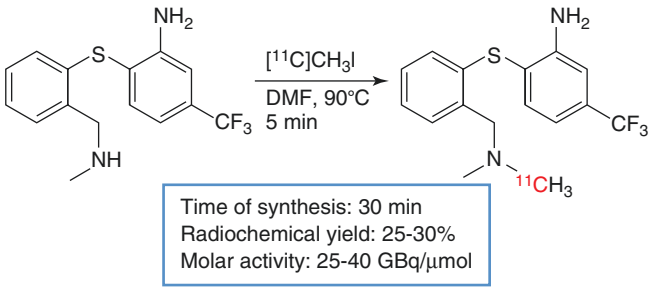

Fig. 19 Radiosynthesis of [^{11}C]SERT-5

Test Criterion 1: Good Signal-to-Noise Ratio *In Vivo*

Following the confirmation of the successful labeling of SERT-5, the prototype radiotracer was administered to rats which were sacrificed at selected time points post-injection. Blood samples were collected at the time of sacrifice, selected brain regions were dissected, and the activity levels and weights of selected tissues were determined (Fig. 20).

The activity concentrations in each tissue were determined by expressing the tissue activity as 'activity/tissue weight' or MBq/g tissue. The dissected brain regions were selected based on known *in vitro* expression levels in the rat brain (SERT expression: hypothalamus > thalamus = striatum > cerebellum). As the cerebellum contains almost no SERT, it can be used as a control tissue for comparison with other SERT-rich regions.

The selection of a range of time points allows for the creation of a plot of the activity concentration of the tracer in different tissues over time: the y-axis represents the radioactivity concentration in a given tissue, while the x-axis represents time. These graphs are commonly known as 'time-activity curves' or 'TACs' (Fig. 20). In this way, a comparison between the TACs of regions rich in the target with those that lack the target can provide an indication of

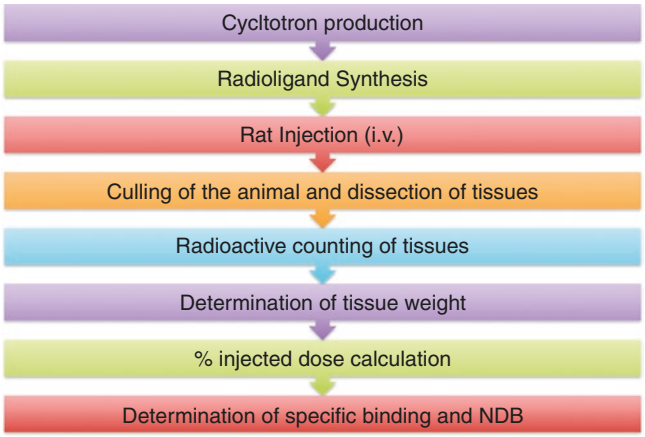

Fig. 20 *In vivo* rat experimental protocol

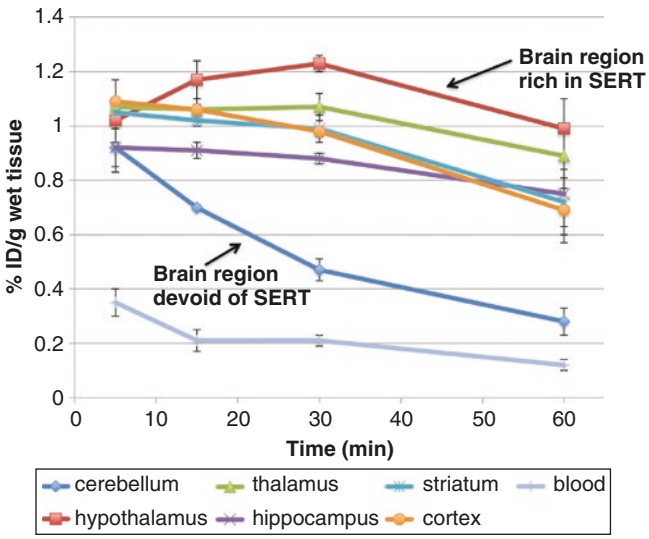

Fig. 21 Biodistribution of [^{11}C]SERT-5 in rat brain

the magnitude of the SERT-specific signal of the radiotracer. The TACs of nontarget tissues will also give an indication of the non-displaceable background signal.

This TAC-based analysis answers two critical questions: (1) 'Does [^{11}C]SERT-5 access the target organ?' and (2) 'Does [^{11}C]SERT-5 bind to the SERT with adequate contrast *in vivo*?' The TACs in Fig. 21 clearly show that the activity concentration in the hypothalamus (which is rich in SERT) at 20–60 min post-administration is much higher than that of the cerebellum (which is low in SERT). In addition, regions containing intermediate levels of SERT have intermediate radioactivity concentrations.

Taken together, the data thus far confirmed that the lead compound could be labeled with ^{11}C and that the resulting radiotracer produces an *in vivo* distribution in the brain that is consistent with the known literature distribution of SERT. Furthermore, it also shows that the radioactivity washout from regions devoid of SERT is more rapid than

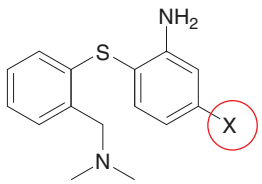

Name	X	SERT (K_i, nM)	NET (K_i, nM)	DAT (K_i, nM)
SERT-5	CF_3	0.33	1205	2038
SERT-21	Cl	0.27	230	115
SERT-24	OCH_3	1.89	1990	2650
DASB	CN	1.10	1350	1420

Fig. 22 Binding affinity of 2-(phenylthio)arylamine derivatives to cloned human transporters

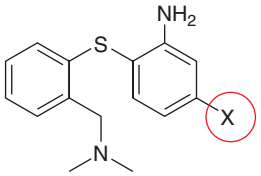

Name	X	LogD
SERT-5	CF_3	3.77
SERT-21	Cl	3.55
SERT-24	OCH_3	2.83
DASB	CN	2.71

Fig. 23 LogP of 2-(phenylthio)arylamine derivatives

the washout regions which contain significant levels of SERT. Furthermore, the TACs also show that the radiotracer reversibly binds to SERT within the timescale of the experiment.

As [^{11}C]SERT-5 showed promising *in vivo* SERT-targeting characteristics, a number of close analogues of the prototype—containing chlorine, methoxy, or nitrile substituents in place of the CF_3 moiety—were subsequently synthesized to determine if the properties of the prototype could be further improved (Fig. 22).

The affinity of the SERT-5 analogues were determined using cloned human cell lines expressing the serotonin transporter. These data show that all of the analogues have high affinity for SERT as well as hundred- to thousand-fold selectivity for the target over NET and DAT. The LogP values of the compounds were also measured using the octanol-water 'shake-flask' method, revealing that [^{11}C]SERT-5 had the highest log P value (3.77) of the compounds assayed (Fig. 23).

According to the 'logP 1–3' rule of thumb, the candidates with methoxy and nitrile substituents appear to have optimal lipophilicities for imaging the CNS. The regional distribution of these ^{11}C-labeled analogues of [^{11}C]SERT-5 was subsequently compared using an approach identical to that used in the initial evaluation of the parent radiotracer (Fig. 24).

The signal-to-noise ratios of each of these ^{11}C-labeled analogues were compared using the hypothalamus-to-cerebellum activity concentration ratios (Fig. 25) (Table 5).

In this analysis, the cerebellum—which has low expression of SERT—is treated as a reference region (the noise), while the hypothalamus, which has high expression of SERT, is the 'target-rich' region (the signal). In comparison to SERT-5, the data shows that DASB has the superior signal-to-noise ratio at time points 30–60 min post-injection. SERT-24 and SERT-21 also have good signal-to-noise ratios throughout the period studied compared to the prototype tracer.

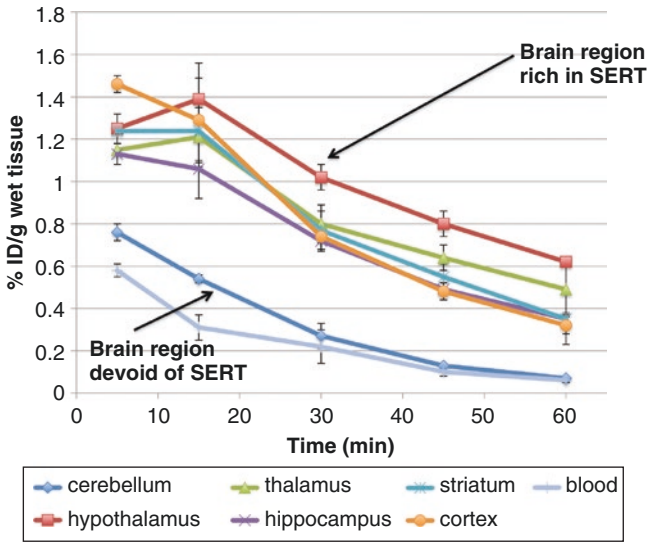

Fig. 24 Biodistribution of [^{11}C]DASB in rat brain

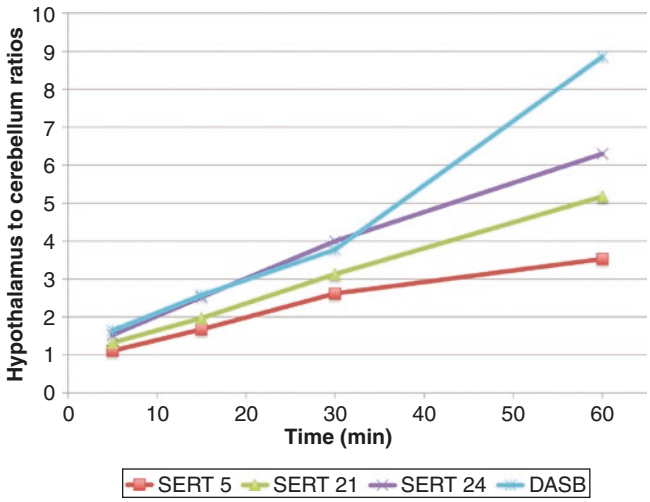

Fig. 25 Comparison of SERT radiotracers: signal-to-noise ratios in rats over 60 min

Table 5 Relationship between logD values, cerebellar clearance washout rates, and signal-to-noise ratios

Name	LogD	Cerebellar clearance rate (t_{half} min)	Signal-to-noise ratio
SERT-5	3.77	32	2.5
SERT-21	3.55	25	4.2
SERT-24	2.83	19	6.3
DASB	2.71	16	7.9

SERT serotonin transporter

Test Criterion 2: Appropriate *In Vivo* Pharmacokinetics

The TAC analysis also allows for an assessment of the pharmacokinetic profile of the radiotracer. More specifically, these data facilitate the determination of whether the kinetics of the tracer are reversible or irreversible over the time period studied. In all cases, [^{11}C]SERT-5 and its ^{11}C-labeled analogues displayed reversible kinetics *in vivo*. That is to say, their activity concentrations reached a plateau in the target tissue and then subsequently washed out of tissue during the timescale of the experiment). At this stage, in the evaluation procedure, it has been confirmed that the radiotracers are able to enter the brain, have appropriate regional distributions, have suitable pharmacokinetic profiles (*i.e.* are compatible with the half-life of carbon-11), and produce good signal-to-noise ratios *in vivo*. The most promising of these compounds—[^{11}C]DASB—was selected for further characterization.

Test Criterion 3: Appropriate *In Vivo* Pharmacology

To assess the appropriateness of [^{11}C]DASB *in vivo* pharmacology, rats were pretreated with a non-radioactive 'blocking agent' prior to the administration of the radiotracer. Tissue and blood TACs were then generated in a manner similar to that described above in order to explore whether or not there are any significant alterations to the radiotracer's signal-to-noise ratio alterations upon blocking.

The choice of blocking agents depends on a variety of factors. In the case of a SERT radiotracer, the selectivity of the radiotracer for SERT over DAT and NET is critical given the structural similarities between these proteins and the known off-target pharmacology of SERT compounds for these transporters. As a result, experiments in which animals are pretreated with selective SERT-, DAT-, and NET-targeting blocking agents are important (in addition to a 'vehicle'-only control experiment, of course). In addition, it is also useful to perform 'self-block' experiments in which a non-radioactive variant of the tracer is administered as a blocking agent (Fig. 26).

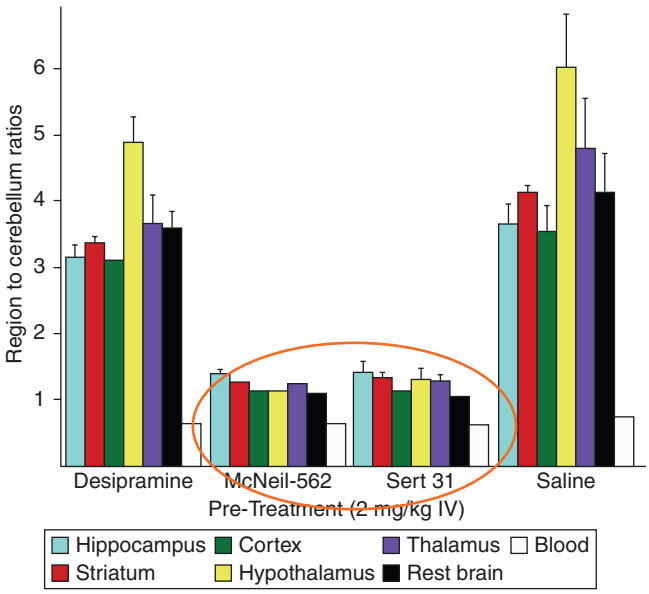

Fig. 26 Region-to-cerebellum activity concentration ratios of [^{11}C]DASB in rats pretreated with desipramine, McN-5652, SERT-31, and saline

These data reveal that [^{11}C]DASB administration with saline 'vehicle' results in the accumulation of the radiotracer in the hypothalamus as well as regions with intermediate expression of SERT. In contrast, blocking with non-radiolabeled DASB and McN-5652 (a known selective SERT blocker) dramatically reduces the radioactivity concentration in the hippocampus. In addition, the administration of desipramine (a reasonably selective NET blocker) does not significantly perturb the accumulation of the radiotracer in SERT-rich regions.

Similar experiments can be performed using inhibitors of the DAT as well as any other receptors enzymes that the radiotracer may be binding in a non-selective manner. In this case, pretreatment experiments using GB12909 (a DAT inhibitor), haloperidol (a dopamine D2 blocker), WAY100635 (a serotonin 5-HT$_{1A}$ blocker), ketanserin (a 5-HT$_{2A}$ blocker), and raclopride (a dopamine D2/D3 receptor blocker) produce no significant reductions in the regional distribution of [^{11}C]DASB. Based on this evidence, [^{11}C]DASB appears to have appropriate pharmacology for imaging SERT in the CNS, though the off-target binding of the radiotracer to other receptors/transporters cannot be absolutely ruled out unless tested.

Test Criterion 4: Radiolabeled Metabolites in the Region of Interest

After their administration, most radiotracers are subject to enzymatic breakdown or metabolism *in vivo*. This frequently results in the generation of radiolabeled metabolites that differ in structure from the parent compound. To test this possibility, [^{11}C]DASB was administered intravenously, and at selected

time points post-administration, blood samples and brain tissue were collected. The blood was analysed using radioHPLC to determine the amount of intact [^{11}C]DASB as well as the presence of ^{11}C-labeled metabolites. Figure 27 shows a profile of the radiometabolites of [^{11}C]DASB in the blood at 30 min post-administration, revealing that only 25% of the [^{11}C]DASB remains intact in the blood at this time point.

If any of these radiolabeled metabolites are capable of penetrating the brain, they can lead to background signal that can obscure the specific binding signal of [^{11}C]DASB. Yet conversely, if the metabolites cannot penetrate the brain, their influence on the signal in the area of interest is minimized.

A similar analysis of brain tissue at 30 min after the administration of [^{11}C]DASB can reveal if these blood-borne metabolites can cross into brain tissue. To this end, the brains of rats that had been administered [^{11}C]DASB were collected 30 mins following the administration the tracer, homogenized, and analysed via radioHPLC.

Figure 28 shows that over 95% of the radioactivity in the brain at 30 min postinjection corresponds to [^{11}C]DASB. Although 5% of the radioactivity corresponds to radiometabolites, the majority of the signal in the brain is due to parent compound. As a result, [^{11}C]DASB was considered suitable for further evaluation as a SERT-targeted imaging agent.

Test Criterion 5: Sensitivity Towards the Target

The ultimate purpose of a radiotracer is to test sensitivity of the imaging agent towards its target. In the case of [^{11}C]DASB, this was explored via an experiment aimed at determining whether the radiotracer could follow the differential occupancy of the SERT by an antidepressant drug and follow the drug's natural washout from the SERT over time. To this

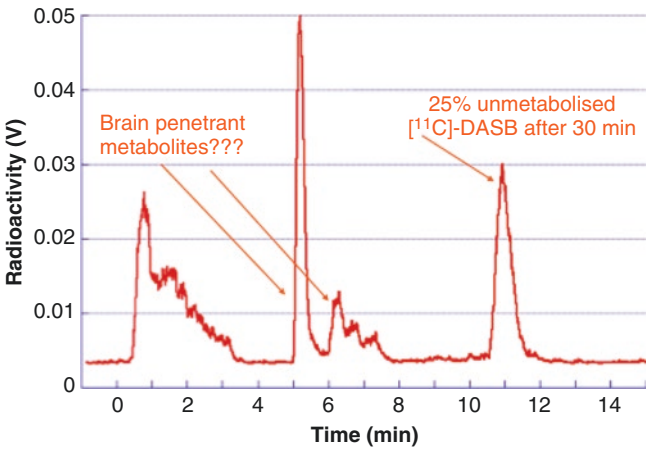

Fig. 27 HPLC analysis of rat plasma after the administration of [^{11}C]DASB

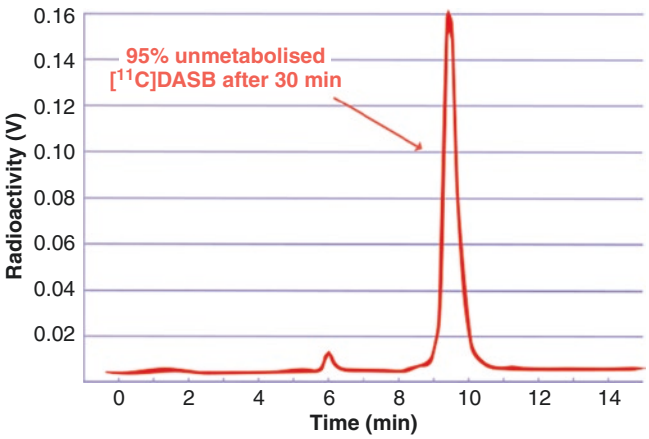

Fig. 28 HPLC analysis of rat brain extract after the administration of [^{11}C]DASB

end, rats were pretreated with paroxetine (a known SERT blocker) at various time intervals (1, 7, 24, and 28 h) and subsequently administered with [^{11}C]DASB. Brain regions were analysed for the presence of [^{11}C]DASB at 60 min post radiotracer administration (Fig. 29) [9].

The tissue (hypothalamus, striatum, cortex, and thalamus)-to-cerebellum activity concentration ratios show that, compared with the baseline condition, the paroxetine quickly occupies the SERT at around 1 h post-administration [9]. At 7 h post-administration of paroxetine, the occupancy of the SERT by paroxetine has slightly decreased (due to washout). And at 24 h following the administration of the paroxetine, the tissue-to-cerebellar activity concentration ratio of [^{11}C]DASB has returned back to the original (control) levels, clearly demonstrating that the radiotracer is sensitive to changes in the occupancy of the transporter by paroxetine [9].

Translation

Some radiotracers that look promising in preclinical studies can be unsuccessful upon translation to humans. [^{11}C]DASB, however, was successfully translated as a radiotracer for *in vivo* human SERT imaging: the clinical data revealed reversible pharmacokinetics and good regional distribution in humans (Fig. 30).

Additional clinical experiments confirmed the selectivity and sensitivity of the radiotracer for imaging SERT *in vivo*, and the tracer has since become a valuable tool for studying the function of SERT in humans (Fig. 31) [10].

Of course, the translation of imaging agents from animals to humans is not always as successful, as with the given example of [^{11}C]DASB. An example of a troublesome translation to humans is provided by the development of the serotonin 5-HT$_{1A}$ radiotracer [^{11}C]WAY100635 (Fig. 32).

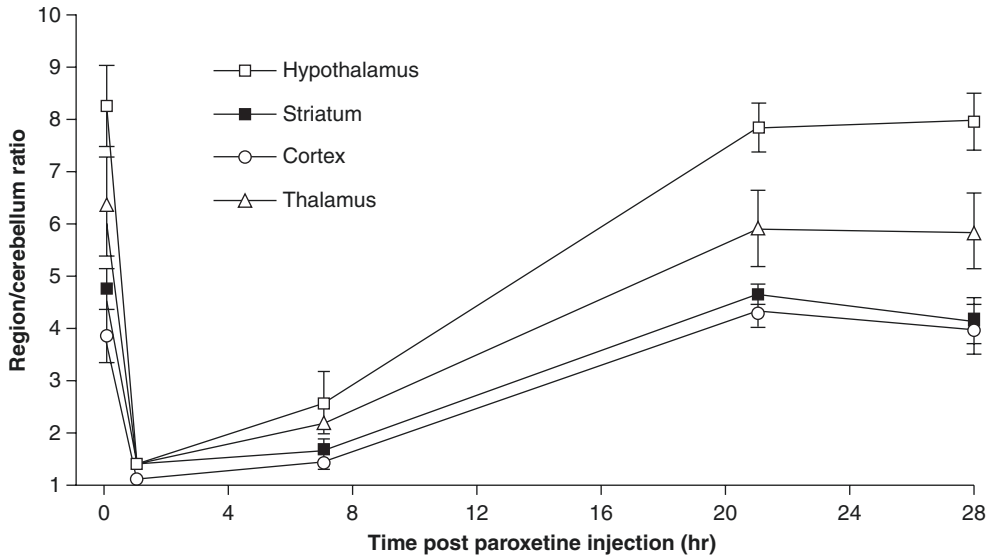

Fig. 29 [^{11}C]DASB: Recovery of binding after pretreatment with paroxetine (2 mg/kg, IV) (From Wilson et al. [9], with permission)

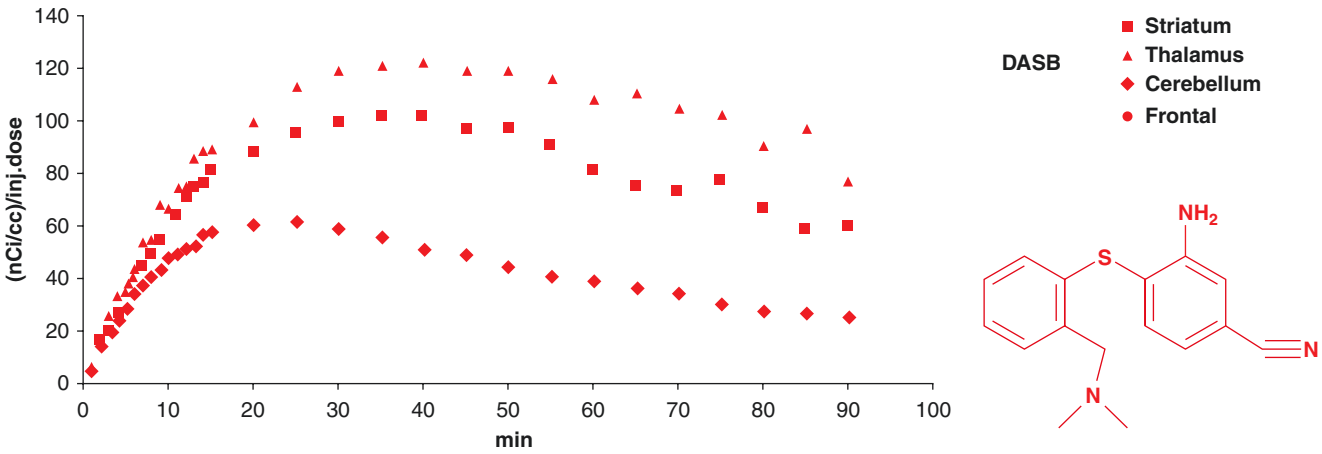

Fig. 30 Time-activity curves of [^{11}C]DASB in the CNS

When evaluated in rats, [^{11}C]WAY100635 demonstrated selective binding for 5-HT$_{1A}$ as well as an excellent signal-to-noise ratio. When first used in humans, however, the radiotracer suffered from poor signal-to-noise ratios, preventing the visualization of 5-HT$_{1A}$ receptor expression. Further analysis showed that there is a difference in the liver metabolism of this compound in humans compared to rats. In humans, an enzyme breaks down the parent molecule to a brain-penetrant metabolite which obscures the binding of the parent molecule to the receptor (Fig. 33a).

This problem was circumvented by labeling the molecule in a different position (Fig. 33a). In the case of [carbonyl-^{11}C]WAY100635, metabolism in the liver produced non-brain-penetrant metabolite instead, allowing this new radiotracer to become a very successful tool for the imaging of 5-HT$_{1A}$ receptors in humans. There are many other excellent examples of the development of radiotracers in the literature, including the creation of amyloid-targeted imaging agents and PSMA-targeting radiotracers.

Summary

In summary, when embarking on the development of a novel radiotracer, time should be taken to assess the design parameters discussed above in 'Part 1'. Only when these have been

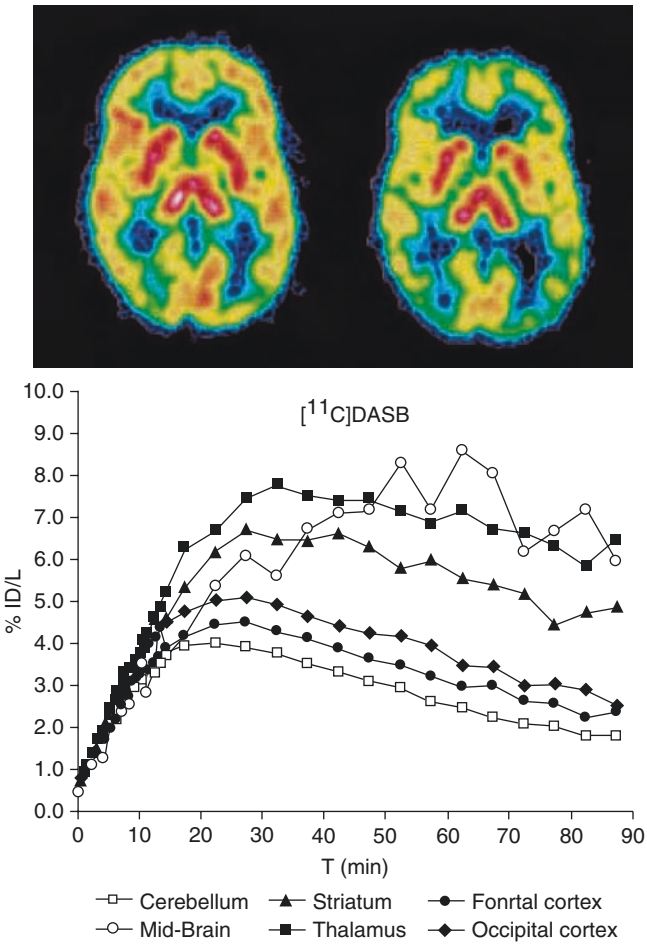

Fig. 31 Effect of citalopram (pretreatment versus post-treatment) upon [^{11}C]DASB scan. Treatment was with 20 mg of citalopram/day for 4 weeks. Images represent summated frames normalized to mean summated cerebellum value. (From Houle *et al.* [10], with permission)

satisfactorily addressed should a prototype compound be labeled and tested. Subsequently, the evaluation of this prototype radiotracer should include the test criteria addressed in 'Part 2'. Problems can arise at any point during the development of a radiotracer. Solving these problems may require revisions to the structure of the prototype radiotracer. In some cases, it may be possible to use an imperfect radiotracer for a particular application. In other cases, however, the project may have to be terminated or pursued using a new starting point or molecular scaffold.

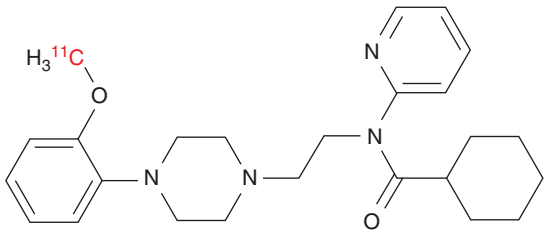

[^{11}C]WAY100635

- High affinity antagonist
- Selective for the 5-HT1A receptor
- Facile radiosynthesis with carbon-11
- Readily crosses the BBB
- Excellent signal-to-noise ration in rats

Fig. 32 Properties of [^{11}C]WAY100635

The Bottom Line

- There are a number of test and design criterion which should be used to maximize the chances of developing a successful radiotracer.
- The following design criteria should be assessed ahead of any experimental work:
  - The choice of an appropriate target
  - High affinity and selectivity for the target
  - Ease of radiosynthesis
  - Maximizing target accessibility while minimizing non-displaceable binding
- A minimum set of test criteria should be examined during the evaluation of a prototype radiotracer:
  - Good signal-to-noise ratio *in vivo*
  - Good *in vivo* pharmacokinetics
  - *In vivo* distribution and pharmacology consistent with literature reports
  - Low levels of radiolabeled metabolites in the region of interest
  - High sensitivity towards the target
- The translation of radiotracers from animals to humans is not always straightforward.

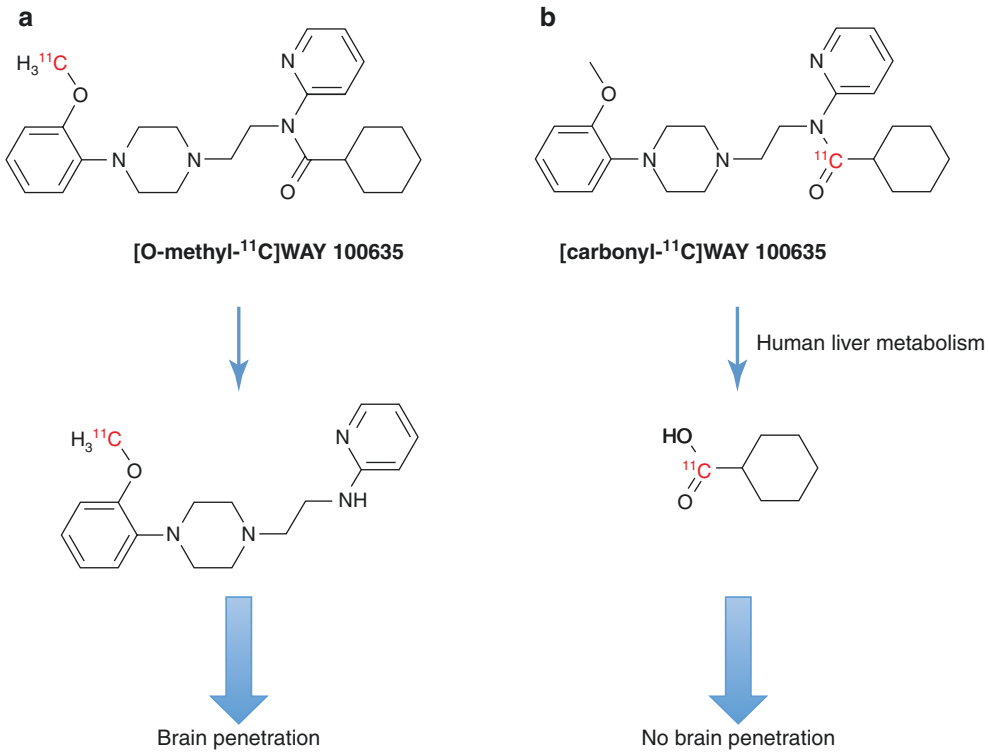

Fig. 33 Radiolabeling of [11C]WAY100635 at methyl and carbonyl positions

References

1. Chaturvedi S, Mishra AK. Small molecule radiopharmaceuticals – a review of current approaches. Front Med (Lausanne). 2016;3:5.
2. Kennedy C, Des Rosiers MH, Jehle JW, Reivich M, Sharpe F, Sokoloff L. Mapping of functional neural pathways by autoradiographic survey of local metabolic rate with (14C)deoxyglucose. Science. 1975;187(4179):850–3.
3. Varrone A, Pappatà S, Quarantelli M. Movement disorders: focus on Parkinson's disease and related disorders. In: Ciarmiello A, Mansi L, editors. PET-CT and PET-MRI in neurology. Cham: Springer International; 2016. p. 103–25.
4. Eckelman WC, Reba RC, Gibson RE, Rzeszotarski WJ, Vieras F, Mazaitis JK, et al. Receptor-binding radiotracers: a class of potential radiopharmaceuticals. J Nucl Med. 1979;20(4):350–7.
5. Patel S, Gibson R. In vivo site-directed radiotracers: a mini-review. Nucl Med Biol. 2008;35(8):805–15.
6. Waterhouse RN. Determination of lipophilicity and its use as a predictor of blood-brain barrier penetration of molecular imaging agents. Mol Imaging Biol. 2003;5(6):376–89.
7. Baciu M, Sebai SC, Ces O, Mulet X, Clarke JA, Shearman GC, et al. Degradative transport of cationic amphiphilic drugs across phospholipid bilayers. Philos Trans A Math Phys Eng Sci. 2006;364(1847):2597–614.
8. Wilson AA, Ginovart N, Schmidt M, Meyer JH, Threlkeld PG, Houle S. Novel radiotracers for imaging the serotonin transporter by positron emission tomography: synthesis, radiosynthesis, and in vitro and ex vivo evaluation of (11)C-labeled 2-(phenylthio)araalkylamines. J Med Chem. 2000;43(16):3103–10.
9. Wilson AA, Ginovart N, Hussey D, Meyer J, Houle S. In vitro and in vivo characterisation of [11C]-DASB: a probe for in vivo measurements of the serotonin transporter by positron emission tomography. Nucl Med Biol. 2002;29(5):509–15.
10. Houle S, Ginovart N, Hussey D, Meyer JH, Wilson AA. Imaging the serotonin transporter with positron emission tomography: initial human studies with [11C]DAPP and [11C]DASB. Eur J Nucl Med. 2000;27(11):1719–22.

Peptides as Radiopharmaceutical Vectors

Ryan A. Davis, Sven H. Hausner, and Julie L. Sutcliffe

The Fundamentals

In this chapter, we describe the core principles of choosing a lead peptide for the development of a radiopharmaceutical (*i.e.* the identification of a peptide sequence) as well as the process of synthesizing, radiolabeling, purifying, characterizing, and validating the *in vitro* and *in vivo* performance of radiolabeled peptides (Fig. 1). Our goals are to identify the most widely used strategies that have advanced radiolabeled peptides toward the clinic and to describe the lessons that have been learned along the way. In addition, some of the most innovative and noteworthy strategies for the radiolabeling of peptides have been included as well.

What Are Peptides? Why Do We Care About Them as Radiopharmaceutical Vectors?

Peptide-based pharmaceuticals have applications in both diagnostic imaging and targeted therapy [1–3]. As of 2014, more than 60 peptide-based pharmaceuticals have gained approval from the United States Food and Drug Administration (US FDA), with ~140 in clinical trials, half of which are diagnostic imaging agents. Remarkably, an estimated 500 more are currently in preclinical development [2–5]. Peptides are short chains of amino acids (AAs) linked by peptide ("amide") bonds (Fig. 2). They are relatively small in size—typically between 5 and 100 amino acids in length (~0.5–10 kDa)—and can have high binding affinity for receptors, high tumor penetration, and favorable pharmacokinetic profiles [4]. Most peptides are non-immunogenic and exhibit short *in vivo* circulation times (typically on the order of minutes to hours) that result in their rapid clearance from the blood pool and other nontarget tissues. Peptides are relatively easy to synthesize in high purity in a cost-effective manner, can be modified to improve their pharmacokinetic properties (*e.g.* via cyclization, AA substitution, capping, multimerization), and are amenable to site-specific radiolabeling. Together, these attributes make peptides a popular and promising choice as a platform for radiopharmaceuticals [1–4].

Peptides, Peptide Receptors, and Their Clinical Relevance

The development of peptides as radiopharmaceuticals for imaging or therapy has gained momentum thanks to advances in biochemistry, most notably the identification and characterization of numerous peptide-binding receptors that are selectively overexpressed in various diseased tissues, especially cancers (Table 1) [6–12]. One of the first examples of clinical imaging with a radiolabeled peptide was the use of [^{123}I-Tyr^3]octreotide to image the density of somatostatin receptors in patients with neuroendocrine tumors (NETs) [13]. Since this first report, a range of somatostatin receptor-targeted peptides labeled with a variety of radionuclides have been used to detect, stage, and treat NETs. The addition of somatostatin receptor imaging to computed tomography (CT) or magnetic resonance imaging (MRI) has been reported to change clinical treatment for 20–60% of patients, data which provides strong evidence for the value of these imaging agents. This success—exemplified by the FDA approval of NETSPOT (^{68}Ga-DOTATATE) in 2016 [14] and LUTATHERA (^{177}Lu-DOTATATE) in early 2018 [15]—has encouraged the field to develop radiolabeled peptides capable of targeting other receptors as well, including gastrin-releasing peptide receptors (GRPRs) and integrin receptors [3].

GRPRs are overexpressed in many cancers, including breast, pancreas, and prostate cancer. GRPR-mediated sig-

R. A. Davis · S. H. Hausner
Department of Internal Medicine, University of California Davis, Sacramento, CA, USA

J. L. Sutcliffe (✉)
Department of Internal Medicine and Department of Biomedical Engineering, University of California Davis, Sacramento, CA, USA
e-mail: jlsutcliffe@ucdavis.edu

J. S. Lewis et al. (eds.), *Radiopharmaceutical Chemistry*, https://doi.org/10.1007/978-3-319-98947-1_8

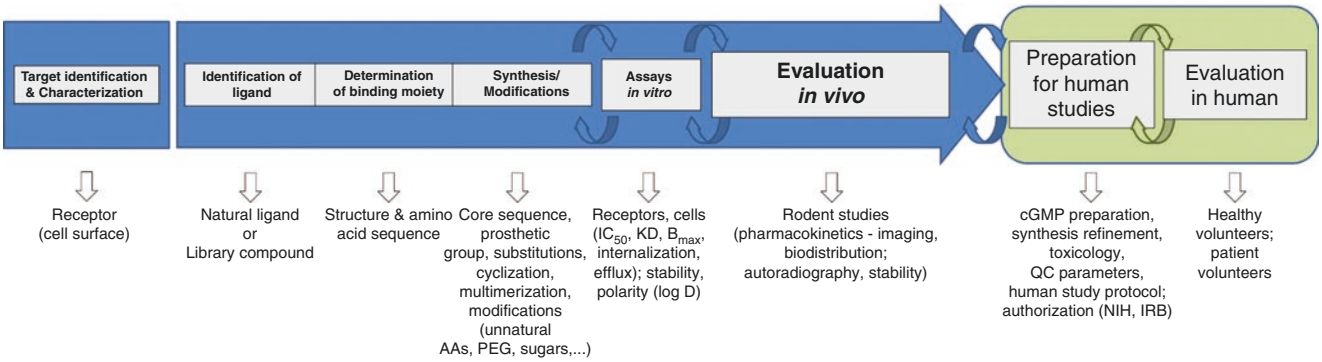

Fig. 1 An overview of the development of radiolabeled peptides

Fig. 2 General structure of a peptide comprised of α-amino acids

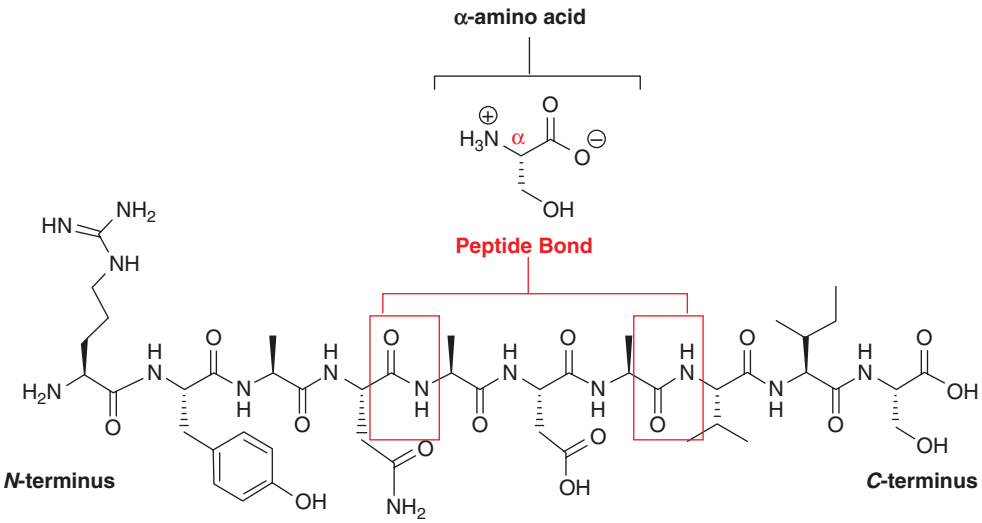

Table 1 Oncological targets for radiolabeled peptides [6–12]

Target	Base peptides
Chemokine receptor (CXCR4)	CPCR4/AcTZ14011
Cholecystokinin/gastrin receptor (CCK1R, CCK2R)	Cholecystokinin (CCK) analogs, Gastrin analogs
Extracellular tumor pH	pH (low) insertion peptide (pHLIP)
Gastrin-releasing peptide receptor (GRPR)	Bombesin (BBN), Gastrin-releasing peptide (GRP) analogs
Glucagon-like peptide-1 receptor (GLP1R)	GLP-1 analogs/Exendin
Integrin receptors ($\alpha_v\beta_3$, $\alpha_v\beta_6$, others)	Arginine-glycine-aspartic acid (RGD) peptides
Matrix metalloproteinase (MMP-2, MMP-9)	Activatable cell-penetrating peptides (ACPP)
Melanocortin 1 receptor (MC1R)	α-Melanocyte-stimulating hormone (α-MSH)
Neuropeptide Y receptors (NPYR)	Neuropeptide Y (NPY)
Neurotensin receptor (NT1, others)	Neurotensin (NT)
Somatostatin receptor (SSTR2, others)	Somatostatin analogs, Octreotide
Vasoactive intestinal peptide receptor (VIPR1)	Vasoactive intestinal peptide (VIP) analogs

naling has been linked to several oncogenic processes such as invasiveness and proliferation. The bombesin (BBN) family of peptides has been used to target GRPRs for both nuclear imaging and therapy, and the efficacy of these radiopharmaceuticals has been examined in several clinical studies [16–18]. The integrin family of cell surface receptors is likewise involved in a number of cellular processes, including cell proliferation, migration, angiogenesis, cell adhesion, and wound healing. In cancer, integrins can be responsible for the growth and metastasis of tumors, with their overexpression showing correlations with both tumor aggressiveness and the overall survival of the patient [19, 20]. The most studied integrin, $\alpha_v\beta_3$ (the vitronectin receptor), is overexpressed in numerous cancers—including melanoma, breast, and head and neck cancer—as well as in neo-angiogenic blood vessels [21]. It has been the target for both imaging and therapy using small peptides containing an arginine-glycine-aspartic acid (RGD) motif [11, 22, 23]. Another integrin, $\alpha_v\beta_6$, has also received significant attention because it is an epithelial-specific cell surface receptor that is undetectable in healthy adult epithelium but is significantly upregulated in a wide range of epithelial-derived cancers, including

pancreas, colon, non-small cell lung, ovarian, breast, and prostate cancer as well as oral squamous cell carcinoma [24, 25]. Radiolabeled peptides—such as those derived from the peptides $R_0$1, A20FMDV2, and H2009.1—have been shown to be effective imaging agents for $\alpha_v\beta_6$-positive tumors in preclinical investigations [26–28].

Peptide Identification

The first step in building a successful peptide-based radiopharmaceutical is the identification of a lead peptide. That initial peptide sequence depends largely on how much is known about the target of interest. Peptides have been developed through "rational design" (based on thoroughly studied target receptors or ligands) as well as through more "random" approaches employing combinatorial libraries (when little or nothing is known about a target). Before heading to the lab, the very first steps should be a thorough review of the literature on the biological and medical relevance of the target and the identification of any available structural and amino acid sequence information for the receptor and its ligands.

Rational Peptide Design Structural information such as X-ray crystallography or nuclear magnetic resonance (NMR) data for the receptor of interest or its natural peptide ligands can provide an excellent starting point for the design of a peptide [29]. For example, the cyclic RGDfV peptide developed by Aumailley *et al.* in 1991—which has become the foundation for numerous radiolabeled peptides targeting the integrin $\alpha_v\beta_3$—was developed through structure-activity relationship studies based on the knowledge that the three amino acid motif Arg-Gly-Asp (RGD) was essential for the binding of $\alpha_v\beta_3$ integrin to the extracellular matrix protein vitronectin [30–32]. Several other peptides derived from naturally occurring sources have also proven to be successful platforms for radiopharmaceuticals:

- The 8-amino acid cyclic peptide octreotide, which targets the somatostatin receptor and is based on the somatotropin-release inhibitory factor (SRIF) somatostatin discovered in hypothalamic extract [33]
- The 14-amino acid peptide bombesin (BBN), which targets gastrin-releasing peptide receptors and was isolated from skin extracts from the European fire-bellied toad [34]
- The 20-amino acid linear peptide A20FMDV2, which targets the integrin $\alpha_v\beta_6$ and was derived from a coat protein on the foot-and-mouth disease virus [35]

Indeed, this handful of examples offers a glimpse at the remarkable diversity of sources for peptide-based radiopharmaceuticals [29, 36].

Combinatorial Library Approaches Because rationally designed ligands cannot necessarily account for all possible targets, the discovery and development of completely novel peptide ligands for cellular targets remains of interest. This can be accomplished via the screening of combinatorial peptide libraries. These libraries contain large numbers (~10^4–10^7) of molecules with different amino acid sequences and structures. In practice, multiple identical copies of individual sequences are anchored on a scaffold that allows for the rapid screening and subsequent identification of potential lead peptides for further testing. Of the many combinatorial library technologies, the "one-bead-one-compound" (OBOC) and phage display libraries are the two most commonly used approaches for the discovery of novel cell-binding peptides [37, 38]. Both technologies are based on the principle of screening a large number of peptide sequences—*i.e.* a large number of beads or phage particles, each containing a unique, randomized peptide sequence—in a high-throughput manner. The scaffold for the phage display libraries is bacteriophage (phage), while the OBOC library relies on the use of solid polymer resin beads (Fig. 3). Each approach has advantages and disadvantages, but both have proven successful for the identification of ligands and have been reviewed in detail in the literature [37, 38].

Briefly, OBOC libraries are not limited to natural amino acids and can include unnatural and D-amino acids as well as peptoid monomers or other chemical modifications which can be exploited for designing highly stable peptide/peptoid libraries that are less susceptible to proteases. While the OBOC method is undeniably successful in identifying new ligands [39], the translation of OBOC-derived peptides into useful imaging agents is slow. Conversely, phage display libraries can be screened *in vivo*, and the generation of a phage display library can be more cost-effective than the synthesis of an OBOC library. Indeed, some phage display libraries are even commercially available. However, the filamentous phage commonly used for this method is prone to amplification bias during screening, and this approach is not amenable to the incorporation of unnatural amino acids or peptides bearing other chemical modifications. Before we move on, it is important to note one caveat that applies to both strategies. Because each individual phage or bead is covered by multiple copies of the same peptide, *avidity* effects can cloud the picture during the initial screening and identification process. More specifically, in the context of the screening assay, multiple copies of a peptide may bind to their cellular target via multivalent interactions that are facilitated by the presence of the phage or bead. As a result, when the peptide in question is later evaluated as a monomer, it is not uncommon to see a significant loss in binding *affinity* to the target.

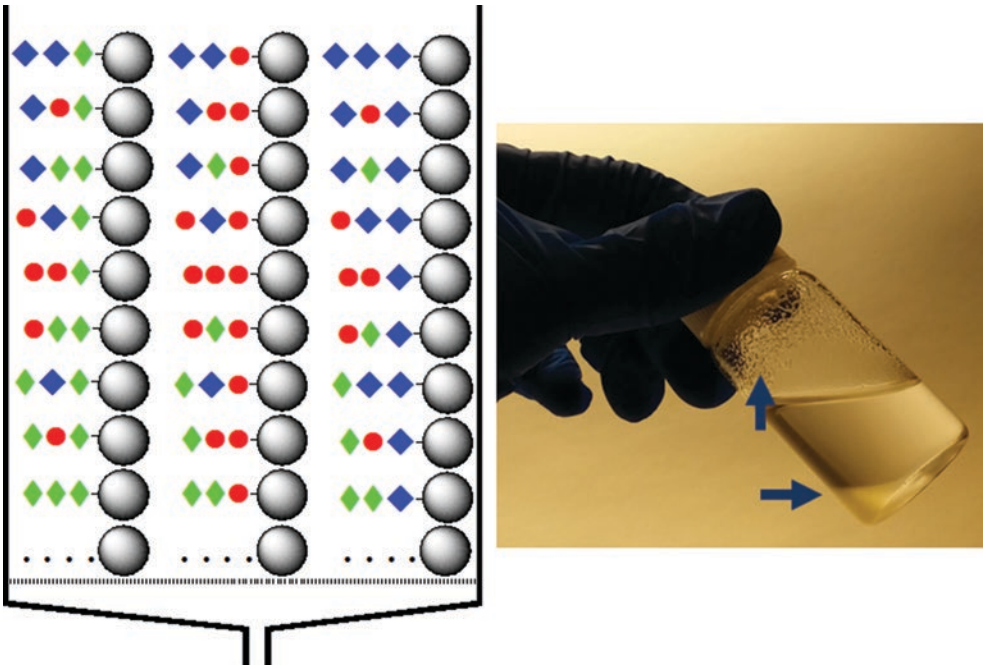

Fig. 3 Left: graphical illustration of a small OBOC library in a fritted reactor. Each polymer resin bead (gray sphere) carries numerous identical copies of the same peptide (*a.k.a* "compound"; one copy shown/bead). The colored shapes represent individual amino acid residues. The reactor, beads, and peptides are not drawn to scale. Right: Photo of an OBOC library in solution; the beads are visible at the bottom of the vial and on the glass wall (arrows)

Peptide Synthesis

Regardless of the origin of the sequence, the peptide of interest has to be synthesized for testing and use. Fortunately, highly reliable procedures and advanced strategies exist for the synthesis of peptides. These are detailed in many widely available protocols—for example, References [40–42]—and on the website of many companies that supply peptide synthesis services or reagents. Though fully assembled peptides (see Fig. 2) can be purchased from companies that perform custom peptide synthesis, we strongly encourage readers to consider in-house synthesis (Fig. 4). In-house synthesis affords the greatest control over the final product, provides the most flexibility (especially with regard to modifications), allows the use of newly developed reagents and functional groups [43], and requires only a small investment by a chemistry laboratory in reagents and consumables. We briefly describe the general peptide synthesis process below because aspects of it are also relevant for the creation of peptide-based radiopharmaceuticals. However, we direct the reader to the primary literature for more detailed information and discussions of more advanced procedures.

Convenience and reliability have made solid-phase peptide synthesis (SPPS) using *N*-9-fluorenylmethyloxycarbonyl (Fmoc) chemistry by far the most widely employed strategy [43]. This approach has been refined and optimized to the point at which the core synthesis of most peptides is a straightforward reiterative process. Many peptides can be prepared using automated SPPS synthesizers, though manual synthesis still allows for the best quality control during the synthesis and permits non-standard modifications.

Peptides are assembled from the *C*-terminus to the *N*-terminus, *i.e.* in the reverse direction as the sequence is written (see Fig. 4). The synthesis of a peptide on a solid support—*i.e.* on a scaffold in the form of surface-modified polymer resin beads bearing multiple copies of a cleavable linker—uses amino acids whose *N*-terminal amines are protected with the base-labile Fmoc-protecting group [40, 41, 43]. Any reactive amino acid side chains are protected in an orthogonal manner, usually with acid-labile protecting groups. This orthogonal protection is necessary to prevent unintended side reactions or polymerization. As shown in Fig. 4, the peptide chain is elongated by attaching each *N*-protected amino acid by reiterative amino acid coupling and Fmoc-removal cycles. The addition of each amino acid during SPPS occurs via the *in situ* activation of the carboxylic acid with an activating agent and subsequent coupling. The completeness of the reaction is ensured by using a multimolar excess of the incoming activated amino acid relative to the amount of peptide on the resin. The progress of each step can be checked using simple colorimetric tests, and excess reagents can be conveniently removed by filtration. To start the next coupling cycle, the *N*-terminal amine of the most recently coupled amino acid is deprotected—*i.e.* the Fmoc group is removed with base—and then the next amino acid is coupled. Once all of the amino acids have been coupled, a cleavage step liberates the peptide from the solid support and often removes the side-chain protein groups as well. The type of *C*-terminus that the peptide will contain—such as a carboxylic acid or an amide (shown in Fig. 4)—is determined at the very beginning of the synthesis by the type of linker on the resin. Following cleavage, the crude peptide is

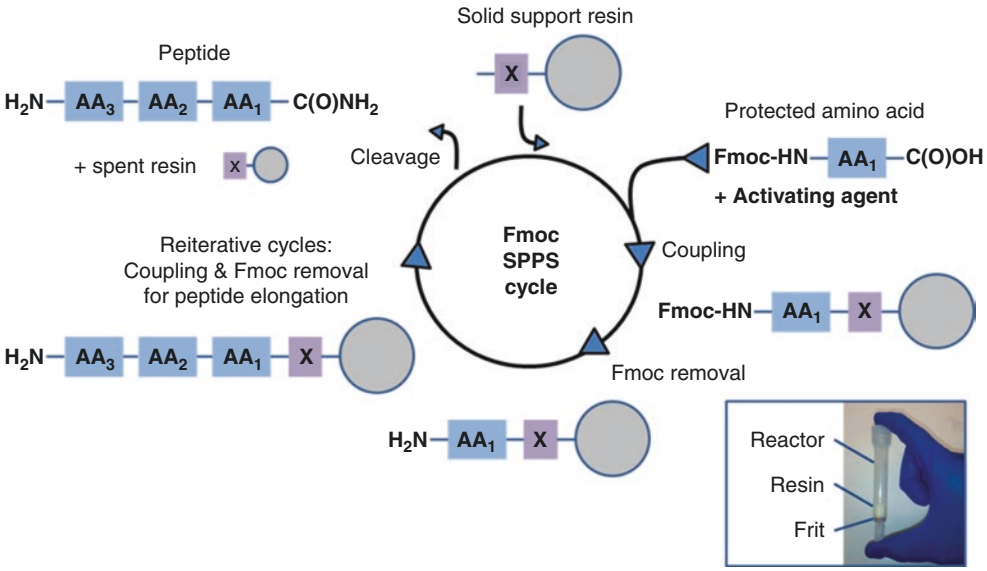

Fig. 4 General flow diagram for solid-phase peptide synthesis (SPPS) following Fmoc chemistry on an acid-cleavable scaffold. X cleavable linker, AA amino acid. The insert shows a typical reactor used for SPPS

ready for purification and/or post-assembly modifications such as cyclization. With regard to the colorimetric coupling test, rather than using the widely mentioned but cumbersome Kaiser (ninhydrin) test, the authors prefer the picrylsulfonic acid (PSA or TNBS) test for 1° amines and the chloranil test for 2° amines during manual synthesis [40, 44]. Several practical matters must be considered during peptide synthesis, including the type of resin (and linker) used, the amino acids and their (side-chain) protection, the coupling agents, and the strategies used for cleavage; reagents and solvents should be of high purity (preferably >99%) and have low moisture content [43].

The Resin (Scaffold) A variety of resins for SPPS can be purchased [41]. The main differences between resin types are the composition of the polymer support, swelling capacity, mechanical stability, loading capacity, linker for peptide attachment (which determines the *C*-terminus of the peptide), and the cleavage conditions required to remove the peptide from the resin. Generally speaking, low loading capacity and high swelling capacity are good for larger peptides, for which steric effects and aggregation can significantly affect coupling efficiencies. Examples of popular resins include Wang (yielding a *C*-terminal acid), 2-chlorotrityl (acid), Rink Amide (amide), and Sieber Amide (amide). When comparing *C*-terminal amides and *C*-terminal acids, peptides bearing the former tend to have higher *in vivo* stability. Therefore, choosing a resin that yields a *C*-terminal amide can be part of a strategy to guard against *in vivo* degradation by exopeptidases [45].

The Amino Acids A wide range of high-purity amino acids for Fmoc-based SPPS are available from commercial suppliers. Both the amino acids and their use have been reviewed in detail in peptide synthesis publications, for example, References [41–43] and the references cited therein. Here, we briefly list the standard orthogonal (acid labile) side-chain protecting groups that the authors routinely use for Fmoc-based SPPS: O-*t*Bu (aspartic acid, glutamic acid); *t*Bu (serine, threonine, tyrosine); Boc (lysine, tryptophan); Trt (cysteine, histidine, asparagine, glutamine), and Pbf (arginine).

The Activating Agent The activation of incoming amino acids to elongate peptide chains during synthesis is done by turning the carboxylic acid into a better leaving group in the form of an "activated ester." Uronium-based peptide coupling agents such as *N,N,N',N'*-tetramethyl-*O*-(*N*-succinimidyl) uronium tetrafluoroborate (TSTU) and 2-(7-aza-*1H*-benzotriazole-1-yl)-1,1,3,3-tetramethyluronium hexafluorophosphate (HATU) and their derivatives are very popular due to their rapid kinetics, low racemization, and easy and safe handling. They can activate the carboxylic acid group of amino acids under basic conditions, usually with Hünig's base (diisopropylethylamine) in DMF. However, because these coupling agents can cause the capping of the free amine when used in excess, they should be used in equimolar or slightly submolar amounts—*e.g.* 0.95-fold the amount of Fmoc-amino acid to be activated—and the Fmoc-amino acid should be activated with the coupling agent and Hünig's base immediately *prior* to addition to the H_2N-peptidyl-resin. Other options for activation include phosphonium-based reagents such as PyBOP and PyBrOP, which are not prone to capping. For peptide radiolabeling, the more stable succinimidyl, nitrophenyl, or polyfluorophenyl esters are preferred, since many protocols require the purification of the activated esters prior to coupling. In this regard, a notable exception is the solid-phase radiolabeling

approach developed by Sutcliffe *et al.* in which [^{18}F]fluoro acids are activated *in situ* with HATU or similar reagents for site-specific radiolabeling [46, 47].

The Solvent *N,N*-Dimethylformamide (DMF) is the most widely used solvent for Fmoc-based SPPS. The use of fresh, high-purity solvents (HPLC grade or better) is highly recommended, because small amounts of amine impurities, water, or solvent-decomposition products can affect coupling reactions and lead to unwanted side reactions. The swelling capacity of resins is solvent-dependent. Therefore, a solvent other than DMF may be advisable in some cases [41] such as incomplete coupling due to peptide aggregation or long peptide chains. *N*-Methylpyrrolidone (NMP), tetrahydrofuran (THF), dimethylsulfoxide (DMSO), dichloromethane (DCM), and 1,4-dioxane are common substitutes for DMF.

The Cleavage The fully assembled peptide is typically cleaved from the resin using acidic conditions, commonly trifluoroacetic acid (TFA) containing a small amount of scavenger reagents to trap highly reactive carbocations formed during the removal of protecting groups [48]. The global removal of the side chain protecting groups of the peptide can occur at this time as well. However, if special protecting groups were chosen, this step can be performed at a later stage [43].

Peptide Purification and Characterization Once a peptide has been synthesized and removed from the resin, it needs to be purified, and its purity, identity, and structure need to be confirmed. High-performance/high-pressure liquid chromatography (HPLC) is used for both purification and purity determination. Mass spectrometry [49], nuclear magnetic resonance [50, 51], Edman sequencing, and possibly even X-ray crystallography can be employed as well.

HPLC is described in greater detail below because it is also used extensively for the evaluation of the radiolabeled peptides. For details on MS, we refer the reader to the specialized literature [49] and only briefly want to highlight that MS can determine the peptide mass and whether cyclization or oxidation has occurred; however, it cannot distinguish between stereoisomers or constitutional isomers or—in its basic form—tell the difference between peptide sequences with the same amino acid composition but different amino acid order.

Radiolabeling of Peptides

The Choice of Radionuclide: The What and the Why? The radioactive half-life, emission profile, and chemistry of the radionuclide are all important considerations when radiolabeling a peptide. The biological half-life of many peptides is on the order of tens of minutes to hours, which suggests that peptides should be paired with radionuclides with similar physical half-lives. Fortunately, a wide selection of radionuclides exists, and many are available at research sites for use in positron emission tomography (PET), single-photon emission computed tomography (SPECT), and peptide receptor radionuclide therapy (PRRT) [15, 42, 52]. Several radionuclides that are often used with peptides are listed in Table 2. While those with half-lives <2 h likely require on-site production capabilities, most of the others are available from commercial suppliers at quantities sufficient for use with peptides. Many of the metallic radionuclides (radiometals) can be handled in quantities required for research on a shielded benchtop, though a shielded fume hood is preferable. In contrast, a hot cell is likely required for most work with fluorine-18.

The Position of the Radiolabel on the Peptide: The Where? The position of the radiolabel in the peptide is important because the behavior of a compound can be affected by the addition of this extra moiety. This is especially important for peptides, since most radionuclides have to be introduced using a bifunctional moiety that can simul-

Table 2 Widely used radionuclides for the radiolabeling of peptides

Radioisotope	Half-life (h)	Decay mode (%)	Production method	Application
Halogens				
F-18	1.8	β^+(97), EC(3)	Cyclotron	Imaging (PET)
I-123	13.2	EC(100), γ	Cyclotron	Imaging (SPECT)
I-124	100.3	β^+(23), EC(77)	Cyclotron	Imaging (PET)
I-131	192.5	β^-(100), γ	Reactor	Therapy
Metals				
Cu-64	12.7	β^+(19), β^-(40), EC(41)	Cyclotron	Imaging (PET); therapy
Ga-67	78.3	EC(100), γ	Cyclotron	Imaging (SPECT)
Ga-68	1.1	β^+(89), EC(11)	Generator	Imaging (PET)
Zr-89	78.4	β^+(23), EC(77)	Cyclotron	Imaging (PET)
Y-86	14.7	β^+(33), EC(67)	Cyclotron	Imaging (PET)
Y-90	64.1	β^-(100)	Generator/ Reactor	Therapy
Tc-99m	6.0	IT(100), γ	Generator	Imaging (SPECT)
In-111	67.2	EC(100), Auger, γ	Cyclotron	Imaging (SPECT); therapy
Lu-177	159.5	β^-(100), γ	Reactor	Imaging (SPECT); therapy

β^+ positron emission, β^- electron emission, *EC* electron capture, γ gamma emission, *IT* internal transition

taneously capture the radionuclide *and* bind to the peptide. When it comes to radiolabeling with prosthetic groups and chelators, peptide chemists are fortunate because peptides offer a range of possible attachment points for site-specific radiolabeling (Fig. 5). However, the size of many prosthetic groups and chelators is not negligible compared to the size of a typical peptide (for examples, see Figs. 6, 7, 8 and 9). As a result, the incorporation of the radiolabeling moiety can result in changes in the chemical, physiochemical, and binding behavior of the labeled peptide compared to its unmodified parent. Those changes can range from relatively minor (*e.g.* alterations in the excretion rate) to far more major (*e.g.* loss of affinity or specificity for their target).

In this regard, the development of integrin $\alpha_v\beta_3$-targeting cycloRGD peptides provides a good case study. In early versions of the peptide [cyclo(RGDyV)], the only seemingly good place for the attachment of a radiolabeling moiety would have been the side-chain carboxylate of the aspartic acid residue (D) (see Fig. 6). Alas, since the RGD motif is critical for binding and the peptide ring size could not be changed without affecting specificity, the peptide was redesigned to cyclo(RGDyK) or cyclo(RGDfK). Here, the side-chain amine of the lysine residue (K) provided a handle for functionalization which allows for the convenient and benign attachment of a prosthetic group. This—along with an additional modification (glycosylation) to improve the pharmacokinetics of the peptide—eventually lead to the [^{18}F] Galacto-RGD peptide used in clinical studies to image the expression of integrin $\alpha_v\beta_3$ [11, 53].

Even though the approaches for radiolabeling peptides can be roughly divided into two major groups—radiolabeling with halogens and radiolabeling with metals—they all share the need for stable attachment to the peptide. Therefore, before going into specifics, we will briefly highlight the most popular functional groups used for the radiolabeling of peptides shown in Fig. 5: (1) amines (*N*-terminus, lysine), (2) thiols (cysteine), (3) amino acids with orthogonal reactive groups (*e.g.* azides or alkynes), and (4) acids (*C*-terminus, aspartic, glutamic acid). If present in the peptide and not required for binding, each of these groups makes for a good first choice to anchor the prosthetic group or chelator. Ideally,

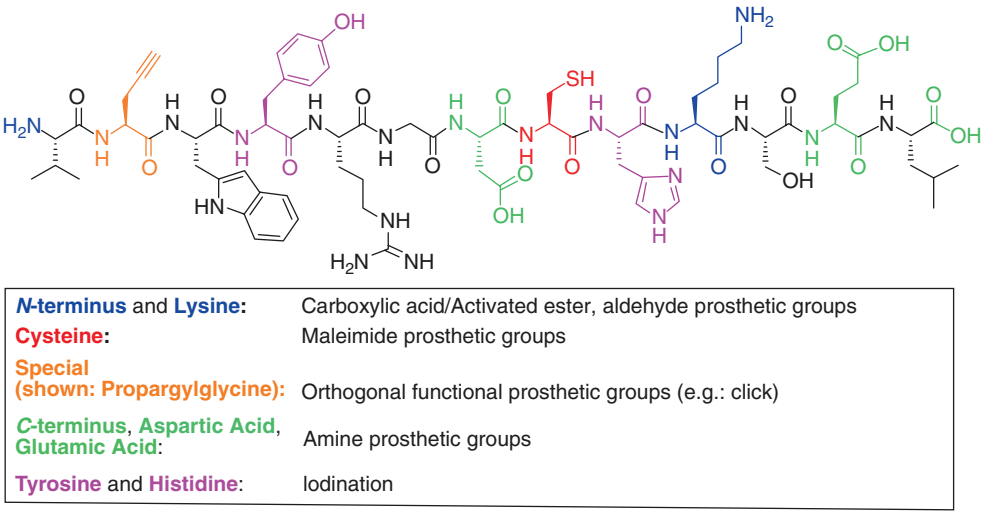

Fig. 5 Reactive sites on a representative peptide that can be used for radiolabeling

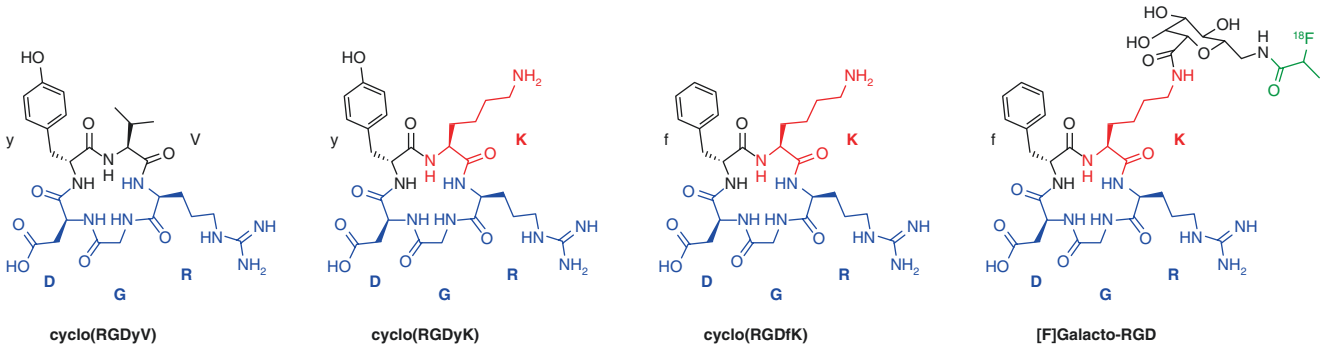

Fig. 6 The structures of several integrin $\alpha_v\beta_3$-targeting cycloRGD peptides. Key amino acid residues required for binding are depicted in blue; the major amino acid residue used for radiolabeling is highlighted in red; and the 2-[^{18}F]fluoropropionyl amide prosthetic group in [^{18}F] Galacto-RGD is shown in green. Standard one-letter amino acid abbreviations are used

only a single copy of the chosen functional group is present in the peptide to guarantee site-specific radiolabeling. In cases in which multiple copies of the chosen functional group are present, advanced (kinetics-based) approaches may work on occasion, but their success is far from guaranteed [54]. Non-site-specific radiolabeling is very much frowned upon in the peptide world and for good reason: as mentioned above, small changes in the structure of a peptide can have big effects on its *in vivo* behavior.

When available, the *N*-terminus is almost certainly the most popular site for radiolabeling, primarily because many amine-reactive prosthetic groups and chelators exist, for example, *N*-succinimidyl 4-[^{18}F]fluorobenzoate ([^{18}F]SFB) [6, 55, 56]. The capping of the *N*-terminus with a chelator or prosthetic group may confer the added benefit of increased *in vivo* stability of the radiolabeled peptide due to the blocking of exopeptidases. The attachment of the prosthetic group somewhere along the peptide backbone can take advantage of the same chemistry by labeling the ε-NH_2 group of lysine (see Fig. 5). The sulfhydryl group of cysteine can also be harnessed for mild radiolabeling (radiofluorination) using maleimide-containing prosthetic groups [57], but attention must be paid to avoid unwanted oxidation or dimerization reactions. Last but not least, the incorporation of an unnatural amino acid with chemistry orthogonal to all other common peptide functional groups provides a versatile and facile approach. In this regard, click chemistry synthons—*e.g.* azides or alkynes—are particularly popular [57].

Peptide Radiolabeling Approaches: The How? As we have mentioned, the strategies for radiolabeling peptides can be roughly divided into two major groups: radiolabeling with halogens and radiolabeling with metals. At present, the vast majority of halogen-based radiolabeling reactions rely upon the formation of covalent bonds between the radionuclide and the peptide. In contrast, radiolabeling reactions with metals are often predicated on the coordination of the radiometal with a chelator that has been attached to the peptide. Not surprisingly, these fundamental differences make for different kinds of practical approaches. For example, a chelator can be introduced at almost any time during the synthesis of a peptide, whereas a ^{18}F-labeled prosthetic group should only be incorporated closer to or at the end of the synthesis of the radiolabeled peptide.

Radiohalogens

As is evident in Table 2, the radionuclides of fluorine and iodine are the principal options for the radiohalogenation of peptides.

Radiofluorination Several very well-established protocols have been developed for the radiolabeling of peptides with fluorine-18 (F-18) for PET, though the field nonetheless continues to benefit from new developments. Fluorine-18 is a particularly suitable radionuclide for peptide-based radiopharmaceuticals because its physical characteristics—most notably its half-life (109 min) but also its low positron (β^+) energy (0.64 MeV) and high fraction of β^+ emission (97%)—pair well with the properties of peptides [58, 59]. The majority of radiosynthetic routes with fluorine-18 use nucleophilic substitution reactions to form the covalent bond with the radionuclide. Three main radiolabeling approaches have evolved over the last few decades:

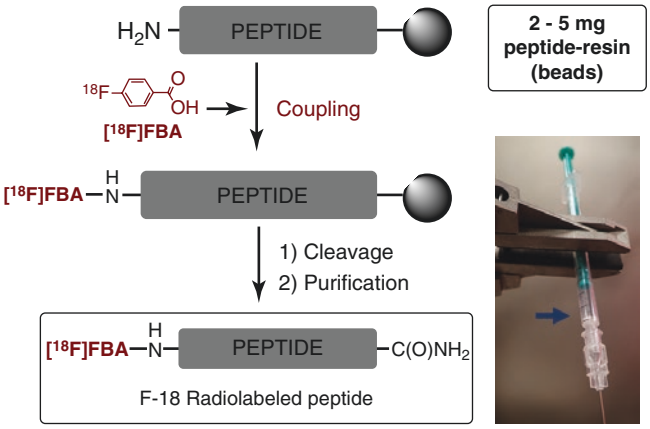

Fig. 7 Schematic showing the solid-phase radiolabeling with [^{18}F]fluoro acid of a selectively deprotected peptide on an acid-cleavable scaffold. The insert shows a photo of a fritted 1 mL syringe containing the beads (arrow)

Radiofluorination via Classic Prosthetic Group Chemistry

This approach is predicated on attaching an ^{18}F-labeled prosthetic group to a functional group within the peptide via a straightforward reaction, for example, an acylation, alkylation, or amidation.

Given the relatively harsh conditions required for the formation of a covalent bond with fluorine, the prosthetic group is first radiolabeled in a separate nucleophilic substitution step prior to the coupling of the ^{18}F-containing prosthetic group to the peptide under milder conditions [55, 60, 61]. While a great variety of ^{18}F-prosthetic groups have been developed, a few examples feature prominently and have been shown to work well with a wide range of peptides to yield radiopharmaceuticals in good radiochemical purity (≥95%) and molar activities (in the range of approximately 40–400 GBq/μmol) (see Fig. 8). However, this approach nonetheless requires a lengthy (~1–2 h) multistep synthesis and subsequent purification (commonly HPLC) to separate

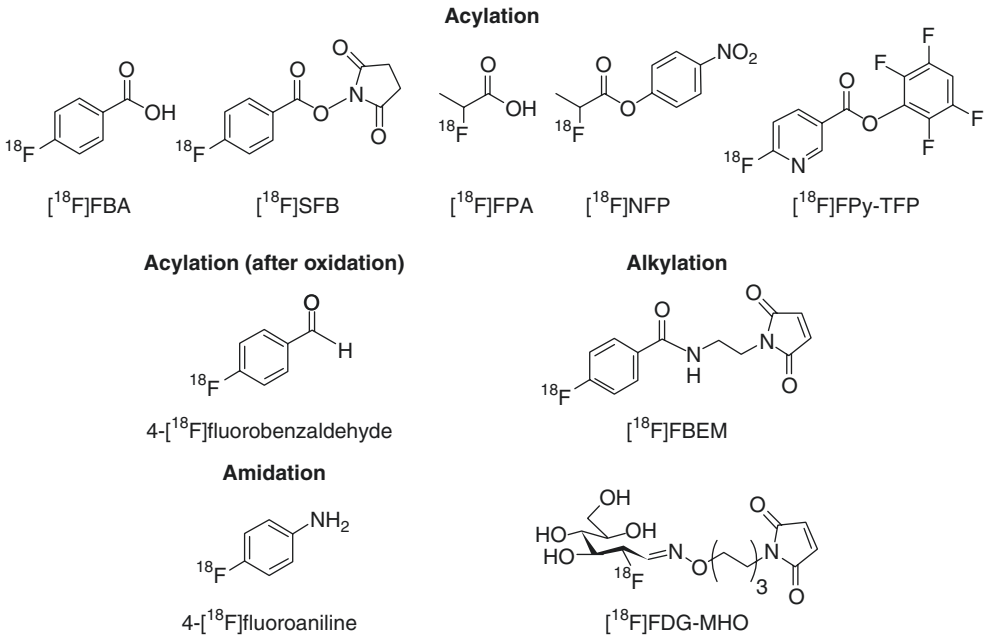

Fig. 8 Notable examples of ^{18}F-labeled prosthetic groups used for the radiolabeling of peptides using classical prosthetic group chemistry

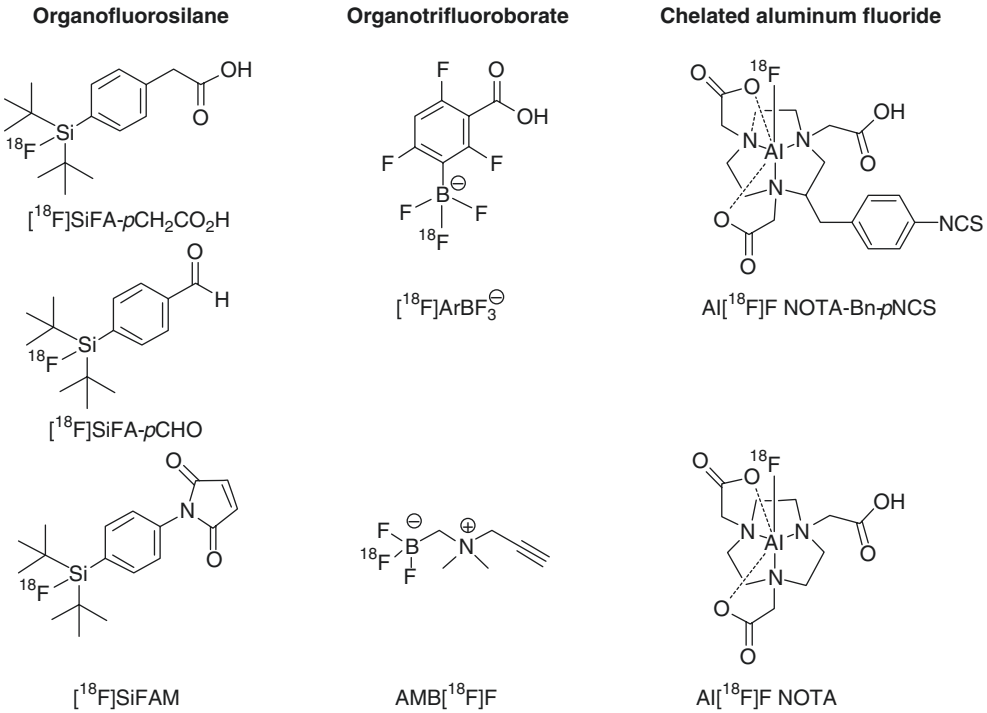

Fig. 9 Notable examples of ^{18}F-labeled prosthetic groups for the radiolabeling of peptides using fluoride capture chemistry. Note the overlap between this chemistry, classic prosthetic group chemistry, and click chemistry. For example, [^{18}F]SiFAM combines fluoride capture with thiol alkylation, while AMB[^{18}F]F combines fluoride capture with click chemistry

the ^{18}F-labeled peptide from unreacted peptide precursor, unreacted prosthetic group, and other by-products.

Amine-reactive ^{18}F-labeled prosthetic groups are typically based on carboxylic acids or activated esters, but aldehyde-based constructs have been used as well [36, 55, 62–64]. [^{18}F]fluoropropionic acid ([^{18}F]FPA), [^{18}F]fluorobenzoic acid ([^{18}F]FBA), and their activated esters—[^{18}F]NFP and [^{18}F]SFB, respectively—are commonly used for peptide radiolabeling via acylation [36, 55, 62, 65]. Initially developed by Vaidyanathan and Zalutsky in 1992 [66], [^{18}F]SFB remains one of the most widely used ^{18}F-labeled prosthetic groups thanks to its relatively reliable synthesis, good stability, good reactivity, and the stability of the [^{18}F]fluorobenzoyl group formed with the peptide. It is routinely synthesized in

three steps by first generating [^{18}F]FBA which is then activated with TSTU to form [^{18}F]SFB for coupling to the peptide (as illustrated in Fig. 10). Depending on the specific peptide, a simple cartridge solid-phase extraction (SPE) purification of the crude [^{18}F]SFB may suffice, though additional purification by reversed-phase HPLC may be required to ensure efficient coupling with the peptide of interest. The pros and cons of this approach, as well as more recent advances in this technology have been discussed in detail in the literature [55, 67, 68]. The case of [^{18}F]SFB offers several interesting insights into the intricacies of developing a successful prosthetic group; notably the development of [^{18}F]SFB took several years [55, 62, 66, 69]. Presently, [^{18}F]SFB is produced in approximately 30–40% decay-corrected (dc) radiochemical yield (RCY) in 60–70 min (SPE purification). The fully automated production of [^{18}F]SFB has paved the way for the solution-phase radiolabeling of a range of peptides, among them constructs targeting the α-melanocyte-stimulating hormone (α-MSH) receptor, integrin receptors, gastrin-releasing peptide receptors (GRPRs), and somatostatin receptors, just to name a few [36, 59].

Refinements to improve fluorine-18 radiolabelings with activated esters continue to this day. Among them is the development of [^{18}F]FPy-TFP (see Figs. 8 and 11), an activated ester in which the *N,N,N*-trimethylammonium triflate precursor is stable enough to withstand the reaction conditions required for the incorporation of fluorine-18, thus allowing for its conjugation to the peptide immediately after radiofluorination [70, 71].

Maleimide-containing prosthetic groups are the preferred choice for thiol-specific radiolabelings, with examples including [^{18}F]FBEM and [^{18}F]FDG-MHO (see Fig. 8) [36, 55, 61, 72]. The sulfhydryl group of the cysteine undergoes a Michael addition with the maleimide to form a thioether linkage that is sufficiently stable on a time scale relevant to most peptide radiopharmaceuticals. This reaction has been used for the solution-phase radiolabeling of integrin receptor-targeting peptides, apoptosis signaling peptides, neurotensin receptor-targeting peptides, human native LDL (nLDL), and tripeptide glutathione (GSH) [36, 55, 72, 73]. Maleimide prosthetic groups can provide an attractive alternative when the amine-based labeling of a peptide is not desirable due to steric reasons or concerns about the presence of multiple amine groups. In addition, this thiol-directed chemistry is very efficient, and thus only low amounts of peptide are typically needed for near-quantitative coupling under mild conditions. However, synthesis times may be long. For example, in a typical coupling reaction, [^{18}F]FBEM must first be prepared from [^{18}F]SFB and purified via HPLC before coupling to the peptide [72].

Solid-Phase Peptide Radiolabeling This approach, illustrated in Fig. 7, can be classified as the progeny of SPPS and classic prosthetic group radiolabeling. Many peptides can be synthesized in high purity on a solid support and may not require cleavage, purification, and formulation prior to radiolabeling. Thus, the peptide can be stored conveniently on solid phase until radiolabeling, thus reducing the number of handling steps and simplifying the workflow. Solid-phase peptide radiolabeling relies on the well-established procedures of SPPS and applies them to radiolabeling with prosthetic groups. As shown in Fig. 7 [46, 47], 4-[^{18}F]fluorobenzoic acid ([^{18}F]FBA) is activated *in situ* with an activating agent for coupling to the H_2N-peptidyl-resin, followed by cleavage and concomitant global deprotection, purification, and formulation. Convenience, reliability, and the possibility of site-specific radiolabeling (via the incorporation of orthogonal protecting groups during SPPS) make solid-phase radiolabeling attractive. The overall radiochemical yield—*i.e.* radiolabeling + cleavage efficiencies—can vary to some extent depending on the peptide sequence and the resin [74]. Good starting points are around 5–10 GBq [^{18}F]FBA, 2–5 mg H_2N-peptidyl-resin, and 15–30 min for coupling and cleavage each. The cleavage step may be extended or facilitated by slight warming, especially if several protecting groups such as Pbf—which can be prone to sluggish removal—are present.

Radiofluorination via [^{18}F]fluoride Acceptor Chemistry

Recently, several research groups have reported the direct incorporation of [^{18}F]fluoride into peptides by taking advantage of the high bond strengths of certain F-X bonds (X = Al, B, Si). These fluoride-capturing prosthetic groups (see Fig. 9) use acceptor moieties connected to the peptide and make radiofluorination considerably simpler by reducing it to as little as a single [^{18}F]fluoride capture step [55, 61, 75, 76]. Three chemistries in particular have been studied for the radiolabeling of peptides and may gain even more popularity in the future: organofluorosilanes, organofluoroborates, and chelated aluminum fluoride.

Organofluorosilanes The use of organosilane as a labeling prosthetic was first proposed by Rosenthal *et al.* who generated [^{18}F]fluorosilane in 65% yield by reacting n.c.a. (no carrier added) [^{18}F]fluoride with chlorotrimethylsilane in aqueous acetonitrile [77]. However, *in vivo* evaluation of the compound revealed poor stability as evidenced by high activity concentrations in the bone. Since this discovery, several silicon-based prosthetic groups—for example, [^{18}F]SiFA-*p*CHO (see Fig. 9)—have been developed for peptide radiolabeling, especially through the laudable efforts of the Schirrmacher laboratory [78]. Numerous derivatives have been synthesized which differ by the attachment point to the peptide and the bulky alkyl groups on the silicon (most com-

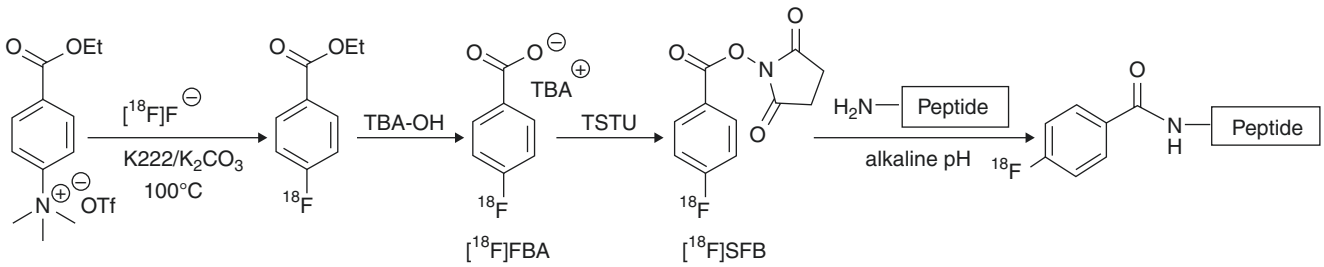

Fig. 10 Schematic showing the synthesis of [^{18}F]SFB using an *N,N,N*-trimethylammonium triflate ethylbenzoate precursor and tetrabutylammonium hydroxide (TBA-OH) base hydrolysis

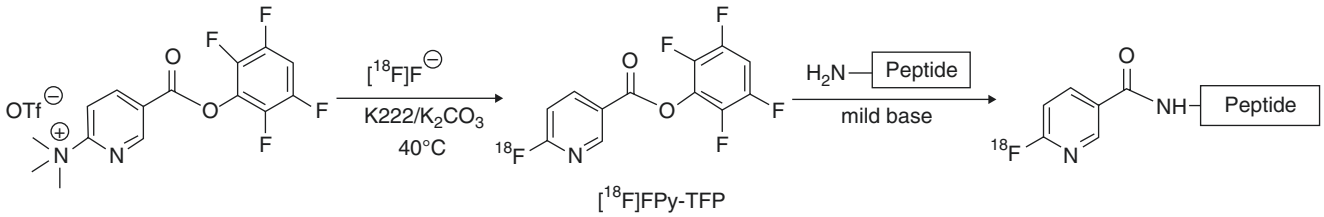

Fig. 11 Schematic showing the synthesis of [^{18}F]FPy-TFP using a *N,N,N*-trimethylammonium triflate precursor. The coupling to the peptide occurs under mildly basic conditions

monly *t*-butyl or isopropyl) that are required to minimize the hydrolysis of the Si-F bond [55, 76]. The prosthetic group is usually pre-attached to the peptide in the form of a hydrosilane or [^{19}F]fluorosilane and reacted with [^{18}F]fluoride in an atom exchange reaction, commonly a H-to-^{18}F or a ^{19}F-to-^{18}F exchange [77]. Somatostatin receptor-targeting peptides, gastrin-releasing receptor-targeting peptides, and integrin receptor-targeting peptides have all been radiolabeled with fluorine-18 using Si-based prosthetic groups. Radiochemical yields range from low single-digits to >75%, and molar activities commonly seen for radiolabeling with classic prosthetic group approaches can be achieved (40–670 GBq/μmol). Notably, in cases in which fluoride exchange is used for radiolabeling, the separation of the ^{19}F-labeled peptide from the ^{18}F-labeled peptide is not possible and, as a result, the molar activity of radiolabeled peptide can be low [77]. Provided that sufficiently bulky groups have been used to shield the Si-[^{18}F]F bond, organofluorosilane prosthetic groups can have excellent hydrolytic stability. However, this comes at the cost of increased lipophilicity and the significant steric demands of the prosthetic group. In addition, the high lipophilicity can result in slow, hepatobiliary clearance of the radiolabeled peptides, a trait which may be counteracted to some degree by the introduction of hydrophilic linkers or a positive charge within the prosthetic group [75–77].

Organofluoroborates This synthetic approach was created in an attempt to make to radiofluorination as easy as capturing the [^{18}F]fluoride ion in aqueous solution. Several different variations have been explored and—largely owing to the persistence of the Perrin group—have resulted in the development of AMB[^{18}F]F (see Fig. 9). AMBF is a zwitterionic trifluoroborate ammonium prosthetic group that has been used for the radiofluorination of bombesin and RGD peptides [79]. The key to this radiolabeling strategy is the ^{19}F-to-^{18}F radionuclide exchange reaction on the tri[^{19}F]fluoroborate prosthetic group attached to the peptide. This approach yields the formulated radiotracer in <30 min in approx 20–25% RCY and a molar activity of 80–160 GBq/μmol [79]. The small amounts of precursor required are essential for good molar activity, since the precursor peptide and the radiolabeled peptide cannot be separated. AMB[^{18}F]F is particularly attractive thanks to its small size and hydrophilicity, and it has been shown to be stable under physiological conditions, thus easing concerns about *in vivo* defluorination [75].

Chelated Aluminum Fluoride The development of aluminum [^{18}F]fluoride chelation chemistry was spearheaded by McBride and co-workers to mimic the facile radiolabeling reactions typically associated with metal ions [55, 80]. The two defining features of this approach are (1) that [^{18}F]fluoride readily reacts with $AlCl_3$ to form an "Al[^{18}F]F"$^{2+}$ species which then (2) can be captured by existing, commercially available chelators (*e.g.* NOTA) that are usually used for radiometals (see Fig. 9). Thus, the NOTA-bearing peptides used for radiometalation can also be used for radiofluorination without any modification. This versatility as well as the ease of the radiochemistry and *in vivo* stability of the Al[^{18}F]F-NOTA moiety have quickly made aluminum [^{18}F]fluoride chelation a popular route for the radiolabeling of

peptides. The radiochemical conversion depends on the concentration of the precursor, reaction temperature, pH, and the specific chelator used. Optimization can yield >90% isolated yield, >95% purity, and molar activities of 100–300 GBq/μmol in 20 min after cartridge purification. Even lyophilized kit formulations have been developed for one-pot syntheses [80]. Numerous peptides have been radiolabeled using this chemistry, beginning with the hapten peptide IMP449 used for pretargeting and including several RGD, octreotide, and bombesin peptides [55, 75, 80].

Radiofluorination via Click Chemistry

Click chemistry was first described in its current form by Sharpless *et al.* in 2001 and quickly adapted for many uses. Radiochemistry, of course, is no exception, and click chemistry has been used for a wide range of applications, ranging from more traditional [^{18}F]fluorine-carbon bond formation (Fig. 12) to fluorine-18 acceptor chemistry (see Fig. 9). With respect to radiofluorination, two types of click chemistry transformations have been particularly useful for radiolabelings using prosthetic groups: (1) the copper-catalyzed 1,3-dipolar cycloaddition reaction between an azide and alkyne [36, 55, 81, 82] and (2) the strain-promoted cycloaddition between cycloalkynes or *trans*-cycloalkenes and azido-compounds [83–85].

Marik and Sutcliffe first described the use of Cu(I)-mediated click chemistry (CuAAC) between azidopropionate-bearing peptides and aliphatic [^{18}F]fluoroalkynes [81]. This was soon followed by Glaser and Årstad, who explored the same chemistry with reversed functional groups [82]. More recently, the click chemistry toolbox has expanded with the development of the even faster and bioorthogonal strain-promoted 1,3-dipolar cycloadditions and inverse-electron demand Diels-Alder (IEDDA) reactions between tetrazines and the strained *trans*-cyclooctene (TCO) [61, 83, 84, 86]. This evolution—particularly the development of IEDDA chemistry—offers the possibility of carrying out click reactions in biological environments.

The use of click chemistry for radiolabeling is certainly worth considering, as evidenced by the numerous peptides successfully radiolabeled with click-based prosthetic groups, including variants of RGD, octreotide, neurotensin-targeting peptides, and others [85]. When choosing a click chemistry pair, it is important to keep several things in mind, as also noted in reference [84]: though the strain-promoted chemistries offer superior reaction rates, the synthesis of prosthetic groups based on these moieties can require much longer preparation times. Moreover, these reagents may not be very stable, and the resulting prosthetic groups are large and lipophilic compared to the peptides that they are being attached to. A big advantage of these reactions, however, is that HPLC purification may not be needed. In contrast, the rate of the CuAAC reaction is still sufficiently high for most peptides, and the Cu(I) can be stabilized with a small amount of commercially available stabilizing chelator such as TBTA, ultimately resulting in good conversion yields within 10–20 min. Importantly, for CuAAC, the precursor reagents are generally widely available at low cost, and the fluorine-18 can be introduced using simple one-step reactions that yield stable [^{18}F]fluoro-click synthons [81, 82]. In this regard, HPLC purification is a small price to pay for the synthesis of the radiolabeled peptide.

Automation of Radiolabeled Prosthetic Groups

Automated radiosyntheses are certainly not limited to fluorine-18 radiochemistry, but the need for speed as well as the multistep nature of many [^{18}F]radiofluorinations certainly

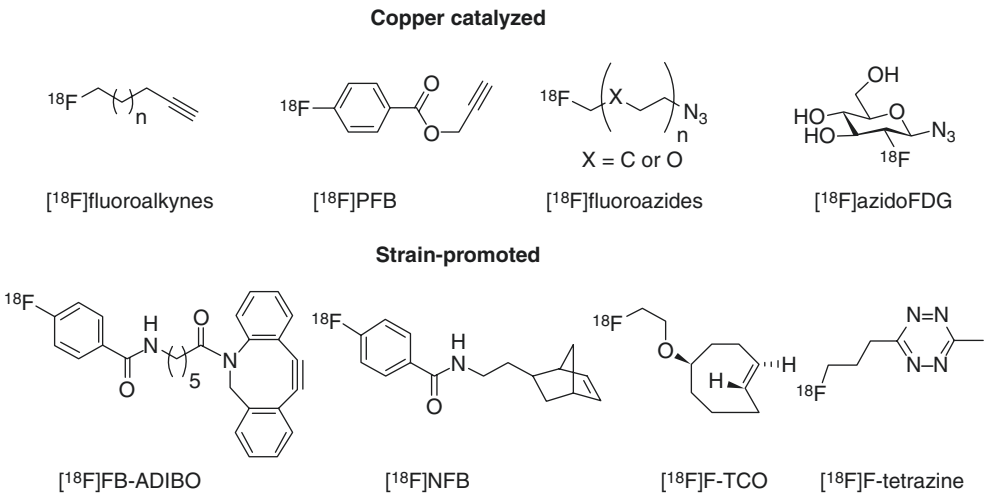

Fig. 12 Notable examples of ^{18}F-labeled prosthetic groups used for the radiolabeling of peptides with click chemistry

warrants automation. All the typical selling points apply: automation minimizes radiation exposure to personnel [87], enables the facile optimization of synthesis conditions, and supports reliable and reproducible reactions under current good manufacturing practice (GMP) procedures. Although automation offers the promise of simplicity, it can also introduce another level of complexity because of the many different types and models of radiosynthesizers being marketed. Each, of course, has its own set of strengths and weaknesses. Luckily for the aspiring radiochemist, this choice is typically made for them by what is available in the laboratory.

All that said, largely *because* of the multistep nature of peptide radiofluorination and the need of purification, the use of automation for the ^{18}F-labeling of peptides has focused mainly on the synthesis of the prosthetic groups themselves. Here, numerous automated syntheses have been reported, including preparations of [^{18}F]SFB, [^{18}F]FBA, [^{18}F]FBEM, azido-^{18}F-sugars [88], [^{18}F]hexafluorobenzene [89], and [^{18}F]fluoroethylazide [55, 90]. Yields, molar activities, and purities are generally similar or better than those obtained via manual synthesis, with predictable reaction times as well. Fully automated protocols capable of generating ^{18}F-labeled peptides from [^{18}F]fluoride with no manual interventions are still lacking, even for peptides under clinical investigation. This is due in large part to the instrumental complexity required to prepare and purify both a prosthetic group and a final ^{18}F-labeled peptide [55, 67, 91]. Therefore, the automation of peptide radiolabeling from the delivery of the radionuclide to the final formulation of the radiotracer remains an area of active research. Thanks to the continued strong interest in clinical tracers, progress can be expected in the coming years.

Radioiodination

Radioiodination continues to be an option for the radiolabeling of peptides, though it is pursued much less frequently than radiofluorination or radiometalation. That is at least partially due to the somewhat limited availability of radionuclides of iodine as well as concerns about handling the various radioisotopes of the element. That said, the use of radioiodine has not completely fallen out of favor because several nuclides are available, enabling both imaging (I-123 for SPECT; I-124 for PET) and therapy (I-131). The direct incorporation of iodine via oxidative chemistry provides the most straightforward approach to radioiodination, typically with chloramine-T as the oxidant [12, 36, 56].

The direct incorporation of radioiodine can take place at tyrosine or histidine residues by electrophilic addition. For tyrosine, the radioiodine is incorporated at one of the two positions *ortho* to the hydroxyl group; for histidine, the radionuclide is attached at one of the two imidazole methine positions. If these residues are not present in the peptide, cannot be used for radiolabeling because they are required for target binding, or if the peptide contains other oxidization-sensitive residues, then amine functionalities can be leveraged for radioiodination using a pre-labeled prosthetic group: the Bolton-Hunter reagent [(3-(4-hydroxyphenyl) propionic acid *N*-hydroxysuccinimide ester; Fig. 13] [12, 36, 56]. Once the radioiodinated Bolton-Hunter reagent has been synthesized, the coupling chemistry is identical to that of the other succinimidyl ester-based prosthetic groups discussed above (*e.g.* [^{18}F]SFB).

Radiometals

Most of the peptide-based imaging agents in the later stages of preclinical development and beyond—and certainly all of the peptide-based radiopharmaceuticals intended for PRRT—have at least one radiometalated variant currently being studied or used. Indeed, radiometalated peptides have been extensively described and discussed in many excellent reviews [3, 6, 15, 52, 92–94]. As illustrated in Table 2, a wide range of radiometals can be used to radiolabel peptides. This variety of options—together with simple "bake & shake" radiolabeling protocols—makes radiometals particularly attractive for peptide-based radiopharmaceuticals. Overall, there is considerable overlap between the radiolabeling of peptides and the radiolabeling of proteins and antibodies, both in terms of radionuclides used and metal-capturing chemistries employed. However, because of their rapid pharmacokinetics, several shorter-lived radionuclides (*e.g.* gallium-68) are especially useful in conjunction with peptides.

Just as for radiolabeling of antibodies with radiometals, the introduction of a radiometal into a peptide involves five basic steps: (1) the selection of the radiometal, (2) the selec-

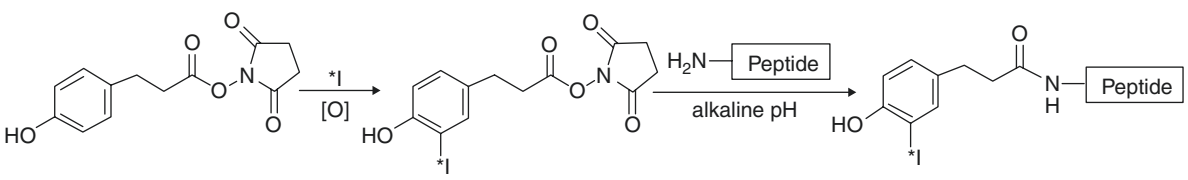

Fig. 13 Synthetic route for the radioiodination of peptides using the Bolton-Hunter reagent

tion of the appropriate chelator for that radiometal, (3) the conjugation of the chelator to the peptide, (4) the chelation of the radiometal, and (5) the purification and formulation of the final radiolabeled construct. Chelators are small molecules that sequester metal ions by using several donor atoms to form a number of bonds with the metal. Over the last 20 years, both the number of radiometals and the variety of chelators have rapidly increased along with growing knowledge about preferable metal-chelator pairings (Fig. 14) [6, 92, 93].

While the actual radiolabeling of the peptide is done in solution, the conjugation of the chelator to the peptide can occur in solution or, even more conveniently, during SPPS. Frequently, the chelator is attached at the amine of the *N*-terminus or a lysine side chain (Fig. 15). In solution, this can be done by using a chelator bearing an activated ester or through in situ activation. For conjugation during SPPS, selectively protected chelators—*e.g.* tri-*tert*-butyl 1,4,7,10-tetraazacyclododecane-1,4,7,10-tetraacetate, DOTA tris(*t*-Bu ester)—can be used with the standard protocols for in situ activation and protecting group removal. Fortunately for radiochemists, a variety of chelators is commercially available to work with a wide range of chemistries, as illustrated in Fig. 15. Catalogs commonly list the chelators as "bifunctional chelators" (BFCs), since they are designed to be covalently conjugated to a biomolecule *and* to coordinate the radiometal ion.

A brief note of caution should be added here when considering BFCs conjugated via an isothiocyanate group (-NCS). Though these bifunctional chelators are quite popular for conjugation to antibodies, isothiocyanates *can* result in unintended Edman degradation when used with peptides. Isothiocyanates are amine-reactive, and—as long as they are conjugated in solution and strongly acidic conditions are avoided—there should not be any peptide-related concerns. However, isothiocyanates should not be coupled to the *N*-terminus of a typical α-amino acid *on solid phase* because the thiourea formed by the conjugation will undergo Edman degradation involving a five-membered ring species during the TFA-induced cleavage step (Fig. 16). Luckily, the conjugation of isothiocyanates to β-amino acids and the side chains of lysines proceeds without incident. Obviously, the conjugation of chelators is not limited to amine groups within peptides. Several of the other reactive sites discussed previously—including carboxylic acids and thiols—can be used as well (see Fig. 5), and a wide range of bifunctional chelators are also available for couplings to these functional groups (see Fig. 15).

Metallic Radionuclides As listed in Table 2, the main radiometals for PET imaging are gallium-68, copper-64, yttrium-86, and zirconium-89. Gallium-67, technetium-99m, indium-111, and lutetium-177 are used for SPECT imaging, and the radiometals used for therapeutic applications include yttrium-90, indium-111, and lutetium-177 [6, 93]. Since several metals have multiple radioisotopes with different types of decay, simply choosing a different isotope of the same metal can result in a peptide-based radiopharmaceutical useful imaging, radiotherapy, or even both (*a.k.a.* a theranostic radiopharmaceutical). Examples of elements for which there are multiple radioisotopes include gallium-67/68, yttrium-86/90, and copper-60/61/62/64. Since all isotopes of a given element have identical chemical characteristics, switching from one radioisotope to another will result in a pair of peptide-based radiopharmaceuticals that behave identically with respect to chemistry and pharmacokinetics.

Selecting a metal radionuclide for peptide radiolabeling can feel a bit overwhelming because of the large number of options available. The candidate pool can usually be narrowed down by the application (*i.e.* emission type), availability, and radioactive half-life of the radionuclides. Because many peptides have rapid pharmacokinetic profiles, short-lived radionuclides are often appropriate choices, especially in the context of imaging. As a result, gallium-68 ($t_{1/2}$ = 68 min) is an especially popular choice for radiolabeled peptides for PET imaging.

The selection of a metallic radionuclide for peptide radiolabeling can also be influenced by the stability of the peptide at various pH values. Some radiometals must be coordinated at low pH to avoid the formation of insoluble precipitates, while others capture the radiometal most efficiently at higher pH. For example, when radiolabeling with tricationic radiometals—such as indium-111, yttrium-86/90, lutetium-177, gallium-67/68—the pH needs to be kept below 5, as higher pH ranges lead to the formation of insoluble colloidal metal-hydroxide species. Along these lines, the dicationic radioisotopes of copper are popular choices because of their flexible coordination chemistry, which can tolerate a wide range of pH values, roughly pH 4–9.

Radiolabeling Peptides with Radiometals As discussed, the chelator is generally covalently attached as part of the peptide synthesis prior to radiolabeling. High-purity (low trace metal) solvents should be used throughout the synthesis and purification of the chelator-bearing peptide in order to avoid contamination with trace metals. The radiolabeling is then carried out in a separate step by incubating the chelator-containing peptide with a solution of the radiometal. Since radiometalations are often quantitative, the purification of the radiolabeled construct may consist of a simple cartridge-based purification before the formulation of the final radiopharmaceutical. For detailed optimized reaction protocols, we refer to the primary literature [95]. Typical conditions are illustrated by radiolabelings with copper in which [*Cu]$CuCl_2$ in aqueous ammonium acetate buffer (pH 6–7) is incubated with nano-to-micro molar amounts of a NOTA- or DOTA-containing peptide for several minutes at ambient or slightly elevated temperatures (up to ~50–80 °C). Subsequently, a

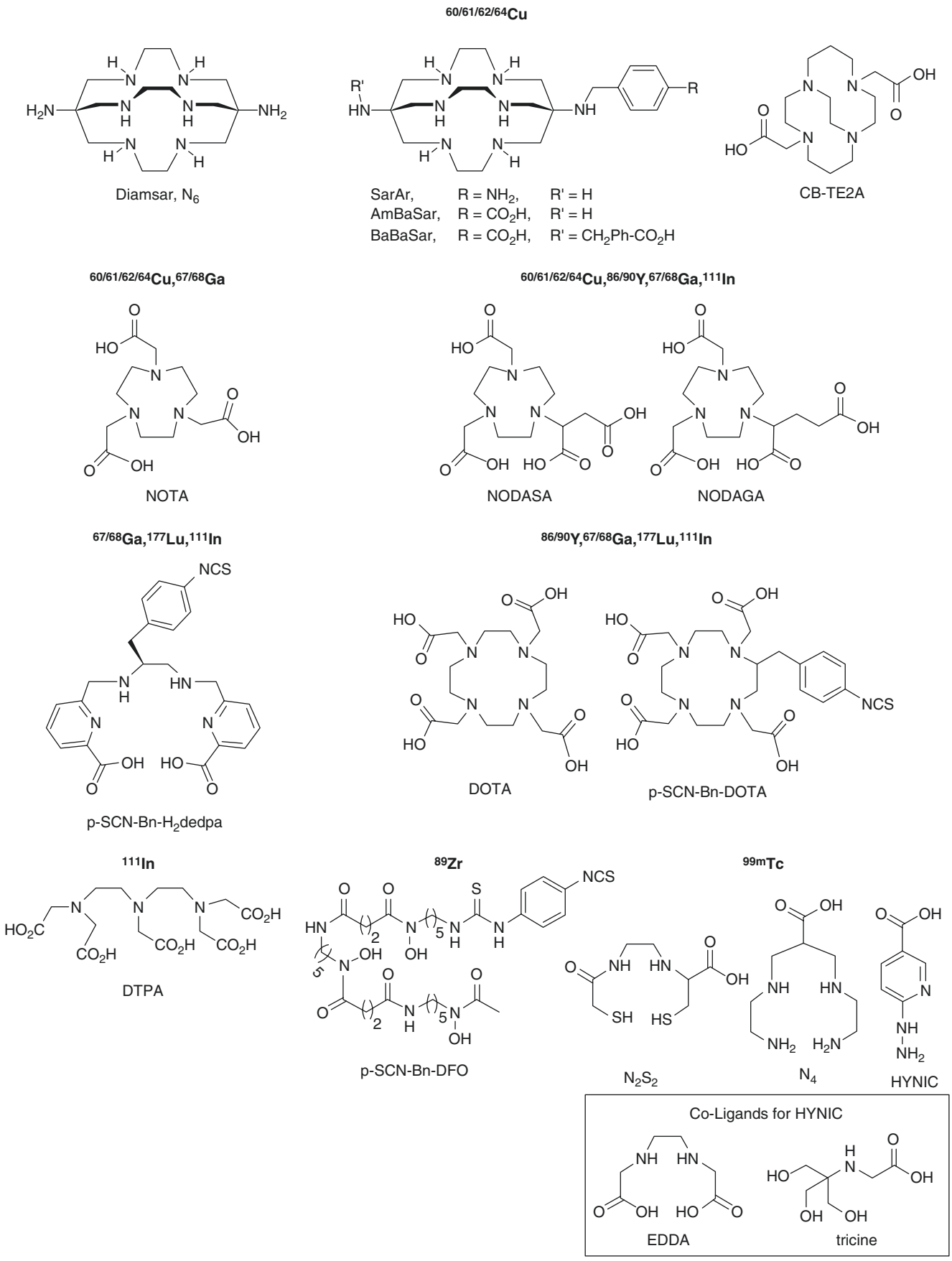

Fig. 14 Examples of common radiometal/chelator pairings used for the radiolabeling of peptides

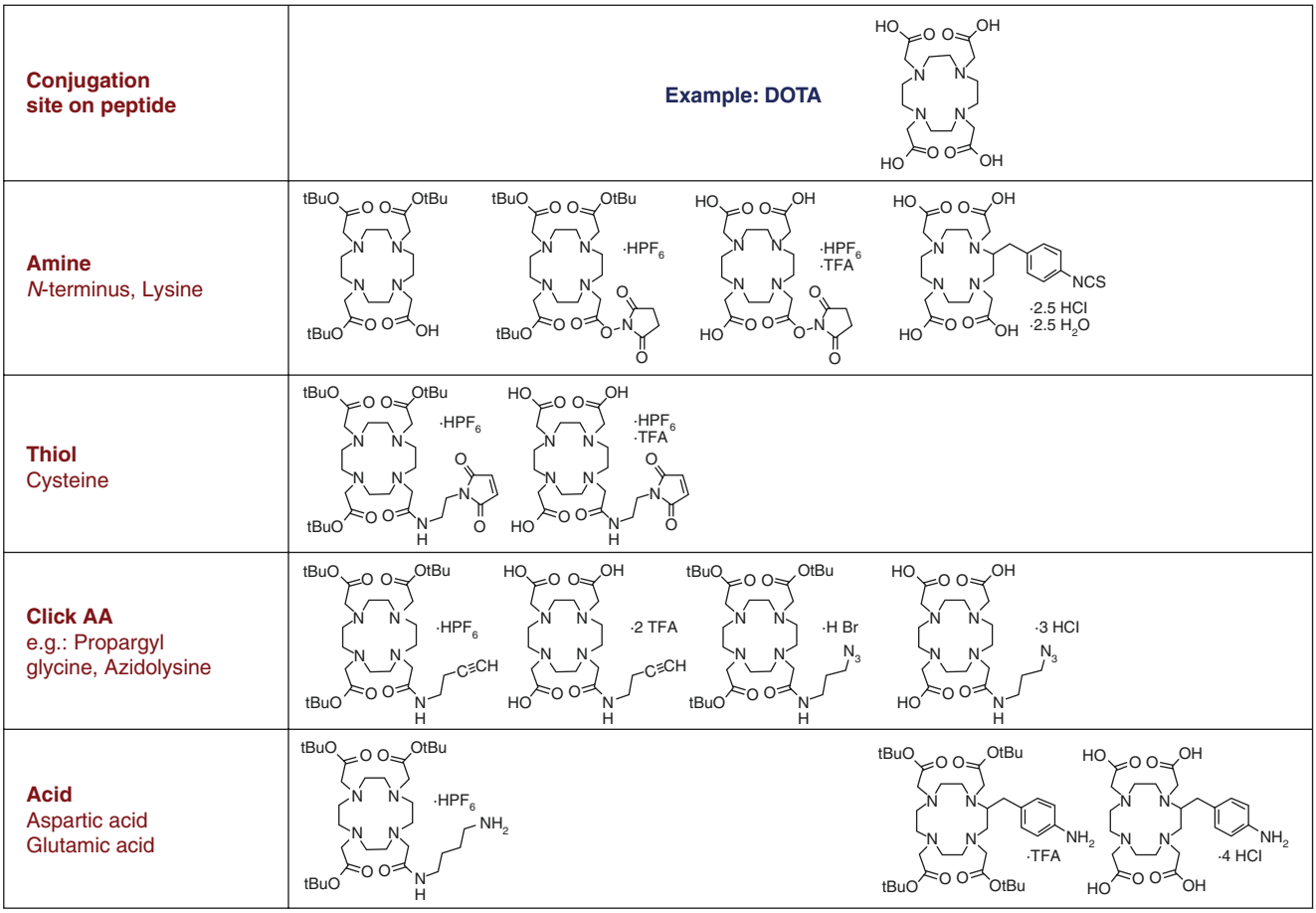

Fig. 15 An example of the breadth of bifunctional chelators that is commercially available, using DOTA as a representative case. Note that in many cases the chelators all are simply—and sloppily—referred to as "DOTA" despite the fact that they have different numbers of carboxylic acids available for binding radiometals. It is therefore always advisable to closely check a paper's experimental section to determine which specific "flavor" of DOTA was used

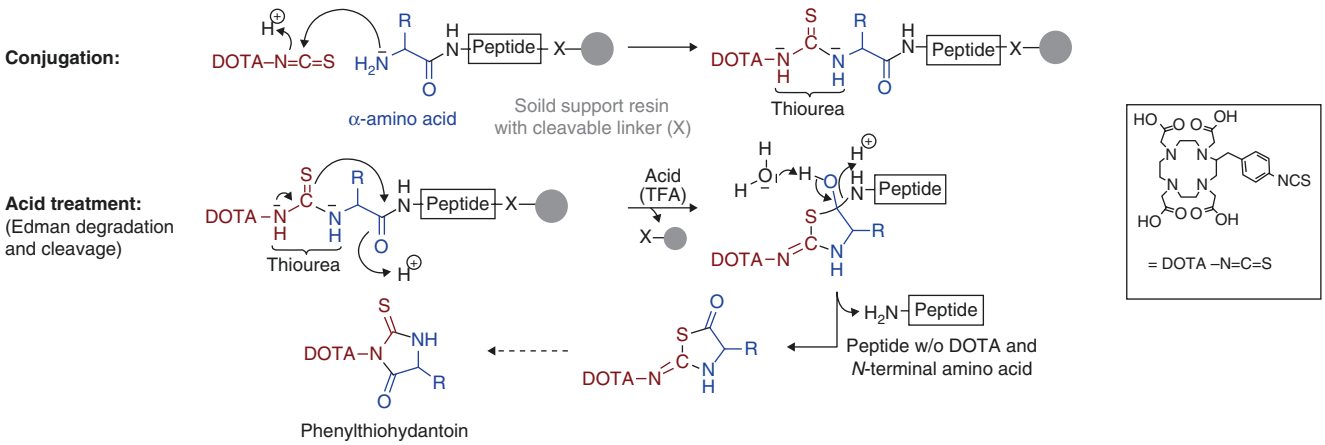

Fig. 16 The conjugation of an isothiocyanate to an amine forms a thiourea linkage. When this conjugation occurs at the *N*-terminus of an *α-amino acid*, the thiourea will undergo Edman degradation during treatment with strong acids such as TFA

cartridge- or HPLC-based purification is performed prior to the formulation of the final radiolabeled peptide [92, 95, 96]. In case any unchelated radiometal remains at the end of the reaction, an excess of a chelator such as EDTA can be added to aid in its removal during purification [95].

The choice of chelator for a given radiometal generally tries to strike a balance between ease of radiolabeling and *in vivo* stability [95, 97]. Acyclic chelators tend to have more rapid radiolabeling kinetics than macrocyclic chelates, but radiometal complexes of the latter typically have exhibited

greater stability *in vivo* [6, 92]. Figure 14 contains several radiometal/chelator pairings that *typically* work well for simple, rapid, and high-yield chelation reactions as well as for producing stable peptide-based radiotracers. It has to be pointed out, however, that the specifics of which chelators work best for a given radiometal are to some extent peptide-dependent. For example, a review of the primary literature reveals differing accounts on the merits of DOTA as chelator for the radioisotopes of copper [6, 93, 98, 99]. At least some of the seemingly conflicting observations can be explained by the differing peptide sequences, as side-chain residues—especially carboxylic acids or amines—can prevent the complete coordination of the radiometal during radiolabeling or facilitate the loss of the radiometal after purification.

Overall, the study of radiometalated peptides is an active and fertile area of research. They are being translated successfully into the clinic for both diagnosis and therapy, as highlighted by the recent FDA approval of the PET imaging agent NETSPOT [14] and its companion radiotherapeutic LUTATHERA. Radiolabeling a peptide with radiometals is a very straightforward procedure that requires little specialized equipment, and the process can also be automated completely for clinical studies. In the context of radiotherapy, radiometalated peptides far outnumber their radioiodinated counterparts. For imaging, radiometalated peptides can provide a convenient alternative to ^{18}F-labeled peptides, both in terms of radiochemistry and imaging time frame (half-life). When choosing between radiometalation and radiohalogenation, several questions should be entertained, including how feasible is this radiosynthesis and how could the prosthetic group or chelator effect the *in vivo* behavior of the peptide.

Purification, Analysis, and Characterization of Radiolabeled Peptides

Chromatographic Methods and Chromatography-Based *In Vitro* Testing

Chromatography plays a key role in the purification, analysis, and characterization of radiolabeled peptides and their precursors. HPLC is the most widely used technique for the purification and analysis of radiolabeled peptides during both radiosynthesis and subsequent analysis. Given the hydrophilic nature and moderate size of most peptide-based radiopharmaceuticals, reversed-phase HPLC conditions are employed. For those unfamiliar with this technique, this means that a lipophilic stationary phase (column) and hydrophilic mobile phase (solvent) are used. Typical solvent systems are based on water and acetonitrile, often containing 0.05–0.1% v/v trifluoroacetic acid (TFA) to keep the peptide fully protonated. Commonly, the HPLC is run using a gradient solvent system in which the fraction of acetonitrile in the solvent mixture is increased over the course of the run (Fig. 17). The use of C-18 reversed-phase columns is common, though—depending on the nature of the peptide—less lipophilic C-12, C-8, or even C-4 columns may be used instead. The use of a matching guard column is recommended, especially for the purification of crude reaction mixtures. This very short pre-column retains particulate impurities and is readily replaced at low cost.

Purification: The "Right" HPLC System, SPE, or "Use Without Further Purification?"

The overall goal when choosing an HPLC column and mobile phase system is to obtain good separation between the peptide and both radioactive and nonradioactive by-products while maintaining reasonable run times (<30 min). Chromatographic data are typically recorded using a UV detector and, for radiolabeled peptides, a radioactivity detector as well. If the two detectors are connected in series, a small offset between the two signals may be observed for the *same* compound (see Fig. 17 bottom). During the development of the radiosynthetic approach, HPLC can be used to determine the possibility of separating the radiolabeled peptide from any by-products, to assess the stability of the peptide under the radiosynthesis conditions, and to determine the purity of the radiolabeled peptide immediately after synthesis, and to assess what level of purification will be required for subsequent use of the radiolabeled peptide (HPLC, simple SPE cartridge purification or—chiefly for radiometals—even use without purification). It is also important to keep in mind that while HPLC does provide excellent resolution, some chemical changes—*e.g.* oxidation or the formation of isomers—are not readily apparent via HPLC alone. It also has to be noted that for a radiolabeled peptide to be usable without purification, all other components present in the radiolabeling mixture need to be compatible with the subsequent experiments.

Analysis and Characterization

Once the purified radiolabeled peptide has been obtained, HPLC can be used to determine the radiochemical purity, molar activity, and radiochemical identity of the radiolabeled peptide. Radiochemical purity can be evaluated by comparing the relative area of the peak of the product in the radiochromatogram to the areas of all of the peaks. *Molar activity*—previously referred to as *specific activity*—can be calculated by determining the UV peak area associated with a known radioactive amount of the radiolabeled peptide and comparing it to a previously obtained standard curve created using the cold peptide. Finally, radiochemical identity can be ascertained by performing a separate "cold spike" HPLC run in which a small amount of analytically verified non-radioactively labeled peptide is mixed into the solution

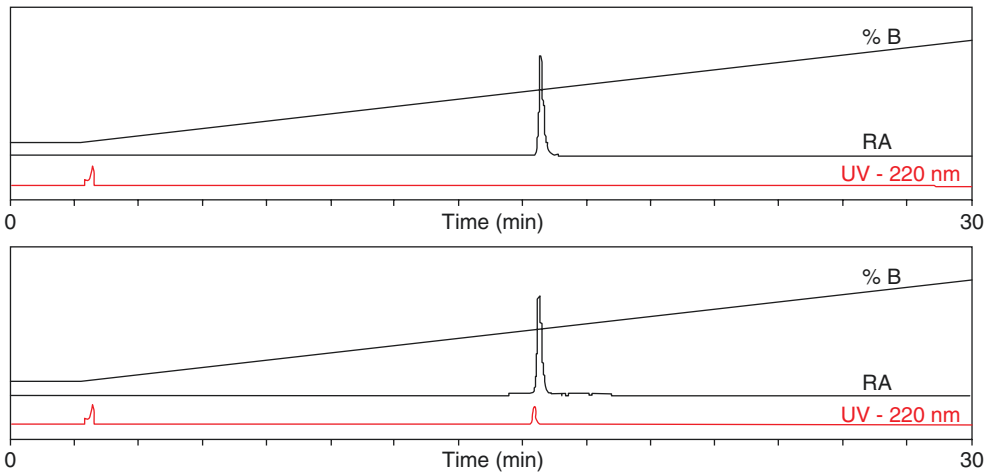

Fig. 17 HPLC traces showing radioactive (black) and UV (red) signals for a purified radiolabeled peptide (top) as well as a purified radiolabeled peptide with a cold spike (bottom). Traces were obtained on an analytical reversed-phase C-12 column at a flow rate of 1.5 mL/min (solvent gradient overlaid in gray; solvent A, water (0.05% v/v TFA); solvent B, acetonitrile; solvent front peak, UV signal at approximately 2.5 min)

of the radiolabeled peptide. In this case, co-elution indicates radiochemical identity. Representative HPLC traces are shown in Fig. 17. For simple radiometalation reactions [6, 93], a complex HPLC setup may not be required. In these cases, radio thin-layer chromatography (radio-TLC) may suffice for some of the tests.

Once the radiolabeled peptide has been formulated—typically in 0.9% saline—the radiolysis of the formulated radiolabeled peptide is evaluated by periodically withdrawing aliquots for HPLC analysis [56, 100]. This is particularly important for peptides labeled with therapeutic radionuclides, since these nuclides undergo high-energy decay. The sampling time frame is largely dependent on the radioactive half-life of the chosen radionuclide and the expected duration of the planned studies. The deterioration of the peak shape or the appearance of new radioactive peaks can indicate radiolysis, aggregation, or—in the case of radiometals—the decomposition of the radiometal-chelator complex. If radiolysis is observed, different storage conditions and formulations containing radioprotectants (*e.g.* ascorbic acid) may be evaluated [100, 101]. In cases in which the crude peptide mixture indicates high radiochemical purity but the formulated radiolabeled peptide shows near-immediate degradation, it may be advisable to check if evaporation to dryness is part of the formulation and/or if the peptide contains particularly sensitive amino acids (*e.g.* aromatics, methionine), as both can be the cause of the rapid degradation.

In Vitro Validation

The specific nature of the *in vitro* tests needed to validate a peptide-based radiopharmaceutical is highly target dependent and determined by a variety of factors, but a standard set of experiments almost always involves serum (or plasma) stability studies and tests with both purified target and whole cells that express the molecular target of the radiopharmaceutical [102–104].

Serum Stability Studies

These studies offer a first indication of the robustness of the radiolabeled peptide *in vivo*. For this experiment, an aliquot of the formulated radiolabeled peptide is mixed with serum and incubated at 37 °C. Over a time frame covering at least the expected duration of the *in vivo* experiment, samples are withdrawn, and serum proteins are precipitated via the addition of ethanol or acetonitrile. To determine the fraction of protein-bound radioactivity, both the precipitate and the supernatant are measured in a gamma counter. Next, a diluted aliquot of the supernatant is injected onto the HPLC to determine the fraction of the radiolabeled peptide that remains intact. Corroboration that the peak of the intact radiolabeled peptide has been identified correctly can be obtained by performing a separate "hot spike" HPLC run in which the injected solution is mixed with a small amount of fresh radiolabeled peptide. It is important to point out that sera from different species can differ in their peptidase profile [105]. As a result, mouse (or rat) serum stability studies may be more relevant for preclinical *in vivo* experiments, while human serum studies are far more important with respect to clinical translation. If available, human plasma, which still contains the blood clotting factor fibrinogen, may be used. Regardless of the specifics, it is important to completely remove all precipitable proteins before HPLC to avoid difficult-to-remove protein deposits on the HPLC column.

ELISA

Enzyme-linked immunosorbent assay (ELISA) experiments with purified target protein can shed light on the binding of the peptide in a simple test environment (Fig. 18). While many variations exist, a typical ELISA consists of incubating a range of different concentrations of the (radiolabeled) peptide over the immobilized target protein in a 96-well plate in the presence of a ligand (at a fixed concentration) competing

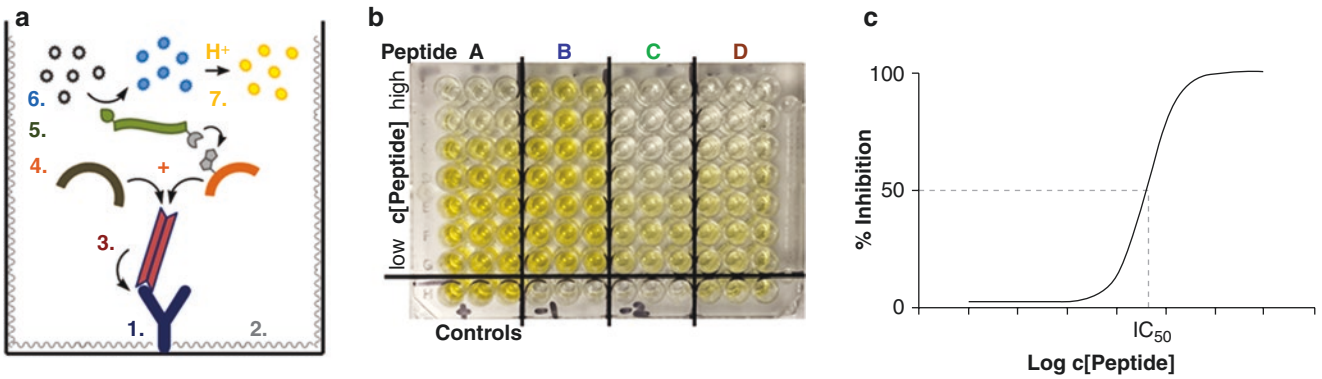

Fig. 18 (**a**) A schematic representation of the key steps in a typical competitive ELISA using an optical readout. See the main text for a description of the individual steps. (**b**) Photo of a 96-well plate measured on an optical plate reader with an ELISA of four peptides (**A**–**D**) run in triplicate for seven concentrations each. (**c**) A plot of the relative % inhibition of biotinylated ligand binding vs. peptide concentration on a semilogarithmic scale reveals the peptide concentration (IC_{50}) at which 50% of the natural ligand binding is inhibited. (Photo (**b**) courtesy of Dr. Sarah Tang-Wu, Department of Chemistry, University of California, Davis CA, USA)

for binding to the target. The resulting binding curve—plotted as relative % of competing ligand binding inhibited vs. log[peptide]—will provide the "inhibitory concentration" IC_{50}: the concentration at which the peptide inhibits 50% of a competing ligand's binding to the target. Lower IC_{50} values indicate better peptide binding. ELISAs are often carried out using nonradioactive cold analogs of the radiotracer by allowing them compete for binding with a validated ligand that bears a tag for detection, typically either a long-lived radionuclide or a biotin moiety. A visual guide to such a "competitive ELISA" assay is provided in Fig. 18. Figure 18a depicts a vertical cross section through a single well of a multi-well plate. The standard procedure for this assay involves first coating the well with a capturing antibody for the target of interest (1) and then blocking any non-specific binding sites within the well with bovine serum albumin (BSA) or casein (2). Next, the target of interest (3) is introduced and captured in the well by the antibody. This is followed by the incubation of a pre-mixed solution (4) of the peptide and the biotinylated competing ligand. Once equilibrium has been reached (*e.g.* after 1 h), an avidin-bearing protein (*e.g.* ExtrAvidin-HRP; 5) is introduced and allowed to bind to the biotinylated ligand. The concentration of the avidin-bearing protein is then visualized by its conversion of the colorless TMB substrate (6) to the blue TMB oxidation product. This reaction can be stopped via the addition of acid, and the acidified TMB oxidation product (yellow, 7) can be quantified on a plate reader.

Cell-Based Assays

Assays involving cells provide models that are (slightly) closer to *in vivo* conditions. In these tests, cell lines with high levels of natural or transfection-induced expression of the receptor of interest ("positive controls") are used alongside cell lines that exhibit low or no expression of the target ("negative controls") [103]. A variety of factors must be carefully considered to ensure reliable results, including the characterization of the cell line and control of the environmental conditions under which the cells are grown. If adherent, cells can also be used for cell-based ELISAs in which the cells themselves take the place of the immobilized target protein.

Cells are routinely used for *binding, internalization, and efflux studies* [102]. These assays provide important insight into how well a peptide binds to, is taken up by, and is retained in the cells of interest. These studies can also provide an indication of whether the radiolabeled peptide is acting as an agonist (is internalized) or an antagonist (is not internalized) [56]. In a typical experiment, sets of cells in multi-well plates or in microcentrifuge tubes are exposed to media containing the radiolabeled peptide for different lengths of time. This incubation is typically performed at 37 °C to encourage metabolism (*i.e.* binding and internalization), though a temperature of 4 °C is used in some steps to suppress metabolism (*e.g.* for certain washing steps). A control (*i.e.* blocking) experiment that demonstrates the specificity of the peptide for its target can be carried out by adding an excess of a validated ligand to the media along with the radiolabeled peptide. Following the removal of the media and washing solutions, total binding is determined by comparing the amount of radioactivity in the cells to the amount of radioactivity in the supernatant. The subsequent washing of the cells with a mildly acidic buffer can remove surface-bound radioactivity, thereby providing insight into the internalization of the radiolabeled peptide. For *efflux studies*, cells are first incubated and washed as above to determine total binding. Then, they are incubated further in fresh media, and the efflux of radioactivity from the cells is determined at

various time points by comparing the radioactivity in the fresh media to the radioactivity remaining in the cells.

If warranted by promising initial *in vitro* studies, more advanced cell-based *saturation binding assays* may be carried out as well [56, 104, 106]. These allow for the determination of the peptide's equilibrium binding constant (K_d) for the receptor of interest expressed on a cell line. K_d can be considered independent from the experimental procedure, a key difference relative to IC_{50} values, which are highly dependent on the specifics of the procedure. In brief, to determine K_d, cells are incubated with media containing increasing concentrations of the (radiolabeled) peptide. After reaching binding equilibrium, the cells are then washed, and the amount of cell-associated radioactivity is counted. The amount of bound peptide [mol] is plotted against the concentration of peptide used [M], and these data are analyzed with nonlinear regression analysis to reveal the K_d value as well as the number of binding sites (receptors) in the assay (B_{max}). However, it is important to keep in mind that these results are predicated on certain assumptions, notably the equilibrium conditions and the absence of internalization (Fig. 19) [106, 107].

Additional *In Vitro* Tests of Interest

- *Cell viability* studies are very important as well when evaluating peptides radiolabeled with therapeutic radionuclides [101]. Here, cells are incubated with media containing varying amounts of the radiolabeled peptide, and the viability and proliferation of the cells are monitored over time. This should provide some indication of how well the radiolabeled peptide may work for PRRT [3, 15, 52].
- The *hydrophilicity (log D)* of the radiolabeled peptide can be determined using the octanol/aqueous solution shake-flask method [108]. While this measurement is typically not particularly important for radiolabeled peptides—unless, of course, if their *in vivo* target is in the brain—it

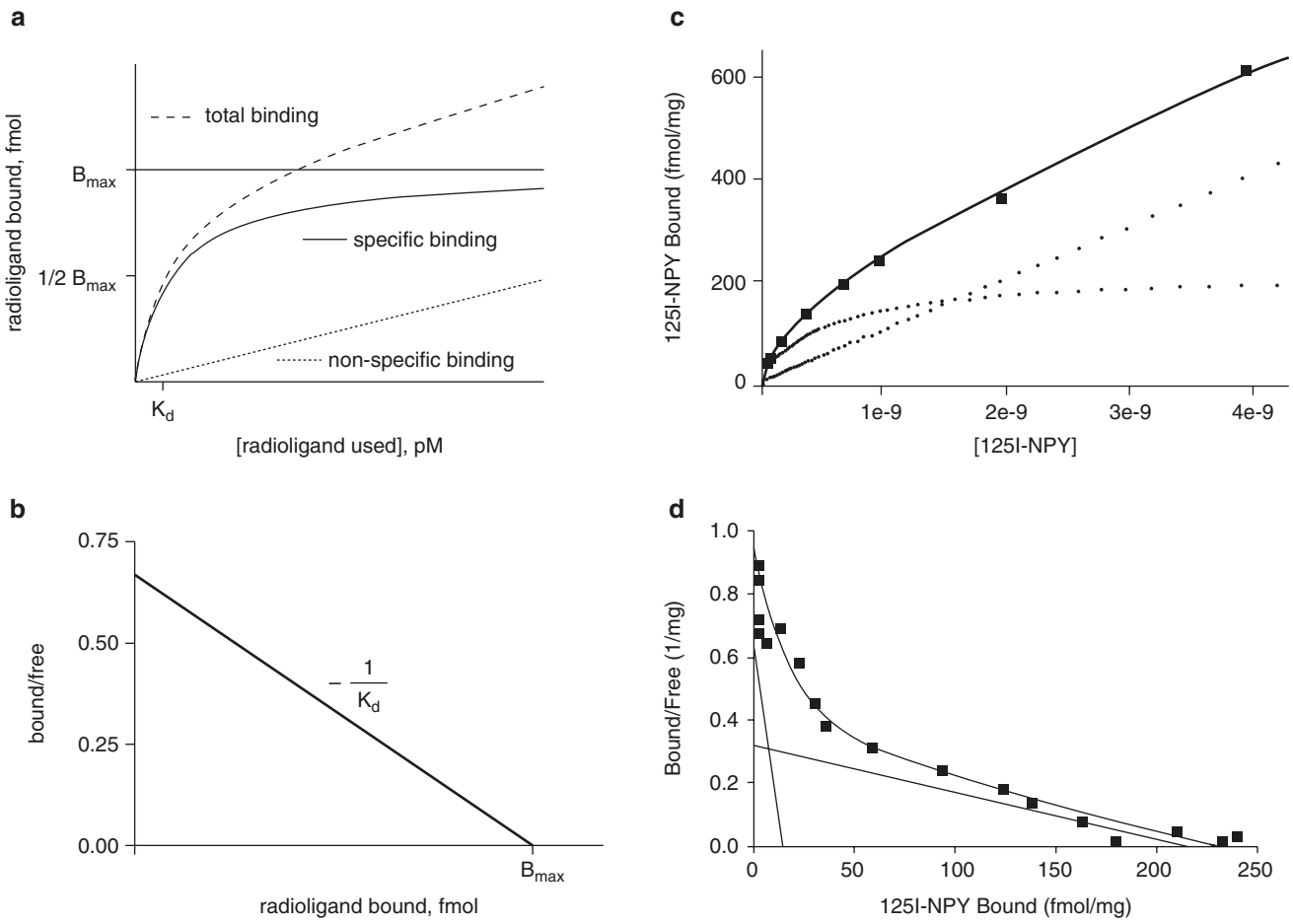

Fig. 19 Graphical determination of K_d and B_{max} using Rosenthal (or Scatchard) plots. (**a**) and (**b**) depict the theoretical case; (**c**) and (**d**) show corresponding experimental data. Because of the potential for significant errors in the graphical data analysis, the data are processed by computer programs that perform iterative nonlinear regression analysis. (**a** and **b** from Hein *et al.* [106], with permission; **c** and **d** from Walker and Miller [107] with permission)

may offer a first indication of their dominant clearance pathway *in vivo* [109].

- Once the radiosynthesis and formulation of a radiolabeled peptide have been optimized, the suitability of the filters and storage vessels used should also be confirmed prior to *in vivo* experimentation. The last step in the formulation of radiolabeled peptides for *in vivo* experiments is filtration through a sterile 0.2 μm filter. To avoid unpleasant surprises, it is recommended to test the compatibility of the radiolabeled peptide and the sterile filter before commencing any *in vivo* experiments to make sure that the formulated radiotracer does not stick to the filter membrane (low protein-binding PVDF membranes are a good first choice). The same is true for storage vessels; certified low-binding vessels may work best [56].

In Vivo Validation

As promising radiolabeled peptides move from *in vitro* to *in vivo* evaluation, the typical sets of experiments and analyses become more similar to those employed for other radiopharmaceuticals. In order to identify and improve promising candidates for use in humans, these experiments remain necessary because, as eloquently pointed out by Eberle *et al.*, "despite [many years] of experience with radiopeptides, based on thousands of analogs designed, synthesized, and tested *in vivo*, the biological characteristics of a radiopeptide in an organism cannot be predicted" [56]. In other words, experiments that elucidate the pharmacokinetics (PK) of radiolabeled peptides in small animal models are crucial because few general rules exist.

Preclinical *in vivo* experiments are closely overseen by institutional review committee and are commonly supported by specially trained staff in dedicated facilities [110]. Proper animal handling practices—along with the careful planning, control, and documentation of the experimental conditions—are key for protecting animal welfare and ensuring the quality of the scientific data [111]. Initial experiments are most often carried out in small animals, specifically mice or rats. Cell or tissue xenograft models in immunodeficient mice are especially common for the evaluation of tumor-targeted radiopharmaceuticals and, when possible, should include target-negative control tumors.

Studies with radiolabeled peptides intended for imaging commonly include a set of animals that are imaged at certain time points after the administration of the radiolabeled peptide. The time points and the duration of each individual scan are determined by the radioactive half-life of the radionuclide as well as the pharmacokinetic profile of the peptide. These imaging data can be quantified via the calculation of standard uptake values (SUVs) [112, 113]. Furthermore, if the behavior of the radiolabeled peptide at very early time points is of interest, a dynamic (multi-frame) scan may be performed immediately after the administration of the tracer, and the resulting data can be displayed as time-activity curves (TACs) [109].

As the uptake of a radiolabeled peptide cannot be readily quantified by imaging alone for some key organs—for example, the urinary bladder wall, gall bladder, pancreas, skin, glands, intestines—additional *biodistribution studies* are commonly carried out as well. Here, groups of animals are sacrificed and dissected at selected time points after the administration of the radiolabeled peptide, and tissues of interest are weighed and their radioactivity counted using a gamma counter. The uptake of the radiotracer in each tissue is then expressed as a decay-corrected relative radioactivity concentration per unit weight: "percent of injected dose per gram" (%ID/g) [109]. Unsurprisingly, the number of animals required for a biodistribution study with multiple time points is considerably higher than that needed for an imaging study. On the flip side, however, biodistribution studies offer ample opportunity for tissue sampling. The samples may be used for stability studies or autoradiography of tissue slices, which, along with immunohistochemical staining, can facilitate the correlation of target expression with the uptake of the radiotracer [27, 103]. Additional correlation and confirmation on the molecular level is desirable and can be done by performing *in vivo blocking* experiments. To this end, an excess of a validated ligand for the receptor of interest is co-administered along with the radiolabeled peptide. While blocking experiments are often performed via the co-administration of a cold analog of the radiolabeled peptide rather than a separate validated ligand, these experiments are of questionable value, because both hot and cold analogs of the same peptide can be expected to compete for the same *in vivo* target.

If peptides radiolabeled with therapeutic radionuclides are evaluated for PRRT, longitudinal therapy studies have to be performed in which the administration of the peptide is followed by the long-term monitoring of the animals (including their body weight, tumor size, and blood chemistry). For these studies, the cohort size, treatment regimen, animal monitoring, control groups, and end points need to be carefully planned. In this regard, previously optimized strategies and protocols can be used as guides for experiments with new compounds [36, 101].

Predictably, many variations and adaptations of the *in vivo* experiments mentioned here exist. The specifics are typically based on the particular goals and constraints of individual studies [103], though new developments, insights, and techniques are often incorporated as well. For example, patient-derived xenografts (PDX) are being investigated as more realistic preclinical models of disease [114, 115]. Furthermore, veterinary hospitals are increasingly becoming

aware of molecular imaging and can provide access to animal populations with spontaneous diseases [116, 117]. Even within the context of classic rodent models, important improvements are being introduced which are particularly relevant for the evaluation of radiolabeled peptides. Particularly noteworthy are studies on the reduction of renal retention [118, 119] and the co-administration of protease inhibitors [120].

Peptide Modifications and Optimization: From Lead Compounds to Trials, Tribulations, and Triumphs (*a.k.a.* Particularly Important Works)

Few if any lead peptides possess all the *in vitro* and *in vivo* characteristics required for a good radiopharmaceutical. A review of some of the most notable peptide-based radiopharmaceuticals reveals that even the most promising candidates need to undergo a thorough process of optimization in order to produce a construct that combines high affinity and selectivity with sufficient stability and a suitable pharmacokinetic profile. To this end, the strategies listed in Fig. 20 have been used with great success. Starting with the identification of the core motif required for binding, approaches for the optimization of a radiolabeled peptide include—but are not limited to—cyclization, *N*- and *C*-terminal modifications, the use of unnatural amino acids or other modifiers, multimerization, and the co-administration of protease inhibitors. Most of the time, myriad modifications have to be evaluated, and more than one of these strategies have to be applied to produce a final radiopharmaceutical that is suitable for translation to the clinic.

This quest is delightfully summarized in the brief review by Pless [121], which recounts how in 1973, Brazeau, Guillemin, and co-workers were studying growth hormone-releasing hormones (GHRH). As Brazeau *et al.* describe in their original publication, the team started with "chloroform-methanol-glacial acetic acid extract of about 500,000 sheep hypothalamic fragment extracts" [122] and eventually isolated "8.5 mg of a product" from which they identified a tetradecapeptide GHRH antagonist—which they named "somatostatin"—"through stepwise Edman degradation" (Fig. 21) [122]. They gained some promising insights by testing a synthetic peptide prepared through "solid-phase methodology" (*a.k.a.* SPPS), but further efforts were hampered by the peptide's very short biological half-life of approximately 2 min. This triggered a worldwide collaborative effort to screen libraries of somatostatin analogs in order to determine the minimal chain length required for biological activity and to evaluate the key enzymatic degradation sites, an effort which culminated in the identification of octreotide in 1980. This octapeptide retains the cyclic structure and main binding motif characteristics of somatostatin but contains two D-amino acids and a modified *C*-terminus (an alcohol instead of a carboxylic acid). As octreotide compares favorably to somatostatin both in terms of growth hormone (GH) inhibition and biological half-life (approximately 1.5 h), it has been used successfully as a peptide pharmaceutical since 1988 for the treatment of GH-expressing (*i.e.* somatostatin receptor-positive) tumors.

In the historical review by Levine and Krenning [13], the authors recount how small amounts of ^{125}I-labeled octreotide analogs were used for the initial staining of neuroendocrine tumor samples in 1982. In addition, it is related how radiochemists struggled—and nearly gave up—in their worldwide search for sufficiently high molar activity iodine-123, before finally succeeding in 1987 in the preparation [^{123}I-Tyr^3] octreotide for planar and SPECT imaging. Within 3 years, [^{123}I-Tyr^3]octreotide had been used in hundreds of patients for the detection of tumors, but the high cost and limited supply of the iodine-123 (as well as the high intestinal uptake of tracer) spurred the search for octreotide analogs labeled with different radionuclides.

The radiometalated ^{111}In-octreotide (OctreoScan; see Fig. 21 [123, 124]) emerged as an early success thanks to its easy radiolabeling chemistry and good imaging results. By 1993, more than 1000 patients had been imaged by Krenning

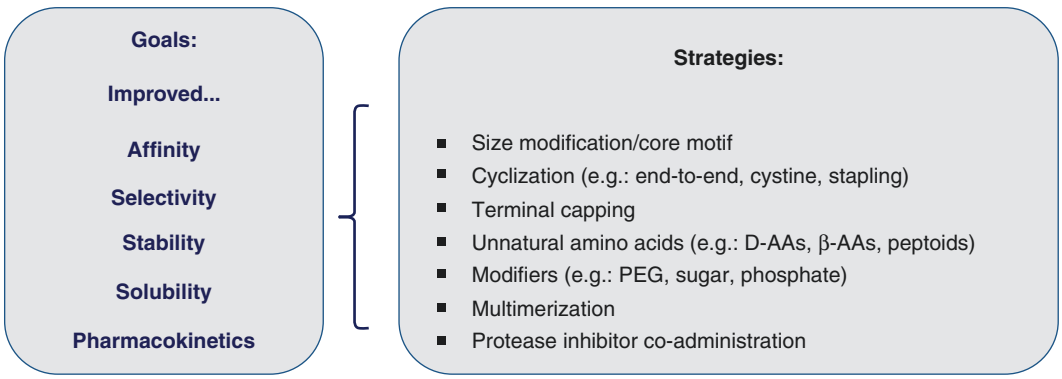

Fig. 20 Key goals for the optimization of peptide-based radiopharmaceuticals and the major strategies used to achieve these goals

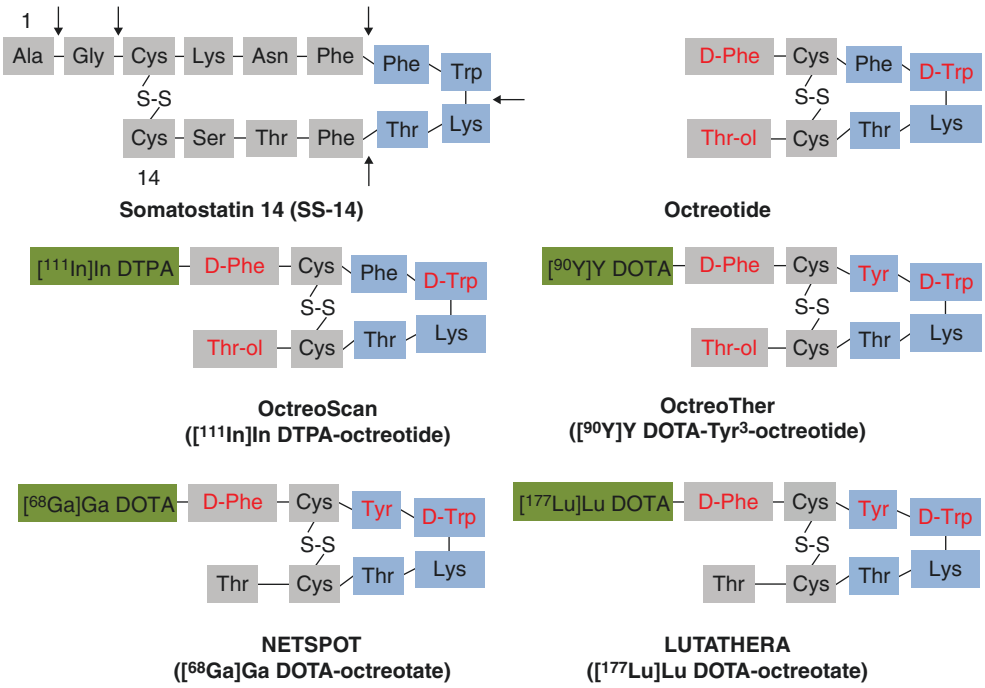

Fig. 21 Schematic highlighting key modifications to the native somatostatin-14 (SS-14) peptide that led to the development of octreotide and the radiopharmaceuticals OctreoScan, OctreoTher, NETSPOT, and LUTATHERA. Key enzymatic degradation sites on SS-14 are indicated by arrows; blue residues form the binding motif; red amino acids indicate modified residues; and the radiolabeling moieties are indicated in green [123, 124]

and co-workers, and in 1994, the US FDA approved OctreoScan as an imaging radiopharmaceutical. High doses of OctreoScan were soon given in attempts at PRRT, though these efforts produced only mixed results because of the suboptimal energy spectrum of the indium-111 emissions as well as the need for radioprotection of the kidneys. This led to the evaluation of ^{90}Y-labeled analog OctreoTher (see Fig. 21), which boasts more penetrating β^- radiation and thus produces more favorable response rates.

While studies with these agents continued, other radiolabeled octreotide analogs were developed and investigated. Along these lines, the key criteria included (1) maintaining simple radiochemistry and (2) expanding and improving the usefulness and the efficacy of the peptide radiopharmaceutical. In the realm of imaging, this lead to the development of the ^{68}Ga-labeled peptide NETSPOT (see Fig. 21), which has enabled the widespread use of PET for the imaging of neuroendocrine tumors. For therapy, beginning in 1998, a worldwide multicenter effort developed, evaluated, and eventually validated the ^{177}Lu-labeled peptide LUTATHERA (see Fig. 21). The US FDA approved NETSPOT for imaging in 2016 [14] and LUTATHERA for radiotherapy in early 2018 [15].

The circuitous route from Brazeau, Guillemin, and their sheep hypothalami to these most recent developments clearly demonstrates how collaborative, multidisciplinary, complex, and rewarding the process of developing radiolabeled peptides can be. It is clear that these efforts and the lessons learned en route have set the stage for the future development of a wide range of clinically effective and useful peptide-based radiopharmaceuticals.

The Bottom Line

- Radiolabeled receptor-binding peptides are very important radiopharmaceuticals for both nuclear imaging and therapy.
- Interest in radiolabeled receptor-binding peptides has surged in part due to their ease of synthesis, flexibility with regard to structural modifications, rapid pharmacokinetics, and lack of immunogenicity.
- Combinatorial library approaches have enabled the rapid screening of large numbers of peptides sequences. These techniques take advantage of both chemical (OBOC) and bacterial (phage display) libraries.
- Peptide radiopharmaceuticals under development should be tested *in vivo* as soon as possible after initial *in vitro* tests such as ELISAs have demonstrated their affinity and selectivity. This helps with the early identification and mitigation of possible pharmacokinetic and metabolic issues.
- In the coming years, radiolabeled peptides will have a significant clinical impact as theranostics, as underscored by the FDA-approval of NETSPOT for imaging in 2016 and LUTATHERA for radiotherapy in 2018.

References

1. Kaspar AA, Reichert JM. Future directions for peptide therapeutics development. Drug Discov Today. 2013;18(17–18):807–17.
2. Okarvi SM, Maecke HR. Radiolabelled peptides in medical imaging. In: Koutsopoulos S, editor. Peptide applications in biomedicine, biotechnology and bioengineering. Duxford: Woodhead Publishing; 2018. p. 431–83.
3. Chatalic KLS, Kwekkeboom DJ, de Jong M. Radiopeptides for imaging and therapy: a radiant future. J Nucl Med. 2015;56(12):1809–12.
4. Fosgerau K, Hoffmann T. Peptide therapeutics: current status and future directions. Drug Discov Today. 2015;20(1):122–8.
5. Wetzler M, Hamilton P. Peptides as therapeutics. In: Koutsopoulos S, editor. Peptide applications in biomedicine, biotechnology and bioengineering. Duxford: Woodhead Publishing; 2018. p. 215–30.
6. Correia JD, Paulo A, Raposinho PD, Santos I. Radiometallated peptides for molecular imaging and targeted therapy. Dalton Trans. 2011;40(23):6144–67.
7. Demoin DW, Wyatt LC, Edwards KJ, Abdel-Atti D, Sarparanta M, Pourat J, et al. PET imaging of extracellular pH in tumors with 64Cu- and 18F-labeled pHLIP peptides: a structure–activity optimization study. Bioconjug Chem. 2016;27(9):2014–23.
8. van Duijnhoven SMJ, Robillard MS, Nicolay K, Grull H. Tumor targeting of MMP-2/9 activatable cell-penetrating imaging probes is caused by tumor-independent activation. J Nucl Med. 2011;52(2):279–86.
9. Dufresne M, Seva C, Fourmy D. Cholecystokinin and gastrin receptors. Physiol Rev. 2006;86(3):805–47.
10. Maschauer S, Einsiedel J, Hübner H, Gmeiner P, Prante O. 18F- and 68Ga-Labeled neurotensin peptides for PET imaging of neurotensin receptor 1. J Med Chem. 2016;59(13):6480–92.
11. Haubner R, Maschauer S, Prante O. PET radiopharmaceuticals for imaging integrin expression: Tracers in clinical studies and recent developments. Biomed Res Int. 2014;2014:1–17.
12. Okarvi SM. Peptide-based radiopharmaceuticals: future tools for diagnostic imaging of cancers and other diseases. Med Res Rev. 2004;24(3):357–97.
13. Levine R, Krenning EP. Clinical history of the theranostic radionuclide approach to neuroendocrine tumors and other types of cancer: historical review based on an interview of Eric P. Krenning by Rachel Levine. J Nucl Med. 2017;58(Suppl. 2):3S–9S.
14. Barrio M, Czernin J, Fanti S, Ambrosini V, Binse I, Du L, et al. The Impact of somatostatin receptor–directed PET/CT on the management of patients with neuroendocrine tumor: a systematic review and meta-analysis. J Nucl Med. 2017;58(5):756–61.
15. Jadvar H, Chen X, Cai W, Mahmood U. Radiotheranostics in cancer diagnosis and management. Radiology. 2018;286(2):388–400.
16. Morgat C, Mishra AK, Varshney R, Allard M, Fernandez P, Hindie E. Targeting neuropeptide receptors for cancer imaging and therapy: perspectives with bombesin, neurotensin, and neuropeptide-Y receptors. J Nucl Med. 2014;55(10):1650–7.
17. Sah BR, Burger IA, Schibli R, Friebe M, Dinkelborg L, Graham K, et al. Dosimetry and first clinical evaluation of the new 18F-radiolabeled bombesin analogue BAY 864367 in patients with prostate cancer. J Nucl Med. 2015;56(3):372–8.
18. Yu Z, Ananias HJK, Carlucci G, Hoving HD, Helfrich W, Dierckx RAJO, et al. An update of radiolabeled bombesin analogs for gastrin-releasing peptide receptor targeting. Curr Pharm Des. 2013;19(18):3329–41.
19. Danhier F, Le Breton A, Preat V. RGD-Based strategies to target alpha(v) beta(3) integrin in cancer therapy and diagnosis. Mol Pharm. 2012;9(11):2961–73.
20. Desgrosellier JS, Cheresh DA. Integrins in cancer: biological implications and therapeutic opportunities. Nat Rev Cancer. 2010;10(1):9–22.
21. Ruoslahti E, Pierschbacher MD. New perspectives in cell adhesion: RGD and integrins. Science. 1987;238(4826):491–7.
22. Haubner R, Decristoforo C. Radiolabelled RGD peptides and peptidomimetics for tumour targeting. Front Biosci. 2009;14:872–86.
23. Gaertner FC, Kessler H, Wester HJ, Schwaiger M, Beer AJ. Radiolabelled RGD peptides for imaging and therapy. Eur J Nucl Med Mol Imaging. 2012;39:126–38.
24. Gagnon MKJ, Hausner SH, Marik J, Abbey CK, Marshall JF, Sutcliffe JL. High-throughput in vivo screening of targeted molecular imaging agents. Proc Natl Acad Sci U S A. 2009;106(42):17904–9.
25. Bandyopadhyay A, Raghavan S. Defining the role of integrin alpha(v)beta(6) in cancer. Curr Drug Targets. 2009;10(7):645–52.
26. Hackel BJ, Kimura RH, Miao Z, Liu H, Sathirachinda A, Cheng Z, et al. 18F-Fluorobenzoate-labeled cystine knot peptides for PET imaging of integrin alpha(v)beta(6). J Nucl Med. 2013;54(7):1101–5.
27. Hausner SH, Bauer N, Hu LY, Knight LM, Sutcliffe JL. The effect of bi-terminal PEGylation of an integrin alpha(v)beta(6)-targeted 18F peptide on pharmacokinetics and tumor uptake. J Nucl Med. 2015;56(5):784–90.
28. Li S, McGuire MJ, Lin M, Liu YH, Oyama T, Sun X, et al. Synthesis and characterization of a high-affinity alpha(v)beta(6)-specific ligand for in vitro and in vivo applications. Mol Cancer Ther. 2009;8(5):1239–49.
29. Charron CL, Hickey JL, Nsiama TK, Cruickshank DR, Turnbull WL, Luyt LG. Molecular imaging probes derived from natural peptides. Nat Prod Rep. 2016;33(6):761–800.
30. Aumailley M, Gurrath M, Müller G, Calvete J, Timpl R, Kessler H. Arg-Gly-Asp constrained within cyclic pentapoptides. Strong and selective inhibitors of cell adhesion to vitronectin and laminin fragment P1. FEBS Lett. 1991;291(1):50–4.
31. Ruoslahti E. RGD and other recognition sequences for integrins. Annu Rev Cell Dev Biol. 1996;12(1):697–715.
32. Haubner R, Finsinger D, Kessler H. Stereoisomeric peptide libraries and peptidomimetics for designing selective inhibitors of the alpha(v)beta(3) integrin for a new cancer therapy. Angew Chem Int Ed Engl. 1997;36(1314):1374–89.
33. Burgus R, Ling N, Butcher M, Guillemin R. Primary structure of somatostatin, a hypothalamic peptide that inhibits the secretion of pituitary growth hormone. Proc Natl Acad Sci U S A. 1973;70(3):684–8.
34. Anastasi A, Erspamer V, Bucci M. Isolation and structure of bombesin and alytesin, two analogous active peptides from skin of European amphibians Bombina and Alytes. Experientia. 1971;27(2):166–7.
35. Logan D, Abughazaleh R, Blakemore W, Curry S, Jackson T, King A, et al. Structure of a major immunogenic site on foot-and-mouth-disease virus. Nature. 1993;362(6420):566–8.
36. Fani M, Maecke HR. Radiopharmaceutical development of radiolabelled peptides. Eur J Nucl Med Mol Imaging. 2012;39(S1):11–30.
37. Hu LY, Kelly KA, Sutcliffe JL. High-throughput approaches to the development of molecular imaging agents. Mol Imaging Biol. 2017;2:163–82.
38. Liu R, Li X, Xiao W, Lam KS. Tumor-targeting peptides from combinatorial libraries. Adv Drug Deliv Rev. 2017;110–111:13–37.
39. Aina OH, Liu RW, Sutcliffe JL, Marik J, Pan CX, Lam KS. From combinatorial chemistry to cancer-targeting peptides. Mol Pharm. 2007;4(5):631–51.
40. Amblard M, Fehrentz J-A, Martinez J, Subra G. Methods and protocols of modern solid phase peptide synthesis. Mol Biotechnol. 2006;33(3):239–54.
41. Shelton PT, Jensen KJ. Linkers, resins, and general procedures for solid-phase peptide synthesis. In: Jensen KJ, Shelton PT, Pedersen S, editors. Peptide synthesis and applications. methods in molecular biology (methods and protocols), vol. 1047. Totowa: Humana Press; 2013. p. 23–41.
42. Koutsopoulos S. Peptide applications in biomedicine, biotechnology and bioengineering. Duxford: Woodhead Publishing; 2018.

43. Behrendt R, White P, Offer J. Advances in Fmoc solid-phase peptide synthesis. J Pept Sci. 2016;22(1):4–27.
44. Boas U, Mirsharghi S. Color test for selective detection of secondary amines on resin and in solution. Org Lett. 2014;16(22):5918–21.
45. Galati R, Verdina A, Falasca G, Chersi A. Increased resistance of peptides to serum proteases by modification of their amino groups. Z Naturforsch C. 2003;58(7–8):558–61.
46. Sutcliffe-Goulden JL, O'Doherty MJ, Marsden PK, Hart IR, Marshall JF, Bansal SS. Rapid solid phase synthesis and biodistribution of 18F-labelled linear peptides. Eur J Nucl Med Mol Imaging. 2002;29(6):754–9.
47. Davis RA, Lau K, Hausner SH, Sutcliffe JL. Solid-phase synthesis and fluorine-18 radiolabeling of cycloRGDyK. Org Biomol Chem. 2016;14(37):8659–63.
48. Petrou C, Sarigiannis Y. Peptide synthesis: methods, trends, and challenges. In: Koutsopoulos S, editor. Peptide applications in biomedicine, biotechnology and bioengineering. Duxford: Woodhead Publishing; 2018. p. 1–21.
49. Zhang G, Annan RS, Carr SA, Neubert TA. Overview of peptide and protein analysis by mass spectrometry. Curr Protoc Mol Biol. 2014;108:10.21.1–10.21.30.
50. Beck JG, Frank AO, Kessler H. NMR of peptides. In: Bertini I, McGreevy KS, Parig G, editors. NMR of biomolecules. Weinheim: Wiley-VCH; 2012. p. 328–44.
51. Westermann JC, Craik DJ. NMR in peptide drug development. In: Otovos L, editor. Peptide-based drug design. Methods in molecular biology, vol. 494. Totowa: Humana Press; 2008. p. 87–113.
52. Sabet A, Biersack HJ, Ezziddin S. Advances in peptide receptor radionuclide therapy. Semin Nucl Med. 2016;46(1):40–6.
53. Haubner R, Weber WA, Beer AJ, Vabuliene E, Reim D, Sarbia M, et al. Noninvasive visualization of the activated alpha(v)beta(3) integrin in cancer patients by positron emission tomography and [18F]Galacto-RGD. PLoS Med. 2005;2(3):e70.
54. Kuchar M, Pretze M, Kniess T, Steinbach J, Pietzsch J, Löser R. Site-selective radiolabeling of peptides by 18F-fluorobenzoylation with [18F]SFB in solution and on solid phase: a comparative study. Amino Acids. 2012;43(4):1431–43.
55. Richter S, Wuest F. 18F-Labeled peptides: The future is bright. Molecules. 2014;19(12):20536–56.
56. Eberle AN, Mild G. Receptor-mediated tumor targeting with radiopeptides. J Recept Signal Transduct Res. 2009;29(1):1–37.
57. Miller PW, Long NJ, Vilar R, Gee AD. Synthesis of C-11, F-18, O-15, and N-13 radiolabels for positron emission tomography. Angew Chem Int Ed Engl. 2008;47(47):8998–9033.
58. Link JM, Shoner SC, Krohn KA. Sources of carrier F-19 in F-18 fluoride. AIP Conf Proc. 2012;1509(61):61–5. https://doi.org/10.1063/1.4773941.
59. Okarvi SM. Recent progress in fluorine-18 labelled peptide radiopharmaceuticals. Eur J Nucl Med. 2001;28(7):929–38.
60. Olberg DE, Hjelstuen OK. Labeling strategies of peptides with 18F for positron emission tomography. Curr Top Med Chem. 2010;10(16):1669–79.
61. Krishnan HS, Ma L, Vasdev N, Liang SH. 18F-Labeling of sensitive biomolecules for positron emission tomography. Chemistry. 2017;23(62):15553–77.
62. Vaidyanathan G, Zalutsky MR. Synthesis of N-succinimidyl 4-[18F]fluorobenzoate, an agent for labeling proteins and peptides with 18F. Nat Protoc. 2006;1(4):1655–61.
63. Namavari M, Cheng Z, Zhang R, De A, Levi J, Hoerner JK, et al. A novel method for direct site-specific radiolabeling of peptides using [18F]FDG. Bioconjug Chem. 2009;20(3):432–6.
64. Carberry P, Carpenter AP, Kung HF. Fluoride-18 radiolabeling of peptides bearing an aminooxy functional group to a prosthetic ligand via an oxime bond. Bioorg Med Chem Lett. 2011;21(23):6992–5.
65. Hausner SH, Marik J, Gagnon MKJ, Sutcliffe JL. In vivo positron emission tomography (PET) imaging with an alpha(v) beta(6) specific peptide radiolabeled using 18F-"click" chemistry: Evaluation and comparison with the corresponding 4-[18F]fluorobenzoyl- and 2-[18F]fluoropropionyl-peptides. J Med Chem. 2008;51(19):5901–4.
66. Vaidyanathan G, Zalutsky MR. Labeling proteins with fluorine-18 using N-succinimidyl 4-[18F]fluorobenzoate. Int J Rad Appl Instrum B. 1992;19(3):275–81.
67. Thonon D, Goblet D, Goukens E, Kaisin G, Paris J, Aerts J, et al. Fully automated preparation and conjugation of N-succinimidyl 4-[18F]fluorobenzoate ([18F]SFB) with RGD peptide using a GE FASTlab synthesizer. Mol Imaging Biol. 2011;13(6):1088–95.
68. Mäding P, Füchtner F, Wüst F. Module-assisted synthesis of the bifunctional labelling agent N-succinimidyl 4-[18F]fluorobenzoate ([18F]SFB). Appl Radiat Isot. 2005;63(3):329–32.
69. Haka MS, Kilbourn MR, Watkins GL, Toorongian SA. Aryltrimethylammonium trifluoromethanesulfonates as precursors to aryl [18F]fluorides: Improved synthesis of [18F]GBR-13119. J Labelled Comp Radiopharm. 1989;27(7):823–33.
70. Basuli F, Zhang X, Woodroofe CC, Jagoda EM, Choyke PL, Swenson RE. Fast indirect fluorine-18 labeling of protein/peptide using the useful 6-fluoronicotinic acid-2,3,5,6-tetrafluorophenyl prosthetic group: A method comparable to direct fluorination. J Labelled Comp Radiopharm. 2017;60(3):168–75.
71. Olberg DE, Arukwe JM, Grace D, Hjelstuen OK, Solbakken M, Kindberg GM, et al. One step radiosynthesis of 6-[18F]fluoronicotinic acid 2,3,5,6-tetrafluorophenyl ester ([18F]F-Py-TFP): A new prosthetic group for efficient labeling of biomolecules with fluorine-18. J Med Chem. 2010;53(4):1732–40.
72. Wu Z, Li Z-B, Chen X. 18F-labeling of peptides using FBEM. Protoc Exch. 2007; https://doi.org/10.1038/nprot.2007.286.
73. Wuest F, Köhler L, Berndt M, Pietzsch J. Systematic comparison of two novel, thiol-reactive prosthetic groups for 18F labeling of peptides and proteins with the acylation agent succinimidyl-4-[18F] fluorobenzoate ([18F]SFB). Amino Acids. 2009;36(2):283–95.
74. White JB, Hausner SH, Carpenter RD, Sutcliffe JL. Optimization of the solid-phase synthesis of F-18 radiolabeled peptides for positron emission tomography. Appl Radiat Isot. 2012;70(12):2720–9.
75. Bernard-Gauthier V, Lepage ML, Waengler B, Bailey JJ, Liang SH, Perrin DM, et al. Recent advances in F-18 radiochemistry: a focus on B-18F, Si-18F, Al-18F, and C-18F radiofluorination via spirocyclic iodonium ylides. J Nucl Med. 2018;59(4):568–72.
76. Smith GE, Sladen HL, Biagini SC, Blower PJ. Inorganic approaches for radiolabelling biomolecules with fluorine-18 for imaging with positron emission tomography. Dalton Trans. 2011;40(23):6196–205.
77. Bernard-Gauthier V, Wängler C, Schirrmacher E, Kostikov A, Jurkschat K, Wängler B, et al. 18F-labeled silicon-based fluoride acceptors: potential opportunities for novel positron emitting radiopharmaceuticals. Biomed Res Int. 2014;2014:1–20.
78. Wangler C, Niedermoser S, Chin J, Orchowski K, Schirrmacher E, Jurkschat K, et al. One-step 18F-labeling of peptides for positron emission tomography imaging using the SiFA methodology. Nat Protoc. 2012;7(11):1946–55.
79. Liu Z, Pourghiasian M, Radtke MA, Lau J, Pan J, Dias GM, et al. An organotrifluoroborate for broadly applicable one-step 18F-labeling. Angew Chem Int Ed Engl. 2014;53(44):11876–80.
80. McBride WJ, Sharkey RM, Goldenberg DM. Radiofluorination using aluminum-fluoride (Al18F). EJNMMI Res. 2013;3(1):36.
81. Marik J, Sutcliffe JL. Click for PET: rapid preparation of [18F] fluoropeptides using CuI catalyzed 1,3-dipolar cycloaddition. Tetrahedron Lett. 2006;47(37):6681–4.
82. Glaser M, Årstad E. "Click labeling" with 2-[18F]fluoroethylazide for positron emission tomography. Bioconjug Chem. 2007;18(3):989–93.
83. Zeng D, Zeglis BM, Lewis JS, Anderson CJ. The growing impact of bioorthogonal click chemistry on the development of radiopharmaceuticals. J Nucl Med. 2013;54(6):829–32.

84. Pretze M, Pietzsch D, Mamat C. Recent trends in bioorthogonal click-radiolabeling reactions using fluorine-18. Molecules. 2013;18(7):8618–65.
85. Kettenbach K, Schieferstein H, Ross TL. 18F-labeling using click cycloadditions. Biomed Res Int. 2014;2014:1–16.
86. Denk C, Svatunek D, Filip T, Wanek T, Lumpi D, Fröhlich J, et al. Development of a 18F-labeled tetrazine with favorable pharmacokinetics for bioorthogonal PET imaging. Angew Chem Int Ed Engl. 2014;53:9655–9.
87. Lazari M, Collins J, Shen B, Farhoud M, Yeh D, Maraglia B, et al. Fully automated production of diverse 18F-labeled PET tracers on the ELIXYS multireactor radiosynthesizer without hardware modification. J Nucl Med Technol. 2014;42(3):203–10.
88. Collet C, Maskali F, Clement A, Chretien F, Poussier S, Karcher G, et al. Development of 6-[18F]fluoro-carbohydrate-based prosthetic groups and their conjugation to peptides via click chemistry. J Labelled Comp Radiopharm. 2016;59(2):54–62.
89. Jacobson O, Yan X, Ma Y, Niu G, Kiesewetter DO, Chen X. Novel method for radiolabeling and dimerizing thiolated peptides using [18F]-hexafluorobenzene. Bioconjug Chem. 2015;26(10):2016–20.
90. Ackermann U, Plougastel L, Goh YW, Yeoh SD, Scott AM. Improved synthesis of [18F]FLETT via a fully automated vacuum distillation method for [18F]2-fluoroethyl azide purification. Appl Radiat Isot. 2014;94:72–6.
91. Ackermann U, Plougastel L, Wichmann C, Goh YW, Yeoh SD, Poniger SS, et al. Fully automated synthesis and coupling of [18F]FBEM to glutathione using the iPHASE FlexLab module. J Labelled Comp Radiopharm. 2014;57(2):115–20.
92. Zeglis BM, Lewis JS. A practical guide to the construction of radiometallated bioconjugates for positron emission tomography. Dalton Trans. 2011;40(23):6168–95.
93. Wadas TJ, Wong EH, Weisman GR, Anderson CJ. Coordinating radiometals of copper, gallium, indium, yttrium, and zirconium for PET and SPECT imaging of disease. Chem Rev. 2010;110(5):2858–902.
94. Färber SF, Wurzer A, Reichart F, Beck R, Kessler H, Wester H-J, et al. Therapeutic radiopharmaceuticals targeting integrin alpha(v) beta(6). ACS Omega. 2018;3(2):2428–36.
95. Roosenburg S, Laverman P, Joosten L, Cooper MS, Kolenc-Peitl PK, Foster JM, et al. PET and SPECT imaging of a radiolabeled minigastrin analogue conjugated with DOTA, NOTA, and NODAGA and labeled with 64Cu, 68Ga, and 111In. Mol Pharm. 2014;11(11):3930–7.
96. Hu LY, Bauer N, Knight LM, Li Z, Liu S, Anderson CJ, et al. Characterization and evaluation of 64Cu-labeled A20FMDV2 conjugates for imaging the integrin alpha(v)beta(6). Mol Imaging Biol. 2014;16(4):567–77.
97. Lin M, Welch MJ, Lapi SE. Effects of chelator modifications on 68Ga-labeled [Tyr3]octreotide conjugates. Mol Imaging Biol. 2013;15(5):606–13.
98. Cai Z, Anderson CJ. Chelators for copper radionuclides in positron emission tomography radiopharmaceuticals. J Labelled Comp Radiopharm. 2014;57(4):224–30.
99. De León-Rodríguez LM, Kovacs Z. The synthesis and chelation chemistry of DOTA−peptide conjugates. Bioconjug Chem. 2008;19(2):391–402.
100. Liu S, Edwards DS. Stabilization of 90Y-labeled DOTA-biomolecule conjugates using gentisic acid and ascorbic acid. Bioconjug Chem. 2001;12(4):554–8.
101. Banerjee S, Pillai MRA, Knapp FF. Lutetium-177 therapeutic radiopharmaceuticals: Linking chemistry, radiochemistry, and practical applications. Chem Rev. 2015;115(8):2934–74.
102. Kiesewetter DO, Gao H, Ma Y, Niu G, Quan Q, Guo N, et al. 18F-radiolabeled analogs of exendin-4 for PET imaging of GLP-1 in insulinoma. Eur J Nucl Med Mol Imaging. 2011;39(3):463–73.
103. James ML, Gambhir SS. A molecular imaging primer: modalities, imaging agents, and applications. Physiol Rev. 2012;92(2):897–965.
104. Bigott-Hennkens HM, Dannoon S, Lewis MR, Jurisson SS. In vitro receptor binding assays: general methods and considerations. Q J Nucl Med Mol Imaging. 2008;52(3):245–53.
105. Jenssen H, Aspmo SI. Serum stability of peptides. In: Otvos L, editor. Peptide-based drug design. Methods In molecular biology, vol. 494. Totowa: Humana Press; 2008. p. 177–86.
106. Hein P, Michel MC, Leineweber K, Wieland T, Wettschureck N, Offermanns S. Receptor and binding studies. In: Dhein S, Mohr FW, Delmar M, editors. Practical methods in cardiovascular research. Berlin: Springer; 2005. p. 723–83.
107. Walker MW, Miller RJ. 125I-neuropeptide Y and 125I-peptide YY bind to multiple receptor sites in rat brain. Mol Pharm. 1988;34(6):779–92.
108. Waterhouse R. Determination of lipophilicity and its use as a predictor of blood–brain barrier penetration of molecular imaging agents. Mol Imaging Biol. 2003;5(6):376–89.
109. Richter S, Wuest M, Bergman CN, Way JD, Krieger S, Rogers BE, et al. Rerouting the metabolic pathway of 18F-labeled peptides: the influence of prosthetic groups. Bioconjug Chem. 2015;26(2):201–12.
110. Stout DB, Chatziioannou AF, Lawson TP, Silverman RW, Gambhir SS, Phelps ME. Small animal imaging center design: the facility at the UCLA Crump Institute for Molecular Imaging. Mol Imaging Biol. 2005;7(6):393–402.
111. David JM, Knowles S, Lamkin DM, Stout DB. Individually ventilated cages impose cold stress on laboratory mice: a source of systemic experimental variability. J Am Assoc Lab Anim Sci. 2013;52(6):738–44.
112. Keyes JW Jr. SUV: standard uptake or silly useless value? J Nucl Med. 1995;36(10):1836–9.
113. Visser EP, Boerman OC, Oyen WJG. SUV: from silly useless value to smart uptake value. J Nucl Med. 2010;51(2):173–5.
114. Pompili L, Porru M, Caruso C, Biroccio A, Leonetti C. Patient-derived xenografts: a relevant preclinical model for drug development. J Exp Clin Cancer Res. 2016;35(189):1–8.
115. Jackson SJ, Thomas GJ. Human tissue models in cancer research: looking beyond the mouse. Dis Model Mech. 2017;10(8):939–42.
116. Randall EK. PET-computed tomography in veterinary medicine. Vet Clin North Am Small Anim Pract. 2016;46(3):515–33.
117. Spriet M, Espinosa P, Kyme AZ, Phillips KL, Katzman SA, Galuppo LD, et al. 18F-sodium fluoride positron emission tomography of the equine distal limb: exploratory study in three horses. Equine Vet J. 2018;50:125–32.
118. Akizawa H, Uehara T, Arano Y. Renal uptake and metabolism of radiopharmaceuticals derived from peptides and proteins. Adv Drug Deliv Rev. 2008;60(12):1319–28.
119. Sleep D. Albumin and its application in drug delivery. Expert Opin Drug Deliv. 2014;12(5):793–812.
120. Nock BA, Maina T, Krenning EP, de Jong M. "To serve and protect": enzyme inhibitors as radiopeptide escorts promote tumor targeting. J Nucl Med. 2013;55(1):121–7.
121. Pless J. The history of somatostatin analogs. J Endocrinol Invest. 2005;28(11 Suppl International):1–4.
122. Brazeau P, Vale W, Burgus R, Ling N, Butcher M, Rivier J, et al. Hypothalamic polypeptide that inhibits secretion of immunoreactive pituitary growth-gormone. Science. 1973;179(4068):77–9.
123. Okarvi SM. Peptide-based radiopharmaceuticals and cytotoxic conjugates: potential tools against cancer. Cancer Treat Rev. 2008;34(1):13–26.
124. Martino MCD, Hofland LJ, Lamberts SWJ. Somatostatin and somatostatin receptors: from basic concepts to clinical applications. In: Martini L, editor. Progress in brain research, vol. 182. Amsterdam: Elsevier; 2010. p. 255–80.

Immunoglobulins as Radiopharmaceutical Vectors

Danielle J. Vugts and Guus A. M. S. van Dongen

Fundamentals

The discovery of target-specific molecules has revolutionized medicine. While only generic drugs were available at first, the development of hybridoma technology made possible the creation of immunoglobulins that target a specific antigen or protein. Since then, the development of immunoglobulins has evolved, and not only tumor-associated antigens but also antigens involved in angiogenesis and immune control can be targeted. Furthermore, these antibodies can be decorated with payloads such as dyes, radionuclides, and toxins to expand their utility.

It is remarkable to note that all of the radioimmunoconjugates that have been approved by the FDA and EMA to date are murine antibodies. Furthermore, 90% of these are diagnostic agents, and the most recent approval occured almost a decade ago. While no radioimmunoconjugates have been approved since 2010, the application of these radiopharmaceuticals in early phase clinical trials has increased dramatically in recent years. This advent has been driven by the idea that imaging can aid in the understanding of therapeutic drugs during early phase clinical trials with fewer patients. As a result, one of the primary aims in the creation of antibody-based radiotracers is not preparing stand-alone diagnostics but rather creating companion imaging agents that can guide the development and application of therapeutics.

Details

Immunoglobulins

The Discovery of Immunoglobulins More than 100 years ago, Dr. Paul Ehrlich received the Nobel Prize in Physiology or Medicine for his contribution to immunology. His immunological achievements evolved into what is now called the "magic bullet concept": the idea that diseases can be treated using drugs that target specific receptors or biochemical pathways. In theory, these "magic bullets" do not harm healthy tissues, since the receptor that is targeted is not present in healthy tissue. Ehrlich applied this concept during the development of an antisyphilitic drug by synthesizing and screening hundreds of organic arsenical compounds. His ideas inspired many others and have had a profound impact on the field of cancer therapy.

The development of monoclonal antibodies as magic bullets for tracing and killing microbes and tumor cells took off in 1975 with the discovery of hybridoma technology by Georges Kohler and César Milstein, for which the pair received the Nobel Prize for Medicine and Physiology in 1984 [1]. In its most basic form, hybridoma technology is predicated on injecting a mouse with an antigen or antigen-containing cells to provoke an immune response. The mouse's B cells (also known as B lymphocytes)—a type of white blood cells of the lymphocyte subtype—then produce antibodies that bind the antigen. These B cells can be isolated, fused with immortalized myeloma cells, and cloned to produce what is termed a "hybridoma" cell line that continually produces murine monoclonal antibodies (mAbs) against the original antigen.

Although useful for *in vitro* purposes and *in vivo* murine preclinical studies, murine mAbs suffer from immunogenicity problems in human patients, since the human body recognizes them as foreign and thus produces human anti-mouse antibodies (HAMAs). This HAMA response, observed in about 90% of patients, is an allergic reaction that can range from a mild rash to life-threatening anaphylactic shock and has hampered the use of murine mAbs in the clinic. Furthermore, mouse mAbs suffer from short serum half-lives, inefficient disease targeting, and an inability to efficiently trigger human effector functions. After the repeated administration of murine antibodies, HAMAs can be formed, and the clearance of the mouse mAbs can become even faster [2].

D. J. Vugts (✉) · G. A. M. S. van Dongen
Department of Radiology & Nuclear Medicine, VU University Medical Center, Amsterdam, The Netherlands
e-mail: d.vugts@vumc.nl

J. S. Lewis et al. (eds.), *Radiopharmaceutical Chemistry*, https://doi.org/10.1007/978-3-319-98947-1_9

In response to these limitations, the technology underpinning the development of mAbs has matured and enabled the creation of chimeric, humanized, and human antibodies (Fig. 1). Chimeric mAbs consist of a variable region of murine origin and a constant region of human origin. With these mAbs, the chance of provoking an unwanted immune response is decreased to about 50% because of the human origin of the constant region. Humanized mAbs were developed to overcome the remaining immunogenicity issue. Humanized mAbs have murine complementarity-determining regions (CDRs) and human variable and constant regions. Further innovations have led to the ability to create fully human antibodies, for which the chance of immune response is decreased even further (to less than 20%), though not eliminated completely.

Engineered mAb Development and Functionalization of mAbs There are five different classes of immunoglobulins: IgG, IgM, IgA, IgD, and IgE (Fig. 2). For more detailed information regarding the structure and function of antibodies, the reader is referred to *Roitt's Essential Immunology* [3].

IgGs are the most common class used for the creation of radioimmunoconjugates and antibody-drug conjugates. IgGs consist of two identical light chains and two identical heavy chains linked to each other via disulfide bonds. The variable heavy (V_H) and variable light (V_L) chains are collectively called the variable region (F_v), the part of the antibody that contains the antigen-binding complementarity-determining regions (CDRs). The V_H and V_L chains together with the constant light chain (C_L) and the C_H1 constant heavy chain are collectively called the Fab region, while the constant heavy chains C_H2 and C_H3 together form the constant region (F_C) (see IgG in Fig. 2). The Fc region interacts with effector cells and is involved in the activation of the complement cascade.

Multiple engineered immunoglobulins and antibody-like protein scaffolds such as affibody molecules and Adnectins [4] have been developed to complement the natural antibodies displayed in Figs. 1 and 2. Table 1 provides an overview of the different formats of engineered antibodies and antibody-like protein scaffolds as well as several of their characteristics, such as their molecular weight, composition, and typical serum half-life. Finally, a great deal of effort has also been dedicated to the creation of other antibody-based constructs, including immunocytokines, bispecific and multispecific mAbs [5] capable of targeting two or more distinct antigens, and glycoengineered mAbs [6].

The In Vivo Mechanisms of Action of Immunoglobulins Most of the immunoglobulins developed for medical applications are therapeutic agents. These constructs—mostly anticancer drugs—can be distinguished via the several modes of action through which they function [7]:

1. Antibody-Dependent Cell-Mediated Cytotoxicity (ADCC): After the binding of the antibody to a target on the surface of the cell, an immune effector cell such as a natural killer (NK) cell, monocyte, macrophage, or granulocyte interacts with the Fc part of the antibody and actively lyses the targeted cell (Fig. 3a).
2. Complement-Dependent Cytotoxicity (CDC): Via its Fc region, the antibody activates a complement cascade which triggers cell death via the formation of a membrane attack complex on the surface of the cell (Fig. 3a).

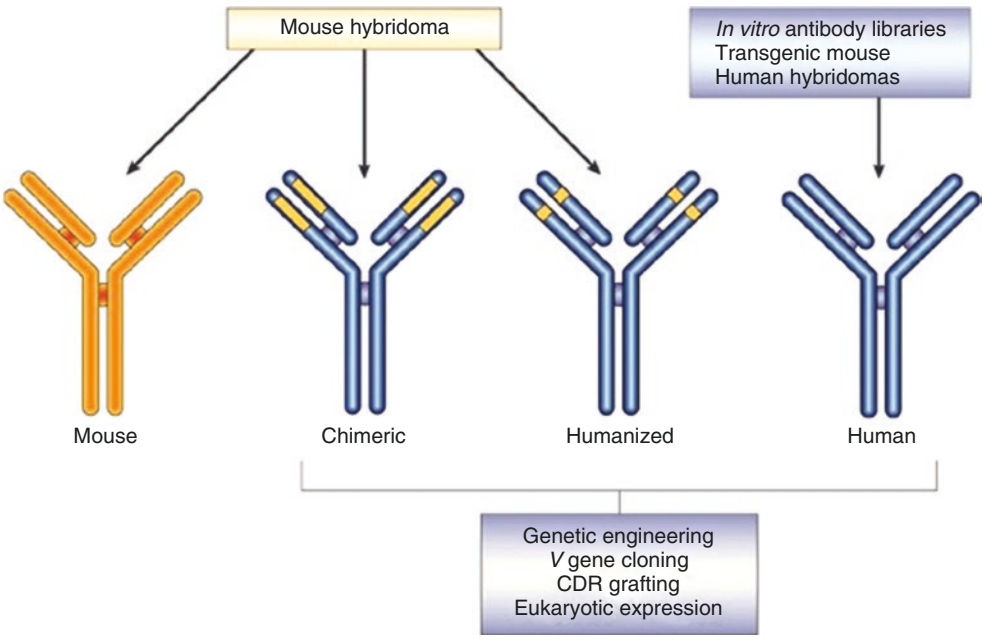

Fig. 1 Overview of mouse, chimeric, humanized, and human antibodies (From Brekke *et al.* [2], with permission)

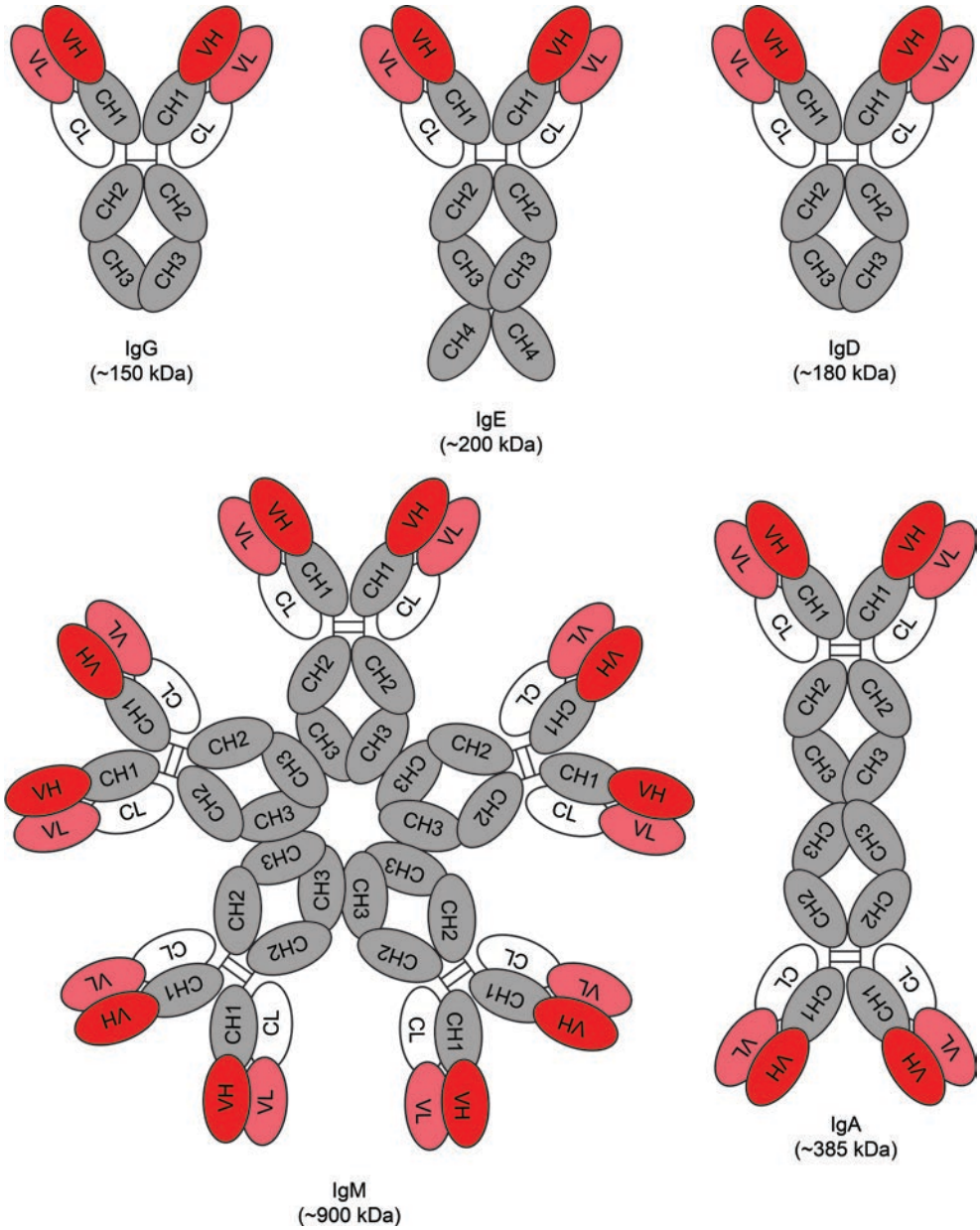

Fig. 2 Overview of the structure of IgG, IgA, IgM, IgD, and IgA immunoglobulins

3. Signal Transduction: The binding of the antibody to its target generates an intracellular signal or blocks signal transduction, which can affect a broad range of cellular functions, including growth, differentiation, and death (Fig. 3a).
4. Inhibition of Angiogenesis: Angiogenesis is the growth of new blood vessels from existing vasculature. The new vessels supply the growing tumor with oxygen and nutrients, allowing the tumor to enlarge, invade nearby tissue, and spread throughout the body (Fig. 3b).
5. Checkpoint Blockade: Immune checkpoints regulate the immune system, and they can be used by tumors to protect themselves from attacks by the immune system. Via checkpoint blockade, the inhibitory checkpoints are blocked and the immune system competence restored. (Fig. 3c).

The therapeutic effect of antibodies can also be mediated via the conjugation of therapeutic radionuclides or highly toxic chemotherapeutics to immunoglobulins, creating radioimmunoconjugates and antibody-drug conjugates (ADCs), respectively (Fig. 3d, e). Moving on to slightly more complex technologies, bispecific mAbs are available targeting two different antigens, *e.g.* one arm recognizes an antigen on a tumor cell, and the other arm activates antigens on immune effector cells (Fig. 3f). Finally, chimeric antigen receptor (CAR) T-cell-based therapy is highly promising as well. T-cells from a patient are collected and genetically engineered by intro-

Table 1 Comparison of the properties of engineered mAbs

Format		Molecular weight (kDa)	Typical serum $t_{1/2}$	Clearance route
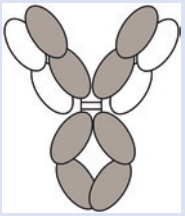	IgG	~150	1–3 weeks	Hepatic
	F(ab')2	~110	1–7 days	Hepatic
	Fab	~50	12–20 h	Renal
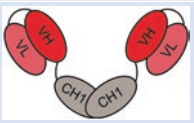	Minibody	~75	5–10 h	Hepatic
	scFv	~25	2–4 h	Renal
	Diabody	~50	3–5 h	Renal
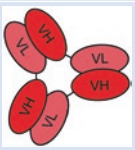	Triabody	~75		Hepatic
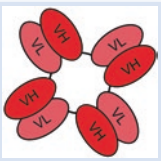	Tetrabody	~100		Hepatic
	Domain antibody	~15	30–60 min	Renal
	Nanobody (dimer)	12–15 (per nanobody)	30–60 min	Renal
	Affibody	6	30–60 min	Renal
	Adnectin/monobody (fibronectin type III domain)	10	<2 h	Renal

ducing DNA into them, thereby producing CARs on the surface of the cells. The CARs are proteins that allow the T cells to recognize an antigen on targeted tumor cells (Fig. 3g).

Application in Different Disease Areas The majority of the immunoglobulins under evaluation and approved by the FDA and EMA are directed against cancer or autoimmune diseases such as Crohn's disease. The number of immunoglobulins in phase III clinical trials has doubled between 2010 (26 mAbs) and 2017 (52 mAbs). The series *Antibodies to Watch in [20XX]* published in the journal MABS is an interesting source describing both mAbs in late-stage clinical trials and recently approved mAbs [8].

The newest area in which immunoglobulins are being used is the field of neurology. Although up to now this has not been very successful, there is an increasing interest in the development of immunoglobulins for diagnosis and therapy

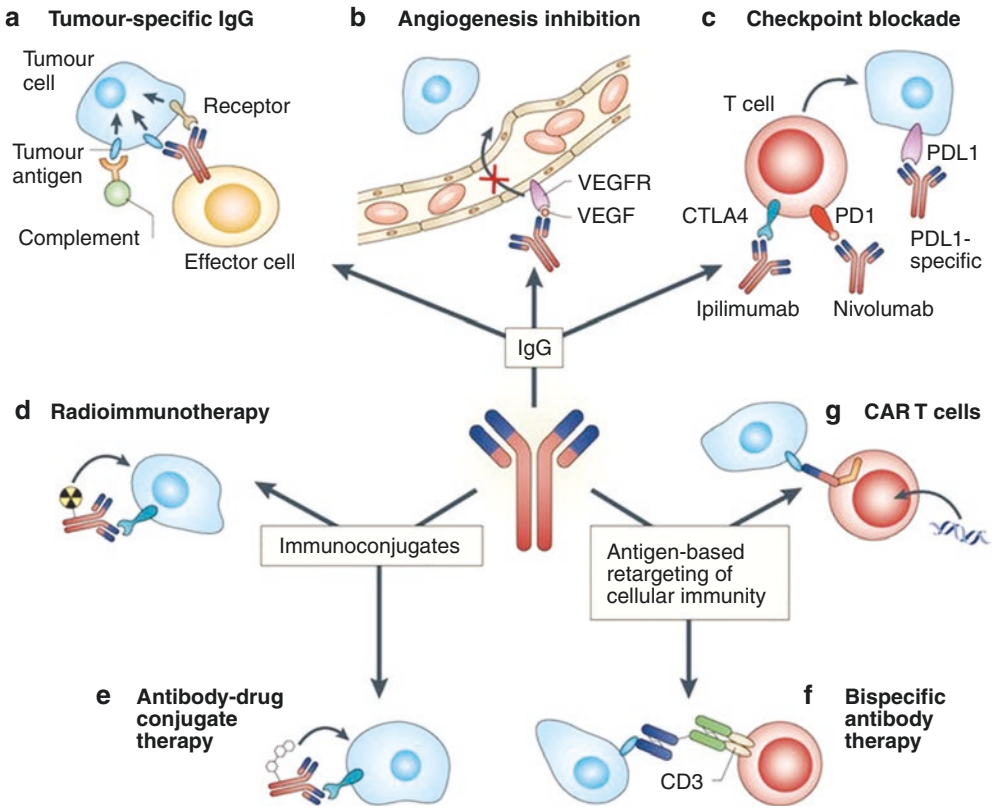

Fig. 3 Successful monoclonal antibody (mAb) therapeutics have been based on a number of strategies. Immunoglobulin G (IgG) molecules that bind to target cancer cells (**a**) can mediate antibody-dependent cellular cytotoxicity (ADCC) by immune effector cells, induce complement-mediated cytotoxicity (CMC) or result in the direct signalling-induced death of cancer cells (for example, herceptin and rituximab). IgG mAbs can also be used to inhibit angiogenesis (**b**) (for example, bevacizumab) or block inhibitory signals (**c**), thereby resulting in a stronger antitumour T cell response (for example, ipilimumab and nivolumab). Radioimmunoconjugates (**d**) (for example, ^{131}I-labeled tositumomab and ^{90}Y-labeled ibritumomab tiuxetan) deliver radionuclides to the cancer cells, whereas antibody–drug conjugates (**e**) (for example, brentuximab vedotin and trastuzumab emtansine) deliver highly potent toxic drugs to the cancer cells. mAb variable regions are also used to re-target immune effector cells towards cancer cells through the use of bispecific mAbs that recognize cancer cells with one arm and activating antigens on immune effector cells with the other arm (**f**) (for example, blinatumomab) or through a gene therapy approach in which DNA for a mAb variable region fused to signalling peptides is transferred to T cells, thereby rendering them chimeric antigen receptor (CAR) T cells (**g**) specific for the tumour. CD3, T cell surface glycoprotein CD3 ε-chain; CTLA4, cytotoxic T lymphocyteassociated antigen 4; PD1, programmed cell death protein 1; PDL1, PD1 ligand; VEGF, vascular endothelial growth factor; VEGFR, VEGF receptor

of neurodegenerative diseases. Antibodies by themselves have a very limited brain penetration because they cannot pass through the blood-brain barrier (BBB), a fact which has prompted debate on whether intact antibodies could ever be useful as therapeutic agents in neurology. However, the development of immunoglobulins that are actively transported across the BBB has allayed some of these concerns, making this area an exciting new frontier for research [9].

Target Expression and Accessibility

When discussing antibodies in the context of radiopharmaceuticals vectors, cancer provides most of the targets of interest. Two important parameters in the development of mAb-based radioimmunoconjugates are the expression and accessibility of the target.

Target Expression The ideal antigen is only expressed in the tissue of interest—usually a tumor. Unfortunately, very few *truly* tumor-*specific* antigens exist. Instead, most antigens found on tumors are also expressed on healthy tissues, therefore making them tumor-*associated* antigens. Generally speaking, tumor-associated antigens are expressed in greater abundance on tumor cells than on healthy tissues. Furthermore, it might be that the antigen expressed on normal tissues is poorly accessible for intravenously injected mAbs, and therefore these antigens are called "operationally" tumor selective. Not surprisingly, high densities of antigen favor the accumulation of the radioimmunoconjugate at the tumor site, and large differences between the expression of antigen on tumor tissue and healthy tissues will result in better tumor-to-background contrast, which is important for diagnostic as well as for therapeutic purposes.

Unfortunately, the uptake of a mAb or radioimmunoconjugate is often a more complicated issue than the simple presence or absence of the antigen. For example, the shedding or secretion of antigens into the blood can result in the formation of immunocomplexes in the blood, which can limit the amount of mAb available for tumor binding. In addition, upon the binding of the mAb or radioimmunoconjugate to the antigen, the expression of some antigens can be downregulated or modulated, a change which can hamper the efficacy of mAb-based treatments.

In conclusion, the target of a radioimmunoconjugate should be expressed with high density on diseased cells like tumor cells and low density in healthy tissues. This combination should produce the highest signal-to-background concentration ratios. It is important to remember that the expression of antigen in healthy organs can create an "antigen sink" which must be saturated before the antibody can effectively target tumor tissue [10]. Thus, the lowest dose of antibody does not necessarily—or even usually—produce the highest activity concentration in the tumor. The optimal antibody dose for radioimmunodetection and radioimmunotherapy should therefore be determined via dose escalation studies in humans.

Target Accessibility The accessibility of a molecular target is governed by several factors, including vascularization, interstitial fluid pressure, the nature of the disease (*i.e.* hematological tumors vs. solid tumors), and the location of the disease in the body [11, 12]. For example, tumors can grow up to 1–2 mm^3 without the need of vasculature. However, if they want to grow larger, they must find a way to gather blood supply from the host organism. Angiogenesis—the formation of new blood vessels from preexisting ones—is the most well-known mechanism by which tumors supply themselves with nutrients and oxygen, although other mechanisms have been described by Hillen and Griffioen [13]. Notably, the vasculature of tumors is relatively disordered compared to that of normal tissues and thus has low and irregular blood flow. This can result in the inconsistent supply of nutrients to the tumor and the creation of hypoxic regions within the tumor.

In addition to tumor cells and blood vessels, tumors are also composed of the extracellular matrix (ECM), stroma, and tumor interstitial fluid (TIF). All of these components can affect the accessibility of the target within the tumor [14]. For example, the presence of TIF can increase the interstitial pressure within tumors, impairing the ability of antibodies to penetrate the tumor and thus reducing the accessibility of the target. Finally, both the type of tumor and the location of the tumor can influence the accessibility of the target (and thus the effectiveness of the mAb). Hematological tumors ("liquid tumors") are easy to access, whereas solid tumors can be more complicated and difficult to penetrate. Moreover, natural barriers in the human body can have an impact on the accessibility of the tumor and target. For example, macromolecules such as antibodies cannot penetrate the blood-brain barrier, while the poor permeability of organs such as the skin and the lungs can prevent the access of the antibody as well. The aforementioned factors may account for the variable uptake of mAbs in different types of tumors as well as the heterogeneous distribution of radioimmunoconjugates within an individual tumor. Therefore, these factors should always be considered when evaluating radioimmunoconjugates.

Radioimmunoconjugates

Selection of the Appropriate Radionuclide-Immunoglobulin Combination Table 2 provides a summary of the most common radionuclides used in conjunction with antibodies for positron-emission tomography (PET), single photon emission computed tomography (SPECT), and radioimmunotherapy. The properties that are most important for the selection of the ideal radionuclide-immunoglobulin combination are included as well. The most crucial directive to take into account when selecting a radionuclide for imaging is matching the physical half-life of the radionuclide with the biological half-life of the immunoglobulin. This is essential to ensure that there is sufficient time for the immunoglobulin to accumulate in the tumor prior to the decay of the radionuclide, that the tumor can be visualized, and that the radiation exposure to normal tissues is as low as possible. When selecting the radionuclide for radioimmunotherapy, the most important factor to consider is that the radiation dose to the tumor in comparison with normal tissues is optimal. The biological half-life of the immunoglobulin is mainly determined by its molecular weight and structure. The general rule of thumb is that a protein with a molecular weight lower than 70 kDa is cleared very rapidly (within hours) via the kidneys, whereas larger macromolecules have longer *in vivo* half-lives. The half-life of an immunoglobulin also depends on its subtype as well as its origin: mouse, chimeric, humanized, or human.

Taken together, all of this means that intact IgG1s are typically labeled with radionuclides with physical half-lives of several days. Furthermore, when radiolabeling immunoglobulins, the use of so-called residualizing radionuclides is generally preferred. Residualizing radionuclides will be trapped inside the cell after internalization and will not be released from the target tissue. In contrast, non-residualizing nuclides such as iodine are released upon the internalization and catabolism of the immunoglobulin. As a result, the uptake and biodistribution of the radionuclide do not reflect the uptake and biodistribution of the radioimmunoconjugate. If the immunoglobulin is not internalized, the residualizing nature of the nuclide

Table 2 Radionuclides used in radioimmunoconjugates for PET, SPECT, and radioimmunotherapy

Radionuclide	Physical half-life	β^+_{max} in keV (yield)	β^-_{max} in MeV (yield)	γ-energies in MeV (yield)	Properties
^{18}F	109.77 min	634 (97%)	–	0.14 (41%)	Tracers can be transported over short distances, imaging up to 6 h after injection, cyclotron product, only suitable for imaging of fast-clearing antibody fragments
^{86}Y	14.72 h	3141 (34%)	–	1.08 (83%)	Forms an ideal theranostics pair with ^{90}Y, cyclotron product, relatively short half-life for imaging antibodies, only suitable for imaging small antibody fragments
^{89}Zr	78.41 h	902 (23%)	–	0.9 (99%)	Ideal $t_{1/2}$ for IgG imaging, cyclotron product, transportation worldwide (including radioimmunoconjugates), bone-seeking radionuclide
^{124}I	100.22 h	2138 (24%)	–	0.6 (61%)	Ideal $t_{1/2}$ for IgG imaging, cyclotron product, transportation worldwide (including radioimmunoconjugates)
^{64}Cu	12.70 h	653 (18%)	0.58 (39%)	–	Cyclotron product, relatively short half-life for imaging antibodies, only suitable for imaging small antibody fragments
^{68}Ga	67.71 min	1899, 822 (90%)	–	1.08 (3%)	Germanium generator product, only suitable for imaging of fast-clearing antibody fragments
^{123}I	13.22 h	–	–	0.16 (83%)	Cyclotron product, suitable for imaging antibody fragments; dehalogenation can occur resulting in thyroid uptake
^{131}I	8.03 d	–	0.63 (90%)	0.36 (82%)	Dehalogenation can occur resulting in thyroid uptake, nuclear reactor product, used for RIT
^{111}In	67.3 h	–	–	0.17, 0.25 (100%)	Ideal $t_{1/2}$ for IgG imaging, cyclotron product, bone-seeking isotope
^{67}Cu	61.83 h	–	0.56 (20%), 0.47 (35%), 0.38 (45%)	0.18 (40%)	Ideal $t_{1/2}$ for RIT with intact IgG, not easily available, accelerator product
^{177}Lu	159.5 h	–	0.18 (12%), 0.39 (9%), 0.50 (79%)	0.11, 0.21 (100%)	RIT and imaging possible at the same time, nuclear reactor product
^{99m}Tc	6.0 h	–	–	0.14 (890%)	Molybdenum generator product, only suitable for imaging of fast-clearing antibody fragments, cheap
^{90}Y	64.1 h	–	2.28 (100%)	–	RIT only, forms an ideal theranostics pair with ^{86}Y, ^{90}Sr generator product
^{67}Ga	78.3 h	–	–	0.09 (39%), 0.18 (21%), 0.3 (17%)	Ideal $t_{1/2}$ for imaging with intact IgG, cyclotron product

PET positron-emission tomography, *SPECT* single photon emission computed tomography, *RIT* radioimmunotherapy

becomes less important. In most of the cases, however, the immunoglobulin is at least partially internalized, and thus the choice for a so-called residualizing isotope is preferred.

Another important consideration is that the radioimmunoconjugate should be as stable as possible. Therefore, it is important to exert careful control over the radiochemistry and select the appropriate chelator for the radiometal at hand (if applicable). Furthermore, the radiolabeling should be done inertly and should not change the biodistribution of the mAb. Finally, the costs of preparing a radioimmunoconjugate should be considered as well. Although this is not relevant from a scientific perspective, it certainly is from a clinical care viewpoint. If a radionuclide is very costly to produce (and thus to use), this will inevitably adversely affect the availability and applicability of the radioimmunoconjugate.

Approved Radioimmunoconjugates in the Clinic The number of radioimmunoconjugates approved by the US Food and Drug administration (FDA) and European Medicines Agency (EMA) is rather limited. Table 3 presents an overview of the approved radioimmunoconjugates, including their antibody format, target, production method, radiolabel, and approved indications [15]. In general, it is clear that most of these radioimmunoconjugates are of murine origin. Furthermore, they are all radiolabeled with SPECT radionuclides or contain a therapeutic radionuclide (*i.e.* I-131 or Y-90). Since 2010, no new radioimmunoconjugates have been approved by the FDA or EMA, yet the use of radioimmunoconjugates in phase I–III clinical trials has grown tremendously (see clinical trials.gov) [16, 17].

Application of Radioimmunoconjugates in Drug Development In addition to pure diagnostic and therapeutic agents, radioimmunoconjugates have also been used as imaging tracers to aid in the development, evaluation, and applica-

Table 3 Overview of approved immunoglobulin-based imaging or therapeutic radiopharmaceuticals

Trade name	Generic name	Company	EMA approval	FDA approval	Antibody format	Target	Cell line	Radiolabel	Approved indications
OncoScint	Satumomab pendetide	Cytogen	Not approved	1992	B72.3, mouse IgG1	TAG-72	Hybridoma	^{111}In	Colorectal and ovarian carcinoma
CEA-Scan	Arcitumomab	Immunomedics	1996 (withdrawn in 2005)	1996	IMMU-4, mouse IgG Fab'	Human CEA	Hybridoma	^{99m}Tc	Colorectal cancer
Myoscint	Imciromab pentetate	Centocor	Not approved	1996 (discontinued)	R11D10, mouse IgG2a Fab'	Human cardiac myosin	Murine ascites	^{111}In	Myocardial infarction
Verluma	Nofetumomab merpentan	Boehringer Ingelheim, NeoRx	Not approved	1996	NR-LU-10, mouse IgG2b Fab	40 kDa glycoprotein antigen (carcinoma-associated antigen)	Hybridoma	^{99m}Tc	Small-cell lung cancer
ProstaScint	Capromab pendetide	Cytogen	Not approved	1996	7E11-C5.3, mouse IgG1	Tumor surface antigen PSMA, 100 kDa glycoprotein	Hybridoma	^{111}In	Prostate carcinoma
Zevalin	Ibritumomab tiuxetan	Spectrum Pharms/ Biogen	2004	2002	2B8, mouse IgG1	CD20	CHO	^{90}Y	Non-Hodgkin lymphoma
Bexxar	Tositumomab	Corixa and GSK	Not approved	2002 (discontinued in 2014)	B1, mouse IgG2a	CD20	Hybridoma	^{131}I	Non-Hodgkin lymphoma
NeutroSpec formerly LeuTech	Fanolesomab	Palatin Technologies	Not approved	2004	RB5, mouse IgM	CD15	Hybridoma	^{99m}Tc	Appendicitis
Lymphoscan	Bectumomab	Immunomedics		Not approved	LL2, mouse IgG2a Fab'	CD22		^{99m}Tc	Non-Hodgkin lymphoma
HumaSPECT	Votumumab	KS Biomedix Ltd./Organon Teknika	1998 (withdrawn in 2003)	Not approved	88BV59, human IgG3	Cytokeratin tumor-associated antigen	Human lymphoblastoid cell line transformed with EBV	^{99m}Tc	Carcinoma of the colon and rectum
Indimacis-125	Igovomab	CIS Bio International	1996 (discontinued)	Not approved	OC125, mouse IgG1 F(ab')2	CA-125		^{111}In	Ovarian cancer
LeukoScan	Sulesomab	Immunomedics	1997	Not approved	IMMU-MN3, mouse IgG Fab'	NCA-90	NS0	^{99m}Tc	Osteomyelitis and appendicitis, including patients with diabetic foot ulcers
Scintimun	Besilesomab	CIS Bio	2010	Not approved	Murine IgG1	NCA-95	Hybridoma	^{99m}Tc	Inflammation/infection

tion of therapeutic drug candidates. Indeed, they have been used in numerous preclinical studies as well as early phase clinical trials. In general, drug development is inefficient, time-consuming, and expensive: timelines of 10–15 years from target discovery to drug approval are typical. Notably, the approval and success rates of immunoglobulins are much higher than those of new small molecules; however, the success rate remains low. About 8% of all small molecules in phase I clinical trials are approved, compared to ~14% for biologics [18]. In oncology (the field in which radioimmunoconjugates are most often used), the numbers are even more dire: only 7% of the drugs in phase I studies will ultimately be approved. In light of these numbers, it is not surprising that the use of imaging has attracted attention as an approach to improve the odds for small molecules and biologicals in early phase clinical trials.

Choice for PET or SPECT Imaging Twenty years ago, most radioimmunoconjugates available were for SPECT imaging. Today, however, the pendulum has swung heavily in favor of PET. The preference for PET is largely driven by the increased availability of clinical PET scanners and the intrinsic advantages of PET over SPECT. More specifically, PET has a better spatial resolution than SPECT and is more sensitive, and PET data can be quantified. When a choice has to be made between developing a PET and SPECT radioimmunoconjugate, at least five questions should spring to mind: (A) What types of scanners are available in the clinic? (B) What resolution is required? (C) Are quantitative results required? (D) What is the cost of the radionuclide? (E) What are the costs associated with the preparation of the radioimmunoconjugate? When both PET and SPECT are available, PET should be favored due to its intrinsic advantages.

Theranostics and Radioimmunotherapy (RIT) While many definitions have been offered for the term "theranostics," the essence of the idea is clear: the use of diagnostic imaging to improve the efficacy of therapy. To this end, patients can be imaged using a diagnostic radioimmunoconjugate, and the imaging data can be used to design a treatment regimen based on an analogous radioimmunoconjugate labeled with a therapeutic radionuclide (see Table 2). The ideal theranostic combination of radioimmunoconjugates should have the same biodistribution, and as a result, the imaging radioimmunoconjugate will provide an accurate prediction of the internal dosimetry—including tumor dose—created by the therapeutic radioimmunoconjugate. In this regard, the imaging helps in selecting patients suitable for RIT and can be used to determine the total dose of RIT needed to have an optimal therapeutic effect without causing deleterious side effects. For this, the radionuclides should behave identically *in vivo* and should not accumulate in radiosensitive organs, even if they are released from their chelators. For example, if a theranostic pair of radioimmunoconjugates are both internalized in the tumor and catabolized by the liver, the redistribution of the free radionuclides should be the same.

Considerations for the Development of Radioimmunoconjugates At this juncture, we believe that it would be helpful to lay out several guidelines that should be considered during the design and development of radioimmunoconjugates. Generally speaking, the strategies that have been developed for the preparation of radioimmunoconjugates are generic. For example, the conjugation of isothiocyanate-bearing chelators to the lysines of antibodies works the same way—or *nearly* the same way—for all antibodies (see Chap. 25). The same is true for labeling, say, DFO-bearing immunoconjugates with zirconium-89. This marks a substantial departure from the preparation of small-molecule radiotracers and radiotherapeutics, for which radiosynthetic strategies can vary widely.

Inert Radiolabeling As discussed in the previous section, it is critical to modify and radiolabel each antibody in an inert manner in order to ensure that the biodistribution of the radioimmunoconjugate is identical to that of its parental antibody. This can be achieved in most cases by keeping the ratio of chelators to mAb as low as possible. The effect of the number of chelators per antibody can—and should—be explored both *in vitro* and *in vivo*. Even if *in vitro* binding assays suggest that the act of radiolabeling does not affect the ability of the antibody to bind its molecular target, the pharmacokinetic profile of the construct may nonetheless have been altered. Thus, both methods of interrogation are critical. Most of the time, the effect of bioconjugation is marginal, and on average, up to four chelators per antibody can be randomly accommodated without affecting the *in vivo* performance of the immunoconjugate. It is recommended, however, to stay on the safe side and attach fewer than two chelators per antibody. It is especially important to ensure the inert nature of radiolabeling in the context of radioiodination reactions. When direct radioiodinations are performed using oxidizing agents, the radiolabeling efficiency can increase with longer reaction times and more oxidants. However, this increase in yield comes at a price, as longer reaction times or more oxidants are often associated with oxidative damage to the immunoglobulin itself [19].

Radiolabeling Efficiency and Purification Both the ease of radiolabeling and the radiolabeling efficiency should also be considered while developing a new radiolabeling procedure for an immunoconjugate. The premodification of the mAb with a chelator to create a storable chelator-mAb construct allows for easy-to-use post-labeling procedures that result in excellent labeling efficiencies. Excellent radiolabeling effi-

ciencies can facilitate kit preparations—as are often used for ^{99m}Tc-radiopharmaceuticals—as well as direct injections. However, reagents used during radiolabeling must often be removed prior to formulation and injection into animals or patients. To this end, size-exclusion chromatography using disposable columns or spin filter filtration are often applied for the purification of radioimmunoconjugates. For both methods, the size of the radioimmunoconjugate is the basis for its separation from other reagents (mostly small molecules and salts) present during radiolabeling. The immunoconjugate precursor is not typically separated from the radioimmunoconjugate, and the specific activity is thus expressed as amount of radioactivity divided by the total mass of immunoglobulin in the solution (MBq/mg). Good radiolabeling efficiencies also help to control costs by reducing the amount of radionuclide needed for radiosynthesis reactions and minimize the presence and influence of impurities.

It is important to note that both the immunoconjugate and the radionuclide should be highly pure prior to even beginning a radiolabeling experiment. Even relatively minute impurities in the radiolabeling mixture can adversely affect both the yield of the radiolabeling reaction as well as the quality of the final product. Along these lines, when selecting reagents to be used in the preparation of radioimmunoconjugates, their chemical composition should be evaluated to determine whether any impurities might influence the efficiency of radiolabeling. For example, the metal content of solvents should be as low as possible. Interestingly, this can lead to the selection of chemical grade materials rather than pharmaceutical grade materials for use in the clinic, because the pharmaceutical grade material may contain too many metal impurities. Similarly, when radiometals are used for radiolabeling, it is often advisable to pretreat solvents and disposables with Chelex resin in order to minimize the presence of (competing) metallic impurities.

Stability of Radioimmunoconjugates The *in vitro* and *in vivo* stability of both diagnostic and therapeutic radioimmunoconjugates should be excellent. For this purpose, the *in vitro* stability of radioimmunoconjugates is mostly evaluated upon storage at 4 °C and 37 °C in storage buffer or in human serum. In case of therapeutic radioimmunoconjugates, the high radioactivity concentration might cause radiation damage due to radical formation resulting in deterioration of the therapeutic radioimmunoconjugate. Antioxidizing agents can prevent the radiation damage. Furthermore, the *in vivo* stability is especially critical for therapeutic radioimmunoconjugates, since many therapeutic radionuclides deliver their radiation dose over long periods of time, and it is preferable that the radioimmunoconjugates remain stable for as much of this time period as possible.

Current Good Manufacturing Practice (cGMP) In the development of radioimmunoconjugates, it is of utmost importance to develop processes that are compliant with GMP. Of course, this can be less of an issue when developing radioimmunoconjugates for preclinical studies. However, in these cases, the animal welfare and the reproducibility of results should be paramount considerations as well. With regard to cGMP, the use of hazardous chemicals in the preparation of radioimmunoconjugates should be avoided if possible, and the chemicals with the lowest risk and environmental impact ("green chemistry") should be used if several options can produce the same high-quality product. If this is not the case, it should be proven that these hazardous chemicals do not end up in the final product after purification and formulation. Along these lines, a good purification procedure is absolutely critical and should be evaluated very carefully.

The Evaluation of Radioimmunoconjugates

When a radioimmunoconjugate is prepared for the first time, the quality of the radioimmunoconjugate must be determined as well as its *in vitro* and *in vivo* performance. Protection against radiolytic degradation is of utmost importance, and the stability of the radioimmunoconjugates should be evaluated carefully before performing any *in vivo* applications.

Quality Control of Radiolabeled Immunoconjugates The following three parameters form the core of the quality control evaluation of any radioimmunoconjugate before its release for (pre)clinical application: immunoglobulin integrity, (radio)chemical purity, and immune reactive fraction.

Immunoglobulin Integrity The integrity of an immunoglobulin may become impaired upon the conjugation of a chelator or its subsequent radiolabeling. Therefore, it is important to monitor the effects that these procedures might have on the immunoglobulin's structural integrity. This can be done via a variety of different methods, including size-exclusion chromatography (SEC), sodium dodecyl sulfate polyacrylamide gel electrophoresis (SDS-PAGE), surface plasmon resonance (SPR), and liquid chromatography-mass spectrometry (LC-MS).

Size-Exclusion Chromatography (SEC) It is mostly done via HPLC using UV and radioactivity detectors. A size-

exclusion column separates molecules based on size: small molecules can enter pores of the stationary phase of the column, while large molecules cannot. As a result, larger molecules travel faster through the column than small molecules and elute from the column more quickly. The selection of a suitable column for this purpose depends on the desired recovery of radioactivity from the column as well as the need to separate out aggregates and high and low molecular weight side products from starting materials. The validation of a column using a protein standard to test separation efficiency and recovery is advised and also allows for the evaluation of changes in the performance of the column over its lifetime.

Sodium Dodecyl Sulfate Polyacrylamide Gel Electrophoresis (SDS-PAGE) It employs an electric field to separate proteins based on their molecular weight. Proteins are amphoteric molecules, having both positive and negative charges. Upon mixing with SDS, the 3D structure of the protein is disrupted and the protein gets a uniform negative charge. The denatured protein is loaded onto the polyacrylamide gel, which is actually composed of two phases: a stacking gel and a separating gel. When an electric field is applied, the protein begins to move through the gel toward the anode as a function of molecular weight, with small proteins moving faster. The stacking gel concentrates the protein, and then the separating gel resolves the proteins according to their molecular weight. After the run, the gel can be stained, and the molecular weight of the proteins within the gel can be compared to a standard molecular weight ladder.

Surface Plasmon Resonance (SPR) It can be used to measure the interaction between immobilized target proteins and immunoglobulins in solution. Polarized light is directed toward the surface of the antigen-coated sensor ship, and changes in the refraction index caused by the binding of various concentrations of the immunoglobulin to its target protein are detected by the hardware. This technique can be used to determine not only binding affinities (K_d) but also kinetic rate constants (k_a and k_d) and thermodynamic parameters.

LC-MS/MS It is the combination of SEC-HPLC and mass spectrometry which allows for the determination of the chelator-to-immunoglobulin ratio and distribution of the ratios as well as the presence of proteinaceous side products derived from the immunoglobulin.

Radiochemical Purity The radiochemical purity of the radioimmunoconjugate can also be determined using SEC-HPLC and SDS-PAGE in conjunction with radioactivity detectors. In this respect, it is important to determine the recovery of the radioimmunoconjugate from the column as well as that of any radiolabeled side products that can be present as well (such as the free radionuclide and the free radionuclide-chelator complex). Recovery from the column should be near 100% to ensure that the HPLC and radioactivity profiles are representative of the test sample. Along these lines, it is important to pay particular attention to the radionuclide itself as a possible impurity, as it may stick to the column and cause the radiochemical purity of the radioimmunoconjugate to be overestimated. Generally speaking, the radiochemical purity of a radioimmunoconjugate should also be analyzed with instant thin-layer chromatography (iTLC). In iTLC, the product mixture is spotted on a paper strip (stationary phase) and eluted with a mobile phase. The more polar the mobile phase, the more easily the compounds will migrate on the TLC strip. Importantly, however, iTLC does not allow for the determination of protein integrity, since any protein—irrespective of size—will migrate in the same manner.

Immunoreactive Fraction The immunoreactive fraction is easily one of the most important metrics used for the quality control of radioimmunoconjugates as it provides information as to whether the radiolabeled immunoglobulin is still capable of binding its target antigen. The immunoreactive fraction can either be determined using an assay based on the serial dilution of cells expressing the antigen or via a binding assay similar to an ELISA (enzyme-linked immunosorbent assay). The former method is colloquially known as the "Lindmo assay" [20]. In this technique, a serial dilution of fixed or unfixed cells is prepared followed by the addition of a constant concentration of radioimmunoconjugate. After a certain incubation period, the cells are separated from the supernatant, and the amount of radioactivity in each phase is determined in order to calculate the immunoreactive fraction. In the second type of assay, a constant amount of antigen is attached to the wells of a 96-well plate. A serial dilution of the radioimmunoconjugate is added, and after a certain incubation period, the supernatant is separated from the coated plates. Subsequently, the plates are washed, and the amount of bound and free radioimmunoconjugate is determined in order to calculate the immunoreactive fraction. Unfortunately, the assays used to calculate immunoreactive fraction often require quite a bit of optimization, involving variables including the cell type, the amount of cells, the amount of antigen, the incubation period, and the temperature. For both assays, it is advisable to always include appropriate controls, such as the blockage of binding with an excess of unlabeled parental mAb.

The Performance of Radioimmunoconjugates After all of the appropriate quality control tests have been performed, *in vitro* and *in vivo* experiments can be performed to evaluate the performance of the radioimmunoconjugate. To this end, *in vitro* autoradiography can be performed to determine the expression level of the antigen in question in tumor slices. The expression level and saturation of the target can be investigated via the co-incubation of the slides with the radioimmunoconjugate as well as increasing amount of cold, non-radiolabeled immunoglobulin.

The *in vivo* evaluation of radioimmunoconjugates with oncological targets is typically performed in mice bearing tumor xenografts. It is important to keep the following questions and issues surrounding both the model and the immunoglobulin in mind when using tumor-bearing mice:

- If the radioimmunoconjugate targets a human protein, does it cross-react with the murine antigen? Is its affinity for the mouse equivalent of the antigen known? Is that affinity comparable to its affinity for the human antigen?
- Is the expression level of the antigen the same in the healthy tissues of humans and mice?
- What is the expression level of the antigen in xenograft tissue, and is it representative of human tumors? Low expression levels can be difficult to visualize, even in preclinical models.
- The endogenous antibody levels in young immune-deficient mice (nu/nu) have not yet matured. This can result in the rapid clearance of the radioimmunoconjugate and can therefore produce large standard deviations during biodistribution experiments [21]. This effect is not observed when using increased amounts of the radiolabeled mAb (*e.g.* > 100 μg/mouse) or when slightly older mice are used (>8 weeks).
- The use of Matrigel should be carefully evaluated, and it should be clearly established whether the uptake of the radioimmunoconjugate is mediated by the target and not by Matrigel-induced granulation tissue.

There are several typical preclinical *in vivo* biodistribution experiments that can be used to determine whether a new radioimmunoconjugate has clinical potential as an imaging agent:

1. The determination of the saturation of a target by the co-injection of increasing amounts of non-radiolabeled immunoglobulin
2. The determination of the uptake of the radioimmunoconjugate in control tumors that do not express the target antigen
3. The use of an isotype control, nontargeted radioimmunoconjugate to validate the specificity of the novel targeted radioimmunoconjugate and to discriminate between tumor uptake that is target-mediated and not target-mediated
4. The determination of the therapeutic efficacy of the radiolabeled immunoglobulin (if the radioimmunoconjugate is meant for RIT, of course)
5. Immunohistochemistry on tumor sections to correlate target expression with the uptake of the radioimmunoconjugate

Radioimmunodetection: ImmunoPET and ImmunoSPECT

Introduction The primary reason for selecting immunoglobulins as vectors for PET and SPECT imaging is their specificity. Generally speaking, immunoglobulins are developed to target a specific antigen or protein with high affinity and do not cross-react with other targets. An ideal radioimmunoconjugate would target an antigen or protein solely expressed on the tissue of interest, though such selectivity is almost never the case (see the section on "Target Expression and Accessibility"). In the following pages, we will discuss the findings that can be gleaned from imaging in early phase clinical studies as well as the considerations that must be undertaken when using immunoglobulins for imaging and therapy. At the end of this chapter—in the "Particular Important Works" section—we will highlight some recent important successes in the field of nuclear imaging with antibodies. We refer readers with a particular interest in RIT to Chap. 5 for more details. What will become clear from these previous achievements is that nuclear imaging with antibodies can enhance and complement data obtained with *in vitro* biomarkers and also add power and value of early clinical trials.

What Can Be Learned from Clinical Imaging? The question above is especially relevant for pharmaceutical companies developing new immunoglobulins and physicians performing clinical studies with new antibodies. The following information can potentially be obtained with immunoPET as well as immunoSPECT [16, 22–27].

Target Expression and Accessibility The confirmation of the presence of a target is an important information, since it can be used to tailor accompanying treatment regimens. For example, if a given target is absent in a tumor, other treatment strategies can be considered. This reduces the time wasted treating a patient with a drug that does not accumulate in the target tissue and spares the patient adverse effects associated with the erstwhile ineffective therapeutic. Typically, this confirmation of a target's presence is done via, for example, immunohistochemistry

(IHC) or quantitative polymerase chain reaction (PCR) using tumor biopsies. However, tissue samples that have been previously collected and stored may not represent the current status of the tumor. Furthermore, heterogeneity—which cannot be assessed by tumor biopsies—can exist between and within lesions. In contrast, imaging can non-invasively provide real-time information about the expression of a target *and* its heterogeneity in diseased and normal tissues. It follows that imaging is a promising tool for screening patients that may or may not respond to treatment with a given targeted therapeutic. Imaging also provides information about the modulation of target expression (like in combination therapy) and about the accessibility of a given target. Simply put, while IHC and qPCR may be able to confirm the expression of a target, they cannot provide information as to whether a therapeutic will be able to accumulate in the target-bearing tissue.

Target Saturation Imaging with the radiolabeled antibody can also help determine the dose necessary to obtain homogeneous tumor targeting, achieve target saturation, and overcome the sink of antigen present in healthy tissue. Since most antigens are not solely expressed on the target tissue, it is often important to saturate the antigen sink present in normal tissues before the drug begins to accumulate in the target tissue [10, 17]. During standard phase I trials, this is not feasible, and only the maximum tolerated dose can be determined without any information on tumor targeting. With imaging, however, much more information can be obtained in early phase clinical research. The determination of target saturation might be very beneficial in the context of RIT or ADC-based treatments as well. Indeed, the dose of an ADC or radioimmunotherapeutic agent can be tailored based on data obtained with imaging. In this way, clinicians can increase the therapeutic window by minimizing side effects while maximizing the tumoricidal effects of the therapeutic.

Pharmacokinetics and Biodistribution In addition to data on the expression and saturation of targets, radioimmunoconjugates can also provide information on the whole-body biodistribution and pharmacokinetic profile of immunoglobulins. Indeed, theranostic imaging can provide insight into the accumulation of a therapeutic antibody in healthy tissue and thus help predict the toxicity profile of an immunoglobulin. Not surprisingly, this can be especially important for highly potent ADCs and radioimmunotherapeutics.

Target Modulation and Monitoring Response The use of imaging to monitor response requires imaging before, during, and/or after therapy and allows for the rationalization of drug response. Response monitoring is often done using [^{18}F]FDG PET. However, [^{18}F]FDG PET does not provide any information about the modulation of the target and instead only tells us about the metabolic activity of the tumor and the tumor load. Imaging with a target-specific imaging agent is thus preferred when monitoring response to therapy. For example, the modulation of the expression of HER2 and VEGF by heat shock protein 90 (HSP90) has been monitored using ^{89}Zr[Zr]-trastuzumab and ^{89}Zr[Zr]-bevacizumab [28].

Table 4 Advantages and disadvantages of imaging with radioimmunoconjugates

Advantages	Limitations
Minimally invasive	Slow kinetics
Quantitative (PET)	Relatively high radiation burden
Determination of whole-body target expression	High background uptake
Target accessibility is taken into account	Scanning over multiple days
Repetition of scans is possible	Stability of radiopharmaceutical is very important
	HAMA due to the use of murine antibodies in humans
Transportation worldwide is possible, although logistically challenging because of radioactivity	

PET positron-emission tomography, *HAMA* human anti-mouse antibodies

Modulation of Antibody Delivery to the Target Finally, the delivery of antibodies and radioimmunoconjugates can be changed by inhibitors of angiogenesis such as bevacizumab, because they decrease vessel density and thereby reduce the permeability of tumors for macromolecules. Along these lines, ^{89}Zr[Zr]-bevacizumab can be used to image vascular permeability and VEGF levels after antiangiogenic therapy, providing a visual readout of tumor accessibility for follow-up treatment [29–31].

Advantages and Limitations of ImmunoPET and ImmunoSPECT Although most of the advantages of imaging with radioimmunoconjugates have been mentioned in previous sections, it is important to summarize them and also discuss some of the technique's limitations as well. Table 4 provides an overview of the advantages and limitations of imaging with radioimmunoconjugates. The main limitation of the modality is the relatively high radiation dose received by patients. Pretargeted imaging in which the administration of immunoglobulin and radionuclide is decoupled may offer a solution that combines the specificity of antibodies with the radiation dosimetry of small molecules (see Chap. 26). In addition, the newest generation of whole-body PET scanners may also facilitate the reduction of radiation doses, as less radioactivity can be injected while obtaining images with better resolution.

Tricks of the Trade

The Preparation of Radioimmunoconjugates

Although many of the important issues to keep in mind when developing radioimmunoconjugates have been mentioned in the previous sections, the most critical ones are summarized again here. When preparing and evaluating radioimmunoconjugates, it is of the utmost importance that the immunoglobulin is radiolabeled in an inert manner. Only then will the uptake of the radioimmunoconjugate reflect the uptake of the parent antibody. In this regard, it is important to pay particular attention to the bioconjugation process, as coupling too many chelators per antibody can accelerate blood clearance and increase activity concentrations in the liver; an average chelator:mAb ratio of 2:1 is advised. Additionally, the stability of the radioimmunoconjugate should be excellent. In the case of RIT, this might be challenging due to radiation damage because of high radioactivity concentrations.

Finally, the radioimmunoconjugate should be formulated in a way that prevents "stickiness," a trait that becomes especially troublesome when using low concentrations of radiotracers. To this end, one should take steps to ensure that the product is stored in a manner that prevents sticking to the glass vial or polymeric materials used for administration. To prevent the stickiness of radioimmunoconjugates, the formulation of the construct with mouse serum albumin (only allowed in preclinical experiments in mice) or surfactants such as Tween 80 is useful.

Calibration of Equipment

When developing radiochemical procedures with new radionuclides, one should always remember to calibrate scanners, dose calibrators, and gamma counters. Calibration for different types of vials, syringes, and volumes, resulting in variable geometry, has to be performed in order to ensure the accurate measurement of the amount of radioactivity injected. For example, for zirconium-89 it is known that the material of the container has a strong influence on the measured amount of radioactivity inside the container and that the measured amount of radioactivity in syringes is very much dependent on the volume of solution inside the syringe. Preferably, this calibration is done using validated resources (*e.g.* a highly sensitive GeLi detector and gamma spectrometry).

Particularly Important Works

The ZEPHIR Trial [32]

Trastuzumab emtansine (T-DM1) is a human epidermal growth factor receptor 2 (HER2) targeting antibody-drug conjugate (ADC) that is approved for the treatment of advanced HER2-positive breast cancer after prior treatment with trastuzumab. Currently, patients eligible for treatment with T-DM1 are selected based on biopsy IHC and fluorescence in situ hybridization (FISH) assays. In the ZEPHIR trial, the potential of [^{89}Zr]Zr-trastuzumab PET before treatment and [^{18}F]FDG PET for early response monitoring was evaluated for their predictive value in HER2-positive patients treated with three cycles of T-DM1. Although only HER2-positive patients based on IHC or FISH ($\geq$2.2) were included, a significant percentage of the patients (29%) had negative [^{89}Zr]Zr-trastuzumab PET. Furthermore, intra-patient heterogeneity was observed in 46% of patients. The negative predictive value (NPV) and positive predictive value (PPV) for [^{89}Zr]Zr-trastuzumab PET were 88 and 72%, respectively, while early [^{18}F]FDG PET had corresponding values of 83 and 96%. Taken together, PET with [^{89}Zr]Zr-trastuzumab for confirmation of tumor targeting and [^{18}F]FDG for early response monitoring had a NPV/PPV of 100% and was able to discriminate patients with a median time-to-treatment failure (TTF) of 2.8 months from patients with a median TTF of 15 months. In conclusion, [^{89}Zr]Zr-trastuzumab PET with [^{18}F]FDG PET allows for the selection of patients who will and will not profit from T-DM1 therapy.

The Assessment of Target-Mediated Uptake with ImmunoPET: Analysis of a Phase I Clinical Study with an Anti-CD44 Antibody [33]

In this study, the anti-CD44 mAb RG7356 was radiolabeled with zirconium-89, and a dose escalation was performed in patients with advanced CD44-expressing solid tumors. Differences in the biodistribution of the radioimmunoconjugate were observed in the cohorts who received different doses. In line with the preclinical data obtained in monkeys, the uptake of ^{89}Zr[Zr]-RG7356 in the spleen, liver, and bone marrow decreased with increasing antibody dose, indicating target-mediated specific uptake ("sink") in these normal tissues. The same dose dependency was observed in the kidney and lung in the patients (see Figs. 4 and 5). Above 450 mg, a constant tissue-to-blood area under the curve (AUC) was

observed, indicating antigen saturation. Furthermore, target-independent uptake in healthy organs was observed, since the AUC was higher than expected. For example, based on a blood volume fraction of 30%, the liver-to-blood AUC ratio was expected to be 0.3. However, a liver-to-blood ratio of 0.85 ± 0.08 was observed for the 675 mg dose cohort, suggesting an additional accumulation mechanism in the liver. Finally, the uptake of the radioimmunoconjugate in the tumor could only be observed with a dose of at least 450 mg RG7356, which is not in line with the level of CD44 expression or the percentage of CD44-postive tumor cells also observed in the lower dose cohorts.

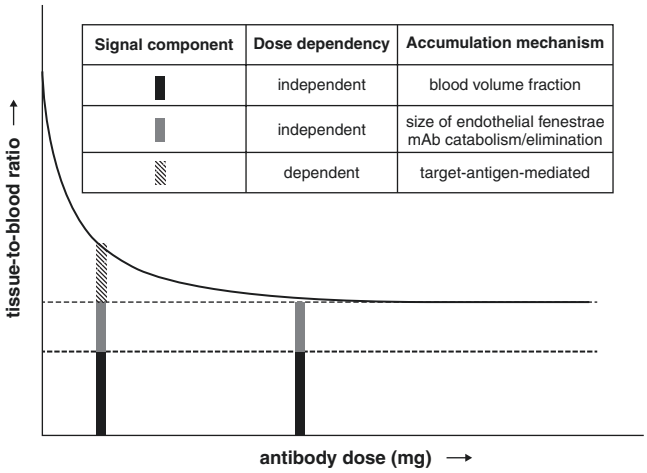

Fig. 4 ImmunoPET signal components in a phase I dose escalation study (From Jauw *et al.* [17], with permission)

Controversial Issues

In the context of radioimmunodetection, one major concern is that the slow kinetics of radioimmunoconjugates are not suitable for imaging because of the high radiation dose received from an immunoPET tracer, and thus constructs with more rapid pharmacokinetic profiles should be developed as alternatives. For example, radiolabeled Fab fragments have far shorter serum half-lives and enable imaging at much earlier time points than full-length radioimmunoconjugates [34, 35]. However, whether the use of alternative vectors is appropriate depends on the question that needs to be answered. More rapidly cleared constructs are generally advantageous for contrast, which is important for tumor detection and the assessment of antigen expression, though for some theranostic applications, slow kinetic full-length radioimmunoconjugates might be more informative. In light of the recent development of whole-body PET scanners, the issue of radiation dosimetry might become irrelevant, since whole-body PET requires the injection of much less radioactivity. Furthermore, whole-body PET also allows for the collection of images at later time points after the administration

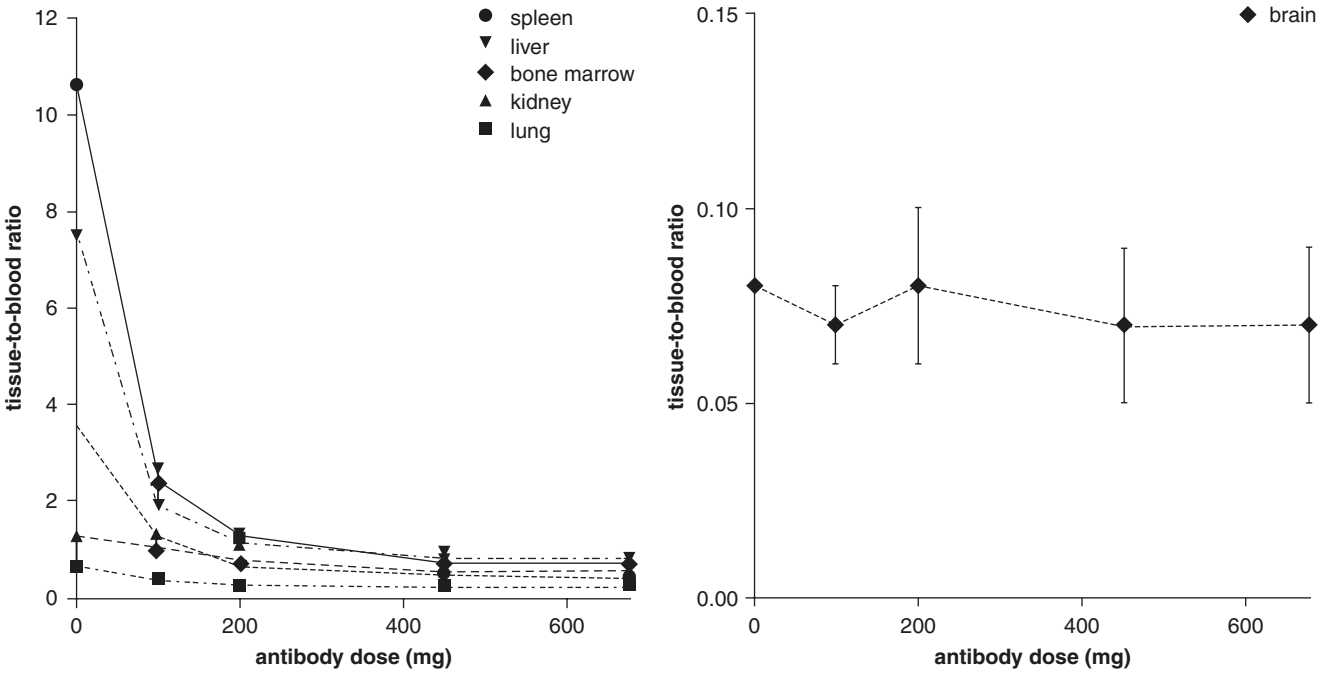

Fig. 5 Tissue-to-blood AUC ratio of RG7356 as a function of antibody dose (From Jauw *et al.* [33], with permission)

of the radioimmunoconjugate, a practice which can dramatically improve the contrast of PET images.

Another controversial issue in the realm of antibody-based nuclear imaging is the influence of the chelator on the toxicological and pharmacological profiles of the antibody. For ^{89}Zr-labeled antibodies, the chelator desferrioxamine (DFO) is typically used for the stable attachment of the radiometal to the antibody. DFO is clinically used for the treatment of iron and aluminum overload. As a result, ^{89}Zr-labeled mAbs using bifunctional chelators based on desferrioxamine have been broadly applied in the clinic without additional toxicity studies. In these cases, it is argued that the toxicity studies of the mAb and DFO itself are sufficient to allow for the clinical translation of the ^{89}Zr[Zr]-DFO-mAbs. Naturally, it has to be proven that the characteristics of the antibody are preserved by performing preclinical biodistribution studies and *in vitro* experiments comparing the original mAb and the ^{89}Zr-labeled mAb. However, this approach is not acceptable to all regulators and thus must be carefully investigated before clinical trial submission.

The Future

The future of nuclear imaging with antibodies, antibody conjugates, and other proteinous vectors is bright. A wide array of immunoglobulins of different sizes and formats are currently in development, and our understanding of their *in vivo* behavior will increase in parallel. Evaluating all of these platforms via classical phase I–III trials will be impossible without creating much longer development times, as an increasing number of compounds would have to be evaluated in a relatively static number of patients. As a result, the field should focus on obtaining more valuable information from a smaller number of patients. Indeed, relatively small imaging studies are performed to help determine which immunoglobulins are the most promising for further development [17]. This is mainly because standardized radiochemistry protocols are available for inert radiolabeling, and direct translation to the clinic without additional toxicity studies is possible as accepted by regulators and pharmaceutical companies.

Furthermore, the development of whole-body PET scanners has made the future even brighter, as the increased sensitivity of these scanners means that antibodies labeled with long-lived radionuclides can be followed over longer periods after their injection with reduced radiation burden to the patient. This will allow for multiple injections of tracers and more sophisticated imaging protocols, thereby increasing the knowledge that can be obtained with imaging.

Bottom Line

- Immunoglobulins are becoming increasingly important for diagnostic, therapeutic, and theranostic purposes.
- The inert radiolabeling of an antibody is necessary for the resulting radioimmunoconjugate to accurately reflect the biodistribution of the parent antibody.
- The radionuclide used in a radioimmunoconjugate should always be tailored to the *in vivo* characteristics of the immunoglobulin.
- The radiochemical purity of the product should be monitored and needs special attention in the case of RIT, since high amounts of radioactivity can induce radiolysis.
- Imaging with radiolabeled immunoglobulins has been recognized by the pharmaceutical industry as an important tool to characterize antibodies as well as target antigens in an efficient way in both preclinical and clinical investigations. For obtaining reproducible and valuable information in a safe manner, the careful consideration of radiochemistry, GMP-compliant production of the conjugate, quality control procedures, and trial design is key.

References

1. Strebhardt K, Ullrich A. Paul Ehrlich's magic bullet concept: 100 years of progress. Nat Rev Cancer. 2008;8(6):473–80.
2. Brekke OH, Sandlie I. Therapeutic antibodies for human diseases at the dawn of the twenty-first century. Nat Rev Drug Discov. 2003;2(1):52–62.
3. Delves PJ, Martin SJ, Burton DR, Roitt IM. Roitt's essential immunology. 13th ed. Chichester/Hoboken: John Wiley & Sons; 2017.
4. Vazquez-Lombardi R, Phan TG, Zimmermann C, Lowe D, Jermutu L, Christi D. Challenges and opportunities for non-antibody scaffold drugs. Drug Discov Today. 2015;20(10):1271–83.
5. Kontermann RE, Brinkmann U. Bispecific antibodies. Drug Discov Today. 2015;20(7):838–47.
6. Liu LM. Antibody glycosylation and its impact on the pharmacokinetics and pharmacodynamics of monoclonal antibodies and Fc-fusion proteins. J Pharm Sci. 2015;104(6):1866–84.
7. Weiner GJ. Building better monoclonal antibody-based therapeutics. Nat Rev Cancer. 2015;15(6):361–70.
8. Reichert JM. Antibodies to watch in 2017. MAbs. 2017;9(2):167–81.
9. Sehlin D, Fang XTT, Cato L, Antoni G, Lannfelt L, Syvanen S. Antibody-based PET imaging of amyloid beta in mouse models of Alzheimer's disease. Nat Commun. 2016;7:10759.
10. Dijkers EC, Oude Munnink TH, Kosterink JG, Brouwers AH, Jager PL, de Jong JR, et al. Biodistribution of 89Zr-trastuzumab and PET imaging of HER2-positive lesions in patients with metastatic breast cancer. Clin Pharmacol Ther. 2010;87(5):586–92.
11. Goldenberg DM. Targeted therapy of cancer with radiolabeled antibodies. J Nucl Med. 2002;43(5):693–713.
12. Jain RK. Transport of molecules, particles and cells in solid tumors. Annu Rev Biomed Eng. 1999;1:241–63.

13. Hillen F, Griffioen AW. Tumour vascularization: sprouting angiogenesis and beyond. Cancer Metastasis Rev. 2007;26(3–4):489–502.
14. Wagner M, Wiig H. Tumor interstitial fluid formation, characterization, and clinical implications. Front Oncol. 2015;5:115.
15. Olafsen T, Wu AM. Novel antibody vectors for imaging. Semin Nucl Med. 2010;40(3):167–81.
16. Lamberts LE, Williams SP, Terwisscha van Scheltinga AG, Lub-de Hooge MN, Schroder CP, Gietema JA, et al. Antibody positron emission tomography imaging in anticancer drug development. J Clin Oncol. 2015;33(13):1491–504.
17. Jauw YW, Menke-van der Houven van Oordt CW, Hoekstra OS, Hendrikse NH, Vugts DJ, Zijlstra JM, et al. Immuno-positron emission tomography with zirconium-89 labeled monoclonal antibodies in oncology: what can we learn from initial clinical trials? Front Pharmacol. 2016;7:131.
18. Hay M, Thomas DW, Craighead JL, Economides C, Rosenthal J. Clinical development success rates for investigational drugs. Nat Biotechnol. 2014;32(1):40–51.
19. Visser GW, Klok RP, Klein-Gebbink JW, Ter Linde T, Van Dongen GA, Molthoff CF. Optimal quality Iodine-131-monoclonal antibodies upon high dose labeling in a large reaction volume and temporarily coating the antibody with iodogen. J Nucl Med. 2001;42(3):509–19.
20. Lindmo T, Boven E, Cuttitta F, Fedorko J, Bunn PA Jr. Determination of the immunoreactive fraction of radiolabeled monoclonal antibodies by linear extrapolation to binding at infinite antigen excess. J Immunol Methods. 1984;72(1):77–89.
21. Van Gog FB, Rakenhoff RH, Snow GB, van Dongen GA. Rapid elimination of mouse/human chimeric monoclonal antibodies in nude mice. Cancer Immunol Immunother. 1997;44(2):103–11.
22. Fleuren ED, Versleijen-Jonkers YM, Heskamp S, van Herpen CM, Oyen WJ, van der Graaf WT, Boerman OC. Theranostic applications of antibodies in oncology. Mol Oncol. 2014;8(4):799–812.
23. Nayak TK, Brechbiel MW. Radioimmuno imaging with longer-lived positron-emitting radionuclides: potentials and challenges. Bioconjug Chem. 2009;20(5):825–41.
24. Van Dongen GA, Poot AJ, Vugts DJ. PET imaging with radiolabeled antibodies and tyrosine kinase inhibitors: immuno-PET and TKI-PET. Tumor Biol. 2012;33(3):607–15.
25. Bourgeois M, Bailly C, Frindel M, Guerard F, Cherel M, Faivre-Chauvet A, et al. Radioimmunoconjugates for treating cancer: recent advances and current opportunities. Expert Opin Biol Ther. 2017;17(7):813–9.
26. Moek KL, Giesen D, Kok IC, de Groot DJA, Jalving M, Fehrmann RS, et al. Theranostics using antibodies and antibody-related therapeutics. J Nucl Med. 2017;58(Suppl 2):83S–90S.
27. Knowles SM, Wu AM. Advances in immuno-positron emission tomography: antibodies for molecular imaging in oncology. J Clin Oncol. 2012;30(31):3884–92.
28. Gaykema SB, Schröder CP, Vitfell-Rasmussen J, Chua S, Oude Munnink TH, Brouwers AH, et al. ^{89}Zr-trastuzumab and ^{89}Zr-bevacizumab PET to evaluate the effect of the HSP90 inhibitor NVP-AUY922 in metastatic breast cancer patients. Clin Cancer Res. 2014;20(15):3945–54.
29. Arjaans M, Oude Munnink TH, Oosting SF, Terwisscha van Scheltinga AF, Gietema JA, Garbacik ET, et al. Bevacizumab-induced normalization of blood vessels in tumors hampers antibody uptake. Cancer Res. 2013;73(11):3347–55.
30. Van der Veldt AA, Lubberink M, Bahce I, Walraven M, de Boer MP, Greuter HN, et al. Rapid decrease in delivery of chemotherapy to tumors after anti-VEGF therapy: implications for scheduling anti-angiogenic drugs. Cancer Cell. 2012;21(1):82–91.
31. Van Asselt SJ, Oosting SF, Brouwers AH, Bongaerts AH, de Jong JR, Lub-de Hooge MN, et al. Everolimus reduces ^{89}Zr-bevacizumab tumor uptake in patients with neuroendocrine tumors. J Nucl Med. 2014;55(7):1087–92.
32. Gebhart G, Lamberts LE, Wimana Z, Garcia C, Emonts P, Ameye L, et al. Molecular imaging as a tool to investigate heterogeneity of advanced HER2-positive breast cancer and to predict patient outcome under trastuzumab emtansine (T-DM1): the ZEPHIR trial. Ann Oncol. 2017;27(4):619–24.
33. Jauw YW, Huisman MC, Nayak TK, Vugts DJ, Christen R, Naegelen VM, et al. Assessment of target-mediated uptake with immuno-PET: analysis of a phase I clinical trial with an anti-CD44 antibody. EJNMMI Res. 2018;8(1):6.
34. Freise A, Wu AM. In vivo imaging with antibodies and engineered fragments. Mol Immunol. 2015;67(2 Pt A):142–52.
35. Wu A. Engineered antibodies for molecular imaging of cancer. Methods. 2014;65(1):139–47.

Nanoparticles as Radiopharmaceutical Vectors

Anyanee Kamkaew, Emily B. Ehlerding, and Weibo Cai

Nanoparticles in Drug Delivery

Nanoparticles are molecular constructs that contain at least one dimension between 1 and 100 nanometers (nm) in size. They possess a greater surface area per unit weight than larger particles, which makes them more reactive than other larger structures. This large surface area also facilitates the modification of nanoparticles for a wide array of purposes. Indeed, nanoparticles are currently being used in many sectors, ranging from medicine [1, 2], manufacturing [3], and materials science [4] to the environment [5, 6], energy, and electronics [7–9].

Over the past decade, nanoparticles have emerged as particularly promising tools for drug delivery in preclinical research. Nanomaterials are effective vectors for the delivery of cargoes—such as drugs or other therapeutic entities—to target tissues since they are small enough to cross the walls of blood vessels and cell membranes in order to interact with cells. Moreover, the pharmacokinetic and pharmacodynamic properties of nanoparticles can be tuned and optimized by choosing appropriate core materials and modifying their surface. Several recent trends in both FDA-approved nanoparticles and nanoparticle-centered clinical trials are shown in Fig. 1. Since the mid-1990s, an average of ~13 nanoparticles have been approved every 5 years [2]. Liposomal and polymeric nanoparticles account for the majority of the nanoparticles approved in the 1990s. Interestingly, approvals dropped dramatically in 2008 after peaking during 2001–2005, a trend that might be related to funding limitations associated with the global financial crisis of 2008. However, the data clearly indicate a new surge in trials in 2014 and 2015. It is important to note that recent years have played witness to the development of significantly more micellar, metallic, and protein-based particles than were created during the earliest days of nanoparticles in the 1990s.

As these data make clear, the use of nanomaterials has received much attention in medicine. However, two major concerns surrounding the *in vivo* use of nanoparticles—specifically their toxicity and their uncertain biological fate—have restricted their clinical utility. While there are several nanomaterials that have been effective and shown no cytotoxicity *in vitro*, the *in vivo* distribution, metabolism, and excretion of these constructs have proven much more complex and have become a bottleneck to clinical translation. To date, more than 200 nanomaterials are in clinical trials. Some of them have been approved; yet, the success of nanoparticles in the clinic remains uncertain. In light of these trends, the advent of radiolabeled nanoparticles could portend a breakthrough, as they could prove indispensable for the *in vivo* tracking of nanoparticles in clinical theranostic approaches [10, 11].

In this chapter, we will focus primarily on recent advances in the study of radiolabeled nanoparticles that could facilitate the clinical application of nanoparticle-based theranostics. The advantages of nanoparticle-based delivery systems, the unique characteristics of many nanoparticles, and several considerations for building effective nanoparticle-based platforms will also be discussed. Finally, tumor targeting and multifunctional radiolabeled nanomaterials will be reviewed as well.

Advantages of Nanoparticles for the Delivery of Radionuclides

Biocompatible nanoparticles have several favorable features that make them promising vectors for the delivery of radionuclides to tissues.

A. Kamkaew (✉)
School of Chemistry, Institute of Science, Suranaree University of Technology, Nakhon Ratchasima, Thailand
e-mail: anyanee@sut.ac.th

E. B. Ehlerding
Department of Medical Physics, University of Wisconsin – Madison, Madison, WI, USA

W. Cai (✉)
Department of Radiology, University of Wisconsin – Madison, Madison, WI, USA
e-mail: wcai@uwhealth.org

J. S. Lewis et al. (eds.), *Radiopharmaceutical Chemistry*, https://doi.org/10.1007/978-3-319-98947-1_10

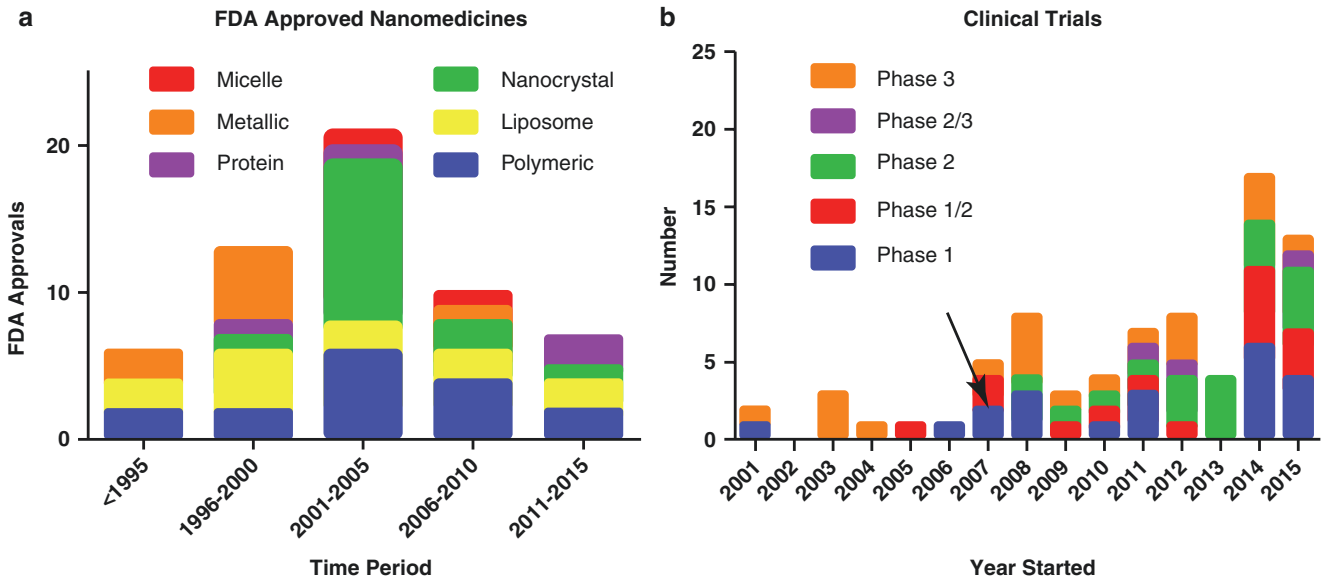

Fig. 1 (**a**) US Food and Drug Administration (FDA)-approved nanoparticles stratified by particle type; (**b**) nanomedicine-centered clinical trials in the United States from 2001 to 2015, as identified on www.clinicaltrials.gov. The arrow indicates the approximate start date of a US law (FDAAA 801) requiring the reporting of clinical trials to an FDA database. (Adapted from Bobo *et al.* [2], with permission)

(i) Multiple radionuclides can be attached to a single nanoparticle, increasing the amount of activity delivered with each particle.
(ii) The surface of nanoparticles can be modified with multiple targeting agents in order to enhance the local accumulation of the radionuclide-bearing nanoparticles.
(iii) The blood circulation time of radiolabeled nanoparticles can be tuned from 30 min to >24 h by altering their size, morphology, materials, and surface modifications (see section "Procedures for Labeling Nanoparticles with Radionuclides").
(iv) Radiolabeled nanoparticles can be decorated with biodegradable polymers to reduce their toxicity.
(v) The possibility of attaching more than one payload to nanoparticles means that combination therapies and multimodal imaging can be performed with a single nanomaterial.
(vi) Nanoparticles have several unique chemical and physical properties that can be harnessed for the delivery of radionuclides to target tissues. For example, the magnetism of some nanoparticles can be leveraged to improve delivery through the use of external magnetic fields.

General Considerations for Designing Nanoplatforms for Radiopharmaceuticals

The size, surface characteristics, and shape of nanoparticles all exert significant influences on their *in vivo* biodistribution. It follows that engineering the physicochemical properties of nanoparticles—including their size, shape, elasticity, surface charge, and surface functionalization—to achieve optimal *in vivo* behavior represents a major challenge in the field [12, 13].

Size Effects

Nanoparticles with diameters less than 5 nm are rapidly cleared from circulation by opsonization (ingestion and elimination by phagocytes), extravasation (leakage from the vasculature), or renal clearance. Larger particles (diameter > 15 nm), in contrast, show a greater tendency to accumulate in the liver, spleen, and bone marrow [14]. The biodistribution of nanoparticles with diameters between 10 and 15 nm is quite variable—and unpredictable—leading to their varied *in vivo* efficacy. Generally speaking, particles with diameters below 15 nm are removed quickly (within 24 h) via the renal system. Particles with sizes above 15 nm—such as 25 nm silica nanoparticles [15] and 17 nm gold nanoparticles [16]—are cleared from the body less quickly (within 2 weeks) through the hepatobiliary system. And finally, nanoparticles above 40 nm typically stay in the body longer, ultimately residing in the liver and spleen. For example, 40 nm gold particles persisted in the Kupffer cells of mice and beagles for at least 6 months [17, 18]. The size and shape of nanoparticles also play a major role in how they are taken up into cells [19]. For example, 14 nm transferrin-coated gold nanoparticles have to be clustered into groups of six or seven before they can be taken into cells, while 50 nm transferrin-coated nanoparticles are able to enter cells alone [20].

Shape Effects

Predicting the *in vivo* behavior of nanoparticles is often quite difficult, because a wide variety of factors—including their stability, composition, size, geometry, surface charge, and route of administration—can influence their biodistribution and pharmacokinetics. However, general trends linking particle geometry and biodistribution can be reasonably predictable. Up to now, most nanomaterials in clinical trials or preclinical studies have been spherical. However, nonspherical nanoparticles have been increasingly explored in the past 2 decades. Compared to their spherical counterparts, elongated particles (*e.g.* filomicelles or rods) have prolonged circulation times, presumably due to flow alignment in circulation. Disc-shaped particles have been shown to localize in organs such as the lungs and heart. Thus, in general, nonspherical particles can enhance accumulation in the target site while simultaneously decreasing side effects [21]. More information on this topic can be found in recent reviews [22, 23].

Inhalation studies suggest that anisotropic particles initiate acute and prolonged inflammatory responses leading to severe adverse effects. On the other hand, the role of particle geometry on the toxicity of intravenously administered nanoparticles is less clear. More long-term *in vivo* toxicity studies as well as trials in larger animals and humans should be conducted to gain a better understanding of these effects.

Surface Modifications and Biocompatibility

A wide variety of strategies can be used to functionalize the surface of nanoparticles with ligands such as small molecules, surfactants, dendrimers, polymers, and biomolecules [24]. Biomolecule-bearing nanoparticles in particular can offer desirable properties for nuclear imaging and therapy, including biocompatibility and the ability to specifically recognize biomarkers of disease. Figure 2 suggests strategies to modify the surface of nanoparticles for multifunctional purposes.

One of the major challenges in the *in vivo* application of nanoparticles is the non-specific uptake of particles by the liver and spleen. In the context of targeted imaging and therapy, the trapping and rapid clearance of nanoparticles by the reticuloendothelial system (RES) effectively reduces the targeting efficiency of the nanomaterials and increases the risk of damage to healthy, nontarget tissues [25]. As a result, it is critical to increase the blood circulation time of particles while simultaneously minimizing—and ideally evading—the uptake of particles by the RES. The most common approach to this problem is coating the surface of nanoparticles with polymers or "stealth molecules." Modifying the surface of nanoparticles with polyethylene glycol (PEG), for example, protects nanoparticles from clearance by the mononuclear phagocytic system (MPS), thereby prolonging their circulation time in the blood and increasing their uptake in target tissue [26]. Several studies have shown that reducing the surface charge of nanoparticle coatings may also significantly reduce uptake by the RES and improve tumor targeting [27].

Nanoparticles Used for the Delivery of Radionuclides

Nanoparticles are versatile and multifunctional materials and thus hold the potential to be modular platforms for nuclear imaging and therapy. A diverse range of nanoparticles have

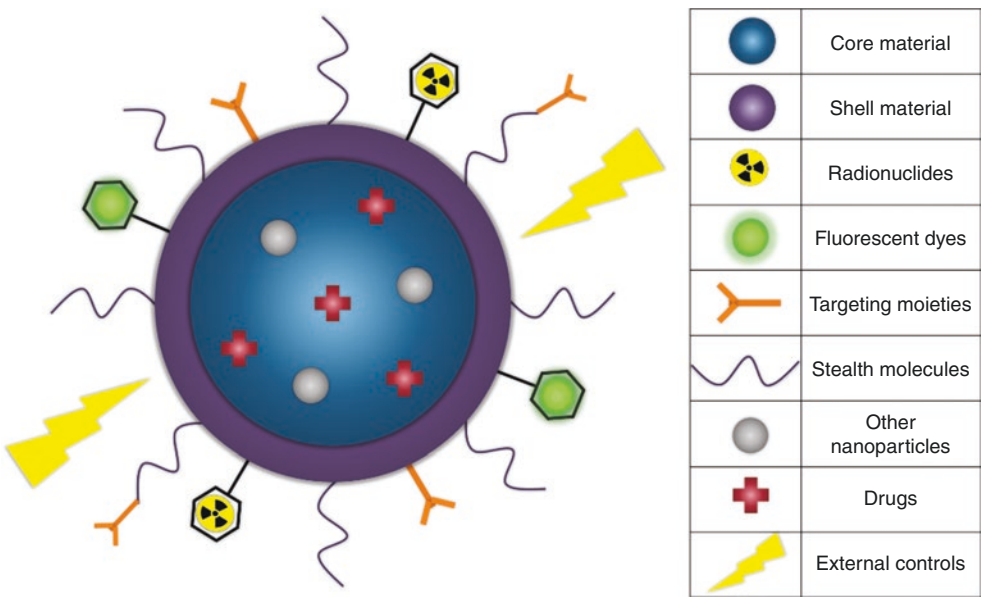

Fig. 2 Strategies to develop multifunctional radiolabeled nanoparticles

been labeled with a wide variety of radionuclides for preclinical studies. In the following section, we will provide an overview of the most commonly used inorganic and organic nanoparticles in nuclear medicine (Fig. 3).

Gold Nanoparticles

Gold nanoparticles (AuNPs) with diameters between 3 and 200 nm can be obtained by forming "colloidal gold" as a suspension of sub-micrometer-sized gold metal particles in aqueous medium. In molecular imaging, AuNPs have gained growing interest due to their extraordinary optical and electronic properties, stability, biological compatibility, controllable morphology and size dispersion, and facile surface functionalization [28]. AuNPs have demonstrated safe profiles both *in vivo* and *in vitro,* are easily modified, and can be targeted to tissues of interest both passively or actively [29, 30]. Therefore, many subtypes of gold nanoparticles—including gold nanorods, nanospheres, nanoshells, and nanocages as well as gold surface-enhanced Raman scattering (SERS) nanoparticles—have been developed and investigated for applications in molecular imaging [31]. AuNPs have been labeled with a number of radionuclides for SPECT or PET. These radiolabeled particles have also been combined with treatment modalities such as PTT (photothermal therapy), PDT (photodynamic therapy), and radiotherapy to create nanoparticle-based theranostics. Figure 4 shows an example of the *in vivo* use of ^{64}Cu-labeled AuNPs. Dynamic PET imaging of [^{64}Cu]Cu-NOTA-Au-GSH showed rapid renal clearance (>75%ID at 24 h postinjection) of radiolabeled gold nanoparticles [32]. As another example, AuNPs coated with plasma-polymerized allylamine (PPAA) with a mean diameter of 5 nm were conjugated to [^{89}Zr]Zr-DFO-cetuximab to form AuNPs-PPAA-[^{89}Zr]Zr-cetuximab. *In vivo* biodistribution studies revealed no significant differences in the uptake of the cetuximab-nanoparticle conjugates and unconjugated cetuximab in A431 tumors out to 72 h after injection. Furthermore, immunoPET studies showed that AuNPs-PPAA-[^{89}Zr]Zr-cetuximab provided high tumor-to-background activity concentration ratios, but the liver uptake of AuNPs-PPAA-[^{89}Zr]Zr-cetuximab was higher than that of [^{89}Zr]Zr-DFO-cetuximab [33]. Although AuNPs have been better studied than other inorganic nanomaterials, major challenges have limited their translational potential as cancer theranostics, including their instability in the blood and insufficient targeting to desired cells.

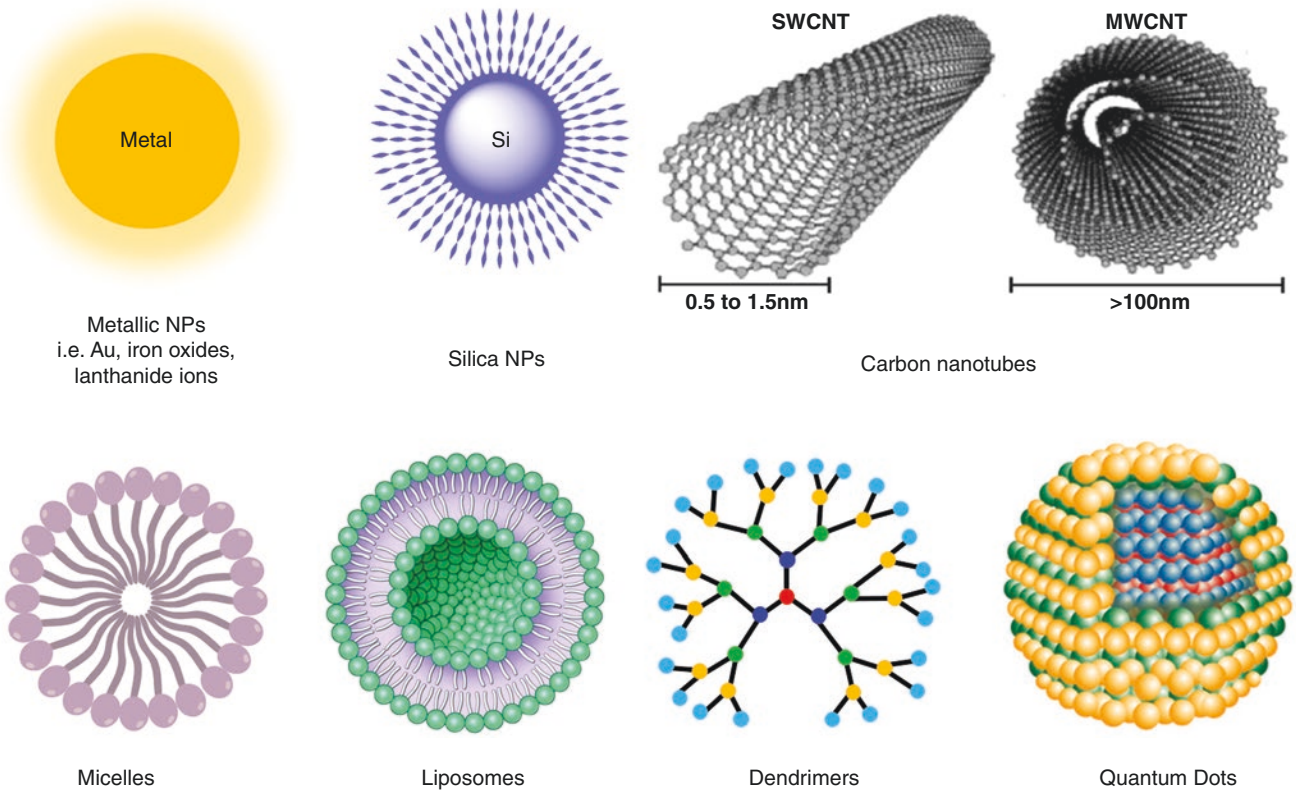

Fig. 3 Various types of nanoparticles used to create radio-nanomaterials

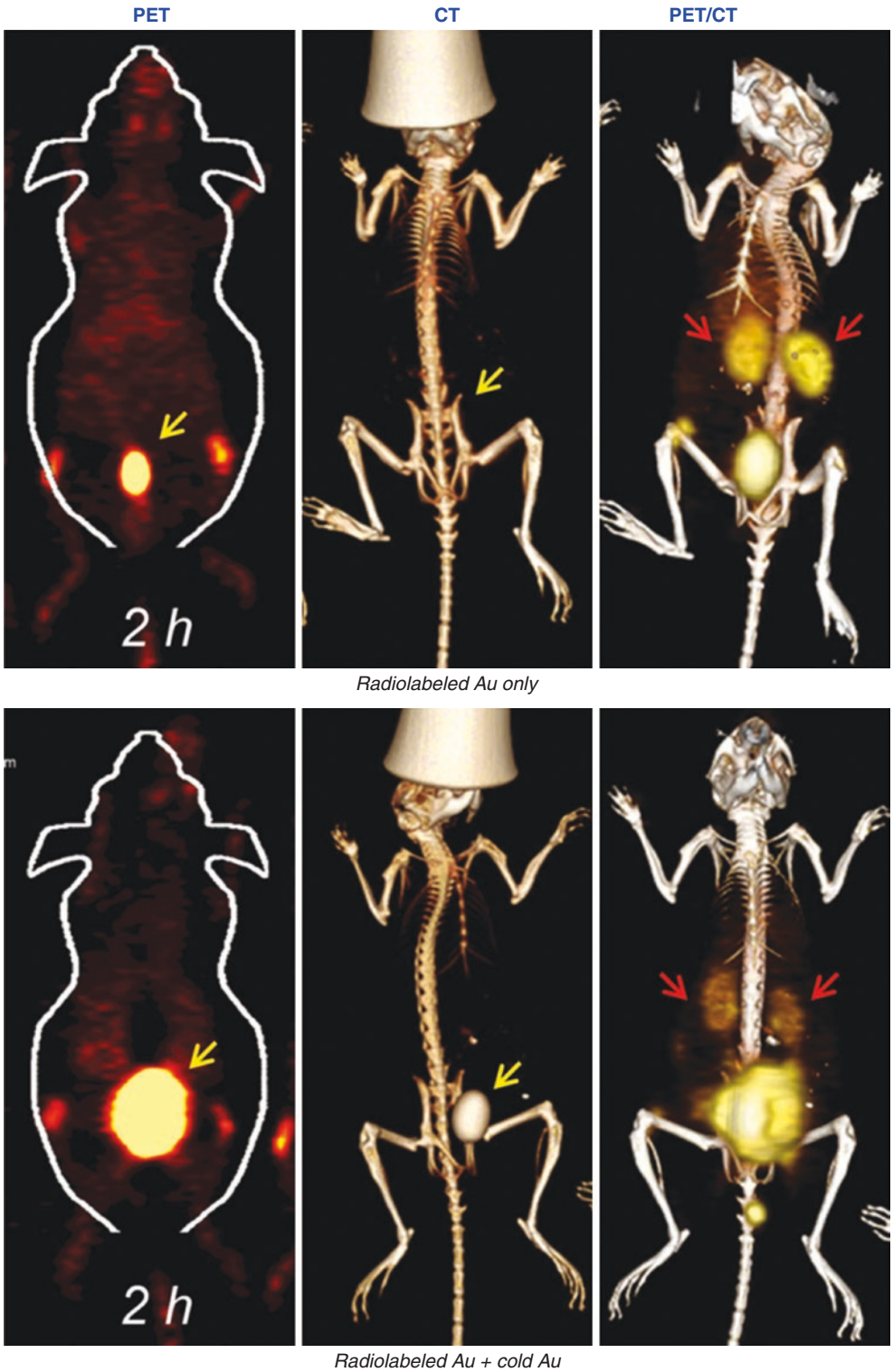

Fig. 4 *In vivo* PET/CT imaging of [^{64}Cu]Cu-NOTA-Au-GSH and NOTA-Au-GSH at 2 h p.i. Yellow arrows indicate the bladder, and red arrows mark the kidneys. (Adapted from Chen *et al.* [32], with permission)

Magnetic Nanoparticles

Magnetic nanoparticles (MNPs) have been studied for a wide variety of applications in medicine, including imaging, cell labeling, and the delivery of drugs and genes [34, 35]. Indeed, the ready availability of MNPs and their physicochemical properties—including their simple and robust preparation, the ease of incorporating reactive functional groups on their surface, and their magnetic responsiveness—have made them particularly promising nanomaterials for translational science. In addition, compared with other multifunctional nanomaterials such as quantum dots or car-

bon nanotubes, MNPs possess excellent biocompatibility because they are more easily degraded and eliminated from the body [36, 37].

Generally speaking, a MNP is comprised of three parts: (1) a magnetic core that provides contrast enhancement, (2) a polymer shell that provides stability and biocompatibility, and (3) surface-bound or embedded molecules that facilitate *in vivo* targeting and/or multifunctionality [38]. Furthermore, the unique magnetic properties of MNPs, including their ability to enhance the relaxation of protons within specific tissues, enable their *in vivo* detection using magnetic resonance imaging (MRI) [39]. Finally, the ability of MNPs to be functionalized and concurrently respond to a magnetic field has made them a useful platform for the development of theranostic tools [40–42]. For instance, external magnetic fields can be used to concentrate and retain MNPs in a specific area or tissue [43].

Several approaches for the radiolabeling of MNPs—including chelator-based and chelator-free radiolabeling techniques—have been reported. To date, iron oxide nanoparticles (IONPs) have been radiolabeled with several radionuclides for SPECT imaging. For example, [^{99m}Tc]TcO^{4-} was conjugated to the functionalized PEG coating on the surface of IONPs to form [^{99m}Tc]Tc-IONPs with high radiolabeling yields (~99%) for multimodality SPECT/MR imaging of sentinel lymph nodes [44]. IONPs have also been labeled with other radionuclides for SPECT, such as iodine-125 [45] and iodine-131 [46].

IONPs were also radiolabeled with numerous positron-emitting radionuclides, including copper-64 [47–49], fluorine-18 [50], and zirconium-89 [51]. For example, a nanoplatform for targeted anticancer drug delivery and PET/MR imaging was developed by radiolabeling cRGD- and DOX-functionalized superparamagnetic iron oxide nanoparticles (SPIONs) with copper-64 [48]. Moreover, chelator-free radiolabeled ultrasmall SPIONs, [^{89}Zr]Zr–USPIONs, were found to be thermodynamically and kinetically stable *in vitro*. *In vivo* imaging and biodistribution studies showed the potential of using [^{89}Zr]Zr–USPIONs for PET/CT (and possibly MRI) of tissues enriched with activated macrophages. The feasibility of chelator-free radiolabeling of SPIONs with germanium-69 [52] and arsenic-72 [53] was also verified.

Lanthanide Nanoparticles

The term "lanthanides"—abbreviated "Ln"—refers to the 15 metallic chemical elements from lanthanum through lutetium (atomic numbers 57 through 71), collectively known as the rare-earth elements. Lanthanides are often found as oxides and fluorides in rocks, ores, and minerals since they are extremely unstable when isolated in elemental form. As methods for the extraction and separation of these lanthanide salts continue to improve, many researchers have turned their attention toward using these elements in cancer imaging and therapy. Several unique properties of lanthanides make them suitable for biological applications. First, the redox stability of Ln^{3+} ions makes them highly stable in the presence of biological reducing agents like ascorbate and thiols. Second, their 4f electron configurations, 4f ↔ 5d charge transfer, and f ↔ f transitions give them favorable luminescent properties [54]. For example, gadolinium complexes such as gadopentetic acid (Magnevist) and gadoteric acid (Artirem) are commonly used as MRI contrast agents for cancer imaging in the clinic. Moreover, the lanthanide radionuclide lutetium-177 has been used in cancer imaging and therapy, as it emits both gamma and beta particles [55]. In the form of nanomaterials, lanthanide oxide nanoparticles, nanodrums, and nanocrystals show potential for use as imaging agents and anticancer drugs [56].

Ln^{3+}-based nanoparticles have been radiolabeled for SPECT and PET imaging. Li and co-workers studied the long-term *in vivo* distribution of ^{153}Sm-labeled $Gd(OH)_3$ nanorods *in vivo* using SPECT imaging [57]. Time-resolved SPECT imaging showed that the uptake and retention of the $Gd(OH)_3$ nanorods occurred mainly in the liver, spleen, and lungs. Due to the similarity of their atomic radii and chemical properties, samarium-153 can be readily incorporated into other Ln^{3+}-based nanoparticles containing elements such as Y^{3+}, Yb^{3+}, or Er^{3+} [58–61]. For PET imaging, Cheng and Cai *et al.* demonstrated chelator-free ^{89}Zr radiolabeling of ten different types of lanthanide metal oxide nanomaterials (M_xO_y, M = Gd, Ti, Te, Eu, Ta, Er, Y, Yb, Ce, or Mo, x = 1–2, y = 2–5) modified with polyethylene glycol (PEG). Among them, [^{89}Zr]Zr−Gd_2O_3−PEG was employed as an *in vivo* multimodal imaging probe that revealed deep-seated draining lymph node networks via PET and MR imaging (Fig. 5) [62].

Silica Nanoparticles

Unlike the previous examples we have discussed, silica nanoparticles do not possess intrinsic properties that allow them to serve as contrast agents or therapeutics. However, the well-defined siloxane chemistry that underpins the creation of silica nanoparticles facilitates the facile tuning of their size, morphology, porosity, and functionalization. This gives silica nanomaterials a distinct edge over their counterparts in biomedical applications [63]. Moreover, their high surface area-to-volume ratio, rigid and stable skeletal network, and well-established, scalable synthetic procedures are added advantages of silica nanoparticles which have propelled their application in medicine. Indeed, one type of small silica nanoparticle dubbed "C-dots" is currently in

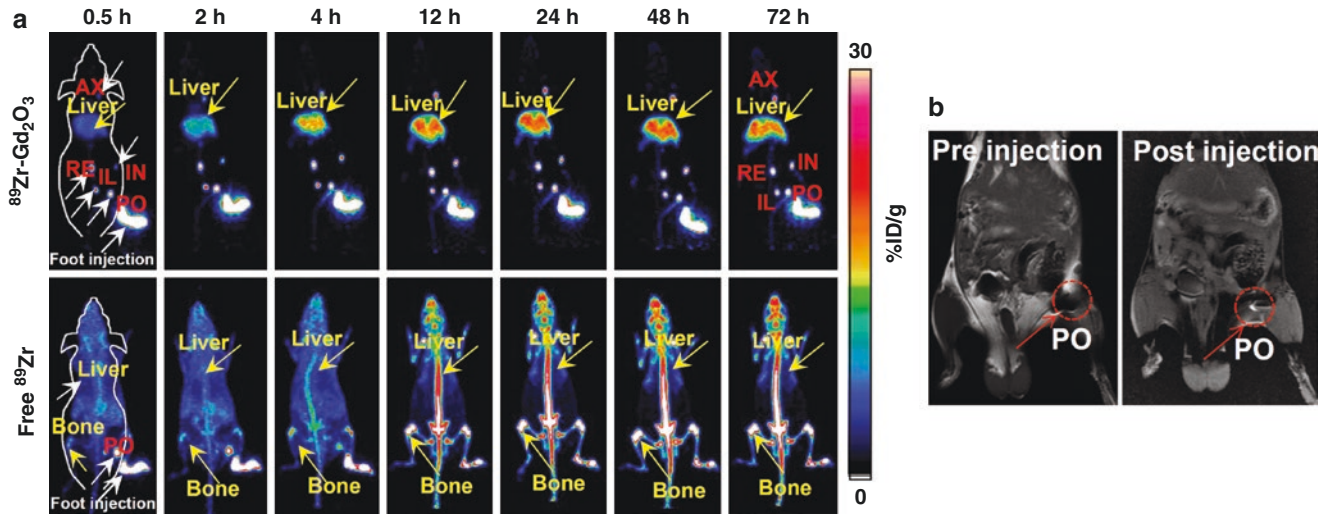

Fig. 5 *In vivo* lymph node (LN) mapping after local injection of radiolabeled Gd_2O_3-PEG nanoparticles into the right rear footpad of mice. (**a**) *In vivo* MIP of lymph node imaging with PET after the local injection of [^{89}Zr]Zr-Gd_2O_3–PEG nanorods (top) or free [^{89}Zr]Zr^{4+} (bottom) into the right footpad of each mouse: *PO* popliteal LN, *IL* iliac LN, *RE* renal LN, *IN* inguinal LN, *AX* axillary LN. (**b**) *In vivo* MRI LN mapping using Gd_2O_3-PEG nanorods. MR images were taken before (left) and after (right) the injection of the Gd_2O_3-PEG nanorods. (Adapted from Cheng *et al.* [62], with permission. © American Chemical Society)

clinical trials as of 2017 [64]. Cornell dots—or cRGDY-PEG-C-dots—were radiolabeled with ^{124}I to obtain [^{124}I]I-cRGDY–PEG–C-dot particles that were inherently fluorescent due to the embedding of Cy5 dye within the particle. Findings from the first-in-human study (a single-injection tracer dose in metastatic melanoma) evaluated the safety, pharmacokinetics, clearance properties, and radiation dosimetry of [^{124}I]I-cRGDY–PEG–C dots and suggested that these particles are safe to use in humans. Another example—ultrasmall silica nanoparticles synthesized in water-based environments called Cornell prime dots or cRGDY-PEG-C′-dots [65]—were radiolabeled with zirconium-89 via two different strategies: chelator-free and chelator-based radiolabeling [66]. High *in vitro* radiostability was found for both radioconjugates; however, the constructs labeled using a chelator-based strategy were significantly more stable *in vivo*. The renal clearance of the particles was confirmed by pharmacokinetic studies and PET imaging. Finally, both versions of the radiolabeled C'-dots displayed low accumulation in the RES, improved tumor uptake, and high target-to-background activity concentration ratios in $\alpha_v\beta_3$ integrin-expressing human melanoma xenograft models.

With their tailored porous structure and high surface area, mesoporous silica nanoparticles (MSNs) have additional advantages over traditional drug nanocarriers, resulting in a dramatic rise in their biomedical use since their first report in 2001 [67, 68]. These nanostructures have been radiolabeled with radionuclides ranging from fluorine-18 ($t_{1/2}$ = 109.8 min) [69] to zirconium-89 ($t_{1/2}$ = 72.8 h) [10] via both chelator-based and chelator-free strategies. For example, a technique for the chelator-free labeling of MSNs with zirconium-89 was developed [70]. The results showed that zirconium-89 has strong binding affinity for both MSNs and dense silica ($dSiO_2$) without the detachment of the radiometal for 48 h. Compared to [^{89}Zr]Zr-$dSiO_2$, [^{89}Zr]Zr-MSN exhibited higher *in vivo* stability, with very little bone uptake for over 3 weeks (Fig. 6).

Carbon Nanoallotropes

Carbon nanomaterials are lower-dimensional carbon allotropes that have garnered great attention since the discovery of fullerenes in 1985 [71]. In recent years, their popularity has been compounded further by the discoveries of carbon nanotubes (CNTs) [72], graphene [73], carbon dots [74, 75], and nanodiamonds [76]. These nanomaterials typically range in size from 1 nm to 1 μm and have been employed in optical and photoacoustic imaging as well as photothermal imaging and therapy due to their strong absorption in the NIR I (750–1000 nm) and NIR II (1000–1700 nm) windows that facilitates deep tissue imaging with high resolution, enhanced contrast, and minimized autofluorescence and photobleaching [77].

In nuclear medicine, the biological properties of CNTs have been explored for both PET and SPECT imaging using radionuclides such as iodine-125 [78], indium-111 [79], and technetium-99 m [80]. Both single-walled (SWNT) and multi-walled nanotubes (MWNT) have demonstrated small molecule-like clearance from systemic blood circulation, rapid transportation through tissues and organs, rapid renal clearance, and no retention in the RES. The unique electronic

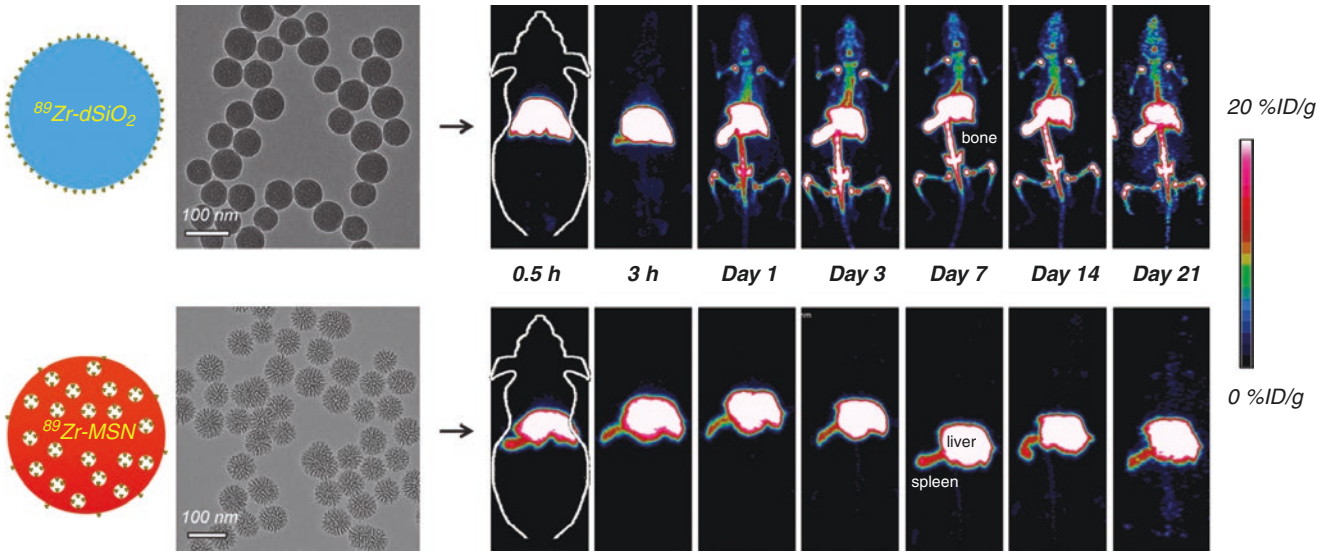

Fig. 6 Maximum intensity projection PET images, schematic, and transmission electron microscopy (TEM) images of ^{89}Zr-labeled mesoporous silica nanoparticles ([^{89}Zr]Zr-MSN) (bottom) and ^{89}Zr-labeled dense silica nanoparticles ([^{89}Zr]Zr–dSiO$_2$) (top). The absence of radioactivity in the bones in the case of [^{89}Zr]Zr-MSN demonstrates the high *in vivo* stability of these intrinsically radiolabeled nanoparticles when compared to [^{89}Zr]Zr–dSiO$_2$. (From Chen *et al.* [70], with permission. © American Chemical Society)

and optical properties of graphene have also been harnessed for phototherapy [81], while the surface itself can be used for the attachment of various materials for multimodality imaging and theranostics [82, 83]. While their potential has been heralded for decades, concerns over their long-term toxicity have severely impeded the clinical implementation of CNTs and graphene, prompting the recent introduction of other lower-dimensional nanocarbons into the biomedical arena [77].

Quantum Dots (QDs)

QDs are semiconductor crystals composed of elements from groups II–VI or III–V with physical dimensions smaller than the exciton Bohr radius [84]. Semiconductor metal combinations such as CdS, CdSe, CdTe, ZnS, and PbS can be used to make QDs, and they can range from 2 and 10 nm in diameter (10–50 atoms) [85]. Generally, a QD's structure is composed of a semiconductor core coated by a shell (*e.g.* ZnS) to improve their optical properties and another layer to enhance their solubility in aqueous buffers. Cadmium selenide (CdSe) is the typical core of QDs that absorbs incident photons, leading to the generation of electron-hole pairs. These pairs then rapidly recombine, prompting the emission of less-energetic photons and giving QDs unique optical properties [86]. Compared to organic dyes and fluorescent proteins, QDs offer several unique advantages, including their size- and composition-tunable emission from visible to infrared wavelengths, large absorption coefficients across a wide spectral range, and very high levels of brightness and photostability [84].

Radiolabeled QDs have been explored as potential platforms for the construction of multimodal agents for optical and PET/SPECT imaging. This is an especially appealing combination of modalities, as optical imaging provides high resolution, while PET and SPECT offer high sensitivity, quantification, and limitless tissue penetration [87]. Since chelated radionuclides are sometimes unstable in living animals, chelator-free strategies for the radiolabeling of QDs have been investigated extensively. QDs have been intrinsically radiolabeled with various radionuclides such as copper-64, indium-111, zinc-59, selenium-81, and others [88]. Sun *et al.* [89] reported self-illuminating, chelator-free, ^{64}Cu-radiolabeled QDs and their Cherenkov luminescence and PET imaging capabilities *in vivo*. Copper-64 was encapsulated into these ionic QDs via the ion exchange method with nearly 100% radiolabeling yield and high radiostability (section "Procedures for Labeling Nanoparticles with Radionuclides"). PET images of mice bearing U87MG xenografts showed ~5 %ID/g in the tumor at 1 h postinjection and 12.7 %ID/g at 17 h p.i. Similar results were also obtained from Cherenkov resonance energy transfer (CRET) imaging, suggesting the potential use of these ^{64}Cu-doped QDs for both PET and CRET imaging (Fig. 7 top and bottom). Other works on intrinsically radiolabeled QDs have also been published [90, 91].

Although a number of preclinical studies have been conducted with radiolabeled QDs to elucidate their biodistribution and clearance mechanisms, the toxicity of the cadmium ions in the core of CdSe QDs is a serious concern that has posed a major challenge to clinical imaging using QDs [92, 93].

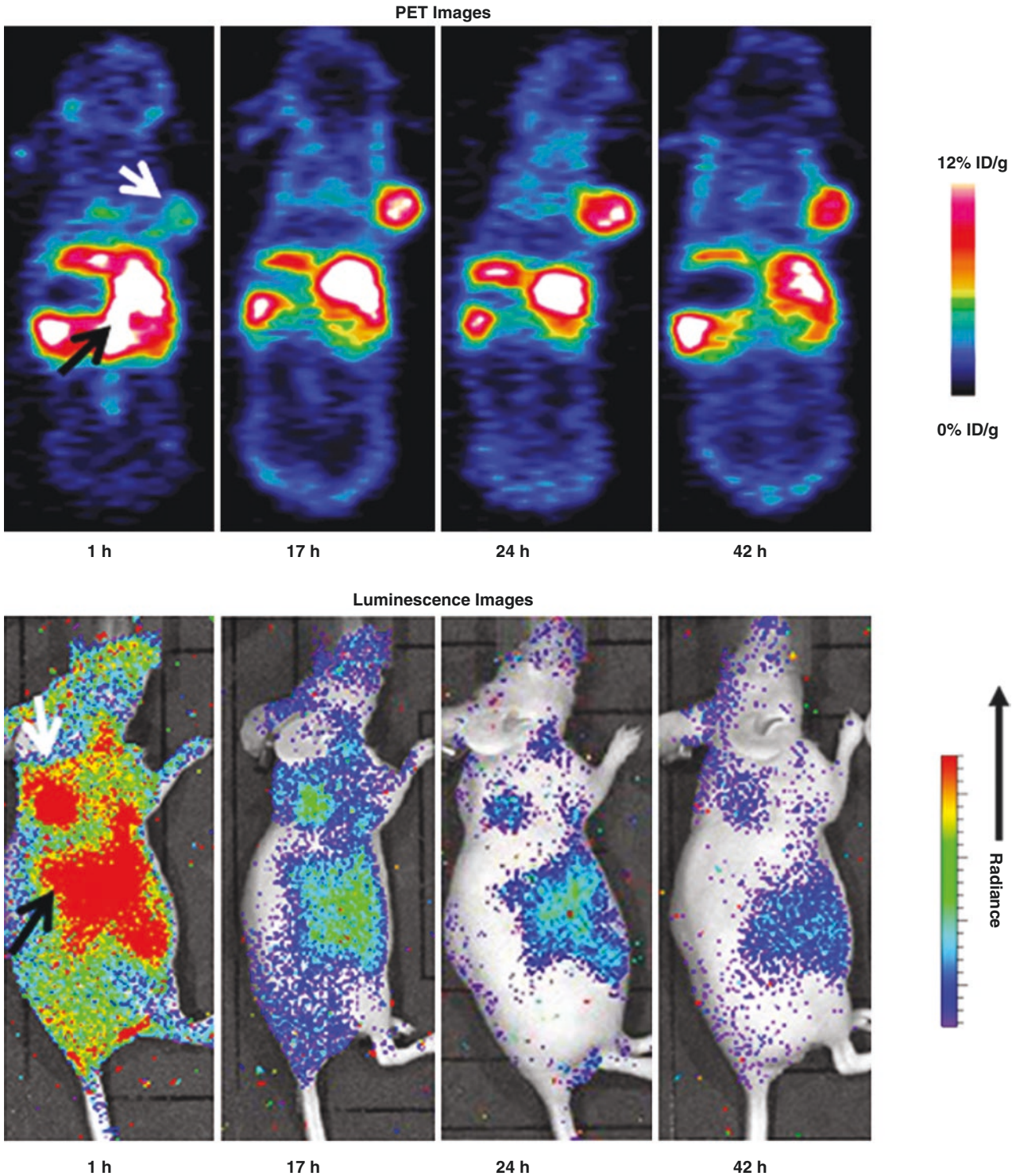

Fig. 7 (Top) Coronal PET images of U87MG tumor-bearing mice at 1, 17, 24, and 42 h after the intravenous injection of ^{64}Cu-doped QD580. (Bottom) Whole-body luminescence images of U87MG tumor-bearing mice at 1, 17, 24, and 42 h p.i. of ^{64}Cu-doped QD580 (Ex: Closed; Em: Open). White arrowheads indicate tumors; black arrowheads indicate livers. (Adapted from Sun *et al.* [89], with permission. © American Chemical Society)

Liposomes

Liposomes are composed of a lipid bilayer that encloses an aqueous compartment, enabling the loading of either lipophilic or hydrophilic cargoes. They have been widely used for the reformulation of drugs and can accumulate in tumor tissue either passively (via extravasation through abnormal tumor vasculature) or actively (via target-specific ligands). A variety of different modification methods can be used to sequester cargoes within the inner space, in the lipid bilayer,

or on the surface of liposomes. Furthermore, the size, structure, and size distribution of liposomes can be tailored in rather straightforward ways. As a result, liposomes are excellent platforms for the delivery of therapeutic entities [94]. Besides being a drug carrier, liposomes can be efficiently radiolabeled to monitor their *in vivo* distribution [95]. Indeed, a variety of different radionuclides have been incorporated into liposomes, including gallium-68, copper-64, zirconium-89, technetium-99m, manganese-52, and indium-111. For example, Jensen *et al.* [96] reported the optimized protocols for radiolabeling liposomes with ^{52}Mn via both chelator-based and chelator-free strategies.

Micelles

Micelles are self-assembled nanostructures with a hydrophobic inner core and a hydrophilic outer shell. Micelles passively accumulate in areas with leaky vasculature such as tumors and sites of inflammation and infarction, and—like liposomes—have been used for the reformulation of hydrophobic drugs [97, 98]. With their high stability and biocompatibility, radiolabeled micelles have begun to be used for tumor imaging. For example, Starmans *et al.* reported a micelle that was labeled with zirconium-89 and Fe^{3+} (^{89}Zr/Fe-DFO-micelles) for dual-modality PET/MR imaging [99]. *In vivo* PET/MR studies in mice bearing LS174T tumors showed tumor targeting of the ^{89}Zr/Fe-DFO-labeled micelles through the enhanced permeability and retention (EPR) effect, yielding high tumor-to-blood (10.3 ± 3.6) and tumor-to-muscle (15.3 ± 8.1) activity concentration ratios at 48 h postinjection. In another study by Jensen *et al.* ABC-type (PEG-PHEMA-PCMA) triblock copolymers were prepared to form micelles bearing primary alcohols to enable the conjugation of chelators [100]. These micelle systems were used to compare the *in vivo* stabilities of DOTA and CB-TE2A as chelators for copper-64 in micelles. The *in vivo* results showed that both micelles have long circulation properties, high tumoral accumulation, and similar stability.

Dendrimers

Dendrimers—one of the promising nanopolymeric carrier systems—are highly branched macromolecules with spherically controlled 3D architecture. In general, dendrimers are comprised of three components: (i) a central core which is a single atom or a molecule possessing two identical functional groups, (ii) repeating interior building blocks, and (iii) numerous functional groups on the spherical surface that can be coupled to guest molecules. The presence of branches with repeating functional groups allows dendrimers to be modified for several purposes, such as molecular imaging and drug delivery. The modification of nanomaterials with small molecule anticancer drugs (which are usually hydrophobic) can enhance the solubility of the drugs such that they can cross biological membranes. Moreover, the increase in size and molecular weight when using dendrimers can suspend elimination via macrophages and enhance the accumulation of the nanomaterials in cancer cells [101–103].

Dendrimers can be efficiently labeled with various radionuclides using both prosthetic groups and chelators [104, 105]. For example, Almutairi *et al.* prepared ^{76}Br-labeled biodegradable dendrimers for the PET imaging of tumor angiogenesis [106]. To this end, the pentaerythritol core of dendrimers was modified with tyrosine to enable radiolabeling with bromine-76. Protective shells were formed to prevent *in vivo* dehalogenation using heterobifunctional polyethylene oxide (PEO) chains conjugated to the periphery of the dendrimers. The outer layer was decorated with lysine-modified RGD peptides to enable tumor targeting. The cell binding affinity of the targeted dendrimers was 50-fold higher than that of the RGD peptide alone. Moreover, the targeted dendrimers exhibited a six-fold increase in $\alpha_v\beta_3$ receptor-mediated endocytosis compared to nontargeted analogs.

Strategies to Target Cancer with Nanoparticles

Passive Targeting

In contrast to normal tissues, rapidly growing tumors must stimulate the production of blood vessels to maintain their supply of energy and oxygen. This neovasculature is usually abnormal in form and architecture and exhibits several hallmarks, including poorly aligned and defective endothelial cells with wide fenestrations, a lack of a smooth muscle layer, impaired functional receptors, and innervation with a wider lumen. Moreover, tumor tissues usually have minimal lymphatic drainage. Taken together, these factors lead to abnormal fluid transport dynamics in tumors, especially with respect to macromolecular drugs [107]. Nanoparticles larger than 8 nm in size can take advantage of this irregular tumor vasculature and passively target tumors by passing through their inter-endothelial junctions, which are much larger than those of healthy tissues. This phenomenon is known as the "enhanced permeability and retention" (EPR) effect [108].

In 1979, styrene maleic acid neocarzinostatin (SMANCS) was reported as the first anticancer protein (neocarzinostatin, NCS) conjugated to a polymer (styrene maleic acid copolymer, SMA) [109]. Interestingly, it was found that SMANCS accumulated to a greater degree than NCS alone in tumor tissues [110]. Soon thereafter, it

was found that other plasma proteins larger than 40 kDa also displayed selective accumulation in tumors, leading to the generalization of the EPR effect [108]. Traditionally, the EPR effect was investigated using an intravenous injection of the dye Evans Blue, which binds to plasma albumin and forms a macromolecule which accumulates in tumor tissue but not normal tissues [111]. Since the first report of EPR effect, nanocarrier-based antitumor drugs have been explored extensively. The study of the EPR effect in large animals has led to improved understandings of differences in the EPR effect between tumor types, the heterogeneity of the EPR effect within patient groups, and the dependency of the EPR effect on tumor stage in humans. Hansen *et al.* labeled PEGylated liposomes with copper-64 and evaluated the EPR effect in 11 dogs with spontaneous solid tumors via PET/CT. The results showed that the EPR effect was strong in some tumor types [112]. However, this was not a general feature of solid tumors, since they observed a high degree of heterogeneity in the uptake of the nanoparticles in the tumors of different dogs [112]. Discussions of the EPR effect of radiolabeled nanoparticles—liposomes in most cases—primarily focus on the long circulation half-life of the nanoparticles. Yet a long circulation half-life is a double-edged sword: while it can lead to higher levels of tumor accumulation, it also causes prolonged radiation exposure to normal organs [113, 114].

Active Targeting

Targeting Cancer Cells Active targeting is predicated on the conjugation of bioactive ligands to the surface of nanoparticles in order to facilitate the specific uptake and retention of the particles in target tissues. Generally speaking, these ligands selectively bind cell surface proteins or receptors that are overexpressed in diseased organs, tissues, cells, or subcellular domains. Widely used targets include the epidermal growth factor receptor (EGFR/Her1), human epidermal growth factor receptor 2 (Her2), folate receptor, and prostate-specific membrane antigen (PSMA) [115].

Both specificity and delivery capacity are keys to the efficiency of an active targeting system. The specificity of the ligand-functionalized nanoparticles, of course, is determined by the differential interaction of the particles with target and nontarget tissues and cells. Figure 8 shows a schematic representation of how ligand-functionalized nanoparticles interact with cell surface receptors and internalize via receptor-mediated endocytosis. Currently, active targeting is envisioned as a promising complementary strategy to the EPR effect to augment the efficiency of nanoparticles in cancer. Discussions of the conjugation strategies used to create actively targeted nanoparticles can be found in several recent reviews [13, 14, 116].

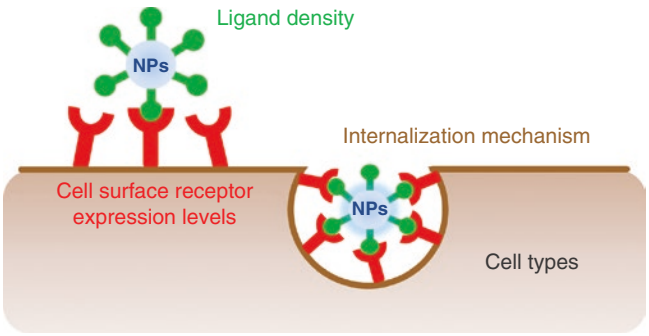

Fig. 8 A schematic illustrating the ways in which ligand-functionalized nanoparticles interact with cell surface receptors

In nuclear medicine, an array of radiolabeled antibody-conjugated nanoparticles have been reported. For example, Chen *et al.* developed functionalized mesoporous silica ($mSiO_2$) nanoparticles for actively targeted PET imaging and drug delivery. In this case, TRC105 antibodies (specific for CD105/endoglin) were conjugated to ^{64}Cu-labeled $mSiO_2$ nanoparticles (uniform 80 nm diameter size) to form [^{64}Cu]Cu-NOTA-$mSiO_2$-PEG-TRC105 [117]. Systematic studies of the targeting efficacy of [^{64}Cu]Cu-NOTA-$mSiO_2$-PEG-TRC105 in 4T1 murine breast tumors clearly suggested that the nanoparticles prominently accumulated at the tumor site *via* both the EPR effect and TRC105-mediated targeting. Small molecule ligands like folic acid (FA; the target ligand for folate receptor) have also been used to decorate radiolabeled nanoparticles. Li *et al.* radiolabeled FA-bearing liposomes to quantitatively measure the *in vivo* pharmacokinetics of [^{89}Zr]Zr-FA-DFO-liposomes. Here, the cellular uptake of [^{89}Zr]Zr-FA-DFO-liposomes by folate receptor-overexpressing KB cells was about 15-fold higher than the nontargeted [^{89}Zr]Zr-DFO-liposomes.

Targeting Tumor Vasculature As we have discussed above, angiogenesis (*i.e.* the formation of new blood vessels) is a characteristic of most solid tumors. As a result, it stands to reason that targeting tumor angiogenesis and neovasculature represents a nearly universal approach to localizing nanoparticles in tumor tissues [118]. Moreover, tumor endothelial cells are directly exposed to circulating blood, eliminating the need for extravasation and therefore increasing the delivery of the nanoparticles to the target cells. In addition, many proteins—such as endoglin (CD105), epithelial cell adhesion molecule (EpCAM), CD20, CD44, CD90, and CD133—are overexpressed on the surface of the endothelial cells of tumor vasculature, providing ample potential targets for tumor-seeking particles. To provide an example, integrin $\alpha_v\beta_3$ is dramatically overexpressed on neovasculature and

has been leveraged effectively as a target for ^{64}Cu-labeled quantum dots [119], single-walled carbon nanotubes [120], and SPIONs [48].

Interactions with the Tumor Microenvironment Tumor cells do not act alone but rather in close interaction with the extracellular matrix (ECM) as well as nongenetically altered stromal cells that constitute the tumor microenvironment (Fig. 9). The interactions between tumor cells and the tumor microenvironment have a deep influence on the progression of cancer and contribute to almost all of the hallmarks of cancer. In the past decade, the tumor microenvironment has been explored intensively as a new target for cancer therapy [121, 122].

Along these lines, several of the telltale characteristics of the tumor microenvironment—including its acidic pH, hypoxic milieu, *etc.*—have been exploited to stimulate morphological changes in nanoparticles [123]. For example, pH-responsive nanoparticles have been developed that enable signal amplification in the slightly acidic pH within solid tumors in order to facilitate sensitive imaging of tumors with high contrast [124]. Gao *et al.* reported pH-responsive [^{99m}Tc]Tc-Mn-MSNs-PEG for SPECT-MRI dual-modal imaging that show increased T1-MRI relaxivity (r1 = 6.60 $mM^{-1}s^{-1}$) in the acidic tumor microenvironment [125].

Furthermore, multistage drug delivery systems triggered by tumor microenvironment-specific stimuli have also emerged for tumor therapy and imaging [123]. Figure 10 outlines several strategies for tumor microenvironment-activatable nanoparticles. For example, Rao and co-workers created a caspase-sensitive nanoaggregation PET imaging probe called [^{18}F]F-C-SNAT [126]. This probe used a caspase-3-/caspase-7-dependent reaction that leads to an enhanced accumulation and retention of fluorine-18 within apoptotic tumors.

Procedures for Labeling Nanoparticles with Radionuclides

Medical Radionuclides

The radionuclides used in medicine have a wide variety of half-lives, decay modes, production routes, and radiosynthetic chemistries. Generally speaking, medical radionuclides are grouped according to their application: imaging or therapy.

Radionuclides for Imaging The term "nuclear imaging" describes two modalities: positron emission tomography (PET) and single-photon emission computed tomography (SPECT). SPECT is predicated on the detection of gamma rays emitted from a radionuclide. Commonly used radionuclides for clinical SPECT imaging include technetium-99m, iodine-123, indium-111, and thallium-201. As its name suggests, PET imaging requires a positron-emitting nuclide. The vast majority of clinical PET scans utilize fluorine-18 (t1/2 = 109 min), though several other positron-emitting radionuclides—including gallium-68. zirconium-89, and copper-64—are beginning to be used in the clinic as well. Readers interested in additional details should refer to Chap. 6 for a detailed discussion of the fundamentals of each imaging modality as well as Chap. 4 for an in-depth treatment of the production of radionuclides for imaging.

Radionuclides for Therapy In recent years, targeted radiotherapy has increasingly become a common treatment for certain cancers [55]. In these treatments, a targeting ligand is labeled with a radionuclide which emits therapeutic particles—*i.e.* beta or alpha particles—and then injected into a patient and allowed to accumulate at sites of disease. A wide variety of radionuclides can be used for targeted therapy, including beta-emitters such as yttrium-90, iodine-131, and lutetium-177 and alpha-emitters such as actinium-225 and

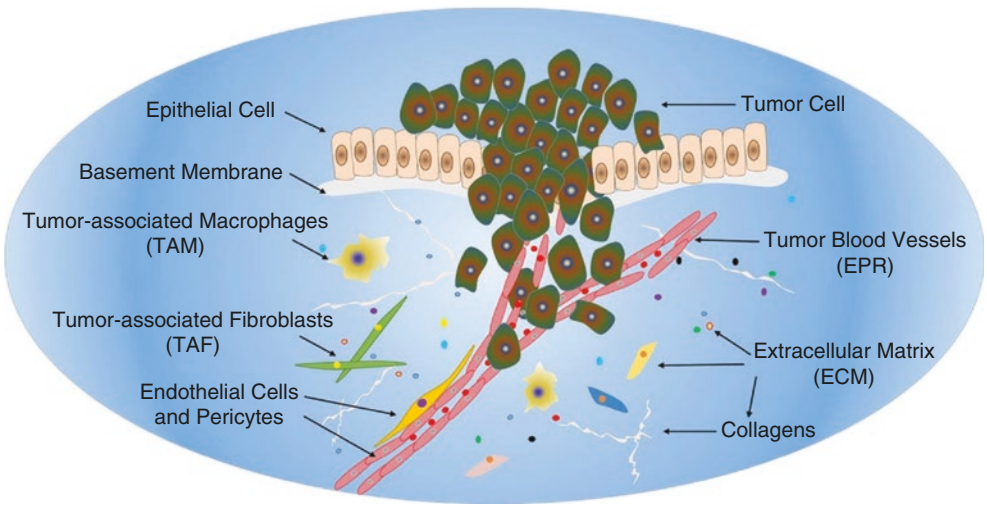

Fig. 9 Schematic representation of the tumor microenvironment. Various cell types and non-cell components are involved in supporting the proliferation, invasion, and metastasis of tumors. (From Yang and Gao [121], with permission)

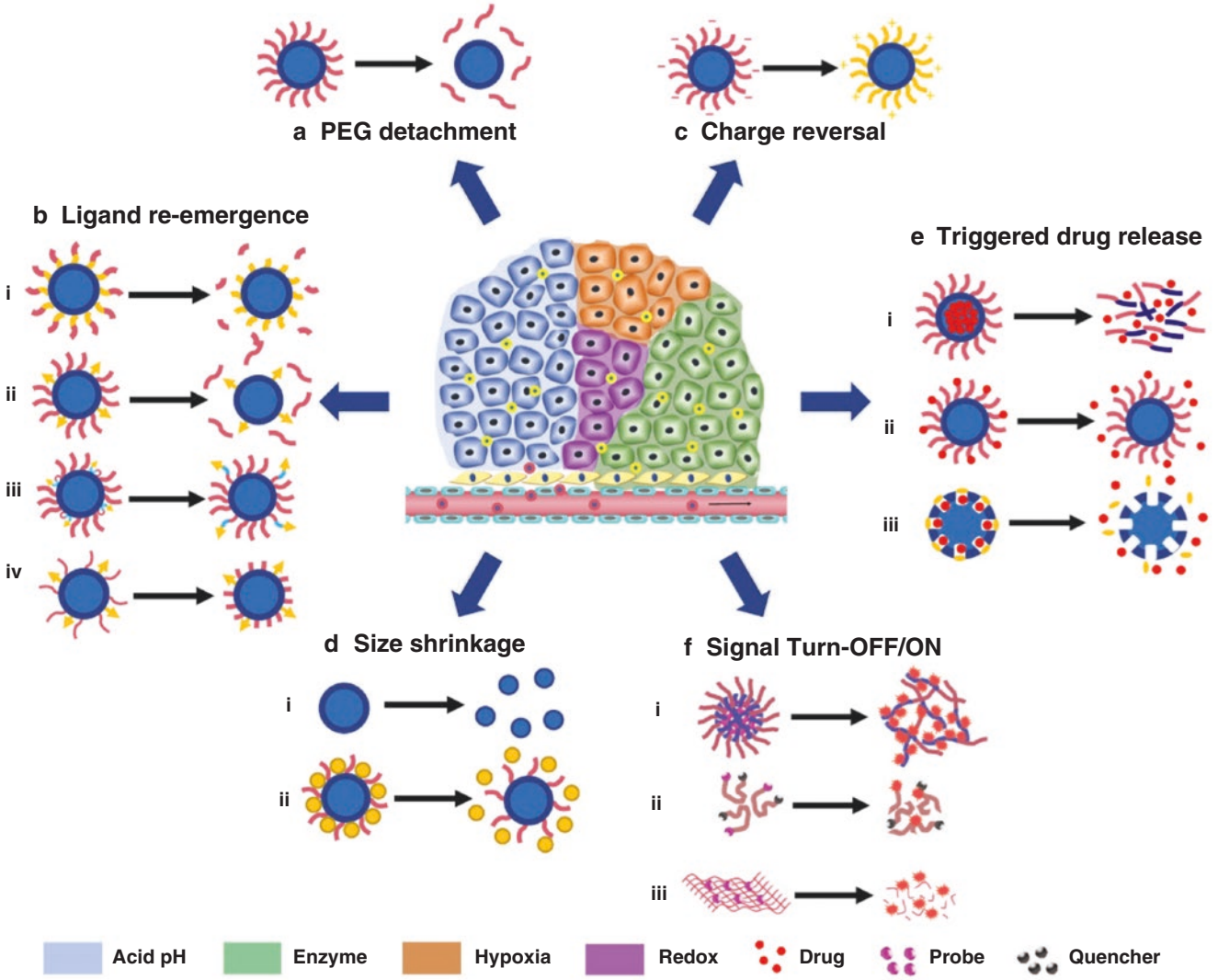

Fig. 10 Strategies for tumor microenvironment-responsive nanoparticles: (**a**) PEG detachment; (**b**) ligand re-emergence; (**c**) charge reversal; (**d**) size shrinkage; (**e**) triggered drug release; (**f**) stimuli-based signal activation nanoplatforms (From Chen *et al.* [123], with permission. © 2017 Ivyspring International Publisher)

bismuth-213. The treatment of hematological cancers and neuroendocrine tumors has been the primary clinical application of targeted radiotherapy, though it has recently begun to be applied to several other solid tumors as well. Readers interested in additional details should refer to Chap. 5 for a detailed discussion of the fundamentals of targeted radiotherapy as well as Chap. 4 for an in-depth treatment of the production of therapeutic radionuclides.

Covalent Labeling with Nonmetallic Radionuclides

Covalent attachment strategies are often used to label nanoparticles (or the ligands attached to nanoparticles) with nonmetallic radionuclides such as fluorine-18, carbon-11, bromine-76, and iodine-124/125. In each case, the properties of the nanoparticle dictate both the radionuclide used and the method of radiolabeling. The serum half-life of the nanoparticle needs to be matched to the physical half-life of the radionuclide. In addition, the surface chemistry of the nanoparticle decides the type of radiosynthetic chemistry that is needed to attach the radionuclide to the nanoparticle.

Carbon-11 is often incorporated into organic synthons, allowing for the straightforward incorporation of carbon-11 into radiotracers through reactions such as the methylation of amines or carboxyl groups on the surface of iron oxide nanoparticles [42] (see Chaps. 11 and 12). For fluorine-18, similar direct reactions can be employed. However, a different approach can also be used in which reactive prosthetic groups are first labeled with fluorine-18 and then attached to the nanoparticle (see Chaps. 15, 16, and 17). More recently,

several other unique methods have been explored for the ^{18}F-labeling of nanoparticles, including the direct activation of nanoparticles via proton beam irradiation [127]. The radiobromination and radioiodination of nanoparticles likewise proceeds through typical organic chemistry techniques, generally through the substitution of the halogens on the surface of the particles (see Chaps. 22 and 24). In each of these cases, the surface of the nanoparticle must be modified with appropriate reactive groups or leaving groups to facilitate the desired covalent chemistry.

Because these reactions involve the direct covalent attachment of radionuclides to the either the surface of the nanoparticle or its ligands, the resultant linkages are often very stable. Furthermore, two of the radionuclides that we have discussed in this section—carbon-11 and fluorine-18—are among the most widely available, making these techniques accessible to wide range of scientists and clinicians. However, the news isn't all good. Indeed, these strategies often require complicated chemical reactions and purifications that can be avoided by using other, more facile techniques (see below).

Labeling Nanoparticles with Radiometals

In addition to carbon-11 and the halogen-based radionuclides discussed above, several metallic radionuclides are also available for the radiolabeling of nanoparticles. As some nanomaterials circulate for a long time in the body, they must be radiolabeled with nuclides with long radioactive half-lives. Commonly used radiometals for the radiolabeling of nanoparticles include copper-64, gallium-68, and zirconium-89 for PET and technetium-99 m and indium-111 for SPECT.

Chelator-Based Labeling Most radiolabelings using metallic nuclides employ bifunctional chelators. This is facilitated by the widespread commercial availability of a variety of bifunctional chelators that have been optimized for use with various nuclides [128–130]. While the suitability of the chelator for the radiometal of choice is certainly of the utmost importance for the nanoparticle radiochemist, it is actually the conjugation of the chelator to the nanoparticle that is the chief concern. The proper functionalization of the surface of the nanoparticle is critical for the successful conjugation of a chelator to its surface, as many commercially available chelators are designed to react with amines, thiols, or carboxylic acids. Depending on the nanoparticle in question, a few options are available for modifying the surface to allow for the conjugation of a chelator. (3-Mercaptopropyl) trimethoxysilane and (3-aminopropyl)triethoxysilane are used to modify the surface of nanoparticles with thiol (-SH) and amine (-NH_2) groups, respectively. In each case, the preformed nanoparticles are incubated with the given chemical to modify the surface, followed by reaction with the bifunctional chelator of choice.

Once a chelator has been attached to the surface of a nanoparticle, the labeling reaction with the radiometal is usually quite straightforward. The incubation—often at high temperature—of the chelator-modified nanoparticles with an aqueous solution of the radiometal usually facilitates the successful chelation of the nuclide. Typically, this is followed by some sort of purification step that depends on the type of nanoparticle involved. Methods such as EDTA challenge, HPLC, and size-exclusion chromatography have been used to remove excess unchelated radiometals from the crude solution of radiolabeled nanoparticles.

The ease of chelator-based techniques makes them the most widely used radiosynthetic approach for nanoparticles. However, this strategy relies on the availability of an optimal chelator for the radiometal of choice, which is not always available. The release of the radiometal *in vivo* can result in the accumulation of the radiometal in nontarget tissues, a phenomenon which can negatively impact contrast in imaging and create unwanted radiation dose to healthy organs during targeted radiotherapy. As a result, many nanoparticle radiochemists are turning to intrinsic radiolabeling techniques.

Intrinsic Radiolabeling The term "intrinsic labeling" describes any technique for the radiolabeling of nanoparticles that does not use a chelator or a direct covalent chemical reaction [131]. In some instances—such as cases in which a well-established chelator does not exist for a radiometal—this may be the only viable option for a given nuclide. As we outline below, a number of synthetic routes are available for the generation of intrinsically labeled nanoparticles.

Hot-Plus-Cold Synthesis In a "hot-plus-cold" strategy, a radionuclide is directly incorporated into a nanoparticle during its synthesis. This involves using both hot (radioactive) and cold (nonradioactive) precursors during the formation of a nanoparticle. This provides nanoparticles that are quite stably labeled and is a relatively straightforward technique. For example, copper sulfide nanoparticles are often used in photothermal treatments since they strongly absorb near-infrared radiation and convert it to heat. If the nanoparticle is localized in cancerous tissues, the heat that is given off can kill the cells around it. Since these nanoparticles already contain copper, the substitution of cold copper with copper-64 provides a means for the *in vivo* tracking of these nanoparticles with PET.

While the hot-plus-cold strategy provides some of the most stable radiolabeled nanoparticles, it is important to note that this approach requires a particular combination of radionuclide and nanoparticle, so it is not universally applicable. Additionally, "crystal mismatch" may occur within the nanoparticle as the radionuclide decays or if a foreign ele-

ment is incorporated (for instance, using copper-64 as a substitute for Au in the synthesis of gold nanoparticles). This could lead to issues with the structural integrity of the nanoparticle, as the strength of the crystalline structure is degraded. Furthermore, the synthesis of some nanoparticles requires harsh conditions or long reaction times, further limiting the use of certain radionuclides.

Specific Trapping Rather than forming actual covalent bonds, very strong interactions between certain atoms can allow for the "specific trapping" of ions within nanoparticle structures. Many metal ions are inherently oxophilic, meaning they form particularly stable bonds with oxygen atoms. This, of course, is the basis of many chelators, and a wide variety of nanoparticles also display a multitude of oxygen atoms on their surface. Perhaps not surprisingly, this property has enabled the radiolabeling of platforms ranging from silica to iron oxide nanoparticles with a variety of radiometals, including zirconium-89, germanium-69, lutetium-177, and copper-64. Furthermore, this type of radiolabeling is not necessarily predicated solely on the presence of oxygen atoms. Indeed, fluoride ions display a strong affinity for rare-earth metals. The affinity of fluoride for yttrium, for example, has been exploited for the radiolabeling of $NaYF_4$ nanoparticles with fluorine-18. Moving on, other inherent properties of a nanoplatform can also be used for specific trapping of radionuclides. For example, porphysomes—liposome-like particles containing porphyrins—are also capable of coordinating radiometals. As is the case with the "hot-plus-cold" synthesis strategies discussed above, these trapping strategies require specific combinations of radionuclides and nanoplatforms. Furthermore, even when there is an inherent affinity between the two, the stability of the bond—especially *in vivo*—must be fully evaluated (see section "Tests for Nanoparticle Radiopharmaceuticals").

Cation Exchange Cation exchange has been a widely used technique in materials science for quite some time [132]. In essence, an ion in a crystal (or nanoparticle) is replaced by a different ion in solution. The driving force for these reactions is the relative thermodynamic stability of the reactants versus the products, and this relative stability can be adjusted through the appropriate choice of solvent. This technique has been exploited for developing novel nanomaterials; however, its application in radiolabeling has not been fully explored. Indeed, only a small handful of nanoparticles have been radiolabeled in this manner. In one case, copper-64 was used to label quantum dots by replacing the pre-existing zinc cations in commercially available CdSe/ZnS particles. Likewise, the lanthanide ions in $NaLuF_4$:Yb,Gd,Tm nanoparticles have been exchanged with samarium-153 to create a SPECT imaging agent. It is known that with the correct choice of ions, these cation exchange reactions proceed quickly, suggesting that this technique may not have reached its full potential. Again, as with other the intrinsic radiolabeling techniques that we have discussed, cation exchange requires a specific combination of nanoparticle and radio-cation. And in addition, this strategy also requires the detailed optimization of reaction conditions in order to obtain products in reasonable time frames (Fig. 11).

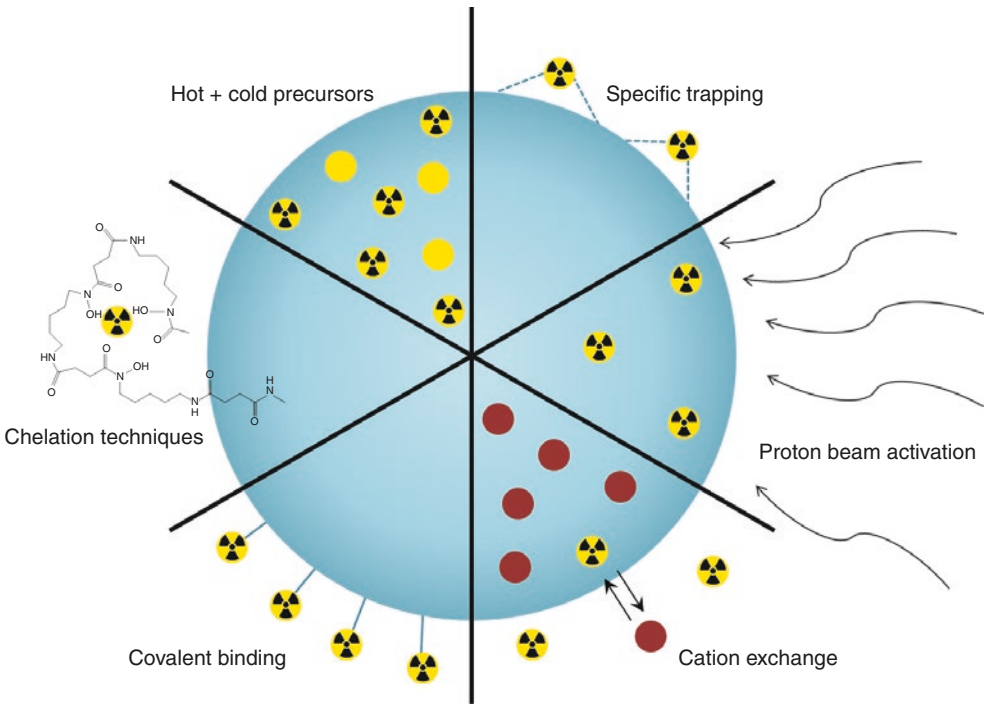

Fig. 11 A wide variety of strategies are available for the radiolabeling of nanoparticles

Tests for Nanoparticle Radiopharmaceuticals

Once a radiolabeled nanoparticle has been designed and synthesized, a number of chemical and biological tests must be performed in order to ensure that the nanoparticle will behave as expected *in vivo*. While the small size of nanoparticles undeniably gives them interesting properties, this exact property also presents unique challenges in the context of creating radiopharmaceuticals for *in vivo* applications. More specifically, tests on three different levels—in solution, *in vitro*, and *in vivo*—are needed before a radiolabeled nanoparticle has been fully evaluated.

Solution-Based Studies

Several solution-based tests should be the first steps in the validation of nanoparticle-based radiopharmaceuticals.

Stability and Degradation Studies The use of nanoparticles for *in vivo* applications requires a delicate balance. They must simultaneously be stable enough to ensure delivery to their intended targets, yet they must also biodegrade over time in the interest of long-term safety. Common tests for the structural stability of nanoparticles involve the incubation of the constructs in various solutions (biological or otherwise) over time. For studies of the shelf life of the nanoparticles, this solution should be whatever is used for their storage: buffers, aqueous media, etc. To simulate the *in vivo* environment, solutions of fetal bovine serum (FBS) or simulated bodily fluid (SBF) can be used to study how the nanoparticles interact with proteins.

Following these incubations, samples of the nanoparticles may be analyzed in a number of ways to probe for decomposition or other structural changes. Tools such as atomic force microscopy (AFM), scanning electron microscopy (SEM), and transmission electron microscopy (TEM) can provide highly magnified images and important structural information. For example, Fig. 12 shows TEM images illustrating the degradation of silica nanoparticles upon incubation in SBF at 37 °C [133]. Clearly, these bMSNs (biodegradable mesoporous silica nanoparticles) become smaller over time, indicating their dissolution in bodily fluids. Other tests that can be used for the analysis of nanoparticles after incubation include dynamic light scattering (DLS), zeta-potential measurements, and x-ray scattering techniques.

Radiolabeling Efficiency and Stability The stable attachment of the radionuclide to the particle is critical for both nuclear imaging and therapy. Generally speaking, tests for radiochemical stability are similar to those for structural stability: after the nanoparticles are radiolabeled, they are incubated in solution and analyzed over time. These analyses can be performed in a number of ways. One method involves the use of radio-thin layer chromatography (radioTLC).

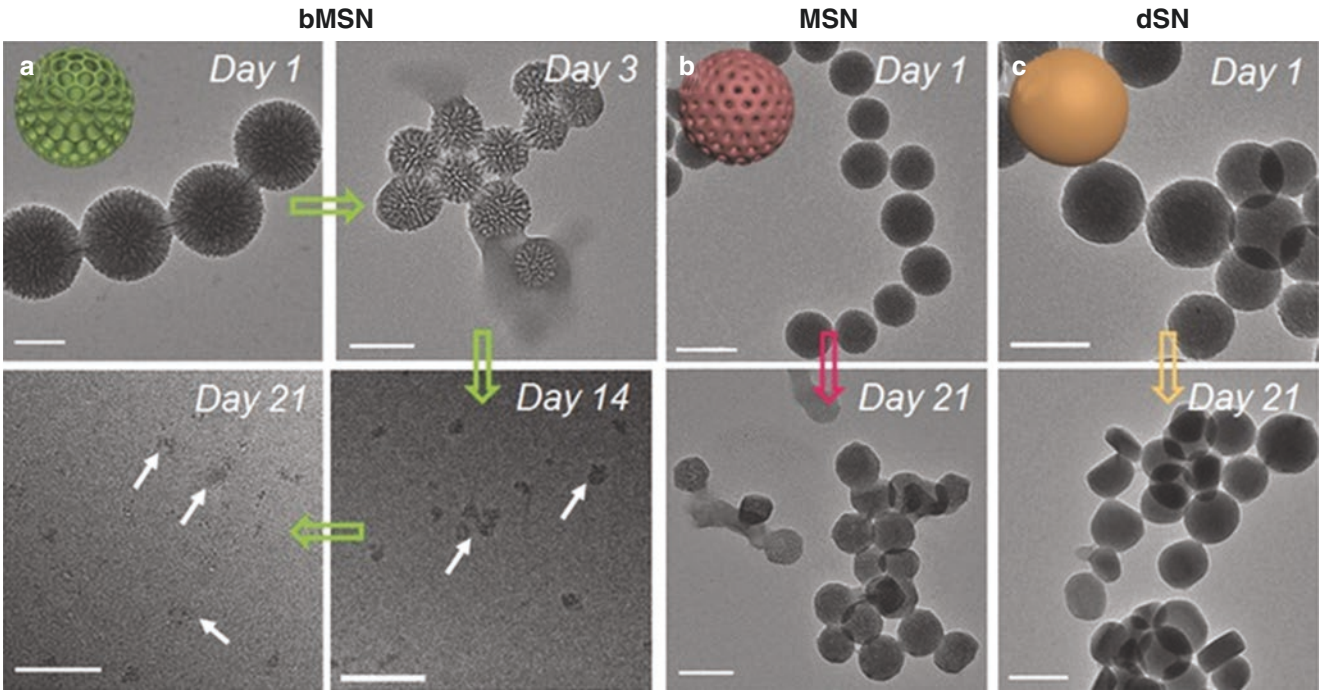

Fig. 12 Transmission electron microscopy analysis of nanoparticle structures following incubation in simulated bodily fluid: (**a**) biodegradable mesoporous silica nanoparticles; (**b**) mesoporous silica nanoparticles; (**c**) dense silica nanoparticles (From Goel *et al.* [133], with permission)

RadioTLC enables the separation of free radionuclides and radiolabeled particles as well as the analysis of the relative amounts of each (Fig. 13). The "spin-down" method is another tool for the analysis of radiolabeled nanoparticles, which—unlike radioTLC—does not involve finding a proper mobile phase. In this test, the solution of nanoparticles is centrifuged in order to form a pellet of nanoparticles. The amount of radioactivity in both the pellet and the supernatant can then be assessed using a gamma counter, providing a measurement of the amount of radioactivity that has detached from the nanoparticles.

One final test is known as the EDTA challenge. Since EDTA binds many metals tightly, the stability of the coordination of a given radiometal to a nanoparticle can be tested by incubating the radiolabeled nanomaterial with an excess of EDTA. Following this incubation, the EDTA-bound and nanoparticle-bound radionuclides can be separated, often using one of the aforementioned techniques, and the relative amounts of each can be analyzed.

In Vitro Studies

In vitro studies with cultured cells represent a second layer of sophistication for the testing of radiolabeled nanoparticles. These may be performed with either cancerous or normal cell lines or with more advanced models such as organoids or patient-derived tissue samples. These tests serve to build a foundation for understanding how a given radiolabeled nanoparticle interacts with living cells. At a minimum, these tests should be performed with the non-radiolabeled nanoparticles to determine their effects on cellular function. Testing with radiolabeled nanoparticles is a good idea as well, especially when therapeutic nuclides are involved.

If nanoparticles are meant to be internalized into cells or are simply actively targeted to cancer tissues, cell-based assays can verify their behavior *in vitro* [134, 135]. These tests rely on the detection of nanoparticles in some way, though whether this is achieved via fluorescence imaging or radioactivity counting depends on the nanoparticle in question. Both approaches can provide information about the proportion of the nanoparticles that are surface-bound or internalized into cells. If optical imaging is utilized, confocal imaging may aid in visualizing the localization of nanoparticles in specific subcellular compartments.

Sometimes, nanoparticles can interfere with cellular functions to the extent that they compromise the viability of the cells. This, of course, needs to be identified prior to performing any *in vivo* studies. Perhaps the most common assay of cell viability is the MTT assay (MTT = 3-(4,5-dimethylthiazol-2-yl)-2,5-diphenyltetrazolium bromide) [136]. This colorimetric assay involves the incubation of cells with the MTT substrate (which begins yellow) and its subsequent reduction in viable cells to a purple metabolite. This color change can then be detected using a plate reader. In short, the more intense the purple color, the healthier the cells. Alternative methods for measuring the metabolism of nanoparticle-treated cells also exist, including ATP assays. The production of ATP (adenosine triphosphate) is one of the hallmarks of healthy cells, so the detection of ATP—often using luminescent sensors—can provide an indirect measure of the health of cells.

While nanoparticles are often used to detect and treat diseases such as cancer, the nanoparticles themselves could—under some circumstances—have carcinogenic effects. A simple method for monitoring the mutagenic effects of

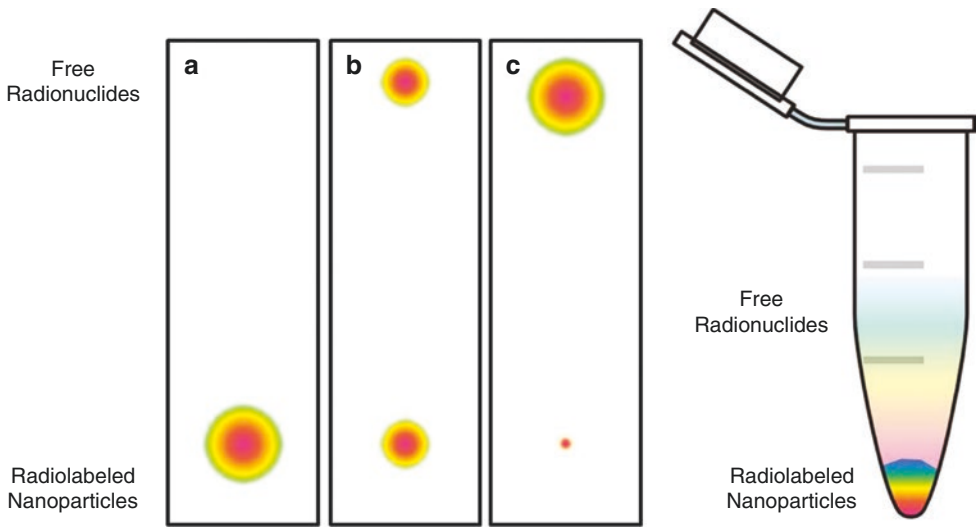

Fig. 13 Left: Examples of radioTLC plates. (**a**) Complete retention of radiolabel on the nanoparticles; (**b**) 50% retention of radiolabel on the nanoparticles; (**c**) nearly complete dissociation of the radiolabel from the nanoparticles. Right: Example of the "spin-down" method of analyzing radiolabeling stability

nanoparticles is the Ames assay [137]. This test utilizes bacterial DNA as a model for mutagenesis. In brief, this test involves the use of genetically modified bacterial strains that are unable to produce histidine (his^-). These strains are incubated with the nanoparticle in question, and then the number of mutant bacterial colonies that have reverted back to the his^+ genotype are determined. While this test is centered upon only a single type of mutation in an admittedly simple model, it is a well-recognized first step in mutagenic testing.

One limitation of many cell culture models is the lack of sophistication; that is, two-dimensional systems (*i.e.* cells in a culture plate) often cannot recapitulate the three-dimensional properties of tissues. For that reason, advanced *in vitro* systems such as 3D cell culture and flow models have been developed. A 3D culture model includes a matrix that supports three-dimensional growth, a variety of cell types, and more advanced elements such as nerve and immune cells [138]. These models allow for more sophisticated investigations into the interactions between radiolabeled nanoparticles and organized cells and are thus often more accurate predictors of *in vivo* results than traditional methods.

As with any chemical or biological assay, each of these aforementioned techniques has pros and cons. For this reason, a wide variety of chemical and biological characterization methods should be used for the evaluation of radiolabeled nanoparticles. Simple tests such as MTT and Ames assays represent a valuable start, but they should certainly be followed with studies using more advanced models. In addition, other factors such as dosing of nanoparticles need to be considered during *in vitro* assays. For instance, many *concentrations that could not* tests use artificially high concentrations of investigative compounds, concentrations that could not be achieved *in vivo* but can provide a "worst-case scenario" *in vitro* result. While testing at these concentrations may have value, the use of biologically relevant concentrations should be explored as well. Finally, the intended dosing regimen of the nanoparticles—*e.g.* whether the nanoparticle will be administered in a single dose or multiple doses—should be considered during *in vitro* assays as well. In the end, we believe that it is important to note that even after a radiolabeled nanoparticle has been characterized thoroughly using a plethora of different *in vitro* assays, its *in vivo* behavior can still be quite different than anticipated.

***In Vivo* Preclinical Evaluation** Once a nanoparticle has been fully evaluated *in vitro*, it is fit for evaluation in preclinical *in vivo* models. A variety of *in vivo* models may be appropriate depending on the intended clinical application, though murine models are the most common choice for initial testing.

Biodistribution Studies The pharmacokinetic profile of a nanoparticle depends on a large number of factors, including its size, surface charge, shape, coating, composition, deformability, and route of administration [139]. Oftentimes, however, even knowing all these characteristics in advance does not allow for an accurate prediction of a nanoparticle's *in vivo* behavior.

Several trends are evident in biodistribution studies of radiolabeled nanoparticles. Compared to non-nanoparticle formulations of drugs and small molecules, nanoparticles produce higher activity concentrations in the kidneys, liver, and spleen, with the relative uptake in each mainly determined by the size and surface characteristics of the nanoparticle. Large, cationic, and hydrophobic nanoparticles are rapidly cleared through the mononuclear phagocyte system (MPS), which contains both the liver and spleen. In these organs, nanoparticles are often bound irreversibly and—as a result—are cleared very slowly from the body. As a result, it is often desirable to create nanoparticles that are excreted through the kidneys, so-called "renal-clearable" nanoparticles [140]. Nanoparticles with diameters under 10 nm are more easily cleared through the kidneys, often enhancing their safety profiles.

One of the major benefits of radiolabeled nanoparticles *in vivo* is the relative ease of monitoring their biodistribution. If solution studies and *in vitro* tests indicate that the labeling is quite stable, PET, SPECT, and biodistribution studies can provide sensitive measures of the *in vivo* behavior of the nanoparticles. Generally speaking, a long-lived radionuclide should be used for these studies in order to facilitate monitoring for the longest possible amount of time possible. In most cases, nanoparticles do not clear out of the body quickly; thus, their long-term *in vivo* fate should be explored. Moreover, the choice of preclinical model is crucial when determining the biodistribution of a nanoparticle. It has been shown that the clearance of nanoparticles can vary across species: while larger nanoparticles often accumulate in the livers of humans, mice, rats, monkeys, chickens, and rabbits, the same nanoparticles are preferentially retained in the lungs of sheep, pigs, goats, and cats [139].

***In Vivo* Safety Profiles** Any time a foreign substance is introduced into the body, the safety of the agent—both short- and long-term—needs to be thoroughly evaluated [141, 142]. Perhaps not surprisingly, the acute and chronic effects of nanoparticles in the body vary widely. The toxicity of nanoparticles stems primarily from causing the aggregation and misfolding of proteins. The interactions of nanoparticles with cell membranes may be another cause of toxicity through structural damage to the lipid bilayer. Taken together, these mechanisms of cytotoxicity can lead to organ-wide problems which need to be thoroughly explored during the evaluation of any nanoparticle-based radiopharmaceutical.

A number of *in vivo* tests should be performed to assess the toxicology of nanoparticles. For example, the analyses of

blood cell counts and serum biomarker levels can provide a non-specific strategy for evaluating toxicity. Both complete blood counts—which provide more general whole-body information—and assays for organ-specific biomarkers should be evaluated. The latter includes assays for ALT, AST, and bilirubin to assess liver function as well as tests for creatinine to measure the performance of the kidneys. Tissue-based analyses should also be performed. These often take the form of *ex vivo* pathological examinations. Specifically, tissues of interest can be removed, sliced, and stained to look for markers of cellular damage. Conventional hematoxylin and eosin (H&E) staining can help probe for damage to cellular structures, while staining for specific biomarkers of apoptosis (caspase-3), oxidative stress (superoxide dismutase), or inflammation (INF-γ) can provide more complementary information. The nanoparticles themselves—depending on their size, of course—may also be visible on tissue slices. These tissue-specific analyses should be performed not only for the targeted tissue but also for nontarget organs as well.

Challenges and Future Directions for Nanoparticle Delivery of Radionuclides

The targeted delivery of nanoparticles for theranostic purposes holds significant clinical promise due to the flexible and multifunctional nature of nanomaterials. However, the clinical utilization of nanoparticles has been limited by concerns over their toxicity and *in vivo* behavior. Radiolabeled nanoparticles have the potential to provide insights into the *in vivo* behavior of nanoparticles and thus could prove instrumental in the success of these materials in the clinic.

Of course, several issues surrounding radiolabeled nanoparticles should be carefully considered prior to their implementation in the clinic. For example, the *in vivo* behavior of large doses of nanoparticles is too complex to be inferred using radiolabeled tracers because the amount of nanoparticles introduced into a system can impact their physicochemical and biological characteristics. Furthermore, these behaviors can vary on a patient-by-patient basis, rendering generalizations about the behavior of nanoparticles problematic [143].

Nonetheless, the clinical potential of radiolabeled nanoparticles as diagnostics, therapeutics, and theranostics certainly warrants more research. The development of more facile procedures for the surface modification and radiolabeling of nanoparticles is therefore urgently needed. In addition, strategies for the production and characterization of nanoparticles with minimal batch-to-batch variation are required as well. As the field of "nanomedicine" continues to grow, it is expected that standard procedures for the synthesis, characterization, and radiolabeling of nanoparticles will be agreed upon by the field as a whole. Ultimately, it is our hope that the introduction of nanoparticles—and especially radiolabeled nanoparticles—into routine clinical practice will positively impact the diagnosis and treatment of a wide variety of disease.

The Bottom Line

- Nanoparticles hold promise as radiopharmaceuticals due to their modularity, flexibility, and high capacity for functionalization and loading with radionuclides. However, the toxicity of nanoparticles remains controversial and requires more investigation.
- Traits one should consider when deciding whether a nanoparticle will make a good platform for a radiopharmaceutical include the type of nanoparticle as well as its size, surface chemistry, and shape.
- The choice of radionuclide for labeling a nanoparticle depends on many factors, including the application (imaging or therapy) and the nanoparticle's pharmacokinetic profile.
- When radiolabeling a nanoparticle, the surface chemistry should be taken into account to determine the proper approach to radiolabeling and thus ensure sufficient radiochemical stability.
- After a radiolabeled nanoparticle has been synthesized, it needs to be properly evaluated both *in vitro* and *in vivo* to determine its stability, toxicity, and pharmacokinetic behavior.

References

1. Zhang L, Gu FX, Chan JM, Wang AZ, Langer RS, Farokhzad OC. Nanoparticles in medicine: therapeutic applications and developments. Clin Pharmacol Ther. 2008;83(5):761–9.
2. Bobo D, Robinson KJ, Islam J, Thurecht KJ, Corrie SR. Nanoparticle-based medicines: a review of FDA-approved materials and clinical trials to date. Pharm Res. 2016;33(10):2373–87.
3. Hu Q, Tuck C, Wildman R, Hague R. Application of nanoparticles in manufacturing. In: Aliofkhazraei M, editor. Handbook of nanoparticles. Cham: Springer International; 2015. p. 1–53.
4. Niemeyer CM. Nanoparticles, proteins, and nucleic acids: biotechnology meets materials science. Angew Chem Int Edit. 2001;40(22):4128–58.
5. Kabalan I, Lebeau B, Nouali H, Toufaily J, Hamieh T, Koubaissy B, et al. New generation of zeolite materials for environmental applications. J Phys Chem C. 2016;120(5):2688–97.
6. Patil SS, Shedbalkar UU, Truskewycz A, Chopade BA, Ball AS. Nanoparticles for environmental clean-up: a review of potential risks and emerging solutions. Environ Technol Innov. 2016;5:10–21.
7. Raimondi F, Scherer GG, Kötz R, Wokaun A. Nanoparticles in energy technology: examples from electrochemistry and catalysis. Angew Chem Int Ed Engl. 2005;44(15):2190–209.
8. Lai X, Halpert JE, Wang D. Recent advances in micro-/nano-structured hollow spheres for energy applications: from simple to complex systems. Energy Environ Sci. 2012;5(2):5604–18.

9. Darr JA, Zhang J, Makwana NM, Weng X. Continuous hydrothermal synthesis of inorganic nanoparticles: applications and future directions. Chem Rev. 2017;117(17):11125–38.
10. Miller L, Winter G, Baur B, Witulla B, Solbach C, Reske S, et al. Synthesis, characterization, and biodistribution of multiple 89Zr-labeled pore-expanded mesoporous silica nanoparticles for PET. Nanoscale. 2014;6(9):4928–35.
11. Ehlerding EB, Grodzinski P, Cai W, Liu CH. Big potential from small agents: nanoparticles for imaging-based companion diagnostics. ACS Nano. 2018;12(3):2106–21.
12. Pelaz B, Alexiou C, Alvarez-Puebla RA, Alves F, Andrews AM, Ashraf S, et al. Diverse applications of nanomedicine. ACS Nano. 2017;11(3):2313–81.
13. Shi J, Kantoff PW, Wooster R, Farokhzad OC. Cancer nanomedicine: progress, challenges and opportunities. Nat Rev Cancer. 2017;17(1):20–37.
14. Blanco E, Shen H, Ferrari M. Principles of nanoparticle design for overcoming biological barriers to drug delivery. Nat Biotechnol. 2015;33(9):941–51.
15. Kumar R, Roy I, Ohulchanskky TY, Vathy LA, Bergey EJ, Sajjad M, et al. In vivo biodistribution and clearance studies using multimodal organically modified silica nanoparticles. ACS Nano. 2010;4(2):699–708.
16. Hardonk MJ, Harms G, Koudstaal J. Zonal heterogeneity of rat hepatocytes in the in vivo uptake of 17 nm colloidal gold granules. Histochemistry. 1985;83(5):473–7.
17. Sadauskas E, Danscher G, Stoltenberg M, Vogel U, Larsen A, Wallin H. Protracted elimination of gold nanoparticles from mouse liver. Nanomedicine. 2009;5(2):162–9.
18. Gad SC, Sharp KL, Montgomery C, Payne JD, Goodrich GP. Evaluation of the toxicity of intravenous delivery of auroshell particles (gold-silica nanoshells). Int J Toxicol. 2012;31(6):584–94.
19. Behzadi S, Serpooshan V, Tao W, Hamaly MA, Alkawareek MY, Dreaden EC, et al. Cellular uptake of nanoparticles: journey inside the cell. Chem Soc Rev. 2017;46(14):4218–44.
20. Zhang S, Li J, Lykotrafitis G, Bao G, Suresh S. Size-dependent endocytosis of nanoparticles. Adv Mater. 2009;21:419–24.
21. Albanese A, Tang PS, Chan WC. The effect of nanoparticle size, shape, and surface chemistry on biological systems. Annu Rev Biomed Eng. 2012;14:1–16.
22. Kinnear C, Moore TL, Rodriguez-Lorenzo L, Rothen-Rutishauser B, Petri-Fink A. Form follows function: nanoparticle shape and its implications for nanomedicine. Chem Rev. 2017;117(17):11476–521.
23. Fish MB, Thompson AJ, Fromen CA, Eniola-Adefeso O. Emergence and utility of nonspherical particles in biomedicine. Ind Eng Chem Res. 2015;54(16):4043–59.
24. Weissleder R, Kelly K, Sun EY, Shtatland T, Josephson L. Cell-specific targeting of nanoparticles by multivalent attachment of small molecules. Nat Biotechnol. 2005;23(11):1418–23.
25. Yu M, Zheng J. Clearance pathways and tumor targeting of imaging nanoparticles. ACS Nano. 2015;9(7):6655–74.
26. Salatin S, Maleki Dizaj S, Yari Khosroushahi A. Effect of the surface modification, size, and shape on cellular uptake of nanoparticles. Cell Biol Int. 2015;39(8):881–90.
27. Fröhlich E. The role of surface charge in cellular uptake and cytotoxicity of medical nanoparticles. Int J Nanomedicine. 2012;7:5577–91.
28. Zhang X. Gold nanoparticles: recent advances in the biomedical applications. Cell Biochem Biophys. 2015;72(3):771–5.
29. Sperling RA, Rivera Gil P, Zhang F, Zanella M, Parak WJ. Biological applications of gold nanoparticles. Chem Soc Rev. 2008;37(9):1896–908.
30. Shah M, Badwaik VD, Dakshinamurthy R. Biological applications of gold nanoparticles. J Nanosci Nanotechnol. 2014;14(1):344–62.
31. Cai W, Gao T, Hong H, Sun J. Applications of gold nanoparticles in cancer nanotechnology. Nanotechnol Sci Appl. 2008;1:17–32.
32. Chen F, Goel S, Hernandez R, Graves SA, Shi S, Nickles RJ, et al. Dynamic positron emission tomography imaging of renal clearable gold nanoparticles. Small. 2016;12(20):2775–82.
33. Karmani L, Labar D, Valembois V, Bouchat V, Nagaswaran PG, Bol A, et al. Antibody-functionalized nanoparticles for imaging cancer: influence of conjugation to gold nanoparticles on the biodistribution of 89Zr-labeled cetuximab in mice. Contrast Media Mol Imaging. 2013;8(5):402–8.
34. Erathodiyil N, Ying JY. Functionalization of inorganic nanoparticles for bioimaging applications. Acc Chem Res. 2011;44(10):925–35.
35. Conde J, Dias JT, Grazu V, Moros M, Baptista PV, de la Fuente JM. Revisiting 30 years of biofunctionalization and surface chemistry of inorganic nanoparticles for nanomedicine. Front Chem. 2014;2:48.
36. Banerjee R, Katsenovich Y, Lagos L, McIintosh M, Zhang X, Li CZ. Nanomedicine: magnetic nanoparticles and their biomedical applications. Curr Med Chem. 2010;17(27):3120–41.
37. Amirfazli A. Nanomedicine: magnetic nanoparticles hit the target. Nat Nanotechnol. 2007;2(8):467–8.
38. Gupta AK, Naregalkar RR, Vaidya VD, Gupta M. Recent advances on surface engineering of magnetic iron oxide nanoparticles and their biomedical applications. Nanomedicine (Lond). 2007;2(1):23–39.
39. Tietze R, Alexiou C. Improving cancer imaging with magnetic nanoparticles: where are we now? Nanomedicine (Lond). 2017;12(3):167–70.
40. Shubayev VI, Pisanic TR 2nd, Jin S. Magnetic nanoparticles for theragnostics. Adv Drug Deliv Rev. 2009;61(6):467–77.
41. Zhu L, Zhou Z, Mao H, Yang L. Magnetic nanoparticles for precision oncology: theranostic magnetic iron oxide nanoparticles for image-guided and targeted cancer therapy. Nanomedicine (Lond). 2017;12(1):73–87.
42. Ai F, Ferreira CA, Chen F, Cai W. Engineering of radiolabeled iron oxide nanoparticles for dual-modality imaging. Wiley Interdiscip Rev Nanomed Nanobiotechnol. 2016;8(4):619–30.
43. Li C, Li L, Keates AC. Targeting cancer gene therapy with magnetic nanoparticles. Oncotarget. 2012;3(4):365–70.
44. Madru R, Kjellman P, Olsson F, Wingardh K, Ingvar C, Stahlberg F, et al. 99mTc-labeled superparamagnetic iron oxide nanoparticles for multimodality SPECT/MRI of sentinel lymph nodes. J Nucl Med. 2012;53(3):459–63.
45. Tang Y, Zhang C, Wang J, Lin X, Zhang L, Yang Y, et al. MRI/SPECT/fluorescent tri-modal probe for evaluating the homing and therapeutic efficacy of transplanted mesenchymal stem cells in a rat ischemic stroke model. Adv Funct Mater. 2015;25(7):1024–34.
46. Chen J, Zhu S, Tong L, Li J, Chen F, Han Y, et al. Superparamagnetic iron oxide nanoparticles mediated (131)I-hVEGF siRNA inhibits hepatocellular carcinoma tumor growth in nude mice. BMC Cancer. 2014;14:114.
47. Jarrett BR, Gustafsson B, Kukis DL, Louie AY. Synthesis of 64Cu-labeled magnetic nanoparticles for multimodal imaging. Bioconjug Chem. 2008;19(7):1496–504.
48. Yang X, Hong H, Grailer JJ, Rowland IJ, Javadi A, Hurley SA, et al. cRGD-functionalized, DOX-conjugated, and (6)(4)Cu-labeled superparamagnetic iron oxide nanoparticles for targeted anticancer drug delivery and PET/MR imaging. Biomaterials. 2011;32(17):4151–60.
49. Torres Martin de Rosales R, Tavaré R, Paul RL, Jauregui-Osoro M, Protti A, Glaria A, et al. Synthesis of 64cu(II)–bis(dithiocarbamatebisphosphonate) and its conjugation with superparamagnetic iron oxide nanoparticles: in vivo evaluation as dual-modality PET–MRI agent. Angew Chem Int Ed Engl. 2011;50(24):5509–13.

50. Devaraj NK, Keliher EJ, Thurber GM, Nahrendorf M, Weissleder R. 18F labeled nanoparticles for in vivo PET-CT imaging. Bioconjug Chem. 2009;20(2):397–401.
51. Boros E, Bowen AM, Josephson L, Vasdev N, Holland JP. Chelate-free metal ion binding and heat-induced radiolabeling of iron oxide nanoparticles. Chem Sci. 2015;6(1):225–36.
52. Chakravarty R, Valdovinos HF, Chen F, Lewis CM, Ellison PA, Luo H, et al. Intrinsically germanium-69-labeled iron oxide nanoparticles: synthesis and in-vivo dual-modality PET/MR imaging. Adv Mater. 2014;26(30):5119–23.
53. Chen F, Ellison PA, Lewis CM, Hong H, Zhang Y, Shi S, et al. Chelator-free synthesis of a dual-modality PET/MRI agent. Angew Chem Int Ed Engl. 2013;52(50):13319–23.
54. Chatterton N, Bretonniere Y, Pecaut J, Mazzanti M. An efficient design for the rigid assembly of four bidentate chromophores in water-stable highly luminescent lanthanide complexes. Angew Chem Int Ed Engl. 2005;44(46):7595–8.
55. Larson SM, Carrasquillo JA, Cheung NK, Press OW. Radioimmunotherapy of human tumours. Nat Rev Cancer. 2015;15(6):347–60.
56. Park JY, Chang Y, Lee GH. Multi-modal imaging and cancer therapy using lanthanide oxide nanoparticles: current status and perspectives. Curr Med Chem. 2015;22(5):569–81.
57. Yang Y, Sun Y, Liu Y, Peng JJ, Wu YQ, Zhang YJ, et al. Long-term in vivo biodistribution and toxicity of Gd(OH)(3) nanorods. Biomaterials. 2013;34(2):508–15.
58. Peng J, Sun Y, Zhao L, Wu Y, Feng W, Gao Y, et al. Polyphosphoric acid capping radioactive/upconverting NaLuF4:Yb,Tm,153Sm nanoparticles for blood pool imaging in vivo. Biomaterials. 2013;34(37):9535–44.
59. Yang Y, Sun Y, Cao TY, Peng JJ, Liu Y, Wu YQ, et al. Hydrothermal synthesis of NaLuF4:Sm-153,Yb,Tm nanoparticles and their application in dual-modality upconversion luminescence and SPECT bioimaging. Biomaterials. 2013;34(3):774–83.
60. Cao T, Yang Y, Sun Y, Wu Y, Gao Y, Feng W, et al. Biodistribution of sub-10 nm PEG-modified radioactive/upconversion nanoparticles. Biomaterials. 2013;34(29):7127–34.
61. Liu Y, Sun Y, Cao C, Yang Y, Wu Y, Ju D, et al. Long-term biodistribution in vivo and toxicity of radioactive/magnetic hydroxyapatite nanorods. Biomaterials. 2014;35(10):3348–55.
62. Cheng L, Shen S, Jiang D, Jin Q, Ellison PA, Ehlerding EB, et al. Chelator-free labeling of metal oxide nanostructures with zirconium-89 for positron emission tomography imaging. ACS Nano. 2017;11(12):12193–1220.
63. Vivero-Escoto JL, Huxford-Phillips RC, Lin W. Silica-based nanoprobes for biomedical imaging and theranostic applications. Chem Soc Rev. 2012;41(7):2673–85.
64. Phillips E, Penate-Medina O, Zanzonico PB, Carvajal RD, Mohan P, Ye Y, et al. Clinical translation of an ultrasmall inorganic optical-PET imaging nanoparticle probe. Sci Transl Med. 2014;6(260):260ra149.
65. Ma K, Mendoza C, Hanson M, Werner-Zwanziger U, Zwanziger J, Wiesner U. Control of ultrasmall sub-10 nm ligand-functionalized fluorescent core–shell silica nanoparticle growth in water. Chem Mater. 2015;27(11):4119–33.
66. Chen F, Ma K, Zhang L, Madajewski B, Zanzonico P, Sequeira S, et al. Target-or-clear zirconium-89 labeled silica nanoparticles for enhanced cancer-directed uptake in melanoma: a comparison of radiolabeling strategies. Chem Mater. 2017;29(19):8269–81.
67. Tang F, Li L, Chen D. Mesoporous silica nanoparticles: synthesis, biocompatibility and drug delivery. Adv Mater. 2012;24(12):1504–34.
68. Vallet-Regi M, Rámila A, del Real RP, Pérez-Pariente J. A new property of MCM-41: drug delivery system. Chem Mater. 2001;13(2):308–11.
69. Lee SB, Kim HL, Jeong H-J, Lim ST, Sohn M-H, Kim DW. Mesoporous silica nanoparticle pretargeting for pet imaging based on a rapid bioorthogonal reaction in a living body. Angew Chem Int Ed Engl. 2013;125(40):10743–6.
70. Chen F, Goel S, Valdovinos HF, Luo H, Hernandez R, Barnhart TE, et al. In vivo integrity and biological fate of chelator-free zirconium-89-labeled mesoporous silica nanoparticles. ACS Nano. 2015;9(8):7950–9.
71. Kroto HW, Heath JR, O'Brien SC, Curl RF, Smalley RE. C60: Buckminsterfullerene. Nature. 1985;318:162–3.
72. Iijima S. Helical microtubules of graphitic carbon. Nature. 1991;354:56–8.
73. Novoselov KS, Geim AK, Morozov SV, Jiang D, Zhang Y, Dubonos SV, et al. Electric field effect in atomically thin carbon films. Science. 2004;306(5696):666–9.
74. Xu X, Ray R, Gu Y, Ploehn HJ, Gearheart L, Raker K, et al. Electrophoretic analysis and purification of fluorescent single-walled carbon nanotube fragments. J Am Chem Soc. 2004;126(40):12736–7.
75. Baker SN, Baker GA. Luminescent carbon nanodots: emergent nanolights. Angew Chem Int Ed Engl. 2010;49(38):6726–44.
76. Mochalin VN, Shenderova O, Ho D, Gogotsi Y. The properties and applications of nanodiamonds. Nat Nanotechnol. 2012;7(1):11–23.
77. Hong G, Diao S, Antaris AL, Dai H. Carbon nanomaterials for biological imaging and nanomedicinal therapy. Chem Rev. 2015;115(19):10816–906.
78. Wang H, Wang J, Deng X, Sun H, Shi Z, Gu Z, et al. Biodistribution of carbon single-wall carbon nanotubes in mice. J Nanosci Nanotechnol. 2004;4(8):1019–24.
79. Singh R, Pantarotto D, Lacerda L, Pastorin G, Klumpp C, Prato M, et al. Tissue biodistribution and blood clearance rates of intravenously administered carbon nanotube radiotracers. Proc Natl Acad Sci U S A. 2006;103(9):3357–62.
80. Guo J, Zhang X, Li Q, Li W. Biodistribution of functionalized multiwall carbon nanotubes in mice. Nucl Med Biol. 2007;34(5):579–83.
81. Rong P, Yang K, Srivastan A, Kiesewetter DO, Yue X, Wang F, et al. Photosensitizer loaded nano-graphene for multimodality imaging guided tumor photodynamic therapy. Theranostics. 2014;4(3):229–39.
82. Yang K, Feng L, Hong H, Cai W, Liu Z. Preparation and functionalization of graphene nanocomposites for biomedical applications. Nat Protoc. 2013;8(12):2392–402.
83. Yang K, Feng L, Shi X, Liu Z. Nano-graphene in biomedicine: theranostic applications. Chem Soc Rev. 2013;42(2):530–47.
84. Chan WC, Maxwell DJ, Gao X, Bailey RE, Han M, Nie S. Luminescent quantum dots for multiplexed biological detection and imaging. Curr Opin Biotechnol. 2002;13(1):40–6.
85. Ghasemi Y, Peymani P, Afifi S. Quantum dot: magic nanoparticle for imaging, detection and targeting. Acta Biomed. 2009;80(2):156–65.
86. Bruchez M Jr, Moronne M, Gin P, Weiss S, Alivisatos AP. Semiconductor nanocrystals as fluorescent biological labels. Science. 1998;281(5385):2013–6.
87. Goel S, England CG, Chen F, Cai W. Positron emission tomography and nanotechnology: a dynamic duo for cancer theranostics. Adv Drug Deliv Rev. 2017;113:157–76.
88. Sun M, Hoffman D, Sundaresan G, Yang L, Lamichhane N, Zweit J. Synthesis and characterization of intrinsically radiolabeled quantum dots for bimodal detection. Am J Nucl Med Mol Imaging. 2012;2(2):122–35.
89. Sun X, Huang X, Guo J, Zhu W, Ding Y, Niu G, et al. Self-illuminating 64Cu-doped CdSe/ZnS nanocrystals for in vivo tumor imaging. J Am Chem Soc. 2014;136(5):1706–9.

90. Kennel SJ, Woodward JD, Rondinone AJ, Wall J, Huang Y, Mirzadeh S. The fate of MAb-targeted Cd125mTe/ZnS nanoparticles in vivo. Nucl Med Biol. 2008;35(4):501–14.
91. Cai W, Hong H. In a "nutshell": intrinsically radio-labeled quantum dots. Am J Nucl Med Mol Imaging. 2012;2(2):136–40.
92. Sharma VK, McDonald TJ, Sohn M, Anquandah GAK, Pettine M, Zboril R. Assessment of toxicity of selenium and cadmium selenium quantum dots: a review. Chemosphere. 2017;188:403–13.
93. Mo D, Hu L, Zeng G, Chen G, Wan J, Yu Z, et al. Cadmium-containing quantum dots: properties, applications, and toxicity. Appl Microbiol Biotechnol. 2017;101(7):2713–33.
94. Akbarzadeh A, Rezaei-Sadabady R, Davaran S, Joo SW, Zarghami N, Hanifehpour Y, et al. Liposome: classification, preparation, and applications. Nanoscale Res Lett. 2013;8(1):102.
95. van der Geest T, Laverman P, Metselaar JM, Storm G, Boerman OC. Radionuclide imaging of liposomal drug delivery. Expert Opin Drug Deliv. 2016;13(9):1231–42.
96. Jensen AI, Severin GW, Hansen AE, Fliedner FP, Eliasen R, Parhamifar L, et al. Remote-loading of liposomes with manganese-52 and in vivo evaluation of the stabilities of 52Mn-DOTA and 64Cu-DOTA using radiolabelled liposomes and PET imaging. J Control Release. 2018;269:100–9.
97. Khadka P, Ro J, Kim H, Kim I, Kim JT, Kim H, et al. Pharmaceutical particle technologies: an approach to improve drug solubility, dissolution and bioavailability. Asian J Pharm Sci. 2014;9(6):304–16.
98. Kalepu S, Nekkanti V. Insoluble drug delivery strategies: review of recent advances and business prospects. Acta Pharm Sin B. 2015;5(5):442–53.
99. Starmans LW, Hummelink MA, Rossin R, Kneepkens EC, Lamerichs R, Donato K, et al. (89) Zr- and fe-labeled polymeric micelles for dual modality pet and t1 -weighted mr imaging. Adv Healthc Mater. 2015;4(14):2137–45.
100. Jensen AI, Binderup T, Kumar Ek P, Kjær A, Rasmussen PH, Andresen TL. Positron emission tomography based analysis of long-circulating cross-linked triblock polymeric micelles in a u87mg mouse xenograft model and comparison of dota and cb-te2a as chelators of copper-64. Biomacromolecules. 2014;15(5):1625–33.
101. Xu L, Zhang H, Wu Y. Dendrimer advances for the central nervous system delivery of therapeutics. ACS Chem Neurosci. 2014;5(1):2–13.
102. Noriega-Luna B, Godnez LA, Rodriguez FJ, Rodriguez A, Zaldvar-Lelo de Larrea G, Sosa-Ferreyra CF, et al. Applications of dendrimers in drug delivery agents, diagnosis, therapy, and detection. J Nanomater. 2014;2014:19.
103. Rai AK, Tiwari R, Maurya P, Yadav P. Dendrimers: a potential carrier for targeted drug delivery system. Pharm Biol Eval. 2016;3(3):275–87.
104. Zhao L, Zhu M, Li Y, Xing Y, Zhao J. Radiolabeled dendrimers for nuclear medicine applications. Molecules. 2017;22(9):pii: E1350.
105. Sarko D, Eisenhut M, Haberkorn U, Mier W. Bifunctional chelators in the design and application of radiopharmaceuticals for oncological diseases. Curr Med Chem. 2012;19(17):2667–88.
106. Almutairi A, Rossin R, Shokeen M, Hagooly A, Ananth A, Capoccia B, et al. Biodegradable dendritic positron-emitting nanoprobes for the noninvasive imaging of angiogenesis. Proc Natl Acad Sci U S A. 2009;106(3):685–90.
107. McDonald DM, Choyke PL. Imaging of angiogenesis: from microscope to clinic. Nat Med. 2003;9(6):713–25.
108. Fang J, Nakamura H, Maeda H. The EPR effect: unique features of tumor blood vessels for drug delivery, factors involved, and limitations and augmentation of the effect. Adv Drug Deliv Rev. 2011;63(3):136–51.
109. Maeda H, Takeshita J, Kanamaru R. A lipophilic derivative of neocarzinostatin. A polymer conjugation of an antitumor protein antibiotic. Int J Pept Protein Res. 1979;14(2):81–7.
110. Maeda H, Matsumoto T, Konno T, Iwai K, Ueda M. Tailor-making of protein drugs by polymer conjugation for tumor targeting: a brief review on smancs. J Protein Chem. 1984;3(2):181–93.
111. Greish K. Enhanced permeability and retention (EPR) effect for anticancer nanomedicine drug targeting. Methods Mol Biol. 2010;624:25–37.
112. Hansen AE, Petersen AL, Henriksen JR, Boerresen B, Rasmussen P, Elema DR, et al. Positron emission tomography based elucidation of the enhanced permeability and retention effect in dogs with cancer using copper-64 liposomes. ACS Nano. 2015;9(7):6985–95.
113. Hong H, Zhang Y, Sun J, Cai W. Molecular imaging and therapy of cancer with radiolabeled nanoparticles. Nano Today. 2009;4(5):399–413.
114. Ngoune R, Peters A, von Elverfeldt D, Winkler K, Pütz G. Accumulating nanoparticles by EPR: a route of no return. J Control Release. 2016;238:58–70.
115. Byrne JD, Betancourt T, Brannon-Peppas L. Active targeting schemes for nanoparticle systems in cancer therapeutics. Adv Drug Deliv Rev. 2008;60(15):1615–26.
116. Bertrand N, Wu J, Xu X, Kamaly N, Farokhzad OC. Cancer nanotechnology: the impact of passive and active targeting in the era of modern cancer biology(). Adv Drug Deliv Rev. 2014;66:2–25.
117. Chen F, Hong H, Zhang Y, Valdovinos HF, Shi S, Kwon GS, et al. In vivo tumor targeting and image-guided drug delivery with antibody-conjugated, radiolabeled mesoporous silica nanoparticles. ACS Nano. 2013;7(10):9027–39.
118. Matter A. Tumor angiogenesis as a therapeutic target. Drug Discov Today. 2001;6(19):1005–24.
119. Cai W, Chen K, Li ZB, Gambhir SS, Chen X. Dual-function probe for PET and near-infrared fluorescence imaging of tumor vasculature. J Nucl Med. 2007;48(11):1862–70.
120. Liu Z, Cai W, He L, Nakayama N, Chen K, Sun X, et al. In vivo biodistribution and highly efficient tumour targeting of carbon nanotubes in mice. Nat Nanotechnol. 2007;2(1):47–52.
121. Yang S, Gao H. Nanoparticles for modulating tumor microenvironment to improve drug delivery and tumor therapy. Pharmacol Res. 2017;126(Suppl C):97–108.
122. Miao L, Huang L. Exploring the tumor microenvironment with nanoparticles. Cancer Treat Res. 2015;166:193–226.
123. Chen B, Dai W, He B, Zhang H, Wang X, Wang Y, et al. Current multistage drug delivery systems based on the tumor microenvironment. Theranostics. 2017;7(3):538–58.
124. Feng L, Dong Z, Tao D, Zhang Y, Liu Z. The acidic tumor microenvironment: a target for smart cancer nano-theranostics. Natl Sci Rev. 2018;5(2):269–86.
125. Gao H, Liu X, Tang W, Niu D, Zhou B, Zhang H, et al. 99mTc-conjugated manganese-based mesoporous silica nanoparticles for SPECT, pH-responsive MRI and anti-cancer drug delivery. Nanoscale. 2016;8(47):19573–80.
126. Palner M, Shen B, Jeon J, Lin J, Chin FT, Rao J. Preclinical kinetic analysis of the caspase-3/7 PET tracer 18F-C-SNAT: quantifying the changes in blood flow and tumor retention after chemotherapy. J Nucl Med. 2015;56(9):1415–21.
127. Perez-Campana C, Gomez-Vallejo V, Martin A, San Sebastian E, Moya SE, Reese T, et al. Tracing nanoparticles in vivo: a new general synthesis of positron emitting metal oxide nanoparticles by proton beam activation. Analyst. 2012;137(21):4902–6.
128. Wang L, Zhao Z, Meyer MB, Saha S, Yu M, Guo A, et al. CARM1 methylates chromatin remodeling factor BAF155 to enhance tumor progression and metastasis. Cancer Cell. 2014;25(1):21–36.

129. Burke BP, Clemente GS, Archibald SJ. Recent advances in chelator design and labelling methodology for 68Ga radiopharmaceuticals. J Labelled Comp Radiopharm. 2014;57(4):239–43.
130. Deri MA, Zeglis BM, Francesconi LC, Lewis JS. PET imaging with (89)Zr: from radiochemistry to the clinic. Nucl Med Biol. 2013;40(1):3–14.
131. Goel S, Chen F, Ehlerding EB, Cai W. Intrinsically radiolabeled nanoparticles: an emerging paradigm. Small. 2014;10(19):3825–30.
132. Beberwyck BJ, Surendranath Y, Alivisatos AP. Cation exchange: a versatile tool for nanomaterials synthesis. J Phys Chem C. 2013;117(39):19759–70.
133. Goel S, Chen F, Luan S, Valdovinos HF, Shi S, Graves SA, et al. Engineering intrinsically Zirconium-89 radiolabeled self-destructing mesoporous silica nanostructures for in vivo biodistribution and tumor targeting studies. Adv Sci (Weinh). 2016;3(11):1600122.
134. Gottstein C, Wu G, Wong BJ, Zasadzinski JA. Precise quantification of nanoparticle internalization. ACS Nano. 2013;7(6):4933–45.
135. Gonzalez-Rodriguez D, Barakat AI. Dynamics of receptor-mediated nanoparticle internalization into endothelial cells. PLoS One. 2015;10(4):e0122097.
136. Almutary A, Sanderson BJS. The MTT and crystal violet assays: potential confounders in nanoparticle toxicity testing. Int J Toxicol. 2016;35(4):454–62.
137. Mortelmans K, Zeiger E. The Ames Salmonella/microsome mutagenicity assay. Mutat Res. 2000;455(1–2):29–60.
138. Edmondson R, Broglie JJ, Adcock AF, Yang L. Three-dimensional cell culture systems and their applications in drug discovery and cell-based biosensors. Assay Drug Dev Technol. 2014;12(4):207–18.
139. Zamboni WC, Torchilin V, Patri AK, Hrkach J, Stern S, Lee R, et al. Best practices in cancer nanotechnology: Perspective from NCI Nanotechnology Alliance. Clin Cancer Res. 2012;18:3229–41.
140. Ehlerding EB, Chen F, Cai W. Biodegradable and renal clearable inorganic nanoparticles. Adv Sci (Weinh). 2016;3(2):pii: 1500223.
141. Dobrovolskaia MA. Pre-clinical immunotoxicity studies of nanotechnology-formulated drugs: challenges, considerations and strategy. J Control Release. 2015;220(Pt B):571–83.
142. Wolfram J, Zhu M, Yang Y, Shen J, Gentile E, Paolino D, et al. Safety of nanoparticles in medicine. Curr Drug Targets. 2015;16(14):1671–81.
143. Prabhakar U, Maeda H, Jain RK, Sevick-Muraca EM, Zamboni W, Farokhzad OC, et al. Challenges and key considerations of the enhanced permeability and retention (EPR) effect for nanomedicine drug delivery in oncology. Cancer Res. 2013;73(8):2412–7.

Part II

Radiochemistry

The Radiopharmaceutical Chemistry of Carbon-11: Basic Principles

Gunnar Antoni

Historic View on Carbon-11 Chemistry

Carbon-11 was produced for the first time in 1934 by Crane and Lauritsen. It was the first available radioisotope of carbon and thus particularly suitable for biological research [1]. They found that this new radionuclide of carbon had a short half-life of only 20.4 min and decayed via 99.81% positron emission and 0.19% electron capture to the stable nuclide boron-11. One of the principal reasons for the interest in carbon-11 stems from the fact that carbon, oxygen, hydrogen, sulfur, phosphorus, and nitrogen are the "atoms of life": these six basic elements build up the organic molecules that constitute all living organisms. This means that radiolabeling a molecule with carbon-11 will produce a compound that is indistinguishable from its natural stable counterpart and can thus be used as a true "tracer" to investigate biological processes without influencing their rate or outcome to any measurable extent. In light of this, carbon-11 immediately attracted the interest of researchers in the field of biology. Another important aspect was that the cyclotron-produced radionuclide could be retrieved as [^{11}C]carbon dioxide, which is easily isolated and can be transformed into more complex biomolecules using relatively simple technical equipment compatible with the handling of large amounts of radioactivity. Just 5 years after its initial discovery, Ruben *et al.* used [^{11}C]carbon dioxide for the study of photosynthesis in plants [2]. Although radiation detector technology at that time was far away from today's standard equipment, these instruments were sufficiently sophisticated to allow for measurements in living organisms. In 1945, the first human study was performed by Tobias *et al.,* who investigated the fixation of [^{11}C] carbon monoxide by red blood cells in humans [3].

Over time, the inaccessibility of particle accelerators and laboratories with equipment for work with short-lived radionuclides—as well as problems encountered in performing quantitative measurements of radioactivity within a living subject—led to a halt in the use of carbon-11 in biological research. However, some researchers continued the work, and in 1966, two of the pioneers in PET research, Michael Ter-Pergossian and Henry Wagner, published an article entitled, "*A New Look at the Cyclotron for Producing Short-Lived Radionuclides.*" They showed how practical amounts of carbon-11, nitrogen-13, oxygen-15, and fluorine-18 could be produced using a cyclotron and claimed that the short half-lives of these radionuclides were not an insurmountable obstacle to their use in living organisms [4].

After the Second World War, the long-lived radionuclide carbon-14 ($t_{1/2}$ = 5730 y) became available, thus creating new opportunities for biological research and providing easy access to versatile tools for biological studies. However, the drawback of carbon-14 is that the β-particle emitted is not energetic enough to penetrate tissue and is also difficult to detect, traits which limited the use of carbon-14 to *in vitro* and *ex vivo* studies. Therefore, many researchers continued to look for radionuclides that could be used to determine the time-resolved spatial distribution of a radiolabeled compound within a living organism. Carbon-11 thus fulfilled these expectations. Medical research with carbon-11 and fluorine-18 therefore commenced during the 1960s. Meanwhile, technical progress was well on its way to facilitating *in vivo* research with compounds labeled with positron emitting radiocnuclides. In the 1950s, David E. Kuhl and coworkers at Pennsylvania University introduced the concept of emission and transmission, which led to the construction of the first tomographic instruments. This technique was further developed in the beginning of the 1970s by Michael E. Phelps and Michael Ter-Pergossian at Washington University in St. Louis, Missouri, USA.

As we move along in this historical review, it is important to mention two groundbreaking radiochemical developments related to carbon-11. The first is the publication of practical methods for the production of useful amounts of high molar activity [^{11}C]carbon dioxide, [^{11}C]carbon monoxide, ammonium [^{11}C]cyanide, and [^{11}C]methane by Christman in 1975.

G. Antoni (✉)
PET Centre, Uppsala University Hospital, Uppsala, Sweden
e-mail: gunnar.antoni@akademiska.se

J. S. Lewis et al. (eds.), *Radiopharmaceutical Chemistry*, https://doi.org/10.1007/978-3-319-98947-1_11

The second is the synthesis of [^{11}C]methyl iodide, which was performed independently and roughly contemporaneously in 1976 by Långström in Uppsala and Comar in Orsay [5, 6]. The easy access to simple precursors such as [^{11}C]carbon dioxide and ammonium [^{11}C]cyanide opened the doors for labeling several classes of organic compounds, including carboxylic acids, alcohols, nitriles, and amines. However, the availability of [^{11}C]methyl iodide provided even greater opportunities and started the era of receptor-ligand studies with PET. Starting in the 1980s, brain receptor studies have been a large part of PET research and have had a significant impact on our knowledge of how the brain functions and interacts with drugs. In this context, the importance of [^{11}C]methyl iodide cannot be overestimated.

The development of methods for ^{11}C-based radiosynthesis is a field of research that continues to grow, but we should acknowledge that it builds upon inventions dating 50 years back in time. Indeed, since these pioneering innovations, the literature surrounding carbon-11 has increased substantially. These methods will be covered in this chapter as well as Chap. 12. Without a doubt, the development of novel approaches to radiochemistry—and radiochemistry with carbon-11 in particular—has been among the most important driving forces in the emergence of PET as a standard clinical modality that benefits individual patients as well as the healthcare system in general.

This chapter is not intended to provide a fully comprehensive review of carbon-11 chemistry. Rather, it is our hope that this chapter can give the reader a grasp of the essence and overall principles governing radiochemistry with carbon-11. Along these lines, detailed descriptions of syntheses are outside the scope of this chapter, but the reader is encouraged to consult the primary literature and reviews for further information [7–9].

General Aspects of Carbon-11 in Imaging and Labeling Synthesis

Decay Characteristics of Carbon-11

There is no such thing as the perfect radionuclide for PET. Characteristics such as the physical half-life, the fraction of β^+ emission decay, and the maximum positron energy of a radionuclide determine its usefulness for imaging qualities, while the chemistry of the element determines the synthetic methodologies that can be used during its incorporation into biomolecules. From an imaging point of view, the lower the β^+ energy and the higher the fraction of β^+ emission, the better. The positrons emitted from carbon-11 have a maximum energy of 0.960 MeV, and they traverse about 4.3 mm in soft tissue before their annihilation. In comparison, the positrons emitted by fluorine-18 decay have a maximum energy of 0.634 MeV and a range of about 2.4 mm in tissue. However, since the median energy of the positrons is around 1/3 of the maximum energy, the mean range of the positrons from carbon-11 and fluorine-18 is about 1.2 mm and 0.6 mm, respectively. In practice, the difference in resolution provided by carbon-11 and fluorine-18 is of minor clinical importance.

When it comes to the half-life, things become more complicated for carbon-11. Now, we must consider several things, such as time required for the synthesis of the tracer, the biological half-life of the process to be studied, and the logistics of the transport and delivery of the compound. As a rule of thumb, the production time for a PET tracer including quality control and delivery to the clinical PET facility should not exceed three half-lives. For carbon-11, this is about 60 min. Not surprisingly, this limits the choice of synthesis methods that can be used for carbon-11, but the currently available arsenal of labeling reactions and quality control methods effectively circumvents these restrictions and allows for a broad range of synthesis schemes. For example, the chemoenzymatic syntheses of aromatic amino acids—as shown in (Fig. 1)—require a total of seven different chemical transformations followed by workup, HPLC purification, formulation, sterile filtration, and quality control. This is all accomplished within a total production time of about 55 min [10].

Briefly, racemic [^{11}C]alanine—labeled either in the carboxylic- or 3-position—is synthesized from [^{11}C]cyanide or [^{11}C]methyl iodide, respectively. In a one-pot multienzymatic synthesis, [^{11}C]pyruvate is formed as an intermediate which can be further transformed into a range of aromatic amino acids. Indeed, this approach provides access to enantiomerically pure L-tyrosine, L-DOPA, L-tryptophan, and 5-hydroxy-L-tryptophan labeled with carbon-11 either in the carboxylic- or β-positions. Of special interests are the

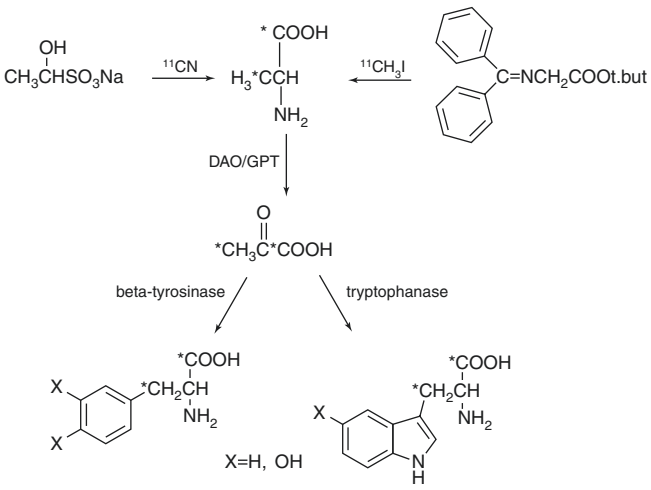

Fig. 1 Chemoenzymatic synthesis of aromatic amino acids

two neurotransmitter precursors—L-DOPA and 5-hydroxy-L-tryptophan—which are enzymatically transformed *in vivo* to dopamine and serotonin, respectively. Analogues of tryptophan and DOPA such as 6-fluoro-L-[^{11}C]DOPA and 5-fluoro-L-[^{11}C]tryptophan are also available through the same synthetic procedure. It is thus clear that although carbon-11 has a short half-life, it is possible to perform complicated multistep syntheses and produce sufficient amounts of radiotracers for routine clinical applications. It is also important to note that carbon-11 is especially well suited for the labeling of endogenous compounds, as exemplified in Scheme 1.

Another important aspect of the production of radiotracers is the option to distribute the compounds to nearby medical centers that do not have production capabilities. Generally speaking, the half-life carbon-11 is too short for this. However, it should be mentioned that carbon-11 has been transported from a laboratory at Uppsala University to the PET clinic at Karolinska Hospital, Stockholm, a distance of 70 kilometers. This is certainly not routinely applicable, but it is nonetheless important in the context of showing what is possible.

Apart from the production of radiotracers, we also need to consider logistical concerns that can arise in routine clinical situations. Several clinically used carbon-11 PET tracers—for example, L-[*methyl*-^{11}C]methionine and [1-^{11}C]acetate—can be produced in rather large quantities, and one batch is typically sufficient for several patients. Furthermore, there is a growing understanding that a multi-tracer protocol may have value for diagnostic settings. A very good example of this is the diagnosis of neurodegenerative disorders such as Alzheimer's disease (AD) and other dementias for which the clinical differential diagnosis is both important and difficult. A multi-tracer PET investigation showing a decrease in the glucose consumption by the brain (as measured with [^{18}F]fluorodeoxyglucose) as well as the high uptake of a β-amyloid tracer (such as [^{11}C]PIB) is indicative of AD. This highly synergistic information can guide clinicians in the diagnosis of which type of dementia the patient is suffering from. In a multi-tracer PET protocol, the two PET investigations should preferably be performed on the same day, which is possible using two ^{11}C-labeled tracers or by combining one ^{11}C- and one ^{18}F-labeled compound.

We should also consider the radiation dose to the subject. As a rule of thumb, the radiation dose from ^{11}C-labeled radiotracers is about 0.4 mSv/100 MBq. The general guideline for radiation dose to healthy controls sets a limit of 10 mSv. Although higher doses can be accepted, the risks of ionizing radiation should always be considered, and it is especially important to minimize radiation doses during PET investigations in children. In conclusion, the half-life of carbon-11 is sufficiently long for multistep synthesis and sufficiently short enough to allow patients to be scanned with several tracers on the same day with favorable dosimetry.

Tracer Principle and Molar Activity

Positron emission tomography is based on the "tracer principle" as defined by 1943 Nobel laureate George de Hevesy and which can be expressed as follows: *A tracer is a compound or an atom that can be used to study or follow a process in a living system without to any measurable extent influence the rate or outcome of the studied process.* To perform true tracer studies, the amount of a radiotracer administered must be very small in mass but high in radioactivity. Thus, the quotient radioactivity/mass defined as specific activity (A_s) in Bq/g should be high. In PET, molar activity (A_M) in units of GBq/μmol is generally more useful and preferred. The theoretical maximum molar activity of carbon-11 is 3.4×10^5 GBq/μmol, but in practice, due to isotopic dilution, most reported carbon-11 PET tracers are in the range of 50–200 GBq/μmol, though values as high as 2000 GBq/μmol can be found in the literature.

Isotopic Dilution and Molar Activity

Why can't the theoretical molar activity of carbon-11 be reached in practice [11]?

A typical carbon-11 PET tracer has a carbon-12 to carbon-11 ratio of around 10,000 to 1. Basically, most of the product obtained consists of stable material. This means that the molar activity decreases with time due to the decay of carbon-11. Consequently, if the theoretical molar activity could be achieved, the molar activity would not be time dependent. The explanation is straightforward: if all atoms are carbon-11, the ratio of radioactivity/mass is constant with time, since the mass of carbon and the amount of radioactivity decrease at the same rate. However, with a starting ^{12}C/^{11}C ratio of 10,000/1, the decay results in a time-dependent decrease in the amount of radioactivity but does not result in any measurable change in mass. Since carrier-free carbon-11 cannot be obtained, time becomes an important parameter in the context of molar activity.

It is practically impossible to avoid the isotopic dilution of carbon-11 with stable isotopes of carbon that have been introduced to the target at the time of production or during the post-processing of [^{11}C]carbon dioxide. The irradiation of the target gas with accelerated protons produces a plasma in which all carbon-containing molecules are stripped down to "naked" carbon atoms and free electrons and converted to the primary precursor formed in the target—[^{11}C]carbon dioxide or [^{11}C]methane—by reaction with oxygen or hydrogen, respectively. The isotopic dilution emanating from

radionuclide production is more or less constant in a well-functioning target system, and it is difficult to reduce this any further. The quality of the target gas mixture (N_2/O_2 or N_2/H_2) is thus essential. The main contribution to the isotopic dilution comes from the target, and during post-processing, [^{11}C]carbon dioxide is further subjected to isotopic dilution due to the presence of atmospheric carbon dioxide in the synthesis equipment, process gases, and reagents. In this sense, [^{11}C]methane is the perfect precursor, since methane is not found in the atmosphere or in any of the reagents used. When the secondary precursor or the product has been obtained, the risk of isotopic dilution is typically nonexistent, and therefore, from this point on, time is the only cause of further decreases in molar activity. In summary, the choice of primary precursor, the reaction pathway, and the quality of reagents all introduce higher degrees of variation in isotopic dilution compared to the production of the radionuclide. Therefore, it is important for the radiochemist to consider each of these variables. For instance, chemicals such as Grignard reagents and lithium aluminum hydride are usually contaminated with atmospheric carbon dioxide which will decrease molar activity.

Stoichiometric Aspects of High Molar Activity

High molar activity has implications for radiochemistry. As a result, the pros and cons associated with it as well as examples of how it influences the synthesis of PET tracers need attention. High molar activity of the precursor is mainly an advantage, but in some cases, it can be a disadvantage. The amount of carbon—in the form of CO_2 or CH_4—produced in the target is in the range of 1–50 nmol, and this low amount changes the stoichiometric relationships as compared to standard organic chemistry. This can easily be understood by considering that the ratio between the total mass of a ^{11}C-labeled precursor (carbon-12 and carbon-11) and the precursor for labeling typically is in the order of 1/100. With such a ratio between the reaction components, a bimolecular reaction that normally follows second-order kinetics can be better described by pseudo-first-order kinetics (Fig. 2).

In such a situation, the concentration of the reagent in excess (B in this case) is practically constant during the course of the reaction, and the rate of conversion of labeled precursor A to labeled product C can thus be significantly increased by a 100-fold excess of B. Consequently, many reactions can be completed with high conversion of the carbon-11 precursor to product within a few minutes' time. This stoichiometric relationship may also influence the outcome of the reaction with respect to the ratio between the product and side products. The methylation of an amine with [^{11}C]methyl iodide is an informative example of this phenomenon. In almost any organic chemistry textbook, it is stated that the methylation of a primary amine with methyl iodide will lead to a complex mixture of mono-, di-, and trimethylated products, as the nucleophilicity of the amine increases in the following order: R-NH_2 < RR′-NH < RR′R″-N. In practice, with [^{11}C]methyl iodide and a ratio of R-NH_2/CH_3I > 100, only the monomethylated product is formed. Consequently, access to high molar activity [^{11}C]methyl iodide revolutionized PET radiochemistry because it allows for this ideal stoichiometry during the ^{11}C-methylation of amines.

There are of course exceptions to the positive effect of the low amount of the carbon-11 precursor. One example is the synthesis of [1-^{11}C]acetate via the Grignard reaction between methylmagnesium bromide and [^{11}C]carbon dioxide. In this particular case, the stoichiometry with a large excess of the Grignard reagent over carbon dioxide is a disadvantage, and [^{11}C]carbon dioxide can react with one, two, or three equivalents of methylmagnesium bromide to form [^{11}C]acetate, [^{11}C]acetone, and [^{11}C]tertiary butanol, respectively. There is a critical balance between optimizing the radiochemical yield of [^{11}C]acetate and simultaneously avoiding either large amounts of unreacted [^{11}C]carbon dioxide or the formation of the side products. There are, however, several useful methods for overcoming this problem and optimizing the radiochemical yield of [1-^{11}C]acetate. Another example of how stoichiometry changes the distribution of products in radiochemistry lies in the synthesis of [4-^{11}C]gamma-aminobutyric acid. In this case, the direct translation of an organic synthetic method to radiochemistry conditions was not possible. An intermediate nitrile was required which could be produced by a simple nucleophilic substitution reaction on an alkyl bromide with excess potassium cyanide as shown in Fig. 3.

When translating this approach to carbon-11 reaction conditions with excess alkyl bromide, no product was

$$A + B \longrightarrow C \qquad r = k[A][B]$$

with [A] and [B] denoting the concentration of carbon-11 precursor and precursor for labelling, respectively, the equation reduces to

$$r = k'[A]$$

where $k' = k[B]$

Fig. 2 Pseudo-first-order kinetics approximation

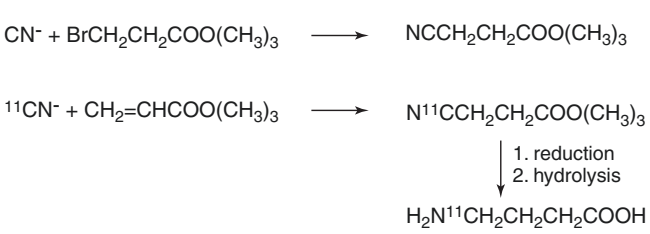

Fig. 3 Synthesis of [4-^{11}C]GABA

obtained, and only unreacted [^{11}C]cyanide was found in the reaction mixture. As an alternative, a Michael addition reaction with [^{11}C]cyanide was investigated which produced the carbon-11-labeled nitrile in high radiochemical yield. [4-^{11}C] gamma-aminobutyric acid was then subsequently obtained after the selective reduction of the nitrile with cobalt boride/sodium borohydride to the corresponding primary amine and then the alkaline hydrolysis of the ester protecting group. From this, we can speculate that the mechanism of the reaction between cyanide and the alkyl bromide is probably not a simple nucleophilic substitution reaction. The results suggest that cyanide first acts as a base and abstracts a proton, leading to the elimination of bromide and the formation of the unsaturated ester which then undergoes a Michael addition with cyanide. With an alkyl bromide/CN ratio of 100/1, the concentration of the intermediate unsaturated precursor is very low (in the same range as cyanide), and the rate of the Michael addition becomes extremely slow. Furthermore, the reactive cyanide anion is converted to unreactive hydrogen cyanide. Such a mechanism requires an excess of cyanide over alkyl bromide, which is not the case with [^{11}C]cyanide. Therefore, no product is obtained.

In this context, other complicating factors must also be considered when working with nanomolar amounts of the radiolabeled reagent. Occasionally, the radiochemist will encounter reactions that are unexpectedly slow or do not give any product without any reasonable explanation. In this event, it cannot be ruled out that the presence of small amounts of impurities in any of the reagents or solvents—amounts that would not affect the reaction under normal stoichiometric conditions—might be inhibiting the reaction or resulting in the formation of side products. This phenomenon can be investigated by adding small amount of unlabeled precursor to the reaction mixture. It is important to note, however, that this approach necessarily reduces the molar activity of the final product and is therefore not useful as a solution to this problem in and of itself. Importantly, the direct translation of traditional synthetic reaction conditions to radiochemistry is not always possible, and carbon-11 syntheses usually require their own optimizations. It is therefore recommended to investigate new ^{11}C-based syntheses directly with radioactive material instead of performing optimizations with unlabeled material. As stated above, the subsequent translation to the radiochemical scale can produce unwanted surprises!

Carbon-11 Precursors for Labeling

Production of Carbon-11

Today, carbon-11 is exclusively produced using the ^{14}N(p,α)^{11}C reaction via the bombardment of nitrogen gas containing trace or small amounts of either oxygen or hydrogen with 8–17 MeV protons. The only expected radionuclidic impurity formed in the target gas during the bombardment is nitrogen-13, created via the ^{16}O(p,α)^{13}N nuclear reaction. In practice, carbon-11 is obtained in very high radionuclidic purity due to the high concentration of nitrogen and low amounts of oxygen-16 in the target gas. This high purity is also fueled by the low cross section of the ^{16}O(p,α)^{13}N reaction compared to that of the ^{14}N(p,α)^{11}C transformation as well as the simple online process for the separation of the ^{11}C-bearing precursor from any ^{13}N-containing products.

In-Target-Produced Primary Precursors

By definition, precursors that are produced within the target (*i.e.* "in target") are denoted *primary precursors*, while those that are obtained during the subsequent processing of the target are called *secondary precursors*. Importantly, neither of these should be confused with the *precursor for labeling*, the molecule to be labeled with the radioactive precursor to produce the final radiotracer.

The ^{14}N(p,α)^{11}C reaction using gas mixtures of either N_2/O_2 or N_2/H_2 produces [^{11}C]carbon dioxide or [^{11}C]methane, respectively, as the primary precursors. Other primary precursors such as [^{11}C]carbon monoxide and ammonium[^{11}C] cyanide can be produced in the target by adjusting the relative concentrations of oxygen and hydrogen or the beam current. However, the yields for these synthons are not very high, and thus post-processing synthetic routes to these precursors are typically preferred. Even [^{11}C]methyl iodide can be produced directly in the target, but that approach has proven to be more of a scientific curiosity than of any practical use.

Secondary Precursors

It is truly important to have several methods available for radiolabeling molecules with carbon-11. Thankfully, there are a large number of secondary precursors available from [^{11}C]carbon dioxide and [^{11}C]methane, with the former being the most important starting material for more complex reactive molecules. Unlike [^{11}C]methane, [^{11}C]carbon dioxide can be used directly to produce PET tracers such as [^{11}C] acetate and [^{11}C]palmitate. In addition, a number of useful building blocks can be obtained through on-line or one-pot syntheses starting with [^{11}C]carbon dioxide. For example, Fig. 4 illustrates several secondary precursors the can be obtained from [^{11}C]carbon dioxide.

[^{11}C]Methyl iodide is by far the most often employed ^{11}C-labeled secondary precursor, and there are two methods for the production of this very important synthon (Fig. 5).

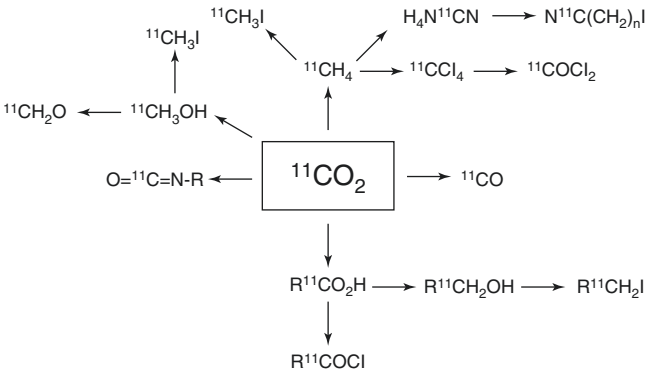

Fig. 4 Synthesis of secondary precursors from [^{11}C]carbon dioxide

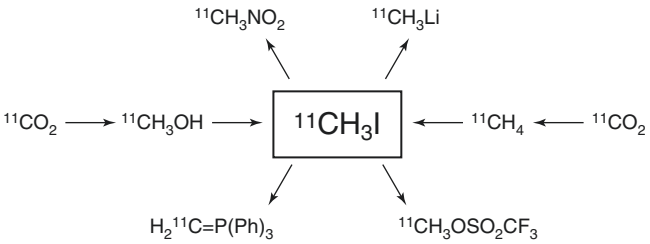

Fig. 5 Synthesis [^{11}C]methyl iodide and derivatives thereof

The classical "wet-chemistry method" from the 1970s is predicated on the reduction of [^{11}C]carbon dioxide to [^{11}C]methanol. The subsequent treatment of the latter with hydroiodic acid provides [^{11}C]methyl iodide in very high radiochemical yield in a short synthesis time. The drawback of this method is the isotopic dilution arising from lithium aluminum hydride contaminated with CO_2. In contrast, the "gas-phase method" provides very high molar activity, but the radiochemical yield of this approach is lower, and it requires a longer synthesis time. In addition, [^{11}C]methyl iodide can also be transformed into the more reactive [^{11}C]methyl triflate—which in some reactions is superior to methyl iodide—in a subsequent online process. Another transformation that can widen the range of synthetic options is reacting [^{11}C]methyl iodide with a lithium base (*e.g.* BuLi) to obtain the nucleophilic methylating agent [^{11}C]methyl lithium.

Shifting gears a bit, alkyl and aryl halides have been used as electrophilic reagents, primarily for the production of ^{11}C-amino acids. Alkyl groups are found in many drugs, and the possibility of producing libraries of alkylated analogues of a tracer of interest using ^{11}C-labeled methyl, ethyl, propyl, isopropyl, butyl, or benzyl halides remains an underdeveloped area of study. Other important secondary ^{11}C-labeled precursors include [^{11}C]CO, [^{11}C]CN, $^{11}CH_3NO_2$, [^{11}C]CH_2O, and [^{11}C]$COCl_2$. There are surprisingly few examples of the use of [^{11}C]formaldehyde, most likely due to the lack of a simple and reliable method for the production of this useful reagent. Indeed, several methods (all with significant flaws) have been developed over the years, but a recently developed improved method—shown in Fig. 6—may lead to renewed interest in [^{11}C]CH_2O as a precursor.

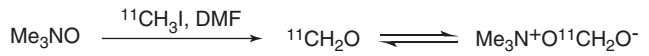

Fig. 6 Synthesis of [^{11}C]formaldehyde

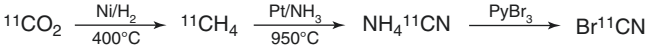

Fig. 7 Synthesis of [^{11}C]cyanide and [^{11}C]cyanogen bromide

Ammonium [^{11}C]cyanide is of special interest, both because the nitrile is an interesting functional group in its own right and due to the possibility of transforming nitriles into amines, amides, or carboxylic acids. The production method of choice for [^{11}C]cyanide is an online post-target process as presented in Fig. 7.

[^{11}C]Cyanide is obtained from [^{11}C]carbon dioxide via the reduction of the latter with H_2/Ni to create [^{11}C]CH_4, followed by a platinum-catalyzed reaction with ammonia. This process usually yields the product in high molar activity and moderate to high radiochemical yield. [^{11}C]Cyanide has also been used to produce what could be called "tertiary precursors," halonitriles of different chain lengths that can be used as alkylating agents. A special feature of [^{11}C]cyanide is that through *umpolung*, it can be transformed from a nucleophile to the electrophilic reagent cyanogen bromide. This possibility further enriches the broad palette of synthetic options for [^{11}C]cyanide. For example, [^{11}C]cyanogen bromide gives access to guanidine-like structures via its reaction with amines, and it can also be used for the unspecific "tagging" of biomolecules.

Moving on, carbonyls are present in many biomolecules and drugs and are therefore an interesting and suitable position for radiolabeling. [^{11}C]Phosgene has been used to label carbonyls, but its production is laborious, the necessary equipment requires demanding maintenance, and the subsequent radiochemistry is problematic due to the high reactivity of [^{11}C]$COCl_2$. [^{11}C]CO is another highly versatile precursor available via the catalytic reduction of [^{11}C]CO_2 either by zinc or molybdenum at high temperatures [12]. Recently, an alternative method for the one-pot conversion of [^{11}C]carbon dioxide to [^{11}C]carbon monoxide using a silacarboxylic acid as the reducing agent has been presented. [^{11}C]Carbon monoxide is a useful building block for the ^{11}C-labeling of carbonyls, a topic which will be discussed in greater detail below.

A final—yet seldom used—class of precursors is ^{11}C-nitroalkanes (*e.g.* [^{11}C]nitromethane). ^{11}C-Labeled nitroalkanes are useful reagents and can either undergo condensation or nucleophilic substitution reactions. As we wrap up this section, we would like to remind the reader that there are indeed a number of other secondary precursors that we have not mentioned. After all, this is not intended to be a comprehensive review of all available carbon-11 precursors. If interested, the reader should consult the primary literature for more detailed and comprehensive information.

Labeling Strategies with Carbon-11

The radiosynthetic chemistry of carbon-11 is undoubtedly challenging. However, it is not the only issue that demands attention when working with the radionuclide. Indeed, both the radiation protection of the radiochemist and the technological challenges associated with using the radionuclide must be considered as well. In this sense, technology becomes critical for carbon-11 chemistry. To wit, the development of new radiosynthetic methods often parallels the emergence of innovations in synthesis technology. As mentioned earlier, the short half-life of carbon-11 restricts both the number of synthetic options available and the time permitted to use enact these options. The radiochemical yield of the final product is thus a function of the chemical yield of the reaction and the time needed to perform the reaction. As a consequence, the reaction should be stopped before the radioactive decay of the product exceeds the rate of formation of the product. Apart from normal optimization procedures, there are three key aspects to an effective strategy for ^{11}C-based radiosynthesis:

- Introducing the carbon-11 atom as late as possible in the reaction sequence
- Minimizing the synthesis time to optimize radiochemical yield and molar activity
- Minimizing isotopic dilution

With these three imperatives in mind, there are several different methodologies that can be applied for the synthesis of ^{11}C-based radiotracers. Generally speaking, these methodologies can be distilled into four approaches:

- Organic synthesis
- Enzymatic catalysis
- Biosynthesis
- Recoil labeling

Of these, only the first two are of practical value. Biosynthetic methods using algae or leaves and recoil synthesis by, for example, the spallation reaction ^{16}O(*p,3p3n*)^{11}C are mentioned only for the sake of completeness. In light of the access to an array of different precursors, a multitude of different chemical reactions are available to the radiochemist. Furthermore, the vast literature on carbon chemistry suggests that there are great opportunities for the further development of carbon-11 chemistry. Although the methylation of heteroatoms with [^{11}C]methyl iodide gives access to a large number of compounds, this labeling position is not always available or preferred. As a result, a great deal of effort has been devoted to the development of methods for the formation of C-C bonds with carbon-11. For example, the following methods have been applied to this problem:

- The carboxylation of organometallic reagents with [^{11}C] carbon dioxide
- The alkylation of stabilized carbanions with ^{11}C-labeled alkyl halides
- The use of reactions of [^{11}C]cyanide with electrophilic carbons
- The use of the anion of ^{11}C-labeled nitroalkanes
- The use of transition metal-mediated reactions with [^{11}C] methyl iodide and [^{11}C]carbon monoxide

The simple reaction between a Grignard reagent and [^{11}C] carbon dioxide is an excellent method for the production of clinically useful tracers such as [^{11}C]acetate and [^{11}C]palmitate. The alkylation of stabilized carbanions with alkyl halides is more complicated and, as mentioned, has been used mainly for the enantioselective synthesis of amino acids. The methods listed above open the door to a number of synthetic pathways; however, apart from [^{11}C]acetate, only a few PET tracers in clinical use are produced using any of these reactions. Nonetheless, the inherent potential they possess warrants some additional discussion.

Transition Metal-Mediated Reactions

The use of metals as catalysts in organic chemistry is widespread and has been successfully translated to carbon-11 chemistry. The most important examples involve the use of transition metal catalysts such as palladium and rhodium, though reactions mediated by selenium—though technically a metalloid—are also worth mentioning in this context. The stoichiometry in carbon-11 chemistry again affects the mechanism of these reactions. To wit, the low concentration of the ^{11}C-precursor changes these reactions from “catalytic” to “mediated,” since completing the catalytic cycle with the regeneration of the catalyst is highly unlikely. Two highly useful types of transition metal-catalyzed, C-C bond formation reactions have been found to

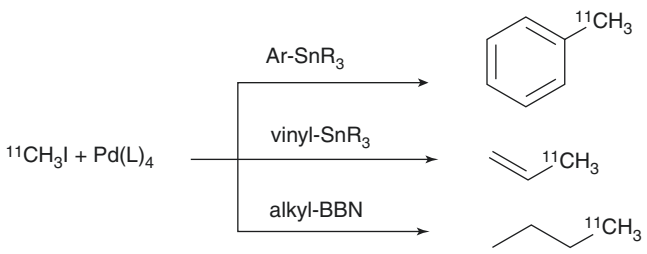

Fig. 8 Synthetic options provided by Stille and Suzuki cross-coupling reactions

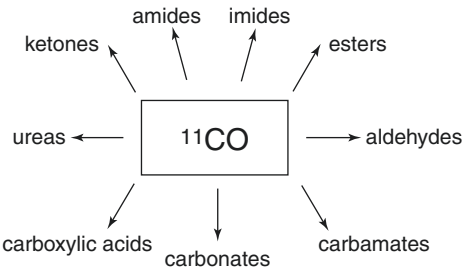

Fig. 9 Synthetic options provided by transition metal-mediated ^{11}C-carbonylations

significantly expand the synthetic opportunities with carbon-11: (1) palladium-mediated Stille and Suzuki cross-coupling reactions with [^{11}C]methyl iodide (Fig. 8) and (2) palladium-, rhodium-, and selenium-mediated ^{11}C-carbonylations (Fig. 9).

The Stille and Suzuki cross-couplings use organostannanes and organoboranes, respectively, as the nucleophiles reacting with [^{11}C]methyl iodide. These substrates are compatible with a number of functional groups, and the reactions can be performed under mild conditions. It is important to note that if the Stille reaction is performed with a trimethylstannane as the leaving group, the reaction is susceptible to isotopic dilution and reductions in molar activity. This is caused by an exchange reaction between [^{11}C]methyl iodide and the methyl groups on the stannane. The Stille coupling presents the option of using a carbonylation reaction for radiolabeling a molecule in two different positions (Fig. 10).

Stannanes are often rather toxic compounds, and therefore, the Suzuki reaction is generally preferred. One example of the use of this approach is the synthesis of the aromatase enzyme inhibitor [*methyl*-^{11}C]Cetrozole via a palladium-mediated Suzuki cross-coupling as presented in Fig. 11.

Interestingly, the cyano group of cetrozole can also be labeled via a Pd-mediated cyanation with [^{11}C]cyanide, exemplifying the strength and flexibility offered by this transition metal-based approach.

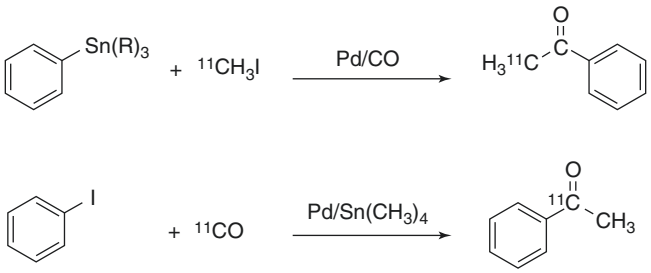

Fig. 10 Labeling a molecule in two different positions using the Stille coupling

^{11}C-Carbonylations

[^{11}C]Formylpiperidine and *N*-[^{11}C]acetylpiperidine were the first ^{11}C-carbonylation reactions reported and were performed by passing [^{11}C]CO in a stream of helium into a cold solution of lithium piperidide in tetrahydrofuran/dimethoxyethane. This resulted in the trapping of 10–20% of the [^{11}C]CO in the reaction mixture, producing an isolated radiochemical yield on the order of 1–3%. The same low radiochemical yield was also reported in the first report of a palladium-mediated carbonylation using Pd(0)-triphenylphosphine (tetrakis) ligands. The inherent inertness of carbon monoxide is not the problem, as the metal circumvents this issue. Instead, the low radiochemical yield can be partly explained by the low solubility of CO in all useful solvents. The carrier gas—typically nitrogen or helium—efficiently passes [^{11}C]CO through the reaction mixture, and only very small amounts of [^{11}C]CO are retained, resulting in low overall radiochemical yields. The main problem in ^{11}C-carbonylations can thus be broken down to a simple technical issue: how to quantitatively transfer and retain [^{11}C]CO in a reaction mixture. To overcome this problem and to take complete advantage of the synthesis options with [^{11}C]CO, the following technical and chemical solutions have been developed:

- Synthesizing a reactive derivative of [^{11}C]CO
- Increasing the efficiency of the reaction of [^{11}C]CO with a catalyst
- Recycling the [^{11}C]CO
- Quantitatively transferring the [^{11}C]CO to a closed reaction vial

The synthesis of BH_3-[^{11}C]CO provided the first successful example of an approach that could quantitatively transfer and retain [^{11}C]CO in the reaction mixture [13]. The volatile BH_3-[^{11}C]CO is distilled to the reaction mixture, a procedure which imposes a temperature limitation on this method due to the need for temperatures below −70 °C to trap the reagent in the solvent. However, such low temperatures may not be

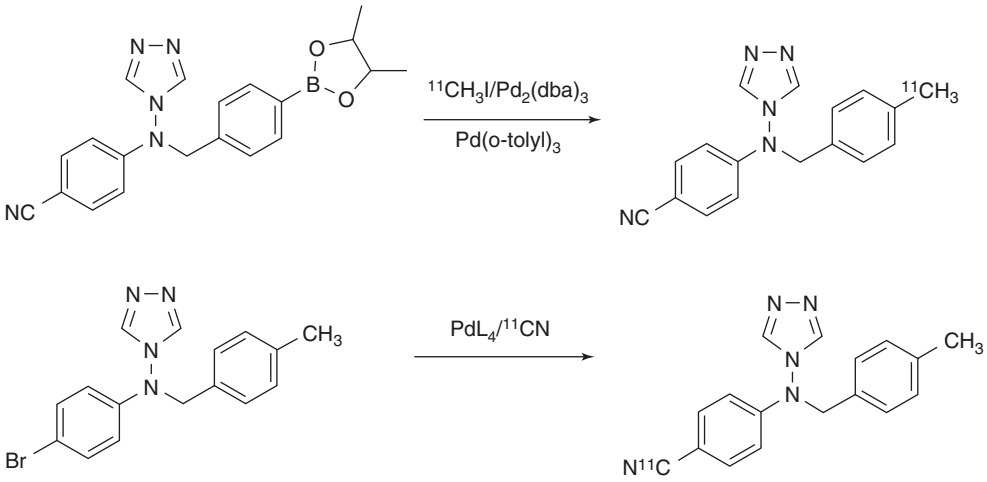

Fig. 11 Synthesis of [^{11}C]Cetrozole

compatible with certain reaction mixtures, rendering this methodology useful only in certain cases. Alternatively, Cu(I) tris(pyrazolyl)borate derivatives—coined "scorpionates"—can also be used to trap [^{11}C]CO in the reaction solution. [^{11}C]Carbon monoxide is subsequently released *in situ* by the addition of triphenylphosphine. Although both methods have been shown to result in good radiochemical yields, there are only a few published examples of their use in the synthesis of tracers.

Technical solutions such as recycling of [^{11}C]CO can also increase yields, but perhaps the most general methods are the autoclave approach and the use of xenon as carrier gas. Both of these solutions directly address the problem of how to quantitatively transfer and retain [^{11}C]CO in the reaction vessel [14, 15]. The low solubility of CO in most solvents distributes [^{11}C]CO mainly into the gas phase, and a very high liquid-phase/gas-phase ratio is needed to achieve high conversion rates of [^{11}C]CO into the product.

The first generally useful technical solution for ^{11}C-carbonylations was the autoclave method. It addresses two of the crucial parameters: the quantitative transfer of [^{11}C]CO to the reaction vessel and the optimization of the ratio of liquid phase/gas phase. In the autoclave method, [^{11}C]CO is concentrated on a solid support—which together with the tubing has a very small volume in comparison to the autoclave—and is transferred in helium gas at 5 bar to the 200 μL autoclave. The autoclave is loaded with the reaction mixture at a pressure of 400 bar, which reduces the gas volume (He/^{11}CO) in accordance with the standard gas law ($P_1V_1 = P_2V_2$) for pressure (P) and volume (V). The resulting liquid-phase/gas-phase ratio is about 100/1 with a gas-phase volume of around 2 μL. [^{11}C]Carbon monoxide is thus quantitatively transferred into the autoclave and confined in a very small volume of gas. Another important factor is that the autoclave can withstand high pressures and solvents such as tetrahydrofuran (THF) that can be used at temperatures exceeding 175 °C. This method has proven to give high radiochemical yields in conjunction with Pd-, Rh-, and Se-mediated reactions. Indeed, this approach provides a nice example of the synergism between developments in synthesis and technology. One drawback is that the use of the same autoclave for different syntheses imposes several GMP-related issues, such as the potential for carry-over from a previous production.

The xenon method uses a much simpler technical setup and is based on the high solubility of xenon in certain solvents. [^{11}C]CO is concentrated on a solid support and transported in xenon to a capped reaction vessel containing the reaction mixture (preferably in THF). Due to the high solubility of xenon in THF, [^{11}C]CO is quantitatively transferred and retained in the reaction vessel. It is important to understand that there is no change in solubility of CO in the solvent used, and xenon functions only as a transporting media. Examples of ^{11}C-carbonylation reactions using the autoclave or xenon methods are presented in Fig. 12.

Radiotracers based on the antimigraine drug [*carbonyl*-^{11}C]zolmitriptan and the antiepileptic drug [*carbonyl*-^{11}C]phenytoin have been used to study regional brain uptake in humans [16].

Enzymatic Catalysis and Carbon-11

Organic synthetic methods dominate the carbon-11 field, and a useful and common approach in organic synthesis is the use of catalysts to increase the rate and selectivity of a reaction. Yet metal complexes are not the only catalysts to which ^{11}C-radiochemists can turn. Indeed, the potential of enzymes for carbon-11 radiochemistry became obvious early on. While enzymes are predominantly applied to the synthesis of endogenous compounds such amino acids, other examples of

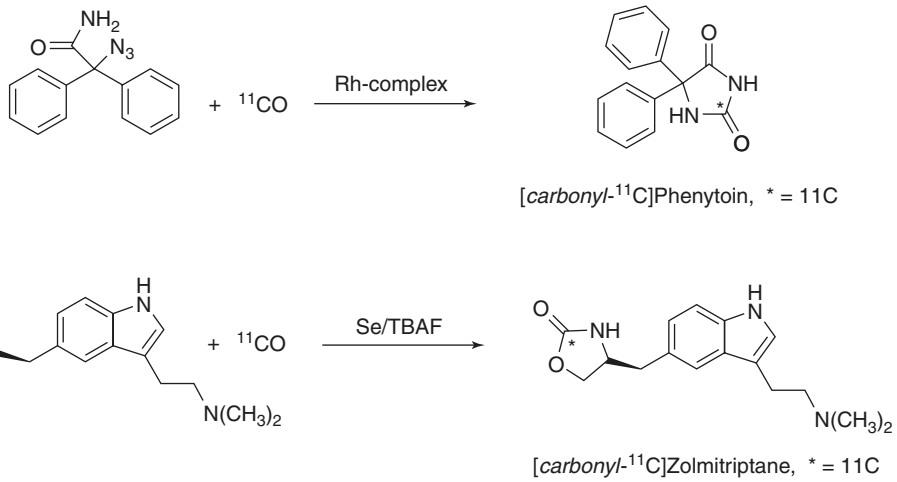

Fig. 12 Synthesis of [*carbonyl*-^{11}C]zolmitriptan and [*carbonyl*-^{11}C]phenytoin using the autoclave and xenon methods, respectively

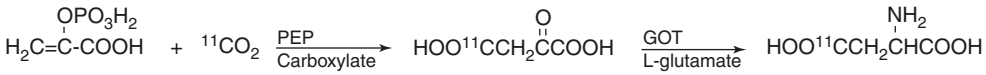

Fig. 13 Enzymatic synthesis [4-^{11}C]aspartic acid

this approach exist as well, including the chemical and multi-enzymatic syntheses of ^{11}C-labeled pyruvate and lactate and the multi-enzymatic synthesis of [4-^{11}C]aspartic acid (Fig. 13) [17].

Position-Specific Labeling and Labeling in Different Positions in a Molecule

One important aspect in the design of a radiotracer is choosing the most appropriate position within the molecule for radiolabeling. Here, there are several things to consider. One obvious and important chemical consideration is the ease with which the radiolabel can be incorporated into the molecule in question. This will influence both the radiochemical yield and the molar activity of the radiotracer and will have an impact on the purification of the construct as well. Biology can also play a role in the selection of site for radiolabeling, though in this case the situation gets more complicated and can require *in vivo* experiments to provide a final answer. In most cases, radiotracers are subjected to metabolism after their administration, and the position of the radiolabel determines which radiolabeled metabolites are formed. It is therefore important to know how these radiometabolites will distribute within the body and how they may interact with the intended molecular target of the radiotracer. A labeled metabolite that binds to the same target as the intact tracer can confound the interpretation of the PET data, while radiometabolites that accumulate in healthy organs can decrease signal-to-background ratios.

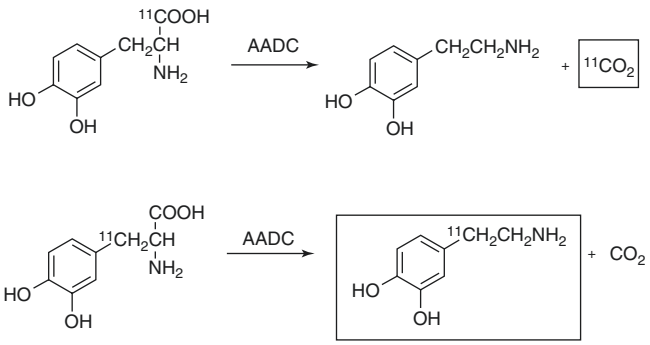

Fig. 14 *In vivo* synthesis of dopamine

The importance of the labeling position is nicely illustrated by [*carboxy*-^{11}C]DOPA and [β-^{11}C]DOPA, radiotracers synthesized for the study of the dopaminergic neurotransmitter system in the brain. Depending on the labeling position, two very different PET images are obtained. With [*carboxy*-^{11}C]DOPA, a low and uniform uptake of radioactivity is obtained in the brain, whereas with [β-^{11}C]DOPA, high radioactive uptake is found in the striatum in brain, a region known to contain a high density of dopaminergic neurons. How can this be understood? Both radiotracers are the same molecule, but they display very different uptake patterns in the brain! In this case, the explanation is rather simple since we have full understanding of the *in vivo* metabolism of DOPA. The enzyme aromatic amino acid decarboxylase (AADC) is found in high concentrations in dopaminergic neurons in the striatum and decarboxylates DOPA to form the neurotransmitter dopamine (Fig. 14). This

highlights the potential value of the position-specific radiolabeling of a molecule at different sites, which is often possible with carbon-11 but is rarely feasible with fluorine-18.

Depending on the labeling position, metabolism via AADC produces either [^{11}C]carbon dioxide (from [*carboxy*-^{11}C]DOPA) or [β-^{11}C]dopamine (from [β-^{11}C]DOPA). The former is excreted from tissue, and the latter is stored in vesicles in the neurons. Clearly, only [β-^{11}C]DOPA can be used to study and quantify this important process in the brain. However, [*carboxy*-^{11}C]DOPA has some value, since it can be used to verify that what is measured in the PET scanner actually represents the *in vivo* synthesis of dopamine from DOPA [17].

Another example of the importance of the labeling position is provided by the synthesis of ^{11}C-labeled WAY1000635, a 5-HT$_{1A}$ receptor ligand. WAY1000635 has an *O*-methyl group that is easily labeled with [^{11}C]methyl iodide. However, when the product of this ^{11}C-methylation—[*O-methyl*-^{11}C]WAY100635—was used for PET imaging, the interpretation of the data was hampered by the presence of a radiolabeled metabolite (identified as WAY100634) that entered the brain and had significant affinity for the 5-HT$_{1A}$ receptors. Instead, the more difficult and technically demanding synthesis of [*carbonyl*-^{11}C]WAY100635 was developed using [^{11}C]cyclohexanecarbonyl chloride. The metabolism of this tracer produces a radiolabeled metabolite which does not pass through the blood-brain barrier (Fig. 15) [18].

In general, the most appropriate labeling position for radiotracers that are used for studying the brain is one that results in the formation of polar radiometabolites with limited or no BBB penetration. Along these lines, the ^{11}C-methylation of nitrogen is a useful approach, because demethylation is often the major metabolic pathway, producing hydrophilic radiometabolites with low brain uptake. This explains the many examples of useful receptor ligands that are radiolabeled in this manner. Clearly, when designing a new brain-targeted radiotracer, one would ideally have a complete understanding of how the tracer is metabolized. If these data are unavailable, the ability to label a molecule in different positions and perform preclinical studies provides a route to determining the most appropriate position for labeling.

Double-Isotope Labeling: The Kinetic Isotope Effect

In theory, the strength of a covalent bond between carbon-11 bond and another atom differs compared to the same bond with carbon-12 due to the lower zero-point energy of the heavier isotope. It follows that larger amounts of energy are required to break the bond with the heavier isotope, a phenomenon which can lead to lower rates of reaction if bond breakage is the rate-limiting step. This is called the kinetic isotope effect (KIE), and it is of interest as a tool to elucidate reaction mechanisms and to fine-tune the properties of PET radiotracers. The most often used illustration of the KIE is substituting hydrogen for deuterium, a switch that can lead to dramatic changes in rates of a reaction. Indeed, the substitution of hydrogen for a deuterium on a carbon that is involved in a rate-limiting carbon-carbon bond formation induces a primary KIE.

Fowler *et al.* demonstrated the usefulness of this phenomenon in the study of the expression of the enzyme monoamine oxidase type B (MAO-B) in the brain with the MAO-B inhibitors L-[^{11}C]deprenyl and L-[^{11}C]dideuteriumdeprenyl

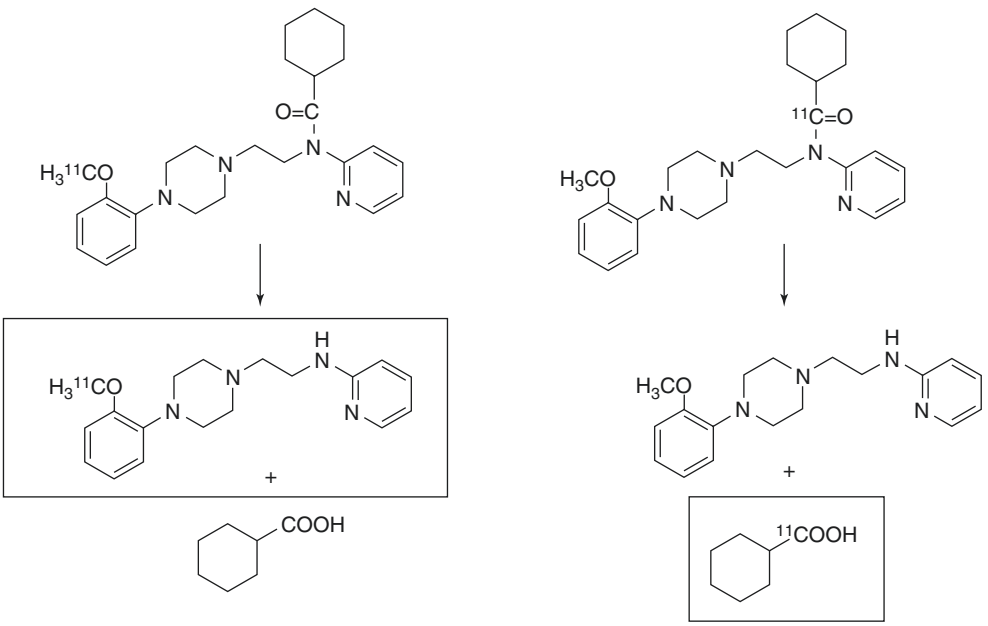

Fig. 15 Metabolism of [^{11}C]WAY100635

[19]. Deprenyl forms a covalent bond with the enzyme, and it was found that in regions of the brain with high MAO-B expression, the very high affinity of L-[^{11}C]deprenyl resulted in flow-dependent kinetics (*i.e.* the delivery of the tracer is the rate-limiting step, making the quantification of MAO-B expression difficult since we can only measure the rate-limiting step in a kinetic analysis). This can be understood by a compartmental analysis in which L represents the PET tracer and R the molecular target—in this case MAO-B—with K_1 and k_3 the rate constants for transport from plasma into tissue and ligand-enzyme binding, respectively:

$$L_P \underset{K_1}{\overset{k_2}{\rightleftharpoons}} L_F + L_{NS} \overset{R}{\underset{k_3}{\rightarrow}} L - R$$

(Lp = ligand in plasma; L_F = free ligand in tissue; L_{NS} = non-specifically bound ligand in tissue; L-R = ligand-enzyme complex; K_1, k_2, k_3 = rate constants for transport into tissue, out of tissue, and enzyme binding, respectively.)

If $k_3 >> K_1$, transport into tissue is rate-limiting, but if the reaction rate to form the complex L-R is reduced (*i.e.* $K_1 > k_3$), the binding of ligand to enzyme becomes the rate-limiting process.

In contrast, with L-[^{11}C]dideuteriumdeprenyl, a secondary KIE was observed which reduced the rate of the reaction. As a result, the rate-limiting step for the tracer was changed from the delivery of the radiotracer to its binding to the enzyme, and the regional expression of MAO-B in the brain could be determined.

Future Developments and Where to Go with Carbon-11-Labeled Tracers

As we conclude this chapter, we would like to spend some time addressing a very important question: Which technical and synthetic strategies should we pursue and what should we strive toward the future development of carbon-11 chemistry? From a technology point of view, we could adopt the current trend that dominates fluorine-18 and gallium-68 chemistry and use cassettes and develop premade commercially available reagent kits for the production of radiotracers. This is somewhat more challenging for carbon-11 chemistry because it relies on gaseous precursors such as [^{11}C]methyl iodide, [^{11}C]carbon dioxide, [^{11}C]carbon monoxide, and ammonium [^{11}C]cyanide. It is possible that further innovations in microfluidics technology and flow reactors could solve the problems associated with handling gaseous precursors. This could potentially lead to the development of a fully automated and GMP-compliant "PET Coffee Machine," in which a reagent kit and single-use synthesis card are integrated with the production of the radionuclide to enable the synthesis of ^{11}C-labeled PET tracers. In essence, "press a button to select a PET tracer." Simplicity at this level would allow a laboratory technician to perform the production of a large variety of tracers without special knowledge of PET radiochemistry. This, of course, is the perfect solution for the production of radiopharmaceuticals.

But what about research and development? What can we foresee as the pathway forward? There will never be a situation in which there is nothing more to explore. Therefore, we should constantly focus on the development of new methods and collaborations with other scientific disciplines to fill the gaps of unmet clinical needs. Radiopharmaceutical chemistry has always relied on collaboration with pharmaceutical companies and medicinal chemists at universities to develop libraries of compounds that could be transformed into tracers. Carbon-11 is a perfect match in this sense, since all organic compounds can be labeled with this radionuclide (at least in theory!). This type of collaboration could most likely be performed in a more efficient manner by establishing a larger consortium with long-term relationships between radiochemists, PET scientists, clinicians, and medicinal chemists. Such a group could outline strategies that could speed up the processes of development and validation for new tracers. We should also consider placing more emphasis on the radiolabeling of endogenous compounds to better understand biochemical and physiological processes. In this context, carbon-11 is also the most appropriate radionuclide.

As scientists, we often learn that what is regarded as out of reach today could be the standard practice tomorrow. With this in mind, we must realize that future developments in carbon-11 chemistry may enable new opportunities that are currently hidden below the radiochemical horizon. Accordingly, although most of reported tracer syntheses use a few ^{11}C-labeled precursors—with ^{11}C-methylation reactions dominating—it is nonetheless imperative that we continue our research in the field of basic carbon-11 radiochemistry and further expand what can be achieved.

From a clinical perspective, it is important to keep several considerations in mind when discussing the use of carbon-11 as the basis for PET radiotracers:

- The radiation dose to patients
- The logistical aspects of multi-tracer protocols
- The logistics of the production of PET tracers

The ALARA (As Low As Reasonably Achievable) principle of radiation dose should always govern the routine clinical diagnostic operations. Multi-tracer protocols are increasingly becoming of clinical value, and from a logistical point of view, carbon-11 can facilitate repeated scans in the same patients on the same day. The production of

^{11}C-labeled PET tracers requires the use of large amounts of radioactivity, and for most syntheses, the cycle time for the equipment between two productions is dependent on the decay of the remaining radioactivity to levels that permit operators access to the hot cell. The short half-life of carbon-11 may allow up to four productions per synthesis unit per day. In contrast, for fluorine-18, it is generally challenging to perform more than one tracer production per day. This is important in economic terms, since the number of hot cells and synthesis units can be kept to a reasonable number. Is carbon-11 then the perfect radionuclide for PET? Unfortunately, the answer is no. As we stated in the beginning of this chapter, there is no such thing as "the perfect" radionuclide. With carbon-11, we have restrictions related to its short half-life, which is a constraint that we cannot overcome and is the principal drawback of the radionuclide. In addition, the use of ^{11}C-labeled tracers is limited to hospitals with a PET production facility in close proximity to the PET cameras.

In sum, the journey that begins with the pioneering work in the 1930s and continues with today's diagnostic imaging is by no means over. We should continue to strive toward a situation in which ^{11}C-labeled tracers are clinically available to all patients that require a PET scan for diagnostic purposes.

The Bottom Line

- Carbon-11 is an accelerator-produced, positron-emitting radionuclide. Its physical half-life of 20.4 min is sufficiently long to allow for multistep syntheses while short enough to enable multiple PET scans of the same individual on the same day.
- Carbon-11 is exclusively produced using the $^{14}N(p,\alpha)^{11}C$ reaction via the bombardment of nitrogen gas containing trace or small amounts of either oxygen or hydrogen with 8–17 MeV protons.
- Both time and isotopic dilution are critical factors in determining the specific activity of a radiotracer labeled with carbon-11.
- Precursors that are produced within the target are denoted *primary precursors*, while those that are obtained during the subsequent processing of the target are called *secondary precursors*. The $^{14}N(p,\alpha)^{11}C$ reaction using gas mixtures of either N_2/O_2 or N_2/H_2 produces [^{11}C]carbon dioxide or [^{11}C]methane, respectively, as primary precursors.
- The most useful secondary precursor is [^{11}C]methyl iodide, though other important secondary precursors include [^{11}C]CO, [^{11}C]CN, $^{11}CH_3NO_2$, [^{11}C]CH_2O, and [^{11}C]$COCl_2$.
- Two transition metal-catalyzed, C-C bond formation reactions have been found to significantly expand the synthetic opportunities with carbon-11: palladium-mediated Stille and Suzuki cross-coupling reactions with [^{11}C]methyl iodide and palladium-, rhodium-, and selenium-mediated ^{11}C-carbonylations.
- The direct translation of traditional synthetic reaction conditions to radiochemistry is not always possible. It is therefore recommended to investigate new ^{11}C-based syntheses directly with radioactive material instead of performing optimizations with unlabeled material.
- The short half-life of carbon-11 restricts the synthetic options available for the creation of ^{11}C-labeled radiotracers as well as the time permitted for synthesis. The radiochemical yield of the final product is thus a function of the chemical yield of the reaction and the time needed to perform the reaction.
- Carbon-11 can be used for the position-specific radiolabeling of different sites within a molecule. This can be particularly useful if the *in vivo* metabolism of a radiotracer creates unwanted radiolabeled by-products.

References

1. Crane HR, Lauritsen CC. Radioactivity from carbon and boron oxide bombarded with deutons and the conversion of positrons into radiation. Phys Rev. 1934;45(6):430–2.
2. Ruben S, Hassid WZ, Kamen MD. Radioactive carbon in the study of photosynthesis. J Am Chem Soc. 1939;61(3):661–3.
3. Tobias CA, Lawrence JH, Roughton F, Root W, Gregersen M. The elimination of carbon monoxide from the human body with reference to the possible conversion of CO to CO_2. Am J Phys. 1945;145:253–63.
4. Ter-Pogossian MM, Wagner HN. A new look at the cyclotron for making short-lived isotopes. Nucleonics. 1966;24:50–62.
5. Christman DR, Finn RD, Karlstrom KI, Wolf AP. The production of ultra high activity ^{11}C-labeled hydrogen cyanide, carbon dioxide, carbon monoxide and methane via the $^{14}N(p,\alpha)^{11}C$ reaction. Int J Appl Radiat Isot. 1975;26(8):435–42.
6. Långström B, Lundqvist H. The preparation of [^{11}C]methyl iodide and its use in the synthesis of [methyl-^{11}C]-L-methionine. Int J Appl Radiat Isot. 1976;27(7):357–63.
7. Antoni G, Kihlberg T, Långström B. Aspects on the synthesis of ^{11}C-labeled compounds. In: Welch M, Redvanly C, editors. Handbook of radiopharmaceuticals, radiochemistry and applications. Chichester: John Wiley & Sons Ltd.; 2003. p. 141–94.
8. Wuest F, Berndt M, Kniess T. Carbon-11 labeling chemistry based upon [^{11}C]methyl iodide. In: Schubiger PA, Lehmann L, Friebe M, editors. PET chemistry. Ernst Schering Research Foundation Workshop, vol. 64. Heidelberg/Berlin: Springer-Verlag; 2007. p. 183–213.
9. Antoni G, Kihlberg T, Långström B. ^{11}C: Labeling chemistry and labeled compounds. In: Vértes A, Nagy S, Klencsár Z, editors. Handbook of nuclear chemistry, Vol. 4, Radiochemsitry and radiopharmaceutical chemistry in life sciences. Dordrecht, the Netherlands: Kluwer Academic; 2003. p. 119–57.
10. Bjurling P, Watanabe Y, Tokushige M, Oda T, Långström B. Syntheses of β-^{11}C-labeled L-tryptophan and 5-hydroxy-L-

tryptophan by using a multi-enzymatic route. J Chem Soc Perkin Trans. 1989;1:1331–4.
11. Gómez-Vallejo V, Gaja V, Koziorowski J, Llop J. Specific activity of 11C-labeled radiotracers. In: Hsieh C-H, editor. A big challenge for PET chemists, positron emission tomography—current clinical and research aspects. InTech; 2012. p. 183–210. https://doi.org/10.5772/31491.
12. Långström B, Itsenko O, Rahman O. [11C]Carbon monoxide, a versatile and useful precursor in labelling chemistry for PET-ligand development. J Labelled Comp Radiopharm. 2007;50(9–10):794–810.
13. Audrain H, Martarello L, Gee A, Bender D. Utilisation of [11C]-labeled boron carbonyl complexes in palladium carbonylation reaction. Chem Commun (Camb). 2004;5:558–9.
14. Kihlberg T, Långström B. Method and apparatus for production and use of [^{11}C]carbon monoxide in labeling synthesis. PCT Int Appl. 2002; WO, 2002102711 A1
15. Eriksson J, van den Hoek J, Windhorst AD. Transition metal mediated synthesis using [^{11}C]CO at low pressure – a simplified method for 11C-carbonylation. J Labelled Comp Radiopharm. 2012;55(6):223–8.
16. Verbeek J, Eriksson J, Syvänen S, Labots M, de Lange EC, Voskuyl RA, et al. [^{11}C]phenytoin revisited: synthesis by [^{11}C]CO carbonylation and first evaluation as a P-gp tracer in rats. EJNMMI Res. 2012;2(1):36.
17. Torstenson R, Tedroff J, Hartvig P, Fasth KJ, Långström B. A comparison of ^{11}C-labeled L-DOPA and L-fluorodopa as positron emission tomography tracers for the presynaptic dopaminergic system. J Cereb Blood Flow Metab. 1999;19(10):1142–9.
18. Osman S, Lundkvist C, Pike VW, Halldin C, McCarron JA, Swahn CG, et al. Characterization of the radioactive metabolites of the 5-HT$_{1A}$ receptor radioligand, [O-*methl*-^{11}C]WAY-100635, in monkey and human plasma by HPLC: comparison of the behaviour of an identified radioactive metabolite with parent radioligand in monkey using PET. Nucl Med Biol. 1996;23(5):627–34.
19. Fowler JS, Wang GJ, Logan J, Xie S, Volkow ND, MacGregor RR, et al. Selective reduction of radiotracer trapping by deuterium substitution: comparison of carbon-11-L-deprenyl and carbon-11-deprenyl-D2 for MAO B mapping. J Nucl Med. 1995;36(7):1255–62.

The Radiopharmaceutical Chemistry of Carbon-11: Tracers and Applications

Verena Pichler, Neydher Berroterán-Infante, Marius Ozenil, Sarah Pfaff, Cécile Philippe, and Wolfgang Wadsak

Introduction

In this chapter, several different aspects of carbon-11 radiochemistry are discussed, including general and technical considerations surrounding setup for ^{11}C-radiosyntheses and specific radiolabeling routes for the preparation of representative ^{11}C-labeled radiotracers. The optimization of equipment and labeling procedures—especially with respect to time—is a must when dealing with the short-lived radionuclide carbon-11. Time reduction in all processes (including quality control) is of the utmost importance, though both accuracy and reproducibility must be maintained. The synthetic possibilities for ^{11}C-labeled radiotracers resemble a multicolored bouquet of flowers, with methods ranging from gas-phase reactions to in-loop syntheses and from straightforward ^{11}C-methylations to tricky multistep Grignard reactions. A variety of synthons—including [^{11}C]CH_3I, [^{11}C]HCN, [^{11}C]CS_2, and [^{11}C]CO—are used to prepare a multitude of radiotracers incorporating a ^{11}C-radiolabel at desired positions in the target molecule without altering its physicochemical and biological properties. Although several critical limitations are placed upon ^{11}C-radiochemists—including time constraints as well as the need for sufficient yields and molar activities—you will find plenty of examples within this chapter of instances in which scientists have overcome these obstacles and were able to set up feasible synthetic routes that demonstrate the beauty of ^{11}C-radiochemistry.

V. Pichler · N. Berroterán-Infante · M. Ozenil · S. Pfaff
C. Philippe · W. Wadsak (✉)
Department of Biomedical Imaging and Image-guided Therapy, Division of Nuclear Medicine, Medical University of Vienna, Vienna, Austria
e-mail: wolfgang.wadsak@meduniwien.ac.at

Technical Aspects of Carbon-11: Commercially Available Synthesizers and Optimization

General Considerations for Radiotracer Production and the Setup of Synthesizers

The routine production of ^{11}C-labeled radiotracers requires equipment that ensures the safety of the attending radiochemists. This suite of equipment typically involves a lead-shielded working space, so-called hot cells, an active gas compression system for storing exhaust air in tanks during the decay process and radiation monitoring systems. The heart of every ^{11}C-radiochemistry laboratory is the semi-automated or fully automated synthesizer, in which the actual chemical conversion of the precursor to the radiolabeled product takes place.

Carbon-11 synthesis modules—like any other synthesizer in radiochemistry—should comply with a set of specific properties in order to fulfill the demands of routine production with a high degree of reproducibility [1]. As a result, the modules must facilitate or allow for the following:

- The possibility for the automation of all processes
- The reproducibility of robust processes
- Modifications for challenging syntheses (*e.g.* in-loop reactions)
- Constant quality of the radiolabeled product in terms of molar activity and radiochemical yield
- The production of multiple doses per day
- Reduced maintenance efforts

Independent of the manufacturer, versatile synthesis modules for carbon-11 radiochemistry must have a minimum configuration featuring four major parts (for an overview, see Fig. 1). The first part consists of an instrument for the production of [^{11}C]methyl iodide ([^{11}C]iodomethane)—with or without an extension to prepare [^{11}C]methyl triflate—either via the "wet" method (see the section on "'Wet' Production

J. S. Lewis et al. (eds.), *Radiopharmaceutical Chemistry*, https://doi.org/10.1007/978-3-319-98947-1_12

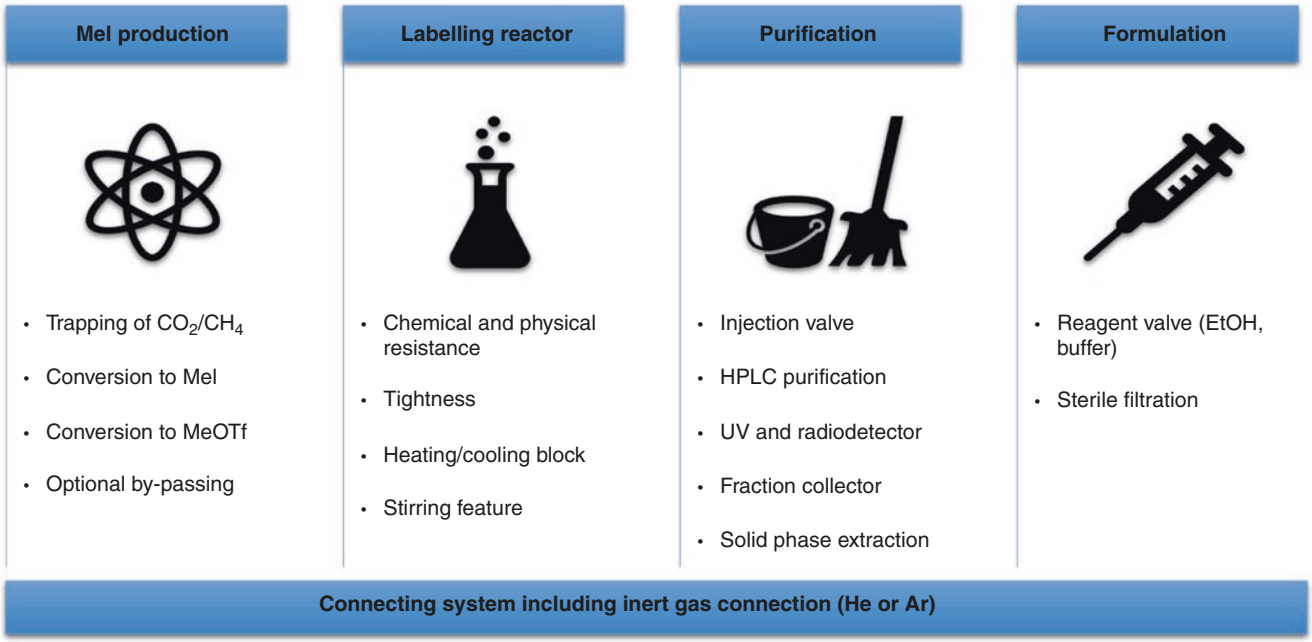

Fig. 1 Overview of the four necessary procedures for a successful radiosynthesis

of [^{11}C]CH_3I") or the "gas-phase" method (see the section on "'Gas-Phase' Production of [^{11}C]CH_3I"). The next part is composed of the reaction and reagent vessels necessary for conducting the radiolabeling procedure, including a heating/cooling block. This part has to be connected via an injection valve to the third component: a purification system including an HPLC for the separation of precursors, possible by-products, and the radiotracer of interest (see the section on "Purification and Separation") and often also a solid-phase extraction (SPE) system or a rotary evaporator to get rid of residual solvents used during HPLC. For clinical purposes, a fourth component is built in to facilitate the formulation of the radiolabeled compound in a manner suitable for intravenous injections. All four of these parts are connected via tubes and externally controllable valves, and the transportation of all gaseous or liquid/dissolved precursors, intermediates, and products is realized via an inert gas flow (mainly helium or argon).

Reactors and Reagent Vessels

The reaction vessel—which contains the dissolved non-radiolabeled organic precursor—is directly connected to the [^{11}C]CO_2/[^{11}C]methyl iodide production unit (Fig. 2; see Part 2). In addition, exhaust tubing should be present to prevent overpressure and to ensure a constant gas flow during the delivery of the radioactive precursor. In most cases, there is at least one additional segment of tubing for the addition of reagents or solvents to quench the reaction. The tubing for the addition of the radioactive intermediate—*e.g.* [^{11}C]methyl iodide—reaches down to the bottom of the reaction vessel to facilitate the ideal trapping of the radioactivity. In some cases, the height of the position of this inlet tubing can be adjustable. All other tubes are positioned in the upper part of the vessel to prevent an inadvertent backflow of the reaction mixture. Furthermore, this component also includes a heating/cooling block that enables diverse reaction conditions as well as a stirring unit.

The first step of the radiolabeling reaction is the trapping of the radioactive precursor/intermediate in the solution containing the nonradioactive precursor. Subsequently, the reaction vessel is closed for the entirety of the reaction time, and the reaction mixture is heated to the desired temperature. The tightness of the reactor is a key factor for successful radiosyntheses, as this reduces the possibility of losing radioactivity due to evaporation. After the completion of the reaction, the mixture is cooled to room temperature, and the reaction is quenched (*e.g.* by addition of HPLC solvent or water). As time efficiency is crucial when working with such a short-lived radionuclide, an efficient heating/cooling system can save precious time.

It is important to mention—though perhaps obvious—that all tubes and vessels must be chemically resistant and need to display a high degree of stability over a wide range of temperatures. As many ^{11}C-based radiotracers are highly lipophilic—especially those designed to permeate the blood-brain barrier, such as [^{11}C]PIB or [^{11}C]DASB—the reactor should preferably be made of either glass or plastic with a polar surface in order to avoid non-specific binding between

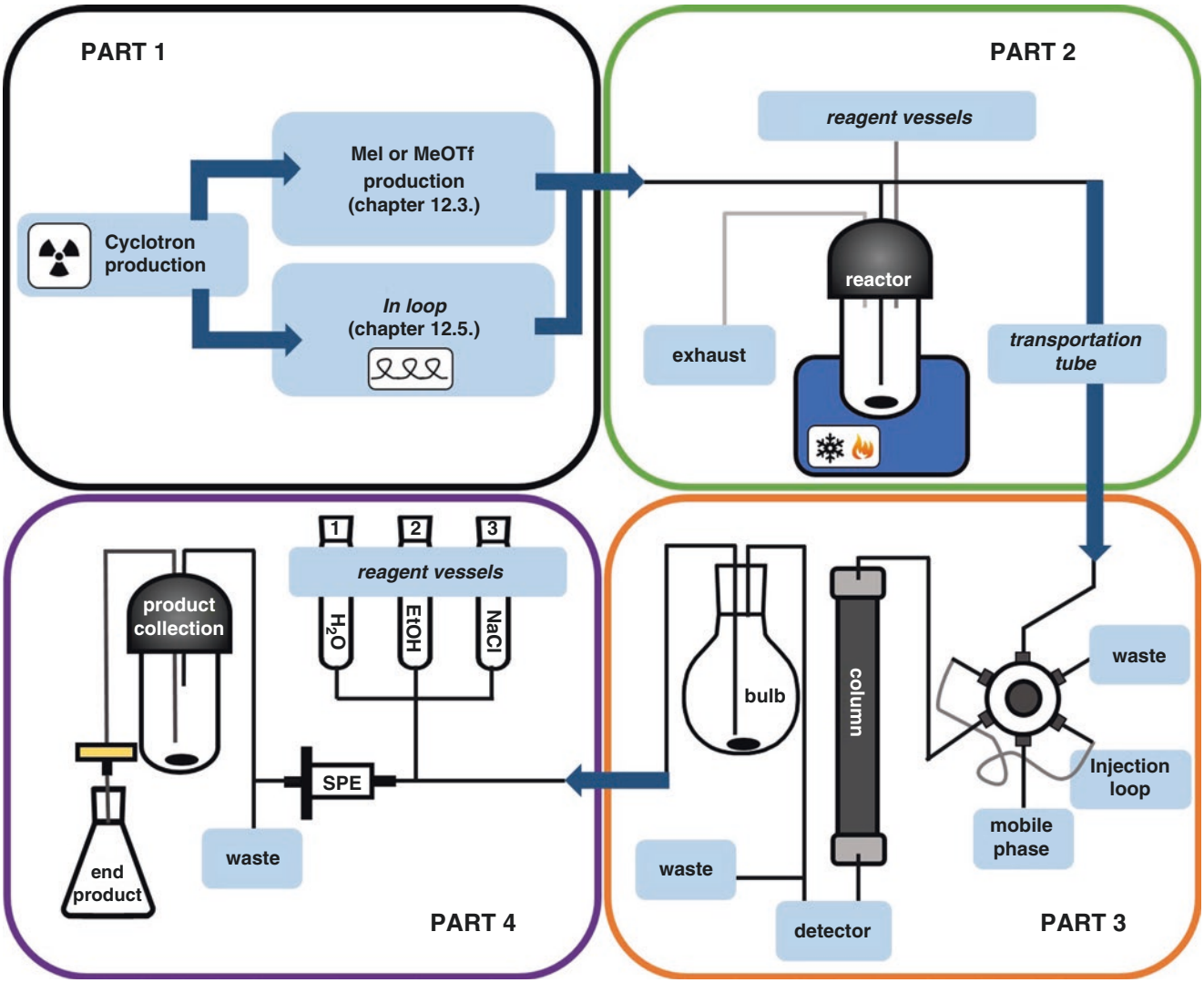

Fig. 2 The four essential parts of carbon-11 radiosynthetic modules

the tracer and the surfaces of the instrument. Moisture- and air-sensitive reactions often require modifications to the module array in order to increase turnover and yield. One potential modification of the module involves using a loop instead of a vessel-based reactor as a platform for either conversion steps or whole radiosyntheses. For example, radiochemical Grignard reactions are often performed "in-loop," bypassing the [^{11}C]methyl iodide production unit (see the section on "Grignard Reactions in Carbon-11 Radiochemistry (In-Loop)").

Purification and Separation

One characteristic of carbon-11 radiochemistry is that vast excesses of non-radioactive precursor typically remain even after the creation of a new radiotracer. Hence, the majority of carbon-11 syntheses require a purification process to separate the ^{11}C-labeled compound from unreacted precursor, side products, and organic solvents from the conversion process (see Fig. 2, Part 3).

To this end, the crude reaction mixture is typically transferred to an HPLC system, including an injection valve, a column, a UV/Vis and radioactivity detectors, and an apparatus enabling the collection of the peak of interest. The collected product peak still contains organic solvents from the mobile phase—*e.g.* acetonitrile or methanol—which must be removed prior to the formulation of the radiotracer for patients. In order to remove these solvents, the collected product is first diluted with large amounts of water. This solution is then transferred to a reversed-phase C_{18} cartridge for purification via SPE. The dilution step is necessary in order to reduce the amount of nonpolar solvents, as the presence of these solvents can reduce the efficiency of the cartridge. Depending on the physicochemical parameters of the product, the use of other cartridges—including those

containing ion-exchange resins—or even combinations thereof can be advantageous as well.

The last part of the module consists of additional reagent vessels, a product collection vial, and a final segment of tubing including a sterile filter for the filling of the final product vial under aseptic conditions (see Fig. 2, Part 4). These reagent vessels are connected to the SPE cartridge with the retained product, and the cartridge is washed with water to remove the final traces of organic solvents. Then, the purified product is recovered from the SPE cartridge via elution with a small amount of an organic solvent that is well tolerated in living organisms (such as ethanol) into the product collection vial where formulation takes place.

Formulation

Following synthesis and purification, the radiolabeled product must be prepared for intravenous administration to patients [2], as a so-called *parenteral preparation*. Parenteral preparations are sterile aqueous preparations that may include excipients for the adjustment of osmolality and pH. In the final steps described in the section on "Purification and Separation," the radiotracer is washed out of the SPE cartridge with ethanol and directly into the product collection vial already containing a buffered solution for the adjustment of pH and osmolality (*e.g.* phosphate-buffered saline). Depending on the specifications within the applicable pharmacopeia, up to 10% v/v ethanol is allowed in injections. Last but not least, the cartridge is rinsed with physiological sodium chloride solution (0.9% w/v) to ensure the complete transfer of the product from the SPE cartridge and through the lines. The well-stirred solution is then transferred from the product collection vial in the production hot cell into the final sterile product vial in the filling hot cell, where it is sterile filtered under aseptic conditions (*i.e.* laminar airflow) and subsequently ready to use.

Optimizing Possibilities Within the Synthesizer

Careful handling and maintenance significantly extend the lifetime of every module. Before starting a synthesis, the synthesizer should be checked, and all tubings and vessels must be washed and dried. Checking the system thoroughly for leakages reduces the loss of radioactivity during syntheses and is mandatory when dealing with gaseous reagents such as $[^{11}C]CO_2$, $[^{11}C]CH_4$, and [^{11}C]methyl iodide. The cleaning of all necessary tubing and connections within the module removes residues or particles from prior syntheses and thus reduces the likelihood of synthesis failures due to blockages within the tubes and valves. The exclusion and elimination of humidity is not only essential for highly moisture-sensitive reactions like Grignard reactions but can also increase radiochemical yields by preventing the hydrolysis of reagents. For example, [^{11}C]methyl iodide can be hydrolyzed to form the unwanted byproduct [^{11}C]methanol.

The optimization of yields is an essential practice for every radiochemist. In this regard, a particularly useful strategy—especially when working with short-lived radionuclides—lies in minimizing reaction, purification, and transfer times. For carbon-11 and its 20-min physical half-life, reducing the total synthesis time by just 3 min will result in a 10% increase in the yield of the reaction! Shortening the connecting tubes and miniaturizing reactor vessels can lead not only to reduced transportation times but also to reductions in the amount of product lost within the tubes and on vessel walls.

In addition, the consistent performance of radiotracer production ensures high molar/specific activity [3]. In general, every CO_2 source within the early components of the synthesizer can significantly affect molar activity. The main sources for nonradioactive CO_2 are the target gas itself and the connection tube between the target and the synthesizer. Therefore, the quality of the target gas as well as that of the inert gas used for transportation is the most important factor when it comes to low molar activity. Additional CO_2 contamination can also be caused by leaks in the system as well as poor quality traps for humidity or CO_2, especially traps based on molecular sieves or charcoal. Furthermore, one should also pay careful attention to the absence of CO_2 in the hydrogen gas used for the reduction of $[^{11}C]CO_2$ to $[^{11}C]CH_4$. In the end, it becomes clear that comprehensive and constant monitoring of the module is the best way to detect alterations or deteriorations within the system as early as possible and thus to reduce the probability of poor quality productions or even failed syntheses.

Post-target Production: From $[^{11}C]CO_2$ to $[^{11}C]CH_3I$

General Aspects of $[^{11}C]CH_3I$ Production

^{11}C-based methylations are used to introduce a $[^{11}C]CH_3$-moiety into a molecule. They are—by far—the most widely used method for the ^{11}C-labeling of organic molecules. The most commonly used methylation agent is [^{11}C]methyl iodide ($[^{11}C]CH_3I$; [^{11}C]iodomethane), which can be produced either via the so-called "wet" method (Fig. 3) or the gas-phase method (Fig. 4; see also Chap. 11 "Carbon-11-Labeled Precursors for Labeling").

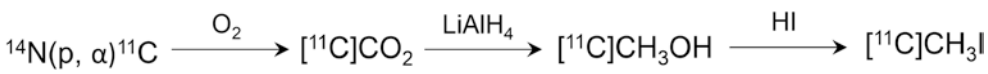

Fig. 3 "Wet" method for the preparation of [^{11}C]methyl iodide

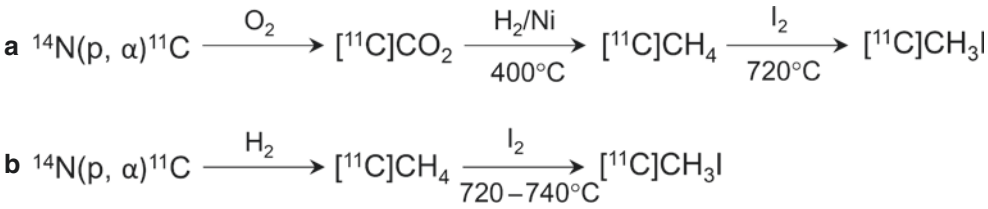

Fig. 4 "Gas-phase" method for the preparation of [^{11}C]methyl iodide. (**a**) Starting from cyclotron-produced [^{11}C]carbon dioxide and (**b**) starting from cyclotron-produced [^{11}C]methane

"Wet" Production of $[^{11}C]CH_3I$

The "wet" chemistry method for the production of [^{11}C]methyl iodide [4] consists of the reduction of [^{11}C]carbon dioxide ($[^{11}C]CO_2$) to [^{11}C]methanol ($[^{11}C]CH_3OH$) via reduction with lithium aluminum hydride ($LiAlH_4$) and subsequent reaction with hydroiodic acid (HI). More specifically, $[^{11}C]CO_2$ is produced in the cyclotron via the $^{14}N(p,\alpha)^{11}C$-reaction and is then trapped in a solution of $LiAlH_4$ in tetrahydrofuran (THF). Thereby $[^{11}C]CO_2$ is reduced to $[^{11}C]CH_3OH$. After the evaporation of the THF, HI is slowly added to the precipitate, and the reaction mixture is heated to 90 °C. The resultant $[^{11}C]CH_3I$ can then be distilled using an ascarite/phosphorus pentoxide trap into the solution containing the organic molecule to be ^{11}C-methylated. This trap is needed to remove excess HI (via ascarite) and to eliminate traces of water (via phosphorus pentoxide), both of which are essential for good methylation yields. This method is not without its drawbacks, of course. For example, the use of $LiAlH_4$ can be associated with low molar activities, and HI can degrade tubing and valves.

Tricks of the Trade To minimize contamination with atmospheric carbon, all sensitive tubes and vials should be flushed with inert gas (such as helium or argon) whenever possible.

"Gas-Phase" Production of $[^{11}C]CH_3I$

Although the "wet" chemistry method is very reliable in terms of radiochemical yields, the "gas-phase" method [5] is more commonly used for the production of [^{11}C]methyl iodide today. This approach is simpler than the "wet" chemistry method and results in higher molar activities due to its avoidance of the use of $LiAlH_4$ (a source of CO_2).

As in the "wet" method, the "gas-phase" method begins when $[^{11}C]CO_2$ is produced in the cyclotron. This $[^{11}C]CO_2$ is commonly trapped on a molecular sieve (4 Å) and converted to $[^{11}C]CH_4$ in the presence of Ni catalyst and hydrogen at 400 °C (Fig. 5). Afterward, $[^{11}C]CH_4$ is reacted with elemental iodine (I_2) at 720–740 °C to produce $[^{11}C]CH_3I$. Since the efficiency of the conversion of $[^{11}C]CH_4$ to $[^{11}C]CH_3I$ is only 20–30%, this process might be repeated a couple of times. Indeed, there are several different technical solutions for this repetition. For example, a pump can be used to pass $[^{11}C]CH_4$ several times through the iodine column in a circulating process to increase the conversion yield. In this approach, a trap has to be installed to collect $[^{11}C]CH_3I$ produced during the reaction. Following the reaction, $[^{11}C]CH_3I$ can be released from the trap via heating and transferred to the reactor using a gentle gas flow (*e.g.* He, 5 mL/min).

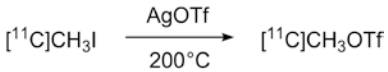

Fig. 5 Synthesis of [^{11}C]methyl triflate

Tricks of the Trade In order to achieve high molar activities of $[^{11}C]CH_3I$, it is essential to continually flush all sensitive tubes and vials with an inert gas such as helium or argon. Furthermore, both the $[^{11}C]CO_2$ trap and the $[^{11}C]CH_3I$ trap must be heated to 400 °C and 190 °C, respectively, immediately prior to the start of synthesis for a couple of minutes in order to remove moisture and atmospheric carbon. During the heating process, the inert gas should constantly flow (20–50 mL/min) through the traps. Before starting the synthesis, the traps have to be cooled down to room temperature again in order to enable efficient trapping.

Transformation of $[^{11}C]CH_3I$ to $[^{11}C]CH_3OTf$

[^{11}C]Methyl triflate ($[^{11}C]CH_3OTf$) is a much more reactive reagent for ^{11}C-methylations and, therefore, is used for the ^{11}C-methylation of nucleophiles with low reactivity (Fig. 6). [^{11}C]Methyl triflate can be produced easily via the passage of $[^{11}C]CH_3I$ through a heated (200 °C) column loaded with graphitized carbon impregnated with silver triflate (AgOTf) [6].

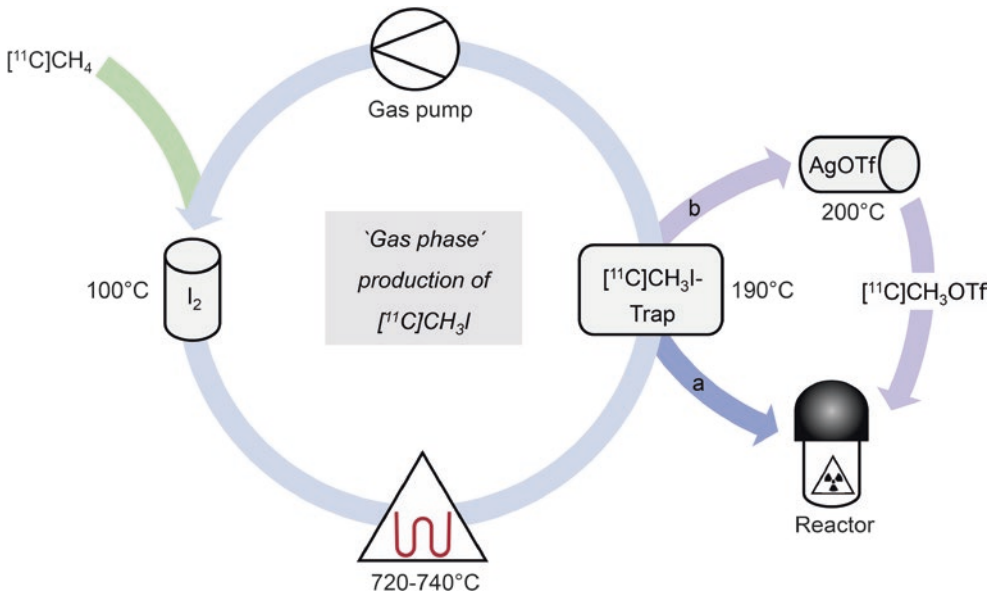

Fig. 6 "Gas-phase" production of [^{11}C]methyl iodide. (a) Direct delivery of [^{11}C]CH_3I into the reactor and (b) online passage of [^{11}C]CH_3I through AgOTf for conversion into [^{11}C]CH_3OTf

Tricks of the Trade The silver triflate (AgOTf)-impregnated graphitized carbon is extremely sensitive to moisture. If it comes into contact with humid air or other sources of moisture, the conversion of [^{11}C]CH_3I into [^{11}C]CH_3OTf will no longer occur, and the AgOTf-impregnated graphitized carbon has to be exchanged. Furthermore, the carbon substrate is sensitive to light and therefore has to be stored in the dark (the column in which this reagent is used has to be "light-proof" as well). After filling the column with the AgOTf-impregnated graphitized carbon, the column must be heated to 200 °C for 2 h under a continuous flow of inert gas (50–100 mL/min) to remove any contamination. The filled column can be reused for multiple syntheses but has to be kept closed under an inert atmosphere or needs to be heated up to 200 °C for 15–20 min under a continuous flow of inert gas (50–100 mL/min) before every synthesis.

A Comparison of the [^{11}C]-Methylation of Amines, Acids/Alcohols, and Thiols

Amines, acids, alcohols, and thiols can all be labeled with [^{11}C]CH_3 moieties. To this end, the functional group in question is reacted with [^{11}C]CH_3I/[^{11}C]CH_3OTf via nucleophilic substitution to create a secondary or tertiary amine, ester, ether, or thioether. ^{11}C-Methylations are quite simple and fast. Indeed, the reaction can often be performed by transferring [^{11}C]CH_3I or [^{11}C]CH_3OTf into a solution containing the precursor and quickly heating (<5 min) up this reaction solution. Solvents like DMSO, acetone, 2-butanone, or acetonitrile are commonly used depending on the temperature and polarity required for the reaction. For the methylation of hydroxyl and carboxyl groups, the addition of a base (*e.g.* NaOH or TBAH) is needed to deprotonate the functional group. In contrast, amines and thiols can be methylated without prior deprotonation. Examples of ^{11}C-methylations are provided in the sections on "Applications of Carbon-11 Tracers Produced Using [^{11}C]MeI" and "[^{11}C]CO_2 Fixation and Its Application."

Tricks of the Trade The precursor for methylation should be dissolved shortly before starting the synthesis. It is best to add the base directly into the solution of the precursor. In addition, one should always remember that heating and cooling might take significant extra time. As a result, gains in radioactive yield created by performing reactions at elevated temperatures may be offset by corresponding losses in yield due to decay.

Applications of Carbon-11 Tracers Produced Using [^{11}C]MeI

As previously mentioned in the section on "Post-target Production: From [^{11}C]CO_2 to [^{11}C]CH_3I", ^{11}C-methylations are the most common type of ^{11}C-labeling reactions. As a result, they have contributed to the development of a variety of important radiotracers with different applications.

^{11}C-Amino Acids

Due to the essential role of amino acids in all kinds of biological processes, several PET tracers based on amino acid scaffolds have been developed and have proved to be a versatile research tools. A variety of ^{11}C-labeling reactions—*e.g.*

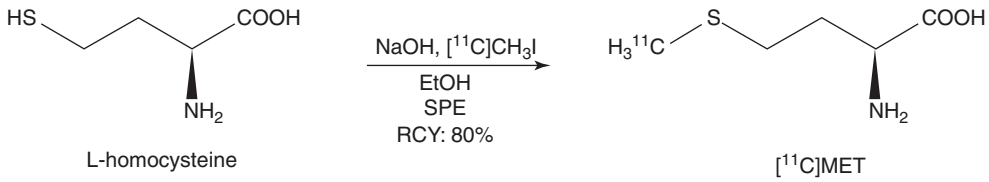

Fig. 7 Radiochemical synthesis of [^{11}C]MET

alkylations, carboxylations, and cyanations—can provide standard and non-standard amino acids which share the (bio) chemical properties of their nonradioactive counterparts. This latter point is particularly important, since ^{18}F-labeled amino acids have been proposed as more practical alternatives to ^{11}C-labeled amino acids. However, the introduction of fluorine atoms can significantly change the chemical properties of an amino acid [7].

L-[Methyl-^{11}C]Methionine The high uptake of [^{18}F]FDG in healthy brain tissues has been described as a major limitation for its use in the imaging of brain tumors. Radiolabeled amino acids such as L-[*methyl*-^{11}C]methionine were proposed as a way to circumvent this issue, since their uptake in a healthy brain is low. Moreover, the upregulation of type L-amino acid carriers in several brain tumors can lead to the increased accumulation of L-[*methyl*-^{11}C]methionine [8]. Although several ^{11}C-labeled amino acids have been used in neuro-oncology, L-[*methyl*-^{11}C]methionine is indisputably the most often employed due to its fast, convenient, and high-yield radiochemical synthesis which enables scans for two to three consecutive patients with the same production batch. While various methods have been described to synthesize L-[*methyl*-^{11}C]methionine, in our hands the most practical way utilizes L-homocysteine as the precursor (in EtOH and activated with 0.1 M NaOH) and [^{11}C]CH_3I as methylation agent (Fig. 7).

Alpha-[^{11}C]Methyl-L-Tryptophan ([^{11}C]AMT) Serotonergic neurotransmission is known to be relevant in different pathways of the brain, such as mood, sleep, feeding, and sexual behavior. Moreover, its dysregulation has been related to numerous neurologic and psychiatric disorders, including depression, affective diseases, and epilepsy. Therefore, the *in vivo* measurement of the rate of serotonin synthesis can provide a reliable view of ongoing serotonergic processes [9]. [^{11}C]AMT is the methylated form of the amino acid tryptophan—a precursor of serotonin (also known as 5-HT)—which is further enzymatically converted to α-[^{11}C]methyl-serotonin ([^{11}C]AM-5HT) in the brain. Unlike native 5-HT, [^{11}C]AM-5HT is not further metabolized by the enzyme monoamine oxidase A and therefore accumulates in serotonergic nerve terminals, a phenomenon which facilitates the evaluation of the synthesis rate of 5-HT [10]. More recently, [^{11}C]AMT has also been used in PET imaging of different tumors, such as breast, brain, and lung cancers [11]. The radiosynthesis [12] of [^{11}C]AMT is quite complex and highly sensitive to traces of moisture (Fig. 8). To wit, the synthesis requires the fresh preparation of lithium diisopropylamide (LDA) at −78 °C as well as the use of gastight syringes for the addition of liquids. LDA serves as a strong base to yield the activated enolate precursor under argon atmosphere that further reacts with [^{11}C]CH_3I. After the ^{11}C-methylation reaction, an acid-catalyzed decyclization steps the basic hydrolysis of the protecting groups, and finally SPE purification provides the desired product: [^{11}C]AMT.

^{11}C-Amino Acid Derivatives

[^{11}C]Choline Prostate carcinomas are the most common type of cancer in men, with particularly high rates of disease in 60–70-year-old men [13]. Although [^{18}F]FDG is by far the most used tracer in oncology, its utility in the diagnosis and staging of prostate cancer is limited due to several factors, including the uptake of the radiotracer in the adjacent urinary bladder, inflammatory conditions, and scar tissue. Therefore, radiotracers such as [^{11}C]choline and its ^{18}F-analogues were developed to target the biosynthesis of cellular membrane (phospholipids), since this process is known to be increased in prostate cancer cells. [^{11}C]Choline is also utilized similarly to L-[*methyl*-^{11}C]methionine in the diagnosis of brain tumors. The radiosynthesis of [^{11}C]choline has been amply described, and excellent yields are always obtained in short synthesis times (Fig. 9). For instance, the reaction takes place smoothly when using a solution of dimethylaminoethanol in DMF as the precursor and [^{11}C]CH_3I as the labeling agent. Purification by means of SPE (without HPLC) is sufficient, since a cation exchange resin can be used due to the cationic nature of the product.

^{11}C-Labeled Neuroimaging Tracers

Neuroimaging is one of the main applications of PET. In fact, the brain was the initial focus of PET imaging when the technology was first introduced, and over the years, numerous PET tracers have been developed to visualize brain functions and characterize neurological and psychiatric disorders. From a chemical point of view, methylated amines are a frequent structural motif in drugs designed for the central

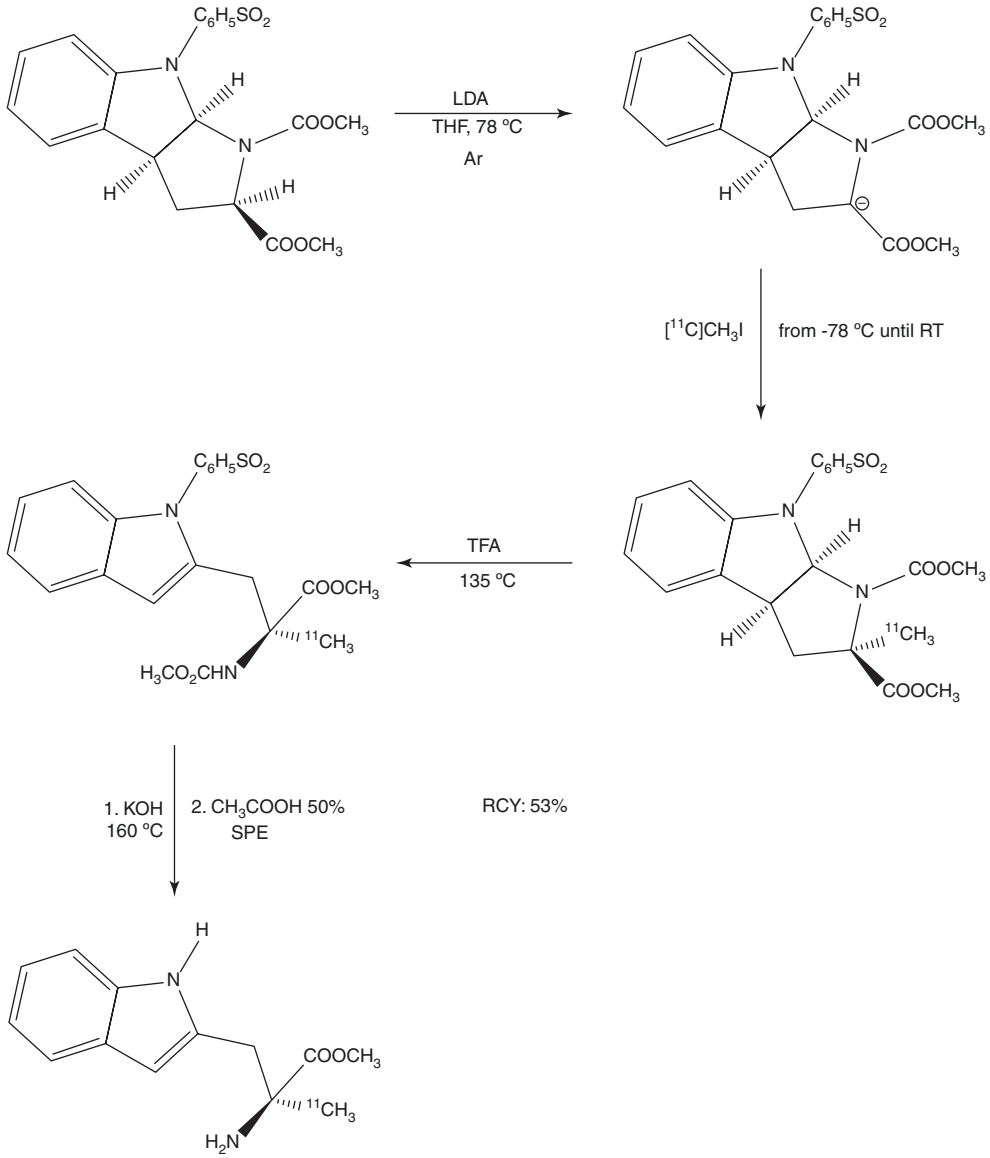

Fig. 8 Radiochemical synthesis of [^{11}C]AMT

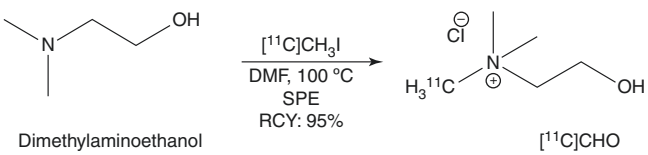

Fig. 9 Radiochemical synthesis of [^{11}C]CHO

nervous system [14]. This has fueled the development of corresponding radiotracers via amine-directed ^{11}C-methylations, although tracers have been developed via the ^{11}C-methylations of alcohols, amides, and thiols as well. Moreover, the metabolic fate of these ^{11}C-methylated tracers usually follows a pathway that involves demethylation, thus producing radioactive metabolites that are more polar and have a lower molecular weight than the parent radiotracer and which often possess low uptake in the brain.

[^{11}C]Pittsburgh Compound B ([^{11}C]PiB) Alzheimer's disease (AD) is a type of dementia characterized by significant loss of neurons and deficiencies in neurotransmitter systems. It accounts for the majority of dementia cases, and its prevalence is estimated to quadruple over the next 50 years [15]. The occurrence of symptoms similar to those present in other types of dementia (*e.g.* mild cognitive impairment) impedes the accurate diagnosis of this disease. Autopsies, however, have revealed that the deposition of β-amyloid (in conjunction with the aggregation of tau protein) is an important hallmark of AD. Therefore, PET imaging of these β-amyloid deposits, also known as plaques, has been described as an effective technique to confront this problem. To this end, [^{11}C]PiB—a thioflavin T analogue—was developed as a tracer to visualize such plaques. It is until now the most applied tracer for the *in vivo* visualization of amyloid plaques, although a couple of ^{18}F-labeled analogues have

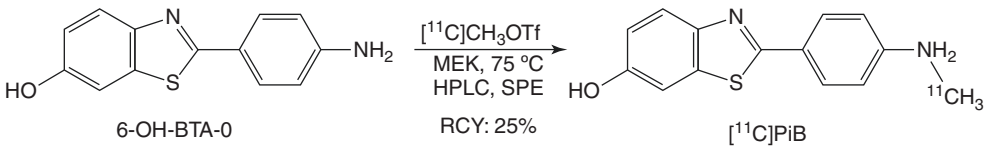

Fig. 10 Radiochemical synthesis of [^{11}C]PiB

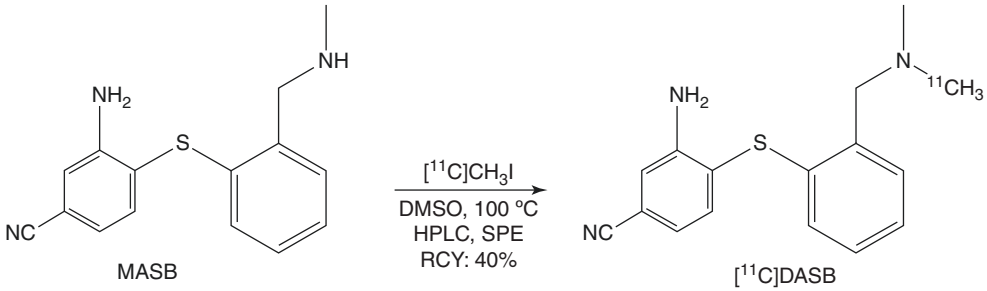

Fig. 11 Radiochemical synthesis of [^{11}C]DASB

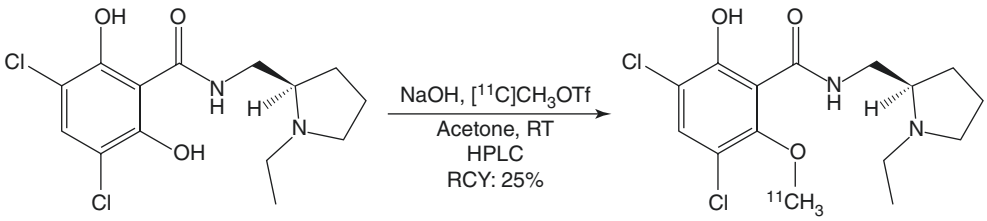

Fig. 12 Radiochemical synthesis of [^{11}C]raclopride

been developed as well. The radiochemical synthesis of [^{11}C]PiB (Fig. 10) initially employed [^{11}C]CH_3I as the labeling agent but was later optimized using [^{11}C]CH_3OTf [16]. In light of the lower nucleophilicity of anilines, the higher reactivity of [^{11}C]CH_3OTf proves beneficial, ultimately creating a simple and efficient strategy for radiolabeling. As usual, purification via HPLC and SPE after the labeling reaction yields the product [^{11}C]PiB.

[^{11}C]3-Amino-4-(2-Dimethylaminomethylphenylsulfanyl)Benzonitrile ([^{11}C]DASB) The serotonin transporter (5-HTT) is a protein located in the plasma membrane of serotonergic neurons which regulates 5-HT concentrations from the synaptic cleft through reuptake into the presynaptic neuron. The *in vivo* assessment of 5-HTT expression and density—although sometimes intricate—can enable enhanced analysis of neuropsychiatric disorders. Dysregulation of 5-HTT has been reported in several conditions, especially depression. Moreover, parallel investigations have suggested the involvement of the 5-HTT polymorphisms in such conditions. Therefore, 5-HTT has been proposed as a target for drugs known as selective serotonin reuptake inhibitors (SSRIs). Although several compounds have been nominated as potential PET radiotracers for 5-HTT, [^{11}C]DASB is widely acknowledged as the gold standard tracer for PET studies of the 5-HTT due to its high affinity and selectivity for its target, high brain uptake, and fast binding equilibrium. The synthesis of [^{11}C]DASB (Fig. 11) occurs in a straightforward manner after the trapping of [^{11}C]CH_3I in a solution containing the precursor—3-amino-4-(2-methylaminomethylphenylsulfanyl)-benzonitrile (MASB)—in DMSO. Afterward, the product is purified using HPLC and SPE [17].

[^{11}C]3,5-Dichloro-N-[[(2S)-1-Ethylpyrrolidin-2-yl] Methyl]-2-Hydroxy-6-Methoxy Benzamide ([Methoxy-^{11}C]Raclopride) The neurotransmitter dopamine exerts its functions through five G-protein-coupled receptors—D_1 and D_5 (both D_1-type receptors) as well as D_2, D_3, and D_4 (all three D_2-type receptors)—which possess a broad distribution in the brain and also in the peripheral nervous system. Moreover, the involvement of the dopamine receptor system in a variety of diseases has been reported, including movement disorders such as Parkinson's and Huntington's diseases. In particular, the role of the D_2/D_3 receptors in these conditions has been investigated with [*methoxy*-^{11}C]raclopride (Fig. 12) by evaluating the density of these postsynaptic receptors in the striatum. [*Methoxy*-^{11}C]Raclopride is a benzamide derivative and a highly selective D_2/D_3 receptor antagonist which possesses a moderate affinity toward these receptors. The synthesis of [*methoxy*-^{11}C]raclopride has been reported using both [^{11}C]CH_3I and [^{11}C]CH_3OTf, though the latter has shown to produce higher radiochemical yields. To this end, a solution of desmethyl-raclopride in acetone or 2-butanone together with 5 M sodium hydroxide is commonly used as precursor solution and kept at low temperatures (15–20 °C) during the trapping of [^{11}C]CH_3OTf. After the labeling reaction, the product is purified via HPLC. By using the

appropriate conditions for this purification, the fraction containing the product can be directly filtered into the product vial without further treatment (*i.e.* no SPE necessary).

[^{11}C]Harmine ([^{11}C]HAR) The degradation of monoamine neurotransmitters (*e.g.* 5-HT, dopamine, or norepinephrine) plays a key role in the regulation of neurotransmission. A type of enzymes known as monoamine oxidases (MAO)—and more specifically the enzyme MAO-A—is responsible for the degradation of the neurotransmitters mentioned above. MAO-A is primarily found in catecholaminergic neurons, and its dysregulation has been correlated with several behavioral and neuronal disease states, including panic, bipolar affective, and major depressive disorders. Besides its expression in the brain, MAO-A is also located in cardiac muscle cells, where it has been identified as a major source of reactive oxygen species (ROS) that can affect function and viability of the myocardium. The *in vivo* measurement of the density of MAO-A has been achieved with a couple of PET ligands, including the β-carboline derivative [^{11}C]HAR, which is a reversible inhibitor of MAO-A that displays high affinity and selectivity for the enzyme. The radiosynthesis of [^{11}C]HAR requires a base for the formation of the phenoxide anion (Fig. 13) that subsequently reacts with [^{11}C]CH_3I [18]. Therefore, a solution of the precursor harmol in DMSO must be freshly prepared for each radiosynthesis prior to the addition of 5 M sodium hydroxide. The resulting solution should be light yellow; a green-colored solution should not be obtained.

[^{11}C]CO_2 Fixation and Its Application

Introduction to [^{11}C]CO_2 Fixation Chemistry

The application of [^{11}C]CO_2 as a starting material for ^{11}C-radiosyntheses is attractive for accessing functional groups with high oxidation states such as carboxylic acids, ureas, and carbamates (Fig. 14). From a chemical point of view, the direct incorporation of [^{11}C]CO_2 into radiotracers is quite challenging, as carbon dioxide is unreactive, and thus

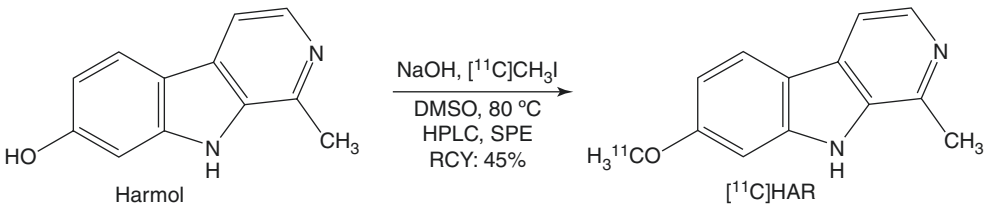

Fig. 13 Radiochemical synthesis of [^{11}C]HAR

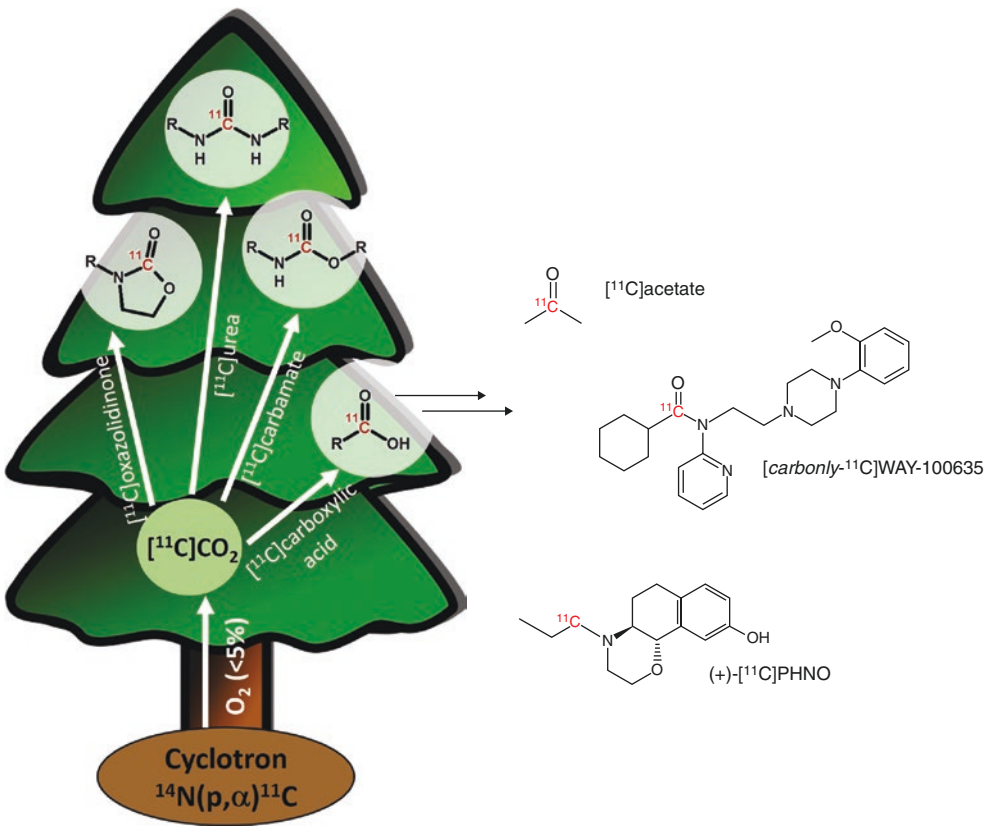

Fig. 14 Reaction pathways to [^{11}C]CO_2 fixation products yielding in high oxidation state functional groups

highly reactive nucleophiles or catalysts must be used to facilitate the effective fixation of [^{11}C]CO_2 [19].

A successful synthetic procedure for the fixation of [^{11}C]CO_2 uses organometallic reagents such as Grignard reagents, organolithiums, or silanamines. The functional groups formed through these reactions are mostly carboxylic acids and derivatives thereof such as carboxyamides. In general, these very reactive reagents are moisture sensitive and unstable, which makes automation cumbersome and reproducibility difficult (for a discussion of Grignard reactions, see the section on "Grignard Reactions in Carbon-11 Radiochemistry (In-Loop)." In contrast, transition metal-mediated carboxylation reactions involving organoboron and organozinc reagents are superior in terms of the stability of the reagents.

The spectrum of CO_2 fixation agents has recently expanded, especially due to the growing field of "green" chemistry and approaches involving guanidines and amidines. These strategies facilitate the formation of functional groups with even higher oxidation states than carboxylic acid derivatives, including ureas, carbamates, and oxazolidinones [20].

Grignard Reactions in Carbon-11 Radiochemistry (In-Loop)

Grignard reactions involve organometallic compounds—alkyl or aryl magnesium halides—which work as nucleophiles, attacking electrophilic carbons and leading to the formation of carbon-carbon bonds. In radiochemistry, [^{11}C]CO_2 typically serves as the electrophilic reagent for these reactions. Grignard reactions can be performed rapidly and quantitatively. These traits, along with the direct availability of [^{11}C]CO_2 from cyclotrons, make this approach highly attractive for the production of PET radiotracers. One of the most popular PET tracers, [^{11}C]acetate, was developed by Pike *et al.* more than 35 years ago and is produced via a Grignard reaction using [^{11}C]CO_2 [21]. Since then, the most common radioactive carboxylation reactions have been the syntheses of [^{11}C]acetate and [^{11}C]palmitate. Grignard reactions have also been applied to the production of [*carbonyl*-^{11}C]WAY100635 and (+)-[^{11}C]PHNO, two important radiotracers in neuroimaging. The syntheses of both were described by Mark *et al.* using a loop for the Grignard reaction [22].

Moisture Sensitivity, Solvents, and Preparation

Grignard reagents are extremely sensitive to moisture, and any contact with water results in the formation of magnesium hydroxides that precipitate in organic solvents. Therefore, the synthesis module in which the Grignard reaction takes place must be moisture-free. It is not possible to keep the whole hot cell under inert atmosphere, but the operator should avoid any water contamination inside the cell while preparing the synthesizer. The optimal strategy for cleaning and preparing a synthesizer prior to Grignard reactions is comprised of three washing steps. First, the system is washed with water to remove all hydrophilic impurities. Afterward, acetone is used as a cleaning agent to eliminate any water residue. Finally, an additional wash is performed with a nonpolar organic solvent, typically the same substance used for performing the reaction. The last washing is critical, as acetone itself contains an electrophilic carbon (a ketone) that is susceptible to attack by Grignard reagent. In addition, all lines must be properly dried with an inert gas, typically helium or argon. Grignard reactions require dry and aprotic solvents such as diethylether or tetrahydrofuran (THF). Furthermore, it is important to consider that these solvents may contain stabilizing agents that can hinder the synthesis or lead to the formation of by-products. Hence, the use of freshly distilled solvents is recommended, as they are free of any stabilizers and completely dry. Moreover, the organometallic reagent must be used within a short period of time to obtain good molar activities. The reason is clear: the ubiquitous presence of CO_2. The diffusion of air (containing atmospheric CO_2) through the septum of the storage bottle may take place, leading to the incorporation of this CO_2—rather than [^{11}C]CO_2—into the Grignard reagent even at room temperature or during storage.

Technical Considerations: Reaction Vessels Versus In-Loop Syntheses for Grignard Reactions

Grignard reactions can be performed in every vial or vessel that enables reactions under inert atmosphere. Two approaches are commonly used for Grignard-based radiosyntheses. The first is the "classical" vessel-based method using a reactor. The second approach, in contrast, uses a polymeric loop as the site of the reaction. Both approaches have advantages and disadvantages. As a result, preparations of [^{11}C]acetate, for example, using both methods have been published [23, 24]. For reactions in a conventional reactor, the metal halide precursor is dissolved in an aprotic and dry solvent, and [^{11}C]CO_2 is bubbled through the precursor solution. Subsequently, the reaction is quenched and the solvents are evaporated. Thereafter, the product is purified by a distillation step, leaving metal-hydroxyl impurities inside the reactor vessel and transferring the clean product to a product vial. On the one hand, this purification method is relatively elegant and efficient for one-step reactions. On the other hand, the distillation step is time-consuming and requires a tight system that is both temperature- and pressure-stable. Therefore, this approach is not practical for radiosyntheses involving multistep reactions during which the decay of carbon-11 plays a dominant role in the determination of yield.

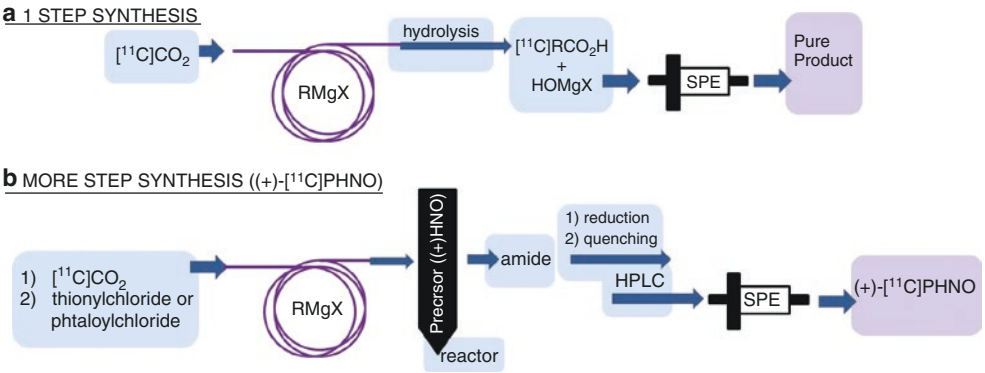

Fig. 15 Scheme of in-loop syntheses for (**a**) a one-step reaction and (**b**) a multistep synthesis of (+)-[^{11}C]PHNO

The alternative method is the "in-loop" synthesis (Fig. 15). In this case, the inner surface of a polymer loop is coated with the Grignard solution by pushing it through the loop with a flow of an inert gas. Subsequently, [^{11}C]CO_2 is passed through the impregnated loop, and it reacts with the organometallic reagent. When performing a one-step reaction that forms a carboxylic acid salt, the crude mixture can then be purified using an HPLC system. In case of multistep reactions (e.g., (+)-[^{11}C]PHNO and [*carbonyl*-^{11}C]WAY-100635), the intermediate species remain in the loop and are eluted into a reaction vessel during the subsequent step. Perhaps not surprisingly, the length and material of the loop must be tested and optimized for each application. The loop material must exhibit low non-specific binding and resistance to both the Grignard reagent and its solvent. The in-loop reaction boasts high conversion rates due to reaction of the reagents on the large surface area of the loops. Accordingly, one significant advantage of the in-loop method is the possibility of fast conversion reactions without the need for cooling or heating. Additionally, plastic tubes are usually available in each laboratory, so in-loop syntheses are easily accessible for anyone and offer a plethora of synthesis possibilities. However, the crude reaction mixture of multistep "in-loop" reactions must be purified via distillation or the use of SPE cartridges in a manner similar to that used for vial-based systems.

Other Applications: Neuroimaging Using (+)-[^{11}C]PHNO and [Carbonyl-^{11}C]WAY-100635

In neuroimaging, radiotracers that specifically target receptors or transporters with high (subtype) selectivity are used. In this respect, (+)-[^{11}C]PHNO and [*carbonyl*-^{11}C]WAY-100635 are applied to target dopamine D_2/D_3 receptors ((+)-[^{11}C]PHNO) or serotonin-1A receptors ([*carbonyl*-^{11}C]WAY-100635), respectively, for the visualization of physiological processes in the brain or mental disorders like schizophrenia or depression. The production of these radiotracers requires multistep syntheses, after which by-products are removed. Both syntheses start with the Grignard reaction followed by the conversion of the carboxyl group to the respective carboxylic acid chloride using thionyl chloride. The crude mixture is transferred to a reactor containing the dissolved precursor—(+)HNO or WAY-100634, respectively—by pushing the thionyl chloride/THF solution through the loop. While the reaction of [*carbonyl*-^{11}C]WAY-100635 is stopped after a heating step, the synthesis of (+)-[^{11}C]PHNO requires an additional step in which $LiAlH_4$ is used to reduce the acyl intermediate to the alkyl product [25–27]. The purification of both compounds takes place via semi-preparative HPLC, and SPE is subsequently used to remove the organic solvents used during chromatography (as described in the section on "Technical Aspects of Carbon-11: Commercially Available Synthesizers and Optimization"). To conclude, Grignard reactions are a versatile tool for the incorporation of carbon-11 into radiotracers and have become well-established in the clinic. Moreover, the advent of in-loop syntheses has made them even more accessible for multistep reactions in radiochemistry.

Tricks of the Trade Careful attention should be dedicated to the removal of all traces of water/moisture from all equipment used with reactive Grignard species. Ideally, single-use materials should be employed for these steps. Stabilizers (*e.g.* xylene) in reagents and solvents should also always be avoided, as they might lead to the formation of by-products.

Application of Other Carbon-11 Precursors in Tracer Preparation

Overview of Other Methodologies for the Production of ^{11}C-Labeled Radiotracers

The vast majority of carbon-11 tracers are produced via reaction with electrophilic methylating agents such as [^{11}C]CH_3I or [^{11}C]CH_3OTf. In the section on "[^{11}C]CO_2 Fixation and Its Application," we have seen that the reaction between

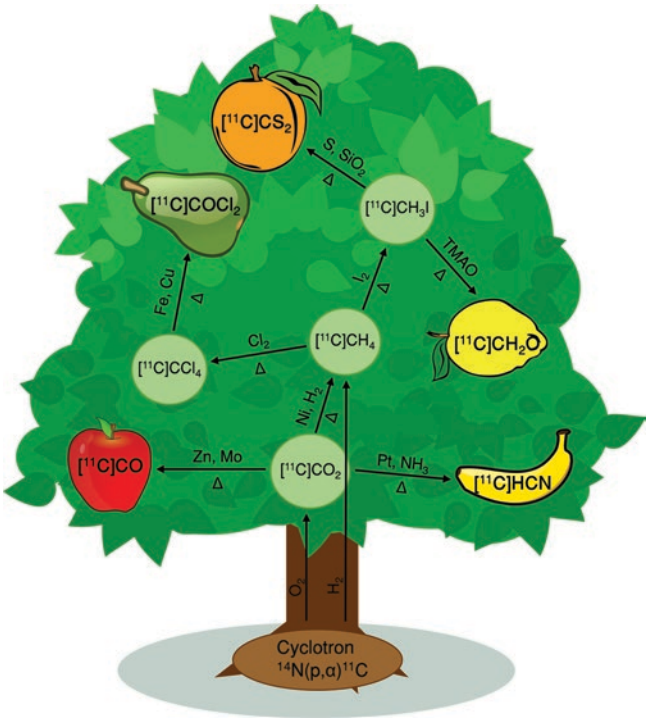

Fig. 16 Reaction pathways to less-common carbon-11 precursors

Grignard reagents and $[^{11}C]CO_2$ has also become a well-established route to ^{11}C-based radiotracers. Considering the breadth of carbon chemistry, it is surprising that ^{11}C-labeled radiotracers are almost exclusively synthesized from a small variety of radiolabeled precursors. This imbalance between what is *possible* and what is *feasible* can be attributed to the high degree of automation and time constraints associated with ^{11}C-based radiosyntheses. However, unconventional carbon-11 precursors are nonetheless important tools that can both open up synthetic pathways to otherwise inaccessible radiotracers and enable the labeling of a higher number of positions within a molecule. An assortment of such rarely used carbon-11 precursors is shown in Fig. 16 as lower- and higher-hanging fruits [28].

Carbonylation

The term "carbonylation" refers to the introduction of carbon monoxide into organic or inorganic molecules. $[^{11}C]CO$ can be straightforwardly and rapidly (<5 min) obtained via the reduction of $[^{11}C]CO_2$ over zinc or molybdenum in high radiochemical yields. However, compared to the other carbon-11 precursors discussed in this chapter, $[^{11}C]CO$ is quite unreactive. One strategy to increase the reactivity of $[^{11}C]CO$ is to apply pressures of 350+ bar within an autoclave system in order to increase its solubility and shift the reaction equilibrium toward nongaseous products. Obviously, however, this high-pressure process comes with disadvantages such as high-maintenance intervals and complexity. In response to the drawbacks of high-pressure processes, lower-pressure methods have been developed. Generally, ^{11}C-carbonylations are typically performed using transition metal-mediated cross-couplings between nucleophilic and electrophilic reagents, thereby enabling the synthesis of a variety of carbonyl-labeled moieties (*e.g.* esters, amides, hydrazines, acrylamides, and carbamates). Not surprisingly, the ligand system of the transition metal strongly affects the efficiency of $[^{11}C]CO$ trapping and therefore the radiochemical yield [29]. One example of ^{11}C-carbonylation is the synthesis of [*carbonyl*-^{11}C]raclopride, which is labeled at a metabolically more stable position than the better known [*methoxy*-^{11}C] raclopride (Fig. 17).

Reactive C=O Species: $[^{11}C]$Formaldehyde and $[^{11}C]$Phosgene

Formaldehyde is a well-studied and multifaceted reagent which can be used for a myriad of reactions. As early as 1972, $[^{11}C]$formaldehyde ($[^{11}C]HCHO$) was prepared via the ferric-molybdenum oxide-catalyzed oxidation of $[^{11}C]$methanol. However, the specialized equipment required for this procedure hampered the application of this approach in most carbon-11 laboratories. Recently, $[^{11}C]$formaldehyde has been prepared in a one-pot synthesis by treating $[^{11}C]CH_3I$ with trimethylamine *N*-oxide (TMAO), a strategy which has greatly widened the scope of its application and led to a series of novel radiotracers [30]. Examples of radiosyntheses performed with $[^{11}C]$formaldehyde include reductive aminations, ring closure reactions, and electrophilic aromatic substitution. Depending on the substrate, a reductive amination approach can have several advantages compared to conventional $[^{11}C]CH_3I$-based methylations, including insensitivity to moisture, reduced cross-reactivity with other nucleophiles, and avoidance of alkaline reaction conditions. This, in turn, helps radiochemists eschew protecting groups when using this strategy, as illustrated by the conversion of serotonin to *N*-$[^{11}C]$methylserotonin (see Fig. 17) [31].

Considering its high reactivity and the high number of functional groups that it could theoretically label, $[^{11}C]$phosgene ($[^{11}C]COCl_2$) is a very promising carbon-11 precursor. However, the use of $[^{11}C]COCl_2$ has remained limited to a small number of groups due to its cumbersome synthesis. Typical procedures for the synthesis of $[^{11}C]$phosgene involve the chlorination of $[^{11}C]CH_4$ to form $[^{11}C]CCl_4$, which is then oxidized at high temperature in the presence of iron or copper catalysts without the intentional addition of oxygen. In another synthetic route which has increased the reliability of the synthesis of $[^{11}C]$phosgene, the ^{11}C-labeled synthon is formed in the pretreatment tube of a commercially

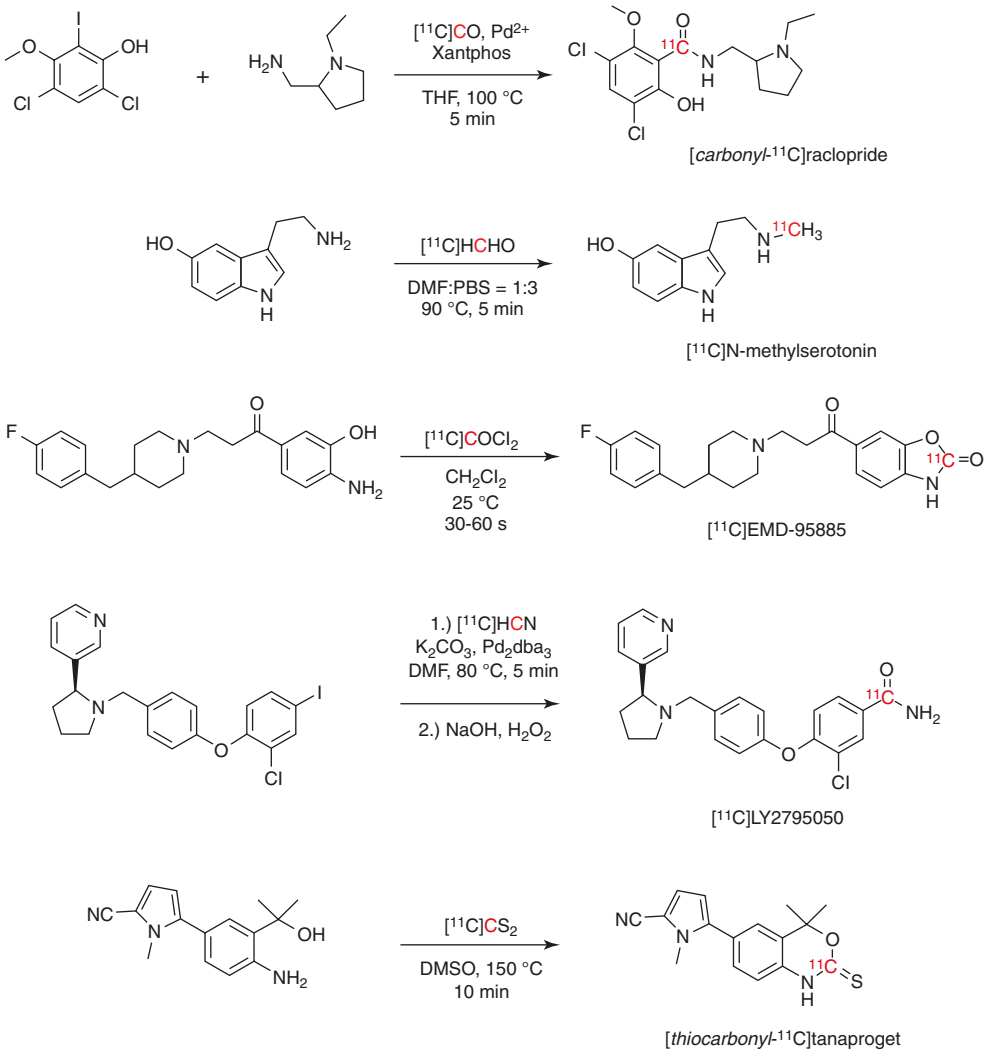

Fig. 17 Representative reactions of the carbon-11 precursors discussed in this chapter

available CCl_4 gas detection system. A variety of structures are accessible using [^{11}C]phosgene-based radiolabeling reactions, including amides, carbamates, ureas, and uric acids [32]. Indeed, the high reactivity of [^{11}C]phosgene is exemplified by the almost instantaneous formation of [^{11}C]EMD-95885 (see Fig. 17) [33].

[^{11}C]Hydrogen Cyanide ([^{11}C]HCN)

Due to the cataclysmic combination of toxicity with volatility, even experienced synthetic chemists try to avoid using hydrogen cyanide. Radiochemists, however, can work with [^{11}C]HCN as carbon-11 precursor without fear, since the amount used lies far below that which is dangerous. [^{11}C]HCN can be prepared by reacting [^{11}C]CH_4 with NH_3 over a platinum catalyst at 950 °C [34]. [^{11}C]HCN is then typically reacted with nitriles bearing aromatic halides or aryl-boronic acids under transition metal-catalyzed conditions. Furthermore, aryl nitriles can be obtained via nucleophilic aromatic substitution with activated arenes. Alpha-amino acids can be synthesized via the nucleophilic ring opening of activated aziridines or the Strecker reaction from aldehydes or ketones. Radiolabeling with [^{11}C]HCN offers more than just a one-step reaction to nitriles, since amides, carboxylic acids, and amines can be readily generated from subsequent reactions. For example, in the synthesis of [^{11}C]LY2795050, the radiolabeled nitrile is hydrolyzed to a primary amide (see Fig. 17) [35]. However, it is important to note that HCN readily adsorbs on stainless steel, and thus inert tubing (*e.g.* Teflon™) must be used in order to avoid the loss of [^{11}C]HCN in transport lines.

[^{11}C]Carbon Disulfide ([^{11}C]CS_2)

Compared to CO_2, carbon disulfide (CS_2) has weaker double bonds and thus increased reactivity. CS_2 is a liquid under standard conditions and is readily condensed and trapped in solution, making it a relatively easy-to-handle carbon-11

precursor. [^{11}C]CS_2 can be obtained by passing [^{11}C]CH_3I over a column containing elemental sulfur and sand at 500 °C. [^{11}C]Dithiocarbamate salts can be formed by reacting [^{11}C]CS_2 at room temperature with a variety of primary amines. Upon heating these salts, they release H_2S and further react to form symmetrical [^{11}C]thiocarbonyl-labeled thioureas. In the presence of electrophilic alkylating agents, thioureas can furthermore be S-alkylated, thereby opening up access to a wide variety of target structures. The three-step reaction from [^{11}C]CS_2 to *S*-alkylated thioureas can be performed in a one-pot setup which is rapid enough for carbon-11 chemistry and results in high radiochemical yields and purities. [^{11}C]Carbon disulfide can also be used for ring closure reactions between amines and alcohols, as illustrated by the synthesis of [*thiocarbonyl*-^{11}C]tanaproget (see Fig. 17) [36].

Technical Advantages: Solid Support, Online, or Other Approaches

The chemical behavior of most carbon-11 precursors (*e.g.* [^{11}C]CH_3I) is best studied (and understood) in solution. Therefore, it appears logical that the majority of ^{11}C-labeling reactions are conducted in the solution phase as well. Indeed, vial-based "in-solution" reactions are predominantly used in carbon-11 chemistry, but reactions on solid supports—such as "on-cartridge" or "in-loop" reactions (see the section on "[^{11}C]CO_2 Fixation and Its Application")—have been developed as well. Syntheses using solid supports offer several advantages that are especially important in carbon-11 chemistry, such as decreased reaction times, higher degrees of automation, and enhanced reliability. This is illustrated by the "on-cartridge" synthesis of [*N-methyl*-^{11}C]choline, in which the precursor 2-dimethylaminoethanol is loaded onto a C_{18} cartridge prior to synthesis. [^{11}C]CH_3I is then distilled across the C_{18} cartridge, and a cationic exchange cartridge is sufficient for the subsequent purification of the product, enabling an overall synthesis time of 12 min from the end of bombardment (EOB) [37].

The Bottom Line

- Speed up! Time is crucial when dealing with carbon-11. All processes from EOB to product release after quality control need to be optimized for minimal time consumption in order to obtain sufficient yields and high molar activities.
- The most important reaction pathway for ^{11}C-radiochemistry is ^{11}C-methylation, and the most important synthon is [^{11}C]methyl iodide ([^{11}C]CH_3I). For higher reactivity, [^{11}C]methyl triflate ([^{11}C]CH_3OTf) can be prepared directly from [^{11}C]CH_3I.
- The use of other ^{11}C-labeled synthons opens additional routes for ^{11}C-radiolabeling in different positions and makes it possible to incorporate carbon-11 into some molecules for which [^{11}C]CH_3I and [^{11}C]CH_3OTf are unsuitable. Along these lines, [^{11}C]CO_2, [^{11}C]CS_2, [^{11}C]$COCl_2$, [^{11}C]HCHO, [^{11}C]CO, or [^{11}C]HCN is used.
- Grignard reactions are attractive due to their ability to incorporate [^{11}C]CO_2, but they are extremely moisture-sensitive and require the use of aggressive chemicals. This makes the automation of these ^{11}C-radiosyntheses very challenging.
- The most widely applied ^{11}C-radiotracer is the amino acid L-[*methyl*-^{11}C]methionine. Clinically, it is mainly used to assess brain tumors.
- ^{11}C-Labeled compounds play a particularly important role in neuroimaging and studying specific processes of nerve cells. Important radiotracers in this respect are [^{11}C]raclopride, [^{11}C]DASB, and [^{11}C]PiB (among many others).

References

1. Shao X, Hoareau R, Runkle AC, Tluczek LJM, Hockley BG, Henderson BD, et al. Highlighting the versatility of the Tracerlab synthesis modules. Part 2: fully automated production of [11C]-labeled radiopharmaceuticals using a Tracerlab FX C-pro. J Label Compd Radiopharm. 2011;54(14):819–38.
2. European Directorate for the Quality of Medicines (EDQM). Parenteral Preparations. In: European Pharmacopoeia, 9th Edition. Strasbourg: Council of Europe; 2015. pp. 871–3.
3. Gómez-Vallejo V, Llop J. Specific activity of [11C]CH3I synthesized by the "wet" method: main sources of non-radioactive carbon. Appl Radiat Isotop. 2009;67(1):111–4.
4. Långström B, Lundqvist H. The preparation of 11C-methyl iodide and its use in the synthesis of 11C-methyl-L-methionine. Int J Appl Radiat Isot. 1976;27(7):357–63.
5. Larsen P, Ulin J, Dahlstrom K, Jensen M. Synthesis of [11C] iodomethane by iodination of [11C]methane. Appl Radiat Isotop. 1997;48(2):153–7.
6. Jewett DM. A simple synthesis of [11C]methyl triflate. Int J Radiat Appl Instrum A. 1992;43(11):1383–5.
7. Ermert J, Coenen HH. Methods for 11C- and 18F-labelling of amino acids and derivatives for positron emission tomography imaging. J Label Compd Radiopharm. 2013;56(3–4):225–36.
8. Crippa F, Alessi A, Serafini GL. PET with radiolabeled aminoacid. Q J Nucl Med Mol Imaging. 2012;56(2):151–62.
9. Visser AKD, van Waarde A, Willemsen ATM, Bosker FJ, Luiten PGM, den Boer JA, et al. Measuring serotonin synthesis: from conventional methods to PET tracers and their (pre)clinical implications. Eur J Nucl Med Mol Imaging. 2011;38(3):576–91.
10. Diksic M, Nagahiro S, Sourkes TL, Yamamoto YL. A new method to measure brain serotonin synthesis in vivo. I. Theory and basic data for a biological model. J Cereb Blood Flow Metab. 1990;10(1):1–12.
11. Huang X, Xiao X, Gillies RJ, Tian H. Design and automated production of 11C-alpha-methyl-l-tryptophan (11C-AMT). Nucl Med Biol. 2016;43(5):303–8.
12. Chakraborty PK, Mangner TJ, Chugani DC, Muzik O, Chugani HT. A high-yield and simplified procedure for the synthesis of α-[11C]methyl-l-tryptophan. Nucl Med Biol. 1996;23(8):1005–8.

13. Reske SN, Blumstein NM, Neumaier B, Gottfried H-W, Finsterbusch F, Kocot D, et al. Imaging prostate cancer with 11C-choline PET/CT. J Nucl Med. 2006;47(8):1249–54.
14. Engkvist O, Wrede P, Rester U. Prediction of CNS activity of compound libraries using substructure analysis. J Chem Inf Comput Sci. 2003 Jan 1;43(1):155–60.
15. Cohen AD, Klunk WE. Early detection of Alzheimer's disease using PiB and FDG PET. Neurobiol Dis. 2014;72(Pt A):117–22.
16. Philippe C, Haeusler D, Mitterhauser M, Ungersboeck J, Viernstein H, Dudczak R, et al. Optimization of the radiosynthesis of the Alzheimer tracer 2-(4-N[11C]methylaminophenyl)-6-hydroxybenzothiazole ([11C]PIB). Appl Radiat Isot. 2011;69(9):1212–7.
17. Haeusler D, Mien L-K, Nics L, Ungersboeck J, Philippe C, Lanzenberger RR, et al. Simple and rapid preparation of [11C] DASB with high quality and reliability for routine applications. Appl Radiat Isot. 2009;67(9):1654–60.
18. Philippe C, Zeilinger M, Mitterhauser M, Dumanic M, Lanzenberger R, Hacker M, et al. Parameter evaluation and fully-automated radiosynthesis of [11C]harmine for imaging of MAO-A for clinical trials. Appl Radiat Isot. 2015;97:182–7.
19. Rotstein BH, Liang SH, Holland JP, Collier TL, Hooker JM, Wilson AA, Vasdev N. 11CO2 fixation: a renaissance in PET radiochemistry. Chem Commun (Camb). 2013;49(59):5621–9.
20. Mossine AV, Brooks AF, Jackson IM, Quesada CA, Sherman P, Cole EL, et al. Synthesis of diverse 11C-labelled PET radiotracers via direct incorporation of [11C]CO2. Bioconjug Chem. 2016;27(5):1382–9.
21. Pike VW, Eakins MN, Allan RM, Selwyn AP. Preparation of [1−11C]acetate—an agent for the study of myocardial metabolism by positron emission tomography. Int J Appl Radiat Isot. 1982;33(7):505–12.
22. Rami-Mark C, Unbergsboek J, Haeusler D, Nics L, Philippe C, Mitterhauser M, et al. Reliable set-up for in-loop 11C-carboxylations using Grignard reactions for the preparation of [carbonyl-11C]WAY-100635 and [11C]-(+)-PHNO. Appl Radiat Isot. 2013;82:75–80.
23. Mitterhauser M, Wadsak W, Krcal A, Schmaljohann J, Bartosch E, Eidherr H, et al. New aspects on the preparation of [11C]acetate—a simple and fast approach via distillation. Appl Radiat Isot. 2004;61(6):1147–50.
24. Soloviev D, Tamburella C. Captive solvent [11C]acetate synthesis in GMP conditions. Appl Radiat Isot. 2006;64(9):995–1000.
25. Plisson C, Huiban M, Pampols-Maso S, Singleton G, Hill SP, Passchier J. Automated preparation of the dopamine D2/3 receptor agonist ligand [11C]-(+)-PHNO for human PET imaging studies. Appl Radiat Isot. 2012;70(2):380–7.
26. Wilson AA, McCormick P, Kapur S, Willeit M, Garcia A, Hussey D, et al. Radiosynthesis and evaluation of [11 C]-(+)-4-Propyl-3,4,4a,5,6,10b-hexahydro-2 H -naphtho[1,2- b][1,4]oxazin-9-ol as a potential radiotracer for in vivo imaging of the dopamine D2 high-affinity state with positron emission tomography. J Med Chem. 2005;48(12):4153–60.
27. Oya S, Joseph SK, Carberry P, Divgi CR, Koren AO. Preparation of [11C]-(+)-PHNO using an automated synthesizer coupled with a stand-alone system for making [11C]propionyl chloride. J Label Compd Radiopharm. 2013;56:466.
28. Dahl K, Halldin C, Schou M. New methodologies for the preparation of carbon-11 labeled radiopharmaceuticals. Clin Transl Imaging. 2017;5(3):275–89.
29. Kealey S, Gee A, Miller PW. Transition metal mediated [11C] carbonylation reactions: recent advances and applications. J Label Compd Radiopharm. 2014;57(4):195–201.
30. Hooker JM, Schönberger M, Schieferstein H, Fowler JS. A simple, rapid method for the preparation of [11C]formaldehyde. Angew Chem Int Ed Engl. 2008;47(32):5989–92.
31. Wu C, Li R, Dearborn D, Wang Y. Reductive amination with [11C] formaldehyde: a versatile approach to radiomethylation of amines. Int J Org Chem. 2012;2(3):202–23.
32. Ogawa M, Takada Y, Suzuki H, Nemoto K, Fukumura T. Simple and effective method for producing [11C]phosgene using an environmental CCl4 gas detection tube. Nucl Med Biol. 2010;37(1):73–6.
33. Roger G, Dollé F, de Bruin B, Liu X, Besret L, Bramoullé Y, et al. Radiosynthesis and pharmacological evaluation of [11C]EMD-95885: a high affinity ligand for NR2B-containing NMDA receptors. Bioorg Med Chem. 2004;12(12):3229–37.
34. Scott PJH. Radiochemical syntheses. Volume 2: further radiopharmaceuticals for positron emission tomography and new strategies for their production. Hoboken: John Wiley & Sons; 2015.
35. Ma L, Placzek MS, Hooker JM, Vasdev N, Liang SH. [11C] Cyanation of arylboronic acids in aqueous solutions. Chem Commun (Camb). 2017;53(49):6597–600.
36. Haywood T, Kealey S, Sánchez-Cabezas S, Hall JJ, Allott L, Smith G, et al. Carbon-11 radiolabelling of organosulfur compounds: 11C synthesis of the progesterone receptor agonist tanaproget. Chem Eur J. 2015;21:9034–8.
37. Pascali C, Bogni A, Iwata R, Cambiè M, Bombardieri E. [11C] Methylation on a C18 Sep-Pak cartridge: a convenient way to produce [N-methyl-11C]choline. J Labelled Comp Radiopharm. 2000;43:195–203.

The Radiopharmaceutical Chemistry of Nitrogen-13 and Oxygen-15

Vanessa Gómez-Vallejo, Luka Rejc,
Fernando López-Gallego, and Jordi Llop

Nitrogen-13 (^{13}N) and oxygen-15 (^{15}O) are positron-emitting radionuclides, and their main properties are described in Table 1. Due to their short half-lives ($t_{1/2}$), it is usually not possible to distribute ^{13}N- or ^{15}O-labeled radiotracers from production facilities to remote end-users. They also have high positron energies and, consequently, large positron ranges (5.5 and 8.4 mm for ^{13}N and ^{15}O, respectively; see Table 1), especially compared to other commonly used positron emitters such as ^{11}C or ^{18}F (maximum ranges of 4.1 and 2.4 mm, respectively). These factors have limited the use of ^{13}N and ^{15}O in radiopharmaceutical chemistry.

However, there are several reasons to consider these two radionuclides as potential alternatives to other positron-emitting radionuclides for the preparation of positron emitter-labeled radiotracers: (i) stable isotopes of both oxygen and nitrogen are ubiquitous in biologically active molecules; (ii) both radionuclides can be produced efficiently in a variety of chemical forms using biomedical cyclotrons; and (iii) short-lived radionuclides reduce the radiation doses to subjects, enable repeated studies within a single day, and significantly ease the logistics of waste disposal. These advantages—taken together with the widespread installation of biomedical cyclotrons as well as recent advances in automation and microfluidic chemistry—promise to usher in a new era for ^{15}O and ^{13}N in nuclear medicine. These two radionuclides could be valuable options for the preparation of new radiolabeled compounds, particularly those in which the position of the radionuclide can be changed within the molecule without changing its overall structure. This promises to be extremely useful in helping understand the *in vivo* behavior and metabolism of radiotracers.

Table 1 Main properties of ^{13}N and ^{15}O

Isotope	Half-life	E_{max} (MeV)[a]	E_{mean} (MeV)[b]	R_{max} (mm)[c]
^{13}N	9.97 min	1.199	0.492	5.5
^{15}O	122 s	1.732	0.735	8.4

[a]Maximum energy of the emitted positrons
[b]Mean energy of the emitted positrons
[c]Maximum range in water

In this chapter, we discuss the main aspects of the production and use of ^{13}N and ^{15}O from both historical and contemporary perspectives. Particular considerations when applying "classical chemical reactions" to radiochemistry will be discussed. Our ultimate goals are to provide the reader with a comprehensive overview of the different options available and to inspire researchers new to the field to pursue new applications for these challenging but interesting radionuclides.

Details and Tricks of the Trade

The Discovery of ^{13}N and ^{15}O

In 1934, F. Joliot and I. Joliot-Curie irradiated a boron nitride foil with α particles produced in a polonium preparation [1]. As reported by the authors, "the emission of positrons did not cease immediately when the active preparation was removed. The foil remained radioactive, and the emission of radiation decayed exponentially as for an ordinary radio-element with a half life period of 14 min." Joliot and Curie treated the irradiated sample with sodium hydroxide and observed the formation of gaseous ammonia carrying the radioactivity. They concluded that they had discovered a new radioactive nuclide (^{13}N), and, despite their inaccurate estimation of its half-life, in 1935 they were awarded the Nobel Prize "for their synthesis of new radioactive elements." In the same year, Cockcroft,

V. Gómez-Vallejo
Radiochemistry Platform, Center for Cooperative Research in Biomaterials, CIC biomaGUNE, San Sebastián, Guipúzcoa, Spain

L. Rejc · J. Llop (✉)
Radiochemistry and Nuclear Imaging, Center for Cooperative Research in Biomaterials, CIC biomaGUNE, San Sebastián, Guipúzcoa, Spain
e-mail: jllop@cicbiomagune.es

F. López-Gallego
Institute of Synthetic Chemistry and Catalysis (IQSCH), University of Zaragoza, Zaragoza, Spain

Fundación ARAID, Zaragoza, Spain

J. S. Lewis et al. (eds.), *Radiopharmaceutical Chemistry*, https://doi.org/10.1007/978-3-319-98947-1_13

Gilbert, and Walton described the production of ^{13}N via the proton irradiation of ^{13}C-enriched graphite and the deuteron irradiation of natural graphite [2]. They had just discovered the $^{13}C(p,n)^{13}N$ and $^{12}C(d,n)^{13}N$ nuclear reactions but—remarkably—had to wait until 1951 to receive the Nobel Prize for "their pioneering work on the transmutation of atomic nuclei by artificially accelerated atomic particles."

Not coincidentally, ^{15}O was also discovered in 1934, a few months after the discovery of ^{13}N. Inspired by Joliot and Curie's results, Livingston and McMillan irradiated nitrogen gas with deuterons [3]. The gas was then transferred to a bulb vessel and the activity measured. The authors estimated that one nitrogen atom was activated per million incident deuterons and that the half-life of the activated species was 126 s. To identify the radioactive nuclide, the irradiated gas was mixed with oxygen and hydrogen and passed over heated platinized asbestos to form water, which was collected in a $CaCl_2$ drying tube. The activity was found to pass entirely into the drying tube, confirming the formation of a radioactive oxygen isotope in the deuteron beam.

Efficient methods for the production of ^{13}N and ^{15}O have been thoroughly investigated since these pioneering efforts, and currently, most of the commercially available biomedical cyclotrons are equipped with specific targets that enable their efficient and routine production. Radiochemical methods for the preparation of a plethora of ^{15}O- and especially ^{13}N-labeled tracers have also been developed, some with clinical applications. The aim of the following sections is to provide a comprehensive overview of the main production methods and applications for both radionuclides and, in doing so, emphasize some historical aspects and practical tips that will provide the reader with an overview of the radiochemistry of these exciting radionuclides.

^{13}N: Production

^{13}N does not exist naturally and must be produced using nuclear reactions. As shown in Table 2, different nuclear reactions can be used to produce ^{13}N in different chemical forms by simply modifying the incident particle and the physicochemical form of the irradiated material.

Table 2 Nuclear reactions used for ^{13}N production

Target material	Nuclear reaction	In-target product
CO_2 (trace N_2)	$^{12}C(d,n)^{13}N$	$[^{13}N]N_2$
Graphite	$^{12}C(d,n)^{13}N$	Trapped $[^{13}N]CN$
Charcoal	$^{12}C(d,n)^{13}N$	$[^{13}N]N_2$ + trapped $[^{13}N]CN$
^{13}C-enriched charcoal	$^{13}C(p,n)^{13}N$	$[^{13}N]CN$
H_2O/ethanol	$^{16}O(p,\alpha)^{13}N$	$[^{13}N]NH_3$
H_2O	$^{16}O(p,\alpha)^{13}N$	$[^{13}N]NH_3$ + $[^{13}N]NO_3^-$ + $[^{13}N]NO_2^-$
$NaNO_3$ (aq)	$^{14}N(n,2n)^{13}N$	$[^{13}N]NH_3$
Al_4C_3	$^{12}C(d,n)^{13}N$	Matrix-trapped ^{13}N

From a technical standpoint, the most convenient route for the production of ^{13}N is the irradiation of liquid water with protons, which directly results in the formation of three major labeled species: $[^{13}N]NO_3^-$, $[^{13}N]NO_2^-$, and $[^{13}N]NH_3$. The relative amount of these species varies depending on the dose to the target as well as the presence of other species, either impurities or substances that have been intentionally added to the irradiated water. For example, the irradiation of aerated water at doses as low as 0.01 μAh results in the formation of approximately 50% $[^{13}N]NO_3^-$, 10% $[^{13}N]NO_2^-$, and 40% $[^{13}N]NH_3$. When the dose is increased to 25 μAh, the relative amounts of $[^{13}N]NO_3^-$ and $[^{13}N]NO_2^-$ are 95% and 5%, respectively, while the generation of $[^{13}N]NH_3$ is negligible [4]. It is important to note that adding radical scavengers to the target water can cause an increase in $[^{13}N]NH_3$ levels at a given dose.

These observations can be explained in terms of the reactions taking place within the cyclotron target. During the first few seconds of irradiation, the incident protons generate ^{13}N atoms, which are (obviously) surrounded by water molecules. $[^{13}N]NH_3$ is produced initially by the abstraction of hydrogen from the target water matrix, a process that also results in the formation of •OH radicals, ultimately leading to the formation of oxo anions of nitrogen ($[^{13}N]NO_3^-$ and $[^{13}N]NO_2^-$) by radiolytic oxidation. The formation of primarily $[^{13}N]NH_3$ can be achieved by preventing this radiolytic oxidation either by using solid (frozen) water as the target material [5] or by adding a reducing agent such as ethanol or acetic acid to the irradiated water [6]. These particular findings absolutely revolutionized the production and use of $[^{13}N]NH_3$, a species that can be used directly as a tracer for blood flow and perfusion [7] and as the synthon in the preparation of other, more complicated tracers (see below). In light of this, most PET centers equipped with a cyclotron produce $[^{13}N]NH_3$ using a target configuration similar to that depicted in Fig. 1. The target has a cavity that can be filled with a few milliliters of 5 mM aqueous ethanol solution using a remote loading system connected to the target via a six-port valve. This solution is irradiated with protons for a few minutes to produce ^{13}N, and the activity is finally transferred to hot cells for further manipulation. In the integrated current range typically used for medical applications (1–4 μAh), $[^{13}N]NH_3$ is the major species, which is obtained as an aqueous solution and can easily be purified with a cation-exchange resin.

The production of $[^{13}N]NH_3$ following the procedure discussed above is efficiently carried out in many facilities worldwide. However, prior to the first report in 1991 that the addition of a radical scavenger favors the production of $[^{13}N]NH_3$, the production of labeled ammonia was more

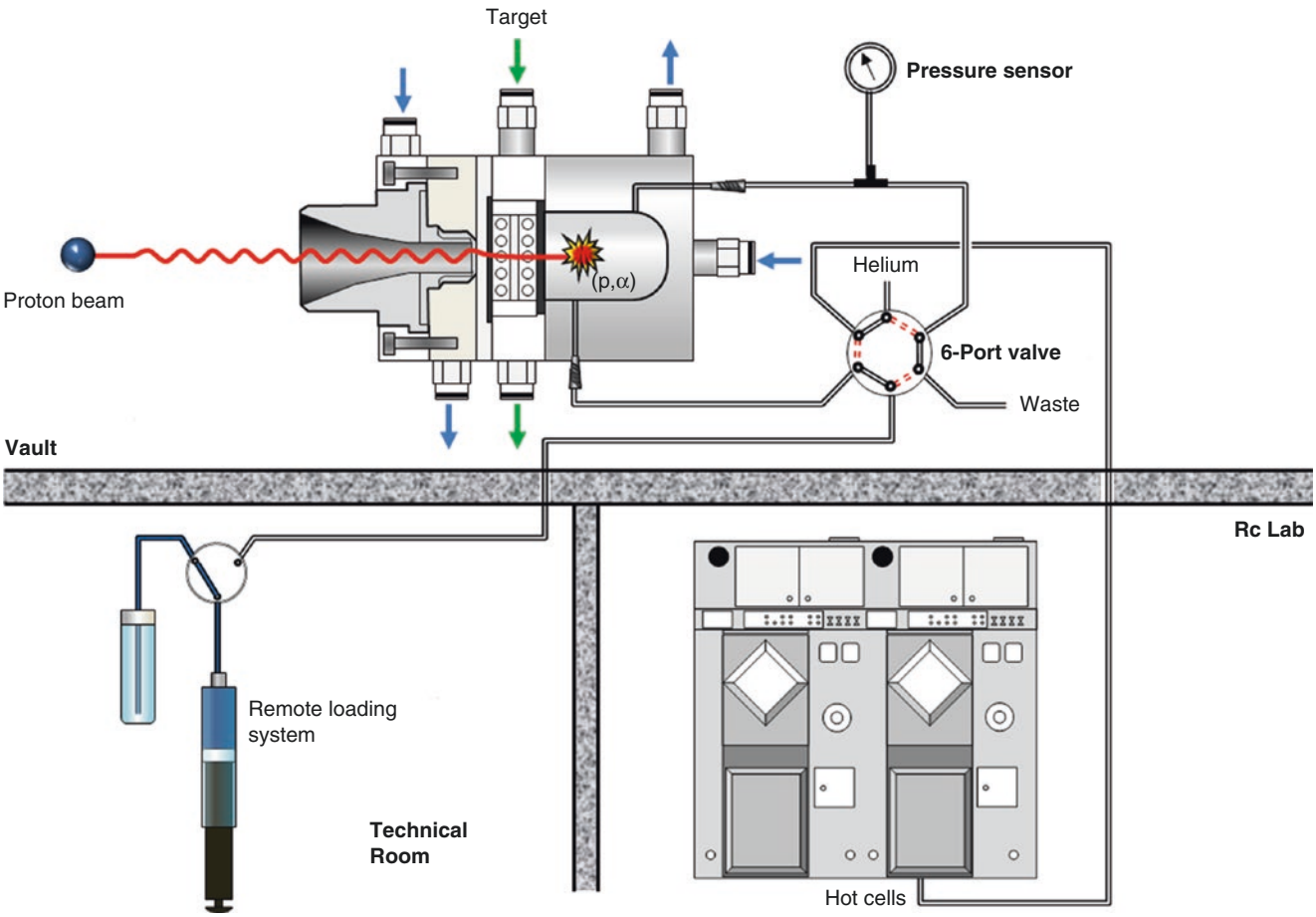

Fig. 1 Schematic of a typical target for the production of $[^{13}N]NH_3$ via the $^{16}O(p,\alpha)^{13}N$ reaction. In the six-port valve, the black and red lines represent the positions during the loading of the target and the transfer of the activity to the hot cells, respectively. The blue and green arrows represent water and helium cooling, respectively

laborious. Earlier works relied on the irradiation of solid targets to produce ^{13}N. For example, for many years, the Washington University School of Medicine used the irradiation of Al_4C_3 with deuterons [8]. In this approach, carbide (in powder form) was introduced in an aluminum capsule, irradiated with 7 MeV deuterons, and dissolved in hydrochloric acid. The solution was then basified, and the labeled ammonia was distilled. As an alternative, the same laboratory developed a method for the *in-cyclotron* production of ammonia by the irradiation of methane [8] (see Fig. 2). The target chamber (100 mm in diameter and 450 mm long) was filled with methane (P = 100 kPa) and irradiated with deuterons. During irradiation, the gas was recirculated using a peristaltic pump and passed through both an acid trap to absorb ammonia and a calcium chloride trap to avoid excess moisture circulating through the irradiated chamber. After irradiation, the acid solution containing the $[^{13}N]NH_3$ was removed and brought to basic pH, and the ammonia was distilled and trapped in acidic solution. Two important details need to be considered in this process. First, the irradiated chamber needs to be large,

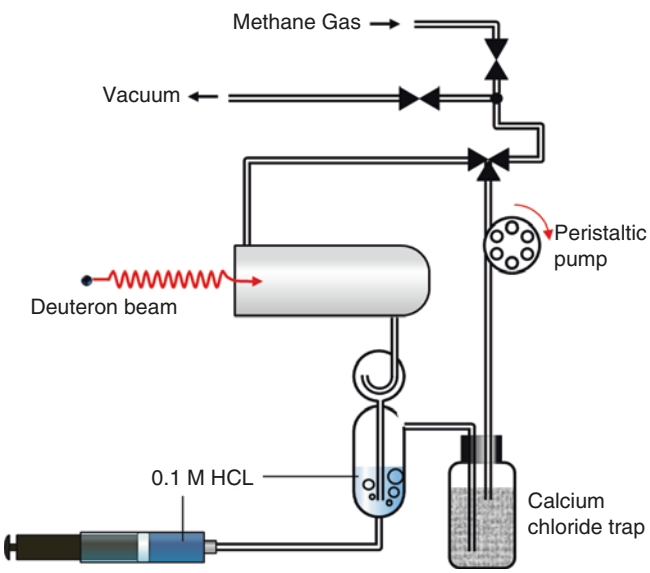

Fig. 2 A recirculated gas target used for the production of $[^{13}N]NH_3$ from methane (Adapted from Straatmann and Welch [8], with permission)

especially compared to the gas target chambers currently used in which gas irradiation is performed at high pressures (a few tens of MPa). In the process described by this laboratory, the irradiated gas was not pressurized, thereby decreasing the probability of interactions between the gas molecules and the incident particles; hence, longer paths were required [8]. The second issue is that "only" 740 MBq of $[^{13}N]NH_3$ could be produced after 10 min of irradiation (target current = 30 μA). A similar amount of aqueous $[^{13}N]NH_3$ can be produced using the target shown in Fig. 1 in less than 1 min.

Another sophisticated procedure described in the literature for the production of $[^{13}N]NH_3$ includes the post-processing of $[^{13}N]NO_3^-$ generated in the cyclotron, e.g., by treatment with a strong reducing agent such as $Ti(OH)_3$ or Devarda's alloy. A description of these methods lies outside the scope of this chapter, but details can be found in a recent review [9].

^{13}N can also be produced as nitrogen gas ($[^{13}N]N_2$). While this chemical form is less useful from a synthetic point of view, $[^{13}N]N_2$ has been applied in nitrogen fixation studies in plants [10] and ventilation studies in both humans and animals [11]. Several different methodologies have been reported for the production of $[^{13}N]N_2$, both in the target and via post-processing of other cyclotron-produced labeled species. One of the most convenient methods is by recovering $[^{13}N]N_2$ as a byproduct generated during the production of $[^{11}C]CO_2$, which is usually produced via the irradiation of a N_2/O_2 mixture with protons. In this method, the stable ^{14}N atom undergoes a (p,α) nuclear reaction to yield ^{11}C, which immediately reacts with the oxygen present in the gas mixture to yield $[^{11}C]CO_2$. During this process—and in the energy range in which ^{11}C is usually produced—^{14}N can undergo a second nuclear reaction (p,pn) which results in the formation of ^{13}N. Atoms of ^{13}N undergoing recoil can undergo isotopic exchange with N_2, resulting in the formation of $[^{13}N]N_2$. The probability that the $^{14}N(p,pn)^{13}N$ reaction occurs is lower than the probability that the $^{14}N(p,\alpha)^{11}C$ reaction occurs, but it is still high enough to yield significant amounts of the ^{13}N-labeled gas. This was recently exploited using the target configuration shown in Fig. 3 [12]. During irradiation, considerable amounts of $[^{14}O]O_2$, $[^{15}O]O_2$, $[^{11}C]CO$, and (obviously) $[^{11}C]CO_2$ were produced along with $[^{13}N]N_2$, and hence, a purification step was required. After irradiation, the gas was first passed through a soda lime trap to quantitatively trap $[^{11}C]CO_2$, after which it was circulated through a CuO trap (at 700 °C) to oxidize $[^{11}C]CO$ to $[^{11}C]CO_2$. A second soda lime trap removed the *in situ*-generated $[^{11}C]CO_2$, while the radioactive oxygen species were eliminated by exchange on CuO and by radioactive decay (the half-lives of ^{14}O and ^{15}O are 70 s and 122 s, respectively).

^{13}N: Radiochemistry

As mentioned in the previous section, ^{13}N can be produced in different chemical forms: $[^{13}N]NO_3^-$, $[^{13}N]NO_2^-$, $[^{13}N]NH_3$, and $[^{13}N]N_2$. Of these, $[^{13}N]NH_3$ and $[^{13}N]NO_2^-$ have been exploited to prepare different radiotracers by translating macroscopic chemical reactions into the radiochemistry field.

The Synthesis of ^{13}N-Labeled Compounds Using $[^{13}N]NH_3$ Ammonia is a nucleophile, and as such, its ^{13}N-labeled form has been used in the preparation of several different families of compounds, including amines, amides, ureas, and carbamates. One of the most convenient methods for the preparation of primary amines under nonradioactive conditions is the reductive amination reaction (Fig. 4a). This method starts with the incorporation of ammonia in a carbonyl compound (aldehyde or ketone) to produce the corresponding hemiaminal, which readily loses water to form a carbon-nitrogen double bond (imine) and can be further reduced to yield the corresponding primary amine. This method has been successfully applied to the preparation of ^{13}N-labeled amines, for example, in the radiosynthesis of $[^{13}N]$amphetamine (Fig. 4b). This product was prepared with 3.5% overall radiochemical yield through the reaction of phenylacetone with $[^{13}N]NH_3$ in the presence of carrier ammonia, aluminum, and mercuric chloride, with the latter two acting as reducing agents via the *in situ* formation of aluminum amalgam [13]. If this one-pot reaction is carried out in the absence of carrier NH_3, the concentration of the labeling agent ($[^{13}N]NH_3$) is very low compared to that of the carbonyl compound. As a consequence, the resulting primary ^{13}N-labeled amine competes with $[^{13}N]NH_3$ to react with the carbonyl compound, leading to the formation of the ^{13}N-labeled secondary amine and decreasing the overall yield (see Fig. 4b). This side reaction can be minimized by mimicking non-radioactive conditions, that is, by adding a large excess of ammonia, which consumes the carbonyl compound and prevents the formation of the secondary amine at the expense of a dramatic decrease in molar activity.

Primary amines can also be prepared from amides, which can be converted into amines via the Hofmann degradation (also called the Hofmann rearrangement) or by the reduction of the carbonyl group. The Hofmann degradation reaction begins with the deprotonation of the nitrogen atom to form the amidate ion. After the halogenation of the nitrogen, the second proton of the nitrogen atom is abstracted by additional base to give an *N*-haloamidate. This *N*-haloamidate then spontaneously eliminates the halide to form a nitrene, in which the nitrogen atom is surrounded by only a sextet of electrons. This reactive species subsequently undergoes a

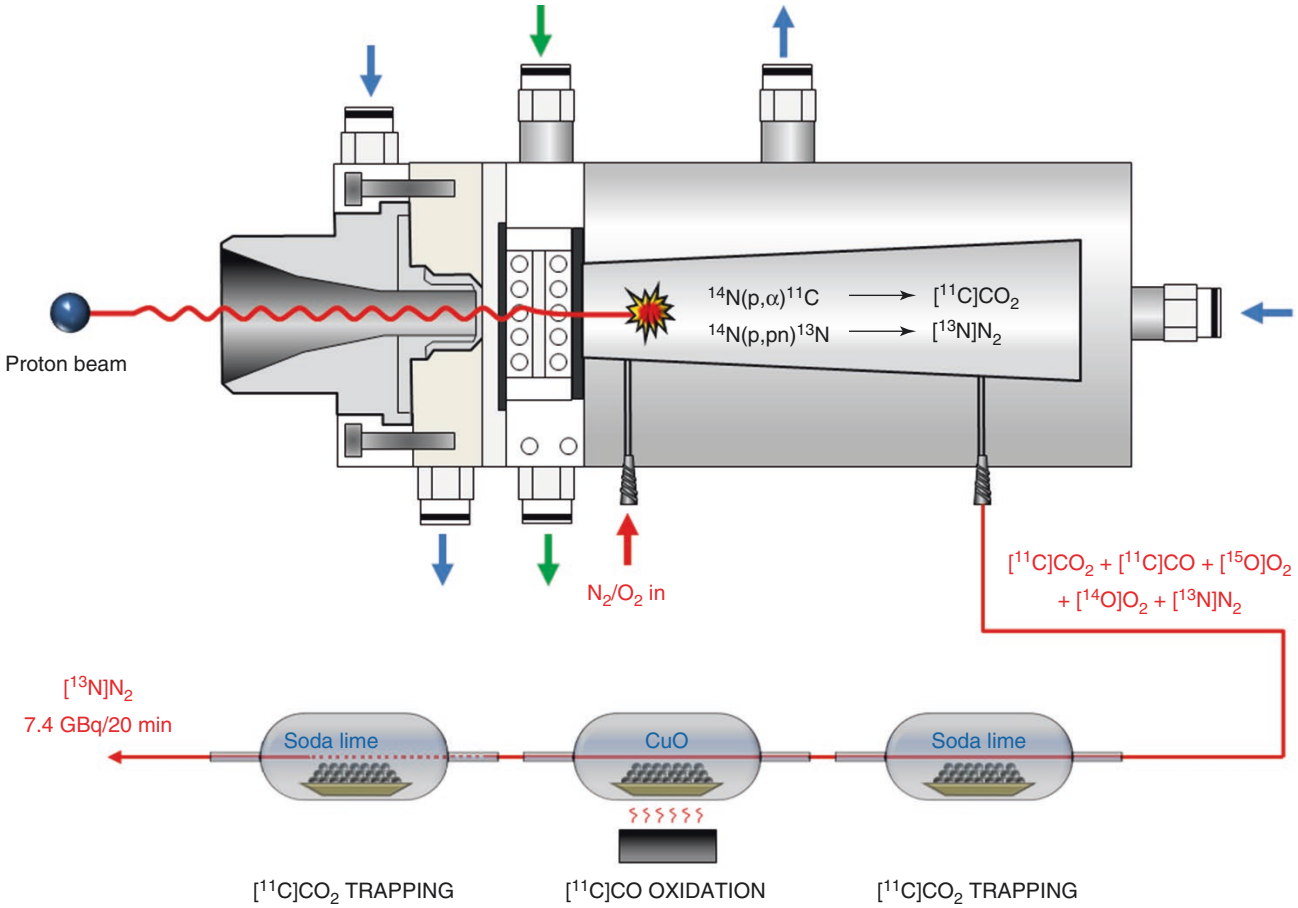

Fig. 3 Schematic of the configuration for the production of $[^{13}N]N_2$ using the $^{14}N(p,pn)^{13}N$ reaction. The blue and green arrows represent water and helium cooling, respectively

1,2-shift of an alkyl group to give an isocyanate R-N=C=O, which is attacked by water to produce an unstable carbamic acid. This finally decomposes to yield carbon dioxide as well as the corresponding amine (Fig. 4c).

This reaction—which results in the net loss of one carbon atom—has been employed in radiochemistry to synthesize ^{13}N-labeled β-phenethylamine (PEA), an important neuromodulator [14]. In a first step, phenylpropionyl chloride was reacted with $[^{13}N]NH_3$-containing water and sodium hydroxide to yield the corresponding amide (Fig. 4d, left). The subsequent treatment of this intermediate with sodium hypobromite under heating resulted in the formation of the amine via the Hofmann rearrangement. For the formation of the amide, good radiochemical yields (around 50%) were obtained under optimal experimental conditions, even under no-carrier-added conditions. However, the reduction step only resulted in 5% radiochemical yields when no-carrier ammonia was added. This value could be increased to 50% by adding carrier ammonia in a 1:2 ratio with sodium hypobromite. Indeed, keeping appropriate relative proportions of sodium hypobromite and the amide is paramount to obtaining good yields, and this is very difficult to achieve when the reaction is conducted under no-carrier-added conditions, because the concentration of (labeled) amide is extremely low and unknown a priori.

Unlike the Hofmann degradation, the amine reduction can lead to the production of ^{13}N-labeled amines with high specific activity [15] (Fig. 4d, right). In this case, the main limitation is that the reaction cannot be conducted in water, which is incompatible with the reducing agent (lithium aluminum hydride). However, the reduction step is not sensitive to an excess of $LiAlH_4$ with respect to the intermediate-labeled amide, and good radiochemical yields of 60–70% can be obtained even when the reaction is conducted under no-carrier-added conditions.

Another alternative for preparing ^{13}N-labeled amines in conventional organic chemistry is via aminolysis. In this reaction, a halogen in an alkyl group is replaced by an amine (or ammonia) with the elimination of hydrogen halide. In radiochemistry, this method has been applied to the preparation of ^{13}N-labeled adenosine [16] starting with two different substrates: 6-chloro-9-β-D-ribofuranosylpurine and 6-fluoro-9-β-D-ribofuranosylpurine (Fig. 5). Despite the reaction working better in the presence of non-radioactive ammo-

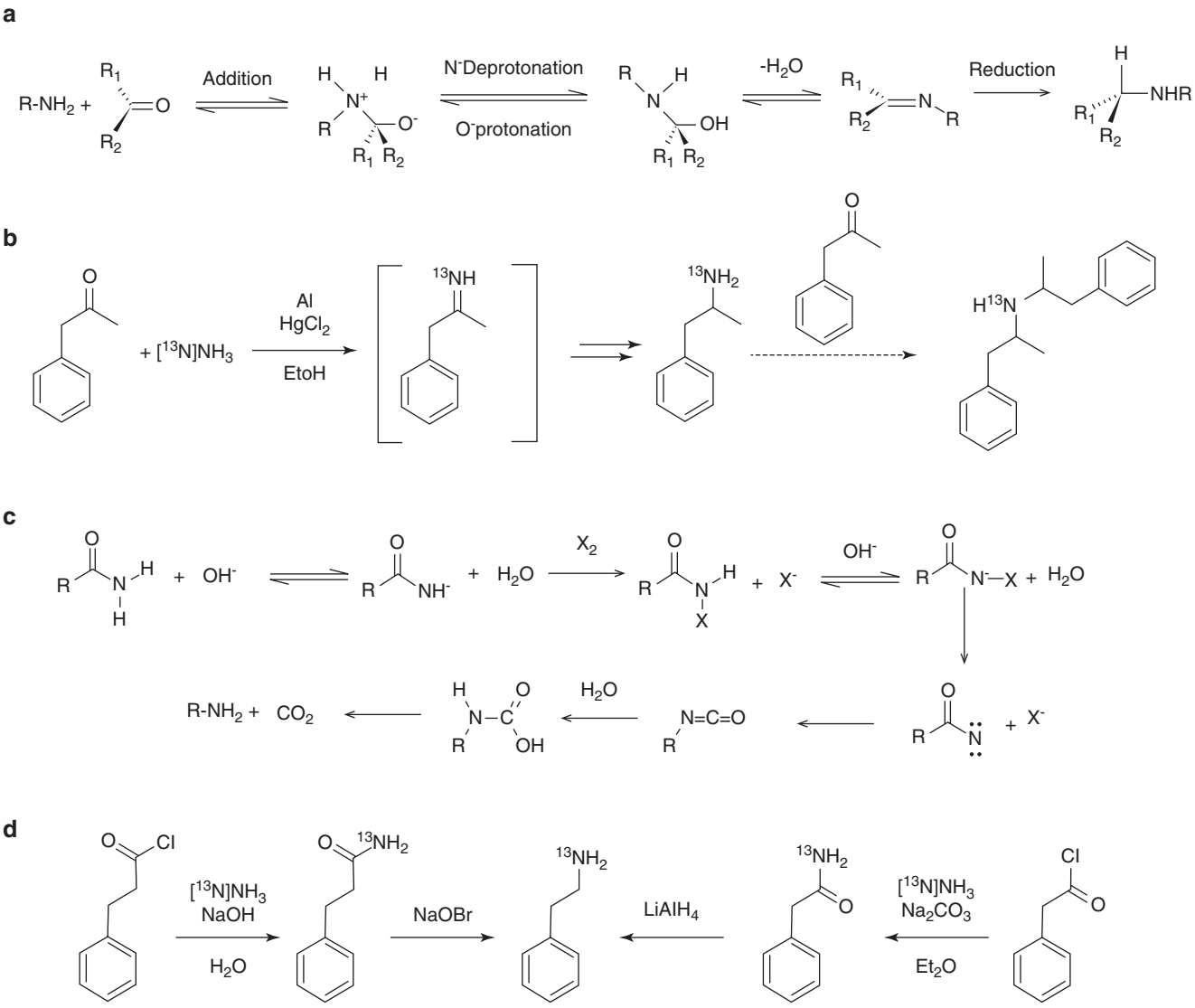

Fig. 4 (**a**) General mechanism for the formation of amines via reductive amination. (**b**) Synthesis of ^{13}N-labeled amphetamine via reductive amination. An excess of the carbonyl compound can lead to the formation of the secondary amine, as it occurs in no-carrier-added conditions. (**c**) The formation of amines from amides via the Hofmann degradation. (**d**) The synthesis of ^{13}N-labeled β-phenethylamine (PEA) via the Hofmann degradation (left) and the subsequent reduction of the amide (right). Note that the starting amide is different in both cases because the Hofmann degradation results in a net loss of one carbon atom

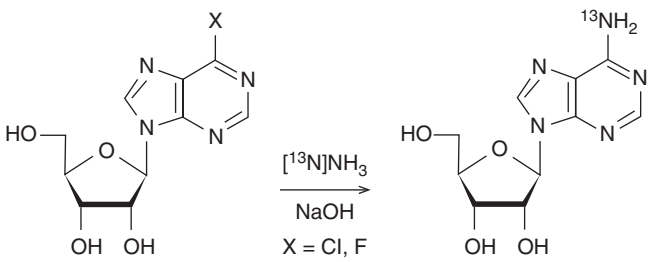

Fig. 5 Synthesis of [^{13}N]adenosine via the ammonolysis of 6-chloro and 6-fluoro-9-β-D-ribofuranosylpurine

nia—a molar ratio 1:2 with respect to the precursor—yields of around 10% have been obtained even in no-carrier-added conditions. However, NaOH needed to be added to maintain a basic pH. This was not required in carrier-added reactions in which the nonradioactive ammonia was sufficient to keep the pH above 10 and keep the ammonia in the neutral (nucleophilic) form.

As a nucleophile, ammonia can react with electrophiles other than those described above including isocyanates, carbamoyl chlorides, and chloroformates. This reactivity can be exploited to prepare ^{13}N-labeled ureas and carbamates (Fig. 6) [17]. Of course, water can also react with these electrophiles, so the use of anhydrous [^{13}N]NH_3 is of paramount

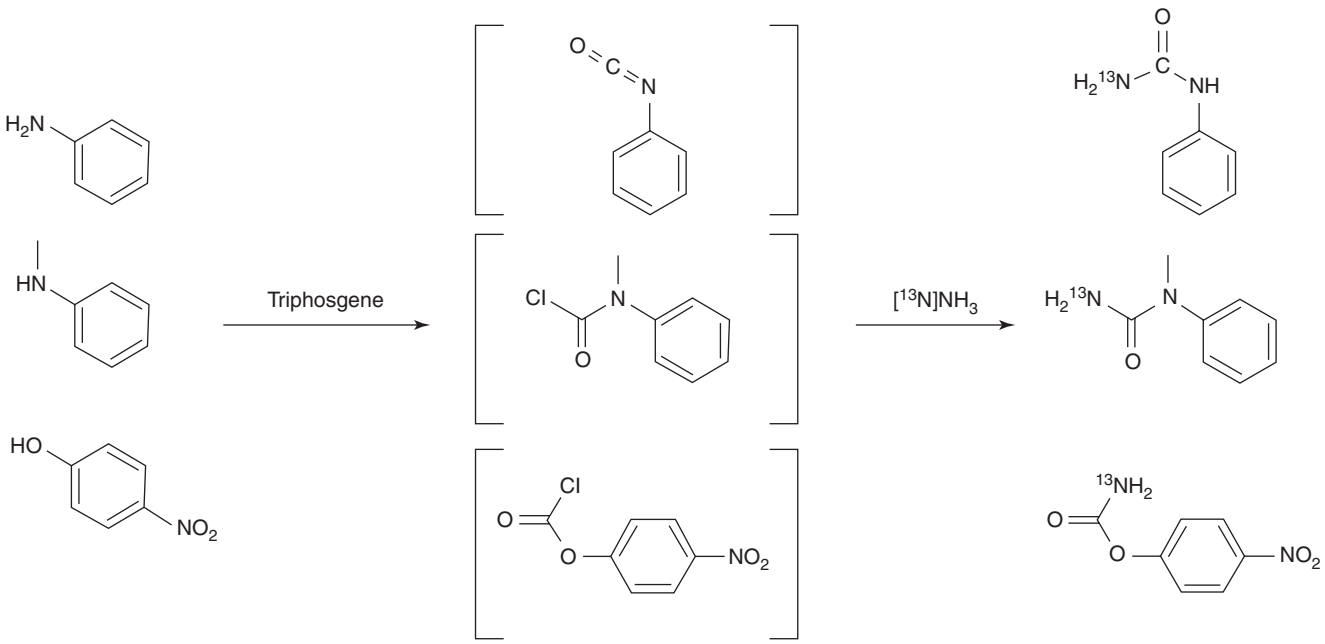

Fig. 6 Synthesis of [^{13}N]urea and [^{13}N]carbamate analogues using anhydrous [^{13}N]NH_3

importance. This can be obtained by trapping [^{13}N]NH_3—produced by proton irradiation of water/ethanol—in a cation-exchange resin. The radioactivity is eluted with aqueous KOH under an inert gas flow, passed over a CaO trap, and bubbled into an anhydrous organic solvent such as dimethylformamide.

The Enzymatic Synthesis of Amino Acids Using [^{13}N]NH_3 Amino acids are organic compounds containing amine (-NH_2) and carboxyl (-COOH) functional groups and a side chain (R group) specific to each amino acid. Every amino acid (except glycine) can exist in two isomeric forms due to the possibility of forming two different enantiomers around the central carbon atom. These are called the *L* and *D* forms; only *L*-amino acids are manufactured in cells and incorporated into proteins.

The preparation of amino acids labeled with an ^{13}N within the R group in the *L* configuration can be achieved using chemical methods by taking advantage of the nucleophilic character of ammonia. For example, *L*-[^{13}N]asparagine can be synthesized via the reaction of the activated ester *L*-α-N-Boc-aspartate with [^{13}N]NH_3 to form the corresponding amide, followed by hydrolysis of the protecting groups (Fig. 7) [18]. That said, chemical methods are usually time-consuming and inefficient and require protection and deprotection steps that adversely affect the radiochemical yield of the reaction. Additionally, the synthesis of only a single particular enantiomer is usually challenging. In response to these difficulties, enzymatic methods have been developed.

Enzymes are specialized proteins that speed up the biochemical reactions of cellular metabolism; in other words, enzymes are the catalysts of life. Over many hundreds of thousands of years, enzymes have evolved to work under physiological conditions with exquisite chemo-, regio-, and enantioselectivity. Generally speaking, enzymes have an active site formed by a molecular cavity or cleft in which the catalytic groups are displayed [19]. These "catalytic groups" are either amino acids within the peptide backbone of the enzyme or non-peptidic cofactors bound to the protein scaffold through supramolecular interactions. The substrates of the enzyme bind to this cavity and thus acquire a suitable conformation for the chemical reaction to take place. In 1894, Emil Fisher proposed the "lock-and-key" model to explain the binding of a substrate to an enzyme active site (Fig. 8a) [20]. In this model, both the substrate and active site present excellent chemical and geometric congruence in order to ensure a perfect fit of the substrate into the active cavity. Unfortunately, this early model only explained the specificity and selectivity of enzymes but not their high catalytic efficiency. Sixty years later, Daniel Koshland proposed the "induced-fit" model to explain the ability of enzymes to catalyze reactions by stabilizing transition states (Fig. 8b) [20]. In this model, enzymes undergo conformational changes induced by the substrate that reshape the binding site, molding the catalytic residues into precise positions to efficiently perform catalysis. In this process, the molecular structure of the substrate is sometimes also reoriented.

Beyond their essential role in life, enzymes have been exploited for biotechnological purposes since ancient times. Fermentation to produce alcoholic beverages such as wine

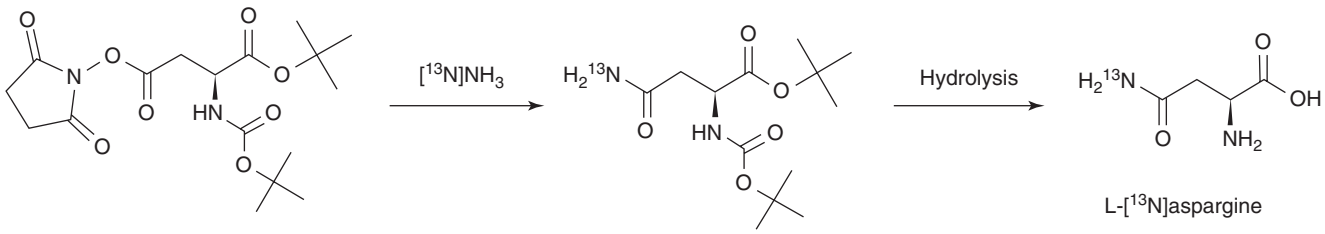

Fig. 7 Synthesis of *L*-[^{13}N]asparagine by a synthetic chemistry method

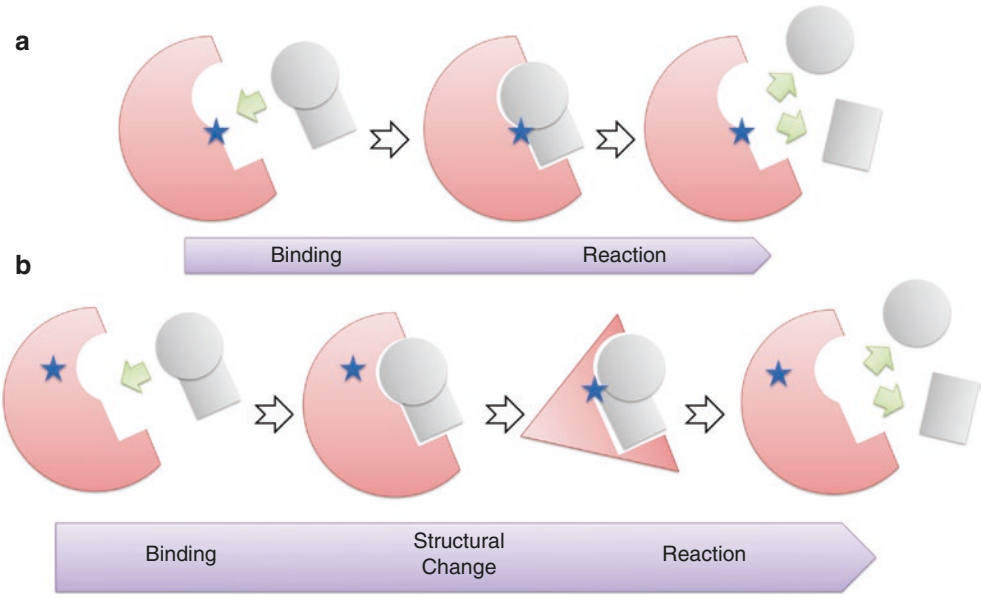

Fig. 8 Different mechanisms for the action of enzymes. (**a**) The *lock-and-key model:* the substrate (gray) binds to an active site of the enzyme (red) with the same shape as the molecular shape of the substrate. Once the substrate binds, the reaction takes place by the action of the catalytic residues (blue), and the products are released. (**b**) The *induced-fit model*: the substrate (gray) binds the active site of the enzyme and triggers a conformational change in the protein structure (red) that positions the catalytic residues (blue) in the correct positions to start the chemical reaction. The substrate is then transformed into the product, which is then released from the active site

and beer is probably the oldest example [21], although it wasn't until the second half of the nineteenth century that Louis Pasteur first proved that microorganisms were responsible for the fermentation process. Thirty years later, Eduard Buchner demonstrated that yeast could transform sugars from fruits and grains into ethanol and CO_2 [22]. He was awarded the Nobel Prize in 1907, and his discovery is considered the birth of biochemistry.

The unique selectivity of enzymes as well as their capacity to work with high efficiency under mild conditions means that they have been used as a very convenient method to prepare ^{13}N-labeled amino acids since the early 1970s. Three enzymatic routes have been used to create several different ^{13}N-labeled amino acids (Fig. 9):

(i) Amino acid dehydrogenase—which catalyzes the reductive amination of α-keto acids—can be used with nicotinamide adenine dinucleotide (NADH) as a redox cofactor and [^{13}N]NH_3 as the source of the amine.

(ii) Amino acid synthase can catalyze the insertion of [^{13}N]NH_3 into the ω-carboxylic group of acidic amino acids using adenosine triphosphate (ATP).

(iii) A bi-enzymatic system can be employed in which an amino acid dehydrogenase—usually glutamate dehydrogenase—catalyzes the reductive amination of α-ketoglutarate to produce *L*-[^{13}N]glutamate, which is then used by a transaminase that transfers the radiolabeled amine group to an α-keto acid to form the desired *L*-[^{13}N]amino acid.

Despite their practical utility, the biological origin of enzymes poses some limitations on their use in radiochemistry, primarily because enzymes are generally soluble in aqueous media. This hampers the use of isolated enzymes, because the separation of the catalyst and the product can become difficult once the reaction is complete. However, such separation can be achieved using chromatographic methods. For example, column chromatography was used to purify *L*-[^{13}N]glu-

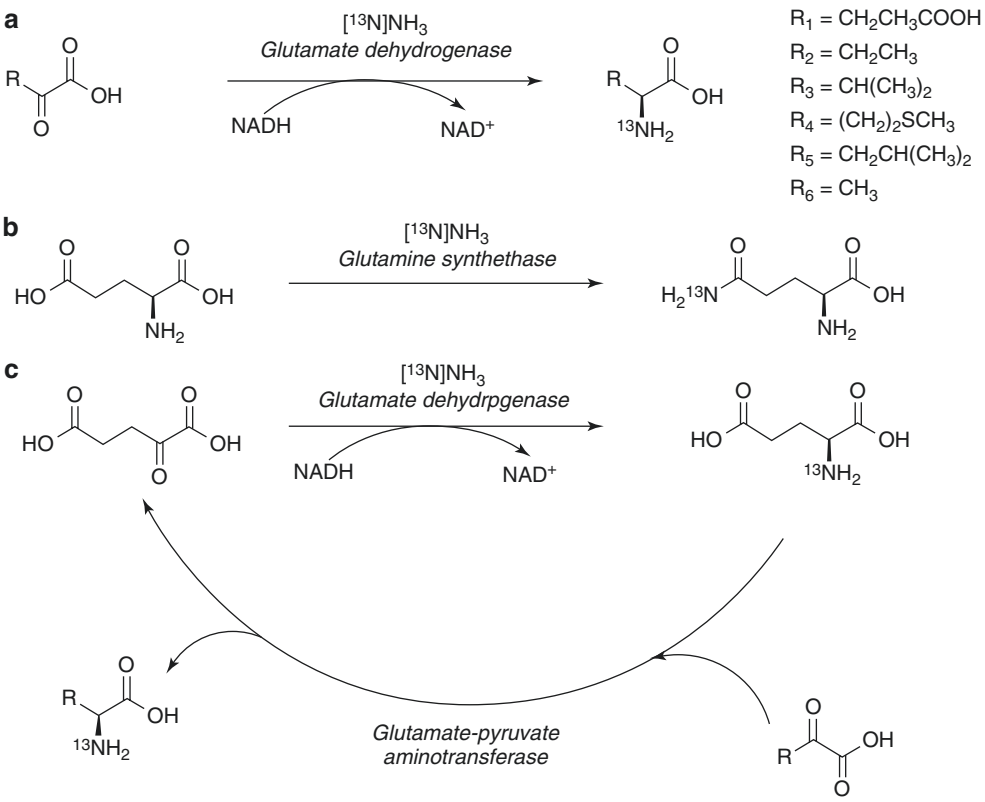

Fig. 9 Examples of the main enzymatic routes for the incorporation of $[^{13}N]NH_3$ into amino acids: (**a**) using amino acid dehydrogenases; (**b**) using amino acid synthetases; and (**c**) using a bi-enzymatic system consisting of an amino acid dehydrogenase and a transaminase

tamic acid and *L*-[^{13}N]alanine after their synthesis via enzymatic methods. When the column was eluted by gravity, the enzyme appeared to be bound to the top of the column, and the resulting radiopharmaceutical product proved pure. While pressure could be applied to accelerate this process, this reduces the efficacy of the separation, resulting in the observation of enzyme within the final product mixture [23].

In light of these difficulties, efforts have been focused on improving the ways in which enzymatic reactions are applied to radiochemistry. One such approach is predicated on the immobilization of enzymes on an insoluble matrix (carrier). In this case, the enzymes act as heterogeneous biocatalysts that can be manipulated easily and separated from the products once the reaction is complete. In addition, immobilization may also enhance the operational and storage stability of enzymes as well as facilitate their recycling or integration into continuous chemical processes [24]. It is important to note, however, that immobilization can completely quench catalytic activity of an enzyme. Therefore, the appropriate selection of both the solid support and the immobilization chemistry is essential to create an efficient immobilized catalyst. Unfortunately, no universal immobilization protocols have been described, and even today the immobilization of enzymes remains an empirical approach in which trial and error are far too common. Going forward, the knowledge gained from over 40 years of research into the immobilization of enzymes together with computational methods capable of providing structural information about the enzyme promises to guide the selection of the best immobilization protocol.

The first successful application of immobilized enzymes to the synthesis of ^{13}N-labeled amino acid was reported in 1974. In this work, *L*-[^{13}N]glutamic acid was prepared by dissolving $[^{13}N]NH_3$, α-ketoglutarate, and NADPH in buffered solution. The solution was passed through a reaction column containing glutamic acid dehydrogenase immobilized on derivatized silica beads. The resulting (pure) labeled amino acid could even be eluted with pyruvic acid through a second column containing immobilized glutamate-pyruvate transaminase, ultimately yielding *L*-[^{13}N]alanine [23]. Since then, radiochemical reactions using immobilized enzymes have been exploited to prepare several different labeled amino acids. For a detailed list of examples, we refer the interested reader to a recent review [25].

The Synthesis of ^{13}N-Labeled Compounds Using [^{13}N] NO_2 Nitrite (NO_2^-) is widely used in organic chemistry, usually as a sodium salt. Of all the chemical reactions involving nitrite, four have found applications in radiochemistry: the synthesis of *S*-nitrosothiols, *N*-nitrosamines, azo compounds, and azides (the latter can subsequently be used for the preparation of ^{13}N-labeled triazoles).

It is well known that the reaction of thiols with sodium nitrite under acidic conditions produces *S*-nitrosothiols at a

wide range of pHs. While the exact mechanism of this reaction is not fully understood, it is generally accepted that under strong acidic conditions, NO^+ (or H_2ONO^+) is likely to be the nitrosating agent (Fig. 10a). The reaction proceeds rapidly and is almost quantitative, making it a good candidate for ^{13}N radiochemistry. This reaction has been translated to the radiochemistry: different *S*-[^{13}N]nitrosothiols have been prepared using [^{13}N]NO_2^-, which is readily produced via the reduction of [^{13}N]NO_3^- generated during the proton irradiation of pure water. Initially, this reaction was described in solution and applied to the synthesis of *S*-nitrosoglutathione (see Fig. 10b) [26]. The synthesis—which was quite straightforward—was based on the reaction of [^{13}N]NO_2^- with glutathione in the presence of 0.125 M HCl. The formation of ^{13}N-labeled *S*-nitrosoglutathione ([^{13}N]GSNO) could be observed in just 1 min, with chromatographic purity close to 90%. Interestingly, this value decreased with time, suggesting the instability of the ^{13}N-nitroso derivative at these low pH values.

This method was successfully applied to the preparation of [^{13}N]GSNO. However, the reaction was conducted in aqueous media and was thus incompatible with many precursors—such as organic thiols—that are not soluble in water. Solid-phase reactions may represent an interesting alternative to overcome this problem. The labeling species [^{13}N]NO_2^- is an anion, and as such, it can be quantitatively trapped in an anion-exchange resin when dissolved in pure water. Water can then be removed from the cartridge, leaving [^{13}N]NO_2^- ready to react in organic media. Taking advantage of this, a simplified method for the preparation of different *S*-[^{13}N]nitrosothiols was described [27]. The process consisted of first trapping [^{13}N]NO_2^- in an anion-exchange resin. The water was then removed from the cartridge first by rinsing the cartridge with water, then rinsing with a water-miscible organic solvent, and finally purging with an inert gas. After the removal of the water, the dead volume of the cartridge was filled with an acidic solution of the corresponding thiol to form ^{13}N-labeled *S*-nitrosothiol. This method was applied to the preparation of [^{13}N]GSNO and a small library of thiols (Fig. 10c). The reaction in the cartridge worked efficiently, and the purification of the final tracers was achieved via high-performance liquid chromatography (HPLC). However, the automation of this process presents a number of challenges, because the [^{13}N]NO_2^- is pushed out of the cartridge when the acidic precursor solution is loaded. Hence, accurate control of both the volume and flow rate of the acidic solution containing the thiol during this step is of paramount importance for guaranteeing good radiochemical yields. Despite the facts that this process is fully automatable *and* that the amount of activity obtained is sufficient for *in vivo* experiments, these studies have never been conducted.

As mentioned above, nitrite can also be used to prepare nitrosamines by reacting secondary amines with sodium nitrite in aqueous media in the presence of a strong acid. As in the case of nitrosothiols, NO^+ is the most likely nitrosating agent, which reacts with the amine. In this case, however, the strong acidic conditions result in the formation of the protonated amine. This decreases its nucleophilic character and consequently negatively impacts the yield of the reaction. Under non-radioactive conditions, this is solved by the slow addition of the acid to an

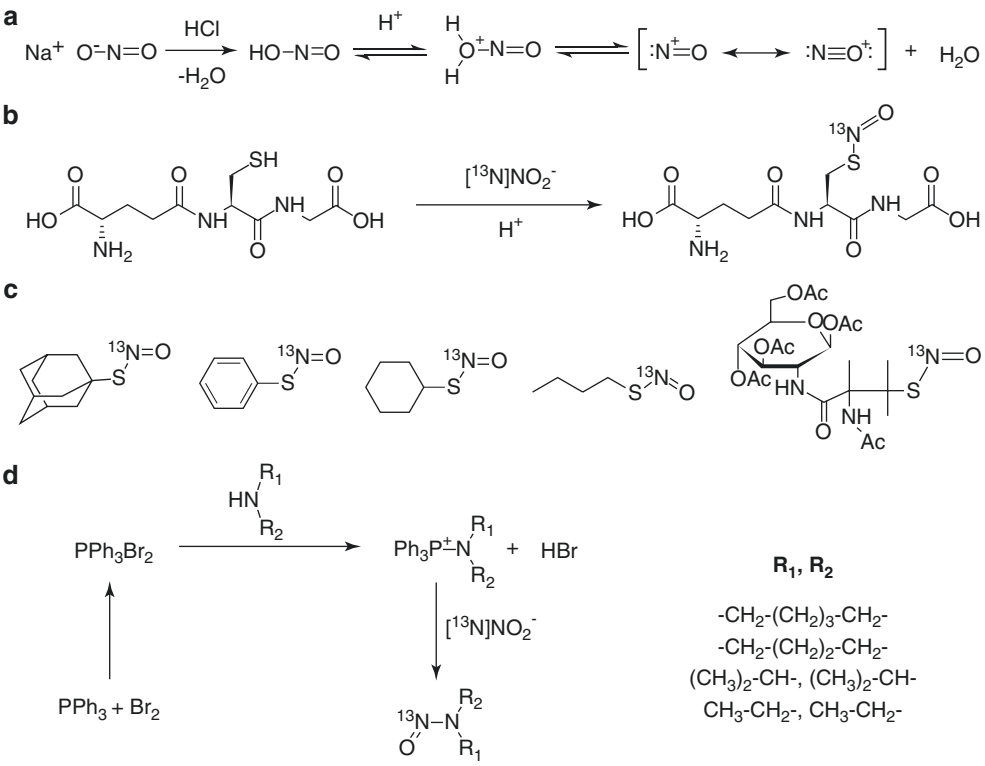

Fig. 10 (**a**) Mechanism for the formation of the nitrosating agent. (**b**) Synthesis of *S*-[^{13}N] nitrosoglutathione. (**c**) Synthesis of other *S*-[^{13}N] nitrosothiols created using a solid-phase support-based approach. (**d**) Reaction scheme for the formation of *N*-[^{13}N]nitrosamines

equimolar amount of the amine and sodium nitrite to maintain a solution with a weakly acidic pH [28]. Even following this strategy, the reaction takes several hours, a time-scale that is incompatible with the short half-life of ^{13}N. Obviously, it cannot be applied to the preparation of *N*-[^{13}N]nitrosamines.

This limitation was overcome by combining a solid phase-supported method with the activation of the amine in the presence of a mixture of PPh_3 and Br_2 [29]. In this case, the [^{13}N]NO_2^- was first trapped in an anion-exchange resin. After rinsing the cartridge with water and tetrahydrofuran, a solution containing Ph_3P, Br_2, and the amine in dichloromethane was loaded onto the cartridge, and the reaction allowed to proceed at room temperature. While it has not been proven, it is believed that the PPh_3 first quantitatively reacts with Br_2 to form bromotriphenylphosphonium bromide, which then reacts *in situ* with the secondary amine to yield the nitrosation reaction precursor: triphenyl(amin-1-yl)phosphonium bromide (see Fig. 10d for reaction scheme). This method has been used to prepare several different ^{13}N-labeled nitrosamines (Fig. 10d). However, the methodology poses major experimental drawbacks. Chief among these is that the reaction cannot be performed in water due to the incompatibility of the nitrosation reaction with water. This has two main implications: (i) the water must be removed from the anion-exchange cartridge after trapping [^{13}N]NO_2^-, and (ii) the dichloromethane would need to be completely and assiduously removed prior to any *in vivo* applications.

Another major use of the nitrite anion in organic chemistry is in the preparation of azo compounds. To this end, an aromatic amine is first reacted with sodium nitrite in the presence of a mineral acid to produce the corresponding aryldiazonium ion, which can then couple with a nucleophile in basic conditions to produce the corresponding azo compound. In non-radioactive chemistry, both reactions are carried out at low temperature (0 °C) in just a few minutes, and the final product is isolated by precipitation. As in previous cases, however, such conditions are not suitable for ^{13}N due to the short half-life of the radionuclide and its low concentration under no-carrier-added conditions. However, a similar strategy to that previously described for the preparation of *S*-[^{13}N]nitrosothiols can be used to prepare ^{13}N-labeled azo compounds [30, 31]. In a first step, [^{13}N]NO_2^- is trapped on an anion-exchange cartridge, and, after rinsing with water, the cartridge is loaded with an acidic solution of the aromatic amine to form the ^{13}N-labeled aryldiazonium salt. This reaction is fast and efficient at room temperature, even at the low concentration of no-carrier-added [^{13}N]NO_2^-. The resulting ^{13}N-labeled diazonium salt is a cation, which has no affinity for the anion-exchange resin and can easily be eluted from the cartridge into a reaction vial, in which the ^{13}N-labeled azo compound can be formed via reaction with either an aromatic amine or alcohol under basic conditions (Fig. 11a). This methodology, while useful, is rather tricky: the first and second steps occur under acidic and basic conditions, respectively, and the implementation of an intermediate purification step is challenging due to the short half-life of the radionuclide. Hence, the optimization of the experimental conditions (pH, temperature, and reaction time) is required on a case-by-case basis.

It is important to note that ^{13}N-labeled azo compounds—unlike *S*-[^{13}N]nitrosothiols and *N*-[^{13}N]nitrosamines—have *in vivo* applications. Azo compounds have a similar structure to Congo red, which has been used for decades to identify amyloid deposits in brain tissue postmortem. Yet Congo Red does not cross the blood-brain barrier, which obviously impairs its potential for *in vivo* applications. However, ^{13}N-labeled azo compounds smaller than Congo Red and with appropriate physicochemical properties have shown promise for the detection of β-amyloid plaques in a mouse model of Alzheimer's disease (Fig. 11b–d).

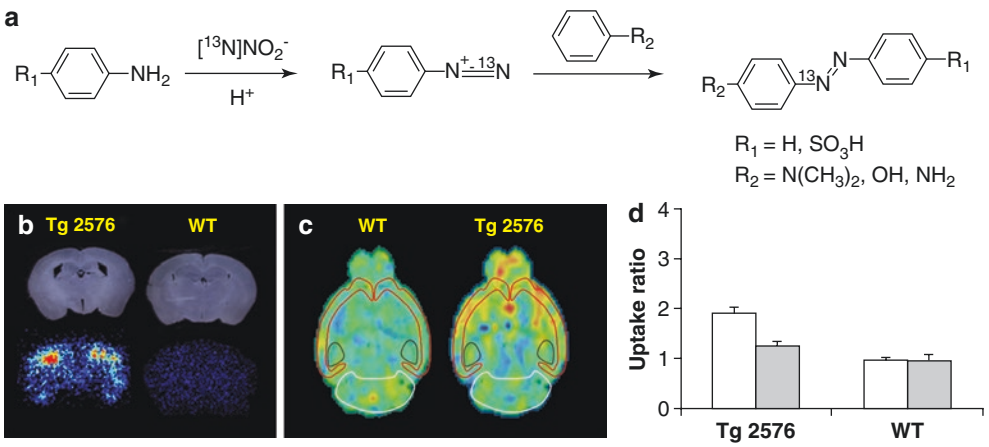

Fig. 11 (**a**) General scheme for the synthesis of ^{13}N-labeled azo compounds. (**b**) Microscopy (top) and autoradiography (bottom) images of tissue sections including the dorsal hippocampus from non-transgenic (WT) and transgenic (Tg2576) mice incubated with a ^{13}N-labeled azo compound [R_1 = SO_3H; R_2 = $N(CH_3)_2$]. (**c**) Representative coronal sections of *in vivo* PET images obtained using the same ^{13}N-labeled azo compound in WT and Tg2576 mice. (**d**) Cortex-to-cerebellum (white bars) and hippocampus-to-cerebellum (gray bars) activity concentration ratios obtained *in vivo* with the same compound

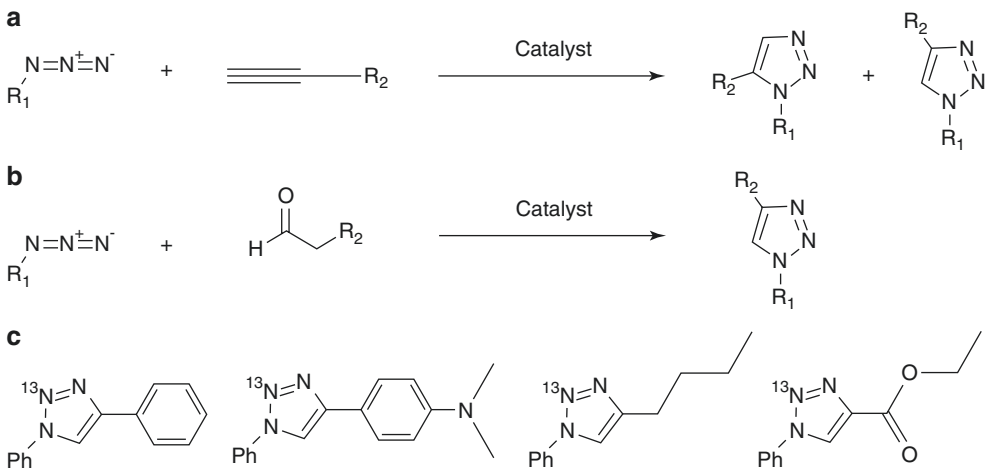

Fig. 12 (**a**) Preparation of triazoles by the [3 + 2] cycloaddition of azides with alkynes. (**b**) Preparation of triazoles by the [3 + 2] cycloaddition of azides with aldehydes. (**c**) Some ^{13}N-labeled triazoles reported in the literature

Table 3 Nuclear reactions used for the production of ^{15}O

Target material	Nuclear reaction	In-target product
N_2	$^{14}N(d,n)^{15}O$	$[^{15}O]O_2 + [^{15}O]N_2O + [^{15}O]NO_2 + [^{15}O]O_3$
N_2/O_2	$^{14}N(d,n)^{15}O$	$[^{15}O]O_2$
N_2/CO_2	$^{14}N(d,n)^{15}O$	$[^{15}O]CO_2$
N_2/H_2	$^{14}N(d,n)^{15}O$	$[^{15}O]H_2O$
N_2/CH_4	$^{14}N(d,n)^{15}O$	$[^{15}O]CH_3OH + [^{15}O]C_2H_5OH + [^{15}O]H_2O$
O_2	$^{16}O(p,pn)^{15}O$	$[^{15}O]O_2$
H_2O	$^{16}O(p,pn)^{15}O$	$[^{15}O]H_2O$
$[^{15}N]N_2/H_2$	$^{15}N(p,n)^{15}O$	$[^{15}O]H_2O$

The last application of $[^{13}N]NO_2^-$ that we will mention here is in the preparation of labeled triazoles starting from ^{13}N-labeled azides via [3 + 2] "click" cycloaddition reactions (see Fig. 12 and Chap. 26). The synthesis of ^{13}N-labeled azides is considered in more detail below in the section on "Particularly Important Works." Briefly, by using the appropriate catalyst—$[Cu(Icy)_2]PF_6$—different ^{13}N-labeled triazoles can be synthesized by reacting ^{13}N-labeled phenyl azides with alkynes at room temperature. This methodology works well with both aromatic and aliphatic terminal alkynes and could be extended to the reaction of labeled azides with aldehydes as well [32].

^{15}O: Production

^{15}O does not exist naturally, so it must be produced using nuclear reactions. As shown in Table 3, different nuclear reactions can be used to produce ^{15}O in different chemical forms. By far the most frequently used nuclear reaction is $^{14}N(d,n)^{15}O$, which works efficiently in an energy range of 3–15 MeV. This range can be achieved either by biomedical cyclotrons equipped with a deuteron source (usually by accelerating deuterons at 5 or 9 MeV) or by using so-called ^{15}O-generators, which are small cyclotrons capable of accelerating deuterons up to 3–4 MeV.

Historically, one of the most widely used reactions for ^{15}O production was the irradiation of a N_2/O_2 mixture with deuterons to produce primarily $[^{15}O]O_2$ with a minor amount of $[^{15}O]N_2O$ [33]. The ^{15}O-labeled molecular oxygen can be used to prepare other tracers such as $[^{15}O]CO_2$ by heating it over activated charcoal at 600 °C [34] or $[^{15}O]H_2O$ by heating it with H_2 in the presence of palladium at 150 °C [35]. The latter reaction is usually utilized in an "in-flow process." More specifically, the target is flushed continuously with a mixture of N_2/O_2 to produce $[^{15}O]O_2$. This ^{15}O-labeled dioxygen is then transferred to a hot cell where it is mixed with H_2 and circulated through an oven containing the catalyst to yield $[^{15}O]H_2O$, which is finally trapped in saline.

Nowadays, most biomedical cyclotrons only have proton sources because accelerated protons are used to produce other commonly used cyclotron-generated radionuclides (*e.g.* ^{18}F, ^{11}C, and ^{13}N). The installation of two proton sources rather than one proton source and one deuteron source minimizes downtime and guarantees the availability of such radionuclides even when one of the two sources fails. Hence, alternative methods for the production of ^{15}O using protons have been developed [36]. This can be achieved by irradiating $[^{15}N]N_2$ (Fig. 13). First, the target chamber is flushed several times with H_2 and finally vented to the atmosphere in order to leave a residual amount of H_2. Using a pneumatically driven syringe, the target is then loaded to a pressure of around 1.65 MPa with $[^{15}N]N_2$, and the irradiation is performed (note that the concentration of hydrogen in the final mixture is around 5%). After irradiation, the contents of the target are removed to recover the expensive $[^{15}N]N_2$ gas, and the $[^{15}O]H_2O$ is trapped in the cold trap (T = −40 °C). Afterward, the cold trap is heated, and the ^{15}O-labeled water can be transferred to the radiochemistry lab using an inert gas flow.

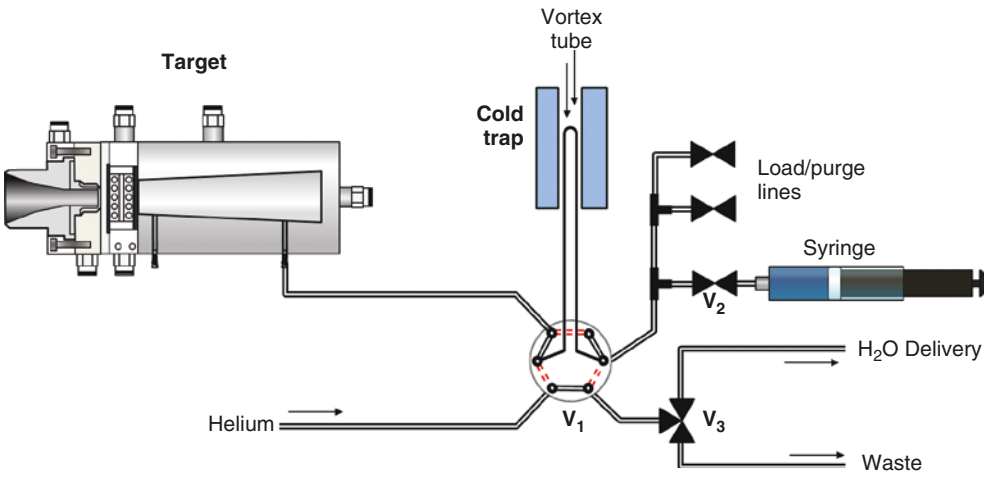

Fig. 13 Schematic of a system for the production and separation of [^{15}O]water. The cyclotron target is unloaded and reloaded by a 200 mL syringe. A trap cooled by a vortex tube retains the water vapor. The six-port valve V_1 switches the trap between the target syringe and the helium-delivery lines. An electric current can be applied to the trap to re-vaporize the water for delivery in a flow of helium. (Adapted from Powell and O'Neil [36], with permission)

^{15}O: Radiochemistry

Syntheses of more complex chemical species labeled with ^{15}O are vanishingly rare, mainly due to its extremely short half-life. One of the few examples is the preparation of [^{15}O]butanol—a radiotracer later on used for the determination of cerebral blood flow [37, 38]—using organoboranes. This molecule was obtained by reacting cyclotron-produced [^{15}O]O_2 with tri-*n*-butylborane in solution [39], and the process was later optimized by using tributylborane adsorbed on solid surfaces [40].

The chemical synthesis of ^{15}O-labeled hydrogen peroxide was also achieved using a solid supported process (Fig. 14) [41]. To this end, C-18 cartridges were conditioned with a solution containing 2-ethylanthrahydroquinol and then flushed with a stream of helium gas to remove the solvent. [^{15}O]O_2 was then passed through the cartridges to undergo a redox reaction with 2-ethylanthrahydroquinol, yielding [^{15}O]H_2O_2 as well as the corresponding (unlabeled) quinone. The resulting [^{15}O]H_2O_2 was eluted with saline. While the authors suggested that this compound could be used to investigate oxygen metabolism, such studies were never carried out.

Particularly Important Works

When reading the word "nitrogen-13," the first thing that comes to the minds of most radiochemists is that it is "the radionuclide used to prepare [^{13}N]NH_3, a tracer used to assess myocardial perfusion." Yet ^{13}N does not always need to remain confined to this somewhat limited perception. Indeed, those more experienced in its radiochemistry may foresee a radionuclide that—either in the form of ammonia or nitrite—can be used to prepare a few radiotracers, most of them described in previous sections. This section aims to provide an overview of other uses of the radionuclide which are by essence "different."

Mechanistic Studies Using ^{13}N

Radionuclides can be used to investigate the mechanisms of certain reactions, and ^{13}N is no exception. There are two aspects of radionuclides that make them particularly attractive for mechanistic studies: (i) the detection of radioactivity is extremely sensitive, meaning that the species can be detected even at very low concentrations, and (ii) unlike other analytical techniques, the detection of radioactivity is quantitative and linear. In other words, if two radioactive species labeled with the same radionuclide are present and the concentration of one is double that of the other, the signal corresponding to the first species will be double the signal corresponding to the second.

One clear example of the application of ^{13}N to mechanistic investigations lies in the study of the formation of aryl azides [42]. Under non-radioactive conditions, these molecules can be synthesized by reacting an aromatic amine with $NaNO_2$ and hydrazine hydrate in the presence of acetic acid. This reaction is effective, and it has been postulated that one equivalent of sodium nitrite reacts with the aromatic amine to yield the corresponding diazonium salt. Simultaneously, another equivalent of nitrite reacts with hydrazine hydrate to generate the azide ion *in situ*, resulting in the formation of the aryl azide. In light of this, three reaction mechanisms are possible (Fig. 15):

(i) An Sn_2Ar process (SN in the figure)
(ii) A thermal [3 + 2] cycloaddition to form a ^{1}H-pentazole cycloadduct, which ultimately yields the product via a second retro-[3 + 2] reaction (CA in the figure)
(iii) An addition-elimination process via an acyclic intermediate (AE in the figure)

The actual reaction mechanism was elucidated by exploring two different experimental scenarios: in scenario A (see Fig. 15a), aniline was reacted with sodium nitrite in the

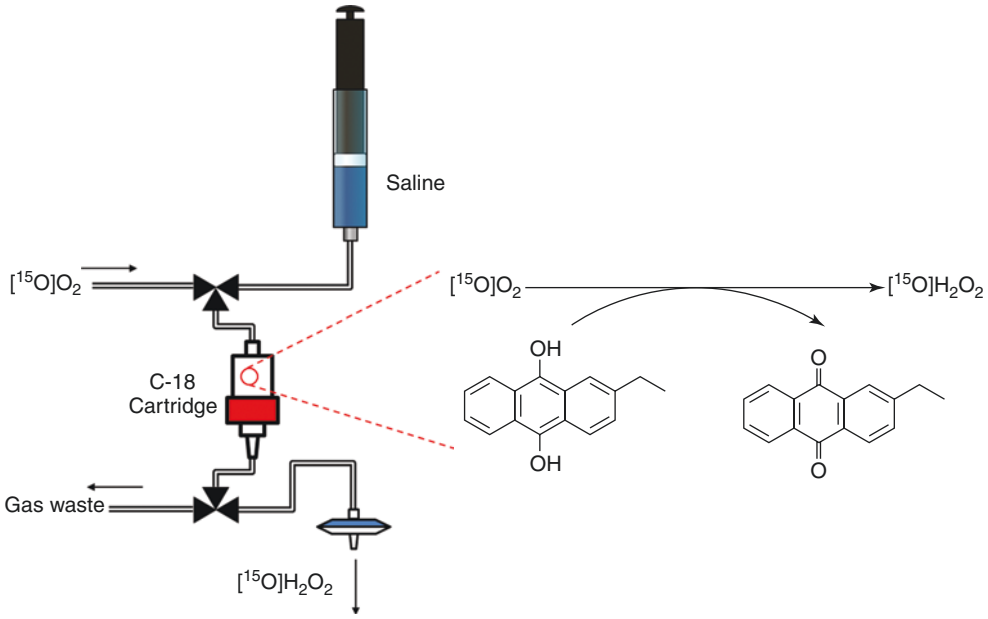

Fig. 14 Scheme for the production of $[^{15}O]H_2O_2$ (Adapted from Takahashi et al. [41], with permission)

presence of hydrochloric acid to yield the non-labeled diazonium salt. In a separate vial, hydrazine hydrate was reacted with $[^{13}N]NO_2^-$ in the presence of acetic acid to yield the ^{13}N-labeled azide ion. Finally, both solutions were mixed to enable the formation of the ^{13}N-labeled phenyl azide. In scenario B (see Fig. 15b), aniline was reacted with $[^{13}N]NO_2^-$ in the presence of hydrochloric acid to yield the ^{13}N-labeled diazonium salt. Separately, hydrazine hydrate was reacted with sodium nitrite in the presence of acetic acid to yield the non-labeled azide ion. Both solutions were finally mixed to enable the formation of ^{13}N-labeled phenyl azides. In both cases, the relative amounts of ^{13}N-labeled phenyl azide and $[^{13}N]N_2$ were determined. The experimental results showed that in scenario A, 50% of the radioactivity was present as the ^{13}N-labeled phenyl azide and the other 50% was present as $[^{13}N]N_2$. In scenario B, 100% of the radioactivity was present as the ^{13}N-labeled phenyl azide, and $[^{13}N]N_2$ was almost undetectable. These results suggested that the aryl azide from the corresponding diazonium salts occurs via a stepwise mechanism through an acyclic zwitterionic intermediate, a conclusion that was supported by computational methods.

Nanoparticle Radiolabeling with ^{13}N

Metal oxide nanoparticles (NPs) have broad applications in industry and in the manufacture of both commercial and personal healthcare products. The rapid and ever-expanding development of nanotechnology has raised concerns about the risks that these nanostructures may pose to human health and the environment. However, NPs are extremely difficult to detect and quantify once distributed in a biological system, thwarting safety evaluations and assessments of their biological fate. One way to overcome this problem is to label the NPs with a positron-emitting radionuclide.

Usually, long-lived radionuclides are employed to radiolabel NPs because the residence time of NPs in the body is relatively long (typically hours to days). However, the incorporation of a short-lived positron emitter may provide interesting information about the biodistribution immediately after administration. In the work described here, NPs were labeled with ^{13}N using direct proton beam activation [43] by taking advantage of the $^{16}O(p,\alpha)^{13}N$ nuclear reaction (Fig. 16). Experimentally, aluminum oxide NPs were placed in an aluminum capsule, which was then placed in a solid target holder (see Fig. 16b) and irradiated with a proton beam (target current = 5 μA; integrated current = 0.5 μAh). In this process, ^{13}N is produced in the sinus of the crystal lattice of the NPs (see Fig. 16a). Two main issues bear consideration here: (i) one particle is activated by the recoil implantation of the radioisotope generated in a different particle; that is, the ^{13}N produced as a consequence of the $^{16}O(p,\alpha)^{13}N$ nuclear reaction in one particle travels a few micrometers until its kinetic energy is lost, and it stays in a different particle; (ii) the nuclear reaction releases a significant amount of energy, resulting in a macroscopic temperature increase. This limits this methodology to the activation of NPs that do not contain temperature-sensitive components. In addition, appropriate cooling during irradiation is required to prevent heating at the nanoscale, which may melt the particles.

By carefully considering these issues, however, aluminum oxide NPs with four different nominal sizes were labeled, and their biodistribution profiles were evaluated in rats up to 1 h after intravenous administration. A relationship between the nominal size of the NPs and the organs in which the NPs accumulated could be established (Fig. 16c).

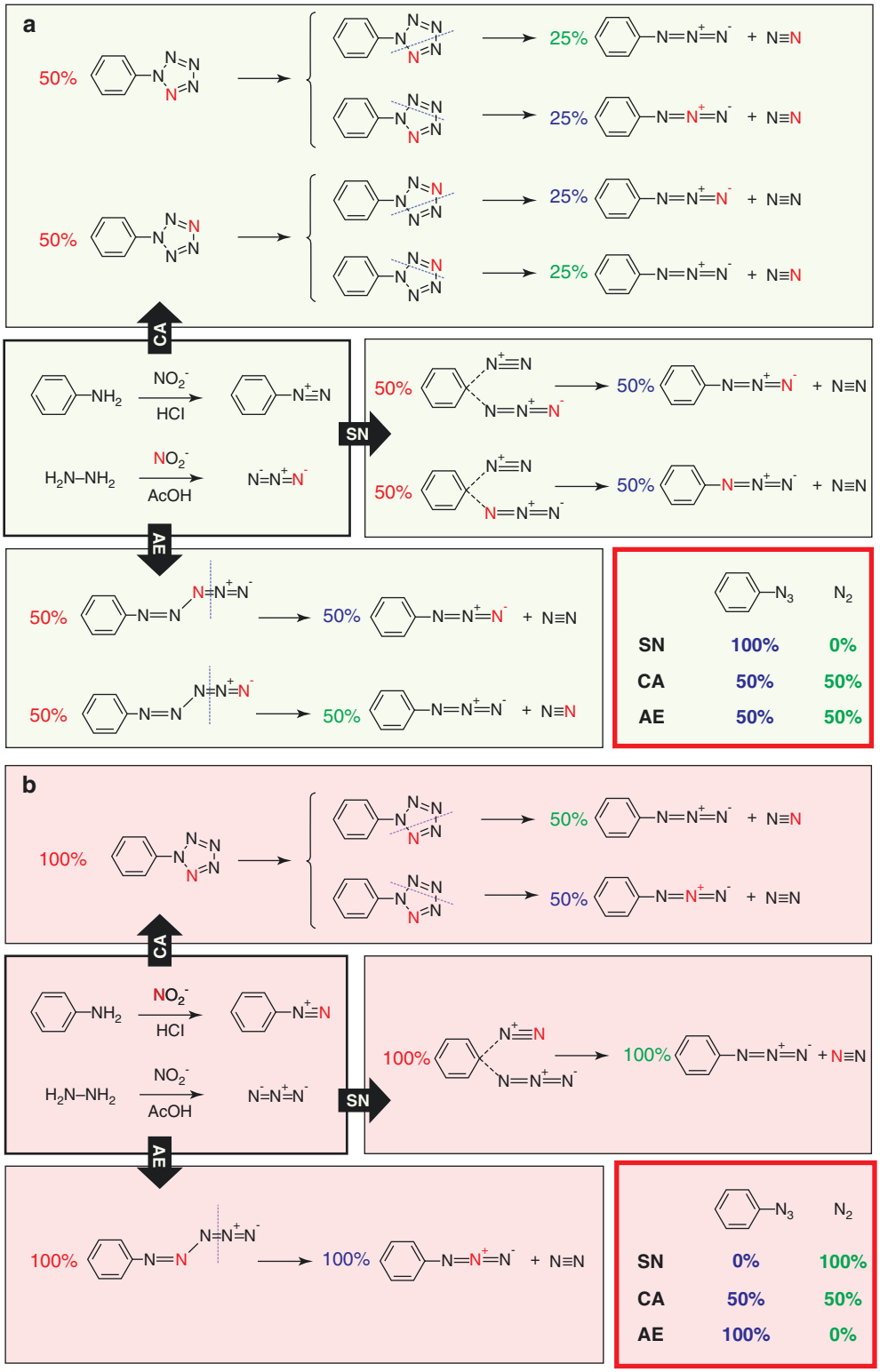

Fig. 15 The two strategies (**a** and **b**) followed to synthesize ^{13}N-labeled phenyl azide. In both scenarios, the three different possible mechanisms are shown: SN, aromatic nucleophilic substitution; CA, thermal cycloaddition followed by retro-(3 + 2) reaction; and AE, an addition-elimination process via an acyclic intermediate. For each scenario, the expected percentage of radioactivity for each labeled species is shown (numbers in red for intermediates, in green for $[^{13}N]N_2$, and in blue for ^{13}N-labeled phenyl azide). The global expected % values for $[^{13}N]N_2$ and ^{13}N-labeled phenyl azide in each scenario and mechanism are summarized in the highlighted squares

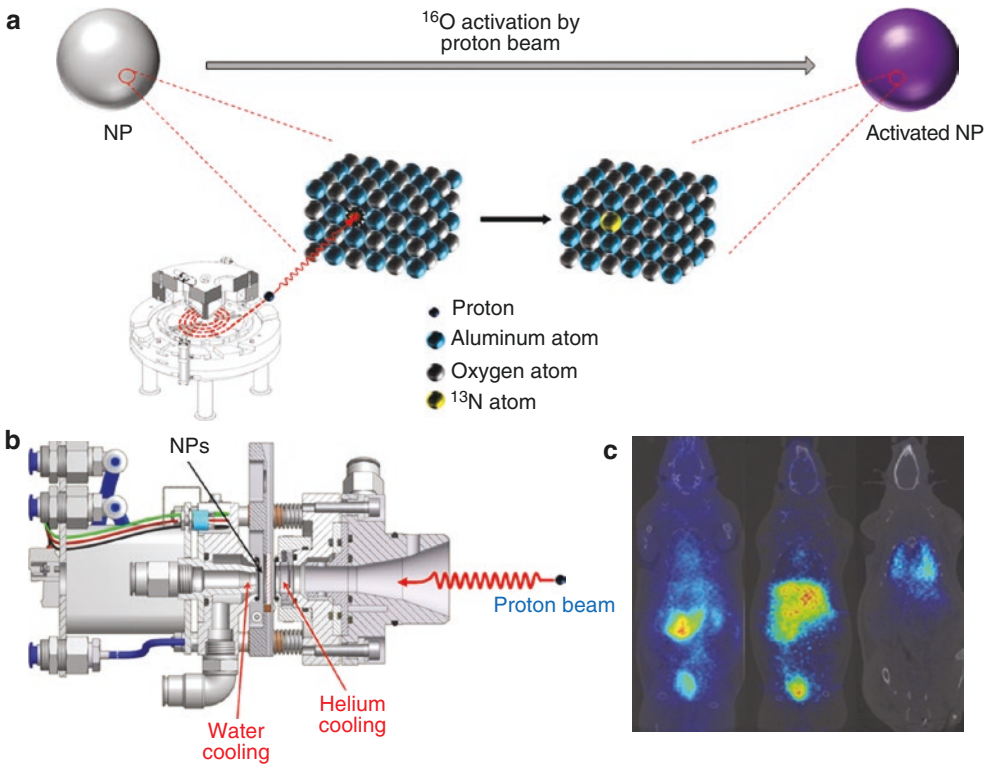

Fig. 16 (**a**) Schematic of the generation of ^{13}N-labeled aluminum oxide NPs by direct proton irradiation. The ^{13}N atom is generated in the sinus of the crystal lattice. (**b**) Scheme of the solid target holder used for the irradiation of the NPs. (**c**) Representative PET images obtained after the administration of three different sized labeled NPs (nominal sizes from left to right, 10, 40, and 10,000 nm)

The Future

It is clear that the main limitation to the routine use of ^{13}N and ^{15}O is their extremely short physical half-lives. This has three main consequences. First, it limits the application of ^{13}N- and ^{15}O-labeled tracers to centers equipped with a cyclotron of sufficient energy to efficiently produce these radionuclides. Second, it demands fast, efficient, and robust synthetic methods in order to prevent decay-associated radioactivity loss. And last but not least, the use of these radionuclides is limited to investigations of biological phenomena with fast kinetics because the effective half-life of ^{13}N- or ^{15}O-labeled tracers—which is a combination of the physical half-life of the nuclide and the biological half-life of the tracer—is very short.

The need for an on-site cyclotron can be considered a major limitation, because the installation of a cyclotron still requires a significant economic investment in terms of equipment, building works, and specialized personnel. However, different companies are currently working to develop compact cyclotrons. These efforts may result in products that are easier to operate, less logistically demanding, and more affordable than conventional cyclotrons. In theory, this could pave the way for the progressive implementation of a "dose on demand" PET scenario, in which more and more centers would have access to their own particle accelerator. If this were to become the case, short-lived radionuclides may gain significance. Two main limitations of compact cyclotrons are the potential lack of a source of deuterons (preventing ^{15}O production) and the limited energy of the accelerated protons, which might be insufficient to produce ^{13}N via the ^{16}O(p,α)^{13}N reaction (>10 MeV are usually needed for efficient production). Alternatively, other nuclear reactions could be employed, including ^{13}C(p, n)^{13}N, which is very efficient in the energy range 4–10 MeV. However, new targets compatible with compact cyclotrons might need to be developed to make these alternate approaches viable.

The need for fast and efficient synthetic routes for the preparation of ^{13}N- and ^{15}O-labeled tracers has been partially satisfied by some recent advances. The first relates to microfluidics technology, which has recently emerged as an interesting alternative to conventional methods of radiosynthesis because the radionuclide can be more efficiently incorporated in shorter time frames. Microfluidics technology has been applied to the preparation of radiotracers using several different radionuclides, including ^{13}N [44]. Although the real application of microfluidics to the preparation of pure ^{13}N-labeled compounds in sufficient quantities for *in vivo* studies still remains a challenge, realistic expectancies have been created, and future improvements are quite likely.

The second advance relates to the application of biosynthetic methods, which have been successfully applied to the preparation of ^{13}N-labeled tracers for decades and have also been suggested for ^{15}O-based agents [45]. However, a trial and error process was often used because understanding of the precise mechanisms underlying biocatalytic reactions

was very limited. Recently, significant advances in genomics and computational biology have resulted in novel experimental and computational protein engineering tools which have significantly enhanced the available toolbox of enzymes. Additionally, protein engineering and improvements in industrialized and commercial methods for the preparation of enzymes have introduced a new safety paradigm compatible with good manufacturing practices. Indeed, a variety of enzymes can now be purchased through certified companies that ensure biological safety and an absence of pyrogens or cell-derived residues. Finally, the development of innovative immobilization strategies and the application of computational tools can overcome some of the traditional limitations of enzymes in radiosynthesis, including poor stability in the presence of nonpolar solvents, under high temperatures, or under extreme pH values; limited reactivity toward artificial substrates; and high solubility in water, which ultimately limit their reusability in batch reactions or their applicability in continuous flow processes. All these developments may contribute to the wider application of enzymatic methods to the preparation of ^{13}N- and ^{15}O-labeled tracers.

The third limitation derived from the short half-lives of ^{13}N and ^{15}O is probably the most difficult to overcome, because the acquisition of images beyond 60 min after the administration of ^{13}N and 10 min after the administration of ^{15}O becomes unfeasible. However, the literature is full of useful examples in which the acquisition of images over short periods is sufficient to acquire relevant information.

Taking all these issues into account, it is expected that the use of ^{15}O- and especially ^{13}N-labeled compounds may increase in the future and that previously unexplored synthetic approaches will be investigated. While only a handful research groups are currently developing novel strategies for the preparation of compounds labeled with these radionuclides, the various issues mentioned above bring some hope to possibility of a new era for these short-lived radionuclides.

The Bottom Line

- ^{13}N and ^{15}O are positron emitters that, despite having short half-lives, can be efficiently produced by the majority of biomedical cyclotrons.
- ^{13}N has been employed in the production of radiolabeled amines, amides, azo compounds, triazoles, ureas, carbamates, and amino acids. Enzymatic reactions have played a pivotal role in the radiosynthesis of the latter.
- ^{15}O has been employed in the preparation of radiolabeled gases and water. It has only very rare been used in the preparation of more complex molecules.
- Recent technological advances may aid in the implementation of simple, affordable, and easy-to-handle cyclotron-synthesizer combinations, facilitating the use of these short-lived radionuclides in a wide range of applications.

References

1. Joliot F, Curie I. Artificial production of a new kind of radio-element. Nature. 1934;133(3354):201–2.
2. Cockcroft JD, Gilbert CW, Walton ETS. Production of induced radioactivity by high velocity protons. Nature. 1934;133(3357):328.
3. Livingston MS, McMillan E. The production of radioactive oxygen. Phys Rev. 1934;46(5):437–8.
4. Tilbury RS, Dahl JR. ^{13}N species formed by proton irradiation of water. Radiat Res. 1979;79(1):22–33.
5. Firouzbakht ML, Schlyer DJ, Wolf AP, Fowler JS. Mechanism of nitrogen-13-labeled ammonia formation in a cryogenic water target. Nucl Med Biol. 1999;26(4):437–41.
6. Wieland B, Bida G, Padgett H, Hendry G, Zippi E, Kabalka G, et al. In-target production of [^{13}N]ammonia via proton irradiation of dilute aqueous ethanol and acetic acid mixtures. Appl Radiat Isot. 1991;42(11):1095–8.
7. DeGrado TR, Hanson MW, Turkington TG, Delong DM, Brezinski DA, Vallée JP, et al. Estimation of myocardial blood flow for longitudinal studies with ^{13}N-labeled ammonia and positron emission tomography. J Nucl Cardiol. 1996;3(6):494–507.
8. Straatmann MG, Welch MJ. Enzymatic synthesis of nitrogen 13 labeled amino acids. Radiat Res. 1973;56(1):48–56.
9. Gómez-Vallejo V, Gaja V, Gona KB, Llop J. Nitrogen-13: historical review and future perspectives. J Labelled Comp Radiopharm. 2014;57(4):244–54.
10. Peter Wolk C, Austin SM, Bortins J, Galonsky A. Autoradiographic localization of ^{13}N after fixation of ^{13}N-labeled nitrogen gas by a heterocyst-forming blue-green alga. J Cell Biol. 1974;61(2):440–53.
11. Wellman TJ, Winkler T, Costa ELV, Musch G, Harris RS, Venegas JG, et al. Measurement of regional specific lung volume change using respiratory-gated PET of inhaled ^{13}N-nitrogen. J Nucl Med. 2010;51(4):646–53.
12. Le Bars D. A convenient production of [^{13}N]nitrogen for ventilation studies using a nitrogen gas target for ^{11}C production. J Labelled Comp Radiopharm. 2001;44(1):1–5.
13. Finn RD, Christman DR, Wolf AP. A rapid synthesis of nitrogen-13 labelled amphetamine. J Labelled Comp Radiopharm. 1981;18(6):909–13.
14. Tominaga T, Inoue O, Irie T, Suzuki K, Yamasaki T, Hirobe M. Preparation of ^{13}N-β-phenethylamine. Appl Radiat Isot. 1985;36(7):555–60.
15. Tominaga T, Inoue O, Suzuki K, Yamasaki T, Hirobe M. Synthesis of ^{13}N-labelled amines by reduction of ^{13}N-labelled amides. Appl Radiat Isot. 1986;37(12):1209–12.
16. Toshiaki I, Osamu I, Kazutoshi S, Toshiyoshi T. Labeling of ^{13}N labeled adenosine and nicotinamide by ammonolysis. Appl Radiat Isot. 1985;36(5):345–7.
17. Kumata K, Takei M, Ogawa M, Kato K, Suzuki K, Zhang MR. One-pot radiosynthesis of [^{13}N]urea and [^{13}N] carbamate using no-carrier-added [^{13}N]NH_3. J Labelled Comp Radiopharm. 2009;52(5):166–72.
18. Elmaleh DR, Hnatowich DJ, Kulprathipanja S. A novel synthesis of ^{13}N-*L*-asparagine. J Labelled Comp Radiopharm. 1979;16(1):92–3.
19. Benkovic SJ, Hammes-Schiffer S. A perspective on enzyme catalysis. Science. 2003;301(5637):1196–202.
20. Koshland DE. The key–lock theory and the induced fit theory. Angew Chem Int Ed. 1995;33(23–24):2375–8.

21. Chambers PJ, Pretorius IS. Fermenting knowledge: the history of winemaking, science and yeast research. EMBO Rep. 2010;11(12):914–20.
22. Barnett JA. A history of research on yeasts 5: the fermentation pathway. Yeast. 2003;20(6):509–43.
23. Cohen MB, Spolter L, Chang CC, MacDonald NS, Takahashi J, Bobinet DD. Immobilized enzymes in the production of radiopharmaceutically pure amino acids labeled with ^{13}N. J Nucl Med. 1974;15(12):1192–5.
24. Brena B, González-Pombo P, Batista-Viera F. Immobilization of enzymes: A literature survey. Methods Mol Biol. 2013;1051:15–31.
25. da Silva ES, Gómez-Vallejo V, López-Gallego F, Llop J. Biocatalysis in Radiochemistry; Enzymatic Incorporation of PET radionuclides into molecules of biomedical interest. J Labelled Comp Radiopharm. 2017;61(4):332–54.
26. Llop J, Gómez-Vallejo V, Bosque M, Quincoces G, Peñuelas I. Synthesis of *S*-[^{13}N]nitrosoglutathione (^{13}N-GSNO) as a new potential PET imaging agent. Appl Radiat Isot. 2009;67(1):95–9.
27. Gómez-Vallejo V, Kato K, Oliden I, Calvo J, Baz Z, Borrell JI, et al. Fully automated synthesis of ^{13}N-labeled nitrosothiols. Tetrahedron Lett. 2010;51(22):2990–3.
28. Sabaté CM, Delalu H. Synthesis and characterization of secondary nitrosamines from secondary amines using sodium nitrite and p-toluenesulfonic acid. Chem Asian J. 2015;10(3):674–8.
29. Gómez-Vallejo V, Kato K, Hanyu M, Minegishi K, Borrell JI, Llop J. Efficient system for the preparation of [^{13}N]labeled nitrosamines. Bioorg Med Chem Lett. 2009;19(7):1913–5.
30. Gaja V, Gómez-Vallejo V, Puigivila M, Pérez-Campaña C, Martin A, García-Osta A, et al. Synthesis and evaluation of ^{13}N-labelled azo compounds for β-amyloid imaging in mice. Mol Imag Biol. 2014;16(4):538–49.
31. Gómez-Vallejo V, Borrell JI, Llop J. A convenient synthesis of ^{13}N-labelled azo compounds: a new route for the preparation of amyloid imaging PET probes. Eur J Med Chem. 2010;45(11):5318–23.
32. Joshi SM, Gómez-Vallejo V, Salinas V, Llop J. Synthesis of 13 N-labelled polysubstituted triazoles: via Huisgen cycloaddition. RSC Adv. 2016;6(111):109633–8.
33. Welch MJ, Ter-Pogossian MM. Preparation of short half-lived radioactive gases for medical studies. Radiat Res. 1968;36(3):580–7.
34. Nichols AB, Cochavi S, Hales CA, Strauss HW, McKusick KA, Waltman AC, et al. Scintigraphic detection of pulmonary emboli by serial positron imaging of inhaled ^{15}O-labeled carbon dioxide. New Engl J Med. 1978;299(6):279–84.
35. Sajjad M, Liow JS, Moreno-Cantu J. A system for continuous production and infusion of [^{15}O]H_2O for PET activation studies. Appl Radiat Isot. 2000;52(2):205–10.
36. Powell J, O'Neil JP. Production of [15O]water at low-energy proton cyclotrons. Appl Radiat Isot. 2006;64(7):755–9.
37. Wunderlich G, Knorr U, Stephan KM, Tellmann L, Azari NP, Herzog H, et al. Dynamic scanning of ^{15}O-butanol with positron emission tomography can identify regional cerebral activations. Hum Brain Mapp. 1997;5(5):364–78.
38. Ingvar M, Eriksson L, Greitz T, Stone-Elander S, Dahlbom M, Rosenqvist G, et al. Methodological aspects of brain activation studies: cerebral blood flow determined with [^{15}O]butanol and positron emission tomography. J Cereb Blood Flow Metab. 1994;14(4):628–38.
39. Kabalka GW, Lambrecht RM, Sajjad M, Fowler JS, Kunda SA, McCollum GW, et al. Synthesis of ^{15}O-labeled butanol via organoborane chemistry. Appl Radiat Isot. 1985;36(11):853–5.
40. Kabalka GW, Green JF, Goodman MM, Maddox JT, Lambert SJ. The synthesis of oxygen-15 butanol via the oxidation of tributylborane adsorbed on solid surfaces. J Labelled Comp Radiopharm. 1994;35:186–8.
41. Takahashi K, Murakami M, Hagami E, Sasaki H, Kondo Y, Mizusawa S, et al. Radiosynthesis of ^{15}O-labeled hydrogen peroxide. J Labelled Comp Radiopharm. 1989;27(10):1167–75.
42. Joshi SM, De Cózar A, Gómez-Vallejo V, Koziorowski J, Llop J, Cossío FP. Synthesis of radiolabelled aryl azides from diazonium salts: experimental and computational results permit the identification of the preferred mechanism. Chem Commun. 2015;51(43):8954–7.
43. Pérez-Campaña C, Gómez-Vallejo V, Martin A, San Sebastián E, Moya SE, Reese T, et al. Tracing nanoparticles in vivo: a new general synthesis of positron emitting metal oxide nanoparticles by proton beam activation. Analyst. 2012;137(21):4902–6.
44. Gaja V, Gómez-Vallejo V, Cuadrado-Tejedor M, Borrell JI, Llop J. Synthesis of ^{13}N-labelled radiotracers by using microfluidic technology. J Labelled Comp Radiopharm. 2012;55(9):332–8.
45. Maddaluno JF, Faull KF. Fast enzymatic preparation of l-DOPA from tyrosine and molecular oxygen: a potential method for preparing [^{15}O]l-DOPA. Appl Radiat Isot. 1990;41(9):873–8.

The Radiopharmaceutical Chemistry of the Radionuclides of Gallium and Indium

Julia E. Blower, Maggie S. Cooper, Cinzia Imberti, Michelle T. Ma, Christopher Marshall, Jennifer D. Young, and Philip J. Blower

Fundamentals

Gallium and indium share the same group in the periodic table (group 13) and provide a trio of radionuclides—gallium-68, gallium-67 and indium-111—with a range of applications in nuclear medicine, including scintigraphy, SPECT, PET and targeted radiotherapy. Indium-111 and gallium-67 are gamma-emitting radionuclides with long half-lives (67.3 h and 78.3 h, respectively) which can be coupled to biomolecular vectors using bifunctional chelators. Gallium-68 is a positron-emitting radionuclide with a very short half-life (68 min) that has gained great traction in the last decade by virtue of its availability from several commercially available generators, one of which has recently gained marketing authorization in Europe [1].

Despite their chemical and radiological parallels, the paths of these three radionuclides in nuclear medicine have scarcely crossed. Indium-111 has played a seminal role in nuclear medicine since the 1970s [2, 3]. Because of its long half-life and its amenability to stable chelation, it quickly found applications as a radiolabel for both monoclonal antibodies (via bifunctional chelators) and white blood cells (via metastable complexes with ionophores such as 8-hydroxyquinoline and tropolone [4]). While gallium-67 has similar physical properties to indium-111, it—somewhat curiously—never became widely employed in either of these roles. Since the Ga^{3+} cation is significantly smaller and more labile than the In^{3+} cation (vide infra), the early chelators developed for indium-111 (*e.g.* diethylenetriaminepentaacetic acid, DTPA [3]) proved unsuitable for the coordination of gallium-67. Instead, the clinical use of gallium-67 has been based on exploiting the biological behaviour of the Ga^{3+} ion itself, particularly its parallels with Fe^{3+} and its participation in some aspects of iron metabolism (*e.g.* delivery to lymphoma by transferrin [5]).

Similarly, despite being isotopes of the same element, gallium-68 and gallium-67 have historically shared virtually no applications or chemical methodologies. The clinical use of gallium-67 became routine in the 1970s. However, very little progress was made in the development of effective bifunctional chelators for the nuclide until the advent of the gallium-68 generator in the 1990s/2000s. In particular, the last decade has played witness to the rapid development of several effective bifunctional chelators for gallium [6]. This recent push very clearly reflects the increasing recognition of the clinical potential of the gallium-68 generator for making PET tracers accessible to patients. During this period, the focus of radiopharmaceutical chemists has turned towards making radiolabeling with [^{68}Ga]Ga^{3+} as simple as possible [7]. The goal is to emulate the straightforward processing to which radiopharmacists have become accustomed for the preparation of ^{99m}Tc-labeled radiopharmaceuticals since the 1970s. Of course, these improved chelators could also be used for the coordination gallium-67, but the emergence of gallium-67's positron-emitting isotopologue has largely sidelined the nuclide. Moreover, [^{18}F]FDG has at least partially supplanted gallium-67 even for the most well-established applications of the latter: the imaging of lymphoma and inflammation [8]. Interestingly, the iron-mimicking properties of gallium that have underpinned many of the applications of gallium-67 have not been exploited in the use of gallium-68, largely because the half-life of gallium-68 is too short to match the long circulation time of transferrin. Recently, however, the ability of gallium-68 to form complexes with bacterial and fungal siderophores that are isostructural with Fe^{3+} analogues has sparked some interest in the use of the nuclide for the imaging of infectious disease [9].

In a marked departure from the trend with many other radiometals, the creation of chelators for both indium and gallium has focused not only upon the development of

J. E. Blower · M. S. Cooper · C. Imberti · M. T. Ma · J. D. Young
P. J. Blower (✉)
School of Biomedical Engineering & Imaging Sciences, King's College London, St. Thomas' Hospital, London, UK
e-mail: Philip.Blower@kcl.ac.uk

C. Marshall
Wales Research and Diagnostic PET Imaging Centre, University Hospital of Wales, School of Medicine, Cardiff University, Cardiff, UK

J. S. Lewis et al. (eds.), *Radiopharmaceutical Chemistry*, https://doi.org/10.1007/978-3-319-98947-1_14

ligands designed to offer maximal kinetic stability but also upon ligands designed to facilitate the controlled release of the metal. Examples of the latter include ionophores such as 8-hydroxyquinoline—used to enable the intracellular release of [^{111}In]In^{3+} during the radiolabeling of cells—and ligands (*e.g.* citrate) intended to allow for the transchelation of gallium-67 to transferrin within the blood. An additional consideration in the design of chelators for Ga^{3+}—of particular importance in light of the ever-widening use of gallium-68—is the need for fast chelation to make radiolabeling reactions simple and straightforward.

The gamma emissions of both indium-111 and gallium-67 are accompanied by the emission of low-energy secondary electrons such as Auger electrons, mostly with ranges in the tissue of <1 μm. The exploitation of this phenomenon for targeted radionuclide therapy has been explored both in the laboratory and in the clinic [10–13]. To date, however, these studies have remained rather superficial and have not led to the widespread clinical adoption of these isotopes for targeted radiotherapy.

The growth of the clinical use of gallium-68 seems assured, driven both by the availability of the nuclide (via cyclotron- and generator-based production methods) and the development of quick, easy-to-use radiolabeling methods that can be performed on-site without costly infrastructure. On the other hand, the rise of PET imaging may lead to a decline in the use of indium-111 for SPECT, as long-lived positron-emitting radionuclides such as zirconium-89 become more established as radiolabels for both antibodies [14] and cells [15]. Already, the clinical nuclear medicine community has to adapt to the reduced commercial availability of indium-111 and gallium-67, while the supply of zirconium-89 is growing.

Details

The Radioactive Emissions of Gallium and Indium

The most medically useful radioisotope of indium is indium-111, although both Indium-114m and Indium-113m have been used for medical applications in the past. Indium-111 has a half-life of 67.3 h, making it a suitable radiolabel for vectors with longer pharmacokinetic profiles. It is imageable with a gamma camera, but its multiple photopeaks at 171 keV and 245 keV leave something to be desired in terms of image quality (technetium-99m, in contrast, has a monoenergetic photopeak that is nearly ideal). The physical properties of gallium-67 are quite similar to those of indium-111: gallium-67 has a half-life of 78.3 h and an even more complex gamma spectrum, with the highest abundance of gamma emissions at 93, 185 and 300 keV contributing to its non-ideal imaging characteristics.

The decays of indium-111 and gallium-67 are accompanied by the emission of low-energy Auger electrons with short path lengths (<< 1 cell diameter). For imaging applications, this phenomenon contributes to unwanted cellular radiation dose. However, it also creates the possibility of using these radionuclides for targeted radionuclide therapy. Indeed, when these radionuclides are internalized, these Auger electrons have the potential to cause cell death through mechanisms such as DNA damage. This possibility has been evaluated both in preclinical [12, 13] and clinical studies [11, 16], though not necessarily in the contexts most likely to produce optimal results. As a result, it remains unclear whether Auger electron-based therapies with these radionuclides will be useful in the future. The secondary electron emissions of indium-111 and gallium-67 differ significantly. Although the total energies of the emitted electrons are similar (6.3 and 6.8 keV, respectively), indium-111 emits far more electrons per decay (14.7 vs. 4.7). Consequently, the electrons emitted from gallium-67 are more energetic, giving them a greater range in water (up to 2.4 μm). One might expect, therefore, that the lethality of these electrons from gallium-67 would depend less on the localization of the radionuclide within the cell nucleus. This may explain the significantly greater potency of gallium-67 than indium-111 per intracellular decay. Clearly, more research is needed in this field.

Gallium-68 decays to zinc-68 by positron emission (89%) and electron capture. The energy of its positrons (1.9 MeV) is significantly higher than those emitted by fluorine-18 and copper-64, a trait which leads to PET images with lower resolution. While this effect is significant in small-animal PET, it ultimately proves marginal with the current generation of human PET scanners.

The Coordination Chemistry of Gallium and Indium

Gallium and indium are *p*-block elements in group 13 of the periodic table with electronic configurations [Ar]$3d^{10}$ $4s^2$ $4p^1$ and [Kr]$4d^{10}5s^25p^1$, respectively. Their full *d*-orbitals simplify their chemistry compared to their neighbouring transition metals that have unfilled *d*-shells. Their ionization energies predispose them to be predominantly trivalent and electrochemically inert, with only Ga(III) and In(III) stable under biological conditions. Ga^{3+} and In^{3+} are both relatively "hard" Lewis acid metal ions, with high charge density and a preference for oxygen and nitrogen donor atoms. As d^{10} metal ions, they exhibit no ligand field or crystal field stabilization energies, and their coordination geometries are governed by the steric requirements of their ligands. Their bonding is highly ionic, and the lability of their coordinate bonds means that their incorporation into receptor-targeted radiopharmaceuticals requires well-designed chelators to achieve adequate stability.

Although Ga^{3+} and In^{3+} share similar periodic properties, the conditions needed to ensure their stable coordination are

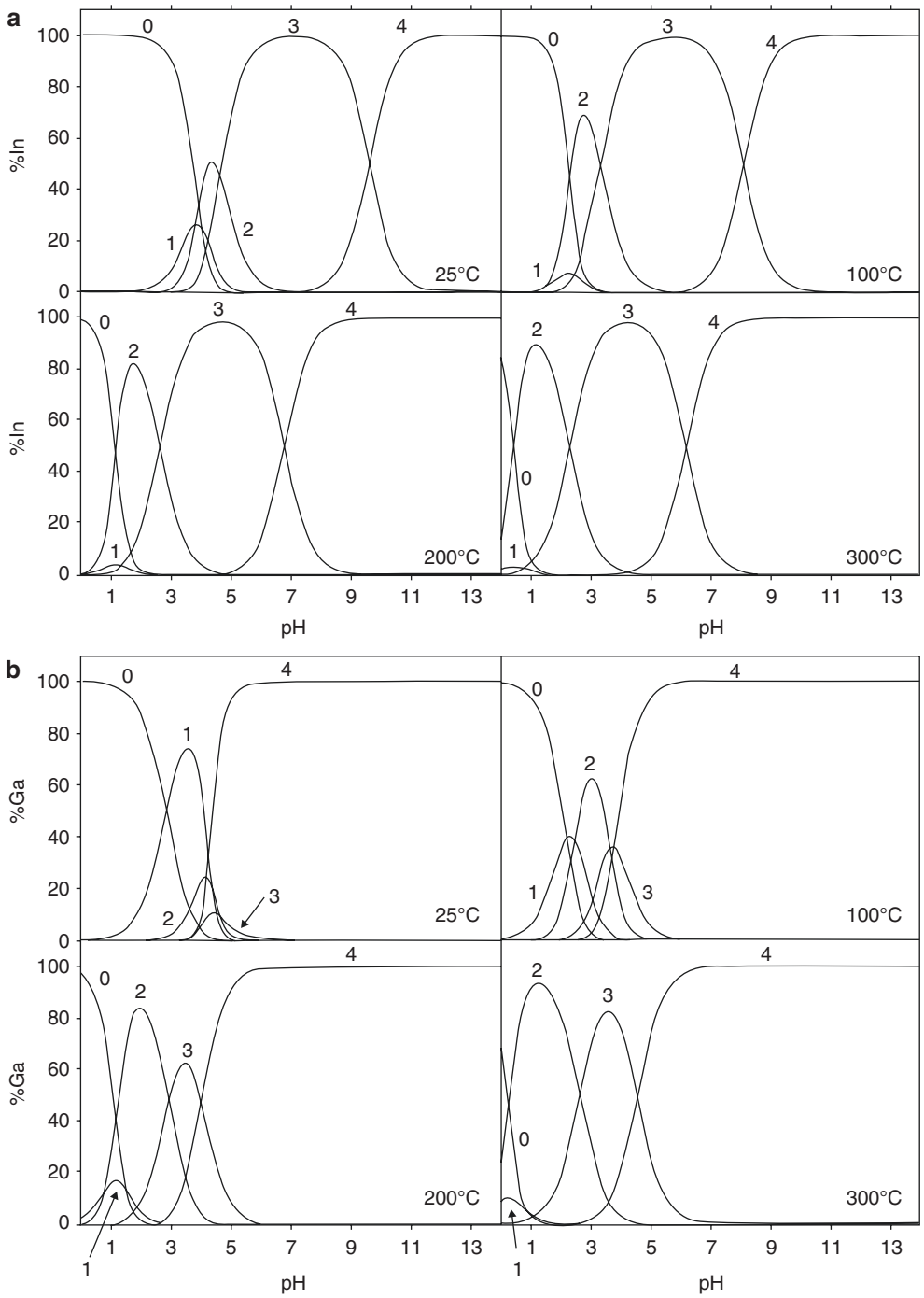

Fig. 1 Distribution of mononuclear In-hydroxide (**a**) and Ga-hydroxide (**b**) species as a function of temperature and pH at infinite dilution. The species shown are (M = Ga or In): 0 = M^{3+}, 1 = $M(OH)^{2+}$, 2 = $M(OH)_2^{+}$, 3 = $M(OH)_3$ and 4 = $M(OH)_4^{-}$ (From Wood and Samson [17], with permission)

significantly different. Ga^{3+} is relatively small, with an ionic radius of 0.62 Å. It forms complexes with up to six donor atoms and frequently adopts octahedral geometries. In contrast, In^{3+} is significantly larger (0.8 Å) and forms stable complexes with up to nine donor atoms in its coordination sphere. As a result, ideal chelators for In^{3+} typically incorporate more than six donor atoms. In aqueous solution, both hydrated cations are acidic and subject to the formation of hydroxide complexes. Under acidic conditions (pH <3), fully hydrated Ga^{3+} exists as $[Ga(H_2O)_6]^{3+}$. As the pH rises, however, the hydrated cation is readily deprotonated, forming strong hydroxide complexes including $[Ga(OH)]^{2+}$, $[Ga(OH)_2]^{+}$, $[Ga(OH)]_3$ and $[Ga(OH)_4]^{-}$. The distribution of these species as a function of pH at 25 °C and 100 °C is shown in Fig. 1. The major species include $[Ga(H_2O)_6]^{3+}$ below pH 3 at both temperatures, $[Ga(OH)]^{2+}$ from pH 3–5 at 25 °C, but $[Ga(OH)_2]^{+}$ at 100 °C, and $[Ga(OH)_4]^{-}$ above pH 5 at both temperatures [17].

Indium, like gallium, forms strong complexes with OH^{-} ions as pH rises above about pH 3.5 (see Fig. 1). These hydrolytic equilibria govern the reactivity of aqueous Ga^{3+} and In^{3+} with chelators, and the design of the chelators and

the pH at which they are used must take this into account. A particularly critical requirement is the selection of chelators and conditions to overcome the tendency of both $Ga(OH)_3$ and $In(OH)_3$ to precipitate from solution.

Bifunctional Chelators

The choice of chelator is critical for the development of an effective receptor-targeted radiopharmaceutical labeled with Ga^{3+} or In^{3+}. The ideal chelator should meet several criteria:

(i) It should rapidly and quantitatively bind to very low (micro- to nanomolar) concentrations of the radiometal typically present, enabling the simple, on-site preparation of radiopharmaceuticals.
(ii) It should bind the radiometal quantitatively even at low concentrations of the chelator. After the synthesis of a radiolabeled bioconjugate, the unlabeled, "cold" precursor is typically not easily separable from the radiolabeled construct. As a result, relatively large amounts of the unlabeled bioconjugate can compete with the radiopharmaceutical for binding sites *in vivo*, effectively blocking the binding of the latter. The quantitative measure of the amount of radioactivity bound per biologically active molecule is called *molar activity* and has units of activity (Bq) per mole of conjugate.
(iii) It should stably retain the radiometal *in vivo* so that dissociation does not lead to the unwanted accumulation of the radiometal in healthy, nontarget tissues.

It follows that any chelator for a bioconjugate radiolabeled with gallium-67/68 or indium-111 should be capable of binding the radiometal with high thermodynamic stability, high kinetic stability and fast complexation kinetics. Favourable *thermodynamics* are important to drive the formation of the complex under conditions in which the concentrations of both the chelator and the metal ion are very low. Polydentate chelators generally form more thermodynamically stable complexes with Ga and In than homologous monodentate ligands. Indeed, all of the ligands that are useful for gallium- and indium-based radiopharmaceuticals are polydentate chelating systems. Once circulating *in vivo*, radiopharmaceuticals are diluted even further, endogenous biomolecules with higher concentration can compete to bind the radiometal and endogenous metal ions can compete to bind the chelator. Even the most thermodynamically stable radiometal-chelator complexes will dissociate under these conditions unless the radiolabeled metal complex possesses high *kinetic stability* as well. If suitably designed, polydentate chelators—and especially macrocyclic chelators—can impart the requisite kinetic stability. If a donor atom from a polydentate or macrocyclic ligand dissociates from the metal centre, the likelihood of its rapid re-coordination is high because the dissociated donor atom (being linked to other coordinated atoms) remains proximal to the metal centre. This is a kinetic manifestation of the *chelate effect*.

The rapid and quantitative chelation of radiometal is desirable because many radiopharmaceuticals—particularly those based on Gallium-68—will be prepared on-site at hospitals and clinics. Rapid radiolabeling kinetics are not only a must when working with radionuclides with short half-lives (*e.g.* Gallium-68), but they also simplify radiolabeling protocols and eliminate the need for separation or purification procedures to remove uncoordinated radiometal.

The extent to which complexation kinetics and *in vivo* kinetic stability influence the choice of a chelator depends largely on the half-life of the radionuclide and the imaging protocol employed. Gallium-68 has a half-life of 68 min, so rapid radiolabeling kinetics is critical. However, since PET imaging with ^{68}Ga-based radiopharmaceuticals is typically performed within 2 h of administering the tracer, prolonged *in vivo* stability (> 4 h) is not required. Not surprisingly, these requirements are reversed when we consider indium-111. Its half-life of 67 h means that rapid radiolabeling kinetics is much less of priority. However, the use of the radionuclide as a label for vectors with multi-day pharmacokinetic profiles means that *in vivo* stability is of paramount importance.

Metastable Chelates of Gallium and Indium

Somewhat counterintuitively, complexes with high thermodynamic and kinetic stability are undesirable in some applications. In these cases, ligands with lower affinity and greater lability are used, with the aim of deliberately exploiting the controlled dissociation and transchelation of the radiometal in the biological milieu.

For example, indium-111 is used in this way for labeling whole cells, using uncharged, lipophilic complexes of 8-hydroxyquinoline and other bidentate, monobasic ligands. In addition, complexes of gallium-67 with weakly binding ligands such as citrate are employed to insert the radiometal into the biological pathways of iron trafficking. In both of these cases, the chelators do not form highly stable complexes with the radiometal: rather, these complexes form *only* in the presence of a large excess of chelator. To delve a bit deeper into the first example, these uncharged, lipophilic indium-111 complexes can diffuse across cell membranes. Once inside cells—where the concentration of the chelator is (obviously) much lower—the complexes dissociate, releasing $[^{111}In]In^{3+}$. It is supposed that the free radiometal then binds to endogenous intracellular biomolecules, a process which underpins the use of these complexes for cell labeling (see below). Analogous complexes of gallium-67 have not found widespread use in this application,

though it would be feasible in principle. However, the use of [^{67}Ga]Ga-citrate for the imaging of lymphoma is mechanistically similar: the metastable [^{67}Ga]Ga-citrate complex undergoes transchelation to the iron-transporting protein transferrin in the plasma, allowing for the selective imaging of tumours that express high levels of the transferrin receptor.

Bifunctional Chelators for Gallium

Chelators for the incorporation of gallium into targeted radiopharmaceuticals must simultaneously provide enough kinetic stability for the complex to remain intact during imaging—a few hours for gallium-68, often days for gallium-67—without imposing high kinetic barriers to the initial formation of the complex (particularly in the case of gallium-68) [6]. An effective chelator for gallium must also compete with OH^- for the metal. Although $[Ga(OH)_3]$ is never the dominant species in solution, its presence is important due to its very low solubility. The precipitation of $[Ga(OH)_3]$ removes it from solution, thus driving the further formation of colloids. This process leads to a greater loss of gallium than predicted by the distribution shown in Fig. 1, which was derived at infinite dilution. The formation of $[Ga(OH)_3]$ is greatest at pH 4–5 and increases with both temperature and the presence of other metals in solution. The chelator must bind gallium rapidly enough to avoid the simultaneous formation of $[Ga(OH)_3]$ colloid, which, once precipitated from solution, is no longer available for chelation. In order to circumvent this issue, stabilizing ligands such as citrate, acetate and oxalate are often used. The affinity of these ligands for Ga^{3+} is sufficient to reduce the formation of $[Ga(OH)_3]$ but not strong enough to prevent the formation of complexes with the bifunctional chelator.

As Ga^{3+} is a hard Lewis acid, it favours binding to hard Lewis bases such as nitrogen and oxygen. With its small radius, it is most stable as a six-coordinate (distorted) octahedron, whereas In^{3+} favours higher coordination numbers. Ga^{3+} can also form four and five coordinate complexes, but these are typically more sensitive to hydrolysis.

Macrocyclic Chelators for Gallium

DOTA (1,4,7,10-tetraazacyclododecane-1,4,7,10-tetraacetic acid, Fig. 2) is a macrocyclic chelator with a 12-membered ring containing four donor amine nitrogen atoms and four pendant carboxylic acids. It is the most commonly used chelator for radiometals because it forms stable complexes with a wide range of metals in a variety of oxidation states, including Bi(III), Cu(II), Ga(III), In(III), Lu(III), Pb(II), and Sc(III). DOTA is suitable for binding gallium-67/68 and readily does so upon heating to 100 °C for 10–30 min at pH 4 [18]. It is important to note, however, that DOTA was designed not for gallium but rather for larger metals with higher coordination numbers (hence its eight donor groups). Crystal structures

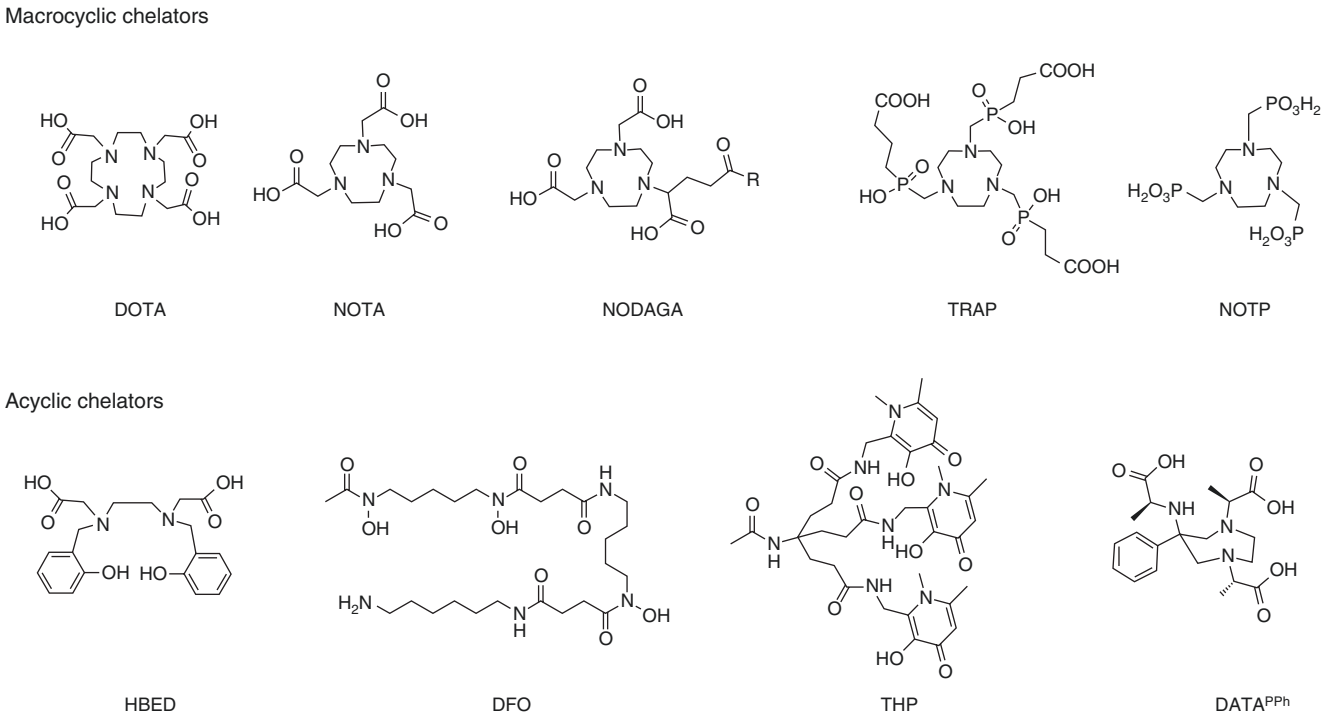

Fig. 2 Structures of common macrocyclic (top) and acyclic (bottom) chelators for gallium

show that DOTA binds gallium as an N_4O_2 donor, with two pendant carboxylic acid groups uninvolved in the coordination of the metal. In addition, the formation of the Ga-DOTA complex produces steric strain in the backbone of the macrocyclic [19]. Consequently, the DOTA complex of Ga^{3+} has a lower formation constant (log K_{ML}) than the NOTA complex of Ga^{3+} (21.33 compared to 30.98) [20]. Despite these deficiencies, DOTA remains—at least for now—the most widely used chelator for clinical studies with [^{68}Ga]Ga^{3+} due to its widespread availability and the favourable biodistribution of many [^{68}Ga]Ga-DOTA-labeled conjugates.

NOTA (1,4,7-triazacyclononane-1,4,7-triacetic acid; see Fig. 2), on the other hand, is a nine-membered ring containing three amines and three pendant carboxylic acids. NOTA binds to Ga^{3+} in an N_3O_3 coordination environment and is well suited to the size of the metal as well as its preferences in coordination number and geometry. The formation of gallium-67/68 complexes with NOTA requires incubation at pH 4 for 10 min but not heating (unlike DOTA). Ga-NOTA has a higher formation constant than Ga-DOTA as well as excellent *in vivo* kinetic stability. As a result, it is currently accepted as the "gold standard" chelator for gallium-67/68, even though DOTA is used more often in the clinic [6]. NOTA can be turned into a bifunctional chelator by adding a linker to one of its carboxylic acid arms, but doing so reduces the number of carboxylic acids available for binding gallium. An alternative which leaves all of the pendant carboxylic acids intact is NODAGA, a relative of NOTA in which a linking group is added via one of the CH_2 groups in the backbone of the macrocycle (see Fig. 2), thus allowing the chelator to retain the optimal metal-binding properties of NOTA.

A number of NOTA-based derivatives are also used for the chelation of gallium, notably TRAP and NOTP, two chelators in which phosphinic or phosphonic acid groups (respectively) replace the carboxylic acid arms of NOTA (see Fig. 2). These modifications enable the chelators to bind gallium in the presence of metal impurities [21], but both TRAP and NOTP still require acidic conditions (pH 3–4) for optimal radiolabeling.

Acyclic Gallium Chelators

HBED (bis(2-hydroxybenzyl)ethylenediaminediacetic acid; see Fig. 2) is a N_2O_4 donor that binds to Ga^{3+} through its amine, carboxylic acid and phenol functional groups. HBED can be labeled with gallium-67/68 via incubation for 10 min at room temperature at pH 4. A drawback of the chelator is that the three pairs of donor groups allow for the formation of multiple geometric isomers which are distinguishable by HPLC and NMR (Fig. 3) [22].

DFO (desferrioxamine B; see Fig. 2) is a potent microbially derived acyclic iron chelator (siderophore) used for treating iron overload diseases. It binds gallium as an O_6 donor through its three hydroxamate groups. The chelation of [$^{67/68}$Ga]Ga^{3+} can be achieved at room temperature via incubation for 30 min at pH 3.5 [6] or 1 h at pH 5 [23]. One early radiopharmaceutical application of DFO was the labeling of antibodies with gallium-67, but the resulting radioimmunoconjugates displayed poor *in vivo* stability [23].

The THP (*tris*(hydroxypyridinone)) chelator, like DFO, is based on the design of chelators for iron(III), and its three 1,6-dimethyl-3-hydroxypyridin-4-one units provide an O_6 donor set. The radiolabeling of THP is performed at room temperature and pH 6.5 and is complete within 5 min [18]. These conditions not only support quick and convenient labeling but also enable the labeling of biological vectors that are sensitive to low pH or heat, such as antibodies [24]. THP is the first chelator that allows for the production of ^{68}Ga-labeled imaging agents using a one-step, room-temperature radiopharmaceutical kit [7].

Importantly, the similarities between the coordination chemistries of Fe^{3+} and Ga^{3+} that underpin the use of DFO and THP extend to the chelation of Ga^{3+} with other siderophores as well. This observation has not only led to the design of improved chelators for the radiometal but also increased interest in the use of gallium-67/68 for the imaging of microbial disease by targeting microbial siderophore receptors. For example, desferri-triacetylfusarinine C (TAFC, Fig. 4) is a

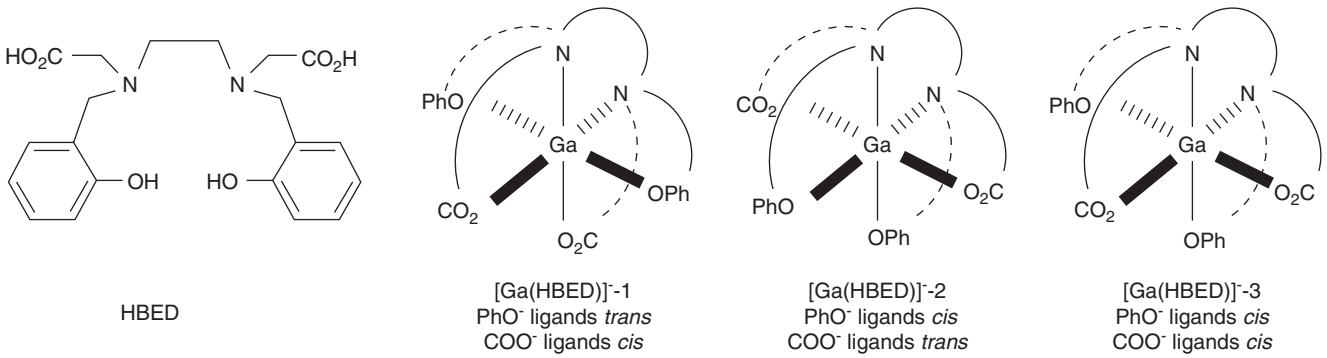

Fig. 3 Possible geometric isomers for hexadentate $[Ga(HBED)]^-$. Note that each isomer depicted here is one representative of a pair of enantiomers (From Tsionou *et al.* [22], with permission)

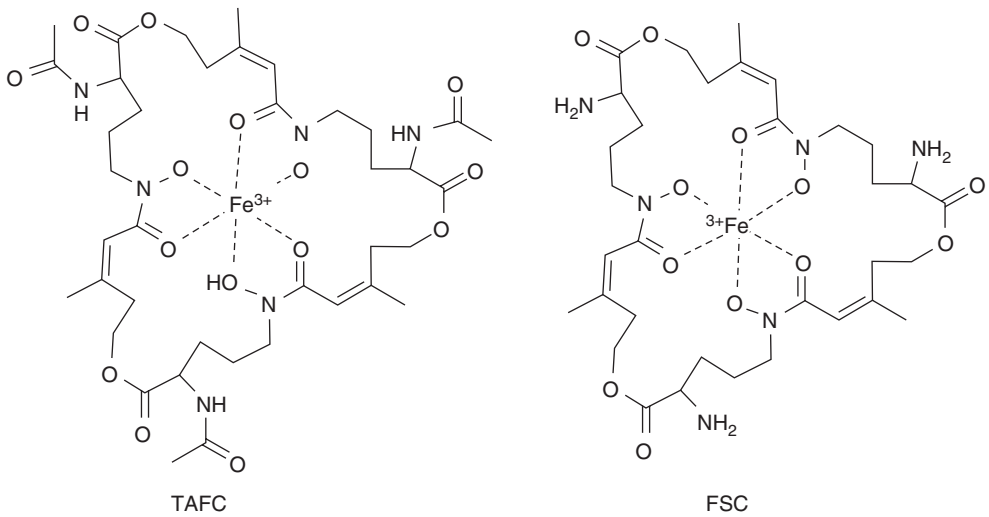

Fig. 4 The Fe^{3+} complexes of TAFC and FSC, siderophores used for the complexation of gallium-68

hydroxamate-based siderophore produced by the fungus *Aspergillus fumigatus*. The radiolabeling of TAFC with gallium-68 was first investigated as a way to detect fungal infections [9], but the facility of the radiolabeling reaction itself prompted further explorations into the use of TAFC as a bifunctional chelator for gallium-68. As a proof of principle, its deacetylated version fusarinine C (FSC; see Fig. 4) was conjugated to three different RGD-based peptides via their lysine sidechains and radiolabeled with gallium-68, producing excellent radiolabeling yields and specific activities over a wide range of pH values (3–8) [25].

Bifunctional Chelators for indium-111

In the 1980s, indium-111 became the first-choice radionuclide for the labeling of peptides and proteins. Its longer half-life corresponds well with the pharmacokinetic profiles of antibodies and other large proteins, facilitating the collection of images several days after the administration of the radiopharmaceutical. Effective chelators for indium-111 were developed quickly, easily outstripping the development of chelators for other radiometals. Consequently, indium-111 also became the first widely used radiolabel for small peptides—including octreotide—even though other radionuclides with shorter half-lives would have been preferable with regard to both image quality and radiation dosimetry.

The earliest studies with indium-111 centred upon the creation of DTPA-bearing bioconjugates using either cyclic diethylenetriaminepentaacetic acid anhydride (cDTPA, Fig. 5) or mixed anhydride DTPA (mDTPA). This strategy proved remarkably effective, but optimizations were nonetheless necessary. The conjugation of cDTPA and mDTPA uses one of the chelators' carboxylate arms to form an amide link with the biomolecule, rendering this group unavailable for the coordination of the radiometal. This is, not surprisingly, not an ideal scenario, as all five of the ligands' carboxylate groups are needed to complex the radiometal with maximum stability [26]. As a result, [^{111}In]In-DTPA-labeled conjugates formed in this manner are kinetically and thermodynamically unstable *in vivo* over the multi-day periods needed for imaging with radiolabeled antibodies. The indium-111 released is taken up by the liver and the reticuloendothelial system, a significant problem for clinical imaging.

In light of these issues, more stable chelators for indium-111 were sought. Due to its large size and preference for forming complexes with high coordination numbers, [^{111}In]In^{3+} can bind all eight donor atoms offered by DTPA (and an additional water molecule as well [26]). Brechbiel *et al.* first reported the use of isothiocyanatobenzyl-bearing derivatives of DTPA that allowed all five of the ligand's carboxylates to be available for the coordination of the metal even *after* bioconjugation [27]. ^{111}In-labeled constructs using these bifunctional chelators were more stable *in vivo* than their forerunners. Reducing the flexibility of the backbone of DTPA via alkyl substitutions or the incorporation of cyclic elements, as in CHX-A-DTPA, for example (see Fig. 5), further improved the *in vivo* stability of [^{111}In]In-DTPA complexes [28]. Over the years, macrocylic chelators such as DOTA and NOTA—described above in connection with gallium-68—have also become established for use with indium-111 [29].

Despite the importance of indium-111 as a radiolabel for monoclonal antibodies, the ^{111}In-labeled radiopharmaceutical with the greatest clinical impact is easily [^{111}In]In-octreotide, which has been used for many years for the imaging of neuroendocrine tumours. Indeed, the use of [^{111}In]In-octreotide predates PET imaging with two similar ^{68}Ga-labeled peptides—[^{68}Ga]Ga-DOTATATE and [^{68}Ga]Ga-DOTATOC—which are preferable both in terms of image quality and patient dosimetry.

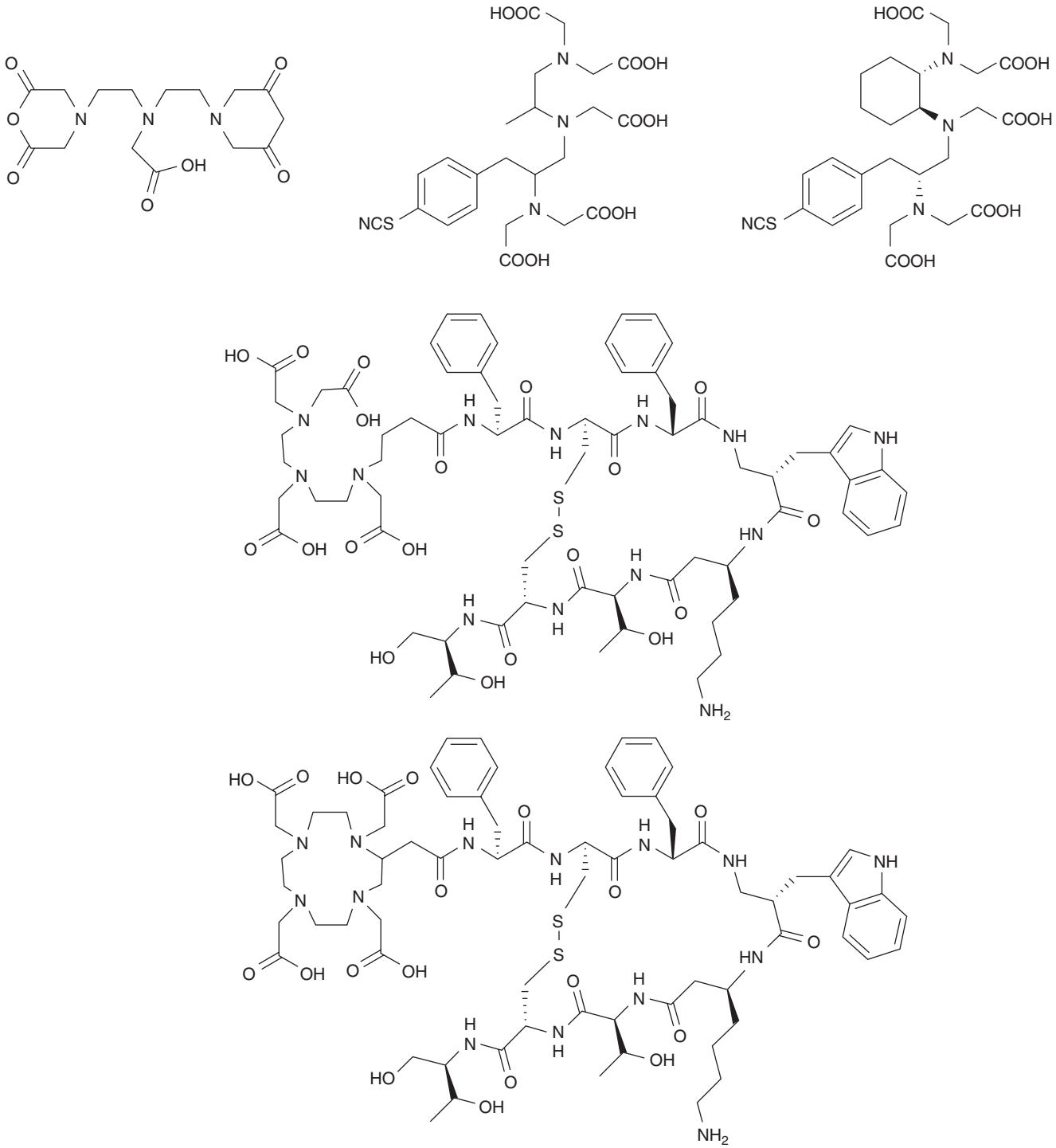

Fig. 5 Bifunctional chelators and bioconjugates for labeling with indium-111. Top: DTPA cyclic anhydride (left), 1B3M-DTPA (centre) [30] and CHX-A-DTPA (right). Middle: DTPA-(D)Phe^{1} Octreotide (Octreoscan). Bottom: DOTA^{0}-(D)Phe^{1}-Tyr^{3}-octrotide (DOTATOC) [28]

Cell Tracking with In-111

Indium-111 has become established as the most widely used radionuclide for radiolabeling white blood cells and platelets. More recently, indium-111 has been adopted for the radiolabeling other types of cells as well, as novel cell-based therapies enter clinical trials. Most early studies used [^{111}In]In-oxine—a complex of [^{111}In]In^{3+} with three 8-hydroxyquinolinate ligands (Fig. 6)—which became commercially available in the 1980s. The putative mechanism of this

approach relies upon [^{111}In]In-oxine first crossing the cell membrane by virtue of its lipophilicity. Once the complex is exposed to higher-affinity In^{3+}-binding species within the cell, the radiometal undergoes transchelation and is thus trapped in the cell. Because of the instability of the complex, the blood cells must be freed from plasma and washed with saline in order to ensure efficient labeling; otherwise, the indium-111 will bind to plasma proteins.

A number of closely related alternatives to 8-hydroxyquinoline have been evaluated as ionophores for indium-111. The most successful has been tropolone. The [^{111}In]In-tropolonate complex (see Fig. 6) was proposed for labeling platelets [5] but can also be used for labeling white blood cells. Like oxine, tropolone forms a 3:1 complex with indium but has the advantage that labeling can be carried out in the presence of plasma. With the recently reduced commercial availability of [^{111}In]In-oxine, [^{111}In]In-tropolone—which is readily prepared in hospital radiopharmacies—has become a useful alternative.

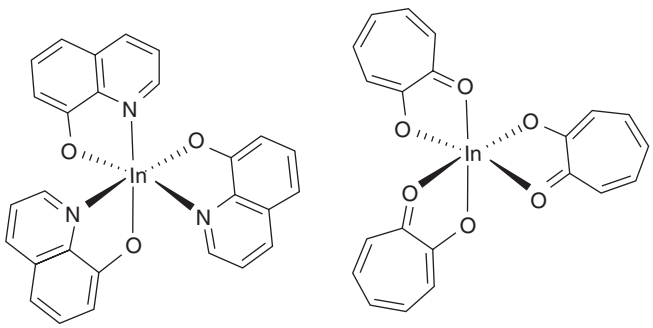

Fig. 6 [^{111}In]In-ionophore complexes used for the labeling of blood cells: indium oxinate (left) and indium tropolonate (right)

Generator Production of Gallium-68

One of the most advantageous features of gallium-68 is that it can be produced conveniently using a ^{68}Ge/^{68}Ga generator, without the need for an on-site cyclotron. The ^{68}Ge/^{68}Ga generator is based on the parent radionuclide germanium-68 ($t_{1/2}$ = 271 d), which can be produced by the proton irradiation (23 MeV) of natural gallium via the ^{69}Ga(p,2n)^{68}Ge reaction and decays to gallium-68 via electron capture. The generator itself consists of a lead-shielded short glass column containing the solid support onto which germanium-68 is adsorbed (see Fig. 7). When this immobilized germanium-68 decays, it produces gallium-68 that can be eluted from the solid support. Of course, it is critical to selectively elute the gallium-68 such that no germanium-68 "breaks through" and interferes with subsequent radiolabeling reactions or delivers a prolonged radiation dose to the patient. The methods used for elution depend on the type of solid support as well as the chemical form of gallium-68 required. The elution of a fresh generator typically yields 70–80% of the gallium-68 present, though this value decreases as the generator ages. Generators can be eluted multiple times daily, with the yield increasing with the time between elutions. To wit, eluting the generator 68 min (one half-life of gallium-68) after the previous elution results in the collection of only 50% of the total possible yield of the radiometal, while waiting 136 min (two half-lives of gallium-68) allows for the collection of 75% of the total possible yield.

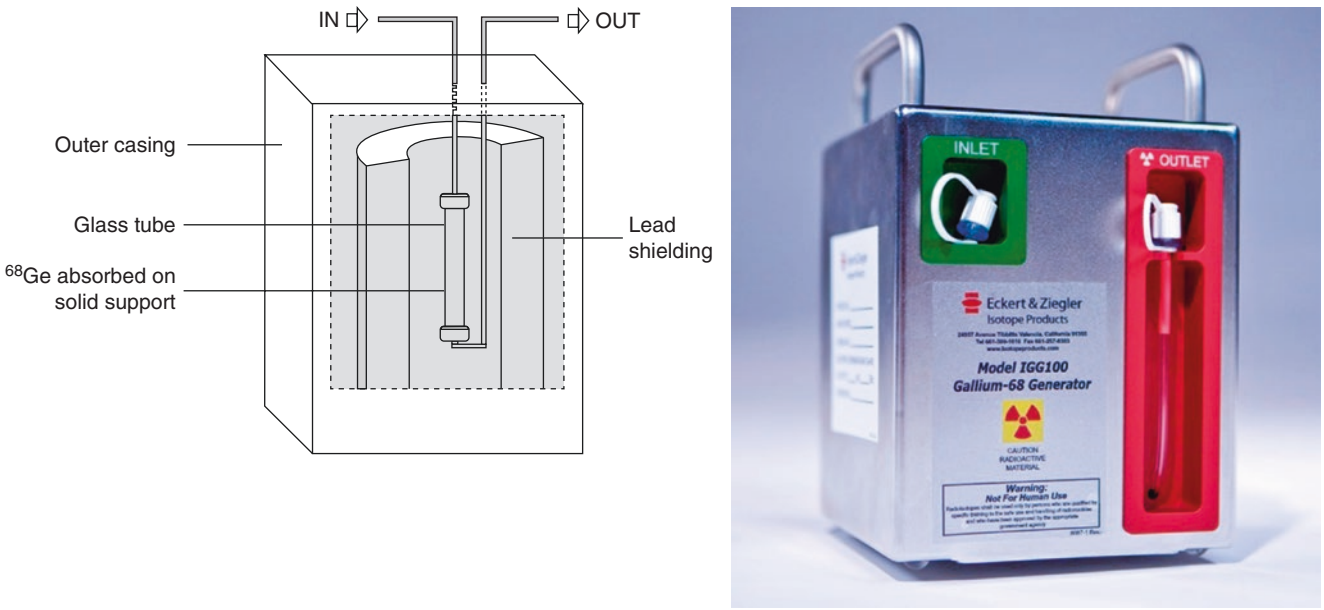

Fig. 7 Schematic of a ^{68}Ge/^{68}Ga generator (left) and a commercial ^{68}Ge/^{68}Ga generator (right, courtesy of Eckert & Ziegler)

The earliest generators relied on a liquid-liquid extraction method to separate gallium-68 from germanium-68 [31]. Later versions, however, turned to solid-phase ion-exchange extraction. Using Al_2O_3 as the solid phase, gallium-68 could be eluted with an EDTA solution (typically 10 mL), resulting in the formation of directly injectable [^{68}Ga]Ga-EDTA [32]. The main limitation of this design is that it can only produce [^{68}Ga]Ga-EDTA, since the transchelation of gallium-68 from Ga-EDTA is challenging due to the high thermodynamic stability of this complex (logK = 21.7). As a result, new, more versatile separation techniques were sought. One such approach relied upon the adsorption of ^{68}Ge(IV) on solid-phase matrices of MO_2 (M = Ti, Sn). In this case, [^{68}Ga]Ga^{3+} can be extracted in the far more labile form of [^{68}Ga]$GaCl_3$ using a 0.1 N solution of hydrochloric acid. Several commercially available ^{68}Ge/^{68}Ga generators—including the "Obninsk" generator (Cyclotron Co., Ltd., Obninsk, Russia) and the IGG100 generator (Eckert & Ziegler Radiopharma, Hopkinton MA, USA)—are based on this design. The iThemba generator (iThemba Labs, Somerset West, South Africa) is similar but employs a SiO_2 stationary phase and requires a higher concentration hydrochloric acid eluent (0.6–1 M). The ITG GmbH generator, on the other hand, employs an organic solid phase consisting of silica gel modified with dodecyl 3,4,5-trihydroxybenzoate [33]. The use of this non-metallic solid phase reduces metal breakthrough and enables the elution of gallium-68 at lower concentrations of hydrochloric acid (0.05 M HCL, 4 mL).

Despite their rise to prominence in the clinic, ^{68}Ge/^{68}Ga generators are still limited by several factors:

1. **Contamination with Trace Metals and Radionuclides.** Non-radioactive metals such as zinc-68 (the decay product of gallium-68), Al and Fe can compete with gallium-68 in reactions with chelators, decreasing radiolabeling efficiency and reducing molar activity. Ti—which originates in the TiO_2 solid phase—is particularly problematic. High concentrations of Ti (up to 3 μM) are often found in the eluate, and the metal can interfere with the radiolabeling of chelators [22]. "Breakthrough" of the parent germanium-68 is also problematic because of the potential for undesirable radiation dose to patients due to the long half-life. Ensuring that this breakthrough can be kept below acceptable thresholds has been one of the main obstacles to garnering marketing authorization for pharmaceutical-grade generators.
2. **Low pH.** Eluting generators with solutions of hydrochloric acid can interfere with radiolabeling chemistry, can degrade biomolecules and may require buffering of the final product.
3. **High Volume.** Typical elution volumes of hydrochloric acid are in the range of 5–10 mL. Unfortunately, this creates very dilute solutions of gallium-68 that often result in poor radiochemical yields and inconveniently large volumes of injection (particularly for small animal studies). Indeed, in some cases, fractionation—the isolation of the eluate fractions with the highest concentration of gallium-68—is required in order to reach an acceptable concentration of gallium-68.

To address these issues, several chemical and physical techniques were developed for the post-processing of the eluate. Although each approach solves some of these problems, they may introduce others and inevitably add to the complexity of labeling procedures. The anion-exchange method involves combining the gallium-68 eluate (10 mL of 0.1 M HCl) with an additional 15 mL of 9.5 M HCl, resulting in the formation of [^{68}Ga]$GaCl_4^-$, which can be adsorbed on a strong anion-exchange column and subsequently eluted with small volumes of water [34]. This method effectively reduces both the volume of the eluent and the amount of germanium-68 breakthrough but does not sufficiently remove other metal contaminants. Furthermore, it requires additional steps and relatively long processing times—in the context of the half-life of the radionuclide, of course—which can combine to severely reduce yields.

The cation-exchange method is based on adsorbing cationic complexes of [^{68}Ga]Ga^{3+} onto an organic cation-exchange resin and subsequently eluting [^{68}Ga]Ga^{3+} with a small volume of a mixture of acetone and HCl (97.6% acetone/0.05 M HCl, 400 μL) [35]. This method removes germanium-68 breakthrough and reduces other metal impurities, facilitating high-yield radiolabeling reactions. However, the presence of acetone in the final product is problematic for GMP production. An ethanol-based elution system was developed by Eppard *et al.* as part of a search for a more widely acceptable final formulation, though this approach uses higher concentrations of HCl (0.9 M) [36]. In these cases, metal impurities were again significantly reduced, and high radiolabeling yields were achieved, removing the need for further purification. However, the use of higher concentrations of HCl can affect the radiolabeling chemistry and reactivity of the selected chelators.

More recently, improvements in post-processing methods using cation-exchange silica monolith columns have been sought to achieve fast, high-yielding gallium-68 radiochemistry for direct injection into patients [37]. It is thought that these methods could be integrated into microfluidic systems to enable the automated preparation of ^{68}Ga-labeled tracers. This method currently facilitates the quantitative recovery of [^{68}Ga]Ga^{3+} from the monolith in a mixture of ethanol/HCl with a reduced eluate volume (0.5 mL) and HCl concentration (0.5 M) compared to the method referred to above due to Eppard *et al.* [36].

Cyclotron-Based Production of Ga-68

The simplicity of the gallium-68 generator has made it popular in the nuclear medicine community. However, the increasing demand for ^{68}Ga-labeled radiopharmaceuticals and the limited life span, high cost and limited availability of generators have prompted interest in the development of

cyclotron-based methods for the production of gallium-68 via the ^{68}Zn(p,n)^{68}Ga reaction. This is particularly true in areas with high population density where many patients can be served within a short travelling time.

The earliest attempts at the cyclotron-based production of gallium-68 involved the irradiation of a solid target of zinc-68 electrodeposited on a copper substrate. However, the need for expensive systems for solid target irradiation and post-irradiation processing as well as the time-consuming nature of the methodology and its vulnerability to contamination by other metal ions have limited its adoption. Nevertheless, ongoing work on this approach has produced promising results: yields of up to 2.2 GBq/μA.h, target processing times of 30–35 min and radionuclidic impurities of <99.8% [38]. Liquid targets have been investigated as a more convenient alternative to solid-state targetry. Pandey *et al.*, for example, reported the irradiation of aqueous solutions of [^{68}Zn]$ZnCl_2$, resulting in high target pressure due to radiolysis-mediated evolution of hydrogen and oxygen; the use of nitrate salts in dilute nitric acid solutions significantly reduced rates of water radiolysis [39].

The main difference between gallium-68 produced on a cyclotron and via generator is radionuclidic purity. Of course, the germanium-68 breakthrough concerns characteristic of generators are absent from cyclotron-based methods. However, small amounts of gallium-67 and gallium-66 are produced via the cyclotron method due to impurities in the zinc-68 target material and competing transformations such as the ^{68}Zn(p,2n)^{67}Ga reaction. That said, radionuclidic impurities can be minimized by increasing the isotopic purity of zinc-68 and limiting the cyclotron beam energy to below 13 MeV to avoid the (p,2n) reaction. While it is still under development, cyclotron-produced GMP-grade gallium-68 is close to being available commercially as a viable and economical alternative to ^{68}Ge/^{68}Ga generators.

The Production of Indium-111 and Gallium-67

By far the most common route for the production of indium-111 is the cyclotron-based proton irradiation of natural cadmium. Two of the most common isotopes of cadmium—cadmium-111 (12.8%) and cadmium-112 (24.1%) [40]—are the true targets of this method. The Cd is electroplated on copper and irradiated with protons at the excitation function peaks of 12 MeV and 20 MeV, respectively, to induce the ^{111}Cd(p,n)^{111}In and ^{112}Cd(p,2n)^{111}In reactions. The target material is dissolved in concentrated HBr and the indium-111 purified by solvent extraction with diisopropyl ether. Gallium-67 is usually produced by proton bombardment (ca. 20 MeV) of enriched zinc-68 electroplated on copper, via the ^{68}Zn(p,2n)^{67}Ga reaction. The gallium-67 is purified by dissolving the zinc target in hydrochloric acid followed by ion-exchange chromatography or solvent extraction with diisopropyl ether.

The Biology of Gallium and Its Role in Imaging

Since the serendipitous discovery of the accumulation of gallium-67 in tumours in the 1960s, this phenomenon and the overarching bioinorganic chemistry of gallium have been the topics of study [6]. Although gallium is not an endogenous metal, it interacts with several biological systems, primarily due to its chemical similarities with iron(III). While these interactions may not be important when gallium is stably chelated *in vivo* (as in ^{68}Ga-labeled biomolecules), they are relevant for any application of salts and loosely chelated forms of the radiometal (such as [^{67}Ga]Ga-citrate).

The most prominent interaction of gallium in plasma involves the iron transport protein transferrin, a monomeric glycoprotein with two metal-binding sites that can sequentially bind to Fe(III) upon the synergistic coordination of a carbonate ion. Its affinity for Ga^{3+} is lower than for Fe^{3+} (log K_1 = 20.3 and log K_2 = 19.3 for Ga^{3+}; log K_1 = 22.8 and log K_2 = 21.5 for Fe^{3+} [41]). However, only one third of its iron-binding sites are typically occupied under physiological conditions, leaving the others free to coordinate gallium. Experimental data and mathematical models agree that gallium in serum is primarily bound to transferrin in equilibrium with the gallate species $[Ga(OH)_4]^-$.

Despite their association with the same protein in serum, the pharmacokinetics and biodistribution of iron and gallium are significantly different. Unlike iron, gallium is redox-inactive and cannot bind to haemoglobin (which would require its reduction to Ga(II)). Consequently, while iron is primarily associated with red blood cells, gallium is more widely distributed into tissues and clears more slowly from plasma. Preclinical imaging studies using gallium-67 have shown the accumulation of radioactivity in the bone, liver, spleen, kidneys, intestine and—notably—tumours [6], particularly lymphoma (Fig. 8).

The mechanisms of gallium uptake in cancer have been debated for several decades and are still not completely understood. However, there is consensus that the radiometal's coexistence in transferrin-bound and gallate ($[Ga(OH)_4]^-$) forms *in vivo*—unlike iron, which is fully associated with transferrin in healthy individuals—is critical. The uptake of gallium in cancer cells [5] is mainly mediated by transferrin receptors which are often upregulated in rapidly proliferating cancer cells. Upon binding to transferrin receptors, the gallium-transferrin complex can be internalized by endocytosis [7]. To interact with the transferrin receptors of a tumour, the gallium-bearing transferrin has to penetrate into the extravascular space. This is a slow process for a macromolecule such as transferrin [7] and can only account for the uptake of gallium in the tumour long after the administration of the radiotracer. The gallate ion, on the other hand, can rapidly penetrate the endothelium and bind to extravascular transferrin molecules (and subsequently transferrin receptors) on the surface of tumour cells. This process is

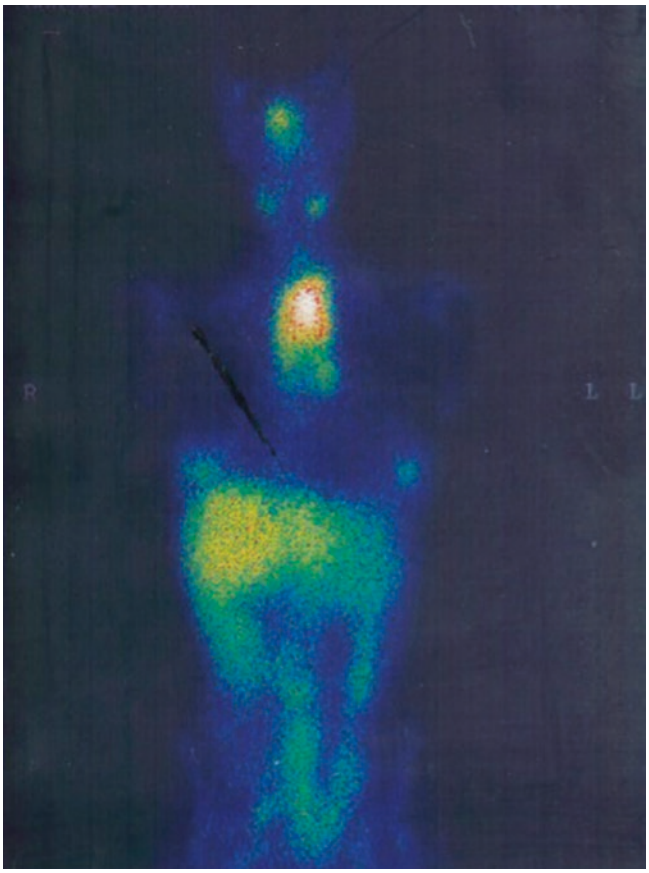

Fig. 8 Gallium-67-citrate planar scan of a female with Hodgkin's lymphoma, showing pathological uptake of gallium-67 in tumour tissue as well as physiological uptake in the salivary glands, mammary tissue, liver and gut (Image courtesy of Dr. A. J. Coakley, East Kent Hospitals NHS Trust, Kent, UK)

more likely to be responsible for tumoural uptake at early time points and is controlled by the mobile equilibrium between the gallate and gallium-transferrin species. In blood vessels, the extravasation of gallate results in the dissociation of more gallium from transferrin to restore the equilibrium, thus feeding the extravasation process. Conversely, the relatively high concentration of gallate in the extravascular space compared to gallium-transferrin drives the binding of gallium to extravascular transferrin molecules.

Transferrin-independent pathways for the accumulation of gallium in cancer cells also exist alongside these pathways. These mechanisms are not clear, but they are expected to be different from the transferrin-independent mechanisms for the uptake of iron, which involve iron(II). The accumulation of gallium in the bone is independent of transferrin, as demonstrated by experiments using carrier-added gallium (to reach Ga(III) concentrations above the threshold of transferrin saturation), which showed increased accumulation of the radiometal in bones as well as its accelerated clearance from the blood [7]. Mechanisms regulating the skeletal uptake of gallium are largely unknown but are likely to involve the gallate ion.

Finally, gallium-67 was also found to accumulate in sites of infection and inflammation, an observation that has been exploited for the clinical imaging of those processes [42]. In these pathologies, the localization of gallium is probably linked to the increased permeability and blood flow in these lesions. Once there, gallium can bind to lactoferrin (another iron-binding protein that is secreted from leukocytes as part of the inflammatory process) and become incorporated in leukocytes and macrophages. In addition, the uptake of gallium in infections might also be mediated by siderophores secreted by bacteria to fulfill their iron requirements [9].

Tricks of the Trade

Gallium-68 Generator Use

If a generator has not been eluted within 48 h, the first eluate should be discarded, and the generator should be re-eluted a few hours later to obtain an eluate with minimized contamination by trace metals and zinc-68 (the decay product of gallium-68). Ultrahigh purity HCl solutions should be used to elute the generator, and all other reagents should have minimal trace metal content. Ideally, buffers should be added to the chelator/ligand prior to mixing with the HCl-based gallium-68 eluate solution rather than mixing the buffer with the gallium-68 eluate first. This minimizes the formation of poorly soluble hydroxide species (colloidal gallium). An alternative way to minimize the formation of colloids may be to keep the gallium-68 in alkaline buffer prior to chelation to ensure the formation of soluble $[Ga(OH)_4]^-$; however, this approach has not been widely tested.

Instant Thin-Layer Chromatography (ITLC) with Gallium-67/68

Citrate is a useful mobile phase for the development of ITLCs, but it does not allow for the precise quantification of "colloidal gallium". The percentage of colloidal gallium in a given reaction is variable and not reproducible and therefore cannot be accurately controlled by comparison to a control ITLC of unchelated gallium. Therefore, an additional ITLC method—such as using a mobile phase of 1 M ammonium acetate in 50:50 methanol/water—should be used in parallel.

Radioactivity Measurements

Both indium-111 and gallium-67 have significant low-energy gamma and X-rays in their emission spectra, making measurements in gamma counters and dose calibrators highly dependent on the geometry and material of the containers in which the samples are assayed. Sample containers and solution volumes must therefore be carefully standardized.

Problems with Sampling Indium-111

During the development of labeling methodologies for indium-111, we have noticed that labeling yields can deteriorate—sometimes dramatically—when taking multiple samples from vials of [^{111}In]In-chloride over a period of time. This phenomenon is likely due to contact with syringe and pipette tips, as [^{111}In]In-chloride is particularly sensitive to contamination both from metal ions within hydrochloric acid, needles and tips and from organic contaminant leaching from the plastic pipette tips. Therefore, it is advisable to avoid using metal needles and plastic pipette tips when repeatedly sampling [^{111}In]In-chloride. Sampling and other manipulations should be minimized, and when it cannot be avoided, the use of acid-washed, preferably glass, tips is recommended. Taking multiple samples from the stock vials is not advisable from the viewpoint of Good Manufacturing Practice, as commercial indium-111 and gallium-67 typically contain no preservatives, and puncturing the vial multiple times can lead to microbiological contamination.

Cell Labeling

As noted above, cell labeling with [^{111}In]In-tropolone can be carried out in plasma. The volume of the labeling reaction should be kept low to improve the efficiency of the labeling reaction. For some cell types, labeling at 37 °C can be more efficient than at room temperature.

[^{67}Ga]Ga-Chloride

Gallium-67 is typically available from suppliers as [^{67}Ga]Ga-citrate, the form used clinically for tumour imaging. However, citrate can reduce the radiolabeling efficiency of gallium-67 with some chelators. Therefore, the conversion of [^{67}Ga]Ga-citrate to [^{67}Ga]Ga-chloride and the removal of citrate are often useful. This can be done easily by slowly passing the [^{67}Ga]Ga-citrate solution over a silica light Sep-Pak cartridge (120 mg sorbent, 55- to 105-μm particle size) to trap the [^{67}Ga]Ga^{3+}, followed by washing the cartridge with water to remove the excess citrate. The [^{67}Ga]Ga^{3+} can then be eluted from the cartridge using 0.1 M HCl, yielding [^{67}Ga]Ga-chloride [7]. Radiolabeling reactions can then be performed using the same methods used with generator-produced [^{68}Ga]Ga-chloride.

Particularly Important Works

In the preceding pages, we have discussed some of the most important developments in the radiopharmaceutical chemistry of indium-111, gallium-67 and gallium-68 from the 1970s and 1980s. These include the elucidation of production methods for indium-111 and gallium-67, the development of methods for labeling both antibodies and cells with indium-111, and the revelation of the interplay between the bioinorganic chemistry of gallium and the use of gallium-67 for the imaging of tumours, infection and inflammation. More recently, the dominant story for this family of radionuclides has been the rise of PET imaging with gallium-68. In this section, we will discuss several of the developments that have led to the advent of gallium-68 PET.

Imaging Neuroendocrine Tumours: From [^{111}In]In-Octreotide to ^{68}Ga-Labeled Radiopharmaceuticals

The era of molecular imaging with receptor-targeted peptides began with the first report by Krenning *et al.* of imaging somatostatin-positive human tumours with [^{111}In]In-DTPA-D-Phe1-octreotide [43]. [^{111}In]In-DTPA-D-Phe1-octreotide was subsequently marketed in kit form as Octreoscan® in the mid-1990s and has been used routinely in the clinic for more than 20 years. As early as 1993, Maecke *et al.* [44] first proposed the use of a ^{68}Ga-labeled analogue (DFO-octreotide conjugate) for PET studies. In 2001, Hofmann *et al.* [45] reported the superiority of PET with [^{68}Ga]Ga-DOTATOC compared to SPECT with [^{111}In]In-DTPA-D-Phe1-octreotide: 100% of lesions found by CT/MRI could be identified via imaging with [^{68}Ga]Ga-DOTATOC compared to only 85% with [^{111}In]In-DTPA-D-Phe1-octreotide (Fig. 9). Over the next 5–10 years, additional studies with alternatives such as [^{68}Ga]Ga-DOTANOC and [^{68}Ga]Ga-DOTATOC confirmed the clinical superiority of gallium-68 PET over indium-111 SPECT. The use of an on-site generator was pivotal to the clinical adoption of these radiotracers, as it allowed radiopharmacies to prepare these products on demand. In recent years, generator technology has improved as well, and the recent introduction of kit-based ^{68}Ga-labeled imaging agents (*e.g.* SomaKit TOC®; Advanced Accelerator Applications SA, Saint-Genis-Pouilly, France) means that ^{68}Ga-based radiopharmaceuticals are now available not just to specialist centres but to the radiopharmacy community as a whole.

Imaging Prostate-Specific Membrane Antigen

The second major contributor to the expansion of gallium-68 PET has been the development of a series of ^{68}Ga-labeled probes for the imaging of prostate-specific membrane antigen (PSMA). The imaging of PSMA expression in prostate cancer patients has proven to be a highly sensitive and effective tool for informing patient management. In recent years, these ^{68}Ga-labeled small molecule radiotracers have supplanted similarly targeted radiopharmaceuticals based on antibodies such as mAb 7E11 (ProstaScint®; Aytu Bioscience, Englewood CO, USA) and humanized J591. The targeting

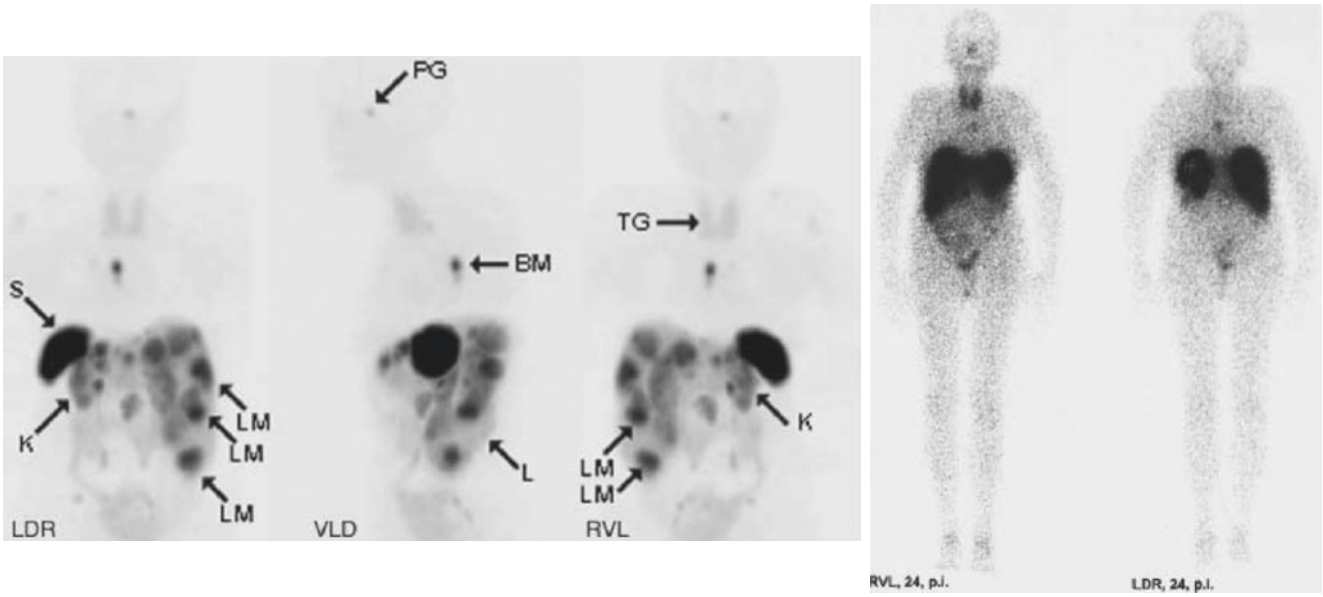

Fig. 9 Comparative imaging results obtained with [^{68}Ga]Ga-DOTATOC (left: PET, 90 min postinjection) and [^{111}In]In-DTPA-D-Phe1-octreotide (right: planar scans, 24 h postinjection) in patients with somatostatin-positive neuroendocrine tumours (From Hofmann *et al.* [45], with permission)

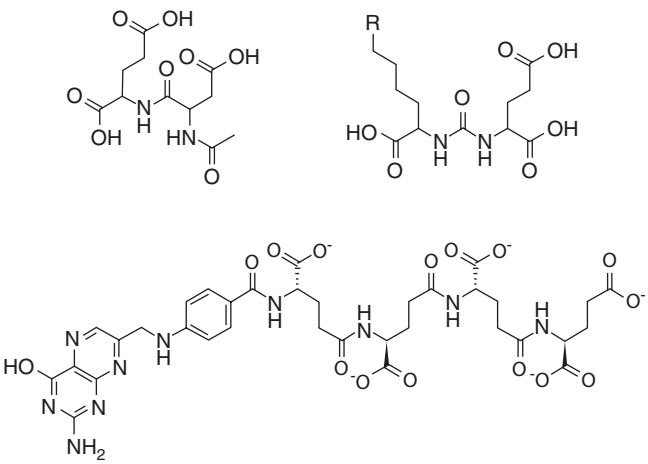

Fig. 10 Ligands for PSMA: NAAG (top left), polyglutamated folate (bottom) and a urea-based inhibitor PSMA targeting motif (top right)

motif that forms the core of these probes is based on the natural substrates of PSMA: NAAG (N-acetylaspartylglutamic acid) and polyglutamated folate (also shown in Fig. 10). However, the peptide bonds in these constructs (see Fig. 10) are replaced with a urea bond in order to make it stable to enzymatic cleavage. This small molecule can be modified at the lysine terminus to incorporate various chelators, which has led to development of several ^{68}Ga-labeled tracers. Currently, the most popular variant is [^{68}Ga]Ga-HBED-CC-PSMA, which can detect metastasis more accurately than CT or [^{18}F]fluoro-choline PET and has become the most widely used imaging agent for prostate cancer [46]. Alternative variants with DOTA as the chelator have also become accepted into clinical practice, including [^{68}Ga]Ga-DOTA-PSMA [47] and [^{68}Ga]Ga-DOTA-PSMA-I&T [48]. These constructs allow for both imaging and therapy using the same core structure, as DOTA can also bind therapeutic isotopes such as ^{177}Lu. Like [^{68}Ga]Ga-DOTATOC and [^{68}Ga]Ga-DOTATATE, [^{68}Ga]Ga-HBED-CC-PSMA and [^{68}Ga]Ga-DOTA-PSMA (617 and I&T) tracers are synthesized using automated synthesis modules. These methods are robust but time-consuming (over 35 min) and are (of course) limited to sites with the infrastructure necessary for automated synthesis. To simplify and speed up the radiolabeling process—and reduce the need for costly capital infrastructure—an alternative gallium-68 PSMA tracer, [^{68}Ga]Ga-THP-PSMA, has been developed. It exploits the THP chelator which allows for radiolabeling in a single step [7] by adding eluate directly from a gallium-68 generator to a vial containing THP-PSMA, a neutralizing agent and a buffer [49].

Controversial Issues

Gallium-68: More Generators, Bigger Generators or Cyclotron Production?

For the time being, the use of gallium-68 radiopharmaceuticals is increasing rapidly. The historical analogy with technetium-99m—with its generator- and kit-based distribution model—is obvious. Indeed, there are those who advocate replacing some of the long-established ^{99m}Tc-

based nuclear medicine tests (*e.g.* dynamic renal scanning [50], lung V/Q scanning, etc.) with analogous tests using gallium-68 in order to exploit the improved image quality and quantification offered by PET. It is important to consider whether this increasing demand is best met by generators with higher activity, more generators or the cyclotron-based production of the nuclide.

Larger generators offer the possibility of producing more patient doses per elution, but many nuclear medicine centres—particularly those in smaller centres that benefit most from the generator concept—do not have enough scanners to manage the larger number of patients that could be scanned using the output from these larger generators. In such centres, a more effective solution is to have several smaller generators that are eluted sequentially, with each producing enough activity for one or two simultaneous scans. In conjunction with improvements to synthesis units and automation—or, even better, simple kit-based labeling methods—this approach could facilitate the creation of doses of ^{68}Ga-labeled radiopharmaceuticals throughout the day. In larger centres with more PET scanners serving more populous regions, larger generators or cyclotron-based production methods are viable alternatives.

Ga-68 vs. F-18

Paradoxically, the dramatic rise in the use of ^{68}Ga-labeled radiopharmaceuticals—especially the recent advent of [^{68}Ga]Ga-PSMA—has prompted questions regarding whether gallium-68 has a long-term future in nuclear medicine. The emergence of automated synthesis units and simple kit-based labeling protocols has made performing gallium-68 radiolabelings at hospital sites a relatively straightforward practice. As a result, the on-site production of ^{68}Ga-labeled radiopharmaceuticals is simpler and quicker, and failures are much reduced. However, a parallel trend towards the use of centralized radiopharmacy services is exerting a downward pressure on the capabilities of local radiopharmacies. In light of this, it is hard to deny that fluorine-18 is a better fit than gallium-68 for this centralized production model due to its longer half-life (110 min). Ultimately, the short half-life of gallium-68 may be its Achilles' heel. Nevertheless, it may be premature to announce the demise of gallium-68: a balanced view is that a mixed economy—able to cope with the wide range of geographical and social contexts of the PET market—is the most likely outcome. Time will tell.

GMP Issues with ^{68}Ge/^{68}Ga Generators

A ^{68}Ge/^{68}Ga generator can be used for about 1 year. It is regularly eluted with hydrochloric acid, and while the hydrochloric acid reservoir needs to be replaced at intervals, the lines running into and out of the generator tend to stay in place and, although usually in a grade A environment, are not free from the risk of microbiological contamination. Such matters have made it a long haul to achieve marketing authorization for gallium-68 generators. Although the regulatory authorities currently seem to be happy with the measures that the generator producers have put in place, complacency is a perpetual enemy, and it is advisable for users to take steps to reduce and monitor the risk of contamination.

The Future

Gallium-68 and Gallium-68 Chemistry

As discussed above, it is clear that the use of gallium-68 is on the rise. The potential of simply and conveniently using gallium-68 generator eluates for labeling biomolecule-chelator conjugates is clear. Yet in recent years, this simplicity has not been realized. Now that chelators capable of rapid chelation under mild conditions have emerged [7], there is no justification for new tracers that require complex processing, harsh conditions or poor radiolabeling efficiencies. The industry and user community should focus on radiosyntheses that are amenable to simple kit-based methods, even for centres equipped with cyclotrons, hot cells, and automated synthesizers.

Molar Activity of ^{68}Ga-Labeled Peptides

The maximum theoretically achievable molar activity of radiolabeled peptides is reached when all molecules are labeled or, in the case of radiometal-based probes, when all chelator sites are occupied by a radionuclide. Under these conditions, molar activity is limited by, and inversely proportional to, the half-life of the radionuclide. For example, indium-111—with a half-life that is 50 times longer than that of gallium-68—might be expected to yield products with a 50-fold lower specific activity than analogous ^{68}Ga-labeled constructs. In practice, however, the molar activities of ^{111}In-labeled constructs are typically 50-fold *higher* than those of comparable ^{68}Ga-labeled probes. If we are to improve on this, as may be necessary for targeting receptors with particularly low abundance, we must identify the causes of this phenomenon and find solutions. Possible causes include the contamination of eluates with trace metals that compete with gallium-68 for chelator sites, particularly titanium from the generator's stationary phase. This has barely been investigated and clearly deserves a closer look in the future.

Auger Electron Emitter Therapy

Targeted radionuclide therapy is currently enjoying a renaissance. However, the therapeutic use of the Auger electrons emitted by indium-111 and gallium-67 has barely been explored [10]. Clinical results are very sparse and not encouraging, but this should not necessarily discourage further work. The biological basis of Auger electron therapy is far from understood, and more extensive studies on the relationship between the subcellular localization of radionuclides, the biological effects of the Auger process, and the resulting mechanisms of cellular toxicity are needed to determine whether therapy with these radionuclides is viable. Similarly, a more thorough understanding of the biological effects of Auger electrons on the function, phenotype, and survival of cells labeled with indium-111 for cell tracking is necessary if ^{111}In-labeled cells are to be trusted to reflect the bulk in vivo behaviour of administered cells.

Commercial Availability of Indium-111

Despite the clinical importance of cell labeling with indium-111, the commercial availability of indium-111 and [^{111}In]In-oxine has diminished in recent years. The economic and commercial value of reinstating this supply remains unclear, primarily due to the concurrent growth in PET. Zirconium-89, for example, has now supplanted indium-111 as the radionuclide of choice for the radiolabeling antibodies. Furthermore, the feasibility of labeling cells with zirconium-89 has recently been demonstrated, and this technique will undoubtedly reach the clinic as the age of cell-based therapies arrives [15]. Similarly, the commercial availability of gallium-67 has also dwindled, and it is unclear whether this trend will have detrimental effects in the clinic or whether gallium-67 will join the ranks of nuclides that are only of historical interest.

The Bottom Line

The next few years will see marked changes in the use of gallium-67, gallium-68 and indium-111. As the use of PET expands in the clinic, the use of gallium-68 will grow apace. New commercial generators are on the verge of receiving marketing authorization, and the field has played witness to rapid developments in several other areas, including the development of cyclotron-based production methods, the creation of novel chelators and the emergence of kit-based radiolabeling protocols. It remains to be seen whether this growth is sustainable in the face of changing models for the production and distribution of radiopharmaceuticals, particularly as the centralized production of fluorine-18 and scandium-44 gains momentum. At the same time, PET-based methods are emerging that could supplant applications that were once the preserve of indium-111, such as the radiolabeling of antibodies and cells. Likewise, the importance of gallium-67 has waned in recent years as well. While it remains popular in some countries for the imaging of infection and inflammation, its use in lymphoma imaging has been supplanted by PET with [^{18}F]FDG. On the other hand, however, the Auger electron emissions of both indium-111 and gallium-67 are—at least in theory—attractive for therapeutic applications, though much more research is needed to determine whether the use of these radionuclides for therapy can become a clinical reality.

References

1. Velikyan I. Ga-68-based radiopharmaceuticals: production and application relationship. Molecules. 2015;20(7):12913–43.
2. Paik CH, Herman DE, Eckelman WC, Reba RC. Synthesis, plasma-clearance, and in vitro stability of protein containing a conjugated In-111 chelate. J Radioanal Chem. 1980;57(2):553–64.
3. Segal AW, Arnot RN, Thakur ML, Lavender JP. Indium-111-labeled leukocytes for localization of abscesses. Lancet. 1976;2(7994):1056–8.
4. Kotze HF, Heyns AD, Lotter MG, Pieters H, Roodt JP, Sweetlove MA, et al. Comparison of oxine and tropolone methods for labeling human platelets with indium-111. J Nucl Med. 1991;32(1):62–6.
5. Weiner RE. The mechanism of Ga-67 localization in malignant disease. Nucl Med Biol. 1996;23(6):745–51.
6. Price EW, Orvig C. Matching chelators to radiometals for radiopharmaceuticals. Chem Soc Rev. 2014;43(1):260–90. Review
7. Young JD, Abbate V, Imberti C, Meszaros LK, Ma MT, Terry SYA, et al. Ga-68-THP-PSMA: a PET imaging agent for prostate cancer offering rapid, room-temperature, 1-step kit-based radiolabeling. J Nucl Med. 2017;58(8):1270–7.
8. Hicks RJ. Ga-67SPECT: ave atque vale! Or have we bid a premature farewell to a trusted friend? Leuk Lymphoma. 2006;47(12):2440–2.
9. Petrik M, Haas H, Dobrozemsky G, Lass-Florl C, Helbok A, Blatzer M, et al. Ga-68-siderophores for PET imaging of invasive pulmonary aspergillosis: proof of principle. J Nucl Med. 2010;51(4):639–45.
10. Othman MF, Mitry NR, Lewington VJ, Blower PJ, Terry SY. Re-assessing gallium-67 as a therapeutic radionuclide. Nucl Med Biol. 2017;46:12–8.
11. Jonkhoff AR, Plaizier MA, Ossenkoppele GJ, Teule GJ, Huijgens PC. High-dose gallium-67 therapy in patients with relapsed acute leukaemia: a feasibility study. Br J Cancer. 1995;72(6):1541–6.
12. Michel RB, Brechbiel MW, Mattes MJ. A comparison of 4 radionuclides conjugated to antibodies for single-cell kill. J Nucl Med. 2003;44(4):632–40.
13. Ochakovskaya R, Osorio L, Goldenberg DM, Mattes MJ. Therapy of disseminated B-cell lymphoma xenografts in severe combined immunodeficient mice with an anti-CD74 antibody conjugated with ^{111}indium, ^{67}gallium, or ^{90}yttrium. Clin Cancer Res. 2001;7(6):1505–10.
14. van de Watering FC, Rijpkema M, Perk L, Brinkmann U, Oyen WJ, Boerman OC. Zirconium-89 labeled antibodies: a new tool for molecular imaging in cancer patients. Biomed Res Int. 2014;2014:203601.
15. Charoenphun P, Meszaros LK, Chuamsaamarkkee K, Sharif-Paghaleh E, Ballinger JR, Ferris TJ, et al. [^{89}Zr]oxinate$_4$ for long-term in vivo cell tracking by positron emission tomography. Eur J Nucl Med Mol Imaging. 2015;42(2):278–87.
16. Krenning EP, Kooij PP, Bakker WH, Breeman WA, Postema PT, Kwekkeboom DJ, et al. Radiotherapy with a radiolabeled somatostatin analogue, [^{111}In-DTPA-D-Phe1]-octreotide. A case history. Ann N Y Acad Sci. 1994;733:496–506.

17. Wood SA, Samson IM. The aqueous geochemistry of gallium, germanium, indium and scandium. Ore Geol Rev. 2006; 28(1):57–102.
18. Berry DJ, Ma Y, Ballinger JR, Tavare R, Koers A, Sunassee K, et al. Efficient bifunctional gallium-68 chelators for positron emission tomography: tris(hydroxypyridinone) ligands. Chem Commun (Camb). 2011;47(25):7068–70.
19. Viola NA, Rarig RS, Ouellette W, Doyle RP. Synthesis, structure and thermal analysis of the gallium complex of 1,4,7,10-tetraazacyclo-dodecane-N,N ',N ",N "'-tetraacetic acid (DOTA). Polyhedron. 2006;25(18):3457–62.
20. Sun YZ, Anderson CJ, Pajeau TS, Reichert DE, Hancock RD, Motekaitis RJ, et al. Indium(III) and gallium(III) complexes of bis(aminoethanethiol) ligands with different denticities: Stabilities, molecular modeling, and in vivo behavior. J Med Chem. 1996;39(2):458–70.
21. Simecek J, Hermann P, Wester HJ, Notni J. How is Ga-68 labeling of macrocyclic chelators influenced by metal ion contaminants in Ge-68/Ga-68 generator eluates? ChemMedChem. 2013;8(1):95–103.
22. Tsionou MI, Knapp CE, Foley CA, Munteanu CR, Cakebread A, Imberti C, et al. Comparison of macrocyclic and acyclic chelators for gallium-68 radiolabelling. RSC Adv. 2017;7(78):49586–99.
23. Govindan SV, Michel RB, Griffiths GL, Goldenberg DM, Mattes MJ. Deferoxamine as a chelator for Ga-67 in the preparation of antibody conjugates. Nucl Med Biol. 2005;32(5):513–9.
24. Nawaz S, Mullen GED, Sunassee K, Bordoloi J, Blower PJ, Ballinger JR. Simple, mild, one-step labelling of proteins with gallium-68 using a tris(hydroxypyridinone) bifunctional chelator: a Ga-68-THP-scFv targeting the prostate-specific membrane antigen. EJNMMI Res. 2017;7(1):86.
25. Knetsch PA, Zhai CY, Rangger C, Blatzer M, Haas H, Kaeopookum P, et al. [Ga-68]FSC-$(RGD)_3$ a trimeric RGD peptide for imaging $alpha_vbeta_3$ integrin expression based on a novel siderophore derived chelating scaffold-synthesis and evaluation. Nucl Med Biol. 2015;42(2):115–22.
26. Maecke HR, Riesen A, Ritter W. The molecular-structure of indium-DTPA. J Nucl Med. 1989;30(7):1235–9.
27. Brechbiel MW, Gansow OA, Atcher RW, Schlom J, Esteban J, Simpson DE, et al. Synthesis of 1-(para-isothiocyanatobenzyl) derivatives of DTPA and EDTA – antibody labeling and tumor-imaging studies. Inorg Chem. 1986;25(16):2772–81.
28. Camera L, Kinuya S, Garmestani K, Pai LH, Brechbiel MW, Gansow OA, et al. Evaluation of a new DTPA-derivative chelator – comparative biodistribution and imaging studies of In-111 labeled B3 monoclonal-antibody in athymic mice bearing human epidermoid carcinoma xenografts. Nucl Med Biol. 1993;20(8):955–62.
29. Meares CF, Moi MK, Diril H, Kukis DL, Mccall MJ, Deshpande SV, et al. Macrocyclic chelates of radiometals for diagnosis and therapy. Br J Cancer. 1990;62(Suppl 10):21–6.
30. Kozak RW, Raubitschek A, Mirzadeh S, Brechbiel MW, Junghaus R, Gansow OA, et al. Nature of the bifunctional chelating agent used for radioimmunotherapy with Y-90 monoclonal-antibodies – critical factors in determining in vivo survival and organ toxicity. Cancer Res. 1989;49(10):2639–44.
31. Gleason GI. A positron cow. Int J Appl Radiat Isot. 1960;8:90–4.
32. Yano Y, Anger HO. A gallium-68 positron cow for medical use. J Nucl Med. 1964;5:484–7.
33. Tworowska I, Ranganathan D, Thamake S, Delpassand E, Mojtahedi A, Schultz MK, et al. Radiosynthesis of clinical doses of ^{68}Ga-DOTATATE (GalioMedix) and validation of organic-matrix-based ^{68}Ge/^{68}Ga generators. Nucl Med Biol. 2016;43(1):19–26.
34. Meyer GJ, Macke H, Schuhmacher J, Knapp WH, Hofmann M. ^{68}Ga-labelled DOTA-derivatised peptide ligands. Eur J Nucl Med Mol Imaging. 2004;31(8):1097–104.
35. Zhernosekov KP, Filosofov DV, Baum RP, Aschoff P, Bihl H, Razbash AA, et al. Processing of generator-produced ^{68}Ga for medical application. J Nucl Med. 2007;48(10):1741–8.
36. Eppard E, Wuttke M, Nicodemus PL, Rosch F. Ethanol-based post-processing of generator-derived ^{68}Ga toward kit-type preparation of ^{68}Ga-radiopharmaceuticals. J Nucl Med. 2014;55(6):1023–8.
37. He P, Burke BP, Clemente GS, Brown N, Pamme N, Archibald SJ. Monolith-based Ga-68 processing: a new strategy for purification to facilitate direct radiolabelling methods. React Chem Eng. 2016;1(4):361–5.
38. Lin M, Mukhopadhyay U, Waligorski G, Balatoni J, Gonzalez-Lepera C. Production of Curie quantities of Ga-68 with a medical cyclotron via the Zn-68(p, n)Ga-68 reaction (abstract). J Nucl Med. 2017;58:336.
39. Pandey MK, Engelbrecht HP, Byrne JF, Packard AB, DeGrado TR. Production of Zr-89 via the Y-89(p,n)Zr-89 reaction in aqueous solution: Effect of solution composition on in-target chemistry. Nucl Med Biol. 2014;41(4):309–16.
40. Haji-Saeid M, Pillai MRA, Ruth TJ, Schlyer DJ, Van den Winkel P, Vora MM. Cyclotron produced radionuclides: physical characteristics and production methods. Vienna: International Atomic Energy Agency; 2009.
41. Harris WR, Pecoraro VL. Thermodynamic binding constants for gallium transferrin. Biochemistry. 1983;22(2):292–9.
42. Palestro CJ. The current role of gallium imaging in infection. Semin Nucl Med. 1994;24(2):128–41.
43. Krenning EP, Bakker WH, Kooij PP, Breeman WA, Oei HY, de Jong M, et al. Somatostatin receptor scintigraphy with indium-111-DTPA-D-Phe-1-octreotide in man: metabolism, dosimetry and comparison with iodine-123-Tyr-3-octreotide. J Nucl Med. 1992;33(5):652–8.
44. Macke HR, Smith-Jones P, Maina T, Stolz B, Albert R, Bruns C, et al. New octreotide derivatives for in vivo targeting of somatostatin receptor-positive tumors for single photon emission computed tomography (SPECT) and positron emission tomography (PET). Horm Metab Res Suppl. 1993;27:12–7.
45. Hofmann M, Maecke H, Borner AR, Weckesser E, Schoffski P, Oei ML, et al. Biokinetics and imaging with the somatostatin receptor PET radioligand Ga-68-DOTATOC: preliminary data. Eur J Nucl Med. 2001;28(12):1751–7.
46. Afshar-Oromieh A, Zechmann CM, Malcher A, Eder M, Eisenhut M, Linhart HG, et al. Comparison of PET imaging with a Ga-68-labelled PSMA ligand and F-18-choline-based PET/CT for the diagnosis of recurrent prostate cancer. Eur J Nucl Med Mol Imaging. 2014;41(1):11–20.
47. Benešová M, Schäfer M, Bauder-Wüst U, Afshar-Oromieh A, Kratochwil C, Mier W, et al. Preclinical evaluation of a tailor-made DOTA-conjugated psma inhibitor with optimized linker moiety for imaging and endoradiotherapy of prostate cancer. J Nucl Med. 2015;56(6):914–20.
48. Weineisen M, Schottelius M, Simecek J, Baum RP, Yildiz A, Beykan S, et al. Ga-68- and Lu-177-labeled PSMA I&T: optimization of a PSMA-targeted theranostic concept and first proof-of-concept human studies. J Nucl Med. 2015;56(8):1169–76.
49. Hofman MS, Eu P, Jackson P, Hong E, Binns D, Iravani A, et al. Cold Kit PSMA PET imaging: Phase I study of ^{68}Ga-THP-PSMA PET/CT in patients with prostate cancer. J Nucl Med. 2018;59(4):625–31.
50. Hofman MS, Hicks RJ. Gallium-68 EDTA PET/CT for renal imaging. Semin Nucl Med. 2016;46(5):448–61.

The Radiopharmaceutical Chemistry of Fluorine-18: Nucleophilic Fluorinations

Johannes Ermert and Bernd Neumaier

Introduction of Fluorine-18

Due to its favourable nuclear decay properties, the positron-emitting radiohalogen fluorine-18 is one of the most important radionuclides for the production of radiopharmaceuticals for positron emission tomography (PET). ^{18}F decays into ^{18}O with a half-life $t_{1/2}$ = 110 min (Fig. 1).

Fluorine decays by 96.9% β⁺-emission and 3.1% EC. The emitted positron has a maximum energy of E_{max} = 0.634 MeV and a mean energy of E_{mean} = 0.250 MeV, which corresponds to a maximum range in water of R_{max} = 2.4 mm and a mean range of R_{mean} = 0.6 mm [1, 2]. In the context of PET, these decay properties translate into several advantages that make ^{18}F the most widely used radionuclide in PET:

- A convenient half-life of 109 min poses fewer constraints on synthesis time and permits longer imaging protocols.
- A high branching ratio for β⁺ decay produces many positrons, increasing the sensitivity of imaging and reducing the safety and logistical concerns associated with other radioactive emissions.
- A low positron energy of 649 keV results in high-resolution PET images.

Fluorine is monovalent, and it forms a covalent and stable bond with carbon. When bound to carbon, a covalently bound fluorine atom has a van der Waals radius of 1.47 Å; this is larger than that of a hydrogen atom (1.2 Å) but occupies a smaller volume than methyl, amino, or hydroxyl groups [3]. Generally speaking, fluorine possesses some extreme properties. For example, it is the most electronegative element on the periodic table, and it has the highest oxidation potential. As a result, the introduction of a fluorine atom into a molecule can have significant effects on the physicochemical properties of the compound. For example, the presence of fluorine can shift the pKa values of nearby acidic and basic functional groups by several log units. Furthermore, the replacement of a hydrogen atom by a fluorine can reduce the basicity of a compound, leading to increased lipophilicity and modifying its *in vivo* biodistribution profile [4]. Fluorine substitution can also enhance the binding affinity of a compound for its target or even improve the metabolic stability of a compound by blocking metabolically labile sites. These effects are often exploited in drug design, and an increasing number of pharmaceuticals contain fluorine atoms in their structures. It is important to consider the physicochemical implications of fluorination during the development of ^{18}F-labeled radiotracers. For example, endogenous compounds like amino acids, sugars, neurotransmitters, or fatty acids do not contain fluorine. Thus, the introduction of fluorine-18 into these compounds may affect their physiological behaviour [4].

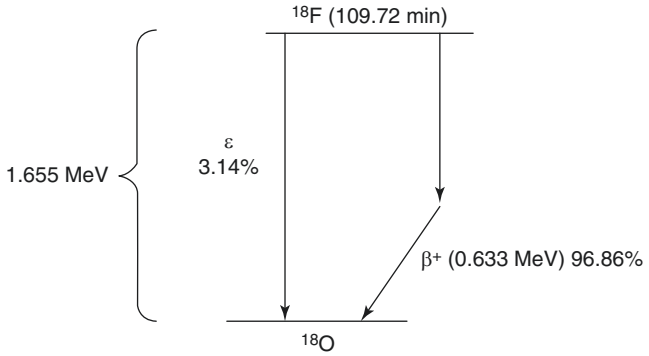

Fig. 1 Scheme 1. Decay scheme of ^{18}F

There are two different ways to introduce fluorine-18 into molecules: electrophilic substitution reactions of electron-rich systems and nucleophilic substitution reactions of electron poor systems.

The starting material of electrophilic ^{18}F-substitution reactions is ^{18}F-labeled elemental fluorine ($[^{18}F]F_2$) (see Chap. 16 for a more detailed discussion). $[^{18}F]F_2$ is produced using a

J. Ermert · B. Neumaier (✉)
Institute of Neuroscience and Medicine, INM-5: Nuclear Chemistry, Forschungszentrum Jülich GmbH, Jülich, Germany
e-mail: b.neumaier@fz-juelich.de

J. S. Lewis et al. (eds.), *Radiopharmaceutical Chemistry*, https://doi.org/10.1007/978-3-319-98947-1_15

medium-energy cyclotron via the $^{20}Ne(d,\alpha)^{18}F$ nuclear reaction using neon gas in a passivated Ni target chamber or via the $^{18}O(p,n)^{18}F$ nuclear reaction on highly enriched $^{18}O_2$-gas in an aluminium target chamber [5]. The latter reaction is more effective, but the starting material is much more expensive. In both cases, the fluorine-18 is adsorbed on the walls of the target and requires the addition of elemental fluorine gas to prompt an isotopic exchange that facilitates the removal [^{18}F]F_2. This procedure limits the maximum molar activity of any tracers created using this [^{18}F]F_2. Furthermore, the theoretical achievable maximum radiochemical yield (RCY) is limited to 50%, because every [^{18}F]F_2-molecule carries only one ^{18}F-atom.

Yet high specific activities are often needed to avoid pharmacological or toxicological effects of the labeled compound. In addition, the use of radiotracers with low specific activity can compromize imaging when targeting low-abundance receptors or transporters [6]. Until recently, ^{18}F-labeled molecules in no-carrier-added (n.c.a.) form could only be obtained via *nucleophilic* ^{18}F-substitution reactions. However, an alternative method has also been developed to improve the specific activity of electrophilic [^{18}F]F_2. In this method, the first step consists of the production of [^{18}F]fluoride via the irradiation of ^{18}O-enriched water. Subsequently, the [^{18}F]fluoride is converted into [^{18}F]fluoromethane which is then transformed in a discharge chamber in the presence of low amounts of F_2 into [^{18}F]F_2 with higher specific activity [7].

The most important route for the production of nucleophilic [^{18}F]fluoride is the $^{18}O(p,n)^{18}F$ reaction (Ep = 16 → 3 MeV) using ^{18}O-enriched water in liquid targets. The body of the target chamber can consist of titanium, silver, niobium, or tantalum. Nb or Ta targets are particularly suitable for high beam currents and enable the production of up to 500 GBq of [^{18}F]fluoride (after proton irradiation for 120 min at 18 MeV with a beam current of 145 µA [8]).

Nucleophilic ^{18}F-Substitution

Generally speaking, it is preferable to avoid time-consuming radiosyntheses (> 1 $t_{1/2}$) in order to obtain high amounts of the short-lived ^{18}F-labeled products. Thus, the introduction of ^{18}F into a molecule should occur as late as possible in the synthesis. This approach is often termed a "late-stage radiofluorination" or a "direct labeling method" [9, 10]. A major advantage of this approach is that late-stage radiofluorinations can often be carried out using automated synthesis modules. Multistep syntheses, in contrast, are more elaborate and are thus far more difficult to adapt to automated synthesis modules. In many of these multistep methods, the first step is the preparation of a ^{18}F-labeled small building block—often called a "prosthetic group"—which is further used to obtain a more complex labeled molecule.

General Aspects of ^{18}F-Labeling

^{18}F-labeling reactions can involve a number of difficulties due to the physicochemical properties of [^{18}F]fluoride in aqueous solution (in which it is typically obtained after irradiation). To wit, [^{18}F]fluoride is strongly hydrated due to its high charge density, and it is easily protonated to form hydrogen fluoride. As a result, it is not suitable for nucleophilic substitution reactions unless it is liberated from its aqueous surroundings. Consequently, water has to be removed carefully during the preprocessing of fluorine-18. After the removal of water, naked ^{18}F can react with its precursor partner by nucleophilic substitution. Yet in polar aprotic solvents, the addition of a phase transfer catalyst or a suitable cation like Cs^+ or tetraalkylammonium ions for charge separation is often needed to aid in the dissolution of $^{18}F^-$. If protecting groups have been used, they must also be removed. Protecting groups are often necessary to eliminate acidic protons in the molecule that would diminish the nucleophilicity of $^{18}F^-$. Finally, the product has to be purified by solid phase extraction or preparative HPLC.

In sum, nucleophilic ^{18}F-fluorination reactions consist of the following steps:

1. ^{18}F-Preprocessing: the removal of target water and the addition of a phase transfer catalyst, tetraalkylammonium, or Cs^+ to enhance the nucleophilicity of [^{18}F]fluoride.
2. The reaction with the labeling precursor in a polar aprotic solvent.
3. The removal of any protecting groups.
4. The purification and formulation of the final ^{18}F-labeled product.

^{18}F-Preprocessing

Before [^{18}F]fluoride can be used in nucleophilic substitution reactions, several preprocessing steps must be performed. First, the irradiated water received from the target is passed through an anion cartridge to trap the [^{18}F]fluoride. After that, the [^{18}F]fluoride can be eluted using weak bases like Cs_2CO_3 or Rb_2CO_3. The bases employed for elution must be non-nucleophilic in order to avoid competing substitution reactions. As a result, the phase transfer catalyst Kryptofix®2.2.2 in combination with potassium (bi)carbonate or tetraalkylammonium bicarbonate (alkyl = ethyl or

butyl) are typically used for elution rather than heavy alkali bases. After elution, the [^{18}F]fluoride is repeatedly dried via azeotropic distillation with acetonitrile to fully remove any water; the loss of [^{18}F]fluoride as volatile hydrogen [^{18}F]fluoride during this step is prevented by the base used for the elution. This step results in the creation of "naked", highly nucleophilic [^{18}F]fluoride due to the formation of weak ion pairs between [^{18}F]F$^-$ and the heavier alkali metal cations. In this regard, the use of the phase transfer catalyst Kryptofix®2.2.2/potassium (bi)carbonate or tetraalkylammonium bicarbonate is advantageous because the "naked" [^{18}F]fluoride is solubilized in a polar aprotic solvent such as acetonitrile. This whole procedure can be—and often is—conducted in commercially available remote-controlled synthesis devices. Nevertheless, this approach has two disadvantages. First, the use of base can lead to the formation of side products and prevents the use of base-sensitive precursors. And second, azeotropic drying is a highly time-consuming process.

In response to these problems, several alternative methods have been developed over the last two decades. These include the use of less basic inorganic anions like potassium phosphate, oxalate, triflate, or mesylate for the elution of the [^{18}F]fluoride from the anion exchange cartridge [11, 12]. To avoid the thermal drying step, the cartridge is washed with dry solvents, and the elution is performed with an organic solution of these inorganic anions and a phase transfer catalyst [13–15]. Even more notably, a recently described "minimalist" method enables the efficient preparation of different aliphatic and aromatic ^{18}F-labeled compounds using only an alcoholic solution of the "onium" precursor—for example, a sulfonium, iodonium, or ammonium derivative—for the elution of [^{18}F]fluoride [14]. This protocol obviates the need for azeotropic drying as well as base or any other additives.

Aliphatic ^{18}F-Substitution

The subsequent ^{18}F-fluorination step can be classified as a nucleophilic *aliphatic* or *aromatic* substitution. In general, nucleophilic aliphatic ^{18}F-substitutions are more effective, and most of the ^{18}F-labeled radiopharmaceuticals in routine clinical use are prepared via this route. A prerequisite for aliphatic ^{18}F-substitutions is the presence of a good leaving group. Along these lines, the halides Cl, Br, and I or the different types of sulfonates—tosylate, nosylate, mesylate, and triflate—are used most often in radiofluorination reactions. The selection of the appropriate leaving group depends on the structure and reactivity of the labeling precursor. In highly reactive precursors, no significant influence of the type of leaving group can be observed on the radiochemical yield of the reaction. In contrast, in less reactive or more sterically hindered precursors, the use of sulfonates—which are best suited to stabilize the additional electron density that results from bond heterolysis—are preferred. Depending on the kind of precursor and the reaction conditions, nucleophilic aliphatic ^{18}F-substitutions proceed via S_N1 or S_N2 mechanisms. The S_N2 substitution reaction takes place via a "backside attack" mechanism called the Walden inversion, leading to an inversion of configuration (Fig. 2).

Walden inversion is observed in the synthesis of 2-[^{18}F]fluoro-2-deoxy-D-glucose ([^{18}F]FDG), the most widely used PET tracer in nuclear medicine. It is used to sensitively detect different kinds of tumour lesions and plays an important role in modern clinical diagnosis. 1,3,4,6-Tetra-O-*acetyl*-2-O-trifluoromethanesulfonyl-β-D-mannopyranose serves as the radiolabeling precursor [16]. The nucleophilic attack of [^{18}F]fluoride takes place in the 2-position, resulting in an inversion of the stereo configuration. After the hydrolysis of the acetyl groups, [^{18}F]FDG is formed in a radiochemical purity of almost 100%, showing that the reaction occurs almost solely via an S_N2 mechanism (Fig. 3).

The ^{18}F-radiofluorination of complex molecules is often challenging. Complex molecules contain functional groups which can hamper nucleophilic ^{18}F-substitution reactions owing to their acidity or steric hindrance. Another example that underscores the complex interplay of leaving and protecting groups is the synthesis of 3′-deoxy-3′-[^{18}F]fluorothymidine ([^{18}F]FLT). In this case, an array of different protecting and leaving groups were studied to find the best

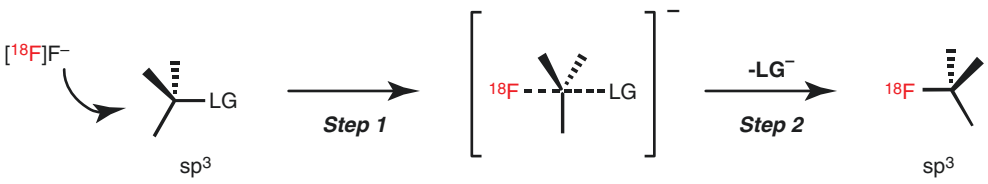

Fig. 2 S_N2 mechanism with Walden inversion

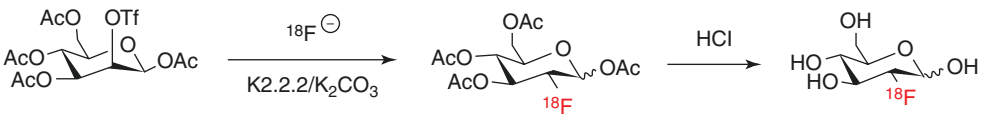

Fig. 3 Nucleophilic synthesis of [^{18}F]FDG

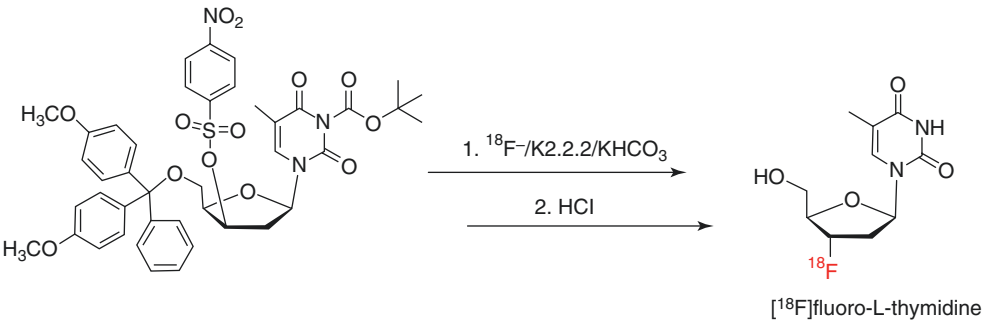

Fig. 4 Synthesis of [^{18}F]FLT from the corresponding precursor using a nosyl leaving group and *tert*-butoxycarbonyl and dimethoxytrityl protecting groups for the amide and hydroxyl, respectively

combination that provides the highest radiochemical yield. The highest RCYs of 30–40% were obtained using a nosyl leaving group and *tert*-butoxycarbonyl and dimethoxytrityl protecting groups for the amide and hydroxyl, respectively (Fig. 4) [17].

Aliphatic nucleophilic ^{18}F-substitutions are usually performed at higher temperatures (~80–100 °C) in polar aprotic solvents like acetonitrile, *N,N*-dimethylformamide (DMF), or dimethyl sulfoxide (DMSO). However, it was discovered that nucleophilic aliphatic ^{18}F-substitution reactions can also be performed in *tert*-alcohol media [18]. These results contradict previous observations concerning the deleterious effect of protic solvents, including alcohols, on nucleophilic fluorination, usually explained by extensive hydrogen bonding that reduces the nucleophilicity of fluoride. The combination of acetonitrile and *tert*-butanol provides higher RCYs—especially when sulfonate leaving groups are used—and is particularly useful with base-sensitive precursors. There are several hypotheses regarding why tertiary alcohols improve the yields of nucleophilic aliphatic ^{18}F-fluorination reactions: (1) the strength of the alkali-F ionic bond is reduced by hydrogen bonding; (2) the coordination of [^{18}F]fluoride by the *tert*-alcohols limits the solvation of the radionuclide; (3) hydrogen bonding between the tertiary alcohol and the oxygen atoms of the sulfonate group enhances the leaving group's ability; and (4) the protic medium and hydrogen bonding between the *tert*-alcohol and reactive heteroatoms in the substrate obviates side reactions like eliminations, hydroxylations, and intramolecular alkylations [19]. The advantages of *tert*-butanol as a solvent for ^{18}F-substitution reactions are demonstrated in the synthesis of [^{18}F]fluoropropylcarbomethoxyiodophenylnortropane ([^{18}F]FP-CIT), which was obtained with high reproducibility in total RCY of 36 ± 5% after HPLC purification (Fig. 5) [20]. In comparison, the synthesis afforded only <5% RCY under conventional conditions [21].

To return to the production of [^{18}F]FLT, the use of the bulky alcohol 3-methyl-pentan-3-ol in acetonitrile also produced higher and more robust RCYs (see Fig. 4). Using this bulky alcohol, RCYs of up to 54% were obtained in a mixture of 3-methyl-pentan-3-ol in acetonitrile in comparison to only maximum 30–40% RCY in pure acetonitrile [22].

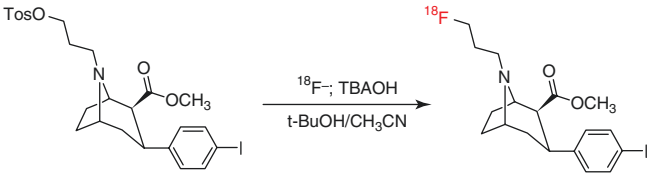

Fig. 5 Synthesis of [^{18}F]FP-CIT using a solution of tert-BuOH/acetonitrile

Synthesis of ^{18}F-Labeled Arenes by Aromatic Nucleophilic ^{18}F-Substitution (S_NAr)

The earliest attempts at synthesizing ^{18}F-labeled arenes sought to leverage the Balz-Schiemann and Wallach reactions (Fig. 6). Unfortunately, however, both methods provided RCYs of <3% due to the formation of aryl cations as intermediates that are susceptible to many side reactions. Furthermore, products obtained by the Balz-Schiemann reaction are characterized by a low specific activity because tetrafluoroborate—which contains ^{19}F—is used as the counter anion of the diazonium salt.

The most successful route to no-carrier-added [^{18}F]fluoroarenes is nucleophilic aromatic ^{18}F-substitution via the S_NAr (addition-elimination) mechanism (Fig. 7). This requires not only a good leaving group in the aromatic ring but also an activating electron-withdrawing group, preferably in the ortho- or para-position relative to the leaving group. Typical leaving groups include I, Br, Cl, F, NO_2, and $^+NMe_3$, with the last two providing the best performance because their electron-withdrawing character helps them stabilize the developing negative charge on the aromatic ring.

In stark contrast to nucleophilic aliphatic substitutions, the fluoride itself can serve as a good leaving group in S_NAr reactions. Greater amounts of energy are needed for the formation of the resonance-stabilized Meisenheimer complex intermediates compared to the intermediates of aliphatic substitutions. Thus, ^{18}F-substitutions via the S_NAr mechanism often require higher temperatures, leading to side reactions and lower RCYs. Accordingly, higher-boiling solvents like DMSO, DMF, and *N,N*-dimethylacetamide (DMA) are normally preferred for this type of reaction. The synthesis of [^{18}F]altanserin was one of the first examples in which a S_NAr

reaction was successfully applied to facilitate the synthesis of this radiotracer in one step without the need for protecting groups (Fig. 8) [23].

The precursor for [^{18}F]altanserin is an electron-deficient arene, enabling the direct introduction of ^{18}F. Non-activated or even electron-rich arene rings, however, require another strategy. In this case, the aromatic precursor needs an activating group in the ortho- or para-position relative to the leaving group; in the majority of cases, the activating group must be removed or further functionalized in order to obtain the desired product. This strategy is exemplified by the nucleophilic synthesis of 6-[^{18}F]fluoro-3,4-dihydoxy-L-phenylalanine (6-[^{18}F]FDOPA). The first synthesis of 6-[^{18}F]FDOPA for clinical use was performed using a rapid electrophilic ^{18}F-fluorination method yielding a high enantiomeric excess (ee > 99%). However, the disadvantages of this procedure are its low molar activity, its relatively low radiochemical yield (<25%), and the low starting activity of [^{18}F]F_2 [24]. The first nucleophilic synthesis of 6-[^{18}F]FDOPA was realized using a dimethoxybenzaldehyde building block with a nitro or trimethylammonium leaving group [25]. The aldehyde served as an activating group and was converted to an acid after the introduction of fluorine-18. To achieve this, ^{18}F-labeled benzaldehyde was first converted into [^{18}F]fluorobenzylbromide or iodide and subsequently coupled to a chiral auxiliary to form 6-[^{18}F]FDOPA after acidic hydrolysis. Different auxiliaries were examined, but the best results were obtained with a chiral phase transfer catalyst reaction that couples benzyl bromide to a protected glycine derivative (Fig. 9, *left*) [26]. The transfer of this highly cumbersome and multistep procedure to automated synthesis modules was sophisticated. Every reaction step had to be carefully optimized to obtain a reliable synthesis procedure. Yet still, the process is now available on a cassette-based synthesis module, affording [^{18}F]FDOPA in a high enantiomeric excess of 97%, a total synthesis time of 63 min, and a radiochemical yield of 36% [27].

In order to implement the concept of late-stage radiofluorination, an alternative synthesis route of 6-[^{18}F]FDOPA was developed that makes use of the direct nucleophilic ^{18}F-fluorination of a protected amino acid derivative (Fig. 9, *centre*) [28]. The isotopic ^{18}F-for-^{19}F exchange reaction is activated by a carbonyl in the para-position. Subsequently, the carbonyl is converted into an ester via a Baeyer-Villiger oxidation and further hydrolysed yielding 6-[^{18}F]FDOPA. One major disadvantage of this procedure is its sensitivity to the basic ^{18}F-labeling conditions, which can lead to

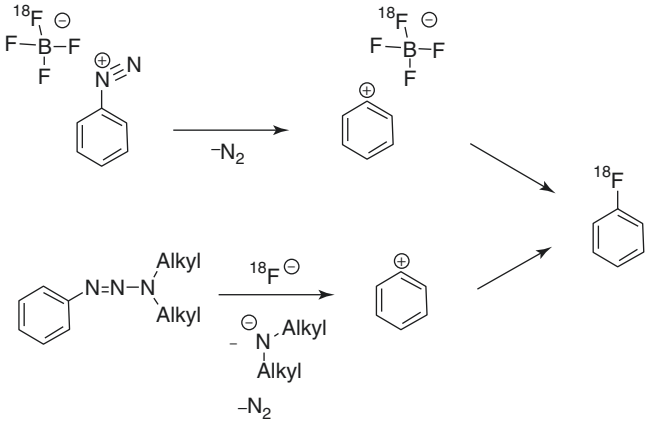

Fig. 6 Preparation of ^{18}F-labeled arenes via the Balz-Schiemann (top) and Wallach reactions (bottom)

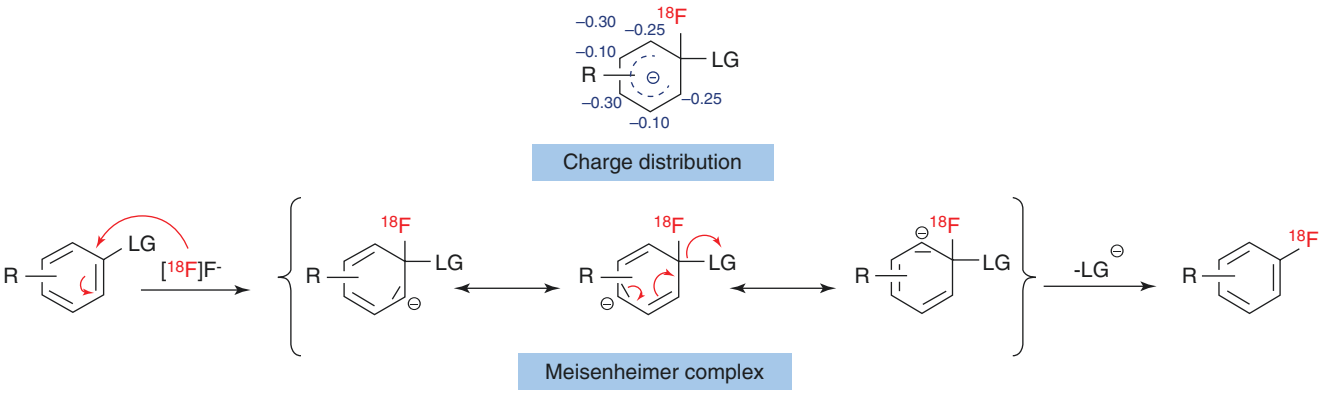

Fig. 7 Aromatic nucleophilic substitution (S_NAr)

Fig. 8 One-step radiosynthesis of [^{18}F]altanserin

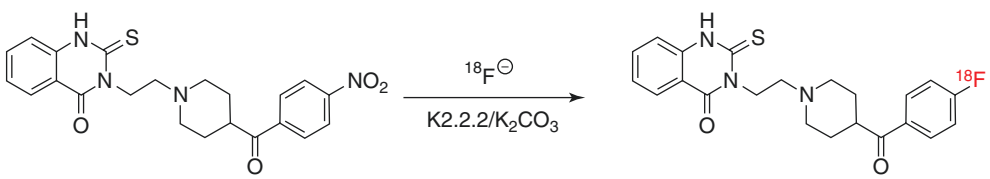

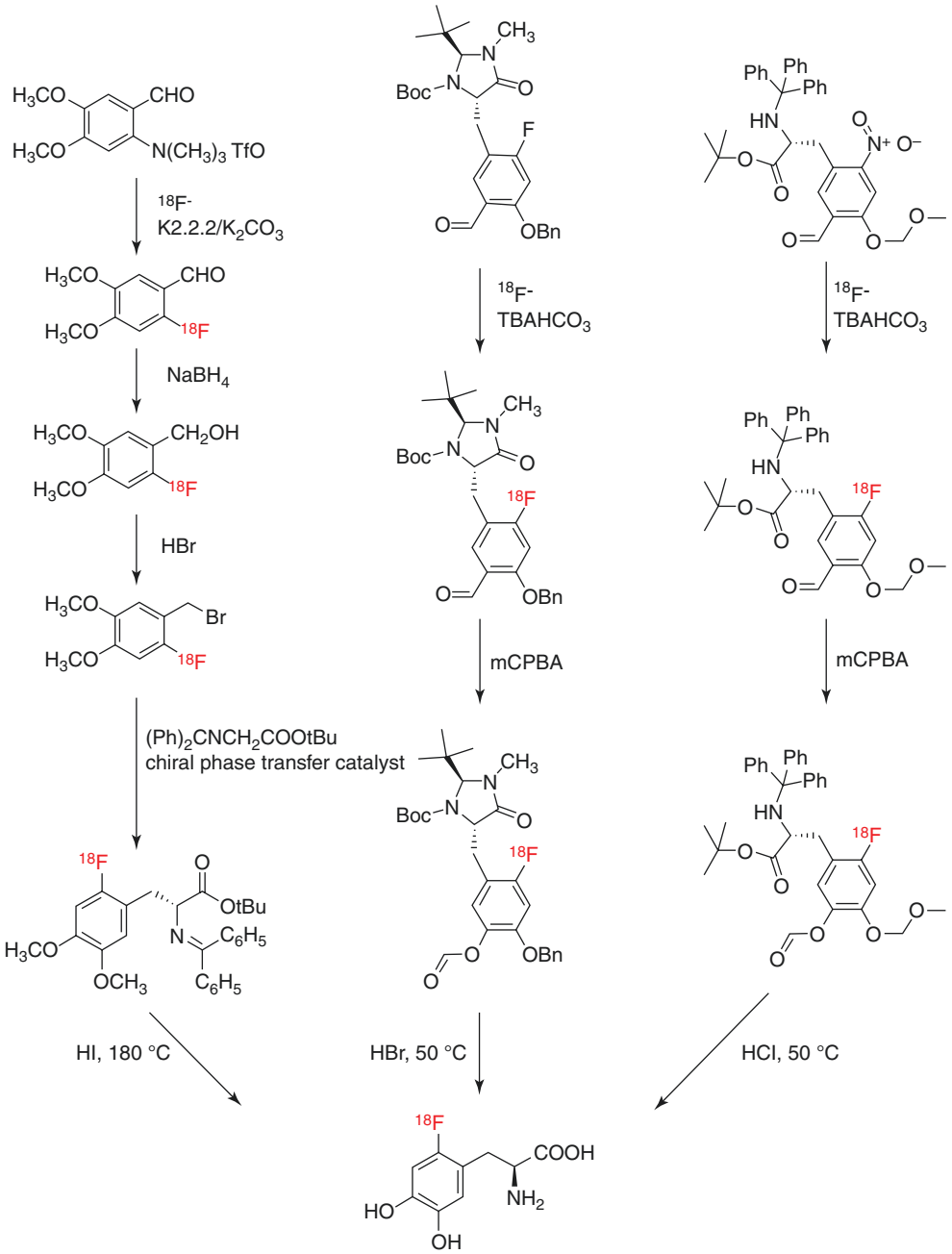

Fig. 9 Three multistep, nucleophilic syntheses of 6-[^{18}F]FDOPA

the epimerization of the amino acid. A further variation on this approach was created by developing an alternative precursor that is less sensitive to base-mediated epimerisation. Furthermore, the use of other protecting groups—*tert*-butyl and *tert*-butoxycarbonyl—enabled the use of milder deprotection conditions (Fig. 9, *right*) [29]. In this case, a nitro group was used as a leaving group instead of a fluoride, facilitating the synthesis of 6-[^{18}F]FDOPA in high specific activity.

Aromatic ^{18}F-Substitution of Heteroarenes via Classical S_NAr Approach

Nucleophilic substitution reactions with [^{18}F]fluoride have also been applied to the synthesis of ^{18}F-labeled *hetero*arenes [30, 31]. Along these lines, the 2- and 4-positions of pyridine are particularly highly activated for nucleophilic exchange reactions using I, Br, Cl, F, NO_2, or $^{+}NMe_3$ as leaving groups. Interestingly, the synthesis of 2-[^{18}F]fluoropyridine deriva-

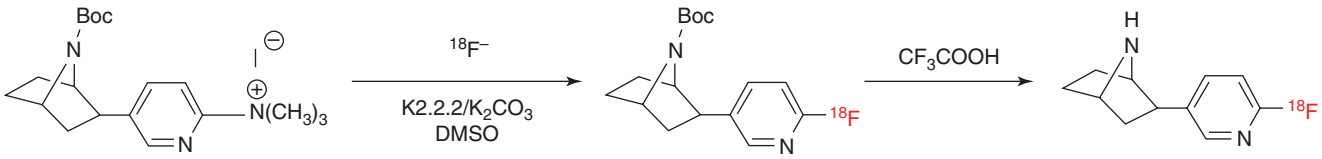

Fig. 10 Synthesis of norchloro[^{18}F]fluoroepibatidine

Table 1 Prerequisites for nucleophilic ^{18}F-substitutions

Aliphatic ^{18}F-substitution	Aromatic ^{18}F-substitution
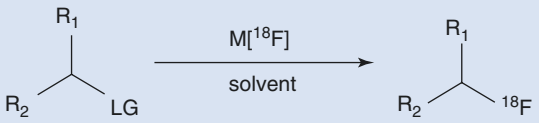	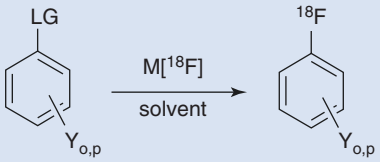
LG = Cl, Br, I, sulfonates	LG = Cl, Br, I, F, NO_2 [35], $(CH_3)_3N^+$ [36], Ar_2S^+ [37], ArI^+ [38], IL_2 [39, 40], $I(OAc)_2$ [41], ArSO [42], ArSeO [43], N-arylsydnones [44]
R_1 = alkyl, aryl; R_2 = alkyl, aryl, H	Y = COOR, COR, CHO, CN, NO_2
M = Cs^+, Rb^+, R_4N^+, K2.2.2./K^+, R = alkyl	M = Cs^+, Rb^+, R_4N^+, K2.2.2./K^+ R = alkyl
Solvent: acetonitrile, DMF, DMSO, *tert*-butanol/acetonitrile	Solvent: DMSO, DMF, DMA

LG = leaving group, *Y* = activating group, *DMSO* = dimethyl sulfoxide, *DMF* = *N,N*-dimethylformamide, *DMA* = *N,N*-dimethylacetamide

tives has been preferred because of its efficiency [32]. The labeling conditions for 2-[^{18}F]fluoropyridines are similar to the S_NAr conditions used for the *homo*arenes discussed above: both high temperatures and high-boiling solvents like DMSO or DMF are needed. This approach was used for the one- and two-step syntheses of norchloro[^{18}F]fluoroepibatidine ((±)-exo-2-(6-[^{18}F]fluoro-3-pyridyl)-7-azabicyclo [2.2.1]heptane) (Fig. 10). In the initial study, the amino group of the labeling precursor was not protected, leading to isolated RCYs of only ~10% [33]. However, the introduction of a Boc group on the amine improved the isolated RCY to >55% [34].

In Table 1 [35–44], the prerequisites for both aliphatic and aromatic ^{18}F-nucleophilic substitution reactions are summarized.

Aromatic ^{18}F-Substitution Using "Onium" Salts

As we have mentioned, direct nucleophilic aromatic substitutions with [^{18}F]fluoride of electron-deficient aromatic substrates bearing "conventional" leaving groups such as halogens, nitro groups, and trimethylammonium groups provide convenient access to n.c.a. ^{18}F-labeled compounds. On the other hand, the preparation of radiofluorinated arenes labeled at inactivated and especially electron-rich positions using [^{18}F]F^- has been very challenging [28]. However, the utilization of suitable aryliodonium [38, 45] and diarylsulfonium [37, 46] leaving groups has facilitated the radiolabeling of electron-neutral and moderately electron-rich aromatics (Fig. 11). Iodonium ylides based on Meldrum's acid [39] or spirocyclic iodonium ylides [40, 47] were also successfully employed for the same purpose (Fig. 12). In the case of aryl-substituted onium salts, the nucleophilic attack of the [^{18}F]fluoride preferentially takes place at the more electron-deficient position. Furthermore, in the case of diaryliodonium salts, an *ortho*-effect is observed. Accordingly, substituents like alkyls or halogens direct the incoming ^{18}F nucleophile to attack the same ring at the *ortho*-position [48, 49]. The possibility of radiolabeling even electron-rich arene rings using symmetrical substituted bisaryliodonium or arylthienyliodonium salts was also intensively studied. For example, this approach enabled the synthesis of 2- and 4-[^{18}F]fluoroanisoles in RCYs of 29% and 61%, respectively [45].

These "onium" salts have also been used for the synthesis of ^{18}F-labeled building blocks like 1-bromo-4-[^{18}F]fluorobenzene [50] or 4-[^{18}F]fluoroiodobenzene [51, 52] that can be used for palladium-mediated ^{18}F-coupling reactions [53]. This concept is exemplified by the synthesis of the selective cyclooxygenase (COX-2) inhibitor 3-(4-[^{18}F]fluorophenyl)-4-(4-methanesulfonylphenyl)-5*H*-furan-2-one using the Stille reaction (Fig. 13) [54].

The main challenge of this approach lines in the preparation of the onium salt and iodonium ylide precursors, which often requires harsh oxidative and acidic conditions. Consequently,

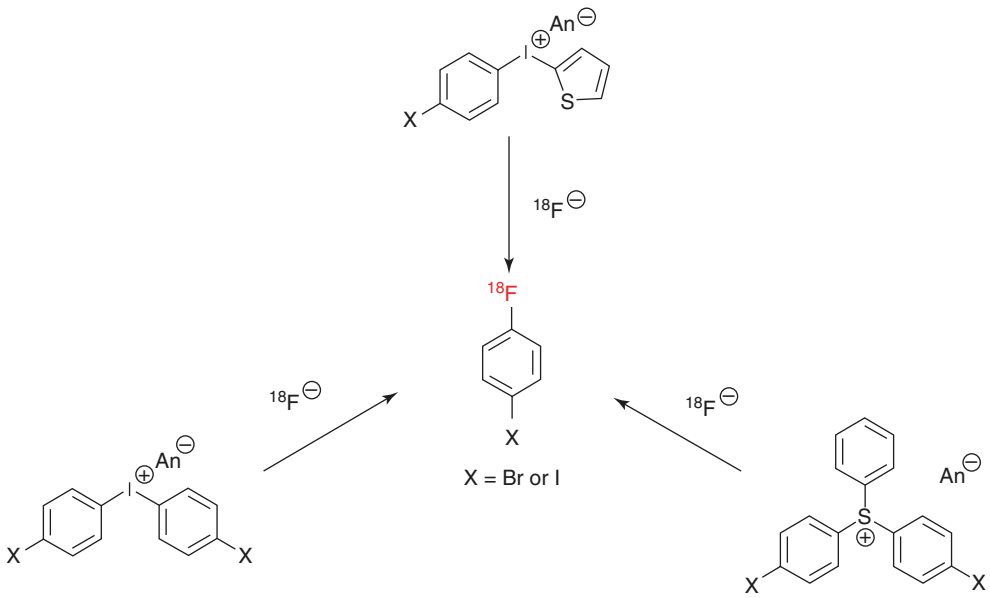

Fig. 11 Synthesis of [^{18}F] fluoro-4-halobenzenes using sulfonium or iodonium salt precursors. An = counter ion

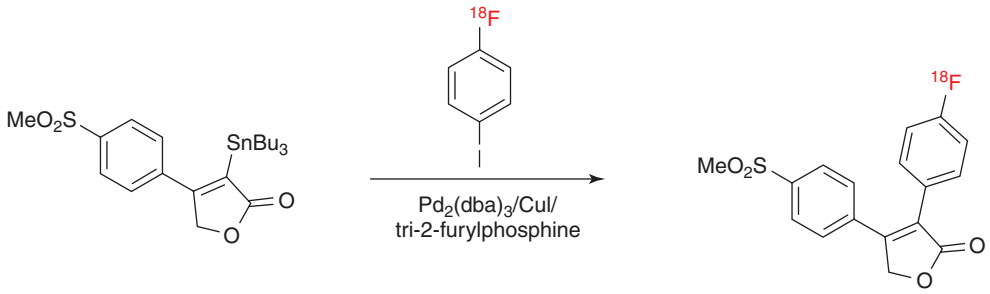

Fig. 12 Iodonium ylides for the preparation of complex ^{18}F-labeled arenes

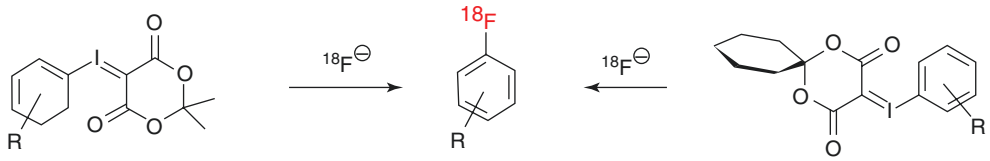

Fig. 13 Synthesis of a ^{18}F-labeled COX-2 inhibitor using the Stille reaction

polyfunctionalized iodonium salts are relatively difficult to prepare. Furthermore, in many cases, these compounds suffer from limited storage capability [47]. Nevertheless, a recently published procedure facilitates the preparation of densely functionalized and sensitive iodonium salt precursors [55]. In this approach, the treatment of an iodoarene with a mixture of trimethylsilyl acetate and Selectfluor™ as oxidation agents leads to the formation of the corresponding (diacetoxyiodo)arenes, which are subsequently coupled with potassium (4-methoxyphenyl)trifluoroborate to create iodonium salts. This enables the synthesis of precursors with acid-sensitive and base-sensitive functionalities. These syntheses were performed using glove box techniques; however, highly purified reagents and solvents are not required under these rigorously anhydrous conditions. This method has enabled the synthesis of iodonium salts for the preparation of both 4-[^{18}F]fluorophenylalanine and 6-[^{18}F]FDOPA. The synthesis of the iodonium salt for the latter is shown in Fig. 14: a three step procedure enables the synthesis of ((S)-methyl-3-(4,5-bis(ethoxymethoxy)2-iodophenyl)-2-(di-(*tert*-butoxycarbonyl))amino)propanoate)(4-methoxyphenyl)-λ_3-iodane trifluoromethanesulfonate in a yield of 63% [56].

The synthesis of 6-[^{18}F]FDOPA via this iodonium precursor has been established for routine clinical production (Fig. 15) [56].

In the following section, we provide some practical notes on several things that radiochemists should consider before starting work with [^{18}F]fluoride and performing nucleophilic substitution reactions.

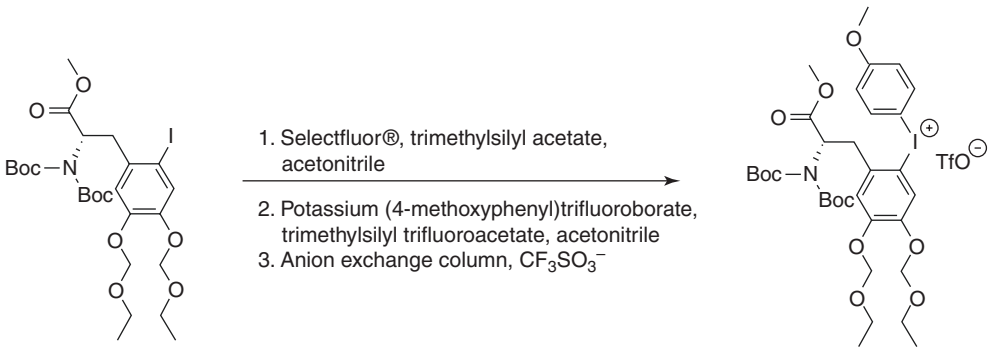

Fig. 14 Synthesis of the iodonium precursor for the synthesis of 6-[^{18}F]FDOPA

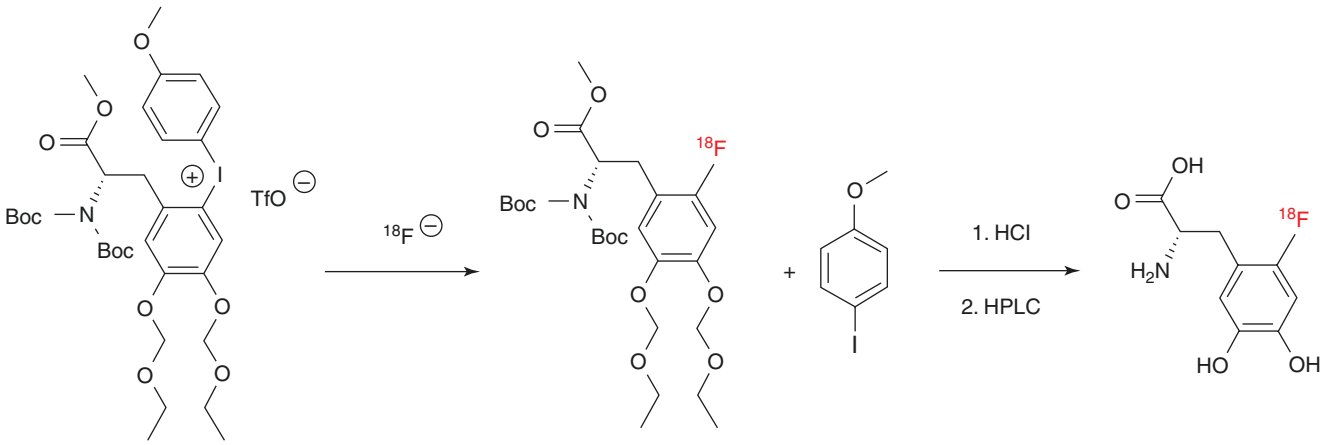

Fig. 15 Synthesis of 6-[^{18}F]FDOPA via an iodonium salt [56]

Rules for Performing Nucleophilic ^{18}F-Fluorinations

- All necessary radiation protection and safety measures must be employed.
- The careful consideration of the position for the introduction of ^{18}F is crucial, particularly with regard to pharmacological properties, metabolic stability, and labeling efficiency.
- The intended position of the ^{18}F label determines the appropriate precursor and the radiofluorination protocol, especially for aromatic nucleophilic radiofluorinations. For example, 2- and 4-[^{18}F]fluorobenzaldehyde are prepared using nitro- or *N*,*N*,*N*-trimethylanilinium precursors, while 3-[^{18}F]fluorobenzaldehyde is only efficiently produced using iodonium or sulfonium salts.
- Sufficient shelf life, synthetic accessibility, and stability under fluorination reaction conditions are indispensable for a precursor.
- If possible, the radiolabeled product should be easily separable from the precursor and any impurities.
- Owing to the relatively short half-life of ^{18}F, the radiosynthetic method should have as few reaction steps as possible and be as fast as possible.
- Traces of water substantially diminish the nucleophilicity of $^{18}F^-$ and can lead to reduced RCYs. In light of this, nucleophilic radiofluorinations should be carried out under absolutely anhydrous conditions. Dry solvents, carrier gases, and lab equipment should always be used.
- In the case of more demanding radiofluorinations, radiolabeling can be substantially hampered by the adsorption of $^{18}F^-$ onto the walls of the reaction vessel (up to >50%). In order to correctly determine the yield of ^{18}F incorporation using TLC or HPLC, the adsorbed [^{18}F]fluoride should be dissolved via the addition of H_2O.
- Under acidic conditions, $^{18}F^-$ forms volatile [^{18}F]HF; it is crucial to make sure that this gas is trapped by appropriate equipment.

The Bottom Line

- Nucleophilic substitutions with $^{18}F^-$ provide simple access to radiofluorinated PET probes in high molar activity. In contrast, the preparation of ^{18}F-labeled radiotracers with high molar activity using the electrophilic ^{18}F-fluorination is cumbersome.
- In nucleophilic radiofluorinations, $^{18}F^-$ can be entirely incorporated into precursor molecules. In contrast, the RCY of electrophilic ^{18}F-fluorinations is limited to a maximum of 50%.
- The highly efficient $^{18}O(p,n)^{18}F$ reaction allows for the convenient production of up to 500 GBq [^{18}F]fluoride in a single run using a liquid target.
- Numerous remotely controlled synthesis modules are commercially available which permit the expedient cGMP production of a broad spectrum of PET tracers for preclinical and clinical applications.
- Emerging methods of radiofluorination using nucleophilic [^{18}F]fluoride allow for the introduction of fluorine-18 into (almost) any position of (almost) any small molecule.
- The protection of acidic groups—hydroxyls, thiols, carboxyls, and amines—is often necessary in order to achieve acceptable labeling yields.
- The rather harsh reaction conditions—high temperatures, strong basic conditions, organic solvents, *etc.*—typically employed for direct nucleophilic radiofluorination are usually not compatible with sensitive biomolecules like proteins. In such cases, an indirect radiolabeling approach using radiolabeled building blocks bearing reactive groups (*i.e.* "prosthetic groups") must be used.

References

1. Coenen HH. Fluorine-18 labeling methods: features and possibilities of basic reactions. In: Schubiger PA, Lehmann L, Friebe M, editors. PET chemistry: The driving force in molecular imaging. Ernst Schering Research Foundation Workshop 62. Berlin/Heidelberg: Springer; 2007. p. 15–50.
2. Miller PW, Long NJ, Vilar R, Gee AD. Synthesis of ^{11}C, ^{18}F, ^{15}O, and ^{13}N radiolabels for positron emission tomography. Angew Chem Int Ed Engl. 2008;47(47):8998–9033.
3. Bondi AJ. van der Waals volumes and radii. J Phys Chem. 1964;68(3):441–51.
4. Purser S, Moore PR, Swallow S, Gouverneur V. Fluorine in medicinal chemistry. Chem Soc Rev. 2008;37:320–30.
5. Qaim SM, Clark JC, Crouzel C, Guillaume M, Helmeke HJ, Nebeling B, et al. PET radionuclide production. In: Stöcklin G, Pike VW, editors. Radiopharmaceuticals for positron emission tomography – methodological aspects. Dordrecht: Springer Netherlands; 1993. p. 1–42.
6. Wadsak W, Mitterhauser M. Basics and principles of radiopharmaceuticals for PET/CT. Eur J Radiol. 2010;73(3):461–9.
7. Bergman J, Solin O. Fluorine-18-labeled fluorine gas for synthesis of tracer molecules. Nucl Med Biol. 1997;24(7):677–83.
8. Devillet F, Geets J-M, Ghyoot M, Kral E, Nactergal B, Mooij R, Vosjan M. Performance of IBA new conical shaped niobium [^{18}O] water targets. Proceedings of the 15th international workshop on targetry and target chemistry. WTTC15 August 18-21, 2014, Prague, Czech Republic. https://core.ac.uk/download/pdf/35205875.pdf. Accessed 21 May 2018.
9. Ermert J, Coenen HH. Nucleophilic ^{18}F-fluorination of complex molecules in activated carbocyclic aromatic position. Curr Radiopharm. 2010;3(2):109–26.
10. van der Born D, Pees A, Poot AJ, Orru RVA, Windhorst AD, Vugts DJ. Fluorine-18 labelled building blocks for PET tracer synthesis. Chem Soc Rev. 2017;46(15):4709–73.
11. Lee SJ, Oh SJ, Chi DY, Moon DH, Ryu JS. High yielding [^{18}F] fluorination method by fine control of the base. Bull Kor Chem Soc. 2012;33(7):2177–80.
12. Seo JW, Lee BS, Lee SJ, Oh SJ, Chi DY. Fast and easy drying method for the preparation of activated [^{18}F]fluoride using polymer cartridge. Bull Kor Chem Soc. 2011;32(1):71–6.
13. Wessmann SH, Henriksen G, Wester HJ. Cryptate mediated nucleophilic ^{18}F-fluorination without azeotropic drying. Nuklearmedizin. 2012;51(1):1–8.
14. Richarz R, Krapf P, Zarrad F, Urusova EA, Neumaier B, Zlatopolskiy BD. Neither azeotropic drying, nor base nor other additives: a minimalist approach to ^{18}F-labeling. Org Biomol Chem. 2014;12(40):8094–9.
15. Lemaire CF, Aerts JJ, Voccia S, Libert LC, Mercier F, Goblet D, et al. Fast production of highly reactive no-carrier-added [^{18}F]fluoride for the labeling of radiopharmaceuticals. Angew Chem nt Ed Engl. 2010;49(18):3161–4.
16. Hamacher K, Coenen HH, Stöcklin G. Efficient stereospecific synthesis of no-carrier-added 2-[^{18}F]fluoro-2-deoxy-D-glucose using aminopolyether supported nucleophilic substitution. J Nucl Med. 1986;27(2):235–8.
17. Suehiro M, Vallabhajosula S, Goldsmith SJ, Ballon DJ. Investigation of the role of the base in the synthesis of [^{18}F]FLT. Appl Radiat Isot. 2007;65(12):1350–8.
18. Kim DW, Ahn DS, Oh YH, Lee S, Kil HS, Oh SJ, et al. A new class of S 2 reactions catalyzed by protic solvents: facile fluorination for isotopic labeling of diagnostic molecules. J Am Chem Soc. 2006;128(50):16394–7.
19. Kim DW, Jeong LST, Sohn MH, Katzenellenbogen JA, Chi DY. Facile nucleophilic fluorination reactions using tert-alcohols as a reaction medium: significantly enhanced reactivity of alkali metal fluorides and improved selectivity. J Org Chem. 2008;73(3):957–62.
20. Lee SJ, Oh SJ, Chi DY, Kang SH, Kil HS, Kim JS, Moon DH. One-step high-radiochemical-yield synthesis of [^{18}F]FP-CIT using a protic solvent system. Nucl Med Biol. 2007;34(4):345–51.
21. Chaly T, Dhawan V, Kazumata K, Antonini A, Margouleff C, Dahl JR, et al. Radiosynthesis of [^{18}F] N-3-fluoropropyl-2-β-carbomethoxy-3-β-(4-iodophenyl) nortropane and the first human study with positron emission tomography. Nucl Med Biol. 1996;23(8):999–1004.
22. Marchand P, Ouadi A, Pellicioli M, Schuler J, Laquerriere P, Boisson F, Brasse D. Automated and efficient radiosynthesis of [^{18}F]FLT using a low amount of precursor. Nucl Med Biol. 2016;43(8):520–7.
23. Lemaire C, Cantineau R, Guillaume M, Plenevaux A, Christiaens L. Fluorine-18-altanserin: a radioligand for the study of serotonin receptors with PET: radiolabeling and in vivo biologic behavior in rats. J Nucl Med. 1991;32(12):2266–72.
24. Pretze M, Wängler C, Wängler B. 6-[^{18}F]fluoro-L-DOPA: a well-established neurotracer with expanding application spectrum and strongly improved radiosyntheses. Biomed Res Int. 2014;2014:674063.
25. Lemaire C, Guillaume M, Cantineau R, Christiaens L. No-carrier-added regioselective preparation of 6-[^{18}F]fluoro-L-dopa. J Nucl Med. 1990;31(7):1247–51.

26. Lemaire C, Gillet S, Guillouet S, Plenevaux A, Aerts J, Luxen A. Highly enantioselective synthesis of no-carrier-added 6-[^{18}F] fluoro-L-dopa by chiral phase-transfer alkylation. Eur J Org Chem. 2004;2004(13):2899–904.
27. Libert LC, Franci X, Plenevaux AR, Ooi T, Maruoka K, Luxen AJ, Lemaire CF. Production at the curie level of no-carrier-added 6-^{18}F-fluoro-L-dopa. J Nucl Med. 2013;54(7):1154–61.
28. Wagner FM, Ermert J, Coenen HH. Three-step, "one-pot" radiosynthesis of 6-fluoro-3,4-dihydroxy-L-phenylalanine by isotopic exchange. J Nucl Med. 2009;50(10):1724–9.
29. Martin R, Baumgart D, Hubner S, Juttler S, Saul S, Clausnitzer A, et al. Automated nucleophilic one-pot synthesis of ^{18}F-L-DOPA with high specific activity using the GE TRACERlab MXFDG (abstract). J Label Compd Radiopharm. 2013;56:S126.
30. Dollé F. Fluorine-18-labelled fluoropyridines: advances in radiopharmaceutical design. Curr Pharm Des. 2005;11(25):3221–35.
31. Dollé F. [^{18}F]Fluoropyridines: From conventional radiotracers to the labeling of macromolecules such as proteins and oligonucleotides. In: Schubiger PA, Lehmann L, Friebe M, editors. PET chemistry: the driving force in molecular imaging. Ernst Schering Research Foundation Workshop 62. Berlin/Heidelberg: Springer Berlin; 2007. p. 113–57.
32. Preshlock S, Tredwell M, Gouverneur V. ^{18}F-labeling of arenes and heteroarenes for applications in positron emission tomography. Chem Rev. 2016;116(2):719–66.
33. Horti A, Ravert HT, London ED, Dannals RF. Synthesis of a radiotracer for studying nicotinic acetylcholine receptors: (+/−)-exo-2-(2-[^{18}F]fluoro-5-pyridyl)-7-azabicyclo[2.2.1]heptane. J Label Compd Radiopharm. 1996;38(4):355–65.
34. Ding YS, Liang F, Fowler JS, Kuhar MJ, Carroll FI. Synthesis of [^{18}F]norchlorofluoroepibatidine and its N-methyl derivative: new PET ligands for mapping nicotinic acetylcholine receptors. J Label Compd Radiopharm. 1997;39(10):827–32.
35. Attiná M, Cacace F, Wolf AP. Displacement of a nitro-group by [^{18}F]fluoride ion. A new route to aryl fluorides of high specific activity. J Chem Soc Chem Commun. 1983:108–9.
36. Haka MS, Kilbourn MR, Watkins GL, Toorongian SA. Aryltrimethylammonium trifluoromethanesulfonates as precursors to aryl [^{18}F]fluorides: improved synthesis of [^{18}F]GBR-13119. J Label Compd Radiopharm. 1989;27(7):823–33.
37. Mu L, Fischer CR, Holland JP, Becaud J, Schubiger PA, Schibli R, et al. ^{18}F-radiolabeling of aromatic compounds using triarylsulfonium salts. Eur J Org Chem. 2012;2012(5):889–92.
38. Pike VW, Aigbirhio FI. Reactions of cyclotron-produced [^{18}F] fluoride with diaryliodonium salts – a novel single-step route to no-carrier-added [^{18}]fluoroarenes. J Chem Soc Chem Commun. 1995:2215–6.
39. Cardinale J, Ermert J, Humpert S, Coenen HH. Iodonium ylides for one-step, no-carrier-added radiofluorination of electron rich arenes, exemplified with 4-(([^{18}F]fluorophenoxy)-phenylmethyl) piperidine NET and SERT ligands. RSC Adv. 2014;4:17293–9.
40. Rotstein BH, Stephenson NA, Vasdev N, Liang SH. Spirocyclic hypervalent iodine(III)-mediated radiofluorination of non-activated and hindered aromatics. Nat Commun. 2014;5:4365.
41. Haskali MB, Telu S, Lee Y-S, Morse CL, Lu S, Pike VW. An investigation of (diacetoxyiodo)arenes as precursors for preparing no-carrier-added [^{18}F]fluoroarenes from cyclotron-produced [^{18}F] fluoride ion. J Org Chem. 2016;81(1):297–302.
42. Chun J-H, Morse CL, Chin FT, Pike VW. No-carrier-added [^{18}F] fluoroarenes from the radiofluorination of diaryl sulfoxides. Chem Commun (Camb). 2013;49(21):2151–3.
43. Simeon FG, Lu S, Pike VW. Diarylselenoxides as precursors to no-carrier-added [^{18}F]fluoroarenes (abstract). J Label Compd Radiopharm. 2015;58:S149.
44. Narayanam MK, Ma G, Champagne PA, Houk KN, Murphy JM. Synthesis of [^{18}F]fluoroarenes by nucleophilic radiofluorination of N-arylsydnones. Angew Chem Int Ed. 2017;56(42):13006–10.
45. Ross TL, Ermert J, Hocke C, Coenen HH. Nucleophilic ^{18}F-fluorination of heteroaromatic iodonium salts with no-carrier-added [^{18}F]fluoride. J Am Chem Soc. 2007;129(25):8018–25.
46. Sander K, Gendron T, Yiannaki E, Cybulska K, Kalber TL, Lythgoe MF, Arstad E. Sulfonium salts as leaving groups for aromatic labelling of drug-like small molecules with fluorine-18. Sci Rep. 2015;5:9941.
47. Rotstein BH, Wang L, Liu RY, Patteson J, Kwan EE, Vasdev N, Liang SH. Mechanistic studies and radiofluorination of structurally diverse pharmaceuticals with spirocyclic iodonium(III) ylides. Chem Sci. 2016;7(7):4407–17.
48. Coenen HH, Ermert J. Direct nucleophilic ^{18}F-fluorination of electron rich arenes: present limits of no-carrier-added reactions. Curr Radiopharm. 2010;3(3):163–73.
49. Pike VW. Hypervalent aryliodine compounds as precursors for radiofluorination. J Label Compd Radiopharm. 2018;61(3):196–227.
50. Ermert J, Hocke C, Ludwig T, Gail R, Coenen H. Comparison of pathways to the versatile synthon of no-carrier-added 1-bromo-4-[^{18}F]fluorobenzene. J Label Compd Radiopharm. 2004;47(7):429–41.
51. Wüst FR, Kniess T. Synthesis of 4-[^{18}F]fluoroiodobenzene and its application in Sonogashira cross-coupling reactions. J Label Compd Radiopharm. 2003;46(8):699–713.
52. Way JD, Wuest F. Automated radiosynthesis of no-carrier-added 4-[^{18}F]fluoroiodobenzene: a versatile building block in ^{18}F radiochemistry. J Label Compd Radiopharm. 2014;57(2):104–9.
53. Way J, Bouvet V, Wuest F. Synthesis of 4-[^{18}F]fluorohalobenzenes and palladium-mediated cross-coupling reactions for the synthesis of ^{18}F-labeled radiotracers. Curr Org Chem. 2013;17(19):2138–52.
54. Wüst FR, Höhne A, Metz P. Synthesis of ^{18}F-labelled cyclooxygenase-2 (COX-2) inhibitors via Stille reaction with 4-[^{18}F]fluoroiodobenzene as radiotracers for positron emission tomography (PET). Org Biomol Chem. 2005;3:503–7.
55. Qin L, Hu B, Neumann KD, Linstad EJ, McCauley K, Veness J, et al. A mild and general one-pot synthesis of densely functionalized diaryliodonium salts. Eur J Org Chem. 2015;2015(27):5919–24.
56. Kuik WJ, Kema IP, Brouwers AH, Zijlma R, Neumann KD, Dierckx RA, et al. In vivo biodistribution of no-carrier-added 6-^{18}F-fluoro-3, 4-dihydroxy-L-phenylalanine (^{18}F-DOPA), produced by a new nucleophilic substitution approach, compared with carrier-added ^{18}F-DOPA, prepared by conventional electrophilic substitution. J Nucl Med. 2015;56(1):106–12.

The Radiopharmaceutical Chemistry of Fluorine-18: Electrophilic Fluorinations

Michael Wagner and Frank Wuest

The Fundamentals of Electrophilic Radiofluorination Chemistry

Electrophilic radiofluorinations are defined as a class of chemical reactions between an electrophilic ^{18}F source—$^{18}F^+$—and electron-rich reactants like alkenes, aromatic rings, or carbanions to form carbon-[^{18}F]fluorine bonds. Electrophilic radiofluorination reactions are an efficient and fast way to introduce an ^{18}F atom into organic molecules. The labeling procedures are usually fairly simple, and the incorporation of the radiohalogen is typically performed in one of the last reaction steps of the radiosynthesis. Historically, electrophilic radiofluorination reactions were among the first methods used for the preparation of some of the most important ^{18}F-labeled radiopharmaceuticals, including 2-[^{18}F]fluorodeoxyglucose (2-[^{18}F]FDG) and 6-[^{18}F]fluoro-3,4-dihydroxy-L-phenylalanine (6-[^{18}F]F-DOPA), for the imaging of glucose and dopamine metabolism, respectively [1, 2] (Fig. 1).

Despite recent advances in conventional electrophilic fluorination chemistry with ^{19}F, several technical challenges associated with fluorine-18 have limited the application of these approaches to electrophilic ^{18}F-*radio*fluorinations. As in conventional electrophilic fluorination reactions—which commonly utilize elemental fluorine gas (F_2) as the primary source of electrophilic fluorine—all electrophilic radiofluorination reactions are based on ^{18}F-labeled reagents that are ultimately derived from cyclotron-produced [^{18}F]F_2 fluorine gas. [^{18}F]F_2 can be produced in small biomedical cyclotrons via the $^{20}Ne(d,\alpha)^{18}F$ or $^{18}O(p,n)^{18}F$ nuclear reactions using ^{20}Ne or enriched [^{18}O]O_2 as target gases, respectively. In both cases, non-radioactive F_2 gas has to be added as a carrier to remove the radioactivity as carrier-added (c.a.) [^{18}F]F_2 gas from the target following bombardment [3].

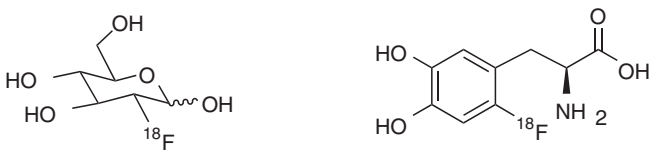

Fig. 1 Structures of 2-[^{18}F]FDG (left) and 6-[^{18}F]F-DOPA (right)

Today, [^{18}F]F_2 is typically obtained through the $^{18}O(p,n)^{18}F$ reaction using enriched [^{18}O]O_2 as the target. Following the initial irradiation and the subsequent addition of 0.2% of carrier F_2 gas, a second irradiation provides extractable c.a. [^{18}F]F_2 gas. This "two-shot" irradiation protocol—including the cryogenic trapping and recovery of the expensive enriched [^{18}O]O_2 target gas after the first irradiation—is needed to remove the [^{18}F]F_2, which is trapped on the walls of the aluminum-, nickel-, or gold-plated copper target after the initial irradiation [4]. A useful method to determine the total production yield of [^{18}F]F_2 and its molar activity is based on a demetallation reaction with phenyltrimethyltin (see the section on "Direct Electrophilic ^{18}F-radiofluorinations versus ^{18}F-fluorodemetallation Reactions," below) [5].

The addition of nonradioactive F_2 carrier gas results in the formation of c.a. [^{18}F]F_2 at rather low molar activities, typically in the range of ~0.05–0.5 GBq/μmol. This is significantly lower than the molar activity of cyclotron-produced no-carrier-added (n.c.a.) [^{18}F]fluoride (up to 5500 GBq/μmol) and several orders of magnitude lower than the theoretical molar activity of ^{18}F (6.3×10^4 GBq/μmol). To understand the implications of this, consider that an ^{18}F-labeled compound synthesized with n.c.a. [^{18}F]fluoride is diluted by ~1000 analogous ^{19}F-containing molecules. In contrast, an ^{18}F-labeled radiotracer synthesized with c.a. [^{18}F]F_2 is diluted by up to 10^6 ^{19}F-containing molecules(!)

This discrepancy can have drastic pharmacological consequences for c.a. ^{18}F-labeled radiotracers. First, c.a. ^{18}F-labeled radiotracers with low molar activity are more likely to exert pharmacological—including toxicological—effects, thus violating the basic concept of the tracer principle.

M. Wagner · F. Wuest (✉)
Department of Oncology, University of Alberta, Edmonton, AB, Canada
e-mail: wuest@ualberta.ca

J. S. Lewis et al. (eds.), *Radiopharmaceutical Chemistry*, https://doi.org/10.1007/978-3-319-98947-1_16

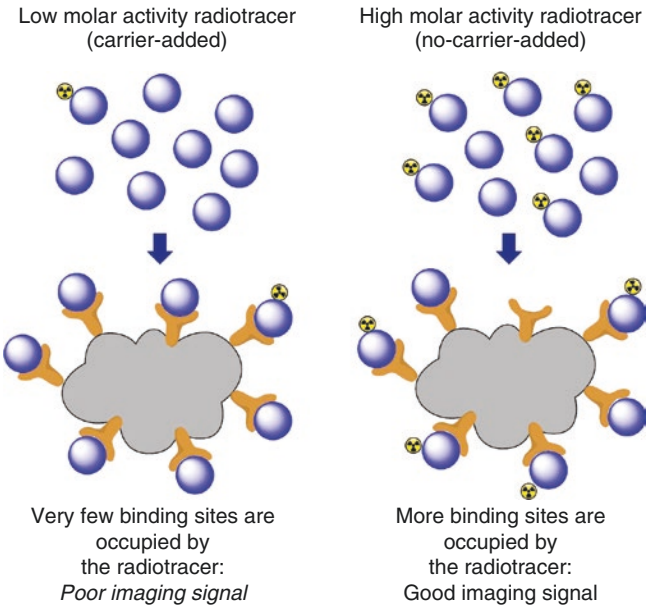

Fig. 2 Influence of molar activity on the quality of the imaging signal (Adapted from Kim [6], with permission)

Second, c.a. ^{18}F-labeled radiotracers cannot typically be used for the imaging of saturable binding sites *in vivo*. In this case, most of the binding sites would be occupied by the nonradioactive compound, and only a very few would be bound by the radiotracer, resulting in poor signal. The situation is illustrated in Fig. 2 [6].

As a consequence, electrophilic radiofluorination reactions are usually limited to the synthesis of radiotracers that (a) can compete with high concentrations of endogenous analogues like amino acids, hexoses, and nucleosides or (b) interact with binding sites with low saturation capacity, for example, transporter proteins like facilitative hexose transporters (*e.g.* GLUT1) or enzymes (*e.g.* hexokinase II).

Another inherent limitation of electrophilic radiofluorination chemistry with $[^{18}F]F_2$ is the maximum achievable theoretical radiochemical yield of 50%. This limit is due to the fact that every labeling with an ^{18}F atom is inevitably accompanied by a labeling with a nonradioactive ^{19}F atom. This also applies to electrophilic radiofluorination reagents that are prepared from $[^{18}F]F_2$. Additional challenges and limitations of electrophilic radiofluorination chemistry stem from the chemical nature of $[^{18}F]F_2$ gas, as it is a highly reactive and, as a result, poorly selective electrophilic radiofluorination agent. However, the reactivity and selectivity of $[^{18}F]F_2$ can be controlled somewhat by using low reaction temperatures and diluted $[^{18}F]F_2$/inert gas mixtures (typically Ne).

Alternatively, the chemical conversion of highly reactive $[^{18}F]F_2$ into less reactive (and therefore more selective) ^{18}F-labeled electrophilic fluorination reagents has become a method of choice for controlling reactivity and selectivity in electrophilic radiofluorination chemistry.

Based on this array of limitations and challenges, it is not surprising that electrophilic radiofluorination chemistry has usually only been applied to radiolabeling reactions which could otherwise not be performed with widely used nucleophilic n.c.a. [^{18}F]fluoride. This situation is somewhat surprising in light of recent advances in traditional organic fluorine chemistry that have provided a highly versatile toolbox of both nucleophilic and electrophilic fluorination methods [7, 8]. The translation of these innovative synthetic approaches to radiochemistry with fluorine-18 would facilitate the preparation of a wide variety of ^{18}F-labeled radiotracers. Consequently, intense research efforts have been made over the last 20 years to improve the utility of electrophilic radiofluorination chemistry, with special emphasis on (1) developing novel ^{18}F-labeled electrophilic fluorination agents with improved reactivity-selectivity profiles and (2) increasing the specific activity of ^{18}F-labeled compounds produced via electrophilic radiofluorination chemistry.

Secondary Labeling Precursors and Building Blocks for Electrophilic Radiofluorinations with ^{18}F

Direct electrophilic radiofluorination reactions of electron-rich compounds like arenes and alkenes with elemental $[^{18}F]F_2$ gas are characterized either by the substitution of a hydrogen with a ^{18}F or the addition of two fluorine atoms to a double bond.

Direct electrophilic radiofluorinations with electron-rich arenes follow the typical mechanism for electrophilic aromatic substitution reactions (S_EAr). The first step involves the nonspecific complexation of the $\{^{18}F^+\}$ electrophile with the π-electron system of the aromatic ring. No specific positional selectivity is usually associated with this donor-acceptor-type complex. In order to undergo a substitution, a σ-complex must be formed in which the carbon at the site of substitution is bonded to both the $\{^{18}F^+\}$ electrophile and the proton to be displaced. The formation of the σ-complex is usually the rate-determining step, followed by the rapid elimination of the proton to form the final ^{18}F-labeled product. However, the exact mechanism of the addition of $[^{18}F]F_2$ to the double bond remains unclear, since the formation of a proposed bridged fluoronium ion as the typical halonium intermediate during halogen (X_2; X = Cl, Br, I) additions to alkenes has not yet been confirmed.

From a chemistry prospective, direct electrophilic radiofluorinations are among the most straightforward radiolabeling methods in ^{18}F radiochemistry. However, the difficulties in handling $[^{18}F]F_2$ and the lack of selectivity due to the high reactivity of $[^{18}F]F_2$ are major disadvantages that have hampered the widespread application of this method for the synthesis of ^{18}F-labeled radiotracers. However, solutions for

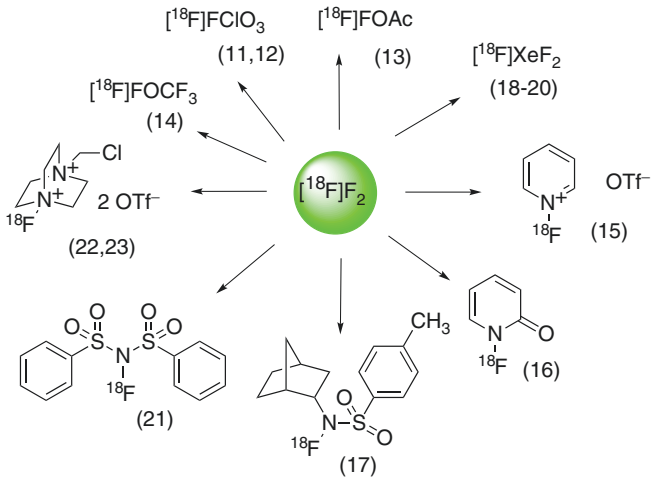

Fig. 3 Secondary precursors for electrophilic ^{18}F-labeling derived from $[^{18}F]F_2$

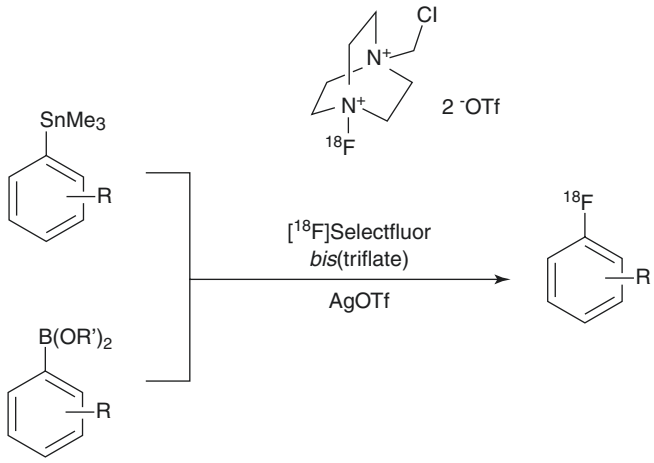

Fig. 4 Ag-mediated radiofluorinations with [^{18}F]Selectfluor® *bis*(triflate)

these problems of reactivity and selectivity can be found in the use of less reactive electrophilic ^{18}F-labeled agents or the application of radiofluorodemetallation reactions rather than direct radiofluorinations.

In an effort to create building blocks for electrophilic radiofluorination reactions, elemental $[^{18}F]F_2$ can be converted into less oxidizing secondary labeling precursors with reduced reactivity but enhanced chemo- and regioselectivity. More specifically, this can be achieved by binding fluorine to elements with slightly lower electronegativity like oxygen, nitrogen, or xenon to generate c.a. $\{^{18}F^+\}$ synthons as secondary labeling precursors. An overview of existing electrophilic ^{18}F secondary labeling precursors is provided in Fig. 3.

Except for $[^{18}F]XeF_2$—which is admittedly an exotic secondary ^{18}F-radiofluorination agent—all of the other secondary electrophilic radiolabeling precursors are *O*-^{18}F and *N*-^{18}F compounds containing an electropositive ^{18}F that is transferred as $\{^{18}F^+\}$ to electron-rich arenes or alkenes either directly or through ^{18}F-fluorodemetallation chemistry. Among all of the reported *O*-^{18}F compounds, [^{18}F]acetylhypofluoride ([^{18}F]FOAc) has found several applications [9], most notably the synthesis of 6-[^{18}F]F-DOPA via ^{18}F-fluorodemetallation reactions using organotin or organomercury compounds. Other ^{18}F-labeled compounds like [^{18}F]perchloryl fluoride [10, 11] and trifluoromethyl hypofluorite [12], and some *N*-[^{18}F]F derivatives based upon pyridinium salts [13], pyridones [14], and sulfonamides [15], have found only a handful of applications in the synthesis of ^{18}F-labeled radiotracers.

Several electrophilic fluorination reagents commonly employed in organic synthesis—for example, xenon difluoride [16–18], *N*-fluorobenzenesulfonimide (NFSI) [19], and Selectfluor® (chloromethyl-4-fluoro-1,4-diazoniabicyclo[2.2.2]octane bis(triflate)) [20, 21]—have been used more extensively in ^{18}F chemistry for the introduction of an electrophilic $\{^{18}F^+\}$ equivalent into electron-rich compounds. While $[^{18}F]XeF_2$ can also be conveniently synthesized from n.c.a. [^{18}F]fluoride using an isotopic exchange reaction [17, 18], [^{18}F]NFSI and [^{18}F]Selectfluor® bis(triflate) are prepared from the primary labeling precursor $[^{18}F]F_2$, preferably in a reaction chamber made of Teflon or quartz (also referred to as discharge chamber) at higher molar activities. The successful use of both [^{18}F]NFSI and [^{18}F]Selectfluor® bis(triflate) has been spearheaded by the Gouverneur laboratory, who have used these reagents in Ag-mediated electrophilic radiofluorination reactions with arylboronic esters and arylstannanes (Fig. 4) [19–21].

Direct Electrophilic ^{18}F-Radiofluorinations Versus ^{18}F-Fluorodemetallation Reactions

The utility of steering the reactivity-selectivity profile of $[^{18}F]F_2$ versus the use of less reactive secondary electrophilic labeling precursors like [^{18}F]FOAc is best demonstrated by the electrophilic radiosyntheses of 2-[^{18}F]FDG. Notably, the first successful radiosynthesis of 2-[^{18}F]FDG was based on an electrophilic radiofluorination reaction with $[^{18}F]F_2$, which provided 2-[^{18}F]FDG in a radiochemical yield of 8–10% [1]. However, the use of less reactive [^{18}F]FOAc instead of $[^{18}F]F_2$ gave higher radiochemical yields and better selectivity for the electrophilic synthesis of 2-[^{18}F]FDG. Figure 5 shows the addition of $[^{18}F]F_2$ and [^{18}F]FOAc to the double bond of triacetoxyglucal followed by acidic deprotection with HCl to form 2-[^{18}F]FDG and the corresponding mannose derivative 2-[^{18}F]FDM.

The use of the less reactive [^{18}F]FOAc leads to a radiochemical yield (RCY) of 30% and a favorable 2-[^{18}F]FDG:2-[^{18}F]FDM chemoselectivity of 7:1. These results compare favorably to the 10% RCY and 3:1 2-[^{18}F]FDG:2-[^{18}F]FDM chemoselectivity obtained in the synthetic scheme using $[^{18}F]F_2$.

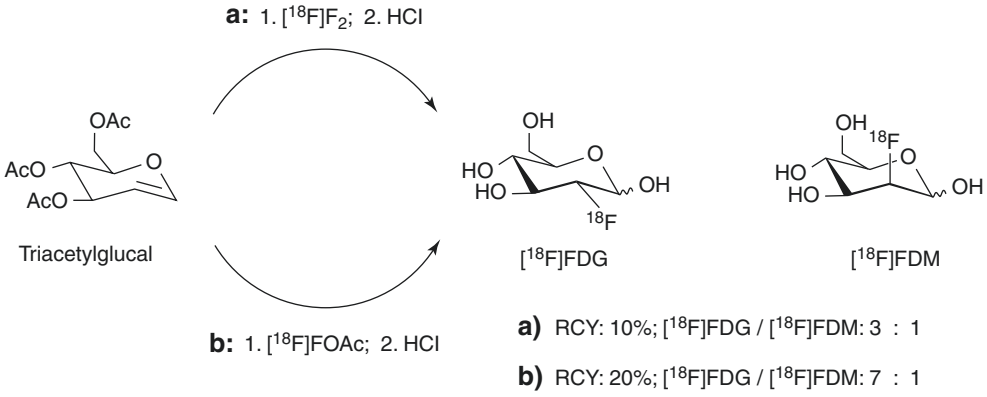

Fig. 5 Radiosynthesis of 2-[^{18}F]FDG and 2-[^{18}F]FDM via electrophilic radiofluorination with [^{18}F]F_2 and [^{18}F]FOAc

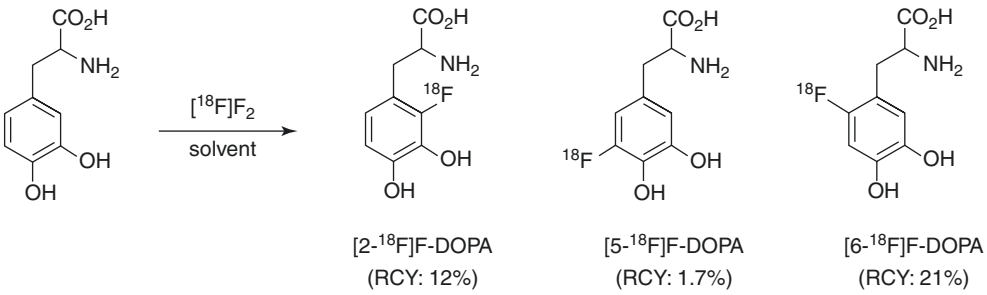

Fig. 6 Radiosynthesis of 6-[^{18}F]F-DOPA via direct electrophilic radiofluorination with [^{18}F]F_2

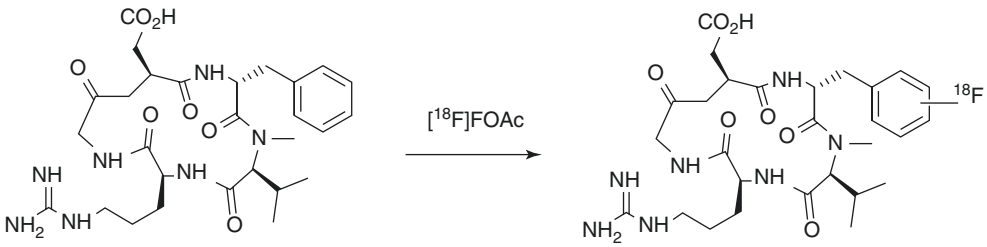

Fig. 7 Radiosynthesis of an on ^{18}F-labeled RDG peptide by direct electrophilic radiofluorination with [^{18}F]FOAc

The adjustment of the reactivity-selectivity profile of [^{18}F]F_2 in direct electrophilic radiofluorination reactions can also be achieved through the selection of different acidic solvents [22]. Electrophilic radiofluorination of L-DOPA with [^{18}F]F_2 in acids like trifluoroacetic acid (TFA), 10% TFA in glacial acetic acid, and formic acid mainly leads to the formation of undesired 2- and 5-substituted regioisomers, whereas reaction in stronger acids (HF or HF/BF_3) leads to the formation of the desired 6-substituted regioisomer (6-[^{18}F]F-DOPA). The direct electrophilic radiofluorination of 3,4-dihydroxyphenyl-L-alanine (L-DOPA) with [^{18}F]F_2 in HF at low temperatures (−65 °C) resulted in the formation of all three possible regioisomers—2-[^{18}F]F-DOPA, 5-[^{18}F]F-DOPA, and 6-[^{18}F]F-DOPA—in radiochemical yields of 12, 1.7, and 21%, respectively [22] (Fig. 6).

The choice of HF as the solvent is particularly important, because it is both a very polar solvent and an acid which promotes electrophilic fluorinations of activated aromatic compounds like phenols. Moreover, liquid HF keeps the two hydroxyl groups in L-DOPA well protonated and may therefore also protect the labeling precursor L-DOPA against oxidation by the highly reactive and oxidative F_2 gas.

A rather exotic application of direct electrophilic radiofluorination chemistry with [^{18}F]FOAc has recently been reported for the synthesis of an ^{18}F-labeled cyclic RGD peptide for the PET imaging of tumor-associated integrins. This radiosynthesis resulted in the formation of at least three different regioisomers—reinforcing the selectivity challenges associated with direct electrophilic ^{18}F-radiofluorinations—but no attempts were described to resolve the regioselectivity problem [23] (Fig. 7).

Significant improvements in radiofluorinations have been achieved through the application of ^{18}F-fluorodemetallation reactions. More specifically, aromatic fluorodemetallation reactions of group IVb metalloarenes (Si, Ge, and Sn) and organomercury arenes with [^{18}F]F_2 and [^{18}F]FOAc have proven valuable for the regiospecific incorporation of ^{18}F into aromatic compounds. An early comparative study of group IVb metalloarenes revealed aromatic trimethylstannane compounds as superior labeling precursors than the analogous Si and Ge compounds [24] (Fig. 8).

In addition, the effects of both different substitution patterns and the identity of the group IVb metal on the radiochemical yields of ^{18}F-fluorodemetallation reactions with [^{18}F]F_2 and [^{18}F]FOAc are summarized in Table 1 [24]. Interestingly, the reaction of both radiofluorination agents—[^{18}F]F_2 and [^{18}F]FOAc—was not affected by perhalogenated solvents (*e.g.* $CFCl_3$), though the reactions failed completely when solvents with active hydrogens were used (*e.g.* CH_3CN).

Clearly, both the regioselectivity and high yields associated with this methodology make the use of ^{18}F-fluorodemetallation reactions with [^{18}F]F_2 and [^{18}F]FOAc—especially with organostannanes—a very attractive method for the synthesis method for ^{18}F-labeled electron-rich aromatic compounds. Regioselective ^{18}F-fluorodemetallation chemistry was also tested successfully with organomercury compounds [25, 26]. In practice, the usefulness of regioselective ^{18}F-fluorodemetallation is best demonstrated by the preparation of 6-[^{18}F]F-DOPA, an important radiotracer for studying dopamine metabolism in the brain (Fig. 9).

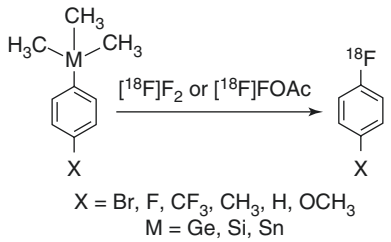

Fig. 8 Aromatic ^{18}F-fluorodemetallation of aryltrimethyl group IVb organometallics with [^{18}F]F_2 and [^{18}F]FOAc

Early preparations of 6-[^{18}F]F-DOPA involved the reaction of 6-substituted organomercury compounds with [^{18}F]FOAc to afford 6-[^{18}F]F-DOPA in 12% RCY after the removal of the protecting groups under acidic conditions [25, 26]. In order to avoid the use of highly toxic organomercury compounds, however, regioselective ^{18}F-fluorodestannylation reactions are now method of choice for the preparation of 6-[^{18}F]F-DOPA [27–29] as well as other catecholamines such as 6-[^{18}F]fluorometaraminol [30] and aromatic amino acids like 2-[^{18}F]fluoro-L-tyrosine [31]. In the ^{18}F-fluorodestannylation-based synthesis of 6-[^{18}F]F-DOPA, the radiochemical yields obtained with [^{18}F]F_2 (26–33%) are superior to those achieved when [^{18}F]FOAc is used as the electrophilic radiofluorination reagent (8%) [27–29]. It is important to note, however, that recent advancements in

Table 1 Effects of the substituent and metal on the yield of the ^{18}F-fluorodemetallation of *para*-substituted trimethylaryl group IVb organometallics using [^{18}F]F_2 and [^{18}F]FOAc (Data from Firnau *et al.* [24])

	% [^{18}F]fluorodemetallation yield					
	M = Sn		M = Ge		M = Si	
Ar-X	[^{18}F]F_2	[^{18}F]FOAc	[^{18}F]F_2	[^{18}F]FOAc	[^{18}F]F_2	[^{18}F]FOAc
X = OCH_3	70.4 ± 6.6	66.0 ± 4.3	35.4 ± 1.4	–	19.8 ± 3.0	–
X = CH_3	78.4 ± 6.4	–	40.6 ± 5.8	16.4 ± 1.8	22.4 ± 4.0	9.1 ± 1.1
X = F	73.8 ± 6.8	–	55.8 ± 3.6	–	30.4 ± 3.2	–
X = H	64.4 ± 6.6	68.2 ± 5.7	40.4 ± 4.0	8.5 ± 0.5	23.0 ± 4.0	3.5 ± 0.3
X = Br	34.2 ± 3.4	–	24.8 ± 0.8	–	10.2 ± 0.6	–
X = CF_3	35.0 ± 2.8	36.3 ± 1.6	10.4 ± 1.6	–	2.4 ± 0.5	–

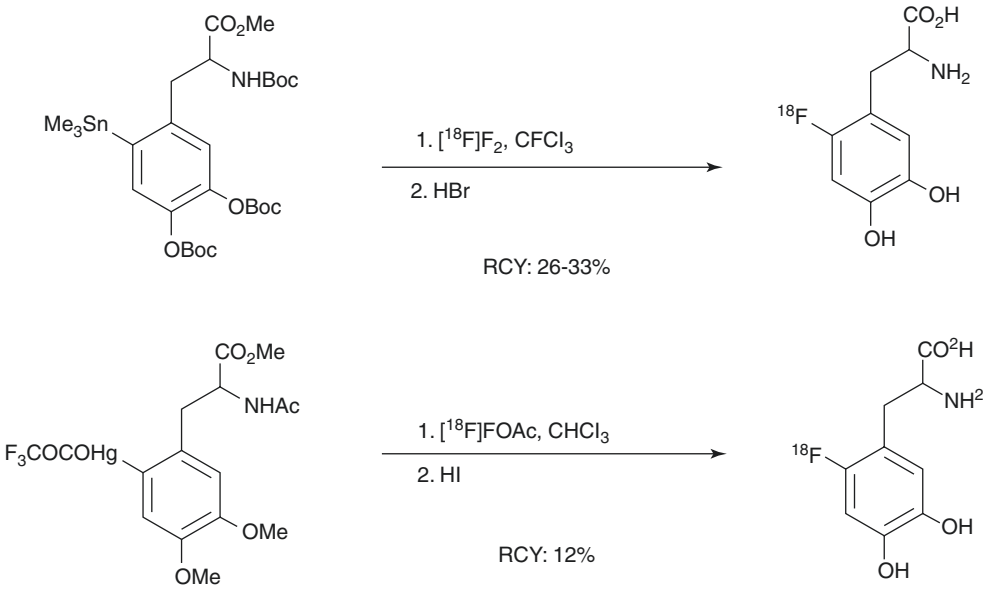

Fig. 9 Radiosynthesis of 6-[^{18}F]F-DOPA via ^{18}F-fluorodemetallation reactions

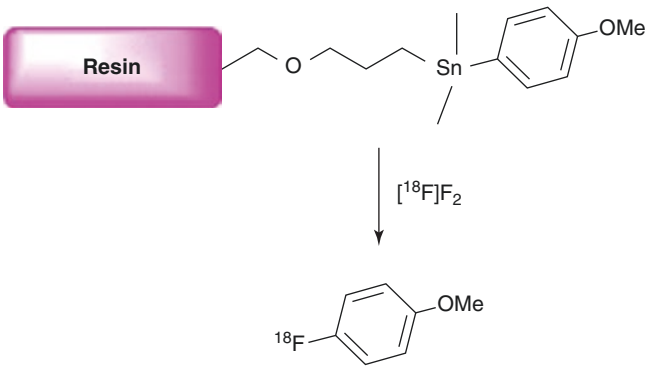

Fig. 10 Solid phase ^{18}F-fluorodemetallation reactions

radiochemistry with n.c.a. [^{18}F]fluoride have led to high-yielding, automated preparations of both n.c.a 6-[^{18}F]F-DOPA and 2-[^{18}F]fluoro-L-tyrosine becoming the preferred synthesis routes for the clinical production of these radiotracers [32].

The feasibility of ^{18}F-fluorodemetallation reactions was also tested on solid phase [33]. To this end, an allyl ether-functionalized polystyrene resin was prepared by coupling chloromethylated polystyrene with 2-propen-1-ol. Subsequently, the reaction of 2-propen-1-ol with trimethyltin chloride (Me_3SnCl) under photolytic conditions produced a resin-bound organotin derivative which could react with several aryl intermediates. One example of a solid phase ^{18}F-fluorodemetallation is provided by the radiosynthesis of 4-[^{18}F]fluoroanisole using [^{18}F]F_2 as the electrophilic radiofluorination agent (Fig. 10).

Table 2 summarizes selected radiopharmaceuticals prepared via direct electrophilic ^{18}F-radiofluorinations or ^{18}F-fluorodemetallation reactions discussed in this section of the chapter [1, 22, 25–27, 29–31, 34–43].

Preparation and Use of High Molar Activity Electrophilic ^{18}F-Labeled Synthons from n.c.a. [^{18}F]Fluoride

One of the principal limitations of using electrophilic ^{18}F-labeled synthons for the preparation of radiopharmaceuticals is the rather low molar activity of the resulting ^{18}F-labeled compounds, a trait which can exclude them from the imaging of saturable binding sites like receptors. Over the last two decades, various attempts have been made to address this major drawback. All of the solutions are predicated on the concept of reversing the polarity (*umpolung*) of nucleophilic and high molarity n.c.a [^{18}F]fluoride to create an electrophilic {^{18}F$^+$} synthon with high molar activity.

This chemical *umpolung* concept was tested with three different strategies:

1. The homolysis of n.c.a. [^{18}F]CH_3F in the presence of minute amounts of F_2 gas [45, 46]
2. The formation of electrophilic radiofluorination agents through the reaction of n.c.a. [^{18}F]fluoride with strong oxidizing agents [47]
3. The oxidative addition of n.c.a. [^{18}F]fluoride into transition metal complexes followed by reductive elimination chemistry [48–51]

Homolysis of [^{18}F]CH_3F in the Presence of Minute Amounts of F_2 Gas

A first strategy to reduce the amount of carrier F_2 gas needed for the production of [^{18}F]F_2 at high molar activity is based on the homolytic cleavage of n.c.a. [^{18}F]CH_3F in an electrical discharge chamber or via the use of UV laser pulses at constant power [45, 46] (Fig. 11).

In the first step, high molar activity n.c.a. [^{18}F]fluoride is converted into [^{18}F]CH_3F in the presence of methyl iodide. Constituents of a mixture of [^{18}F]CH_3F and minute amounts of carrier F_2 gas (0.1–1.7 μmol) in an inert neon matrix are then atomized using an electric discharge or a UV laser pulse to form [^{18}F]F_2. Under optimal conditions, molar activities of [^{18}F]F_2 gas were up to 55 GBq/μmol using this method. This high molar activity [^{18}F]F_2 has been used for the radiosynthesis of various radiotracers—including 6-[^{18}F]F-DOPA, [^{18}F]CFT, [^{18}F]fluoro-oxoquazepam, and [^{18}F]fluoroatipamezole—exploiting the regioselective ^{18}F-fluorodestannylation chemistry discussed in section (Fig. 12).

This strategy has been used to produce radiotracers with molar activities exceeding 15 GBq/μmol in sufficient amounts for human PET studies (400–800 MBq). However, since highly specialized equipment is needed, the widespread use of this interesting method for the production of [^{18}F]F_2 has remained somewhat limited [45, 46].

Formation of Electrophilic Radiofluorination Agents Through the Reaction of n.c.a. [^{18}F] Fluoride with Strong Oxidizing Agents

Another innovative strategy to obtain electrophilic ^{18}F with higher molar activity lies in the reaction of nucleophilic n.c.a. [^{18}F]fluoride with strong oxidizing agents such as XeF_2 or perchloric acid. The electrophilic labeling agent [^{18}F]XeF_2 can readily be obtained via an isotopic exchange reaction with n.c.a. [^{18}F]fluoride starting from XeF_2 [16–18]. However,

Table 2 Selection of radiopharmaceuticals prepared via electrophilic ^{18}F-radiofluorination methods

Radiopharmaceutical	Synthesis method	Application	References
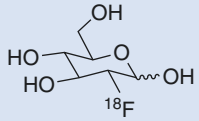 2-[^{18}F]Fluoro-deoxyglucose (2-[^{18}F]FDG) 2-[^{18}F]Fluorodeoxyglucose (2-[^{18}F]FDG)	Addition of [^{18}F]F_2, [^{18}F]XeF_2, or [^{18}F]FOAc to the double bond in triacetoxyglucal precursor	PET imaging of glucose metabolism	[1] ([^{18}F]F_2) [34] ([^{18}F]XeF_2) [35] ([^{18}F]FOAc)
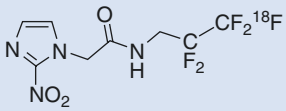 [^{18}F]-2-(2-Nitro-1[H]-imidazole-1-yl)-*N*-(2,2,3,3,3-pentafluoropropyl)-acetamide ([18F]EF5) [^{18}F]-2-(2-Nitro-1[H]-imidazole-1-yl)-*N*-(2,2,3,3,3-pentafluoropropyl)-acetamide ([^{18}F]EF5)	Addition of [^{18}F]F_2 to the double bond in trifluoroallyl precursor	PET imaging of hypoxia	[36]
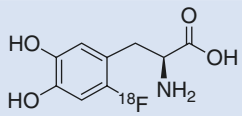 6-[^{18}F]Fluoro-3,4-dihydroxy-L-phenylalanine (6-[^{18}F]F-DOPA) 6-[^{18}F]Fluoro-3,4-dihydroxy-L-phenylalanine (6-[^{18}F]F-DOPA)	Direct electrophilic radiofluorination with [^{18}F]F_2 or [^{18}F]FOAc	PET imaging of dopamine metabolism	[22] ([^{18}F]F_2) [37] ([^{18}F]FOAc)
	^{18}F-fluorodemetallation using HgR_2 or $SnMe_3$ precursors with [^{18}F]F_2 or [^{18}F]FOAc		[25, 26] ([^{18}F]FOAc, HgR_2) [27, 29] ([^{18}F]F_2, $SnMe_3$) [29] ([^{18}F]FOAc, $SnMe_3$)
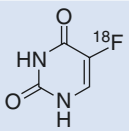 5-[^{18}F]Fluorouracil 5-[^{18}F]Fluorouracil	Direct electrophilic radiofluorination with [^{18}F]F_2 or [^{18}F]FOAc	Tumor imaging	[38, 39] ([^{18}F]F_2) [40] ([^{18}F]FOAc)
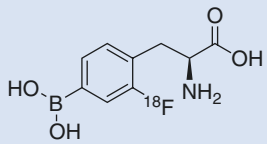 4-Borono-2-[^{18}F]fluoro-L-phenylalanine 4-Borono-2-[^{18}F]fluoro-L-phenylalanine	Direct electrophilic radiofluorination with [^{18}F]FOAc	PET imaging of amino acid metabolism	[41, 42]
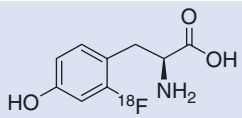 2-[^{18}F]Fluoro-L-tyrosine 2-[^{18}F]Fluoro-L-tyrosine	^{18}F-fluorodestannylation with [^{18}F]F_2	PET imaging of amino acid metabolism	[31]

(continued)

Table 2 (continued)

Radiopharmaceutical	Synthesis method	Application	References
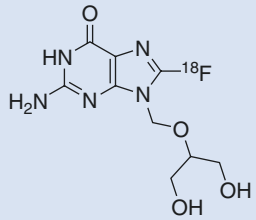 8-[^{18}F]Fluoroganciclovir 8-[^{18}F]Fluoroganciclovir	Direct electrophilic radiofluorination with [^{18}F]F_2	PET imaging of HSV1-tk expression	[43]
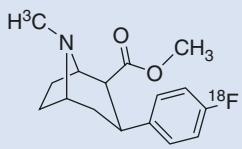 [^{18}F]CFT [^{18}F]CFT	^{18}F-fluorodestannylation with [^{18}F]FOAc	PET imaging of dopamine metabolism	[44]
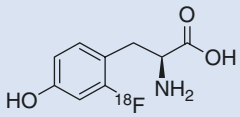 [^{18}F]Fluorometaraminol [^{18}F]Fluorometaraminol	^{18}F-fluorodestannylation with [^{18}F]F_2	PET imaging of cardiac sympathetic nerve integrity	[30]

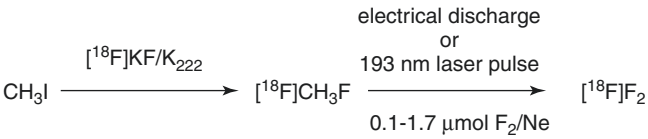

Fig. 11 Synthesis of high molar activity [^{18}F]F_2 starting from n.c.a. [^{18}F]fluoride

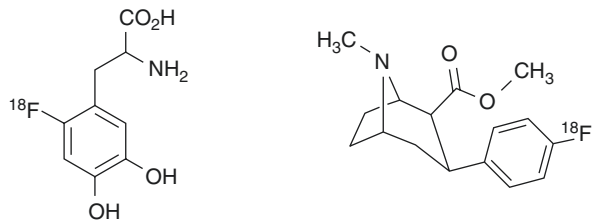
6-[^{18}F]F-DOPA

[^{18}F]CFT

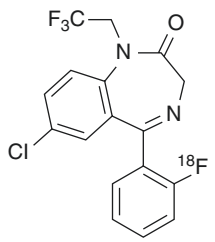
[^{18}F]Fluoro-oxoquazepam

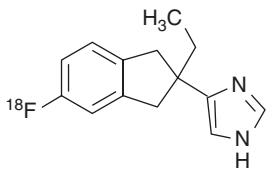
[^{18}F]Fluoroatipamezole

Fig. 12 Structures of radiotracers 6-[^{18}F]F-DOPA, [^{18}F]CFT, [^{18}F]fluoro-oxoquazepam, and [^{18}F]fluoroatipamezole prepared via electrophilic radiofluorinations starting from high molar activity [^{18}F]F_2 [45]

the synthesis of [^{18}F]perchloryl fluoride from $HClO_4/H_2SO_4$ and n.c.a. [^{18}F]fluoride was characterized by poor reproducibility, which has—not surprisingly—limited its use [10, 11]. More recently, Szabó *et al.* described a highly elegant approach using a hypervalent iodine tosylate and n.c.a. [^{18}F]fluoride to form [^{18}F]fluoro-benziodoxole, a reagent which was then used for electrophilic fluorocyclization reactions with *o*-styrilamides (Fig. 13) [47]. The molar activities of the resulting [^{18}F]fluoro-benzoxazepines were up to 400 GBq/µmol, values much higher than the molar activities typically obtained in electrophilic radiofluorination experiments.

Oxidative Addition of n.c.a. [^{18}F]Fluoride into Transition Metal Complexes Followed by Reductive Elimination Chemistry

The use of transition metal-based chemistry and the ability to harness the *umpolung* concept through reductive elimination are highly elegant methods to circumvent the otherwise delicate and challenging preparation of high molar activity [^{18}F]F_2. Recently, the Ritter group developed an elegant *umpolung* method based on the incorporation of nucleophilic n.c.a. [^{18}F]fluoride into organopalladium(IV) or organonickel(III) intermediates and their subsequent fast reductive elimination to form a structurally diverse array of ^{18}F-labeled aryl fluorides [48, 49] (Fig. 14).

The major drawback of this approach, however, is the need to prepare and handle air- and moisture-sensitive transition metal complexes as radiofluorination precursors [50, 51].

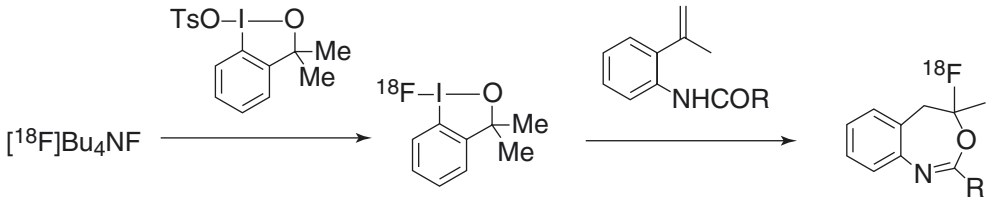

Fig. 13 *Umpolung* of nucleophilic n.c.a. [^{18}F]fluoride by its conversion into the electrophilic ^{18}F-fluorination reagent [^{18}F]fluoro-benziodoxole, followed by fluorocyclization to give [^{18}F]fluoro-benzoxazepines in high molar activity

Fig. 14 *Umpolung* of nucleophilic n.c.a. [^{18}F] fluoride by its oxidative introduction into Pd- and Ni-complexes, followed by reductive elimination to form various ^{18}F-labeled aryl fluorides (Ar-^{18}F)

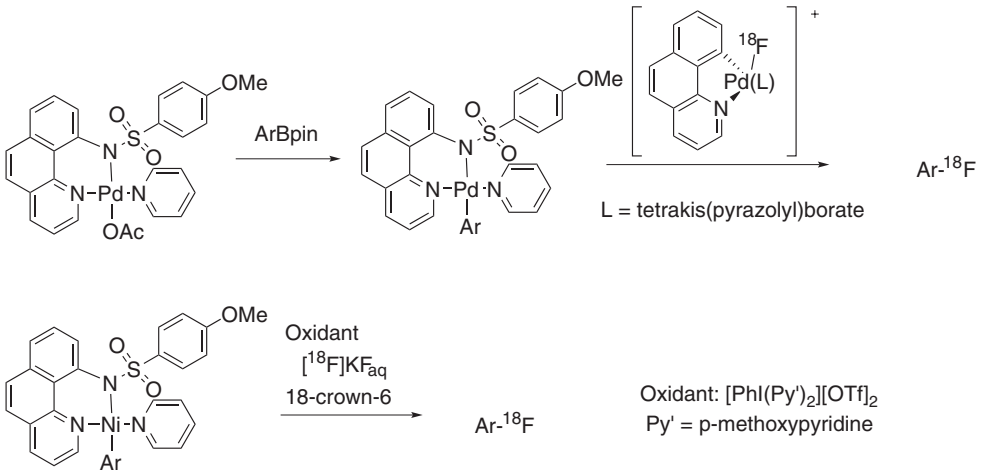

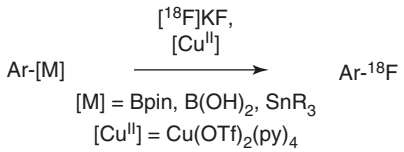

Fig. 15 Oxidative introduction of [^{18}F]fluoride by reductive elimination to form various ^{18}F-labeled aryl fluorides (Ar-^{18}F)

The sensitive nature of these transition metal complexes has unquestionably hampered their use for radiolabeling experiments with ^{18}F.

Another recently developed—and now widely used—method for the *umpolung* of nucleophilic n.c.a. [^{18}F]fluoride is the copper-mediated oxidative introduction of n.c.a. [^{18}F] fluoride into aryl boron and aryl tin compounds. The development of this innovative chemistry for electrophilic radiofluorinations was pioneered by the groups of Gouverneur [50] and Scott [51] (Fig. 15).

It has been proposed that an organocopper(III) species is involved in the *umpolung* process and that the corresponding aryl [^{18}F]fluorides are obtained through reductive elimination [52].

This approach to the oxidative functionalization of aryl pinacol boronates (Bpin) and arylboronic acids has been continuously improved. Recent work by the Neumaier group reported the beneficial effect of primary and secondary alcohols on Cu-mediated ^{18}F-labeling reactions [53]. The group developed a protocol for the rapid radiolabeling of a broad range of boronic and stannyl substrates in high radiochemical yields of 80–99%. Notably, radiofluorinated indoles, phenols, and anilines could be synthesized directly from the corresponding unprotected labeling precursors [53]. Finally, it is important to note that the Cu-mediated electrophilic [^{18}F]fluorination of organoborons has recently become clinically viable, as very good molar activities and yields can be achieved and a wide variety of the nontoxic aryl boron precursors are readily accessible [53, 54].

Conclusion

Electrophilic ^{18}F-radiofluorination chemistry pioneered the synthesis of ^{18}F-labeled radiopharmaceuticals. However, more powerful radiosynthetic strategies developed in the 1980s based on nucleophilic radiofluorinations with n.c.a. [^{18}F]fluoride have almost completely replaced electrophilic radiofluorinations for the preparation of ^{18}F-labeled radiopharmaceuticals. Yet the last decade has played witness to an impressive renaissance in electrophilic ^{18}F-radiofluorination chemistry. The application of transition metal-based chemistry and the ability to harness the *umpolung* concept for the preparation of electrophilic {^{18}F^{+}} synthons with high molar activity starting from n.c.a. [^{18}F]fluoride have stimulated a remarkable rediscovery of electrophilic ^{18}F radiochemistry. The arsenal of compounds which now can be labeled with ^{18}F at high molar activity has vastly expanded and now

includes many electron-rich aromatic molecules that previously could only be labeled using classical electrophilic ^{18}F-radiofluorination methods.

As electron-rich aromatic compounds are common in many classes of drugs, these novel radiosynthetic approaches will undoubtedly aid in the future preparation of innovative ^{18}F-labeled radiopharmaceuticals for clinic testing. Along these lines, the recent emergence of Cu-mediated electrophilic radiofluorinations is a particularly promising development. And indeed, the first compounds prepared via Cu-mediated electrophilic ^{18}F-radiofluorinations have already entered the clinic.

The Bottom Line

- Electrophilic ^{18}F-radiofluorinations have pioneered ^{18}F radiochemistry, as demonstrated by the first successful synthesis of 2-[^{18}F]FDG and 6-[^{18}F]F-DOPA.
- Electrophilic ^{18}F-radiofluorination chemistry is an efficient and fast way to introduce an ^{18}F atom into organic molecules.
- All electrophilic ^{18}F-radiofluorinations created using cyclotron-produced [^{18}F]F_2 gas have two important inherent limitations: (1) a 50% maximum achievable radiochemical yield and (2) low molar activity.
- The reactivity and selectivity profile of electrophilic radiofluorination reactions can be tuned somewhat through the preparation of *O*-^{18}F and *N*-^{18}F compounds as secondary radiolabeling precursors.
- Direct ^{18}F-radiofluorinations and ^{18}F-fluorodemetallations are the most popular types of electrophilic radiofluorination reactions based on [^{18}F]F_2.
- Recent developments have successfully applied the *umpolung* concept to the preparation of electrophilic radiofluorination agents with high molar activity.
- The first compounds prepared via Cu-mediated electrophilic ^{18}F-radiofluorination reactions have entered the clinic.

References

1. Ido T, Wan CN, Casella V, Fowler JS, Wolf AP. Labeled 2-deoxy-D-glucose analogs. 18F-labeled 2-deoxy-2-fluoro-D-glucose, 2-deoxy-2-fluoro-D-mannose and 14C-2-deoxy-2-fluoro-D-glucose. J Labelled Comp Radiopharm. 1978;14(2):175–83.
2. Garnett ES, Firnau G, Nahmias C. Dopamine visualized in the basal ganglia of living man. Nature. 1983;305(5930):137–8.
3. Qaim SM. Cyclotron production of medical radionuclides. In: Vértes A, Nagy S, Klencsár Z, Lovas RG, Rösch F, editors. Handbook of nuclear chemistry, vol. 4. 2nd ed. Dordrecht: Springer Science+Business Media BV; 2011. p. 1903–34.
4. Hess E, Blessing G, Coenen HH, Qaim SM. Improved target system for production of high purity [18F]fluorine via the 18O(p,n)18F reaction. Appl Radiat Isot. 2000;52(6):1431–40.
5. Blessing G, Coenen HH, Franken K, Qaim SM. Production of [18F]F2, H18F and 18F$^-$ aq using the 20Ne(d, α)18F process. Appl Radiat Isot. 1986;37(11):1135–9.
6. Kim DW. Bioorthogonal click chemistry for fluorine-18 labeling protocols under physiologically friendly reaction condition. J Fluor Chem. 2015;174:142–7.
7. Liang T, Neumann CN, Ritter T. Introduction of fluorine and fluorine-containing functional groups. Angew Chem Int Ed Engl. 2013;52(32):8214–64.
8. Hollingworth C, Gouverneur V. Transition metal catalysis and nucleophilic fluorination. Chem Commun (Camb). 2012;48(24):2929–42.
9. Lerman O, Rozen S. Acetyl hypofluorite, a new moderating carrier of elemental fluorine and its use in fluorination of 1,3-dicarbonyl derivatives. J Org Chem. 1983;48(5):724–7.
10. Ehrenkaufer RE, MacGregor RR. Synthesis of [18F]perchloryl fluoride and its reaction with functionalized aryl lithiums. Int J Appl Radiat Isot. 1983;34(3):613–5.
11. Hiller A, Fischer C, Jordanova A, Patt JT, Steinbach J. Investigations to the synthesis of n.c.a. [18F]FClO3 as electrophilic fluorination agent. Appl Radiat Isot. 2008;66:152–7.
12. Neirincx RD, Lambrecht RM, Wolf AP. Cyclotron isotopes and radiopharmaceuticals – XXV. An anhydrous 18F-fluorinating intermediate: Trifluormethyl hypofluorite. Int J Appl Radiat Isot. 1978;29:323–7.
13. Oberdorfer F, Hofmann E, Maier-Borst W. Preparation of 18F-labeled N-fluoropyridinium triflate. J Label Compd Radiopharm. 1988;25(9):999–1005.
14. Oberdorfer F, Hofmann E, Maier-Borst W. Preparation of a new 18F-labelled precursor: 1-[18F]fluoro-2-pyridone. Appl Radiat Isot. 1988;39(7):685–8.
15. Satyamurthy N, Bida GT, Phelps ME, Barrio JR. N-[18F]Fluoro-N-alkylsulfonamides: Novel reagents for mild and regioselective radiofluorination. Appl Radiat Isot. 1990;41(8):733–8.
16. Schrobilgen G, Firnau G, Chirakal R, Garnett ES. Synthesis of [18F] XeF2, a novel agent for the preparation of 18F-radiopharmaceuticals. J Chem Soc Chem Commun. 1981;4:198–9.
17. Constantinou M, Aigbirhio FI, Smith RG, Ramsden CA, Pike VW. Xenon difluoride exchanges fluoride: a simple preparation of [18F]xenon difluoride for PET and mechanistic studies. J Am Chem Soc. 2001;123:1780–1.
18. Lu S, Pike VW. Synthesis of [18F]xenon difluoride as a radiolabeling reagent from [18F]fluoride ion in a micro-reactor and at a production scale. J Fluor Chem. 2010;131:1032–8.
19. Teare H, Robins EG, Årstad E, Luthra SK, Gouverneur V. Synthesis and reactivity of [18F]-N-Fluorobenzenesulfonimide. Chem Commun. 2007;22:2330–2.
20. Stenhagen ISR, Kirjavainen AK, Forsback SJ, Jørgensen CG, Robins EG, Luthra SK, et al. [18F]Fluorination of an arylboronic ester using [18F]selectfluor bis(triflate): application to 6-[18F] fluoro-L-DOPA. Chem Commun. 2013;49:1386–8.
21. Teare H, Robins EG, Kirjavainen A, Forsback S, Sandford G, Solin O, et al. Radiosynthesis and evaluation of [18F]selectfluor bis(triflate). Angew Chem Int Ed. 2010;49:6821–4.
22. Firnau G, Chirakal R, Garnett ES. Aromatic radiofluorination with [18F]fluorine gas: 6-[18F]fluoro-L-dopa. J Nucl Med. 1984;25(11):1228–33.
23. Ogawa M, Hatano K, Oishi S, Kawasumi Y, Fujii N, Kawaguchi M, Doi R, Imamura M, Yamamoto M, Ajito K, Mukai T, Saji H, Ito K. Direct electrophilic radiofluorination of a cyclic RGD peptide for in vivo alpha(v)beta3 integrin related tumor imaging. Nucl Med Biol. 2003;30(1):1–9.

24. Coenen HH, Moerlein SM. Regiospecific aromatic fluorodemetallation of group IVb metalloarenes using elemental fluorine or acetyl hypofluoride. J Fluor Chem. 1987;36:63–75.
25. Adam MJ, Jivan S. Synthesis and purification of L-6-[18F]fluorodopa. Int J Rad Appl Instrum A. 1988;39(12):1203–6.
26. Luxen A, Perlmutter M, Bida GT, Van Moffaert G, Cook JS, Satyamurthy N, Phelps ME, Barrio JR. Remote, semiautomated production of 6-[18F]fluoro-L-dopa for human studies with PET. Int J Rad Appl Instrum A. 1990;41(3):275–81.
27. Dolle F, Demphel S, Hinnen F, Fournier D, Vaufrey F, Crouzel C. 6-[18F]Fluoro-L-DOPA by radio-fluorodestannylation: A short and simple synthesis of a new labelling precursor. J Labelled Comp Radiopharm. 1998;41:105.
28. de Vries EF, Luurtsema G, Brüssermann M, Elsinga PH, Vaalburg W. Fully automated synthesis module for the high yield one-pot preparation of 6-[18F]fluoro-L-DOPA. Appl Radiat Isot. 1999;51:389–94.
29. Namavari M, Bishop A, Satyamurthy N, Bida G, Barrio JR. Regioselective radiofluorodestannylation with [18F]F2 and [18F]CH3COOF: A high yield synthesis of 6-[18F]fluoro-L-dopa. Int J Rad Appl Instrum A. 1992;43:989–96.
30. Eskola O, Grönroos T, Bergman J, Haaparanta M, Marjamäki P, Lehikoinen P, et al. A novel electrophilic synthesis and evaluation of medium specific radioactivity (1R,2S)-4-[18F]fluorometaraminol, a tracer for the assessment of cardiac sympathetic nerve integrity with PET. Nucl Med Biol. 2004;31(1):103–10.
31. Hess E, Sichler S, Kluge A, Coenen HH. Synthesis of 2-[18F] fluoro-L-tyrosine via regiospecific fluoro-de-stannylation. Appl Radiat Isot. 2002;57(2):185–91.
32. Lemaire C, Libert L, Franci X, Genon JL, Kuci S, Giacomelli F, Luxen A. Automated production at the curie level of no-carrier-added 6-[(18)F]fluoro-L-dopa and 2-[(18)F]fluoro-L-tyrosine on a FASTlab synthesizer. J Labelled Comp Radiopharm. 2015;58(7):281–90.
33. Brown GD, Hernan AG, Wadsworth H, Kilburn JD, Gibson A, Brady F, Luthra SK. Solid phase [18F]fluorodemetallation reactions. J Labelled Comp Radiopharm. 2003;46:S152.
34. Shiue C-Y, To K-C, Wolf AP. A rapid synthesis of 2-deoxy-2-fluoro-D-glucose from xenon difluoride suitable for labeling with 18F. J Labelled Comp Radiopharm. 1983;20(2):157–62.
35. Shiue CY, Salvadori PA, Wolf AP, Fowler JS, MacGregor RR. A new improved synthesis of 2-deoxy-2-[18F]fluoro-d-glucose from 18F-labeled acetyl hypofluorite. J Nucl Med. 1982;23(10):899–903.
36. Dolbier WR Jr, Li AR, Koch CJ, Shiue CY, Kachur AV. [18F]-EF5, a marker for PET detection of hypoxia: synthesis of precursor and a new fluorination procedure. Appl Radiat Isot. 2001;54(1):73–80.
37. Adam MJ, Ruth TJ, Grierson JR, Abeysekara B, Pate BD. Routine synthesis of L-[18F]6-fluorodopa with fluorine-18 acetyl hypochlorite. J Nucl Med. 1986;27:1462–6.
38. Fowler JS, Finn RD, Lambrecht RM, Wolf AP. The synthesis of 18F-5-fluorouracil. VII J Nucl Med. 1973;14(1):63–4.
39. Vine EN, Young D, Vine WH, Wolf W. An improved synthesis of 18F-5-fluorouracil. Int J Appl Radiat Isot. 1979;30(7):401–5.
40. Diksic M, Farrokhzad S, Yamamoto YL, Feindel W. A simple synthesis of 18F-labelled 5-fluorouracil using acetylhypofluorite. Int J Nucl Med Biol. 1984;11(2):141–2.
41. Ishiwata K, Ido T, Mejia AA, Ichihashi M, Mishima Y. Synthesis and radiation dosimetry of 4-borono-2-[18F]fluoro-D,L-phenylalanine: a target compound for PET and boron neutron capture therapy. Appl Radiat Isot. 1991;42(4):325–8.
42. Ishiwata K, Ido T, Mieko K, Kubota K, Ichihashi M, Mishima Y. 4-Borono-2-[18F]fluoro-D,L-phenylalanine as a target compound for boron neutron capture therapy: tumor imaging potential with positron emission tomography. Nucl Med Biol. 1991;18(7):745–51.
43. Namavari M, Barrio JR, Toyokuni T, Gambhir SS, Cherry SR, Herschman HR, Phelps ME, Satyamurthy N. Synthesis of 8-[(18)F]fluoroguanine derivatives: in vivo probes for imaging gene expression with positron emission tomography. Nucl Med Biol. 2000;27(2):157–62.
44. Haaparanta M, Bergman J, Laakso A, Hietala J, Solin O. [18F]CFT ([18F]WIN 35,428), a radioligand to study the dopamine transporter with PET: biodistribution in rats. Synapse. 1996;23(4):321–7.
45. Bergman J, Solin O. Fluorine-18-labeled fluorine gas for synthesis of tracer molecules. Nucl Med Biol. 1997;24(7):677–83.
46. Krzyczmonik A, Keller T, Kirjavainen AK, Forsback S, Solin O. Vacuum ultraviolet photon-mediated production of [(18) F]F(2). J Labelled Comp Radiopharm. 2017;60(4):186–93.
47. Cortés González MA, Nordeman P, Bermejo Gómez A, Meyer DN, Antoni G, Schou M, Szabó KJ. [(18)F]fluoro-benziodoxole: a no-carrier-added electrophilic fluorinating reagent. Rapid, simple radiosynthesis, purification and application for fluorine-18 labelling. Chem Commun (Camb). 2018;54(34):4286–9.
48. Kamlet AS, Neumann CN, Lee E, Carlin SM, Moseley CK, Stephenson N, et al. Application of palladium-mediated 18F-fluorination to PET radiotracer development: overcoming hurdles to translation. PLoS ONE. 2013;8(3):e59187.
49. Campbell MG, Ritter T. Late-stage fluorination: from fundamentals to application. Org Process Res Dev. 2014;18:474–80.
50. Tredwell M, Preshlock SM, Taylor NJ, Gruber S, Huiban M, Passchier J, Mercier J, Génicot C, Gouverneur V. A general copper-mediated nucleophilic 18F fluorination of arenes. Angew Chem Int Ed Engl. 2014;53(30):7751–5.
51. Mossine AV, Brooks AF, Makaravage KJ, Miller JM, Ichiishi N, Sandford MS, Scott PJ. Synthesis of [18F]arenes via the copper-mediated [18F]fluorination of boronic acids. Org Lett. 2015;17(23):5780–3.
52. Ye Y, Schimler SD, Hanley PS, Sandford MS. Cu(OTf)2-mediated fluorination of aryltrifluoroborates with potassium fluoride. J Am Chem Soc. 2013;135:16292–5.
53. Zischler J, Kolks N, Modemann D, Neumaier B, Zlatopolskiy BD. Alcohol-enhanced Cu-mediated radiofluorination. Chem Eur J. 2017;23:3251–6.
54. Mossine AV, Brooks AF, Bernard-Gauthier V, Bailey JJ, Ichiiski N, Schirrmacher R, et al. Automated synthesis of PET radiotracers by copper-mediated 18F-fluorination of organoborons: Importance of the order of addition and competing protodeborylation. J Label Compd Radiopharm. 2018;61:228–36.

The Radiopharmaceutical Chemistry of Fluorine-18: Next-Generation Fluorinations

Anu J. Airaksinen

Abbreviations

$AMBF_3$	Alkylammoniomethyltrifluoroborate
DFO	Desferrioxamine
DMA	*N,N*-Dimethylacetamide
DMF	Dimethylformamide
DMSO	Dimethyl sulfoxide
DTPA	Diethylenetriaminepentaacetic acid
DOTA	1,4,7,10-Tetraazacyclododecane-1,4,7,10-tetraacetic acid
EDTA	Ethylenediaminetetraacetic acid
EtOH	Ethanol
HPLC	High-pressure liquid chromatography
Kryptofix 2.2.2	4,7,13,16,21,24-Hexaoxa-1,10-diazabicyclo[8.8.8]hexacosane
MPAEM	Methyl phenyl acetamido ethyl maleimide
NFSI	*N*-Fluorobenzenesulfonimide
NODA	1,4,7-Triazacyclononane-1,4-diiacetic acid
NOTA	1,4,7-Triazacyclononane-1,4,7-triacetic acid
PBS	Phosphate-buffered saline
PET	Positron emission tomography
PPTS	Pyridinium *p*-toluenesulfonate
PSMA	Prostate-specific antigen
QMA	Quaternary ammonium ion-exchange resin
RCY	Radiochemical yield
S_NAr	Aromatic nucleophilic substitution
SPE	Solid-phase extraction
USP	*United States Pharmacopeia*

Fundamentals

One of the great advantages of fluorine-18 in radiopharmaceutical chemistry is its ability to form covalent bonds with carbon. However, as discussed in the chapter on "The Radiopharmaceutical Chemistry of Fluorine-18: Nucleophilic Fluorinations", basic conditions and elevated temperatures are typically needed to promote the formation of C-F bonds in nucleophilic substitution reactions. Many biomolecules—including antibodies, antibody fragments, and proteins—are sensitive to harsh reaction conditions such as these and therefore cannot be radiolabeled with [^{18}F]fluoride via direct nucleophilic substitution. Instead, milder labeling approaches are needed, such as the bioconjugation of ^{18}F-labeled prosthetic groups. Fluorine readily forms bonds with several group 13–15 elements: boron, carbon, nitrogen, aluminum, silicon, and phosphorous (Table 1) [1, 2]. Of these, N-F bonds are too weak to be candidates for stable radiofluorinations: in fact, N-^{18}F compounds are important reagents for electrophilic ^{18}F-fluorination chemistry (see the chapter on "The Radiopharmaceutical Chemistry of Fluorine-18: Electrophilic Fluorinations"). Moving on, there are some examples of the radiofluorination of P(IV) compounds. However, the resulting P-^{18}F bond has exhibited low hydrolytic stability, hampering its use in radiopharmaceutical chemistry [3]. The same is true for compounds with Si-^{18}F bonds, though there are cases in which steric hindrance has been used to mask—and thus stabilize—Si-^{18}F moieties (see the chapter on "The Radiopharmaceutical Chemistry of Fluorine-18: Nucleophilic

Table 1 Comparison of the bond dissociation energies (kJ/mol) of the bond between fluorine and carbon as well as some heteroatoms

Bond	Bond dissociation energy (kJ/mol)
B-F	732
C-F	514
N-F	290
Al-F	675
Si-F	576
P-F	405

A. J. Airaksinen (✉)
Department of Chemistry – Radiochemistry, University of Helsinki, Helsinki, Finland

J. S. Lewis et al. (eds.), *Radiopharmaceutical Chemistry*, https://doi.org/10.1007/978-3-319-98947-1_17

Fluorinations"). In the first part of this chapter, we will discuss radiolabeling methods based on the reactions of [^{18}F]fluoride with boron and aluminum. The bonds between these elements and fluorine are stronger than the C-F bond, and, consequently, less harsh conditions are needed to promote their formation. For this reason, these reactions are especially useful for the radiofluorination of sensitive substrates. Furthermore, these radiofluorination reactions can also be performed in protic media because boron and aluminum can react with solvated [^{18}F]fluoride. This advantageous trait has paved the way for the development of kit-based fluorination methods based on B-F and Al-F chemistry.

The field of medicinal chemistry has increasingly turned to fluorination as an approach to adjusting the pharmacokinetic and chemical properties of drug candidates [4]. Selective fluorinations can be deployed to control the conformation, decrease the basicity, and increase the metabolic stability and binding affinity of drug candidates. Due to recent advances in the development of reagents for selective electrophilic fluorinations—such as Selectfluor, NFSI, and other *N*-fluoroamines—the fluorination of molecules at electron-rich positions has become easily accessible, and fluorinated (hetero)arenes are increasingly employed in the design of lead structures. Despite the impressive progress in the creation of reagents for electrophilic radiofluorinations (see the chapter on "The Radiopharmaceutical Chemistry of Fluorine-18: Electrophilic Fluorinations"), there remains an unfulfilled demand for more robust and translational tools for the radiofluorination of electron-rich substrates with high molar activity. Recent efforts have been focused upon finding new strategies for the late-stage fluorination of electron-rich substrates with [^{18}F]fluoride. In the second part of this chapter, methods for the transition metal-mediated ^{18}F-fluorination of electron-rich arenes will be introduced.

Radiofluorination of Heteroatoms

Radiolabeling with [Al[^{18}F]F]$^{2+}$

Fluoride forms a strong complex with the metallic Al^{3+} cation [5]. The bond energy of this $[AlF]^{2+}$ complex is 675 kJ/mol, higher than that of any other Al-halogen bond. Critically, the Al-F bond is also stable *in vivo*, but—as is the case for [^{18}F]fluoride—the free [Al[^{18}F][F]$^{2+}$ complex accumulates in the bone. Several studies have demonstrated that the formation of a 1:1 aluminum-fluoride complex is favored at pH 4 and therefore[Al[^{18}F]F]$^{2+}$ complexes are typically synthesized between pH 4.0 and 5.5 [6]. The pH of the reaction is critically important for the formation of the complex: if the pH is too high, insoluble aluminum hydroxide complexes may form and precipitate; if the pH is too low, the reaction will produce H[^{18}F]F. Bifunctional chelators are needed to incorporate the[Al[^{18}F]F]$^{2+}$ complex into targeted biomolecules such as proteins and peptides. Along these lines, aluminum forms octahedral complexes, so chelators that offer five donor atoms as well as one open binding site for the fluoride anion are considered ideal. The purification of the cyclotron-produced [^{18}F]fluoride from trace metals is important for achieving optimal RCYs of the [Al[^{18}F]F]$^{2+}$ complex. These trace metals may originate from the target window (usually made from Havar or titanium) during the irradiation of ^{18}O-enriched water and are typically removed using ion-exchange methods. The commercially available sterile USP grade [^{18}F]fluoride in saline has also been found to be adequate for [Al[^{18}F]F]$^{2+}$-based radiolabeling reactions [7].

One of the first chelators studied for complexing [Al[^{18}F]F]$^{2+}$ was diethylenetriaminepentaacetic acid (DTPA) [5]. DTPA is an acyclic chelator which is widely used for complexing several different radiometals, including indium-111, luthetium-177, and gallium-68 (see the chapters on "The Radiopharmaceutical Chemistry of the Radionuclides of Gallium and Indium" and "The Radiopharmaceutical Chemistry of the Radionuclides of Lutetium and Yttrium"). The [Al[^{18}F]F]$^{2+}$ synthon is readily complexed with DTPA with high (>90%) radiochemical yields, but the aqueous stability of the Al[^{18}F]F-DTPA complex is insufficient for applications in radiopharmaceutical chemistry. As a result, several other acyclic and cyclic chelators have been explored, including desferrioxamine (DFO), 1,4,7,10-tetraazacyclododecane-1,4,7,10-tetraacetic acid (DOTA), and ethylenediaminetetraacetic acid (EDTA). This search leads to the discovery that NOTA (1,4,7-triazacyclononane-1,4,7-triacetic acid), a macrocyclic hexadentate chelator, forms a very stable complex with [^{18}F]F]$^{2+}$ [5]. Macrocyclic chelators are less flexible than their acyclic cousins and thus typically form complexes with higher stability. However, higher temperatures are usually required to rearrange the cyclic ligand structure for the complexation of metal ions. Consequently, lower radiochemical yields are often achieved using macrocyclic chelators. Generally, the [Al[^{18}F]F]$^{2+}$ complex is formed by mixing a solution of $AlCl_3$ with a small volume of aqueous [^{18}F]fluoride (50–100 μl) in a sodium-acetate buffer (pH 4.0). This mixture is then added to a solution of the NOTA-bearing biomolecule and subsequently heated to 100 °C for 15 min, leading to non-decay-corrected RCYs between 5% and 20%. When conjugated to peptides, the [NOTA-Al[^{18}F]F complex has shown a high level of stability both in serum and *in vivo*.

Five donor atoms are needed for binding the [^{18}F]F]$^{2+}$ complex to the macrocyclic chelator. Any additional substituents around the macrocycle can have a significant influence on the formation and stability of the chelator-[^{18}F][AlF]$^{2+}$ complex. As a result, several peptides bearing NOTA-based chelators have been labeled with [Al[^{18}F]F]$^{2+}$ in order to find the optimal chelation system (Fig. 1) [8]. In this work, it was found that the addition of a pendent bis(carboxymethyl)

amino donor group near the macrocycle significantly improves radiolabeling yields, in some cases producing RCYs as high as 87% (IMP467 in Fig. 1). On the other hand, consistently higher labeling efficiencies were found when using a pentadentate cousin of NOTA: NODA (1,4,7-triazacyclononane-1,4-diiacetic acid; Fig. 2a) [9]. This result suggests that the third carboxylate group in NOTA may actually *interfere* with the binding of the fluoride anion to aluminum. Radiochemical yields of up to 95% have been achieved with NODA, though the concentration of the radiolabeling precursor can have a significant influence on RCYs, making small reaction volumes critical [9]. For NODA, significant decreases in RCY were observed when the concentration of chelator was decreased below 30 μM (Fig. 2b). The same trend was observed for NOTA-based chelators: for IMP467, RCYs dropped to 55% when amount of the precursor was decreased from 500 nmol to 20 nmol. It is important to bear in mind that controlling the amount of precursor is often essential for achieving sufficient effective molar activities for imaging. In this particular study, a smaller amount of the chelator-bearing precursor (20 nmol) was necessary to optimize the molar activity of the radiolabeled peptide [^{18}F]IMP467 (115 GBq/μmol). The addition of cosolvents has also been reported to increase RCYs, and several different solvents—including DMSO, DMF, CH_3CN, and EtOH—have been found to be effective in this regard [10].

The coordination of the [Al[^{18}F]F]$^{2+}$ core by macrocyclic chelators such as NOTA or NODA requires heating to 100–120 °C. This is too harsh for many biomolecules. Therefore, several Al^{18}F-bearing prosthetic groups have been developed in order to enable the use of this chemistry with more sensitive biomolecules. For example, NODA-MPAEM is a maleimide-containing prosthetic group that can be attached to sulfhydryl groups in a biomolecule *after* the coordination of [Al[^{18}F]F]$^{2+}$ (Fig. 3) [11]. For example, [Al[^{18}F]F]$^{2+}$NODA-MPAEM has been efficiently coupled to a reduced Fab fragment in 10–15 min at room temperature with 69–80%

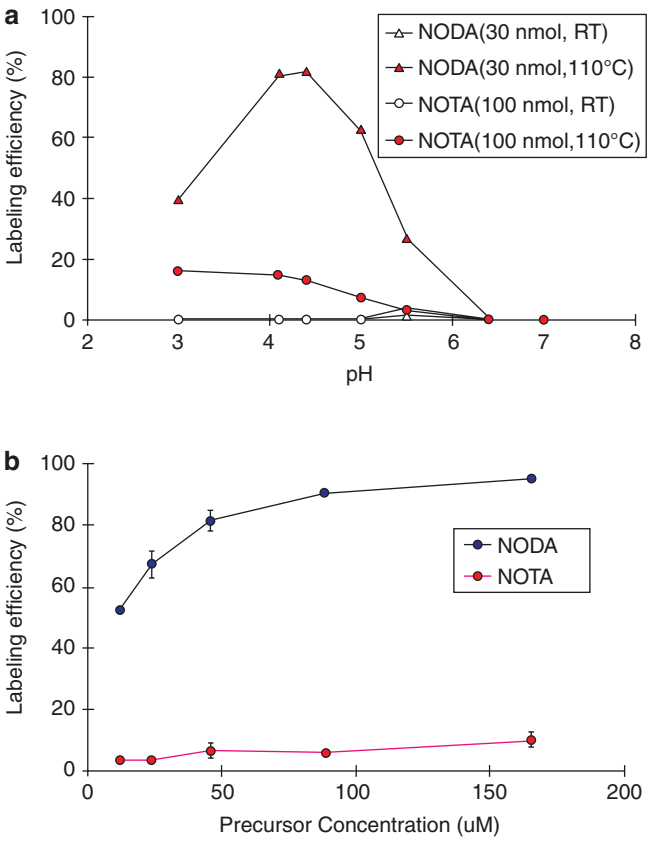

Fig. 2 A comparison of the radiolabeling efficiencies of NODA and NOTA with [Al[^{18}F]F]$^{2+}$. (**a**) The influence of pH and temperature at two different concentrations of precursor (30 nm and 100 nmol); (**b**) the influence of the concentration of precursor on the efficiency of radiolabeling (From Shetty *et al.* [9], with permission)

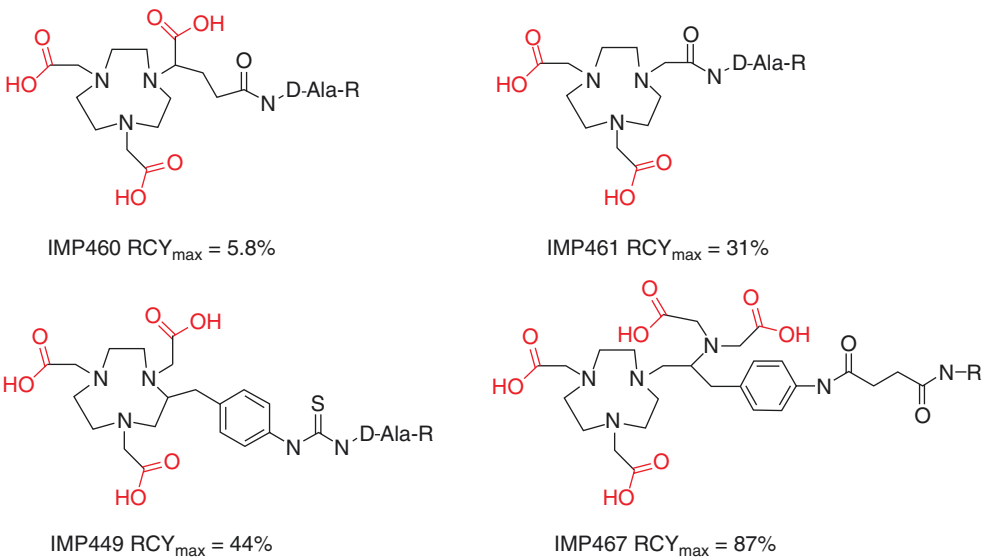

Fig. 1 The influence of the structure of NOTA-based chelators on radiolabeling yields (isolated RCYs) with [Al[^{18}F]F]$^{2+}$ (500 nmol of peptide: R = *D*-Lys(HSG)-*D*-Tyr-*D*-Lys(HSG)-NH_2)

RCY. The labeled product was found to retain its integrity and immunoreactivity.

In addition, several new acyclic polydentate ligands have been developed to facilitate the stable complexation of $[Al[^{18}F]F]^{2+}$ at low temperatures [12]. Of these, H_3L3 was found to exhibit the highest stability *in vitro* and will serve as a lead structure for the development of new ligand architectures for $[Al[^{18}F]F]^{2+}$ (Fig. 4). The optimal pH range for complexing $[Al[^{18}F]F]^{2+}$ with H_3L3 is between 4 and 5, but high RCYs can be achieved even at pH 5.5. The highest RCY 95% was achieved through heating to 40 °C in a solution containing 20% acetonitrile or ethanol as a co-solvent. While $[Al[^{18}F]F]^{2+}$-L3 is not stable at pH <4, it was found to be stable in phosphate-buffered saline (PBS) at pH 7.4 and in rat serum *in vitro*. Even more importantly, after derivatization (R = -COOH in Fig. 4) and subsequent conjugation to a PSMA targeting vector, Glu-NH-CO-NH-Lys, it was found to be stable against defluorination *in vivo*, as the administration of the $[Al[^{18}F]F]^{2+}$L3-labeled tracer to mice produced no significant uptake of $[^{18}F]$fluoride in the bone.

The principal advantage of the Al[^{18}F]F method is its exceptional tolerance to aqueous conditions, eliminating the need for the laborious azeotropic drying steps typically needed in radiofluorination methods that employ $[^{18}F]$fluoride (see the chapters on "The Radiopharmaceutical Chemistry of Fluorine-18: Nucleophilic Fluorinations" and "The Radiopharmaceutical Chemistry of Fluorine-18: Electrophilic Fluorinations"). This trait has enabled the development of ^{18}F-labeling kits which are optimized with respect to buffer, pH, and the optimal molar ratio of peptide to Al^{3+}. These kits also typically contain a bulking agent as well as a radioprotectant (*e.g.* ascorbic acid) [7]. Bulking agents—such as mannitol or α,α-trehalose—are needed to aid in the production of an acceptable lyophilized "cake" when using very small amounts of starting materials. Generally speaking, the radiolabeling of a lyophilizated kit is accomplished via the addition of 100–200 μL of USP grade $[^{18}F]F^-$ in saline and then heating the mixture to 90–110 °C for 15 min. The radiolabeled product can then be isolated via cartridge purification, typically providing the final product in high radiochemical yield (45–97%) and high molar activity (up to 223 GBq/μmol) [7].

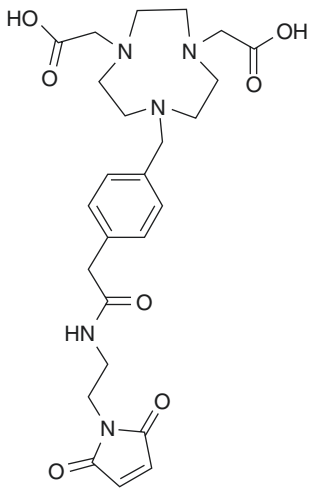

Fig. 3 A maleimide-based prosthetic group—NODA-MPAEM—for the radiolabeling of heat-sensitive biomolecules with $[Al[^{18}F]F]^{2+}$

[^{18}F]Fluoroborates

The boron-fluorine bond is one of the strongest known, with a bond dissociation energy of 732 kJ/mol. Arylboronic acids can be fluorinated with KHF_2 in acidic pH to yield aryltrifluoroborate salts with high yields [13]. This has been exploited for the development of reactions for the aqueous ^{18}F-fluorination of organoboronic acids and their esters. The reaction exhibits a third-order dependence on the concentration of fluoride (see Eq. 1) [14]. As a result, exceptionally low reaction volumes are essential for ensuring high yields, especially under no-carrier-added conditions. For this reason, ^{18}F-fluorination reactions of boronic precursors are often performed under carefully controlled carrier-added conditions in which nanomolar amounts of KHF_2 are added to the reaction mixture:

$$K_{eq}\left(\text{formation pH 4}\right) = \frac{\left[ArBF_3^-\right]}{\left[ArB(OH)_2\right]\left[F^-\right]^3} \qquad (1)$$

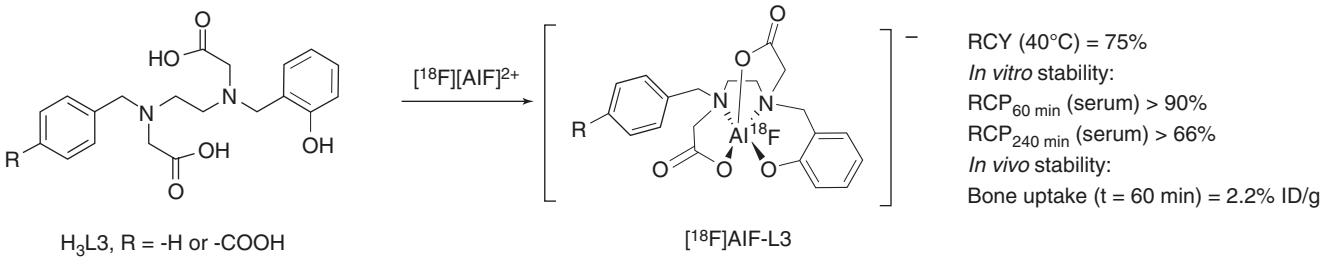

H_3L3, R = -H or -COOH

$[^{18}F]AlF$-L3

Fig. 4 H_3L3, an acyclic polydentate chelator (R = -H) for complexing $[Al[^{18}F]F]^{2+}$ and its bifunctional variant (R = -COOH) for conjugation to biomolecules and other targeting vectors

Each trifluoroborate anion contains three fluorides: two fluorine-19 atoms and one fluorine-18. This three-to-one stoichiometry means that under optimal conditions, two atoms of stable fluorine and one atom of fluorine-18 are consumed to create each RBF_3^- group [15]. This leads to a molar activity for the RBF_3^- moiety which is three times lower than that of the target water. However, due to the high critical concentration of fluoride needed to facilitate this reaction, these conditions are practically never achieved.

Despite the high bond dissociation energy of the B-F bond, [^{18}F]organotrifluoroborate salts exhibit poor hydrolytic stability at pH >7 unless they are stabilized by appropriate substituents within the structure. Inductive effects caused by the substituents influence the polarization of the B-F bond and can adjust its susceptibility to hydrolytic attack. One of the first reported boron-^{18}F compounds was a biotinylated *p*-aminophenyl [^{18}F] trifluoroborate. This aromatic [^{18}F]organotrifluoroborate was later found to be hydrolytically unstable [16]. A kinetic analysis of the hydrolysis demonstrated that at neutral pH and under sufficiently dilute conditions, [^{18}F]aryltrifluoroborate salts suffer thermodynamically favorable and kinetically irreversible solvolysis. During this process, the [^{18}F] aryltrifluoroborate salts revert back to their starting materials: an arylboronic acid and a free [^{18}F]fluoride anion (Fig. 5) [14]. The release of free [^{18}F]fluoride is especially detrimental for PET imaging, since free [^{18}F]fluoride accumulates in the bone and interferes with the quantification of images. Thankfully, it was found that electron-withdrawing groups—especially in an *ortho* position relative to the boron atom—decrease the rate of this solvolysis reaction. Not surprisingly, electron-donating groups have the opposite effect. Indeed, depending on the substituents on the aromatic ring, the rates of this solvolysis reaction can range from very fast ($k_{obs} \approx 0.3\ min^{-1}$) to very slow ($k_{obs} \approx 10^{-4}\ min^{-1}$) (Table 2) [14].

The thermodynamics of the solvolytic reversion to free fluoride at pH > 7 can be defined by a third-order equilibrium constant:

$$K_{eq}\left(\text{solvolysis pH 7.5}\right) = \frac{\left[ArB(OH)_2\right]\left[F^-\right]^3}{\left[ArBF_3^-\right]} \qquad (2)$$

Generally speaking, the ^{18}F-fluorination of aromatic organoborate precursors is achieved by incubating the aqueous [^{18}F]fluoride with an arylboronic ester and KHF_2

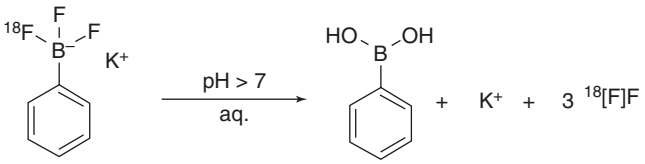

Fig. 5 The irreversible solvolysis of an [^{18}F]aryltrifluoroborate salt to an arylboronic acid and free [^{18}F]fluoride

Table 2 Rate constants of solvolysis (k_{obs}) as well as defluorination half-lives of several substituted aryltrifluoroborates. The rate constants and half-lives were determined via ^{19}F-NMR

Compound	Defluorination rate constant k_{obs} (min^{-1})	Defluorination half-life (min)
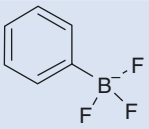	0.345 ± 0.007	2.01 ± 0.04
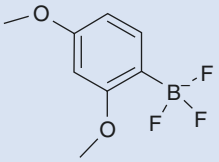	0.19 ± 0.2	3.7 ± 0.3
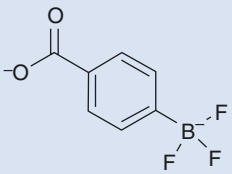	0.082 ± 0.006	8.4 ± 0.6
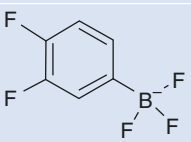	0.077 ± 0.009	9 ± 1
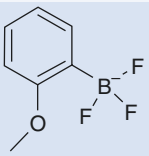	0.046 ± 0.003	15 ± 1
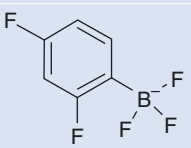	0.016 ± 0.001	43 ± 4
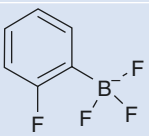	0.014 ± 0.001	50 ± 3
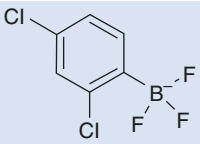	0.0037 ± 0.0001	185 ± 7
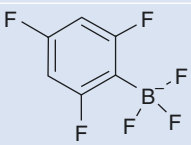	0.0024 ± 0.0002	280 ± 20

(as a carrier) between pH 2 and 3 (Fig. 6a) [14]. In the case of ^{18}F–^{19}F isotopic exchange reactions, no additional carrier KHF_2 is needed, though sufficient concentrations of precursor are essential to achieve efficient radiofluorinations (Fig. 6b). In a typical procedure, the cyclotron-

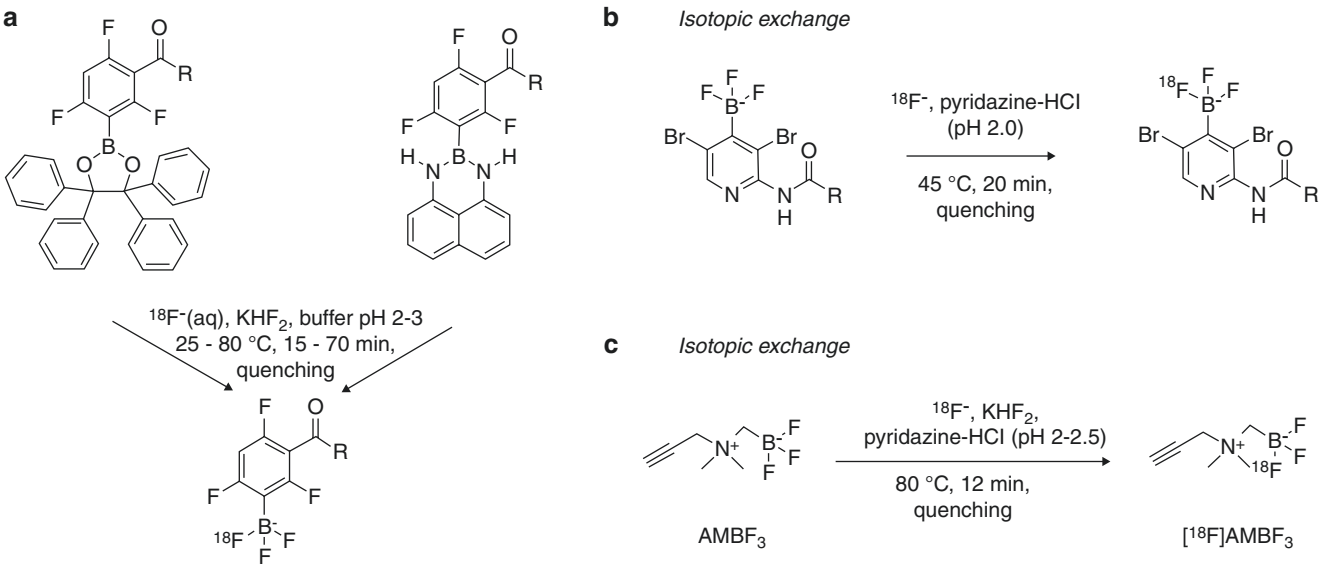

Fig. 6 Synthesis of [^{18}F]aryltrifluoroborate salts (**a**) from boronic ester precursors via a substitution reaction under carrier-added conditions or (**b**) via an isotopic exchange reaction. (**c**) Synthesis of [^{18}F]alkylammoniomethyltrifluoroborate salt ([^{18}F]AMBF$_3$) via an isotopic exchange reaction

produced [^{18}F]fluoride is trapped on an anion-exchange resin and subsequently eluted using either $NaClO_4$ or saline. The use of carbonate buffer for this elution is not recommended in this case, although it is commonly employed for the elution of [^{18}F]F$^-$ from anion-exchange resins during the production of anhydrous [^{18}F]fluoride for nucleophilic substitution reactions. The synthesis of [^{18}F]fluoroborates is enhanced at low pH because the alkoxy groups of the boric ester are protonated under acidic conditions and can thus facilitate the substitution reaction with fluoride. The neutralization of the carbonate buffer would unnecessarily increase the volume of the reaction mixture. High concentrations of fluoride are critical for the efficient formation of B-^{18}F bonds. To reach appropriate concentrations, the [^{18}F]fluoride-containing eluate is typically concentrated via azeotropic distillation with acetonitrile and then redissolved in a small amount of water (~10 μL). Reaction times and temperatures can range from 15 to 70 min and 25–80 °C, respectively, and typical radiochemical yields can vary from 10% to 50%. The reaction is stopped by elevating the pH of the solution and by diluting the reaction mixture, after which the product is purified in order to remove unreacted [^{18}F]fluoride. If any mono- or di-fluorinated species are produced, they are quickly hydrolyzed when the pH is elevated, providing the chemically pure organotrifluoroborate salt. The molar activity of the final product can be controlled by varying the volume of the reaction (15–100 μL, depending on the starting activity), which in turn determines the amount of carrier (see Eq. 1) and precursor needed for efficient radiofluorination. Molar activities around 50–100 GBq/umol are generally achieved, but values as high as 555 GBq/umol have been reported [15, 17].

Recently, a nonaromatic and zwitterionic [^{18}F]alkylammoniomethyltrifluoroborate ([^{18}F]AMBF$_3$) synthon was reported with superior stability against *in vitro* and *in vivo* defluorination [18]. The terminal alkyne group facilitates the bioconjugation of AMBF$_3$ to azide-functionalized biomolecules using copper-catalyzed click chemistry (see the chapters on "Bioconjugation Methods for Radiopharmaceutical Chemistry" and "Click Chemistry in Radiopharmaceutical Chemistry"). The discovery of [^{18}F]AMBF$_3$ was based on the unexpected observation that the rate constants for the solvolysis of non-aromatic organotrifluoroborates correlate well with the pK_a values of their corresponding carboxylic acids (Table 3) [19]. Betaine—the corresponding carboxylic acid of AMBF$_3$—has a pK_a of 1.84, and AMBF$_3$ has a low-defluorination rate constant (k_{obs}) of 3.13×10^{-5} min^{-1}. As a point of reference, the pK_a of valeric acid is 4.88, and the rate constant (k_{obs}) for the solvolysis of its cousin butyltrifluoroborate is much higher: 0.3 min^{-1}.

The AMBF$_3$-conjugated biomolecules can be radiolabeled under aqueous conditions using an ^{18}F–^{19}F isotopic exchange reaction (Fig. 6c). ^{18}F-Fluorination is typically achieved in a single step at 80 °C, providing molar activity values similar to those achieved with [^{18}F]trifluoroborates. The reaction provides [^{18}F]AMBF$_3$-labeled biomolecules in RCYs between 20% and 35%, values that are slightly lower than those typically achieved using aromatic organotrifluoroborates. In the end, however, the simple labeling procedure for the [^{18}F]AMBF$_3$ group and its better *in vivo* stability make it a superior choice compared to aromatic [^{18}F]trifluoroborates.

Table 3 Rate constants (k_{obs}) for the solvolysis of selected organofluoroborates at pH 7.5 as well as pK_a values for their corresponding carboxylic acids

Compound	Defluorination rate constant k_{obs} (min^{-1})	Corresponding carboxylic acid	pK_a of the carboxylic acid
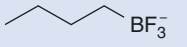	0.3	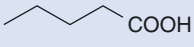	4.88
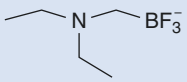	1.76×10^{-4}	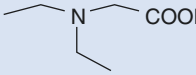	2.04
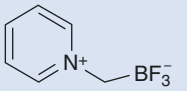	6.44×10^{-5}	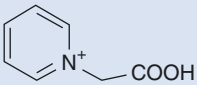	2.0
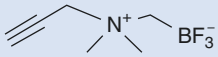	3.13×10^{-5}	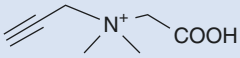	1.84
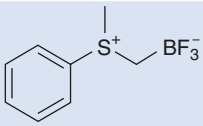	1.51×10^{-6}	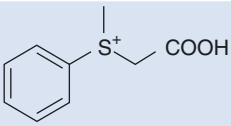	1.1

Tricks of the Trade

The ^{18}F-Fluorination of Biomolecules Using Alkylammoniomethyltrifluoroborate ($AMBF_3$)

The first step in this procedure is the conjugation of alkylammoniomethyltrifluoroborate ($AMBF_3$) to an azide-modified biomolecule via the Cu(I)-catalyzed 1,3-dipolar cycloaddition reaction (see the chapters on "Bioconjugation Methods for Radiopharmaceutical Chemistry" and "Click Chemistry in Radiopharmaceutical Chemistry"). The radiolabeling procedure is started by trapping the cyclotron-produced [^{18}F]fluoride (37 GBq) on a small amount of quaternary ammonium (QMA) ion-exchange resin, followed by drying the resin by blowing it with the ^{18}F-labeled transfer gas. This "μQMA cartridge" is assembled by loading the resin (9 mg) into a 16-gauge needle, preconditioning the "cartridge" with saturated NaCl solution (3 ml), and then washing the system with an equal volume of deionized water [18, 20]. The trapped [^{18}F]fluoride is eluted from the resin using 60 μL of 0.9% NaCl in deionized water, followed by drying the resin with the transfer gas. The resulting aqueous [^{18}F]fluoride solution is directly added to a preheated reaction mixture (80 °C) containing 100 nmol of the $AMBF_3$-conjugated precursor, 15 μL of pyridazine-HCl buffer (1.0 M, pH 2.0–2.5), 15 μL of DMF, and 1 μL of 7.5 mM KHF_2 solution. It is important to note that suitable pH values (2.0–2.5) and low reaction volumes (< 100 μl) are critical for the efficiency of the ^{18}F–^{19}F-exchange reaction. This mixture is heated at 80 °C for 12 min, after which the reaction is quenched by adding 2 ml of 5% NH_4OH (v/v). The ^{18}F-fluorinated product can then be purified with an appropriate solid-phase extraction (SPE) or HPLC procedure, yielding the product in 20–35% RCY and a molar activity of 40–111 GBq/μmol.

Transition Metal-Mediated ^{18}F-Fluorinations

Palladium- and Nickel-Mediated ^{18}F-Fluorination

Despite recent advancements in the development of more selective reagents for electrophilic radiofluorinations, the selective radiofluorination of sp^2 carbons at aromatic and allylic positions has remained a challenge (see the chapter on "The Radiopharmaceutical Chemistry of Fluorine-18: Electrophilic Fluorinations"). In 2011, however, Ritter *et al.* presented an unprecedented and sophisticated system for circumventing the hurdles related to performing electrophilic radiofluorinations with the high-molar-activity fluorine-18 [21]. In this approach, high-molar-activity nucleophilic [^{18}F]fluoride is used as a starting material for synthesizing a palladium-based electrophilic radiofluorination reagent, which can be used for labeling electron-rich arenes with fluorine-18 (Fig. 7). The palladium center of the radiofluorination reagent is in the +IV oxidation state and can function as an electron acceptor. While reduced to a + II oxidation state, the electrophilic radiofluorination reagent can transfer [^{18}F]fluorine to a nucleophile. The nucleophile in this reaction is a *second* Pd compound: a preformed Pd(II)-aryl complex, which introduces the electron-rich arene to the reaction. The [^{18}F]fluorine transfer from the reagent to the Pd(II)-aryl complex leads to the oxidation of the complex and the formation of a Pd(IV)-aryl-[^{18}F]fluoride intermediate. This intermediate subsequently undergoes C-[^{18}F]F reductive elimination to produce the final ^{18}F-fluorinated arene. The reaction has been applied successfully for the radiosynthesis of both electron-rich and electron-neutral [^{18}F]aryl fluorides (Table 4) [21, 22].

The electrophilic [^{18}F]fluorination reaction is performed in a typical two-step sequence. First, the Pd(IV)-picoline

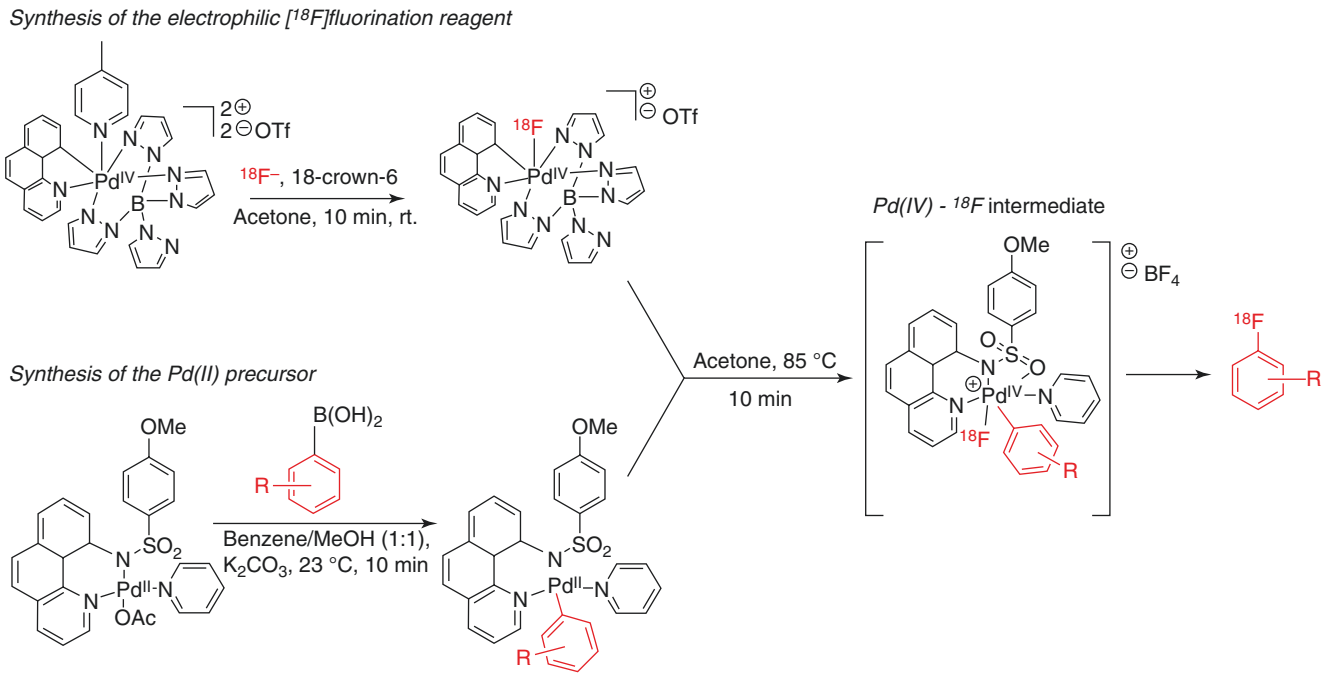

Fig. 7 The palladium(IV)-based electrophilic radiofluorination of electron-rich arenes via a two-step sequence in which the electrophilic ^{18}F-fluorination reagent is first synthesized from its Pd(IV)-picoline precursor and then used for the ^{18}F-fluorination of a preformed Pd(II) precursor that introduces the arene to the reaction. The final ^{18}F-fluorinated arene is achieved as a result of the C-[^{18}F]F reductive elimination of the Pd(IV)-^{18}F intermediate

complex is ^{18}F-fluorinated via incubation with azeotropically dried K[^{18}F]F/18-crown-6 at room temperature for 10 min. The more conventional phase-transfer reagent Kryptofix 2.2.2 cannot be used, because its amine residues may react with the Pd(IV)-picoline complex. This ^{18}F-fluorination reaction tolerates the presence of some water but yields drop as the concentration of water increases. After the initial formation of the ^{18}F-fluorination reagent, the reaction mixture is filtered over a pyridine-functionalized resin that captures excess starting material and some by-products which may precipitate during the reaction. After this simple purification step, the Pd(II)-aryl complex is added. The reaction mixture is then heated at 85 °C for 10 min, ultimately producing the final ^{18}F-labeled arene in RCYs of 10–30% and molar activities up to 480 GBq/μmol [21, 22]. Because high-molar-activity [^{18}F]fluoride is used as the primary source of fluorine-18, the RCYs of this reaction are not limited to 50%, as is the case for electrophilic radiofluorinations starting with [^{18}F]F_2 produced in target. Regardless of the groundbreaking nature of the discovery and its obvious potential, this method has some shortcomings which have constrained its translation to nuclear medicine. First, the reaction does not tolerate basic functional groups such as amines which are common in both existing drugs and new drug candidates; this can be overcome, however, via the appropriate protection of the basic functional groups. Second, steric hindrance at the *ortho* position to the arene substitution reduces the efficiency of the reaction. Third, the synthesis of the Pd complexes is challenging without significant expertise in synthetic organometallic chemistry; indeed, the Pd-based starting materials can be only briefly manipulated in air. And finally, the scale-up and automation of the synthetic procedures have proven difficult, a problem which has compromised radiochemical yields when this procedure has been applied to clinical-scale productions [22].

In light of these difficulties, newer, more translational methods based on Ni(II)-aryl complexes have been developed [23]. In these approaches, there is no need for a palladium-based electrophilic radiofluorination reagent. Instead, the oxidative radiofluorination is achieved using a hypervalent iodine(III) oxidant—PhI(4-OMe-pyridine)$_2$(OTf)$_2$—and K[^{18}F]F/18-crown-6 (Fig. 8). The reaction has proven effective for the synthesis of electron-rich and electron-deficient [^{18}F]aryl fluorides as well as [^{18}F]alkenyl fluorides (see Table 4) [23]. Furthermore, the reaction is not particularly sensitive to steric hindrance, and it has been applied to the synthesis of *ortho*-substituted and densely functionalized [^{18}F]aryl fluorides.

In a typical procedure, small volumes of aqueous [^{18}F]fluoride (2–5 μL) and 18-crown-6 phase-transfer reagent are

Table 4 The radiochemical yields of palladium- and nickel-mediated ^{18}F-fluorination reactions using either the electrophilic Pd(IV) radiofluorination reagent (see Fig. 7) and the Pd(II)-complex of the precursor *or* [^{18}F]fluoride in conjunction with a hypervalent iodine oxidant (see Fig. 8) and and the Ni(II)-complex of the precursor

[M]	Precursor	Product	RCY (%)
Pd(II)-complex	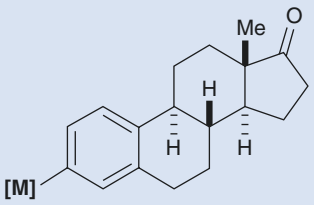	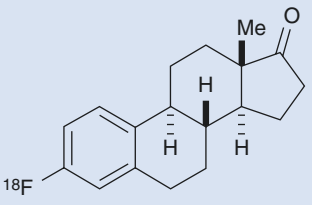	33 ± 7%
Ni(II)-complex			58 ± 6%
Pd(II)-complex	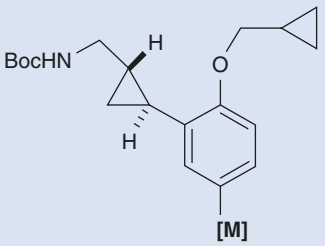	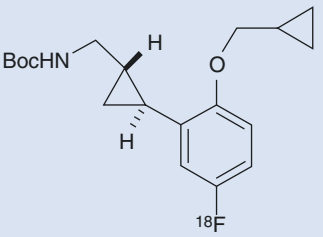	18 ± 5%
Ni(II)-complex			43 ± 9%
Pd(II)-complex	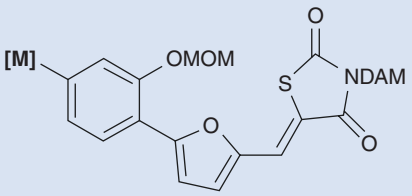	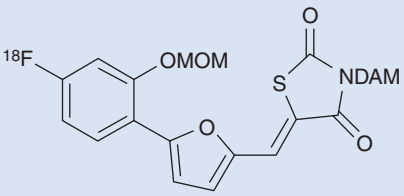	10 ± 2%

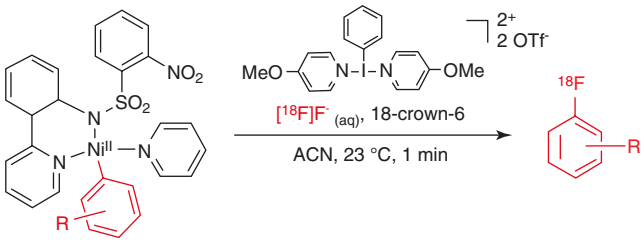

Fig. 8 The nickel-mediated ^{18}F-fluorination of electron-rich arenes

added to a mixture of the Ni(II)-aryl complexes and the oxidant. The reaction mixture is allowed to react 1 min at 23 °C and subsequently purified. In reactions with starting activities of <20 MBq, yields have varied between 15% and 41%. Disappointingly, the RCYs in clinical-scale productions have been lower. For example, for the synthesis of [^{18}F]5-fluorouracil, the radiochemical yield of its *tert*-butyl protected ^{18}F-labeled intermediate dropped from 15% to 3% when increasing the starting activity of ^{18}F to >50 GBq [24]. This low yield was found to be caused by side reactions between the oxidant and high-valent nickel intermediates in the alkaline and aqueous media.

Copper(II)-Mediated ^{18}F-Fluorination

Arenes can also be ^{18}F-fluorinated using their boronic acid-, boronic ester-, or stannane-bearing derivatives using copper(II)-mediated nucleophilic ^{18}F-fluorination processes reported by both Gouverneur and Scott [25–27]. These methods provide access to ^{18}F-fluorinated arenes which are not easily accessible—or accessible at all—via aromatic nucleophilic substitutions (S_NAr) with [^{18}F]fluoride, and they are compatible with electron-rich, electron-neutral, and electron-deficient arenes. Unlike methods based on bulky Pd complexes, copper-mediated radiofluorinations enable the creation of *ortho*-substituted [^{18}F]fluoroarenes. Furthermore, these methods tolerate numerous functional groups and can be applied with boronic acids and esters containing heteroatoms. However, alcohol and amine functionalities must be protected before the reaction, and heterocycles with cyclic secondary amines, amides, or ureas need to be protected as well [28]. For some primary amines, more extensive *N,N*-di-Boc protection is required to prevent competing copper-mediated reactions leading to the oxidative coupling of the boronic ester and the N-H group [25].

In the method reported by Gouverneur, pinacol-derived aryl boronate esters are fluorinated under no-carrier-added conditions with azeotropically dried [^{18}F]KF/K222 in the presence of tetrakis(pyridine)copper(II) triflate [Cu(OTf)$_2$(py)$_4$] (Fig. 9a). The reaction is base sensitive, and thus $K_2C_2O_4$ with a minimal amount of K_2CO_3 (10% w/w) is recommended for the elution of [^{18}F]fluoride from the anion-exchange resin (QMA) instead of strongly basic K_2CO_3, especially when working with high starting activities. Oxygen is essential for the progress of the reaction, and therefore the reaction vial is purged with air after the drying of the [^{18}F]KF/K222 complex and before the addition of the aryl boronate precursor and copper salt. The optimal reaction stoichiometry of the precursor and copper salt depends on the structure of the aryl boronate ester as well as the amount of starting activity. For small-scale reactions (A_0 < 50 MBq), an excess of precursor can be used with a typical borate ester:Cu(OTf)$_2$(py)$_4$ ratio of 10:1. When using activities exceeding 3 GBq, higher concentrations of the copper salt are needed to maintain the efficiency of the reaction. For electron-deficient arene substrates, borate ester:Cu(OTf)$_2$(py)$_4$ ratios of 1:1.5 and 1: 1.3 have provided the best results. For electron-rich arenes, however, equimolar amounts have proven optimal. Either DMF or dimethylacetamide (DMA) can be used as a solvent, though DMA has been found to be superior for electron-rich arenes [29]. Depending on the aryl boronate, reaction conditions of heating to 110–140 °C for 10–20 min have produced RCYs from 5% to 83% and molar activities >100 GBq/μmol [25, 29].

The method reported by Scott is centered upon using boronic acids as precursors for Cu(OTf)$_2$-mediated radiofluorination (Fig. 9b). In this approach, no-carrier-added [^{18}F]fluoride is eluted from an anion-exchange cartridge (QMA) using a weakly basic mixture of KOTf and K_2CO_3 (molar ratio 73:1) and subsequently azeotropically dried. After drying, pyridinium *p*-toluenesulfonate (PPTS) and pyridine are added, followed by the copper(II) salt and the boronic acid precursor in DMF. The optimal molar ratio of boronic acid precursor:Cu(OTf)$_2$:pyridine was found to be 1:5:125, and the addition of the pyridine is essential for the reaction. Unlike the method reported by Gouverneur, this reaction can be carried out in an inert atmosphere, which may prove beneficial in the context of automation. Yields comparable to those achieved via the method published by Gouverneur have been achieved (Table 5) [25–27]. Depending on the precursor and starting activity, heating to 110 °C for 20 min has produced RCYs from 8% to 73% and molar activities up to 28 GBq/μmol [27].

Arylstannanes can also be used for the copper-mediated radiofluorination of arenes bearing electron-donating, electron-neutral, or electron-withdrawing substituents [26] (Fig. 9c). Ortho-substitution is also well tolerated. It has been postulated that the transmetalation of the aryl group to

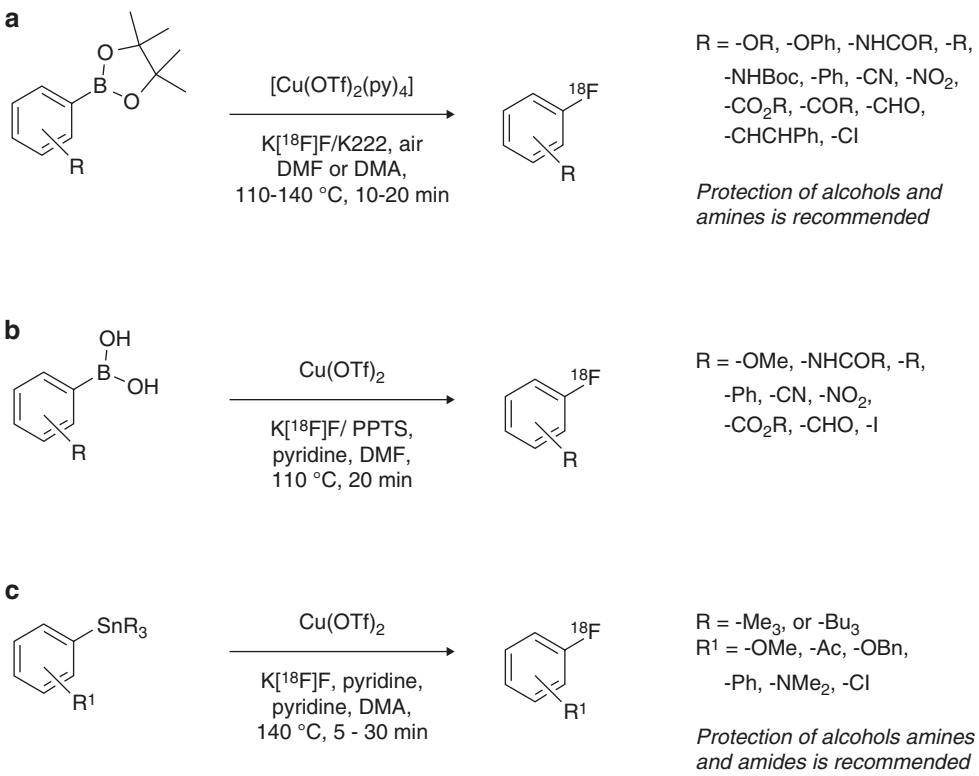

Fig. 9 Methods for copper-mediated ^{18}F-fluorinations using no-carrier-added [^{18}F]-fluoride and starting from (**a**) aryl boronate esters, (**b**) aryl boronic acids, or (**c**) arylstannanes

Table 5 A comparison of the yields of copper(II)-mediated ^{18}F-fluorination reactions starting from selected boronic esters (-BPin), boronic acids [-$B(OH)_2$], and tributylstannanes [-$Sn(Bu)_3$]. All yields are non-isolated, decay-corrected yields (RCYs)

	Precursor		
Product	-BPin	-$B(OH)_2$	-$Sn(Bu)_3$
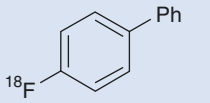	74 ± 5%	46 ± 6%	55 ± 9%
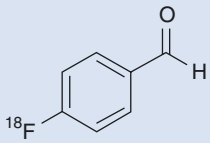	47 ± 7%	49 ± 6%	nd
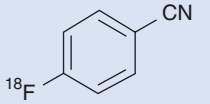	39 ± 7%	47 ± 11%	nd
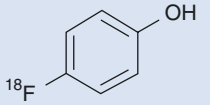	7 ± 2%	15 ± 3%	nd
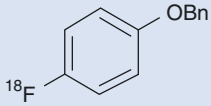	43 ± 5%	nd	49 ± 4%
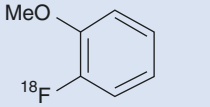	11 ± 2%	nd	48 ± 4%
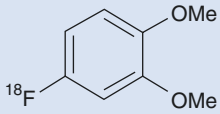	54 ± 3%	nd	54 ± 8%
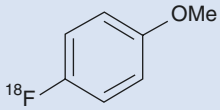	nd	19 ± 3%	57 ± 4%
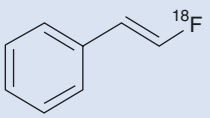	26 ± 4%	nd	64 ± 6%

the copper would even proceed faster for tin compared to boron. In this case, [^{18}F]fluoride is trapped on an anion-exchange cartridge (QMA) and eluted into a reaction vial containing potassium trifluoromethanesulfonate and potassium carbonate in a molar ratio 125:1. After azeotropic distillation, the residue is dissolved in DMA, and the arylstannane precursor—either as -$SnMe_3$ or -$SnBu_3$—$Cu(OTf)_2$—and pyridine are added in a molar ratio of 1:2:15. After heating at 140 °C for 5–30 min, the ^{18}F-radiofluorinated products are typically produced with RCYs between 7% and 59% (see Table 5) [26]. In clinical-scale productions, with starting activities of [^{18}F]fluoride >50 GBq, molar activities as high as 89 GBq/μmol have been achieved.

The discovery of copper-mediated radiofluorinations has had a tremendous impact on PET radiochemistry by providing access to ^{18}F-fluorinated products with high molar activity that were previously inaccessible using no-carrier-added [^{18}F]fluoride. As we have noted, this method is tolerant of numerous functional groups and heterocycles. However, when using aryl boron reagents, functional groups which can act as nucleophiles in the copper-catalyzed Chan-Lam coupling—such as -NH, -OH, and -SH—may be detrimental to the reaction and need to be protected. Similarly, some heterocycles may prevent the ^{18}F-fluorination by generating unreactive copper species, while others may facilitate the reaction. Many drugs contain one or multiple heterocycles, and the outcome of the reaction is difficult to predict when multiple heterocycles are involved. Gouverneur has presented a robust "derisking" approach which is practical for screening potential heterocycle-containing compounds before making any actual retrosynthetic schemes for ^{18}F-fluorination of a new tracer candidate [28]. In this method, the influence of the heterocycles existing in the molecular structure of the tracer candidate is investigated by radiolabeling a known model compound (ArBPin) in the presence of the heterocycles. The influence of these "contaminants" on the radiolabeling reaction is utilized to predict the optimal radiosynthetic route for the proposed tracer. For example, if the results indicate that the reaction does not tolerate certain heterocycle, the radiosynthesis of the new tracer candidate can be planned so that the incompatible heterocycle is introduced to the molecule after the ^{18}F-fluorination step. However, caution should be exercised when using these results to predict the labeling efficiency of the heterocycle itself, as several other factors—such as steric and electronic effects—may contribute as well.

The Future

The methods based on Al[^{18}F]F chemistry have already established their position in radiopharmaceutical chemistry, and have been successfully utilized for the radiolabeling of several biomolecules, including peptides [8, 30, 31], affibodies [32], and antibody fragments [11]. The pharmacokinetic evaluation of Al[^{18}F]F-labeled tracers has revealed that they behave similarly to their ^{68}Ga-labeled counterparts, produce low-activity concentrations in healthy tissues, and are typically eliminated via urinary excretion (Fig. 10) [33]. These results also suggest that coordination to aluminum converts fluorine-18 from a non-residualizing radionuclide to a residualizing species, a significant shift that leads to the increased accumulation of radiolabeled metabolites in target tissues [34]. Of course, this method is not perfect, and increased

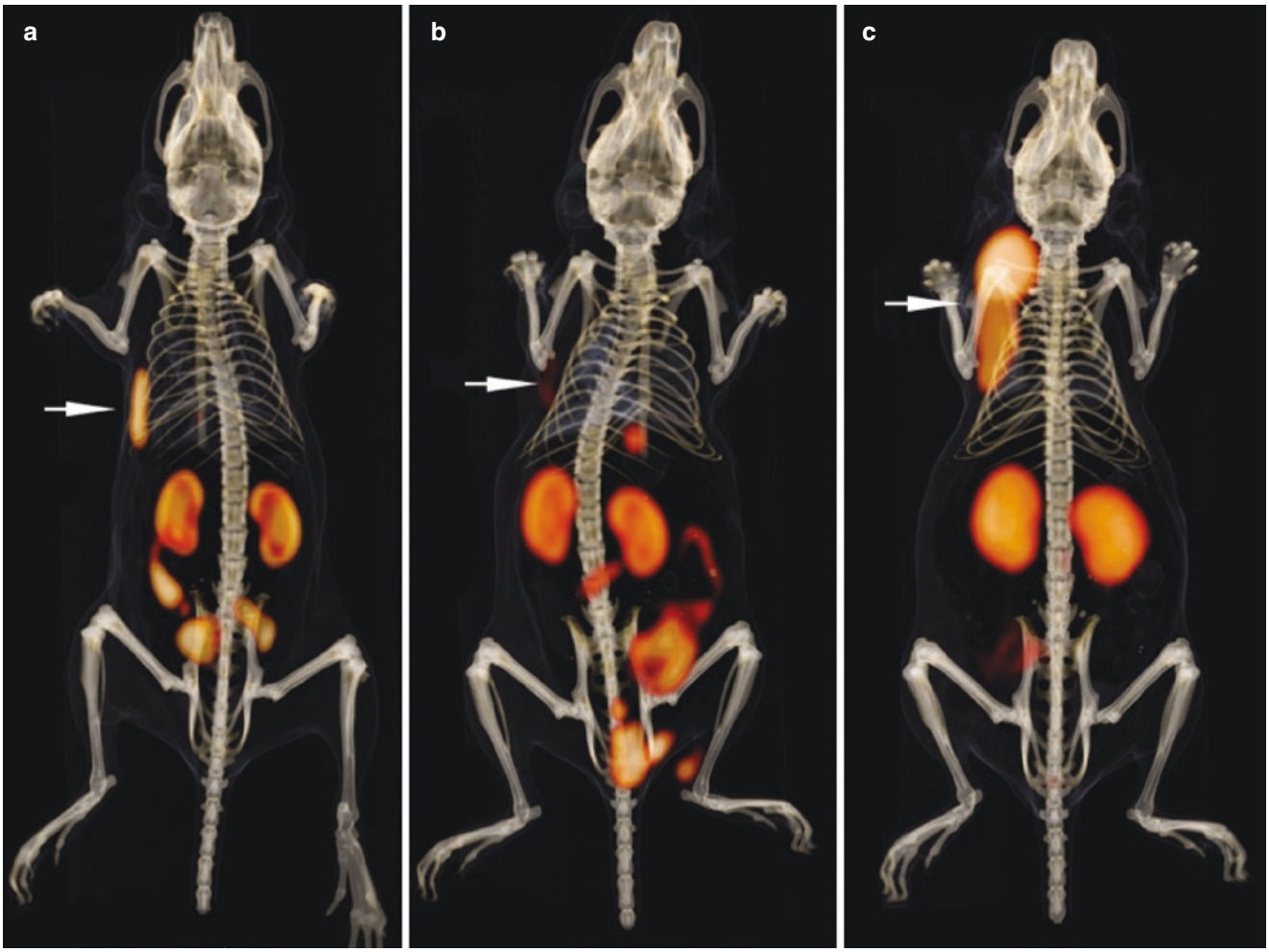

Fig. 10 Anterior three-dimensional volume-rendered projections of fused PET and CT scans of mice bearing subcutaneous AR42J tumors on the right flank injected with NOTA-octreotide [^{18}F]IMP466 (**a**), [^{18}F]IMP466 in the presence of excess unlabeled IMP466 (**b**), and ^{68}Ga-IMP466 (**c**) (From Laverman *et al.* [33], with permission. © Society of Nuclear Medicine and Molecular Imaging, Inc.)

activity concentrations in the kidneys have been observed *in vivo* using Al[^{18}F]F-labeled tracers.

Like Al[^{18}F]F complexes, both ArB[^{18}F]F_3^- and the zwitterionic AMB[^{18}F]F_3 are polar moieties that increase the hydrophilicity of their tracers and therefore accelerate their renal excretion. This increased hydrophilicity is advantageous for optimizing the target-to-background activity concentration ratios of PET images. However, it should not be overlooked that this same shift in hydrophilicity may also influence the pharmacokinetic profiles of small compounds such as peptides and peptidomimetics. Several peptides, proteins, and small molecules have been labeled using ArB[^{18}F]F_3^- and AMB[^{18}F]F_3 chemistry [35–39]. However, due to its superior *in vivo* stability, AMB[^{18}F]F_3 has emerged as the most promising approach. Ultimately, one of the greatest advantages of these B[^{18}F]F- and Al[^{18}F]F-based methods is their tolerance to water. This trait has already enabled the development of ^{18}F-labeling kits based on Al[^{18}F]F chemistry, and kits based on AMB[^{18}F]F_3 can be expected soon as well.

Transition metal-catalyzed ^{18}F-fluorination reactions have revolutionized radiochemistry, providing access to a wide variety of ^{18}F-fluorinated aromatic and allylic substrates with formerly unattainable molar activities (GBq/μmol). Currently, the most significant hurdle for the widespread utilization of these approaches is scaling up these reactions for fully automated production. The excellent yields of the small-scale reactions (< 1 GBq) are rarely achieved when these procedures are scaled up to activity levels designed to produce several clinical doses (> 5 GBq) (Fig. 11) [25, 27, 29, 40]. The reasons for this phenomenon are multiform and have their roots in several factors centered on the differences between small-scale and clinical-scale productions, such as the volume of the reaction mixture, the amount of base in the aqueous solution of [^{18}F]fluoride, and the total concentration of fluoride. Furthermore, differences in the amount of radioactivity used in the reactions may contribute as well, since higher levels of activity (>10 GBq) may induce excitation, ionization, and the formation of radicals. On top of these

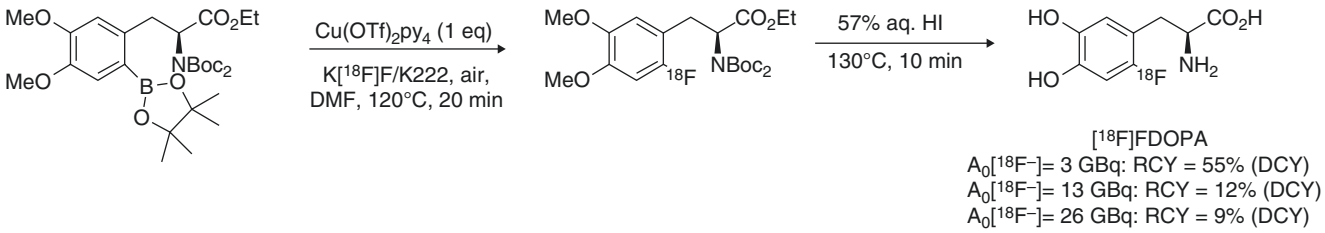

Fig. 11 The synthesis of [^{18}F]FDOPA from its boronic ester-bearing precursor via copper-mediated radiofluorination as well as the radiochemical yields for this reaction under different conditions

issues, there are also important differences between manual, semi-automated, and automated synthesis procedures that must be considered. Extensive research is currently being dedicated to solving these problems, and it can be expected that these transformations—especially the copper-mediated ^{18}F-fluorination reactions—will fulfill their potential, speed up the discovery of new PET radiopharmaceuticals, and even replace some of the established clinical production methods.

The Bottom Line

- Fluorine forms bonds with several group 13–15 elements, including carbon, boron, nitrogen, aluminum, silicon, and phosphorous. However, not all of these bonds are hydrolytically stable.
- [^{18}F]Fluoride forms a stable [Al[^{18}F]F]$^{2+}$ complex with the metallic Al^{3+} cation. The complex can be incorporated into macromolecules using bifunctional chelators such as NODA.
- [^{18}F]Fluoroborates can be synthesized via the ^{18}F-fluorination of organoboronic acids or their esters. [^{18}F]Fluoroborates are hydrolytically stable when stabilized by appropriate substituents within their structure.
- Transition metals can catalyze the ^{18}F-fluorination of electron-rich and other aromatic compounds with no-carrier-added, high-molar-activity [^{18}F]fluoride. Palladium-, nickel-, and copper-mediated reactions can be used.
- In copper(II)-mediated nucleophilic ^{18}F-fluorinations, arenes are ^{18}F-fluorinated with no-carrier-added [^{18}F]fluoride using their boronic acid-, boronic ester-, or stannane-bearing derivatives.

References

1. Luo YR. Comprehensive handbook of chemical bond energies. 1st ed. Boca Raton: CRC Press; 2007.
2. O'Reilly RJ, Karton A, Radom L. Effect of substituents on the strength of N–X (X = H, F, and cl) bond dissociation energies: a high-level quantum chemical study. J Phys Chem A. 2011;115(21):5496–504.
3. Studenov AR, Adam MJ, Wilson JS, Ruth TJ. New radiolabelling chemistry: synthesis of phosphorus–[18F]fluorine compounds. J Label Compd Radiopharm. 2005;48:497–500.
4. Gillis EP, Eastman KJ, Hill MD, Donnelly DJ, Meanwell NA. Applications of fluorine in medicinal chemistry. J Med Chem. 2015;58(21):8315–59.
5. McBride WJ, Sharkey RM, Karacay H, D'Souza CA, Rossi EA, Laverman P, et al. A novel method of 18f radiolabeling for PET. J Nucl Med. 2009;50(6):991–8.
6. McBride WJ, Sharkey RM, Goldenberg DM. Radiofluorination using aluminum-fluoride (Al18F). EJNMMI Res. 2013;3(1):36.
7. McBride WJ, D'Souza CA, Karacay H, Sharkey RM, Goldenberg DM. New lyophilized kit for rapid radiofluorination of peptides. Bioconjug Chem. 2012;23(3):538–47.
8. McBride WJ, D'Souza CA, Sharkey RM, Karacay H, Rossi EA, Chang C-H, et al. Improved 18F labeling of peptides with a fluoride-aluminum-chelate complex. Bioconjug Chem. 2010;21(7):1331–40.
9. Shetty D, Choi SY, Jeong JM, Lee JY, Hoigebazar L, Lee Y-S, et al. Stable aluminium fluoride chelates with triazacyclononane derivatives proved by X-ray crystallography and 18F-labeling study. Chem Commun (Camb). 2011;47(34):9732–4.
10. D'Souza CA, McBride WJ, Sharkey RM, Todaro LJ, Goldenberg DM. High-yielding aqueous 18F-labeling of peptides via Al18F chelation. Bioconjug Chem. 2011;22(9):1793–803.
11. McBride WJ, D'Souza CA, Sharkey RM, Goldenberg DM. The radiolabeling of proteins by the [18F]AlF method. Appl Radiat Isot. 2012;70(1):200–4.
12. Cleeren F, Lecina J, Billaud EMF, Ahamed M, Verbruggen A, Bormans GM. New chelators for low temperature Al18F-labeling of biomolecules. Bioconjug Chem. 2016;27(3):790–8.
13. Vedejs E, Chapman RW, Fields SC, Lin S, Schrimpf MR. Conversion of Arylboronic acids into potassium aryltrifluoroborates: convenient precursors of arylboron difluoride Lewis acids. J Org Chem. 1995;60(10):3020–7.
14. Ting R, Harwig CW, Lo J, Li Y, Adam MJ, Ruth TJ, et al. Substituent effects on aryltrifluoroborate solvolysis in water: implications for Suzuki−Miyaura coupling and the design of stable 18F-labeled aryltrifluoroborates for use in PET imaging. J Org Chem. 2008;73(12):4662–70.
15. Liu Z, Li Y, Lozada J, Schaffer P, Adam MJ, Ruth TJ, et al. Stoichiometric leverage: rapid 18F-aryltrifluoroborate radiosynthesis at high specific activity for click conjugation. Angew Chem Int Ed Engl. 2013;52(8):2303–7.
16. Ting R, Adam MJ, Ruth TJ, Perrin DM. Arylfluoroborates and alkylfluorosilicates as potential PET imaging agents: high-yielding aqueous biomolecular 18F-labeling. J Am Chem Soc. 2005;127(38):13094–5.
17. Ting R, Harwig C, auf dem Keller U, McCormick S, Austin P, Overall CM, et al. Toward [18F]-labeled aryltrifluoroborate radiotracers: in vivo positron emission tomography imaging of

stable aryltrifluoroborate clearance in mice. J Am Chem Soc. 2008;130(36):12045–55.
18. Liu Z, Pourghiasian M, Radtke MA, Lau J, Pan J, Dias GM, et al. An organotrifluoroborate for broadly applicable one-step 18F-labeling. Angew Chem Int Ed. 2014;53(44):11876–80.
19. Liu Z, Chao D, Li Y, Ting R, Oh J, Perrin DM. From minutes to years: predicting organotrifluoroborate solvolysis rates. Chemistry. 2015;21(10):3924–8.
20. Liu Z, Lin K-S, Bénard F, Pourghiasian M, Kiesewetter DO, Perrin DM, et al. One-step 18F labeling of biomolecules using organotrifluoroborates. Nat Protoc. 2015;10(9):1423–32.
21. Lee E, Kamlet AS, Powers DC, Neumann CN, Boursalian GB, Furuya T, et al. A fluoride-derived electrophilic late-stage fluorination reagent for PET imaging. Science. 2011;334(6056):639–42.
22. Kamlet AS, Neumann CN, Lee E, Carlin SM, Moseley CK, Stephenson N, et al. Application of palladium-mediated 18F-fluorination to PET radiotracer development: overcoming hurdles to translation. PLoS One. 2013;8(3):e59187.
23. Lee E, Hooker JM, Ritter T. Nickel-mediated oxidative fluorination for PET with aqueous [18F] fluoride. J Am Chem Soc. 2012;134(42):17456–8.
24. Hoover AJ, Lazari M, Ren H, Narayanam MK, Murphy JM, van Dam RM, et al. A transmetalation reaction enables the synthesis of [18F]5-fluorouracil from [18F]fluoride for human PET imaging. Organometallics. 2016;35(7):1008–14.
25. Tredwell M, Preshlock SM, Taylor NJ, Gruber S, Huiban M, Passchier J, et al. A general copper-mediated nucleophilic 18F fluorination of arenes. Angew Chem Int Ed Engl. 2014;53(30):7751–5.
26. Makaravage KJ, Brooks AF, Mossine AV, Sanford MS, Scott PJH. Copper-mediated radiofluorination of arylstannanes with [18F]KF. Org Lett. 2016;18(20):5440–3.
27. Mossine AV, Brooks AF, Makaravage KJ, Miller JM, Ichiishi N, Sanford MS, et al. Synthesis of [18F]arenes via the copper-mediated [18F]fluorination of boronic acids. Org Lett. 2015;17(23):5780–3.
28. Taylor NJ, Emer E, Preshlock S, Schedler M, Tredwell M, Verhoog S, et al. Derisking the copper-mediated 18F-fluorination of heterocyclic positron emission tomography radioligands. J Am Chem Soc. 2017;139(24):8267–76.
29. Preshlock S, Calderwood S, Verhoog S, Tredwell M, Huiban M, Hienzsch A, et al. Enhanced copper-mediated 18F-fluorination of aryl boronic esters provides eight radiotracers for PET applications. Chem Commun (Camb). 2016;52(54):8361–4.
30. Dijkgraaf I, Franssen GM, McBride WJ, D'Souza CA, Laverman P, Smith CJ, et al. PET of tumors expressing gastrin-releasing peptide receptor with an 18F-labeled bombesin analog. J Nucl Med. 2012;53(6):947–52.
31. Zhang Z, Amouroux G, Pan J, Jenni S, Zeisler J, Zhang C, et al. Radiolabeled B9958 derivatives for imaging bradykinin B1 receptor expression with positron emission tomography: effect of the radiolabel–chelator complex on biodistribution and tumor uptake. Mol Pharm. 2016;13(8):2823–32.
32. Da Pieve C, Allott L, Martins CD, Vardon A, Ciobota DM, Kramer-Marek G, et al. Efficient [18F]AlF radiolabeling of ZHER3:8698 affibody molecule for imaging of HER3 positive tumors. Bioconjug Chem. 2016;27(8):1839–49.
33. Laverman P, McBride WJ, Sharkey RM, Eek A, Joosten L, Oyen WJG, et al. A novel facile method of labeling octreotide with 18F-fluorine. J Nucl Med. 2010;51(3):454–61.
34. Schoffelen R, Sharkey RM, Goldenberg DM, Franssen G, McBride WJ, Rossi EA, et al. Pretargeted immuno-positron emission tomography imaging of carcinoembryonic antigen-expressing tumors with a bispecific antibody and a 68Ga- and 18F-labeled hapten peptide in mice with human tumor xenografts. Mol Cancer Ther. 2010;9(4):1019–27.
35. auf dem Keller U, Bellac CL, Li Y, Lou Y, Lange PF, Ting R, et al. Novel matrix metalloproteinase inhibitor [18F]marimastat-aryltrifluoroborate as a probe for in vivo positron emission tomography imaging in cancer. Cancer Res. 2010;70(19):7562–9.
36. Liu Z, Hundal-Jabal N, Wong M, Yapp D, Lin KS, Bénard F, et al. A new 18F-heteroaryltrifluoroborate radio-prosthetic with greatly enhanced stability that is labelled by 18F–19F-isotope exchange in good yield at high specific activity. Med Chem Commun. 2014;5(2):171–9.
37. Li Y, Guo J, Tang S, Lang L, Chen X, Perrin DM. One-step and one-pot-two-step radiosynthesis of cyclo-RGD-18F-aryltrifluoroborate conjugates for functional imaging. Am J Nucl Med Mol Imaging. 2013;3(1):44–56.
38. Li Y, Liu Z, Harwig CW, Pourghiasian M, Lau J, Lin K-S, et al. 18F-click labeling of a bombesin antagonist with an alkyne-18F-ArBF3 -: in vivo PET imaging of tumors expressing the GRP-receptor. Am J Nucl Med Mol Imaging. 2013;3(1):57–70.
39. Walker D, Li Y, Roxin Á, Schaffer P, Adam MJ, Perrin DM. Facile synthesis and 18F-radiolabeling of α4β1-specific LLP2A-aryltrifluoroborate peptidomimetic conjugates. Bioorg Med Chem Lett. 2016;26(20):5126–31.
40. Zhang Z, Lau J, Kuo H-T, Zhang C, Colpo N, Bénard F, et al. Synthesis and evaluation of 18F-labeled CJ-042794 for imaging prostanoid EP4 receptor expression in cancer with positron emission tomography. Bioorg Med Chem Lett. 2017;27(10):2094–8.

The Radiopharmaceutical Chemistry of Technetium-99m

Stephanie M. Rathmann, Zainab Ahmad, Samantha Slikboer, Holly A. Bilton, Denis P. Snider, and John F. Valliant

Nuclear Chemistry

Isotopes of Technetium

Technetium, a transition metal, is the 43rd element in the periodic table and was the first synthetic element reported [1]. It has a $4d^5 5s^2$ (d^7) electron configuration and forms a wide variety of coordination and organometallic complexes [2–4]. Remarkably, there are 51 isotopes of technetium ranging from technetium-85 to technetium-120. Of these, the two most studied are technetium-99—which has a half-life of 211,000 y and is sometimes referred to as technetium-99g—and ^{99m}Tc. The latter is our primary concern here. The half-life of ^{99m}Tc is 6.01 h and is nearly ideal for nuclear medicine. Indeed, it is long enough to facilitate the preparation, transportation, and administration of radiopharmaceuticals as well as the imaging of patients. At the same time, it is short enough to allay concerns surrounding radiation exposure and disposal. In addition, the primary gamma rays emitted by ^{99m}Tc have an energy of 140 keV, which is sufficient to allow for clinical tomographic whole-body imaging at any depth without imparting a burdensome radiation dose. These features—along with its low cost and widespread availability—have made ^{99m}Tc one of the most important radionuclides in clinical diagnostic nuclear medicine [5]. Across the globe, approximately 25 million medical imaging procedures are performed using ^{99m}Tc-based radiopharmaceuticals every year [5, 6].

S. M. Rathmann · Z. Ahmad · S. Slikboer · H. A. Bilton
D. P. Snider · J. F. Valliant (✉)
Department of Chemistry and Chemical Biology, McMaster University, Hamilton, ON, Canada
e-mail: valliant@mcmaster.ca

Method of Production

It is critical that any radionuclide destined for routine clinical use have a plentiful and secure supply at reasonable cost. ^{99m}Tc is a daughter radionuclide formed via the β^--emission of molybdenum-99 (^{99}Mo) [7]. There are two principal ways in which ^{99}Mo is produced: (i) as a by-product of nuclear fission or (ii) via the direct irradiation of molybdenum-98 in a nuclear reactor. In the former case, ^{99}Mo can be isolated from the fission of uranium-235 in a nuclear reactor with a yield of 6% [8]. In the latter case, molybdenum-98 is bombarded with neutrons to produce ^{99}Mo. This method requires intense neutron sources to generate sufficient amounts of ^{99}Mo [9]. The recent global shortage of ^{99}Mo has spurred the development of alternative strategies for the production of ^{99}Mo, including production using linear accelerators [10]. Here, a molybdenum-100 (^{100}Mo) source is irradiated with gamma rays, resulting in the release of a neutron in what is otherwise known as the ^{100}Mo(γ,n)^{99}Mo reaction. The direct production of ^{99m}Tc on cyclotrons is also a possibility. In this scenario, the proton bombardment of a solid ^{100}Mo source—the ^{100}Mo(p,2n)^{99m}Tc reaction—is used [8, 11].

The ^{99}Mo/^{99m}Tc Generator

The ^{99}Mo/^{99m}Tc generator is a convenient way to obtain ^{99m}Tc and is one key reason that ^{99m}Tc became one of the most widely used in nuclear imaging. A ^{99}Mo/^{99m}Tc generator contains ^{99}Mo—in the form of molybdate $[^{99}Mo]MoO_4^{2-}$—absorbed onto an aluminum oxide column. Importantly, the product formed via the decay of the ^{99}Mo is $[^{99m}Tc]TcO_4^-$ that does not have the same affinity for the aluminum oxide. As a result, the $[^{99m}Tc]TcO_4^-$ can be eluted from the generator in high purity [12]. Conveniently, a simple 0.9% saline (9 mg/ml NaCl) solution can be used to selectively elute the $[^{99m}Tc]TcO_4^-$. A schematic of a ^{99}Mo/^{99m}Tc generator and series of photographs depicting how it is used are shown in Fig. 1 (see the section on "Eluting a ^{99}Mo/^{99m}Tc Generator"

J. S. Lewis et al. (eds.), *Radiopharmaceutical Chemistry*, https://doi.org/10.1007/978-3-319-98947-1_18

for more details). ^{99}Mo/^{99m}Tc generators are typically eluted once every 24 h, but it is possible to do 2–3 elutions per day. Depending on the "size" of the generator (*i.e.* the activity of ^{99}Mo), sufficient ^{99m}Tc can be obtained to produce 50–80 patient doses per day.

The Chemistry of Technetium

General

Technetium complexes have been reported with oxidation states ranging from −1 to +7 [13]. Examples highlighting the diversity of ^{99m}Tc chemistry are shown in Table 1. The oxidation state formed when working with ^{99m}Tc—as is the case for other transition metals—is controlled by several factors, including pH, the type and "strength" of the reducing agent, and the nature of the coordinating ligands [14]. The structures of technetium complexes vary widely. Indeed, ^{99m}Tc complexes with tetrahedral (N = 4), tetragonal pyramidal (N = 5), octahedral (N = 6), capped octahedral (N = 7), and pentagonal bipyramidal (N = 8) geometries have been reported [15]. The formation of multiple structural isomers is also common, which must be taken into account when designing ^{99m}Tc-based radiopharmaceuticals. For example, for Tc(V) complexes of amino acid-based chelators—such as [^{99m}Tc]TcO(RP294)—it is possible to form both *syn*- and *anti*-isomers (Fig. 2) [16]. Such isomers can create substantial issues (particularly at the stage of regulatory approval), as they may have different physical and biochemical properties.

Characterizing ^{99m}Tc Complexes

Characterizing ^{99m}Tc complexes can be a challenge because the doses used for nuclear imaging typically contain only a very small molar amount of the metal complex. For instance, the dose of a ^{99m}Tc-labeled radiopharmaceutical used for a clinical scan—typically, 185–925 MBq—corresponds to only 0.95–4.7 nanograms (ng) of metal. This is below the detection limit of methods typically used for the macroscopic characterization of metal complexes. Furthermore, as there are no stable isotopes of technetium, ^{99}Tc must be used to develop new complexes and study the chemistry of ^{99m}Tc. ^{99}Tc has a half-life of 2.11×10^5 years, and because it undergoes a low-energy beta decay, it can be easily shielded, and milligram quantities can be handled safely. However, the long half-life does create challenges with regard to contamination and disposal. Consequently, rhenium, technetium's 5d congener, is often used to prepare reference standards for ^{99m}Tc-containing compounds.

Re and Tc have similar atomic radii due to the lanthanide contraction and regularly form structurally analogous complexes. A notable exception to the similarity in their chemistry

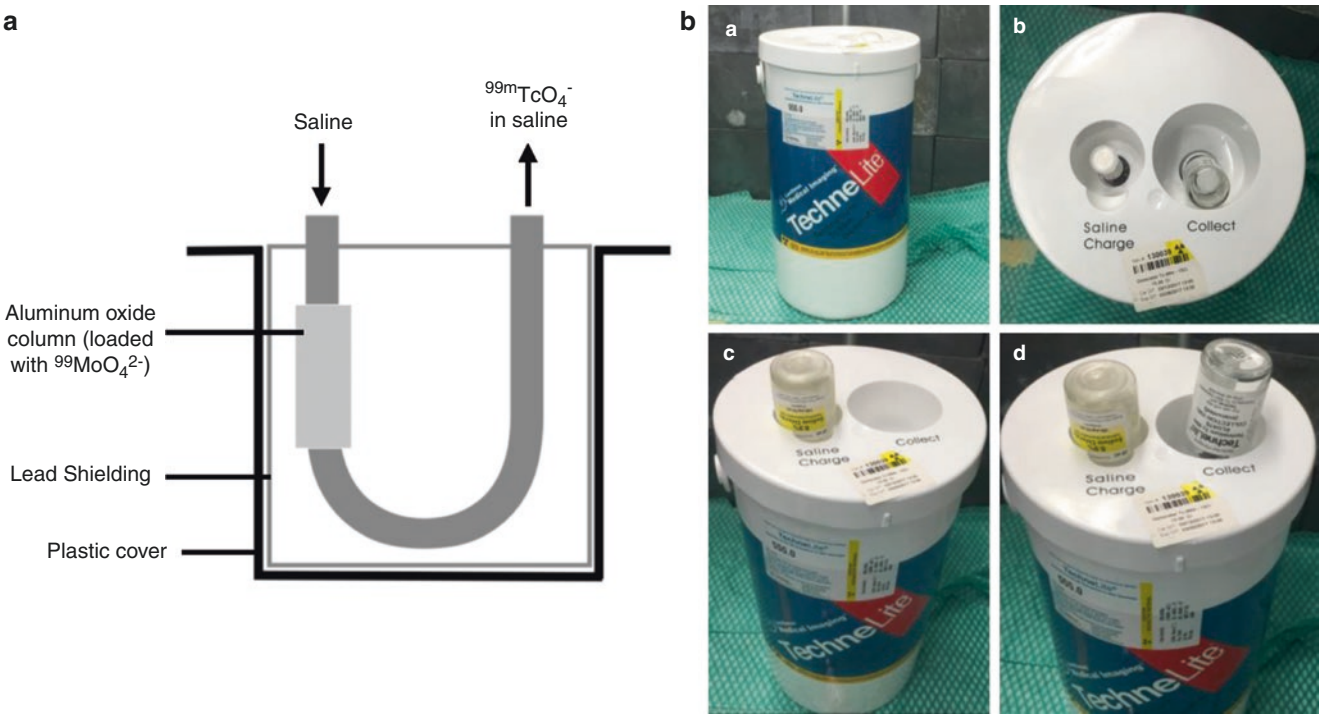

Fig. 1 ^{99}Mo/^{99m}Tc generator. (**a**) Schematic representation of a ^{99}Mo/^{99m}Tc generator. (**b**). A typical ^{99}Mo/^{99m}Tc generator. (**a**) Side view; (**b**) top view; (**c**) vial of saline containing the desired volume to elute attached to the inlet; (**d**) ^{99m}Tc collection vial attached to collection port (Note that the collection vial is often enclosed in a specially designed lead pig)

is the fact that ReO_4^- is harder to reduce than TcO_4^-. This can require the use of different reducing agents and reaction conditions to prepare analogous Re and Tc complexes. For example, the preparation of the ^{99m}Tc(I)- and Re(I)-based analogues of $[(M(CO)_3(OH_2)_3]^+$ requires significantly different conditions and reagents [17–19]. For the ^{99m}Tc complex, the product can be prepared in a single step using boranocarbonate ($[CO_2BH_3]^{2-}$). For radioisotopes of Re, however, a two-step kit must be used since it is necessary to first employ a mixture H_3PO_4 and BH_3-NH_3 to get the second step (treatment with boranocarbonate) to proceed in high yield [14, 20]. Re(V) and Tc(V) chelator complexes are similarly prepared under different conditions, as the formation of complexes of Re(V) often requires higher temperatures, lower pH, and higher concentrations of reducing agents than complexes of Tc(V) [19]. Another important difference between the chemistries of Tc and Re is that it is common for analogous complexes of each element to have disparate stabilities toward oxidation and disproportionation reactions [21].

When developing a new ^{99m}Tc-based radiopharmaceutical, convention dictates that a Re analogue be prepared on a multi-milligram scale and characterized by NMR, mass spectrometry, and X-ray crystallography (when possible). Once the ^{99m}Tc-labeled compound is synthesized, both the ^{99m}Tc and Re complexes can be co-injected into an HPLC. Subsequently, the elution of the Re complex can be monitored via UV or MS, the elution of the ^{99m}Tc complex can be monitored using a radiation detector, and their retention times can be compared to verify co-elution.

Table 1 The oxidation states of technetium and examples of different Tc complexes

Oxidation state	Archetypal examples	Application in nuclear medicine
−1	$[Tc(CO)_5]^-$	N/A
0	$Tc_2(CO)_{10}$	N/A
+1	$[Tc(CO)_3(H_2O)_3]^+$, $[Tc(CNCH_2C(CH_3)_2OCH_3)_6]^+$	Prostate cancer, cardiac imaging
+2	$[TcCl_4]^{2-}$, $[Bu_4N][Tc(NO)Br_4]$	N/A
+3	Teboroxime, $[TcCl_3(Et_2PhP)_3]$	Myocardial perfusion
+4	Bisphosphonates,$[TcO(OH)EDTA]^{3-}$	Bone injury and metabolism
+5	Tc-MAG_3, Tc-BAT	Renal function, brain imaging
+6	TcF_6, $[TcNCl_4]^-$	N/A
+7	TcO_4^-	Thyroid imaging

N/A = Not applicable

Current ^{99m}Tc-Based Radiopharmaceuticals: Structure, Synthesis, and Clinical Use

^{99m}Tc-based radiopharmaceuticals have dominated the field of nuclear medicine for the past several decades, though recent advances in the use of radionuclides for positron emission tomography (PET) have changed this predominant role [5, 22]. Notwithstanding, ^{99m}Tc-labeled agents are used daily around the globe to diagnose a wide spectrum of pathologies, including ischemia, coronary artery disease, renal failure, bone disease and fractures, cerebrovascular diseases, liver and gall bladder disorders, and cancer.

^{99m}Tc-based radiopharmaceuticals are obtained using "instant kits," which facilitate robust and high-yielding ^{99m}Tc-labeling reactions using simple and typically one-step procedures [23]. This technology—as with ^{99}Mo/^{99m}Tc generators—greatly simplified the production and ease of access to ^{99m}Tc-based radiopharmaceuticals. These kits typically contain a lyophilized mixture of the compound (ligand) to be labeled, buffers, and various additives. The latter include antioxidants (to increase stability of the product), catalysts, solubilizing agents, and fillers (for quick solubilization prior to lyophilization when preparing the kits). The buffers utilized in these kits are crucial, as the pH of the reaction mixture following the addition of the metal can have a significant influence on the yield of the radiolabeling reaction, as well as how simple and multifunctional ligands coordinate ^{99m}Tc. Detailed information regarding specific additives for approved radiopharmaceuticals can be found in the package inserts, which are referenced for the examples provided below.

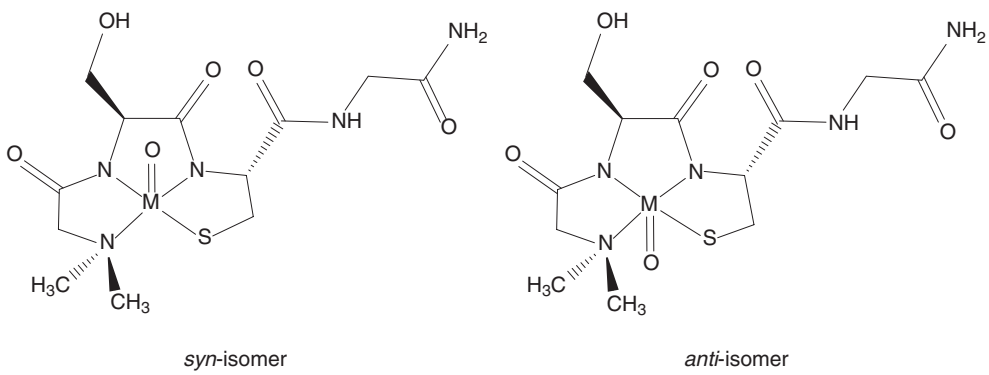

Fig. 2 The *syn*- and *anti*-isomers of [^{99m}Tc]TcO(RP294)

Agents for Cardiac Perfusion Imaging

[^{99m}Tc]Tc-Sestamibi

[^{99m}Tc]Tc-Sestamibi (Cardiolite™) is an approved radiopharmaceutical used primarily for the imaging of myocardial perfusion. In this context, it can be used to identify both cardiac ischemia and necrosis by comparing SPECT images collected during resting and stress (postexercise) states. Interestingly, it is also often employed as a second-line diagnostic for the imaging of breast tumors after positive mammography [24]. [^{99m}Tc]Tc-Sestamibi is an octahedral, cationic ^{99m}Tc(I) complex (Fig. 3a) that was developed as a replacement for an older cardiac imaging agent—[^{201}Tl]TlCl (thallous chloride)—because it produces images of superior quality and reduces radiation doses to patients [25, 26]. [^{99m}Tc]Tc-Sestamibi accumulates in tissues in proportion to blood flow by localizing quickly within the mitochondria of cardiomyocytes [24, 27]. In healthy patients, it clears primarily through both the hepatobiliary (33%) and renal (27%) systems with a blood half-life of 4.3 min at rest and 1.6 min following exercise-induced stress [27].

[^{99m}Tc]Tc-Sestamibi contains six isonitrile ligands and is a unique example of an organometallic complex that can be prepared in water under dilute conditions. It is produced using a high-yielding, single-step instant kit, which contains the isonitrile ligands as their copper(I) complex, a series of buffers and antioxidants, and stannous chloride as the reducing agent. [^{99m}Tc]TcO_4^- in saline is added to the kit to form the product, and the purity of the final radiopharmaceutical is verified by instant thin layer chromatography (iTLC) [27]. iTLC, which typically employs silica-impregnated chromatography paper, is a rapid and convenient method for determining the purity of radiopharmaceuticals [23].

[^{99m}Tc]Tc-Tetrofosmin

[^{99m}Tc]Tc-Tetrofosmin (Myoview™), like [^{99m}Tc]Tc-sestamibi, is an approved agent used for myocardial perfusion imaging. Specifically, it is used to identify regions of reversible myocardial ischemia and infarcted myocardium in patients with suspected coronary artery disease [28, 29] In addition, it is used for evaluating ventricular function in patients with known or suspected heart disease [30]. As shown in Fig. 3b, [^{99m}Tc]Tc-tetrofosmin—([^{99m}Tc]Tc-(tetrofosmin)$_2O_2$)$^+$—is a cationic, trans-dioxo-bis(diphosphine)-technetium(V) complex [28–30]. It is prepared using a high-yielding kit by combining an ether-functionalized diphosphine ligand (1,2-bis[bis(2-ethoxyethyl)phosphino] ethane) with stannous chloride as the reducing agent, disulfosalicylate as an antimicrobial, and the appropriate buffers. The uptake of [^{99m}Tc]Tc-tetrofosmin is proportional to the blood flow, and its mechanism of uptake and retention is seemingly identical to that of [^{99m}Tc]Tc-sestamibi. Quantitative SPECT imaging with [^{99m}Tc]Tc-tetrofosmin is used to assess the presence of ischemia or necrosis by detecting differing levels of signal in the heart before, during, or after exercise. This radiopharmaceutical shows rapid uptake in the myocardium, quick clearance from the blood, liver, and lungs, and primarily renal excretion.

Agent for Bone Imaging

[^{99m}Tc]Tc-MDP

[^{99m}Tc]Tc-Medronate (DraxImage® MDP-25 and TechneScan® MDP) is a radiopharmaceutical used for bone scintigraphy in which the radiometal is chelated by methylene diphosphonate (Fig. 4) [31]. [^{99m}Tc]Tc-MDP is believed to be a Tc(IV) complex with one ^{99m}Tc atom complexed by two diphosphonate ligands. However, at the macroscopic scale with ^{99}Tc, X-ray crystallography reveals that each diphosphonate ligand is bound to two Tc centers, resulting in a mixture of polymers and oligomers. Importantly, this is not likely to be the structure for [^{99m}Tc]

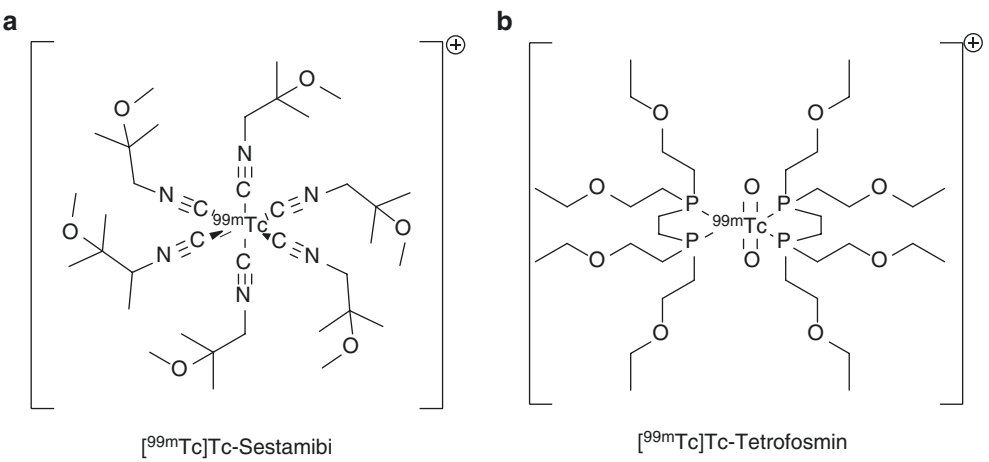

Fig. 3 ^{99m}Tc-labeled cardiac perfusion agents currently used in nuclear medicine. (**a**) [^{99m}Tc]Tc-Sestamibi and (**b**) [^{99m}Tc]Tc-tetrofosmin

Tc-MDP, since the ^{99m}Tc-radiosynthesis reactions are performed using small amounts of the radiometal in the presence of a large excess of ligand [23, 32, 33]. [^{99m}Tc]Tc-MDP is obtained by combining [^{99m}Tc]TcO_4^- with a lyophilized and sterile mixture of medronic acid, ascorbic acid, and stannous fluoride [34]. [^{99m}Tc]Tc-MDP is used to detect bone metastases as well as osteonecrosis because it localizes to the sites of high calcium metabolism, typically by binding to hydroxyapatite [31, 34]. This allows for the imaging of skeletal tumors as well as soft tissue malignant sarcomas and adenocarcinomas in which calcium deposits accumulate. Note that ^{99m}Tc-labeled bisphosphonates can also be used for the imaging of osteomyelitis (infection in the bone) and have recently been reported to accumulate in tumor-associated macrophages found in non-osseous lesions [35].

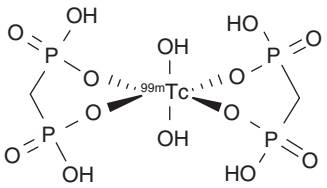

[^{99m}Tc]Tc-MDP

Fig. 4 The ^{99m}Tc-labeled bone scanning agent, [^{99m}Tc]Tc-MDP [23]

Agents for Renal Imaging

[^{99m}Tc]Tc-DMSA

[^{99m}Tc]Tc-DMSA (dimercaptosuccinic acid) is an approved radiopharmaceutical for renal cortical scintigraphy and is largely used for the delineation of renal scars [36, 37]. This radiopharmaceutical is obtained in a kit formulation as a vial containing a lyophilized, sterile mixture of dimercaptosuccinic acid (90% meso-isomer and 10% D- and L-isomers), stannous chloride dihydrate, ascorbic acid, and inositol to which a solution of [^{99m}Tc]TcO_4^- in saline is added. The mixture is incubated for 10 min to obtain the final product (Fig. 5a) [23, 34, 36]. The mechanism of [^{99m}Tc]Tc-DMSA is predicated on the ability of the complex to bind plasma proteins. Once protein-bound, the [^{99m}Tc]Tc-DMSA clears from the plasma and eventually concentrates in the renal cortex by 1 h postinjection, with approximately 20% of injected dose still present in each kidney 6 h following the administration of the radiotracer [36, 38]. [^{99m}Tc]Tc-DMSA is also used to

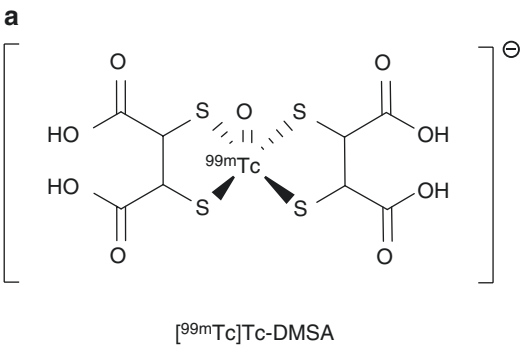

[^{99m}Tc]Tc-DMSA

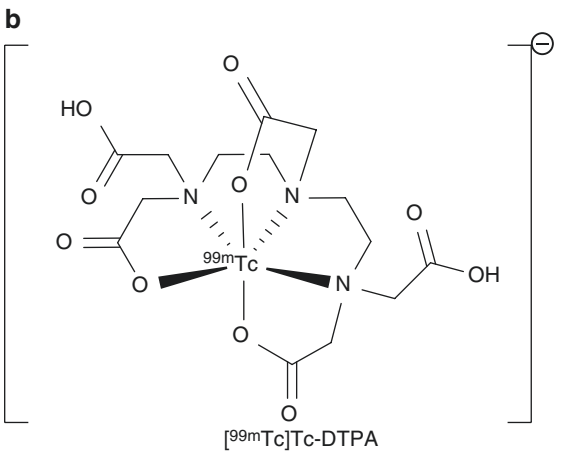

[^{99m}Tc]Tc-DTPA

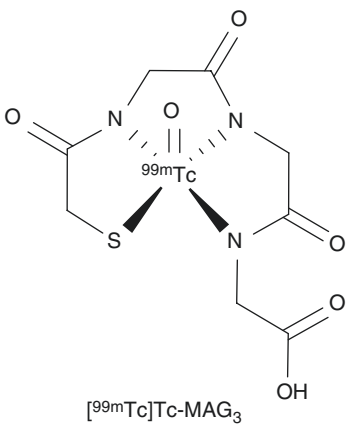

[^{99m}Tc]Tc-MAG_3

Fig. 5 Three ^{99m}Tc-labeled agents used in renal function testing:
(**a**) [^{99m}Tc]Tc-DMSA,
(**b**) [^{99m}Tc]Tc-DTPA, and
(**c**) [^{99m}Tc]Tc-MAG_3

evaluate kidney function, as patients with advanced renal failure will exhibit little renal uptake of the agent [36].

[^{99m}Tc]Tc-DTPA

[^{99m}Tc]Tc-DTPA (diethylenetriaminepentaacetate)—also known as [^{99m}Tc]Tc-Pentetate™—is also an approved radiopharmaceutical used for renal scintigraphy [34, 39, 40]. The product is obtained by adding [^{99m}Tc]TcO_4^- to vials containing diethylenetriaminepentaacetic acid (pentetic acid) as well as buffers, stabilizers, and stannous chloride dehydrate [34, 39, 40]. [^{99m}Tc]Tc-DTPA (Fig. 5b) is administered intravenously and used to assess renal perfusion and glomerular filtration rate. It also has applications for brain imaging, in which it is used to detect intracranial lesions associated with excessive neovascularity or a compromised blood-brain barrier (BBB) [39]. For renal studies, imaging is done within a few minutes of injection because the rapid excretion through the kidneys allows for the assessment of the glomerular filtration rate as well as renal blood flow.

[^{99m}Tc]Tc-MAG_3

[^{99m}Tc]Tc-MAG_3 (^{99m}Tc-mercaptoacetyltriglycine) is a radiopharmaceutical sold under the name of TechneScan MAG_3™ that is also utilized to assess kidney function, notably renal failure and urinary tract obstruction [40–42]. [^{99m}Tc]Tc-MAG_3 renograms are often performed on kidney donors prior to kidney transplantation to evaluate the health of a donor kidney. It is obtained in a kit for formulation with each vial containing a lyophilized and sterile mixture of the ligand, reducing agent, and buffers to maintain a pH between 5 and 6 during labeling [34, 41]. [^{99m}Tc]Tc-MAG_3 is a tetradentate, monooxo complex of Tc(V), and mercaptoacetyltriglycine (Fig. 5c). Like [^{99m}Tc]Tc-DMSA, the mechanism of [^{99m}Tc]Tc-MAG_3 is predicated on the ability of the complex to bind plasma proteins [41, 43]. This binding is reversible, and the unbound complex is cleared quickly from the blood. Healthy individuals have a faster clearance rate in comparison with patients with impaired renal function. Unlike [^{99m}Tc]Tc-DMSA, which stays as a protein-bound complex for imaging purposes, the reversible protein binding and clearing of [^{99m}Tc]Tc-MAG3 from the blood are utilized for assessment of renal function. Thus, the presence of the free hydrophilic metal complex in the blood and subsequent glomerular filtration through the kidneys with active tubular secretion provides data on kidney function and areas of obstruction [41, 44]. The clearance of the compound is correlated with effective renal plasma flow, with 40–50% of the injected dose extracted by the proximal tubules by 5 min post-injection. Almost 90% of the injected dose is cleared via the renal system within 3 h of injection [41].

Other Imaging Agents

[^{99m}Tc]TcO_4^-

Pertechnetate ([^{99m}Tc]TcO_4^-) (Fig. 6a) is used in conjunction with other imaging agents—notably [^{99m}Tc]Tc-sestamibi and [^{201}Tl]TlCl—for the detection of thyroid cancer, via parathyroid scintigraphy [24, 34]. It is taken up by functional thyroid tissue through the Na^+/I^- symporter in a manner similar to iodide due to the similar ionic radii and charge [34, 45]. This pertechnetate "background" signal can be subtracted from the ^{99m}Tc-sestamibi or [^{201}Tl]TlCl scans to identify the diseased tissue corresponding to parathyroid carcinoma [24, 34].

[^{99m}Tc]Tc-Exametazime

[^{99m}Tc]Tc-Exametazime (Ceretec™) is an approved radiopharmaceutical used to detect altered regional cerebral perfusion in patients suffering from various cerebrovascular diseases [46, 47]. In addition, it can be used to label leukocytes for the localization of abdominal infections and inflammatory bowel disease [48]. [^{99m}Tc]Tc-Exametazime is a neutral Tc(V) complex of (RR,SS)-4,8-diaza-3,6,6,9-tetramethyl-undecane-2,10-dione bisoxime—a ligand commonly referred to as hexamethyl propylene amine oxime (HMPAO)—that exists as a mixture of D and L enantiomers (Fig. 6b). [^{99m}Tc]Tc-Exametazime is lipophilic and is thus able to cross the BBB, where it is converted by hydrolysis (at approximately 12% per hour) to a charged, hydrophilic complex that cannot recross the BBB, resulting in the intracerebral accumulation of the radiotracer [23, 46]. The activity concentration in the brain reaches a maximum of 3.5–7.0% of the injected dose within 1 min of injection, and up to 15% of the retained activity is cleared from the brain by 2 min after injection. Otherwise, moderate uptake is found throughout the body in muscle and soft tissue, with 50% and 40% of the injected dose being cleared via the hepatobiliary and renal systems, respectively.

[^{99m}Tc]Tc-DISIDA

[^{99m}Tc]Tc-DISIDA (diisopropyl iminodiacetic acid)—also known as [^{99m}Tc]Tc-disofenin (Hepatolite™)—is a metal complex of iminodiacetic acid that is used for imaging the hepatobiliary tract, gallbladder, and bile ducts (Fig. 6c) [49–51]. Prior to the advent of [^{99m}Tc]Tc-disofenin, another ^{99m}Tc-based radiopharmaceutical, [^{99m}Tc]Tc-dimethyl acetanilide iminodiacetic acid ([^{99m}Tc]Tc-HIDA), was used for these applications. The two radiotracers are derived from ligands that have the same group bound to ^{99m}Tc, though they differ structurally in the nature of the substituents. [^{99m}Tc]Tc-disofenin is currently used in a test that is anachronistically referred to as a "HIDA scan" [49, 50]. [^{99m}Tc]Tc-DISIDA

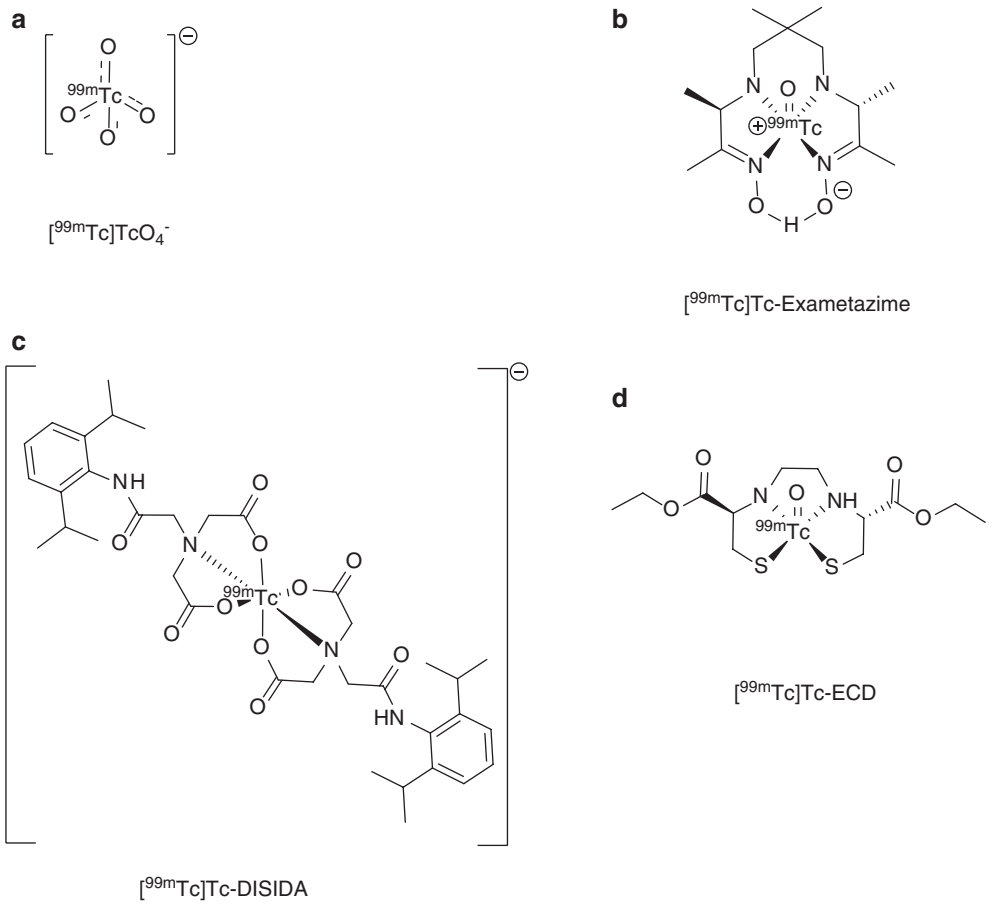

Fig. 6 Common ^{99m}Tc-labeled compounds used in nuclear medicine: (**a**) [^{99m}Tc]TcO_4^-, (**b**) [^{99m}Tc]Tc-exametazime, (**c**) [^{99m}Tc]Tc-DISIDA, and (**d**) [^{99m}Tc]Tc-ECD

is used for the diagnosis of gallbladder disease, as it rapidly clears from the liver to the gallbladder. The ^{99m}Tc complex binds to albumin resulting in decreased renal clearance and increased hepatic accumulation. Following uptake into the hepatocytes, the metal dissociates from the chelator. Patients are imaged for approximately 1 h following the administration of the radiotracer in order to track the production and flow of bile from the liver first to the gall bladder and then to the intestines [50, 51]. In the absence of gallbladder disease, the gallbladder is visualized within an hour; the lack of uptake in the gallbladder past 4 h is indicative of disease, the presence of gallstones, or the obstruction of the bile duct.

[^{99m}Tc]Tc-ECD

[^{99m}Tc]Tc-ECD (ethylene cysteine dimer; Neurolite™) is an approved radiopharmaceutical that is used for brain imaging in patients that have had a stroke [40, 52, 53]. This radiopharmaceutical is a stable and lipophilic complex that can pass through the BBB via passive diffusion. [^{99m}Tc]Tc-ECD is a neutral, square pyramidal complex containing a $[Tc(V)O]^{3+}$ core and a diaminedithiol ligand (Fig. 6d) [23]. The L,L stereoisomer crosses the cell membrane of brain cells in which it is metabolized via ester hydrolysis to create more polar and less diffusible compounds [52, 53]. If, on the other hand, the metal complex is hydrolyzed prior to crossing the BBB, the resulting metal-bound dicarboxylate anion is excreted via the renal system [23]. At 1 h post-injection, little activity remains in the blood. The uptake of [^{99m}Tc]Tc-ECD in the brain is cleared in a bi-exponential decay, with 40% of the activity being cleared with a 1.3-h half-life, and the remaining 60% cleared slowly with a half-life of 42.3 h [54]. By 2 h, 50% of the injected dose is cleared through the renal system, reducing background signals. SPECT imaging of the brain can begin 10 min following the administration of the radiotracer but should be performed 30–60 min postinjection to acquire optimal images [52]. The related complex, [^{99m}Tc]TC-ethylene dicysteine, [^{99m}Tc]Tc-EC, which is also a metabolite of [^{99m}Tc]Tc-ECD, is used to assess renal function and provides scintigraphy data equivalent to that obtained by [^{99m}Tc]Tc-MAG_3 [40]. [^{99m}Tc]Tc-EC is cleared through active tubular transport, allowing for the assessment of renal clearance in patients with suspected or known renal

failure. [^{99m}Tc]Tc-EC can be produced directly using an instant kit [40].

^{99m}Tc-Sulfur Colloid

^{99m}Tc can be used to label sulfur-based colloids to detect lymph node metastases associated with breast cancer as well as and to image peritoneovenous shunt patency, gastroesophageal reflux, and functional reticuloendothelial cells in the spleen, bone marrow, and liver [55, 56]. The product is obtained from a lyophilized mixture of anhydrous sodium thiosulfate, EDTA, and gelatin [55]. Mixing the contents of this kit with [^{99m}Tc]TcO_4^- and adjusting the pH with mixtures of NaOH and HCl results in the formation of the ^{99m}Tc-sulfur colloids for which the optimal size range is 15–100 nm [56]. ^{99m}Tc-sulfur colloid is administered differently depending on intended use. For lymphatic mapping, they are injected subcutaneously into the tissue surrounding the tumor [57]. When administered by intraperitoneal injection, ^{99m}Tc-sulfur colloid mixes with the peritoneal fluid, and its rate of clearance from the peritoneal cavity is used to evaluate peritoneovenous shunt patency [55]. When ^{99m}Tc-sulfur colloid is administered orally, it enters the gastroesophageal tract, allowing for gastric scintigraphy [55]. And finally, when administered intravenously, the uptake of the ^{99m}Tc-sulfur colloid in the reticuloendothelial system of the liver and spleen is dependent on the blood flow and the number and function of the phagocytic cells.

Tricks of the Trade: Practical Technetium Chemistry

The following section contains descriptions of selected practical procedures and calculations routinely used by researchers working with ^{99m}Tc. These were chosen by graduate students for new students interested in developing ^{99m}Tc radiopharmaceuticals.

Eluting a ^{99}Mo/^{99m}Tc Generator

To obtain [^{99m}Tc]TcO_4^- from a ^{99}Mo/^{99m}Tc generator, a sealed vial containing 0.9% (9 mg/mL) saline is placed on the inlet needle at the top of the generator (see Fig. 1b(c)). Next, an evacuated vial (which often comes with the generator) is situated in a lead container and placed on the collection inlet needle (see Fig. 1b(d)). Once the needle has pierced the collection vial, the saline from the stock vial will travel through the generator "carrying" the [^{99m}Tc]TcO_4^- into the collection vial. Once emptied, the saline vial can be removed followed by the collection vial. At this point, the needles should be wiped with a tissue or a suitably absorbent material held using tweezers, making sure to wipe the saline needle first. The storage caps should then be placed on the inlet needles until the next elution, and the amount of activity in the sample measured using a dose calibrator.

Determining the Mass of ^{99m}Tc

Understanding the amount of material you are working with when labeling compounds is a critical part of radiochemistry. To determine the amount of technetium in a sample, you simply need to know the half-life of the radionuclide and the amount of activity present in the sample. A sample calculation shown in Fig. 7a highlights the relationship between half-life, activity, and the amount of material in a sample. Another widely used term is specific activity (A_s), which is the amount of activity per unit of mass of a sample [23]. A_s is typically expressed in Ci/g or Bq/g, and a sample calculation for the specific activity in a 3.7×10^8 Bq sample of [^{99m}Tc]Tc-MDP is shown in Fig. 7b. Note that there is another term, effective specific activity, which is defined as the specific activity divided by the amount of ligand present in the sample. This is a critical factor which is often erroneously used interchangeably with specific activity. For targeted radiopharmaceuticals, the presence of too much unlabeled ligand can result in competition between the said ligand and the radiotracer for binding to the target. On the other hand, however, effective specific activities that are *too* high can result in nonspecific binding and low uptake at the desired target or a compound that has poor stability (*e.g.* [^{99m}Tc]Tc-MDP) [23].

The Preparation of ^{99m}Tc Complexes

The predominant method for the preparation of ^{99m}Tc-based radiopharmaceuticals is to combine [^{99m}Tc]TcO_4^- with a reducing agent and a suitable ligand [58]. The yield and nature of the product are greatly influenced by several factors, including the identity and concentration of the ligand, the identity and concentration of the reducing agent, temperature, and pH. As discussed previously, a wide array of ligands and labeling conditions have been reported for the synthesis of ^{99m}Tc complexes, and a selection of commonly used methods is provided below [6, 59–62]. Note that when preparing novel ^{99m}Tc complexes, graphs of yield versus key factors (*e.g.* pH, temperature, ligand concentration, time, *etc.*) should be generated to help identify the optimal labeling conditions.

Tc(V) Complexes of Hydrazinonicotinic Acid (HYNIC)

One of the more prevalent oxidation states of ^{99m}Tc in radiopharmaceuticals is ^{99m}Tc(V). Here, stannous chloride ($SnCl_2$) has proven to be an effective and biocompatible reducing

a

$$\text{half life} = \tau_{1/2} = \frac{\ln 2}{\lambda}$$

$$\text{Decay Constant} = \lambda = \frac{\ln 2}{21600\,\text{sec}}$$

$$= 3.2 \times 10^{-5}\,{}^{1}\!/_{\text{sec}}$$

$$\text{Activity in Sample} = A = 10\,\mu\text{Ci}$$

$$1\text{Ci} = 3.7 \times 10^{10}\,\text{Bq}$$

$$A = 10\,\mu\text{Ci} = 1.0 \times 10^{-5}\,\text{Ci}/3.7 \times 10^{10}$$

$$= 3.7 \times 10^{5}\,\text{Bq}$$

$$A = N\lambda$$

$$\text{Number of moles} = N = \frac{A}{\lambda}$$

$$= \frac{3.7 \times 10^{5}\,\text{Bq}}{3.2 \times 10^{-5}\,{}^{1}\!/_{\text{sec}}}$$

$$= 1.2 \times 10^{10}$$

$$\text{Moles} = n = \frac{N}{N_A}$$

$$= \frac{1.2 \times 10^{10}}{6.022 \times 10^{23}}$$

$$= 1.99 \times 10^{-14}\,\text{mol}$$

$$= 0.02\,\text{pmol}$$

b

$$\lambda = \frac{\ln 2}{\tau_{\frac{1}{2}}}$$

$$= \frac{\ln 2}{21600\,\text{sec}}$$

$$= 3.2 \times 10^{-5}\,{}^{1}\!/_{\text{sec}}$$

$$A = N\lambda$$

$$\text{Activity} = 10\,\text{mCi} = 3.7 \times 10^{8}\,\text{Bq}$$

$$N = \frac{A}{\lambda}$$

$$= \frac{3.7 \times 10^{8}\,\text{Bq}}{3.2 \times 10^{-5}\,{}^{1}\!/_{\text{sec}}0}$$

$$= 1.2 \times 10^{13}$$

$$n = \frac{N}{N_A}$$

$$= \frac{1.2 \times 10^{13}}{6.022 \times 10^{23}}$$

$$= 1.99 \times 10^{-11}\,\text{mol}$$

$$m = n \times MW_{\text{Tc-MDP}}$$

$$= 1.99 \times 10^{-11}\,\text{mol} \times 274.907\,{}^{\text{g}}\!/_{\text{mol}}$$

$$= 5.47 \times 10^{-9}\text{g}$$

$$\text{Specific Activity} = A_s = \frac{A}{m}$$

$$= \frac{3.7 \times 10^{8}\,\text{Bq}}{5.47 \times 10^{-9}\,\text{g}}$$

$$= 1.83 \times 10^{6}\,\text{Bq/g}$$

Fig. 7 Example calculations for ^{99m}Tc-labeled compounds. (**a**) Sample calculation showing the amount of ^{99m}Tc in 10 μCi and (**b**) sample calculation showing the theoretical specific activity of [^{99m}Tc]Tc-MDP

agent for the conversion of pertechnetate into ^{99m}Tc(V) complexes. As a result, $SnCl_2$ is currently used in several kits for the commercial production of [^{99m}Tc]Tc-DMSA, [^{99m}Tc]Tc-ECD, [^{99m}Tc]Tc-DTPA, [^{99m}Tc]Tc-exametazine, and [^{99m}Tc]Tc-tetrofosmin [30, 36, 39, 46, 52, 63].

The reduction of [^{99m}Tc]TcO_4^- with $SnCl_2$ in the presence of bifunctional ligands and their biomolecular conjugates has also been widely used to prepare targeted radiopharmaceuticals. For example, hydrazinonicotinic acid (HYNIC) readily forms stable complexes with ^{99m}Tc(V) and, as a result, was developed as a convenient way to introduce a ^{99m}Tc-binding chelating group into proteins and peptides [64]. As HYNIC does not occupy the entire coordination sphere of the metal, co-ligands such as tricine and ethylenediamine diacetic acid are often added to radiolabeling reactions involving HYNIC-bearing bioconjugates [65, 66]. Methods for the conjugation of HYNIC to biomolecular vectors have been well established in the literature and typically rely upon the use of a bifunctional variant of HYNIC that has an amine-reactive functionality. Once prepared, typical labeling conditions involve the incubation of the HYNIC ligand (3–100 μg), a co-ligand (5–50 mg), and stannous chloride (50–200 μg) for 15–30 min either at room temperature (for sensitive proteins) or 100 °C (for thermally robust molecules) [64, 66–70]. HYNIC labeling yields are generally high, and impurities can be identified using iTLC or HPLC [64, 67].

[^{99m}Tc][Tc(CO)$_3$]$^+$ Complexes

[^{99m}Tc]Tc(I) complexes have also become commonplace in the literature as a result of the ease with which a unique organometallic precursor—[^{99m}Tc][Tc(CO)$_3$(H$_2$O)$_3$]$^+$—can be prepared from pertechnetate in aqueous solutions [71–73]. This synthon is highly useful not only because the carbonyl ligands create a remarkably stable complex but also because the water ligands can be replaced by a variety of donor groups, enabling the formation of a large number of different Tc(I) complexes [17, 74–79]. [^{99m}Tc][Tc(CO)$_3$(H$_2$O)$_3$]$^+$ is formed via the reaction of [^{99m}Tc]TcO_4^- and potassium boranocarbonate ($K_2[BH_3CO_2]$), which acts as both a reducing agent and a source of carbonyl ligands. In the presence of the appropriate buffers, high yields of [^{99m}Tc]

$[Tc(CO)_3(H_2O)_3]^+$ can be obtained in a single step (Table 2). In order to reduce the time required for preparation, these reagents can also be heated in a microwave following purging with argon for 10 min. It is important to note that only a microwave approved for laboratory use should be employed [71, 72, 75, 80–82]. This microwave procedure facilitates the formation of $[^{99m}Tc][Tc(CO)_3(H_2O)_3]^+$ in quantitative yields in only 3.5 min when the reaction is performed at 110 °C [72]. After the reaction is complete, the pH of the $[^{99m}Tc][Tc(CO)_3(H_2O)_3]^+$ solution should be adjusted using 1 M HCl since the reaction solution is highly basic.

Table 2 Roles of each reagent in the preparation of $[^{99m}Tc]Tc[(CO)_3(H_2O)_3]^+$

Reagent	Role
Potassium boranocarbonate ($K_2[BH_3CO_2]$)	Reducing agent, solid source of CO
Sodium carbonate (Na_2CO_3) and sodium tetraborate decahydrate ($Na_2B_4O_7{\cdot}10H_2O$)	Buffers, where optimal pH is 8.0.
Potassium sodium tartrate $KOCO[CH(OH)]_2COONa{\cdot}4H_2O$	Stabilizes ^{99m}Tc-complexes of intermediate oxidation states

$K_2[BH_3CO_2]$—first reported by Alberto and colleagues—is a critical component for the preparation of complexes containing the $[^{99m}Tc]Tc[(CO)_3]^+$ synthon [83]. The experimental setup used to prepare this unique reagent is shown in Fig. 8. First, carbon monoxide gas is passed through 1 M KOH and subsequently a column containing a calcium sulfate drying agent to remove any residual water (flask A). The gas is then passed into a solution of 1.0 M $BH_3{\cdot}THF$ (flask B) which is cooled in an ice bath to 0 °C and connected to an ammonia condenser that is cooled to −60 °C using dry ice in acetone. The ammonia condenser allows for the THF to be condensed and remain in flask B, while the gaseous $BH_3{\cdot}CO$ can travel to flask C, where it is passed through a solution of KOH in ethanol for 5 h at −80 °C to produce $K_2[BH_3CO_2]$, which precipitates from the solution. The solution is allowed to warm to room temperature, and $K_2[BH_3CO_2]$ is collected by filtration and washed with cold ethanol. The isolated $K_2[BH_3CO_2]$ is then dried under vacuum, leaving a white solid which can be stored at room temperature and used for several months. Prior to the preparation of this material, readers should refer to the original publications for important details regarding the method and hazards [72, 75, 79, 83].

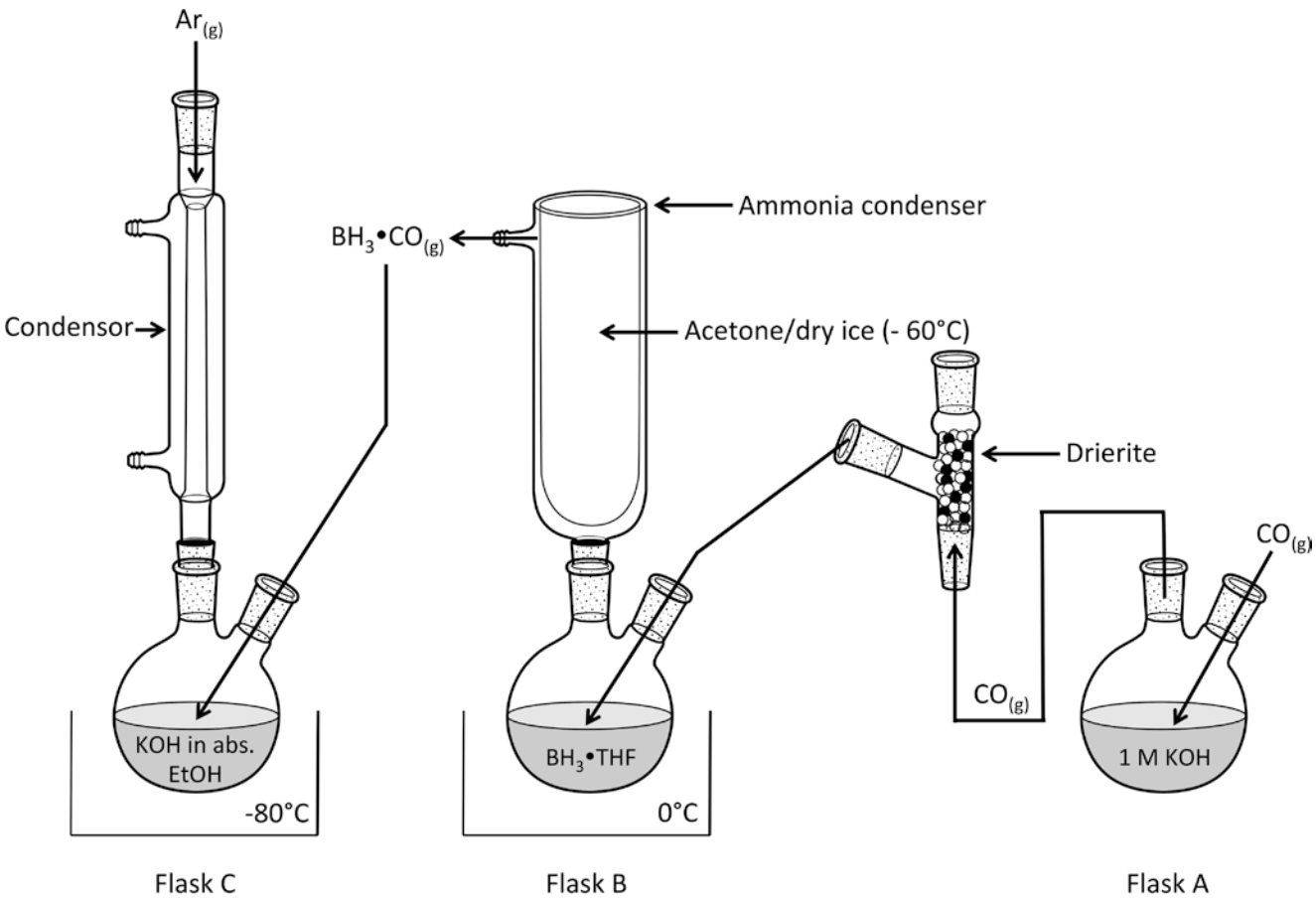

Fig. 8 Reaction setup for the synthesis of $K_2[BH_3CO_2]$

Preparing ^{99m}Tc Compounds for Biodistribution Studies

Once a ^{99m}Tc complex has been prepared, there are several studies that should be performed prior to assessing the performance of the complex *in vivo*. First, the purity of the ^{99m}Tc-labeled complex must be confirmed using HPLC and radio-TLC, and the structure of the product should be verified, preferably using a fully characterized rhenium (or ^{99}Tc) reference standard. When determining the purity of a ^{99m}Tc complex by HPLC, it is important to use two different elution methods or columns. Ideally, the compound should have a radiochemical purity greater than 95%, with no single impurity in an abundance higher than 1%. Once the optimal radiosynthesis conditions have been determined and the desired product obtained, the yield and reproducibility of the synthesis for the ^{99m}Tc complex should be assessed using a minimum of three independent labeling experiments. If yields vary by more than 5–10%, the conditions should be further optimized to ensure the robustness of the reaction.

Two common impurities that can form during the preparation of ^{99m}Tc complexes are $[^{99m}Tc]TcO_4^-$ and colloidal $[^{99m}Tc]TcO_2$. The latter is often a result of conditions in which the ligands do not form adequately stable complexes with ^{99m}Tc, the ligands are poorly soluble, or the amount of the ligand and reducing agent is not optimal. Residual $[^{99m}Tc]TcO_4^-$ can result from cases in which insufficient amounts of the reducing agent have been added, the reducing agent decomposes, or the metal complex itself decomposes. The quality of the reducing agent should be checked if labeling yields are low or highly variable. RadioTLC is a convenient way to identify the presence of colloidal $[^{99m}Tc]TcO_2$ and $[^{99m}Tc]TcO_4^-$ [31]. A simple procedure to assess the presence of both compounds is provided in Table 3.

Once the purity and nature of a ^{99m}Tc-labeled compound have been confirmed, the product must be formulated in an appropriate biocompatible solvent (*e.g.* 0.9% saline, PBS) prior to administration to a test animal. Solvents should be pharmaceutical grade and preferably passed through a microporous filter (0.2 μm) before use. A general checklist for formulating a compound for testing in preclinical models is provided in Fig. 9a. However, additional regulations regarding formulation may be also required by an institution's animal ethics committee.

Table 3 TLC conditions for the separation of chelate complexes of ^{99m}Tc, $[^{99m}Tc]TcO_2$ colloid and $[^{99m}Tc]TcO_4^-$

TLC plate	Eluent	Location of $[^{99m}Tc]TcO_2$ colloid	Location of $[^{99m}Tc]TcO_4^-$	Typical location of ^{99m}Tc-chelate
iTLC-SG glass microfiber chromatography paper	Acetone	Baseline	Solvent front	Baseline
	Distilled water	Baseline	Solvent front	Solvent front

Because of the small molar amounts of material being handled, ^{99m}Tc-labeled complexes can adhere to surfaces. As a result, adhesion ("stickiness") testing should also be performed to ensure that novel ^{99m}Tc-compounds do not bind to surfaces, including—and most frustratingly—the syringe at the time of injection. To test this, the optimal formulation and concentration of activity for injection should be drawn into the exact type of syringe to be used during the administration of the radiopharmaceutical to the animal. Ideally, this should be done in triplicate, with the activity in each syringe measured in a dose calibrator and the volume and amount of activity recorded. The dose should then be dispensed into a vial, and the residual activity in the syringe and vial should be measured. The amount of activity remaining in the syringe should be less than 10% of the total activity. If the amount of activity in the syringe is >10%, the formulation should be adjusted accordingly. There are several options available for reducing adherence, including the addition of a surfactant (*e.g.* Polysorbate 80), 0.5% BSA, or a small amount of a biocompatible solvent (*e.g.* 1–5% ethanol, 0.1–2% DMSO).

Once the final formulation has been determined, the next step is to perform stability testing. This requires incubating the complex in the formulation solution at 37 °C for up to 24 h and checking the purity of the sample at various time points using either iTLC or HPLC. The fraction of intact compound should be calculated at each time point to determine the rate of the decomposition process. The time between formulation and injection should not exceed a window during which the compound remains ≥95% pure.

The lipophilicity of the compound should also be measured. The lipophilicity of a new imaging agent is an important aspect in predicting and understanding its absorption and binding to plasma proteins as well as in guiding the further optimization of its pharmacokinetics [84]. The log *P* value of a compound is a measure of its partition coefficient between water and 1-octanol and can be calculated using the "shake flask" method [84]. In this method, equal amounts of the ^{99m}Tc complex are dissolved in three vials containing equal parts 1-octanol and water, and these vials are placed on a shaker for 20 min. Following the agitation, the vials are centrifuged, and fractions are taken from each layer and transferred to pre-weighed tubes suitable for use in a gamma counter. The log *P* value for the compound can then be calculated by dividing the mass of the solution in each of the tubes by the counts per minute (CPM) values obtained from a gamma counter. Note that it is important to follow the detailed procedure described in the paper by Wilson *et al.* [82, 84] in order to understand the limitations of the method and to ensure reproducible and accurate results.

Given that there are endogenous ligands that can promote the transmetalation of ^{99m}Tc from a radiopharmaceutical,

a

- ❑ Removal of all non-biocompatible salts
- ❑ Removal of all non-biocompatible solvents
- ❑ Prepared in sterile biocompatible solvent (i.e. saline, PBS)
- ❑ Contain less than 10% EtOH, or 1% DMSO in final formulation (if appropriate)
- ❑ Ensure pH is within the range 6-8
- ❑ Osmolality should be >450 mOsm/kg

b

- ❑ Mouse/small animal restraint device and/or anesthetic machine
- ❑ Alcohol wipes
- ❑ 30 gauge needles (2 per mouse)
- ❑ 25 gauge needles (2 per mouse)
- ❑ 1 ml polycarbonate syringes (2 per mouse)
- ❑ Lead containers for transport of ^{99m}Tc complexes
- ❑ Dose calibrator, calibrated for ^{99m}Tc
- ❑ Gamma counter, set for ^{99m}Tc
- ❑ Gamma tubes with caps and tube racks (one tuber per organ/tissue, per mouse, pre-weighed and recorded)
- ❑ Analytical balance
- ❑ 2 sets of forceps (1 fine tip, 1 regular tip)
- ❑ 1 pair of surgical scissors
- ❑ 1 beaker of PBS (for rinsing tissues/organs)
- ❑ Paper towels
- ❑ Anesthetic (i.e. isoflurane, ketamine, etc.)
- ❑ Oxygen tank or medical air
- ❑ Documentation records (notebooks with tables) prepared in advance

Fig. 9 Practical checklists for *in vivo* studies. (**a**) Checklist for formulating a compound for testing in preclinical models and (**b**) checklist of standard equipment and supplies required for a biodistribution study

ligand challenge experiments are also valuable when developing novel ^{99m}Tc-based agents. Two common tests are the cysteine and histidine challenges, in which the purified and formulated ^{99m}Tc complex is incubated separately with 2 mM cysteine or 2 mM histidine—the approximate concentration of these ligands in the blood—in PBS (pH 7.4) at 37 °C, typically for 6 h [85]. The stability of the ^{99m}Tc complex can be monitored at selected time points (typically hourly) using HPLC or iTLC [75, 86]. The appearance of new peaks and changes in retention time or peak shape versus that of the purified ^{99m}Tc complex would suggest that the metal complex may not have adequate stability for use *in vivo*.

For targeted radiopharmaceuticals, the next step is typically *in vitro* cell binding studies. The goal here is to test the ability of new ^{99m}Tc complexes to bind to a specific target that is overexpressed as a result of disease or injury. Although the experimental aspects of these studies vary depending on the nature of the target and targeting ligand, a commonly used approach involves the incubation of the formulated ^{99m}Tc complex with a cell line that overexpresses the target of interest. As a control to ensure binding is not due to non-specific, non-selective, or off-target binding, blocking studies are performed with increasing concentrations of a ligand that is known to bind the target of interest. Alternatively, substitution of the cell line for one that does not express the target can also be used as a control.

Biodistribution Studies

Once all of the appropriate formulation, stability, and *in vitro* testing studies have been completed, biodistribution and imaging studies can be performed. For the former, several time points will be needed to get an accurate picture of

the pharmacokinetic profile of the radiopharmaceutical, and multiple animals per time point are required to ensure reproducibility and address biological variability. The number of animals needed per study depends on the robustness of the model being used but typically lies between three and five animals per time point (see the chapter on "An Introduction to Biostatistics") [87]. With respect to timing, an early time point (5–30 min) should be taken to observe the initial distribution of the tracer as well as the activity concentration in the blood. Intermediate time points (1–2 h) should also be used to determine the clearance pathways, and finally, a later time point at least one half-life (6 h) following the administration of the tracer should be employed as well. However, the signal to background noise may not always be ideal at 6 h, so later time points such as 12 and 24 h can also be used, provided there is adequate activity remaining in the organs of interest.

The choice of animal model to evaluate new radiopharmaceuticals is a complex issue that requires careful consideration (see the Chapters on "Preclinical Experimentation in Oncology" and "Preclinical Experimentation in Neurology"). Once the ideal model has been chosen, it is important to realize that in the weeks leading up to a biodistribution study, the animals may need a specific diet (*e.g.* high fat, fasting, etc.) or other regimens to yield reproducible and representative results. All animal care and preparation should be in accordance with the animal care and use protocols of the research institution where the studies are performed. It is almost impossible to be *too* prepared for a preclinical biodistribution study. This is particularly true for scientists new to this field. Before beginning, it is essential to prepare materials akin to what is done in an operating room. A list of standard equipment and supplies for a biodistribution study can be found in the checklist in Fig. 9b. Students who are new to the field should consider repeating a biodistribution study of a known radiopharmaceutical (*e.g.* ^{99m}Tc-sestamibi) prior to working with an experimental agent, in order to ensure that their procedures and techniques are robust [88].

On the day of a biodistribution study, doses of the formulated ^{99m}Tc complex should be prepared along with standards for the gamma counter and dose calibrator. It is important to note that when labeling and purifying a ^{99m}Tc complex, excess radiopharmaceutical should always be prepared, because standards are certainly necessary and backup doses may be needed in the event of a problem. For the dose calibrator standard, the volume equivalent of a single dose should be used, and the activity of the standard and time of measurement should both be recorded. When preparing the gamma counter standards, small aliquots from the stock solution should be used (~18.5–37 kBq; 0.5–1 μCi) so as to not saturate the gamma counter. Replicates (typically 4–6) of the gamma standard should be prepared and measured to determine an average count value per unit of activity. The volume of the standards used should be recorded. It is also important to ensure that the gamma counter has been properly calibrated, that the dose calibrator has been maintained according to the manufacturer's directions, and that the limits of detection and linear dynamic ranges are known for both instruments.

When preparing doses, each dose should be placed in a separate syringe fitted with a new needle; a reused needle can quickly dull and make injections difficult. When drawing up a dose, it is also imperative to ensure that there are no air bubbles in the syringe or needle hub. The injection volume should be no more than 20% of the total blood volume of the mouse. A formula for calculating the blood volume of a mouse as a function of its weight is shown below, where 0.049 is the percent of total body mass attributed to the blood [89].

$$\text{Blood volume}(\text{mL}) = \text{body weight}(\text{g}) \times 0.049$$

At the chosen time points for the biodistribution study, the mice of each cohort should be euthanized according to the protocols outlined by the institution where the experiment is being performed [72]. Subsequently, the blood of the mice can be collected via cardiac puncture, and the other organs and tissues can be removed, washed in saline or PBS, and dried before transfer to pre-weighed tubes for gamma counting. The weight of each filled tube should then be recorded, and then the tubes containing the organs, tissues, and standards can be loaded onto the gamma counter. Following the counting of the samples, the gamma counter will print or display the counts from each gamma tube, typically reported as counts per minute (CPM). Measuring the gamma counter standards at the same time as the organs and tissues removes the need for decay correction, as this correction will be integrated into the CPM/μCi calculation. After determining the average CPM values for the standards, the volume of the dose calibrator standard should be divided by the volume of the gamma counter standard. Using these calculated values and the activity of the dose calibrator standard, the following formula can be used:

$$\frac{(\text{Average gamma standard CPM}) \times \left(\dfrac{\text{volume dose cal standard}}{\text{volume gamma standard}} \right)}{\text{Dose cal standard activity}} = \frac{\text{CPM}}{\mu\text{Ci}}$$

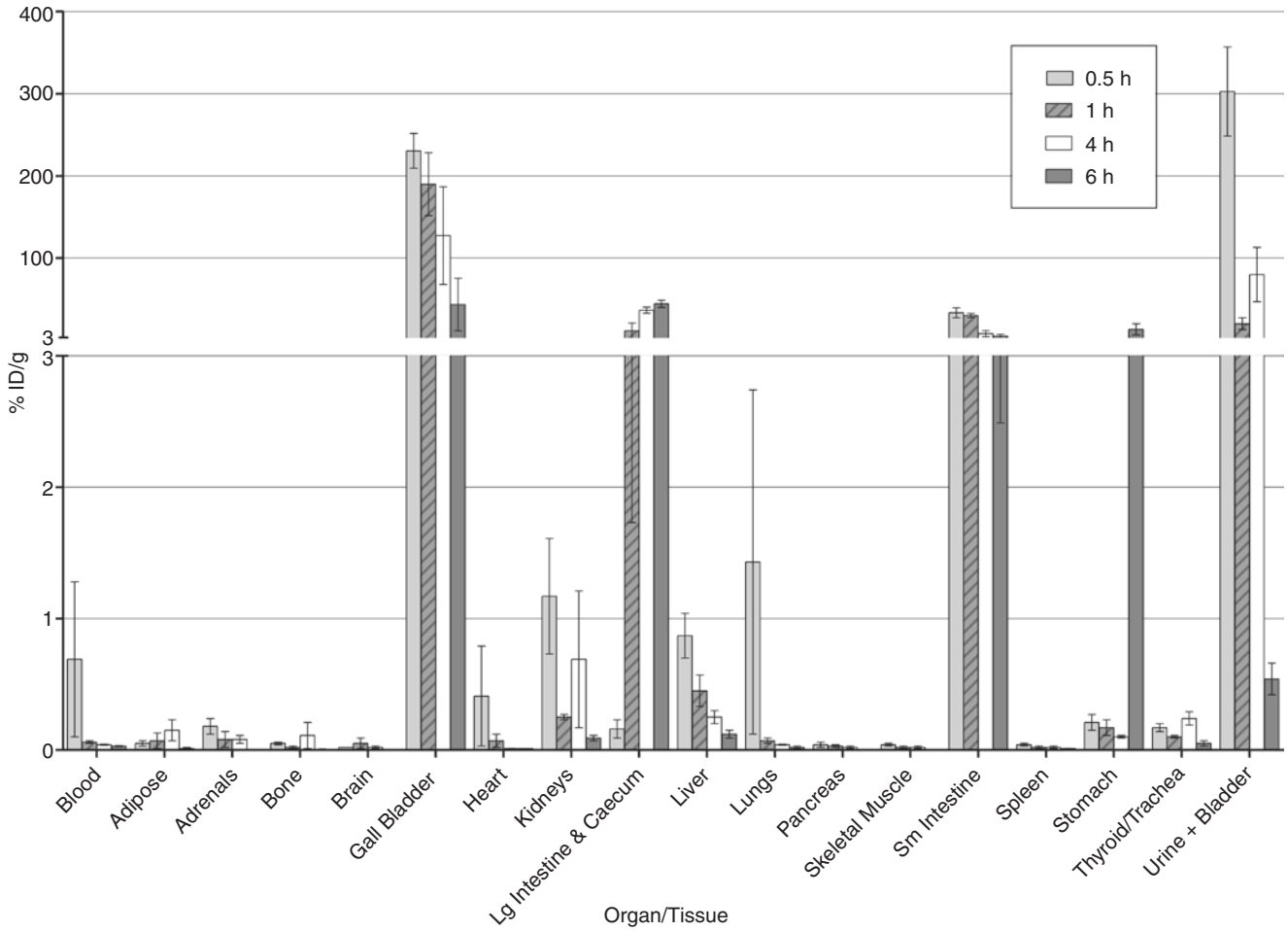

Fig. 10 Example biodistribution study results. Typical graph of biodistribution data. These results were for a ^{99m}Tc-labeled tetrazine, and the animals (Balb/c mice) were sacrificed at 0.5, 1, 4, and 6 h post-injection (n = 3 mice). Activity was normalized to the weight of various tissues or fluids (x-axis), as mean percent injected dose per gram of tissue or fluid (%ID/g) ± SEM (y-axis) (From Bilton *et al.* [72], with permission)

Using this calculated value, the raw CPM values of each organ/tissue can be converted to μCi/organ

$$\frac{\text{Organ CPM value}}{\text{Standard CPM} / \mu\text{Ci}} = \mu\text{Ci} / \text{organ}$$

After obtaining these values, the amount of activity can then be divided by the total activity injected, giving the percent injected dose (%ID) per organ. This value can further be divided by the mass of each tissue, organ, or fluid to give the normalized value reported as %ID/g.

When reporting biodistribution data, graphs of the %ID/g and the %ID per tissue/fluid are typically generated (Fig. 10). The former is especially important, as it gives a sense of the amount of activity normalized to the weight of the organ/tissue. Note also that high and unexpected activity concentrations in the liver, lung, and spleen can indicate the presence of colloidal [^{99m}Tc]TcO_2 [90]. In contrast, the presence of [^{99m}Tc]TcO_4^-—which can be the result of poor labeling yields or decomposition—can produce high activity concentrations the stomach and thyroid.

Bifunctional Chelators and the Importance of Optimized Pharmacokinetics for Creating Next-Generation Targeted ^{99m}Tc Radiopharmaceuticals

Bifunctional Chelators for Developing Targeted ^{99m}Tc Radiopharmaceuticals

One would expect that the ideal nuclear properties, low cost, and prevalence of ^{99m}Tc would make it the leading medical radionuclide for the creation of new radiopharmaceuticals [91]. However, other diagnostic radionuclides—notably ^{18}F, ^{68}Ga, and ^{89}Zr—are playing a greater role in this regard. The reasons for this are multifaceted, but one major issue is

the difficulty in linking ^{99m}Tc to biomolecular targeting vectors without having a detrimental influence on the *in vivo* distribution of the parent biomolecule itself.

While a number of innovative strategies for labeling targeted vectors with ^{99m}Tc have been developed, none have become widely available in the clinic. When considering the development of new ^{99m}Tc-based radiopharmaceuticals, the design and optimization of the ligands for ^{99m}Tc are critical considerations. Much can be learned from work done on chelators for Tc(V) and Tc(I). For example, knowledge gained from the study of ^{99m}Tc(I) complexes was ultimately used to create a radiopharmaceutical for imaging the expression of prostate specific membrane antigen (PSMA) [81].

Chelators for Tc(V)

N_xS_y Tetradentate Chelators

Over the past several decades, there has been a tremendous body of work on developing bifunctional tetradentate chelators for Tc(V). These include mixed amine- and thiol-based chelators (N_xS_y, x + y = 4), most notably N_2S_2 [*e.g.* bis(aminoethanethiol) (BAT)] and N_3S [*e.g.* mercaptoacetylglycylglycylglycine (MAG_3)] variants (Fig. 11a, b) [62]. These ligands are extremely efficient at forming ^{99m}Tc complexes, and their radiometalation can be performed via a ligand exchange reaction with [^{99m}Tc]Tc-glucoheptonate or through direct reduction of pertechnetate. For example, technetium-labeled BAT complexes have been used to image targets in the brain, as they are capable of crossing the blood-brain barrier. ^{99m}Tc-labeled MAG_3 compounds, in contrast, can be used to prepare targeted radiopharmaceuticals and, as noted previously, to assess kidney function (see Fig. 11b) [42]. While substituted analogues of these ligands have been reported, these variants often form isomers, which can hinder translation because it may be necessary to assess the *in vivo* properties of each isomer (see Fig. 2).

Hydrazinonicotinamide (HYNIC)

HYNIC ligands were created as a convenient method for radiolabeling biomolecules with ^{99m}Tc (see the section on "The Preparation of ^{99m}Tc Complexes"). The active ester of HYNIC can readily be conjugated to small molecules and proteins, and the hydrazine donor can form a stable metal-nitrogen multiple bond complexes with ^{99m}Tc [60]. To occupy the remaining coordination sites, HYNIC—which can act as a monodentate ligand or a bidentate ligand with the added coordination of its pyridine nitrogen—requires co-ligands. These co-ligands create a convenient handle for fine-tuning the pharmacokinetic properties of the imaging agent by varying the polarity and charge of the additional ligands (Fig. 11c). A wide range of biomolecules have been labeled with HYNIC, but none have yet made it to routine clinical use. The reason for this lack of success remains unclear; however, it may be due to the absence of an optimal co-ligand.

Chelators for Tc(I)

As we have discussed, [^{99m}Tc][$Tc(CO)_3(H_2O)_3$]$^+$ can be used to prepare a wide range of chelator complexes via the substitution of the labile water ligands. Numerous examples of bidentate and tridentate chelators have been reported, including bifunctional derivatives that can be linked to targeting molecules [59, 92–94]. Tridentate chelators bearing nitrogen, oxygen, and sulfur donor groups and featuring a range

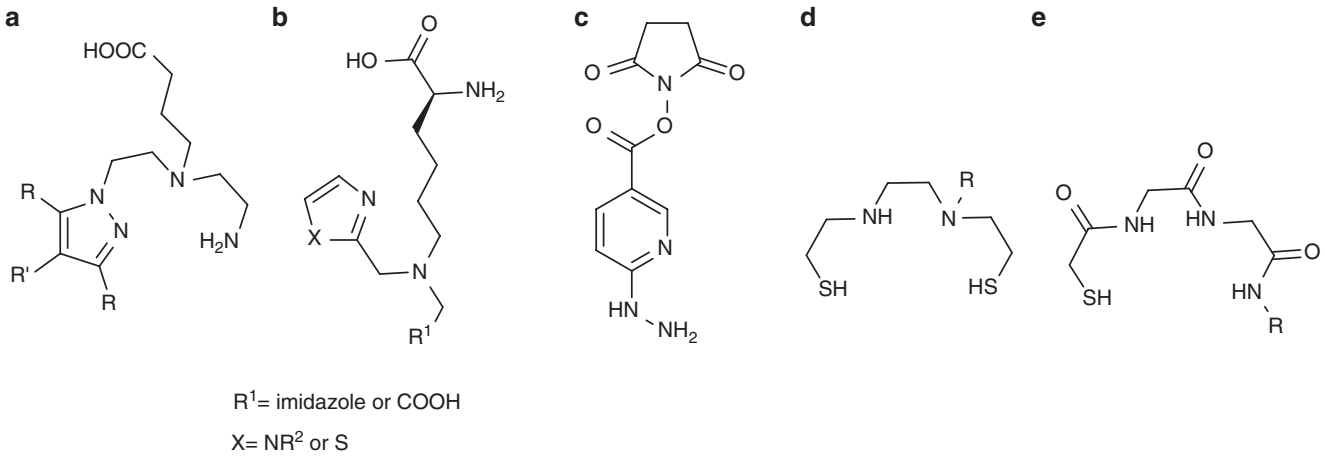

Fig. 11 Structures of different technetium chelators. (**a**) Pyrazole derivatives [94]; (**b**) single-amino-acid chelators [59]; (**c**) HYNIC [60]; (**d**) BAT [62]; and (**e**) MAG_3 [43]

of different heterocycles including pyridines, triazoles, imidazoles, and pyrazoles have been reported (see Fig. 11).

This chemical technology has been used to create many ^{99m}Tc(I)-based radiopharmaceuticals. Raposinho and colleagues, for example, designed a technetium probe to image the melanocortin-1 receptor through the functionalization of a peptidic α-melanocyte-stimulating hormone [94]. A cyclic peptide was synthesized and labeled with the $[^{99m}Tc][Tc(CO)_3]^+$ core through a variety of functionalized pyrazole-diamine chelators. Four pyrazole derivatives were tested, and it was found that the addition of a carboxylate group on the pyrazole ring significantly reduced the uptake of the imaging agent in the kidneys and liver compared to the parent compound (see Fig. 11a). More specifically, the addition of the carboxylate acid groups decreased the activity concentrations in the kidneys and liver by more than 89% and 91%, respectively, clearly demonstrating the sensitivity of these constructs to subtle changes in the structure of the chelator.

In analogous work, Pomper and coworkers synthesized a library of PSMA-targeted compounds and evaluated their uptake in murine models of prostate cancer [92]. The authors synthesized chelators based on quinolone and pyridine, and the ^{99m}Tc complex of the former suffered from high uptake in the liver. The pyridine derivatives, on the other hand, resulted in better clearance profiles, and their pharmacokinetic profiles were further improved by changing the nature of the spacer between the targeting molecule and the chelator.

It is undeniably time-consuming to synthesize a library of different chelators with various linker groups in order to optimize the pharmacokinetics of a ^{99m}Tc-labeled radiopharmaceutical. Nonetheless, when creating ^{99m}Tc-based imaging agents, it is important to ensure that the synthetic methods allow for the introduction of structural variations. For example, click chemistry has been used as a convenient means to create libraries of structurally diverse chelators for Tc(I) (Fig. 12) [6]. In this system—in which the additional two donor atoms are present on the molecule containing the alkyne—the N3 of the triazole ring coordinates the metal. This is termed a "regular" click ligand. If, one the other hand, the donor groups are on the azide, the N2 of the triazole will coordinate the metal. This, not surprisingly, is called an "inverse" click ligand. Both variants are easily synthesized and can be used to produce a variety of different chelators. However, it is important to note that the radiolabeling chemistry of these two constructs is different. For instance, "inverse" click ligands require 10^{-3}–10^{-2} M ligand to achieve quantitative labeling, while "regular" click ligands need only 10^{-5}–10^{-6} M. Moreover, ^{99m}Tc-labeled variants of bombesin bearing "inverse" click ligands showed reduced *in vivo* stability relative to analogues containing "regular" click ligands [6]. Mindt, Schibli and coworkers further exploited the "click-to-chelate" concept to prepare a variety of chelators through the use of functionalized L-propargylglycine and L-azido alanine [93].

Amino acids have also been widely used to introduce structural diversity into chelators for ^{99m}Tc(I) as well as help optimize the pharmacokinetic properties of bioconjugates [59]. For example, a class of compounds known as single amino acid chelators (SAACs) was developed using a lysine backbone that can be easily modified to introduce different heterocycles as donor groups (see Fig. 11b). These compounds are easy to prepare, and the products form robust complexes with Tc and Re in high yield. Unfortunately, the first generation of SAAC ligands was too lipophilic, resulting in high activity concentrations in the hepatobiliary system regardless of the biomolecular targeting vector. To circumvent this problem, Babich and coworkers modified the ligand to include more polar heterocycles [59]. Through the addition of a carboxylic acid-containing donor or an acetate-functionalized imidazole, the off-target binding of these bioconjugates was decreased dramatically. More specifically, these ^{99m}Tc-bearing compounds are typically eliminated through the kidneys and have low uptake in the hepatobiliary system. This study reinforces the notion that simple modifications to the structure of the chelator can have a dramatic influence on the distribution and effectiveness of ^{99m}Tc-labeled bioconjugates.

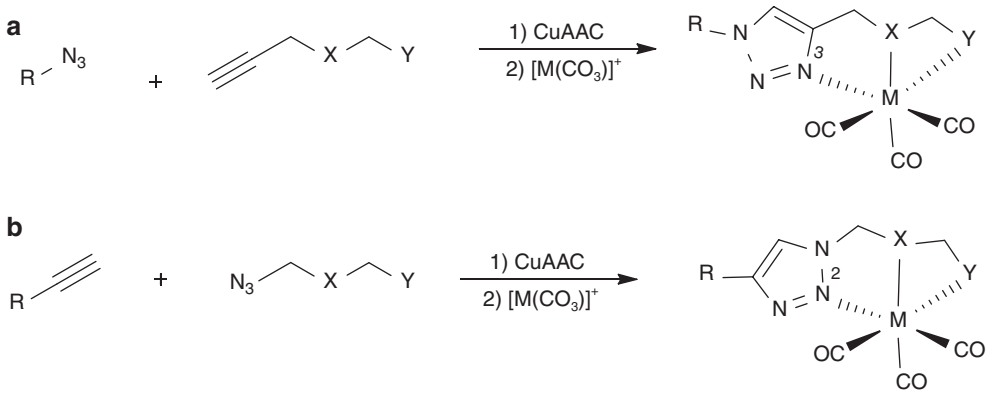

Fig. 12 Examples of the "click-to-chelate" concept [6]. (**a**) A "regular" click ligand and (**b**) an "inverse" click ligand. X and Y represent various donor atoms (*e.g.* O, N, S)

Next-Generation ^{99m}Tc Radiopharmaceuticals

^{99m}Tc-Labeled Radiopharmaceuticals that Target Prostate-Specific Membrane Antigen (PSMA)

Improvements in chelator design have led to the advent of a new generation of ^{99m}Tc-based radiopharmaceuticals. One recent example of this phenomenon is the emergence of a ^{99m}Tc radiopharmaceutical for imaging PSMA, a transmembrane protein that is overexpressed on prostate cancers [73]. By linking a suitable chelator for ^{99m}Tc(I) to a PSMA inhibitor, Babich and coworkers were able to produce an imaging agent with high tumor uptake and good clearance from nontarget tissue [81]. The product—which is called [^{99m}Tc]Tc-trofolastat and can be produced in an instant kit—has successfully completed a phase II clinical trial focused on the detection of intermediate- and high-grade prostate cancers prior to radical prostatectomy [95].

The development of [^{99m}Tc]Tc-trofolastat provides an excellent case study in the creation of a "next-generation" ^{99m}Tc-labeled radiopharmaceutical. Early in the development of [^{99m}Tc]Tc-trofolastat, two compounds composed of glutamate-urea inhibitors of PSMA, referred to in the literature as MIP-1404 and MIP-1405 (Fig. 13a, b), were prepared and used to visualize tumors in the prostate bed and metastatic disease in the bone and lymph nodes [73]. The chelators used in these imaging agents are both based on two imidazole derivatives and contain three nitrogen atoms bound to ^{99m}Tc(I); they differ in the pharmacokinetic modifying groups attached to the chelate. Each imidazole in MIP-1405 has one terminal carboxymethyl group, whereas MIP-1404 has a biscarboxymethyl amino-2-oxoethyl group attached to each heterocycle. In a comparative clinical trial, MIP-1404 showed low uptake in the kidney and demonstrated more lesions than MIP-1405, which produced higher activity concentrations in the kidneys [96]. MIP-1404—which would later become [^{99m}Tc]Tc-trofolastat—was ultimately selected as the lead compound for further testing. In a clinical trial, it identified 94% of prostate cancer lesions, higher than the 86% detected through MRI. The sensitivity and specificity of [^{99m}Tc]Tc-trofolastat toward positive lymph nodes were 33.3% and 88.4%, respectively, and the sensitivity increased to 50.0% when patients receiving androgen deprivation therapy were excluded. Interestingly, MRI results in patients under androgen deprivation therapy had much lower sensitivity (15.8%) but somewhat higher specificity (96.2%). For the sake of clarity, in the context of imaging studies, sensitivity refers to the proportion of true positive results, while specificity refers to the proportion of true negative results [97].

Another recently reported PSMA-targeted imaging agent is [^{99m}Tc]Tc-PSMA I&S [98]. This radiopharmaceutical is based on a molecule that had previously been radiolabeled with indium-111 using a DOTA chelator. However, due to the high cost and limited availability of ^{111}In, the development of technetium analogue was pursued. Synthetic modifications were performed to remove the DOTA chelator and replace it with a N_3S mercaptoacetyl triserine ligand which forms stable ^{99m}Tc(V) complex (Fig. 13c). Although prior *in vitro* studies determined that the IC_{50} for the ^{99m}Tc derivative was fivefold higher than that of the ^{111}In version, biodistribution studies showed that the two constructs produced similar activity concentrations in PSMA-positive LNCaP tumors at 1 h postinjection: 8.1 ± 1.1 and 8.3 ± 3.3% ID/g for the ^{111}In- and ^{99m}Tc-labeled compounds, respectively. While clinical results with a limited number of patients are promising, they must necessarily be regarded as preliminary.

^{99m}Tc-Labeled Agents for the Imaging of Neuroendocrine Tumors

Neuroendocrine tumors (NETs) typically overexpress somatostatin receptors. As a result, a number of different radiopharmaceuticals have been developed for imaging this target, including ^{111}In-DPTA-octreotide (Octreoscan™) and several ^{68}Ga-labeled peptides (including DOTA-TOC, DOTA-TATE, and DOTA-NOC) [99–102]. While [^{68}Ga]Ga-DOTA-TATE (NETSPOT™) has received approval for imaging NETs, it is nonetheless costly and requires access to a ^{68}Ge/^{68}Ga generator. To address this problem, work has been ongoing on the development of a ^{99m}Tc-labeled somatostatin-targeting imaging agent, with one example [^{99m}Tc]Tc-HYNIC-TOC (Fig. 13d) [103]. While this tracer showed greater sensitivity than [^{111}In]In-DTPA-octreotide, it also suffers from significant nontarget uptake in the pancreas. Consequently, there is an opportunity to develop more effective ^{99m}Tc-labeled radiopharmaceuticals for imaging NETs.

^{99m}Tc-Labeled Agents that Target Angiogenesis

Recently, a tracer known as [^{99m}Tc]Tc-3PRGD$_2$ was developed for imaging diseases characterized by increased angiogenesis. This agent—which is currently in phase I trials [104–106]—targets the $\alpha_v\beta_3$ integrin that is overexpressed on the endothelial cells of newly formed blood vessels. Targeting is achieved through the use of the well-known cyclic RGD dimer peptide, and a PEG-4-modified variant HYNIC is used for radiolabeling with ^{99m}Tc (Fig. 13e) [107]. [^{99m}Tc]Tc-3PRGD$_2$ is currently the subject of three clinical trials for patients with rheumatoid arthritis (RA), esophageal cancer, or breast cancers [108]. In preclinical studies, [^{99m}Tc]Tc-3PRGD$_2$ was able to detect arthritic joints as early as 30 min post-injection, and the lesions were still visible at 6 h post-injection [105]. The tracer produced high uptake in the kidneys and yielded a positive correlation between the severity of the arthritic disease and the uptake values in the joints, with more severe cases displaying higher activity concentrations.

Because they are capable of imaging a target that is associated with different disease states, radiopharmaceuticals

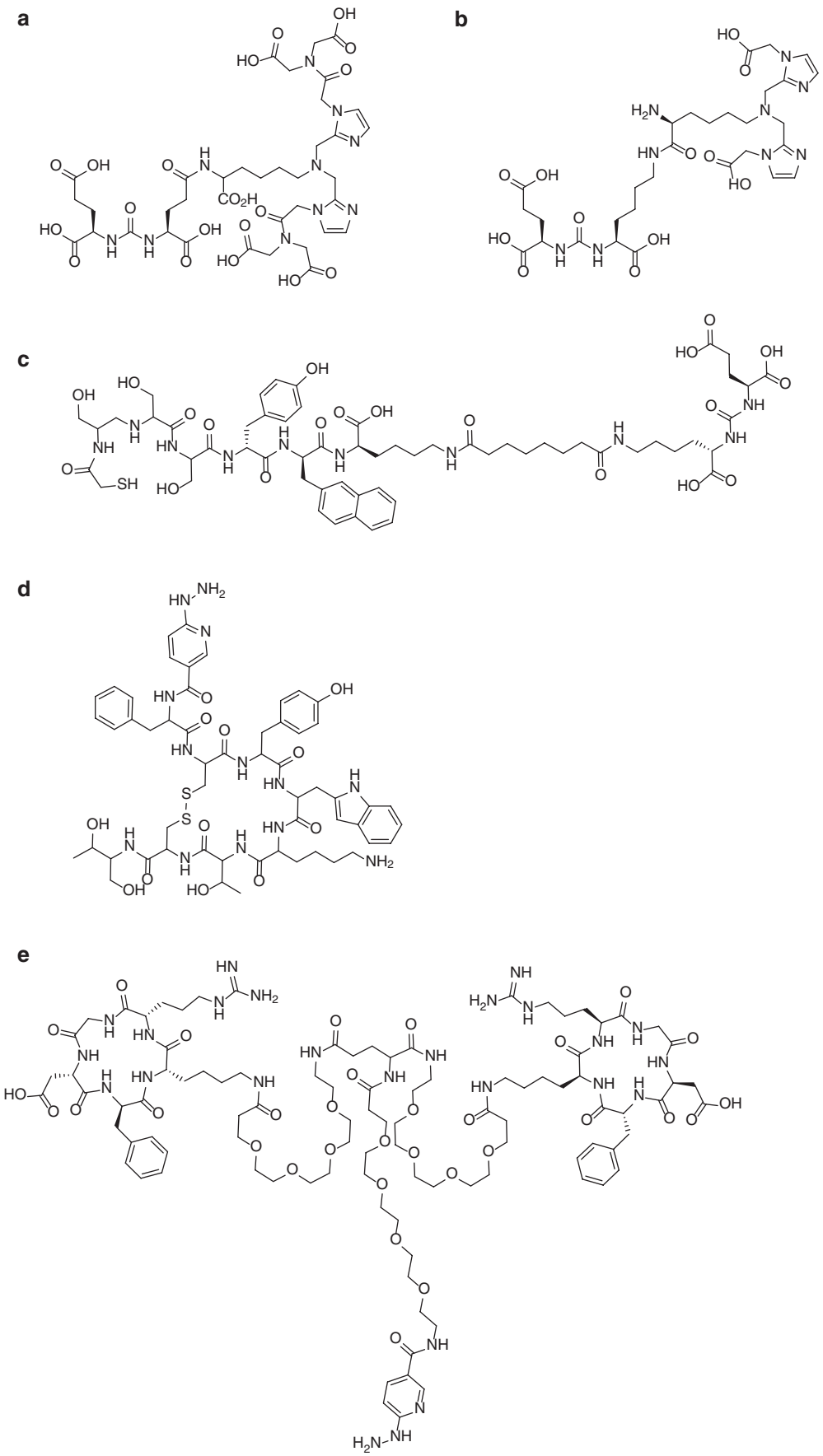

Fig. 13 Technetium-binding radiopharmaceuticals that are currently in clinical trials. (**a**) MIP-1404; (**b**) MIP-1405 [73]; (**c**) PSMA I&S [98]; (**d**) HYNIC-TOC [103]; and (**e**) $3PRGD_2$ [110]

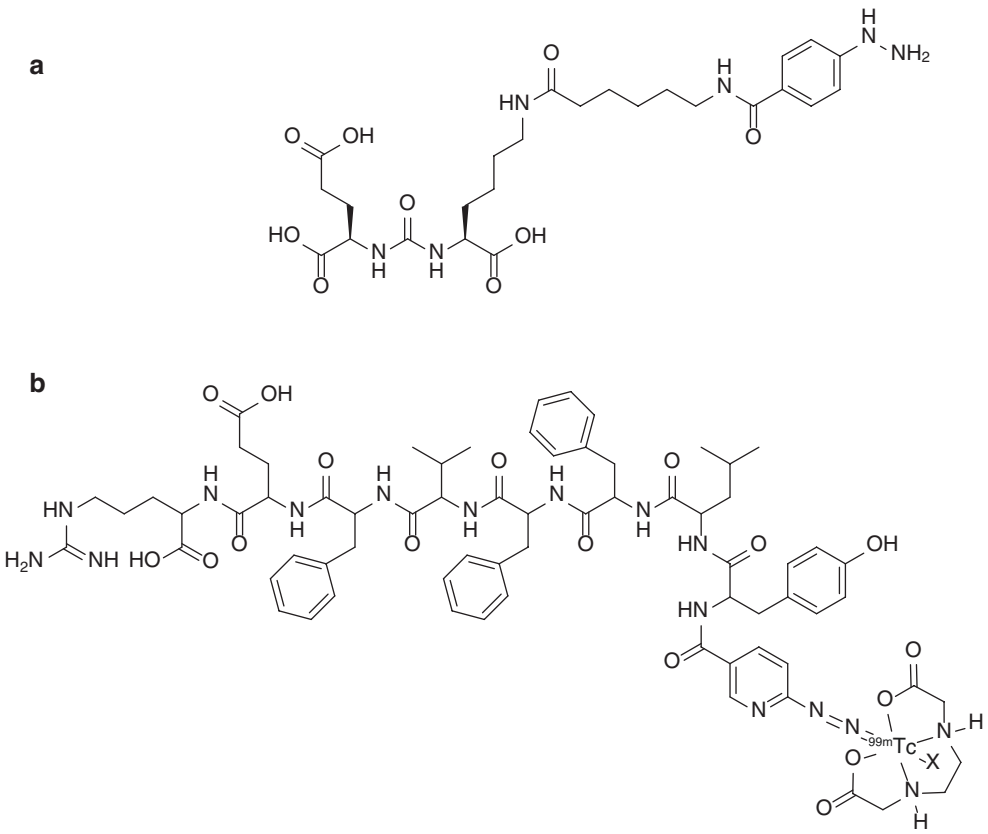

Fig. 14 Two recent examples of targeted ^{99m}Tc-labeled radiopharmaceuticals: (**a**) HYNIC-ALUG [108] and (**b**) [^{99m}Tc]Tc-HYNIC-H6F (X is likely H_2O or Cl^-) [109]

like [^{99m}Tc]Tc-3PRGD$_2$ have the potential to have widespread clinical utility. A comparative study of [^{99m}Tc]Tc-3PRGD$_2$ and [^{99m}Tc]Tc-MIBI showed comparable uptake for the two tracers in breast cancer lesions [106]. [^{99m}Tc]Tc-3PRGD$_2$ was capable of distinguishing between benign lesions and breast cancer as well as detecting ductal carcinoma *in situ*. [^{99m}Tc]Tc-3PRGD$_2$ had sensitivity, specificity, and accuracy values of 89.3%, 90.9%, and 89.7%, respectively, compared to 87.5%, 72.7%, and 82.1%, respectively, for [^{99m}Tc]Tc-MIBI. There continues to be a major unmet clinical need for radiopharmaceuticals that can help characterize suspicious lesions that are seen by mammography and reduce the number of unnecessary biopsies.

^{99m}Tc-Labeled Agents with Interesting Preclinical Data

A recent publication described [^{99m}Tc]Tc-HYNIC-ALUG, an agent for imaging prostate cancer that combines the HYNIC core with a small molecule glutamate-urea-lysine PSMA inhibitor (Fig. 14a) [109]. The radiolabeling reaction was performed in 15 min at 100 °C, resulting in a radiochemical purity of >99% and specific activity of 200 GBq/μmol. In a biodistribution study, the compound produced very high activity concentrations in LNCaP tumors at early time points (14 and 19%ID/g at 1 and 2 h, respectively) as well as low non-specific binding. Due to its rapid rate of excretion, the effective dose delivered by the agent was 8.4×10^{-4} mSv/MBq, which is lower than that created by MIP-1404 and MIP-1405 (8.78×10^{-3} and 7.87×10^{-3} mSv/MBq, respectively).

Another recent publication combined a HER2-targeted peptide with a HYNIC ligand for the imaging of breast cancer (Fig. 14b) [110]. In this case, the radiolabeling reaction was performed in 25 min, producing the tracer in a radiochemical purity greater than 95% and a specific activity of 35 MBq/nmol. A biodistribution study in mice bearing MDA-MB-453 xenografts produced tumor activity concentrations of 2.5 ± 0.1, 0.7 ± 0.2, and 0.2 ± 0.1 %ID/g at 0.5, 1, and 2 h, respectively. Importantly, these values were significantly higher at most time points than those in nontarget tissues such as the heart, spleen, intestine, and muscle. Due to its rapid accumulation in tumor tissue and low background uptake, [^{99m}Tc]Tc-HYNIC-H6F has the potential to be used to monitor HER2 expression non-invasively. This could help improve the detection and characterization of breast cancer as well as inform choices of therapy. However, further preclinical development is needed to increase the uptake and retention of the agent in tumor tissue, an improvement that could be driven by the modification of the tracer's ligands.

The Bottom Line

A key message that we hope to convey with this chapter is that while ^{99m}Tc remains a mainstay of nuclear medicine, the development of next-generation ^{99m}Tc radiopharmaceuticals

has not kept pace with the advancement of the field as a whole. That said, the impressive results recently seen with several PSMA-targeted constructs illustrate that advancements in ^{99m}Tc chemistry can create transformative diagnostic tools that can improve patient management. The field must build on this recent momentum and continue to exploit the low cost and low dose burden of ^{99m}Tc as well as the logistical advantages offered by instant kits. The latter are vastly simpler than the multi-step and automated production methods typically used with a large number of other radionuclides and thus help to lower the cost and time required to translate novel imaging agents.

With respect to opportunities, the ability to image infection and inflammation remains an important unmet medical need. Despite early, unsuccessful attempts to use ^{99m}Tc-labeled antibiotics and peptides, new ^{99m}Tc-based agents that bind biomarkers unique to these conditions would offer a cost-effective way to diagnose a wide range of diseases and to monitor response to therapy. The same is true in the field of immuno-oncology. Here, major investments are being made in pharmaceuticals that stimulate the immune system to attack tumors. Responses, particularly in melanoma, have been dramatic. However, there is a serious unmet medical need for techniques for monitoring early response to these expensive treatments, many of which can come with serious side effects. As multiple imaging sessions for assessing immune cell migration and tumor response are needed, ^{99m}Tc is the ideal medical radionuclide for such an imaging agent.

References

1. Perrier C, Segrè E. Radioactive isotopes of element 43. Nature. 1937;140:193–4.
2. Abram U, Alberto R. Technetium and rhenium – Coordination chemistry and nuclear medical applications. J Braz Chem Soc. 2006;17(8):1486–500.
3. Méndez-Rojas MA, Kharisov BI, Tsivadze AY. Recent advances on technetium complexes: coordination chemistry and medical applications. J Coord Chem. 2006;59(1):1–63.
4. Morais GR, Paulo A, Santos I. Organometallic complexes for SPECT imaging and/or radionuclide therapy. Organometallics. 2012;31(16):5693–714.
5. Amato I. Nuclear medicine's conundrum. Chem Eng News. 2009;87(36):58–64.
6. Kluba CA, Mindt TL. Click-to-Chelate: development of technetium and rhenium-tricarbonyl labeled radiopharmaceuticals. Molecules. 2013;18(3):3206–26.
7. Pillai MR, Dash A, Knapp FF Jr. Sustained availability of ^{99m}Tc: possible paths forward. J Nucl Med. 2013;54(2):313–23.
8. Boschi A, Martini P, Pasquali M, Uccelli L. Recent achievements in Tc-99m radiopharmaceutical direct production by medical cyclotrons. Drug Dev Ind Pharm. 2017;43(9):1402–12.
9. Ross CA, Diamond WT. Predictions regarding the supply of ^{99}Mo and ^{99m}Tc when NRU ceases production in 2018. Phys Can. 2015;71(3):131–8.
10. Jang J, Yamamoto M, Uesaka M. Design of an X-band electron linear accelerator dedicated to decentralized ^{99}Mo/^{99m}Tc supply: From beam energy selection to yield estimation. Phys Rev Accel Beams. 2017;20(10):104701.
11. Schaffer P, Bénard F, Bernstein A, Buckley K, Celler A, Cockburn N, et al. Direct production of ^{99m}Tc via ^{100}Mo(p,2n) on small medical cyclotrons. Phys Procedia. 2015;66:383–95.
12. Lebowitz E, Richards P. Radionuclide generator systems. Semin Nucl Med. 1974;4(3):257–68.
13. Jones AG, Davison A. The chemistry of technetium I, II, III and IV. Int J Appl Radiat Isot. 1982;33(10):867–74.
14. Papagiannopoulou D. Technetium-99m radiochemistry for pharmaceutical applications. J Label Compd Radiopharm. 2017;60(11):502–20.
15. Technetium-99m Radiopharmaceuticals: Manufacture of Kits. International Atomic Energy Agency, 2008. Technical Reports Report No.: 466.
16. Wong E, Fauconnier T, Bennett S, Valliant J, Nguyen T, Lau F, et al. Rhenium(V) and technetium(V) oxo complexes of an N2N'S peptidic chelator: evidence of interconversion between the syn and anti conformations. Inorg Chem. 1997;36(25):5799–808.
17. Alberto R, Schibli R, Egli A, Schubiger AP, Abram U, Kaden TA. A Novel organometallic aqua complex of technetium for the labeling of biomolecules: synthesis of $[^{99m}Tc(OH_2)_3(CO)_3]^+$ from $[^{99m}TcO_4]^-$ in aqueous solution and its reaction with a bifunctional ligand. J Am Chem Soc. 1998;120(31):7987–8.
18. Alberto R, Schibli R, Egli A, Schubiger PA, Herrmann WA, Artus G, et al. Metal-carbonyl syntheses XXII. Low-pressure carbonylation of $[MOCl_4)]^-$ and $[Mo_4]^-$: the technetium(I) and rhenium(I) complexes $[NEt_4]_2[MCl_3(CO_3]$. J Organomet Chem. 1995;493(1–2):119.
19. Egli A, Alberto R, Tannahill L, Schibli R, Abram U, Schaffland A, et al. Organometallic ^{99m}Tc-aquaion labels peptide to an unprecedented high specific activity. J Nucl Med. 1999;40(11):1913–7.
20. Schibli R, Schwarzbach R, Alberto R, Ortner K, Schmalle H, Dumas C, et al. Steps toward high specific activity labeling of biomolecules for therapeutic application: preparation of precursor $[^{188}Re(H_2O)_3(CO)_3]^+$ and synthesis of tailor-made bifunctional ligand systems. Bioconjug Chem. 2002;13(4):750–6.
21. Deutsch E, Libson K, Vanderheyden JL, Ketring AR, Maxon HR. The chemistry of rhenium and technetium as related to the use of isotopes of these elements in therapeutic and diagnostic nuclear medicine. Int J Rad Appl Instrum B. 1986;13(4):465–77.
22. Farwell MD, Pryma DA, Mankoff DA. PET/CT imaging in cancer: current applications and future directions. Cancer. 2014;120(22):3433–45.
23. Zolle I, editor. Technetium-99m pharmaceuticals: preparation and quality control in nuclear medicine. Berlin/Heidelberg: Springer; 2007.
24. Coover LR. The role of technetium tc 99m sestamibi in the early detection of breast carcinoma. Hosp Physician. 1999;35(2):16–21.
25. Berman DS, Kiat H, Friedman JD, Wang FP, Van Train K, Matzer L, et al. Separate acquisition rest thallium-201/stress technetium-99m sestamibi dual-isotope myocardial perfusion single-photon emission computed tomography: a clinical validation study. J Am Coll Cardiol. 1993;22(5):1455–64.
26. Wackers FJ, Berman DS, Maddahi J, Watson DD, Beller GA, Strauss HW, et al. Technetium-99m hexakis 2-methoxyisobutyl isonitrile: human biodistribution, dosimetry, safety, and preliminary comparison to thallium-201 for myocardial perfusion imaging. J Nucl Med. 1989;30(3):301–11.
27. Yaes RJ. Clinical review, Tc 99m Sestamibi. U.S. Food and Drug Administration 2 Apr 2008. NDA 19-785. https://www.fda.gov/downloads/Drugs/.../DevelopmentResources/ucm072825.pdf. Accessed 7 Apr 2018.
28. Kelly JD, Forster AM, Higley B, Archer CM, Booker FS, Canning LR, et al. Technetium-99m-tetrofosmin as a new

radiopharmaceutical for myocardial perfusion imaging. J Nucl Med. 1993;34(2):222–7.
29. Sinusas AJ, Shi Q, Saltzberg MT, Vitols P, Jain D, Wackers FJ, et al. Technetium-99m-tetrofosmin to assess myocardial blood flow: experimental validation in an intact canine model of ischemia. J Nucl Med. 1994;35(4):664–71.
30. Myoview 30 mL Kit for the preparation of technetium Tc99m tetrofosmin for Injection. GE Healthcare. 2011. http://www3.gehealthcare.com/en/products/categories/nuclear_imaging_agents/nuclear_pharmacies. Accessed Oct 2017.
31. Yazdani A, Bilton H, Vito A, Genady AR, Rathmann SM, Ahmad Z, et al. A bone-seeking trans-cyclooctene for pretargeting and bioorthogonal chemistry: a proof of concept study using ^{99m}Tc- and ^{177}Lu-labeled tetrazines. J Med Chem. 2016;59(20):9381–9.
32. Jurisson S, Berning D, Jia W, Ma DS. Coordination-compounds in nuclear-medicine. Chem Rev. 1993;93(3):1137–56.
33. Libson K, Deutsch E, Barnett BL. Structural characterization of a technetium-99-diphosphonate complex. Implications for the chemistry of technetium-99m skeletal imaging agents. J Am Chem Soc. 1980;102(7):2476–8.
34. Atkins HL. Radiopharmaceuticals. Phys Rep. 1975;21(6):315–67.
35. Junankar S, Shay G, Jurczyluk J, Ali N, Down J, Pocock N, et al. Real-time intravital imaging establishes tumor-associated macrophages as the extraskeletal target of bisphosphonate action in cancer. Cancer Discov. 2015;5(1):35–42.
36. DMSA kit for the preparation of technetium Tc99m Succimer Injection. GE Healthcare. 2006. http://www3.gehealthcare.com/en/products/categories/nuclear_imaging_agents/nuclear_pharmacies. Accessed Oct 2017.
37. Handmaker H, Young BW, Lowenstein JM. Clinical experience with ^{99m}Tc-DMSA (dimercaptosuccinic acid), a new renal-imaging agent. J Nucl Med. 1975;16(1):28–32.
38. de Lange MJ, Piers DA, Kosterink JG, van Luijk WH, Meijer S, de Zeeuw D, et al. Renal handling of technetium-99m DMSA: evidence for glomerular filtration and peritubular uptake. J Nucl Med. 1989;30(7):1219–23.
39. Draximage DTPA kit for the preparation of technetium Tc99m pentate injection. GE Healthcare. 2016. http://www.draximage.com/products/us/draximage-dtpa/. Accessed Oct 2017.
40. Kabasakal L. Technetium-99m ethylene dicysteine: a new renal tubular function agent. Eur J Nucl Med. 2000;27(3):351–7.
41. Technescan MAG3 kit for the preparation of technetium Tc99m mertiatide. Curium Pharma. 2015. https://curiumpharma.com/wp-content/uploads/2017/02/Tscan-MAG3-a096i0-in-1015.pdf. Accessed Oct 2017.
42. Klingensmith WC 3rd, Briggs DE, Smith WI. Technetium-99m-MAG3 renal studies: normal range and reproducibility of physiologic parameters as a function of age and sex. J Nucl Med. 1994;35(10):1612–7.
43. Eshima D, Fritzberg AR, Taylor A Jr. ^{99m}Tc renal tubular function agents: current status. Semin Nucl Med. 1990;20(1):28–40.
44. Jurgens S, Herrmann WA, Kuhn FE. Rhenium and technetium based radiopharmaceuticals: development and recent advances. J Organomet Chem. 2014;751:83–9.
45. Ponto JA. Mechanisms of radiopharmaceutical localization (Norenberg J, editor). Albuquerque: University of New Mexico College of Pharmacy 2012;16(4). Program No. 0039-000-12-164-H04-P 2.5.
46. Ceretec kit for the preparation of technetium Tc99m exametazime injection. GE Healthcare. 2013. http://www3.gehealthcare.com/en/products/categories/nuclear_imaging_agents/nuclear_pharmacies. Accessed Oct 2017.
47. Neirinckx RD, Canning LR, Piper IM, Nowotnik DP, Pickett RD, Holmes RA, et al. Technetium-99m d,l-HM-PAO: a new radiopharmaceutical for SPECT imaging of regional cerebral blood perfusion. J Nucl Med. 1987;28(2):191–202.
48. Robins PD, Salazar I, Forstrom LA, Mullan BP, Hung JC. Biodistribution and radiation dosimetry of stabilized ^{99m}Tc-exametazine-labeled leukocytes in normal subjects. J Nucl Med. 2000;41(5):934–40.
49. Chervu LR, Nunn AD, Loberg MD. Radiopharmaceuticals for hepatobiliary imaging. Semin Nucl Med. 1982;12(1):5–17.
50. Krishnamurthy GT, Turner FE. Pharmacokinetics and clinical application of technetium 99m-labeled hepatobiliary agents. Semin Nucl Med. 1990;20(2):130–49.
51. Weissmann HS, Frank MS, Bernstein LH, Freeman LM. Rapid and accurate diagnosis of acute cholecystitis with 99mTc-HIDA cholescintigraphy. AJR Am J Roentgenol. 1979;132(4):523–8.
52. Neurolite kit for the preparation of technetium Tc99m bicisate for injection. Lantheus Medical Imaging. 2015. http://www.lantheus.com/assets/Neurolite-US-PI-513073-0415-format-6-1-29-2016.pdf. Accessed Oct 2017.
53. Vanbilloen HP, Cleynhens BJ, Verbruggen AM. Importance of the two ester functions for the brain retention of ^{99m}Tc-labelled ethylene dicysteine diethyl ester (^{99m}Tc-ECD). Nucl Med Biol. 1998;25(6):569–75.
54. Vallabhajosula S, Zimmerman RE, Picard M, Stritzke P, Mena I, Hellman RS, et al. Technetium-99m ECD: a new brain imaging agent: in vivo kinetics and biodistribution studies in normal human subjects. J Nucl Med. 1989;30(5):599–604.
55. Kit for the preparation of technetium Tc 99m sulfur colloid injection. Rev. 1.1 Pharmalucence. 2013. http://www.pharmalucence.com/images/SC_PI.pdf. Accessed Oct 2017.
56. Michenfelder MM, Bartlett LJ, Mahoney DW, Herold TJ, Hung JC. Particle-size and radiochemical purity evaluations of filtered ^{99m}Tc-sulfur colloid prepared with different heating times. J Nucl Med Technol. 2014;42(4):283–8.
57. Kern KA, Rosenberg RJ. Preoperative lymphoscintigraphy during lymphatic mapping for breast cancer: improved sentinel node imaging using subareolar injection of technetium 99m sulfur colloid. J Am Coll Surg. 2000;191(5):479–89.
58. Dewanjee MK. The chemistry of ^{99m}Tc-labeled radiopharmaceuticals. Semin Nucl Med. 1990;20(1):5–27.
59. Maresca KP, Marquis JC, Hillier SM, Lu G, Femia FJ, Zimmerman CN, et al. Novel polar single amino acid chelates for technetium-99m tricarbonyl-based radiopharmaceuticals with enhanced renal clearance: application to octreotide. Bioconjug Chem. 2010;21(6):1032–42.
60. Meszaros LK, Dose A, Biagini SCG, Blower PJ. Hydrazinonicotinic acid (HYNIC) – Coordination chemistry and applications in radiopharmaceutical chemistry. Inorg Chim Acta. 2010;363(6):1059–69.
61. Ogawa K, Mukai T, Inoue Y, Ono M, Saji H. Development of a novel ^{99m}Tc-chelate-conjugated bisphosphonate with high affinity for bone as a bone scintigraphic agent. J Nucl Med. 2006;47(12):2042–7.
62. Zhang XY, Yu PR, Yang YP, Hou YQ, Peng C, Liang ZG, et al. ^{99m}Tc-labeled 2-arylbenzothiazoles: a beta imaging probes with favorable brain pharmacokinetics for single-photon emission computed tomography. Bioconjug Chem. 2016;27(10):2493–504.
63. Eckelman W, Richards P. Instant ^{99m}Tc-DTPA. J Nucl Med. 1970;11(12):761.
64. Abrams MJ, Juweid M, tenKate CI, Schwartz DA, Hauser MM, Gaul FE, et al. Technetium-99m-human polyclonal IgG radiolabeled via the hydrazino nicotinamide derivative for imaging focal sites of infection in rats. J Nucl Med. 1990;31(12):2022–8.
65. Garcia MF, Zhang X, Shah M, Newton-Northup J, Cabral P, Cerecetto H, et al. ^{99m}Tc-bioorthogonal click chemistry reagent for in vivo pretargeted imaging. Bioorg Med Chem. 2016;24(6):1209–15.
66. von Guggenberg E, Behe M, Behr TM, Saurer M, Seppi T, Decristoforo C. ^{99m}Tc-labeling and in vitro and in vivo evaluation

of HYNIC- and (Na-His)acetic acid-modified [D-Glu^1]-minigastrin. Bioconjug Chem. 2004;15(4):864–71.
67. Babich JW, Solomon H, Pike MC, Kroon D, Graham W, Abrams MJ, et al. Technetium-99m-labeled hydrazino nicotinamide derivatized chemotactic peptide analogs for imaging focal sites of bacterial infection. J Nucl Med. 1993;34(11):1964–74.
68. Faintuch BL, Santos RLSR, Souza ALFM, Hoffman TJ, Greeley M, Smith CJ. ^{99m}Tc-HYNIC-Bombesin (7–14)NH_2: Radiochemical evaluation with co-ligands EDDA (EDDA = ethylenediamine-N,N ′-diacetic acid), tricine, and nicotinic acid. Synth React Inorg Met Org Chem. 2005;35(1):43–51.
69. Vito A, Alarabi H, Czorny S, Beiraghi O, Kent J, Janzen N, et al. A ^{99m}Tc-labelled tetrazine for bioorthogonal chemistry. synthesis and biodistribution studies with small molecule *trans*-cyclooctene derivatives. PLoS One. 2016;11(12):e0167425.
70. von Guggenberg E, Sarg B, Lindner H, Alafort LM, Mather SJ, Moncayo R, et al. Preparation via coligand exchange and characterization of [^{99m}Tc-EDDA-HYNIC-D-Phe$_1$,Tyr$_3$]octreotide (^{99m}Tc-EDDA/HYNIC-TOC). J Label Compd Radiopharm. 2003;46(4):307–18.
71. Alberto R, Schibli R, Schubiger AP, Abram U, Pietzsch HJ, Johannsen B. First application of *fac*-[^{99m}Tc$(OH_2)_3(CO)_3]^+$ in bioorganometallic chemistry: design, structure, and in vitro affinity of a 5-HT_{1A} receptor ligand labeled with ^{99m}Tc. J Am Chem Soc. 1999;121(25):6076–7.
72. Bilton HA, Ahmad Z, Janzen N, Czorny S, Valliant JF. Preparation and evaluation of ^{99m}Tc-labeled tridentate chelates for pre-targeting using bioorthogonal chemistry. J Vis Exp. 2017;120:e55188.
73. Goffin KE, Joniau S, Tenke P, Slawin K, Klein EA, Stambler N, et al. Phase 2 study of ^{99m}Tc-trofolastat SPECT/CT to identify and localize prostate cancer in intermediate- and high-risk patients undergoing radical prostatectomy and extended pelvic LN dissection. J Nucl Med. 2017;58(9):1408–13.
74. Banerjee SR, Levadala MK, Lazarova N, Wei L, Valliant JF, Stephenson KA, et al. Bifunctional single amino acid chelates for labeling of biomolecules with the {$Tc(CO)_3$}+ and {$Re(CO)_3$}+ Cores. Crystal and molecular structures of [ReBr$(CO)_3(H_2NCH_2C_5H_4N)$], [$ReCO)_3${$(C_5H_4NCH_2)_2NH$}]Br, [$Re(CO)_3${$(C_5H_4NCH_2)_2NCH_2CO_2H$}]Br, [$Re(CO)_3${X(Y)$NCH_2CO_2CH_2CH_3$}]Br (X =Y = 2-pyridylmethyl; X = 2-pyridylmethyl, Y = 2-(1-methylimidazolyl)methyl; X = Y) 2-(1-methylimidazolyl)methyl), [$ReBr(CO)_3${$(C_5H_4NCH_2)NH(CH_2C_4H_3S)$}], and [$Re(CO)_3${$(C_5H_4NCH_2)N(CH_2C_4H_3S)(CH_2CO_2)$}]. Inorg Chem. 2002;41(24):6417–6425.
75. Bayly SR, Fisher CL, Storr T, Adam MJ, Orvig C. Carbohydrate conjugates for molecular imaging and radiotherapy: Tc-99m(I) and Re-186(I) tricarbonyl complexes of N-(2′-hydroxybenzyl)-2-amino-2-deoxy-D-glucose. Bioconjug Chem. 2004;15(4):923–6.
76. Karagiorgou O, Patsis G, Pelecanou M, Raptopoulou CP, Terzis A, Siatra-Papastaikoudi T, et al. (S)-(2-(2′-Pyridyl)ethyl)cysteamine and (S)-(2-(2′-pyridyl)ethyl)-d,l-homocysteine as ligands for the "*fac*-[$M(CO)_3]^+$" (M = Re, ^{99m}Tc) core. Inorg Chem. 2005;44(12):4118–20.
77. Lazarova N, Babich J, Valliant J, Schaffer P, James S, Zubieta J. Thiol- and thioether-based bifunctional chelates for the $[M(CO)_3]^+$ core (M = Tc, Re). Inorg Chem. 2005;44(19):6763–70.
78. Liu Y, Pak JK, Schmutz P, Bauwens M, Mertens J, Knight H, et al. Amino acids labeled with [^{99m}Tc$(CO)_3]^+$ and recognized by the L-type amino acid transporter LAT1. J Am Chem Soc. 2006;128(50):15996–7.
79. Schweinsberg C, Maes V, Brans L, Blauenstein P, Tourwe DA, Schubiger PA, et al. Novel glycated [^{99m}Tc$(CO)_3$]-labeled bombesin analogues for improved targeting of gastrin-releasing peptide receptor-positive tumors. Bioconjug Chem. 2008;19(12):2432–9.
80. Banerjee SR, Pullambhatla M, Foss CA, Falk A, Byun Y, Nimmagadda S, et al. Effect of chelators on the pharmacokinetics of Tc-99m-labeled imaging agents for the prostate-specific membrane antigen (PSMA). J Med Chem. 2013;56(15):6108–21.
81. Hillier SM, Maresca KP, Lu G, Merkin RD, Marquis JC, Zimmerman CN, et al. ^{99m}Tc-labeled small-molecule inhibitors of prostate-specific membrane antigen for molecular imaging of prostate cancer. J Nucl Med. 2013;54(8):1369–76.
82. Jiang H, Kasten BB, Liu H, Qi S, Liu Y, Tian M, et al. Novel, cysteine-modified chelation strategy for the incorporation of $[M^I(CO)_3]^+$(M = Re, ^{99m}Tc) in an α-MSH peptide. Bioconjug Chem. 2012;23(11):2300–12.
83. Alberto R, Ortner K, Wheatley N, Schibli R, Schubiger AP. Synthesis and properties of boranocarbonate: a convenient in situ co source for the aqueous preparation of [^{99m}Tc$(OH_2)_3(CO)_3]^+$. J Am Chem Soc. 2001;123(13):3135–6.
84. Wilson AA, Jin L, Garcia A, DaSilva JN, Houle S. An admonition when measuring the lipophilicity of radiotracers using counting techniques. Appl Radiat Isot. 2001;54(2):203–8.
85. Stein WH, Moore S. The free amino acids of human blood plasma. J Biol Chem. 1954;211(2):915–26.
86. Schibli R, La Bella R, Alberto R, Garcia-Garayoa E, Ortner K, Abram U, et al. Influence of the denticity of ligand systems on the in vitro and in vivo behavior of ^{99m}tc(i)-tricarbonyl complexes: a hint for the future functionalization of biomolecules. Bioconjug Chem. 2000;11(3):345–51.
87. Eckelman WC, Kilbourn MR, Joyal JL, Labiris R, Valliant JF. Justifying the number of animals for each experiment. Nucl Med Biol. 2007;34(3):229–32.
88. Jones AG, Abrams MJ, Davison A, Brodack JW, Toothaker AK, Adelstein SJ, et al. Biological studies of a new class of technetium complexes: the hexakis(alkylisonitrile)technetium(I) cations. Int J Nucl Med Biol. 1984;11(3–4):225–34.
89. Brown RP, Delp MD, Lindstedt SL, Rhomberg LR, Beliles RP. Physiological parameter values for physiologically based pharmacokinetic models. Toxicol Ind Health. 1997;13(4):407–84.
90. Psimadas D, Baldi G, Ravagli C, Bouziotis P, Xanthopoulos S, Franchini MC, et al. Preliminary evaluation of a ^{99m}Tc labeled hybrid nanoparticle bearing a cobalt ferrite core: in vivo biodistribution. J Biomed Nanotechnol. 2012;8(4):575–85.
91. Kendi AT, Moncayo VM, Nye JA, Galt JR, Halkar R, Schuster DM. Radionuclide therapies in molecular imaging and precision medicine. PET clin. 2017;12(1):93–103.
92. Banerjee SR, Foss CA, Castanares M, Mease RC, Byun Y, Fox JJ, et al. Synthesis and evaluation of technetium-99m- and rhenium-labeled inhibitors of the prostate-specific membrane antigen (PSMA). J Med Chem. 2008;51(15):4504–17.
93. Mindt TL, Struthers H, Brans L, Anguelov T, Schweinsberg C, Maes V, et al. "Click to chelate": synthesis and installation of metal chelates into biomolecules in a single step. J Am Chem Soc. 2006;128(47):15096–7.
94. Morais M, Oliveira BL, Correia JD, Oliveira MC, Jimenez MA, Santos I, et al. Influence of the bifunctional chelator on the pharmacokinetic properties of ^{99m}Tc$(CO)_3$-labeled cyclic a-melanocyte stimulating hormone analog. J Med Chem. 2013;56(5):1961–73.
95. Scherr D, Karnes J, Slawin K, Keane T, Trabulsi E, Ellis W, et al. A phase 2 study with MIP-1404 in men with high-risk PC scheduled for RP and EPLND compared to histopathology. 2012. clinicaltrials.gov/ct2/show/NCT01667536. Acceessed 8 Apr 2018.
96. Vallabhajosula S, Nikolopoulou A, Babich JW, Osborne JR, Tagawa ST, Lipai I, et al. ^{99m}Tc-labeled small-molecule inhibitors of prostate-specific membrane antigen: pharmacokinetics and biodistribution studies in healthy subjects and patients with metastatic prostate cancer. J Nucl Med. 2014;55(11):1791–8.
97. Altman DG, Bland JM. Diagnostic tests. 1: sensitivity and specificity. BMJ. 1994;308(6943):1552.
98. Robu S, Schottelius M, Eiber M, Maurer T, Gschwend J, Schwaiger M, et al. Preclinical evaluation and first patient application of

^{99m}Tc-PSMA-I&S for SPECT imaging and radioguided surgery in prostate cancer. J Nucl Med. 2017;58(2):235–42.
99. Buchmann I, Henze M, Engelbrecht S, Eisenhut M, Runz A, Schafer M, et al. Comparison of ^{68}Ga-DOTATOC PET and ^{111}In-DTPAOC (Octreoscan) SPECT in patients with neuroendocrine tumours. Eur J Nucl Med Mol Imaging. 2007;34(10):1617–26.
100. Shi W, Johnston CF, Buchanan KD, Ferguson WR, Laird JD, Crothers JG, et al. Localization of neuroendocrine tumours with [^{111}In] DTPA-octreotide scintigraphy (Octreoscan): a comparative study with CT and MR imaging. QJM. 1998;91(4):295–301.
101. Srirajaskanthan R, Kayani I, Quigley AM, Soh J, Caplin ME, Bomanji J. The role of ^{68}Ga-DOTATATE PET in patients with neuroendocrine tumors and negative or equivocal findings on ^{111}In-DTPA-octreotide scintigraphy. J Nucl Med. 2010;51(6):875–82.
102. Wild D, Bomanji JB, Benkert P, Maecke H, Ell PJ, Reubi JC, et al. Comparison of ^{68}Ga-DOTANOC and ^{68}Ga-DOTATATE PET/CT within patients with gastroenteropancreatic neuroendocrine tumors. J Nucl Med. 2013;54(3):364–72.
103. Behera A, De K, Chandra S, Chattopadhyay S, Misra M. Synthesis, radiolabelling and biodistribution of HYNIC-Tyr^3 octreotide: a somatostatin receptor positive tumour imaging agent. J Radioanal Nucl Chem. 2011;290(1):123–9.
104. Gao S, Ma Q, Wen Q, Jia B, Liu Z, Chen Z, et al. ^{99m}Tc-3P$_4$-RGD$_2$ radiotracers for SPECT/CT of esophageal tumor. Nucl Sci Tech. 2013;24(4):040302.
105. Huang C, Zheng Q, Miao W. Study of novel molecular probe ^{99m}Tc-3PRGD2 in the diagnosis of rheumatoid arthritis. Nucl Med Commun. 2015;36(12):1208–14.
106. Ma Q, Chen B, Gao S, Ji T, Wen Q, Song Y, et al. ^{99m}Tc-3P4-RGD2 scintimammography in the assessment of breast lesions: comparative study with ^{99m}Tc-MIBI. PLoS One. 2014;9(9):e108349.
107. Jia B, Liu Z, Zhu Z, Shi J, Jin X, Zhao H, et al. Blood clearance kinetics, biodistribution, and radiation dosimetry of a kit-formulated integrin $\alpha_v\beta_3$-selective radiotracer ^{99m}Tc-$_3$PRGD$_2$ in non-human primates. Mol Imaging Biol. 2011;13(4):730–6.
108. Chen B, Zhao G, Ma Q, Ji B, Ji T, Xin H, et al. 99mTc-3P-RGD2 SPECT to monitor early response to bevacizumab therapy in patients with advanced non-small cell lung cancer. Int J Clin Exp Pathol. 2015;8(12):16064–72.
109. Xu X, Zhang J, Hu S, He S, Bao X, Ma G, et al. 99mTc-labeling and evaluation of a HYNIC modified small-molecular inhibitor of prostate-specific membrane antigen. Nucl Med Biol. 2017;48:69–75.
110. Li L, Wu Y, Wang Z, Jia B, Hu Z, Dong C, et al. SPECT/CT imaging of the novel HER2-targeted peptide probe 99mTc-HYNIC-H6F in breast cancer mouse models. J Nucl Med. 2017;58(5):821–6.

The Radiopharmaceutical Chemistry of the Radioisotopes of Copper

Xiaoxi Ling, Cathy S. Cutler, and Carolyn J. Anderson

Abbreviations

AD	Alzheimer's disease
ALS	Amyotrophic lateral sclerosis
AmBaSar	4-((8-Amino-3,6,10,13,16,19-hexaazabicyclo[6.6.6]icosan-1-yl)amino) benzoic acid
ATSM	Diacetyl-*bis*(N^4-methylthiosemicarbazone)
Aβ	Amyloid-β
BLIP	Brookhaven Linac Isotope Producer
BNL	Brookhaven National Laboratory
BTS	Bis(thiosemicarbazone)
c(RGDfD)	cyclo(Arg-Gly-Asp-d-Phe-Asp)
c(RGDyK)	cyclo(Arg-Gly-Asp-d-Tyr-Lys)
CB-TE1A1P	1,4,8,11-Tetraazabicyclo[6.6.2]hexadecane-4-acetic acid-11-methylphosphonic acid
CB-TE2A	1,4,8,11-Tetraazabicyclo[6.6.2]hexadecane-4,11-diacetic acid
CT	Computed tomography
DiamSar	1,8-Diamino-3,6,10,13,16,19-hexaazabicyclo[6,6,6]-eicosane
DOTA	1,4,7,10-Tetraazacyclododecane-1,4-7,10-tetraacetic acid
E^0	Standard reduction potentials
EDTA	Ethylenediaminetetraacetic acid
ETS	Ethylglyoxal bis(thiosemicarbazone)
FAZA	1-(5-Fluoro-5-deoxy-α-D-arabinofuranosyl)-2-nitroimidazole
FMISO	Fluoromisonidazole
FRIB	Facility for Rare Isotope Beams
GTS	Glyoxal-bis(thiosemicarbazone)
GTSM	Glyoxal-bis(N^4-methylthiosemicarbazone)
h	Hours
keV	Kilo-electron volts (10^3)
LANL	Los Alamos National Lab
mAb	Monoclonal antibody
MeCOSar	5-(8-methyl-3,6,10,13,16,19-hexaazabicyclo[6.6.6]icosan-1-ylamino)-5-oxopentanoic acid
MeV	Mega-electron volts (10^6)
MicroPET	Miniaturized positron emission tomography
min	Minutes
MSU	Michigan State University
NODAGA	1-(1,3-Carboxypropyl)-4,7-dicarboxymethyl-1,4,7-triazacyclononane
NOTA	1,4,7-Tricarboxymethyl-1,4,7-triazacyclononane
NSCL	National Superconducting Cyclotron Laboratory
PCBA	1-[(1,4,7,10,13-Pentaazacyclopentaadec-1-yl)methyl]benzoic acid
PCB-TE2A	1,4,8,11-Tetraazabicyclo[6.6.3] heptadecane-4,11-diacetic acid
PEG	Polyethylene glycol
PET	Positron emission tomography
pH	Potential of hydrogen
PTSM	Pyruvaldehyde-*bis*(N^4-methylthiosemicarbazone)

X. Ling · C. J. Anderson (✉)
Department of Medicine, University of Pittsburgh, Pittsburgh, PA, USA
e-mail: lingx@upmc.edu; andersoncj@upmc.edu

C. S. Cutler
Medical Isotope Research & Production (MIRP) Program, Collider Accelerator Department, Brookhaven National Laboratory, Upton, NY, USA

J. S. Lewis et al. (eds.), *Radiopharmaceutical Chemistry*, https://doi.org/10.1007/978-3-319-98947-1_19

Sar/Sarcophagine	3,6,10,13,16,19-Hexaazabicyclo(6,6,6) eicosane
SarAr	N^1-(4-aminophenyl)-3,6,10,13,16,19-hexaazabicyclo[6.6.6] icosane-1,8-diamine
SOD1	Superoxide dismutase 1
SPECT	Single-photon emission computed tomography
SSR	Somatostatin receptor
TATE	Octreotate
TE2A(1,4-)	1,4,8,11-Tetraazacyclotetradecane-1,4-biacetic acid
TE2A(1,8-)	1,4,8,11-Tetraazacyclotetradecane-1,8-biacetic acid
TETA	1,4,8,11-Tetraazacyclotetradecane-1,4,8,11-tetraacetic acid
Y3-TATE	Tyrosine-3-octreotate

Introduction

There are five radioisotopes of copper that are suitable for use in nuclear imaging or targeted radionuclide therapy: copper-67, copper-64, copper-62, copper-61, and copper-60 (Table 1). These radionuclides have diverse nuclear properties, including half-lives ranging from 10 min to 62 h and decay modes such as positron (β^+)- and beta particle (β^-) emission. Copper-67 can be harnessed for single-photon emission computed tomography (SPECT) as well as radionuclide therapy, while the quartet of radioisotopes of copper decay via positron emission for positron emission tomography (PET). Perhaps not surprisingly, this array of radioisotopes has been exploited for the development of PET tracers as well as agents for targeted radionuclide therapy. Two current foci of research into the radiopharmaceutical chemistry of copper are the creation of new coordination architectures for the radiometal as well as the development of relatively simple radiolabeling techniques that will lead to agents that remain intact *in vivo*. This chapter will discuss the production of the various radionuclides, the development of chelators for copper(II), and the applications of copper-based radiopharmaceuticals in imaging and therapy.

Table 1 Decay characteristics of copper radionuclides

Isotope	$T_{1/2}$	β- MeV (%)	β+ MeV (%)	EC (%)	γ MeV (%)
^{60}Cu	23.4 min	–	3.92 (6%) 3.00 (18%) 2.00 (69%)	7.4%	0.85 (15%) 1.33 (80%) 1.76 (52%) 2.13 (6%)
^{61}Cu	3.32 h	–	1.22 (60%)	40%	0.284 (12%) 0.38 (3%) 0.511(120%)
^{62}Cu	9.76 min	–	2.91 (97%)	2%	0.511(194%)
^{64}Cu	12.8 h	0.573 (39.6%)	0.655 (19.3%)	41%	1.35 (0.6%) 0.511(38.6%)
^{67}Cu	62.0 h	0.577 (20%) 0.484 (35%) 0.395 (45%)	–	–	0.184 (40%) 0.092 (23%)

Historical Use of Copper Radionuclides

There is a long history of tumor detection and imaging using copper-64 and copper-67. ^{64}Cu-labeled porphyrins were the first radiocopper agents to be investigated in humans and were used in patients with tumors of the tongue, neck, brain, breast, and lung [1]. These imaging studies were done before SPECT or PET scanners were available, and the detection of the [^{64}Cu]Cu-porphyrin was accomplished using a 1-inch thallium-activated sodium iodide crystal connected to a transistorized rate meter and recording device. Patients were scanned 24 h after the injection of the radiotracer, and a range of uptakes was observed in the various types of tumors. [^{67}Cu] copper citrate was used for the imaging of patients with lung cancers or tuberculosis using a gamma camera, and the retention patterns of this radiotracer between these two diseases were very different: while it was cleared from inflammatory lesions, it was retained in tumors [2]. There is still interest in the use of radioactive copper-labeled porphyrins that are taken up by tumor cells [3, 4] as well as "free" radioactive Cu(II), which binds to copper transport proteins and is taken up in tumors by known copper transporter proteins [5, 6].

Copper is an essential element for all living organisms due to its redox chemistry and is an integral component in several essential proteins, including superoxide dismutase, ceruloplasmin, and metallothionein. Indeed, there are actually diseases related to imbalances of copper homeostasis [7]. Menkes disease—an X-linked inherited disorder—is caused by a mutation in the ATP7A gene that encodes a copper-transporting ATPase and leads to mental retardation, abnormalities in hair, bone fractures, and aortic aneurysms [8]. Wilson's disease—an autosomal recessive genetic disease—is caused by disabling mutations in both copies of the ATP7B gene, results in high hepatic copper levels, and causes both liver disease and neurological damage. Copper-64 and copper-67 have been used as biomedical tracers to investigate the biology of copper proteins and their role in Wilson's disease [9–11] and Menkes disease [12].

The Production of the Radioisotopes of Copper

The family of copper radionuclides includes a diverse array of diagnostic (copper-60, copper-61, copper-62, and copper-64) and therapeutic (copper-64 and copper-67) radioisotopes

(Table 1). The positron-emitting nuclides have a range of half-lives (10 min to 12.7 h) and can be produced by a cyclotron or a generator. A major challenge in the production of the radioisotopes of copper is obtaining the nuclides with high specific activity. This is due to the presence of cold copper and other metallic impurities. The production of these radionuclides typically involves the irradiation of a solid metal target followed by a separation step to remove the desired copper radionuclide from the target material and other impurities.

The Production of Copper-67 Copper-67 is an attractive radionuclide for targeted radionuclide therapy, as it is a pure beta emitter with a reasonably long half-life (62 h) that is compatible with the pharmacokinetic profiles of biomolecules such as proteins or peptides. Copper-67 decays to stable zinc-67 ($E_{\beta 1}$ = 577 keV, 20% abundance; $E_{\beta 2}$ = 484 keV, 23%; $E_{\beta 3}$ = 395 keV, 56%) and emits gamma emissions at a suitable energy for gamma scintigraphy or SPECT imaging [91.3 keV (7.3%), 93.3 keV (16.6%), 185 keV (46.7%)]. These are ideal properties for a therapeutic radionuclide. However, the production of copper-67 requires higher-energy cyclotrons or accelerators, and there are only a few facilities worldwide with these machines.

Brookhaven National Laboratory (BNL) has been producing copper-67 on a limited basis since the 1980s by bombarding natural zinc metal or oxide targets with 200 MeV protons using the Brookhaven Linac Isotope Producer (BLIP) [13, 14]. Natural zinc foils are bombarded with protons (20–50 μA) for 18–48 h to induce the $^{nat}Zn(p,2pxn)^{67}Cu$ reaction (Fig. 1) [14]. A drawback of using natural zinc as a target is that significant quantities of copper-61 and copper-64 are produced simultaneously—via the $^{66}Zn(p,2pn)$, $^{67}Zn(p,\alpha)$, $^{68}Zn(p,\alpha\nu)$, and $^{70}Zn(p,\alpha 3\nu)$ reactions—and therefore the copper-67 must be allowed to decay for at least 2 days to allow for the shorter-lived copper-64 contaminant

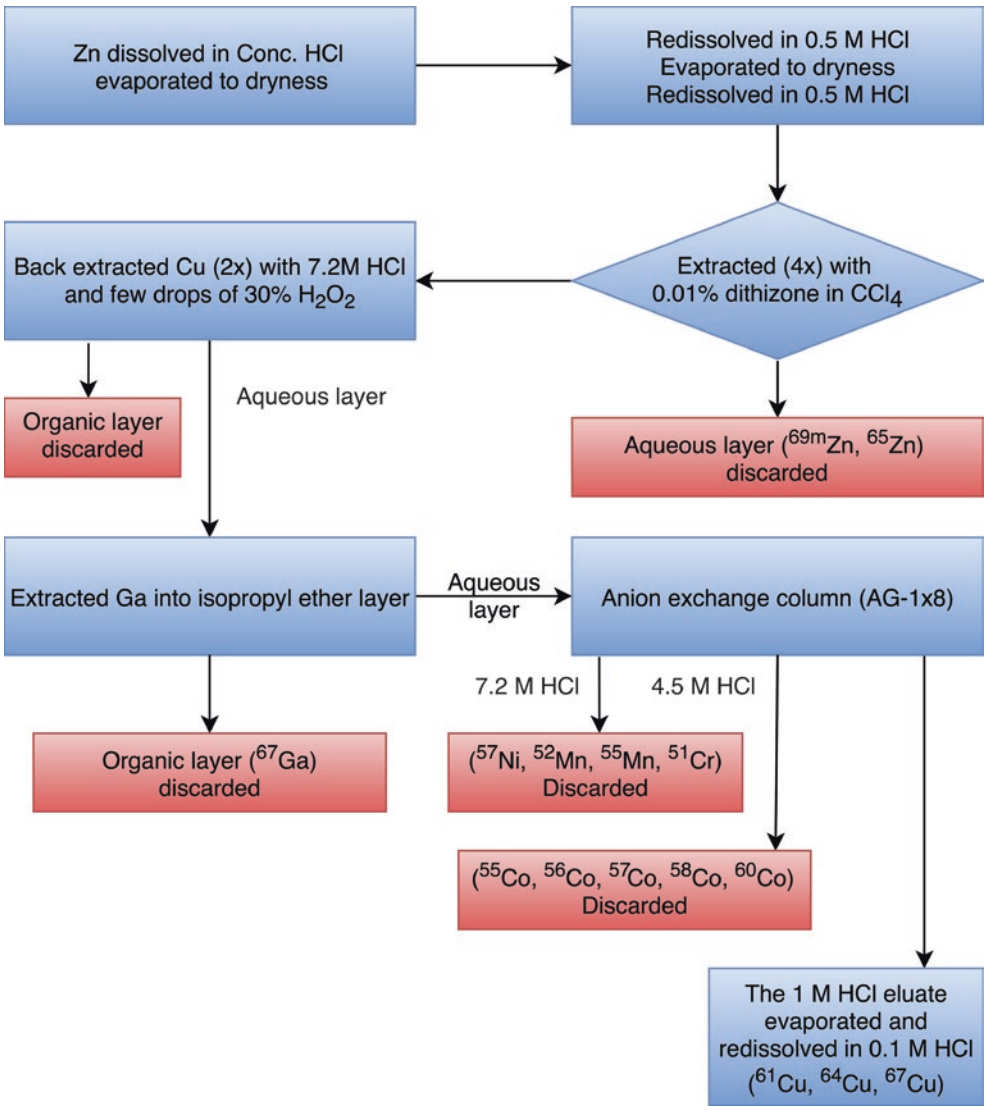

Fig. 1 Flowchart of the copper-67 separation strategy at BLIP used in 1991 (From Dasgupta *et al.* [13], with permission)

to decay away. A further drawback to the production of copper-67 is that the specific activity obtained—ranging from 74–222 MBq/mg (2–6 mCi/μg)—is too low for receptor-targeted radiotracers. To improve upon this, BNL switched to irradiating enriched zinc-68 targets, which had previously been shown to increase production yields by 4.5-fold [15] and eliminate the production of the stable impurities copper-63 and copper-65. Due to the increased cost of using a zinc-68 target, methods were developed to facilitate the recycling of the target; however, this involved handling long-lived zinc-65 ($T_{1/2}$ = 244 d) that is produced via the ^{68}Zn(p,p3n) nuclear reaction. To ameliorate the high dose from the zinc-65, a target processing protocol was developed to electroplate zinc (0.7–8 g) onto a titanium disk and remotely load the irradiated target into an aluminum capsule into a hot cell. The new aluminum targets were designed such that they could be irradiated simultaneously with other production targets, reducing the overall cost of the production of copper-67 by sharing the cost of running the linear accelerator (LINAC).

Generally speaking, the targets for the production of copper-67 are processed using a modified ion-exchange procedure [16]. Briefly, the target is dissolved with 20–40 mL of 12 M hydrogen chloride. The resultant solution is then loaded onto a Bio-Rad AG50-X4 cation exchange column (12–15 mL, 100–200 mesh). The zinc is washed off with 2 column volumes of 10 M hydrogen chloride, dried down, and then taken up in 0.5 M sodium acetate buffer. After the addition of 1 mL of sodium hydroxide, the resultant solution was loaded onto a Chelex column on which the copper cation is retained and the zinc cation is eluted from the column. The column is then washed with varying concentrations of hydrogen chloride to remove unwanted metals, and the copper is eluted with 2 M hydrogen chloride. This procedure was modified to improve the separation of the copper-67 from both the coproduced cobalt impurity and the zinc starting material.

In the past, Los Alamos National Lab (LANL) has produced copper-67 for the nuclear medicine community. However, at the time of writing, BNL is the only facility that is producing copper-67 for external customers. The Facility for Rare Isotope Beams (FRIB) at the Michigan State University (MSU) is under construction at the time of this writing, and this facility will allow harvesting of usable quantities of difficult-to-produce medical radionuclides, such as copper-67. Mastren *et al.* showed the feasibility of producing copper-67 by isotope harvesting from an aqueous beam dump at a heavy-ion fragmentation facility at the National Superconducting Cyclotron Laboratory (NSCL) at the MSU campus [17, 18]. A liquid-water target system/beam stop at NSCL was used to collect samples of copper-67 that were also produced as a secondary beam (76 MeV/A) at the NSCL. A series of separation steps were performed to remove radioactive isotopes of germanium, gallium, zinc, and nickel, as well as stable zinc (Fig. 2) [18]. Copper-67 produced by this method was used to label a NOTA-bearing immunoconjugate of panitumumab at relatively low molar activity (128 MBq/μmol), demonstrating the feasibility of this approach [17]. It has been estimated that FRIB will be

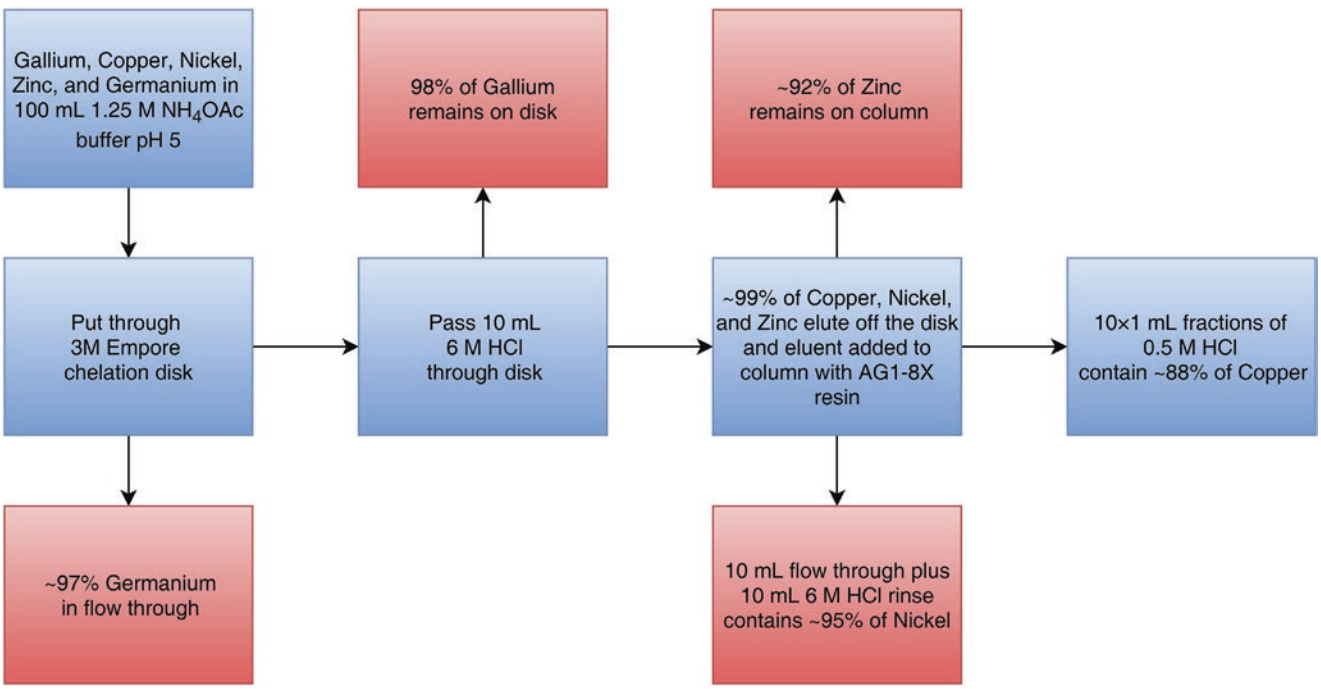

Fig. 2 Flowchart of separation strategies for the isolation of copper-67 at the NSCL (From Mastren *et al.* [18], with permission)

able to produce up to 74 GBq (2 Ci) of copper-67 and that weekly harvesting will provide a reliable and continuous supply of this isotope [18].

The Production of Copper-64 Copper-64 can be efficiently produced on both a reactor and a biomedical cyclotron. Zinn *et al.* developed an approach to the production of copper-64 via the $^{nat}Zn(n,p)^{64}Cu$ reaction in a nuclear reactor [19]. Utilizing fast neutrons, high specific activity copper-64 was produced at the Missouri University Research Reactor (MURR) in amounts averaging 9.3 GBq (250 mCi); however, the coproduction of long-lived zinc-65—and the cost and complexity of the disposal of this radionuclide—eventually ended production by this method. Copper-64 has also been produced in Australia as a by-product of the cyclotron-based production of gallium-67 via the $^{68}Zn(p,2n)^{67}Ga$ reaction [20]. Although this mode of production is economical and allows for the production of very large amounts [> 0.11 TBq (3 Ci)] of material with reasonably high molar activity [~ 31.8 TBq/mmol (860 Ci/mmol)], a drawback is that on-demand production would be problematic, given that the major radionuclide produced is longer-lived gallium-67 ($T_{1/2}$ = 72 h).

Copper-64 is currently produced primarily by the $^{64}Ni(p,n)^{64}Cu$ nuclear reaction on a biomedical cyclotron [21] using methodology first proposed by Szelecsenyi *et al.* [22]. This reaction involves the irradiation of enriched nickel-64 which has been electroplated on a gold or rhodium platform [21–25]. An enriched nickel-64 target has been designed that can be efficiently recovered post irradiation (Fig. 3) [21]. The principal advantages of using the $^{64}Ni(p,n)^{64}Cu$ transmutation reaction are that very high molar activity copper-64 is produced (> 370 TBq/mmol (10 KCi/mmol)) and that curie-scale amounts can be prepared on demand. Using a 12 MeV cyclotron, Obata *et al.* reported yields of >111 MBq/μAh and averaged 74 MBq/μAh with >99% radionuclidic purity (Fig. 4) [24], while Avila-Rodriguez *et al.* improved yields to >260 MBq/μAh with 11.4 MeV protons [26]. The use of copper-64 has dramatically increased over the past decade [27], and it is being produced—in some cases routinely—in the United States [21, 28], Europe [25], and Japan [24].

The Production of Copper-60/61 Large quantities of copper-60 (up to 32 GBq) and copper-61 (up to 5 GBq) have also been produced on a biomedical cyclotron using enriched nickel-60 and nickel-61 targets, respectively [23]. The methods for the purification of these nuclides from their targets follow methods similar to those developed for copper-64. These radionuclides have shorter half-lives—23 min and 3.3 h, respectively—and while copper-60 has been used in conjunction with the thiosemicarbazone ATSM to image hypoxia (Fig. 5) [29], the use of copper-60 has been replaced by the more practical copper-64 [30].

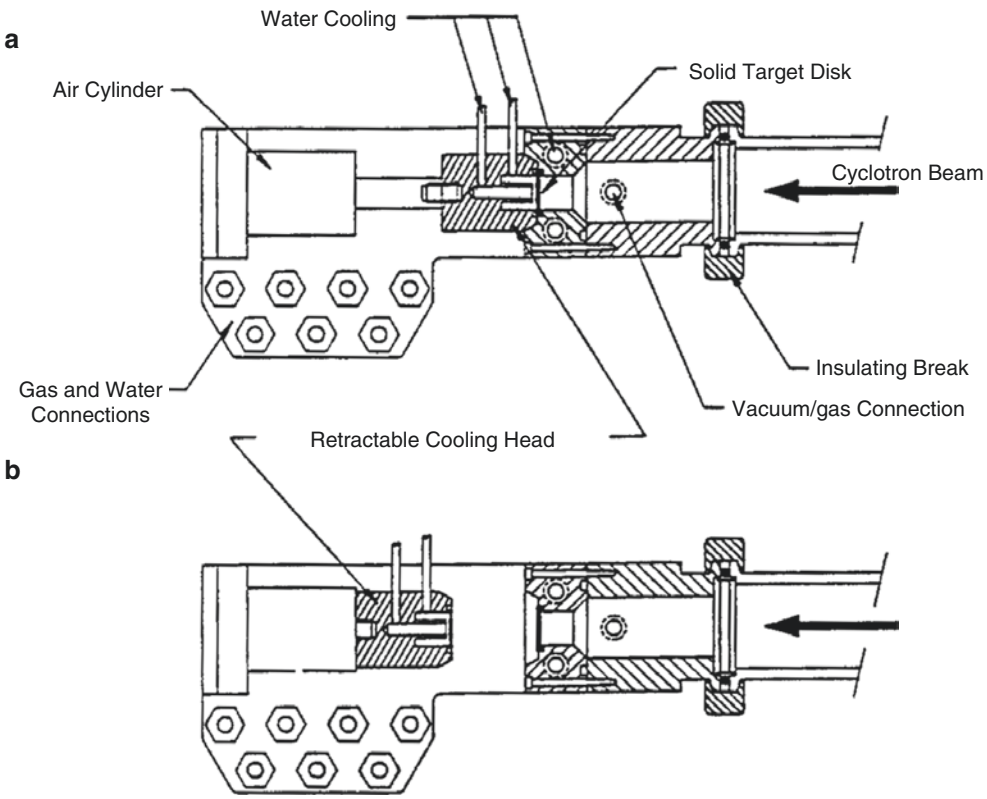

Fig. 3 Remotely controlled solid target (gold disk plated with nickel-64) holder with retractable cooling head for the production of copper-64: (**a**) configured for irradiation and (**b**) retracted for the transfer of the target disk after irradiation (From McCarthy *et al.* [21], with permission)

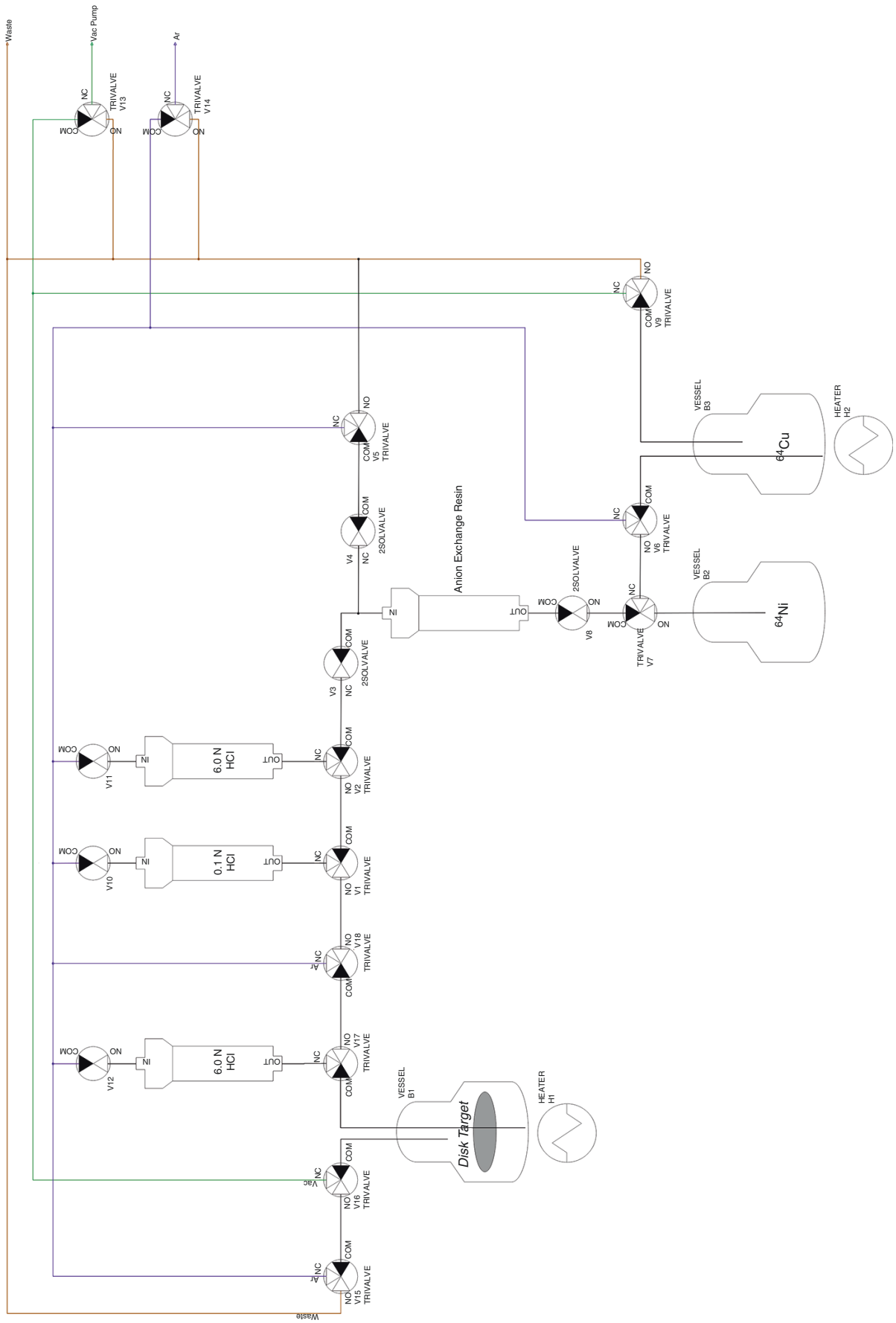

Fig. 4 Scheme of the apparatus for the separation of copper-64. The apparatus consists of three parts: a heater to remove the irradiated nickel-64, a column to separate copper-64 from nickel-64, and a vial to collect the copper-64. The parts are connected with Teflon tubing and electric valves. The electric valves are operated using a remote controller (From Obata *et al.* [24], with permission)

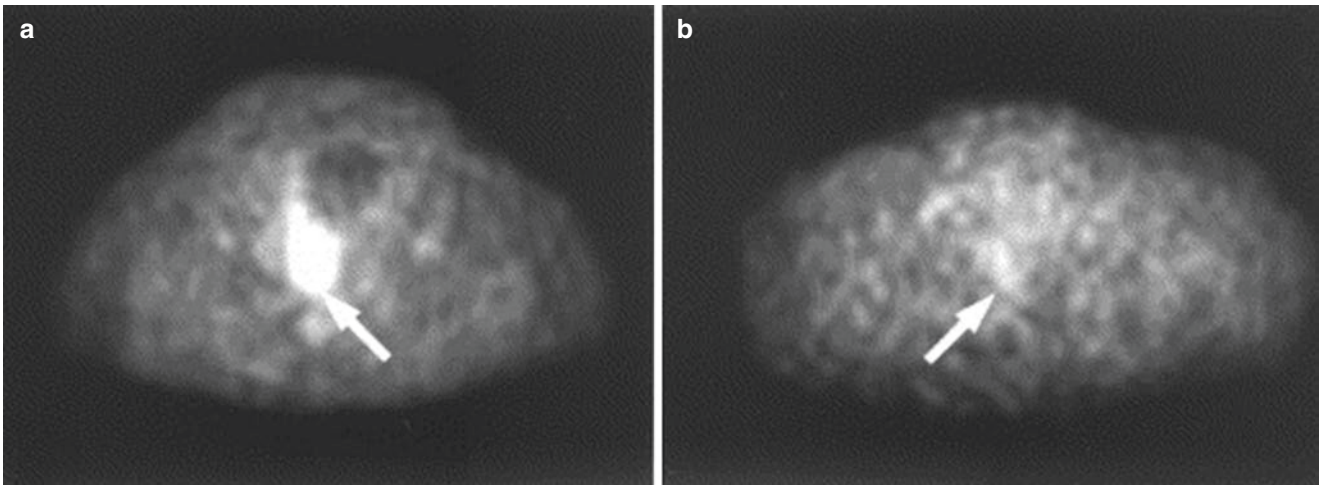

Fig. 5 Transaxial pelvic PET images of two patients 30–60 min after the injection of [^{60}Cu]Cu-ATSM. (**a**) Intense uptake in the primary tumor (arrow) of Patient 2, who developed recurrent disease at 6 months. (**b**) Low uptake in the primary tumor (arrow) of Patient 12, who was free of disease after 23 months (From Dehdashti *et al.* [29], with permission)

The Production of Copper-62 Copper-62 is the daughter radionuclide of cyclotron-produced zinc-62 ($T_{1/2}$ = 9.2 h). The use of a ^{62}Zn/^{62}Cu generator as a source of copper-62 for radiopharmaceuticals was first reported by Robinson *et al.* [31], and even with the short lifetime of the generator (1–2 days), there has been significant interest in radiopharmaceuticals labeled with copper-62. Historically, the generator consisted of zinc-62 loaded onto a Dowex 1x10 anion-exchange column and can be eluted with 2 M hydrogen chloride followed by buffering with 3 M sodium acetate [32]. The latest version is a ^{62}Zn/^{62}Cu 50 μL microgenerator that utilizes 0.2 M hydrogen chloride and 1.8 M sodium chloride as the elution buffer [33], though this configuration also requires buffering with sodium acetate (Fig. 6). Another type of generator—first reported by Fujibayashi *et al.*—involved loading zinc-62 in 2 mL water at pH 5.0 on CG-120 Amberlite cation-exchange resin [34]. The generator eluent (200 mM glycine) is advantageous because as formulated, ready-to-inject thiosemicarbazone tracers could be produced without further purification. Unfortunately, however, leakage of zinc-62 using this elution scheme proved to be a problem, prompting Fukumura *et al.* to add a Sep-Pak CM cartridge—a silica-based weak acidic cation exchanger—to the system in order to reduce the levels of zinc-62 to less than 0.1% (Fig. 7) [35].

The Chelation Chemistry of Copper-Based Radiopharmaceuticals

Introduction to Copper-Based Radiopharmaceuticals

Copper-based radiopharmaceuticals fall into two major categories. The first class of agents consists of small copper coordination complexes, most often compounds bearing bis(thiosemicarbazone) (BTS) ligands. These metal complexes—though relatively unstable *in vivo*—are planar and lipophilic and can thus diffuse into the heart and brain for the imaging of blood flow or, in some cases, become trapped selectively in hypoxic tissues. The second class of Cu-based radiopharmaceuticals is predicated on the attachment of highly stable radiocopper-chelator complexes to vectors that target proteins that are upregulated in disease. These vectors are typically biomolecules such as proteins or peptides but can also be macromolecules such as nanoparticles. In addition, there are several less common copper-based radiotracers that defy classification in this two-tiered system, including [^{62}Cu]$CuCl_2$ (which is taken up in tumors by copper transporters, *e.g.* CTR1). Indeed, this chapter will feature some discussion of the recent resurgence of [^{64}Cu]$CuCl_2$ as a PET agent for tumor imaging. Finally, radioactive copper has also been incorporated into elemental copper-based nanoparticles [36].

Coordination Chemistry of Copper(I) and Copper(II)

The aqueous solution coordination chemistry of copper is limited to two oxidation states: Cu(I) and Cu(II) [37–39]. The Cu(III) cation can exist, though it is relatively rare and difficult to attain without the use of strong π-donating ligands [40]. Copper(I) must be stably complexed under aqueous conditions since the free ion disproportionates to Cu(II) cation and Cu(0) metal. Due to their lability, most Cu(I) complexes lack sufficient kinetic stability for *in vivo* applications. Cu(II) has d^9 electronic configuration and "prefers" forming 4-coordinate, square planar complexes. It is common for two additional ligands to bind Cu(II) as well, resulting in the formation of six-coordinate complexes that exhibit axial elongation or tetragonal compression due to the Jahn-Teller effect. Copper(II) complexes typically have color, with both

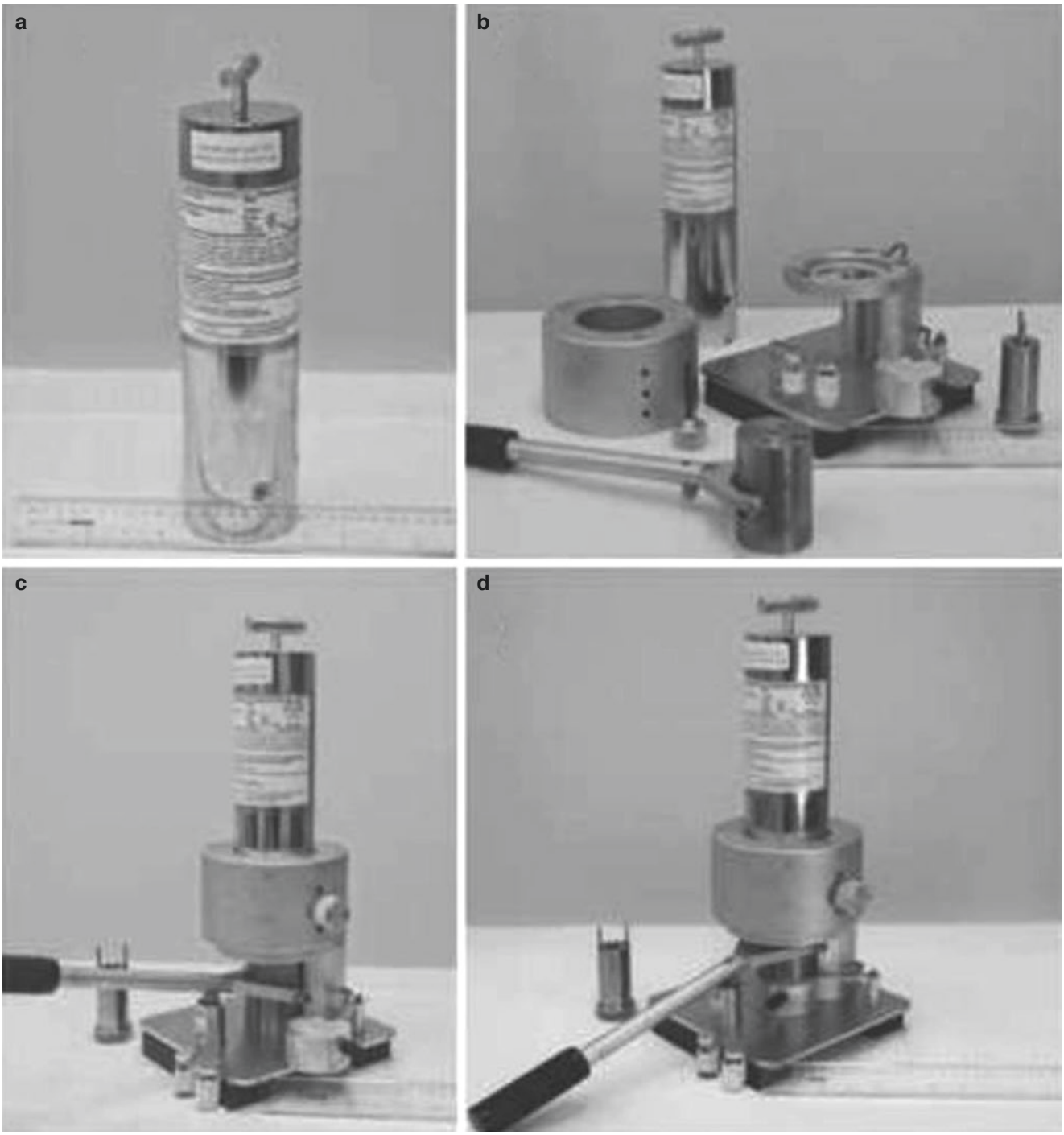

Fig. 6 The $^{62}Zn/^{62}Cu$ microgenerator produced by Proportional Technologies, Inc. (Houston, TX). (**a**) Generator unit. (**b**) Generator and disassembled stand and shielding. (**c**) Assembled generator stand and shielded elution vial. (**d**) Generator with shielded vial positioned for elution (From Ng *et al.* [33], with permission)

the λ_{max} and extinction coefficients dependent on the nature of the ligands. Copper(II) has borderline softness, which means that the metal favors nitrogen- and sulfur-containing ligands but will also coordinate phosphorous and oxygen atoms to form square planar, distorted square planar, trigonal pyramidal, square pyramidal, and distorted octahedral geometries.

Although Cu(II) is less labile than Cu(I), the kinetic stability of Cu(II) complexes *in vivo* is much more important from a radiopharmaceutical point of view than their thermo-

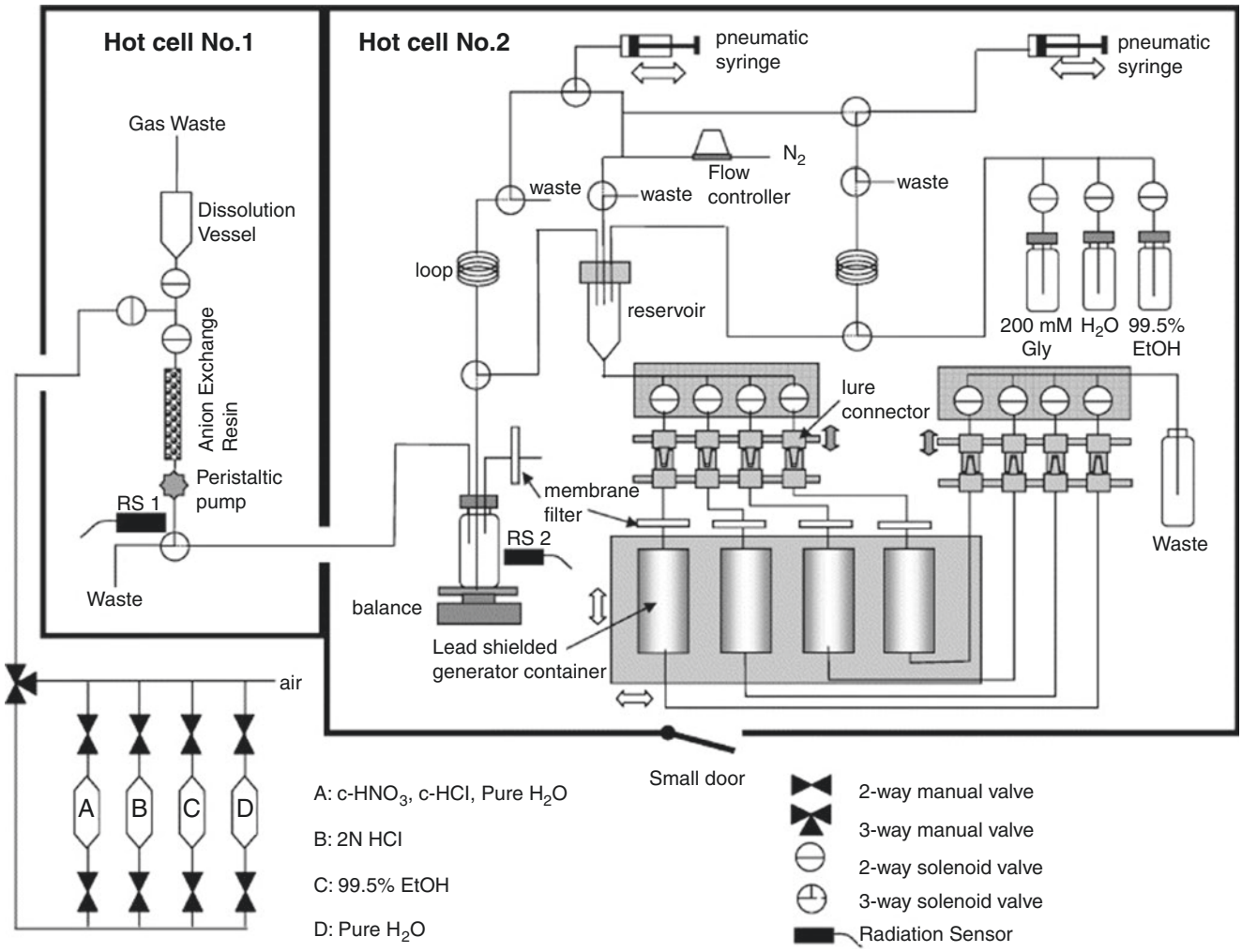

Fig. 7 Dispensing system for the $^{62}Zn/^{62}Cu$ generator (From Fukumura *et al.* [35], with permission)

dynamic stability in aqueous solution. Caution should be paid when selecting chelators for copper complexes, as the choice of chelators for copper can have a major impact on the biodistribution of the tracer (Fig. 8). Therefore, the development of novel chelation systems for copper radionuclides that have long-term *in vivo* stability has been an active area of investigation. Indeed, the stability, charge, hydrophilicity, and even the size of the copper complex can all impact *in vivo* distribution. It is important to remember that the biodistribution data for a given radiocopper complex is also indicative of "free" radioactive copper cations that dissociate from the chelator *in vivo* via reduction or transchelation [41]. Last but not least, the renaissance of imaging with copper chloride [5, 42] as well as the advent of quantum dots containing radioactive copper [43] underscores the fact that organic chelators are not necessarily required for copper-based PET imaging. Hence, there is no simple answer to the question "what is the best chelator for copper?"

Radiotracers Based on Copper Bis(thiosemicarbazones) (BTS)

Several copper complexes labeled with copper-62 and copper-60 have been designed to be sufficiently stable to clear from circulation while passively and efficiently diffusing into tissues of interest such as the heart, brain, kidneys, or tumor. A historical example from 30 years ago that still remains relevant today is centered upon copper complexes bearing bis(thiosemicarbazone) (BTS) ligands [45, 46]. Nonradioactive copper(II)-bis(thiosemicarbazone) (Cu-BTS) complexes were found to be toxic to tumor cells in the 1960s [47]. In the 1980s, Green, Welch, and others began investigating copper-62-labeled pyruvaldehyde bis(N^4-methylthiosemicarbazone) ([^{62}Cu]Cu-PTSM) for the imaging of various tissues, such as the brain [48–52], heart [53–55], kidneys, and tumors [56]. Figure 9 shows some most common BTS compounds as well as GTS (glyoxal

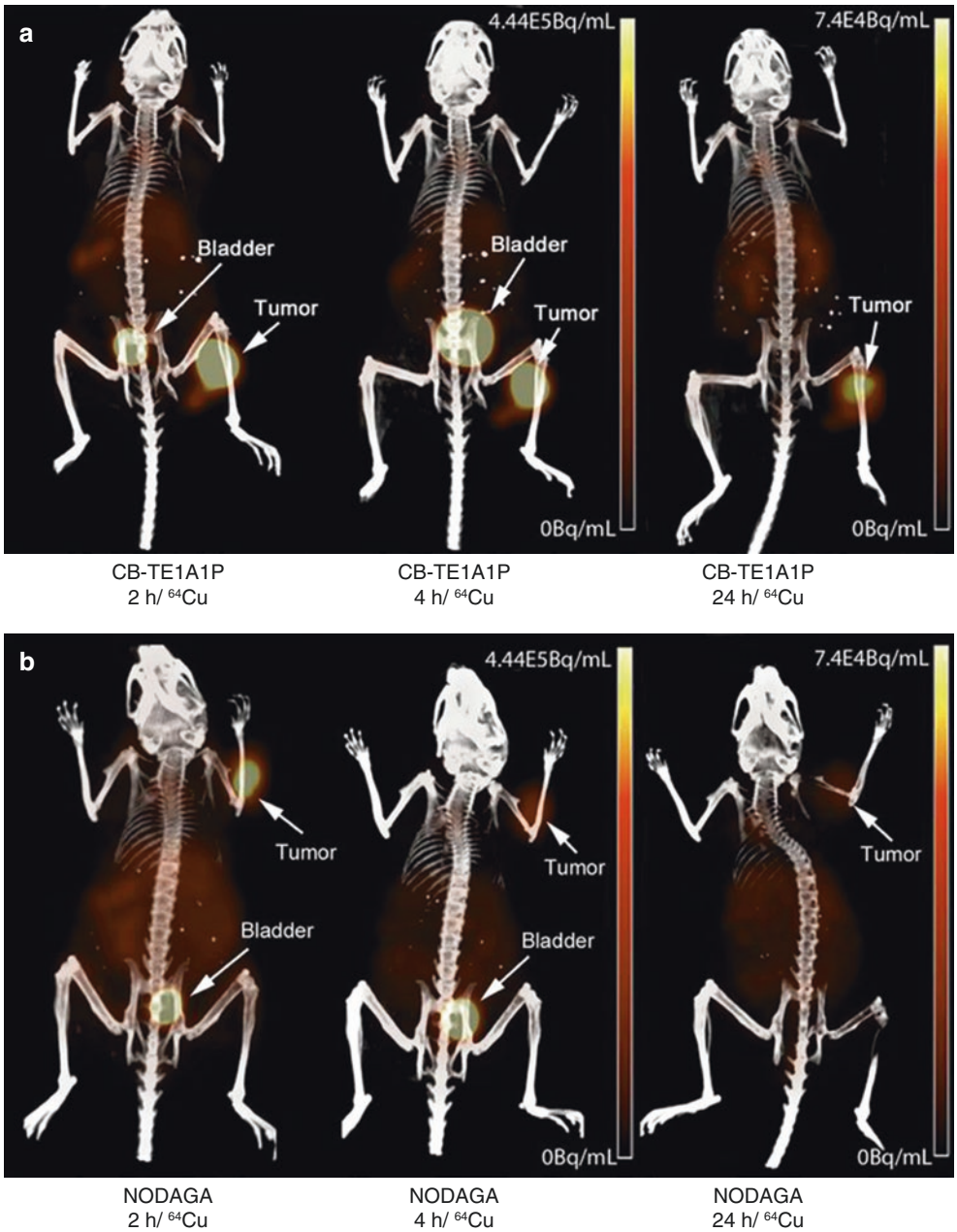

Fig. 8 Small-animal PET/CT imaging of B16F10 tumor-bearing mice at 2, 4, and 24 h after the administration of (**a**) [^{64}Cu]Cu-CB-TE1A1P-PEG4-LLP2A or (**b**) [^{64}Cu]Cu-NODAGA-PEG4-LLP2A (From Beaino and Anderson [44], with permission)

bis(thiosemicarbazone)) derivatives that can form copper complexes, some of which are capable of penetrating the blood-brain barrier [57–59]. Upon reaching the tissue of interest, some of these complexes can release their radioactive copper cation, a trait that is actually advantageous, since this copper will then remain trapped in the tissue.

The synthesis and radiolabeling of the BTS ligands are fairly straightforward and based on a procedure published by Petering *et al.* (Fig. 10) [47]. The appropriate α-ketoaldehyde is added to an aqueous solution of a thiosemicarbazide with 5% glacial acetic acid at 50–60 °C under continuous stirring. The product can subsequently be recrystallized readily using boiling methanol with the quick addition of water. The radiolabeling procedures for BTS analogs are equally facile and involve adding acidic [^{64}Cu]copper chloride to acetate buffer (25 mM, pH 6.0) [33] or glycine buffer (200 mM, pH 5.0–6.0) [61]. The labeling reaction proceeds rapidly: ~5 min at room temperature.

While the practice is somewhat uncommon, BTS chelators can be functionalized with receptor-targeting ligands to enhance their target-specific uptake. For example, Donnelly *et al.* appended a stilbene or styrylpyridine group to one side of the BTS complex (Fig. 11), and this agent bound to amyloid-β (Aβ) plaques as illustrated by PET imaging in a

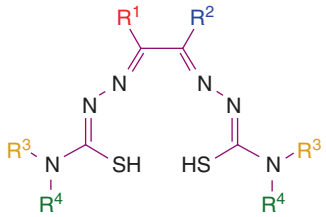

ATSM	R^1=R^2 = CH_3; R^3 = CH_3; R^4 = H
PTSM	R^1 = H; R^2 = CH_3; R^3 = CH_3; R^4 = H
ETS	R^1 = H; R^2 = CH_2CH_3; R^3=R^4 = H
GTSM	R^1=R^2 = H; R^3 = CH_3; R^4 = H
GTSE	R^1=R^2 = H; R^3 = CH_2CH_3; R^4 = H
GTSP	R^1=R^2 = H; R^3 = C_6H_5; R^4 = H
$GTSM_2$	R^1=R^2 = H; R^3=R^4 = CH_3
$GTSE_2$	R^1=R^2 = H; R^3=R^4 = CH_2CH_3
GTSPY	R^1=R^2 = H; R^3=R^4 = -$(CH_2)_4$-

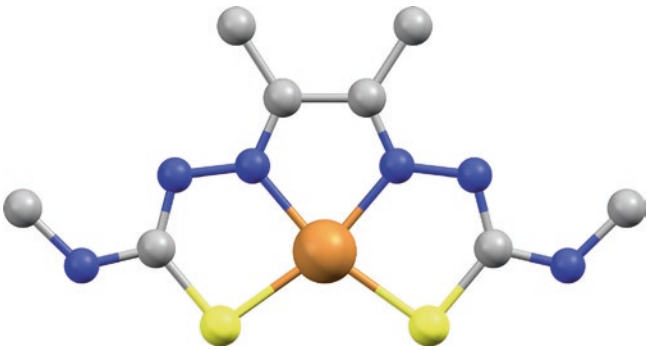

Fig. 9 (Top) Structures of BTS and GTS chelators for copper. (Bottom) Crystal structure of Cu-ATSM [60], showing a square planar configuration (*carbon, gray; nitrogen, blue; sulfur, yellow; copper, bronze; hydrogen atoms are omitted for the sake of clarity*)

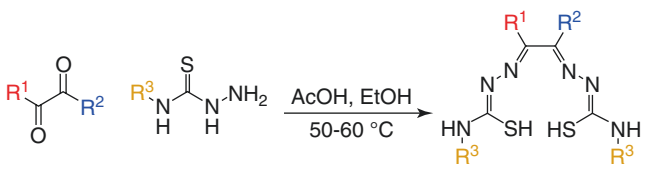

Fig. 10 The synthesis of BTS chelators

transgenic mouse model of Alzheimer's disease (AD) [62, 63]. Along these lines, bifunctional BTS ligands have also been used for the radiolabeling of peptide-based conjugates with radionuclides of copper [64, 65].

Copper(II)-labeled BTS complexes have been extensively evaluated as ^{62}Cu-radiopharmaceuticals for the PET imaging of perfusion [32, 52, 54, 55, 66–69]. However, in humans, the myocardial uptake of [^{62}Cu]Cu-PTSM is markedly attenuated at high rates of flow [68], undermining the tracer's potential clinical utility for quantification of myocardial perfusion under hyperemic conditions [54, 55, 70]. Subsequent work [71, 72] revealed the source of this problem to be interspecies variability in the binding of Cu-PTSM to serum albumin (*i.e.* $K_{human\ albumin} > K_{dog\ albumin}$; Fig. 12). A more recently developed BTS-based tracer—[^{62}Cu]Cu-ETS—has been investigated for imaging tumor blood flow, and this agent does not exhibit the interspecies variations in albumin binding that proved problematic with Cu-PTSM [73, 74].

Imaging of Hypoxia with Copper-Labeled BTS Agents

Hypoxia (low oxygenation) can affect the entire body (*e.g.* altitude sickness) or can occur locally in many types of tissues and organs. Hypoxia often occurs in tumors and/or the tumor microenvironment, where cells are rapidly growing and overutilizing oxygen from the surrounding blood supply [75]. Nitroimidazole-based agents—such as ^{18}F-labeled fluoromisonidazole (FMISO) and 1-(5-fluoro-5-deoxy-α-D-arabinofuranosyl)-2-nitroimidazole (FAZA)—that can be reduced and selectively retained in hypoxic tissues are widely used PET tracers for imaging hypoxia [76–78].

Several Cu-BTS complexes labeled with copper-60, copper-62, and copper-64 have been developed as hypoxia-targeted PET imaging probes [46]. Before we move on to our discussion of these constructs, a short discussion of the redox chemistry of copper is warranted. As we have discussed above, the most common oxidation states of copper are Cu(I) and Cu(II), and the standard reduction potential (E^0) from Cu(II) to Cu(I) is relatively low (about 0.15 V). This means Cu(I) can be readily oxidized to Cu(II), yet Cu(II) is also susceptible to being reduced to Cu(I). For Cu(II) complexes, reduction potentials decrease as the ligand stabilizes the complex. Furthermore, after the Cu(II) center is reduced to Cu(I), some complexes may dissociate as the metal changes its coordination geometry preferences, leading to the release of Cu(I) [79]. Other Cu(I) complexes, however, are resistant to dissociation and can be readily re-oxidized to Cu(II) by molecular oxygen. For example, Cu-GTSM is a Cu-BTS complex derived from glyoxal (GTS). Its structure is very similar to the well-studied hypoxia imaging agent, Cu-ATSM, though there are no methyl groups in the R_1 or R_2 positions (see Fig. 9). Crystallographic analysis tells us that the lack of alkyl groups results in a slightly shorter C=C double bond, which further stretches the two sulfur atoms away from the copper ion and creates a weaker ligand for copper [80]. As a result, Cu-ATSM has a reduction potential ($E_{1/2}$) of −0.60 V (vs AgCl/Ag) [81], while Cu-GTSM has an $E_{1/2}$ of −0.44 V (vs AgCl/Ag). Put simply, Cu(II)-GTSM is easier to reduce. These seemingly minor differences in structure and reduc-

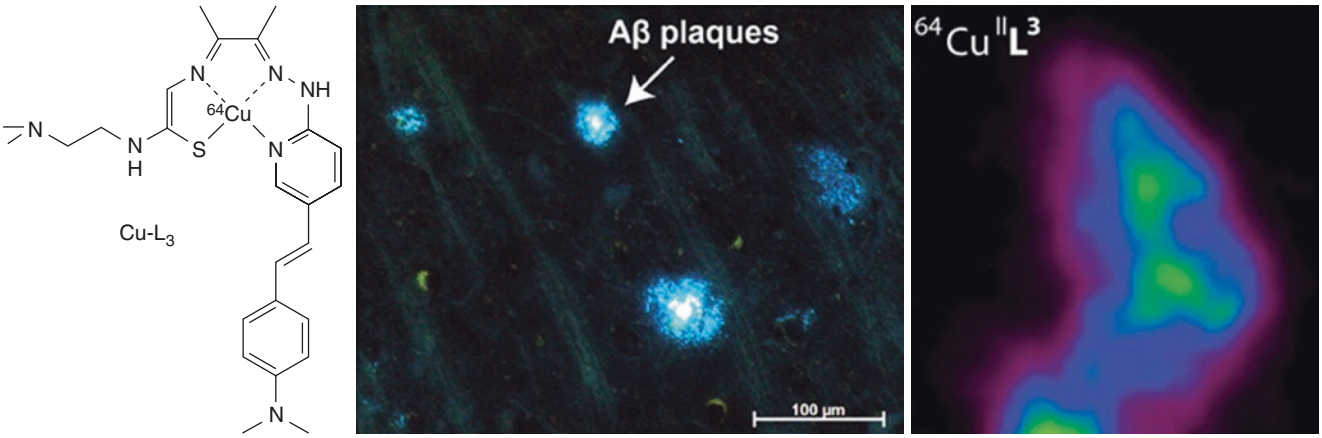

Fig. 11 (Left) Structure of styrylpyridine-functionalized BTS chelator L^3. (Middle) Epifluorescence of Cu-L^3 in a frontal cortex sample of a transgenic mouse with AD showing binding of the complex to Aβ plaques. (Right) PET scan of [^{64}Cu]Cu-L^3 in the brain of a mouse (From Hickey *et al.* [63], with permission)

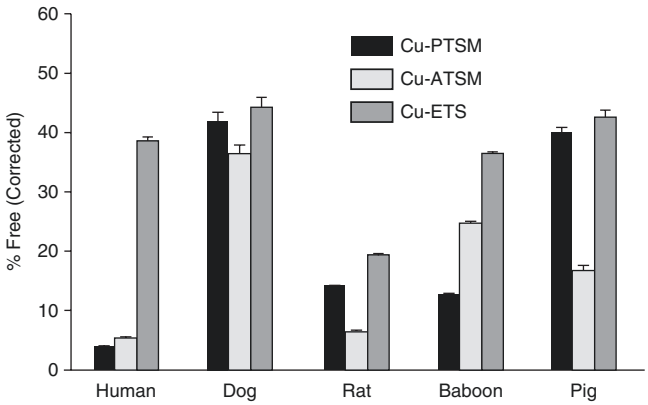

Fig. 12 Species dependence of the binding of ^{64}Cu-labeled BTS complexes to serum albumin (40 mg/mL) (From Basken *et al.* [74], with permission)

tion potentials lead to significant differences in the applications of radiotracers based on Cu-ATSM and the family of Cu-GTS compounds. Cu-ATSM is used for the PET imaging of hypoxia, as the molecule is retained selectively in hypoxic cells but not in normal cells. In contrast, radiotracers based on the Cu-GTS family of compounds are trapped in all cells, regardless of their oxygen saturation levels [81]. These Cu-GTS agents release the Cu(I) cation under even normoxic intracellular conditions due to their more positive (or less negative) reduction potentials [82]. While this means that Cu-GTS complexes cannot be used for hypoxia imaging, they have shown some promise for the PET imaging of copper metabolism in murine models of neurodegenerative diseases [58, 59].

[^{60}Cu]Cu-ATSM has been investigated in women with cervical cancer and was found to be a predictor of recurrence [83]. Patients with glioma were imaged with [^{62}Cu]Cu-ATSM, and the radiotracer distinguished tumor grades and tissue hypoxia (Fig. 13) [84]. Nie *et al.* imaged hypoxia in mouse and rabbit models of atherosclerosis and showed that the uptake of a macrophage marker (RAM-11) and a hypoxia indicator (pimonidazole) correlated with the uptake of [^{64}Cu]Cu-ATSM in the plaques [85, 86]. [^{64}Cu]Cu-ATSM and [^{18}F]-FMISO have been compared for imaging hypoxia in several tumor types, and these findings note the advantages of both tracers [87].

^{64}Cu-Labeled Macrocyclic Chelators and Chelator-Bearing Bioconjugates

Traditional Macrocyclic Chelators

The development of chelators capable of forming complexes with radiocopper that are highly stable *in vivo* has been a major area of research since the 1980s, when Meares *et al.* showed that macrocyclic chelators were required to prevent the immediate dissociation of the copper(II) cation in living subjects [88]. The traditional macrocycles used to chelate copper radionuclides are cyclen and cyclam structures modified with carboxylic groups, *e.g.* DOTA (a cyclen derivative) and TETA (a cyclam derivative) (Fig. 14) [89]. These macrocyclic complexes can be labeled under relatively mild conditions. For example, TETA-bearing peptides can be radiolabeled in about 30 min at room temperature and pH 5.5 [90], while DOTA-bearing constructs can be radiolabeled at room temperature and pH 6.5 [91] or with heat (50 °C) and pH 5.5 [92]. However, radiocopper-labeled complexes of DOTA and TETA have been shown to be relatively unstable *in vivo* [93].

A more promising macrocycle for the coordination of radiocopper is TE2A, in which two of the macrocyclic nitrogens are modified with acetate arms and two remain protonated (see Fig. 14). Pandya *et al.* reported that the acid

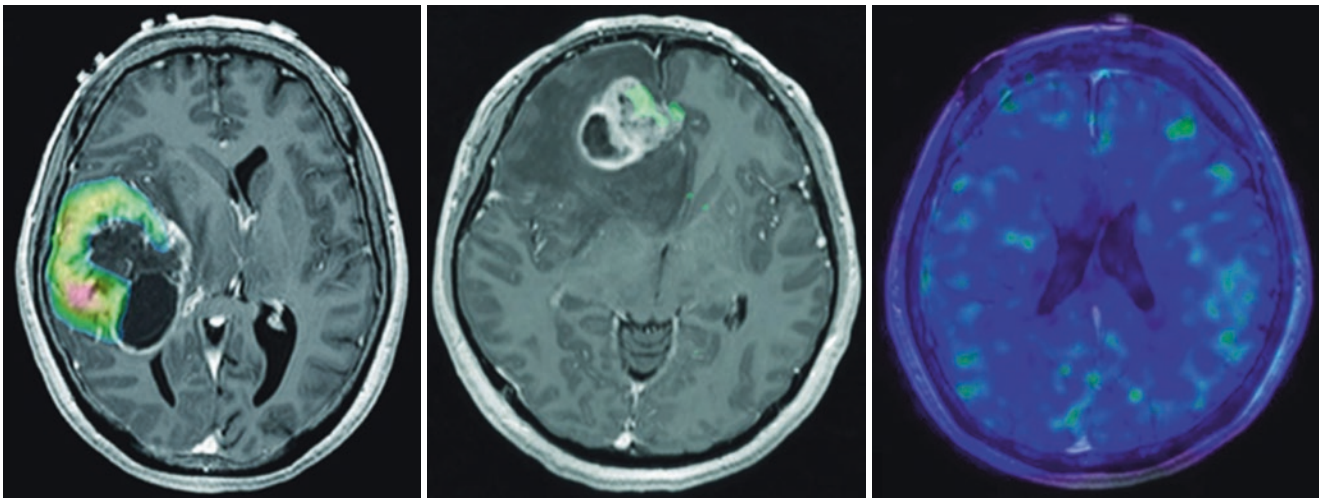

Fig. 13 Merged PET/MR [^{62}Cu]Cu-ATSM images of patients with glioma. Left*:* Patient 1 with glioblastoma. Middle: Patient 2 with glioblastoma. Right: Patient 3 with oligoastrocytoma. Original magnification × 200 (From Tateishi *et al.* [84], with permission)

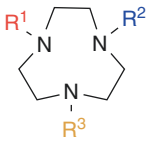

NOTA $R^1=R^2=R^3 = CH_2CO_2H$

NODAGA $R^1=R^2= CH_2CO_2H$; $R^3 = CH(CO_2H)(CH_2)_2CO_2H$

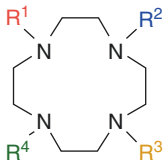

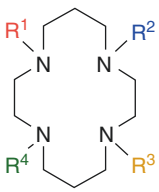

Cyclen $R^1=R^2=R^3=R^4 = H$

DOTA $R^1=R^2=R^3=R^4 = CH_2CO_2H$

DO3A $R^1=R^2=R^3 = CH_2CO_2H$; $R^4 = H$

Cyclam $R^1=R^2=R^3=R^4 = H$

TETA $R^1=R^2=R^3=R^4 = CH_2CO_2H$

TE2A(1,4-) $R^1=R^4 = CH_2CO_2H$; $R^2=R^3 = H$

TE2A(1,8-) $R^1=R^3 = CH_2CO_2H$; $R^2=R^4 = H$

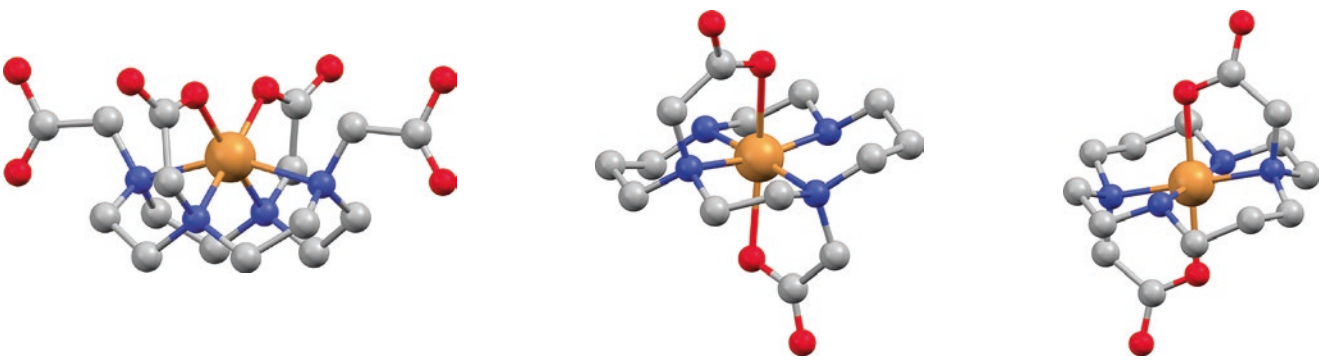

Fig. 14 (Top) Structures of selected traditional macrocyclic chelators. (Bottom) Crystal structure of Cu-DOTA [94], Cu-TE2A(1,4-) [95], and Cu-TE2A(1,8-) [96] (*carbon, gray; nitrogen, blue; oxygen, red; copper, bronze; hydrogen atoms, counterions, and crystallization water molecules are omitted for clarity*)

decomplexation stability of Cu-TE2A was improved compared to Cu-TETA, and rat biodistribution data showed significantly lower activity concentrations in the kidneys and liver 24 h after the administration of [^{64}Cu]Cu-TE2A compared to [^{64}Cu]Cu-TETA, results which strongly suggest reduced dissociation of the metal *in vivo* [97]. More recently, TE2A-benzyl isothiocyanate was conjugated to the CD138-targeting murine monoclonal antibody (mAb) 9E7.4. The radiolabeling of the TE2A-antibody was facile and achieved by brief warming of a mixture of [^{64}Cu]copper chloride and the antibody in a mild buffer. The ^{64}Cu-labeled TE2A-9E7.4 showed decent tumor uptake and tumor-to-blood activity concentration ratios in mice bearing 5T33 xenografts, suggesting that the TE2A chelator may work well for other antibodies (Fig. 15) [98].

The use of Cu-DOTA-like complexes for PET neuroimaging is not advisable. Ono *et al.* attempted to use ^{64}Cu-cyclen- and ^{64}Cu-DOTA-labeled benzofuran compounds for Aβ aggregate-targeted imaging. However, the charged complexes proved unable to penetrate the blood-brain barrier [99].

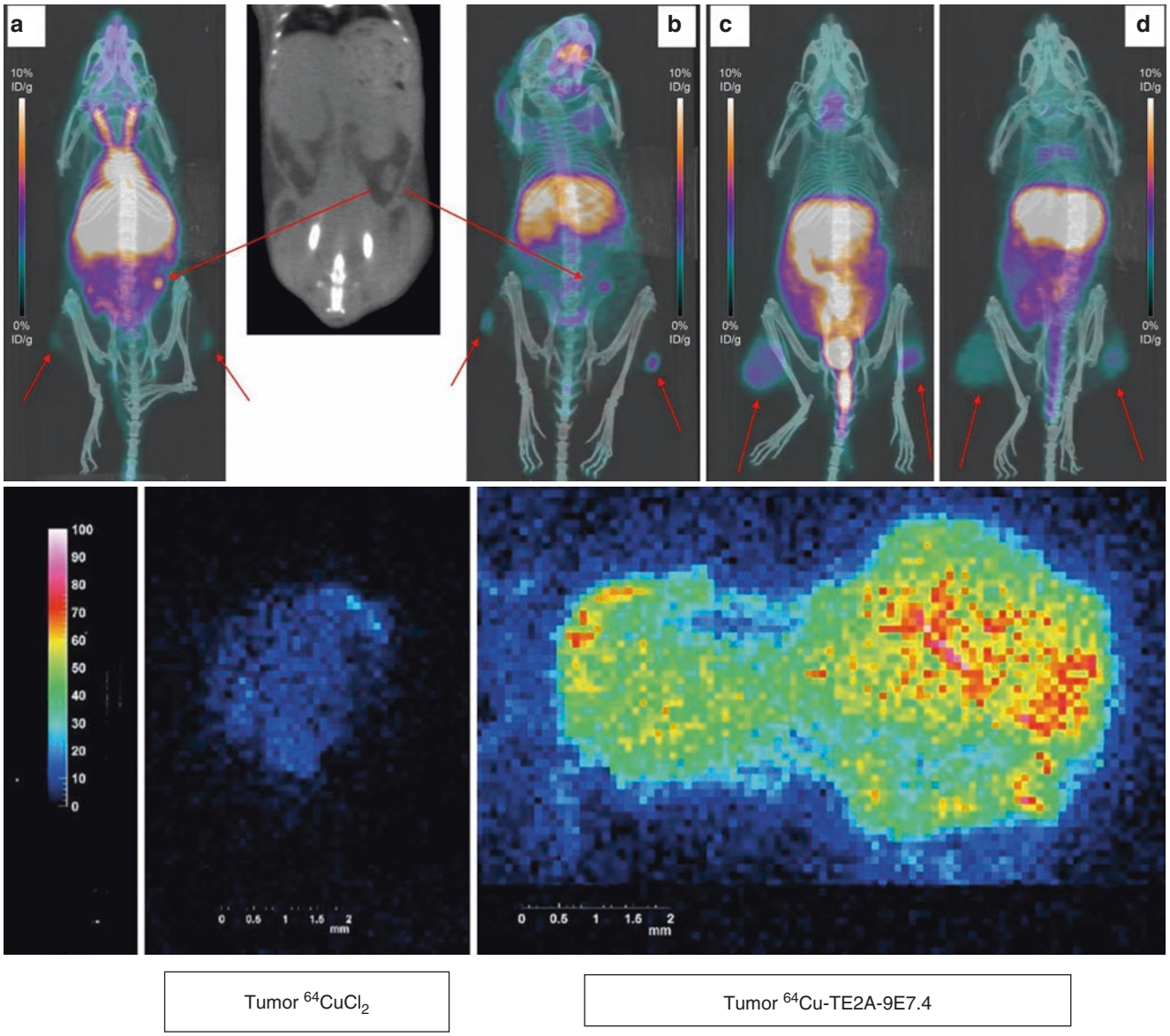

Fig. 15 (Top) PET imaging of [^{64}Cu]Cu-TE2A-9E7.4 and [^{64}Cu]copper chloride ([^{64}Cu]$CuCl_2$) in tumor-bearing mice. Maximum intensity projections PET-CT imaging of [^{64}Cu]Cu-TE2A-9E7.4 at 2 h (**a**) and 24 h (**b**) post-injection, showing uptake in both subcutaneous tumors and an iliac lymph node (tumors are indicated by arrows). Maximum intensity projections of PET-CT imaging with [^{64}Cu]$CuCl_2$ at 2 h (**c**) and 24 h (**d**) post-injection, showing uptake in both subcutaneous tumors. (Bottom) Digital autoradiography of subcutaneous tumors using [^{64}Cu]Cu-TE2A-9E7.4 (right) and [^{64}Cu]$CuCl_2$ (left) (From Bailly *et al.* [98], with permission)

The Sarcophagine Family of Chelators

The sarcophagine family of chelators was first developed by Sargeson *et al.* [100] and was initially investigated for their *in vivo* stability by Smith *et al.* (Fig. 16) [101]. The Sar, DiamSar, and SarAr chelators coordinate copper-64 extremely quickly over a pH range of 4.0–9.0 and are excreted from normal mice very rapidly, though significant uptake in kidneys—likely due to the positive charge of the complexes—is observed [101]. DiamSar was conjugated to c(RGDfD) through a terminal aspartic acid carboxylic acid moiety on the peptide and subsequently labeled with copper-64 at room temperature for 1 h at pH 8.0 [102]. In tumor-bearing mice, [^{64}Cu]Cu-DiamSar-c(RDGfD) cleared from the blood and liver out to 4 hours post-injection, and the uptake of the tracer in M21 melanoma xenografts peaked at 1.5% ID/g at 1 h post-injection. Cai *et al.* synthesized a different sarcophagine-based bifunctional chelator—AmBaSar—which has a benzoic acid moiety for conjugation to primary amines on peptides. This chelator was conjugated to c(RGDyK) and labeled with copper-64 at room temperature for 60 min, pH 5.0 [103]. Biodistribution studies were performed in mice bearing U87MG glioma xenografts, and the construct produced improved tumor-to-non-tumor activity concentration ratios compared to an analogous construct bearing DOTA [104].

Paterson *et al.* developed a sarcophagine-based chelator functionalized with 5-oxopentanoic acid (MeCOSar) and attached it to the somatostatin receptor-targeting peptide octreotate for the imaging of neuroendocrine tumors [106]. The radiolabeling of Sar-TATE with copper-64 was very facile (20 min at room temperature, pH 7.4). In mice bearing A427–7 non-small cell lung cancer xenografts, [^{64}Cu]Cu-Sar-TATE showed very high and persistent tumoral uptake (~30 %ID/g) (Fig. 17); however, the retention of the radiotracer in the kidney was high as well (~10 %ID/g at 24 h) [106]. This same group also conjugated an isothiocyanate-bearing derivative of sarcophagine—(CH_3)(*p*-SCN-Ph)Sar—to an HER2-targeting antibody to image the expression levels of the antigen in a mouse model of breast cancer [107]. This chelator-bearing antibody was radiolabeled with copper-64 readily at room temperature in 5 min and exhibited very high tumoral uptake and reasonable activity concentrations in the liver and kidneys (Fig. 18) [107]. Dearling *et al.* performed a very nice comparison study in which four members of the sarcophagine family as well as DOTA, TETA, and NOTA were conjugated to an engineered antibody fragment (ch14.18-ΔC_H2) for the imaging of neuroblastoma [108]. In this case, the goal was to determine whether decreasing the net positive charge on the sarcophagine chelator would decrease kidney uptake. Although the imaging agents bearing [^{64}Cu]Cu-(SO_3)(CO_2)Sar and [^{64}Cu]Cu-(NH_2)(CO_2)Sar produced lower activity

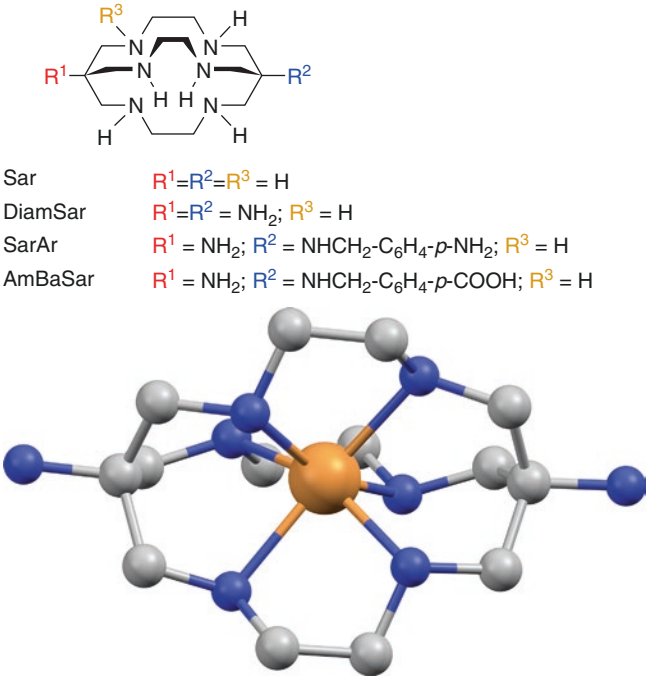

Fig. 16 (Top) Structures of selected sarcophagine chelators. (Bottom) Crystal structure of Cu-DiamSar [105] (*carbon, gray; nitrogen, blue; oxygen, red; copper, bronze; hydrogen atoms, counterions, and crystallization water molecules are omitted for clarity*)

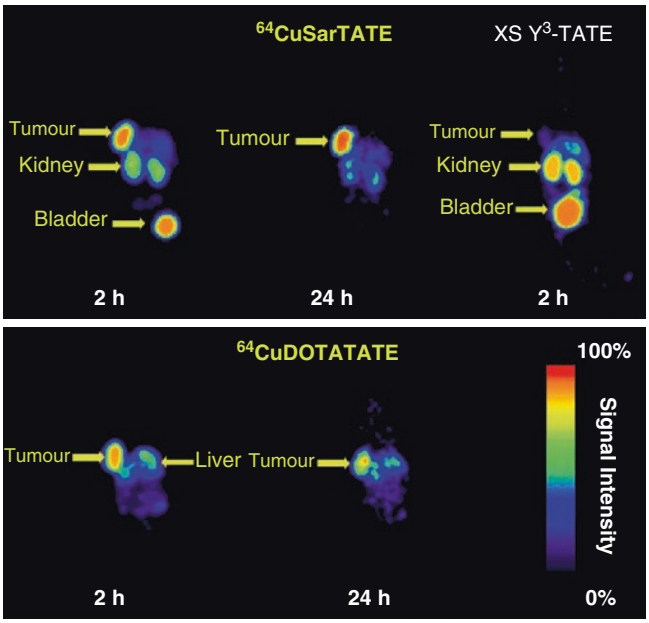

Fig. 17 (Top) PET images of mice bearing A427-7 tumors at 2 h and 24 h post-injection of [^{64}Cu]Cu-Sar-TATE (with and without the co-injection of Tyr^3-octreotate as a blocking agent) and (bottom) PET images of mice bearing A427-7 tumors at 2 h and 24 h post-injection of [^{64}Cu]Cu-DOTA-TATE (From Paterson *et al.* [106], with permission)

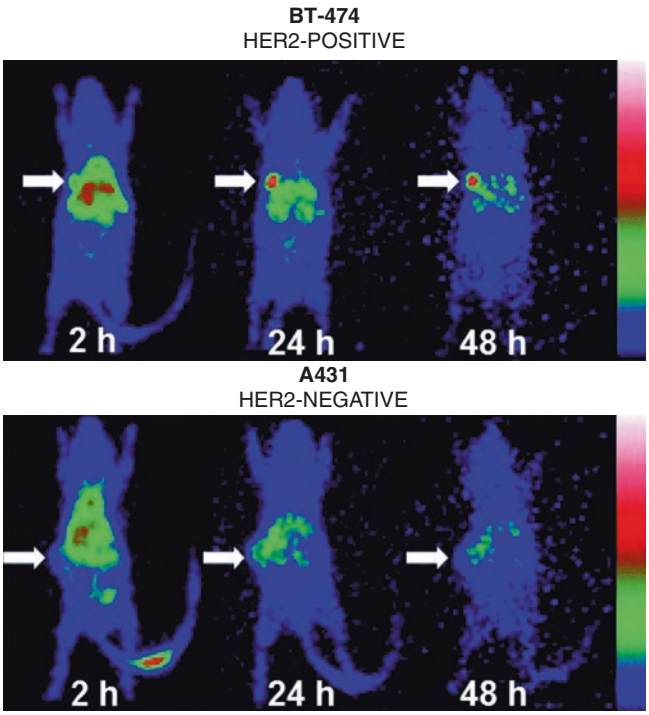

Fig. 18 PET images of mice bearing HER2-positive BT-474 xenografts (top) and HER2-negative A431 xenografts (bottom) at 2 h, 24 h, and 48 h following the administration of [^{64}Cu]Cu-(CH_3)(*p*-NCS-Ph) Sar-trastuzumab. *Arrows* indicate tumors (From Paterson *et al.* [107], with permission)

concentrations in the kidneys, the NOTA-containing construct ultimately proved to have the optimal biodistribution.

Cross-Bridged Macrocyclic Chelators

The development of the cross-bridged macrocyclic chelators represented another important step in the advancement of copper-based biomolecular radiopharmaceuticals. CB-TE2A—which has a cyclam backbone, an ethylene bridge between two nonadjacent nitrogens, and acetic acid moieties on the other two nitrogens—was the first cross-bridged chelator that was shown to dramatically improve the *in vivo* stability of ^{64}Cu-complexes compared to traditional macrocycles (Fig. 19) [93, 109]. In a proof-of-concept experiment, CB-TE2A was conjugated to the somatostatin receptor-targeting peptide Y3-TATE directly through one of the carboxylates. The resulting ^{64}Cu-labeled conjugate, [^{64}Cu]Cu-CB-TE2A-Y3-TATE, showed dramatic improvement in tumor uptake and nontarget organ clearance compared to [^{64}Cu]Cu-TETA-Y3-TATE (Fig. 20) [110]. Since this work, several other peptides have been coupled to CB-TE2A for PET imaging with copper-64 [111–115]; the drawback, however, is that the conditions required for radiolabeling are rather harsh (1 h at 90 °C, pH 8.0).

Recently, a "2nd-generation" cross-bridged chelator has been developed: CB-TE1A1P (see Fig. 20). The structure of

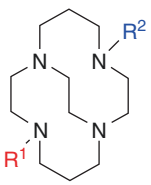

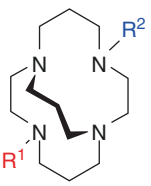

CB-Cyclam R^1=R^2 = H
CB-TE2A R^1=R^2 = CH_2CO_2H
CB-TE1A1P R^1 = CH_2CO_2H; R^2= $CH_2PO_3H_2$

PCB-TE2A R^1=R^2 = CH_2CO_2H
PCB-TE1A1P R^1 = CH_2CO_2H; R^2=$CH_2PO_3H_2$

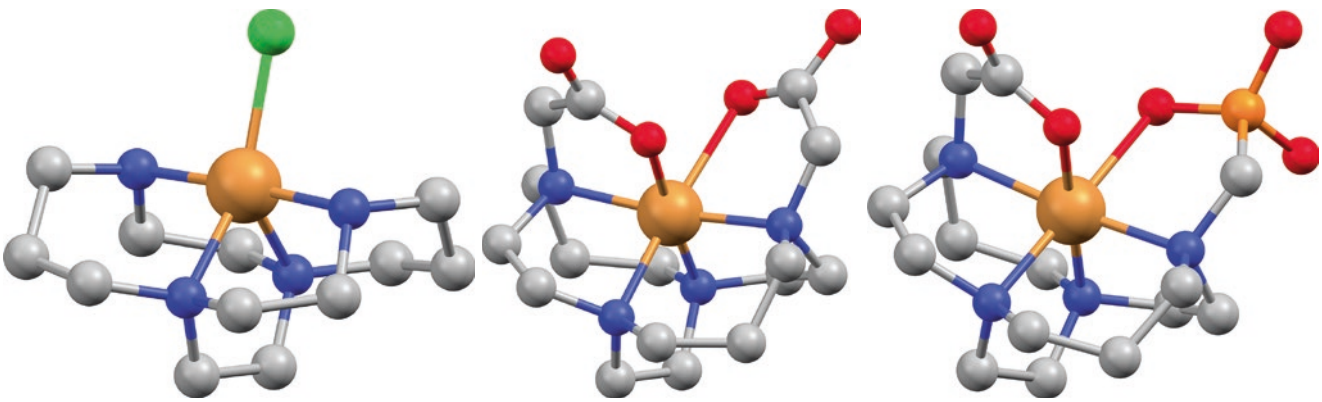

Fig. 19 (Top) Structures of selected cross-bridged macrocyclic chelators. (Bottom) Crystal structure of Cu-CB-TETA [116], Cu-CB-TE2A [117], and Cu-CB-TE1A1P [118] (*carbon, gray; nitrogen, blue; oxygen, red; phosphorus, orange; chloride, green; copper, orange; hydrogen atoms, counterions, and crystallization water molecules are omitted for clarity*)

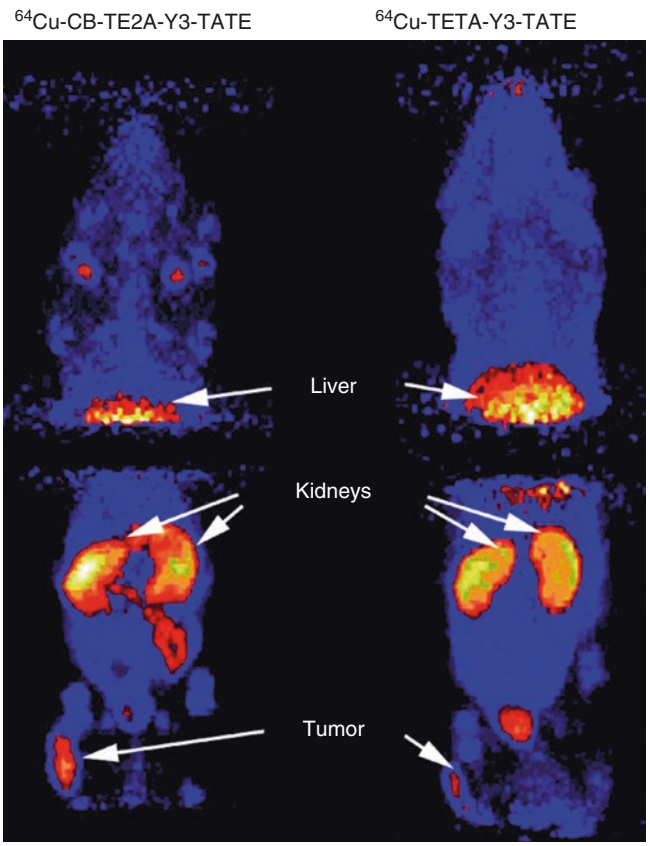

Fig. 20 Small-animal PET projection images of rats bearing AR42J tumors at 4 h after the injection of [^{64}Cu]Cu-CB-TE2A-Y3-TATE (left) and [^{64}Cu]Cu-TETA-Y3-TATE (right) (From Sprague *et al.* [110], with permission)

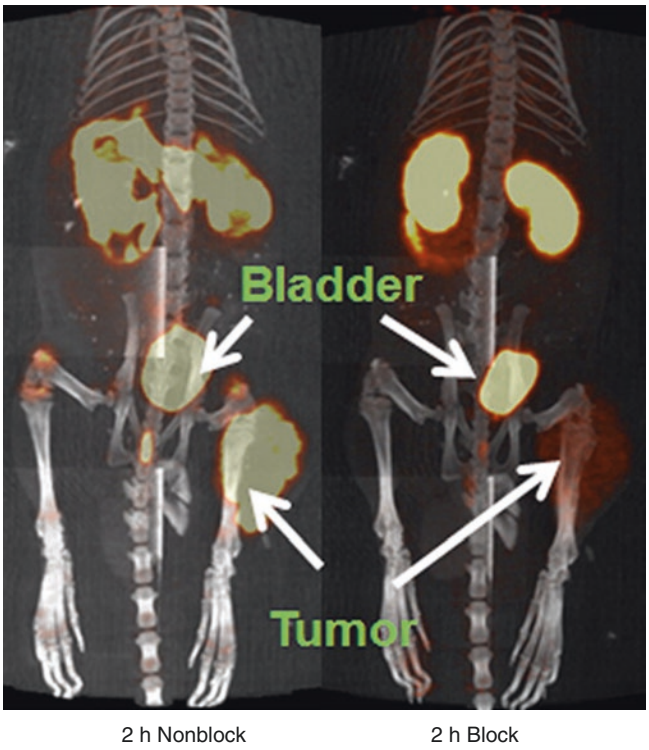

Fig. 21 PET/CT projection images of rats bearing AR42J tumors at 2 h post-injection of [^{64}Cu]Cu-CB-TE1A1P-Y3-TATE, with or without 24 h pre-injection of Y3-TATE as a blocking agent (From Guo *et al.* [119], with permission)

CB-TE1A1P is similar to that of CB-TE2A, though the former boasts one phosphonate coordinating group as well as a carboxylate for conjugation to biomolecules [118]. CB-TE1A1P was initially conjugated to Y3-TATE to facilitate a comparison of its *in vivo* behavior with that of CB-TE2A-Y3-TATE in tumor-bearing rats (Fig. 21) [119]. CB-TE1A1P-Y3-TATE could be labeled at lower temperatures (40 °C for 1 h) than CB-TE2A-Y3-TATE and produced improved clearance through nontarget organs as well as improved tumor-to-background activity concentration ratios. More recently, this chelator has been investigated with other small molecules and peptide-based agents as well (Fig. 22 and see Fig. 8) [44, 120], and click chemistry-based conjugation strategies have been employed to improve synthesis yields and the ease of radiolabeling [121, 122].

Another family of cross-bridged chelators—PCB-TE2A and PCB-TE1A1P—employs a propylene rather than an ethylene bridge across nonadjacent nitrogens (see Fig. 19) [123]. It was postulated that the longer propylene bridge would allow more facile labeling while maintaining or possibly improving *in vivo* stability. PCB-TE2A proved comparable to CB-TE2A with respect to biological clearance, although it can be radiolabeled under milder conditions (70 °C for 10 min). A phosphonate-based agent (PCB-TE1A1P) has also been reported [124], and interestingly, this chelator requires fairly harsh conditions (60 °C for 1 h) compared to CB-TE1A1P, which can be radiolabeled at room temperature in 30 min [118]. A comparison of ^{64}Cu-labeled CB-TE1A1P-RGD and PCB-TE1A1P-RGD in mice bearing U87MG tumors revealed that the two constructs produce similar tumor-to-background activity concentration ratios (Fig. 23) [125].

A summary of the conditions necessary for the radiolabeling of various types of chelators with copper-64 is presented in Table 2. This is not meant to be exhaustive, but it should allow for a rough comparison of the radiolabeling conditions that are typically employed with various types of macrocyclic chelators.

Controversial Issues

There has been controversy throughout the years regarding the mechanism of the hypoxia-dependent uptake of [^{64}Cu]Cu-ATSM. Several years ago, it was shown that the uptake of [^{64}Cu]Cu-ATSM varies between types of tumor cells lines; although hypoxia-mediated uptake of the radiotracer was in

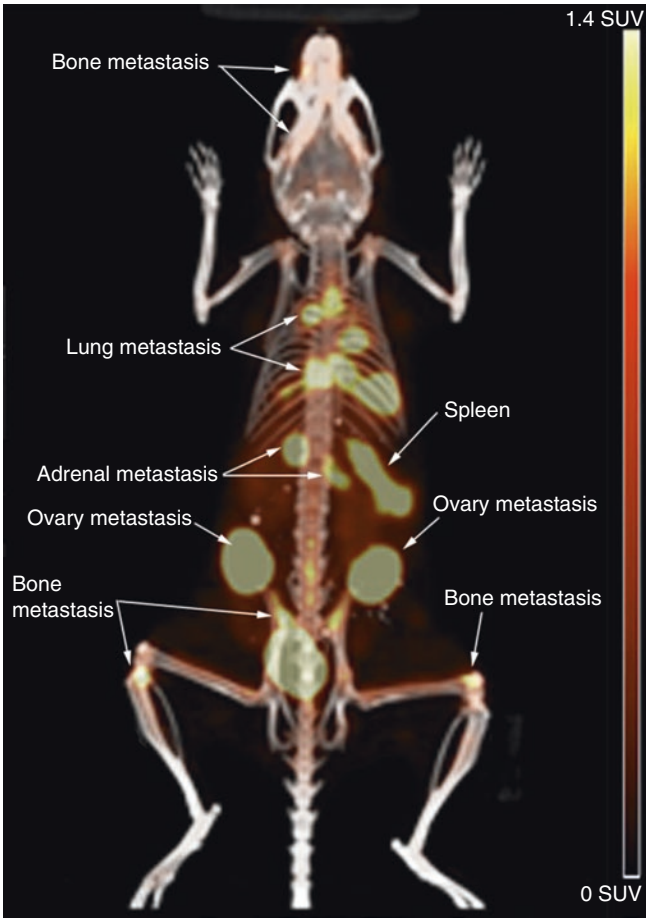

Fig. 22 Small-animal PET/CT imaging of [^{64}Cu]Cu-CB-TE1A1P-PEG4-LLP2A in a mouse bearing B16F10-Luc-tdT melanoma metastases at 2 h post-injection (From Beaino and Anderson [44], with permission)

lung and cervical tumor cells, a rat prostate tumor cell line (R3327-AT) exhibited uptake *in vitro* and *in vivo* that was not dependent on hypoxia [127]. Subsequently, evidence presented by Vavere and Lewis illustrated that the overexpression of the fatty acid synthase pathway in prostate cancer cells consumes reducing agents such as NADPH that are responsible for reducing Cu(II)-ASTM to Cu(I) [128]. Thus, [^{64}Cu]Cu-ATSM cannot be considered a universal hypoxia imaging tracer.

In a more recent study of [^{64}Cu]Cu-ATSM, Hueting *et al.* showed that the tumoral uptake of the radiotracer at 2 and 16 h p.i. in mice bearing EMT6 and CaNT tumors was similar to that of [^{64}Cu]copper acetate, most likely due to the rapid dissociation of [^{64}Cu]Cu-ATSM *in vivo* [129]. However, [^{64}Cu]Cu-ATSM and [^{64}Cu]copper acetate only had similar biodistribution profiles at later time points; the same observation was not made at 15 min after administration. It is therefore important to note that in humans, [^{64}Cu]Cu-ATSM hypoxia imaging was performed at earlier time points (<1 h post-injection). Because of these concerns, there have been essentially no hypoxia imaging studies with [^{64}Cu]Cu-ATSM in humans in recent years.

The Future

There are many reasons to be excited about the future of copper-based radiopharmaceuticals for both imaging and therapy. The radionuclides of copper have been explored for tumor targeting for more than 60 years, and several old agents have recently been repurposed (*e.g.* [^{64}Cu]$CuCl_2$). Furthermore, radiocopper is increasingly being harnessed in the development of theranostic imaging agents as well [130, 131]. The growth in commercially available sources for copper-64 is highly encouraging, and this will fuel the development of the next generation of ^{64}Cu-labeled radiopharmaceuticals for PET imaging. Although the simplicity of using [^{64}Cu]$CuCl_2$ for imaging (and possibly therapy) is alluring, the suboptimal biodistribution of this tracer could inhibit its widespread clinical use. The plethora of novel immunoglobulin-based agents under development—mostly for cancer imaging—will likely continue to be an area of focus for the future. Advances in the creation of stable chelation architectures for Cu(II) will continue, as will the development of novel Cu-labeled small molecule- and peptide-based radiotracers. Finally, we envision that the production of copper-67 will expand and become less cost prohibitive, driving increased investigation into therapeutic copper-based radiopharmaceuticals.

Bottom Line

- Copper-based radiopharmaceuticals have a long history in nuclear medicine, with the earliest studies published in the late 1950s.
- There are five radioisotopes of copper that are suitable for use in nuclear imaging or targeted radionuclide therapy: copper-67, copper-64, copper-62, copper-61, and copper-60.
- Copper-based radiopharmaceuticals fall into two major categories. The first class consists of small copper coordination complexes. The second class is predicated on the attachment of highly stable radiocopper-chelator complexes to vectors that target proteins that are upregulated in disease.

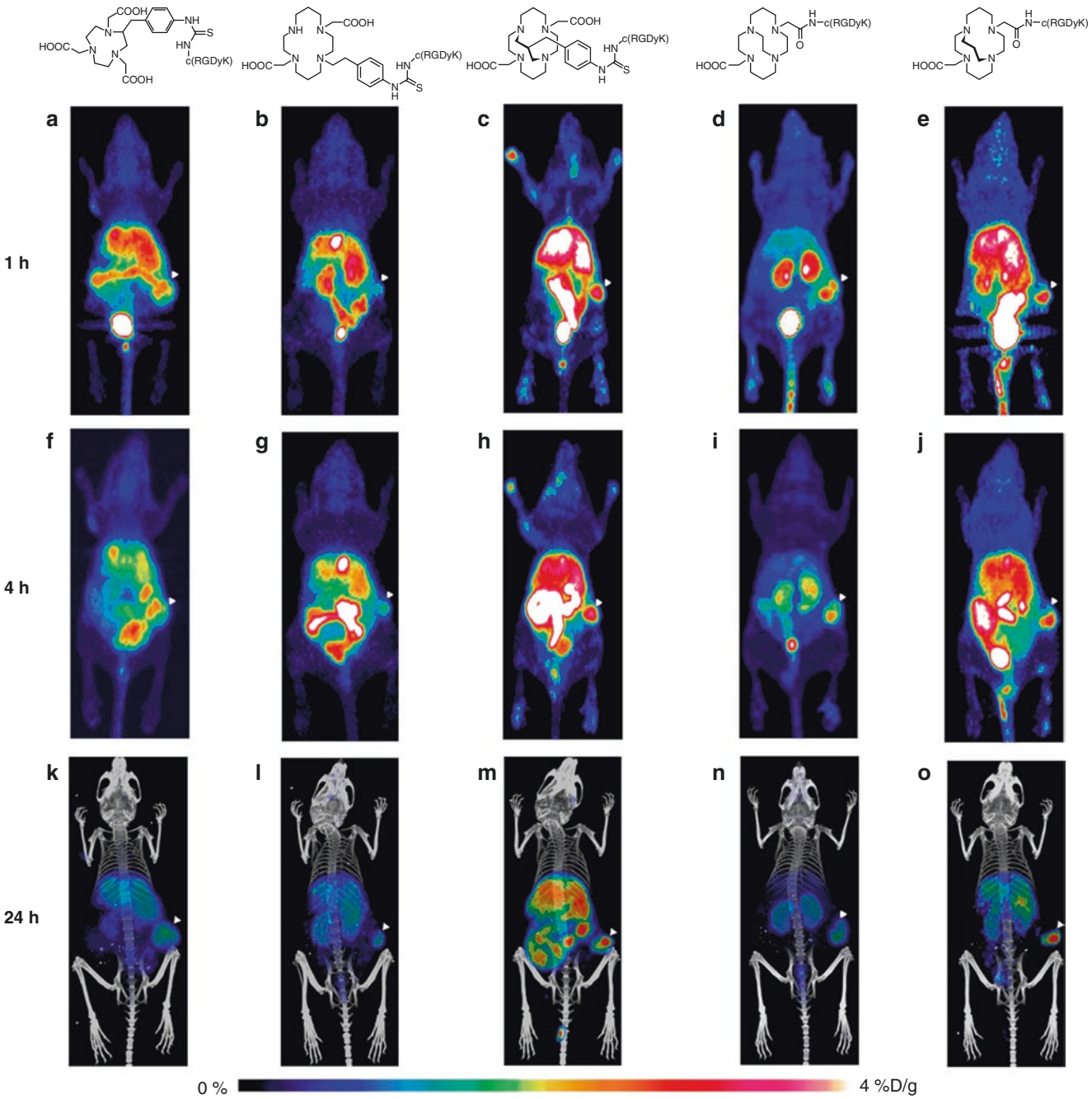

Fig. 23 Representative PET (a–j) and PET/CT (k–o) maximum intensity projection images of c(RGDyK) conjugated with various different ^{64}Cu-labeled chelators in mice bearing U87MG tumors at 1, 4, and 24 h post-injection. *The white arrowheads* indicate tumors (From Sarkar *et al.* [125], with permission)

- Radiocopper complexes based on bis(thiosemicarbazone) ligands have been investigated extensively for imaging blood flow and hypoxia.
- The design of ^{64}Cu-labeled biomolecular conjugates requires macrocyclic Cu(II) chelators to ensure the stable sequestration of the radiometal *in vivo*.
- The widespread production of copper-64 using biomedical cyclotrons has made it a readily available radiometal for PET imaging with antibodies, peptides, and nanoparticles.
- Advances in production technology could fuel a bright future for ^{67}Cu-labeled therapeutic radiopharmaceuticals.

Table 2 Examples of reaction conditions for the radiolabeling of widely used chelators and chelator-peptide conjugates with copper-64

Chelator	Selected labeling conditions (time, temperature, buffer, pH)	Notes and references
TETA	30 min at room temperature, 0.1 M ammonium acetate, pH = 6.5 30 min at room temperature, 0.1 M ammonium acetate, pH = 6.5	TETA chelator alone [93] TETA-Y3-TATE [110]
DOTA	30 min at room temperature, 0.1 M ammonium acetate, pH = 6.5 50 min at 50 °C, 0.1 M ammonium acetate, pH = 5.5	DOTA chelator alone [93] DOTA-c(RGDyK) [92]
NOTA/NODAGA	1 h at 37 °C, 0.1 M ammonium acetate, pH = 7.0 30 min at 70 °C, 0.5 M ammonium acetate, pH = 4.0	NOTA chelator alone [118] NODAGA-PEG4-LLP2A [44]
Sar	5 min at room temperature, 0.1 M sodium acetate, pH = 4–5 30 min at room temperature, 0.1 M PBS, pH = 7.4	Sar, SarAr, DiamSar chelators alone [101] SarTATE (uses MeCOSar) [106]
CB-TE2A	30 min at 75 °C, ethanol/0.1 M ammonium citrate, pH = 6.5 1 h at 95 °C, 0.1 M ammonium acetate, pH = 8.0	CB-TE2A chelator alone [93] CB-TE2A-Y3-TATE [110]
CB-TE1A1P	30 min at room temperature, 0.1 M ammonium acetate, pH = 8.1 30 min at 70 °C, 0.5 M ammonium acetate, pH = 6.5	CB-TE1A1P chelator alone [118] CB-TE1A1P-PEG4-LLP2A [44]
PCB-TE2A	10 min at 70 °C, 0.1 M sodium acetate, pH = 8.0 1 h at 80 °C, 0.1 M sodium acetate, pH = 8.0	PCB-TE2A chelator alone [126] PCB-TE2A-NSC-RGD [126]

References

1. Bases R, Brodie SS, Rubenfeld S. Attempts at tumor localization using Cu 64-labeled copper porphyrins. Cancer. 1958;11(2):259–63.
2. Raynaud C, Comar D, Dutheil M, Blanchon P, Monod O, Parrot R, Rymer M. Lung cancer diagnosis with 67Cu: preliminary results. J Nucl Med. 1973;14(12):947–50.
3. Kilian K, Pegier M, Pyrzynska K. The fast method of Cu-porphyrin complex synthesis for potential use in positron emission tomography imaging. Spectrochim Acta A Mol Biomol Spectrosc. 2016;159:123–7.
4. Shi J, Liu TW, Chen J, Green D, Jaffray D, Wilson BC, Wang F, Zheng G. Transforming a targeted porphyrin theranostic agent into a PET imaging probe for cancer. Theranostics. 2011;1:363–70.
5. Chakravarty R, Chakraborty S, Dash A. (64)Cu(2+) Ions as PET Probe: An emerging paradigm in molecular imaging of cancer. Mol Pharm. 2016;13(11):3601–12.
6. Piccardo A, Paparo F, Puntoni M, Righi S, Bottoni G, Bacigalupo L, et al. (64)CuCl2 PET/CT in prostate cancer relapse. J Nucl Med. 2018;59(3):444–51.
7. Hordyjewska A, Popiolek L, Kocot J. The many "faces" of copper in medicine and treatment. Biometals. 2014;27(4):611–21.
8. Uriu-Adams JY, Keen CL. Copper, oxidative stress, and human health. Mol Asp Med. 2005;26(4–5):268–98.
9. Owen CA. Wilson's disease: The etiology, clinical aspects, and treatment of inherited copper toxicosis (Coppyer in biology and medicine series). Noyes: Park Ridge; 1981.
10. Owen CA. Biochemical aspects of copper: Copper proteins, ceruloplasmin, and copper protein binding. Noyes: Park Ridge; 1982.
11. Osborn SB, Walshe JM. Studies with radioactive copper (64Cu and 67Cu) in relation to the natural history of Wilson's disease. Lancet. 1967;1(7486):346–50.
12. Delhez H, Prins HW, Prinsen L, van den Hamer CJ. Autoradiographic demonstration of the copper-accumulating tissues in mice with a defect homologous to Menkes' Kinky Hair disease. Pathol Res Pract. 1983;178(1):48–50.
13. Dasgupta AK, Mausner LF, Srivastava SC. A new separation for ^{67}Cu from proton irradiated Zn. Appl Radiat Isot. 1991;42:371–6.
14. Mirzadeh S, Mausner LF, Srivastava SC. Production of no-carrier added 67Cu. Int J Rad Appl Instrum A. 1986;37(1):29–36.
15. Novak-Hofer I, Schubiger AP. Copper-67 as a therapeutic nuclide for radioimmunotherapy. Eur J Nucl Med Mol Imaging. 2002;29(6):821–30.
16. Mausner LF, Kolsky KL, Joshi V, Srivastava SC. Radionuclide development at BNL for nuclear medicine therapy. Appl Radiat Isot. 1998;49(4):285–94.
17. Mastren T, Pen A, Loveless S, Marquez BV, Bollinger E, Marois B, et al. Harvesting (67)Cu from the collection of a secondary beam cocktail at the National Superconducting Cyclotron Laboratory. Anal Chem. 2015;87(20):10323–9.
18. Mastren T, Pen A, Peaslee GF, Wozniak N, Loveless S, Essenmacher S, et al. Feasibility of isotope harvesting at a projectile fragmentation facility: (6)(7)Cu. Sci Rep. 2014;4:6706.
19. Zinn KR, Chaudhuri TR, Cheng TP, Morris JS, Meyer WA. Production of no-carrier-added Cu-64 from zinc metal irradiated under boron shielding. Cancer. 1994;73(3):774–8.
20. Smith SV, Waters DJ, Di Bartolo N. Separation of 64Cu from 67Ga waste products using anion exchange and low acid aqueous/organic mixtures. Radiochim Acta. 1997;75:65–8.

21. McCarthy DW, Shefer RE, Klinkowstein RE, Bass LA, Margeneau WH, Cutler CS, et al. Efficient production of high specific activity 64Cu using a biomedical cyclotron. Nucl Med Biol. 1997;24(1):35–43.
22. Szelecsenyi F, Blessing G, Qaim SM. Excitation function of proton induced nuclear reactions on enriched ^{61}Ni and ^{64}Ni: possibility of production of no-carrier-added ^{61}Cu and ^{64}Cu at a small cyclotron. Appl Radiat Isot. 1993;44:575–80.
23. McCarthy DW, Bass LA, Cutler PD, Shefer RE, Klinkowstein RE, Herrero P, et al. High purity production and potential applications of copper-60 and copper-61. Nucl Med Biol. 1999;26(4):351–8.
24. Obata A, Kasamatsu S, McCarthy DW, Welch MJ, Saji H, Yonekura Y, Fujibayashi Y. Production of therapeutic quantities of ^{64}Cu using a 12 MeV cyclotron. Nucl Med Biol. 2003;30:535–9.
25. Zeissler SK, Pavan RA, Orzechowski J, Langlois R, Rodrigue S, van Lier JE. Production of 64Cu on the sherbrooke TR-PET cyclotron. J Radioanal Nucl Chem. 2003;257:175–7.
26. Avila-Rodriguez MA, Nye JA, Nickles RJ. Simultaneous production of high specific activity 64Cu and 61Co with 11.4 MeV protons on enriched 64Ni nuclei. Appl Radiat Isot. 2007;65(10):1115–20.
27. Lewis JS, Welch MJ, Tang L. Workshop on the production, application and clinical translation of "non-standard" PET nuclides: a meeting report. Q J Nucl Med Mol Imaging. 2008;52(2):101–6.
28. Szajek LP, Meyer W, Plascjak P, Eckleman WC. Semi-remote production of [64Cu]CuCl2 and preparation of high specific activity [64Cu]Cu-ATSM for PET studies. Radiochim Acta. 2005;93(4):239–44.
29. Dehdashti F, Grigsby PW, Mintun MA, Lewis JS, Siegel BA, Welch MJ. Assessing tumor hypoxia in cervical cancer by positron emission tomography with 60Cu-ATSM: relationship to therapeutic response-a preliminary report. Int J Radiat Oncol Biol Phys. 2003;55(5):1233–8.
30. Lewis JS, Laforest R, Dehdashti F, Grigsby PW, Welch MJ, Siegel BA. An imaging comparison of 64Cu-ATSM and 60Cu-ATSM in cancer of the uterine cervix. J Nucl Med. 2008;49(7):1177–82.
31. Robinson GD, Zielinski FW, Lee AW. The zinc-62/copper-62 generator: A convenient source of copper-62 for radiopharmaceuticals. Int J Appl Radiat Isot. 1980;31:111–6.
32. Green MA, Mathias CJ, Welch MJ, McGuire AH, Perry D, Fernandez-Rubio F, et al. Copper-62-labeled pyruvaldehyde bis(N4-methylthiosemicarbazonato)copper(II): Synthesis and evaluation as a positron emission tomography tracer for cerebral and myocardial perfusion. J Nucl Med. 1990;31(12):1989–96.
33. Ng Y, Lacy JL, Fletcher JW, Green MA. Performance of a (6)(2) Zn/(6)(2)Cu microgenerator in kit-based synthesis and delivery of [(6)(2)Cu]Cu-ETS for PET perfusion imaging. Appl Radiat Isot. 2014;91:38–43.
34. Fujibayashi Y, Matsumoto K, Yonekura Y, Konishi J, Yokayama A. A new zinc-62/copper-62 generator as a copper-62 source for PET radiopharmaceuticals. J Nucl Med. 1989;30(11):1838–42.
35. Fukumura T, Okada K, Suzuki H, Nakao R, Mukai K, Szelecsenyi F, et al. Improved 62Zn/62Cu generator based on a cation exchanger and its fully remote-controlled preparation for clinical use. Nucl Med Biol. 2006;33(6):821–7.
36. Zhao Y, Sultan D, Detering L, Luehmann H, Liu Y. Facile synthesis, pharmacokinetic and systemic clearance evaluation, and positron emission tomography cancer imaging of 64Cu–Au alloy nanoclusters. Nanoscale. 2041;6(22):13501–9.
37. Linder MC. Biochemistry of copper, Vol 10. Biochemistry of the elements. New York: Plenum Press; 1991.
38. Linder MC, Hazegh-Azam M. Copper biochemistry and molecular biology. Am J Clin Nutr. 1996;63(Suppl):797s–811s.
39. Frieden E. Perspectives on copper biochemistry. Clin Physiol Biochem. 1986;4(1):11–9.
40. Levitzki A, Anbar M. Formation of the bis(biuretat0)-complex of tervalent copper and its redox potential. Chem Commun (London). 1968;403a.
41. Price EW, Orvig C. Matching chelators to radiometals for radiopharmaceuticals. Chem Soc Rev. 2014;43(1):260–90.
42. Panichelli P, Villano C, Cistaro A, Bruno A, Barbato F, Piccardo A, Duatti A. Imaging of brain tumors with copper-64 chloride: early experience and results. Cancer Biother Radiopharm. 2016;31(5):159–67.
43. Guo W, Sun X, Jacobson O, Yan X, Min K, Srivatsan A, et al. Radioactive [64Cu]CuInS/ZnS quantum dots for PET and optical imaging: improved radiochemical stability and controllable cerenkov luminescence. ACS Nano. 2015;9(1):488–95.
44. Beaino W, Anderson CJ. PET imaging of very late antigen-4 in melanoma: comparison of 68Ga- and 64Cu-labeled NODAGA and CB-TE1A1P-LLP2A conjugates. J Nucl Med. 2014;55(11):1856–63.
45. Paterson BM, Donnelly PS. Copper complexes of bis(thiosemicarbazones): from chemotherapeutics to diagnostic and therapeutic radiopharmaceuticals. Chem Soc Rev. 2011;40(5):3005–18.
46. Vāvere AL, Lewis JS. Cu–ATSM: a radiopharmaceutical for the PET imaging of hypoxia. Dalton Trans. 2007;(43):4893–902.
47. Petering HG, Buskirk HH, Underwood GE. The anti-tumor activity of 2-keto-3-ethoxybutyraldehyde bis(thiosemicarbazone) and related compounds. Cancer Res. 1964;24:367–72.
48. Mathias CJ, Welch MJ, Raichle ME, Mintun MA, Lich LL, McGuire AH, et al. Evaluation of a potential generator-produced PET tracer for cerebral perfusion imaging: single-pass cerebral extraction measurements and imaging with radiolabeled Cu-PTSM. J Nucl Med. 1990;31(3):352–9.
49. Okazawa H, Fujibayashi Y, Yonekura Y, Tamaki N, Nishizawa S, Magata Y, et al. Clinical application of 62Zn/62Cu positron generator: perfusion and plasma pool images in normal subjects. Ann Nucl Med. 1995;9(2):81–7.
50. Taniuchi H, Fujibayashi Y, Okazawa H, Yonekura Y, Konishi J, Yokoyama A. Cu-pyruvaldehyde-bis(N4-methylthiosemicarbazone) (Cu-PTSM), a metal complex with selective NADH-dependent reduction by complex I in brain mitochondria: a potential radiopharmaceutical for mitochondria-functional imaging with positron emission tomography (PET). Biol Pharm Bull. 1995;18(8):1126–9.
51. Okazawa H, Yonekura Y, Fujibayashi Y, Mukai T, Nishizawa S, Magata Y, et al. Measurement of regional cerebral blood flow with copper-62-PTSM and a three-compartment model. J Nucl Med. 1996;37(7):1089–93.
52. Okazawa H, Yonekura Y, Fujibayashi Y, Nishizawa S, Magata Y, Ishizu K, et al. Clinical application and quantitative evaluation of generator-produced copper-62-PTSM as a brain perfusion tracer for PET. J Nucl Med. 1994;35(12):1910–5.
53. Green MA. A potential copper radiopharmaceutical for imaging the heart and brain: copper-labeled pyruvaldehyde bis(N^4-methylthiosemicarbazone). Nucl Med Biol. 1987;14:59–61.
54. Beanlands RS, Muzik O, Mintun M, Mangner T, Lee K, Petry N, et al. The kinetics of copper-62-PTSM in the normal human heart. J Nucl Med. 1992;33(5):684–90.
55. Tadamura E, Tamaki N, Okazawa H, Fujibayashi Y, Kudoh T, Yonekura Y, et al. Generator-produced copper-62-PTSM as a myocardial PET perfusion tracer compared with nitrogen-13-ammonia. J Nucl Med. 1996;37(5):729–35.
56. Mathias CJ, Welch MJ, Perry DJ, McGuire AH, Zhu X, Connett JM, Green MA. Investigation of copper-PTSM as a PET tracer for tumor blood flow. Nucl Med Biol. 1991;18:807–11.
57. Acevedo KM, Hayne DJ, McInnes LE, Noor A, Duncan C, Moujalled D, et al. Effect of structural modifications to glyoxal-

bis(thiosemicarbazonato)copper(II) complexes on cellular copper uptake, copper-mediated ATP7A Trafficking, and P-glycoprotein mediated efflux. J Med Chem. 2018;61(3):711–23.
58. Fodero-Tavoletti MT, Villemagne VL, Paterson BM, White AR, Li Q-X, Camakaris J, et al. Bis (thiosemicarbazonato) Cu-64 complexes for positron emission tomography imaging of Alzheimer's disease. J Alzheimers Dis. 2010;20(1):49–55.
59. Torres JB, Andreozzi EM, Dunn JT, Siddique M, Szanda I, Howlett DR, et al. PET imaging of copper trafficking in a mouse model of Alzheimer disease. J Nucl Med. 2016;57(1):109–14.
60. Cowley AR, Dilworth JR, Donnelly PS, Labisbal E, Sousa A. An unusual dimeric structure of a cu(i) bis(thiosemicarbazone) complex: implications for the mechanism of hypoxic selectivity of the Cu(II) derivatives. J Am Chem Soc. 2002;124(19):5270–1.
61. Fujibayashi Y, Cutler CS, Anderson CJ, McCarthy DW, Jones LA, Sharp T, et al. Comparative studies of Cu-64-ATSM and C-11-acetate in an acute myocardial infarction model: ex vivo imaging of hypoxia in rats. Nucl Med Biol. 1999;26(1):117–21.
62. Lim S, Paterson BM, Fodero-Tavoletti MT, O'Keefe GJ, Cappai R, Barnham KJ, et al. A copper radiopharmaceutical for diagnostic imaging of Alzheimer's disease: a bis(thiosemicarbazonato) copper(ii) complex that binds to amyloid-β plaques. Chem Commun. 2010;46(30):5437–9.
63. Hickey JL, Lim S, Hayne DJ, Paterson BM, White JM, Villemagne VL, et al. Diagnostic imaging agents for Alzheimer's disease: copper radiopharmaceuticals that target Aβ plaques. J Am Chem Soc. 2013;135(43):16120–32.
64. Cowley AR, Dilworth JR, Donnelly PS, Heslop JM, Ratcliffe SJ. Bifunctional chelators for copper radiopharmaceuticals: the synthesis of [Cu(ATSM)–amino acid] and [Cu(ATSM)–octreotide] conjugates. Dalton Trans. 2007;(2):209–17.
65. Hueting R, Christlieb M, Dilworth JR, Garayoa EG, Gouverneur V, Jones MW, et al. Bis(thiosemicarbazones) as bifunctional chelators for the room temperature 64-copper labeling of peptides. Dalton Trans. 2010;39(15):3620–32.
66. Bormans G, Janssen A, Adriaens P, Crombez D, Witsenboer A, De Goeij J, et al. A ^{62}Zn/^{62}Cu generator for the routine production of ^{62}Cu-PTSM. Appl Radiat Isot. 1992;43:1437–41.
67. Haynes NG, Lacy JL, Nayak N, Martin CS, Dai D, Mathias CJ, Green MA. Performance of a ^{62}Zn/^{62}Cu generator in clinical trials of PET perfusion agent ^{62}Cu-PTSM. J Nucl Med. 2000;41(2):309–14.
68. Herrero P, Markham J, Weinheimer CJ, Anderson CJ, Welch MJ, Green MA, Bergmann SR. Quantification of regional myocardial perfusion with generator-produced 62Cu-PTSM and positron emission tomography. Circulation. 1993;87:173–83.
69. Wallhaus TR, Lacy J, Whang J, Green MA, Nickles RJ, Stone CK. Human biodistribution and dosimetry of the PET perfusion agent 62Cu-PTSM from a compact modular 62Zn/62Cu generator. J Nucl Med. 1998;39(11):1958–64.
70. Herrero P, Hartman JJ, Green MA, Anderson CJ, Welch MJ, Markham J, Bergmann SR. Regional myocardial perfusion assessed with generator-produced copper-62-PTSM and PET. J Nucl Med. 1996;37(8):1294–300.
71. Mathias CJ, Bergmann SR, Green MA. Development and validation of a solvent extraction technique for determination of Cu-PTSM in blood. Nucl Med Biol. 1993;20(3):343–9.
72. Mathias CJ, Bergmann SR, Green MA. Species-dependent binding of copper(II) bis(thiosemicarbazone) radiopharmaceuticals to serum albumin. J Nucl Med. 1995;36(8):1451–5.
73. Green MA, Mathias CJ, Willis LR, Handa RK, Lacy JL, Miller MA, Hutchins GD. Assessment of Cu-ETS as a PET radiopharmaceutical for evaluation of regional renal perfusion. Nucl Med Biol. 2007;34(3):247–55.
74. Basken NE, Mathias CJ, Lipka AE, Green MA. Species dependence of [64Cu]Cu-Bis(thiosemicarbazone) radiopharmaceutical binding to serum albumins. Nucl Med Biol. 2008;35(3):281–6.
75. Harris AL. Hypoxia – a key regulatory factor in tumour growth. Nat Rev Cancer. 2002;2(1):38–47.
76. Rajendran JG, Krohn KA. F-18 fluoromisonidazole for imaging tumor hypoxia: imaging the microenvironment for personalized cancer therapy. Semin Nucl Med. 2015;45(2):151–62.
77. Bell C, Dowson N, Fay M, Thomas P, Puttick S, Gal Y, Rose S. Hypoxia imaging in gliomas with 18F-fluoromisonidazole PET: toward clinical translation. Semin Nucl Med. 2015;45(2):136–50.
78. Tran LB, Bol A, Labar D, Jordan B, Magat J, Mignion L, et al. Hypoxia imaging with the nitroimidazole 18F-FAZA PET tracer: a comparison with OxyLite, EPR oximetry and 19F-MRI relaxometry. Radiother Oncol. 2012;105(1):29–35.
79. Maurer RI, Blower PJ, Dilworth JR, Reynolds CA, Zheng Y, Mullen GE. Studies on the mechanism of hypoxic selectivity in copper bis(thiosemicarbazone) radiopharmaceuticals. J Med Chem. 2002;45(7):1420–31.
80. Blower PJ, Castle TC, Cowley AR, Dilworth JR, Donnelly PS, Labisbal E, Sowrey FE, Teat SJ, Went MJ. Structural trends in copper(ii) bis(thiosemicarbazone) radiopharmaceuticals. Dalton Trans. 2003;(23):4416–25.
81. Xiao Z, Donnelly PS, Zimmermann M, Wedd AG. Transfer of copper between bis(thiosemicarbazone) ligands and intracellular copper-binding proteins. insights into mechanisms of copper uptake and hypoxia selectivity. Inorg Chem. 2008;47(10):4338–47.
82. Waghorn PA, Jones MW, Theobald MB, Arrowsmith RL, Pascu SI, Botchway SW. Shining light on the stability of metal thiosemicarbazonate complexes in living cells by FLIM. Chem Sci. 2013;4(4):1430.
83. Grigsby PW, Malyapa RS, Higashikubo R, Schwarz JK, Welch MJ, Huettner PC, Dehdashti F. Comparison of molecular markers of hypoxia and imaging with (60)Cu-ATSM in cancer of the uterine cervix. Mol Imaging Biol. 2007;9(5):278–83.
84. Tateishi K, Tateishi U, Sato M, Yamanaka S, Kanno H, Murata H, et al. Application of 62Cu-diacetyl-bis (N4-methylthiosemicarbazone) PET imaging to predict highly malignant tumor grades and hypoxia-inducible factor-1alpha expression in patients with glioma. AJNR Am J Neuroradiol. 2013;34(1):92–9.
85. Nie X, Laforest R, Elvington A, Randolph GJ, Zheng J, Voller T, et al. PET/MRI of hypoxic atherosclerosis using 64Cu-ATSM in a Rabbit model. J Nucl Med. 2015;57(12):2006–11.
86. Nie X, Randolph GJ, Elvington A, Bandara N, Zheleznyak A, Gropler RJ, et al. Imaging of hypoxia in mouse atherosclerotic plaques with (64)Cu-ATSM. Nucl Med Biol. 2016;43(9):534–42.
87. Bourgeois M, Rajerison H, Guerard F, Mougin-Degraef M, Barbet J, Michel N, et al. Contribution of [64Cu]-ATSM PET in molecular imaging of tumour hypoxia compared to classical [18F]-MISO—a selected review. Nucl Med Rev. 2011;14(2):90–5.
88. Moi MK, Meares CF, McCall MJ, Cole WC, DeNardo SJ. Copper chelates as probes of biological systems: stable copper complexes with a macrocyclic bifunctional chelating agent. Anal Biochem. 1985;148(1):249–53.
89. Wadas TJ, Wong EH, Weisman GR, Anderson CJ. Coordinating radiometals of copper, gallium, indium, yttrium, and zirconium for PET and SPECT imaging of disease. Chem Rev. 2010;110(5):2858–902.
90. Wadas TJ, Anderson CJ. Radiolabeling of TETA- and CB-TE2A-conjugated peptides with copper-64. Nat Protoc. 2006;1(6):3062–8.
91. Sprague JE, Li WP, Liang K, Achilefu S, Anderson CJ. In vitro and in vivo investigation of matrix metalloproteinase expression in metastatic tumor models. Nucl Med Biol. 2006;33(2):227–37.
92. Chen X, Sievers E, Hou Y, Park R, Tohme M, Bart R, et al. Integrin alpha v beta 3-targeted imaging of lung cancer. Neoplasia. 2005;7(3):271–9.

93. Boswell CA, Sun X, Niu W, Weisman GR, Wong EH, Rheingold AL, Anderson CJ. Comparative in vivo stability of copper-64-labeled cross-bridged and conventional tetraazamacrocyclic complexes. J Med Chem. 2004;47(6):1465–74.
94. Riesen A, Zehnder M, Kaden TA. Metal complexes of macrocyclic ligands. Part XXIII. Synthesis, properties, and structures of mononuclear complexes with 12- and 14-membered tetraazamacrocycle-N,N′,N″,N‴-tetraacetic acids. Helv Chim Acta. 1986;69(8):2067–73.
95. Tonei DM, Ware DC, Brothers PJ, Plieger PG, Clark GR. Coordination chemistry of 1,4-bis-carboxymethylcyclam, H2(1,4-bcc). Dalton Trans. 2006;(1):152–8.
96. Chapman J, Ferguson G, Gallagher JF, Jennings MC, Parker D. Copper and nickel complexes of 1,8-disubstituted derivatives of 1,4,8,11-tetraazacyclotetradecane. Dalton Trans. 1992;(3):345–53.
97. Pandya DN, Kim JY, Park JC, Lee H, Phapale PB, Kwak W, et al. Revival of TE2A; a better chelate for Cu(II) ions than TETA? Chem Commun. 2010;46(20):3517–9.
98. Bailly C, Gouard S, Lacombe M, Remaud-Le Saec P, Chalopin B, Bourgeois M, et al. Comparison of immuno-PET of CD138 and PET imaging with (64)CuCl2 and (18)F-FDG in a preclinical syngeneic model of multiple myeloma. Oncotarget. 2018;9(10):9061–72.
99. Watanabe H, Kawasaki A, Sano K, Ono M, Saji H. Synthesis and evaluation of copper-64 labeled benzofuran derivatives targeting β-amyloid aggregates. Bioorg Med Chem. 2016;24(16):3618–23.
100. Sargeson AM. The potential for the cage complexes in biology. Coord Chem Rev. 1996;151:89–114.
101. Di Bartolo NM, Sargeson AM, Donlevy TM, Smith SV. Synthesis of a new cage ligand, SarAR, and its complexation with selected transition metal ions for potential use in radioimaging. J Chem Soc Dalton Trans. 2001;(15):2303–9.
102. Wei L, Ye Y, Wadas TJ, Lewis JS, Welch MJ, Achilefu S, Anderson CJ. (64)Cu-labeled CB-TE2A and diamsar-conjugated RGD peptide analogs for targeting angiogenesis: comparison of their biological activity. Nucl Med Biol. 2009;36(3):277–85.
103. Cai H, Fissekis J, Conti PS. Synthesis of a novel bifunctional chelator AmBaSar based on sarcophagine for peptide conjugation and (64)Cu radiolabelling. Dalton Trans. 2009;(27):5395–400.
104. Cai H, Li Z, Huang CW, Shahinian AH, Wang H, Park R, Conti PS. Evaluation of copper-64 labeled AmBaSar conjugated cyclic RGD peptide for improved microPET imaging of integrin alphavbeta3 expression. Bioconjug Chem. 2010;21(8):1417–24.
105. Bernhardt PV, Bramley R, Engelhardt LM, Harrowfield JM, Hockless DCR, Korybut-Daszkiewicz BR, et al. Copper(II) Complexes of substituted macrobicyclic hexaamines: Combined trigonal and tetragonal distortions. Inorg Chem. 1995;34(14):3589–99.
106. Paterson BM, Roselt P, Denoyer D, Cullinane C, Binns D, Noonan W, et al. PET imaging of tumours with a 64Cu labeled macrobicyclic cage amine ligand tethered to Tyr3-octreotate. Dalton Trans. 2014;43(3):1386–96.
107. Paterson BM, Buncic G, McInnes LE, Roselt P, Cullinane C, Binns DS, et al. Bifunctional (64)Cu-labelled macrobicyclic cage amine isothiocyanates for immuno-positron emission tomography. Dalton Trans. 2015;44(11):4901–9.
108. Dearling JL, Paterson BM, Akurathi V, Betanzos-Lara S, Treves ST, Voss SD, et al. The ionic charge of copper-64 complexes conjugated to an engineered antibody affects biodistribution. Bioconjug Chem. 2015;26(4):707–17.
109. Sun X, Wuest M, Weisman GR, Wong EH, Reed DP, Boswell CA, et al. Radiolabeling and in vivo behavior of copper-64-labeled cross-bridged cyclam ligands. J Med Chem. 2002;45(2):469–77.
110. Sprague JE, Peng Y, Sun X, Weisman GR, Wong EH, Achilefu S, Anderson CJ. Preparation and biological evaluation of copper-64-labeled tyr3-octreotate using a cross-bridged macrocyclic chelator. Clin Cancer Res. 2004;10(24):8674–82.
111. Sprague JE, Kitaura H, Zou W, Ye Y, Achilefu S, Weilbaecher KN, et al. Noninvasive imaging of osteoclasts in parathyroid hormone-induced osteolysis using a 64Cu-labeled RGD peptide. J Nucl Med. 2007;48(2):311–8.
112. Hausner SH, Kukis DL, Gagnon MK, Stanecki CE, Ferdani R, Marshall JF, et al. Evaluation of [64Cu]Cu-DOTA and [64Cu]Cu-CB-TE2A chelates for targeted positron emission tomography with an alphavbeta6-specific peptide. Mol Imaging. 2009;8(2):111–21.
113. Dumont RA, Deininger F, Haubner R, Maecke HR, Weber WA, Fani M. Novel (64)Cu- and (68)Ga-labeled RGD conjugates show improved PET imaging of alpha(nu)beta(3) integrin expression and facile radiosynthesis. J Nucl Med. 2011;52(8):1276–84.
114. Fani M, Del Pozzo L, Abiraj K, Mansi R, Tamma ML, Cescato R, et al. PET of somatostatin receptor-positive tumors using 64Cu- and 68Ga-somatostatin antagonists: the chelate makes the difference. J Nucl Med. 2011;52(7):1110–8.
115. Shokeen M, Zheleznyak A, Wilson JM, Jiang M, Liu R, Ferdani R, et al. Molecular imaging of very late antigen-4 (alpha4beta1 integrin) in the premetastatic niche. J Nucl Med. 2012;53(5):779–86.
116. Wong EH, Weisman GR, Hill DC, Reed DP, Rogers ME, Condon JS, et al. Synthesis and characterization of cross-bridged cyclams and pendant-armed derivatives and structural studies of their copper(II) complexes. J Am Chem Soc. 2000;122(43):10561–72.
117. Woodin KS, Heroux KJ, Boswell CA, Wong EH, Weisman GR, Niu W, et al. Kinetic inertness and electrochemical behavior of copper(II) tetraazamacrocyclic complexes: Possible implications for in vivo stability. Eur J Inorg Chem. 2005;(23):4829–33.
118. Ferdani R, Stigers DJ, Fiamengo AL, Wei L, Li BT, Golen JA, Rheingold AL, et al. Synthesis, Cu(II) complexation, 64Cu-labeling and biological evaluation of cross-bridged cyclam chelators with phosphonate pendant arms. Dalton Trans. 2012;41(7):1938–50.
119. Guo Y, Ferdani R, Anderson CJ. Preparation and biological evaluation of (64)cu labeled tyr(3)-octreotate using a phosphonic Acid-based cross-bridged macrocyclic chelator. Bioconjug Chem. 2012;23(7):1470–7.
120. Hu LY, Bauer N, Knight LM, Li Z, Liu S, Anderson CJ, et al. Characterization and evaluation of (64)Cu-labeled A20FMDV2 conjugates for imaging the integrin αvβ 6. Mol Imaging Biol. 2014;16(4):567–77.
121. Cai Z, Ouyang Q, Zeng D, Nguyen K, Modi J, Wang L, et al. 64Cu-labeled somatostatin analogs conjugated with cross-bridged phosphonate-based chelators via strain-promoted click chemistry for PET imaging: in silico through in vivo studies. J Med Chem. 2014;57(14):6019–29.
122. Ocak M, Beaino W, White A, Zeng D, Cai Z, Anderson CJ. (64)Cu-labeled phosphonate cross-bridged chelator conjugates of c(RGDyK) for PET/CT imaging of osteolytic bone metastases. Cancer Biother Radiopharm. 2018;33(2):74–83.
123. Pandya DN, Dale AV, Kim JY, Lee H, Ha YS, An GI, Yoo J. New macrobicyclic chelator for the development of ultra-stable 64Cu-radiolabeled bioconjugate. Bioconjug Chem. 2012;23(3):330–5.
124. Dale AV, An GI, Pandya DN, Ha YS, Bhatt N, Soni N, et al. Synthesis and evaluation of new generation cross-bridged bifunctional chelator for (64)Cu radiotracers. Inorg Chem. 2015;54(17):8177–86.
125. Sarkar S, Bhatt N, Ha YS, Huynh PT, Soni N, Lee W, et al. High in vivo stability of (64)Cu-labeled cross-bridged chelators is a crucial factor in improved tumor imaging of RGD peptide conjugates. J Med Chem. 2018;61(1):385–95.
126. Pandya DN, Bhatt N, An GI, Ha YS, Soni N, Lee H, et al. Propylene cross-bridged macrocyclic bifunctional chelator: a new design for facile bioconjugation and robust (64)Cu complex stability. J Med Chem. 2014;57(17):7234–43.

127. Burgman P, O'Donoghue JA, Lewis JS, Welch MJ, Humm JL, Ling CC. Cell line-dependent differences in uptake and retention of the hypoxia-selective nuclear imaging agent Cu-ATSM. Nucl Med Biol. 2005;32(6):623–30.
128. Vāvere AL, Lewis JS. Examining the relationship between Cu-ATSM hypoxia selectivity and fatty acid synthase expression in human prostate cancer cell lines. Nucl Med Biol. 2008;35(3):273–9.
129. Hueting R, Kersemans V, Cornelissen B, Tredwell M, Hussien K, Christlieb M, et al. A comparison of the behavior of (64) Cu-acetate and (64)Cu-ATSM in vitro and in vivo. J Nucl Med. 2014;55(1):128–34.
130. Boschi A, Martini P, Janevik-Ivanovska E, Duatti A. The emerging role of copper-64 radiopharmaceuticals as cancer theranostics. Drug Discov Today. 2018; 23(8):1489–501.
131. Chatterjee S, Lesniak WG, Miller MS, Lisok A, Sikorska E, Wharram B, et al. Rapid PD-L1 detection in tumors with PET using a highly specific peptide. Biochem Biophys Res Commun. 2017;483(1):258–63.

The Radiopharmaceutical Chemistry of the Radioisotopes of Lutetium and Yttrium

Elaheh Khozeimeh Sarbisheh and Eric W. Price

Fundamentals

The Solution Chemistry of Lu^{3+} and Y^{3+}

To begin our discussion of these versatile radiometals, we will delve into some relevant chemical properties of Lu^{3+} and Y^{3+}. The physiologically relevant oxidation state of yttrium and lutetium is 3+, and these metal ions are redox stable *in vivo*. These 3+ cations are considered hard metal ions with a preference for hard donor atoms such as oxygen and nitrogen [1]. The typical coordination numbers of Lu^{3+} and Y^{3+} are 8 and 9, although 10 is also possible. Furthermore, the effective ionic radius of Lu^{3+} is 98 pm, while that of Y^{3+} is 102 pm [2], and their Pauling electronegativity values are 1.27 and 1.22, respectively [3]. Radiolabeling experiments confirm what these physical properties suggest: radiolabeling conditions and chelator selectivity are effectively the same for $[^{177}Lu]Lu^{3+}$ and $[^{86}Y]/[^{90}Y]Y^{3+}$ ions. Although yttrium is a transition metal, it is often treated as a "pseudo-lanthanide" for the reasons discussed above [4].

The most common coordination geometries for Y^{3+} and Lu^{3+} when bound by chelators are square antiprismatic, distorted square antiprismatic, and monocapped square antiprismatic [5]. The metal ions Y^{3+} (pKa = 7.7) and Lu^{3+} (pKa = 7.6) are not as acidic or prone to hydrolysis as metal ions such as Ga^{3+} (pKa = 2.6) or Zr^{4+} (pKa = 0.22) [6]. However, above pH 3, both Y^{3+} and Lu^{3+} still have a tendency to form insoluble $[M(OH)_3]$ species [7, 8]. As a result, these radiometals are typically formulated in 0.05 or 0.1 M HCl solution to ensure uniform speciation and prevent the formation of insoluble hydroxides. Despite the possibility of forming insoluble hydroxide species above pH 2–4, the buffers used for radiolabeling with Y^{3+} and Lu^{3+} typically reside between pH 4 and pH 6 and, somewhat surprisingly, still work well. This is partially because at very low pH (*e.g.* 1–2), the acidic coordinating groups of chelators (*e.g.* carboxylic acids, pKa ~4–5) may become protonated, a process which can prevent the coordination of the radiometal.

As we embark on our description of the application of these radiometals, we would like to start with an important preface. The chemistry of a radioactive isotope (radionuclide) of an element (*e.g.* yttrium-86 or yttrium-90) is effectively identical to that of its stable, non-radioactive isotopologues (*e.g. yttrium-89*). However, one facet of chemistry that is indeed drastically different when using radionuclides compared to their nonradioactive cousins is that radiochemistry is typically performed under extremely dilute conditions. This extreme dilution partially solves the issue of insoluble hydroxide species that we have discussed. At the concentrations typical for solutions of radiometals, species such as $[M(OH)_3]$—which are normally insoluble—are actually partially soluble. In addition, in radiolabeling reactions, the chelator is present in large molar excess over the radiometal cations (see the section on "Tricks of the Trade: Moles and Specific Activity" for a thought exercise on specific activity). Typically, very small molar quantities of a chelator-vector conjugate (*e.g.* peptide, antibody) are radiolabeled using even smaller molar quantities of radiometal ions. As the radionuclide is essentially always the limiting reagent, a radiolabeling mixture effectively contains a huge excess of unlabeled molecules, with only a small fraction of molecules containing a radionuclide label. Unless the precursor molecule can be separated from the radiolabeled molecule (*e.g.* via chromatography), there will always be a large excess of unlabeled conjugate in the mixture.

Relevant Nuclear Properties of Lutetium and Yttrium Radionuclides

The chart of the nuclides highlights a plethora of radionuclides that have been discovered for both lutetium and yttrium, but only certain nuclides can be produced routinely using existing cyclotron/LINAC/reactor infrastructure and

E. Khozeimeh Sarbisheh · E. W. Price (✉)
Department of Chemistry, University of Saskatchewan, Saskatoon, SK, Canada
e-mail: eric.price@usask.ca

J. S. Lewis et al. (eds.), *Radiopharmaceutical Chemistry*, https://doi.org/10.1007/978-3-319-98947-1_20

Table 1 Relevant nuclear properties of Y^{3+} and Lu^{3+} radionuclides, EC = electron capture [9–11]

Nuclide	$t_{1/2}$ (h)	Decay mode (abundance)	Energy (keV)	Typical production method
[^{177}Lu]Lu^{3+}	159.4	β^- (76%)	γ 112, 208 β^- 177 (12%), 385 (9%), 498 (79%)	^{176}Lu(n,γ)^{177}Lu
[^{86}Y]Y^{3+}	14.7	β^+ (33%) EC (66%)	γ 139–4900 β^+ 1221 (max) β^+ 535 (avg.)	Cyclotron, ^{86}Sr(p,n)^{86}Y
[^{90}Y]Y^{3+}	64.1	β^- (100%)	β^- 2280 (max)	^{90}Zr(n,p)^{90}Y

also possess suitable decay properties for medical applications. For example, a radionuclide such as germanium-68 with a half-life of ~271 days would obviously not be suitable for use inside the human body due to concerns over long-term radiation exposure. However, it may have a compelling use for making a radionuclide generator for a more useful, shorter-lived daughter nuclide (*e.g.* [^{68}Ge]Ge^{4+}/[^{68}Ga]Ga^{3+} generator). As a result, only three nuclides of Y^{3+} and Lu^{3+} have been explored for medical use: yttrium-90 ([^{90}Y]Y^{3+}) for radionuclide therapy, yttrium-86 ([^{86}Y]Y^{3+}) for imaging, and lutetium-177 ([^{177}Lu]Lu^{3+}) for imaging and radionuclide therapy (Table 1) [9–11].

Yttrium-90

Yttrium-90 ($t_{1/2}$ = 64.1 h, $E_{\beta^-(max)}$ = 2280) almost strictly emits β^- (beta) particles and has been clinically used for both radioimmunotherapy (*e.g.* [^{90}Y]Y-Zevalin) and peptide receptor radionuclide therapy (PRRT, *e.g.* [^{90}Y]Y-DOTATATE). The lack of gamma ray or positron emission makes the detection of this radionuclide challenging. It is admittedly possible to perform biodistribution, imaging, and dosimetry studies using its Bremsstrahlung X-rays, though the poor resolution and quality of planar scintigraphic images and the requisite scintillation counting make these processes cumbersome [12]. Interestingly, it has been shown that the positrons emitted from yttrium-90 in very, very low abundance (0.003%) can yield positron emission tomography (PET) images with higher accuracy than Bremsstrahlung imaging, although this is not a routine—or clinically feasible—practice [12]. Ultimately, this lack of facile imaging means that a "matched nuclide pair" surrogate must be used to perform pre-therapy "scout" imaging to enable dosimetric measurements (see the sections on "Yttrium-86" and "Theranostics") [13–15].

One benefit to yttrium-90 compared to other therapeutic radionuclides is that it emits β^- particles with high energy ($E_{\beta^-(max)}$ = 2280 keV; see Table 1). The relatively long mean free path length of these β^- (~12 mm) means that they can be used to treat relatively large and poorly vascularized tumors [9, 16, 17]. Via this "crossfire effect," tumor cells up to ~550 cell diameters away from the radiopharmaceutical can receive therapeutic irradiation [9, 16]. This long β^- range is a double-edged sword, however, as it can lead to heightened damage to healthy tissues such as bone marrow (myelotoxicity) during the circulation of the radiopharmaceutical [18].

Yttrium-86

The positron-emitting radionuclide [^{86}Y]Y^{3+} ($t_{1/2}$ = 14.7 h, β^+ = 33%, $E_{\beta^+(mean)}$ = 535 keV average) can be produced with a cyclotron via the ^{86}Sr(p,n)^{86}Y reaction and can be purified by ion-exchange chromatography or electrolysis. However, this production route is notoriously difficult, and chemically pure yttrium-86 is difficult to obtain, as solutions of the radiometal often contain high concentrations of salts and other metal ion contaminants [19, 20]. Yttrium-86 is typically used for positron emission tomography (PET) by coupling it to targeting vectors such as peptides, antibodies, antibody fragments, and nanoparticles. Yttrium-86 is not used for radionuclide therapy, but its isotopolog yttrium-90 ejects high-energy β^- particles (electrons) and is often used for radionuclide therapy. Due to their chemical equivalence, a cancer-targeting molecule can be radiolabeled with yttrium-86 and used in cancer patients for pre-therapy PET scans to select patients with high tumor uptake and perform dosimetry. Depending on the outcome of the pre-therapy PET scan (scouting scan), the same molecule can then be radiolabeled with yttrium-90 and administered to the same patients for cancer therapy due to the cell-killing abilities of the high-energy β^- particles.

It is often useful to contrast the nuclear properties of exotic positron-emitting nuclides such as yttrium-86 with those of the "gold standard" radionuclide for PET: fluorine-18. Fluorine-18 has a very high positron abundance (96% of decay events result in a positron) and a low average β^+ energy of 252 keV [21, 22]. Yttrium-86, in contrast, has a low branching ratio of ~33%, emits 102 different gamma rays with energies ranging from 139 to 4900 keV (25% of which are within PET detection window of 350–650 keV), and ejects positrons with a significantly higher average energy of 535 keV [10, 23, 24]. This has practical significance for PET imaging. Upon the decay of a radionuclide, the ejected positron travels a distance that is dependent upon its kinetic energy. The ejected positron must lose all of its kinetic energy (net linear momentum = 0) before meeting an electron and annihilating into two 511 keV gamma rays. Positrons that are ejected with higher energy will travel further in the body before coming to rest and annihilating into detectable gamma rays. Consequently, positrons with higher energy produce PET images with lower spatial resolution [24].

The relationship between positron energy and image resolution is illustrated in Fig. 1, which depicts a common device

used for calibrating PET scanners called a phantom. These phantoms are filled with a homogenous aqueous solution containing the radionuclide of interest and three different sealed rods containing water, air, or Teflon. These three different sealed rods have different attenuation coefficients, which are values that describe the degree to which photons are absorbed or scattered by each medium (Teflon > water > air). These phantom images help to predict the spatial resolution that a specific positron-emitting radionuclide will have in animals and humans. In this figure, PET images of phantoms filled with homogenous aqueous solutions of fluorine-18, iodine-124, or yttrium-86 are shown to demonstrate the inferior spatial resolution of yttrium-86 (though modern software background correction can improve this somewhat) [25]. Yttrium-86 is especially poor at detecting bone lesions, as bone has a high attenuation coefficient, which together with the large number of gamma coincidences from yttrium-86 introduces a lot of error and noise. This is demonstrated dramatically by the Teflon rod (see Fig. 1, top rod), as Teflon has a similar attenuation coefficient to bone [26].

Other positron-emitting radiometals could be used for dosimetry scans prior to yttrium-90 therapy, including copper-64 ($E_{\beta^+(\text{mean})}$ = 278 keV, $R_{\beta^+(\text{mean})}$ = 0.7 mm) and zirconium-89 ($E_{\beta^+(\text{mean})}$ = 396 keV, $R_{\beta^+(\text{mean})}$ = 1.3 mm). However, neither of these radiometals are well matched to $[^{90}Y]Y^{3+}$ in terms of coordination chemistry or radionuclidic half-life [27]. A more detailed comparison of $[^{64}Cu]Cu^{2+}$ and $[^{90}Y]Y^{3+}$ highlights these problems. In addition to vastly different half-lives ($t_{1/2}$ = ~13 h for copper-64, $t_{1/2}$ = ~64 h for yttrium-90), the complexes of $[^{90}Y][Y(DOTA)]^{1-}$ compared with $[^{64}Cu][Cu(DOTA)]^{2-}$ have different coordination numbers (CN = 8, 6, respectively) and net charges, which result in significant discrepancies in their tumoral uptake and organ distribution [5]. Yttrium-86 effectively has the same half-life as copper-64 and therefore is a poor match with yttrium-90. However, the coordination chemistry and chemical properties of yttrium-86 are (of course) identical. As an aside, it is important to note that there are many discrepancies in nuclear decay properties reported in the literature, and so the values cited in this chapter should be considered approximate [9].

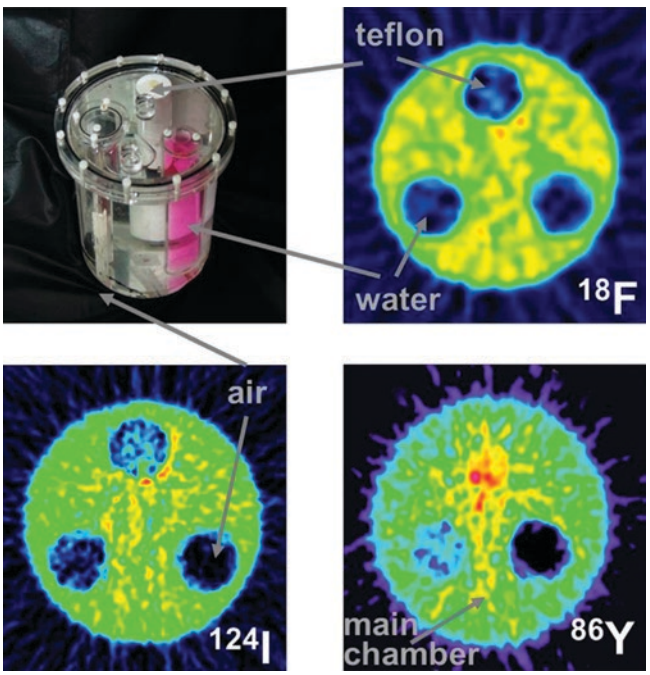

Fig. 1 Positron emission tomography (PET) images of three-rod (air, water, Teflon) phantoms showing the spatial resolution of select PET nuclides with no background subtraction of gamma coincidences (From Rösch *et al.* [26], with permission)

Lutetium-177

Lutetium-177 has a half-life of ~6.6 days and emits both β^- particles for therapy ($E_{\beta^-(\text{max})}$ = 497 keV) and gamma rays for single photon emission computed tomography (SPECT) imaging. As a result, lutetium-177 can be considered a true theranostic radionuclide [28, 29]. In practice, this means that SPECT imaging can be used to help evaluate the *in vivo* biodistribution of ^{177}Lu-labeled radiotherapeutics in the clinic. This approach does have two caveats. First, unlike PET, SPECT is not natively quantitative. And second, only a low abundance of the gamma rays emitted by lutetium-177 lies in the common SPECT imaging window (~30–300 keV), making long imaging times necessary and rendering imaging somewhat cumbersome. In addition to enabling theranostic applications, the gamma ray emissions from lutetium-177 also make biodistribution studies in animals and other *ex vivo* assays much easier. An additional difference between lutetium-177 and yttrium-90 is the energy of the β^- particles ejected from lutetium-177. The β^- particles emitted by lutetium-177 have a mean free path of ~1.6 mm in tissue, almost an order of magnitude shorter than those emitted by yttrium-90 (~12 mm). This shift results in not only lower myelotoxicity from lutetium-177 but also less tumorigenicity from the crossfire effect [18]. Differences in myelotoxicity may be substantial when attaching lutetium-177 and yttrium-90 to traditional peptide and antibody vectors that circulate in the blood for substantial periods of time. While these differences in physical properties may be significant, they *can* be circumvented using cutting-edge techniques in the design and administration of radiopharmaceuticals. Specifically, a recent study utilizing a pretargeted delivery approach vitro assays such as serum has shown improved dosimetry profiles and minimized these differences [30].

Although indium-111 ($t_{1/2}$ = ~67 h, gamma, SPECT) is commonly used for pre-therapy imaging for yttrium-90 and lutetium-177, SPECT imaging is generally inferior to PET. In Fig. 2 the same patient is imaged via SPECT with $[^{111}In]$In-DTPA-octreotide (4 h, 24 h) and via PET with $[^{86}Y]$Y-DOTATOC (4 h, 24 h), showing hepatic and para-aortic metastases of a carcinoid tumor [31]. This figure demonstrates that even though yttrium-86

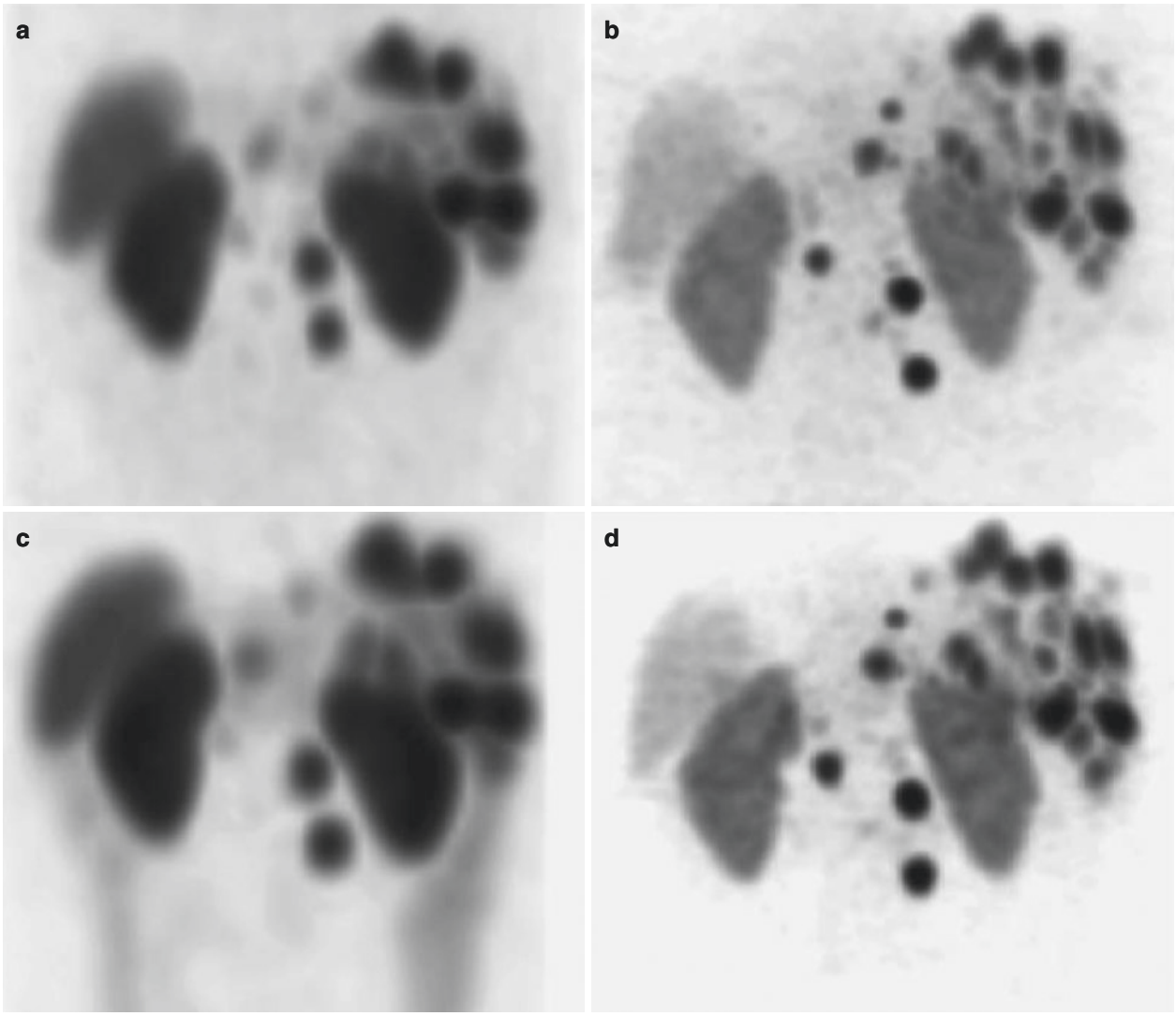

Fig. 2 The same patient imaged via single photon emission computed tomography (SPECT) with [^{111}In]In-DTPA-octreotide (4 h, 24 h, **a, c**) and via positron emission tomography (PET) with [^{86}Y]Y-DOTATOC (4 h, 24 h, **b, d**), showing hepatic and para-aortic metastases of a carcinoid tumor (From Förster *et al.* [31], with permission)

is one of the less desirable PET radionuclides due to its suboptimal nuclear decay properties, the resulting imaging quality is still superior to indium-111 SPECT.

Details

The Bioinorganic Chemistry of Lu^{3+} and Y^{3+}

Bioinorganic chemistry is the study of metals in biology, including the homeostasis and distribution of metals in the human body. Radiopharmaceuticals are administered in minuscule quantities, and so the metal-chelator coordination equilibrium has a strong driving force for dissociation. This is a fundamental reason why chelators must be very carefully tailored for each individual radiometal ion (*vide infra*), as the stability *in vivo* (kinetic inertness) of the metal-chelator complex must be remarkably high to ensure that the radiometal remains bound by the chelator. Within the body, several native ligands—including transferrin, serum albumin, ceruloplasmin, metallothioneins, phosphate, water, and halides—compete for the binding of the radiometal. Indeed, many of these native ligands exist at far higher concentrations than the chelator itself. The body maintains exquisite control and homeostasis of metal ions, and there are essentially no "free" metal ions in the body. Any radiometal that is released from a chelator will be quickly bound by serum proteins and shuttled through the blood either for storage, incorporation or adsorption into bone, binding by proteins/enzymes (*e.g.* superoxide dismutase/ceruloplasmin), or excretion.

To provide an example of metal regulation pertaining to radiometals, the metal ion Fe^{3+} is bound with very high

affinity by the blood serum protein transferrin (a native iron transport protein). However, larger cationic metal ions such as Y^{3+} and Lu^{3+} are not bound as tightly [32–35]. The metal ions Y^{3+} and Lu^{3+} have been shown to bind to transferrin, albeit not as strongly and more transiently than Fe^{3+} [32–35]. An obvious hypothesis for the weaker binding of the lanthanides to transferrin would be their size being too large to fit into the binding sites, as they have smaller charge-to-radius ratios and utilize 4f orbitals, resulting in lower metal ion binding affinity, as 4f orbitals are more diffuse than 3d orbitals [33]. It has been suggested that large metal ions bind poorly to transferrin largely due to steric repulsion at the more crowded *C*-terminus binding site [34], but a more sophisticated argument suggests that the binding strength of metal ions to transferrin is better related to metal ion acidity than size [36–38]. This hypothesis is supported by evaluating the large and very acidic metal ion Bi^{3+}, which has an abnormally high binding affinity for transferrin despite its size, which provides credence to this idea (103 pm, log K_1 = 19.4, and log K_2 = 18.5) [36–38]. Both arguments predict low binding affinities for Y^{3+} and Lu^{3+} for transferrin. The stability constants for binding transferrin with Y^{3+} have not been determined to our knowledge, but log K_1* = 11.08 and log K_2* = 7.93 have been reported for one or two Lu^{3+} ions, which are several orders of magnitude lower than the corresponding values for Fe^{3+} ions [34].

The radionuclides of yttrium and lutetium *do* have high affinity for bone, and the *in vivo* presence of "free" unchelated metal ions results in high uptake in bone. For example, ~50% of $[^{90}Y]Y^{3+}$ injected as unchelated metal ion into a human will primarily deposit in bone, with the next highest uptake being in the liver (~25%) [39]. More concerning is a study that suggests that even intact, cationic lanthanide complexes can adsorb onto the surface of bone. This means that even stably chelated radiometals may accumulate in the bone under certain circumstances, although this is less likely when the chelator is attached to a targeting vector such as an antibody or a peptide [40]. The take-home message from this evaluation of bioinorganic chemistry in relation to $[^{177}Lu]Lu^{3+}$ and $[^{86}Y]/[^{90}Y]Y^{3+}$ is that bone and liver uptake are two of the largest concerns, and abnormally high uptake of radiometal ions in these organs may indicate instability in the metal-chelator complex.

Bifunctional Chelators for Lu^{3+} and Y^{3+}

Chelators generally come in two broad types, macrocyclic and acyclic. Macrocycles are rigid and contain a partially preorganized binding site for the metal ion. The macrocycle effect—an extension of the chelate effect—leads to macrocyclic ligands generally forming more kinetically inert and thermodynamically stable complexes than comparable acyclic chelators [41]. Like the chelate effect, the macrocycle effect is primarily entropy-driven (thermodynamic): the preorganization of the chelator's binding groups means that less reorganization is required to wrap around a metal ion than is typically needed with acyclic chelators [41]. Practically speaking, this means that higher temperatures (*e.g.* 50–95 °C) are typically required to overcome this energetic barrier during radiolabeling reactions with macrocyclic chelators. On the flip side, however, macrocycles also possess high-energy barriers to the release of metal ions, a trait which results in excellent *in vivo* stability (kinetic inertness).

Acyclic chelators are linear (*i.e.* are not covalently cyclized) and are typically radiolabeled efficiently at ambient temperatures in as little as 5–15 min. This ease of radiolabeling portends the fact that acyclic chelators have lower energetic barriers to dissociation and are typically less stable than macrocycles *in vivo* (lower kinetic inertness). Thermodynamic stability constants (K_{ML} = [ML]/[M][L]) can be calculated from experiments such as potentiometric and/or spectrophotometric titrations, but these values offer practically zero predictive power when it comes to *in vivo* stability [42, 43]. Stability constants give a value, direction, and magnitude of the equilibrium in a metal-chelator coordination reaction, but they contain no kinetic information. The "kinetic inertness" of radiometal complexes is generally not quantifiable in terms of formal rate constants but rather tested indirectly via *in vitro* assays such as serum stability or by monitoring *in vivo* demetallation indirectly from characteristics such as bone uptake or liver uptake. Given the luxury, one would always opt for maximum stability and therefore choose macrocyclic chelators. However, sometimes fast radiolabeling kinetics are required (*e.g.* when using a short-lived nuclide), or high temperatures must be avoided (*e.g.* when using heat-sensitive biomolecules). In these cases, acyclic chelators are preferred or sometimes necessary.

A final consideration is that a chelator must be constructed to contain a reactive moiety that enables its facile conjugation to targeting vectors. A selection of these groups includes *N*-hydroxysuccinimidyl esters for the formation of peptide bonds, benzyl isothiocyanates for the formation of thiourea linkages, azides and alkynes for copper-catalyzed click chemistry, thiols and maleimides for the formation of thioether bonds, and tetrazines and *trans*-cyclooctenes for copper-free click chemistry. In the end, the most important experiments to determine the effective stability of both the chelator-radiometal complex and the bioconjugation method are *in vivo* biodistribution and imaging studies with direct comparisons to alternative chelators.

The two most successful and commonly used chelators for yttrium and lutetium are DOTA and CHX-A″-DTPA, but other new chelators such as the picolinic acid-based H_4octapa and the NOTA-based 5p-*C*-NETA have shown promise as well (Fig. 3)

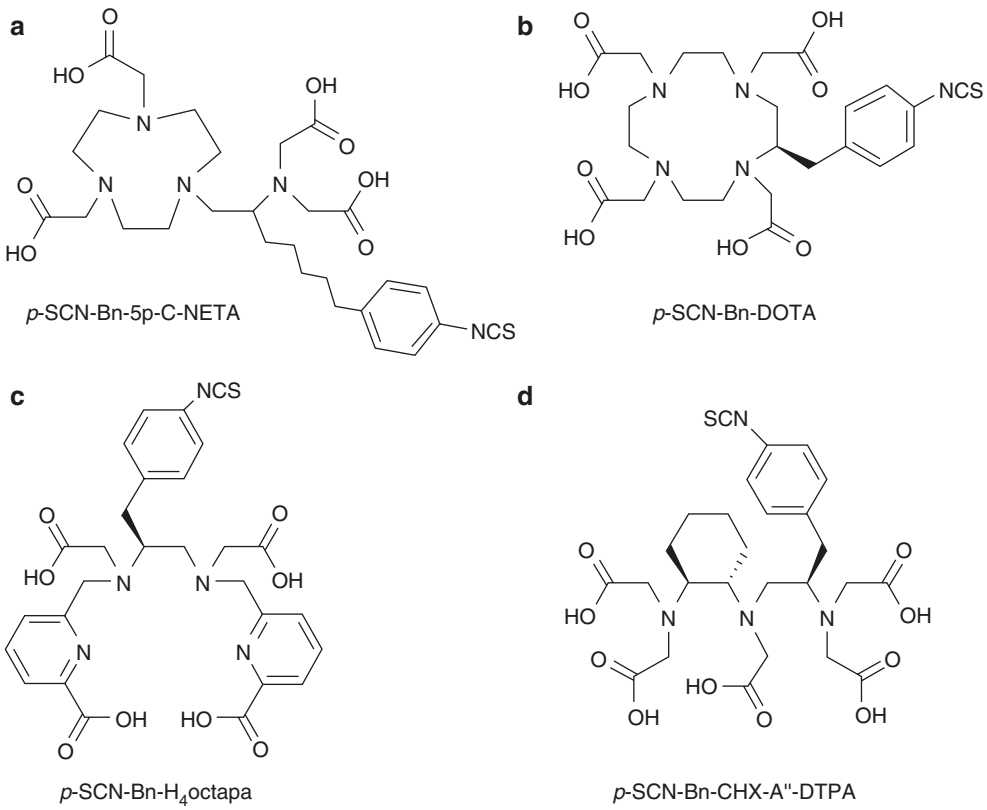

Fig. 3 The most popular and commercially available bifunctional derivatives of the chelators (**a**) 5p-*C*-NETA and (**b**) DOTA (**c**) H_4octapa and (**d**) CHX-A″-DTPA used for radiolabeling with $[^{177}Lu]Lu^{3+}$ and $[^{86}Y]/[^{90}Y]Y^{3+}$

[5, 44–51]. Commercial availability is a huge factor in adoption of chelators, and the front-runners [(*R*)-2-amino-3-(4-isothiocyanatophenyl)propyl]-trans-(*S,S*)-cyclohexane-1,2-diamine-pentaacetic acid (*p*-SCN-Bn-CHX-A″-DTPA) and S-2-(4-Isothiocyanatobenzyl)-1,4,7,10-tetraazacyclododecane tetraacetic acid (*p*-SCN-Bn-DOTA) can be purchased. Despite its slow radiolabeling kinetics and requisite high-temperature labeling conditions, DOTA is perhaps the most ubiquitous chelator used for radiometallation reactions. DOTA is generally considered the "gold standard" chelator for radiometal ions such as $[^{111}In]In^{3+}$, $[^{177}Lu]Lu^{3+}$, $[^{86}Y]/[^{90}Y]Y^{3+}$, $[^{225}Ac]$, $[^{44}Sc]/[^{47}Sc]Sc^{3+}$, and even $[^{68}Ga]Ga^{3+}$.

Particularly Important Works

Chelator Development: The Story of CHX-A″-DTPA

DTPA is the prototypical acyclic chelator for radiochemistry, and although it can bind many radiometal ions quickly at ambient temperature (< 30 min), universally poor *in vivo* stability and the emergence of CHX-A″-DTPA have made it obsolete [42]. The inadequacies of DTPA have been improved through the design of novel derivatives. The first successful alternative to DTPA was 1B4M-DTPA (tiuxetan), a ligand that only differs from DTPA in a single methyl group on one of its ethylene backbones. 1B4M-DTPA was used in the FDA-approved ^{90}Y-based drug Zevalin (Fig. 4) [52]. A further enhancement of DTPA came with CHX-A″-DTPA, in which the placement of a cyclohexyl moiety in the chelator backbone made the chelator more rigid compared to native DTPA. In essence, the inclusion of this cyclohexyl group imposes a degree of covalent preorganization, making CHX-A″-DTPA a "pseudo-macrocycle." The enhanced *in vivo* stability (kinetic inertness) gained from these changes came at the expense of radiolabeling kinetics. That said, the radiolabeling of CHX-A″-DTPA is still very efficient between 20 °C and 37 °C and much more reliable and reproducible than DOTA [42, 53].

In principle, the metal-chelator portion of a radiometal-based radiopharmaceutical should have no influence on the ability of the vector to engage its target (*e.g.* receptor), assuming that there is sufficient space between the chelator and the target-binding portion of the vector. Following this logic, the stereochemistry of a chelator should not affect the *in vivo* behavior of a biomolecular vector, as the chelator itself is not binding to the receptor. However, it is possible that the stereochemistry of the chelator *could* impact the *in vivo* behavior of a radiopharmaceutical by influencing the coordination chemistry, geometry, charge, or stability of the chelator-radiometal complex. In this regard, the family of cyclohexyl-modified DTPA chelators are particularly interesting. Indeed, there are four stereoisomers of

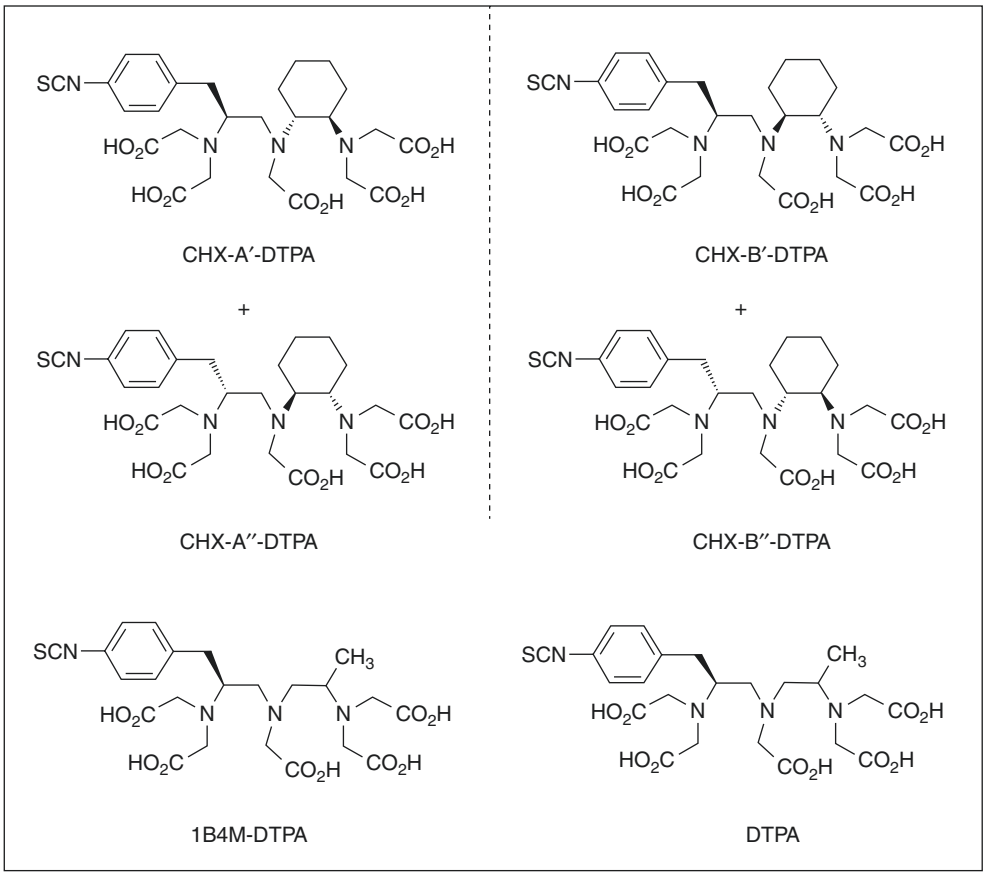

Fig. 4 Chemical structures of the four isomers of CHX-DTPA as well as the chelators 1B4M-DTPA and DTPA, depicted in their bifunctional benzyl isothiocyanate forms

cyclohexyl-modified DTPA: CHX-A′-DTPA, CHX-A″-DTPA, CHX-B′-DTPA, and CHX-B″-DTPA (see Fig. 4). Remarkably, Brechbiel and coworkers went to the trouble of synthesizing each isomer, radiolabeling it with [^{90}Y]Y^{3+}, and assaying its *in vivo* behavior [51]. A critical concept emerged from this study: the [^{90}Y]Y-CHX-B″-DTPA isomer was substantially less stable *in vivo* than the [^{90}Y]Y-CHX-A″-DTPA isomer, as demonstrated by the activity concentrations in the bone (~12 %ID/g vs ~4 %ID/g, respectively) [42, 51]. As previously discussed, when released *in vivo*, unchelated yttrium and lutetium primarily end up adsorbing or otherwise incorporating into bone. This fact allows bone uptake values to be used as surrogate markers for the stability of their radiometal complexes *in vivo*. To our knowledge, the exact reason for this difference in stability between isomers has not been elucidated; however, it is likely that the covalent preorganization imposed by the less stable isomers of CHX-DTPA forces inferior overlap between the orbitals of the metal and ligand. This result highlights the importance of the enantiopurity of chelators in cases in which stereochemistry can impact the coordination of the radiometal. Clearly, the use of a racemic mixture of CHX-DTPA variants would result in higher background uptake of [^{90}Y]Y^{3+} than the use of enantiomerically pure [^{90}Y]Y-CHX-A″-DTPA [42, 51].

Theranostics

Perhaps the most common application of yttrium-86 is as a theranostic pair nuclide for yttrium-90. The term "theranostic" typically refers to the use of the same chemical agent (*e.g.* a chelator-antibody conjugate) for both diagnostic and therapeutic applications in personalized medicine. In some cases, the different emissions from a single radionuclide (*e.g.* lutetium-177) can be harnessed for both imaging and therapy. In other cases, this is not possible, and two different versions of the same radiopharmaceuticals must be employed: one labeled with a nuclide for imaging and one labeled with a nuclide for therapy.

Given that radionuclides that emit both photons for imaging as well as particles for therapy are somewhat rare, the latter approach is more common. In this regard, one can imagine using a chelator-antibody conjugate labeled with a positron-emitting nuclide for PET imaging and dosimetry calculations and then subsequently using the same chelator-antibody conjugate labeled with a β^--emitting nuclide for radioimmunotherapy at a later date. Ideally, a "matched nuclide pair" with nearly identical chemical and nuclear decay characteristics would be used. Unfortunately, these pairs are difficult to find. One common pairing is indium-111 ($t_{1/2}$ = ~67 h, gamma, SPECT) and yttrium-90 ($t_{1/2}$ = ~64 h,

β⁻, therapy). However, this pairing is not ideal due to differences in the coordination spheres and nuclear properties of [^{111}In]In^{3+} and [^{90}Y]Y^{3+}.

It is perhaps not surprising that using yttrium-86 as a theranostic pair nuclide for yttrium-90 has received a great deal of attention. The primary benefit of this pairing is the chemical indistinguishability of [^{86}Y]Y^{3+} and [^{90}Y]Y^{3+}. As a result, radiopharmaceuticals labeled with these two radionuclides of yttrium are biologically equivalent surrogates, making ^{86}Y-labeled constructs ideal for imaging scans used to predict the biodistribution and dosimetry of ^{90}Y-labeled therapeutics. The primary drawback of this theranostic pair is that the half-life of yttrium-86 (14.7 h) is significantly shorter than that of yttrium-90 (64.2 h). As a result, PET data beyond 1–3 days post injection is not available with yttrium-86, though this information could be important when considering the *in vivo* performance of ^{90}Y-labeled radiopharmaceuticals [14, 15]. Despite this limitation of ^{86}Y-PET, PET is generally preferred to SPECT because the former provides improved spatial resolution, produces quantitative data, is natively 3D, and has greater sensitivity, thus enabling more rapid scans with lower injected doses [12].

Several examples of the use of ^{86}Y- and ^{90}Y-labeled theranostic pairs have been published. In one, the authors found that [^{86}Y]Y-CHX-A″-DTPA-trastuzumab provided superior images and more accurate dosimetry data compared to [^{111}In]In-CHX-A″-DTPA-trastuzumab as an imaging surrogate for radioimmunotherapy with [^{90}Y]Y-CHX-A″-DTPA-trastuzumab [14]. Another study compared the accuracy of peptide receptor radionuclide therapy (PRRT) dosimetry performed with [^{86}Y]/[^{111}In]Y/In-DOTATOC for scouting scans prior to [^{90}Y]Y-DOTATOC therapy [31, 54]. This study revealed that [^{111}In]In-DTPA-octreotide and [^{111}In]In-DOTATOC were not biologically equivalent to the ^{90}Y-/^{86}Y-labeled analogues and yielded different organ distributions and inaccurate dosimetry data [31, 54]. These studies demonstrate the well-established principle that performing pre-therapy scouting scans with a chemically identical radiometal surrogate (theranostics) such as yttrium-86 for yttrium-90 is not *required* but is *ideal* when appropriate radionuclides are accessible [14, 31, 54]. The current gold standard in theranostic medicine can be found in the domain of PRRT, where [^{68}Ga]Ga-DOTATATE and other somatostatin-targeting peptide derivatives are used for PET imaging diagnosis and dosimetry, followed by [^{177}Lu]- or [^{90}Y]-DOTATATE therapy (and more recently actinium-225). In fact, [^{177}Lu]Lu-DOTATATE was FDA approved in January 2018 under the brand name LUTATHERA®. A recent clinical study has demonstrated success using tandem PRRT for treating neuroendocrine tumors, which utilized co-injection of both [^{90}Y]Y- and [^{177}Lu]Lu-DOTATATE [55]. The success of this study was reliant on the use of [^{68}Ga]Ga-DOTATATE PET for pre-therapy dosimetry, as well as post-therapy monitoring of treatment response [55].

Tricks of the Trade: Moles and Specific Activity

A thought exercise on specific activity is often useful to put the quantities of a radionuclide used during radiolabeling reactions in perspective and place concrete values on frequently used terms such as "sub-pharmacological." On the information sheets for its products, one of the major radionuclide distributors in North America lists specific activities of 740 GBq/mg for lutetium-177 and 18,500 GBq/mg for yttrium-90. For a research radiolabeling experiment, quantities of 1–20 mCi (37–740 MBq) may typically be used. As summarized in Table 2, a 10 mCi (370 MBq) aliquot of lutetium-177 at a specific activity of 20 Ci/mg (3538 Ci/mmol) is a physical quantity of only ~500 ng and ~2.8 nmol. For yttrium-90, 10 mCi (370 MBq) at a specific activity of 500 Ci/mg (44,954 Ci/mmol) corresponds to a physical quantity of ~20 ng, which is only ~0.2 nmol. To put this in perspective, a standard bottle of concentrated HCl contains ~0.2 ppm iron. It's common to add ~10 μL of concentrated HCl while adjusting the pH of a radiometal solution or buffer, which means adding ~0.036 nmol of Fe^{3+}. To put this into context, a radiolabeling reaction containing 1 mCi (37 MBq) of [^{90}Y]Y^{3+} is only ~0.02 nmol, which means that adding 10 μL of concentrated HCl will introduce a molar excess of iron (~0.036 nmol). This highlights the reason why expensive metal-free acids are typically used for adjusting the pH of radiolabeling buffers (they contain ppb levels of iron instead of ppm), and a metal-scavenging resin such as Chelex® 100 is often used to pretreat buffers. For this thought experiment, we will consider the real-world example of radiolabeling the chelator-bearing immunoconjugate DOTA-trastuzumab. DOTA is a chelator typically used for coordinating [^{90}Y]Y^{3+} and [^{177}Lu]Lu^{3+}, and trastuzumab is a commonly used monoclonal antibody that targets the HER2/*neu* receptor which is overexpressed by a variety of human tumors. In most cases a 1:1 stoichiometric ratio of chelator/radiometal is not achievable when preparing radiopharmaceuticals, as this would mean literally every single molecule of the chelator-antibody conjugate had bound a radiometal ion. Although not realistically achievable, these calculated values effectively provide a value for the "theoretical 100% yield," which would provide the maximum possible specific activity (Max SA; see Table 2).

Tricks of the Trade: Radiolabeling Tips

General radiolabeling protocols for [^{177}Lu]Lu^{3+}, [^{90}Y]Y^{3+}, and [^{86}Y]Y^{3+} dictate that once a solution of radiometal ion is procured (usually as an acidic solution in 0.05–0.1 M HCl or nitric acid), the desired quantity of activity is transferred via auto-pipette to a chelator-vector bioconjugate in buffer. This radiolabeling mixture is allowed to react until radiolabeling yields are as high as possible given the chosen chelator, concentration, and temperature conditions [14, 42, 56, 57]. Radiolabeling yields are typically determined via radioactive instant thin-layer chromatography (called "iTLC") or reverse-phase HPLC coupled to a radiation detector. The chelation of radiometal ions typically requires 15–120 min, depending on the chelator and reaction temperature used. After radiolabeling, the aqueous reaction mixture is purified before use. When the targeting vector is an antibody or large protein, purification is typically performed via size-exclusion chromatography with an appropriate molecular weight cut-off (*e.g.* PD10 Sephadex G25 columns or centrifuge spin filters). Radiometallated peptide conjugates are typically purified via reverse-phase HPLC or small C_{18} Sep-Pak cartridge trap/release. The final prepared doses are typically formulated in saline, are filtered through a 0.22 μm syringe filter for sterilization, and sometimes include a radioprotectant such as ascorbic acid or gentisic acid.

To unpack these variables in more detail, the factor of temperature relates to the type of chelator, with acyclic chelators such as CHX-A″-DTPA typically needing 15–60 min at room temperature or 37 °C to obtain good radiolabeling yields. Even when acyclic chelators are employed, they are sometimes heated to improve radiolabeling efficiency with certain vectors. On the other hand, macrocyclic chelators such as DOTA exhibit slow radiolabeling kinetics and require temperatures in the range of 70–100 °C for 15–60 min for effective and reproducible labeling. To the detriment of reproducibility and radiochemical yields, DOTA-bearing antibodies are routinely radiolabeled at only 37 °C due to the temperature sensitivity of large proteins. The caveats to radiolabeling DOTA at 37 °C are the low and—even more

Table 2 Thought exercise demonstrating common mass and mole quantities of radiometal nuclides used for radiolabeling trastuzumab (10 mCi = 370 MBq). The calculation assumes only one chelator per antibody (146 kDa, 1:1 molar ratio of radiometal/antibody); SA = specific activity

Nuclide	SA (Ci/mg)	SA (Ci/mmol)	Mass of 10 mCi nuclide (ng)	Moles of 10 mCi nuclide (nmol)	Max SA for 1 mg trastuzumab labeling (mCi/mg)
[^{177}Lu]Lu^{3+}	20	3538	500	2.8	24.2
[^{90}Y]Y^{3+}	500	44,954	20	0.2	308

Sample calculations for lutetium-177 →

$$\text{SA of } [^{177}\text{Lu}]\text{Lu}^{3+} = \left[20\frac{\text{Ci}}{\text{mg}}\times 10^{3}\frac{\text{mg}}{\text{g}}\times 176.904\frac{\text{g}}{\text{mol}}\times 10^{-3}\frac{\text{mol}}{\text{mmol}}\right] = 3538\frac{\text{Ci}}{\text{mmol}}$$

$$\text{Mass of 10 mCi of } [^{177}\text{Lu}]\text{Lu}^{3+} = \left[10\,\text{mCi}\times 10^{-3}\frac{\text{Ci}}{\text{mCi}}\times\frac{1\,\text{mg}}{20\,\text{Ci}}\times 10^{6}\frac{\text{ng}}{\text{mg}}\right] = 500\,\text{ng}$$

$$\text{Moles of 10 mCi of } [^{177}\text{Lu}]\text{Lu}^{3+} = \left[10\,\text{mCi}\times 10^{-3}\frac{\text{Ci}}{\text{mCi}}\times\frac{1\,\text{mmol}}{3538\,\text{Ci}}\times 10^{6}\frac{\text{nmol}}{\text{mmol}}\right] = 2.8\,\text{nmol}$$

Maximum theoretical SA for 1 mg trastuzumab labeling →

$$\text{Moles of 1 mg trastuzumab} = \left[\frac{1\,\text{mg}\times 10^{-3}\frac{\text{g}}{\text{mg}}}{146{,}000\frac{\text{g}}{\text{mol}}}\times 10^{9}\frac{\text{nmol}}{\text{mol}}\right] = 6.85\,\text{nmol}$$

1:1 ratio → Moles of lutetium-177 = 6.85 nmol

$$\text{SA } [^{177}\text{Lu}]\text{Lu-trastuzumab} = \left[\left(6.85\times 10^{-6}\,\text{mmol}\right)\times 3538\frac{\text{Ci}}{\text{mmol}}\times 10^{3}\frac{\text{mCi}}{\text{Ci}}\right] = 24.2\frac{\text{mCi}}{\text{mg}}$$

problematically—inconsistent radiochemical yields. The most common buffers used with these radiometal ions are sodium or ammonium acetate at pH 4.5–5.5 (~0.2–2.0 mL, 200–1000 mM). The molarity of these buffers depends on the volume of the acidic solution of radiometal that is added. As radiometals are typically delivered as 0.05–0.1 M HCl solutions, buffers with higher molarities can be used to ensure that the addition of the solution of radiometal to small volumes of the buffer will not change the pH of the radiolabeling reaction. This allows the reaction volume to be kept as small as possible, which improves radiolabeling yields. As mentioned in the thought exercise on specific activity, buffers are typically prepared with trace-level metal-free chemicals and then treated with a metal-scavenging resin such as Chelex® 100 (~1.2 g/L Chelex® in prepared buffer, stirred overnight, and then filtered to remove spent resin) in order to remove as many contaminant metal ions as possible.

The radionuclides $[^{177}Lu]Lu^{3+}$ and $[^{90}Y]Y^{3+}$ emit ionizing β-particles, which causes water molecules to undergo radiolysis (bond cleavage generating free radicals). Free radicals created by the radiolysis of water, including hydroxyl radicals and superoxide radicals, can then destroy the radiopharmaceutical (vector). All radionuclides in high enough quantities and concentrations can induce solvent radiolysis and generate free radicals [58]. Consequently, when radiolabeling with large activities of either of these radionuclides, adding ~1–10 mg/mL (~5–50 mM) of ascorbic acid can act as a radioprotectant to minimize the damage to the radiotracer cause by free radicals [55]. Another consideration when radiolabeling with these radionuclides is that the *chemical purity* differs between radiometals and also between production locations. Excess quantities of non-radioactive contaminant metal ions can drastically interfere with radiolabeling yields, as the chelator may become saturated with other metal ions before it can coordinate the desired radiometal (this is often an issue with yttrium-86).

Controversial Issues: The Dark Side of Yttrium-86

Some shortcomings of yttrium-86 were listed above, such as the poor resolution of its PET images due to the high energy of its ejected positrons, the difficulty of its purification after production, its short half-life compared to its partner nuclide yttrium-90, and its emission of 105 different gamma rays. Some of these deficiencies can be overcome. For example, a software can be used to subtract some of the prompt gamma events after imaging and thus improve the quality of yttrium-86 PET images. Others, however, cannot. For example, the plethora of gamma rays emitted from yttrium-86 require significant shielding, resulting in transportation and logistical problems as well as a radiation dose concern for the personnel handling the radionuclide [9]. In addition, the difficulty in purifying yttrium-86 and the consequent low radiochemical yields obtained by using impure radiometal remain stubborn issues. Indeed, to the knowledge of this chapter's authors, a reliable commercial source of chemically pure yttrium-86 is not currently available in North America, although individual sites may produce it on an ad hoc basis. Taken together, these concerns force the inevitable conclusion that—at least for now—yttrium-86 is undeniably inferior to other positron-emitting nuclides such as fluorine-18, zirconium-89, and gallium-68 (see Figs. 1 and 2) [25, 59].

The Bottom Line

We hope this chapter has illuminated the various chemical and radiochemical properties of lutetium-177, yttrium-90, and yttrium-86 that have made them popular choices for nuclear imaging and therapy over the previous decades. Indeed, these three radionuclides are commonly used with peptide-, antibody-, and nanoparticle-based targeting vectors for SPECT, PET, and radionuclide therapy. Although yttrium-86 remains a troublesome and niche radiometal with very limited availability and many undesirable properties, lutetium-177 and yttrium-90 are two of the most commonly used therapeutic radionuclides worldwide.

- Lutetium-177 ($[^{177}Lu]Lu^{3+}$, $t_{1/2}$ = ~159 h, $E_{\beta^-(max)}$ = 497 keV, $R_{\beta^-(mean)}$ = 1.6 mm, γ = 112, 208 keV):
  - Emits β-particles for radiotherapy as well as gamma rays for SPECT imaging, therefore making it a theranostic radiometal.
  - Emits gamma rays with low abundance. This combined with the low sensitivity of SPECT makes imaging with this radionuclide sub-optimal.
  - Is typically utilized with the chelators DOTA or CHX-A″-DTPA.
  - Is mostly used with peptide- or antibody-based targeting vectors.
  - Has radiochemistry and chelator selection that is effectively identical to that of yttrium-86/yttrium-90.
  - Emits β-particles with a short mean free path length of ~1.6 mm *in vivo*. This not only minimizes radiation toxicity but also reduces crossfire effect and therapeutic efficacy compared to yttrium-90.
  - Emits gamma rays upon decay, which make handling and analysis easier than yttrium-90.
  - Can be purchased with a specific activity of ~20–100 Ci/mg (~740–3700 GBq/mg), which is much lower than that of commercially available yttrium-90 at ~500 Ci/mg (18,500 GBq/mg).

- Yttrium-90 ($[^{90}Y]Y^{3+}$, $t_{1/2}$ = 64.1 h, $E_{\beta^-(max)}$ = 2280 keV, $R_{\beta^-(mean)}$ = 12 mm, 0.003% β^+):
  - Strictly emits high-energy electrons (β^-) for radiotherapy, and its decay produces no substantial quantity of gamma rays or positrons (β^+), making both handling and analysis difficult.
  - Emits β-particles with a longer mean free path length of ~12 mm *in vivo*, which not only increases radiation toxicity but also increases crossfire effect and therapeutic efficacy relative to lutetium-177.
  - Emits a very, very low abundance (0.003%) of positrons which have been imaged with PET. However, this is not trivial or performed routinely.
  - Requires that dosimetry must be performed using a different radionuclide, such as the yttrium-86, indium-111, gallium-68, or zironcium-89.
- Yttrium-86 ($[^{86}Y]Y^{3+}$, $t_{1/2}$ = 14.7 h, β^+ ratio = 33%, $E_{\beta^+(mean)}$ = 535 keV, $R_{\beta^+(mean)}$ = 2.5 mm):
  - Is chemically identical to yttrium-90 and therefore forms bioequivalent chelate complexes, yielding accurate dosimetry data from PET images.
  - Has a shorter half-life (14.7 h vs 64.1 h) that is a poor match for its isotopologue yttrium-90.
  - Produces PET images with relatively poor quality.
  - Emits 105 different gamma rays, which cause radiation shielding issues and dose concerns and require substantial lead shielding for handling and transport.
  - Lacks a reliable commercial source or a long-lived generator system, making the logistics of distribution and procurement challenging.
  - Has not seen much success or clinical interest, with investigators instead favoring gallium-68 or zirconium-89.

References

1. Pearson RG. Hard and soft acids and bases, HSAB, part I: fundamental principles. J Chem Educ. 1968;45(9):581.
2. Shannon R. Revised effective ionic radii and systematic studies of interatomic distances in halides and chalcogenides. Acta Crystallogr. 1976;A32(5):751–67.
3. Barnum DW. Hydrolysis of cations. Formation constants and standard free energies of formation of hydroxy complexes. Inorg Chem. 1983;22(16):2297–305.
4. Liu S. The role of coordination chemistry in the development of target-specific radiopharmaceuticals. Chem Soc Rev. 2004;33(7):445–61.
5. Price EW, Orvig C. Matching chelators to radiometals for radiopharmaceuticals. Chem Soc Rev. 2014;43(1):260–90.
6. Baes CF, Mesmer RE. The thermodynamics of cation hydrolysis. Am J Sci. 1981;281(7):935–62.
7. Baes CF Jr, Mesmer RE. The hydrolysis of cations. New York: Wiley-Interscience; 1976.
8. Martell AE, Smith RM. Critical stability constants. Vol. 3: other organic ligands. New York: Plenum Press; 1977.
9. Holland JP, Williamson MJ, Lewis JS. Unconventional nuclides for radiopharmaceuticals. Mol Imaging. 2010;9(1):1–20.
10. Walrand S, Jamar F, Mathieu I, De Camps J, Lonneux M, Sibomana M, et al. Quantitation in PET using isotopes emitting prompt single gammas: application to yttrium-86. Eur J Nucl Med Mol Imaging. 2003;30(3):354–61.
11. Lederer CM, Shirley VS. Table of isotopes. 7th ed. New York: Wiley; 1978.
12. Walrand S, Flux G, Konijnenberg M, Valkema R, Krenning E, Lhommel R, et al. Dosimetry of yttrium-labelled radiopharmaceuticals for internal therapy: 86Y or 90Y imaging? Eur J Nucl Med Mol Imaging. 2011;38(1):57–68.
13. Nayak TK, Garmestani K, Milenic DE, Baidoo KE, Brechbiel MW. HER1-targeted 86Y-panitumumab possesses superior targeting characteristics than 86Y-cetuximab for PET imaging of human malignant mesothelioma tumors xenografts. PLoS One. 2011;6(3):e18198.
14. Palm S, Enmon RM, Matei C, Kolbert KS, Xu S, Zanzonico PB, et al. Pharmacokinetics and biodistribution of 86Y-trastuzumab for 90Y dosimetry in an ovarian carcinoma model: correlative microPET and MRI. J Nucl Med. 2003;44(7):1148–55.
15. Herzog H, Rösch F, Stöcklin G, Lueders C, Qaim SM, Feinendegen LE. Measurement of pharmacokinetics of yttrium-86 radiopharmaceuticals with PET and radiation dose calculation of analogous yttrium-90 radiotherapeutics. J Nucl Med. 1993;34(12):2222–6.
16. Forrer F, Waldherr C, Maecke HR, Mueller-Brand J. Targeted radionuclide therapy with 90Y-DOTATOC in patients with neuroendocrine tumors. Anticancer Res. 2006;26(1B):703–7.
17. Volkert WA, Goeckeler WF, Ehrhardt GJ, Ketring AR. Therapeutic radionuclides: production and decay property considerations. J Nucl Med. 1991;32(1):174–85.
18. Baum RP, Kluge AW, Kulkarni H, Schorr-Neufing U, Niepsch K, Bitterlich N, et al. [(177)Lu-DOTA](0)-D-Phe(1)-Tyr(3)-octreotide ((177)Lu-DOTATOC) for peptide receptor radiotherapy in patients with advanced neuroendocrine tumours: a Phase-II study. Theranostics. 2016;6(4):501–10.
19. Sadeghi M, Aboudzadeh M, Zali A, Mirzaii M, Bolourinovin F. Radiochemical studies relevant to 86Y production via 86Sr(p,n)86Y for PET imaging. Appl Radiat Isot. 2009;67(1):7–10.
20. Reischl G, Rösch F, Machulla HJ. Electrochemical separation and purification of yttrium-86. Radiochim Acta. 2002;90(4):225–8.
21. Disselhorst JA, Brom M, Laverman P, Slump CH, Boerman OC, Oyen WJG, et al. Image-quality assessment for several positron emitters using the NEMA NU 4-2008 standards in the Siemens Inveon Small-Animal PET Scanner. J Nucl Med. 2010;51(4):610–7.
22. Jødal L, Loirec CL, Champion C. Positron range in PET imaging: an alternative approach for assessing and correcting the blurring. Phys Med Biol. 2012;57(12):3931.
23. Sadeghi M, Aboudzadeh M, Zali A, Zeinali B. 86Y production via 86Sr(p,n) for PET imaging at a cyclotron. Appl Radiat Isot. 2009;67(7):1392–6.
24. Jødal L, Loirec CL, Champion C. Positron range in PET imaging: non-conventional isotopes. Phys Med Biol. 2014;59(23):7419–34.
25. Lubberink M, Herzog H. Quantitative imaging of 124I and 86Y with PET. Eur J Nucl Med Mol Imaging. 2011;38(1):10–8.
26. Rösch F, Herzog H, Qaim S. The beginning and development of the theranostic approach in nuclear medicine, as exemplified by the radionuclide pair 86Y and 90Y. Pharmaceuticals. 2017;10(2):56.
27. Conti M, Eriksson L. Physics of pure and non-pure positron emitters for PET: a review and a discussion. EJNMMI Phys. 2016;3(1):8.
28. Dash A, Pillai MRA, Knapp FF. Production of (177)Lu for targeted radionuclide therapy: available options. Nucl Med Mol Imaging. 2015;49(2):85–107.

29. Baum RP, Kulkarni HR. Theranostics: from molecular imaging using Ga-68 labeled tracers and PET/CT to personalized radionuclide therapy – the Bad Berka experience. Theranostics. 2012;2(5):437–47.
30. Altai M, Membreno R, Cook B, Tolmachev V, Zeglis B. Pretargeted imaging and therapy. J Nucl Med. 2017;58(10):1553–9.
31. Förster GJ, Engelbach MJ, Brockmann JJ, Reber HJ, Buchholz HG, Mäcke HR, et al. Preliminary data on biodistribution and dosimetry for therapy planning of somatostatin receptor positive tumours: comparison of 86Y-DOTATOC and 111In-DTPA-octreotide. Eur J Nucl Med. 2001;28(12):1743–50.
32. Harris WR, Pecoraro VL. Thermodynamic binding constants for gallium transferrin. Biochemistry. 1983;22(2):292–9.
33. Harris WR, Chen Y. Difference ultraviolet spectroscopic studies on the binding of lanthanides to human serum transferrin. Inorg Chem. 1992;31(24):5001–6.
34. Harris WR, Yang B, Abdollahi S, Hamada Y. Steric restrictions on the binding of large metal ions to serum transferrin. J Inorg Biochem. 1999;76(3–4):231–42.
35. Harris WR. Binding and transport of nonferrous metals by serum transferrin. In: Clarke MJ, editor. Less common metals in proteins and nucleic acid probes. Structure and bonding, vol. 92. Berlin/Heidelberg: Springer; 1998. p. 121–62.
36. Sun H, Li H, Sadler PJ. Transferrin as a metal ion mediator. Chem Rev. 1999;99(9):2817–42.
37. Sun H, Cox M, Li H, Sadler P. Rationalisation of metal binding to transferrin: prediction of metal-protein stability constants. In: Hill H, Sadler P, Thomson A, editors. Metal sites in proteins and models. Structure and bonding, vol. 88. Berlin/Heidelberg: Springer; 1997. p. 71–102.
38. Li H, Sadler PJ, Sun H. Rationalization of the strength of metal binding to human serum transferrin. Eur J Biochem. 1996;242(2):387–93.
39. Ando A, Ando I, Hiraki T, Hisada K. Relation between the location of elements in the periodic table and various organ-uptake rates. Int J Rad Appl Instrum B. 1989;16(1):57–80.
40. Wang L, Shi J, Kim Y-S, Zhai S, Jia B, Zhao H, et al. Improving tumor-targeting capability and pharmacokinetics of 99mTc-labeled cyclic RGD dimers with PEG4 linkers. Mol Pharm. 2009;6(1):231–45.
41. Hancock RD. Chelate ring size and metal ion selection. The basis of selectivity for metal ions in open-chain ligands and macrocycles. J Chem Educ. 1992;69(8):615–21.
42. Camera L, Kinuya S, Garmestani K, Wu C, Brechbiel MW, Pai LH, et al. Evaluation of the serum stability and in vivo biodistribution of CHX-DTPA and other ligands for yttrium labeling of monoclonal antibodies. J Nucl Med. 1994;35(5):882–9.
43. Harrison A, Walker CA, Parker D, Jankowski KJ, Cox JPL, Craig AS, et al. The in vivo release of 90Y from cyclic and acyclic ligand-antibody conjugates. Int J Rad Appl Instrum B. 1991;18(5):469–76.
44. Price EW, Carnazza KE, Carlin SD, Cho A, Edwards KJ, Sevak KK, et al. 89Zr-DFO-AMG102 immuno-PET to determine local HGF protein levels in tumors for enhanced patient selection. J Nucl Med. 2017;58(9):1386–94.
45. Price EW, Edwards KJ, Carnazza KE, Carlin SD, Zeglis BM, Adam MJ, et al. A comparative evaluation of the chelators H4octapa and CHX-A″-DTPA with the therapeutic radiometal 90Y. Nucl Med Biol. 2016;43(9):566–76.
46. Price EW, Cawthray JF, Adam MJ, Orvig C. Modular syntheses of H4octapa and H2dedpa, and yttrium coordination chemistry relevant to 86Y/90Y radiopharmaceuticals. Dalton Trans. 2014;43(19):7176–90.
47. Price EW, Zeglis BM, Cawthray JF, Lewis JS, Adam MJ, Orvig C. What a difference a carbon makes: H4octapa vs. H4C3octapa, ligands for In-111 and Lu-177 radiochemistry. Inorg Chem. 2014;53(19):10412–31.
48. Price EW, Zeglis BM, Cawthray JF, Ramogida CF, Ramos N, Lewis JS, et al. H4octapa-trastuzumab: versatile acyclic chelate system for 111In and 177Lu imaging and therapy. J Am Chem Soc. 2013;135(34):12707–21.
49. Kang CS, Chen Y, Lee H, Liu D, Sun X, Kweon J, et al. Synthesis and evaluation of a new bifunctional NETA chelate for molecular targeted radiotherapy using90Y or177Lu. Nucl Med Biol. 2015;42(3):242–9.
50. McMurry TJ, Brechbiel M, Kumar K, Gansow OA. Convenient synthesis of bifunctional tetraaza macrocycles. Bioconjug Chem. 1992;3(2):108–17.
51. Wu C, Kobayashi H, Sun B, Yoo TM, Paik CH, Gansow OA, et al. Stereochemical influence on the stability of radio-metal complexes in vivo. Synthesis and evaluation of the four stereoisomers of 2-(p-nitrobenzyl)-trans-CyDTPA. Bioorg Med Chem. 1997;5(10):1925–34.
52. Hohloch K, Zinzani PL, Linkesch W, Jurczak W, Deptala A, Lorsbach M, et al. Radioimmunotherapy with 90Y-ibritumomab tiuxetan is a safe and efficient treatment for patients with B-cell lymphoma relapsed after auto-SCT: an analysis of the international RIT-Network. Bone Marrow Transplant. 2010;46(6):901–3.
53. Brechbiel MW, Gansow OA, Atcher RW, Schlom J, Esteban J, Simpson D, et al. Synthesis of 1-(p-isothiocyanatobenzyl) derivatives of DTPA and EDTA. Antibody labeling and tumor-imaging studies. Inorg Chem. 1986;25(16):2772–81.
54. Pauwels S, Barone R, Walrand S, Borson-Chazot F, Valkema R, Kvols LK, et al. Practical dosimetry of peptide receptor radionuclide therapy with 90Y-labeled somatostatin analogs. J Nucl Med. 2005;46(1 suppl):92S–8S.
55. Kunikowska J, Pawlak D, Bąk MI, Kos-Kudła B, Mikołajczak R, Królicki L. Long-term results and tolerability of tandem peptide receptor radionuclide therapy with 90Y/177Lu-DOTATATE in neuroendocrine tumors with respect to the primary location: a 10-year study. Ann Nucl Med. 2017;31(5):347–56.
56. Schneider DW, Heitner T, Alicke B, Light DR, McLean K, Satozawa N, et al. In vivo biodistribution, PET imaging, and tumor accumulation of 86Y- and 111In-antimindin/RG-1, engineered antibody fragments in LNCaP tumor-bearing nude mice. J Nucl Med. 2009;50(3):435–43.
57. Rösch F, Herzog H, Stolz B, Brockmann J, Köhle M, Mühlensiepen H, et al. Uptake kinetics of the somatostatin receptor ligand [86Y] DOTA-d Phe1-Tyr3-octreotide ([86Y]SMT487) using positron emission tomography in non-human primates and calculation of radiation doses of the 90Y-labelled analogue. Eur J Nucl Med Mol Imaging. 1999;26(4):358–66.
58. Salako QA, O'Donnell RT, DeNardo SJ. Effects of Radiolysis on Yttrium-90-Labeled Lym-1 Antibody Preparations. J Nucl Med. 1998;39(4):667–70.
59. Barone R, Walrand S, Konijnenberg M, Valkema R, Kvols LK, Krenning EP, et al. Therapy using labelled somatostatin analogues: comparison of the absorbed doses with 111In-DTPA-D-Phe1-octreotide and yttrium-labelled DOTA-D-Phe1-Tyr3-octreotide. Nucl Med Commun. 2008;29(3):283–90.

The Radiopharmaceutical Chemistry of Zirconium-89

Bernadette V. Marquez-Nostra
and Nerissa Viola

Fundamentals

Zirconium is a group IV transition metal with a diverse array of applications in metallurgy, gemology, nuclear power, food packaging, the steel industry, and—of course—nuclear medicine. Zirconium has no known role in biological systems and is generally regarded as non-toxic and environmentally benign. There are five naturally occurring isotopes of zirconium: ^{90}Zr (stable; ~51%), ^{91}Zr (stable; ~11%), ^{92}Zr (stable; ~17%), ^{94}Zr (stable; ~17%), and ^{96}Zr ($t_{1/2} \sim 2.0 \times 10^{19}$ y; ~3%). In nature, the element is typically found as part of the mineral zircon ($ZrSiO_4$). Over 25 different radioisotopes of zirconium have been synthesized, though the relevant radionuclide for nuclear medicine is zirconium-89, which is used for the positron emission tomography (PET) of diseases such as cancer.

PET imaging using ^{89}Zr-labeled radiopharmaceuticals is typically focused on one of three aims: selecting patients who will most likely benefit from a targeted therapy, predicting a patient's response to therapy, or monitoring a patient's response to therapy. The overwhelming majority of preclinical and clinical investigations with ^{89}Zr have involved the radiolabeling of monoclonal antibodies (mAbs). The radiometal's multiday half-life (~3.3 days) extends the time-frame of imaging, improving image contrast by allowing the slow-circulating mAbs to accumulate at sites of disease and clear from the bloodstream. Typically, ^{89}Zr is produced using a biomedical cyclotron via the ^{89}Y(p,n)^{89}Zr reaction and is isolated and purified using hydroxamate-functionalized resins. In biological systems, zirconium-89 exists as a +4 oxidation state and can form complexes with coordination numbers (CN) of up to 8. Desferrioxamine (DFO)—which coordinates Zr^{4+} in a hexadentate fashion, leaving two coordination sites available for exogenous water molecules—is the current "gold standard" chelator for ^{89}Zr. For several years, the less-than-ideal *in vivo* stability of [^{89}Zr]Zr-DFO has been tolerated in preclinical and clinical immunoPET despite the transchelation of the radiometal to the bone over time. The deposition of ^{89}Zr in the bone poses a concern due to both the limited true-positive identification of osseous lesions and, just as importantly, the elevated radiation dose to the sensitive bone marrow. To resolve these issues, several new chelators have been explored to improve the stability of the ^{89}Zr-chelator complex by optimizing both the number of ligands in the coordination sphere (*i.e.* CN = 8) as well as the geometry and morphology of the chelator itself.

B. V. Marquez-Nostra (✉)
Department of Radiology and Biomedical Imaging, PET Center, Yale University, New Haven, CT, USA
e-mail: bernadette.marquez-nostra@yale.edu

N. Viola (✉)
Department of Oncology, Karmanos Cancer Institute, Wayne State University, Detroit, MI, USA
e-mail: villegan@karmanos.org

Details

Biomedical Utility

The importance of zirconium-89 in PET lies in its ability to facilitate the *in vivo* tracking of targeting vectors that require extended amounts of time to achieve optimal target-to-background contrast ratios. Over the last decade, the standardization of its production and commercial availability has paved the way for the development of companion diagnostics for immunotherapy and antibody-based treatments. Indeed, the physical half-life of ^{89}Zr ($t_{1/2}$ = 78.4 h) complements the biological half-lives of variety of larger biomolecules, including monoclonal antibodies (mAbs), antibody fragments, proteins, and nanoparticles. These targeting vectors via typically labeled with zirconium-89 via a bifunctional chelator that is covalently attached to the biomolecule or nanoparticle. Currently, desferrioxamine B (DFO) is the most widely used chelator for Zr-89 in both preclinical and clinical studies. Zirconium-89 is biologically inert and is trapped within the cell once internalized, making it a residualizing radionuclide [1]. This enables better visualization of disease targets and higher target-to-background activity concentration ratios

J. S. Lewis et al. (eds.), *Radiopharmaceutical Chemistry*, https://doi.org/10.1007/978-3-319-98947-1_21

several days after the administration of the [^{89}Zr]Zr-DFO-labeled tracer. However, a disadvantage of imaging with [^{89}Zr]Zr-DFO-labeled biomolecules is the suboptimal stability of [^{89}Zr]Zr-DFO complex, which leads to the decomplexation of [^{89}Zr]Zr^{4+} *in vivo* and its subsequent accumulation in bone. This phenomenon has been observed in both rodents [2] and humans [3].

Coordination Chemistry

The zirconium cation exists predominantly in the +IV oxidation state in aqueous solutions, though lower atypical oxidation states (I, II, III) have been reported [4]. Zr(IV) lacks valence electrons with its [Kr]$4d^0$ electronic configuration, and it has an ionic radius of 85 pm and a covalent radius of 1.48 pm [4, 5]. Because of its high charge and small ionic size, Zr is categorized as a hard Lewis acid with a strong affinity for hard Lewis bases such as oxygen donors. Zr forms metal complexes with varying coordination geometries and coordination numbers ranging from 4 to 12. That said, studies by Intorre and Martell suggest that eight-coordinate complexes of Zr(IV) are ideal [6, 7] . Complexes with lower coordination numbers typically recruit additional ligands to achieve an octacoordinate environment, thereby strengthening the metal complex against polymerization and hydrolysis [5]. Zr(IV) with eight-coordinating ligands conventionally forms a dodecahedral structure. Table 1 lists the geometries of Zr(IV) complexes with various coordination numbers.

Zirconium (IV) has the potential to undergo hydrolysis, forming polynuclear species (*e.g.* dimers, trimers, and tetramers) that are bridged by hydroxo- or oxo-donor groups [5, 8]. In very dilute solutions (10^{-4} M) at pH ~ 2, Zr(IV) exists in a hydrolyzed state in the form $[Zr(OH)_n]^{(4-n)+}$ (note: n is pH-dependent) in very dilute solutions (~ 10^{-8} M) [5]. Hydrolyzed precipitates with very low solubility (~ 10^{-8} M) can also form at pH ~ 2 [8].

Table 1 Coordination geometry of Zr(IV) metallocomplexes

Coordination number	Geometry
4	Tetrahedron
5	Square pyramid
6	Octahedron Trigonal prism
7	Pentagonal bipyramid Capped trigonal prism Capped octahedron
8	Dodecahedron Square antiprism Cube Capped trigonal prism
9	Irregular
10	Irregular

Nuclear Properties of Zr-89

Zirconium-89 has a half-life of 78.4 h, decaying to stable ^{89}Y via positron decay (23%) and electron capture (77%) (Fig. 1) [9]. This decay results in the emission of a characteristic gamma ray of 909 keV (99%), which allows for the fingerprint identification of this radionuclide using high-purity germanium gamma spectroscopy. Importantly, this high-energy gamma does not significantly interfere with imaging because it is not in coincidence with the ß$^+$ decay [9]. ^{89}Zr produces PET images with good spatial resolution due to its low positron energy ($E_{ß[beta]+max}$ = 0.9 MeV), a value comparable to that of the positron emitted by ^{18}F ($E_{ß[beta]+max}$ = 0.64; $t_{1/2}$ ~ 1.8 h) [9, 10]. ^{89}Zr, however, has a much lower positron branching ratio than fluorine-18: 23% vs. 97%, respectively. A comparison of the nuclear properties of ^{89}Zr and ^{18}F is provided in Table 2 [11].

Production and Purification of ^{89}Zr

Early investigations exploring the production of ^{89}Zr were carried out by Link and colleagues [12, 13]. Both this pioneering work as well as more recently published endeavors have contributed to the simplification of the production and

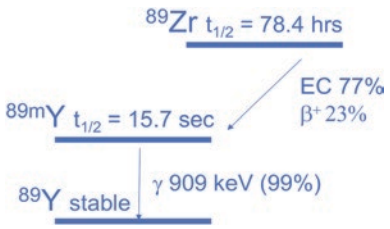

Fig. 1 Simplified decay scheme of Zr-89

Table 2 Physical characteristics of ^{89}Zr versus ^{18}F

Properties	^{18}F	^{89}Zr
Half-life	109.8 min	78.4 h
Mean β+ energy	0.25 MeV	0.4 MeV
Mean β+ range in water	0.62 mm	1.23 mm
Max β+ range in water	2.4 mm	3.8 mm
Single γ energy		909 keV (99.9%) 1657 keV (0.1%) 1713 keV (0.8%)
β+ branching ratio	97%	23%
Mean spatial resolution FWHM FWTM [a]FWHM-to-FWTM ratio	1.81 3.57 0.51	1.99 4.01 0.50

Note: Spatial resolution was analyzed according to National Electrical Manufacturers Association NU 4–2008 guidelines
[a]Suggestive of nonconformity from a Gaussian profile

purification of ^{89}Zr as well as standard operating procedures and semi-automated platforms to make this isotope accessible to researchers worldwide [14–17]. Zirconium-89 is currently produced using a medical cyclotron via the ^{89}Y(p,n)^{89}Zr reaction [16, 18]. The production of ^{89}Zr using solid targets provides the highest yields and will be the main focus in this chapter; however, liquid targets using yttrium solutions such as YCl_3 and $Y(NO_3)_3$ have been employed in cases wherein the cyclotron is incapable of solid targetry [19]. To produce the radiometal from a solid target, a Yttrium foil is secured onto an aluminum or niobium holder [16]. Yttrium-89 is 100% abundant and can be purchased commercially as a foil with varying thickness. In lieu of a foil, yttrium can also be deposited onto a niobium or copper support [18, 20]. To achieve optimal production of ^{89}Zr with the highest possible yields, a number of variables need to be considered, including the energy of the incident protons, the thickness of the target, and the irradiation time. Table 3 lists examples of different production methods developed to optimize yields of ^{89}Zr while minimizing the production of the long-lived ^{88}Zr contaminant.

Proton-induced reactions on yttrium targets at energies relevant to the production of ^{89}Zr can also result in the production of two Zr contaminants: ^{89m}Zr ($t_{1/2}$ = 4.2 min) and ^{88}Zr ($t_{1/2}$ = 83.4 days). Zirconium-89m is short-lived and completely decays to ^{89}Zr within an hour; thus, it is not considered a potential source of impurity [17, 18]. Zirconium-88 is long-lived and inseparable from ^{89}Zr; however, the quantity of ^{88}Zr produced is considered negligible (~ 0.0005%) at the energies (11–15 MeV) used to produce ^{89}Zr (see Table 3) [20]. Other long-lived radioactive contaminants that could be produced from impurities in the yttrium target and/or the target holder are ^{65}Zn, ^{48}V, ^{56}Co, and ^{156}Tb. However, none of these metals bind to the hydroxamate resin used for the purification of ^{89}Zr [20], and thus they can be separated easily from the desired product during the processing of the target.

The processing of the target is performed using a solid-phase extraction system. To this end, the target is dissolved in 2 M HCl, and the ^{89}Zr is separated from the bulk target material via solid-phase extraction using a hydroxamate-functionalized resin. Hydroxamate functions as a bidentate ligand with a high affinity for ^{89}Zr, while ^{89}Y can be washed from the resin with 2 M HCl [16]. At 2–3 M concentrations of HCl, iron can be a challenging contaminant, as it is chemically similar to zirconium. However, it has low affinity for hydroxamate-based resin systems and can be chemically separated from ^{89}Zr through multiple washings of the column.

The affinity of Zr^{4+} for the hydroxamate-functionalized resin was illustrated by the work of Guerard *et al.* [21]. As we have mentioned, [^{89}Zr]Zr^{4+} is a hard acid and has a predilection for binding "hard" Lewis bases such as nitrogen and—especially—oxygen. The solid-state x-ray diffraction analysis of the complex formed by Zr and *N*-methyl acetohydroxamic acid (Me-AHA) shows a 1:4 stoichiometric ratio (CN = 8) between Zr and hydroxamate groups and a log K of 17.3. We adapted this crystal structure into a 2D structure for simplicity (Fig. 2). Based on this work, we can infer that [^{89}Zr]Zr^{4+} binds the hydroxamate groups on the resin with similar affinity. Once it has bound the ^{89}Zr, the resin must be washed with ample volume of 2 M HCl followed by water to remove yttrium, which has a low affinity for hydroxamates. Zirconium-89 is then eluted via transchelation with 1 M oxalic acid ($H_2C_2O_4$), which binds in a 1:4 stoichiometric ratio (similar to the manner in which it coordinates acetohydroxamic acid) [22]. This separation process is depicted in Fig. 3 and is fully described in the seminal paper published by Holland *et al.* In this work, step-by-step procedures were established for preparing the hydroxamate-functionalized resin as well as for the separation of ^{89}Zr from ^{89}Y [16]. In addition, the purification process can be semi-automated to reduce radiation exposure to personnel, making it more feasible to safely isolate large quantities of ^{89}Zr [17, 23].

Table 3 Examples of the parameters used for the production of ^{89}Zr via the ^{89}Y(*p,n*)^{89}Zr reaction. Under these conditions, radionuclidic purity is generally almost quantitative, with very low levels of ^{88}Zr remaining as a radioactive contaminant. Non-radioactive metal contaminants such as iron could be present after the purification process which would affect the effective specific activity of ^{89}Zr

Incident energy, MeV	Description of target (target holder)	Irradiation current × time, μA•h	^{89}Zr produced, MBq (% Recovery)	Yield MBq/μA•h	Radionuclidic purity	Effective specific activity, mCi/μmol	References
13	0.64 mm foil (NR)	10 × 0.67 = 6.67	259 (25%)	38.8	NR	NR	[12]
14	Sputtered 25 μm (copper)	100 × 1 = 100	4810 (NR)	48.1	99.95%	NR	[15]
15	0.1 mm foil with a 10° angle of incidence (custom)	15 × 2.67 = 40	2439 (99.5%)	61.0	>99.99%	470–1195	[16]
14.7	0.64 mm foil (niobium)	15 × 4 = 60	2294 (93%)	38.2	99.998%	353	[17]
12.8	Sputtered 210 μm (niobium)	45 × 2 = 90	1621 (97%)	18	100%	108	[18]

NR not reported

Desferrioxamine: The Current Standard Chelator for ^{89}Zr

Desferrioxamine B (DFO) (Fig. 4) was isolated and characterized by Bickel *et al.* in 1960 from *Streptomyces pilosus* [24]. DFO, marketed as Desferal® for the treatment of iron intoxication, acts as an iron-scavenging siderophore and contains three hydroxamate moieties linked together in a linear scaffold. This hexadentate ligand offers three neutral and three anionic oxygen donors. DFO complexes Fe(III) with a formation constant of 1×10^{30} M^{-1}, forming an octahedral geometry. Other metals with a + 3 charge—*e.g.* Al(III), Ga(III), and Cr(III)—have been shown to bind to this ligand but with lower stability [25]. Importantly, because of its strong affinity and ability to encapsulate Zr(IV), DFO has been widely accepted as the "gold standard" chelator of this metal. However, decomplexation still remains an issue despite the moderate thermodynamic stability of the Zr-DFO complex. A detailed discussion can be found in the following sections.

The emergence of zirconium-89 as an ideal radionuclide for antibodies and large molecules prompted the need to create bifunctional variants of DFO to facilitate bioconjugation reactions to the amines and cysteines of these biomolecules. Several bifunctional derivatives of DFO are now available through commercial sources, and conjugation techniques are discussed below in the section on "Tricks of the Trade."

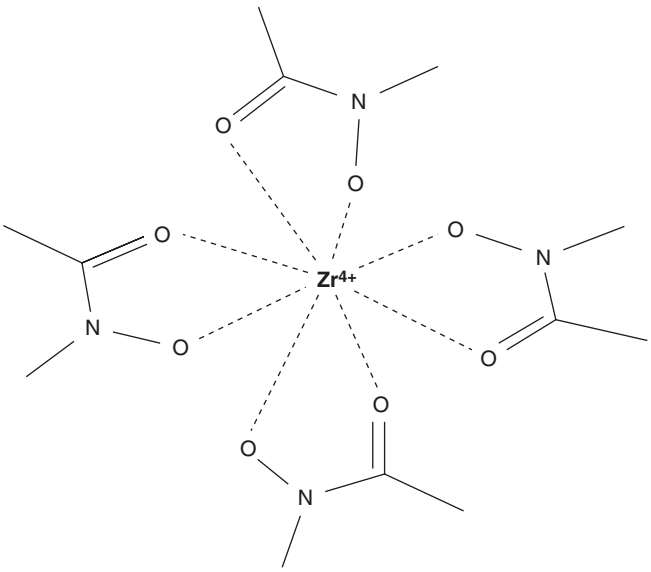

Fig. 2 Zr-Me-AHA forms octacoordinate species based on the crystal structure reported by Guerard *et al.*

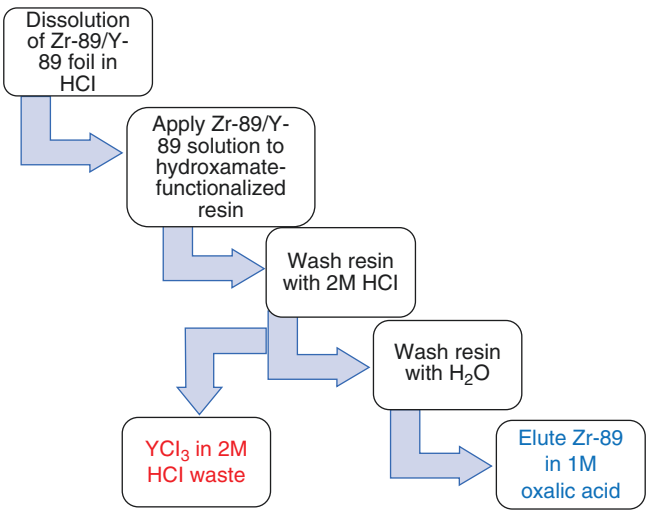

Fig. 3 Flow chart depicting the separation of Zr-89 from Y-89

Tricks of the Trade

Neutralizing the [^{89}Zr]Zr-Oxalate ^{89}Zr is typically supplied as [^{89}Zr]Zr-oxalate in a 1 M solution of oxalic acid. The pH of the [^{89}Zr]Zr-oxalate must be neutralized to pH 6.8–7.4 in order to achieve optimal labeling efficiencies with DFO-bearing conjugates [26]. Several different techniques are employed for neutralization. Choosing a method is often informed by the starting volume of the solution of [^{89}Zr]Zr-oxalate, as the neutralization process can significantly dilute this solution, leading to poor radiolabeling efficiencies. Vosjan *et al.* recommend that the total volume of [^{89}Zr]Zr-oxalate (37–185 MBq) to be neutralized should be 200 µL. If the desired activity for [^{89}Zr]Zr-oxalate is less than 200 µL, then 1 M oxalic acid should be added to obtain this volume. The [^{89}Zr]Zr-oxalate solution can then be neutralized by adding 90 µL of 2 M Na_2CO_3 and 300 µL of 0.5 M HEPES (pH 6.8–7.4) [27]. However, using the carbonate buffer to neutralize larger volumes (>200 µL) of the [^{89}Zr]Zr-oxalate can lead to the formation of insoluble precipitates. Not surprisingly, this phenomenon lowers the amount

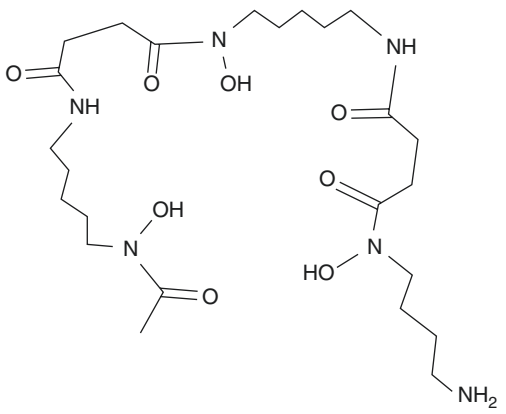

Fig. 4 Desferrioxamine B and its three hydroxamate groups

of ^{89}Zr available in solution for radiolabeling. Alternatively, diluting the starting volume of [^{89}Zr]Zr-oxalate with an equal volume of 1 M HEPES buffer (pH 7.1) prior to adjusting the pH with 2 M NaOH keeps the ^{89}Zr in solution [28].

Conjugation of DFO to Antibodies Meijs and colleagues were the first to develop an approach to the conjugation of DFO to mAbs. This strategy employed a two-step procedure in order to tag the lysine residues (ε-amines) within mAbs [29]. Lysines were first modified to carry maleimide groups (mAb-SMCC). Then a thioester-bearing variant of DFO (Df-SATA) was converted to a free thiol, facilitating the Michael addition between the bifunctional chelator and the modified antibody to form with the DFO-modified immunoconjugate: mAb-SMCC-SATA-Df (Fig. 5). Radiolabeling with ^{89}Zr was achieved by sublimating [^{89}Zr]Zr-oxalate and subsequently adding the Df-mAb immunoconjugate, producing a radiochemical yield of 90% and a specific activity of 185 kBq/μg (5 μCi/μg).

Years later, Verel and colleagues improved upon this SMCC-SATA conjugation chemistry by modifying DFO with an amine-reactive moiety to facilitate the formation of an amide linkage between the chelator and the ε-amine of a lysine residue. This bioconjugation was performed using a five-step procedure (Fig. 6) [20]: (i) the modification of DFO with succinic anhydride, (ii) the chelation of Fe(III) to protect the hydroxamate groups, (iii) the addition of 2,3,5,6-tetrafluorophenol (TFP) to form an amine-reactive TFP ester, (iv) the attachment of the amine-reactive bifunctional chelator to the lysines of the biomolecules, and (v) the removal of the Fe(III). Furthermore, the authors established optimal conditions for radiolabeling with ^{89}Zr *without* the need for the sublimation of the [^{89}Zr]Zr-oxalate.

In an effort to simplify this chemistry further, Perk and colleagues developed isothiocyanato-*p*-benzyl-desferrioxamine (*p*-NCS-Bn-DFO), a bifunctional variant of DFO that is currently commercially available [26]. *p*-NCS-Bn-DFO reacts with the lysines of biomolecules to form thiourea linkages that are similar in stability to the amide bonds formed by other bifunctional variants of DFO (Fig. 7) [26]. The reaction conditions for the conjugation of *p*-NCS-Bn-DFO to a biomolecule—most often an antibody—are mild. The two species are typically incubated in a basic buffer such as sodium carbonate (pH ~ 9) for 30 min at 37 °C, though different buffers

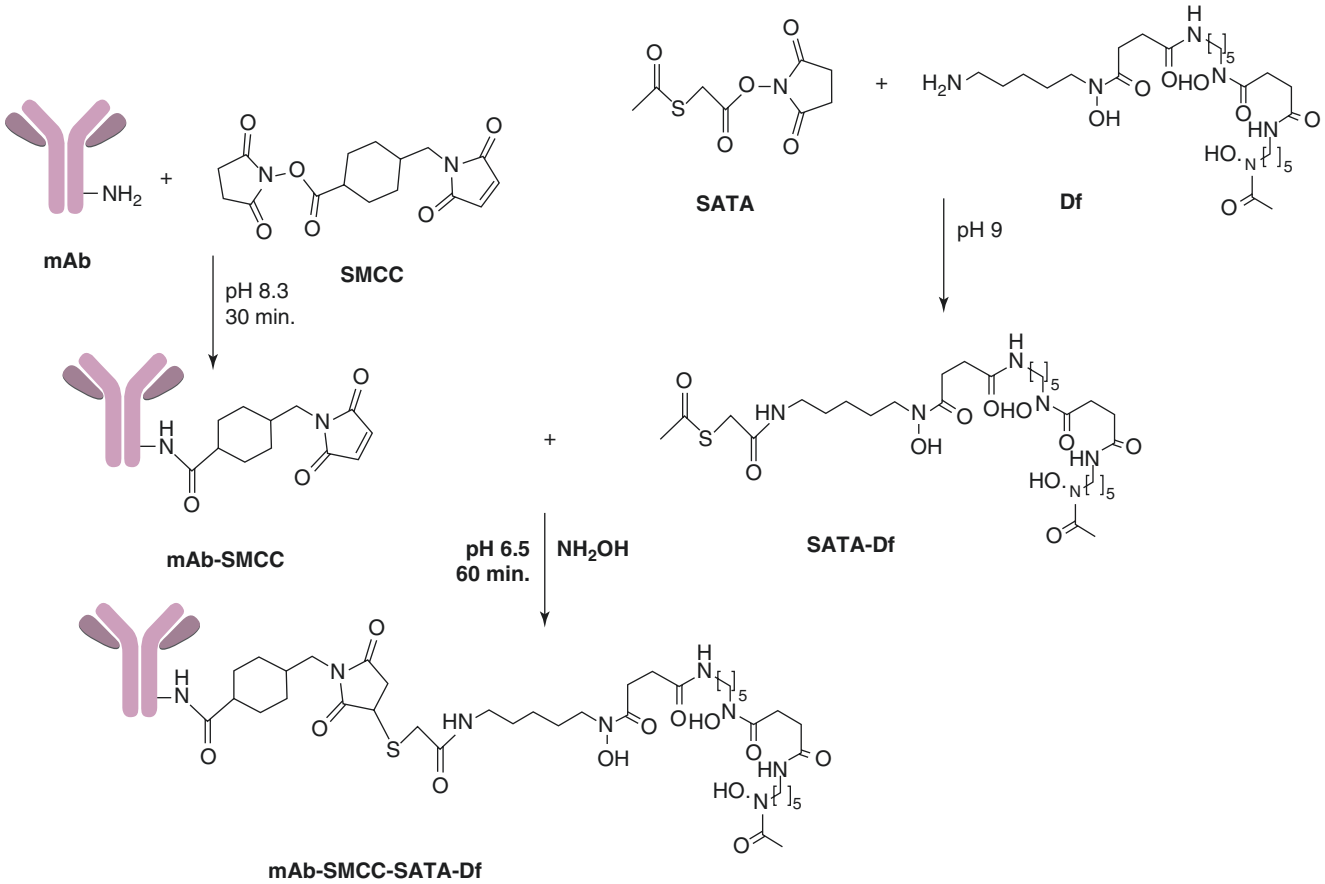

Fig. 5 DFO was derivatized with *N*-succinimidyl-S-acetylthioacetate (SATA), which reacts with maleimide-modified lysines on the mAb

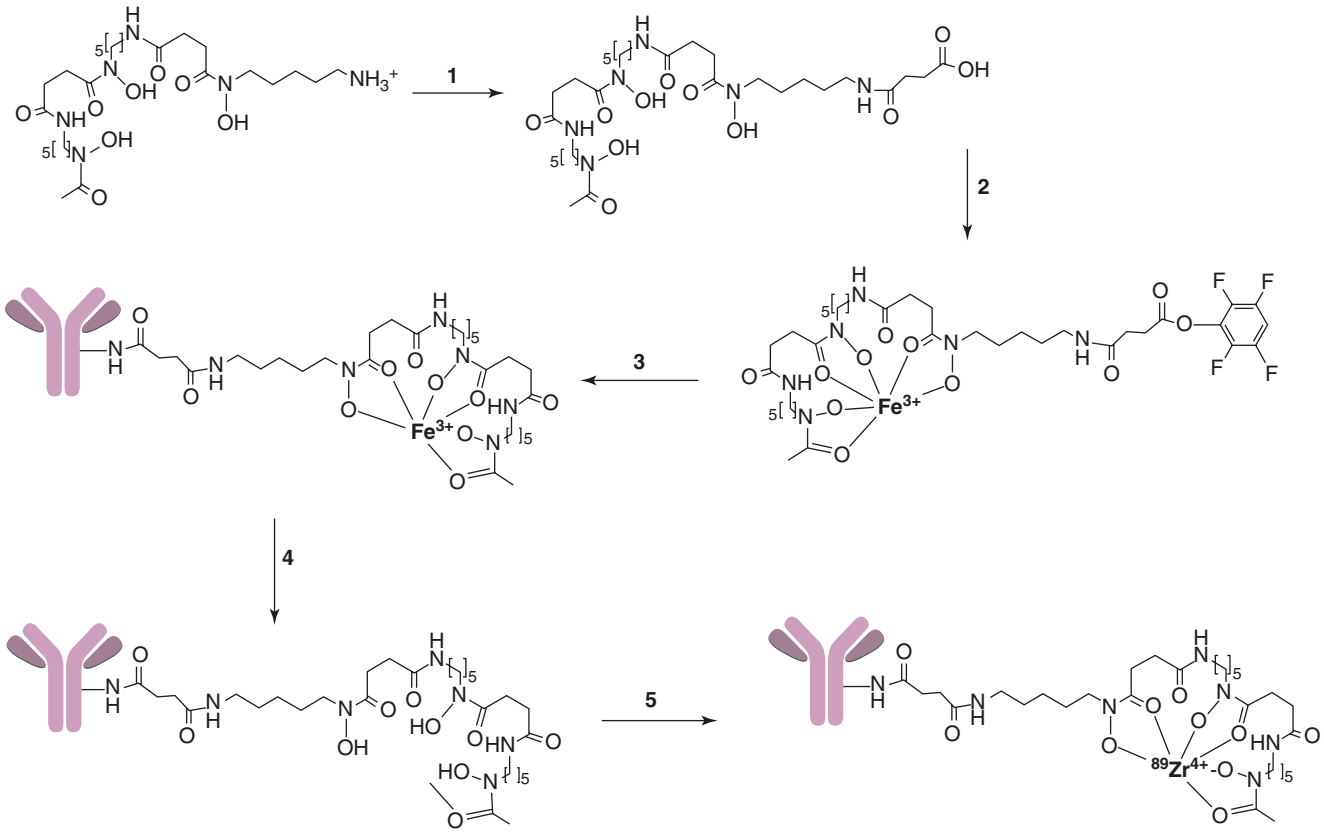

Fig. 6 The attachment of desferrioxamine to antibodies proceeds through a five-step procedure involving (*1*) the conjugation of succinic anhydride to DFO mesylate, (*2*) the coordination of Fe(III) to protect the hydroxamate groups, (*3*) the addition of 2,3,5,6-tetrafluorophenol (TFP), (4) the attachment of the bifunctional chelator to the free amines of the mAb, and (v) the removal of Fe(III) to prepare the chelator for the coordination of $[^{89}Zr]Zr^{4+}$

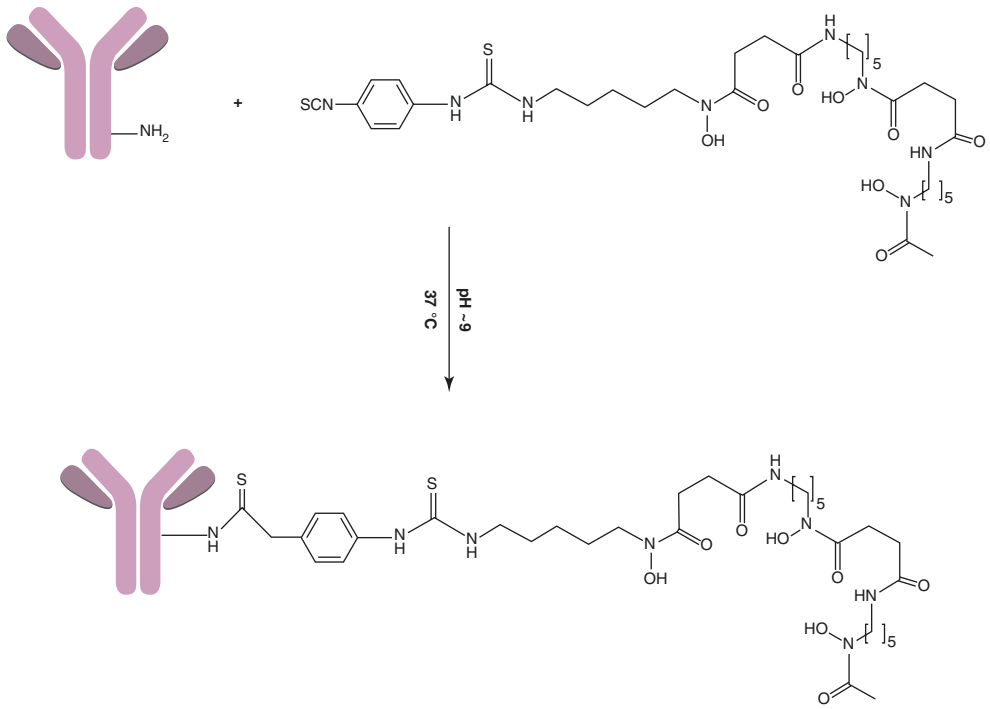

Fig. 7 The conjugation of DFO-Bz-SCN to an amine forms a thiourea linkage

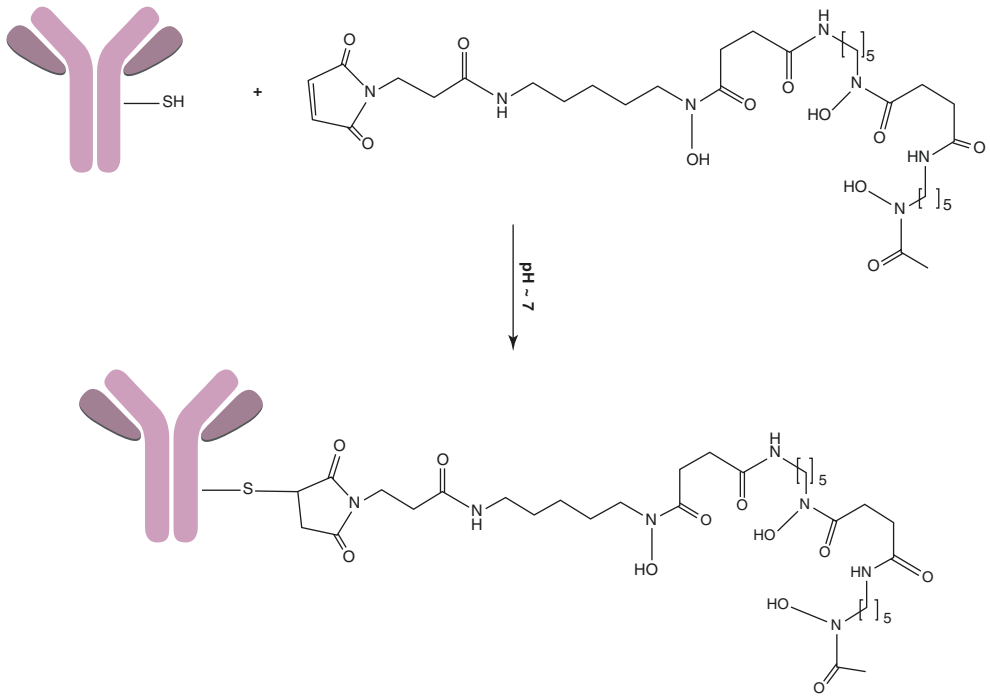

Fig. 8 DFO-maleimide undergoes a Michael addition with engineered cysteine residues to form thioether bonds

(*e.g.* phosphate buffered saline) and longer incubation times have also been used [26]. *p*-NCS-Bn-DFO is not soluble in the aqueous buffer used for conjugation, so it should be dissolved in dimethyl sulfoxide (DMSO) prior to its addition to the reaction mixture containing the biomolecule. We recommend preparing a relatively concentrated stock solution of *p*-NCS-Bn-DFO in DMSO (5–10 mg/mL) so as to limit the amount of DMSO in the conjugation reaction and thus lower the likelihood of the precipitation of the biomolecule. Generally speaking, the final concentration of DMSO in the reaction mixture should not exceed 10% v/v.

Other conjugation methods have been employed to facilitate the site-specific modification of biomolecules with DFO [30, 31]. For example, several studies have used a maleimide-bearing variant of DFO to facilitate Michael additions to engineered cysteine residues in antibodies (Fig. 8) [30, 32]. The buffers used for these ligations are similar to those used with *p*-NCS-Bn-DFO, though they generally have a lower pH (~6.5–7) due to the lower pKa of the sulfhydryl groups of cysteines (pKa = 8.3) compared the ε-amines of lysines (pKa = 10.5). Furthermore, a reducing agent such as tris(2-carboxyethyl)phosphine (TCEP) is necessary to reduce disulfide bridges and produce thiols available for conjugation. It is important to note that sulfhydryl-containing reductants such as dithiothreitol (DTT) and beta-mercaptoethanol (BME) should be avoided in these cases because of their ability to react with the DFO-bearing maleimide.

Radiolabeling with ^{89}Zr Over 20 years ago, Meijs and colleagues first demonstrated the superior stability of [^{88}Zr]Zr-DFO compared to [^{88}Zr]Zr-DTPA by attaching each chelator to a solid support [33]. At the time, ^{88}Zr ($t_{1/2}$ = 83.4 days) was used primarily as a surrogate for ^{89}Zr in proof-of-concept studies *in vitro*. The [^{88}Zr]Zr-DFO was formed in ~90% radiochemical yields after 2 h of incubation using citrate, acetate, or PBS buffers and pH values of 4, 5, 6, or 7. Stability studies in human serum clearly illustrated that DFO provided a more stable coordination environment than DTPA; only 80% of [^{88}Zr]Zr-DTPA remained intact after 24 h, while [^{88}Zr]Zr-DFO proved nearly 100% stable over the same time period [33].

The radiolabeling of DFO-bearing mAbs and biomolecules with neutralized [^{89}Zr]Zr-oxalate can be achieved within 30–60 min in a variety of buffers. Regardless of the buffer, it is critical to ensure that the pH of the reaction lies between pH 6.8–7.2 in order to achieve optimal transchelation of [^{89}Zr]Zr-oxalate to DFO and thus produce high radiochemical yields [20, 26]. The buffers typically used for radiolabeling with ^{89}Zr can be 0.9% saline, 0.25 M sodium acetate, 0.25–1 M HEPES, or 5 mM sodium citrate with 0.5 M HEPES. In our hands, the use of phosphate-buffered saline lowered the yields of ^{89}Zr-labeled mAbs, presumably due to the presence of phosphate anions that can compete with DFO for the coordination of the metal. After the radiolabeling reaction, DTPA (pH 7; final concentration = 1 mM) may be added to the crude solution of [^{89}Zr]Zr-DFO-mAb and incubated for 5 min at room temperature in order to sequester any free [^{89}Zr]Zr^{4+} prior to purification. In addition, if subsequent *in vitro* assays suggest that the reactivity of the [^{89}Zr]Zr-labeled biomolecule has been compromised during radiosynthesis, gentisic acid (5 mg/mL) may be added to the radiolabeling solution to protect the biomolecule from radiolysis [26, 34].

Purification of a DFO-Modified mAb and a [^{89}Zr]Zr-DFO-Labeled Radioimmunoconjugate Size exclusion chromatography can be used to remove any unreacted bifunctional chelator or free [^{89}Zr]Zr^{4+} from DFO-modified immunoconjugates and their ^{89}Zr-labeled analogs, respectively. To this end, desalting gravity flow columns (*e.g.* PD-10) or spin columns (*e.g.* Zeba, Amicon, GE Vivaspin) with molecular weight cutoffs of 10–50 kDa may be used. It is important to note that adding a relatively high concentration of the conjugate (≥0.5 mg/mL) to the column aids in the recovery of high yields of the conjugate after purification. In some cases, the radiolabeled antibody can bind too strongly to the PD10 column, making it "sticky" and difficult to elute. If this occurs, washing the column with 1% bovine serum albumin (BSA) or human serum albumin is suggested to prevent the binding of residual tracer to the resin and thus maximize the recovery of the purified ^{89}Zr-labeled biomolecule.

Non-immunoglobulin Vectors

Relatively Small Molecules Novel vectors based on small molecules may be radiolabeled with ^{89}Zr to assess their biodistribution over several days. For example, Kuda-Wedagedara *et al.* conjugated DFO to cobalamin (vitamin B12) and subsequently labeled this vector with ^{89}Zr using radiolabeling procedures similar to those employed for the labeling of antibodies [27, 35] The resulting [^{89}Zr]Zr-DFO-cobalamin was used to image the nutrient demand of breast cancer xenografts via its interaction with the transcobalamin-CD320 receptor. An important finding in this study was that neither increasing the overall molecular weight of the cobalamin vector (MW = 1190 g/mol) by the addition of the DFO chelator (+752 g/mol) nor changing the overall charge of the molecule to +1 due to the contribution by Zr^{4+} affected the binding of the ^{89}Zr-labeled cobalamin to the transcobalamin receptor.

Other relatively small molecules labeled with ^{89}Zr via DFO-Bz-NCS include peptides such as exendin-4 for the imaging of insulinomas [36]. An aminohexanoic acid spacer was used to link exendin-4 to DFO, producing a final construct with a total molecular weight of ~5 kDa. This strategy was employed to prevent the chelator from interfering with exendin-4's binding to its receptor, GLP-1. Interestingly, however, the ^{89}Zr-labeled exendin-4 had a twofold lower affinity (K_d = 28 nM) than the ^{68}Ga-labeled analog of this peptide (K_d = 11 nM). This difference could be due to the overall charge of the radiolabeled peptide: −1 for the ^{89}Zr-labeled version and neutral for the ^{68}Ga-labeled variant. Thus, considerations for radiolabeling smaller molecules with [^{89}Zr]Zr^{4+} must include how the potential changes to the overall charge of the molecule and the steric hindrance created by the chelator may affect the affinity of the radiotracer to its target.

Cell Labeling A variety of different cell types—including bone marrow cells and immune cells—have been labeled with zirconium-89 to take advantage of the residualizing properties of the radiometal. The delivery of zirconium-89 into the cell can be accomplished by complexing zirconium-89 with oxine ligands in a 1:4 stoichiometric ratio [37]. Ferris *et al.* developed an approach to the ^{89}Zr-labeling of oxines using a biphasic system in which zirconium-89 is in a neutralized aqueous solution and the ligands are in chloroform [37]. The radiolabeling occurs in the interphase of the aqueous and organic layer. The chloroform was then dried to isolate [^{89}Zr]Zr-oxine, which can be resuspended in dimethyl sulfoxide and diluted in PBS for biological studies. The cell permeability of [^{89}Zr]Zr-oxine allows for its rapid, *ex vivo* cellular internalization and subsequent retention [38]. ^{89}Zr-labeled cells can then be administered *in vivo* for PET imaging. An interesting study outlining this concept was conducted by Asiedu *et al.* to image the trafficking of bone marrow cells in an animal model of hematopoietic stem cell transplantation (HSCT) [39]. The radiolabeling efficiency was determined to be 26–30%, producing cells with a specific activity of 16.6 kBq/10^6 cells. Critically, this study revealed that labeling the bone marrow cells did not alter their cellular phenotype, cellular function, or survival. Interestingly, the authors report that the ^{89}Zr-labeled cells quickly accumulated in the lungs, bone marrow, spleen, and liver immediately after bone marrow transfer.

The radiolabeling of the surface of cells is an alternative to intracellular labeling with [^{89}Zr]Zr-oxine. Bansal *et al.* used DFO-Bz-NCS to covalently tag random lysine groups on the surface of stem cells to facilitate labeling with ^{89}Zr [40]. In this study, the cell labeling efficiency was 30–50%, producing cells with specific activities of up to 0.5 MBq/10^6 cells. Efflux studies showed that the zirconium-89 remains associated with the cells after 7 days of incubation in 10% fetal bovine serum in cell medium. Furthermore, the authors conducted a subcellular fractionation study to confirm that the ^{89}Zr remained associated with the membrane. The ^{89}Zr-labeled stem cells in this study accumulated in the lungs (50 ± 27 %ID/g), liver (27 ± 19 %ID/g), and bone (16 ± 5 %ID/g). The authors also comment that the exploration of more stable chelators warrants further investigation.

Label-Free Vectors The term "label-free" refers to the radiolabeling of vectors without the need for conjugating chelators such as DFO. For ^{89}Zr, iron-complexing molecules or nanoparticles containing hard oxygen donors may be used to

directly coordinate this radionuclide within the vector. For example, melanin is a familiar molecule, known for contributing to the pigment of human skin, eyes, and hair. Interestingly, it also contributes to various biological functions, including chelating metal ions such as iron. For this reason, melanin was developed as a water-soluble nanoparticle (7 nm) as an alternative to DFO for the treatment of iron overload [41]. Zhang *et al.* reasoned that the large molecular weight of melanin nanoparticles (MP) could combine with their intrinsic ability to coordinate iron to produce a slowly eliminated platform for the *in vivo* scavenging of excess iron. These nanoparticles would stand in stark contrast to DFO, which must be administered frequently during treatment due to its rapid clearance ($t_{1/2}$ = 5 min in mice). Thus, the goal of these researchers was to determine the pharmacokinetic properties of melanin nanoparticles via radiolabeling them with zirconium-89 for PET imaging [41]. In this study, the MP were labeled with zirconium-89 at pH 5 at 37 °C for 30 min, yielding [^{89}Zr]Zr-MP with a radiochemical yield of 90%, a specific activity of 190 MBq/μmol, and a radiochemical purity of >98%. *In vitro* stability studies in human plasma and PBS determined that the [^{89}Zr]Zr-MP were stable up to 48 h. Subsequent *in vivo* pharmacokinetic studies using a two-compartment open model determined that the elimination half-life of [^{89}Zr]Zr-MP in mice was ~16 h. Notably, [^{89}Zr]Zr-MP had significant accretion in the liver and spleen at 48 h post-injection, promising result given that in patients, excess iron is predominantly deposited in the liver, spleen, and bone marrow.

Another example of a "label-free" vector is Feraheme® (FH), an ultrasmall superparamagnetic iron oxide (USPIO) nanoparticle that is FDA-approved for the treatment of anemia. FH (MW ~ 796 kDa; 17–31 nm) can be labeled directly with various radiometals—including ^{89}Zr—under high temperature with thermodynamic and kinetic stability [42]. The radiolabeling of FH with zirconium-89 was performed in aqueous solution at pH 8.0 via heating at 120 °C for less than 1 h, ultimately producing the radiolabeled particles in 93 ± 3% radiolabeling yield with radiochemical purity of >98%. Boros *et al.* observed that loadings of Zr greater than a Zr:FH molar ratio of 125:1 resulted in the aggregation of the particles. However, keeping this ratio below this threshold allowed the particles to retain their physical, chemical, and magnetic properties. This radiotracer was investigated in animal models of inflammation in the muscle, producing results which suggest that [^{89}Zr]Zr-FH is a promising radiotracer for the detection of inflammation and other diseases in which activated macrophages play a crucial role. However, more investigation is needed to elucidate the mechanism of the binding of zirconium-89 to FH. Other nanoparticles that have been used as platforms for label-free ^{89}Zr-radiopharmaceuticals include paramagnetic octreotide-liposomes [43], nanodots [44], and mesoporous silica nanoparticles [45].

New Chelators for ^{89}Zr

The Zr-DFO complex is stable against decomplexation when monitored for 7 days in PBS and serum at 37 °C [46]. However, the *in vivo* decomplexation of the radiometal from DFO-bearing biomolecules has been observed in several cases. When free in the body, [^{89}Zr]Zr^{4+} is a bone-seeking radiometal, a trait which undermines its ability to resolve true-positive osseous lesions [2, 3]. The deposition of Zr-89 in bone tissue further restricts the dose of the imaging probe that can be administered due to the potential radiation dose to the radiosensitive bone marrow [3]. For this reason, several laboratories have developed new chelators for ^{89}Zr with the goal of improving the *in vivo* kinetic and thermodynamic stability of the ^{89}Zr-chelator complex. In theory, the ideal chelator for ^{89}Zr should be octadentate, provide hard Lewis acid donor atoms, and be able to "wrap" or encapsulate around the cation's 85 pm radius [1, 47].

Several novel chelators for [^{89}Zr] are reviewed in the following section. They are divided into three categories according to their donor groups and structure: (i) linear hydroxamates, (ii) macrocyclic hydroxamates, and (iii) non-hydroxamate ligands. The intrinsic properties of the chelators—such as their hydrophilicity, their affinity for [^{89}Zr]Zr^{4+}, and their susceptibility to the transchelation of [^{89}Zr]Zr^{4+} in the presence of EDTA, DTPA, and serum—are discussed (Table 4). In addition, their performance when conjugated to a protein or peptide (when available from the literature) is addressed as well (Table 5).

Linear Hydroxamates

Desferrioxamine★ (DFO★) DFO★ was developed in response to DFO's inability to provide an octadentate coordination environment for Zr^{4+} [48]. In DFO★, an additional hydroxamic acid is appended onto the amine terminus of DFO. This creates a ligand with four hydroxamic acid moieties that can satisfy Zr(IV)'s preference for a coordination number of 8 (Fig. 9). Issues of solubility were reported for DFO★, but they were largely resolved by using organic cosolvents. The complexation of [^{89}Zr]Zr^{4+} by DFO★ is driven by incubation at elevated temperatures, resulting in a compound with a 1:1 ratio of Zr:DFO★. Isomerization was observed, though this is typical of linear chelators which are not as rigid as macrocycles. After conjugating DFO★ to the GRPR-targeting peptide bombesin and radiolabeling the resulting construct with ^{89}Zr, the authors challenged the stability of [^{89}Zr]Zr-DFO★-bombesin against 300- and 3000-fold excesses of DFO mesylate. Remarkably, the [^{89}Zr]Zr-DFO★ complex remained stable against transchelation after 24 h.

In this proof-of-concept work, the bifunctional chelator DFO★-p-phenyl-isothiocyanate (DFO★-p-Phe-NCS) was

Table 4 Properties of coordination compounds of zirconium-89 with DFO and several "second-generation" chelators

Chelator	Specific activity	Radiolabeling efficiency	Overall charge	Log P/Log D		Excretion route	Bone uptake (%ID/g)			References
				New chelator	DFO		New chelator	DFO	Time point	
DFO★	N.R.	>95%, 5 min, RT	0	NR	NR	NR	NR	NR	NR	[36]
DFO-HOPO	20 MBq/nmol	99% 1 h, RT	0	−0.9 ± 0.3	3 ± 0.01	Kidney, liver	0.004 ± 0.001	0.04 ± 0.002	1 day	[37]
L1	2 mCi/mg	99%, 1 h, RT	0	N.A.		Kidney, liver	0.2 ± 0.03	0.06 ± 0.01	1 day	[39, 40]
L2	0.9 GBq/μmol	RT, 1 h	0	−2 ± 0.03	3 ± 0.04	Kidney, liver	0.27 ± 0.066	0.082 ± 0.16	1 day	[41]
							0.28 ± 0.083	0.078 ± 0.014	3 days	
L3	NR	NR	0	NR	NR	NR	NR	NR	NR	[42]
L4	NR	NR	0	NR	NR	NR		NR	NR	
L5	25 MBq/nmol	>99%, pH~6.5, RT	+1	N.A.	N.A.	Kidney	N.A.	N.A.		[43]
L6	25 GBq/μmol	>90%, pH~6.8–7.2, 90 min, RT	+1	−2.0	NR	Kidney	0.04 ± 0.02	NR	6 h	[45]
L7	NR	>99%, pH~7.4–7.6, 1 h, RT	+1	−3.4	−3.1		0.60 ± 0.19	0.05 ± 0.02	1 day	[47]
L8	NR	65 ± 9.6%, 99 °C, 2 h, pH~7–7.5	0	NR		Kidney	0.03 ± 0.009	0.079 ± 0.014	3 days	[48]
L9	NR	70 ± 10.6%, 99 °C, 2 h, pH~7–7.5	−4	NR		Kidney	2.6 ± 0.012		3 days	
L10	NR	9 ±1%, 99 °C, 2 h, pH~7–7.5	+4	NR		Kidney	N.A.		3 days	
L11	0.7 GBq/μmol	95 °C, 2 h, pH~7–7.5	0	−3 ± 0.02	−3 ± 0.04	Kidney	0.1 ± 0.006		3 days	[49]
L12	0.7 GBq/μmol	50 °C, 1 h, pH~7–7.5	0	−1 ± 0.06		Kidney, liver	0.68 ± 0.33		3 days	

NR not reported
RT room or ambient temperature

Table 5 Activity concentration per gram (%ID/g) in the bone of ^{89}Zr-labeled radiopharmaceuticals containing different bifunctional chelators

Chelator	Bone uptake			References
	New chelator	DFO	Timepoint	
DFO★	1 ± 0.08 0.8 ± 0.1	2.2 ± 0.34 3.9 ± 0.80	1 days 6 days	[36]
DFO-HOPO	NR	NR	NR	[37]
L1	2 ± 0.3	17 ± 4.1	14 days	[39, 40]
L2	15 ± 2.7	11 ± 1.0	6 days	[41]
L3	20 ± 4	8 ± 0.4	3 days	[42]
L4	18 ± 2.9			
L5	29 ± 3	5 ± 0.2	3 days	[43]
	26 ± 0.6	7 ± 0.4	7 days	
L6*	0.7 ± 0.05	NR	1 h	[45]
	0.8 ± 0.3	NR	2 h	
	0.7 ± 0.3	NR	4 h	
L7	19 ± 2.1	2.8 ± 2.2	4 days	[47]
L8	NR	NR		[48]
L9	NR	NR		
L10	NR	NR		
L11	NR	NR		[49]
L12	NR	NR		

Note: All chelators were attached to trastuzumab unless specified
*Conjugated to RGD peptides
NR not reported

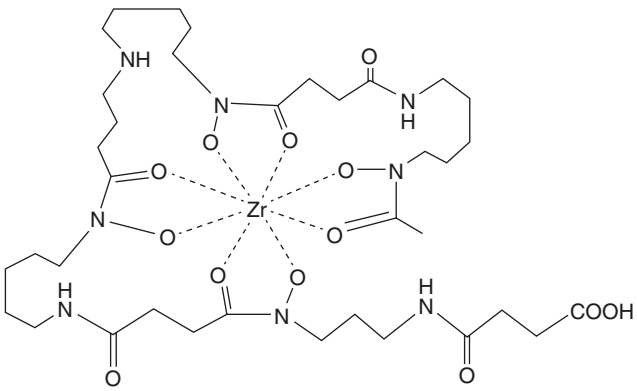

Fig. 9 Structure of Zr-DFO★ complex

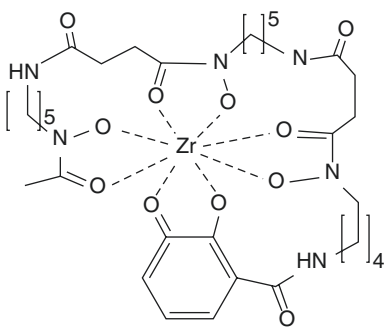

Fig. 10 DFO-HOPO coordinates Zr^{4+} with eight donors

prepared and attached to three different antibodies: trastuzumab (anti-HER2), cetuximab (anti-EGFR), and rituximab (anti-CD20) [47]. The insolubility of DFO★-p-Phe-NCS in aqueous solution necessitated its dissolution in dimethyl sulfoxide (DMSO), which in turn led to modifications to the conjugation protocol aimed at reducing protein aggregation due to the presence of the organic solvent. In addition, rather than adding the DFO★ to the solution of antibody, the antibody was added to the DMSO solution of DFO★. Perhaps as a result, lowered chelator:mAb ratios were achieved for DFO★ compared to analogous conjugation reactions with DFO: 0.6 ± 0.1 vs. 0.9 ± 0.1 for trastuzumab and 0.8 ± 0.1 vs. 1.3 ± 0.1 for rituximab).

Importantly, however, the radiochemical yields obtained with each were comparable (>80%). The stability of [^{89}Zr]Zr-DFO★-trastuzumab was interrogated by monitoring the radiochemical purity and immunoreactivity of the radioimmunoconjugate after storage in 20 mM histidine/240 mM sucrose (93% and 90%, respectively, after 168 h at 4 °C), 0.9% NaCl (89% and 82%, respectively, after 168 h at 4 °C), and serum (96% and 88%, respectively, after 168 h at 37 °C). In all conditions, [^{89}Zr]Zr-DFO★-trastuzumab outperformed [^{89}Zr]Zr-DFO-trastuzumab. The blood-pool residence times and tumoral activity concentrations in mice-bearing N87 xenografts were found to be similar between the two radioimmunoconjugates. Critically, however, decreased bone uptake was observed with the DFO★-bearing radioimmunoconjugate. One interesting observation discussed by Vugts et al. is the attenuated ability of ^{89}Zr-labeled *p*-NCS-Bn-DFO to covalently bind to antibodies. The authors postulate that this may result from the metal center's recruitment of the isothiocyanate to fill its coordination sphere, leaving the isothiocyanate unavailable to react with free amines on the antibody.

DFO-HOPO The addition of a 1,2-hydroxypyridinone (HOPO) moiety to DFO was reported in 1988 by White *et al.* as a ligand for the octadentate complexation of Pu(IV) [49]. The rationale behind the choice of HOPO stemmed from its relatively high acidity, monoprotic nature, and aqueous solubility compared to catechols and hydroxamates, properties that should facilitate facile radiometallation [49]. Because it offers eight possible donor atoms, DFO-HOPO is an appealing ligand for Zr-89. Allott *et al.* reported the investigation of alternative synthetic routes for this chelator and explored the radiochemistry and stability of its complex with zirconium-89 (Fig. 10) [50]. The authors employed radiolabeling conditions similar to those used with DFO, forming [^{89}Zr]Zr-DFO-HOPO in ~99% radiolabeling efficiency and a specific activity of ~ 20 MBq/nmol after incubation at room temperature and neutral pH (~7.4). However, two species—with Rf values of 0.1 and 0.6—were observed upon analysis

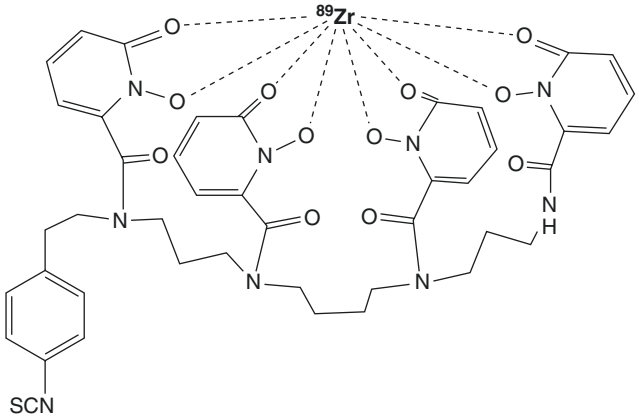

Fig. 11 3,4,3-(L1–1,2-HOPO) (**L1**)—composed of four HOPO moieties linked to a spermine backbone—is an octadentate ligand for Zr

of the radiolabeling reaction mixture via instant thin-layer chromatography (iTLC). The species at Rf ≈ 0.1 was identified as the positively charged kinetic product of the complexation reaction, while the species at Rf ≈ 0.6 was determined to be the neutral, more thermodynamically stable product of the reaction. The conversion of this kinetic product to its more thermodynamically stable cousin seemed to be related to both time and specific activity. More specifically, while heating the reaction to 80 °C does not prevent the formation of the kinetic product, lowering the specific activity of the complex and increasing the incubation time (~24 h at ambient temperature) yielded the neutral species exclusively.

The stability of the [^{89}Zr]Zr-DFO-HOPO complex was assessed via incubation in solutions of EDTA, DFO, and mouse serum at 37 °C. Over 7 days, no demetallation of [^{89}Zr]Zr-DFO-HOPO was observed under all three conditions, while [^{89}Zr]Zr-DFO was observed to decompose in the presence of both EDTA and mouse serum. DFO-HOPO was also able to effectively transchelate [^{89}Zr]Zr^{4+} from [^{89}Zr]Zr-DFO, removing over 60% of the radiometal in only an hour of incubation. *In vivo* biodistribution studies revealed that [^{89}Zr]Zr-DFO-HOPO undergoes both rapid renal clearance and slow biliary and intestinal elimination. The authors believe that the inclusion of a hepatobiliary clearance pathway can be attributed to the increased hydrophobicity of [^{89}Zr]Zr-DFO-HOPO (log $D_{pH\ 7.4}$ ~ −0.9 ± 0.3) compared to [^{89}Zr]Zr-DFO (log $D_{pH\ 7.4}$ ~ −3.0 ± 0.01).

3,4,3-(L1-1,2-HOPO) (L1) Deri *et al.* investigated the zirconium-chelating properties of L1, a ligand composed of four HOPO groups attached to a spermine backbone (Fig. 11) [51]. The complexation of [^{89}Zr]Zr^{4+} with **L1** is achieved under relatively standard conditions: pH ~ 7 and room temperature within 10 min. As with DFO-HOPO, the authors observed distinct kinetic and thermodynamic products whose formation seemed dependent on the concentration of the ligand. The authors proposed that this phenomenon could be due to either the formation of polynuclear dimers or isomers. Interestingly, the kinetic product was not observed when using macroscale amounts during the synthesis of cold ^{nat}Zr-L1. X-ray diffraction of the solid-state structure of ^{nat}Zr-L1 established that the metal was surrounded by an octacoordinate coordination environment composed of the eight oxygen donor atoms of the HOPO [52]. The stability of [^{89}Zr]Zr-L1 was tested against a 100-fold excess EDTA, and the radiolabeled ligand remained >99% over 7 days; [^{89}Zr]Zr-DFO, in contrast, remained only 90 ± 5% intact at 7 days. This EDTA challenge experiment was also performed at pH values of 5–8, and in each case, the stability of [^{89}Zr]Zr-L1 proved superior to that of [^{89}Zr]Zr-DFO. *In vivo* biodistribution assays revealed that [^{89}Zr]Zr-DFO and [^{89}Zr]Zr-L1 boast almost identical pharmacokinetic profiles, though [^{89}Zr]Zr-L1 produced higher activity concentrations in the hepatobiliary tissues (*e.g.* liver, gallbladder and intestines), a newly observed route of clearance. The uptake of the radiometal in the bone at 24 h post-injection was also slightly elevated for [^{89}Zr]Zr-L1 (0.2 ± 0.03 %ID/g) compared to [^{89}Zr]Zr-DFO (0.06 ± 0.01 %ID/g), an observation the authors believe to be due to longer blood residency of [^{89}Zr]Zr-L1.

The functionalization of L1 with *p*-benzyl-isothiocyanate created the bifunctional chelator—*p*-SCN-Bz-HOPO—that could be easily attached to antibodies and other proteins [52]. As a proof-of-concept, the authors conjugated *p*-SCN-Bz-HOPO to trastuzumab and subsequently radiolabeled the immunoconjugate with ^{89}Zr. The radiochemistry was performed according to standard protocols, and comparable specific activities (74 MBq/mg) and immunoreactivities were achieved for both [^{89}Zr]Zr-L1-trastuzumab (92 ± 6.8%) and [^{89}Zr]Zr-DFO-trastuzumab (89 ± 2.1%). However, *in vitro* serum stability studies revealed that the stability of [^{89}Zr]Zr-L1-trastuzumab was slightly lower than that of [^{89}Zr]Zr-DFO-trastuzumab (89% vs. 95% respectively). Next, *in vivo* and pharmacokinetic studies in HER2-positive BT-474 xenografts were conducted to compare the *in vivo* behavior of both constructs. Tissue distribution data showed that the HOPO-containing radiotracer produced lower tumor uptake values than the DFO-bearing construct (61.9 ± 26.4 %ID/g vs. 138 ± 35.3 %ID/g at 336 h p.i.). The authors offered no discussion for this variability, though it is worth pointing out that L1 appears to be more hydrophobic than DFO due to the presence of the aromatic HOPO. This hydrophobicity may affect the pharmacokinetics, tumor penetration, and vascular extravasation of the radioimmunoconjugate depending on the number of L1 chelators conjugated to the antibody. However, the activity concentrations in the bone were significantly lower for [^{89}Zr]Zr-L1-trastuzumab (2 ± 0.3 %ID/g at 336 h p.i.; tumor:bone ratio ~ 26)

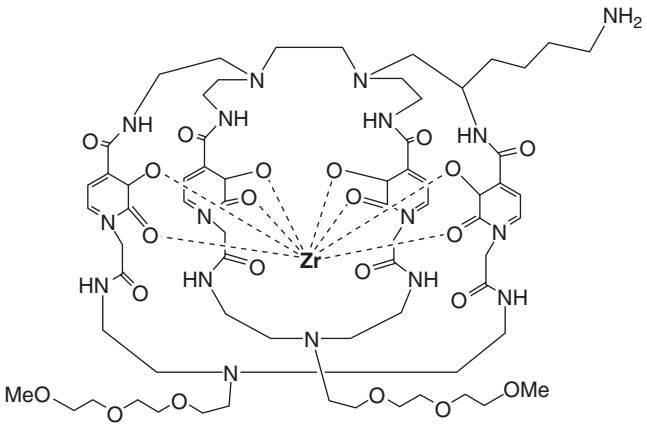

Fig. 12 BPDET-LysH22,2–3-HOPO (**L2**) is a bi-macrocyclic ligand that incorporates 3,2-HOPO groups and displays a "clam shell" appearance. When bound to Zr, an eight-coordinate complex is formed

compared to the [^{89}Zr]Zr-DFO-trastuzumab (17 ± 4.1 %ID/g at 336 h p.i.; tumor:bone ratio ~ 8) h p.i. Taken together, these data—most notably the lowered activity concentrations in the bone—suggest that L1 may be worth exploring as a potential alternative to DFO.

BPDET-LysH22,2-3-HOPO (L2) L2 is an octadentate, bi-macrocyclic bifunctional ligand that incorporates two 3,2-HOPO moieties that form a "clam shell"-like structure (Fig. 12) [53]. Its design was predicated on combining the rigidity of a macrocyclic chelator with the ^{89}Zr-binding properties of HOPO moieties. The incubation of the radiometal and the ligand for 15 min at ambient temperature successfully produced [^{89}Zr]Zr-L2 with a specific activity of ~ 0.9 GBq/μmol and a Log P value of ~ 1.5 ± 0.03, making [^{89}Zr]Zr-L2 more hydrophilic than [^{89}Zr]Zr-DFO (Log P ~ −2.8 ± 0.04). Stability challenge experiments were conducted using both diethylenetriaminepentaacetic acid (DTPA, 50 mM) and human serum for 7 days at 37 °C. [^{89}Zr]Zr-L2 was stable after 1 day of incubation in the presence of DTPA, but only 78% of the complex remained intact after 7 days. The demetallation of [^{89}Zr]Zr-L2 was also studied in serum: 94% of the complex remained intact after 1 day, a value that decreased to 86% after 7 days. Biodistribution studies in healthy mice revealed that the blood clearance of [^{89}Zr]Zr-L2 was relatively slower than the DFO complex. Furthermore, the retention of [^{89}Zr]Zr-L2 in the kidneys was substantially elevated compared to [^{89}Zr]Zr-DFO: 30 ± 7 %ID/g and 15 ± 2 %ID/g for the former and 1.0 ± 0.1 %ID/g and 0.7 ± 0.1 %ID/g for the latter at 1 and 7 days post-injection, respectively. The activity concentrations in the bone were also higher for [^{89}Zr]Zr-L2 compared to [^{89}Zr]Zr-DFO, with the former producing 0.3 ± 0.1 %ID/g in the bone after 1 day p.i., a value which was sustained after 7 days (0.3 ± 0.1 %ID/g) (see Table 3).

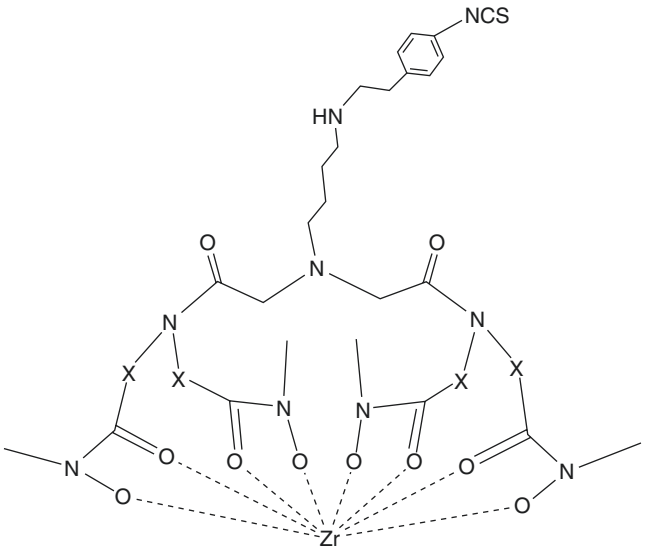

Fig. 13 Tetrahydroxamate chelators **L3** (X = CH_2) and **L4** (X = CH_2CH_2)

The authors proceeded to characterize the *in vitro* and *in vivo* stability of L2 as part of a trastuzumab-based radioimmunoconjugate. [^{89}Zr]Zr-L2-trastuzumab displayed a 50% decrease in the amount of intact radioimmunoconjugate after 24 h in mouse serum. Biodistribution studies revealed that [^{89}Zr]Zr-L2-trastuzumab had a shorter blood residence time than [^{89}Zr]Zr-DFO-trastuzumab, as well as elevated levels of liver uptake (13 ± 4.4 %ID/g and 6.5 ± 2.2 %ID/g, respectively, at 6 days p.i.). Furthermore, the PET images produced by [^{89}Zr]Zr-L2-trastuzumab revealed that the radioimmunoconjugate produces higher activity concentrations in the bone (15 ± 2.7 %ID/g at 6 d pi.) compared to [^{89}Zr]Zr-DFO-trastuzumab (11 ± 1.0% ID/g, p = 0.0003). Clearly, the substandard *in vivo* performance of L2 makes it a less-than-desirable chelator of ^{89}Zr.

Tetrahydroxamate Chelators (L3 and L4) A pair of tetrahydroxamate-based chelators with different linkers (**L3** = −CH2; **L4** = −CH2CH2−) were prepared by Rousseau et al. for the purpose of providing ^{89}Zr with a symmetrical and compact coordination environment (Fig. 13) [54]. The two chelators were functionalized with a *p*-SCN-Bn group and conjugated to trastuzumab, and the *in vitro* and *in vivo* stability of the resulting ^{89}Zr-labeled radioimmunoconjugates were investigated. Radiolabeling yields of >90% were obtained for [^{89}Zr]Zr-L3-trastuzumab, [^{89}Zr]Zr-L4-trastuzumab, and [^{89}Zr]Zr-DFO-trastuzumab. Regrettably, stability assays in mouse plasma revealed that neither [^{89}Zr]Zr-L3-trastuzumab nor [^{89}Zr]Zr-L4-trastuzumab was particularly stable, with 75% and 54% of ^{89}Zr released from L3

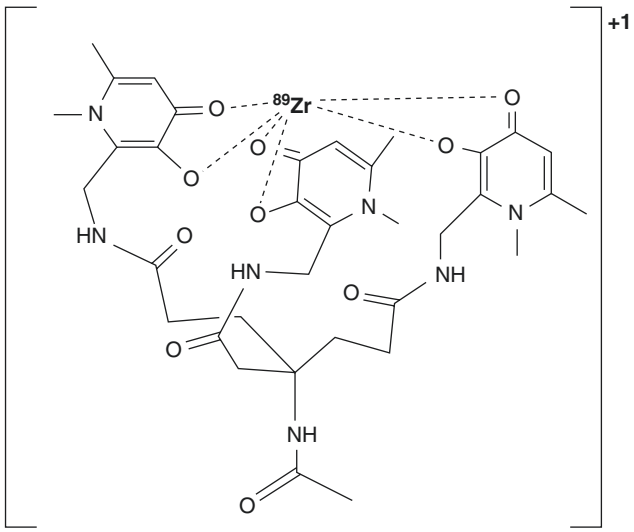

Fig. 14 Tripodal tris(hydroxypyridinone) (**L5**) is composed of three 1,6-dimethyl-3-hydroxypyridin-4-one moieties that form a tripodal ligand that is a hexacoordinate chelator for zirconium-89

and L4, respectively, within 1 day of incubation. The demetallation of ^{89}Zr from each chelator was also evident *in vivo*: [^{89}Zr]Zr-L3-trastuzumab and [^{89}Zr]Zr-L4-trastuzumab produced activity concentrations of 19.5 ± 3.6 %ID/g and 18.3 ± 2.9 %ID/g, respectively, in the bone after 3 days p.i., while the bone uptake from [^{89}Zr]Zr-DFO-trastuzumab was only 7.6 ± 0.4 %ID/g in the same experiment. Ultimately, the authors attributed the release of the radiometal from both chelators to the steric constraints put upon the octacoordinate complex by the short spacer arms of L3 and L4.

Tripodal Tris(Hydroxypyridinone) (L5) In another case, three 1,6-dimethyl-3-hydroxypyridin-4-one moieties were attached to form a tripodal HOPO ligand (Fig. 14) [55]. While this chelator was originally meant as a coordination scaffold for hard, trivalent metals such as Ga(III) and Fe(III), Ma et al. explored extending its utility to zirconium-89. The incubation of ^{nat}Zr^{4+} and L5 produced a mononuclear species—^{nat}Zr-L5—with an overall +1 charge that could be observed via mass spectrometry [56]. A competition assay using a ten-fold excess Fe(III) was conducted against both [^{89}Zr]Zr-L5 and [^{89}Zr]Zr-DFO at room temperature for 20 min. Over this time period, >85% of the ^{89}Zr dissociated from the [^{89}Zr]Zr-L5 complex, compared to only ~7% of ^{89}Zr from [^{89}Zr]Zr-DFO. Not to be deterred, the authors functionalized L5 with maleimidopropionate and conjugated the bifunctional chelator to trastuzumab. The radiolabeling of [^{89}Zr]Zr-L5-trastuzumab proceeded according to standard methods, and the incubation of [^{89}Zr]Zr-L5-trastuzumab and [^{89}Zr]Zr-DFO-trastuzumab in serum over 7 days revealed that both constructs remained >95% intact, though some aggregation was observed for the former. Surprisingly, *in vivo* biodistribution studies showed that [^{89}Zr]Zr-L5-trastuzumab was cleared rapidly by the renal system, with the majority of the injected dose (55–75%) accreting in the bladder after 1 h p.i. [^{89}Zr]Zr-L5-trastuzumab also produced very high activity concentrations in the bone: 29 ± 3.3 %ID/g at 3 days and 26 ± 0.6 %ID/g at 7 days p.i. The demetallation of the [^{89}Zr]Zr-L5 complex is believed to result from the kinetic lability and fluxional behavior of the complex in solution, though the intraconversion of the complex between multiple isomers could also play a role in its rapid dissociation.

Macrocyclic Hydroxamates

Fusarinine (L6) L6 (Fig. 15a) and its triacetylated analog TAFC (L6-$COCH_3$) are produced by the fungus *Aspergillus fumigatus* for the remediation of iron [57]. The 36-membered cyclic backbone of FSC contains three hydroxamic acid moieties for the coordination of metal centers. Both L6 and TAFC formed hexadentate complexes with [^{89}Zr]Zr^{4+} after incubation at room temperature at pH ~6.8–7.2 between 30 and 90 min. A specific activity of ~25 GBq/μmol was achieved for [^{89}Zr]Zr-TAFC. L6 was subsequently conjugated to a succinic anhydride-functionalized cyclic RGD peptide (L6-(RGD), Fig. 15b) by forming an amide bond with a free amine on L6's backbone. The radiolabeling of L6-RGD with zirconium-89 proceeded in a similar fashion to that of TAFC, yielding the product in >90% radiochemical yield after 60 min of incubation at room temperature. No specific activities were reported for either [^{89}Zr]Zr-L6 or the [^{89}Zr]Zr-RGD construct. The stability of [^{89}Zr]Zr-TAFC and [^{89}Zr]Zr-L6-RGD were explored via challenge experiments against EDTA and DFO and compared to that of [^{89}Zr]Zr-DFO as the standard [58]. [^{89}Zr]Zr-TAFC showed high stability in the presence of a 1000-fold excess of EDTA, with ~97% of the metal complex remaining intact after 7 days of incubation. In the presence of DFO at pH~6, however, the transchelation of [^{89}Zr]Zr^{4+} from [^{89}Zr]Zr-TAFC occurred as early as 4 h post-incubation. After this period, ~92% of the complex remained intact, a value which decreased to ~74% after a full day and ~40% after a week. [^{89}Zr]Zr-L6-RGD similarly demonstrated stability in EDTA (pH~7) even after 7 days of incubation (~94% of the metal complex intact), though no studies were performed using [^{89}Zr]Zr-DFO-RGD for the sake of comparison. No data were provided on the performance of the radiolabeled L6 in the EDTA and DFO challenge experiments. Furthermore, no DFO challenge was reported for radiolabeled L6-RGD construct. [^{89}Zr]Zr-TAFC demonstrated fast *in vivo* pharmacokinetics with minimal blood residency (0.05 ± 0.01 %ID/g) at 6 h p.i. The complex also produced minimal bone uptake at this time point (0.04 ± 0.02 %ID/g), and the activ-

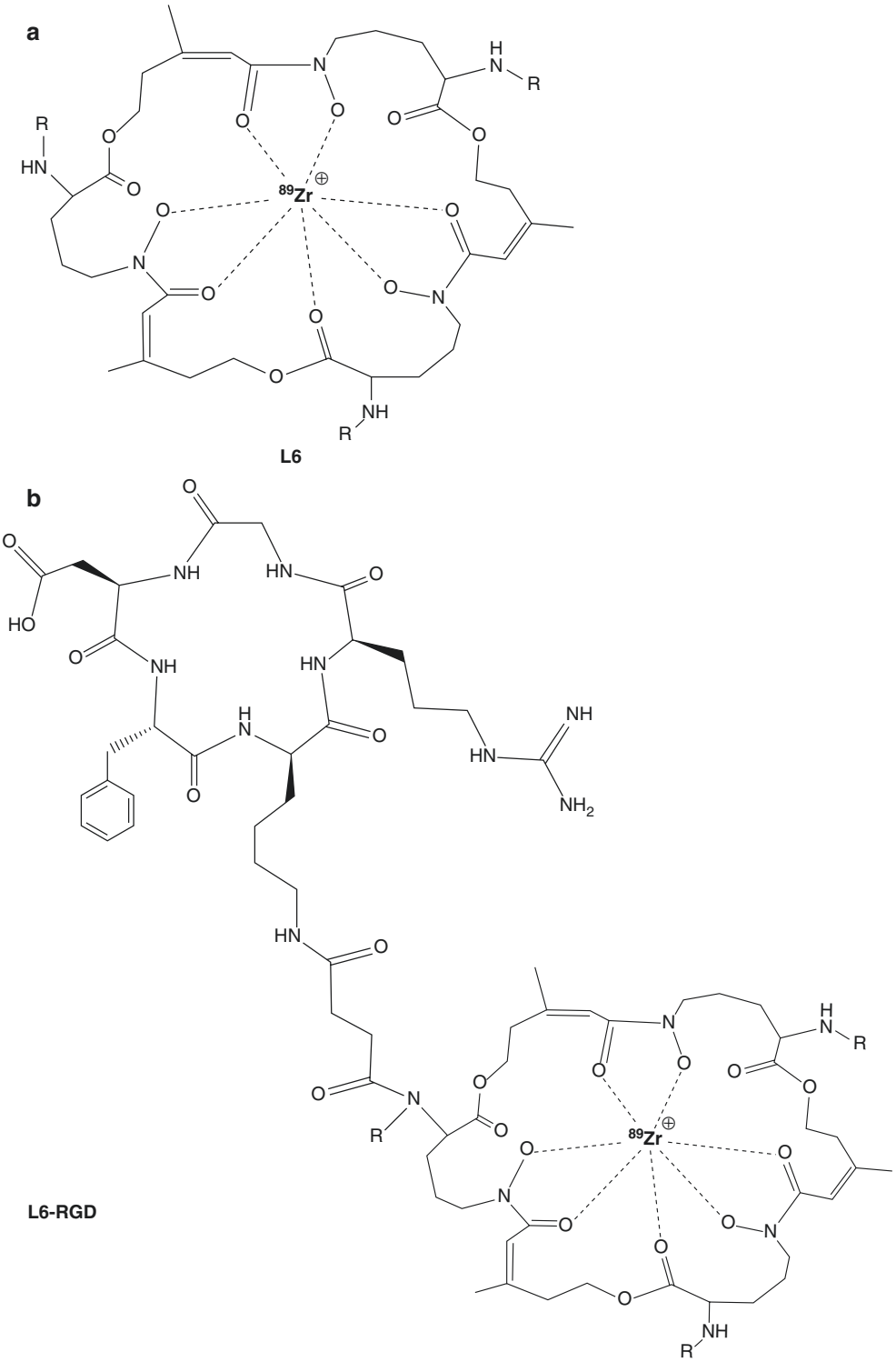

Fig. 15 (**a**) Fusarinine (**L6**) is a macrocyclic chelator comprised of three hydroxamic acids that can coordinate Zr in a hexadentate manner; (**b**) L6 can be attached to RGD through an amide linker

ity concentrations in the spleen, kidneys, liver, and intestines were all <1.5 %ID/g at 6 h p.i. as well. Biodistribution data were also reported for [^{89}Zr]Zr-L6-RGD; however, no comparisons were made against a ^{89}Zr-labeled variant of DFO-RGD nor [^{89}Zr]Zr-L6, experiments which could have made the study more meaningful within the context of this chapter.

Both TAFC and L6 offer unique advantages with regard to the coordination of ^{89}Zr. To wit, TAFC can bind [^{89}Zr]Zr^{4+} at pH 1–5, a significant departure from the established protocols for other chelators such as DFO. In addition, the multiple amines of L6 open the door for simultaneously conjugating the chelator to as many as three vectors, making the creation of multimers possible. Ultimately, L6 and TAFC undoubtedly show some

promise for the coordination of ^{89}Zr. To date, however, the chelators have only been used for the construction of peptide-based radioconjugates, and the use of ^{89}Zr with peptide-based vectors is of dubious merit. The performance of both chelators with radioimmunoconjugates certainly warrants exploration.

Hydroxamate-Functionalized Cyclams (L7) The cyclen 1,4,7,10-tetraazamacrocyclododecane and cyclam 1,4,8,11-tetraazacyclotetradecane were separately derivatized with three and four pendant hydroxamate arms to afford chelators with six and eight oxygen donors, respectively [59]. The radiolabeling of these complexes with [^{89}Zr]Zr^{4+} was performed in typical fashion via incubation at room temperature over 1 h at pH ~ 7.4–7.6. When the radiometal complexes were subjected with a 55 mM EDTA challenge and monitored over 144 h at 37 °C, L7 (Fig. 16)—which possesses long hydroxamate arms—was observed to be the most promising chelator and was selected for further comparison against DFO. The log D values of [^{89}Zr]Zr-L7 and [^{89}Zr]Zr-DFO are comparable at −3.4 vs. −3.1, respectively. Furthermore, both [^{89}Zr]Zr-L7 and [^{89}Zr]Zr-DFO performed similarly when challenged with EDTA, with 91 ± 2% and 87 ± 1% of the complexes remaining intact after 6 days of incubation. Furthermore, [^{89}Zr]Zr-L7 (94% intact) proved more inert than [^{89}Zr]Zr-DFO (53% intact) after 72 h incubation in rat plasma assays. An *in vivo* pharmacokinetic analysis of [^{89}Zr]Zr-L7 and [^{89}Zr]Zr-DFO reveals that the two complexes have similar serum half-lives and are primarily excreted via the renal system. However, the uptake in the bone produced by [^{89}Zr]Zr-L7 (0.60 ± 0.19 %ID/g at 24 h p.i.) was markedly higher than that created by [^{89}Zr]Zr-DFO at the same time point (0.05 ± 0.02 %ID/g). DFT *in silico* analysis validated the thermodynamic stability of [^{89}Zr]Zr-L7, with the ligand providing a favorable coordination geometry with little steric strain.

L7 was functionalized with an *N*-hydroxy-succinimidyl ester to create a bifunctional chelator capable of being attached to antibodies like trastuzumab. Imaging and biodistribution studies in mice bearing both HER2-positive and HER2-negative tumors revealed that [^{89}Zr]Zr-L7-trastuzumab and [^{89}Zr]Zr-DFO-trastuzumab displayed generally similar *in vivo* behavior. The former, however, produced much higher activity concentrations in the bone than the latter. For example, at 96 h post-injection, the activity concentrations in the bone for [^{89}Zr]Zr-L7-trastuzumab and [^{89}Zr]Zr-DFO-trastuzumab were 19.0 ± 2.1 %ID/g and 2.8 ± 2.2 %ID/g, respectively.

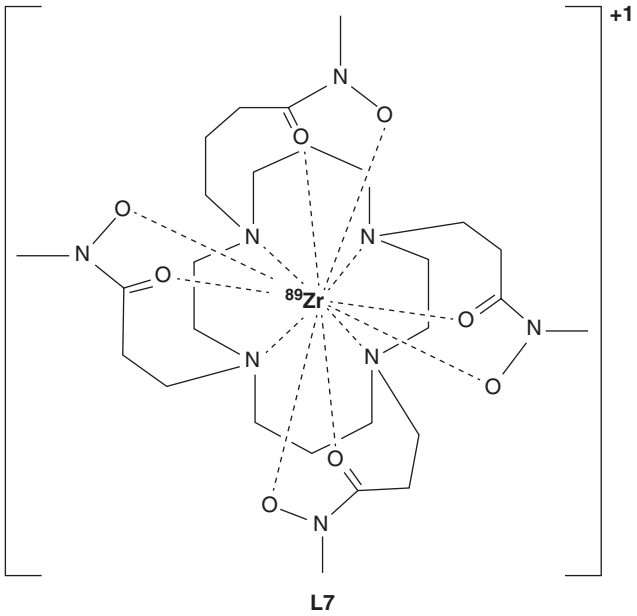

Fig. 16 Hydroxamate-functionalized cyclam **(L7)** is a macrocyclic construct modified with longer tri-hydroxamate arms. It provides the most stable coordinating properties for Zr^{4+} compared to other hydroxamate-modified cyclens and cyclams

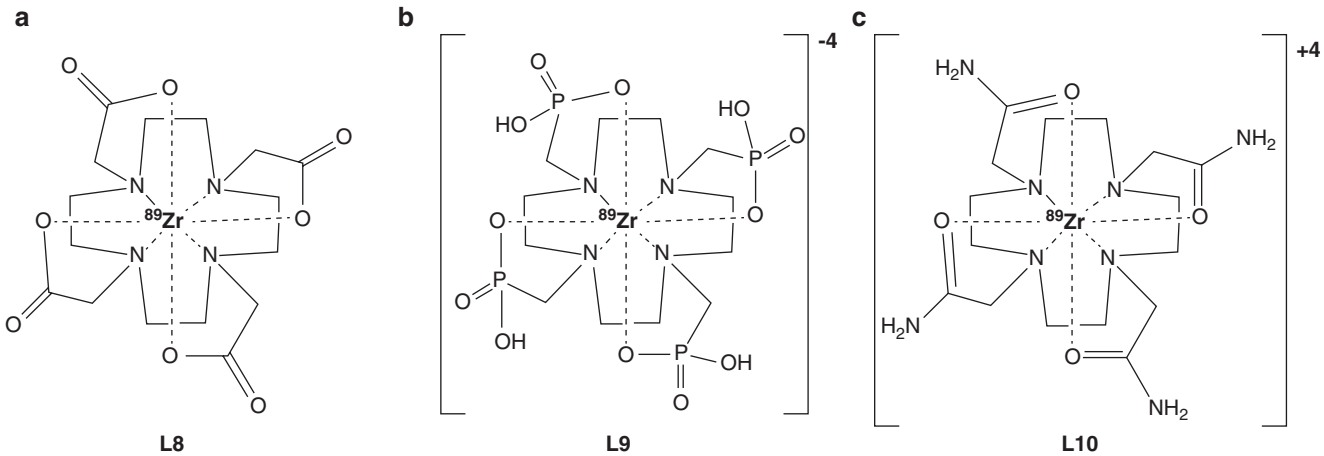

Fig. 17 (**a**) DOTA (**L8**), (**b**) DOTP (**L9**), and (**C**) DOTAM (**L10**) are tetraazamacrocycles with carboxylic acid-, phosphate-, and amine-bearing pendant arms, respectively, that have been explored for the coordination of zirconium-89

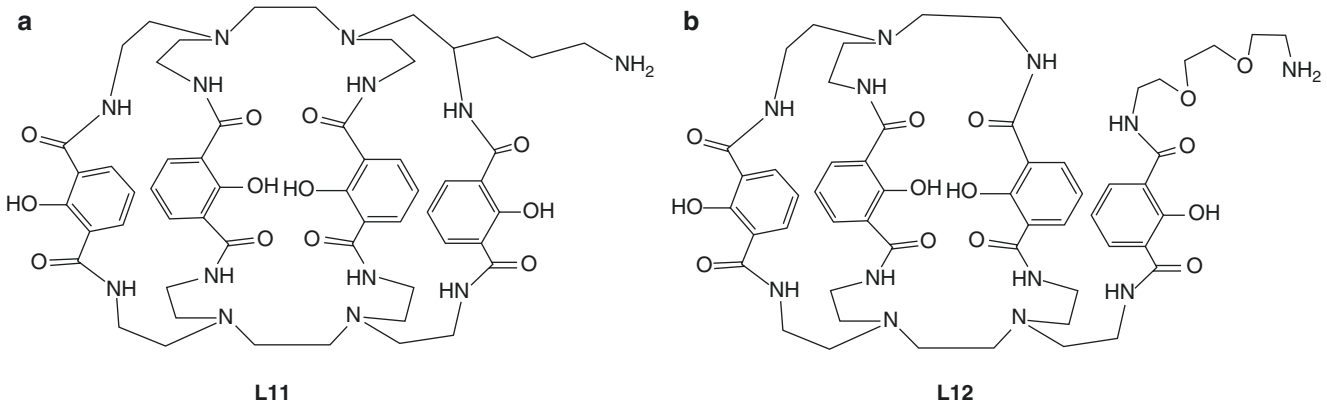

Fig. 18 Four 2-hydroxylisophthalamide (IAM) chelating units were combined to form the octadentate ligands (**a**) **L11** and (**b**) **L12**

Non-hydroxamates

DOTA (L8), DOTP (L9), and DOTAM (L10) Tetraazamacrocycles such as 1,4,7,10-tetraazacyclodo decane-1,4,7,10-tetraacetic acid (DOTA, L8, Fig. 17a) and variants of DOTA with phosphate- (DOTP, L9, Fig. 17b) and amine- (DOTAM, L10, Fig. 17c) derivatized arms have also been investigated for their ability to coordinate zirconium-89 [60]. Unlike acyclic ligands, these macrocycles required heating at 90 °C at 45 min to sufficiently encapsulate the radiometal. This need for heating puts these chelators at a disadvantage in the context of biomolecular vectors, because antibodies and proteins generally cannot tolerate high temperatures. Furthermore, differences in the complexation of [^{89}Zr]Zr^{4+} have been observed when using [^{89}Zr]Zr-oxalate and [^{89}Zr]Zr-Cl_4 as the starting material, with the former providing lower yields, possibly as a result of the competition between the ligand and the oxalates in solution. Competition assays with excess EDTA revealed that the complexes observe the following decreasing ordering of stability: [^{89}Zr]Zr-L8 > [^{89}Zr]Zr-L9 > [^{89}Zr]Zr-L10 = [^{89}Zr]Zr-DFO. Challenging [^{89}Zr]Zr-L8, [^{89}Zr]Zr-L9, and [^{89}Zr]Zr-L10 with excess Fe(III) and Ga(III) did not yield any appreciable loss of [^{89}Zr]Zr^{4+} from the macrocycles, while similar metal competition experiments with [^{89}Zr]Zr-DFO resulted in the partial dissociation of the radiometal from DFO.

The *in vivo* behavior of [^{89}Zr]Zr-L8, [^{89}Zr]Zr-L9, [^{89}Zr]Zr-L10, and [^{89}Zr]Zr-DFO were compared via biodistribution experiments. High levels of [^{89}Zr]Zr-L10 were observed and retained in the liver and spleen over the course of 3 days, primarily due to the aggregation of the complex and its precipitation with serum proteins. Similar biodistribution profiles—*i.e.* accumulation in the blood, liver, and bone—were observed for both [^{89}Zr]Zr-L8 and [^{89}Zr]Zr-DFO within the first hour p.i., with the latter retained in the kidneys at 4 h p.i.. Compared to these two complexes, [^{89}Zr]Zr-L9 exhibited higher accretion in the blood, liver, kidneys, and bone at 72 h p.i. Notably, [^{89}Zr]Zr-L8 produced lower activity concentrations in the bone (0.03 ± 0.009 %ID/g) than both [^{89}Zr]Zr-L9 (2.6 ± 0.1 %ID/g) and [^{89}Zr]Zr-DFO (0.08 ± 0.01 %ID/g). Pandya et al. rationalized that the higher uptake of [^{89}Zr]Zr-L9 in the bone may be due to transchelation and the influence of the ligand's four phosphate moieties (which could theoretically cause the deposition of the intact complex onto bone tissue). This has been observed for other metals complexed by phosphate-containing macrocycles. Moreover, the authors found that L8 appears to provide superior kinetic inertness and *in vivo* stability against transchelation compared to other reported Zr chelators, including TAFC, L1, and L2. In retrospect, the main limitation to L8 is the requirement for elevated temperatures when radiolabeling, which can be circumvented by exploring other synthetic methodologies such as "click" chemistry.

2-Hydroxyisophthalamide (L11-L12) Four 2-hydroxylisophthalamide (IAM) moieties were fused to form the octadentate ligands L11 (Fig. 18a) and L12 (Fig. 18b) [61]. IAMs possess phenolic and carbonyl oxygen donor groups that preferentially bind hard metals and were chosen for these chelators based on their similarities to lanthanide-sequestration moieties produced by bacteria. The coordination of zirconium-89 by L11 and L12 was performed in water at a pH~7.0–7.5. Because of L11's rigidity, it was incubated with zirconium-89 for 2 h at a relatively high temperature, 95 °C. L12 is less rigid but was still heated at 50 °C for 1 h to induce the coordination of zirconium-89. The Log P values for ^{nat}Zr-L11 and ^{nat}Zr-L12 are −2.97 ± 0.02 and − 1.45 ± 0.06, making both more hydrophilic than [^{89}Zr]Zr-DFO.

Stability studies in the presence of 50 mM DTPA suggested that [^{89}Zr]Zr-L11 is more inert to transchelation than both [^{89}Zr]Zr-L12 and [^{89}Zr]Zr-DFO, though parallel experiments in serum somewhat curiously revealed that [^{89}Zr]Zr-DFO (100% intact after 7 days) is more stable than [^{89}Zr]-Zr-L11 (~75.1% intact) or [^{89}Zr]-Zr-L12 (~17% intact) in

serum over 7 days. *In vivo* biodistribution experiments revealed that [^{89}Zr]Zr-L12 had a higher retention in the blood after 1 day than either [^{89}Zr]Zr-L11 or [^{89}Zr]Zr-DFO, with uptake values of 0.01 ± 0.006 %ID/g, 0.003 ± 0.000 %ID/g, and 0.001 ± 0.001 %ID/g, respectively. Furthermore, both [^{89}Zr]Zr-L11 (0.38 ± 0.04 %ID/g) and [^{89}Zr]Zr-L12 (1.52 ± 0.15 %ID/g) were observed to accumulate in the liver to greater degrees than [^{89}Zr]Zr-DFO (0.081 ± 0.012 %ID/g). Finally, and perhaps most importantly, [^{89}Zr]Zr-DFO was observed to produce lower activity concentrations in the bone (0.078 ± 0.014 %ID/g) after 3 days than either of the two IAM-based chelators (0.1 ± 0.01 %ID/g for [^{89}Zr]Zr-L11 and 0.68 ± 0.33 %ID/g for [^{89}Zr]Zr-L12). These disappointing *in vitro* and *in vivo* results seem to disqualify both L11 and L12 as potential chelators of zirconium-89.

The Future

Over the last decade, advances in the production of zirconium-89 as well as the development of chelators to stably sequester the radiometal have fueled the advent of ^{89}Zr-based PET imaging. Perhaps not surprisingly, this rise in ^{89}Zr-based PET has run parallel to a growth in the importance of—and appreciation for—the role of antibodies as vectors for diagnostic and theranostic nuclear imaging. Today, DFO remains the "gold standard" chelator for ^{89}Zr and has been employed in all clinical trials to date. Yet the stability of the [^{89}Zr]Zr-DFO complex in preclinical models has motivated a number of investigations aimed at developing new chelators for the radiometal. A wide range of promising alternatives have been developed, though as we embark on these discoveries, we should be sure to evaluate both the chelator's toxicity and—even more importantly—its potential to change the pharmacokinetic properties of its targeting vector. After all, we should not lose sight of the big picture: ultimately, our overarching goal is to use ^{89}Zr to track targeting vectors in order to accurately stage disease and predict and monitor the response of patients to therapy.

The Bottom Line

In this chapter, we have tried to provide an overview of the production, chemistry, and radiochemistry of zirconium-89 as well as several techniques to consider when working with the radiometal. While a variety of novel chelators have been developed for zirconium-89, only a handful have matched or exceeded DFO's ability to coordinate the radiometal. We understand that this chapter—like all those in this textbook—has provided a great deal of information, so in the end, we sincerely hope the readers keep the following points foremost in their mind.

- Zirconium-89 is a residualizing, positron-emitting radionuclide whose physical half-life provides an excellent match for the pharmacokinetic profiles of many antibodies.
- The current "gold standard" chelator for zirconium-89 in both the laboratory and clinic is desferrioxamine (DFO).
- Over time, [^{89}Zr]Zr-DFO is susceptible to transchelation in the presence of endogenous proteins, producing free [^{89}Zr]Zr^{4+} that can subsequently deposit in the bones. As a result, the imaging of osseous lesions can become difficult, and the radiosensitive bone marrow can be exposed to nontrivial radiation doses.
- Zirconium(IV) is a hard metal, and thus hard donor atoms (*e.g.* oxygens) are necessary for its coordination.
- The ideal chelator for Zr^{4+} should be octadentate in order to saturate the metal's preference for a coordination number of 8. For example, several of the most successful "second-generation" chelators for zirconium-89—*e.g.* DFO★, DFO-HOPO, and L1—possess four hydroxamate groups that collectively offer eight donor atoms.
- The hydrophilicity of a chelator plays a role in the whole body clearance of the radiometal-bearing complex.
- The radiolabeling of antibodies with zirconium-89 must be conducted at or close to neutral pH to preserve the structural integrity of the mAb. As a result, the pKa of the chelator should be within this range. Heating conditions should range from room temperature to 37 °C.
- Zirconium-89 with high effective specific activity should be employed to achieve near quantitative radiolabeling yields and facilitate the creation of ^{89}Zr-labeled mAbs with high specific activities.

References

1. Deri MA, Zeglis BM, Francesconi LC, Lewis JS. PET imaging with (8)(9)Zr: from radiochemistry to the clinic. Nucl Med Biol. 2013;40(1):3–14.
2. Abou DS, Ku T, Smith-Jones PM. In vivo biodistribution and accumulation of 89Zr in mice. Nucl Med Biol. 2011;38(5):675–81.
3. Ulaner GA, Hyman DM, Ross DS, Corben A, Chandarlapaty S, Goldfarb S, et al. Detection of HER2-positive metastases in patients with HER2-negative primary breast cancer using 89Zr-trastuzumab PET/CT. J Nucl Med. 2016;57(10):1523–8.
4. Greenwood NN, Earnshaw A. Chemistry of the elements. 2nd ed. Oxford: Elsevier Butterworth-Heinemann; 1997.
5. Kozak CM, Mountford P. Zirconium & hafnium. Inorganic & coordination chemistry. In: King RB, editor. Encyclopedia of inorganic chemistry. 2nd ed. Chichester/West Sussex: Wiley; 2006.
6. Intorre BI, Martell AE. Zirconium complexes in aqueous solution. I. Reaction with multidentate ligands1. J Am Chem Soc. 1960;82(2):358–64.
7. Intorre BJ, Martell AE. Aqueous zirconium complexes. II. Mixed chelates. J Am Chem Soc. 1961;83(17):3618–23.
8. Ekberg C, Kallvenius G, Albinsson Y, Brown PL. Studies on the hydrolytic behavior of Zr(IV). J Solution Chem. 2004;33(1):47–79.

9. Conti M, Eriksson L. Physics of pure and non-pure positron emitters for PET: a review and a discussion. EJNMMI Physics. 2016;3:8.
10. Moses WW. Fundamental limits of spatial resolution in PET. Nucl Instr Methods Phys Res A. 2011;648(Suppl 1):S236–S40.
11. Disselhorst JA, Brom M, Laverman P, Slump CH, Boerman OC, Oyen WJ, et al. Image-quality assessment for several positron emitters using the NEMA NU 4-2008 standards in the Siemens Inveon small-animal PET scanner. J Nucl Med. 2010;51(4):610–7.
12. Link JM, Krohn KA, Eary JF, Kishore R, Lewellen TK, Johnson MW, et al. Zr-89 for antibody labeling and positron emission tomography. J Labelled Compd Radiopharm. 1986;23(10–12):1297–8.
13. Eary JF, Link JM, Kishore R, Johnson MW, Badger CC, Richter KY, et al. Production of positron emitting Zr89 for antibody imaging by PET. J Nucl Med. 1986;27(6):983.
14. Dejesus OT, Nickles RJ. Production and purification of Zr-89, a potential PET antibody label. Appl Radiat Isot. 1990;41(8):789–90.
15. Meijs WE, Herscheid JDM, Haisma HJ, Wijbrandts R, Vanlangevelde F, Vanleuffen PJ, et al. Production of highly pure no-carrier added Zr-89 for the labeling of antibodies with a positron emitter. Appl Radiat Isot. 1994;45(12):1143–7.
16. Holland JP, Sheh Y, Lewis JS. Standardized methods for the production of high specific-activity zirconium-89. Nucl Med Biol. 2009;36(7):729–39.
17. Wooten A, Madrid E, Schweitzer G, Lawrence L, Mebrahtu E, Lewis B, et al. Routine production of 89Zr using an automated module. Appl Sci. 2013;3(3):593.
18. Queern SL, Aweda TA, Massicano AVF, Clanton NA, El Sayed R, Sader JA, et al. Production of Zr-89 using sputtered yttrium coin targets 89Zr using sputtered yttrium coin targets. Nucl Med Biol. 2017;50:11–6.
19. Pandey MK, Engelbrecht HP, Byrne JP, Packard AB, DeGrado TR. Production of 89Zr via the 89Y(p,n)89Zr reaction in aqueous solution: effect of solution composition on in-target chemistry. Nucl Med Biol. 2014;41(4):309–16.
20. Verel I, Visser GW, Boellaard R, Stigter-van Walsum M, Snow GB, van Dongen GA. 89Zr immuno-PET: comprehensive procedures for the production of 89Zr-labeled monoclonal antibodies. J Nucl Med. 2003;44(8):1271–81.
21. Guerard F, Lee YS, Tripier R, Szajek LP, Deschamps JR, Brechbiel MW. Investigation of Zr(IV) and 89Zr(IV) complexation with hydroxamates: progress towards designing a better chelator than desferrioxamine B for immuno-PET imaging. Chem Commun (Camb). 2013;49(10):1002–4.
22. Hoard JL, Glen GL, Silverton JV. The configuration of Zr(C2O4)4-4 and the stereochemistry of discrete eight-coordination. J Am Chem Soc. 1961;83(20):4293–5.
23. Lin M, Mukhopadhyay U, Waligorski GJ, Balatoni JA, González-Lepera C. Semi-automated production of 89Zr-oxalate/89Zr-chloride and the potential of 89Zr-chloride in radiopharmaceutical compounding. Appl Radiat Isot. 2016;107(Supplement C):317–22.
24. Bickel H, Gaeumann E, Keller-Schierlein W, Prelog V, Vischer E, Wettstein A, Zaehner H. On iron-containing growth factors, sideramines, and their antagonists, the iron-containing antibiotics, sideromycins. Experientia. 1960;16:129–33. [Article in German]
25. Bergeron RJ, McManis JS. Reagents for the stepwise functionalization of spermine. J Org Chem. 1988;53(13):3108–11.
26. Perk LR, Vosjan MJ, Visser GW, Budde M, Jurek P, Kiefer GE, et al. P-Isothiocyanatobenzyl-desferrioxamine: a new bifunctional chelate for facile radiolabeling of monoclonal antibodies with zirconium-89 for immuno-PET imaging. Eur J Nucl Med Mol Imaging. 2010;37(2):250–9.
27. Vosjan MJ, Perk LR, Visser GW, Budde M, Jurek P, Kiefer GE, et al. Conjugation and radiolabeling of monoclonal antibodies with zirconium-89 for PET imaging using the bifunctional chelate p-isothiocyanatobenzyl-desferrioxamine. Nat Protoc. 2010;5(4):739–43.
28. Marquez BV, Ikotun OF, Zheleznyak A, Wright B, Hari-Raj A, Pierce RA, et al. Evaluation of 89Zr-pertuzumab in breast cancer xenografts. Mol Pharm. 2014;11(11):3988–95.
29. Meijs WE, Haisma HJ, Klok RP, van Gog FB, Kievit E, Pinedo HM, et al. Zirconium-labeled monoclonal antibodies and their distribution in tumor-bearing nude mice. J Nucl Med. 1997;38(1):112–8.
30. Tinianow JN, Gill HS, Ogasawara A, Flores JE, Vanderbilt AN, Luis E, et al. Site-specifically 89Zr-labeled monoclonal antibodies for ImmunoPET. Nucl Med Biol. 2010;37(3):289–97.
31. Houghton JL, Zeglis BM, Abdel-Atti D, Aggeler R, Sawada R, Agnew BJ, et al. Site-specifically labeled CA19.9-targeted immunoconjugates for the PET, NIRF, and multimodal PET/NIRF imaging of pancreatic cancer. Proc Natl Acad Sci U S A. 2015;112(52):15850–5.
32. Tavare R, McCracken MN, Zettlitz KA, Salazar FB, Olafsen T, Witte ON, et al. Immuno-PET of murine T cell reconstitution post-adoptive stem cell transplantation using anti-CD4 and anti-CD8 cys-diabodies. J Nucl Med. 2015;56(8):1258–64.
33. Meijs WE, Herscheid JDM, Haisma HJ, Pinedo HM. Evaluation of desferal as a bifunctional chelating agent for labeling antibodies with Zr-89. Int J Rad Appl Instrum A. 1992;43(12):1443–7.
34. Zeglis BM, Lewis JS. The bioconjugation and radiosynthesis of 89Zr-DFO-labeled antibodies. J Vis Exp. 2015;96.
35. Kuda-Wedagedara ANW, Workinger JL, Nexo E, Doyle RP, Viola-Villegas N. (89)Zr-cobalamin PET tracer: synthesis, cellular uptake, and use for tumor imaging. ACS Omega. 2017;2(10):6314–20.
36. Bauman A, Valverde IE, Fischer CA, Vomstein S, Mindt TL. Development of 68Ga- and 89Zr-labeled exendin-4 as potential radiotracers for the imaging of insulinomas by PET. J Nucl Med. 2015;56(10):1569–74.
37. Ferris TJ, Charoenphun P, Meszaros LK, Mullen GE, Blower PJ, Went MJ. Synthesis and characterisation of zirconium complexes for cell tracking with Zr-89 by positron emission tomography. Dalton Trans. 2014;43(39):14851–7.
38. Charoenphun P, Meszaros LK, Chuamsaamarkkee K, Sharif-Paghaleh E, Ballinger JR, Ferris TJ, et al. [(89)Zr]oxinate4 for long-term in vivo cell tracking by positron emission tomography. Eur J Nucl Med Mol Imaging. 2015;42(2):278–87.
39. Asiedu KO, Koyasu S, Szajek LP, Choyke PL, Sato N. Bone marrow cell trafficking analyzed by (89)Zr-oxine positron emission tomography in a murine transplantation model. Clin Cancer Res. 2017;23(11):2759–68.
40. Bansal A, Pandey MK, Demirhan YE, Nesbitt JJ, Crespo-Diaz RJ, Terzic A, et al. Novel (89)Zr cell labeling approach for PET-based cell trafficking studies. EJNMMI Res. 2015;5:19.
41. Zhang P, Yue Y, Pan D, Yang R, Xu Y, Wang L, et al. Pharmacokinetics study of Zr-89-labeled melanin nanoparticle in iron-overload mice. Nucl Med Biol. 2016;43(9):529–33.
42. Boros E, Bowen AM, Josephson L, Vasdev N, Holland JP. Chelate-free metal ion binding and heat-induced radiolabeling of iron oxide nanoparticles. Chem Sci. 2015;6(1):225–36.
43. Abou DS, Thorek DL, Ramos NN, Pinkse MW, Wolterbeek HT, Carlin SD, et al. (89)Zr-labeled paramagnetic octreotide-liposomes for PET-MR imaging of cancer. Pharm Res. 2013;30(3):878–88.
44. Cheng L, Kamkaew A, Shen S, Valdovinos HF, Sun H, Hernandez R, et al. Facile preparation of multifunctional WS2 /WOx nanodots for chelator-free (89) Zr-labeling and in vivo PET imaging. Small. 2016;12(41):5750–8.
45. Chen F, Goel S, Valdovinos HF, Luo H, Hernandez R, Barnhart TE, et al. In vivo integrity and biological fate of chelator-free zirconium-89-labeled mesoporous silica nanoparticles. ACS Nano. 2015;9(8):7950–9.

46. Holland JP, Divilov V, Bander NH, Smith-Jones PM, Larson SM, Lewis JS. 89Zr-DFO-J591 for immunoPET of prostate-specific membrane antigen expression in vivo. J Nucl Med. 2010;51(8):1293–300.
47. Vugts DJ, Klaver C, Sewing C, Poot AJ, Adamzek K, Huegli S, et al. Comparison of the octadentate bifunctional chelator DFO*-pPhe-NCS and the clinically used hexadentate bifunctional chelator DFO-pPhe-NCS for (89)Zr-immuno-PET. Eur J Nucl Med Mol Imaging. 2017;44(2):286–95.
48. Patra M, Bauman A, Mari C, Fischer CA, Blacque O, Haussinger D, Gasser G, Mindt TL. An octadentate bifunctional chelating agent for the development of stable zirconium-89 based molecular imaging probes. Chem Commun (Camb). 2014;50:11523–5.
49. White DL, Durbin PW, Jeung N, Raymond KN. Specific sequestering agents for the actinides. 16. Synthesis and initial biological testing of polydentate oxohydroxypyridinecarboxylate ligands. J Med Chem. 1988;31(1):11–8.
50. Allott L, Da Pieve C, Meyers J, Spinks T, Ciobota DM, Kramer-Marek G, et al. Evaluation of DFO-HOPO as an octadentate chelator for zirconium-89. Chem Commun (Camb). 2017;53(61):8529–32.
51. Deri MA, Ponnala S, Zeglis BM, Pohl G, Dannenberg JJ, Lewis JS, et al. Alternative chelator for (8)(9)Zr radiopharmaceuticals: radiolabeling and evaluation of 3,4,3-(LI-1,2-HOPO). J Med Chem. 2014;57(11):4849–60.
52. Deri MA, Ponnala S, Kozlowski P, Burton-Pye BP, Cicek HT, Hu C, et al. P-SCN-Bn-HOPO: a superior bifunctional chelator for (89)Zr immunoPET. Bioconjug Chem. 2015;26(12):2579–91.
53. Tinianow JN, Pandya DN, Pailloux SL, Ogasawara A, Vanderbilt AN, Gill HS, et al. Evaluation of a 3-hydroxypyridin-2-one (2,3-HOPO) based macrocyclic chelator for (89)Zr(4+) and its use for immunopet imaging of HER2 positive model of ovarian carcinoma in mice. Theranostics. 2016;6(4):511–21.
54. Rousseau J, Zhang Z, Dias GM, Zhang C, Colpo N, Benard F, et al. Design, synthesis and evaluation of novel bifunctional tetrahydroxamate chelators for PET imaging of (89)Zr-labeled antibodies. Bioorg Med Chem Lett. 2017;27(4):708–12.
55. Ma MT, Cullinane C, Imberti C, Baguna Torres J, Terry SY, Roselt P, et al. New tris(hydroxypyridinone) bifunctional chelators containing isothiocyanate groups provide a versatile platform for rapid one-step labeling and PET imaging with (68)Ga(3.). Bioconjug Chem. 2016;27(2):309–18.
56. Ma MT, Meszaros LK, Paterson BM, Berry DJ, Cooper MS, Ma Y, et al. Tripodal tris(hydroxypyridinone) ligands for immunoconjugate PET imaging with (89)Zr(4+): comparison with desferrioxamine-B. Dalton Trans. 2015;44(11):4884–900.
57. Knetsch PA, Zhai C, Rangger C, Blatzer M, Haas H, Kaeopookum P, et al. [(68)Ga]FSC-(RGD)3 a trimeric RGD peptide for imaging alphavbeta3 integrin expression based on a novel siderophore derived chelating scaffold-synthesis and evaluation. Nucl Med Biol. 2015;42(2):115–22.
58. Zhai C, Summer D, Rangger C, Franssen GM, Laverman P, Haas H, et al. Novel bifunctional cyclic chelator for (89)Zr labeling-radiolabeling and targeting properties of RGD conjugates. Mol Pharm. 2015;12(6):2142–50.
59. Boros E, Holland JP, Kenton N, Rotile N, Caravan P. Macrocycle-based hydroxamate ligands for complexation and immunoconjugation of (89)zirconium for positron emission tomography (PET) imaging. ChemPlusChem. 2016;81(3):274–81.
60. Pandya DN, Bhatt N, Yuan H, Day CS, Ehrmann BM, Wright M, et al. Zirconium tetraazamacrocycle complexes display extraordinary stability and provide a new strategy for zirconium-89-based radiopharmaceutical development. Chem Sci. 2017;8(3):2309–14.
61. Bhatt NB, Pandya DN, Xu J, Tatum D, Magda D, Wadas TJ. Evaluation of macrocyclic hydroxyisophthalamide ligands as chelators for zirconium-89. PLoS One. 2017;12(6):e0178767.

The Radiopharmaceutical Chemistry of the Radioisotopes of Iodine

Ganesan Vaidyanathan and Michael R. Zalutsky

Fundamentals

A significant advantage of radiolabeling molecules with iodine is that there are more than 30 known radioisotopes of iodine that possess a variety of physical half-lives and nuclear decay pathways. Many of these are routinely available at a reasonable cost and, as will be discussed below, have properties that are well matched to the needs of molecular imaging, both in preclinical and clinical settings, as well as for targeted radiotherapy. Although in recent years many researchers in radiopharmaceutical chemistry have preferred to work with radionuclides of metals instead of radioisotopes of iodine, in this chapter, we shall attempt to provide a compelling rationale for radiolabeling with iodine. Unlike metal radionuclides, radioisotopes of iodine can easily be incorporated into small organic molecules often without perturbing their biological function. In addition, proteins and peptides can be labeled either directly (not recommended) or by conjugation reactions with biologically inspired prosthetic groups. In this chapter, we shall describe various methods prevalent for the radioiodination of these different types of molecules. After providing an overview of the advantages and disadvantages of iodine radioisotopes, approaches used to label low molecular weight organic compounds are provided. These include radioiodination by both electrophilic and nucleophilic substitution reactions as well as kit methods that can be used to synthesize radioiodinated compounds for routine use. Various strategies for the radioiodination of peptides and proteins including direct labeling, conjugation with pre-labeled prosthetic agents, and click chemistry/bioorthogonal methods are described. Finally, the elephant in the room for radioiodination—the susceptibility of radioiodinated compounds to deiodination *in vivo*—is addressed as well.

G. Vaidyanathan (✉)
Department of Radiology, Duke University Medical Center, Durham, NC, USA
e-mail: ganesan.v@duke.edu

M. R. Zalutsky
Departments of Radiology, Radiation Oncology, Pathology, and Biomedical Engineering, Duke University Medical Center, Durham, NC, USA

Details

Radioisotopes

Although other radioisotopes have been studied as well, the vast majority of radiochemical and preclinical research as well as clinical applications involving radioiodine have involved the four radioisotopes whose relevant properties are summarized in Table 1. Iodine-131 is the most widely utilized radionuclide, including both radiohalogens and radiometals, for therapeutic applications in patients. In most cases, the natural targeting mechanism of free iodide for the thyroid is exploited to treat a variety of diseases of this tissue, while the 2.3-mm average range of its β-particles help limit damage to neighboring tissues. Other therapeutic applications involving ^{131}I in tandem with both small molecules and antibodies have been evaluated, particularly for use in settings where the relatively short β-particle range would be clinically advantageous. On the other hand, the 364-keV γ ray is not an ideal energy for imaging and complicates therapy because of the need for shielding to reduce radiation dose to personnel. Nonetheless, it can be used for both planar imaging and single-photon emission computed tomography (SPECT). Thus, ^{131}I-labeled compounds are true theranostics, because the same radiopharmaceutical can be used for imaging and treatment. This has advantages in terms of gaining regulatory approval, individualizing patient treatment, and cost. The low-cost, widespread availability, minimal shielding issues, and 60-day half-life are features of ^{125}I that have made it the workhorse for radiochemistry, cell culture, and animal model studies for the development of radioiodine-based radiopharmaceuticals. Moreover, ^{125}I can be used in tandem with ^{131}I for so-called paired-label experiments in either cell or animal models, permitting direct comparisons

J. S. Lewis et al. (eds.), *Radiopharmaceutical Chemistry*, https://doi.org/10.1007/978-3-319-98947-1_22

Table 1 Selected iodine radioisotopes of interest for molecular imaging and targeted radiotherapy

Radioisotope	Half-life	Type of decay	Energy (keV)	Imaging application	Therapeutic application
^{123}I	13.2 h	Gamma EC/Auger	159 <5	SPECT	Auger electrons
^{124}I	4.2 days	Positron Annihilation radiation	687 + 975 β^+(mean) 511γ	PET	
^{125}I	60.1 days	Gamma EC/Auger	35.5 <5	Preclinical SPECT	Auger electrons
^{131}I	8.0 days	Gamma β-particle	364 192 (mean)	SPECT	β-particles

EC/Auger electron capture followed by emission of multiple Auger electrons, *SPECT* single-photon emission computed tomography, *PET* positron emission tomography

of different compounds or labeling methods in the same experimental group. This can be a powerful tool because it allows each animal to serve as its own control so differences in parameters such as receptor expression or tumor hemodynamics that can occur in groups of animals can be factored out. Iodine-123 emits a 159-keV γ ray, a nearly ideal energy for SPECT imaging, and ^{124}I has shown promise for PET imaging applications such as immuno-PET where a longer-lived positron emitter is advantageous. Finally, it should be noted that both ^{125}I and ^{123}I emit multiple Auger electrons and are of potential value for therapeutic use in settings where they can be delivered to the cell nucleus.

Radioiodination of Low Molecular Weight Organic Compounds

Organic compounds are labeled with radioisotopes of iodine by electrophilic substitution, nucleophilic substitution or, less commonly, by electrophilic addition to unsaturated bonds. The best method to use is guided to a degree by the structural features of the molecule to be labeled. For example, if the molecule contains an activated/electron-rich ring such as a phenol or aniline, iodine can be easily introduced by electrophilic substitution. Conversely, electron-deficient rings favor nucleophilic substitution. Given that the carbon-iodine bond is weak when the carbon is sp^3 hybridized, radioiodine is almost exclusively introduced onto sp^2 carbons in aromatic rings or vinylic moieties. In addition, compounds with iodine substituted on an sp^3 carbon are susceptible to decomposition by hydrolysis and β-elimination. Nevertheless, radioiodinated compounds where the iodine is attached to a sp^3 carbon such as iodo-fatty acids have been developed.

Radioiodination by Electrophilic Substitution The most common method used for radioiodination is electrophilic substitution. Because radioiodine is routinely available as a solution of sodium iodide, an oxidizing agent is needed to convert iodide to an electropositive form. In addition to electron-rich aromatic rings such as phenols and amino group-substituted benzene rings, electrophilic substitution is possible with less electron-rich rings like imidazole, indole, and benzene. The most widely used electrophilic method, halodemetallation, involves *ipso* substitution on a carbon bearing a metal-containing moiety.

Oxidizing Agents Several oxidizing agents have been used in electrophilic radioiodination chemistry. The structures of some commonly used oxidizing agents are given in Fig. 1. These can be broadly divided into two classes—halogen (generally chlorine)-containing (see Fig. 1a) and those that do not have a halogen (see Fig. 1b). A drawback of halogen-bearing oxidizing agents is the potential formation of byproducts in which the halogen from the oxidizing agent becomes substituted at the position where iodine substitution is desired. Although seldom used anymore, other oxidation methods include electrolytic procedures and enzymes like lactoperoxidase. The sensitivity of the molecule to be labeled to oxidizing conditions can be minimized by using water-insoluble oxidants such as Iodogen and Iodobeads if the reaction can be performed in aqueous media.

Iododeprotonation This method is generally limited to aromatic compounds containing electron-rich rings that are activated by electron-donating substituents such as OH, NH_2, and OMe. It is a very facile reaction and substitution occurs primarily on *ortho* and *para* to these activating groups. As will be described later, the traditional method for radioiodination of proteins and peptides involves the iododeprotonation of constituent tyrosine residues. A method to radiolabel weakly activated or deactivated arenes by radioiododeprotonation also has been reported and involved *N*-chlorosuccinimide as the oxidant and a strong solvent, trifluoromethanesulfonic acid [1]. It was postulated that the "superelectrophilic" iodinating species triflyl hypoiodite is formed *in situ*. The presence of somewhat activating groups resulted in *ortho*- and *para*-iodo products, while electron-withdrawing groups such as NO_2 delivered the *meta*-isomer. A uracil derivative was labeled via radioiododeprotonation using NCS as the oxidant [2]. Excellent radiochemical yields were obtained even though a weaker solvent, 2:1 CH_3CN:H_2O, was used. *N*-iodosuccinimide, activated by metal Lewis

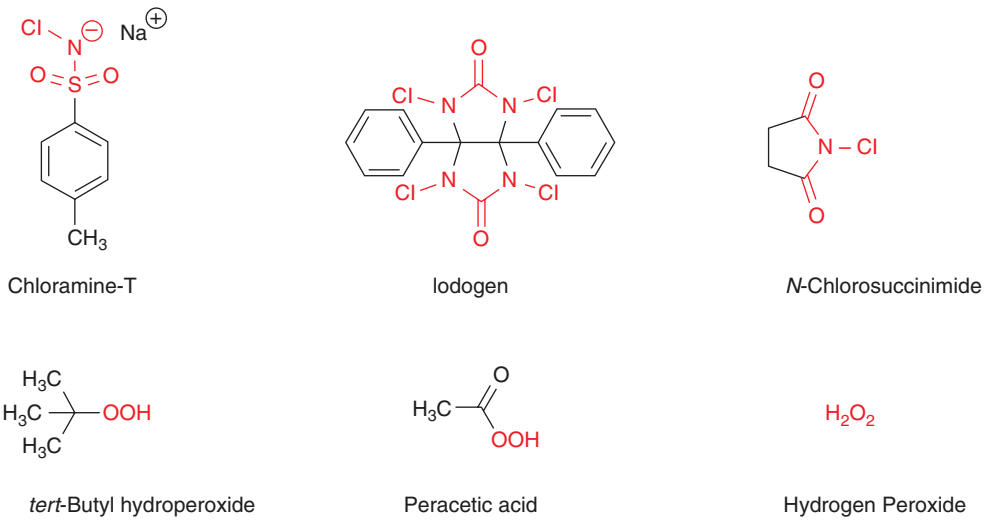

Fig. 1 Structures of oxidizing agents commonly used for electrophilic radioiodination

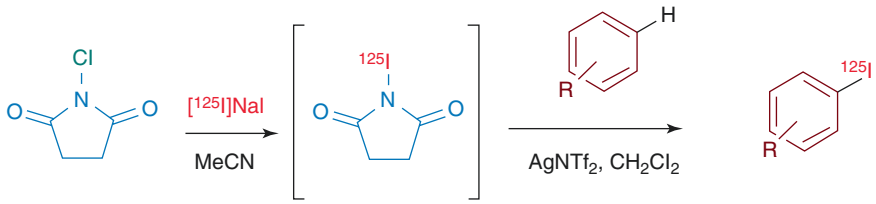

Fig. 2 Radioiododeprotonation of arenes using Lewis acid-activated [^{125}I]*N*-iodosuccinimide

acids, has been used for arene C-H to arene C-I conversion, and this approach has been used for radioiodination as well (Fig. 2) [3].

Iododemetallation Iododemetallation reactions have been utilized extensively for radioiodination (Fig. 3) for several reasons. First, the substitution is regioselective with iodine predominantly going to the same carbon bearing the metal moiety. Secondly, the large difference in polarity between the iodo product and the metal precursor facilitates their easy separation with the result that the radioiodinated product can be obtained in high molar activity. Finally, radiochemical yields for iododemetallation reactions generally are high. However, the metallic precursors are generally very toxic, so it is imperative to insure that they are removed from the final radioiodinated product.

Iododestannylation Iododestannylation is the most commonly used iododemetallation reaction, and numerous radioiodinated compounds have been synthesized by this approach [4–6]. Two alkyl tin precursors—tri-n-butyl- and trimethylstannyl—are used. Although there are some reports indicating higher radiochemical yields with trimethyl analogues [7], excellent radiochemical yields can generally be obtained with either precursor. The interpretation of NMR spectroscopy data is easier with the trimethyl analogues because there will be only one singlet for trimethyl versus four multiplets for the tributyl group. On the other hand, because the

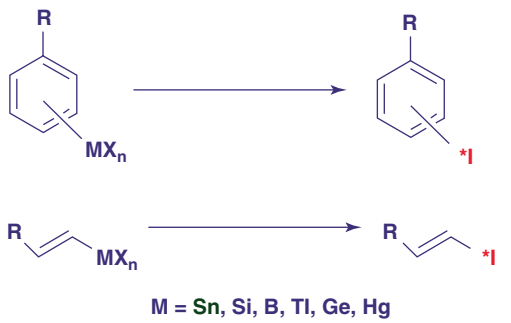

Fig. 3 General scheme for the radioiododemetallation of aryl and vinyl metallic precursors

polarity of the iodo compound and the corresponding trimethylstannyl derivative is similar, the normal-phase chromatographic separation of the two may be challenging; if the tin derivative was synthesized starting with the iodo compound, it will lead to lower molar activity of the final radioiodinated product due to the presence of carrier iodo compound. Conversely, because of its higher lipophilicity, the tributyl analogue can often be easily separated from the halo starting compound by normal-phase chromatography.

There are two main methods to synthesize the tin precursors, generally starting from the iodo compound itself or the bromo, and to a lesser extent, the chloro analogue. In the first approach, the halo compound is subjected to metal (mostly

lithium)-halogen exchange, and the anionic intermediate is treated with electrophilic trialkyltin chloride. This reaction has a couple of drawbacks in that it must be performed at extremely low temperatures and is not compatible with certain functional groups. The preferred method is the palladium-catalyzed Stille coupling of an aryl halide or trifluoromethanesulfonate with hexaalkylditin [8]. A potential side reaction with this method is the Stille coupling of the tin derivative formed with the halo starting material to form dimeric compounds, which can be minimized by using a large excess of hexaalkylditin. In addition to using the Stille coupling, vinylic tin precursors also can be synthesized by the addition of trialkyl tin hydride to corresponding alkenes. The radioiodination of trialkyltin precursors can potentially give rise to two products. The iodine can attach itself to the sp^3 carbon of one of the three alkyl moieties or to the sp^2 carbon of the aryl or vinyl moiety. Substitution on the sp^2 carbon is energetically favored despite a 3:1 statistical advantage for sp^3 carbon substitution [9]. However, the formation of the volatile alkyl iodide has been observed in some cases [10].

Iododesilylation Alternatively, iododesilylation can be used in the synthesis of radioiodinated compounds [11–13]; however, the rate of iododesilylation is much slower than iododestannylation, and harsher conditions often have to be employed [12, 14]. Provided there are no functional groups that are susceptible to these conditions, especially to strong acids, iododesilylation can be utilized for radioiodinations. A potential advantage of silicon precursors is that they are considerably less toxic than tin compounds [15]. In addition, carbon-silicon bonds are stronger than carbon-tin bonds, and, as a result, silicon precursors are less susceptible to protodemetalation, which is a potential problem with tin compounds. Although pentafluorosilicates have been used as precursors for radioiodination [16], most radioiododesilylation reactions have been performed using trimethylsilyl precursors. As with tin precursors, the most common methods for the synthesis of aryl trimethylsilanes are (a) the electrophilic silylation of aryl anions generated via different metal reagents and (b) the palladium-catalyzed silylation using hexamethyldisilane [17], both using a haloarene as the starting material.

Iododemercuration Given that the carbon-mercury bond energy is lower than that for the corresponding carbon-tin bond, halodemercuration should be more facile than iododestannylation [18], and indeed, high radiochemical yields have been reported for this reaction [19, 20]. However, applications of this approach for the synthesis of radioiodinated compounds are few and far between. The mercury precursors were synthesized by the treatment of des-iodo compounds with mercuric salts such as mercuric halide, acetate, or trifluoroacetate, whereby a hydrogen was replaced with HgX (X = F, Cl, Br, I, CH_3COO, or CF_3COO). In some cases, other metallic precursors have been transmetallated to mercury derivatives [21].

Iododeboronation Like silicon compounds, organoborane compounds have relatively low toxicity, an attractive feature for their use as radioiodo precursors when *in vivo* studies are contemplated [22]. A variety of aliphatic and aromatic iodo compounds have been radiolabeled using boron precursors. Initial studies involved the electrophilic radioiodination of trialkylboranes, yielding compounds in which iodine is attached to an sp^3 carbon and hence very susceptible to *in vivo* deiodination. Subsequently, various other precursors such as boronic acids [23], boronates [24], potassium trifluoroborates [25], and triolborates [26] have been utilized for the synthesis of radioiodinated compounds. The synthesis of boronic acid precursors is often problematic, and their stability is frequently an issue. On the other hand, boronate esters, trifluoroborate salts, and triolborate are air-stable crystalline solids. Problems associated with the synthesis of boronate precursors have been alleviated by utilizing Suzuki-Miyura coupling [22]. While reasonable radiochemical yields have been obtained using boron precursors, the presence of electron-withdrawing groups in aromatic rings results in poor yields.

Iododegermylation The energy and length of carbon-germanium bonds are intermediate compared to that of carbon-silicon and carbon-tin bonds; thus, radioiododegermylation is expected to be facile [27]. Furthermore, aryl germanium compounds are stable and less toxic than tin compounds. Good to excellent radiochemical yields have been reported for both activated and deactivated ring systems in various solvents using dichloramine-T as the oxidant. However, this radioiodination strategy has not been used extensively.

Iododethallation Iododethallation is not strictly electrophilic substitution with respect to iodination because in most cases, no oxidizing agent is used; however, thallium trifluoroacetate, used for thallation, can act as an oxidizing agent [1]. The exact mechanism is not clear, but the disproportionation of the diiodothallium intermediate is thought to render the iodo product. Aromatic compounds have been treated with thallium trifluoroacetate first to obtain the thallium derivative, which by itself is an electrophilic substitution reaction. The intermediate thallium derivative *in situ* was then treated with radioiodide [28]. Iododethallation is an *ipso* substitution reaction and predominantly gives one regioisomer. Iododethallation is not very attractive because thallium compounds are extremely toxic, and often carrier iodide must be added [28] for higher radiochemical yields. Ronnest *et al.* reported the synthesis of radioiodinated analogues of griseofulvin and lidocaine by first converting trimethylsilyl precursors to their thallium bis-trifluoroacetate

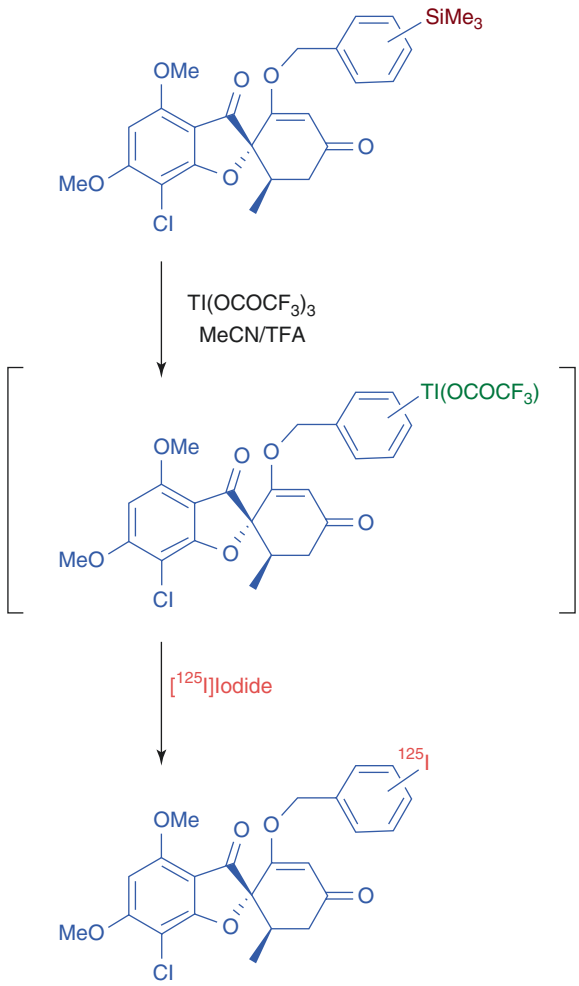

Fig. 4 Synthesis of radioiodinated isomers of Griseofulvin from silicon precursors via thallium intermediates

intermediates, which were treated *in situ* with radioiodide (Fig. 4) [29]. Although the radiochemical yield per se was not provided, HPLC data for the reaction mixtures indicate predominantly one peak corresponding to the product. It is noteworthy that carrier iodide was not used in these cases.

Radioiodination by Nucleophilic Substitution This type of labeling is predominantly carried out for iodoalkanes and iodoarenes by S_N2 and S_NAr reactions, respectively. Because S_N2 substitution is practically not possible on vinylic carbons, radioiodinated iodovinyl compounds are almost always derived from their metallic precursors by the electrophilic method. Depending on the substrate and reaction conditions, S_N1 reactions are also possible with aliphatic compounds. Although halides can be used as leaving groups, sulfonates such as triflate and tosylate are much better leaving groups. As opposed to electrophilic substitution of aromatic compounds, S_NAr reactions are facilitated by electron-withdrawing groups *ortho* and *para* to the nucleofuge.

Exchange Radioiodination There are two types of radioiodination by halogen exchange—homo/isotopic exchange and hetero/halogen exchange. In the former, an existing iodine in the molecule is replaced with an iodine radioisotope (radioiododeiodination). In hetero exchange, a halogen other than iodine, typically a bromine, is replaced with an iodine radioisotope (radioiododehalogenation/bromination). This is often referred to as a Finkelstein reaction. A major drawback of labeling by homo exchange is that the product contains carrier that cannot be separated from the labeled species, which results in low molar activity. Although the chromatographic characteristics of bromo- and iodo-analogues are similar, it is often possible to separate them, with the result that no-carrier-added radioiodinated compounds can be obtained by hetero exchange labeling. These reactions are generally performed at high temperatures in solution, solid-state conditions, or by melt methods. For example, the first radiosynthesis of the adrenomedullary imaging agent *meta*-iodobenzylguanidine (MIBG) was performed by homo iodo-exchange under solid-state conditions [30].

Exchange radioiodinations can be facilitated by metal salts, with copper being the metal most frequently used for this purpose. Initially, Cu(II) salts were used; however, radiochemical yields were only moderate with these reagents. The use of Cu(I) salts did not increase the yield considerably, presumably due to their oxidation to Cu(II) under the reaction conditions [31]. The use of Cu(II) salts along with a reducing agent such as gentisic acid or $SnSO_4$ consistently gave excellent yields for several radioiodinated pharmaceuticals. However, the presence of functional groups in the substrate that are susceptible to reducing conditions is a concern. While various solvents can be used, there are some restrictions when using certain solvents. For example, acetonitrile forms a complex with Cu^+ that leads to decreased radiochemical yields, but a method has been devised to overcome this problem [32]. Similarly, the use of alcoholic solvents can potentially result in the formation of the corresponding alkyl iodide, leading to lower yields of the desired radiopharmaceutical. Many mechanisms, including radical pathways and the formation of an *ipso*-complex of the dihaloarene, have been proposed for Cu^+-assisted radioiodination [33–36]. This exchange method has been extended to the synthesis of radioiodinated heteroaromatic compounds [36]. While conventional Cu^+-assisted radioiodination conditions—including the presence of $SnSO_4$—can be applied to halopyridines, the radioiodination of 2-halopyridine works better without $SnSO_4$.

Other transition metals have been used for exchange radioiodinations. For example, Ni(0)-mediated radioiodination of aryl and heteroaryl bromides has been reported [37]. While high radiochemical yields were generally obtained, the reaction needs to be conducted at a temperature of 180 °C. Despite using such a high temperature, the formation of radioiodinated byproducts was not seen. In addition

to the use of high temperature, another drawback of this method is that it is difficult to handle the nickel reagent, bis(1,5-cyclooctadiene)nickel(0), because it is moisture- and air-sensitive [38].

Copper-Mediated Conversion of Aryl and Heteroaryl Boron Reagents Building upon their work on ^{18}F-labeling with boron precursors, Gouverneur and colleagues have reported the copper-mediated radioiodination of (hetero)aryl boronic acid, boronates, and trifluoroborate salts using anionic radioiodide (Fig. 5a) [38]. Although these investigators tried using Cu_2O as the Cu(I) source, radiochemical yields were only moderate. Optimized reaction conditions involved heating the precursor (15 μmol) and [^{123}I]NaI along with $Cu(OCOCF_3)_2$ (0.30 μmol), 1,10-phenanthroline (0.30 μmol) in MeOH:H_2O (4:1, ~200 μL) at 80 °C for 20 min. Unlike electrophilic iododeborylations, high radiochemical yields were obtained for compounds with both electron-donating and electron-withdrawing substituents; however, *ortho* substituents were a problem. Almost simultaneously, another group published a similar approach for the Cu(I)-mediated radioiodination of (hetero)aryl boronic acids [39]. They used Cu_2O as the Cu(I) source and milder reaction conditions. Their optimized conditions are as follows: the precursor (2 μmol) was added to a solution (50 μL) of Cu_2O (0.4 μmol) and 1,10-phenanthroline (0.8 μmol) in acetonitrile, followed by radioiodide (5 μL), and the reaction was allowed to proceed at 25 °C for 1 h. Almost quantitative radiochemical yields were obtained with several compounds containing electron-donating or electron-withdrawing groups. An active ester-containing *N*-succinimidyl 4-[^{131}I]iodobenzoate (*para*-[^{131}I]SIB) was synthesized in 99% radiochemical yield, but the reaction was performed under anhydrous conditions (Fig. 5b).

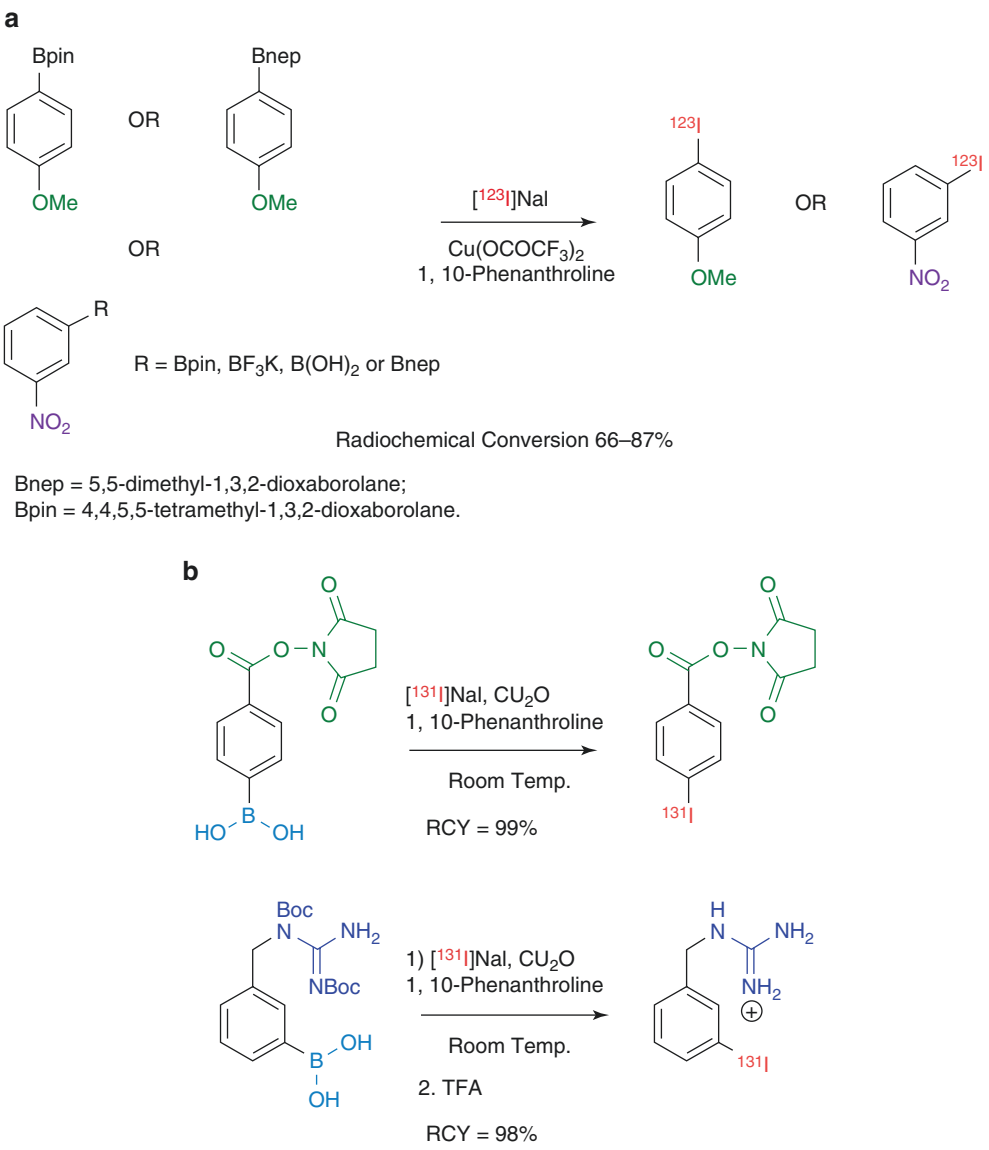

Fig. 5 (**a**) Copper-mediated radioiodination of aryl boronic acid, boronates, and trifluoroborate salts using radioiodide. (**b**) Synthesis of *para*-[^{131}I]SIB and [^{131}I]MIBG via radioiodination of aryl boronic acids using Cu_2O as the Cu(I) source

Iododediazonization A classical method in organic chemistry for the synthesis of aryl iodides utilizes the Sandmeyer reaction, which converts anilines to iodoarenes via an unstable diazonium intermediate. Diazonium salts—formed by treatment of anilines with sodium nitrite and HCl or H_2SO_4 at a low temperature—are reacted with sodium or potassium iodide. While this reaction has been adapted for the synthesis of a few radioiodinated agents [40], it is primarily of historic interest due to a number of significant limitations. First, the substrate should not contain functional groups that are susceptible to acidic conditions, and a suitable aniline precursor should be readily available. The instability of the diazonium intermediate leads to side products such as phenols and desamino derivatives that contribute to low radiochemical yields of the desired product. The Sandmeyer reaction is facilitated by copper salts. An opioid peptide, α-neoendorphin, was radioiodinated by the Sandmeyer reaction using copper catalysts containing non-nucleophilic ligands in about 30% radiochemical yield [41]. Although crown ethers are known to stabilize the diazonium intermediate and help increase the solubility of Cu(I) salts, the addition of 18-crown-6 did not provide any advantage in the radioiodination of α-neoendorphin.

From Triazines The issue of the instability of diazonium salts can be overcome to a degree by converting them to somewhat more stable and isolable triazenes. The Wallach reaction—which involves the transformation of triazenes to iodo derivatives by treatment with protic acids like methane sulfonic acid and sodium/potassium iodide or with a Lewis acid like trimethylsilyl iodide—has been adapted for radioiodination (Fig. 6). Examples include the synthesis of a radioiodinated proteasome inhibitor peptide [42] and SIB [43]. Although dependent on the substrate, solvent, and other conditions, this method generally delivers products in high radiochemical yields and molar activity [44].

Iodonium Salt Precursors Iodonium salt precursors have been used recently for the synthesis of ^{18}F-labeled radiopharmaceuticals. As an alternative to the Sandmeyer reaction, Dimagno and colleagues explored the usefulness of iodonium salts in the synthesis of non-radiolabeled iodoarenes [45]. The potential use of these reagents for the synthesis of radioiodinated compounds such as MIBG has been reported in the patent literature (Fig. 7) [46]. Recently, Guerard *et al.* compared the radiohalogenation of iodonium salts with ^{211}At and ^{125}I [47]. While radiochemical yields for astatination were independent of the solvent used, radioiodination gave highest yields in acetonitrile. Also, radioiodination yields depended on the substituents, but astatination gave almost quantitative yields irrespective of the substituents present. Further, better radiochemical yields were obtained when the counter ion was tosylate or triflate. In another study,

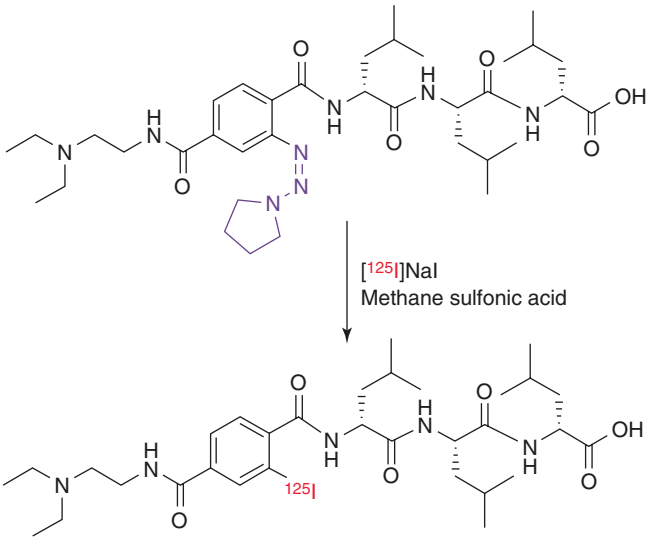

Fig. 6 Radioiodination using triazene precursor exemplified by the synthesis of a radioiodinated proteasome inhibitor peptide

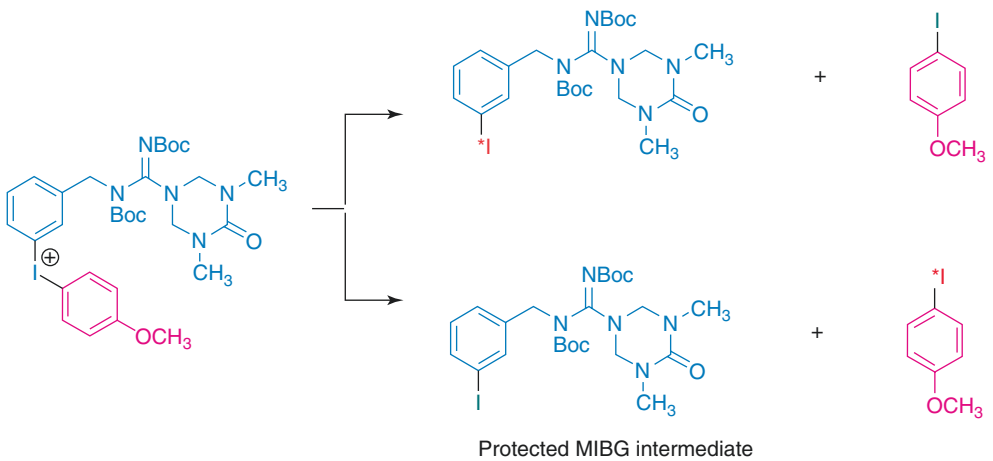

Fig. 7 Synthesis of radioiodinated protected form of MIBG from an iodonium salt precursor, with the desired ring in blue and the expendable ring in pink

the synthesis of a modified Bolton-Hunter reagent (see below), *N*-succinimidyl 3-(4-iodophenyl)propanoate, was achieved starting from an iodonium precursor; however, radiochemical yields were not provided [48]. In addition to the use of relatively high reaction temperatures, a potential drawback of this labeling method is the formation of carrier as a byproduct when the radioiodide attaches to the "expendable" ring versus the "desired" ring of the iodonium precursor, thereby reducing molar activity.

Kit Methods for Radioiodination

To obtain the final radiopharmaceutical in a very pure form, one must almost always rely on HPLC purification, which is time-consuming and requires expensive equipment and skilled technicians. To increase the suitability of promising radiopharmaceuticals for routine use, solid-phase synthesis has been explored for radioiodination. Essentially, an appropriate precursor is attached to an insoluble (or soluble, see below) matrix such as polystyrene. When subjected to radioiodination conditions, the radioiodinated product breaks free, while the excess unreacted precursor remains attached to the support (Fig. 8a). The radioiodinated product can be obtained in a pure form by a simple filtration.

Tin-Based Precursors The pioneering work in this area was done by Hunter and colleagues, who reported the synthesis of radioiodinated *N*-isopropyl-4-iodoamphetamine [49] and MIBG [50] from their respective polymer-supported tin precursors. Using H_2O_2 in acetic acid as the oxidizing agent, near-quantitative radiochemical yields were obtained for [^{131}I]MIBG. Radioiodinated MIBG synthesized by this method has been used in clinical studies [51]. This approach of radioiodination has been extended to the synthesis of SIB [52, 53], Congo Red [54], and other compounds [53]. Tin precursors were synthesized by reacting the polymer-bound dialkyl tin chloride with the corresponding aryl metal (Li or Zn) reagent. It is imperative that functional groups incompatible with these conditions be protected. Unfortunately, attempts to synthesize polymer-bound distannanes that could potentially be used in the alternative palladium-mediated Stille coupling approach to precursor synthesis were futile [55].

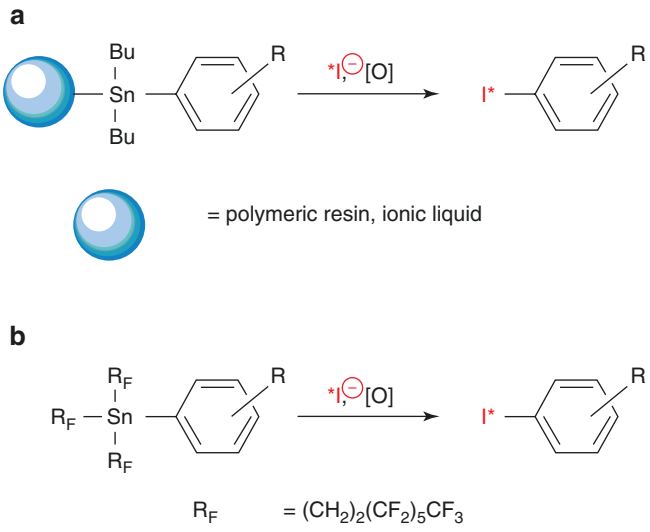

Fig. 8 General scheme for a radioiodination reaction starting with (**a**) a tin precursor anchored to an insoluble support and (**b**) a fluorous tin precursor

A recent study evaluated the usefulness of ionic-liquid-bound tin precursors for radioiodination [56]. The tin precursor of SIB immobilized on an ionic liquid was synthesized and converted to [^{125}I]SIB in 67% radiochemical yield. Purification was achieved by passing the reaction mixture over a silica cartridge to obtain the product in 100% radiochemical purity. However, the synthesis of the precursor was tedious.

Instead of using an immobilized precursor, a recent method exploited the differential solubility of the iodo product and the tin precursor for the development of a synthesis of no-carrier-added [*I]MIBG ([*I] is used to indicate that multiple iodine radioisotopes have been evaluated) that could be potentially adapted for a kit method [57]. The purification involved the treatment of the reaction mixture with an anion-exchange resin and filtration, and [^{131}I]MIBG was synthesized in 72% radiochemical yield and >97% radiochemical purity. Importantly, the tin content of the final preparation was <1.2 parts per billion.

The solid-phase approach described above suffers from some disadvantages, including difficulties in obtaining the precursor in homogeneous form and batch-to-batch variability in its loading. Furthermore, reactions are slower when performed under heterogeneous conditions than homogeneous conditions. An alternative strategy would be to use soluble supports composed of well-defined structures. Based on the "fluorous" technology developed by Curran's group at the University of Pittsburgh, Valliant and colleagues have developed tin precursors for radioiodination that are attached to fluorous supports [58, 59]. These are relatively small, fluorine-rich molecules with defined structure, which can be well-characterized by standard techniques such as NMR and mass spectrometry. The radioiodinated product can be isolated from the reaction mixture by passage over a fluorous solid-phase cartridge, which preferentially retains fluorine-rich compounds compared to those with no (or lower) fluorine content (Fig. 8b). In their first study, several benzamide precursors were made via tetrafluorophenyl (TFP) ester intermediates and radioiodinated with >85% radiochemical yields and 99% radiochemical purity [60]. In addition to adapting this method to several other radioiodinated compounds including MIBG, they developed a hybrid solid-

fluorous phase radioiodination and purification platform that permits solution phase labeling and fluorous phase purification to be performed in one step [59]. Fluorous phase radioiodination has been utilized for the synthesis of a prosthetic agent useful in labeling molecules with either radioiodine or ^{18}F [61]. Currently, the supply of the fluorous reagents at a reasonable cost is unreliable, which is an impediment to the further development of this promising approach.

The application of biotin-containing stannane precursors for radioiodination has been reported in the patent literature [62]. Preliminary data on the feasibility of purifying the radioiodinated products by passing the reaction mixture through a commercially available streptavidin resin cartridge has been presented [63].

Supported Precursors Based on Other Metals Radioiodination using supported precursors of other metals has also been described. The synthesis of [^{123}I]iodometomidate was accomplished using a silicon-based precursor soluble in organic solvents [64]. The radioiodination was performed by heating the polymer along with NCS and [^{123}I] iodide in TFA at 40 °C for 60 min. The TFA was neutralized with a polymer-bound diisopropyl ethylamine, and the reaction mixture was diluted with dichloromethane. The reaction mixture was passed through a silica cartridge to remove the polymer, and the radiolabeled product was isolated in 85% radiochemical yield by subsequent elution of the cartridge with 10% methanol in dichloromethane. Several radioiodinated compounds were synthesized using corresponding Dowex-supported organotrifluoroborates by refluxing a mixture of the precursor, Chloramine-T, and radioiodide in 1:1 THF/water for 20–30 min [65]. Radiochemical yields were a bit lower than those obtained with non-supported precursors presumably due to the heterogeneous reaction conditions. Polymer-supported germanium precursors also have been utilized to synthesize iodinated compounds, with an extension to radioiodination proposed but not performed [66].

Radioiodination of Peptides and Proteins

Unlike small organic molecules, proteins, and in some cases, peptides, cannot be subjected to harsh conditions without loss of biological function. Direct iodination was the original approach for the radioiodination of proteins and peptides, and while several amino acids including histidines can potentially be radioiodinated, tyrosine residues are the most frequent site of radioiodination. Although direct labeling is quite simple, a major disadvantage of direct radioiodination is the extensive deiodination of these labeled molecules *in vivo*. This has led to the development of methods for labeling proteins and peptides via the conjugation of prosthetic agents with enhanced biological stability.

Peptides Unlike the case with proteins, labeling reactions of many peptides can be performed in organic solvents, with oxidants, under acidic conditions, and at higher temperatures. Further, it is often possible to purify radioiodinated peptides by reversed-phase HPLC. If the peptide has a constituent tyrosine residue, then the first choice, particularly for *in vitro* studies, will be to use the direct electrophilic method for iodination unless it adversely affects the peptide function. In peptides lacking a tyrosine, one can be introduced provided it does not affect the overall properties of the peptide. For labeling using radioiodinated prosthetic agents, usually amino (*N*-terminus and lysine side chain) and sulfhydryl (cysteine) groups are modified. There is the option of incorporating unnatural amino acids such as those containing azido or alkyne functions for labeling via a click reaction. If constituent lysine or cysteine residues are important for the biological function of the peptide, it is imperative that they are protected before reacting the peptide with pre-labeled prosthetic agents and then deprotected later.

Direct Radioiodination Many peptides containing tyrosine residues have been radioiodinated by the direct electrophilic approach. Typically, reactions are done in phosphate buffer at room temperature for 5–10 min at a pH of around 7.0–7.5 using oxidants such as Chloramine-T or Iodogen. The reaction is quenched using a reducing agent such as sodium bisulfite, and labeled peptides are often purified by reversed-phase HPLC, although in some cases, simple solid-phase extraction has been used. The formation of the diiodinated by-product has been reported in certain instances [67]. To overcome the problem of *in vivo* instability, L-tyrosine can be replaced with D-tyrosine, which is less susceptible to deiodination, provided this does not affect the peptide's function [68]. The radioiodination of peptides by nucleophilic substitution—either by copper-assisted exchange reaction [69] or iododediazonization [41]—has also been reported.

Radioiodination via Pre-labeled Prosthetic Groups The advantages of this method are that peptides are not subjected to potentially harmful oxidants and with an appropriately designed labeled prosthetic group, the radiolabeled peptide will be stable toward *in vivo* deiodination. However, the prosthetic agent needs to be synthesized and purified beforehand, which requires chemical expertise and time. Furthermore, the overall radiochemical yield and molar activity of the final labeled peptide will be lower. Amine and sulfhydryl groups on the peptide are the sites that are generally modified with prosthetic agents. For modifying amine groups, prosthetic agents containing an active ester such as *N*-hydroxysuccinimidyl (NHS) and, less frequently, tetrafluorophenyl (TFP) or their water-soluble sulfo (SO_3H-substituted) derivatives have been employed (Fig. 9a). The most common prosthetic agents employed for the

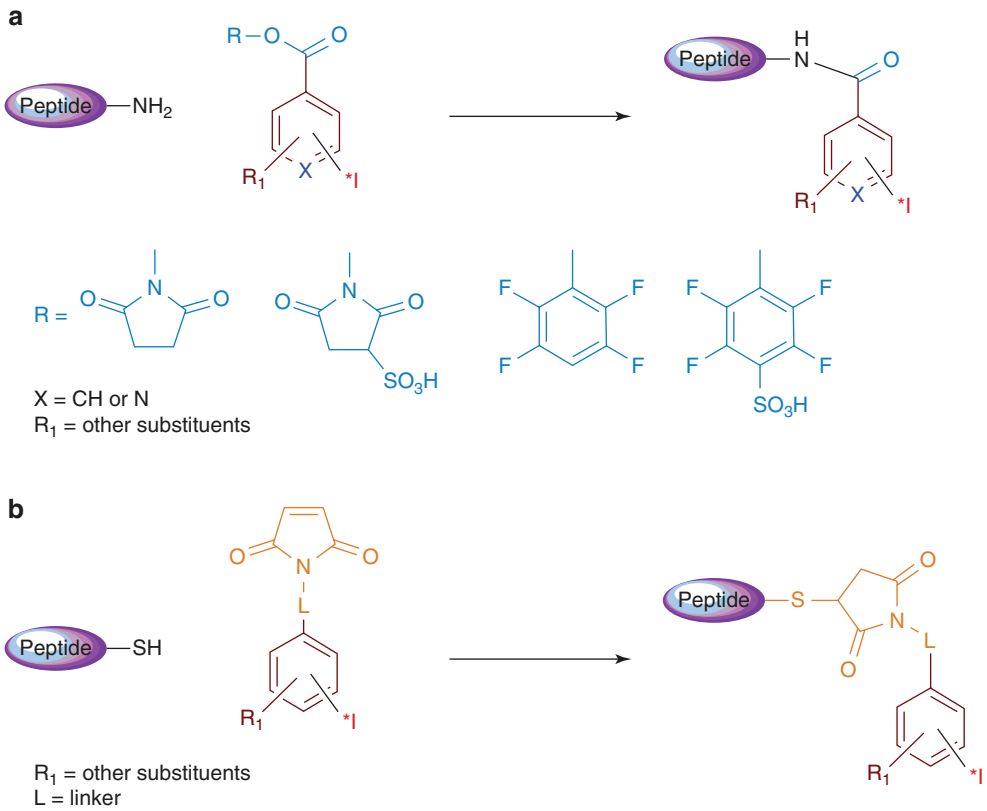

Fig. 9 Radioiodination of peptides by reaction with pre-labeled prosthetic agents: (**a**) via the modification of an amine function and (**b**) via the modification of a sulfhydryl function

radioiodination of peptides by modification of an amine group are *meta* and *para*-[*I]SIB; reagents such as *N*-succinimidyl 5-[*I]iodo-3-pyridine carboxylate ([*I]SIPC), 2,3,5,6-tetrafluorophenyl 5-[^{123}I]iodo-4-pentenoate (TFP-[^{123}I]I-PEA), as well as others also are used [61, 70–72]. Typically, the conjugation reaction is performed by the reaction of the peptide with a labeled prosthetic agent in a solvent such as DMF or acetonitrile in the presence of a tertiary amine. If the peptide is water soluble, the reaction can be performed in pH 8–9 buffers alone or along with a water-miscible organic solvent like acetonitrile [52, 61].

For sulfhydryl group modification, most of the prosthetic agents contain a maleimido function [73, 74] (Fig. 9b); however, agents containing active halides such as bromoacetyl groups as well as disulfides are also used. Often, the introduction of a cysteine onto the peptide is necessary, which facilitates site-specific labeling. The conjugation reaction is performed under physiological conditions and gives relatively high radiochemical yields.

Preconjugation of Precursor Moiety As indicated above, the synthesis and purification of the radioiodinated prosthetic agent takes time and effort. On the other hand, if a tin- or another metal-bearing moiety can be attached to the peptide, radioiodination can be performed in a single step (Fig. 10) [70, 75, 76]. Orthogonal protection strategies may be needed to protect sensitive amino acid residues as well as the tin moiety [76]. The presence of tyrosines on the peptide that can also be labeled is another concern that may be ameliorated in the future by optimizing the pH to favor chemoselective radioiodination at the tin moiety.

Radioiodination by Click Reactions Click reactions such as the copper-catalyzed azide-alkyne cycloaddition (CuAAC), the strain-promoted azide-alkyne cycloaddition (SPAAC) between an azide and dibenzocyclooctyne (DBCO) that does not need a copper catalyst, and the inverse electron demand Diels-Alder reactions (IEDDA) have all been used for radiolabeling biomolecules, especially with ^{18}F. In a few cases, this approach has been adapted for radioiodination of peptides (Fig. 11) [77]. While site-specific labeling can be achieved, the introduction of relatively large moieties onto small peptides can affect their affinity for their biological targets as well as their tissue distribution.

Proteins Unlike most peptides, proteins cannot be subjected to harsh conditions and their radioiodination should be performed under mild conditions in aqueous buffers, ideally at pH values closer to physiological pH. While the most commonly used method of radioiodination of proteins is the direct electrophilic approach, numerous pre-labeled prosthetic agents are now used routinely.

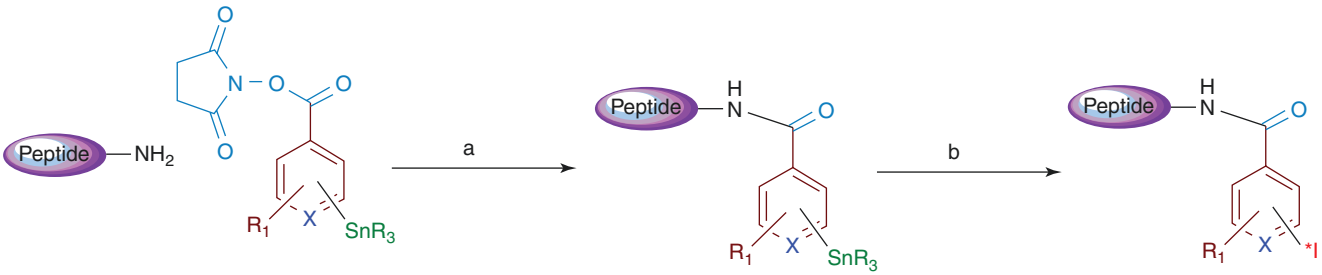

a) Conjugation of a tin moiety-bearing active ester to an orthogonally protected peptide and subsequent removal of protecting groups. b) Radioiodination

R_1 = other substituents; X = CH or N

Fig. 10 Radioiodination of a peptide via preconjugation of a trialkyl tin moiety

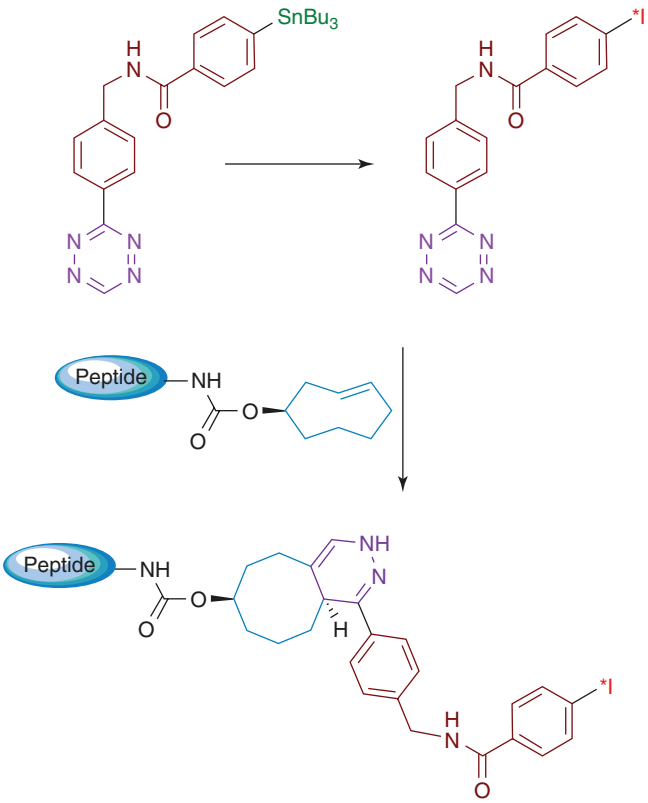

Fig. 11 Radioiodination of a peptide via the inverse electron demand Diels-Alder cycloaddition between tetrazine and *trans*-cyclooctene

Direct Method This procedure involves simple mixing of the protein with radioiodide in the presence of an oxidizing agent for 5–10 min, quenching the reaction with a reducing agent, and isolating the labeled protein by gravity gel filtration. It is easy to perform; however, as in the case with peptides, two major drawbacks of direct labeling are the potential oxidation of amino acids such as tryptophan in the protein and the susceptibility of the products to *in vivo* deiodination. In addition, proteins that undergo extensive internalization after antigen or receptor binding are subjected to degradation by lysosomal proteases, which leads to the rapid washout of free iodide and monoiodotyrosine, the two principle radiolabeled catabolites generated from radioiodinated proteins.

Prosthetic Agents Radioiodination via prosthetic agents avoids subjecting proteins to oxidizing (and reducing) conditions [78] and allows labeling of proteins lacking tyrosines or other iodine-reactive amino acids. Amino groups (*N*-terminal and lysine side chain) and sulfhydryl groups—generated by treatment with Traut's reagent (iminothiolane) or by the site-specific recombinant insertion of cysteine—are the two moieties that are generally used for prosthetic group conjugation. Other conjugation sites that have been modified for radiolabeling include carboxylates and oxidized carbohydrates. The most widely used agents for conjugations to amines include *N*-hydroxysuccinimidyl (NHS) and tetrafluorophenyl (TFP) esters as well as their sulfonated versions. The conjugation efficiency depends on the pH, protein concentration, and temperature. Because the equilibrium shifts from the protonated to the neutral form of the amino group with increasing pH, conjugation efficiency should increase with increasing pH; however, the efficiency of the competing reaction—the hydrolysis of the active ester—also increases with pH. Although TFP esters are more stable than NHS esters at higher pH, NHS esters are used more frequently. Higher conjugation yields can be obtained with higher protein concentrations but at the cost of decreasing molar activity. Reagents containing aldehydes, isothiocyanates, imidate esters, and bromoacetyl/bromoacetamido functionalities have also been employed for amine conjugation. Although not used frequently anymore, radioiodinated acids have been coupled to proteins using water-soluble carbodimides.

The Bolton-Hunter reagent was the first active ester prosthetic agent developed for protein radioiodination (Fig. 12) [79] and has been used to label a variety of proteins with different iodine radioisotopes. The unlabeled precursor and

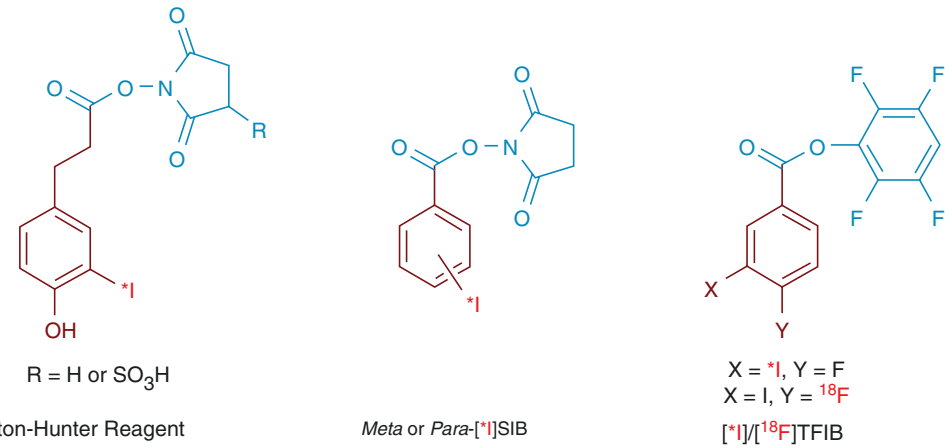

Fig. 12 Structures of the Bolton-Hunter reagent (simple and sulfonated versions), SIB and TFIB

SIB = *N*-succinimidyl iodobenzoate; TFIB = Tetrafluorophenyl 4-fluoro-3-iodobenzoate

mono- and di-radioiodinated versions all are commercially available. Analogues with SO_3H substitution in the succinimidyl ring to increase water solubility also are in use. As with other NHS esters, the conjugation reaction can be performed by incubating the protein in pH 8.5–9.0 buffer at room temperature for 15–20 min.

The Bolton-Hunter reagent suffers from the fact that the iodine is placed on a carbon *ortho* to a hydroxyl group. As a consequence, proteins labeled by the Bolton-Hunter method are susceptible to *in vivo* deiodination because of both reduced carbon-iodine bond strength and the structural similarity of the labeling site to thyroid hormones. To overcome this, two isomeric *N*-succinimidyl [*I]iodobenzoates (SIB) (see Fig. 12) that can be synthesized at high molar activities from the corresponding tin precursors were introduced in the late 1980s [80, 81]. Indeed, a 50–100-fold advantage with respect to deiodination—as demonstrated by lower thyroid uptake (an indicator of deiodination)—was seen for proteins labeled using SIB versus direct radioiodination. Several other prosthetic agents for the radioiodination of proteins have been developed since [82, 83]. Also, several radioiodinated iodo-triazole compounds have been synthesized by a one-pot, three-component Cu(II)-mediated reaction of azide, alkyne, and radioiodide [84], with some of these compounds containing NHS ester and maleimide moieties for conjugation with proteins.

As discussed in a previous section, the availability of iodine radioisotopes with good properties for imaging and therapy makes them ideal for the development of theranostic agents. It is also possible to develop multimodal agents for other modes of imaging and therapy. For example, a radioiodinated BODIPY analogue has been developed that can be conjugated with peptides and proteins for optical/nuclear imaging and targeted radiotherapy (Fig. 13) [85]. Also, a prosthetic agent that can be labeled with either radioiodine or fluorine-18 has been developed (see Fig. 12) [61].

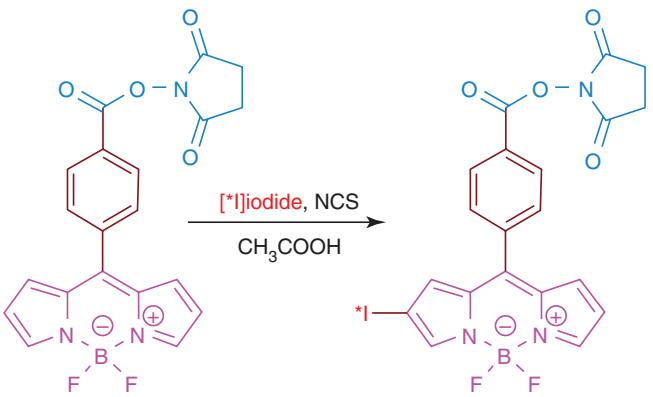

Fig. 13 A prosthetic agent containing both a BODIPY moiety and radioiodine is potentially useful in multimodal imaging as well as for radiotherapy

Residualizing Labels For antibodies and other proteins that undergo extensive internalization after antigen or receptor binding, the cumulative activity in tumor cells is often low when they have been radioiodinated by the direct method or using prosthetic agents like SIB. Several so-called residualizing labels have been developed to overcome this problem [82]. The first-generation ones (*e.g.* cellobiose-tyramine-cyanuric chloride conjugate; Fig. 14) were designed on the premise that radiolabeled catabolites containing nonmetabolized, polar carbohydrate moieties would not cross lysosomal and cellular membranes [86]. Although enhanced tumor retention of activity was achievable when internalizing antibodies were radioiodinated by this approach, poor conjugation efficiencies, protein cross-linking, diminished immunoreactivity, and high liver uptake were problems associated with this labeling chemistry.

Two other residualizing radioiodination strategies involve charged molecules and D-peptide fragments containing at least three amino acids because these species should not

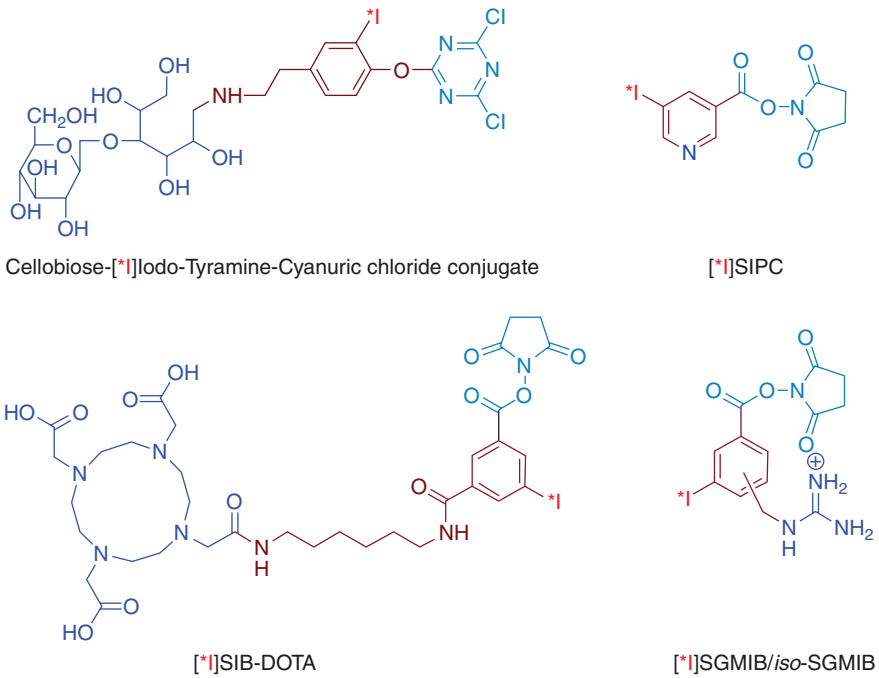

Fig. 14 Structures of selected residualizing labeling agents—cellobiose-iodotyramine-cyanuric chloride, SIPC, SIB-DOTA, and SGMIB. Residualization-enhancing moieties are shown in dark blue, and conjugating moieties in light blue

SPIC = *N*-succinimidyl 5-iodo-pyridine-3-carboxylate; SGMIB = *N*-succinimidyl 4-guanidinomethyl-3-iodobenzoate; *iso*-SGMIB = *N*-succinimidyl 5-guanidinomethyl-3-iodobenzoate; SIB-DOTA = 2,2′,2″-(10-(2-(6-(3-((2,5-dioxopyrrolidin-1-yloxy)carbonyl)-5-iodobenzamido)hexylamino)-2-oxoethyl)-1,4,7,10-tetraazacyclododecane-1,4,7-triyl)triacetic acid

cross cell or lysosomal membranes. Reagents such as SIPC and *N*-succinimidyl 4/5-guanidinomethyl-3-iodobenzoate (SGMIB/iso-SGMIB) (see Fig. 14) contain moieties that should be positively charged at lysosomal pH [7, 87]. Residualizing labels containing negatively charged functional groups [88] and short proteolytically resistant peptides containing positively or negatively charged D-amino acids also have been developed [89–91]. Surprisingly, the tumor targeting of an antibody radioiodinated using a peptide consisting of all D-amino acids was lower than the same antibody labeled via the same peptide but with one constituent D-tyrosine replaced with its L-isomer [91]. Antibodies radiolabeled using chelate-complexed metal radionuclides often have excellent residualizing properties, which has led to the development of chelate-containing residualizing labels for radioiodination (see Fig. 14) [92–94].

While enhanced tumor retention has been observed for antibodies and fragments radioiodinated using all the residualizing labeling methods described above, their synthesis in general is a bit involved. The future development of kit methods for their synthesis should alleviate this problem.

Click Chemistry/Biorthogonal Coupling and Pre-Targeting Strategies In a few instances, click chemistry has been used for the radioiodination of proteins and peptides. For example, an anti-VEGF antibody and insulin were radioiodinated using the IEDDA reaction between tetrazine(Tz) and *trans*-cyclooctene (TCO) [95]. The reaction between the TCO-modified antibody and the radioiodinated Tz was accomplished in a few minutes in 70% radiochemical yield. The labeled antibody bound specifically to its target and had considerably lower deiodination *in vivo* compared with the same antibody radioiodinated by direct labeling or using the Bolton-Hunter reagent. In addition, a DBCO-derivatized antibody was labeled via SPAAC reaction with radioiodinated, azide-containing peptides in moderate radiochemical yields [91].

Deiodination

Before the development of more biologically inspired labeling methods, a significant impediment to the *in vivo* application of many radioiodinated pharmaceuticals was their extensive deiodination *in vivo* [96]. At least two factors contribute to this behavior: (1) the relatively low carbon-iodine bond strength and (2) deiodination induced by enzymes such as iodotyrosine deiodinase, iodothyronine deiodinase, and some nucleophilic and oxidative enzymes. The free iodide generated by these processes is avidly taken up by the thyroid and other tissues such as the stomach and salivary gland, which is problematic because it increases background

signal that can interfere with imaging and increases the radiation dose to these tissues, which can be an impediment for radionuclide therapy. The deleterious effects of deiodination on normal tissues can be minimized by pretreatment with non-radioactive iodide; however, this does not compensate for loss of signal (or therapeutic dose) to the tumor or other cells that were the intended biological target. Certainly, the structure of a radioiodinated molecule plays an important role in its inertness to deiodination. By understanding the factors that contribute to deiodination, this problem can largely be circumvented, particularly in the design of prosthetic agents for labeling proteins and peptides. As exemplified by SIB [80, 81], by designing an iodination site structurally dissimilar to thyroid hormones, deiodination could be reduced by up to two orders of magnitude. Other strategies have focused on improving the stability of the bond between the iodine and the compound. For example, because a boron-iodine bond is much stronger than the analogous carbon-iodine bond, prosthetic agents based on carboranes have been developed, and recently a radioiodinated, carborane-functionalized tetrazine was synthesized for the labeling of antibodies via the IEDDA reaction [97]. Alternatively, the stability of the carbon-iodine bond might be increased through the judicious use of substituents like fluorines *ortho* to the iodine-bearing carbon [98].

Tricks of the Trade

The presence of higher oxidation state species of iodine such as iodate and periodate in commercial radioiodide solutions can have a deleterious effect on radiochemical yields. This is especially the case with ^{123}I and ^{124}I, which has been attributed to the effects of the high-energy processes involved in their production and radiolysis [99]. The proportion of these impurities increase with increasing storage time. One method to remove these impurities is treatment with hydrazine, passage over cation- and anion-exchange columns, and elution from the anion-exchange column with saline [100]. While the use of ascorbic acid also has been prescribed for this, it did not work well with ^{124}I [78]. A "carrier mix" containing NaI and $NaIO_3$ worked for ^{124}I; however, this cannot be used when obtaining high molar activity is essential [78]. In this case, the "Iodogen-coated mAb" method—which gave high radiochemical yields—was used for the radioiodination of monoclonal antibodies, where maximizing molar activity is not critical. Also, it has been shown that the addition of carrier in an amount equivalent to that present in an equidose of ^{125}I can enhance yields when labeling with high specific activity ^{123}I.

The use of solutions with pH values that are appropriate for each radioiodination reaction is essential for optimizing yields. Iododestannylation reactions work best when performed at slightly acidic conditions; for example, in the synthesis of [^{123}I]iomazenil from a tin precursor, radiochemical yields decreased at pH values greater than 5.8 [10]. Copper-assisted nucleophilic exchange radioiodinations are also favored at acidic pH, typically around 2–3. For direct iodinations of tyrosine (either alone, in a protein or peptide) by electrophilic substitution, the optimal pH is about 7.5. Depending on the oxidant, reasonable radiochemical yields can be obtained at lower pH values, but the yield precipitously decreases at higher pH. For labeling peptides and proteins by conjugation with active ester-containing prosthetic agents, the optimal pH is typically around 8.5. Because these procedures mostly involve the modification of lysine side chain amino groups with pKa ~ 10.5, basic pH is needed to shift the equilibrium toward the reactive, unprotonated amino group. However, too high a pH will be counterproductive for two reasons. First, the competitive hydrolysis of the active ester prosthetic agent also increases with higher pH. And second, pH well above physiological pH will not be tolerated by many proteins. Higher conjugation yields also can be obtained by using higher protein/peptide concentrations but at the expense of molar activity for a given amount of activity.

It is important to keep in mind that several functional groups may not be stable under the conditions envisioned for radioiodination. Acid-sensitive groups will be a problem when the radioiodination is conducted at lower pH or when strong acids are used as solvents. Furthermore, functional groups that are susceptible to oxidizing conditions should not be present in the target compound. A case in point is thiourea, which is not stable in the presence of oxidants such as NCS [101]. In addition, the high temperatures used in some procedures may be detrimental to thermally labile functionalities. Although it is best to do radiochemical labeling in the least number of steps (preferably one) to maximize yield and minimize handling, it may be necessary to utilize multistep labeling procedures to overcome stability issues like these.

Particularly Important Works

The development of dehalogenation-resistant prosthetic agents for labeling peptides and proteins was a significant turning point. This helped not only to avoid subjecting delicate biomolecules to harsh oxidizing conditions but also to minimize recognition by deiodinases and thus reduce *in vivo* deiodination. Many such agents have been developed and the introduction of residualizing labeling strategies helped further increase cumulative activity in tumor, which is particularly important in the context of targeted radiotherapy.

It is important to perform radiolabeling reactions efficiently and rapidly to minimize radiation exposure to person-

nel, particularly at the high activity levels required for clinical radionuclide therapy studies. As is the case with radiolabeling procedures for other radionuclides, radioiodination can be achieved through the use of kit methods and automation. Iododemetallation, especially iododestannylation, is the reaction that is most amenable to kit formulation for the synthesis of low molecular weight radioiodinated compounds. In most cases, the radioiodination of compounds from their tin precursors can be achieved in one step. For this reason, the development of tin precursors anchored to a platform, especially the fluorous tin derivatives, is a significant achievement because it greatly facilitates the routine production of radioiodinated compounds. Although the number of radioiodinated agents developed to date using this technology is limited, several important compounds including MIBG, tetrafluorophenyl iodobenzoate (TIB), and TFIB have been synthesized. Perhaps the most noteworthy application of solid-phase/supported synthesis for radioiodinated compounds is the synthesis of radioiodinated MIBG from a tin precursor anchored to an insoluble resin. Subsequently, this technique has been adapted for the synthesis of the active ester SIB, which has many potential applications for protein and peptide labeling. These two methods—as well as the ionic-liquid-based method—should find widespread applications in the future for the synthesis of radioiodinated pharmaceuticals.

The Future

A major impediment to the use of investigational radiopharmaceuticals, including those labeled with radioiodine, is the ability to synthesize them under cGMP conditions in reproducible fashion. As regulatory constraints become more stringent, it will be critical to develop radioiodination procedures that meet these requirements. This will probably involve the adaptation of the automated synthesis devices currently used for PET for use with the radioisotopes of iodine. As noted above, the use of supported precursors will be a major part of this effort because it will greatly facilitate the purification of radiopharmaceuticals and obviate the need for an HPLC step during purification.

Molecular biological advances will make it possible to incorporate various unnatural amino acids into proteins with ease. This development will encourage radiolabeling by the bioorthogonal approach, which has not been investigated extensively with the radioisotopes of iodine. Another area that likely will be investigated intensively in the future is site-specific labeling assisted by ligation enzymes such as sortase, transglutaminase, and lipoic acid ligase. Although these methods require some expertise in molecular biology, the possibilities of introducing the radioiodine-carrying prosthetic agent at a known position (away from the antigen-binding site of the antibody) and with a precise prosthetic agent-to-antibody ratio are very attractive. With the emergence of smaller and smaller protein-based delivery vehicles such as single-domain antibody fragments and affibodies, the probability of conjugating the prosthetic agent in regions of the protein that are critical for target recognition increases, underscoring the importance of site-specific labeling. Moreover, having a radiolabeled protein conjugate with a defined and homogeneous structure should be advantageous from a regulatory perspective. Finally, with the availability of newer hybrid imaging systems, the development of radioiodine-containing multimodal agents for radionuclide imaging and therapy as well as multimodal imaging will be another important area for development.

The Bottom Line

- Electrophilic and nucleophilic substitution reactions, especially the former, are the predominant synthetic approaches used for radioiodination.
- Iododestannylation is the best and most widely used method for the radioiodination of low molecular weight compounds with the proviso that the contamination of the product with unreacted tin precursor can be avoided.
- While the direct radioiodination of peptides and proteins is very easy to perform, it is not recommended because these products undergo extensive deiodination *in vivo.*
- Prosthetic agents have been developed for the radioiodination of proteins and peptides that have largely solved the issue of deiodination.
- Unlike radiometal-labeled peptides and proteins, directly radioiodinated peptides and proteins are typically not residualizing. Although somewhat hard to synthesize, residualizing labels for radioiodination can overcome this problem.
- Anchoring tin precursors to insoluble resins and ionic liquids—as well as the generation of fluorous tin precursors—facilitates the synthesis of radioiodinated compounds via kit methods.

References

1. Mennicke E, Holschbach M, Coenen HH. Direct n.c.a. electrophilic radioiodination of deactivated arenes with N-chlorosuccinimide. J Labelled Compd Radiopharm. 2000;43(7):721–37.
2. Takahashi M, Seki K, Nishijima K, Zhao S, Kuge Y, Tamaki N, et al. Synthesis of a radioiodinated thymidine phosphorylase inhibitor and its preliminary evaluation as a potential SPECT tracer for angiogenic enzyme expression. J Labelled Compd Radiopharm. 2008;51(11–12):384–7.

3. Racys DT, Sharif SA, Pimlott SL, Sutherland A. Silver(I)-catalyzed iodination of Arenes: tuning the Lewis acidity of N-Iodosuccinimide activation. J Org Chem. 2016;81(3):772–80.
4. Tamborini L, Chen Y, Foss CA, Pinto A, Horti AG, Traynelis SF, et al. Development of radiolabeled ligands targeting the glutamate binding site of the N-methyl-d-aspartate receptor as potential imaging agents for brain. J Med Chem. 2016;59(24):11110–9.
5. Jia J, Song J, Dai J, Liu B, Cui M. Optically pure diphenoxy derivatives as more flexible probes for beta-amyloid plaques. ACS Chem Neurosci. 2016;7(9):1275–82.
6. Vaidyanathan G, Affleck DJ, Alston KL, Zalutsky MR. A tin precursor for the synthesis of no-carrier-added [*I]MIBG and [^{211}At]MABG. J Labelled Compd Radiopharm. 2007;50(3–4):177–82.
7. Garg S, Garg PK, Zalutsky MR. N-succinimidyl 5-(trialkylstannyl)-3-pyridinecarboxylates: a new class of reagents for protein radioiodination. Bioconjug Chem. 1991;2(1):50–6.
8. Chen K, He P, Zhang S, Li PF. Synthesis of aryl trimethylstannanes from aryl halides: an efficient photochemical method. Chem Commun. 2016;52(58):9125–8.
9. Seevers RH, Counsell RE. Radioiodination techniques for small organic molecules. Chem Rev. 1982;82(6):575–90.
10. Zea-Ponce Y, Baldwin RM, Zoghbi SS, Innis RB. Formation of 1-[^{123}I]iodobutane in labeling [^{123}I]iomazenil by iododestannylation: implications for the reaction mechanism. Appl Radiat Isot. 1994;45(1):63–8.
11. Arstad E, Hoff P, Skattebol L, Skretting A, Breistol K. Studies on the synthesis and biological properties of non-carrier-added [^{125}I and ^{131}I]-labeled arylalkylidenebisphosphonates: potent bone-seekers for diagnosis and therapy of malignant osseous lesions. J Med Chem. 2003;46(14):3021–32.
12. Vaidyanathan G, Zalutsky MR. No-carrier-added synthesis of meta-[^{131}I]iodobenzylguanidine. Appl Radiat Isot. 1993;44(3):621–8.
13. Green M, Lowe J, Kadirvel M, McMahon A, Westwood N, Chua S, et al. Radiosynthesis of no-carrier-added meta-[^{124}I]iodobenzylguanidine for PET imaging of metastatic neuroblastoma. J Radioanal Nucl Chem. 2017;311(1):727–32.
14. Champion S, Gross J, Robichaud AJ, Pimlott S. Radiosynthesis of ^{123}I-labelled benzimidazoles as novel single-photon emission computed tomography tracers for the histamine H3 receptor. J Labelled Compd Radiopharm. 2011;54(9–10):674–7.
15. Tang P, Ritter T. Silver-mediated fluorination of aryl silanes. Tetrahedron. 2011;67(24):4449–54.
16. Wilbur DS, Svitra ZV. Organopentafluorosilicates – reagents for rapid and efficient incorporation of no-carrier-added radiobromine and radioiodine. J Labelled Compd Radiopharm. 1983;20(5):619–26.
17. McNeill E, Barder TE, Buchwald SL. Palladium-catalyzed silylation of aryl chlorides with hexamethyldisilane. Org Lett. 2007;9(19):3785–8.
18. Coenen HH, Moerlein SM, Stocklin G. No-carrier-added radiohalogenation methods with heavy halogens. Radiochim Acta. 1983;34(1–2):47–68.
19. Foulon CF, Zhang YZ, Adelstein SJ, Kassis AI. Instantaneous preparation of radiolabeled 5-iodo-2′-deoxyuridine. Appl Radiat Isot. 1995;46(10):1039–46.
20. Kawai K, Ohta H, Kubodera A, Channing MA, Eckelman WC. Synthesis and evaluation of radioiodinated 6-iodo-L-DOPA as a cerebral L-amino acid transport marker. Nucl Med Biol. 1996;23(3):251–5.
21. Hylarides MD, Wilbur DS, Hadley SW, Fritzberg AR. Synthesis and iodination of methyl 4-tri-normal-butylstannylbenzoate, para-(methoxycarbonyl) phenylmercuric chloride and para-(methoxycarbonyl) phenylboronic acid. J Organomet Chem. 1989;367(3):259–65.
22. Kabalka GW, Yao ML. No-carrier-added radiohalogenations utilizing organoboranes: the synthesis of iodine-123 labeled curcumin. J Organomet Chem. 2009;694(11):1638–41.
23. Kabalka GW, Sastry KAR, Muralidhar K. Synthesis of iodine-125 labeled aryl and vinyl iodides. J Labelled Compd Radiopharm. 1982;19(6):795–9.
24. Kabalka GW, Akula MR, Zhang J. Synthesis of radioiodinated aryl iodides via boronate precursors. Nucl Med Biol. 2002;29(8):841–3.
25. Kabalka GW, Tang G, Mereddy AR. No-carrier-added radiohalogenations utilizing organoborates. J Labelled Compd Radiopharm. 2007;50(5–6):446–7.
26. Akula MR, Yao ML, Kabalka GW. Triolborates: water-soluble complexes of arylboronic acids as precursors to iodoarenes. Tetrahedron Lett. 2010;51(8):1170–1.
27. Moerlein SM. Regiospecific incorporation of no-carrier-added radiobromine and radioiodine into aromatic rings via halodegermylation. J Chem Soc Perkin Trans 1. 1985;8:1687–92.
28. Haberkorn U, Kinscherf R, Krammer PH, Mier W, Eisenhut M. Investigation of a potential scintigraphic marker of apoptosis: radioiodinated Z-Val-Ala-DL-Asp(O-methyl)-fluoromethyl ketone. Nucl Med Biol. 2001;28(7):793–8.
29. Ronnest MH, Nissen F, Pedersen PJ, Larsen TO, Mier W, Clausen MH. A mild method for regioselective labeling of aromatics with radioactive iodine. Eur J Org Chem. 2013;19:3970–3.
30. Wieland DM, Mangner TJ, Inbasekaran MN, Brown LE, Wu JL. Adrenal medulla imaging agents: a structure-distribution relationship study of radiolabeled aralkylguanidines. J Med Chem. 1984;27(2):149–55.
31. Mertens J, Vanryckeghem W, Bossuyt A. High-yield preparation of ^{123}I-N-isopropyl-para-iodoamphetamine (Iamp) in presence of Cu(I). J Labelled Compd Radiopharm. 1985;22(1):89–93.
32. Eersels JLH, Mertens J, Herscheid JDM. Optimization of the labeling yield by determination of the Cu^{+}-acetonitrile complex constant in Cu^{+}-catalyzed nucleophilic exchange reactions in mixed solvent conditions. J Radioanal Nucl Chem. 2011;288(1):291–6.
33. Eersels JL, Mertens J, Herscheid JD. The Cu^{+}-assisted radioiodination kit: mechanistic study of unexplored parameters concerning the acidity and redox properties of the reaction medium. Appl Radiat Isot. 2010;68(2):309–13.
34. Eersels JLH, Travis MJ, Herscheid JDM. Manufacturing I-123-labelled radiopharmaceuticals. Pitfalls and solutions. J Labelled Compd Radiopharm. 2005;48(4):241–57.
35. Chacko AM, Divgi CR. Radiopharmaceutical chemistry with iodine-124: a non-standard radiohalogen for positron emission tomography. Med Chem. 2011;7(5):395–412.
36. Eersels JLH, Mertens J, Herscheid JDM. New insights into the Cu plus -assisted nucleophilic radioiodination of bromopyridine and iodopyridine analogues. J Labelled Compd Radiopharm. 2012;55(4):135–9.
37. Cant AA, Champion S, Bhalla R, Pimlott SL, Sutherland A. Nickel-mediated radioiodination of aryl and heteroaryl bromides: rapid synthesis of tracers for SPECT imaging. Angew Chem Int Ed Engl. 2013;52(30):7829–32.
38. Wilson TC, McSweeney G, Preshlock S, Verhoog S, Tredwell M, Cailly T, et al. Radiosynthesis of SPECT tracers via a copper mediated ^{123}I iodination of (hetero)aryl boron reagents. Chem Commun (Camb). 2016;52(90):13277–80.
39. Zhang P, Zhuang R, Guo Z, Su X, Chen X, Zhang X. A highly efficient copper-mediated radioiodination approach using aryl boronic acids. Chemistry. 2016;22(47):16783–6.
40. Michelot JM, Moreau MF, Labarre PG, Madelmont JC, Veyre AJ, Papon JM, et al. Synthesis and evaluation of new iodine-125 radiopharmaceuticals as potential tracers for malignant melanoma. J Nucl Med. 1991;32(8):1573–80.
41. Pickett JE, Nagakura K, Pasternak AR, Grinnell SG, Majumdar S, Lewis JS, et al. Sandmeyer reaction repurposed for the site-selective, non-oxidizing radioiodination of fully-deprotected peptides: studies on the endogenous opioid peptide alpha-neoendorphin. Bioorg Med Chem Lett. 2013;23(15):4347–50.

42. Vivier M, Rapp M, Papon J, Labarre P, Galmier MJ, Sauziere J, et al. Synthesis, radiosynthesis, and biological evaluation of new proteasome inhibitors in a tumor targeting approach. J Med Chem. 2008;51(4):1043–7.
43. Khalaj A, Beiki D, Rafiee H, Najafi R. A new and simple synthesis of N-succinimidyl-4-[$^{127/125}$I] iodobenzoate involving a microwave-accelerated iodination step. J Labelled Compd Radiopharm. 2001;44(3):235–40.
44. Foster NI, Dannals R, Burns HD, Heindel ND. A condition variation study for radioiodination via triazene intermediates. J Radioanal Chem. 1981;65(1–2):95–105.
45. Hu B, Miller WH, Neumann KD, Linstad EJ, DiMagno SG. An alternative to the Sandmeyer approach to aryl iodides. Chemistry. 2015;21(17):6394–8.
46. DiMagno SG. WO 2016201128 A1 20161215 preparation of guanidinium compounds; 2016.
47. Guerard F, Lee YS, Baidoo K, Gestin JF, Brechbiel MW. Unexpected behavior of the heaviest halogen astatine in the nucleophilic substitution of aryliodonium salts. Chemistry. 2016;22(35):12332–9.
48. Kothari P, De BP, He B, Chen A, Chiuchiolo MJ, Kim D, et al. Radioiodinated capsids facilitate in vivo non-invasive tracking of adeno-associated gene transfer vectors. Sci Rep. 2017;7:39594.
49. Culbert PA, Hunter DH. Polymer-supported radiopharmaceuticals – ^{123}I labeled and ^{131}I-labeled N-isopropyl-4-iodoamphetamine. React Polym. 1993;19(3):247–53.
50. Hunter DH, Zhu XZ. Polymer-supported radiopharmaceuticals: [^{131}I]MIBG and [^{123}I]MIBG. J Labelled Compd Radiopharm. 1999;42(7):653–61.
51. Chin BB, Kronauge JF, Femia FJ, Chen J, Maresca KP, Hillier S, et al. Phase-1 clinical trial results of high-specific-activity carrier-free ^{123}I-iobenguane. J Nucl Med. 2014;55(5):765–71.
52. Gifford AN, Kuschel S, Shea C, Fowler JS. Polymer-supported organotin reagent for prosthetic group labeling of biological macromolecules with radioiodine. Bioconjug Chem. 2011;22(3):406–12.
53. Janabi M, Pollock CM, Chacko AM, Hunter DH. Resin-supported arylstannanes as precursors for radiolabeling with iodine: benzaldehydes, benzoic acids, benzamides, and NHS esters. Can J Chem. 2015;93(2):207–17.
54. Kabalka GW, Namboodiri V, Akula MR. Synthesis of ^{123}I labeled Congo red via solid phase organic chemistry. J Labelled Compd Radiopharm. 2001;44(13):921–9.
55. Hernan AG, Horton PN, Hursthouse MB, Kilburn JD. New and efficient synthesis of solid-supported organotin reagents and their use in organic synthesis. J Organomet Chem. 2006;691(8):1466–75.
56. Rajerison H, Faye D, Roumesy A, Louaisil N, Boeda F, Faivre-Chauvet A, et al. Ionic liquid supported organotin reagents to prepare molecular imaging and therapy agents. Org Biomol Chem. 2016;14(6):2121–6.
57. Wang G, Chen ZM, Wu EM, Wang Y, Huang HY. A convenient method for the preparation of radioiodinated meta-iodobenzylguanidine at a no-carrier-added level. J Labelled Compd Radiopharm. 2015;58(11–12):442–4.
58. Dzandzi JP, Beckford Vera DR, Genady AR, Albu SA, Eltringham-Smith LJ, Capretta A, et al. Fluorous analogue of chloramine-t: preparation, x-ray structure determination, and use as an oxidant for radioiodination and s-tetrazine synthesis. J Org Chem. 2015;80(14):7117–25.
59. Dzandzi JP, Vera DR, Valliant JF. A hybrid solid-fluorous phase radioiodination and purification platform. J Labelled Compd Radiopharm. 2014;57(9):551–7.
60. Donovan A, Forbes J, Dorff P, Schaffer P, Babich J, Valliant JF. A new strategy for preparing molecular imaging and therapy agents using fluorine-rich (fluorous) soluble supports. J Am Chem Soc. 2006;128(11):3536–7.
61. Billaud EM, Vidal A, Vincenot A, Besse S, Bouchon B, Debiton E, et al. Development and preliminary evaluation of TFIB, a new bimodal prosthetic group for bioactive molecule labeling. ACS Med Chem Lett. 2015;6(2):168–72.
62. Carter RL, Johnson BF, Sood A, Rishel MJ, Valliant JF, Stephenson KA, et al. Biotin stannane for HPLC-free radioiodination. CA 28855223 A1. Google Patents 28 Mar 2013. https://www.google.com/patents/CA2866223A1?cl=en.
63. Wu T, Yang Y, Stephenson K, Valliant J, Carter R, Johnson B, et al. Biotin stannanes for HPLC-free radioiodination (abstract). J Nucl Med. 2013;54(Suppl 2):496.
64. Nakagawa C, Toyama M, Takeuchi R, Takahashi T, Tanaka H. Synthesis of [I-123]-iodometomidate from a polymer-supported precursor with a large excluded volume. RSC Adv. 2016;6(15):12215–8.
65. Yong L, Yao ML, Kelly H, Green JF, Kabalka GW. Radioiodination of polymer-supported organotrifluoroborates. J Labelled Compd Radiopharm. 2011;54(4):173–4.
66. Spivey AC, Tseng CC, Jones TC, Kohler AD, Ellames GJ. A method for parallel solid-phase synthesis of iodinated analogues of the CB1 receptor inverse agonist rimonabant. Org Lett. 2009;11(20):4760–3.
67. Doll S, Woolum K, Kumar K. Radiolabeling of a cyclic RGD (cyclo Arg-Gly-Asp-d-Tyr-Lys) peptide using sodium hypochlorite as an oxidizing agent. J Labelled Compd Radiopharm. 2016;59(11):462–6.
68. Haubner R, Wester HJ, Reuning U, Senekowitsch-Schmidtke R, Diefenbach B, Kessler H, et al. Radiolabeled $\alpha_v\beta_3$ integrin antagonists: a new class of tracers for tumor targeting. J Nucl Med. 1999;40(6):1061–71.
69. Terriere D, Chavatte K, Ceusters M, Tourwe D, Mertens J. Radiosynthesis of new radio neurotensin (8-13) analogues. J Labelled Compd Radiopharm. 1998;41(1):19–27.
70. Vaidyanathan G, Affleck D, Welsh P, Srinivasan A, Schmidt M, Zalutsky MR. Radioiodination and astatination of octreotide by conjugation labeling. Nucl Med Biol. 2000;27(4):329–37.
71. Dissoki S, Hagooly A, Elmachily S, Mishani E. Labeling approaches for the GE11 peptide, an epidermal growth factor receptor biomarker. J Labelled Compd Radiopharm. 2011;54(11):693–701.
72. Rossouw DD. Radioiodine labelling of a small chemotactic peptide, utilizing two different prosthetic groups: a comparative study. J Labelled Compd Radiopharm. 2008;51(1–2):48–53.
73. Kondo N, Temma T, Shimizu Y, Ono M, Saji H. Radioiodinated peptidic imaging probes for in vivo detection of membrane type-1 matrix metalloproteinase in cancers. Biol Pharm Bull. 2015;38(9):1375–82.
74. Bhojani MS, Ranga R, Luker GD, Rehemtulla A, Ross BD, Van Dort ME. Synthesis and investigation of a radioiodinated F3 peptide analog as a SPECT tumor imaging radioligand. PLoS One. 2011;6(7):e22418.
75. Amartey JK, Esguerra C. A facile method for post-conjugation prosthetic radioiodination of "mini-peptides". Appl Radiat Isot. 2006;64(12):1549–54.
76. Vaidyanathan G, Affleck DJ, Schottelius M, Wester H, Friedman HS, Zalutsky MR. Synthesis and evaluation of glycosylated octreotate analogues labeled with radioiodine and ^{211}At via a tin precursor. Bioconjug Chem. 2006;17(1):195–203.
77. Choi MH, Shim HE, Yun SJ, Kim HR, Mushtaq S, Lee CH, et al. Highly efficient method for ^{125}I-radiolabeling of biomolecules using inverse-electron-demand Diels-Alder reaction. Bioorg Med Chem. 2016;24:2589–94.
78. Verel I, Visser GW, Vosjan MJ, Finn R, Boellaard R, van Dongen GA. High-quality ^{124}I-labelled monoclonal antibodies for use as PET scouting agents prior to ^{131}I-radioimmunotherapy. Eur J Nucl Med Mol Imaging. 2004;31(12):1645–52.
79. Lane DJR, Richardson DR. Revolutions in the labelling of proteins with radionuclides of iodine: William Hunter and radioiodination. Biochem J. 2011;4:34–8.

80. Vaidyanathan G, Zalutsky MR. Preparation of N-succinimidyl 3-[*I]iodobenzoate: an agent for the indirect radioiodination of proteins. Nat Protoc. 2006;1(2):707–13.
81. Wilbur DS, Hadley SW, Hylarides MD, Abrams PG, Beaumier PA, Morgan AC, et al. Development of a stable radioiodinating reagent to label monoclonal antibodies for radiotherapy of cancer. J Nucl Med. 1989;30(2):216–26.
82. Tolmachev V, Orlova A, Lundqvist H. Approaches to improve cellular retention of radiohalogen labels delivered by internalising tumour-targeting proteins and peptides. Curr Med Chem. 2003;10(22):2447–60.
83. Sugiura G, Kuhn H, Sauter M, Haberkorn U, Mier W. Radiolabeling strategies for tumor-targeting proteinaceous drugs. Molecules. 2014;19(2):2135–65.
84. Yan R, Sander K, Galante E, Rajkumar V, Badar A, Robson M, et al. A one-pot three-component radiochemical reaction for rapid assembly of ^{125}I-labeled molecular probes. J Am Chem Soc. 2013;135(2):703–9.
85. Ono M, Watanabe H, Ikehata Y, Ding N, Yoshimura M, Sano K, et al. Radioiodination of BODIPY and its application to a nuclear and optical dual functional labeling agent for proteins and peptides. Sci Rep. 2017;7(1):3337.
86. Reist CJ, Archer GE, Kurpad SN, Wikstrand CJ, Vaidyanathan G, Willingham MC, et al. Tumor-specific anti-epidermal growth factor receptor variant III monoclonal antibodies: use of the tyramine-cellobiose radioiodination method enhances cellular retention and uptake in tumor xenografts. Cancer Res. 1995;55(19):4375–82.
87. Choi J, Vaidyanathan G, Koumarianou E, McDougald D, Pruszynski M, Osada T, et al. N-Succinimidyl guanidinomethyl iodobenzoate protein radiohalogenation agents: influence of isomeric substitution on radiolabeling and target cell residualization. Nucl Med Biol. 2014;41(10):802–12.
88. Shankar S, Vaidyanathan G, Affleck DJ, Peixoto K, Bigner DD, Zalutsky MR. Evaluation of an internalizing monoclonal antibody labeled using N-succinimidyl 3-[^{131}I]iodo-4-phosphonomethylbenzoate ([^{131}I]SIPMB), a negatively charged substituent bearing acylation agent. Nucl Med Biol. 2004;31(7):909–19.
89. Karmani L, Leveque P, Bouzin C, Bol A, Dieu M, Walrand S, et al. Biodistribution of ^{125}I-labeled anti-endoglin antibody using SPECT/CT imaging: impact of in vivo deiodination on tumor accumulation in mice. Nucl Med Biol. 2016;43(7):415–23.
90. Pruszynski M, Koumarianou E, Vaidyanathan G, Chitneni S, Zalutsky MR. D-amino acid peptide residualizing agents bearing N-hydroxysuccinimido- and maleimido-functional groups and their application for trastuzumab radioiodination. Nucl Med Biol. 2015;42(1):19–27.
91. Lee FT, Burvenich IJ, Guo N, Kocovski P, Tochon-Danguy H, Ackermann U, et al. l-tyrosine confers residualizing properties to a d-amino acid-rich residualizing peptide for radioiodination of internalizing antibodies. Mol Imaging. 2016. https://doi.org/10.1177/15:1536012116647535.
92. van Schaijk FG, Broekema M, Oosterwijk E, van Eerd JE, McBride BJ, Goldenberg DM, et al. Residualizing iodine markedly improved tumor targeting using bispecific antibody-based pretargeting. J Nucl Med. 2005;46(6):1016–22.
93. Boswell CA, Marik J, Elowson MJ, Reyes NA, Ulufatu S, Bumbaca D, et al. Enhanced tumor retention of a radiohalogen label for site-specific modification of antibodies. J Med Chem. 2013;56(23):9418–26.
94. Vaidyanathan G, White BJ, Affleck DJ, Zhao XG, Welsh PC, McDougald D, et al. SIB-DOTA: a trifunctional prosthetic group potentially amenable for multi-modal labeling that enhances tumor uptake of internalizing monoclonal antibodies. Bioorg Med Chem. 2012;20(24):6929–39.
95. Albu SA, Al-Karmi SA, Vito A, Dzandzi JP, Zlitni A, Beckford-Vera D, et al. ^{125}I-Tetrazines and inverse-electron-demand diels-alder chemistry: a convenient radioiodination strategy for biomolecule labeling, screening, and biodistribution studies. Bioconjug Chem. 2016;27(1):207–16.
96. Cavina L, van der Born D, Klaren PHM, Feiters MC, Boerman OC, Rutjes F. Design of radioiodinated pharmaceuticals: structural features affecting metabolic stability towards in vivo deiodination. Eur J Org Chem. 2017;2017(24):3387–414.
97. Genady AR, Tan J, El-Zaria ME, Zlitni A, Janzen N, Valliant JF. Reprint of: synthesis, characterization and radiolabeling of carborane-functionalized tetrazines for use in inverse electron demand Diels-Alder ligation reactions. J Organomet Chem. 2015;798:278–88.
98. DiMagno SG. US 20140275539 A1. Preparation of radioiodinated and astatinated organic compounds as imaging agents; 2014.
99. Sajjad M, Lambrecht RM, Bakr SA. Autoradiolytic decomposition of reductant-free sodium I-124 iodide and I-123 iodide. Radiochim Acta. 1990;50(1–2):123–7.
100. Sartor J, Guhlke S, Tentler M, Biersack HJ. A simple and efficient method for purification and reduction of radioiodine for pharmaceutical syntheses. J Nucl Med. 1998;39(5):143P.
101. Sahu S, Sahoo PR, Patel S, Mishra BK. Oxidation of thiourea and substituted thioureas: a review. J Sulfur Chem. 2011;32(2):171–97.

The Radiopharmaceutical Chemistry of Alpha-Emitting Radionuclides

D. Scott Wilbur

Fundamentals

Radiopharmaceuticals bearing α-emitting radionuclides have generated significant interest for cancer therapy and the treatment of viral- or bacterial-related diseases [1–6]. This enthusiasm stems from the fact that α particles travel short distances in tissues but have excellent cell-killing properties when carrier molecules bearing α-emitting radionuclides are bound to—or internalized within—target cells. This combination of traits allows targeted α-emitting radiopharmaceuticals to kill single cells while having minimal toxicity to non-targeted tissues. However, three obstacles have hampered the development of radiopharmaceuticals containing α-emitting radionuclides: (1) the low availability of the radionuclides, (2) a critical need for the development of appropriate carriers or targeting vectors, and (3) the requirement to develop chemistry that keeps the α-emitting radionuclide attached to the disease-targeting carrier and its metabolites *in vivo*. In this chapter, the radiobiological rationale for the interest in α-emitting radiopharmaceuticals will be explained, as well as the process of identifying and producing medically useful α-emitting radionuclides. In addition, the chemistry underpinning the incorporation of α-emitting radionuclides into targeting vectors will also be addressed in conjunction with a discussion of the issues surrounding the *in vivo* stability of α-emitting radiopharmaceuticals.

Details

While there has been a recent surge in the development and evaluation of α-emitting radiopharmaceuticals, it should be noted that the very first radionuclide used for targeted radiotherapy of *any* kind was in fact an α-emitting radionuclide. In 1903—only 5 years after the discovery of radioactive elements—an article appeared in the "Medical Record" journal describing the potential use of radium (^{226}Ra) rays in the treatment of cancer [7]. The use of radium for the treatment of cancer, which included both irradiation with external sources as well as the ingestion or injection of salts, increased greatly in the two decades after the turn of the twentieth century [8, 9]. This movement prompted the Curies to donate virtually *all* of the radium they isolated to physicians for the treatment of cancer. Ultimately, this generosity resulted in Marie Curie having to come to the US in 1921 to obtain a single gram of the radionuclide—paid for by donations obtained by "women of America"—so she could continue her research. Unfortunately, without regulations on radioactive materials, radium was used in many non-medical applications that resulted in toxicity to people [10, 11], and interest in this form of therapy diminished. Thankfully, however, much more knowledge about radiochemistry, radiobiology, and radiopharmaceutical development has been gained in the past 100 years, so the potential of α-emitting radiopharmaceuticals for therapy is now beginning to be realized. It is an interesting coincidence that the first US FDA-approved α-particle-emitting radiopharmaceutical is also based on a radioisotope of radium: $^{223}RaCl_2$ (Xofigo™).

Radiobiological Effects of α-Emission

Since the first medical uses of radioactivity in the early 1900s, much has been learned about the effects of radiation on biological materials [12]. It is this knowledge that allows investigators to develop new therapeutic radiopharmaceuticals based on the expected biological responses in target and non-target tissues. To better understand why α-emitters have garnered so much interest as radionuclides for therapy, one only needs to contrast their physical and radiobiological properties with those of the more commonly used β particle emissions. Some important differences in the physical properties of these two particle types are shown in Table 1. It

D. S. Wilbur (✉)
Department of Radiation Oncology, University of Washington, Seattle, WA, USA
e-mail: dswilbur@uw.edu

J. S. Lewis et al. (eds.), *Radiopharmaceutical Chemistry*, https://doi.org/10.1007/978-3-319-98947-1_23

Table 1 Comparison of the physical properties of α particles and β particles

Radionuclide emission	Mass (amu)	Energy distribution[a]	Velocity (% light speed)	Energy range of particles	Range in air (cm)	Range in H_2O[b] (cm)
α particle (He nucleus)	4.0012	Discrete	2%	3 MeV (to) 8 MeV	1.6 cm (to) 7.5 cm	0.0016 cm (to) 0.0075 cm
β particle (electron)	0.000549	Continuous	95%	0.5 MeV (to) 3 MeV	127 cm (to) 1270 cm	0.15 cm (to) 1.9 cm

[a]The term discrete means that the particle has a single energy upon emission, whereas continuous means that the electrons emitted have many different energies and thus travel varying distances (maximum distance is shown).
[b]Biologic tissues are primarily composed of water, so these values can be used an approximation of distance traveled in tissues.

should be noted that the mass of an α particle is 7468 times that of a β particle(!) This large difference in mass—along with differences in the energy, velocity, and charges on the particles—produces very different interactions with biological materials. While it is hard to relate to a ~7,500-fold difference in mass, one can get some appreciation for this by visualizing the damage done to a factory (representing a cell) by a very fast-moving military battle tank weighing 55,000 kg compared to that done by a fast-moving bowling ball weighing 7.3 kg. Indeed, the energy deposited by an α particle can be 1000 times that of a β particle per unit distance traveled. This high deposition of energy over a short distance is referred to as having a high linear energy transfer (or high LET), a term often used in discussions of expected radiobiological response [13].

It should be noted that the distance that an α-particle travels in tissue—16–75 μm—is only a few cell diameters (10–30 μm for eukaryotic cell), whereas a β particle can travel several hundred cell diameters. The 3–8 MeV of energy that an α-particle deposits over the short range of its travel results in a high LET (keV/μm), which in turn results in a high relative biological effectiveness (RBE) when compared to β particles [14]. Radiobiological cell survival studies have shown that the most effective LET for killing mammalian cells is around 100 keV/μm [13]. It has been proposed that at this optimal LET, the ionization events coincide with the diameter of DNA double stands (~2 nm), resulting in lethal double strand breaks in cells. Higher LET radiation (*e.g.* 200 keV/μm) has similar cell-killing properties, but the extra energy deposition might be considered "wasted." However, as α particles interact with biological material, the α energy deposition decreases rapidly on its path, so an average energy of greater than 100 keV might be of value in cell killing. This highly efficient cell killing when an α particle transverses a cell negates two important factors that usually affect cell survival when irradiating with lower LET radiation: the dose rate effect and the oxygen effect. When cells are damaged by low LET dose rates, cellular repairs can occur during the period of irradiation, making it harder to kill the cells. Similarly, if oxygen concentrations are low or absent—as in hypoxic and necrotic tissues—it can be more difficult to kill cells with radiation.

The radiobiological properties of α particle-emitting radiopharmaceuticals make them of particular interest for the treatment of disseminated (micro)metastatic disease and blood-related cancers. Indeed, it has been hypothesized that as few as one transversal of a cell (nucleus) by a single α particle can kill that cell, whereas it might take 400 β particle transversals to kill the same cell. It is generally believed that radiopharmaceuticals containing β-emitters might be more effective at treating large solid tumors than radiopharmaceuticals containing an α-emitter. This belief stems from two phenomena: the expression of target antigen within tumors can be highly heterogeneous, and it can be difficult to access cells in necrotic portions of the tumor. Both of these factors favor radiation delivered over longer distances (a radiation field). However, some investigators believe the fact that α therapy is not affected by the dose rate or the oxygen present in the target tissue may provide advantages over β particle-emitting radionuclides even in treating large tumors. They note that treatment with α-particles may require multiple administrations (fractionated doses) of the radiopharmaceutical to be effective in larger tumors.

Medically Useful α-Emitters

Although there are a large number of α-emitting radionuclides, only a few of them have been identified as appropriate for use in radiopharmaceuticals [15]. There are several important factors to consider when determining whether an α-emitting radionuclide is suitable for the development of therapeutic radiopharmaceuticals: (a) the abundance of α emissions; (b) its physical half-life; (c) the daughters it produces, along with their half-lives and emissions; (d) the availability of facile production routes; and (e) the cost of its production. For example, a radionuclide that has a low abundance of α-emissions may be unattractive, as more radioactivity is required to deliver the α dose than in cases where a radionuclide has a high abundance of α emissions. The requirement for higher quantities of radioactivity being used may result in higher non-target toxicity. The half-life of the radionuclide is also important, as too short a half-life (*e.g.* <30 min) may preclude the radiopharmaceutical from

reaching its target *in vivo* before a large portion has decayed. In addition, the short half-life makes it very difficult to prepare the radiopharmaceutical and conduct quality control on it before significant amounts decay. In contrast, too long a half-life (*e.g.* over a month) prolongs the treatment period, which is not desired since many patients are medically compromised. Another important consideration is the nature of the daughter nuclides produced when the α-emitter decays. The ideal situation is that the radionuclide decays to a stable isotope so that no additional radioactive materials are generated. However, this does not generally occur. Rather, the radionuclide often decays to another radionuclide, which then decays to yet another radionuclide, and so on. If an α-emitting radionuclide is produced from the decay of the parent radionuclide, the resultant daughter or daughters could redistribute in the body and cause unwanted toxicity.

Table 2 lists ten α-emitting radionuclides that have been identified as candidates for medical application [15]. The selection of an α-emitting radionuclide to develop a therapeutic radiopharmaceutical might ideally be accomplished by assessing the intended application and matching the properties of the radionuclide to the disease being treated and the targeting vector to be used. In reality, however, the primary factors in the selection of a radionuclide from the table have all too often been the availability and cost of the radionuclide. Another important consideration in the selection of an α-emitting radionuclide is the chemistry for incorporating it into a targeting molecule. These factors must be considered before entering clinical trials and developing a marketable product. Fortunately, the logistics and economics of availability can be overlooked in the selection of a radionuclide used in early exploratory evaluations, as the availability can change dramatically when technology is advanced.

The decay characteristics of α-emitting radionuclides are critical in the selection of a suitable α-emitter. Table 2 provides information on the energy of α and photon emissions for each radionuclide listed. Major α-emission energies are listed for each radionuclide in the table, and the photon emissions are provided to allow for evaluation of whether each isotope can be used for imaging and quantification of the activity in the patient's organs and tissues. With the move toward theranostic radiopharmaceuticals in personalized or precision medicine, radionuclides that provide "imageable" photons might be favored over others that do not. Many of the photon emissions of the listed radionuclides occur in low abundance, calling into question whether imaging could actually be practically accomplished. It is important to note that one radionuclide—bismuth-213 (^{213}Bi)—has a 440 keV γ emission in high enough abundance to be used for single-photon emission computed tomography (SPECT), and indeed, imaging has been conducted when this isotope was used. In addition, given that ^{213}Bi is a daughter of ^{225}Ac, its 440 keV γ emission can also be used for that radionuclide as well. Another radionuclide, terbium-149 (^{149}Tb), has many photon emissions that might be used for SPECT, but it also has a 511 keV γ emission from positron annihilation that can be used for positron emission tomography (PET) [16]. It is apparent from entries in Table 2 that alternative theranostic

Table 2 α-Emitting radionuclides identified for radiopharmaceutical development[a]

Radionuclide[b]	Half-life	Total of α emissions	α-emission energy in keV (% abundance)	Imageable photon emissions in keV (% abundance)
Thorium-226	30.57 min	100%	6234 (22.8%); 6337 (75.5%)	111 (3.3%); 131 (0.3%); 242 (0.9%)
Bismuth-213	45.61 min	100% (from Po-213)	5875 (2.2%) 8376 (97.8%)	440 (25.9%)
Bismuth-212	60.55 min[c]	100% (from Po-212)	6051 (25.1%); 6090 (9.8%) 8785 (64%)	288 (0.3%); 453 (0.4%)
Terbium-149	4.118 h	16.7%	3967 (16.7%)	165 (26.4%); 352 (29.4%); 389 (18.4%); 511 (14.2%); 652 (16.2%); 817 (11.6%); 853 (15.5%)
Astatine-211	7.214 h	100% (from Po-211)	5870 (41.8%); 7450 (58.1%)	77 (12%); 79 (21%), 687 (0.3%) 569 (0.5%); 898 (0.6%)
Fermium-255	20.07 h	100%	6963 (5%); 7022 (93.4%)	None
Radium-224	3.632 days	100%	5449 (5%); 5685 (94.9%)	241 (4%)
Actinium-225	10.0 days	100%	5732 (8.0%); 5791 (8.6%); 5793 (18.1%); 5830 (50.7%)	108 (0.2%); 112 (0.3%) 154 (0.3%); 157 (0.3%); 188 (0.5%)
Radium-223	11.43 days	100%	5540 (9.0%); 5607 (25.2%); 5716 (51.6%); 5747 (9.0%)	122 (1.2%); 144 (3.3%); 154 (5.7%); 269 (13.9%); 324 (4.0%); 338 (2.8%); 445 (1.3%)
Thorium-227	18.70 days	100%	5709 (8.3%); 5713 (5.0%); 5757 (20.4%); 5978 (23.5%); 6038 (24.2%)	236 (12.9%); 256 (7.0%); 286 (1.7%); 290 (1.9%); 300 (2.2%); 330 (2.9%)

[a]Half-lives and emission information obtained from the National Nuclear Data Center Chart of Nuclides, Brookhaven National Laboratory. https://www.nndc.bnl.gov/chart/. Accessed 6 Apr 2018. Highest abundance emissions are shown; major Auger and β-emissions are omitted for simplicity.

[b]The listed radionuclide order is based on its decay half-life.

[c]When the parent ^{212}Pb ($t_{1/2}$ = 10.64 h) is used, it provides an *in vivo* generator system, and the effective biologic half-life of ^{212}Bi is longer.

pair radionuclides will be required for imaging of most radiopharmaceuticals containing an α emitter.

The daughter radionuclides produced during the decay of an α-emitting radionuclide are also of high importance in selecting a suitable α-emitter. The four panels (a–d) in Fig. 1 show the daughters produced during the decay of ^{225}Ac, ^{213}Bi, ^{227}Th, ^{223}Ra, ^{224}Ra, ^{212}Bi, and ^{226}Th (highlighted in red). All of the radionuclides except for ^{226}Th are produced via naturally occurring radioactive decay processes occurring in the earth's crust. With the exception of the ^{212}Bi and ^{213}Bi, the α-emitters in Fig. 1 identified as acceptable for use in humans (in red) are associated with four or five α emissions arising from their initial decay and their daughters' decay before ultimately decaying to a stable nuclide. Having four or five α decays associated with a radionuclide has been cited as an advantage for therapy, as there is an increased dose to the target tissue. However, the α decay chain can also introduce an unwanted source of toxicity depending on the nature of the daughter radionuclides produced and their half-lives. Although very stable attachments of α-emitting radionuclides to targeting vectors can be obtained, the recoil energy from alpha decay is so high that the resultant daughter nuclide will no longer be associated with the targeting vector. If the released daughter nuclide—or one of the subsequent daughter nuclides—has a long enough half-life, it can redistribute within the body and irradiate non-target tissues elsewhere [17].

For example, during the decay of ^{225}Ac (see Fig. 1, Panel A), ^{213}Bi is formed, which has a long enough half-life

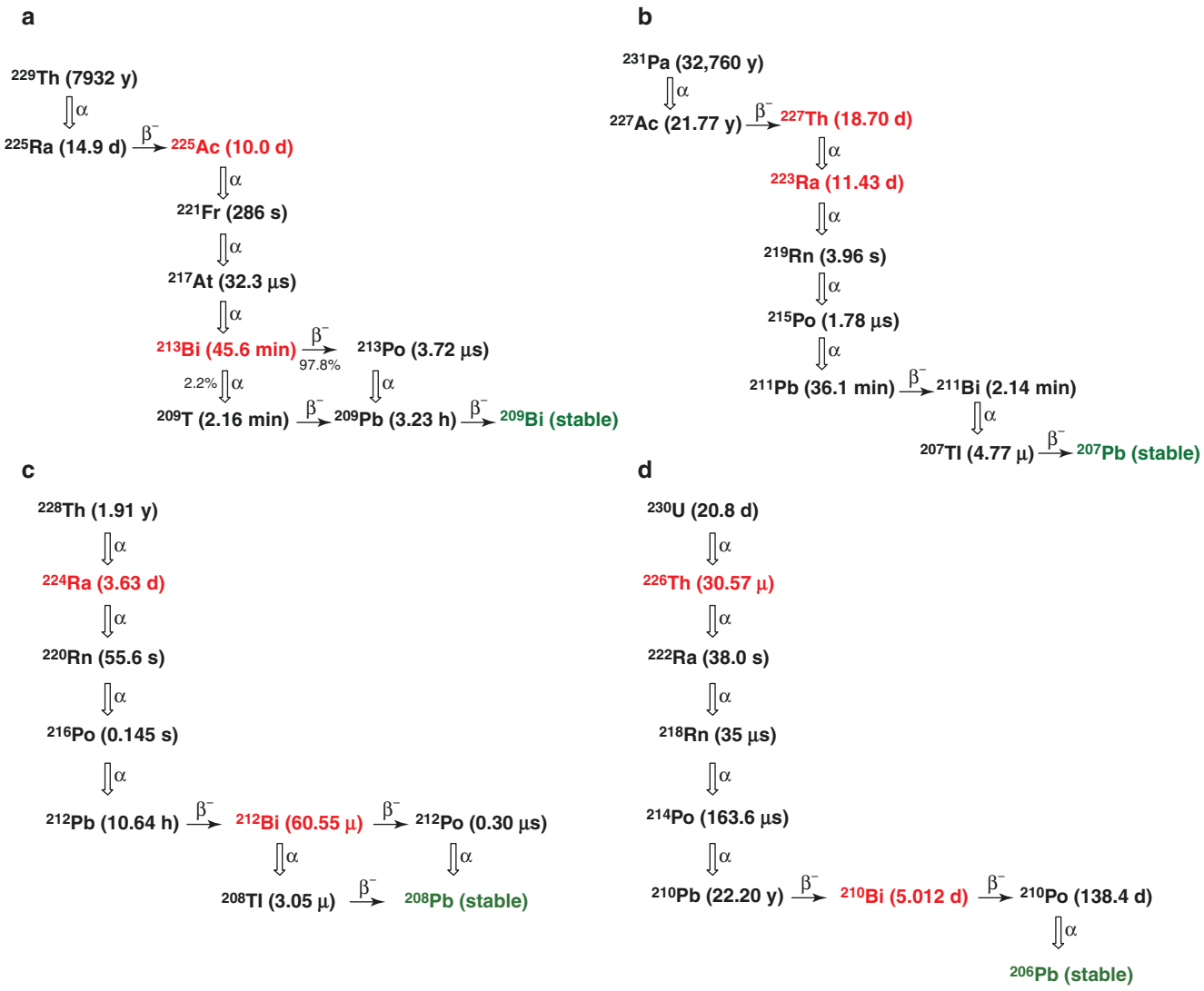

Fig. 1 Radionuclide decay schemes showing α-emitting radionuclides of interest for use in therapeutic radiopharmaceuticals (in red). **Panel A** shows the natural decay scheme (part of Neptunium Series) for ^{225}Ac and ^{213}Bi. **Panel B** shows the natural decay scheme (part of Actinium Series) for ^{227}Th and ^{223}Ra. **Panel C** shows the natural decay scheme (part of Thorium Series) for ^{224}Ra and ^{212}Bi. **Panel D** shows the decay series (that feeds into the Uranium Series) for ^{226}Th. Radionuclide half-lives were obtained from the National Nuclear Data Center Chart of Nuclides, Brookhaven National Laboratory. https://www.nndc.bnl.gov/chart/. (Accessed 6 Apr 2018)

(*i.e.* 45.6 min) to redistribute to non-target tissues. In the decay of ^{224}Ra (see Fig. 1, Panel C), another bismuth nuclide—^{212}Bi—is formed. ^{212}Bi may end up in non-target tissues, as the ^{212}Pb ($t_{1/2}$ ~ 10.6 h) formed in the decay of ^{224}Ra can redistribute prior to its decay to ^{212}Bi. In fact, the redistribution of ^{212}Pb seems very likely, and thus the redistribution of ^{212}Bi is also highly likely. The chief concern with the redistribution of ^{213}Bi or ^{212}Bi is the natural sequestration of bismuth (and thus these radionuclides) in the kidney. Methods to remove bismuth isotopes from the kidney have been somewhat successful, but the potential for kidney damage should be of concern when using ^{225}Ac or ^{224}Ra. Fortunately, thus far no significant kidney toxicity has been noted in clinical trials involving the use of ^{225}Ac.

When employing ^{227}Th there is also a concern about redistribution of its daughter ^{223}Ra (see Fig. 1, Panel B), since the half-life of ^{223}Ra is certainly long enough (11.4 days) for significant redistribution to occur. Fortunately, a lot is known about the distribution and toxicity of ^{223}Ra in humans, as it is an approved therapeutic radiopharmaceutical ($^{223}RaCl_2$). Importantly, ^{223}Ra is not sequestered in normal tissues but rather on bone surfaces (or eliminated quickly through the hepatobiliary system). This knowledge of the distribution and toxicity profile of ^{223}Ra makes the use of ^{227}Th very attractive for targeted alpha therapy. Another thorium isotope, ^{226}Th (see Fig. 1, Panel D), is also very interesting for use in therapeutic applications. While ^{226}Th's short half-life ($t_{½}$ = 30.6 min) will limit its applications, the three α-emitting daughters leading up to ^{210}Pb ($t_{½}$ = 22.2 years) have very short half-lives, making it unlikely that they will redistribute. In contrast, it is very likely that the long-lived ^{210}Pb produced will redistribute, but its lack of damaging particle emissions seems unlikely to cause toxicity. ^{149}Tb (Fig. 2, Panel A) has only one α emission, but it is produced in low abundance (*e.g.* 16.7%). It should be noted that there are several radioactive daughters produced from its decay. Even though these radionuclides do not have α-emissions and will not give a large radiation dose to tissues, radioactivity will likely remain in the patient for an extended time. Another α-emitting radionuclide, ^{211}At, has a branched decay path (Fig. 2, Panel B) that provides 100% α emission. ^{211}At is a very attractive α-emitting radionuclide as it has no α-emitting daughters to cause toxicity through redistribution, but it must be pointed out that ^{211}At has a long-lived ^{207}Bi daughter that could remain in the body for an extended period of time.

Production of Radionuclides

The paucity of production methods and the high costs associated with producing the α-emitting radionuclides of interest have limited their use in preclinical and clinical investigations. Many of the radionuclides studied have been obtained from natural radioactive sources or produced in highly specialized irradiation and isolation facilities. Another issue in obtaining them is that the radionuclides are particularly difficult to handle and purify. These costly facility and difficult technical barriers may ultimately preclude the use of some of the α-emitting radionuclides of interest. Additionally, the radionuclides with half-lives less than 1 day can have limited availability because much (or all) of the radionuclide might be lost in transit. It can be very difficult to prepare a radiopharmaceutical from the short half-lived radionuclides, as they decay rapidly during the processes of radiolabeling, conducting quality control assessments, and transferring to a patient injection area for administration. Fortunately, all the

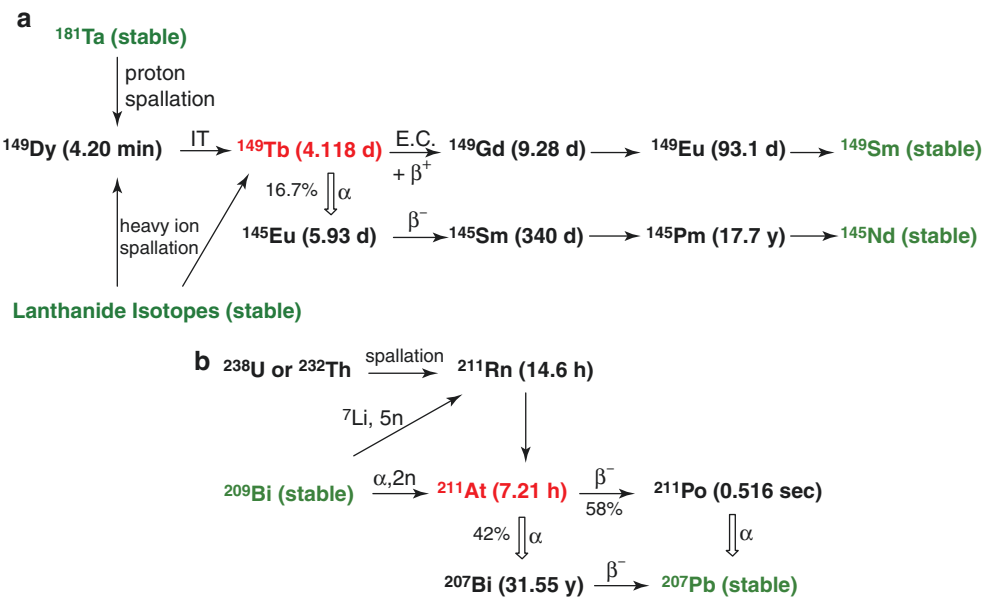

Fig. 2 Schemes showing the production routes and decay schemes for ^{149}Tb (**Panel A**) and ^{211}At (**Panel B**). Radionuclides of interest are in red and stable nuclides are in green. Radionuclide half-lives were obtained from the National Nuclear Data Center Chart of Nuclides, Brookhaven National Laboratory. https://www.nndc.bnl.gov/chart/. (Accessed 6 Apr 2018)

short-lived α-emitting radionuclides of interest, except ^{149}Tb, have longer-lived parent radionuclides that can be used as generators. The use of a generator system allows for the production of the radionuclide at specialized facilities and shipment to multiple sites for the isolation of the α-emitting daughter radionuclide and on-site production of the radiopharmaceutical. As can be seen in the decay schemes in Fig. 1, ^{225}Ac can be used as a generator for ^{213}Bi [18]; ^{224}Ra can be used as a generator for ^{212}Bi [19]; and ^{230}U can be used as a generator for production of ^{226}Th [20]. Also, as shown in Fig. 2, radon-211 (^{211}Rn) can be used as a generator for ^{211}At, potentially allowing broader distribution for radiopharmaceutical development and application.

Table 3 lists some possible production routes for the radionuclides of interest and their parent (generator) radionuclides. Some of the very long-lived radionuclides—for example, ^{238}U, ^{232}Th, and ^{226}Ra—can be irradiated to produce many of the longer-lived parent nuclides, such as ^{227}Ac, ^{228}Th, ^{229}Th, ^{230}Pa, and ^{211}Rn. Thus, the radionuclides listed can be used to produce most of the α-emitting radionuclides of interest. An example in which difficulties in the preparation and isolation of the radionuclide may ultimately preclude

Table 3 Some production routes for α-emitters and their parent radionuclides[a]

α-emitting radionuclide parent and/or daughter[b]	Half-life	Decay type and (% abundance)	Possible production methods for making the α-emitting radionuclide or its generator parent[c]
Radon-211 **Astatine-211** Polonium-211	14.6 h 7.214 h 0.52 s	α (27%); EC (73%) α (41.8%); EC (58.2%) α (100%)	^{238}U(p,xn)^{211}Rn ^{232}Th(p,xn)^{211}Rn ^{209}Bi(^{7}Li,5n)^{211}Rn **^{209}Bi(α,2n)^{211}At**
Thorium-229 Radium-225 **Actinium-225** **Bismuth-213** Polonium-213	7932 years 14.9 days 10.0 days 45.61 min 3.7 μs	α (100%) β (100%) α (100%) α (2.2%); β$^-$ (97.8%) α (100%)	Decay of ^{233}U ^{226}Ra(n,γ)^{229}Th ^{228}Ra(n,γ)^{229}Th ^{227}Ac(n,γ)^{229}Th ^{228}Th(n,γ)^{229}Th ^{226}Ra(γ,n)^{225}Ra **^{226}Ra(p,2n)^{225}Ac** **^{226}Ra(d,3n)^{225}Ac**
Thorium-228 **Radium-224** Radon-220 Polonium-216 Lead-212 **Bismuth-212** Polonium-212	1.91 years 3.63 days 55.6 s 0.15 s 10.64 h 60.55 min 0.299 μs	α (100%) α (100%) α (100%) α (100%) β$^-$ (100%) α (35.9%); β$^-$ (64.1%) α (100%)	**Decay of ^{228}Th** Decay of ^{232}Th ^{226}Ra(n,γ)^{228}Th
Einsteinium-255/	39.8 days	α (8.0%); β$^-$ (92.0%)	^{238}U(^{16}O,xn)^{255}Fm
Fermium-255	20.07 h	α (100%)	Cm(n,γ)^{255}Fm
Actinium-227 **Thorium-227** **Radium-223**	21.77 years 18.70 days 11.43 days	α (1.4%); β$^-$ (98.6%) α (100%) α (100%)	Decay of ^{235}U **^{226}Ra(n,γ)^{227}Ra(β$^-$)^{227}Ac**
Dysprosium-149 **Terbium-149**	4.20 min 4.118 h	EC (100%) α (16.7%); β$^-$ (83.3%)	**^{142,144,146}Nd(^{10,11}B,xn)^{149}Tb** **^{141}Pr(^{12}C,4n)^{149}Tb** **^{140}Ce(^{14,15}N,xn)^{149}Tb** **^{139}La(^{16,18}O,xn)^{149}Tb** **^{133}Cs(^{20,22}Ne,xn)^{149}Tb** ^{142,144}Nd(^{12}C,xn)^{149}Dy to ^{149}Tb ^{141}Pr(^{14,15}N,xn)^{149}Dy to ^{149}Tb ^{140}Ce(^{16,18}O,xn)^{149}Dy to ^{149}Tb ^{138}Ba(^{20,22}Ne,xn)^{149}Dy to ^{149}Tb **^{152}Gd(p,4n)^{149}Tb** **^{151,153}Eu(^{3,4}He,xn)^{149}Tb** **Ta(p,x)^{149}Tb**
Protactinium-230	17.4 days	EC (92.2%); β$^-$ (7.8%)	^{232}Th(p,x)^{230}Pa
Uranium-230	20.8 days	α (100%)	^{232}Th(d,x)^{230}Pa
Thorium-226	30.57 min	α (100%)	**^{231}Pa(p,2n)^{230}U**

[a]The listed radionuclide order alphabetical.

[b]Not all decay radionuclides shown – only long-lived parent and α-emitting daughters of interest (**bold**). Half-lives and emission information was obtained from the National Nuclear Data Center Chart of Nuclides, Brookhaven National Laboratory. https://www.nndc.bnl.gov/chart/. Accessed 6 Apr 2018.

[c]Direct production routes shown in **bold**. Other production routes produce a radionuclide that (ultimately) decays to the desired α-emitter. The production of parent radionuclides can be used to make a generator system, *i.e.* ^{211}Rn/^{211}At.

investigation is fermium-255 (^{255}Fm). While ^{255}Fm has favorable radiochemical properties, such as a reasonable half-life, a decay pathway that ends in a long-lived daughter (^{251}Cf; $t_{1/2}$ = 898 years), and the availability of an einsteinium-255 (^{255}Es; $t_{1/2}$ = 39.8 days) generator system, it is unlikely that sufficient quantities of ^{255}Es or ^{255}Fm will ever be produced for the development of radiopharmaceuticals. In the 1950s, trace quantities of ^{255}Fm were obtained in debris from the first US hydrogen bomb and in Sweden from the irradiation of uranium-238 (^{238}U) with oxygen-16 (^{16}O) atoms. The production of quantities of ^{255}Fm on the order of 37 MBq (1 mCi) was carried out by the neutron activation of curium in the High Flux Isotope Reactor (HIFR) at Oak Ridge National Laboratory, but much more would have to be made to develop and test radiopharmaceuticals containing this radionuclide. Similarly, another man-made radionuclide (not listed in Table 1)—^{253}Es ($t_{1/2}$ = 20.5 days)—has been suggested as a possible therapeutic α-emitter for human use, but both its production [21] and the production of useful quantities of a possible generator (^{253}Cf; $t_{1/2}$ = 17.8 days) would also be extremely difficult. Thus, at this time, neither of these α-emitting radionuclides is really practical for development of therapeutic radiopharmaceuticals.

Another α-emitting radionuclide that is very difficult to produce is terbium-149 (^{149}Tb). It can be produced using heavy-ion irradiations of lanthanide isotopes [22, 23] (as listed in Table 3) as well as by high-energy proton spallation reactions. High-energy proton spallation (1–1.2 GeV) reactions on tantalum foil targets, coupled with mass separation, have provided enough quantities, *e.g.* 1 GBq (37 mCi), of ^{149}Tb to conduct animal studies [24] and conduct PET imaging [25]. Although ^{149}Tb is difficult to produce, the fact that it is a theranostic radionuclide that could be harnessed for therapy as well as PET and SPECT imaging makes it of high interest (Table 2). One can hope that the development of new accelerator technology might make this radionuclide more available in the future for the development of radiopharmaceuticals.

Bonding and Chelation

Another challenge in creating effective α-emitting radiopharmaceuticals has been the development of chemical methods for stably attaching the radionuclide to disease-targeting carrier molecules. Because of the highly cytotoxic nature of α emissions, it is of paramount importance that the radionuclide remain stably attached to the carrier molecule and its metabolites while in the body. If the radionuclide becomes detached from the disease-targeting molecule, the therapy will less efficacious for the quantity of activity injected. Further, it is likely to be more toxic, possibly decreasing the therapeutic window to a point at which treatment with the radiopharmaceutical is not viable. Thus, the bioconjugation method used to attach the radionuclide to the targeting vector is absolutely critical. The low availability and high cost of α-emitting radionuclides has proven troublesome in this regard, too, as these issues have made it difficult to fully optimize bonding or chelation methods. In addition, it is important to note that of the isotopes we have discussed, only terbium and bismuth have stable isotopes. As a result, the characterization of the products in chelation or bonding studies involving the other elements is quite difficult, since macroscopic analytical techniques (*e.g.* NMR, crystallography) are not feasible. An example of this is the difficulty in characterizing ^{211}At-labeled compounds. There are no stable isotopes of astatine, and a radioactivity quantity as high as 2 GBq (54 mCi) of ^{211}At is only ~26 ng, making the physical characterization of ^{211}At-containing radiopharmaceuticals very difficult if not impossible. Importantly, iodinated (and radioiodinated) derivatives can be used as chromatographic standards for ^{211}At-labeled compounds. While this approach generally provides retention times that indicate approximately where the corresponding ^{211}At-labeled compound might elute, it does not necessarily provide unequivocal proof that a radiochromatographic peak in that area comes from an ^{211}At-labeled compound with the expected structure.

The choice of a bonding or chelation method used with α-emitting radionuclides is also somewhat dependent on the emissions from decay of the radionuclide of interest (or its prompt daughter). The ideal scenario is to use a chelation or bonding method that can bind the α-emitting radionuclide and a radionuclide that is useful for imaging. In general, it is important to conduct imaging (PET or SPECT) both to determine if a therapeutic radiopharmaceutical will be efficacious in a particular patient and to follow the course of therapy. If the therapeutic radionuclide has a gamma emission useful for imaging, it is considered a theranostic radionuclide. If, on the other hand, the therapeutic radionuclide does not have an "imageable" gamma, but another isotope of that element *does* have an "imageable" gamma, this is considered a theranostic radionuclide pair. Theranostic pairs are of high value: the same labeling chemistry can be used for both radionuclides, and identical *in vivo* behavior can be expected for each agent. A third situation is where the therapeutic radionuclide is not theranostic and does not have a theranostic pair. In this case, one must use an "imageable" radionuclide of another element to create a diagnostic scout probe for the therapy. Since the same element is not used, a chelation/bonding reagent is chosen such that binding/bonding of both elements results in high *in vivo* stability. The two agents in this situation are typically referred to as a "theranostic matched pair."

Most of the α-emitting radionuclides of interest are radiometals, with the exception of the halogen ^{211}At. As with the

positron- and β-emitting radiometals described in other chapters, the attachment of α-emitting radiometals to carrier molecules can be accomplished by complexation with chelators having the appropriate functional groups. The design of the ligand for stable bonding is based on the chemical nature, preferred oxidation states, and preferred coordination number of the radiometal. A tremendous amount of effort has been dedicated to the creation of effective chelators [26, 27]. An in-depth discussion of the many different types of chelators is beyond the scope of this chapter. However, extensive reviews of the ligands used for the chelation of α-emitting radionuclides have been published [15, 28]. Despite the large number of chelators that have been prepared and tested, there are only a few that are routinely used for labeling targeting molecules with α-emitting radiometals. It is important to note that in addition to the functional part of the chelator that binds the radiometal in question, the molecule must also include a functional group that allows for bioconjugation to disease-targeting molecules. As a result, these modified chelators are typically known as "bifunctional chelators." The most commonly used reactive functional groups on bifunctional chelators are amine-reactive "active esters," such as *N*-hydroxysuccinimidyl or tetrafluorophenyl esters that form amide bonds and phenyl isothiocyanates that form thiourea bonds. Another common reactive functional group is a maleimide, which reacts with sulfhydryl groups to form thioether bonds.

Generally speaking, there two approaches have been used for the radiolabeling targeting molecules with α-emitters: (1) radiolabeling the bifunctional chelator *prior* to its attachment to the targeting molecule and (2) radiolabeling the bifunctional chelator *after* its attachment to the targeting molecule (reaction paths A and B, respectively in Fig. 3). The second approach is typically preferred because it often results in much higher radiolabeling yields, and it is easier to characterize and evaluate the target binding properties of the chelator-bearing targeting vector prior to radiolabeling. However, due to the radiolabeling conditions of some chelators as well as the possibility of side reactions during some radiosyntheses, the first approach has been used in some cases.

The structures of the most commonly used bifunctional chelators are shown in Fig. 4, and information on which chelators have been used with each radionuclide is included in Table 4. In general, acyclic ligands such as DTPA and its analog CHX-A″-DTPA have fast radiolabeling kinetics

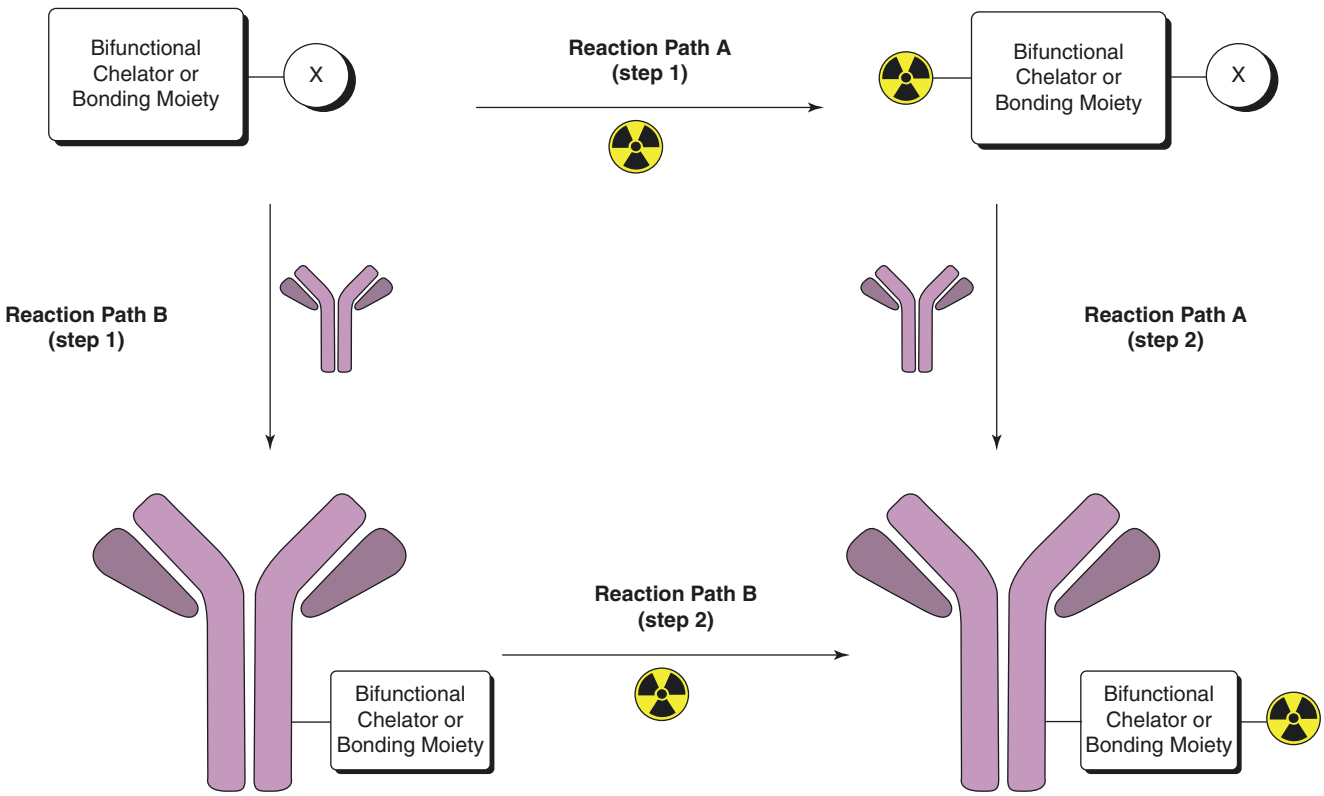

Fig. 3 General scheme depicting alternate reaction paths for radiolabeling of a monoclonal antibody (mAb). **Reaction Path A** depicts radiolabeling of bifunctional chelator or bonding moiety in the first step, followed by conjugation of the radiolabeled reagent with the mAb in a second step. **Reaction Path B** depicts conjugation of the bifunctional chelator or bonding moiety in the first step, followed by radiolabeling of the mAb conjugate in a second step. The circled X signifies a functional group on the chelator or bonding moiety that is reactive with a functional group on the mAb. The radioactivity emblem is representative of an α-emitting radionuclide

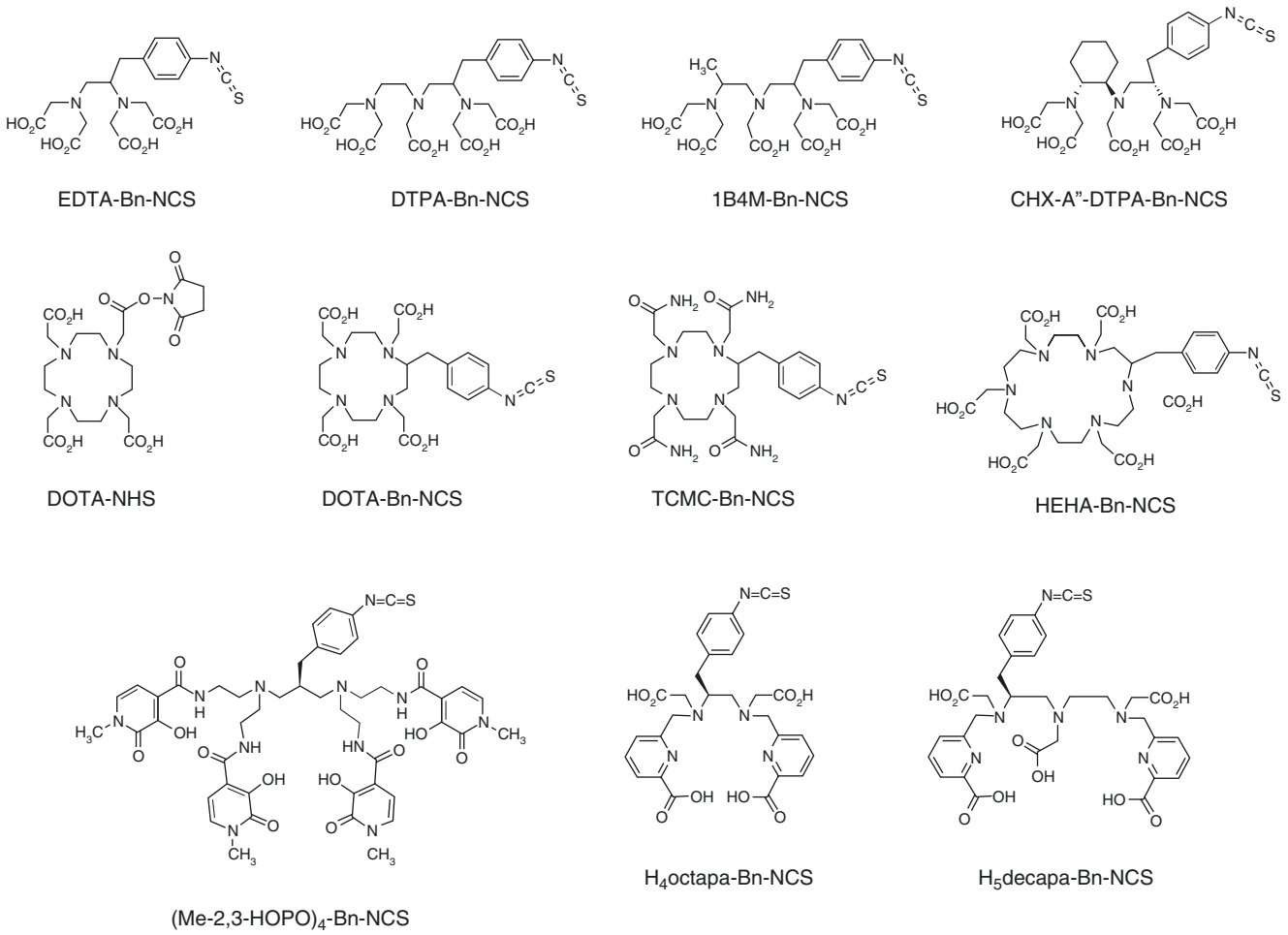

Fig. 4 Chemical structures of bifunctional chelators used to prepare monoclonal antibody (mAb) conjugates for labeling with α-emitting radiometals. The conjugation of these ligands to smaller disease-targeting agents can use reactive functional groups other than the isothiocyanato-benzyl group

under mild reaction conditions, traits that are important when working with radionuclides that have short half-lives or sensitive biomolecules that require mild conditions (*e.g.* proteins). However, while acyclic chelators do have fast complexation kinetics, their complexes are often not stable to *in vivo* demetallation. In contrast, more rigid macrocyclic ligands such as DOTA can require harsh reaction conditions to form complexes, but the resultant complex is often more stable *in vivo*. Because peptides and small molecule targeting moieties are generally less sensitive to high reaction temperatures and lower pH used to facilitate chelation, DOTA can be used to radiolabel them.

The chemistry of bonding astatine to targeting molecules merits a separate discussion as it is fundamentally different from that of the radiometals discussed above. Astatine is a halogen, and it undergoes reactions similar to the other halogens. Interestingly, when astatine was first isolated and its chemistry was evaluated, it was noted that its chemical properties were more similar to its metallic neighbor polonium than its nearest halogen neighbor iodine [29]. More recently, calculations of condensed astatine have shown that it has quite different properties from other halogens (*e.g.* monoatomic) and is metallic in nature [30]. While investigations have been conducted to determine if it can be chelated, no chelators that are stable *in vivo* have yet been found. Some radiolabeling studies involving the binding of ^{211}At to chelated rhodium and iridium have been published [31], but the *in vivo* stability and general utility of this approach remain undefined.

Similar to other halogens, astatine undergoes electrophilic or nucleophilic substitution reactions. Significant effort has been put into development of methods to label molecules with astatine. In those studies, it has been noted that astatine's reactions are generally similar to that of radioiodine, but the properties of the radiolabeled molecules can be quite different, resulting in radioiodine being a poor surrogate for astatine. Nucleophilic substitution reactions involving astatine have not been used much, as they generally

Table 4 Alpha-emitting radionuclides and potential theranostic radionuclide pairs for imaging[a]

α-emitting radiometal[b]	Half-life	Most abundant imageable emissions in keV (% abundance)	Ligand or group most often used[c,d]	Potential theranostic pair radionuclide(s)[c,d]	Half-life of paired nuclide	Imageable photon emissions in keV (abundance)[e]
Astatine-211	7.21 h	77 (12%); 79 (21%)	*m*-benzoate Decaborate(2-)	Iodine-123 Bromine-76	13.2 h 16.2 h	159 (83%) 511 (109%)
Actinium-225	10.0 days	154 (0.3%); 157 (0.3%); 188 (0.5%)	DOTA	Bi-213 daughter	NA	See Bi-213
Bismuth-212	60.55 min	Too low abundance	CHX-A″-DTPA DOTA	Gallium-68 (PET) Scandium-44 (PET)	67.7 min 3.97 h	511 (178%) 511 (189%)
Bismuth-213	45.61 min	440 (26%)	CHX-A″-DTPA DOTA	440 keV (SPECT) Gallium-68 (PET) Scandium-44 (PET)	45.6 min 1.1 h 3.97 h	440 (26%) 511 (178) 511 (189%)
Fermium-255	20.07 h	None	NAOR	NAOR	–	–
Radium-223[f]	11.43 days	154 (5.7%); 269 (14%); 324 (4.0%); 338 (2.8%)	NAC	NAC	–	–
Radium-224[f]	3.632 days	241 (4%)	NAC	NAC	–	–
Terbium-149	4.118 h	165 (26%); 352 (29%); 389 (18%); 511 (14%); 652 (16%); 817 (12%); 853 (16%)	CHX-A″-DTPA DOTA	NA	–	–
Thorium-226	30.57 min	111 (3.3%); 131 (0.3%); 242 (0.9%)	DOTA HOPO	Gallium-68	1.1 h	511 (178%)
Thorium-227	18.70 days	236 (13%); 256 (7.0%); 300 (2.2%); 330 (2.9%)	DOTA HOPO	Zirconium-89	78.4 h	511 (46%)
Lead-212/Bi-212	10.64 h	239 (44%)	TCMC	NA	–	–

[a]The order of radionuclide listing is alphabetical.
[b]When the parent ^{212}Pb ($t_{1/2}$ = 10.64 h) is used, it provides an *in vivo* generator system which makes the effective biologic half-life of ^{212}Bi is longer.
[c]NA is *not applicable* due to the fact that the α-emitting radionuclide has an imageable photon.
[d]NAOR refers to *not able to obtain the radionuclide*; NAC refers to *not able to chelate* the α-emitting radionuclide. In these situations, there is no need to identify a theranostic radionuclide pair for imaging.
[e]Emissions of 511 keV are from positron annihilation (PET imaging); other imageable photons are used in single-photon emission computed tomography (SPECT imaging).
[f]No ligands have been found for use with radium that provide high enough stability for *in vivo* applications.

require more stringent reaction conditions than electrophilic substitution reactions. However, some nucleophilic substitution reactions using iodonium salt intermediates appear to have promise. It should be noted that electrophilic reactions on activated aromatic compounds such as phenols (*e.g.* tyrosine moieties on proteins) can provide a labeling approach, but the resultant astatinated molecules are readily deastatinated. In contrast, the astatination of non-activated or deactivated aromatic compounds provides compounds that are stable (*in vitro*). Of particular importance has been the electrophilic substitution of non-activated aromatic compounds that is facilitated by organometallic intermediates, including organomercury, organosilanes, and organostannanes [32]. Both trimethyl and tri-*n*-butyl organostannanes have proven to be the intermediates of choice for these reactions. Very high astatine labeling yields (>95%) can be achieved using these intermediates.

The critical issue with astatine labeling methods is that most result in an astatine-labeled molecule that is unstable *in vivo* [33]. Not surprisingly, this has made it particularly difficult to develop radiopharmaceuticals containing astatine. This instability appears to be related to the *in vivo* metabolism of the astatine-labeled biomolecule, as the same conjugates are often quite stable *in vitro*. However, the short half-life of astatine is an advantage when the carrier molecule is slowly metabolized—as in the case of monoclonal antibodies (mAb)—because the astatine undergoes decay more rapidly than the protein is metabolized, so the presence of free ^{211}At is kept to a minimum.

An alternate approach for astatine labeling is the use of anionic aromatic boron cage moieties, in which the ^{211}At is bound to an aromatic boron atom rather than a carbon atom. Boron-halogen bonds are in general stronger than carbon-halogen bonds, particularly in aromatic compounds. In studies directed at boron neutron capture therapy, aromatic boron cage moieties—such as the *closo*-decaborate^{2-} moiety (empirical formula of $B_{10}H_{10}^{2-}$)—have been shown to have low toxicity. Furthermore, the dianionic aromatic nature of the *closo*-decaborate^{2-} moiety makes it extremely reactive with electrophilic astatine, resulting in high radiochemical labeling yields. These factors, along with the fact that the aromatic boron cage moieties are similar in size to a phenyl

ring, make them very attractive for use in radiohalogenations. This labeling approach has been shown to provide ^{211}At-labeled compounds that are stable to *in vivo* deastatination [34]. While the use of anionic boron cage moieties for labeling proteins with astatine has been very successful, their use in labeling small molecules has not been demonstrated and may be questionable. This is because the anionic charge on the borate labeling moiety can potentially change the *in vivo* pharmacokinetics and tissue/cell penetration of the small molecule targeting agent. It is apparent that additional astatine labeling methods are needed to develop a broader array of astatinated radiopharmaceuticals.

A description of the most common bifunctional reagents used to modify disease-targeting and receptor-binding molecules for radiolabeling with α-emitting radionuclides is provided in the following sections. Examples of two mAb labeling approaches are also provided for actinium-225 and astatine-211 (see Fig. 3).

Actinium-225 Initial chelation studies with ^{225}Ac were conducted with the commonly used acyclic chelators EDTA and DTPA as well as the latter's more sterically restricted methyl (*e.g.* 1B4M-DTPA) and cyclohexyl (*e.g.* CHX-A″-DTPA) congeners. These ligands were modified with isothiocyanato-benzyl (Bn-NCS) functional groups for conjugation to proteins (see Fig. 4). Unfortunately, when the protein conjugates were radiolabeled with ^{225}Ac, none of them provided adequate *in vivo* stability for use as radiopharmaceuticals. The macrocyclic DOTA ligand was subsequently studied as an alternative. A **DOTA-NHS** derivative (in which an *N*-hydroxysuccinimide ester is attached to an acetate side group) was conjugated with a monoclonal antibody (mAb), and radiolabeling with ^{225}Ac was evaluated. The initial radiolabeling studies provided very low radiochemical yields (<1%) when directly labeling the mAb, so an alternate 2-step labeling approach was evaluated (see *Reaction Path A,* Fig. 3). In this 2-step approach, the bifunctional chelator isothiocyanato-benzyl-DOTA (**DOTA-Bn-NCS**) was radiolabeled in the first step to provide an ^{225}Ac-labeled amine-reactive intermediate **2** that was subsequently conjugated to a mAb to give the radiolabeled mAb **3**. This approach provided higher radiochemical yields (~10%) than the first approach, but these yields remained quite low [35]. More recently, a direct labeling method (see *Reaction Path B*, Fig. 3) in which the mAb is conjugated with **DOTA-Bn-NCS** prior to radiolabeling with ^{225}Ac was reported [36]. This approach provided ~95% labeling yield of the radioimmunoconjugate, and the ^{225}Ac-labeled antibody was found to be stable *in vivo*. The difference in direct labeling yields from the **DOTA-NHS** and **DOTA-Bn-NCS** conjugates—which have 3 or 4 carboxylate groups available, respectively—is striking. Other larger macrocyclic ligands similar to DOTA have been tested for labeling mAbs. Interestingly, a pentaaza-chelate (15 atom ring; PEPA) mAb conjugate was found to be unstable *in vivo*, whereas the mAb conjugate of a hexaaza-derivative (18 atom ring; **HEHA-Bn-NCS**) was found to be stable [37]. Unlike more sensitive mAbs, DOTA-bearing small molecules and peptides can be labeled under elevated temperatures to obtain high radiochemical yields. Other ligands that might improve the labeling conditions for ^{225}Ac are currently under investigation, but it is likely that **DOTA-Bn-NCS** will continue to be used for ^{225}Ac labeling in the future.

Bismuth-212/213 The half-lives of ^{212}Bi and ^{213}Bi are very short (60.6 min and 45.6 min, respectively) for developing radiopharmaceuticals, so the ligand and reaction conditions used in labeling the targeting vector must provide very rapid radiolabeling. Early chelation studies involved the use of a bifunctional DTPA derivative; however, the resulting radioimmunoconjugates were found to be unstable to *in vivo* demetallation. Because of the requirement for rapid labeling and the reaction conditions needed to label DOTA-bearing mAbs with bismuth, the use of DOTA derivatives was not favorable. Thus, considerable efforts were undertaken to find more stable chelator for ^{212}Bi and ^{213}Bi. Since the DTPA ligand provided rapid labeling, DTPA derivatives with rigidifying backbone modifications were developed [27]. These included DTPA variants bearing methyl-substituted backbones (*e.g.* **1B4M-Bn-NCS**) as well as backbones that incorporated a cyclohexyl group (**CHX-A″-DTPA-Bn-NCS**) (see Fig. 4). Unfortunately, substitutions on the DTPA backbone introduced epimers and diastereomeric pairs that affected the *in vivo* stability of the chelate complexes. More information on the *in vivo* stability differences observed for the backbone-modified DTPA derivatives can be obtained from a review on the labeling chemistry of α-emitters [15]. At present, **CHX-A″-DTPA-Bn-NCS** might be considered the bifunctional chelator of choice for labeling heat- and pH-sensitive biomolecules with $^{212/213}$Bi. It must be emphasized that the CHX-A″-DTPA ligand does not provide high *in vivo* stability for bismuth radionuclides, but it has adequate stability for use with slowly metabolized molecules such as mAbs. In contrast, the stability of bismuth-labeled CHX-A″-DTPA chelate complex may not be adequate for labeling small molecules and rapidly metabolized proteins or peptides. Importantly, small molecules and peptides can generally withstand the reaction conditions required to label DOTA derivatives with bismuth isotopes. Examples in which DOTA has been incorporated into a disease-targeting small molecule include a ^{213}Bi-labeled DOTATOC [38] and a ^{213}Bi-labeled biotin-DOTA derivative [39]. Reaction temperatures of 80–100 °C were used to obtain these two products in just 5 min reaction time. Importantly, ^{213}Bi can be used to prepare theranostic radiopharmaceuticals, as it has a 440 keV photon γ emission that can be used for imaging.

Fermium-255 It appears that there are no examples of ^{255}Fm chelation for *in vivo* use, but studies evaluating binding of ^{254}Fm with DTPA suggest that the cyclohexyl-bearing derivative **CHX-A″-DTPA-Bn-NCS** might facilitate the labeling of proteins. However, considering the ~20 h half-life of ^{255}Fm, it would be best if a macrocyclic bifunctional chelator such as **DOTA-Bn-NCS** be evaluated as a labeling moiety. The important point is that it is unlikely that ^{255}Fm will be made available for developing radiopharmaceuticals due to the difficulty of its production.

Radium-223/224 Because of its availability, there is a high interest in the coupling of radium radionuclides—particularly ^{223}Ra—to disease-targeting vectors. Radium's chemistry is similar to that of barium, and in aqueous solution, it is found almost exclusively in the +2 oxidation state [40]. While there have been many attempts to find a ligand that will enable the stable *in vivo* chelation of radium nuclides, none has been developed so far. Attempts with DTPA, DOTA, and calix[4]arene tetraacetic acid have shown that the calix[4]arene provided the most stable complexes, but that stability was not sufficient for *in vivo* use [41]. As an alternative to chelation, incorporation of radium isotopes into nanoparticles may provide an approach that is successful for *in vivo* applications [42].

Terbium-149 The fact that there are several radioisotopes of terbium that have emissions for imaging and therapy makes the α-particle-emitting ^{149}Tb attractive to develop theranostic radiopharmaceuticals [43]. It has been demonstrated that terbium radioisotopes, including ^{149}Tb, can be readily chelated by CHX-A″-DTPA and DOTA. While this is the case, the difficulty in production of ^{149}Tb calls into question the potential of this radionuclide for the development of theranostic radiopharmaceuticals.

Thorium-226/227 The α-emitting isotopes of thorium—^{226}Th and ^{227}Th—have very disparate half-lives: 30.6 min and 18.7 days, respectively. As a result, it seems that different ligand types (*e.g.* acyclic vs. macrocyclic) could be used as bifunctional chelators for labeling radiopharmaceuticals with each of these isotopes. As with the short-lived bismuth isotopes, DTPA derivatives such as CHX-A″-DTPA may be useful for radiopharmaceuticals employing ^{226}Th [44]. Given its much longer half-life, ^{227}Th may be best suited for use with antibody-based vectors, thus making macrocyclic chelators attractive. The labeling of mAbs with ^{227}Th has been accomplished using **DOTA-Bn-NCS** as the bifunctional chelator [45], but the labeling conditions are not optimal and the labeling yields were low. More recently, an octadentate bifunctional chelator containing hydroxypyridinone (HOPO) moieties—**(Me-3,2-HOPO)$_4$-Bn-NCS** (see Fig. 4)—has been developed and facilitates the labeling of mAbs with ^{227}Th under mild conditions [46]. The chelation of ^{227}Th occurred within 30 min and provided >96% labeling yield, making this chelator attractive for labeling with ^{226}Th as well. *In vivo* studies have shown that (Me-3,2-HOPO)$_4$-chelated ^{227}Th has good *in vivo* stability. While ^{226}Th and ^{227}Th do not emit imageable photons in high enough abundance for use in theranostics, HOPO chelators have been shown to bind the positron-emitting radionuclide zirconium-89 (^{89}Zr) [47], perhaps allowing for the development of matched Th/Zr theranostic pairs. Other bifunctional chelators with functional groups similar to the HOPO ligands—such as carboxy-pyridyl derivatives having denticities of 8 (**octapa-Bn-NCS**) and 10 (**decapa-Bn-NCS**)—might also be used for theranostic applications in which the chelation of two different radionuclides are required [26].

Lead-212/Bi-212 The short half-life of ^{212}Bi severely limits its application in therapeutic radiopharmaceuticals. However, investigators have noted that the parent radionuclide ^{212}Pb, which has a 10.6 h half-life, might be used as an *in vivo* generator to produce ^{212}Bi for therapeutic uses. Thus, studies to find an appropriate chelator for ^{212}Pb were conducted. While some of the studies were directed at acyclic ligands, the majority of chelation studies have been conducted with macrocyclic ligands. Of several different macrocyclic chelators, DOTA appeared most stable for both lead and bismuth. Studies with **DOTA-Bn-NCS** conjugated to antibodies provided data that suggested the ^{212}Pb was being released *in vivo*, so another DOTA derivative that had amide bonds rather than the free carboxylates, denoted **TCMC-Bn-NCS** (see Fig. 4), was prepared and tested as it had been previously shown to be particularly stable to the release of chelated lead [27]. The labeling of small molecule targeting agents with ^{212}Pb has been primarily accomplished through the incorporation of DOTA into the small molecule. The issue that arises with this ^{212}Pb/^{212}Bi "*in vivo* generator" approach is that some (>30%) of the ^{212}Bi is released from the chelator upon the decay of ^{212}Pb, and a significant portion of this released ^{212}Bi redistributes to the kidneys. While agents can be administered to release the ^{212}Bi from the kidneys, the potential for latent kidney toxicity remains, so the development of new approaches to the chelation of ^{212}Pb are needed.

Astatine-211 Radiolabeling with ^{211}At is very different from radiolabeling with the other α-emitting radionuclides, as (so far) no methods for the stable chelation of this element from the halogen family have been demonstrated. Being a halogen, ^{211}At can be bound to other molecules through nucleophilic and electrophilic reactions. A large number of studies have been carried out using labeling methods based on these approaches, but many reactions result in products that are not

stable *in vivo* [33]. However, it was found that non-activated aromatic ring-containing bifunctional reagents such as *meta*- or *para*-astatobenzoate esters (Fig. 5) could be radiolabeled and then conjugated with intact mAbs to provide radioimmunoconjugates that are reasonably stable to *in vivo* deastatination. The result reinforces the notion that *in vivo* stability is a function of the rate of metabolism of the astatinated radiopharmaceutical, as small molecules and antibody fragments containing the *same* astatobenzoate functionalities are quite unstable *in vivo*. Unfortunately, due to the insolubility of the tri-*n*-butylstannylbenzoate moiety and the high toxicity of the trimethylstannylbenzoate moiety, the stannylbenzoates are generally radiolabeled prior to conjugation with proteins. This two-step labeling approach (see *Reaction Path A*, Fig. 3) results in a moderate overall radiolabeling yield (*e.g.* 40–50%). An alternative to the benzoate esters is to use phenethylsuccinimide NHS ester conjugates, *i.e.* ***p*-PESA-NHS** (see Fig. 5) [48].

The *in vivo* instability and low labeling yields of the phenyl ring-based conjugates led to the development of new reagents for labeling targeting vectors with ^{211}At that rely upon the formation of aromatic boron-astatine bonds. The underlying concept here is that boron-halogen bonds are generally more stable than carbon-halogen bonds, and aromatic-halogen bonds are more stable than aliphatic-halogen bonds. A number of different aromatic boron cage molecules have been prepared, conjugated with antibody fragments, and tested *in vivo* to evaluate their stability. The nonahydro-*closo*-decaborate^{2-} aromatic moiety was found to provide the best properties for labeling proteins with ^{211}At. Two bifunctional variants of the *closo*-decaborate^{2-} moiety—isothiocyanatophenethylureido (**B10-NCS**) and maleimido-trioxadiamine (**B10-Mal**) derivatives—have been used extensively to radiolabel intact antibodies and antibody fragments (see Fig. 5). The use of these bifunctional reagents has provided immunoconjugates that can be rapidly labeled (under 2 min) to give high radiochemical labeling yields (80–95%) and have been found to be stable to *in vivo* deastatination [34]. While the *closo*-decaborate^{2-} moiety has provided excellent results for labeling proteins, this moiety may be problematic when incorporated into some small molecule carriers, as the dianionic charge may negatively affect their *in vivo* targeting, cell penetration, and pharmacokinetics. This has yet to be determined, however. It should be noted that astatinated benzoate derivatives are being used to prepare mAb-based radiopharmaceuticals, as they undergo minimal deastatination due to the slow metabolism of intact mAbs. Furthermore, an approach that allows for the direct labeling of mAbs conjugated with the trimethylstannylbenzoate moiety has been developed. The direct labeling approach uses a large excess of *N*-iodosuccinimide to cleave the trimethylstannyl group after astatination [49], alleviating the issue of toxicity of the stannylbenzoate conjugate. An improvement in radiolabeling yield was obtained, but the yields were not as high as those obtained using the *closo*-decaborate^{2-}-based conjugates. It should also be noted that the arylstannanes and *closo*-decab-

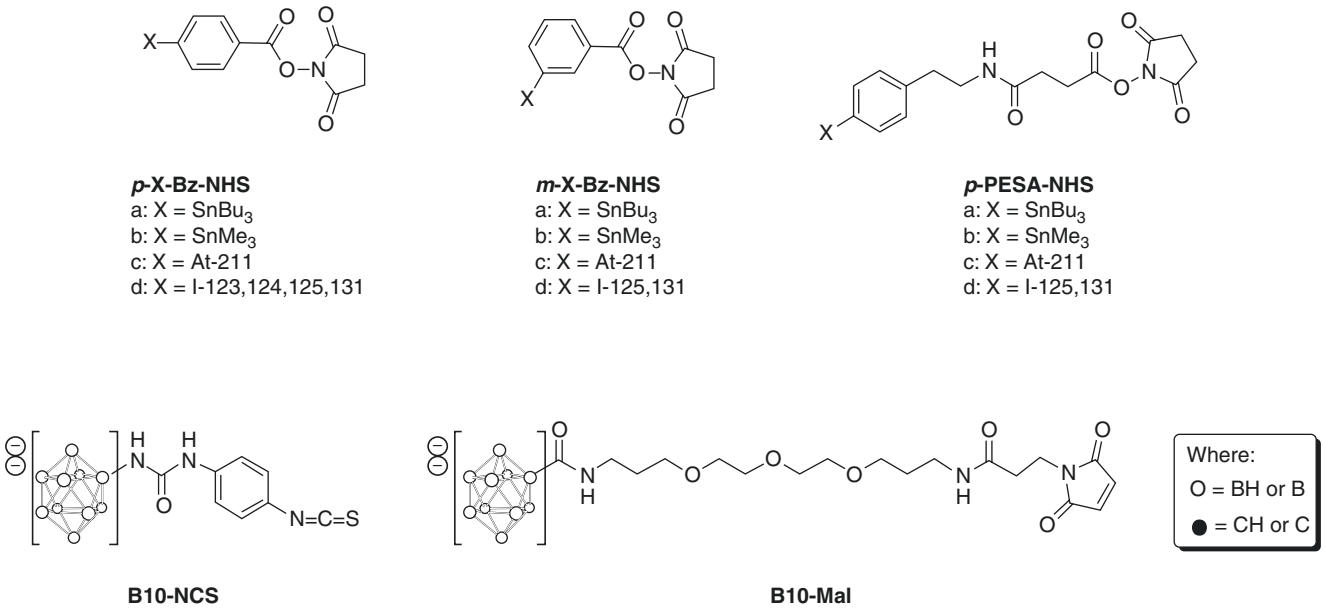

Fig. 5 Chemical structures of benzoate esters, phenethylsuccinimide ester, and *closo*-decaborate$^{(2-)}$ derivatives used to prepare radiohalogen-labeled monoclonal antibody (mAb) conjugates. In the aryl compounds either a $SnBu_3$ or $SnMe_3$ labeling group was used, and the radioiodinated derivatives that have been prepared are shown for the demonstration of their theranostic potential. In the depicted *closo*-decaborate^{2-} cage structure, the open circles represent boron atoms, and the protons attached to the boron atoms are left off for simplicity (as in other aromatic rings)

orate^{2-} moieties readily react with radioiodine and radiobromine, making it possible to develop theranostic matched pair radiopharmaceuticals.

The foregoing description of labeling methods are cursory in nature, as they do not include descriptions of reagents or reaction conditions and do not include a fairly large number of the alternative reagents studied. Of course, one must read reviews and original literature publications to obtain that information. Instead, the descriptions provided cover what might be identified as the most important findings in this area, but such classification is subjective in nature.

Controversial Issues

There are several controversial issues that come up when discussing the potential of α-emitters radionuclides in treating human disease. Some of those issues include (1) the question of how stable the radionuclide bond to the targeting molecule needs to be to develop a useful targeted α-emitting radiopharmaceutical, (2) the belief that only one α-emitting radionuclide can be used for any or all applications, (3) the tendency to dismiss the issue of the redistribution and toxicity of α daughter radionuclides, and (4) the belief that targeted α-emitting radionuclides cannot effectively treat solid tumors. Coming to a consensus on how to address these issues is not easy, as the answers are based on the scientific environment and personal beliefs of individual researchers. Some comments on these issues follow.

With regard to the toxicity introduced by the redistribution of a radionuclide and/or its daughter radionuclides (issues #1 and #3 above), the answer is admittedly not yet clear for α-emitting radiopharmaceuticals. It is likely to be highly dependent on the quantity of radionuclide administered, the natural distribution of the radionuclide and its daughter radionuclides, the rate of release from the organ or tissue, and many other factors. With regard to one α-emitting radionuclide being useful for all/many medical applications, it is important to note that the low availability of α-emitting radionuclides has often resulted in investigators using the same radionuclide with different types of disease-targeting carrier molecules (*e.g.* antibodies, peptides, small molecules) rather than using a radionuclide which has a half-life or decay characteristics that best suites the carrier molecule and disease to be treated. Thus, a particular radionuclide can become that investigator's favorite nuclide. While this belief may have merit for some applications, it seems that short half-lived radionuclides might be optimal in some applications (*e.g.* marrow conditioning) and less optimal in others (*e.g.* solid tumors). The issue of addressing the belief that targeted α-emitters cannot be used to treat solid tumors is perhaps the easiest to address, as it can be—and is currently being—tested, so a definitive answer will be obtained for some cancer types.

The Future

Based on the encouraging results obtained in several ongoing preclinical studies, it seems very likely that α-emitting radiopharmaceuticals will be used in the therapy of human diseases in the future. Perhaps one measure of whether a targeted α-emitting radionuclide might be useful in the therapy of cancer and other human diseases such as viral and bacterial infections is its advancement into clinical trials. While not the first to enter clinical trials, ^{223}Ra ($^{223}RaCl_2$; Xofigo™) was the first α-emitting radiopharmaceutical to obtain approval for use in the therapy of metastatic bone cancer (albeit only for non-resectable metastatic prostate cancer at this time). Presently, five other α-emitting radionuclides listed in Table 2—^{225}Ac, ^{213}Bi, ^{211}At, ^{212}Pb/^{212}Bi, and ^{227}Th—are currently in clinical studies. One of the most important issues that will need to be addressed to bring radiopharmaceuticals to clinical practice is overcoming the low supply of α-emitting radionuclides. Fortunately, the US Department of Energy (US DOE) has focused on providing the quantities of ^{225}Ac and other α-emitting radionuclides required for the commercialization of radiopharmaceuticals containing them. The US DOE is also setting up a network of universities that could ultimately provide regional production of ^{211}At for preclinical and early clinical investigations.

The Bottom Line

The promise of α-emitting radionuclides for treating human diseases is being tested in a number of preclinical and clinical evaluations. Some important points about the development of α-emitting radiopharmaceuticals are listed below:

- Blood-borne and metastatic diseases should be the focus when developing α-emitting radiopharmaceuticals, as radiopharmaceuticals can be of the highest utility and value in these areas.
- At present, the supply of most α-emitting radionuclides is not adequate for routine clinical use, but work is being done to develop larger supplies, including the development of new, less costly methods for their production.
- Highly selective disease-targeting agents with renal or hepatobiliary excretion of metabolites need to be developed to minimize off-target toxicity.

- Methods for stably attaching α-emitting radionuclides to disease-targeting agents have been developed for some radionuclides, and new reagents are being developed for the ones that do not presently have suitable methods for stable attachment.
- α-Emitting radionuclides which have short half-lives can be used with less stable chelators or bonding agents if the carrier molecule is slowly metabolized.
- Methods for removing any free radionuclides from the blood and/or organs need to be developed to minimize the effects of the release of radionuclides from their carrier molecules or the release of their daughters after decay.

References

1. Vaidyanathan G, Zalutsky MR. Targeted therapy using alpha emitters. Phys Med Biol. 1996;41(10):1915–31.
2. McDevitt MR, Sgouros G, Finn RD, Humm JL, Jurcic JG, Larson SM, et al. Radioimmunotherapy with alpha-emitting nuclides. Eur J Nucl Med. 1998;25(9):1341–51.
3. Brechbiel MW. Targeted alpha-therapy: past, present, future? Dalton Trans. 2007;43:4918–28.
4. Mulford DA, Scheinberg DA, Jurcic JG. The promise of targeted alpha-particle therapy. J Nucl Med. 2005;46(Suppl 1):199S–204S.
5. Couturier O, Supiot S, Degraef-Mougin M, Faivre-Chauvet A, Carlier T, Chatal JF, et al. Cancer radioimmunotherapy with alpha-emitting nuclides. Eur J Nucl Med Mol Imaging. 2005;32(5):601–14.
6. Wadas TJ, Pandya DN, Sai KKS, Mintz A. Molecular targeted alpha-particle therapy for oncologic applications. Am J Roentgenol. 2014;203(2):253–60.
7. Cleaves MA. Radium: with a preliminary note on radium rays in the treatment of cancer. Med Rec. 1903;64(16):601–6.
8. Newcomet WS. Internal administration of radium. In: Radium and radiotherapy: radium, thorium, and other radio-active elements in medicine and surgery. New York: Lea & Febiger; 1914. p. 97–105.
9. Simpson FE. Radium therapy. St. Louis: C.V. Mosby Company; 1922.
10. Clark C. Radium girls: women and industrial health reform 1910–1935. Chapel Hill: University of North Carolina Press; 1997.
11. Rowland RE. Radium in humans: a review of U.S. Studies. In: Do U, editor. Energy. Chicago: University of Chicago; 1994. p. 233.
12. Hall EJ, Giaccia AJ. Radiobiology for the radiologist. 6th ed. Philadelphia: Lippincott Williams and Wilkins; 2006.
13. Hall EJ, Giaccia AJ. Linear energy transfer and relative biologic effectiveness. Radiobiology for the radiologist. 6th ed. Philadelphia: Lippincott Williams & Wilkins; 2006.
14. Sgouros G. Alpha-particles for targeted therapy. Adv Drug Deliv Rev. 2008;60(12):1402–6.
15. Wilbur DS. Chemical and radiochemical considerations in radiolabeling with α-emitting radionuclides. Curr Radiopharm. 2011;4(3):214–47.
16. Muller C, Vermeulen C, Koster U, Johnston K, Turler A, Schibli R, et al. Alpha-PET with terbium-149: evidence and perspectives for radiotheragnostics. EJNMMI Radiopharm Chem. 2016:1–5.
17. de Kruijff RM, Wolterbeek HT, Denkova AG. A critical review of alpha radionuclide therapy-how to deal with recoiling daughters? Pharmaceuticals (Basel). 2015;8(2):321–36.
18. McDevitt MR, Finn RD, Sgouros G, Ma D, Scheinberg DA. An $^{225}Ac/^{213}Bi$ generator system for therapeutic clinical applications: construction and operation. Appl Radiat Isot. 1999;50(5):895–904.
19. Atcher RW, Friedman AM, Hines JJ. An improved generator for the production of 212Pb and ^{212}Bi for ^{224}Ra. Appl Radiat Isot. 1988;39:283–6.
20. Morgenstern A, Lebeda O, Stursa J, Bruchertseifer F, Capote R, McGinley J, et al. Production of $^{230}U/^{226}Th$ for targeted alpha therapy via proton irradiation of ^{231}Pa. Anal Chem. 2008;80(22):8763–70.
21. Kulyukhin SA, Auerman LN, Novichenko VL, Mikheev NB, Rumer IA, Kamenskaya AN, et al. Production of microgram quantities of einsteinium-253 by reactor irradiation of californium. Inorg Chim Acta. 1985;110:25–6.
22. Zaitseva NG, Dmitriev SN, Maslov OD, Molokanova LG, Starodub GY, Shishkina TV, et al. Terbium-149 for nuclear medicine. The production of ^{149}Tb via heavy ions induced nuclear reactions. Czechoslov J Phys. 2003;53:A455–A8.
23. Beyer G-J, Comar JJ, Dakovic M, Soloviev D, Tamburella C, Hagebo E, et al. Production routes of the alpha emitting ^{149}Tb for medical application. Radiochim Acta. 2002;90:247–52.
24. Beyer GJ, Miederer M, Vranjes-Duric S, Comor JJ, Kunzi G, Hartley O, et al. Targeted alpha therapy in vivo: direct evidence for single cancer cell kill using ^{149}Tb-rituximab. Eur J Nucl Med Mol Imaging. 2004;31(4):547–54.
25. Muller C, Vermeulen C, Koster U, Johnston K, Turler A, Schibli R, et al. Alpha-PET with terbium-149: evidence and perspectives for radiotheranostics. EJNMMI Radiopharm Chem. 2016;1:1–5.
26. Price EW, Orvig C. Matching chelators to radiometals for radiopharmaceuticals. Chem Soc Rev. 2014;43(1):260–90.
27. Brechbiel MW. Bifunctional chelates for metal nuclides. Q J Nucl Med Mol Imaging. 2008;52(2):166–73.
28. Hassfjell S, Brechbiel MW. The development of the a-particle emitting radionuclides ^{212}Bi and ^{213}Bi, and their decay chain related radionuclides, for therapeutic applications. Chem Rev. 2001;101(7):2019–36.
29. Corson DR, MacKenzie KR, Segre E. Artificially radioactive element 85. Phys Rev. 1940;58:672–8.
30. Hermann A, Hoffmann R, Ashcroft NW. Condensed astatine: monatomic and metallic. Phys Rev Lett. 2013;111(11):116404.
31. Pruszynski M, Bilewicz A, Zalutsky MR. Preparation of Rh[16aneS4-diol]^{211}At and Ir[16aneS4-diol]^{211}At complexes as potential precursors for astatine radiopharmaceuticals. Part I: synthesis. Bioconjug Chem. 2008;19(4):958–65.
32. Wilbur DS. Radiohalogenation of proteins: an overview of radionuclides, labeling methods, and reagents for conjugate labeling. Bioconjug Chem. 1992;3(6):433–70.
33. Wilbur DS. [^{211}At]Astatine-labeled compound stability: issues with released [^{211}at]astatide and development of labeling reagents to increase stability. Curr Radiopharm. 2008;1:144–76.
34. Wilbur DS, Chyan MK, Nakamae H, Chen Y, Hamlin DK, Santos EB, et al. Reagents for astatination of biomolecules. 6. An intact antibody conjugated with a maleimido-*closo*-decaborate(2-) reagent via sulfhydryl groups had considerably higher kidney concentrations than the same antibody conjugated with an isothiocyanato-closo-decaborate(2-) reagent via lysine amines. Bioconjug Chem. 2012;23(3):409–20.
35. McDevitt MR, Ma D, Simon J, Frank RK, Scheinberg DA. Design and synthesis of ^{225}Ac radioimmunopharmaceuticals. Appl Radiat Isot. 2002;57(6):841–7.
36. Maguire WF, McDevitt MR, Smith-Jones PM, Scheinberg DA. Efficient 1-step radiolabeling of monoclonal antibodies to high specific activity with ^{225}Ac for alpha-particle radioimmunotherapy of cancer. J Nucl Med. 2014;55(9):1492–8.

37. Deal KA, Davis IA, Mirzadeh S, Kennel SJ, Brechbiel MW. Improved in vivo stability of actinium-225 macrocyclic complexes. J Med Chem. 1999;42(15):2988–92.
38. Norenberg JP, Krenning BJ, Konings IRHM, Kusewitt DF, Nayak TK, Anderson TL, et al. ^{213}Bi-[DOTA0, Tyr3]octreotide peptide receptor radionuclide therapy of pancreatic tumors in a preclinical animal model. Clin Cancer Res. 2006;12(3, Pt. 1):897–903.
39. Park SI, Shenoi J, Pagel JM, Hamlin DK, Wilbur DS, Orgun N, et al. Conventional and pretargeted radioimmunotherapy using bismuth-213 to target and treat non-Hodgkin lymphomas expressing CD20: a preclinical model toward optimal consolidation therapy to eradicate minimal residual disease. Blood. 2010;116(20):4231–9.
40. Kirby HW, Salutsky ML. The radiochemistry of radium, U.S. Atomic Energy Commission NAS-NS 3057. Springfield: National Academy of Sciences; 1964. p. 172.
41. Gott M, Steinbach J, Mamat C. The radiochemical and radiopharmaceutical applications of radium. Open Chem. 2016;14(1):118–29.
42. Rojas JV, Woodward JD, Chen N, Rondinone AJ, Castano CH, Mirzadeh S. Synthesis and characterization of lanthanum phosphate nanoparticles as carriers for Ra-223 and Ra-225 for targeted alpha therapy. Nucl Med Biol. 2015;42(7):614–20.
43. Muller C, Zhernosekov K, Koster U, Johnston K, Dorrer H, Hohn A, et al. A unique matched quadruplet of terbium radioisotopes for PET and SPECT and for alpha- and beta- radionuclide therapy: an in vivo proof-of-concept study with a new receptor-targeted folate derivative. J Nucl Med. 2012;53(12):1951–9.
44. Le Du A, Sabatie-Gogova A, Morgenstern A, Montavon G. Is DTPA a good competing chelating agent for Th(IV) in human serum and suitable in targeted alpha therapy? J Inorg Biochem. 2012;109:82–9.
45. Larsen RH, Borrebaek J, Dahle J, Melhus KB, Krogh C, Valan MH, et al. Preparation of TH^{227}-labeled radioimmunoconjugates, assessment of serum stability and antigen binding ability. Cancer Biother Radiopharm. 2007;22(3):431–7.
46. Ramdahl T, Bonge-Hansen HT, Ryan OB, Larsen S, Herstad G, Sandberg M, et al. An efficient chelator for complexation of thorium-227. Bioorg Med Chem Lett. 2016;26(17):4318–21.
47. Deri MA, Ponnala S, Kozlowski P, Burton-Pye BP, Cicek HT, Hu C, et al. P-SCN-Bn-HOPO: a superior bifunctional chelator for ^{89}Zr ImmunoPET. Bioconjug Chem. 2015;26(12):2579–91.
48. Yordanov AT, Garmestani K, Zhang M, Zhang Z, Yao Z, Phillips KE, et al. Preparation and in vivo evaluation of linkers for ^{211}At labeling of humanized anti-Tac. Nucl Med Biol. 2001;28(7):845–56.
49. Lindegren S, Andersson H, Back T, Jacobsson L, Karlsson B, Skarnemark G. High-efficiency astatination of antibodies using N-iodosuccinimide as the oxidising agent in labelling of N-succinimidyl 3-(trimethylstannyl)benzoate. Nucl Med Biol. 2001;28(1):33–9.

The Radiopharmaceutical Chemistry of Seldom-Used Radionuclides in Nuclear Medicine

Jason P. Holland

Fundamentals

The chemistry of stable nuclides is a rich and diverse field because elemental properties vary across the entire periodic table. Changes in atomic number, size, charge, ionization potential, electronegativity, oxidation state, bond or coordination number, and other electronic factors dictate the formation and stability of many millions of covalent and ionic species that have been synthesized. When the physical decay properties of radionuclides are superimposed upon this chemical backdrop, a seemingly infinite number of permutations exist for creating radioactive compounds. An overview of the chemical and radiochemical landscape of elements that are of current or potential interest in modern nuclear medicine is shown in Fig. 1 [1–4]. Physical decay data presented in this chapter are taken from the National Nuclear Decay Center (NNDC; Brookhaven National Laboratory, Upton, NY; www.nndc.bnl.gov).

In light of this wealth of possibilities, how can a radiochemist begin to choose the most appropriate radionuclide for their intended application? For the majority of scientists, the answer to this question is dictated by three primary factors. First and foremost is the availability of a given radionuclide. Suffice it to say that only radionuclides that are accessible on a regular basis from either commercial or academic sources have a chance of bridging the gap between the laboratory and the clinic. Many research teams around the world have performed – and continue to perform – sterling work on the nuclear synthesis and separation chemistry of radionuclides, and their efforts underpin all of the radiotracers used in nuclear medicine (see the chapter on "Methods for the Production of Radionuclides for Medicine"). The second consideration is then centred on the application: imaging or therapy? Immutable decay properties predefine which radionuclides are suitable for imaging, which are suitable for radiotherapy, and which can be used for both. Given access to a free choice of radionuclides, the third factor is centred on the chemical and biological properties of the targeting vector. The advantages and disadvantages of radiotracers based on small molecules, peptides, proteins/antibodies, and nanoparticles have been introduced in the chapters on "Small Molecules as Radiopharmaceutical Vectors", "Peptides as Radiopharmaceutical Vectors", "Immunoglobulins as Radiopharmaceutical Vectors", and "Nanoparticles as Radiopharmaceutical Vectors". Matching the physical half-life and decay mode of a radionuclide with not only the intended application but also the anticipated biological half-life of the vector is a logical and highly useful principle adopted by many radiochemists. For instance, radiotracers based on small molecules often exhibit rapid target localization, cellular uptake, washout, and whole-body excretion profiles. In contrast, antibodies require extended circulation times to achieve optimal uptake in target tissue. For a given radiopharmaceutical, the goal is usually to ensure maximal uptake in the target with high image contrast or specific radiotherapeutic dose, all while concomitantly minimizing the overall radiation burden to the patient. The following sections focus on the properties, production methods, separation, radiochemistry, and applications of various radionuclides that, due to limited availability or knowledge of their biochemical properties, are currently considered 'unconventional'. It is worth noting that until recently, radionuclides of copper and zirconium were also considered 'unconventional' but are now part of mainstream nuclear medicine [5]. The hope is that increased research and appreciation of radionuclides from the wider periodic table will expand the repertoire of radiopharmaceutical chemistry.

The Radionuclides of the *s*-Block Elements

The chemistry of the *s*-block metal ions is dominated by the formation of ionic compounds. Moving down the elements of groups 1 and 2 leads to increased atomic radii, decreased

J. P. Holland (✉)
Department of Chemistry, University of Zurich, Zurich, Switzerland
e-mail: jason.holland@chem.uzh.ch

J. S. Lewis et al. (eds.), *Radiopharmaceutical Chemistry*, https://doi.org/10.1007/978-3-319-98947-1_24

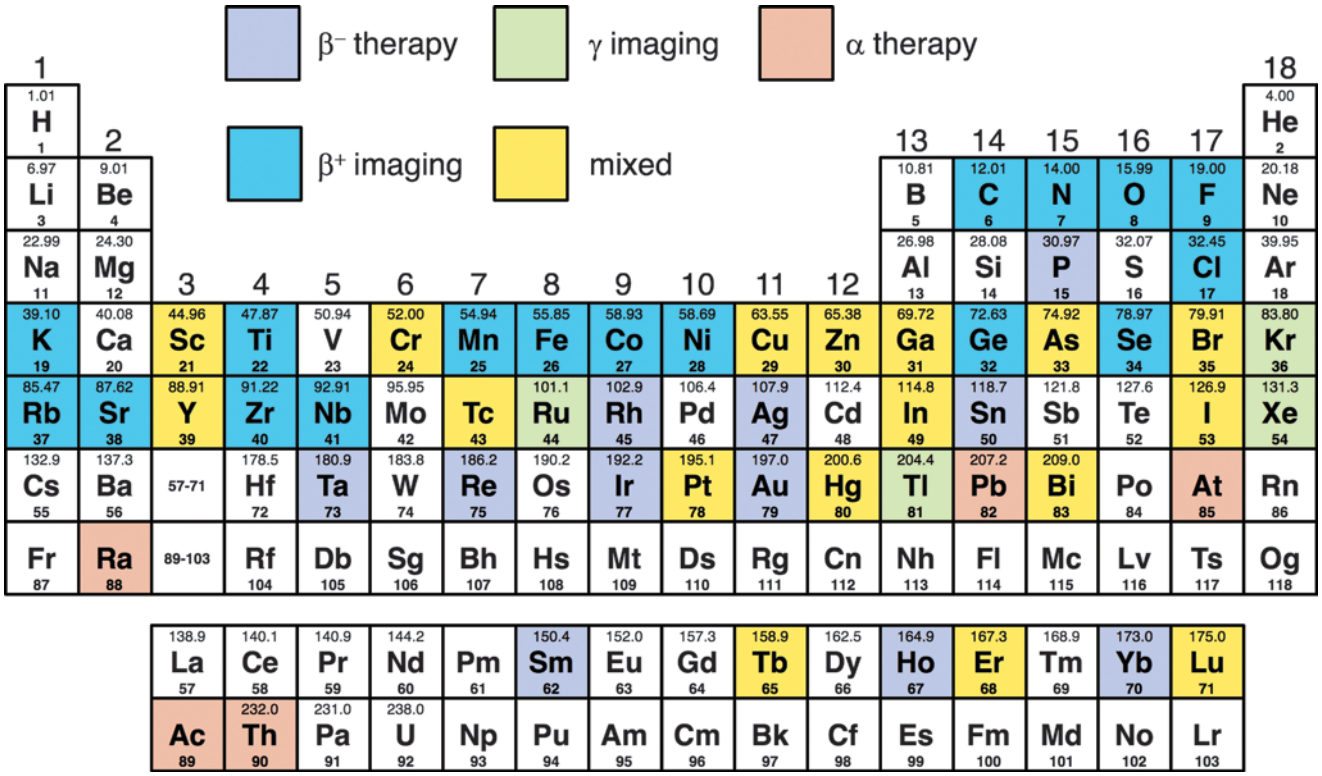

Fig. 1 Periodic table highlighting many of the elements for which at least one radionuclide exists for current or potential use in diagnostic and radiotherapeutic nuclear medicine

first and second ionization energies, and consequently increased chemical reactivity. In water, group 1 alkali and group 2 alkaline earth metal ions exist in their group oxidation states of 1+ and 2+, respectively. The coordination chemistry of *s*-block metal ions is dominated by complexation using ligands bearing small, strongly electronegative, hard, class A donors based on functional groups containing nitrogens and oxygens [6]. Indeed, the first successful ligands for the complexation of alkali metal ions were crown ethers and cryptands introduced by Charles Pedersen, Jean-Marie Lehn, and Donald Cram (Fig. 2; 1987 Nobel Prize in Chemistry). Subsequent work led to the development of sarcophogines and calix[n]arenes that also complex various mono- and divalent metal ions. Four elements from the *s*-block harbour radionuclides of potential use in nuclear medicine (Table 1).

Potassium-38

Potassium ions are essential for life. Membrane flux of K^+ ions is involved in nerve signal transmission, and the dysregulation of potassium is implicated in numerous diseases of the nervous system and myocardium. Potassium-38 ($t_{1/2}$ = 7.64 min) is essentially a pure β^+-emitter that can be produced in a cyclotron via $^{38}Ar(p,n)^{38}K$ or $^{40}Ar(p,3n)^{38}K$ transmutation reactions [2, 7]. Interest in using potassium-38 for PET imaging of myocardial perfusion began in the 1970s, with various clinical studies performed during the 1990s. More recent applications using [^{38}K]KCl(aq.) have measured the kinetics of K^+ ion transport in the kidney and brain. In particular, the perfusion of K^+ ions in the brain is a potential diagnostic measure of the integrity of the blood-brain barrier, which is often compromised in neurological disorders including gliomas and traumatic brain injury [7]. The short half-life of potassium-38 limits radiochemical options, but it is conceivable that combination of potassium-38 with cryptand-222 ($K_{2.2.2}$) – a common reagent used in the form of [^{18}F]KF/$K_{2.2.2}$ for activation of fluoride-18 anions in nucleophilic radiolabeling reactions – could be used to generate novel PET radiotracers for perfusion imaging.

Rubidium-82/Rubidium-82m

Rubidium has at least two radioisotopes of interest in nuclear medicine. The most prevalent radionuclide is rubidium-82 ($t_{1/2}$ = 1.26 min) and is commercially available from ^{82}Sr ($t_{1/2}$ = 25.34 days)/^{82}Rb generators (CardioGen-82® produced by Bracco Diagnostics Inc., Princeton, NJ), which

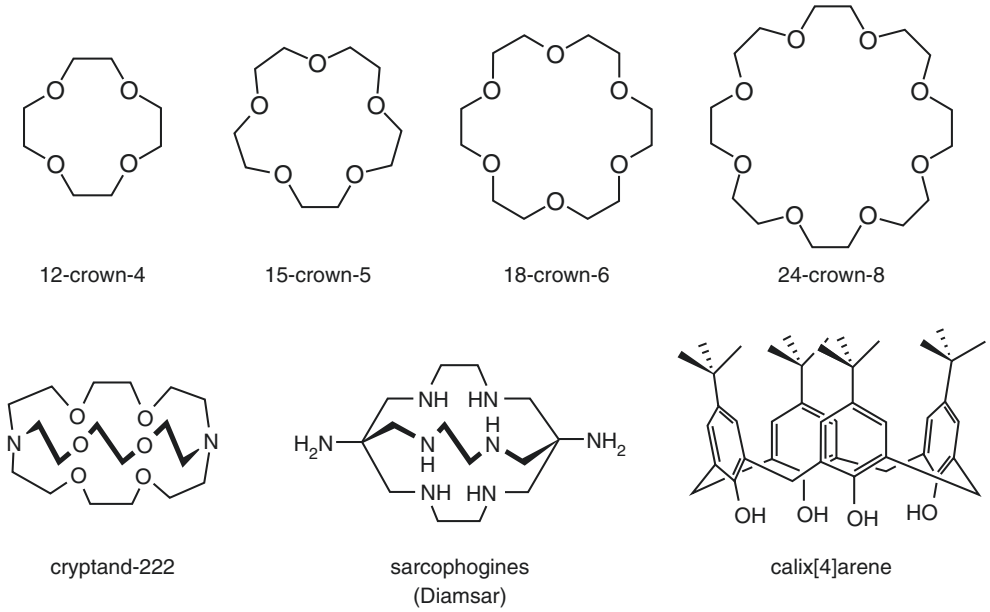

Fig. 2 Chemical structures of representative crown ethers, cryptands, sarcophogines, and calix[n]arenes used for potential complexation of various metal ions including those from groups 1 and 2 of the periodic table

Table 1 Physical decay characteristics and established production routes of various radionuclides from the *s*-block that have potential applications in diagnostic imaging and/or radiotherapy

Radionuclide	Half-life, $t_{1/2}$	Decay mode (% branching ratio)	Production route(s)	*Q*/ keV	Primary applications
Group 1					
^{38}K	7.636 min	ε + β$^+$ (100%) β$^+$ (99.5%)	^{38}Ar(*p*,*n*)^{38}K ^{40}Ar(*p*,3*n*)^{38}K	5914	PET (K$^+$ ion transport, myocardial perfusion, and breakdown of the blood-brain barrier)
^{82}Rb	1.258 min	ε + β$^+$ (100%) β$^+$ (95.4%)	^{82}Sr/^{82}Rb generator	4400	PET (myocardial perfusion and ischaemia)
^{82m}Rb	6.472 h	ε + β$^+$ (99.6%) β$^+$ (21.2%)	^{82}Kr(*p*,*n*)^{82m}Rb		PET (myocardial perfusion)
Group 2					
^{83}Sr	32.41 h	ε + β$^+$ (100%) β$^+$ (27%)	^{85}Rb(*p*,3*n*)^{83}Sr ^{82}Kr(^{3}He,2*n*)^{83}Sr	2273	PET (Ca^{2+} mimic and bone imaging)
^{89}Sr	50.56 days	β$^-$ (100%)	Reactor	1501	Radiotherapy (palliative treatment of bone metastases
^{223}Ra	11.43 days	α (100%)	^{227}Ac/^{227}Th/^{223}Ra generator	5979	Radiotherapy (Xofigo® for treating prostate cancer bone metastases)

received US Federal Drug Administration (US FDA) approval in 1989. Rb$^+$ ions mimic the biochemistry and distribution of K$^+$ ions, and the radiopharmaceutical [^{82}Rb]RbCl(aq.) is used in the clinic to measure myocardial perfusion. Once injected into the bloodstream, Rb$^+$ ions are cleared rapidly from circulation and accumulate in the myocardium (and other tissues) with a kinetic profile that is proportional to the rate of blood flow. The uptake of Rb$^+$ is mediated by Na$^+$/K$^+$-ATPase (adenosine triphosphatase) membrane pumps [8]. The radiotracer is cleared from poorly perfused areas of the myocardium, including necrotic regions and infarcted tissue. The short half-life of rubidium-82 means that radiochemical options are limited with [^{82}Rb]RbCl$_{(aq.)}$ administered directly via intravenous infusion. Until recently, the cost of generators has been a major impediment to the widespread use of rubidium-82. Single doses of [^{82}Rb]RbCl$_{(aq.)}$ have an estimated cost of ~$250, whereas doses of alternative technetium-99m-based SPECT imaging agents cost more than three times less (~70 US dollars).

Rubidium-82m ($t_{1/2}$ = 6.47 h) is a β$^+$-emitting radionuclide (21.2%) that can be produced via the ^{82}Kr(*p*,*n*)^{82m}Rb transmutation reaction [2]. Notably, the main decay pathway of rubidium-82m involves electron capture to krypton-82, with only ~0.3% decaying via isomeric transition. Therefore, the decay of rubidium-82m does not appreciably populate the shorter-lived rubidium-82 ground state. The intermediate half-life of rubidium-82m allows more time to explore the complexation chemistry of [^{82}Rb]Rb$^+$ ions. Also, since Rb$^+$ ions are not chemically degraded *in vivo*, this radionuclide gives scientists an opportunity to study the kinetics of monovalent ion transport over timeframes that are not currently accessible with other *s*-block PET radionuclides.

Strontium-82/Strontium-83/Strontium-89

In addition to strontium-82 – which is used in the production of $^{82}Sr/^{82}Rb$ generators – strontium has at least two radioisotopes of interest in nuclear medicine. Strontium-89 ($t_{1/2}$ = 50.56 days) is a β^--emitter and during the late 1930s was one of the first radionuclides used in radiotherapy [9]. The primary use of strontium-89 was in the palliative care of patients experiencing extreme pain associated with cancer metastasis of the bone. Sr^{2+} ions mimic the chemistry and biodistribution of Ca^{2+} ions and, thus, localize in sites of osteoblastic growth. Recent studies continue to investigate the efficacy of $[^{82}Sr]SrCl_{2(aq.)}$ treatments [9].

For nuclear imaging, strontium-83 ($t_{1/2}$ = 32.41 h) is a β^+-emitting radionuclide (27%) that may be applicable for immunoPET using radiolabeled antibodies. Strontium-83 can be produced via the $^{85}Rb(p,3n)^{83}Sr$ or $^{82}Kr(^3He,2n)^{83}Sr$ transmutation reactions [2, 10]. Studies on the complexation and radiolabeling of antibodies with strontium-83 have not been reported. Much work is needed to develop new bifunctional chelating systems that facilitate the thermodynamically and kinetically stable complexation of Sr^{2+} ions in the presence of a vast excess Mg^{2+} and Ca^{2+} ions. In principle, crown ethers, cryptands, and sarcophogines could be used, but their complexes with *s*-block metal ions often exhibit low formation constants and rapid ion exchange (Fig. 2). In addition, with the notable exception of sarcophogines (which are primarily used to coordinate Cu^{2+} ions), only limited work has been reported on the development of bifunctional versions of these chelators. Nevertheless, increased access to strontium-83 would present radiochemists with an opportunity to revisit the frequently overlooked coordination chemistry of *s*-block elements.

Radium-223

Any discussion of the radionuclides of *s*-block elements eventually gravitates towards radium. Since Marie and Pierre Curie discovered radium in 1898, interest in the chemistry and use of radium has persisted. Indeed, it was Pierre Curie who was one of the first to recognise the potential of using radionuclides to treat cancer. Initial experiments were made in France, and encouraging results established 'radium therapy' as a state-of-the-art technology in the early 1900s [11].

Although Marie Curie isolated the most stable radioisotope of radium – radium-226 ($t_{1/2}$ = 1600 years), which is part of the natural decay series of uranium-238 (4.5×10^9 years) – the α-emitter radium-223 ($t_{1/2}$ = 11.43 days) is of more interest in modern nuclear medicine. In 2013, radium-223 dichloride ($[^{223}Ra]RaCl_{2(aq.)}$; Alpharadin or Xofigo®; Algeta ASA, Oslo, Norway) was approved in the United States and Europe as a radiopharmaceutical for treating patients with advanced prostate cancer. While radium-223 is found naturally as part of the uranium-235 natural decay series, $^{227}Ac/^{227}Th/^{223}Ra$ generators for medical applications are produced artificially via neutron irradiation of ^{226}Ra. Reactor produced radium-227 decays to actinium-227 ($t_{1/2}$ = 21.77 years) which is a convenient radionuclide for making generators.

Like strontium, Ra^{2+}ions mimic the distribution of Ca^{2+} ions and sequester in sites of bone mineral deposition. Prostate cancer frequently metastasises to bone, and the accumulation of $[^{223}Ra]Ra^{2+}$ ions in bone metastases leads to a high radiation dose in these lesions due to the short penetration range of α-particles in tissue. Although the chelation chemistry of Ra^{2+} ions is somewhat limited, interest continues in developing small molecules, peptides, antibodies, and liposomes labeled with radium-223 [12, 13].

The Radionuclides of the *p*-Block Elements

The physical and chemical properties of groups 13–18 arguably make *p*-block elements the most diverse of the periodic table. For instance, the entirety of organic chemistry (and, for that matter, life as we know it) is based on the properties of carbon. Unsurprisingly, *p*-block elements offer a rich source of radionuclides. Previous sections of this book have explored the radiochemistry of carbon-11 ("The Radiopharmaceutical Chemistry of Carbon-11: Basic Principles" and "The Radiopharmaceutical Chemistry of Carbon-11 Chemistry: Tracers and Applications"), nitrogen-13 and oxygen-15 ("The Radiopharmaceutical Chemistry of Nitrogen-13 and Oxygen-15"), fluorine-18 ("The Radiopharmaceutical Chemistry of Fluorine-18: Nucleophilic Fluorinations", "The Radiopharmaceutical Chemistry of Fluorine-18: Electrophilic Fluorinations", and "The Radiopharmaceutical Chemistry of Fluorine-18: Next-Generation Fluorinations"), gallium-68, and indium-111 ("The Radiopharmaceutical Chemistry of the Radionuclides of Gallium and Indium"), as well as radioisotopes of iodine ("The Radiopharmaceutical Chemistry of the Radionuclides of Iodine") in detail. Here, the emphasis is placed on less well-established *p*-block radionuclides (Table 2).

Group 13: The Boron Group (Triels)

Elements of group 13 offer a diverse palette of radionuclides for medical applications. Gallium-67 ($t_{1/2}$ = 3.26 days) and indium-111 ($t_{1/2}$ = 2.805 days) are principally used for SPECT imaging but also emit Auger electrons for radiotherapy [14]. Gallium-68 ($t_{1/2}$ = 67.7 min) is a prevalent PET radionuclide used worldwide for clinical imaging with various peptide-based agents including $[^{68}Ga]$Ga-DOTATE (Netspot®) for detecting somatostatin receptor expression in neuroendocrine tumors. With the exception of thallium,

Table 2 Physical decay characteristics and established production routes of various radionuclides from the *p*-block that have potential applications in diagnostic imaging and/or radiotherapy

Radionuclide	Half-life, $t_{1/2}$	Decay mode (% branching ratio)	Production route(s)	*Q*/ keV	Primary applications
Group 13: The boron group					
^{66}Ga	9.49 h	ε + β$^+$ (100%) β$^+$ (57.0%)	^{66}Zn(*p*,*n*)^{66}Ga ^{63}Cu(^{4}He,*n*)^{66}Ga	5175	PET
^{110m}In	61.9 min	ε + β$^+$ (100%) β$^+$ (61.3%)	^{110}Cd(*p*,*n*)^{110m}In	3878	PET
^{201}Tl	3.042 days	ε (100%)	^{203}Tl(*p*,3*n*)^{201}Pb/^{201}Tl	481	SPECT (myocardial perfusion)
Group 14: The carbon group					
^{69}Ge	39.05 h	ε + β$^+$ (100%) β$^+$ (24%)	^{69}Ga(*p*,*n*)^{69}Ge	2227	PET
^{117m}Sn	13.76 days	IT (100%)	^{116}Cd(*α*,3*n*)^{117m}Sn ^{115}In(*α*,*pn* + *d*)^{117m}Sn		SPECT/radiotherapy
^{212}Pb	10.64 h	β$^-$ (100%)	^{224}Ra/^{212}Pb/^{212}Bi generator	569.9	Radiotherapy (in vivo generation of ^{212}Bi)
Group 15: Pnictogens					
^{32}P	14.268 days	β$^-$ (100%)	Reactor ^{32}S(*n*,*p*)^{32}P	1710	Radiotherapy
^{71}As	65.30 h	ε + β$^+$ (100%) β$^+$ (28.3%)	^{70}Ge(*p*,*γ*)^{71}As	2013	PET
^{72}As	26.0 h	ε + β$^+$ (100%) β$^+$ (87.8%)	^{70}Ge(*α*,2*n*)^{72}Se/^{72}As ^{72}Ge(*p*,*n*)^{72}As	4356	PET
^{74}As	17.77 days	ε + β$^+$ (66%) β$^+$ (29%) β$^-$ (34%)	^{74}Ge(*p*,*n*)^{74}As ^{73}Ge(*d*,*n*)^{74}As	2562	PET and radiotherapy
^{76}As	26.24 h	β$^-$ (100%)	^{76}Ge(*p*,*n*)^{76}As	2962	Radiotherapy
^{77}As	38.79 h	β$^-$ (100%)	Reactor	683	Radiotherapy
^{212}Bi	60.55 min	α (36.0%) β$^-$ (64.0%)	^{224}Ra/^{212}Pb/^{212}Bi generator	6207	Radiotherapy (mix decay mode including alpha and beta particles)
^{213}Bi	45.59 min	α (2.2%) β$^-$ (97.8%)	^{225}Ac/^{213}Bi generator		Radiotherapy
Group 16: Chalcogens					
^{73}Se	7.15 h	ε + β$^+$ (100%) β$^+$ (65.4%)	75As(*p*,3*n*)^{73}Se ^{70}Ge(*α*,*n*)^{73}Se	2740	PET
Group 17: Halogens					
^{34m}Cl	31.99 min	ε + β$^+$ (55.4%) β$^+$ (54.3%) IT (44.6%)	^{34}S(*p*,*n*)^{34m}Cl ^{32}S(*α*,*pn*)^{34m}Cl $^{nat/36}$Ar(*d*,*α*)^{34m}Cl		PET
^{75}Br	96.7 min	ε + β$^+$ (100%) β$^+$ (75%)	^{76}Se(*p*,2*n*)^{75}Br	3062	PET
^{76}Br	16.2 h	ε + β$^+$ (100%) β$^+$ (55%)	^{76}Se(*p*,*n*)^{76}Br	4963	PET
^{77}Br	57.04 h	ε (100%)	^{77}Se(*p*,*n*)^{77}Br	1365	Radiotherapy (Auger electron)
^{211}At	7.214 h	α (41.8%) ε (58.2%)	^{209}Bi(*α*,2*n*)^{211}At	785	Radiotherapy
Group 18: Noble gases					
^{81m}Kr	13 s	IT (99.99%)	^{81}Rb/^{81m}Kr generator		SPECT
^{133}Xe	5.248 days	β$^-$ (97.8%)	Reactor	427	SPECT and radiotherapy

other members of the boron group exist exclusively in a 3+ oxidation state with no accessible redox chemistry. Chelators for Ga^{3+} (ionic radius = 62 pm) and In^{3+} (ionic radius = 80 pm) require ligands with hard, class A donor groups. Ga^{3+} ions form six-coordinate, octahedral complexes, whereas the increased ionic radius of In^{3+} ions allows the central metal cation to accommodate up to eight donor atoms in its first coordination sphere. The chelation chemistry of these two metal ions is dominated by the use of ligands based on *aza*-macrocycles and polydentate chelators like ethylenediaminetetraacetic acid (EDTA) and diethylenetriaminepentaacetic acid (DTPA) (Fig. 3).

Gallium-66 ($t_{1/2}$ = 9.49 h) is a high-energy, β$^+$-emitting radionuclide that can be produced via several transmutation reactions, including the proton irradiation of solid ^{65}Zn targets. As with clinical-grade ^{68}Ge/^{68}Ga generators, the Ga^{3+} ions must be separated from chemical and radiochemical impurities prior to labeling. The purification of gallium-66 is

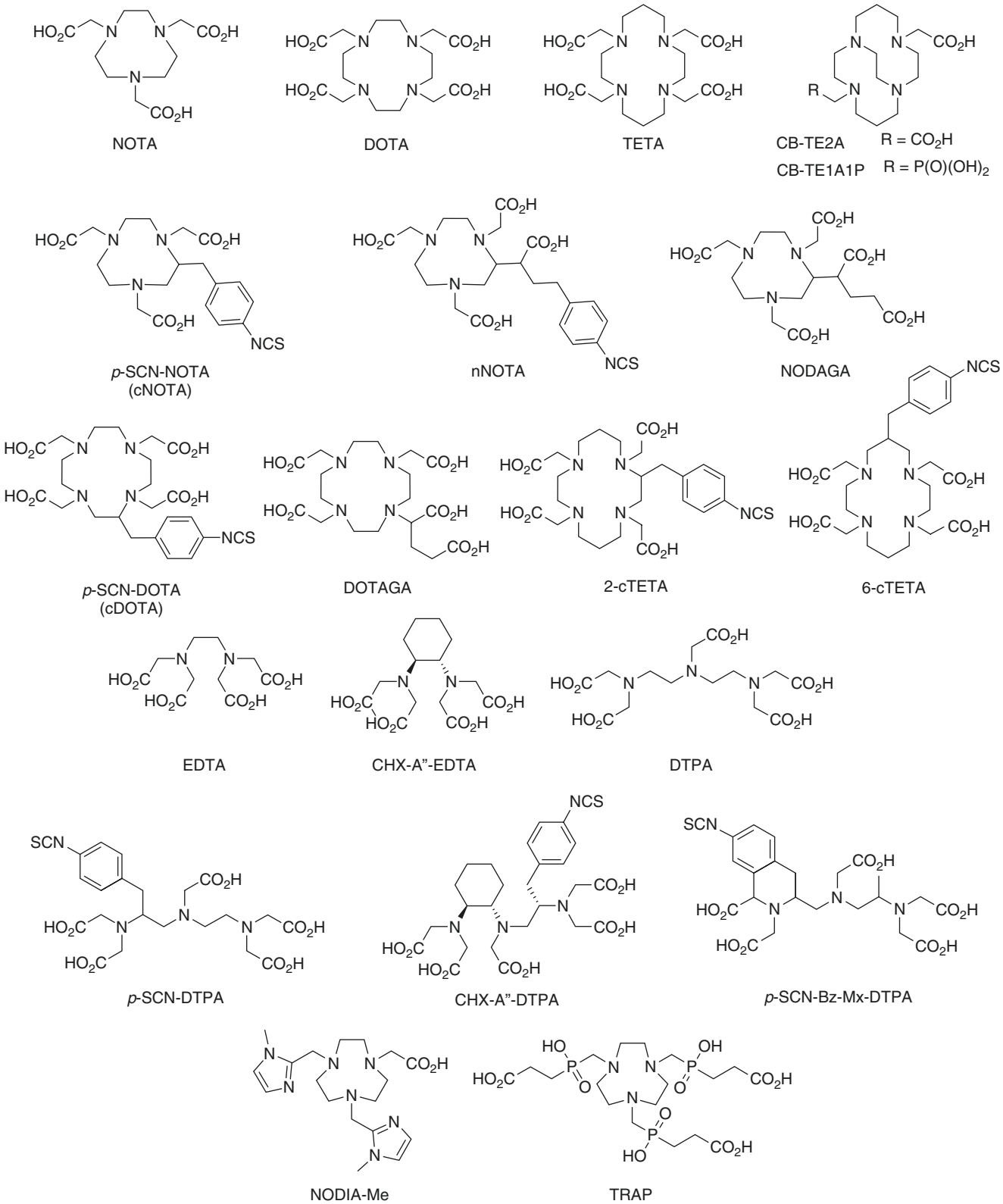

Fig. 3 Structures of selected chelators that complex various radiometal ions and particularly those with a 2+ or 3+ charge

typically accomplished by pre-adsorbing Ga^{3+}ions onto a strong cation exchange resin, followed by washing with ~0.1 M HCl and water to remove divalent metal ion impurities like Zn^{2+}, Cu^{2+}, and Fe^{2+}. The elution of gallium radioisotopes can be achieved in acidic media using a high concentration of NaCl (~5 M). Gallium-66 has an intermediate half-life, which makes it suitable for labeling peptides as well as small proteins and antibody fragments. However, a major drawback of gallium-66 is the high specific gamma ray dose constant (or gamma factor) of 1.296 Rem/h measured at 1 metre from a point source (Oak Ridge National Laboratory, document ORNL/RSIC-45) [15]. For reference, gallium-68 and fluorine-18 have gamma factors of 0.662 and 0.695, respectively. High gamma factors reduce the maximum dose of a given radiopharmaceutical that can be administered to a patient, and high-energy γ-ray emissions require specialized handling procedures to minimize the radiation exposure of radiation workers. As a result, in spite of the possibility of expanding the use of existing gallium-68 radiotracers to longer imaging timeframes, gallium-66 is likely to remain of only academic interest.

Indium-110m ($t_{1/2}$ = 61.9 min) is a relatively high-energy β^+-emitting radioisotope of indium that can be produced via the $^{110}Cd(p,n)^{110m}In$ transmutation reaction. Indium-110m offers the possibility of adapting well-established indium-111 SPECT radiotracers – such as [^{111}In]In-DTPA for measuring renal perfusion imaging – into the realm of PET. The vast majority of existing indium-111 radiolabeled species are based on DTPA-conjugated antibodies and antibody fragments such as [^{111}In]In-capromab pendetide ([^{111}In]In-7E11; ProstaScint®) for imaging prostate-specific membrane antigen (PSMA). Other ^{111}In-labeled radioimmunoconjugates of note include [^{111}In]In-satumomab pendetide (OncoScint®) for imaging TAG-72, a tumor-associated antigen found on colorectal and ovarian carcinomas, as well as the radiolabeled murine Fab fragment [^{111}In]In-imiciromab-pentetate. Formerly used for cardiac imaging, and the murine $F(ab')_2$ fragment [^{111}In]In-igovomab (Indimacis-125®) targets the carcinoma antigen 125 (CA125) and was used in the diagnosis of ovarian cancer. With the exception of ProstaScint®, each of these indium-111 radiotracers have subsequently been withdrawn from clinical practice [16]. However, the combination of the short-lived indium-110m with antibodies is undesirable. Therefore, if this radionuclide is to be used more widely, research is needed to find suitable biological vectors for which the chemistry of indium is preferred over, for example, that of gallium or copper.

Thallium-201 ($t_{1/2}$ = 3.04 days) has a long history in nuclear medicine and was the first radionuclide used for routine myocardial perfusion imaging (launched commercially as [^{201}Tl]TlCl in 1977 by Lantheus Medical Imaging, Billerica, MA). Unlike other metal ions of group 13, thallium readily forms Tl^+ ions due to a pronounced inert pair effect. The inert pair effect describes the scenario in which the two electrons in the outermost *s* subshell become increasingly difficult to ionize. This occurs due to increased 2nd and 3rd ionization energies, which are influenced by the *d*-block and *f*-block contraction of the atomic radius (and for Tl, relativistic effects) as well as the decreased stabilization of complexes due to longer bonds and weaker metal-ligand bond enthalpies. As a result of this phenomenon, the chemistry of Tl^+ ions mimics that of group 1 metal ions. Targeted radiotracers based on thallium-201 have not been reported, but it is likely that ligands bearing soft, class B donors including sulfhydryls will form stable complexes with Tl^+ ions.

Group 14: The Carbon Group (Tetragens)

Beyond the endless depths of carbon chemistry, group 14 has at least 3 radionuclides of potential interest in nuclear medicine.

Germanium-69 ($t_{1/2}$ = 39.05 h) is a relatively long-lived β^+-emitting radionuclide that can be produced in a cyclotron via the proton irradiation of a gallium-69 target [2]. The challenge for radiochemists is that unlike carbon, germanium is a semimetal and exhibits dramatically different chemistry compared to the group's progenitor. The most common oxidation state of germanium is 4+, but 2+ species are also abundant due to a pronounced inert pair effect. The metalloid character of germanium presents itself in the form of complexes and polyatomic germanium clusters with variable oxidation states ranging from 4+ to 4−. Radiochemistry with germanium-69 remains an open challenge to find the best combination of radiolabeling conditions and chelators to complex Ge^{4+} ions under aqueous conditions. In fact, the problem remains such a mystery that to date, no successful radiometal chelation chemistry of germanium-69 has been reported. To circumvent the lack of established chelation chemistry, Chakravarty *et al.* used surface-based chemistry to produce iron oxide nanoparticles intrinsically labeled with germanium-69 for dual-modality PET/MR (magnetic resonance) imaging [17].

Interestingly, the difficulties of adapting traditional 'chelator-based' methods to the chemistry of radionuclides like germanium-69 and various arsenic radioisotopes have spurred radiochemists to explore a range of alternative, 'chelator-free', processes (Fig. 4) [18, 19]. Chelator-free methods take advantage of the intrinsic properties of nanoparticles, including surface reactivity, isotopic/cationic exchange, radiochemical doping, physisorption, and direct chemisorption to facilitate radiolabeling. In most instances,

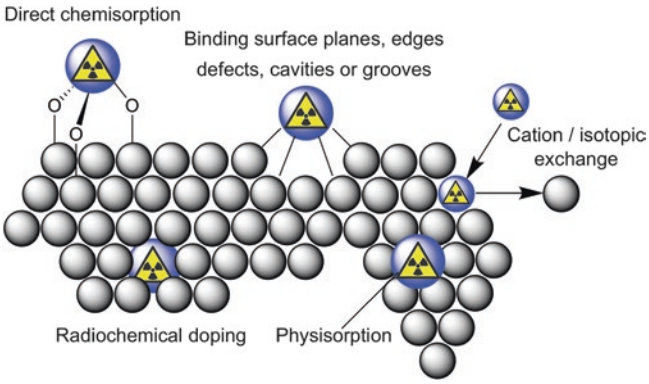

Fig. 4 Overview of several 'chelator-free' mechanisms that have been used to incorporate various radiometals onto the surface or inside the core of nanoparticle-based systems [19]. Such alternative radiolabeling methods are particularly useful when the chelation chemistry of a given radionuclide (like germanium-69 and radionuclides of arsenic) is not well-established

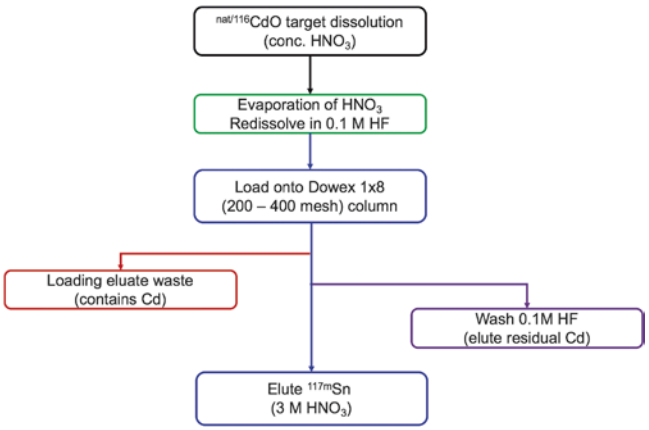

Fig. 5 Schematic flow diagram showing the process developed by Maslov *et al.* for the purification of high specific-activity tin-117m from target cadmium isotopes [20]

radiolabeling is likely mediated by cationic metal ions binding to anionic oxide layers on the particle surface.

Tin-117m ($t_{1/2}$ = 13.76 days) decays via isomeric transition to the stable ground state tin-117. This radionuclide is particularly interesting for potential use in γ-ray imaging and Auger electron radiotherapy. Commercial sources of tin-117m exist (Curative Technologies Corporation, Richland WA, USA), but specific activities (~0.74 GBq/mg) have been restricted by production routes involving the irradiation of isotopically enriched tin-117. Maslov *et al.* recently reported an alternative production route via the $^{nat/116}Cd(\alpha,3n)^{117m}Sn$ reaction and an effective separation protocol based on strong anion exchange columns (Fig. 5) [20]. Using this approach, tin-117m was isolated with a radionuclidic purity >99% and an improved specific activity of >2.4 GBq/mg. Such advances will facilitate more widespread study of the chemistry and potential radiotherapeutic applications of tin-117m. For tin, the 4+ oxidation state, is typically more stable than 2+. Future studies on the radiochemistry and coordination chemistry of tin-117m could conceivably seek to adapt existing macrocyclic chelators like derivatives of NOTA, DOTA, and TETA that stably coordinate many $M^{2+}$and M^{3+}ions from across the periodic table (Fig. 3). The caveat is that the larger size of Sn^{2+} ions and their preference for softer donor atoms may mean that the chemistry of these hard donor-bearing chelators is suboptimal for tin-117m. Alternative chelators that incorporate softer sulfhydryl donors may present a better starting point for advancing tin radiochemistry.

Lead-212 ($t_{1/2}$ = 10.64 h) is a pure β^--emitting radionuclide that can be accessed from commercially available ^{224}Ra generators (AREVA Med LLC, Paris, France). Two lead-212 production facilities are located in the United States. Lead-212 is potentially useful for designing targeted radiotherapy agents. In 2012, the first clinical trials explored [^{212}Pb]Pb-TCMC conjugated to the antibody trastuzumab for the targeted radioimmunotherapy (RIT) of tumors expressing human epidermal growth factor receptor 2 (HER2/*neu*) (Fig. 6; NCT01384253; source: www.clinicaltrials.gov). Lead chemistry encompasses mainly the 2+ and 4+ oxidation states. However, for lead, the inert pair effect is dominant, and Pb^{4+} ions are easily reduced *in aquo* to form Pb^{2+}. The large ionic radius of Pb^{2+} (119 pm) means that this ion has a low charge-to-size ratio and a strong preference to form coordination complexes with ligands bearing soft, class B donors. For this reason, researchers working on the aforementioned clinical trial had to soften the normally hard, carboxylate donors found on DOTA by making neutral amide groups on each of the four carboxylate arms. In previous studies, Chappell *et al.* also found that the $[PbTCMC]^{2+}$ complex was less susceptible to metal ion release than the equivalent $[PbDOTA]^{2-}$ species [21].

From a radiotherapy perspective, lead-212 is interesting because its decay generates bismuth-212 ($t_{1/2}$ = 60.55 h) in situ in addition to emitting β^- particles for direct radiotherapy. Bismuth-212 decays via either α-particle (36%) or β^--particle emission (64%). The α-decay pathway produces thallium-208 ($t_{1/2}$ = 3.1 min), which undergoes rapid β^- decay to stable lead-208. The β^--decay pathway yields polonium-212 which decays instantaneously ($t_{1/2} = 3 \times 10^{-7}$ s) via α-particle emission, again to stable lead-208. This cascade of therapeutic β^-- and α-particles means that lead-212 is potentially a very potent and cytotoxic parent radionuclide. The challenge for designing lead-212-based radiotracers lies not only delivering high activity concentrations to the target with low levels of activity in background organs but also in ensuring that the radionuclide is sequestered *in vivo* to such an extent that none of the lead-212 or daughter nuclides recirculate on the time scale of their complete decay to lead-208. With increased interest and clinical availability of lead-212, it is likely that the near future will see further work exploring

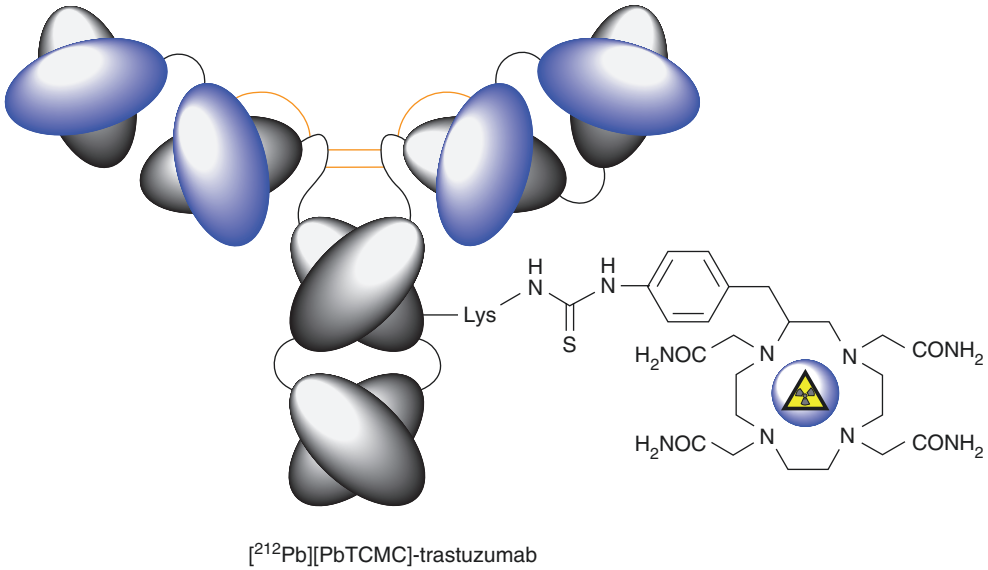

Fig. 6 Schematic diagram showing the chemical conjugation of [^{212}Pb]Pb-TCMC to the antibody trastuzumab via benzyl-thiourea coupling to the ε-NH_2 group of lysine residues

the coordination chemistry, radiochemistry, and radiotherapeutic applications of this exciting radionuclide.

Group 15: Pnictogens

Nitrogen-13 ammonia ([^{13}N]NH_3) is a US FDA-approved radiopharmaceutical for diagnostic PET imaging of myocardial perfusion. [^{13}N]NH_3 PET under stress and rest conditions is used to examine patients with suspected or existing coronary artery disease. Beyond nitrogen-13, at least 3 other elements of group 15 have radionuclides of interest for nuclear medicine.

Phosphorus-32 ($t_{1/2}$ = 14.27 days) is a high-energy β^--emitter that first found application in nuclear medicine during the 1930s [9]. One of the major issues facing cancer patients is how to manage intractable bone pain often associated with advanced metastatic cancer of the prostate, breast, and other tissues. Phosphorus-32, along with other radionuclides including strontium-90, has been widely used in palliative care of these patients. Phosphorus-32 is typically administered as an orthophosphate salt – PO_4^{3-} with Na^+, K^+, Ca^{2+}, or Mg^{2+}counter cations – that readily accumulates in bone minerals. However, the high maximum decay energy of the β^--particle (1710 keV) means that phosphorus-32 delivers a high radiation dose to adjacent bone marrow. The radiochemistry of phosphorus-32 is largely limited to the use of species containing phosphate or polyphosphate groups such as adenosine triphosphate (ATP) [1]. Recently, bisphosphate groups have been used as anchors for attaching drugs, chelators, and other radionuclides onto the surfaces of various nanoparticles. This new chemistry presents an opportunity for combining multimodality nanomedicines with phosphorus-32 [22]. The long half-life of phosphorus-32 is also amenable to the elaborate, multistep syntheses and purification protocols often required to make nanoparticle-based radiotracers.

Arsenic has several radioisotopes that are of potential use in nuclear medicine: Arsenic-71 ($t_{1/2}$ = 65.30 h), arsenic-72 ($t_{1/2}$ = 26.0 h), and arsenic-74 ($t_{1/2}$ = 17.77 days) decay via β^+-emission. Arsenic-74, arsenic-76 ($t_{1/2}$ = 26.24 h), and arsenic-77 ($t_{1/2}$ = 38.79 h) emit β^--particles suitable for radiotherapy. Arsenic compounds typically exist in the 3+ or 5+ oxidation state, but the most challenging aspect of working with radioarsenic is the comparative lack of established chelation chemistry. In the absence of facile chelator-based approaches, Chen *et al.* developed an elegant chelator-free method for radiolabeling the surface of superparamagnetic iron oxide (magnetite, Fe_3O_4) nanoparticles (SPIONs) for PET/MRI [23]. Arsenic ions have a high affinity for Fe_3O_4, attributed to direct a chemisorption process in which $As^{3+}O_3$ trigonal pyramids or $As^{5+}O_4$ tetrahedra occupy vacant FeO_4 tetrahedral sites on the octahedrally terminated {111} surface (Fig. 5). Studies in mice demonstrated that the PEGylated compounds – *As-SPION-PEG – were suitable radiotracers for mapping lymph node drainage with PET/MRI.

Bismuth has two radioisotopes, bismuth-212 ($t_{1/2}$ = 60.55 min) and bismuth-213 ($t_{1/2}$ = 45.59 min), that are of potential use in radiotherapy (see the section on lead-212 vide supra). Typically, bismuth is complexed as Bi^{3+} ions using macrocyclic chelators like DOTA. McDevitt *et al.* [24] and others [25] have studied the efficacy of radioimmunotherapy using bismuth-213-radiolabeled antibodies, including J591 for targeting PSMA expression in prostate cancer. Other studies have also investigated the fate of ^{212}Bi ions formed *in situ* after decay of [[^{212}Pb]Pb]DOTA]$^{2-}$ [26]. Experiments found that ~36% of the bismuth-212 radioactivity dissociated from the complex. Decomplexation is

potentially the result of either the destruction of the complex associated with the recoil energy from the β^--emission of lead-212 or radiolysis in solution. Irrespective of the precise mechanism of decomplexation, the loss of bismuth-212 ions from the chelator has important implications for the design of radiopharmaceuticals based on lead and bismuth. Ideally, the daughter radionuclide would remain stable in complexation with the original targeting vector. However, in situations where a cascade of radiotoxic daughter nuclides occurs, it is important to ensure that the parent lead-212 complex is rapidly taken up and sequestered in the target tissue prior to decay. The search for alternative chelators that enhance the stability of both Pb^{2+} and Bi^{3+} ions *in vivo* must remain a priority before the full potential of radiotherapy with lead and bismuth radionuclides can be attained.

Group 16: Chalcogens

Perhaps surprisingly, radionuclides of the chalcogens and their associated radiochemical reactions are somewhat scarce. Oxygen-15 ($t_{1/2}$ = 122 s; β^+ 100%) is the most well-known group 16 radionuclide, but its very short half-life limits its options for radiochemistry. Most work with oxygen-15 dominated by perfusion studies using [^{15}O]H_2O.

Selenium-73 ($t_{1/2}$ = 7.15 h) is a β^+-emitting radionuclide and has been produced as a no-carrier-added product in elemental form via different automated routes involving cyclotron irradiation and purification from germanium and arsenic targets [27]. From a radiochemistry perspective, the primary interest in using radionuclides of selenium would be to produce analogues of biologically active species or drugs that contain sulphur atoms. For instance, Plenevaux *et al.* synthesized and reported the first human studies with L-2-amino-4-([^{73}Se]methylseleno)butyric acid (also called L-[^{73}Se] selenomethionine) in 1990 [27]. This amino acid analogue can potentially be used for PET of amino acid transport and protein synthesis. Limited access to selenium-73 has restricted further studies. However, given the wealth of important biological processes that involve compounds of sulphur, further investigation of selenium analogues is warranted.

Group 17: Halogens

From fluorine-18 through to the various radionuclides of iodine, radioactive halogens are a cornerstone of nuclear medicine. But what about radiochemistry with molecules containing chlorine, bromine, or astatine atoms?

Chlorine-34m ($t_{1/2}$ = 31.99 min) is a β^+-emitting radionuclide that can be produced via proton or α-particle irradiation of sulphur targets or deuteron irradiation of natural abundant or enriched argon-36 [28]. Engle *et al.* reported detailed optimization and separation studies using argon targets. Radiochemical experiments have been largely restricted to the synthesis of simple compounds, including [^{34m}Cl]chloromethane. Nevertheless, these studies demonstrate that future explorations of the radiochemistry of chlorine-34m might profit from exploiting existing technologies used in the radiosynthesis of tracers bearing carbon-11, fluorine-18, and radioiodine.

Bromine has at least three cyclotron-produced radionuclides of potential use in imaging and radiotherapy [2, 29]. Bromine-75 ($t_{1/2}$ = 96.7 min) and bromine-76 ($t_{1/2}$ = 16.2 h) are β^+-emitters whose half-lives span a time window that make them suitable for labeling small drug molecules and peptides through to small proteins/antibody fragments. Bromine-77 ($t_{1/2}$ = 57.04 h) decays via electron capture and has potential in the design of Auger electron-emitting radiotracers. Moving down the halogen group, the ionic radius of the halide anions increases: F^-(119 pm) < Cl^-(167 pm) < Br^-(182 pm) < I^-(206 pm). So too does their nucleophilicity and leaving group capabilities. As a result, the radiochemistry of bromine radionuclides is closer to that of iodine than fluorine. Electrophilic radiolabeling reactions involving the use of strong oxidising reagents including Chloramine-T and Iodogen® are the most common pathways used for radiolabeling proteins and peptides with iodine (and potentially bromine). Typically, these reactions involve the oxidative radiolabeling of tyrosine or histidine residues (Fig. 7). For radiotracers in which these substrate amino acids are either not present or not available for reaction, alternative pathways – including the use of Bolton-Hunter reagents – allow for the installation of prosthetic groups to facilitate radiohalogenation.

Astatine-211 ($t_{1/2}$ = 7.21 h) is an α-emitting radionuclide that can be produced from the α-particle irradiation of bismuth-209. The chemistry of astatine is quite different from the other halogens. Astatine-211 chemistry is currently of major interest for the development of agents for radiotherapy, but studies have remained limited by the lack of access to the radionuclide [30]. Recent work by Teze *et al.* compared the chemistry of [^{211}At]astatobenzoate with that of iodinated analogues of the same compound and found that the astatine compounds undergo much more rapid oxidation at 37 °C by a factor of 6×10^6 (Fig. 8). In spite of this potentially rapid oxidative metabolism, antibodies labeled with astatine-211 (like trastuzumab for the targeted therapy of tumors expressing HER2/*neu*) as well as *meta*-[^{211}At]astatobenzylguanidine ([^{211}At]MABG) and the ribose nucleic acid (RNA)-base analogue 5-[^{211}At]astato-2′-deoxyuridine ([^{211}At]AUdR) have been synthesized [13].

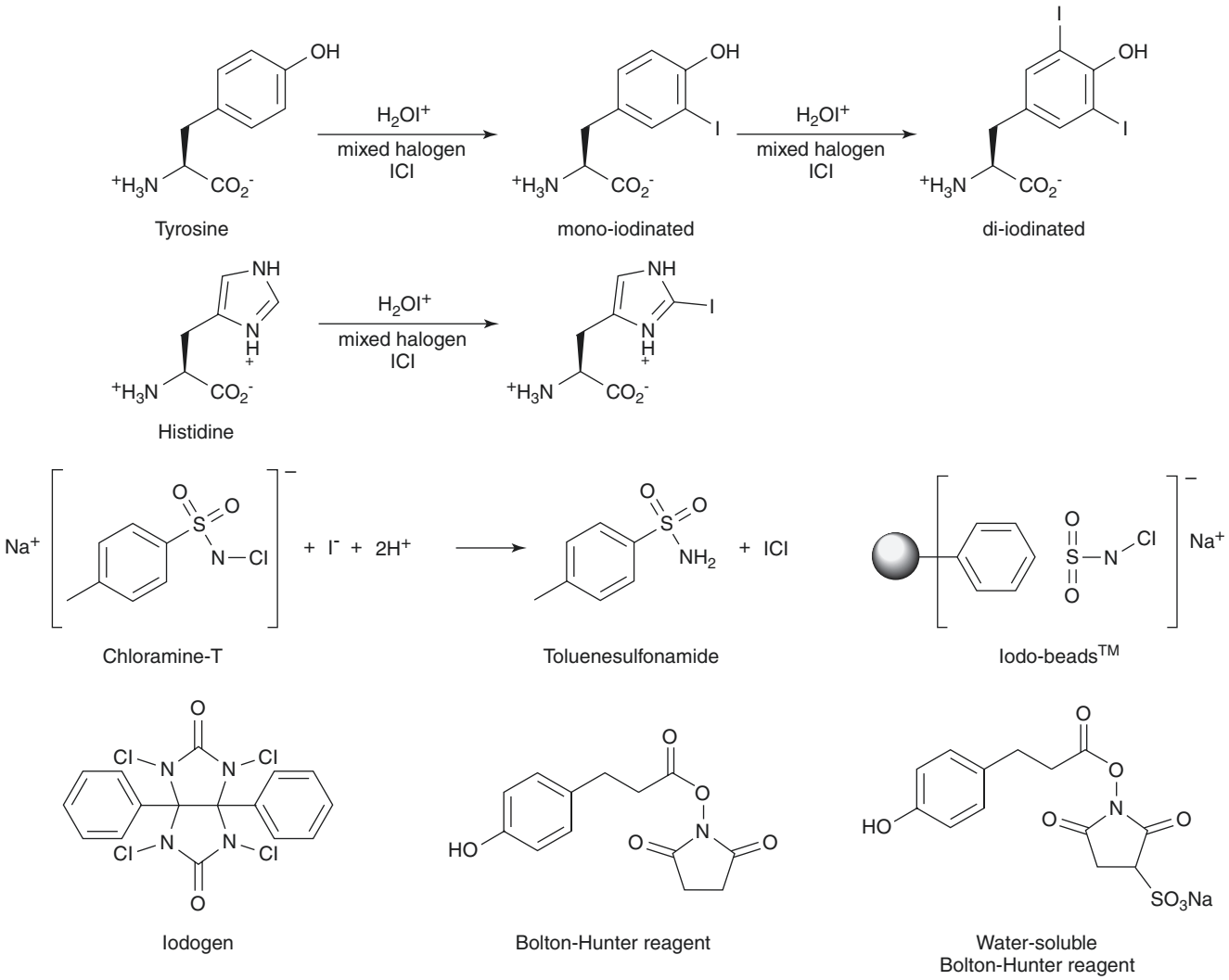

Fig. 7 Scheme showing the radiohalogenation reactions on tyrosine and histidine amino acid side chains and various electrophilic radiolabeling reagents that are commonly used for radioiodination and may be applied in radiolabeling with bromine radionuclides

Group 18: Noble Gases

The chemistry of noble gases is a fascinating topic but is typically restricted to complexes involving highly electronegative ions like fluoride with complexes formed using cold matrix isolation techniques. These compounds and methods are not applicable for radiotracers used *in vivo*. On the other hand, their status as 'noble' presents opportunities for using these gases in lung perfusion studies.

Krypton-81m ($t_{1/2}$ = 13 s) decays via isomeric transition and is useful for γ-ray imaging. The radionuclide is commercially available as a ^{81}Rb/^{81m}Kr generator (KryptoScan™; Cyclotron VU, Amsterdam, Netherlands) in which the parent radionuclide, rubidium-81 ($t_{1/2}$ = 4.57 h), is immobilized on a solid support and the daughter is simply eluted with air. The very short half-life and absence of attainable chemistry in air and water mean that krypton-81m is only suitable for lung ventilation studies. However, in comparison with other radiolabeled perfusion imaging agents like ^{99m}Tc-labeled macroaggregated albumin ([^{99m}Tc]TcMAA), the short half-life of krypton-81m reduces the radiation burden to a patient.

Xenon-133 ($t_{1/2}$ = 5.25 days) is a β^--emitter useful for γ-ray imaging and radiotherapy. Xenon-133 is obtained from reactor sources, but in spite of the more advanced chemistry of xenon, none of the reported species are accessible in a radiochemical or biological setting. As a result, interest in xenon-133 is also restricted to lung perfusion studies.

Radionuclides of the *d*-Block Elements

The sheer depth of chemical and physical properties of the *d*-block elements makes them a rich source of radionuclides for nuclear medicine. Many *d*-block radionuclides like cop-

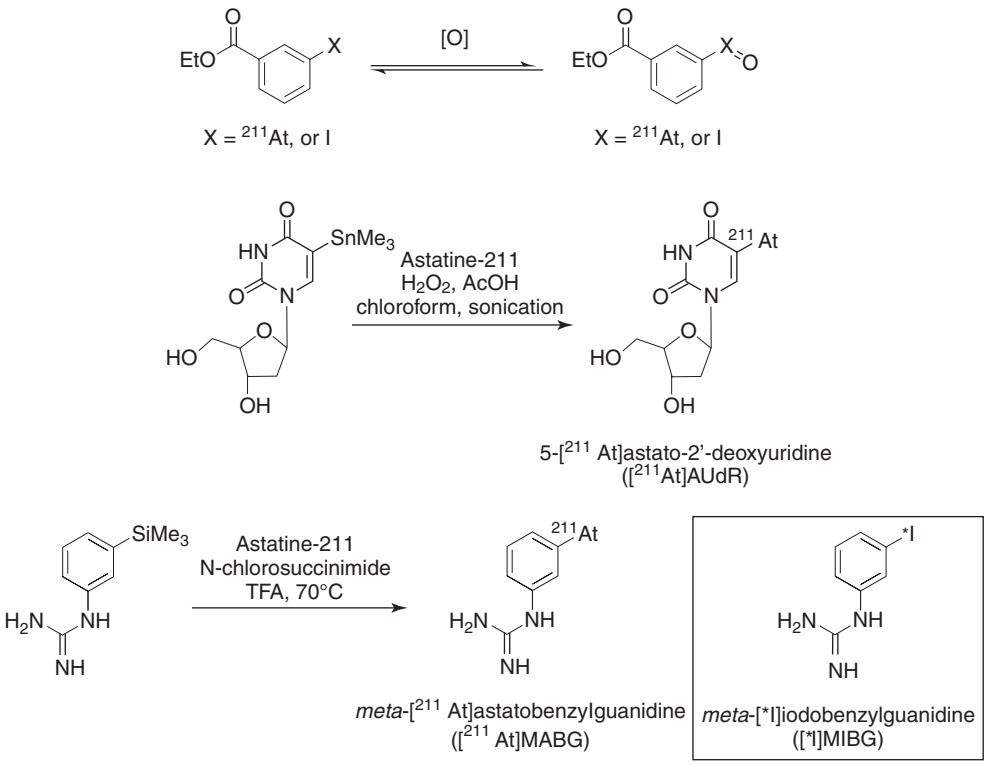

Fig. 8 Scheme showing the oxidative reaction of radiolabeled astatine-211 compounds and the radiosyntheses of [^{211}At]MABG and [^{211}At]AUdR

per-64, zirconium-89, and yttrium-90 have well-established radiochemistry and niche applications. However, the radiochemistry of several other *d*-block radionuclides has yet to be explored in detail (Table 3).

Group 3

Scandium has at least three radionuclides that are of considerable interest for radiotracer design. Scandium is also one of the few elements to have radioisotopes that are highly suited for both imaging and radiotherapy. Scandium-43 ($t_{1/2}$ = 3.89 h) [31] and scandium-44 ($t_{1/2}$ = 3.97 h) [32, 33] are two of the most promising alternative radionuclides for PET [34]. Scandium-47 ($t_{1/2}$ = 3.35 h) is a pure β$^-$-emitter [35]. In addition to cyclotron-produced sources of scandium radioisotopes based on calcium, titanium, or vanadium targetry, scandium-44 can also be obtained from a ^{44}Ti ($t_{1/2}$ = 60.0 years)/^{44}Sc generator [34]. Suitable decay characteristics, simple chelation chemistry, and long-lived titanium-44 generator-based production makes scandium-44 an attractive alternative to gallium-68. In recent years, many studies have investigated the separation chemistry to isolate scandium radionuclides in high specific activity from Ca and Ti targets [33, 36]. The dissolution of the CaO targets is trivial using water or hydrochloric acid, and the separation of Sc^{3+} ions can be achieved using either simple filtration methods or column-based protocols. Various column separation methods have been reported. Solid phase separation media that have been used include hydroxamic acid resins, iminodiacetic acid resins (Chelex 100), and uranium and tetravalent actinides (UTEVA) resins functionalized with dipentyl pentylphosphonate groups have been developed.

The aqueous chemistry of scandium is based entirely on the oxidation state of 3+. The ionic radius of Sc^{3+} ions is quite large (~89 pm), which means that complexes are highly ionic with minimal covalent character in the bonds between donor atoms and Sc^{3+} ions. Standard chelators like DOTA have primarily been used to produce a variety of scandium-44-labeled agents. However, it has been noted that the relatively large ionic radius of Sc^{3+} as well as its preference for hard anionic donors may make bifunctional versions of acyclic chelators like DTPA promising alternatives (Fig. 3) [33].

Yttrium-86 ($t_{1/2}$ = 14.74 h) is a β$^+$-emitter that forms a matched pair with yttrium-90, an established β$^-$-emitter for radiotherapy. The separation of yttrium-86 from strontium-86 targets can be accomplished using electrochemical methods [37]. The radiochemistry and applications of yttrium radionuclides are presented in the chapter on "The Radiopharmaceutical Chemistry of the Radionuclides of Lutetium and Yttrium".

Group 4

Titanium-45 ($t_{1/2}$ = 184.4 min) is also a PET radionuclide that can be produced via the ^{45}Sc(*p*,*n*)^{45}Ti transmutation reaction. From an economic perspective, a major advantage of tita-

Table 3 Physical decay characteristics and established production routes of various radionuclides from the *d*-block that have potential applications in diagnostic imaging and/or radiotherapy

Radionuclide	Half-life, $t_{1/2}$	Decay mode (% branching ratio)	Production route(s)	*Q*/keV	Primary applications
Group 3					
^{43}Sc	3.89 h	ε + β$^+$ (100%) β$^+$ (88.1%)	^{43}Ca(*p*,*n*)^{43}Sc ^{42}Ca(*d*,*n*)^{43}Sc ^{40}Ca(*α*,*p*/*n*)^{43}Sc	2221	PET
^{44}Sc	3.97 h	ε + β$^+$ (100%) β$^+$ (94.3%)	^{44}Ti/^{44}Sc generator	3652	PET
^{47}Sc	3.349 days	β$^-$ (100%)	^{48}Ca(*p*,2*n*)^{47}Sc ^{47}Ca/^{47}Sc generator ^{48}Ti(*n*,*p*)^{47}Sc reactor	600.3	Radiotherapy
^{86}Y	14.74 h	ε + β$^+$ (100%) β$^+$ (31.9%)	^{86}Sr(*p*,*n*)^{86}Y	5240	PET (matched pair with ^{90}Y)
Group 4					
^{45}Ti	184.8 min	ε + β$^+$ (100%) β$^+$ (84.8%)	^{45}Sc(*p*,*n*)^{45}Ti	2062	PET
Group 5					
^{90}Nb	14.60 h	ε + β$^+$ (100%) β$^+$ (51.2%)	^{90}Zr(*p*,*n*)^{90}Nb	6111	PET
^{178}Ta	9.30 min	ε + β$^+$ (100%) β$^+$ (1.4%)	^{178}W/^{178}Ta generator	1937	SPECT
Group 6					
^{51}Cr	27.70 days	ε (100%)	^{51}V(*p*,*n*)^{51}Cr	752	Non-imaging radiotracer applications
Group 7					
^{51}Mn	46.4 min	ε + β$^+$ (100%) β$^+$ (97.1%)	^{50}Cr(*d*,*n*)^{51}Mn ^{nat}Cr(*p*,*x*)^{51}Mn ^{54}Fe(*p*,*α*)^{51}Mn	3207	PET
^{52}Mn	5.591 days	ε + β$^+$ (100%) β$^+$ (29.6%)	^{nat}Cr(*p*,*xn*)^{52}Mn	4711	PET
^{52m}Mn	21.1 min	ε + β$^+$ (98.2%) β$^+$ (96.6%)	^{52}Fe/^{52m}Mn generator	–	PET
^{94m}Tc	52.0 min	ε + β$^+$ (100%) β$^+$ (70.2%)	^{94}Mo(*p*,*n*)^{94m}Tc	–	PET
^{186}Re	3.718 days	ε (7.5%) β$^-$ (92.5%)	Reactor	1070	Radiotherapy
^{188}Re	17.00 h	β$^-$ (100%)	^{188}W/^{188}Re generator	2120	Radiotherapy
Group 8					
^{52}Fe	8.275 h	ε + β$^+$ (100%) β$^+$ (99.6%)	^{nat}Ni(*p*,*x*)^{52}Fe	2375	PET
^{97}Ru	2.83 days	ε (100%)	^{99}Tc(*p*,3*n*)^{97}Ru	1108	SPECT
Group 9					
^{55}Co	17.53 h	ε + β$^+$ (100%) β$^+$ (76%)	^{56}Fe(*p*,2*n*)^{55}Co ^{54}Fe(*d*,*n*)^{55}Co ^{58}Ni(*p*,*α*)^{55}Co	3452	PET
^{105}Rh	35.36 h	β$^-$ (100%)	^{105}Ru/^{105}Rh generator	567	Radiotherapy
^{192}Ir	73.83 days	ε (4.8%) β$^-$ (95.2%)	Reactor	1454	Radiotherapy (high dose rate brachytherapy)
Group 10					
^{57}Ni	35.60 h	ε + β$^+$ (100%) β$^+$ (43.6%)	^{59}Co(*p*,3*n*)^{57}Ni	3264	PET
^{195m}Pt	4.01 days	IT (100%)	^{194}Pt(*n*,*γ*)^{195m}Pt reactor	Stable	SPECT/radiotherapy (Auger electron)
Group 11					
^{111}Ag	7.45 days	β$^-$ (100%)	Reactor	1037	Radiotherapy
^{198}Au	2.694 days	β$^-$ (100%)	Reactor	1379	Radiotherapy
Group 12					
^{62}Zn	9.193 h	ε + β + (100%) β + (8.2%)	Reactor	1620	PET
^{197m}Hg	23.8 h	ε (8.6%) IT (91.4%)	^{197}Au(*p*,*n*)^{197m}Hg	–	Radiotherapy/SPECT
^{197}Hg	64.14 h	ε (100%)	^{197}Au(*p*,*n*)^{197}Hg	3607	Radiotherapy/SPECT

nium is that the target material (scandium-45) is 100% naturally abundant. The targetry and radiochemical protocols for titanium-45 quite closely mirror those used for the more established radiometal zirconium-89 [38]. Group 4 metal ions have a very strong tendency to hydrolyze in aqueous mixtures, and Ti^{4+} ions react rapidly with water to form TiO_2. Early studies used titanium-45 chloride in HCl as a stock labeling source with variable success. However, stock solutions of titanium-45 must first seek to stabilize the ion against hydrolysis using chelators. Most protocols produce titanium trioxalate ($[Ti(C_2O_4)_3]^{2-}$), but Severin *et al.* proposed stabilising Ti^{4+} ions using a combination of salan and pyridine-2,6-dicarboxylic acid (dipic) ligands (Fig. 9). This alternative separation chemistry may open the door to more detailed exploration of titanium-45 radiotracers.

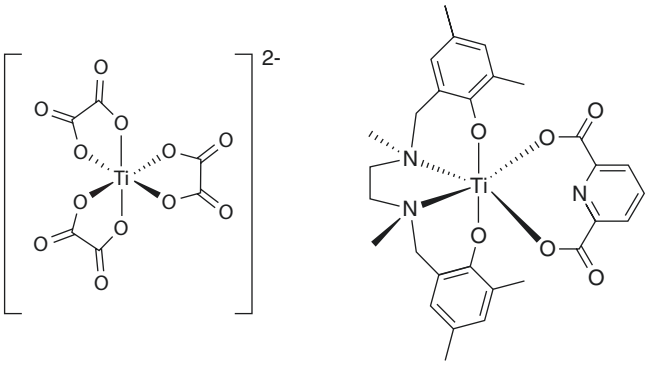

Fig. 9 Structures of two Ti^{4+} complexes that can potentially facilitate radiochemistry by stabilising the ion against facile hydrolysis in water

Group 5

Niobium-90 ($t_{1/2}$ = 14.60 h) is a high-energy β^+-emitting radionuclide that has been proposed as a potential alternative to copper-64 and zirconium-89 for immunoPET imaging. However, its concomitant release of γ-rays at 2186 keV (18.0%) and 2319 keV (82.0%) will likely prevent the clinical translation of this radionuclide based on dosimetry concerns. Yet, niobium-90 may still prove useful as a radionuclide for exploring the basic science of niobium complexes. While the targetry of niobium-90 production is straightforward, its chemical separation from solid zirconium foils is non-trivial. Busse *et al.* [39] reported cross sections for the $^{nat}Zr(p,n)^{90}Nb$ reaction and also the first separation method for isolating no-carrier-added niobium-90 (Fig. 10a). Subsequent work from the same group has produced alternative separation routes (Fig. 10b), and labeling reactions suggested that desferrioxamine B (DFO) is a suitable chelator for producing niobium-90-labeled antibodies [40, 41]. Unfortunately, these separation protocols are time consuming, result in low specific activity tracers, and are not easily reproduced. In addition, the nature of the Nb species present in stock solutions is uncertain. Data on aqueous phase niobium complexes is limited, but Nb ions typical hydrolyze rapidly and form complexes with the group oxidation state of 5+. The oxophilic nature of Nb^{5+} ions may result in the formation of Nb-oxo species. In addition, niobium complexes may under redox chemistry in a similar fashion to technetium. Once separation procedures have been reproduced and made accessible to more laboratories, it will be interesting to explore niobium-90 radiochemistry in greater detail.

Tantalum-178 ($t_{1/2}$ = 9.31 min) can be produced from a tungsten-178 ($t_{1/2}$ = 21.6 days) generator and was proposed as a potentially useful γ-ray imaging radionuclide for myo-

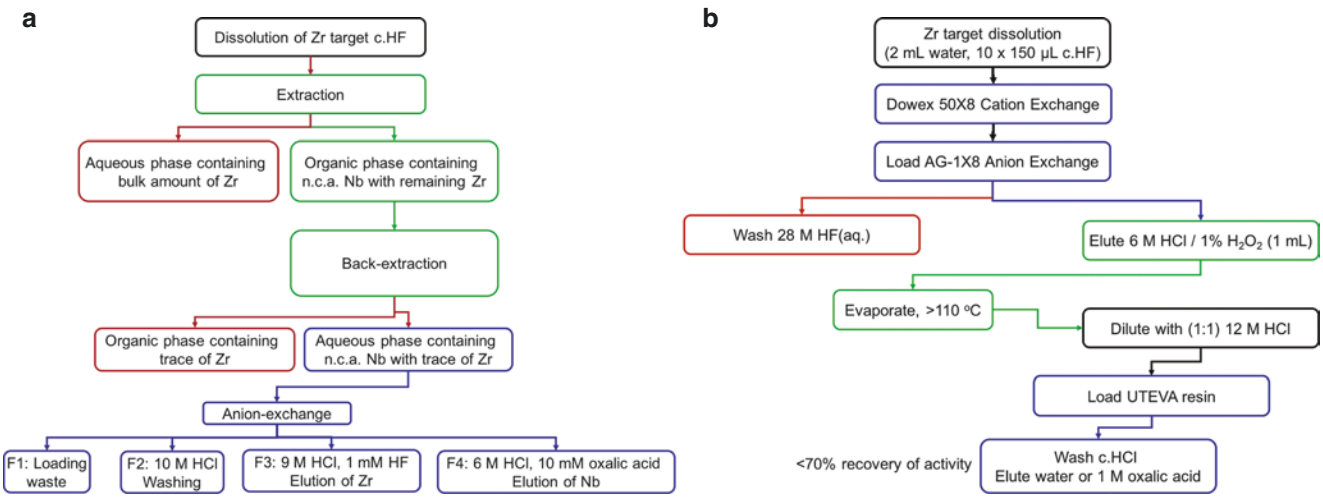

Fig. 10 (**a**, **b**) Proposed isolation protocols for separating niobium-90 from target zirconium based on studies reported

cardial perfusion studies in the 1980s [42]. The aqueous-phase chemistry of tantalum is not well-studied, and in light of the ready access to other radionuclides for myocardial perfusion imaging, more detailed investigations on the properties of tantalum-178 have yet to be performed.

Group 6

Chromium-51 ($t_{1/2}$ = 27.70 days) is a γ-emitting radionuclide, but its half-life and energy of emission are unsuitable for imaging. However, [^{51}Cr][Cr(EDTA)]$^-$ has formerly been used as a 'gold-standard' non-imaging radiotracer to measure glomerular filtration rates as an indicator of kidney function [43]. In addition, chromium-51 forms the basis of a widely used 'release assay' for the accurate quantification of cytotoxicity. The absence of suitable radionuclides for PET or SPECT – and perhaps the extreme toxicity and carcinogenicity of Cr^{6+} species – has limited further exploration of chromium chemistry in nuclear medicine.

Group 7

Manganese has at least three radioisotopes that are currently under development for applications in PET: manganese-51 ($t_{1/2}$ = 46.4 min), manganese-52 ($t_{1/2}$ = 5.59 days), and manganese-52m ($t_{1/2}$ = 21.1 min). Each of these radioisotopes can be produced via the irradiation of chromium or iron targets [2], but manganese-52m can also be obtained from a ^{52}Fe/^{52m}Mn generator. Manganese is redox active, but for biological applications in water, the 2+ and 3+ oxidation states offer the most diverse prospect for developing radiotracers based on existing chelator technologies like DOTA and EDTA (Fig. 3) [44]. Manganese 2+ ions can mimic the distribution of Ca^{2+} ions [45]. The range of half-lives for these manganese radioisotopes is attractive and permits the design of radiotracers ranging from small peptides with rapid pharmacokinetics to full-length antibodies and nanoparticles with prolonged circulation times. In addition, both Mn^{2+} and Mn^{3+} ions have a high magnetic moment and can be used in the design of MRI contrast agents like Teslascan (Mangafodir, [Mn(DPDP)]$^{6-}$; Fig. 11).

Technetium-94m ($t_{1/2}$ = 52.0 min) is a radioisotope of the ubiquitous technetium-99m that can be produced via the ^{94}Mo(p,n)^{94m}Tc transmutation reaction. The radiochemistry of technetium has been presented in the chapter on "The Radiopharmaceutical Chemistry of Technetium-99m". While the number of studies on technetium-94m is rather limited [46], the principal advantages of using this radionuclide are that technetium chemistry is well-established and existing clinical-grade radiotracers produced via kit formulations can be readily adapted.

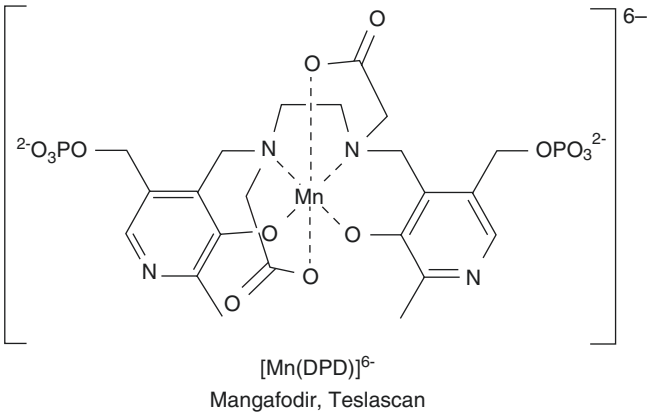

Fig. 11 Chemical structure of Teslascan, an MRI contrast agent based on Mn^{2+} ions with a high-spin d^5 electronic configuration

Rhenium has two isotopes of interest for radiotherapeutic applications. Rhenium-186 ($t_{1/2}$ = 3.72 days) can be obtained from reactor sources, whereas rhenium-188 ($t_{1/2}$ = 17.00 h) is potentially more attractive as a pure β^--emitter obtained from a ^{188}W($t_{1/2}$ = 69.78 days)/^{188}Re generator. The chemistry of rhenium is extremely close – though not identical – to that of technetium, which means established technetium radiotracers and chelation chemistry based on the {Tc=O}, {Tc≡N}, {Tc(HYNIC)}, or *fac*-{Tc(CO)$_3$} cores that can be readily adapted for the production of rhenium-based radiopharmaceuticals [47].

Group 8

Iron-52 ($t_{1/2}$ = 8.28 h) is an almost pure (99.6%) β^+-emitting radionuclide that remains underdeveloped in nuclear medicine. Iron is an essential nutrient for growth, and as an integral cofactor in many enzymes and metalloproteins like haemoglobin, it is the most abundant transition metal in the human body. In aqueous conditions, Fe^{2+} and Fe^{3+} complexes are predominant. The stabilization of Fe^{2+} ions by coordination using multidentate chelators with donor atoms that are high in the spectrochemical series can produce complexes in a low-spin d^6 electronic configuration which are typically exceptionally stable towards hydrolysis. High octahedral crystal field stabilization energies ($-2.4\Delta_o$) combined with kinetic (electronic) stabilization from the filled $(t_{2g})^6$ orbitals decrease the rate of ligand exchange. However, one of the challenges of working with iron in aqueous conditions is the need to use extremely powerful chelators (siderophores like DFO; Fig. 3). Fe^{2+} ions can be oxidized to Fe^{3+} ions, and the solubility product of $Fe(OH)_3$ is very low (log K_{sp} ~2.5×10^{-39}). Therefore, reactions must avoid precipitation of the radionuclide. In addition, iron is one of the principle causes of contamination in a radiochemistry laboratory. The pre-purification of all solvents and working with the highest

purity materials is a prerequisite for generating iron-52 (and other metal-based) radiotracers with high specific activity. One complicating factor is that iron-52 decays to manganese-52m (vide supra), which means that quantification and interpretation of iron-52 PET images are complicated by the concomitant redistribution of the daughter radionuclide.

Ruthenium-97 ($t_{1/2}$ = 2.83 days) decays via electron capture and has been produced by the ^{99}Tc(p,3n)^{97}Ru transmutation reaction using 50 MeV protons [48]. Ruthenium-97 decay is accompanied by γ-ray emissions (215.7 keV; 85.6%) that are suitable for SPECT as well as a host of low-energy Auger electrons that would permit radiotherapy. Early studies in 1981 investigated [^{97}Ru]Ru-DTPA for imaging cerebrospinal fluid [49]. However, since then a number of ruthenium-based polypyridyl and organometallic compounds – including NAMI-A, KP1019, and derivatives of [(η^6-biphenyl)Ru(en)Cl]PF_6 (RAED) and [(η^6-cymene)Ru(pta)Cl_2] (RAPTA) – have been developed as potential antimicrobial and anticancer agents (Fig. 12). Developing SPECT imaging and Auger electron-emitting radiotracers based on the structures of existing drug molecules offers a new route to simultaneously monitor drug distribution and increase their therapeutic efficacy *in vivo*. Notably, the target material technetium-99 is a major radioactive waste and environmental hazard in the United States. The production of ruthenium-97 may offer a modest outlet for using technetium-99.

Group 9

Cobalt-55 ($t_{1/2}$ = 17.53 h) is a relatively high-energy β$^+$-emitter that can be produced via proton or deuteron irradiation of iron or nickel targets [2]. The radiochemistry of cobalt-55 has not been developed, but in 1996, Jansen *et al.* reported pilot studies on five patients with traumatic brain injury [50]. The ^{55}Co-PET imaging was performed at Groningen University Hospital (the Netherlands) 16–24 h after intravenous administration of [^{55}Co]$CoCl_2$ (37 MBq in sterile saline). The authors suggest that Co^{2+} ions mimic the biochemistry of Ca^{2+} and that Co-PET is potentially useful for the diagnostic localization of both structural and functional abnormalities in moderate traumatic brain injury. In terms of radiochemistry, the coordination of cobalt-55 is likely to be successful using standard macrocyclic and acyclic polycarboxylate chelators, including bifunctional derivatives of DOTA and EDTA (Fig. 3). Further work is needed to establish reliable production and radiolabeling protocols.

Rhodium has at least nine radionuclides that are of potential interest in nuclear medicine [2]. Of these, rhodium-105 ($t_{1/2}$ = 35.36 h) for β$^-$ radiotherapy is arguably the most promising. As with many other radionuclides of the *d*-block, the radiochemistry of rhodium-105 remains underdeveloped. However, the larger ionic radius of Ru^{3+} ions (82 pm) leads to a preference for chelators with soft, class B donor atoms and larger cavities [51].

Iridium-192 ($t_{1/2}$ = 73.83 days) is a β$^-$-emitter. Its very long half-life is likely to limit interest in the development of molecularly targeted radiotherapy agents based on iridium-192. Nevertheless, the radionuclide has been used successfully in the clinic for high-dose brachytherapy in prostate cancer patients.

Group 10

Nickel-57 ($t_{1/2}$ = 35.60 h) is a potential PET radionuclide that can be produced using medium-energy cyclotrons (up to 60 MeV incident proton beam energy). Only one study has been performed investigating nickel-57-radiolabeled doxo-

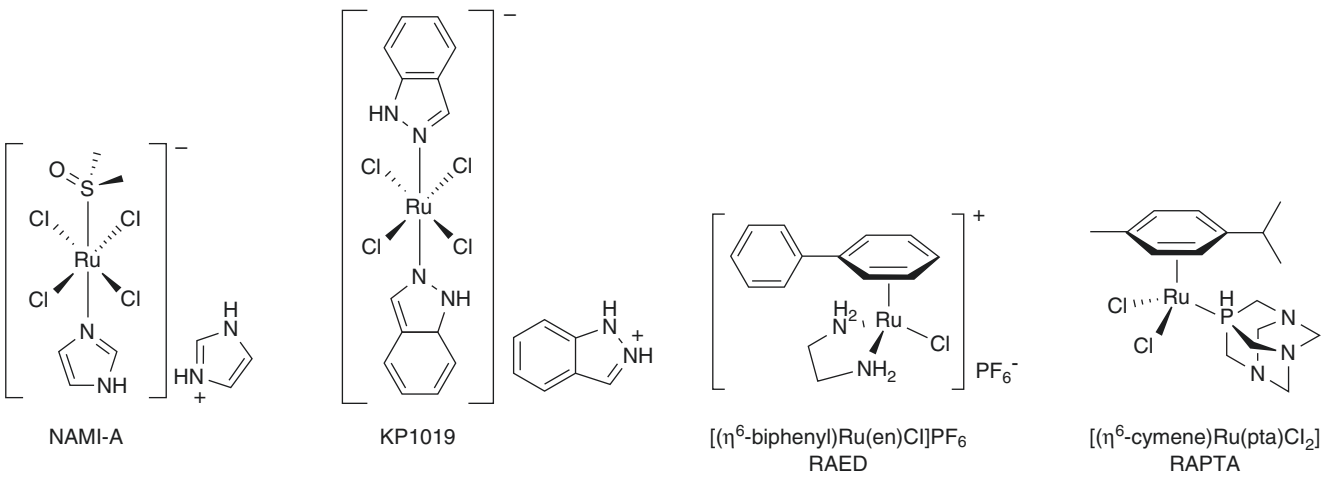

Fig. 12 Chemical structures of several ruthenium-based anticancer agents

rubicin as a drug analogue for measuring efflux associated with multidrug resistance in tumors [52].

Platinum-195m ($t_{1/2}$ = 4.01 days) decays via isomeric transition and is potentially useful for SPECT imaging and Auger electron radiotherapy. Three platinum-based anticancer agents (cisplatin, carboplatin, and oxaliplatin) have received worldwide approval, and several more platinum-based chemotherapeutics are in the pipeline (Fig. 13). The applications of platinum-195m parallel those mentioned for ruthenium and include monitoring drug distribution as well as increasing therapeutic efficacy by turning existing chemotherapeutic drugs into radiotherapeutic Auger-emitting variants.

Group 11

Of the elements of group 11, copper is one of the richest sources of radionuclides for imaging and radiotherapy. Indeed, some of the most well-established metal-based radiotracers have been developed using various radionuclides of copper (see the chapter on "The Radiopharmaceutical Chemistry of the Radionuclides of Copper") [1]. Beyond copper, both silver and gold have radionuclides of potential interest for radiotherapy.

Silver-111 ($t_{1/2}$ = 7.45 days) and *gold-198* ($t_{1/2}$ = 2.69 days) are both pure β^--emitters with similar overall particle energies. Silver-111 emits β^--particles with a mean energy of 360.4 keV (92%), whereas β^--particles from gold-198 have a slightly lower mean energy of 314.8 keV (99.0%) but marginally higher endpoint energy (see *Q*-values/keV; Table 3). Applications of silver-111 remain limited, but with the emergence of nanomedicines (and, in particular, functionalized gold nanoparticles), gold-198 is gaining prominence. One interesting report from Black *et al.* investigated the biodistribution of a range of radiochemically doped [^{198}Au]Au nanostructures with controlled shape and size (Fig. 4) [53]. Remarkably, nanospheres, nanodiscs, nanorods, and cubic nanocages of similar size showed dramatically different distributions and localizations in tumors. Understanding how the physical shape of nanoparticles influences their behaviour *in vivo* is an emerging frontier in nanoscience that will likely impact future design of multimodality radiotracers with silver-111 and gold-198 playing a central role.

Group 12

Zinc-65 ($t_{1/2}$ = 9.19 h) emits β^+-particles with a low abundance (8.2%). Nevertheless, given that zinc has the second highest abundance of transition metal elements in the human body, zinc-65 may be useful in measuring the distribution and biochemical role of Zn^{2+} ions in biology and medicine. Zinc ions are relatively large (ionic radius = 88 pm), and Zn^{2+} is preferentially complexed by ligands bearing soft, class B donor groups including sulfhydryls and imidazoles (histidine). The implications of Zn^{2+} ions in Alzheimer's disease have led to a resurgence of interest in tracking the distribution of zinc complexes *in vivo* [54]. The challenge for radiochemistry is to produce Zn^{2+} complexes of high thermodynamic and kinetic stability that minimize the loss of the radionuclide from the administered agent during the pharmacokinetic window.

Mercury-197m ($t_{1/2}$ = 23.8 h), and to a lesser extent mercury-197 ($t_{1/2}$ = 64.14 h), has been proposed as radionuclides for developing 'theranostic' radiotracers [55]. Mercury ions bind readily to proteins containing a high density of sulfhydryl groups, but in terms of chelation chemistry, the soft donor crown thioether system 1,4,7-trithiacyclonane has been proposed as a suitable chelator [1]. Bifunctional versions have yet to be tested.

Radionuclides of the *f*-Block Elements

Lanthanides

Radionuclides of lanthanide elements have a range of properties suitable for both imaging and radiotherapy. Moving across the period, the chemistry of the 4*f* elements is very

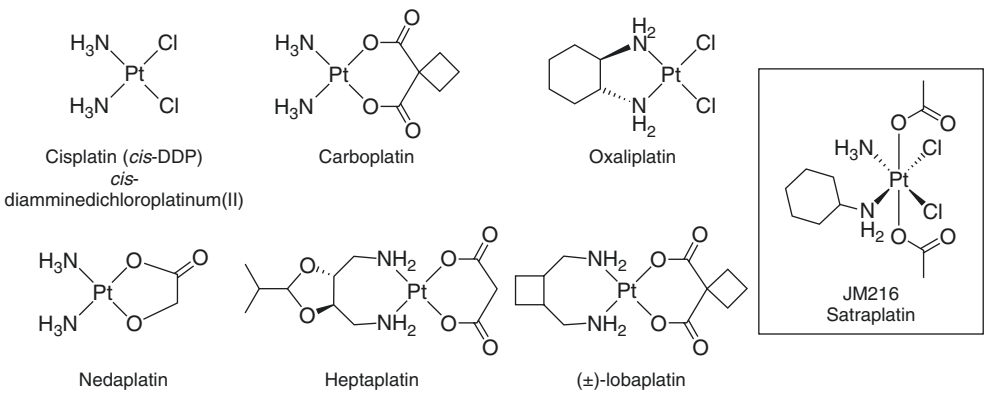

Fig. 13 Chemical structures of several clinically approved and developmental platinum-based drugs for treating cancer

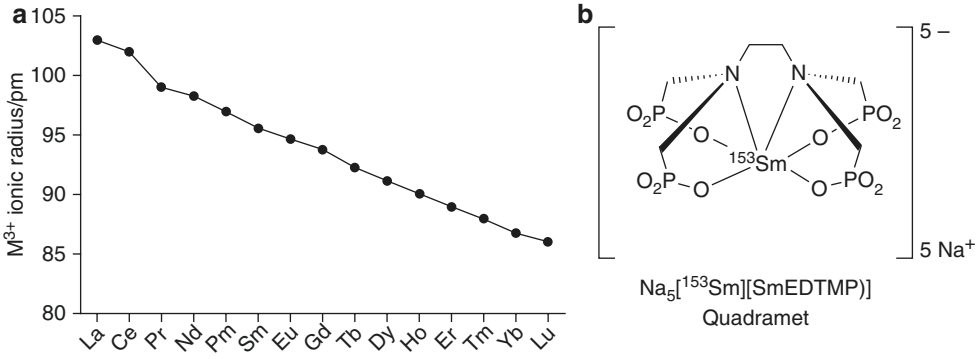

Fig. 14 (**a**) Plot of M^{3+} ionic radius versus 4*f* element showing the pronounced 'lanthanide contraction'. (**b**) Chemical structure of $Na_5[^{153}Sm][Sm(EDTMP)]$ (Quadramet®)

Table 4 Physical decay characteristics and established production routes of various radionuclides from the *f*-block lanthanides and actinides that have potential applications in diagnostic imaging and/or radiotherapy

Radionuclide	Half-life, $t_{1/2}$	Decay mode (% branching ratio)	Production route(s)	Q/keV	Primary applications
Lanthanides					
^{153}Sm	46.50 h	β^- (100%)	Reactor	807	Radiotherapy (Quadramet®)/SPECT
^{149}Tb	17.61 h	α (100%)	Ta spallation	2565	Radiotherapy
^{152}Tb	17.5 h	ε + β + (100%) β + (20.3%)	Ta spallation	3990	PET/radiotherapy (Auger electron)
^{155}Tb	5.32 days	ε (100%)	Ta spallation	823	SPECT/radiotherapy (Auger electron)
^{161}Tb	6.89 days	β^- (100%)	^{160}Gd$(n,\gamma)^{161}$Gd/^{161}Tb	593	SPECT/radiotherapy (beta and Auger electron)
^{166}Ho	26.80 h	β^- (100%)	^{165}Ho$(n,\gamma)^{166}$Ho reactor	1854	Radiotherapy
^{165}Er	10.36 h	ε (100%)	^{165}Ho$(p,n)^{165}$Er	376	SPECT/radiotherapy (Auger electron)
Actinides					
^{225}Ac	10.0 days	α (100%)	Reactor	5935	Radiotherapy
^{227}Th	18.68 days	α (100%)	Reactor	6146	Radiotherapy

similar. Lanthanide ions typically exist in the 3+ oxidation state, and increased nuclear charge induces a contraction in ionic radii from cerium to lutetium (Fig. 14a). Separation protocols for isolating macroscopic and radiochemical quantities of lanthanides typically involve column chromatography using strong cation exchange resins and solutions of α-hydroxyisobutyric acid with pH controlled using buffers (Table 4).

Samarium-153 ($t_{1/2}$ = 46.50 h) is a β^--emitting radionuclide used in radiotherapy. Samarium-153 lexidronam (samarium-153 ethylene diamine tetramethylene phosphonate, $Na_5[^{153}Sm][Sm(EDTMP)]$; Quadramet®; Lantheus Medical Imaging, Billerica MA, USA) is a US FDA-approved radiopharmaceutical used for palliative treatment of pain associated with bone metastases (Fig. 14b). It is most commonly used in patients with cancer of the lung, breast, and prostate as well as osteosarcoma.

Terbium has four radionuclides useful in SPECT, PET, and radiotherapy with β^-- and α-particle emissions [56, 57]. The terbium radioisotopes of interest are terbium-149 ($t_{1/2}$ = 17.61 h) for α-particle radiotherapy, terbium-152 ($t_{1/2}$ = 17.50 h) for PET and Auger electron radiotherapy, terbium-155 ($t_{1/2}$ = 5.32 days) for SPECT imaging, and terbium-161 ($t_{1/2}$ = 6.89 days) for radiotherapy with β^--particles. Several terbium-based radiotracers derived from small molecules, peptides, and antibodies have been studied, including [^{161}Tb]Tb-DOTATATE for the radiotherapy of neuroendocrine tumors [56]. Complexation reactions of Tb^{3+} ions follow similar chemical patterns to the radiochemistry of lutetium-177, and for this reason, DOTA has been the main chelator used so far. It has been suggested that terbium-161 is a potential alternative to lutetium-177. However, the lack of access to radionuclides of terbium as well as the commercial availability of clinical-grade lutetium-177 is likely to limit the adoption of terbium-based radiopharmaceuticals in the near term.

Erbium-165 ($t_{1/2}$ = 10.36 h) is a strong candidate for use in Auger electron radiotherapy and SPECT imaging. Erbium-165 can be produced via proton beam irradiation of holmium-165 (100% naturally abundant). Severin *et al.* also reported the preparation of a novel erbium-165 radionuclide generator. The generator is based on the Szilard-Chalmers reaction of DOTA-bound thulium-165 ($t_{1/2}$ = 10.36 h; ε[epsilon] = 100%, Q-value = 1592 keV) [58]. Up to 200 MBq of erbium-165 was produced, and molar activities of 43 GBq/μmol were suitable for the radiosynthesis of

[^{165}Er]Er-DOTATATE. As interest in the development of Auger-emitting radiopharmaceuticals grows, it will be interesting to see how quickly the nuclear medicine community adopts erbium-165.

Holmium-166 ($t_{1/2}$ = 26.8 h) is a high-energy β^--emitting radionuclide that has been used to generate radiolabeled antibodies for radioimmunotherapy (RIT). For instance, [^{166}Ho]Ho-DOTA-labeled bevacizumab has been evaluated for the targeted RIT of tumors expressing vascular endothelial growth factor A (VEGF-A) [59]. Holmium-166-radiolabeled nanoparticles and chitosan have also been explored for potential radiotherapeutic applications. Radiolabeling with holmium-166 is typically achieved using [^{166}Ho]$HoCl_3$ stock solutions reacted with biological targeting vectors functionalized with DOTA.

Actinides

The chemistry of the 5*f* actinide elements is more diverse than that of the 4*f* lanthanides. In the former, the 5*f* electrons are valence-like and are more readily involved in chemical bonding. Actinides also undergo more extensive redox chemistry, enabling the adoption of a range of oxidation states. A more detailed exploration of the chemistry and radiochemistry of actinides is presented in the chapter on "The Radiopharmaceutical Chemistry of Alpha-Emitting Radionuclides".

Actinium-225 ($t_{1/2}$ = 10.0 days) is the primary radionuclide of the 5*f* elements used in nuclear medicine. Actinium-225 decays via α-particle emission, which generates a decay chain that can be used for generation of various daughter radionuclides *in vivo*. In 2016, Kratochwil *et al.* reported clinical trials in two patients using [^{225}Ac]Ac-PSMA-617 for the targeted radiotherapy of castrate-resistant metastatic prostate cancer [60]. Here, the actinium-225 radionuclide is complexed by the DOTA chelator. Given the high radiotoxicity of actinium-225 and its daughter radionuclides, the kinetically and thermodynamically stable complexation of Ac^{3+} ions is crucial. Further exploration of the radiochemistry and pharmacokinetic properties of Ac^{3+} complexes is essential for the future development of actinium-225-based radiopharmaceuticals.

Tricks of the Trade

In an ideal world, a radiochemist would be free to select any radionuclide for developing radiotracers. Academic or commercially accessible radionuclides cover all groups of the periodic table, but how can we address the original question about how a radiochemist can make the most appropriate choice? Figure 15 shows a flow chart listing the three main criteria of availability, application, and biochemistry. In addition, a selection of common commercially available radionuclides is shown on the left, and a handful of emerging alternatives are displayed on the right.

In practice, logistical considerations often override ambition: if a radionuclide is not available, it cannot be used to build radiopharmaceuticals. On top of this, the potential

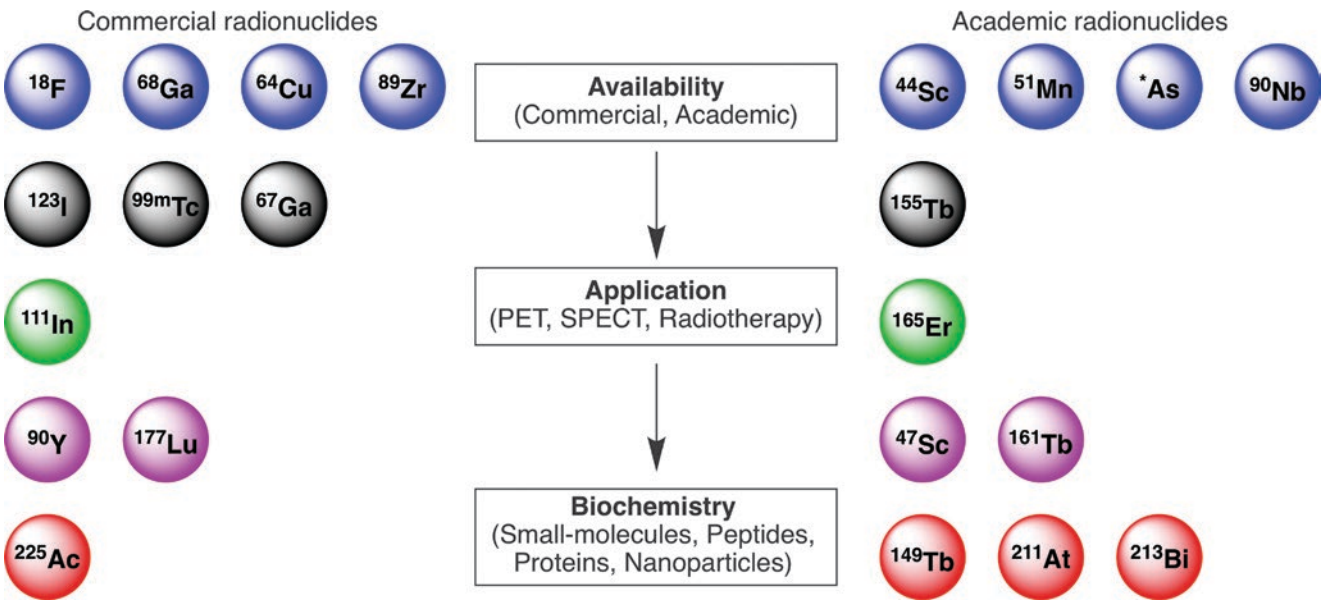

Fig. 15 Scheme showing three proposed criteria for choosing a radionuclide for radiotracer development, as well as a selection of commonly used and emerging radionuclides for different applications (*blue* = PET, *black* = SPECT, *green* = Auger electron radiotherapy, *purple* = β^--particle radiotherapy, and *red* = α-particle radiotherapy)

applications of a radionuclide are governed by its decay properties. That is to say, a positron-emitting radionuclide must (obviously) be chosen when designing a PET imaging agent. In light of these exigencies, when designing a new radiotracer, a radiochemist has the most freedom in the choice of chemistry and biochemistry. The main decisions centre on the nature of the targeting vector, which in turn determines the pharmacokinetics of the putative tracer *in vivo*. For radioactive metal ions, the choice of chelator and conjugation chemistry is crucial to the success of a radiotracer. High kinetic, thermodynamic, and metabolic stability are usually the most desirable properties of a metal ion-chelator complex, and for any new chelator or radiotracer, detailed ligand challenge and stability measurements should always be performed prior to conducting experiments *in vivo*.

An important point that scientists should always keep in mind is that the radionuclide is a *non-innocent*, *integral* component of any radiotracer and as such can have strong influence on its chemical and biochemical properties. While similar chelators can be used to complex different radiometal ions in the same basic radiopharmaceutical structure, switching from one metal ion to another can have dramatic and unpredictable implications on the *in vivo* behaviour of the radiopharmaceuticals. For example, one should not assume that swapping gallium-67/gallium-68 for lutentium-177 will lead to equivalent behaviour *in vivo*. In the end, comprehensive chemical and biological testing is essential to understanding each new radiotracer *ab initio*.

Controversial Issues

As mentioned in the introduction, matching the physical half-life of a radionuclide with the anticipated biological half-life is a common principle used by many radiochemists. This dogma is a useful guide that helps minimize the radiation burden to patients during the application of radiopharmaceuticals, particularly imaging agents. However, the concept does not necessarily hold true for all radiotracers, especially radiotherapeutics. Consider the recent application of [^{225}Ac]Ac-PSMA-617 in patients with advanced metastatic prostate cancer [60]. The reasons for using long-lived actinium-225 in conjunction with a targeting vector with a rapid pharmacokinetic profile are not immediately obvious, and yet the combination is very effective. To find answers as to why this PSMA-targeting small molecule and actinium-225 are a good match, one must consider both decay properties *and* pharmacokinetics.

Many small molecules, urea-based radiotracers labeled with gallium-68 and fluorine-18, have emerged as useful clinical tools for imaging tumors that express PSMA. These diagnostic radiotracers are cleared rapidly from the blood pool and are excreted (usually intact) from the body via the renal system. Their high affinity for PSMA (typically in the nanomolar range) leads to their retention in PSMA-expressing tissues, including tumors and the kidneys. Radiotoxicity to the kidney is normally the dose-limiting factor for these radiotracers.

The effective application of α-radiotherapy is predicated on delivering the maximum amount of the radionuclide to the tumor as quickly as possible while simultaneously minimizing the accumulation and retention of the agent in healthy organs. The radionuclide should also be internalized inside the cells. Internalization has two primary effects. First, the α-particles are closer to the DNA, where ionization has an increased likelihood of causing cytotoxic double-strand breaks. Second, internalized metalloradionuclides often sequester in the target tissue. In the case of actinium-225, decay generates a series of highly energetic, β^-- and α-emitting radionuclides that increase the effective dose. The recirculation of these radiotoxic daughters would increase radiation damage to healthy background tissues. The binding of urea-based radiotracers to PSMA usually leads to the rapid internalization of the radiotracer-PSMA complex. For [^{225}Ac]Ac-PSMA-617, internalization delivers a high radiation dose to tumor while low expression of PSMA in background tissues minimizes off-target damage and associated side effects. The radiotracer is not perfect, and high radiation damage to the kidneys means that further optimization is required to improve tumor-to-kidney ratios. However, this case study provides a clear illustration that while empirical guidelines for developing radiotracers are often useful, sometimes the most effective solutions are found when radiochemists dare to break the rules.

The Future

Only a small fraction of radionuclide space has been developed for use in nuclear medicine. For many of the 'alternative' radionuclides that reside in the deeper corners of the periodic table, the chemistry and interactions of these elements with biological systems are largely unknown. PET and SPECT imaging are the most powerful methods available for non-invasive measurement of the biochemistry of a disease. However, images alone do not improve patient outcome. Having made a diagnosis, clinicians need new imaging tools to monitor patient progress and response to therapy as well as new, more effective drugs to treat disease. Fortunately, radiochemistry is in a strong position to help in both situations. Predicting the future is notoriously dangerous, but as medical and scientific specialists from disciplines outside nuclear medicine continue to gain an appreciation of the benefits of using radiotracers, there is a strong likelihood that the next generation of imaging agents will be designed increas-

ingly as 'companion diagnostics' for improving drug development. In terms of treating diseases like cancer, resistance mechanisms mean that patients often relapse after standard chemotherapy. Here, developing new drugs becomes a 'pharmacological arms race'. For patients with terminal disease who fail to respond to standard chemotherapy, targeted radiotherapeutic drugs are 'nuclear options' that offer hope when no other solutions are available.

The Bottom Line

- Existing radiotracers have only begun to scratch the surface of the available physical, chemical, and biological properties offered by radionuclides from across the periodic table.
- Production methods and availability are the main limitations to the future applications of alternative radionuclides.
- Radionuclides of scandium, titanium, manganese, and arsenic show promise for the future development of PET radiotracers.
- Heavier elements from the *p*-, *d*-, and *f*-block groups are emerging as alternative sources of radionuclides for imaging and especially radiotherapy.
- The exploration of the radiochemistry of niobium, erbium, terbium, astatine, and actinium will generate new knowledge about the chemistry of these 'exotic' elements.

Acknowledgements JPH thanks the Swiss National Science Foundation (SNSF Professorship PP00P2_163683), the European Research Council (ERC-StG-2015, NanoSCAN – 676904), the Swiss Cancer League (Krebsliga Schweiz; KLS-4257-08-2017), and the University of Zurich for financial support.

References

1. Blower PJ. A nuclear chocolate box: the periodic table of nuclear medicine. Dalton Trans. 2015;44(11):4819–44.
2. Nickles RJ. The production of a broader palette of PET tracers. J Label Compd Radiopharm. 2003;46(1):1–27.
3. Qaim SM. The present and future of medical radionuclide production. Radiochim Acta. 2012;100(8–9):635–51.
4. International Atomic Energy Agency. Cyclotron produced radionuclides: physical characteristics and production methods. Technical Report Series No. 468. October. 2009;(468):279.
5. Holland JP, Williamson MJ, Lewis JS. Unconventional nuclides for radiopharmaceuticals. Mol Imaging. 2010;9(1):1–20.
6. Poonia NS, Bajaj AV. Coordination chemistry of alkali and alkaline earth cations. Chem Rev. 1979;79(5):389–445. https://doi.org/10.1021/cr60321a002.
7. Takami A, Yoshida K, Tadokoro H, Kitsukawa S, Shimada K, Sato M, et al. Uptakes and images of 38K in rabbit heart, kidney, and brain. J Nucl Med. 2000;41(4):763–9.
8. Hunter CRRN, Hill J, Ziadi MC, Beanlands RSB, deKemp RA. Biodistribution and radiation dosimetry of 82Rb at rest and during peak pharmacological stress in patients referred for myocardial perfusion imaging. Eur J Nucl Med Mol Imaging. 2015;42(7):1032–42.
9. Nair N. Relative efficacy of 32P and 89Sr in palliation in skeletal metastases. J Nucl Med. 1999;40(2):256–61.
10. Kastleiner S, Qaim SM, Nortier FM, Blessing G, Van Der Walt TN, Coenen HH. Excitation functions of 85Rb(p,xn)85m,g,83,82,81Sr reactions up to 100 MeV: integral tests of cross section data, comparison of production routes of 83Sr and thick target yield of 82Sr. Appl Radiat Isot. 2002;56(5):685–95.
11. Pasachoff N. Marie Curie and the science of radioactivity. New York: Oxford University Press; 1996. p. 48.
12. Henriksen G, Hoff P, Larsen RH. Evaluation of potential chelating agents for radium. Appl Radiat Isot. 2002;56(5):667–71.
13. Vaidyanathan G, Zalutsky MR. Applications of 211At and 223Ra in targeted alpha-particle radiotherapy. Curr Radiopharm. 2011;4(4):283–94.
14. Othman MF, Mitry NR, Lewington VJ, Blower PJ, Terry SY. Re-assessing gallium-67 as a therapeutic radionuclide. Nucl Med Biol. 2017;46:12–8.
15. Unger LM, Trubey DK. Specific gamma-ray dose constants for nuclides important to dosimetry and radiological assessment. ORNL/RSIC-45/Rev.1. International Atomic Energy Agency/International Nuclear Information System. 1982. INIS 14(3):14724519.
16. Walsh G. Biopharmaceutical benchmarks 2010. Nat Biotechnol. 2010;28(9):917–24.
17. Chakravarty R, Valdovinos HF, Chen F, Lewis CM, Ellison PA, Luo H, et al. Intrinsically germanium-69-labeled iron oxide nanoparticle: synthesis and in vivo dual-modality PET/MR imaging HHS public access. Adv Mater. 2014;26(30):5119–23.
18. Boros E, Bowen AM, Josephson L, Vasdev N, Holland JP. Chelate-free metal ion binding and heat-induced radiolabeling of iron oxide nanoparticles. Chem Sci. 2015;6(1):225–36.
19. Lamb JR, Holland JP. Advanced methods for radiolabelling nanomedicines for multi-modality nuclear/MR imaging. J Nucl Med. 2018;59(3):382–9.
20. Maslov OD, Starodub GY, Vostokin GK, Gustova MV, Dmitriev SN, Shvetsov VN, et al. Production of (117m)Sn with high specific activity by cyclotron. Appl Radiat Isot. 2011;69(7):965–8.
21. Chappell LL, Dadachova E, Milenic DE, Garmestani K, Wu C, Brechbiel MW. Synthesis, characterization, and evaluation of a novel bifunctional chelating agent for the lead isotopes 203 Pb and 212 Pb. Nucl Med Biol. 2000;27(1):93–100.
22. Torres Martin de Rosales R, Tavaré R, Glaria A, Varma G, Protti A, Blower PJ. (^{99}m) Tc-bisphosphonate-iron oxide nanoparticle conjugates for dual-modality biomedical imaging. Bioconjug Chem. 2011;22(3):455–65.
23. Chen F, Ellison PA, Lewis CM, Hong H, Zhang Y, Shi S, et al. Chelator-free synthesis of a dual-modality PET/MRI agent. Angew Chem Int Ed Eng. 2013;52(50):13319–23.
24. McDevitt MR, Barendswaard E, Ma D, Lai L, Curcio MJ, Sgouros G, et al. An alpha-particle emitting antibody ([213Bi]J591) for radioimmunotherapy of prostate cancer. Cancer Res. 2000;60(21):6095–100.
25. Milenic DE, Roselli M, Mirzadeh S, Pippin CG, Gansow OA, Colcher D, et al. In vivo evaluation of bismuth-labeled monoclonal antibody comparing DTPA-derived bifunctional chelates. Cancer Biother Radiopharm. 2001;16(2):133–46.
26. Mirzadeh S, Kumar K, Gansow OA. The chemical fate of 212Bi-DOTA formed by β-decay of 212Pb(DOTA)2. Radiochim Acta. 1993;60(1):1–10.
27. Plenevaux A, Guillaume M, Brihaye C, Lemaire C, Cantineau R. Chemical processing for production of no-carrier-added selenium-73 from germanium and arsenic targets and synthesis of l-2-amino-4-([73Se]methylseleno) butyric acid (l-[73Se]selenomethionine). Int J Radiat Appl Instrum A. 1990;41(9):829–38.

28. Engle JW, Barnhart TE, DeJesus OT, Nickles RJ. Production of 34mCl and 38Cl via the (d,α) reaction on 36Ar and natAr gas at 8.4MeV. Appl Radiat Isot. 2011;69(1):75–9.
29. Tolmachev V. Radiobromine-labelled tracers for positron emission tomography: possibilities and pitfalls. Curr Radiopharm. 2011;4(2):76–89.
30. Teze D, Sergentu D-C, Kalichuk V, Barbet J, Deniaud D, Galland N, et al. Targeted radionuclide therapy with astatine-211: oxidative dehalogenation of astatobenzoate conjugates. Sci Rep. 2017;7(1):2579.
31. Walczak R, Krajewski S, Szkliniarz K, et al. Cyclotron production of 43Sc for PET imaging. EJNMMI Phys. 2015;2:33. https://doi.org/10.1186/s40658-015-0136-x.
32. Severin GW, Engle JW, Valdovinos HF, Barnhart TE, Nickles RJ. Cyclotron produced 44gSc from natural calcium. Appl Radiat Isot. 2012;70(8):1526–30.
33. Valdovinos HF, Hernandez R, Barnhart TE, Graves S, Cai W, Nickles RJ. Separation of cyclotron-produced 44Sc from a natural calcium target using a dipentyl pentylphosphonate functionalized extraction resin. Appl Radiat Isot. 2015;95:23–9.
34. Filosofov DV, Loktionova NS, Rösch F. A 44Ti/44Sc radionuclide generator for potential application of 44Sc-based PET-radiopharmaceuticals. Radiochim Acta. 2010;98(3):149–56.
35. Rane S, Harris JT, Starovoitova VN. 47Ca production for 47Ca/47Sc generator system using electron linacs. Appl Radiat Isot. 2015;97:188–92.
36. Pruszyński M, Loktionova NS, Filosofov DV, Rösch F. Post-elution processing of 44Ti/ 44Sc generator-derived 44Sc for clinical application. Appl Radiat Isot. 2010;68(9):1636–41.
37. Yoo J, Tang L, Perkins TA, Rowland DJ, Laforest R, Lewis JS, et al. Preparation of high specific activity 86Y using a small biomedical cyclotron. Nucl Med Biol. 2005;32(8):891–7.
38. Chen F, Valdovinos HF, Hernandez R, Goel S, Barnhart TE, Cai W. Intrinsic radiolabeling of Titanium-45 using mesoporous silica nanoparticles. Acta Pharmacol Sin. 2017;38(6):907–13.
39. Busse S, Brockmann J, Rösch F. Radiochemical separation of no-carrier-added radioniobium from zirconium targets for application of 90Nb-labelled compounds. Radiochim Acta. 2002;90(37438):411–5.
40. Radchenko V, Filosofov DV, Bochko OK, Lebedev NA, Rakhimov AV, Hauser H, et al. Separation of 90Nb from zirconium target for application in immuno-pet. Radiochim Acta. 2014;102(5):433–42.
41. Radchenko V, Hauser H, Eisenhut M, Vugts DJ, Van Dongen GAMS, Roesch F. 90Nb – a potential PET nuclide: production and labeling of monoclonal antibodies. Radiochim Acta. 2012;100(11):857–63.
42. Lacy JL, Layne WW, Guidry GW, Verani MS, Roberts R. Development and clinical performance of an automated, portable tungsten-178/tantalum-178 generator. J Nucl Med. 1991;32(11):2158–61.
43. Moore AEB, Park-Holohan SJ, Blake GM, Fogelman I. Conventional measurements of GFR using 51Cr-EDTA overestimate true renal clearance by 10 percent. Eur J Nucl Med Mol Imaging. 2003;30(1):4–8.
44. Graves SA, Hernandez R, Fonslet J, England CG, Valdovinos HF, Ellison PA, et al. Novel preparation methods of 52Mn for ImmunoPET imaging. Bioconjug Chem. 2015;26(10):2118–24.
45. Graves SA, Hernandez R, Valdovinos HF, Ellison PA, Engle JW, Barnhart TE, et al. Preparation and in vivo characterization of 51MnCl2 as PET tracer of Ca2+ channel-mediated transport. Sci Rep. 2017;7:3033. https://doi.org/10.1038/s41598-017-03202-0.
46. Gagnon K, McQuarrie S, Abrams D, McEwan AJ, Wuest F. Radiotracers based on technetium-94m. Curr Radiopharm. 2011;4(2):90–101.
47. Alberto R, Braband H. SPECT/PET imaging with technetium, gallium, copper, and other metallic radionuclides. In: Alberto R, Braband H, editors. Comprhensive inorganic chemistry II: from elements to applications. 2nd ed. Oxford: Elsevier; 2013. p. 785–817.
48. Zaitseva NG, Stegailov VI, Khalkin VA, Shakun NG, Shishlyannikov PT, Bukov KG. Metal technetium target and target chemistry for the production of 97Ru via the 99Tc(p,3n) 97Ru reaction. Appl Radiat Isot. 1996;47(2):145–51.
49. Oster ZH, Som P, Gil MC, Fairchild RG. Ruthenium-97 DTPA: a new radiopharmaceutical for cisternography. J Nucl. 1981;22(3):269–73.
50. Jansen HM, van der Naalt J, van Zomeren AH, Paans AM, Veenma-van der Duin L, Hew JM, et al. Cobalt-55 positron emission tomography in traumatic brain injury: a pilot study. J Neurol Neurosurg Psychiatry. 1996;60(2):221–4.
51. Jurisson SS, Ketring AR, Volkert WA. Rhodium-105 complexes as potential radiotherapeutic agents. Transit Met Chem. 1997;22(3):315–7.
52. Zweit J, Carnochan P, Goodall R, Ott RJ. Excitation functions of proton induced reactions on cobalt: production of no-carrier added nickel-57, a positron emitting label for doxorubicin. Appl Radiat Isot. 1993;44(12):1411–6.
53. Black KCL, Wang Y, Luehmann HP, Cai X, Xing W, Pang B, et al. Radioactive 198au-doped nanostructures with different shapes for in vivo analyses of their biodistribution, tumour uptake, and intratumoral distribution. ACS Nano. 2014;8(5):4385–94.
54. Watt NT, Whitehouse IJ, Hooper NM. The role of zinc in Alzheimer's disease. Int J Alzheimers Dis. 2011;2011:1–10.
55. Walther M, Preusche S, Bartel S, Wunderlich G, Freudenberg R, Steinbach J, et al. Theranostic mercury: 197(m)Hg with high specific activity for imaging and therapy. Appl Radiat Isot. 2015;97:177–81.
56. Lehenberger S, Barkhausen C, Cohrs S, Fischer E, Grünberg J, Hohn A, et al. The low-energy β – and electron emitter 161Tb as an alternative to 177Lu for targeted radionuclide therapy. Nucl Med Biol. 2011;38(6):917–24.
57. Müller C, Zhernosekov K, Köster U, Johnston K, Hohn DH, et al. A unique matched quadruplet of terbium radioisotopes for PET and SPECT and for α- and β- radionuclide therapy: an in vivo proof-of-concept study with a new receptor-targeted folate derivative. J Nucl Med. 2012;53(12):1951–9.
58. Severin G, Jensen M. A radionuclide generator of Erbium-165, an isotope for Auger Therapy (abstract). Radiother Oncol. 2014;110(Suppl 1):S88–9.
59. Di Pasqua AJ, Yuan H, Chung Y, Kim JK, Huckle JE, Li C, et al. Neutron-activatable holmium-containing mesoporous silica nanoparticles as a potential radionuclide therapeutic agent for ovarian cancer. J Nucl Med. 2012;54(1):111–6.
60. Kratochwil C, Bruchertseifer F, Giesel FL, Weis M, Verburg FA, Mottaghy F, et al. 225Ac-PSMA-617 for PSMA-targeted α-radiation therapy of metastatic castration-resistant prostate cancer. J Nucl Med. 2016;57(12):1941–4.

Part III

Special Topics

Bioconjugation Methods for Radiopharmaceutical Chemistry

Jens Cardinale, Carolina Giammei, Nedra Jouini, and Thomas L. Mindt

Fundamentals

The terms "bioconjugation" and "bioconjugation chemistry" refer to the chemical or biochemical processes used to form a stable linkage between a biomolecule and a second chemical or biological moiety. Broadly defined, biomolecules are relatively large, naturally occurring or nature-inspired molecules that can perform various biological functions. In general, biomolecules can be classified into four groups: (i) polypeptides (peptides, proteins, antibodies, *etc.*), (ii) polysaccharides, (iii) nucleic acids (DNA or RNA), and (iv) lipids. A fifth class of compounds that are often referred to as biomolecules – small molecules that are either building blocks for larger macromolecules or metabolites thereof – will not be covered in this chapter, as they seldom intersect with bioconjugation chemistry. Examples of "secondary moieties" of interest for bioconjugations include drugs (*e.g.* toxins), pharmacological modifiers (*e.g.* polyethylene glycol), and imaging reporters such as fluorophores or radionuclides. While a large number of different chemical transformations and reagents have been employed for bioconjugations, this chapter will focus solely on those employed in the radiopharmaceutical sciences. As a result, several important topics such as cross-linking strategies or the use of cleavable linkers are not included. For a more comprehensive treatment of bioconjugation techniques, some excellent textbooks on the subject are available [1, 2].

In comparison to the radiolabeling approaches outlined in many of the other chapters of this book, the following sections will focus on the direct modification of the functional groups of biomolecules in their native form without the use of protecting group chemistry. In general, these procedures are short and involve no more than 1–2 synthetic steps. We will pay particular attention to protocols that employ mild reaction conditions (*i.e.* aqueous media, neutral pH, and room temperature), a critical consideration for the modification of sensitive biomolecules such as proteins or antibodies. With the exception of a few examples of direct radiolabeling protocols – for example, the radioiodination of tyrosine residues (see the chapter on "The Radiopharmaceutical Chemistry of the Radioisotopes of Iodine") – the attachment of radionuclides to biomolecular vectors is generally accomplished using one of two different strategies: (i) a post-labeling (direct) approach in which the biomolecule is functionalized with a moiety that allows for subsequent radiolabeling and (ii) a pre-labeling (indirect) approach in which a reagent is first radiolabeled and *then* conjugated the biomolecule (Fig. 1).

The first strategy – the post-labeling approach – is most frequently employed for the radiolabeling of molecules with radiometals using bifunctional chelating agents (BFCA; Fig. 2). BFCAs are low molecular weight molecules that contain a chelating system that enables the stable complexation of the radiometal as well as a functional group that facilitates conjugation to a biomolecule. Due to the very low concentrations of radiometals present in radiolabeling reactions, there is almost always a large excess of the BFCA-bearing biomolecule during radiolabeling. As a result, this approach yields mixtures of radiolabeled and non-radiolabeled conjugates that are difficult to separate using common purification techniques. Not surprisingly, the non-labeled biomolecule can compete with the radiolabeled biomolecule for binding sites *in vivo*, thereby lowering the uptake of the more important radiolabeled variant in the tissue of interest. As a result, the optimization of the apparent molar activity of the product mixture becomes critical [3]. This is often accomplished by employing a ratio of precursor-to-radiometal as low as achievable for quantitative complexation of the radiometal. In situations in which a final purification step of the radiotracer is not needed, the post-labeling strategy is particularly suited for the development of radiopharmaceutical "kits."

The second strategy – the pre-labeling approach – is most commonly used for the radiolabeling of molecules with

J. Cardinale · C. Giammei · N. Jouini · T. L. Mindt (✉)
Ludwig Boltzmann Institute Applied Diagnostics, General Hospital Vienna (AKH), Vienna, Austria
e-mail: thomas.mindt@lbiad.lbg.ac.at

J. S. Lewis et al. (eds.), *Radiopharmaceutical Chemistry*, https://doi.org/10.1007/978-3-319-98947-1_25

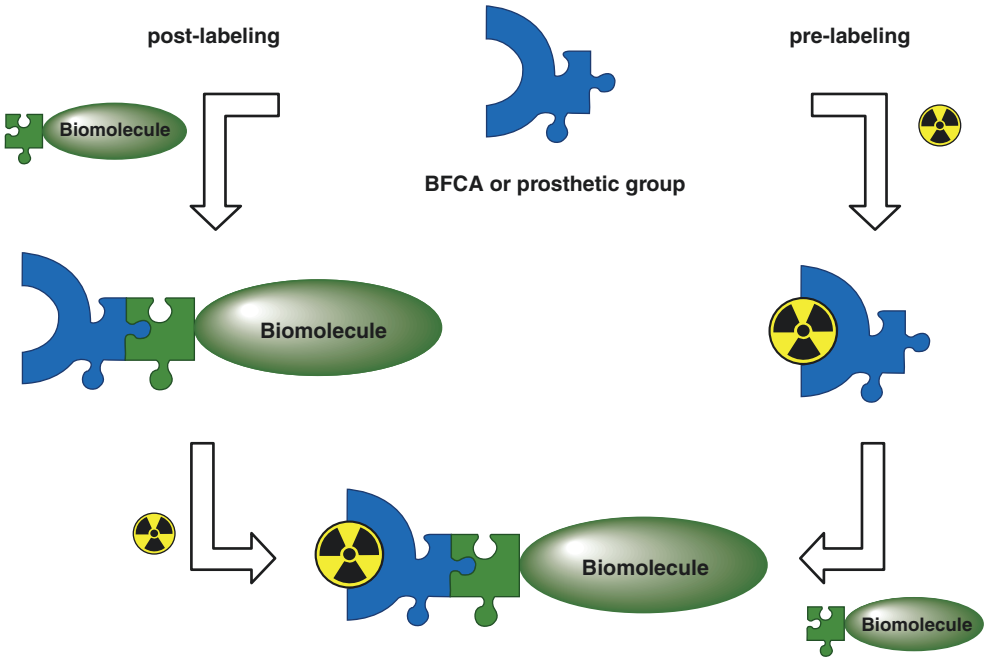

Fig. 1 Pre- and post-labeling approaches for the radiolabeling of biomolecules. The jigsaw pieces symbolize two functional groups forming a covalent linkage in the final conjugate, and the half circle represents a moiety to which a (metallic or nonmetallic) radionuclide can be attached. (Jigsaw puzzle piece courtesy of http://www.clker.com/clipart-group-of-blue-puzzle-pieces.html, with permission)

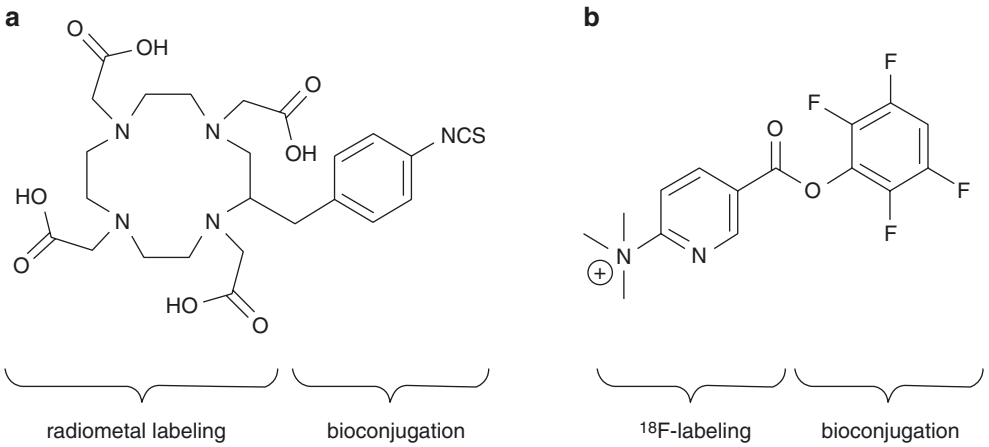

Fig. 2 Representative examples of (**a**) a bifunctional chelating agent (DOTA-*p*BnNCS: S-2-(4-isothiocyanatobenzyl)-1,4,7,10-tetraazacyclododecane tetraacetic acid) and (**b**) a prosthetic group (6-trimethylammoniumnicotinic acid-2,3,5,6-tetrafluorophenyl ester (triflate counterion not shown) for the preparation of 6-[^{18}F]F-Py-TFP: 6-[^{18}F]fluoronicotinic acid-2,3,5,6-tetrafluorophenyl ester)

nonmetallic radionuclides (*e.g.* fluorine-18 or carbon-11). In these cases, the incompatibility of the biomolecule with the conditions needed for radiolabeling is often the driving force behind the adoption of the pre-labeling approach. This strategy is facilitated by so-called prosthetic groups, small molecules that are composed of two domains that allow for both radiolabeling and subsequent conjugation to a biomolecule (see Fig. 2).

Usually, the radiolabeled prosthetic group is separated from its unlabeled precursor to avoid competition for reaction sites on the biomolecule during the bioconjugation step. In light of this separation, only very low (tracer level) concentrations of the radiolabeled prosthetic group are typically available during bioconjugation reactions, which can result in incomplete conversion and, as a result, an additional purification step. Hence, the radiochemical yields obtained using pre-labeling strategies are generally lower than those achieved using post-labeling approaches. Of course, variations of these general radiolabeling strategies have been reported depending on the scientific question. For example, post-labeling approaches are often used for ^{18}F-fluorinations via isotope exchange (see the chapter on "The Radiopharmaceutical Chemistry of Fluorine-18: Next-Generation Fluorinations"), and pre-labeling approaches have been employed for the radiometallation of sensitive biomolecules (or cells) which are unstable under the conditions necessary for radiolabeling (*e.g.* elevated temperatures).

Two important aspects of bioconjugation chemistry to consider are the chemoselectivity and site-specificity of the modification reaction. The term "chemoselectivity" refers to the ability of a reagent to react selectively with one type of functional group in the presence of other moieties. The term "site-specificity" denotes the ability to modify a biomolecule at a single defined position (or, in some cases, a small number of defined positions). Obviously, achieving the latter is a more challenging task. The majority of biomolecules contain not only several different functional groups but also multiple copies of each type at different positions. This means that even if a reactive probe is chemoselective for a given functional group, its reaction with a biomolecule may still – and often does – result in the creation of mixtures of products that differ in both the number of conjugated moieties *and* their position.

To illustrate this phenomenon, let us consider the reaction between a protein with four lysine residues (A, B, C, and D) and an amine-reactive probe (*e.g.* an NHS-ester; Fig. 3). In the absence of any control, this reaction will yield a mixture of 16 regioisomers bearing 0–4 modifications per protein. Moving on, now let's assume that the careful optimization of the conditions (*e.g.* concentration and stoichiometry of reagents, pH, temperature, and time) could enable the creation of products with only two modifications per molecule. Even in this scenario, however, a mixture of six regioisomers would be obtained – with AB, AC, AD, BC, BD, or CD modified – unless other discriminating factors can be exploited to impart site-specificity on the bioconjugation reaction. Of course, this example is a simplification of the situation often encountered in reality. An antibody (Ab), for example, has approximately 30 accessible lysine residues located throughout its macromolecular structure. As a result, the number of potential regioisomers formed via the modifications of an antibody is orders of magnitudes higher than we encounter in our little thought experiment. This heterogeneity can be a serious problem – especially in the context of clinical translation – because different regioisomers may display different biological characteristics. In addition, the over-modification of the biomolecule with too many cargoes as well as the inadvertent conjugation of payloads to positions critical for biological activity can drastically alter the *in vivo* performance of a radiotracer. Thus, it becomes clear that exerting precise control over bioconjugation is crucial for the development of effective radiolabeled conjugates.

When working with chemical reactive probes, it is important to be aware of potential side reactions. For example, activated carboxylic acid esters (*e.g. N*-hydroxysuccinimides or tetrafluorophenol esters) may chemoselectively react with the primary amines of lysine residues at certain pH values. However, the pK_a values – and therefore reactivity – of the nitrogen nucleophiles depend on their microenvironment. Thus, reactions with other amine-containing residues (*e.g.* histidines, tryptophanes, or *N*-terminal amines) can often not be ruled out. As a result, the batch-to-batch variability of bioconjugation reactions must be examined carefully. Despite these shortcomings, it is important to recall that the use of chemical reactive probes for bioconjugations is well established. This is in part due to the widespread commercial availability of reagents (*e.g.* BFCAs and prosthetic groups) as well as the existence of optimized protocols that provide bioconjugates with a narrow distribution of products. In fact, such mixtures can be of quite uniform composition, making them suitable for clinical applications and approval by regulatory bodies.

The chemical functionalization strategies have become a standard tool in radiopharmaceutical chemistry for the chemoselective modification of biomolecules. However, new methodologies are emerging that allow for site-specific bioconjugations. For example, both enzymatic and bioorthogonal

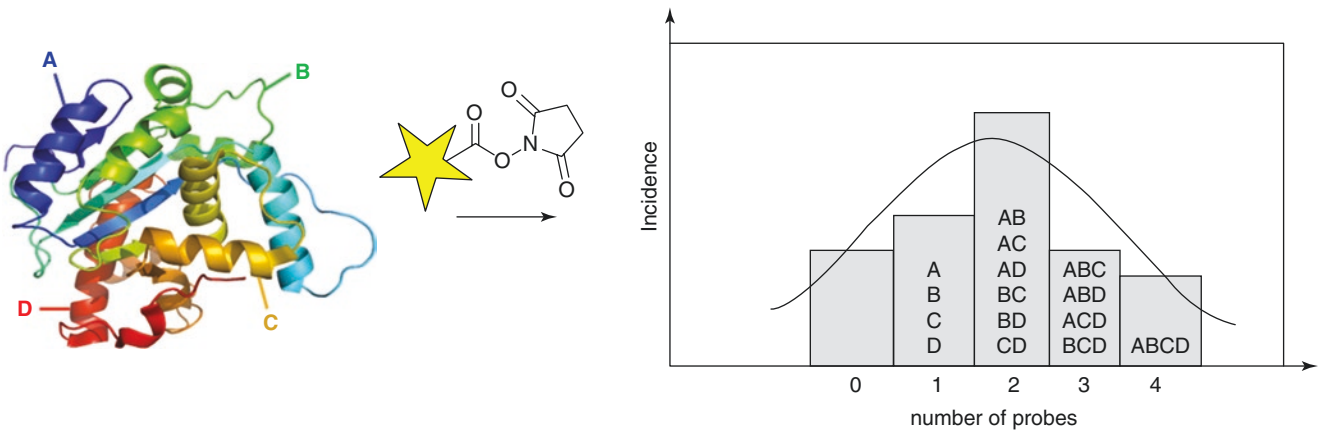

Fig. 3 The product distribution resulting from the functionalization of a protein bearing four lysine residues with an *N*-hydroxysuccinimide-based chemical reactive probe. *Letters* **A–D** represent different lysine residues (or functionalization thereof), and the *star* denotes an imaging entity to be conjugated to the protein. (Image of generic protein courtesy of http://laoblogger.com/structure-of-proteins-clipart.html)

chemistry approaches (*e.g.* click chemistry; see the chapter on "Click Chemistry in Radiopharmaceutical Chemistry") have been developed that enable the formation of well-defined, site-specifically modified bioconjugates that exhibit improved characteristics *in vivo* [4]. In the case study discussed above (see Fig. 3), a site-specific approach would facilitate the controlled formation of a conjugate that is uniform not only in terms of the number (*e.g.* $n = 2$) but also the sites of modifications (*e.g.* the exclusive formation of the lysine adduct "AB"). Such new and promising approaches will undoubtedly expand the repertoire of practitioners in the field. Yet – as is the case for any new technology – it will take time until these methods become established and find more widespread use.

In this chapter, we discuss the various bioconjugation approaches that have been reported for the development of radiopharmaceuticals. The chapter is organized by the different classes of biomolecule, beginning with peptides and proteins and proceeding on to carbohydrates, nucleic acids and, lipids. In addition, we have also included a section on special applications that highlights examples of emerging methodologies for site-specific bioconjugations. In each part, we make an effort to include specific advantages and disadvantages of the methodologies discussed. In the end, the goal is to provide the reader with a practical guide when setting out to use a particular strategy for bioconjugation.

Details

Peptides and Proteins

Introduction

A large number of functions in the human body are orchestrated by peptides and proteins, (bio)polymers formed from amino acids [5]. Although it is not the focus of this chapter, it should be mentioned that a wide variety of methods have been described for the labeling of individual amino acids with radionuclides such as carbon-11 or fluorine-18 [6]. Some products, reactive intermediates, and general reaction schemes from this area of research are also relevant to the bioconjugation of peptides and proteins.

In peptides and proteins, the individual amino acid monomers are linked together by amide bonds formed between the α-amino group of one monomer and the carboxyl group of the next (Fig. 4) [2]. Not surprisingly, these amide bonds are termed "peptide bonds." The common fundamental structure of peptides and proteins is the so-called α-chain, a polyamide chain (usually) composed of the 20 naturally occurring amino acids. The principal difference between peptides and proteins is size. Peptides are typically composed of a chain of no more than approx. 20–40 amino acids. Proteins, in contrast, are large peptides that usually contain more – often many, many more – than 50 or 100 amino acids and form complex yet well-defined three-dimensional structures that are critical for their biological function. Indeed, changes to this three-dimensional structure (*e.g.* misfolding or denaturation) can lead to the loss of functionality, even if the α-chain is still intact. It should be noted that the differentiation between peptides and proteins is arbitrary to some extent. After all, peptides can also exhibit three-dimensional structure. However, the larger the molecule, the more defined the "higher" structures will become. In the simplest of terms, complexity makes the difference.

General Considerations Regarding the Substrates

When it comes to bioconjugation, peptides are simpler substrates than proteins. Due to their smaller size, there is a good chance that a unique residue is present, thereby enabling site-specific bioconjugation using fairly straightforward

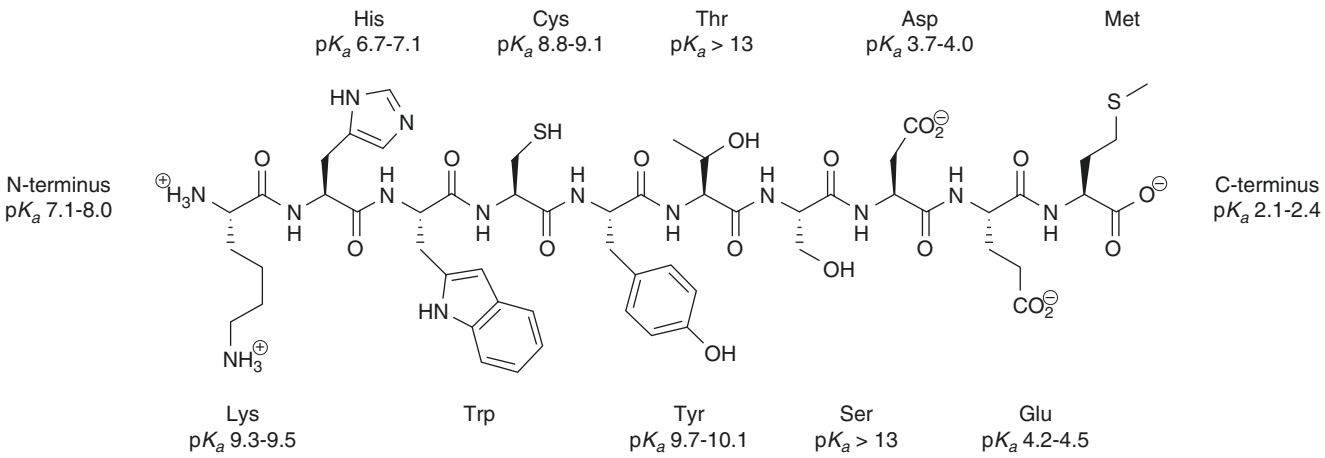

Fig. 4 A model peptide consisting of natural amino acids indicating the reactive groups in their side chains that can be used for bioconjugation (Adapted from Russ *et al.* [2], with permission)

chemical techniques [2, 7]. More importantly, the possibility of using solid-phase peptide synthesis to create peptides can also enable the site-specific incorporation of chemical handles such as chelators for the complexation of radiometals or orthogonal functionalities for subsequent radiolabeling. Another comparative advantage of small peptides is their tolerance of relatively harsh reaction conditions such as increased temperature, nonaqueous media, and both acidic and basic pH. This allows for the application of a broad range of chemical radiolabeling methods. Finally, because of their small size, it is also possible to use HPLC methods for the purification of radiolabeled peptides.

In contrast, most proteins are quite sensitive to the reaction conditions applied during both bioconjugation and radiolabeling. While the addition of small amounts of cosolvents (*e.g.* <10% v/v DMSO) is often tolerated, increased temperatures (approx. >40 °C) or pH values significantly deviating from the biological pH 7.4 can cause the denaturation of the protein. Reactions with proteins are thus typically performed under mild, aqueous reaction conditions, and the purification of products is commonly achieved via size-exclusion techniques which are not capable of separating regioisomeric products. As a result, the modification of proteins with chemical reactive probes usually results in the creation of mixtures of products. If a site-specific conjugation is desired, this can only be achieved using more sophisticated approaches that are discussed in the section on "Special Applications: Site-Specific Modifications".

General Considerations Regarding Possible Reactions

Independent of the radiolabeling method, the bioconjugation reaction should lead to a stable bond, offer some selectivity, and preserve the biological activity of the biomolecule. The first prerequisite is usually fulfilled by common chemical bioconjugation reactions. The second and third requirements depend on the substrate, the bioconjugation method, and the reaction conditions.

Most bioconjugation reactions involving natural amino acids are nucleophilic reactions. Among the natural amino acids, the sulfhydryl – or thiol – group of the cysteine side chain is the strongest nucleophile, followed by the primary amines available at the *N*-terminus of a peptide/protein and the ε-amine of lysine. As a result, thiols and primary amines are the most common functional groups for bioconjugations in radiopharmaceutical chemistry. Although far less reactive, other possible amino acid targets include tyrosine, tryptophan, histidine, arginine, serine, threonine, and methionine, as well as glutamic and aspartic acid and the C-terminus of the peptide [8]. However, examples of bioconjugations using these groups are rare in radiopharmaceutical science. This is due to the *in vivo* instability of esters (*e.g.* derived from Ser) toward esterases as well as the risk of intra- and intermolecular cross-linking side reactions when carboxylic acid residues (*e.g.* Glu or Asp) are activated. It should be noted that for tyrosine and tryptophan residues, some reactions targeting the aromatic core are available, offering a somewhat orthogonal reactivity to the nucleophilic reactions (*e.g.* some of the radioiodinations discussed in the chapter on "The Radiopharmaceutical Chemistry of the Radioisotopes of Iodine") [8].

General Considerations Regarding Selectivity

All of the amino acids mentioned above are shown in a "model peptide" depicted in Fig. 4, including their respective protonation state at physiological pH and nominal pK_a values. The pK_a is a measure of the pH value at which the respective group gets deprotonated. The nucleophilicity of a group is generally higher in the deprotonated state (*e.g.* $RNH_3^+ \ll RNH_2$, $RSH < RS^-$). This is of particular importance for the selectivity of bioconjugation reactions, since controlling the pH of the bioconjugation reaction can be leveraged to control the site of the reaction. While the thiol group of cysteine and the amine of the *N*-terminus show good reactivity at neutral pH, the amino group of the lysine side chain usually requires pH values above 8.0 for efficient deprotonation and conjugation. Conjugation reactions using the hydroxyl group of the tyrosine residue would require pH values above 9.5, thus precluding any selectivity.

The local microenvironment provided by a peptide/protein also plays an important role in the eligibility of a functional group for bioconjugation. To wit, the microenvironment influences the actual pK_a values and the accessibility of nucleophilic groups for reactions with electrophilic reagents. For example, cysteines are often located in the more lipophilic and inaccessible parts of a protein. On the other hand, the hydrophilic ε-amino group of the lysine side chain is usually exposed to surrounding water and therefore readily accessible for conjugation reactions. In some cases, the accessibility of functional groups can be exploited to gain selectivity. For example, the lysine side chain may be targeted site-selectively in the presence of a free *N*-terminus and/or sulfhydryl groups if the latter are not accessible for the reagent. However, these effects are difficult to predict, and the chemoselectivity and site-specificity of a bioconjugation reaction often have to be evaluated experimentally.

Another important consideration in the use of cysteines for bioconjugation is their low natural abundance. Cysteine is the second least abundant amino acid in proteins. Moreover, the sulfhydryl groups of cysteines are frequently part of disulfide bridges and are therefore not available to participate in nucleophilic substitution reactions. Hence, only a fraction of the cysteine residues in peptides/proteins offer possible sites for bioconjugations, making this amino acid one of the most important targets for the modification of proteins. It should be mentioned, however, that disulfide bridges can be partly reduced to form free sulfhydryl groups

[9]. This is a common technique to create conjugation sites within proteins.

Of course, the selectivity of a bioconjugation reaction also strongly depends on the choice of the reagents. In the following section, the most common reactions used for bioconjugation in the field of radiopharmaceutical chemistry are presented. In addition, some examples of novel, chemoselective reagents are given. BFCAs are typically commercially available as activated esters or anhydrides, and as a result, they are often used in these forms. Of course, the activation of carboxylic acid derivatives is also possible in the lab through the reaction of pendant carboxylates with activating reagents such as ethyldimethylcarbodiimide. Whether purchased or homemade, all activated reagents tend to hydrolyze in aqueous media, resulting in their deactivation. This side reaction is usually compensated for by the use of an excess of the activated reagent.

Lysines and the *N*-terminus (Primary Amines)

Due to their relevance in amide-coupling protocols, many synthetic procedures for the coupling of amines are available, including a number of "biocompatible" procedures. The most prominent examples in the radiopharmaceutical sciences are acylations (*e.g.* amide couplings) and the formation of thiourea bonds. Acylation is the conjugation of activated carboxylic acids to amino groups delivering stable amide bonds. Numerous examples of the utilization of amide bonds for bioconjugation can be found in the literature. For example, the modification of the majority of targeted peptides is done *via* the formation of an amide bond with the *N*-terminal amine of the peptide [10]. The activation of the carboxylic acids is often conducted via esterification with *N*-hydroxysuccinimide (NHS) or tetrafluorophenol (TFP) (Fig. 5). These esters exhibit high reactivity toward nucleophiles. For the coupling of primary amines, the pH of the reaction medium should be as low as reasonably possible. The optimal pH range for NHS-esters is 7.0–8.0, while TFP-esters require a pH range of 7.0–9.0. At these relatively low pH values, side reactions with other nucleophilic amino acids (except cysteines) can be minimized. The reaction of activated esters with cysteines may nevertheless lead to thioesters; however, these products are prone to hydrolysis. Similarly, side products formed by the reaction of activated esters with the aromatic amines of histidine and tryptophan also tend to hydrolyze.

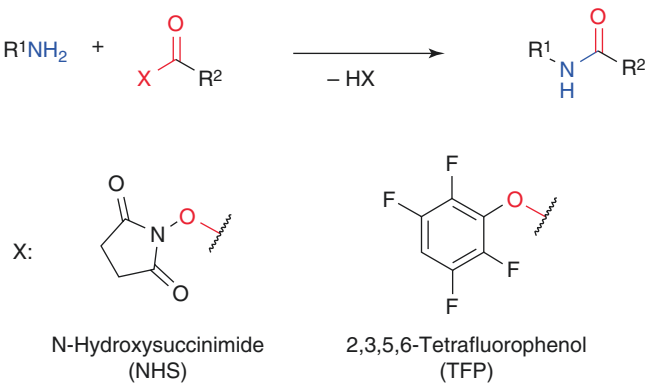

Fig. 5 The acylation of primary amines (R^1 = peptide or protein; R^2 = chelator, linker or prosthetic group; X = OH for non-activated carboxylic acid)

Anhydrides represent an alternative to the acylation reagents discussed thus far. Anhydrides exhibit lower – but still adequate – reactivity toward nucleophiles. A potential drawback of asymmetric anhydrides is the presence of two reactive carbonyls which can give rise to two different products. For example, an amine could attack DOTAGA-anhydride at either carbonyl of the anhydride group, leading to the formation of two isomers (Fig. 6a) [11]. Surprisingly, only one of the two possible isomers was found to be formed in a number of model reactions. This issue can be avoided by using symmetric anhydrides. DTPA-anhydride – a symmetric intramolecular di-anhydride – yields the same product independent on which carbonyl participates in the reaction (Fig. 6b) [12]. Nonetheless, a double substitution reaction leading to cross-linked products may occur. This can be avoided by using an excess of DTPA-anhydride.

Another common conjugation reaction is the formation of thiourea bonds through the reaction of isothiocyanates and primary amines (Fig. 6c). Isothiocyanates are somewhat less reactive compared to activated esters, and their bioconjugation reactions can be performed in a pH range of 8.0–9.5 at room temperature. Notably, isothiocyanates do not react entirely selective with primary amines. Side products from the reaction with hydroxyl or sulfhydryl groups can be formed reversibly, though the thiourea bonds are the only stable products.

Finally, although primary amines can be alkylated to secondary amines using alkyl halogenides or sulfonates (*e.g.* tosylates and mesylates) – a reaction which is very common in fluorine-18 chemistry – no examples of such conjugations could be found in peptide or protein chemistry [13]. That said, activated esters like [^{18}F]4-nitrophenyl 2-fluoropropionate could be used for this purpose.

Cysteines (Sulfhydryl Groups)

The most common conjugation methods that target the sulfhydryl group are alkylation reactions or Michael additions that form thioether linkages. The reagents employed for these reactions include alkyl halogenides, α-halocarbonyls, and – most notably – maleimides (Fig. 7). Examples of the direct alkylation of sulfhydryl groups are rare in radiopharmaceutical chemistry. However, the feasibility of the ^{11}C-methylation of sulfhydryls has recently been demonstrated by the conjugation of [^{11}C]methyl triflate to a cysteine-modified octreotide derivative [14].

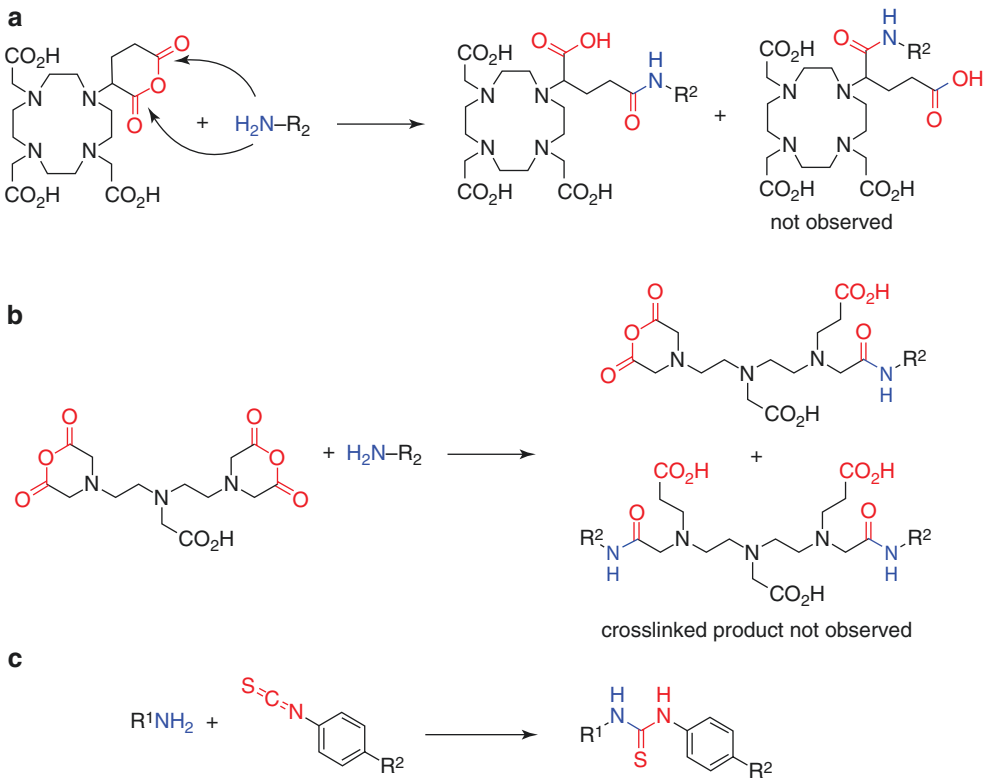

Fig. 6 The conjugation of primary amines to (**a**) DOTAGA-anhydride, (**b**) DTPA-anhydride, and (**c**) isothiocyanates (R^1 = BFCA or prosthetic group, R^2 = peptide or protein)

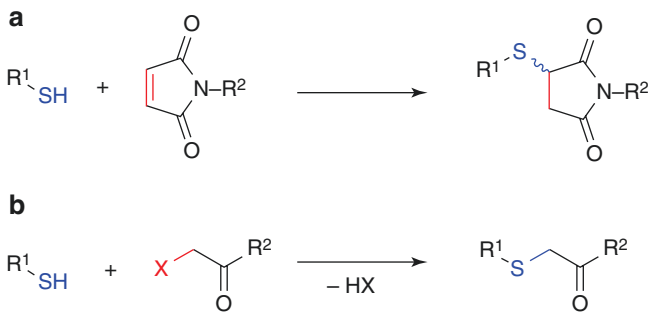

Fig. 7 The addition of thiols to (**a**) maleimides and (**b**) α-halocarbonyls (R^1 = Peptide/protein; R^2 = BFCA or prosthetic group; X = Br, I)

The addition of maleimides to thiols is a far more frequently used approach (Fig. 7a). This reaction can be conducted at neutral pH 6.5–7.5. This is advantageous because amines are protonated at this pH, preventing undesired side reactions. However, the stability of the conjugation product is part of a recent controversy (see the section on "Controversial Issues"). Maleimide-bearing derivatives of various chelators are commercially available, and many examples of this conjugation strategy can be found in the radiopharmaceutical literature [9].

Recently, new methods with great promise for selective bioconjugations via sulfhydryls have been reported (see the section on "Controversial Issues"). For example, a 2-cyanobenzothiazole-based prosthetic group for ^{18}F-labeling was described (Fig. 8a) [15]. This novel reagent reacts with *N*-terminal cysteines, leading to 4,5-dihydro-1,3-thiazole linked products. Another new class of thiol-reactive ^{18}F-labeled prosthetic group is represented by phenyloxadiazole methylsulfonates (Fig. 8b). The conjugation of this reagent to thiols can be conducted at neutral pH in aqueous medium at low to slightly elevated temperatures (RT-50 °C), and the reaction shows good conversion rates even at low concentrations of the substrates.

Tyrosines

In principal, the hydroxyl group of tyrosine can be alkylated by S_N2 reactions under strongly basic conditions using reagents such as alkylsulfonates or halides. However, this reaction is not practical because several side reactions with amines and thiols would result. One helpful characteristic of tyrosine for bioconjugation is the relatively high reactivity of its aromatic core. Recently, the selective conjugation of an aminobenzene-bearing variant of NOTA to a tyrosine residue of the peptide neurotensin was described using an azo-coupling approach [16]. This substitution is achieved in the *ortho*-position to the hydroxyl group of the phenol moiety in a manner analogous to the radioiodination of tyrosines (see the chapter on "The Radiopharmaceutical Chemistry of the Radioisotopes of Iodine").

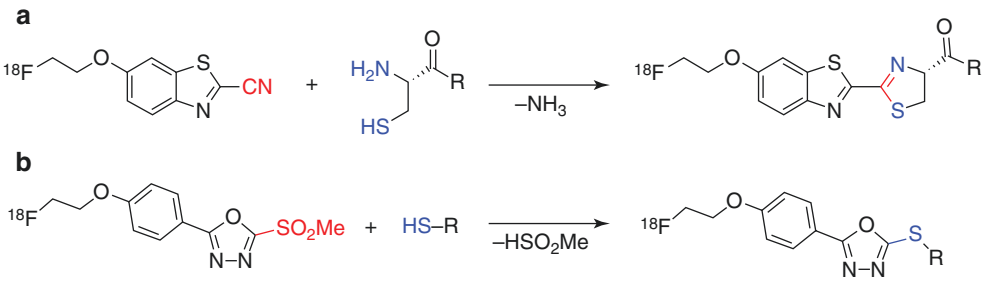

Fig. 8 Novel methods for chemoselective conjugations to cysteines (R = peptide or protein)

Carbohydrates and Saccharides

Carbohydrates are ubiquitously present in all living organisms. They are known for their rich chemistry which has been extensively studied for over a century. While "carbohydrates" refer to substances of the general chemical formula $C_n(H_2O)_n$ (*e.g.* glucose = $C_6H_{12}O_6$), the term "saccharides" is more general and includes derivatives and multimeric forms of carbohydrates. Besides playing key roles in various metabolic processes, these molecules can also be found attached to other classes of biomolecules, including peptides, proteins, and lipids (glycopeptides, glycoproteins, and glycolipids) as well as DNA and RNA [5, 17]. The conjugation of saccharides or polysaccharide chains (glycans) is the most common post-translational modification of proteins, and in fact, more than half of the proteins present in the human body are glycoproteins. Carbohydrates and saccharides are hydrophilic molecules, and when conjugated to small molecules, they often increase their hydrophilicity and solubility. Another important feature of carbohydrates is their ability to form both linear and branched polymers which are not only important biological recognition motifs (*e.g.* by the immune system) but can also offer multiple sites for selective bioconjugation reactions. The radiolabeling of carbohydrates and simple monomeric saccharides – for example [^{18}F]FDG – inevitably involves multistep syntheses using protective groups and, thus, is not covered in this chapter. On the other hand, relatively few examples of the direct radiolabeling of (poly)saccharides have been reported.

An early multistep approach for the site-specific labeling of antibodies is predicated on the initial generation of aldehydes from their glycan side chains. This can be achieved via the oxidation of vicinal diols using reagents such as sodium periodate (Fig. 9a) [9]. Even though this reaction can be conducted at 0 °C and pH 6.0, the strong oxidants employed are also capable of oxidizing other functional groups within the protein, potentially resulting in the loss of its bioactivity. In a second step, the resulting aldehyde is reacted with a nucleophile, for example a primary amine (Fig. 9b) [18]. This reaction leads to the formation of imines, which require stabilization against hydrolysis via reduction to secondary amines (a step that can also lead to the formation of side products). This reaction sequence is also known as reductive amination.

More efficient approaches that eschew the reduction step include the reaction of aldehydes with hydrazine- or hydroxylamine-modified residues, leading to the creation of stable hydrazone and oxime linkages, respectively (Fig. 9c, d) [19, 20]. Both transformations have been used for the bioconjugation of chelators and prosthetic groups; however, they usually yield mixtures of E- and Z-isomers, which can make an additional separation step necessary. Newer methods for the selective modification of glycans employ enzymes, and examples of these approaches are discussed in the section entitled "Special Applications: Site-Specific Modifications".

Another creative radiolabeling procedure makes use of radiolabeled carbohydrates as a prosthetic group. For example, the broadly available [^{18}F]FDG can be used for the radiolabeling of hydroxylamine-modified peptides via its acyclic aldehyde form which is generated in equilibrium with the acetal form during mutarotation (Fig. 10a) [21]. Also, an azide-modified [^{18}F]FDG derivative has been reported for the bioorthogonal conjugation employing the copper-catalyzed azide-alkyne cycloaddition (Fig. 10b; see the chapter on "Click Chemistry in Radiopharmaceutical Chemistry") [22]. Overall, both processes result in the simultaneous formation of glycosylated *and* radiolabeled biomolecules.

Nucleic Acids

Nucleic acids such as deoxyribonucleic acid (DNA) and ribonucleic acid (RNA) are biopolymers mainly found within the nuclei of cells. They are the warehouse of all genetic information and are responsible for its transmission to protein synthesis. In many instances, two single strands of nucleic acids hybridize to form a double helix held together by the specific base-pairing capability described in the classic Watson-Crick model. Nucleic acids are composed of nucleotides that consist of three elements (Fig. 11) [1, 23]:

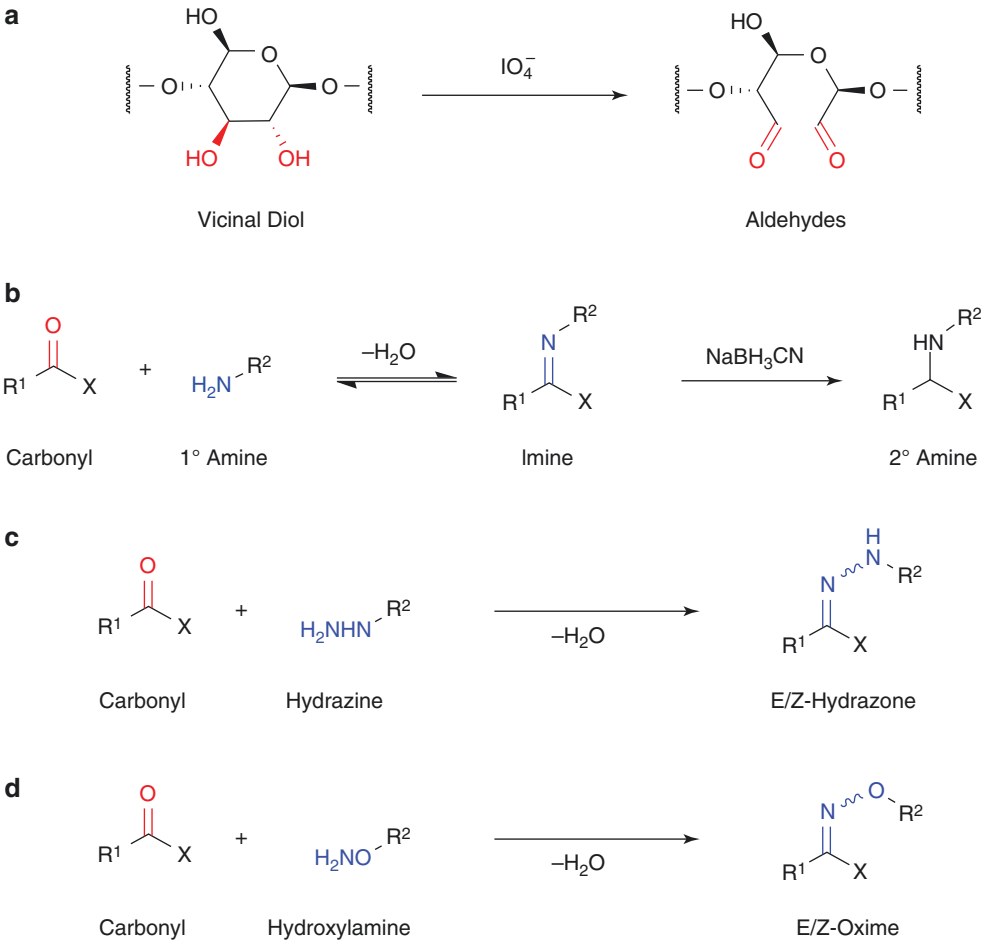

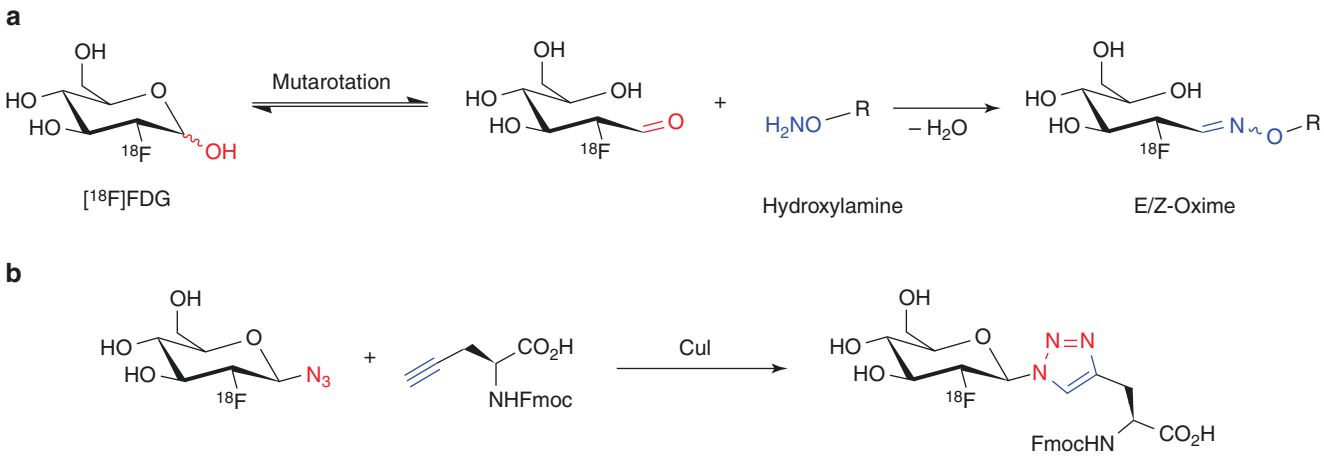

Fig. 9 The oxidative modification of saccharides (R^1 = saccharide, glycoprotein or glycopeptide; R^2 = chelator or prosthetic group; X = H for aldehydes and alkyl for ketones)

Fig. 10 Simultaneous ^{18}F-labeling and glycosylation: (**a**) The formation of oximes using [^{18}F]FDG [mutarotation is the equilibrium interconversion of the α- and β-anomers of a saccharide (squiggled bond) via the open aldehyde form; R = peptide or protein] and (**b**) ^{18}F-fluoroglycosylation via the formation of 1,2,3-triazoles using copper-catalyzed azide-alkyne cycloaddition

1. A nitrogen-containing nucleobase either based on a pyrimidine (uracil, cytosine, or thymine) or a purine (adenine or guanine). Pyrimidines contain a single six-membered ring, whereas purines have a bicyclic fused-ring structure containing a six-membered ring attached to a five-membered ring.
2. A five-membered ring carbohydrate, deoxyribose in the case of DNA and ribose in the case of RNA.

3. A phosphate group through which the nucleobase-bearing carbohydrates are connected. In each nucleotide, the phosphate group is attached to the 3′-hydroxyl of the furanose residue and the 5′-hydroxyl of the adjacent nucleotide, creating a phosphodiester linkage.

Nucleosides have been radiolabeled to create both markers of proliferation and building blocks for incorporation into oligomers. For example, thymidine has been radiolabeled with fluorine-18 and carbon-11. The radiolabeling of building blocks of biomolecules will not be covered in this chapter. In the following pages, we will focus on the applications of oligonucleotides (ONs) [24, 25].

ONs are short sequences of nucleotides that are accessible by solid-phase synthesis. They are able to target biomolecules – such as other nucleic acids – and also carry genetic information [23]. ONs are precise modulators of gene expression and are mainly used as parts of molecular biology techniques for *in vitro* applications (*e.g.* polymerase chain reactions and biochip arrays) [24].

Turning ONs into valuable *in vivo* imaging agents represents a significant challenge for radiopharmaceutical chemists [24]. Radiolabeled ONs hold promise for several applications, including the monitoring of gene expression and *in vivo* pretargeting. However, ONs are highly vulnerable to digestion by nucleases *in vivo*. As a result, structural modifications are necessary not only to increase their stability but also to introduce a reactive handle for selective bioconjugation. The most studied structural modification of ONs involves the replacement of a non-bridging oxygen atom in the phosphate backbone with a sulfur atom, resulting in a phosphorothioate ester (PS, Fig. 12). The introduction of phosphorothioate linkages improves the resistance of the ON toward enzymatic degradation, and the sulfhydryl

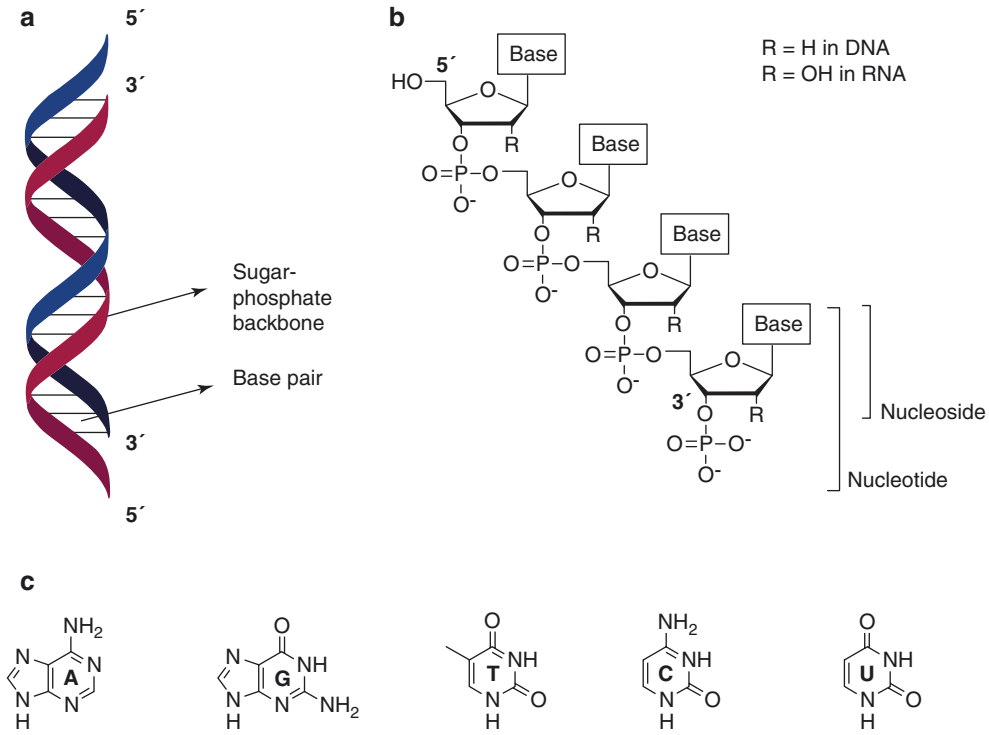

Fig. 11 (**a**) Watson-Crick DNA double helix; (**b**) chemical structure of DNA and RNA; (**c**) Nucleobases: A = adenine, G = guanine, T = thymine, C = cytosine, and U = uracil

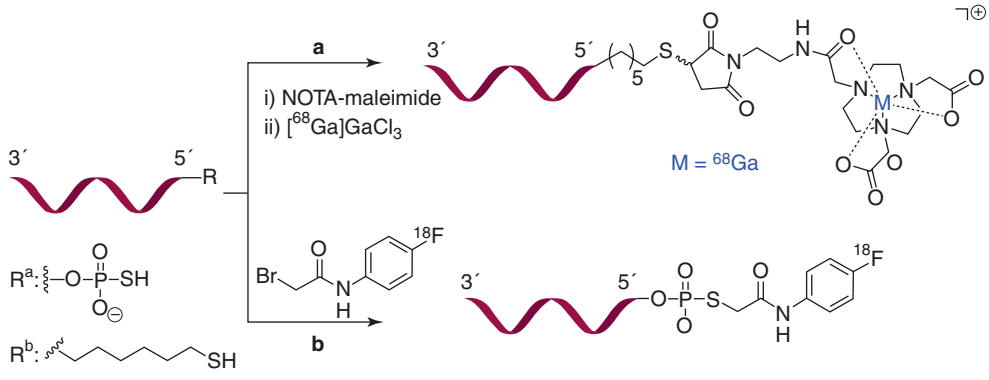

Fig. 12 Examples of the radiolabeling of ONs via their 3′- and 5′-termini. (**a**) A post-labeling approach with BFCAs, the bioconjugation of MMA-NOTA to a hexylthiol-functionalized ON; (**b**) A pre-labeling approach with prosthetic groups, the bioconjugation of *N*-(4-[^{18}F] fluorobenzyl)-2-bromoacetamide to a phosphorothioate-containing ON

group can be used for bioconjugations (see below). However, the chiral center at the phosphorous atom created by this approach can lead to the formation of enantiomers, an undesired complication [23].

Another approach to overcome some of the inherent *in vivo* limitations of ONs hinges on nonnatural analogs. In morpholino nucleic acids (MNAs), the carbohydrate moiety of ONs is replaced by a heterocyclic morpholino structure, and the monomers are linked together through phosphorodiamidate linkages instead of phosphate groups. Peptide nucleic acids (PNAs) are hybrids between ONs and oligopeptides in which the nucleobases are connected via a peptidic backbone. Both analogs mimic the structure of nucleic acids and are able to bind complementary strands of DNA and RNA [23].

The direct radiolabeling of genomic DNA and RNA is rare. Most examples reported in the literature regarding the radiolabeling of this class of biomolecules include shorter ONs – also known as aptamers – and their synthetic analogs (*e.g.* MNA, PNA). In principal, there are three potential sites for the radiolabeling of nucleic acids (see Fig. 11): the nucleobase, the carbohydrate residue, and the phosphate group. In each case, the principal challenge lies in modifying the nucleic acids while not interfering with base pairing [1]. For this reason, the 3′- and 5′-termini are typically exploited for the radiolabeling of ONs [26]. This approach has several advantages, including minimizing structural perturbations, maintaining the ability of the ON to form double-stranded duplexes, protecting the biomolecule from enzymatic degradation, and providing a modular, sequence-independent handle for modification [27].

Several studies report the radiolabeling of the 3′- or 5′-termini of ONs. For labeling with radiometals, ONs have been modified with several different chelators. For instance, the modification of the 5′ terminus of ONs with either hexylamine or hexylthiol has been used to facilitate the subsequent attachment of BFCAs such as *p*-SCN-Bn-NOTA (*p*-isothiocyanatophenyl-NOTA) or MMA-NOTA (maleimido-monoamide-NOTA; see Fig. 12a). In this case, the use of a thiol-maleimide approach proved more effective than an amine-isothiocyanate system [28]. Another general method for the radiolabeling of ONs employs prosthetic groups – for example, *N*-(4-[^{18}F]fluorobenzyl)-2-bromoacetamide – which can be conjugated to ONs bearing a terminal phosphorothioate group (see Fig. 12b). Similar approaches have been applied to the labeling of ONs with other radiohalogens such as bromine-76 and iodine-125 as well as to the radiolabeling of cysteine-containing PNAs [24].

In the end, even though ONs display a number of promising characteristics for the development of radiopharmaceuticals (*e.g.* high specificity, synthetic accessibility, low toxicity, and low immunogenicity), several issues surrounding their stability, transport across biological membranes, and undesired non-specific interactions must still be resolved for them to achieve their potential in *in vivo* applications.

(Phospho)lipids

Lipids are essential for several different purposes within living organisms. Indeed, their functions include serving as precursors of chemical messengers, being a substantial source of energy, and acting as the primary building block of biological membranes. Broadly speaking, lipids can be categorized into the following groups: steroids, fats, waxes, and phospholipids. Phospholipids – the topic of this section – is the principal component of all cell membranes. Their core structure (Fig. 13) consists of two hydrophobic fatty acid tails and a phosphate-containing hydrophilic head joined together by a glycerol moiety (see Fig. 13a). The phosphate group is usually modified with organic molecules, most commonly choline, serine, or ethanolamine (see Fig. 13c). Phosphatidylcholine (PC), for example, is an important phospholipid that is present not only in cell membranes but also used as an additive in the food and cosmetic industries. Due to their amphiphilic character, phospholipids form lipid bilayers in which the fatty acid tails align, thus limiting interactions with water molecules and orienting the hydrophilic phosphate heads toward the surrounding water (see Fig. 13b) [29].

Phospholipids display some interesting properties for medical applications. They are generally nontoxic, nonimmunogenic, bioavailable, and membrane permeable. As a result, they have been investigated for applications in molecular imaging. In nuclear medicine in particular, phospholipids have played two distinct yet essential roles. They can be either the target of a radiotracer or a component of a radiopharmaceutical. With regard to the former, [^{99m}Tc]Tc-lactadherin (a milk fat globule-EGF factor 8 protein) is employed as a cardiovascular imaging probe that specifically targets phosphatidylserine, a phospholipid which is translocated to the outer leaflet of the cell membrane upon early stage apoptosis and necrosis [30]. To continue, both ^{18}F- and ^{11}C-labeled variants of choline have been used as proliferation markers that accumulate in cancerous cells via the choline transporter and subsequently react with phosphatidic acids in a process catalyzed by overexpressed choline kinase [31]. Radiolabeled fatty acids – which are used in diagnostic imaging to detect abnormalities in the fatty acid metabolism of the heart muscle – are building blocks of phospholipids which are not discussed in this chapter [32].

The primary application of radiolabeled phospholipids in nuclear imaging centers on their use as constituents in liposomal formulations. Liposomes are spherical vesicles formed by phosphatidylcholine and other (phospho)lipid derivatives. They can be radiolabeled using several different approaches, including the incorporation of radionuclide-tagged phospholipids into the lipid bilayer [33]. The labeling of phospholipids with radionuclides is generally accomplished through the modification of the organic moiety that is covalently bound to the phosphate group (see Fig. 13a). In the case of

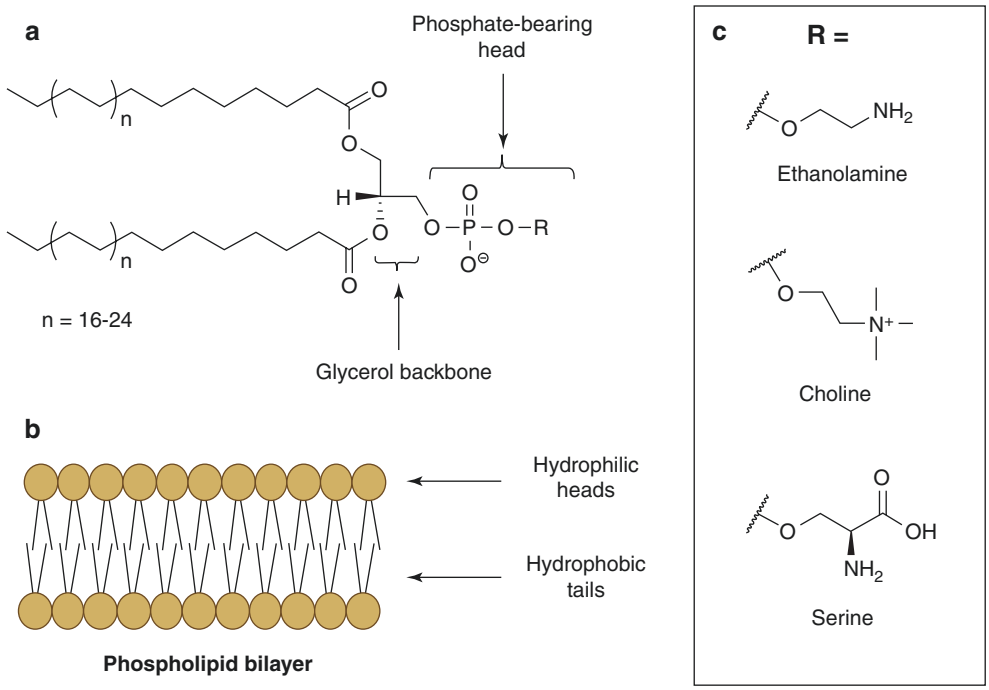

Fig. 13 Structure and composition of phospholipids. (**a**) Phospholipids are composed of a glycerol backbone that links the fatty acid chains to the phosphate head group; (**b**) the phospholipid bilayer in cell membranes; (**c**) the phosphate group can be esterified with alcohols, as in phosphatidylcholine (PC), phosphatidylethanolamine (PE), and phosphatidyl-glycerol (PG)

phosphatidylethanolamine, for example, the amine group can be acylated with the activated ester-bearing derivatives of various BFCAs or prosthetic groups as part of either pre- or post-labeling strategies. To illustrate, the radioiodination of this phospholipid has been performed using the Bolton-Hunter reagent (Fig. 14a; see also the chapter on "The Radiopharmaceutical Chemistry of the Radioisotopes of Iodine") [29]. In addition, the radiolabeling of the same lipid with indium-111 was achieved via a post-labeling approach in which the lipid is first modified with DTPA via the formation of an amide bond (Fig. 14b) [34]. To provide yet another example, phospholipids have also been radiolabeled using a pre-labeling approach that leveraged thiol-maleimide chemistry to ligate a ^{64}Cu-labeled CB-TE2A complex to the biomolecule (Fig. 14c) [35]. Of course, many more examples using similar approaches are reported in the literature, including the conjugation of a variety of chelators for labeling with different radiometals [36].

Special Applications: Site-Specific Modifications

Enzymatic Approaches

Enzymes are nature's catalysts and thus play a crucial role in a multitude of biologically important chemical transformations. Their ability to form covalent bonds in a highly chemoselective and site-specific fashion under mild reaction conditions makes them ideal tools for bioconjugation (Fig. 15). While a number of different enzymes have been employed in this context, only a handful has been used in the development of radiopharmaceuticals [1, 2, 9]. Enzymatic functionalization strategies have mainly been employed for the conjugation of radiometal complexes to proteins, in particular antibodies and antibody fragments, though examples of the enzymatic ^{18}F-fluorination of small molecules have also been described [37].

The success of any enzymatic approach to bioconjugation is predicated on five criteria:

(i) The biomolecule must possess an appropriate substrate sequence for the enzyme, typically either made of amino acids or carbohydrates. This substrate can be naturally occurring within the biomolecule or the product of bioengineering.
(ii) The substrate sequence on the biomolecule must be accessible for modification by the enzyme.
(iii) The modification of the substrate sequence must not interfere with the ability of the biomolecule to bind its target.
(iv) The attachment of a cargo (*e.g.* a chelator) to the complementary substrate that is to be conjugated to the biomolecule must not hinder the enzymatic reaction.
(v) The enzyme itself should be commercially available, robust, and efficient enough to ensure sufficient conversion of the substrates within a reasonable period of time.
(vi) The product of the bioconjugation reaction should be easily and completely separable from both the unreacted substrates and the enzyme.

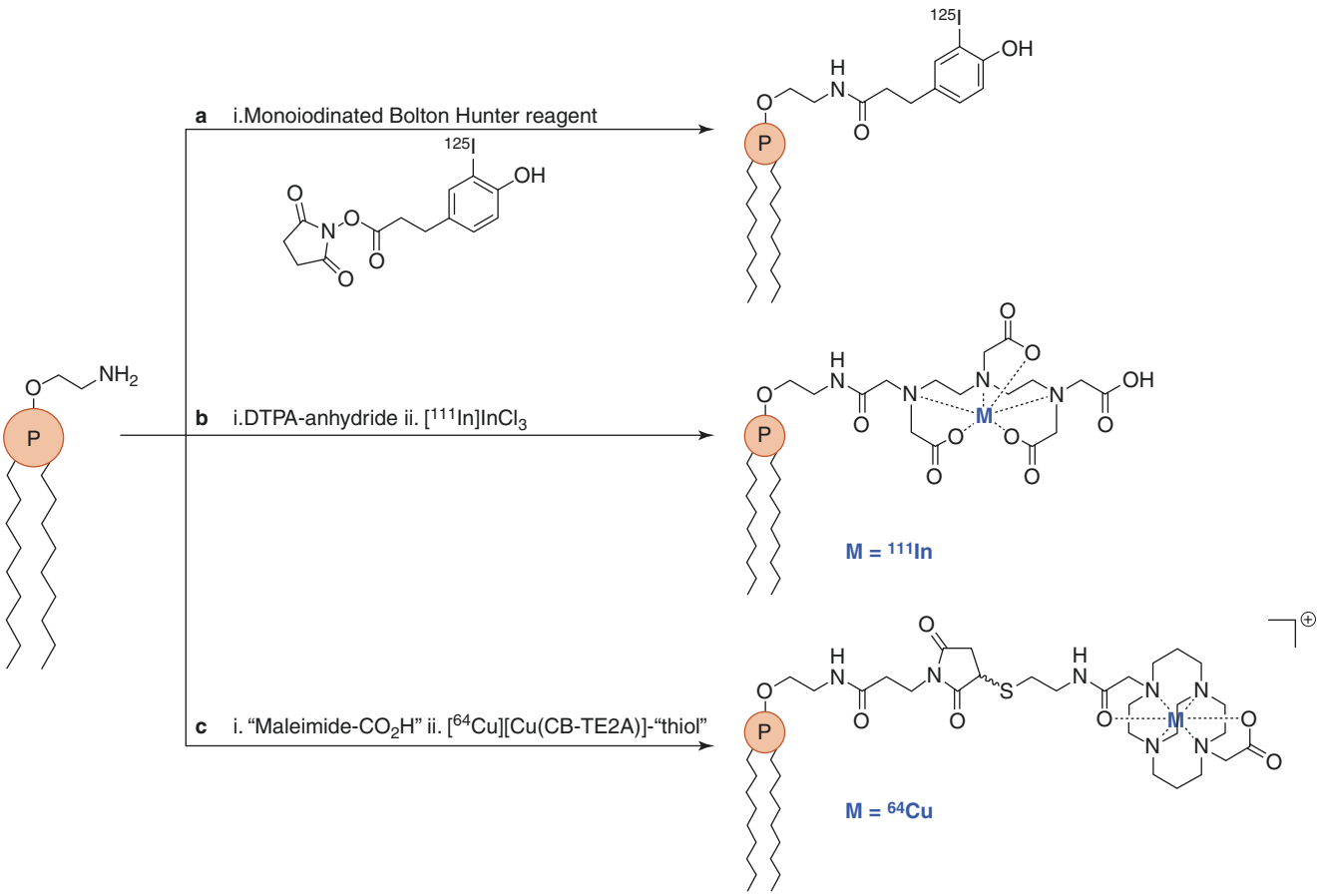

Fig. 14 Examples of the radiolabeling of phosphatidylethanolamine. (**a**) A pre-labeling approach for radioiodination with prosthetic groups; (**b**) A post-labeling approach with indium-111 via DTPA; (**c**) A pre-labeling approach with ^{64}Cu-labeled CB-TE2A

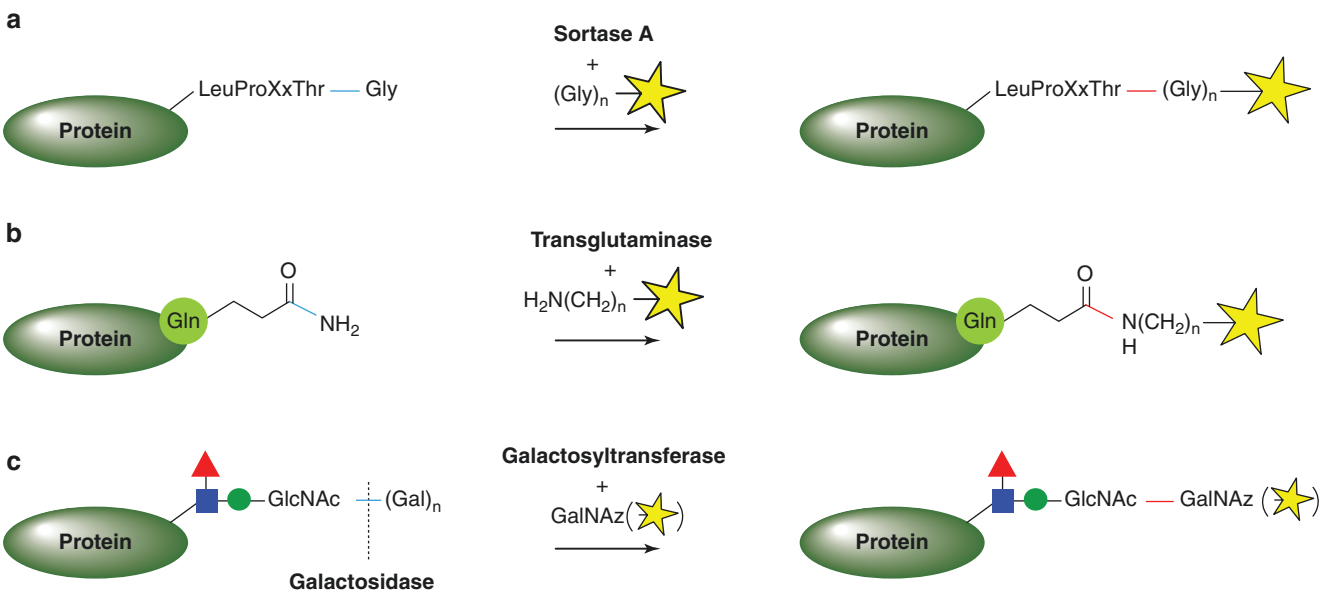

Fig. 15 Three examples of enzymes employed for bioconjugations using (**a**) an engineered amino acid sequence, (**b**) the glutamine residues of the protein, and (**c**) the glycans of an antibody. *Xx* is a placeholder for any amino acid. The *yellow star* symbolizes an imaging entity to be attached to the protein. *Colored squares, triangles, and circles stand* for the carbohydrate residues of the protein's glycans. *Blue and red lines* represent covalent bonds to be enzymatically broken or formed, respectively. In **C**, the *yellow star* is in parentheses because it is linked to an azide-containing GalNAz by click chemistry after the bioconjugation step

In the following paragraphs, we highlight three examples of the enzyme-assisted radiolabeling of antibodies. Each of these methods has been demonstrated to provide homogeneous and well-defined site-selectively modified immunoconjugates that, in some cases, display significantly improved biological characteristics *in vivo*.

Sortase A (EC 3.4.22.70) is an enzyme that belongs to the family of transpeptidases responsible for linking proteins to the cell wall. The enzyme cleaves the amide bond between a threonine (Thr) and a glycine (Gly) residue within its peptide recognition sequence – LeuProXxThrGly (in which Xx = any amino acid) – and forms a new peptide bond between the carboxylic acid of the liberated Thr with the *N*-terminus of a substrate bearing a (poly)Gly tag (see Fig. 15a). Sortase A has been used to modify single-chain and single-domain antibody fragments bearing this recognition motif on their C-termini with several different (poly)Gly-functionalized radiometal chelators, including CHX-A″-DTPA, NOTA, and sarcophagine [38, 39].

Another enzyme that has been leveraged for site-specific bioconjugation is transglutaminase (TGase, EC 2.3.2.13). TGase catalyzes the cross-linking of proteins through the formation of metabolically stable isopeptide bonds between the γ-carboxamide group of glutamine (Gln) – usually embedded within an amino acid recognition sequence (Q-tag) – and primary alkyl amines (*e.g.* the ε-amine group of lysine) (see Fig. 15b). It should be noted that Gln is an amino acid residue that is not typically available for chemical modifications. Microbial TGase has been employed for the attachment of two chelators containing a primary alkyl amine (desferrioxamine and a variant of CPTA) to immunoglobulins for subsequent radiolabeling with gallium-67. More specifically, the modification of the antibody takes place site-specifically at the conserved glutamine residue Gln295 within the Fc region that only becomes accessible for enzymatic modification upon the deglycosylation of a neighboring asparagine residue (Asn297) [40].

Instead of removing the glycans from antibodies in order to make conjugation sites available, one can alternatively use the glycans themselves as substrates for enzymatic modifications [9]. It has been elegantly demonstrated that antibodies can be modified site-selectively at the conserved glycosylation site (Asn297) of the constant Fc region via the manipulation of carbohydrate residues of the oligosaccharide chain using a combination of two enzymes (Fig. 15c). This approach exploits the fact that while the core of the glycans can be heterogenous, most immunoglobulins contain an *N*-acetylglucosamine (GlcNAc) linked to a variable number of galactose (Gal) residues at the termini of the chains. This protocol has three steps: (i) the removal of the terminal Gal residues from the biantennary, complex-type oligosaccharide using β-1,4-galactosidase (EC 3.2.1.23) leading to the exposure of GlcNAc residues; (ii) the incorporation of an azide-modified galactosamine (*N*-azidoacetylgalactosamine; GalNAz) using a mutant, substrate-permissive 1,4,-galactosyltransferase (EC 2.4.1.274), Gal-T(Y289L); and (iii) the conjugation of dibenzocyclooctyne-bearing chelators (*e.g.* desferrioxamine) to the azide-bearing sugars via strain-promoted click chemistry (see the chapter on "Click Chemistry in Radiopharmaceutical Chemistry") followed by labeling with a radiometal (*e.g.* zirconium-89) [41].

In the end, the application of enzymes to bioconjugation reactions often comes at the cost of long reaction times, the need for high concentrations of valuable substrates (the preparation of which can require multistep syntheses), the use of expensive enzymes, and – especially for clinical applications – extensive purifications to remove even trace amounts of the bacterially derived enzymes. However, these efforts seem worthwhile in light of the promise of creating both homogenous and well-defined biomolecular conjugates that display improved performance *in vivo*.

Orthogonal Functionalities

For the purpose of bioconjugation, it would be most convenient to introduce a single orthogonal functionality into a biomolecule at a desired position which can then be modified chemoselectively and site-specifically without the need for any precautions [4]. While this might sound too good to be true, such strategies are already being pursued. For example, the introduction of cysteines (Cys) via site-directed mutagenesis has become a standard tool in protein engineering. These additional Cys residues can be used as handles for the selective conjugation of cargoes – including chelators for radiometals and prosthetic groups – using straightforward chemical methods (see the section on "Cysteines (Sulfhydryl Groups)"). One drawback of introducing extra Cys residues, however, is the risk of the misfolding of the protein due to the formation of nonnative disulfide bridges. Amino acid sequences capable of the coordination of radiometals have also been engineered into proteins. For example, the hexahistidine tag (His_6), ubiquitously used for protein purifications via nickel affinity chromatography, has been used to facilitate the radiolabeling of proteins with the technetium-99m tricarbonyl core [42, 43].

Finally, the most elegant – yet also the most complicated – approach to site-specific bioconjugation is the genetic encoding of bioorthogonal moieties that can react with specific partners under mild reaction conditions (*e.g.* azides and alkynes for click chemistry; see the chapter on "Click Chemistry in Radiopharmaceutical Chemistry"). Once these functionalities have been introduced into proteins, they can be used to attach various cargoes in a highly controlled fashion [44]. A cell's own translational machinery can be leveraged to this end. Indeed, cells can be manipulated into incorporating unnatural amino acids (uAA) in place of structurally related natural variants. For example, both azido-

homoalanine and homopropargylglycine can be used in place of methionine (Fig. 16). However, the global metabolic replacement of an amino acid with unnatural analogs does not necessarily resolve site-specificity issues associated with the modification of multifunctional proteins. To circumvent this issue, recent efforts have been aimed at editing the biosynthetic apparatus *itself*. Based on the pioneering work of Schultz and co-workers, different uAAs can be incorporated site-selectively into proteins by employing a strategy termed the "genetic code expansion technique" [45]. The method utilizes an orthogonal pair of tRNA/tRNA-synthetase which is functionally compatible with the protein translational machinery and genetically encodes for a uAA, leading to the ribosomal incorporation of this uAA in the amino acid sequence of the protein. Among the uAAs incorporated by such methods are key reactive handles that can be used as tags for site-specific modifications via chemistry discussed in this chapter and others (see Fig. 16).

While such advanced biochemical approaches are already frequently employed in protein engineering – *e.g.* for the preparation of antibody drug conjugates (ADC) [46] – there have been only a few reports of the application of these techniques in the radiopharmaceutical sciences. One laboratory employed the genetic code expansion technique to create a variant of the antibody rituximab with the uAA *N*-ε-2-azideoethyloxycarbonyl-lysine (NeaK) incorporated at selected sites. The subsequent reaction of this azide-bearing antibody with a cyclooctyne-containing derivative of DOTA provided an immunoconjugate that could be labeled with several different radiometals, including copper-64 and lutetium-177 [47]. This work enabled the creation of a homogeneous radioimmunoconjugate with precisely two chelators per antibody incorporated *only* at the chosen sites. Moreover, the radioimmunoconjugates created using this approach displayed favorable tumor-targeting properties *in vivo*. In separate work, this methodology has been used for the introduction of a C-terminal selenocysteine (Sec) into a HER2-binding affibody molecule [48]. The unique reactivity of this noncanonical amino acid was exploited for the site-selective radiolabeling of the affibody with $[^{11}C]CH_3$-I as well as the conjugation of a maleimide-bearing DOTA for radiolabeling with gallium-68.

Controversial Issues

Some bioconjugation techniques have become well established in the field even though they have important limitations. For example, the Michael addition between thiols and maleimides that forms a thiosuccinimide linkage is widely used for the radiolabeling of proteins and peptides (see the section on "Cysteines (Sulfhydryl Groups)"). The widespread use of this reaction for bioconjugations can be attributed to the synthetic accessibility and commercial availability of several maleimide-derived BFCAs and prosthetic groups as well as their ability to react chemoselectively with cysteine residues under physiological conditions. However, without chiral auxiliaries, this chemistry affords racemic mixtures of addition products which can be an issue during the regulatory approval process, particularly in the case of small molecules (Fig. 17a). In addition, the suitability of the thiol-maleimide adduct in bioconjugates has recently been disputed due to its potential instability *in vivo*. It is known that adducts of thiols and α,β-unsaturated carbonyls can undergo a retro-Michael reaction (Fig. 17b). In the case of thiosuccinimides, this converts the adduct back to the starting thiols and maleimides. In the presence of excess exogenous thiols (*e.g.* high concentrations of glutathione in reductive and hypoxic tumor tissue),

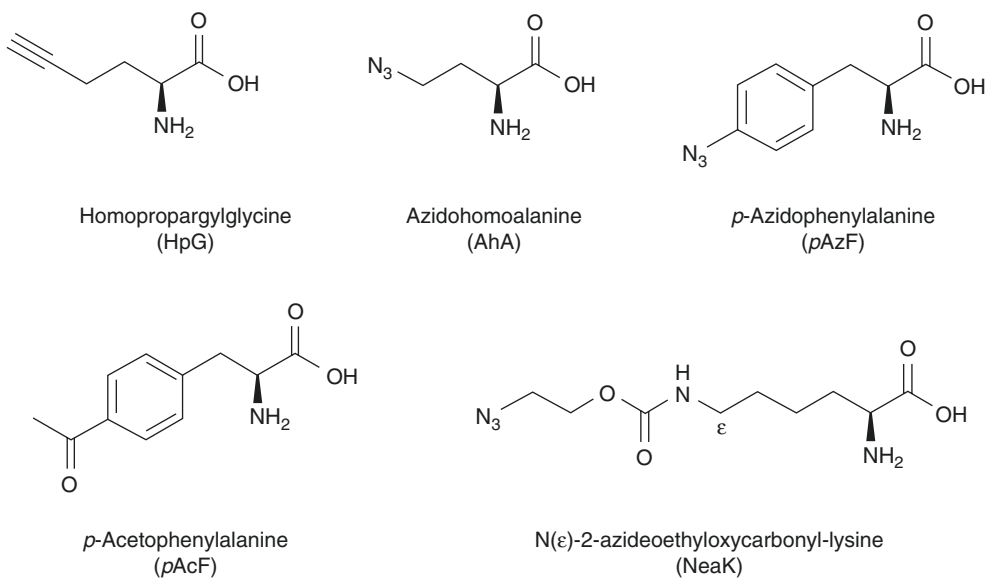

Fig. 16 Examples of unnatural amino acids (uAA) containing bioorthogonal functionalities that have been incorporated into proteins for site-specific modifications

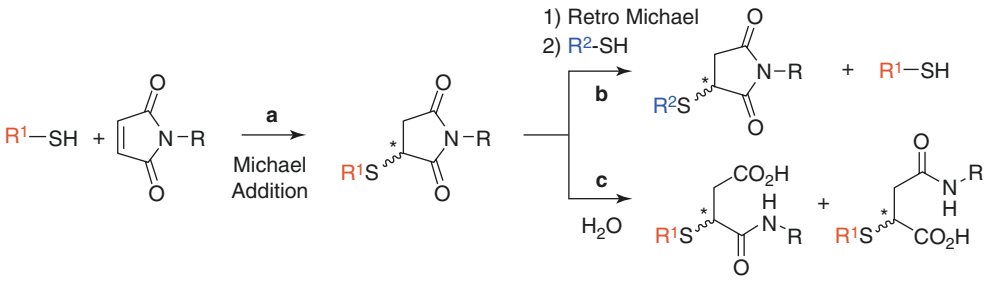

Fig. 17 Michael reaction of thiols and maleimides forming racemic thiosuccinimides (**a**) which can undergo thiol-exchange reactions (**b**) or hydrolysis (**c**). R^1 represents a cysteine residue of, *e.g.* a protein or peptide, R^2 stands for a residue of an exogenous thiol (*e.g.* glutathione), and R represents an imaging probe (*e.g.* a radionuclide) to be attached to the peptide or protein

these maleimides can go on to form new thioether adducts. Overall, this transformation is described as a "thiol-exchange reaction" that can result in the premature loss of the cargo *in vivo*. In fact, in some cases, thiosuccinimides have been considered *as cleavable linkers (!)* rather than stable connectors for bioconjugation [49]. Thiosuccinimides can also undergo irreversible hydrolysis, forming two isomeric succinamic acid thioethers which are not prone to subsequent thiol-exchange reactions (Fig. 17c) [50]. This reaction has been examined for the development of self-hydrolyzing maleimides to improve the stability of ADCs [51].

It is important to note that the thiol-maleimide bioconjugation strategy has been successfully applied countless times. Nonetheless, its utility certainly depends on the intended *in vivo* lifetime of the thiosuccinimide linker, which, in turn, is determined by the conditions to which the bioconjugate is exposed (*e.g.* intracellular versus extracellular environment). It is, however, not surprising that alternative strategies for the modification of thiols have been investigated in order to circumvent the potential limitations discussed above (see the section on "Cysteines (Sulfhydryl Groups)") [9]. A promising substitute for maleimides are phenyloxadiazole methylsulfones, which react chemoselectively with the sulfhydryl group of cysteine residues within minutes under mild aqueous conditions. This reaction forms a single isomer of a heterocyclic thioether product which has been shown to be more stable than thiosuccinimides under physiological conditions [52]. Other examples of emerging methodologies utilizing Cys residues include the condensation reaction between *N*-terminal cysteines and 2-cyanobenzothiazoles as well as the addition reaction of thiols to exocyclic olefinic maleimide derivatives [15, 53]. Several of these new methodologies have the potential to replace the thiol-maleimide-based systems in the future and become the new standard for thiol-selective bioconjugations.

The Future

Today, radiochemists and radiopharmacists have access to a broad set of chemical tools for the modification of (bio)molecules. Yet still, many of the most well-established bioconjugation strategies come with limitations. It is therefore not surprising that practitioners in the field around the world are actively engaged in the design and development of improved bioconjugation methodologies with fine-tuned characteristics. While some novel innovations (*e.g.* click chemistry; see the chapter on "Click Chemistry in Radiopharmaceutical Chemistry") are currently becoming integral parts of the radiopharmaceutical sciences, others have only begun to emerge. Some novel approaches – for example, enzymatic and bioorthogonal methods – have the potential to replace currently established bioconjugation methodologies. However, the broad accessibility of these new technologies as well as the commercial availability of the reagents will be necessary for these techniques to reach their full potential.

The Bottom Line

- Most biomolecules contain multiple copies of functional groups distributed throughout their structure, which makes the chemoselective and site-specific conjugation of radionuclides a challenging task.
- The stringent requirements on the reaction conditions that are often required for the modification of delicate biomolecules in their native form impose further restrictions on the design and development of radiolabeling protocols.
- The use of readily available chemical reactive probes for the direct or indirect radiolabeling of biomolecules often results in the creation of mixtures of conjugates that exhibit heterogeneity in the number of modifications per biomolecule as well as the sites of these modifications. This can be a concern in the development of radiopharmaceuticals because each regioisomeric product can possess different biological properties.
- The careful optimization of the reaction conditions used during modifications with chemical reactive probes can provide mixtures of bioconjugates with narrow product distributions that are suitable for clinical translation. However, the reproducibility of these protocols can be an issue and may require batch-to-batch evaluation.

- Considerable efforts are necessary for the synthesis of site-specifically radiolabeled bioconjugates with well-defined molecular structures and homogenous compositions. State-of-the-art biotechnological approaches, bioorthogonal chemistry, and chemoenzymatic methods represent new and promising tools that are only now becoming available to the field.

References

1. Hermanson GT, editor. Bioconjugate techniques. 3rd ed. Boston: Academic Press; 2013.
2. Algar WR, Dawson P, Medintz IL, editors. Chemoselective and bioorthogonal ligation reactions: concepts and applications. Weinheim: Wiley-VCH Verlag; 2017.
3. Coenen HH, Gee AD, Adam M, Antoni G, Cutler CS, Fujibayashi Y, et al. Consensus nomenclature rules for radiopharmaceutical chemistry – setting the record straight. Nucl Med Biol. 2017;55:v–xi.
4. Sletten EM, Bertozzi CR. Bioorthogonal chemistry: fishing for selectivity in a sea of functionality. Angew Chem Int Ed Eng. 2009;48(38):6974–98.
5. Rodwell VW, Bender D, Botham KM, Kennelly PJ, Weil PA, editors. Harper's illustrated biochemistry. 30th ed. New York: McGraw-Hill Education; 2015.
6. Ermert J, Coenen HH. Methods for ^{11}C- and ^{18}F-labelling of amino acids and derivatives for positron emission tomography imaging. J Label Compd Radiopharm. 2013;56(3–4):225–36.
7. Koniev O, Wagner A. Developments and recent advancements in the field of endogenous amino acid selective bond forming reactions for bioconjugation. Chem Soc Rev. 2015;44(15):5495–51.
8. deGruyter JN, Malins LR, Baran PS. Residue-specific peptide modification: a chemist's guide. Biochemistry. 2017;56(30):3863–73.
9. Adumeau P, Sharma SK, Brent C, Zeglis BM. Site-specifically labeled immunoconjugates for molecular imaging–part 1: cysteine residues and glycans. Mol Imaging Biol. 2016;18(1):1–17.
10. Charron CL, Hickey JL, Nsiama TK, Cruickshank DR, Turnbull WL, Luyt LG. Molecular imaging probes derived from natural peptides. Nat Prod Rep. 2016;33(6):761–800.
11. Bernhard C, Moreau M, Lhenry D, Goze C, Boschetti F, Rousselin Y, et al. DOTAGA-anhydride: a valuable building block for the preparation of DOTA-like chelating agents. Chemistry. 2012;18(25):7834–41.
12. Hnatowich D, Layne W, Childs R, Lanteigne D, Davis M, Griffin T, et al. Radioactive labeling of antibody: a simple and efficient method. Science. 1983;220(4597):613–5.
13. van der Born D, Pees A, Poot AJ, Orru RVA, Windhorst AD, Vugts DJ. Fluorine-18 labelled building blocks for PET tracer synthesis. Chem Soc Rev. 2017;46(15):4709–73.
14. Chin J, Vesnaver M, Bernard-Gauthier V, Saucke-Lacelle E, Wängler B, Wängler C, et al. Direct one-step labeling of cysteine residues on peptides with [^{11}C]methyl triflate for the synthesis of PET radiopharmaceuticals. Amino Acids. 2013;45(5):1097–108.
15. Jeon J, Shen B, Xiong L, Miao Z, Lee KH, Rao J, et al. Efficient method for site-specific ^{18}F-labeling of biomolecules using the rapid condensation reaction between 2-cyanobenzothiazole and cysteine. Bioconjug Chem. 2012;23(9):1902–8.
16. Leier SRS, Wuest F. Radiometal-containing arene diazonium salts for chemoselective bioconjugation of tyrosine residues. J Label Compd Radiopharm. 2017;60(Suppl 1):S94.
17. Moradi SV, Hussein WM, Varamini P, Simerska P, Toth I. Glycosylation, an effective synthetic strategy to improve the bioavailability of therapeutic peptides. Chem Sci. 2016;7(4):2492–500.
18. Rodwell JD, Alvarez VL, Lee C, Lopes AD, Goers JW, King HD, et al. Site-specific covalent modification of monoclonal antibodies: in vitro and in vivo evaluations. Proc Natl Acad Sci U S A. 1986;83(8):2632–6.
19. Jeong JM, Lee J, Paik CH, Kim D-K, Lee DS, Chung J-K, et al. Site-specific^{99m}Tc-labeling of antibody using dihydrazinophthalazine (DHZ) conjugation to Fc region of heavy chain. Arch Pharm Res. 2004;27(9):961–7.
20. Kurth M, Pelegrin A, Rose K, Offord RE, Pochon S, Mach JP, et al. Site-specific conjugation of a radioiodinated phenethylamine derivative to a monoclonal antibody results in increased radioactivity localization in tumor. J Med Chem. 1993;36(9):1255–61.
21. Namavari M, Cheng Z, Zhang R, De A, Levi J, Hoerner JK, et al. A novel method for direct site-specific radiolabeling of peptides using [^{18}F]FDG. Bioconjug Chem. 2009;20(3):432–6.
22. Maschauer S, Prante O. A series of 2-*O*-trifluoromethylsulfonyl-D-mannopyranosides as precursors for concomitant ^{18}F-labeling and glycosylation by click chemistry. Carbohydr Res. 2009;344(6):753–61.
23. Younes C, Boisgard R, Tavitian B. Labelled oligonucleotides as radiopharmaceuticals: pitfalls, problems and perspectives. Curr Pharm Des. 2002;8(16):1451–66.
24. Bogdanov A, Licha K, editors. Molecular Imaging, an essential tool in preclinical research, diagnostic imaging and therapy. Berlin: Springer-Verlag; 2005.
25. Alauddin MM. Nucleoside-based probes for imaging tumor proliferation using positron emission tomography. J Label Compd Radiopharm. 2013;56(3–4):237–43.
26. Gijs M, Aerts A, Impens N, Baatout S, Luxen A. Aptamers as radiopharmaceuticals for nuclear imaging and therapy. Nucl Med Biol. 2016;43(4):253–71.
27. Dolle F, Hinnen F, Vaufrey F, Tavitian B, Crouzel C. A general method for labeling oligodeoxynucleotides with ^{18}F for *in vivo* PET imaging. J Label Compd Radiopharm. 1997;39(4):319–30.
28. Gijs M, Dammicco S, Warnier C, Aerts A, Impens NR, D'Huyvetter M, et al. Gallium-68-labelled NOTA-oligonucleotides: an optimized method for their preparation. J Label Compd Radiopharm. 2016;59(2):63–71.
29. Cevc G, editor. Phospholipid handbook. New York: Marcel Dekker; 1993.
30. Poulsen RH, Rasmussen JT, Bøtker HE, Waehrens LS, Falborg L, Heegaard CW, et al. Imaging the myocardium at risk with ^{99m}Tc-lactadherin administered after reperfusion in a porcine model. Nucl Med Biol. 2014;41(1):114–9.
31. Schwarzenböck S, Souvatzoglou M, Krause BJ. Choline PET and PET/CT in primary diagnosis and staging of prostate cancer. Theranostics. 2012;2(3):318–30.
32. Zeng H, Zhang T, Song F, Wu X. Technetium-99m labeled fatty acid analogues for SPECT imaging in heart and liver. Med Chem. 2014;4:481–6.
33. de Barros AB, Tsourkas A, Saboury B, Cardoso VN, Alavi A. Emerging role of radiolabeled nanoparticles as an effective diagnostic technique. EJNMMI Res. 2012;2(1):39.
34. Lamichhane N, Dewkar GK, Sundaresan G, Mahon RN, Zweit J. [^{18}F]-fluorinated carboplatin and [^{111}In]-liposome for image-guided drug delivery. Int J Mol Sci. 2017;18:1079.
35. Seo JW, Mahakian LM, Kheirolomoom A, Zhang H, Meares CF, Ferdani R, et al. Liposomal Cu-64 labeling method using bifunctional chelators: poly(ethylene glycol) spacer and chelator effects. Bioconjug Chem. 2010;21(7):1206–15.
36. Seo JW, Mahakian LM, Tam S, Qin S, Ingham ES, Meares CF, et al. The pharmacokinetics of Zr-89 labeled liposomes over

extended periods in a murine tumor model. Nucl Med Biol. 2015;42(2):155–63.
37. Onega M, Winkler M, O'Hagan D. Fluorinase: a tool for the synthesis of ^{18}F-labeled sugars and nucleosides for PET. Future Med Chem. 2009;1(5):865–73.
38. Massa S, Vikani N, Betti C, Ballet S, Vanderhaegen S, Steyaert J, et al. Sortase A-mediated site-specific labeling of camelid single-domain antibody-fragments: a versatile strategy for multiple molecular imaging modalities. Contrast Media Mol Imaging. 2016;11(5):328–39.
39. Paterson BM, Alt K, Jeffery CM, Price RI, Jagdale S, Rigby S, et al. Enzyme-mediated site-specific bioconjugation of metal complexes to proteins: sortase-mediated coupling of copper-64 to a single-chain antibody. Angew Chem Int Ed Eng. 2014;53(24):6115–9.
40. Jeger S, Zimmermann K, Blanc A, Grunberg J, Honer M, Hunziker P, et al. Site-specific and stoichiometric modification of antibodies by bacterial transglutaminase. Angew Chem Int Ed Eng. 2010;49(51):9995–7.
41. Zeglis BM, Davis CB, Aggeler R, Kang HC, Chen A, Agnew BJ, et al. Enzyme-mediated methodology for the site-specific radiolabeling of antibodies based on catalyst-free click chemistry. Bioconjug Chem. 2013;24(6):1057–67.
42. Adumeau P, Sharma SK, Brent C, Zeglis BM. Site-specifically labeled immunoconjugates for molecular imaging–part 2: peptide tags and unnatural amino acids. Mol Imaging Biol. 2016;18(2):153–65.
43. Waibel R, Alberto R, Willuda J, Finnern R, Schibli R, Stichelberger A, et al. Stable one-step technetium-99m labeling of His-tagged recombinant proteins with a novel Tc(I)–carbonyl complex. Nat Biotechnol. 1999;17(9):897–901.
44. Spicer CD, Davis BG. Selective chemical protein modification. Nat Commun. 2014;5:4740.
45. Noren CJ, Anthonycahill SJ, Griffith MC, Schultz PG. A general-method for site-specific incorporation of unnatural amino-acids into proteins. Science. 1989;244(4901):182–8.
46. Hallam TJ, Wold E, Wahl A, Smider VV. Antibody conjugates with unnatural amino acids. Mol Pharm. 2015;12(6):1848–62.
47. Wu Y, Zhu H, Zhang B, Liu F, Chen J, Wang Y, et al. Synthesis of site-specific radiolabeled antibodies for radioimmunotherapy via genetic code expansion. Bioconjug Chem. 2016;27(10):2460–8.
48. Wållberg H, Grafström J, Cheng Q, Lu L, Martinsson Ahlzén HS, et al. HER2-positive tumors imaged within 1 hour using a site-specifically ^{11}C-labeled sel-tagged affibody molecule. J Nucl Med. 2012;53(9):1446–53.
49. Baldwin AD, Kiick KL. Tunable degradation of maleimide–thiol adducts in reducing environments. Bioconjug Chem. 2011;22(10):1946–53.
50. Fontaine SD, Reid R, Robinson L, Ashley GW, Santi DV. Long-term stabilization of maleimide–thiol conjugates. Bioconjug Chem. 2015;26(1):145–52.
51. Lyon RP, Setter JR, Bovee TD, Doronina SO, Hunter JH, Anderson ME, et al. Self-hydrolyzing maleimides improve the stability and pharmacological properties of antibody-drug conjugates. Nat Biotechnol. 2014;32(10):1059–62.
52. Chiotellis A, Sladojevich F, Mu L, Muller Herde A, Valverde IE, Tolmachev V, et al. Novel chemoselective ^{18}F-radiolabeling of thiol-containing biomolecules under mild aqueous conditions. Chem Commun (Camb). 2016;52(36):6083–6.
53. Kalia D, Malekar PV, Parthasarathy M. Exocyclic olefinic maleimides: synthesis and application for stable and thiol-selective bioconjugation. Angew Chem Int Ed Eng. 2016;55(4):1432–5.

Click Chemistry in Radiopharmaceutical Chemistry

James C. Knight and Bart Cornelissen

Fundamentals

Radiopharmaceuticals often contain radionuclides with very short physical half-lives. As a result, it is often beneficial to incorporate the radionuclide into the agent during the final step of its synthesis in order to ensure that the radiotracer contains as much activity as possible. However, this requirement can present head-scratching synthetic conundrums that radiochemists often struggle to address. One set of chemical transformations that have proven particularly useful in this regard are grouped under the umbrella of 'click chemistry'. Broadly speaking, click chemistry ligations are reactions between two substrates that can selectively react with one another rapidly, cleanly, and quantitatively under very gentle conditions, in essence, molecular puzzle pieces. Recent advances in this area have led to the creation of a versatile library of ligations with wide applicability and improved efficiency, including reactions which can proceed within the complex environment of living organisms. This latter trait is particularly notable, as it presents an attractive approach for the delivery of radionuclides to sites of disease within the human body via the use of complementary click chemistry reaction pairs. This strategy – known as 'pretargeting' – holds several enticing implications for both nuclear imaging and targeted radiotherapy which will be discussed later in this chapter.

Details

The Utility of Click Chemistry Reactions in Radiochemistry

Click chemistry reactions have been applied most effectively to the preparation of ^{18}F-labeled PET imaging agents, including probes based on peptides, proteins, and – to a lesser extent – small molecules [1–8]. Importantly, these reactions offer the ability to circumvent many of the challenges associated with the direct incorporation of the [^{18}F]fluoride anion, including its poor nucleophilicity and limited reactivity in protic environments (see Chaps. 15, 16, and 17) [9–12]. These limitations often necessitate harsh reaction conditions that can damage the vector being radiolabeled and impair its ability to bind to its biological target (this is particularly true for more sensitive peptides and proteins). Consequently, ^{18}F-labeled prosthetic groups containing click chemistry handles (*e.g.* azides or alkynes) have become popular tools for the radiolabeling of more delicate biomolecules [3].

In practical terms, click chemistry-based ^{18}F-fluorinations begin with the radiosynthesis of the ^{18}F-labeled prosthetic group. This step, of course, can be performed under harsh reaction conditions because the sensitive biomolecule is not yet involved. Once the radiolabeled prosthetic group has been created, it is transferred to a vial containing the biomolecule bearing the complementary moiety, and the two undergo their click ligation under much more mild conditions, ultimately producing the desired radiofluorinated molecule (Fig. 1).

J. C. Knight · B. Cornelissen (✉)
CRUK/MRC Oxford Institute for Radiation Oncology,
Radiobiology Research Institute, Churchill Hospital (Headington),
Department of Oncology, University of Oxford, Oxford, UK
e-mail: bart.cornelissen@oncology.ox.ac.uk

J. S. Lewis et al. (eds.), *Radiopharmaceutical Chemistry*, https://doi.org/10.1007/978-3-319-98947-1_26

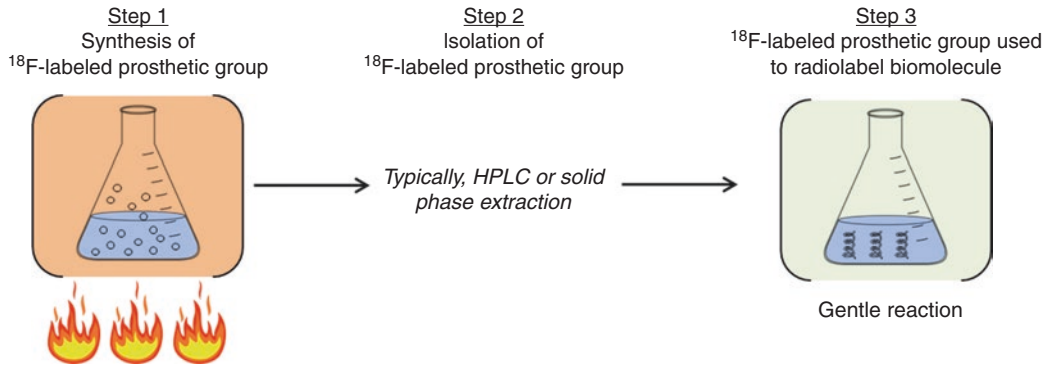

Fig. 1 The general strategy for radiolabeling sensitive biomolecules with ^{18}F-labeled prosthetic groups

While the use of 'clickable' prosthetic groups can yield radiolabeled species which may otherwise be unobtainable, this approach also has some important shortcomings. For example, the synthesis of an ^{18}F-labeled PET imaging agent should ideally be as rapid as possible to combat the inexorably decreasing activity of the decaying radionuclide. This strategy, unfortunately, introduces additional time-consuming steps related to the synthesis and purification of the prosthetic group. A second concern centres on the bulky nature of many clickable prosthetic groups and the linkages formed by the click ligations. The overall impact of incorporating these low molecular weight species onto large proteins (*e.g.* antibodies) can be negligible due to the sheer difference in size. However, these species can – and often do – disrupt the binding properties and biological behaviour of smaller vectors such as peptides and small molecules.

The Archetypal Click Chemistry Reaction

The most popular and widely utilized click chemistry reaction is undoubtedly the Huisgen 1,3-dipolar cycloaddition between an azide and an alkyne which results in the formation of a triazole (Fig. 2a) [13–15]. The earliest version of this reaction – which predates the concept of click chemistry by almost 40 years – was reported in 1963 by its eponym, Rolf Huisgen [14, 15]. In its original form, this reaction has a few critical limitations: it requires elevated temperatures and pressures and also lacks regioselectivity, as it leads to the formation of a mixture of 1,4- and 1,5-substituted triazoles. In the early 2000s, however, this comparatively primitive cycloaddition reaction was revived with the discovery that a copper(I) catalyst allows the reaction to proceed efficiently without heating and leads to the generation of only 1,4-substituted triazoles (Fig. 2b) [13, 16]. The high rate constant of this copper(I)-catalyzed azide-alkyne cycloaddition (CuAAC) – which is increased 10^6-fold compared to the uncatalyzed reaction – and the fact that this reaction is 'so insensitive to the usual reaction parameters as to strain credulity' makes it very attractive for radiosyntheses involving short-lived radionuclides [13].

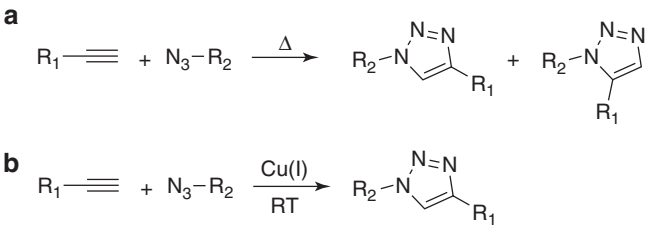

Fig. 2 (**a**) The original Huisgen 1,3-dipolar cycloaddition typically requires heat and/or high pressures and leads to an undesirable mixture of regioisomers. (**b**) Adding a Cu(I) catalyst facilitates an efficient room temperature reaction which only yields the 1,4-substituted triazole

Several examples of ^{18}F-labeled prosthetic groups which undergo CuAAC reactions are provided in Fig. 3. The linear alkyl ^{18}F-labeled alkyne prosthetic groups were among the first developed and have demonstrated promising utility in reactions with azide-bearing small molecules (such as folate receptor-targeting constructs) and peptides (such as A20FMDV2 which targets the integrin $\alpha_v\beta_6$) [4, 5, 17].

Another highly popular ^{18}F-labeled prosthetic group is 2-[^{18}F]fluoroethyl azide ([^{18}F]FEA), which was initially developed in 2007 and has since been used to radiolabel a wide variety of compounds [18–21]. The radiosynthesis of [^{18}F]FEA was originally achieved via the reaction of anhydrous, no-carrier-added K[^{18}F]F/Kryptofix with 2-azidoethyl-4-toluenesulfonate in acetonitrile at 80 °C for 15 min. The recovery of purified [^{18}F]FEA was achieved by distillation at 130 °C, ultimately producing the reagent in a decay-corrected radiochemical yield of 54%. Further refinements in the synthesis and manipulation of [^{18}F]FEA – which can be challenging due to its volatility – have since been reported. These include the simplification of the purification process by incorporating a solid-phase extraction step, a change which has also helped make the radiosynthesis of [^{18}F]FEA compatible with automated synthesis modules [22].

The CuAAC reaction has also been used for the radiolabeling of an alkyne-modified derivative of a Tyr^3-octreotate peptide with a ^{11}C-bearing prosthetic group: [^{11}C]methyl azide ([^{11}C]MeA) [23]. Furthermore, the CuAAC reaction

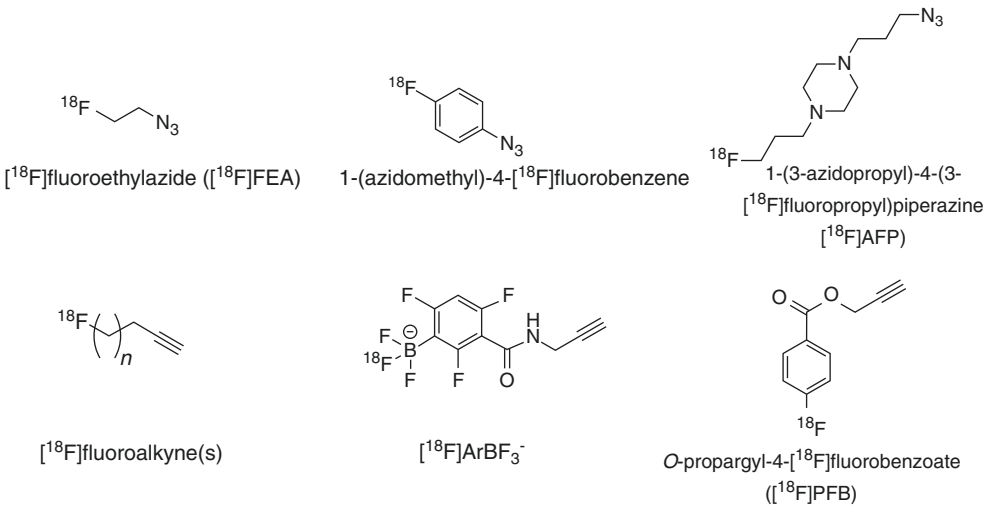

Fig. 3 A selection of commonly used ^{18}F-labeled prosthetic groups for CuAAC-based radiolabelings

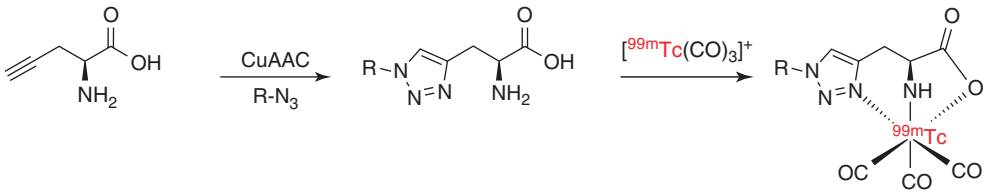

Fig. 4 An example of the 'click-to-chelate' radiolabeling strategy involving ^{99m}Tc(CO)$_3$

has also been elegantly utilized as part of the so-called 'click-to-chelate' strategy for labeling substrates with radiometals such as ^{99m}Tc. In this approach, the click reaction yields a 1,2,3-triazole which forms part of a tridentate scaffold that facilitates the coordination of an M(CO)$_3$ core (Fig. 4). This approach provides a convenient method for radiolabeling compounds with the often mercurial ^{99m}Tc, and – just as importantly – the radiopharmaceuticals created using this strategy have demonstrated high *in vivo* stability [24].

Unfortunately, the 'Cu' in the CuAAC reaction can create several problems. Copper is known to be toxic above certain concentration thresholds, and it is therefore of utmost importance to remove the metal completely from the formulation of the final product. This can be difficult to accomplish, because many peptides and proteins contain amino acids capable of coordinating the metal. The non-specific binding of Cu to proteins and peptides can also adversely affect the ability of the biomolecule to bind its target with high affinity and specificity. Furthermore, a catalyst is an additional reaction parameter which requires thorough optimization and adds complexity to the radiosynthesis protocol.

Strain-Promoted Azide-Alkyne Cycloadditions

Efforts to circumvent this need for a Cu(I) catalyst led to the discovery that building ring strain into the alkyne moiety can promote click chemistry ligations with azide-bearing species in the absence of a catalyst (Fig. 5a) [25–29]. The origin of this steric strain lies in the 'preferences' of the two sp-hybridized alkyne carbon atoms. Under most circumstances, these two atoms would adopt 180° bond angles; however, in a cyclooctyne ring, for example, they are forced to adopt bond angles closer to 163°, creating an associated ring strain of ~18 kcal/mol [30]. The relief of this ring strain is a potent driving force behind this catalyst-free reaction. These strain-promoted [3 + 2] azide-alkyne cycloaddition (SPAAC) reactions – part of a growing group of 'copper-free click' ligations – have now been widely utilized in the preparation of agents for both nuclear imaging and targeted radiotherapy [31, 32].

Compared to analogous CuAAC ligations which typically exhibit rate constants in the range of 10–200 M^{-1} s^{-1}, the reactions between the first generation of these cyclooctynes and azides had relatively modest rate constants (Fig. 5b) [33]. For example, the reaction of the cyclooctyne 'OCT' (see Fig. 5b) with benzyl azide has a second-order rate constant of just 0.0024 M^{-1} s^{-1}. However, it was soon realized that the introduction of electron-withdrawing substituents such as fluorines to positions proximal to the alkyne can lead to substantial increases in reaction rates [34]. To wit, monofluorinated (MOFO) and difluorinated (DIFO) cyclooctynes have yielded SPAAC rate constants of 0.0043 and 0.076 M^{-1} s^{-1}, respectively, under comparable reaction conditions. Other chemical modifications – including the introduction of delocalized aromatic systems into the greater structure of the cycloalkyne – have led to even faster reaction rates [27, 35–39]. Dibenzocyclooctyne (DBCO) and biarylcyclooctyne (BARAC) have achieved rate constants of 0.31 and

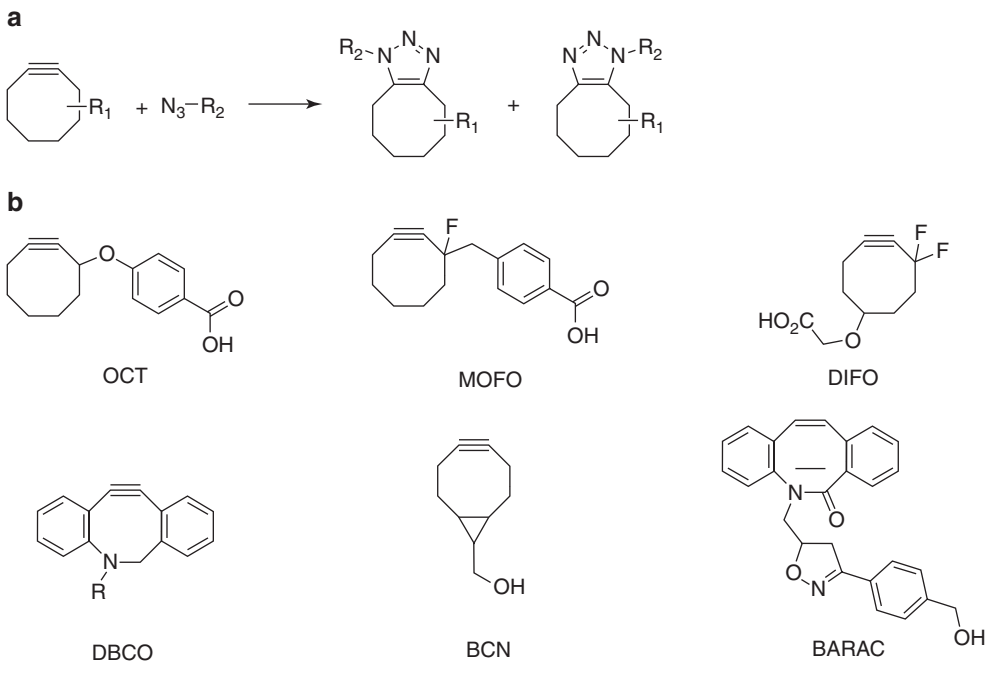

Fig. 5 (**a**) The strain-promoted [3 + 2] azide-alkyne cycloaddition (SPAAC) reaction is an excellent example of a copper-free click chemistry reaction; (**b**) a selection of cyclooctynes commonly used for SPAAC reactions

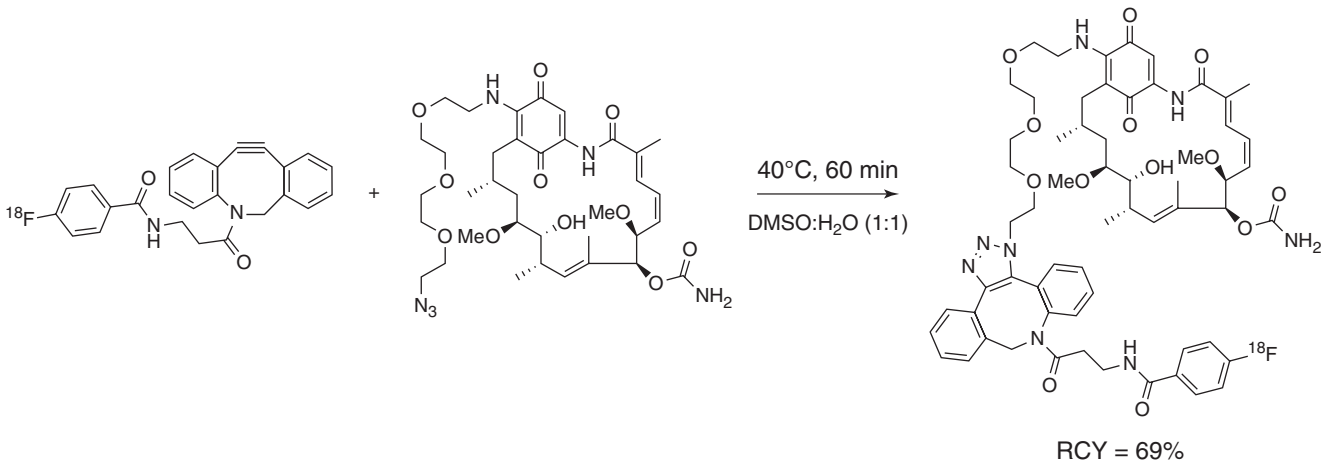

Fig. 6 The radiofluorinated dibenzocyclooctyne – [^{18}F]FB-DBCO – developed by Bouvet *et al.* has been used successfully as a prosthetic group for radiolabeling a variety of azide-containing compounds, including the complex natural product geldanamycin [40]

0.96 M^{-1} s^{-1}, respectively, in reactions with benzyl azide and similar aliphatic azides.

One of the earliest applications of the SPAAC in radiopharmaceutical chemistry is summarized in Fig. 6. In this example, an ^{18}F-labeled prosthetic group derived from DBCO – [^{18}F]-FB-DBCO – was used for the radiolabeling of the complex natural product geldanamycin [40]. The click reaction preceded efficiently under relatively mild reaction conditions (40 °C) and resulted in a radiochemical yield of 69% after 60 min, clearly underscoring the radiochemical value of the SPAAC reaction.

It is also important of course to acknowledge the limitations of SPAAC reactions. Perhaps not surprisingly, the most significant drawback of the ligation is the hydrophobicity of both the ring-strained cycloalkyne reagent and the product of the click ligation. This unfortunate (and often unavoidable) characteristic can often present difficulties during radiosynthesis – for example, the need for solubilizing agents which can be difficult to remove – and can also have a detrimental impact on the *in vivo* pharmacokinetic and pharmacodynamic profiles of the resulting radiopharmaceuticals [41].

The Inverse Electron-Demand Diels-AlderCycloaddition Reaction

Another class of click chemistry reactions which represent an evolutionary progression from the CuAAC ligations discussed earlier are the inverse electron-demand Diels-Alder (IEDDA) [4 + 2] cycloadditions between an electron-rich dienophile – such as norbornene or *trans*-cyclooctene (TCO) – and an electron-deficient diene (*e.g.* tetrazine) [42–44]. This concerted cycloaddition initially forms a highly strained bicyclic adduct that subsequently forms a dihydropyridazine through the loss of $N_{2(g)}$. It is thought that this product may be oxidized further to form an aromatic pyridazine [42].

The importance of the IEDDA reactions stems mostly from their extremely high rate constants – up to k = 380,000 M^{-1} s^{-1} – which are achieved without the need for a catalyst [45–49]. Furthermore, IEDDA ligations often exhibit high chemoselectivity in the presence of other functional groups, including other click chemistry reagents such as azides and alkynes [48, 50, 51]. Due to these favourable attributes, IEDDA reactions have attracted substantial attention from radiochemists and have been successfully employed in a variety of applications relating to radiosynthetic methodology [52–57], protein engineering [58, 59], and *in vivo* click chemistry [60–76]. For example, the IEDDA ligation has demonstrated great utility as the basis of ^{18}F-labeled prosthetic groups, particularly for the radiolabeling of sensitive peptides and proteins. One such prosthetic group based on a norbornene dienophile – [^{18}F]NFB (Fig. 7) – has been employed for the mild radiofluorination of a metabolically stabilized, tetrazine-modified bombesin peptide (TT-BBN) [77]. After a reaction time of 20 min, this approach afforded the desired ^{18}F-labeled peptide with a radiochemical yield of 50%. Notably, this method has been shown to be superior to the more conventional approach of using the primary amine-reactive acylation agent 4-succinimidyl-[^{18}F]fluorobenzoate ([^{18}F]SFB), as the IEDDA-based approach affords comparable radiochemical yields while using fivefold less peptide.

The IEDDA ligation has also been used to facilitate a modular strategy for the radiolabeling antibodies with positron-emitting radiometals. For example, the anti-HER2 antibody trastuzumab was modified with norbornene, and the resulting construct was then reacted with tetrazine-modified versions of DOTA and DFO for the subsequent coordination of copper-64 and zirconium-89, respectively. Importantly, given the sensitive nature of many antibodies, the norbornene conjugation and radiolabeling steps can be performed under gentle reaction conditions, thus eliminating any threat to the immunoreactivity of the antibody [78].

The dienophile TCO has now also been widely utilized as the basis for ^{18}F-labeled prosthetic groups, producing constructs which have demonstrated excellent versatility and efficacy (Fig. 8a). One of these prosthetic groups – [^{18}F]TCO (Fig. 8b) – has been utilized for the preparation of radiofluorinated derivatives of exendin-4 (which targets the glucagon-like protein-1 [GLP-1] receptor) and the cyclic peptide RGD (which targets the $\alpha_v\beta_3$ integrin) [55, 79]. [^{18}F]TCO has also been used in the synthesis of a small molecule PET radiotracer based on the PARP1 inhibitor, AZD2281 (see Fig. 8b) [53]. In this case, the IEDDA cycloaddition afforded a high decay-corrected radiochemical yield of 59.6 ± 5.0% after a reaction time of merely 3 minutes (at room temperature). Interestingly, the use of this relatively bulky prosthetic group had only a slightly detrimental

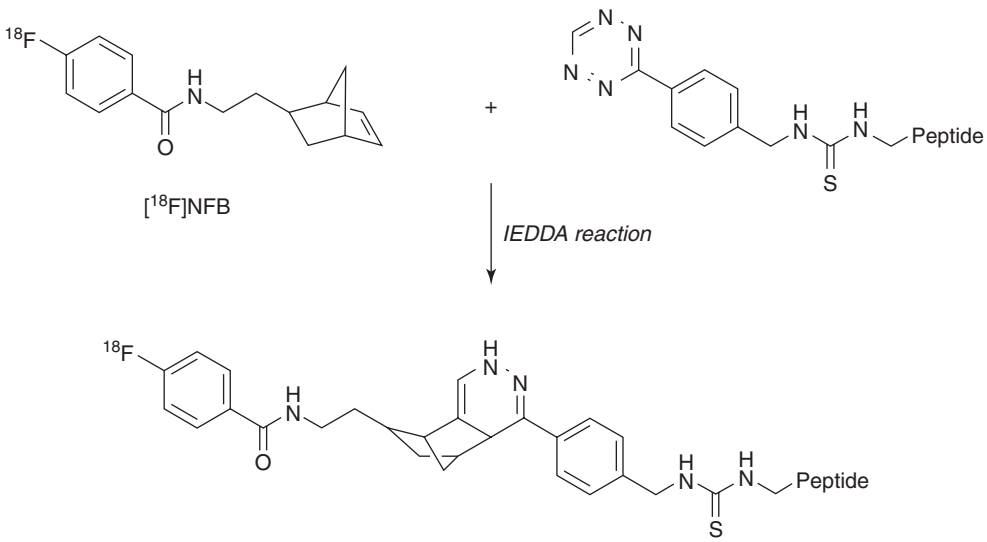

Fig. 7 (**a**) The IEDDA reaction between the norbornene-based prosthetic group [^{18}F]NFB and tetrazine-modified peptides results in the rapid and clean formation of the radiofluorinated peptide under mild reaction conditions

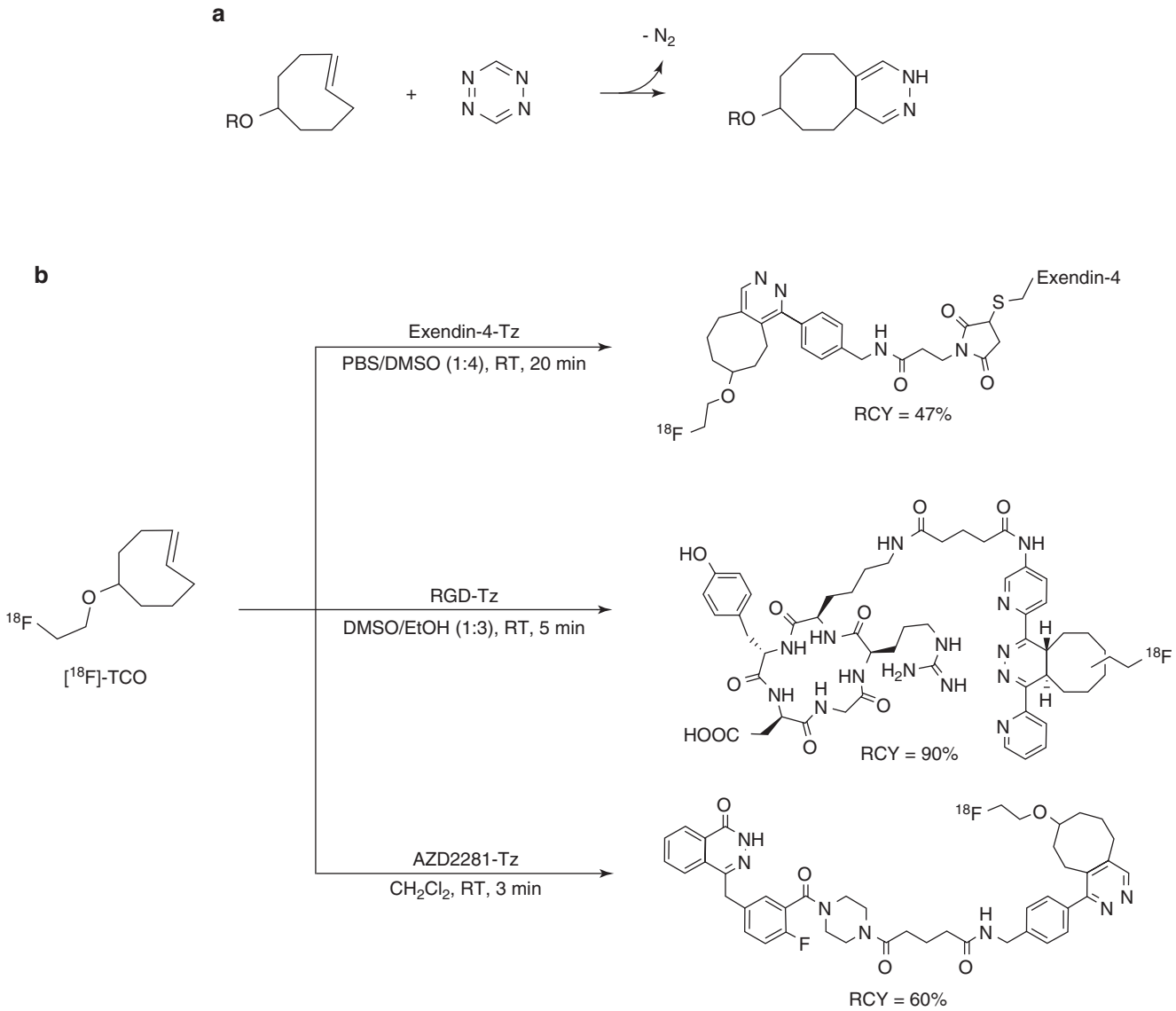

Fig. 8 (**a**) The IEDDA cycloaddition reaction between TCO and tetrazine (Tz) species is a catalyst-free click chemistry reaction that has a high rate constant and excellent chemoselectivity. (**b**) [^{18}F]-TCO is a highly versatile prosthetic group that has been successfully utilized for the synthesis of a diverse array of PET imaging agents, including examples based on exendin-4 [79], the cyclic peptide RGD [55], and the small molecule PARP inhibitor AZD2281 [53]

impact on the ability of [^{18}F]AZD2281 to bind to the PARP1 enzyme compared to the parent compound, AZD2281 (IC_{50} values of ~18 and 5 nM, respectively).

The versatility of these reactions has also been demonstrated by a recent study in which IEDDA chemistry was used to construct a novel bispecific protein (Bs-F(ab)$_2$) [59]. Here, two Fab fragments – one targeting the epidermal growth factor receptor (EGFR) and the other targeting CD105 – were modified with either TCO or tetrazine, thereby facilitating the efficient cross-coupling of the two constructs. The resulting Bs-F(ab)$_2$ was then modified with NOTA via the reaction of an NHS-bearing variant of the chelator with the ε-amino groups of the lysines of the construct and subsequently radiolabeled with ^{64}Cu. This innovative approach highlights the value of IEDDA reactions for applications at the intersection of protein engineering and radiopharmaceutical chemistry.

In Vivo Applications of Click Chemistry

Rejuvenating an Old Concept: Pretargeted Imaging and Therapy

Click chemistry reactions have recently revitalized a concept known as 'pretargeting'[71, 80–82]. The objective of pretar-

geting is to overcome the principal disadvantage of using radiolabeled antibodies to target biomarkers of disease: their slow clearance from the blood. While antibodies can be superb targeting vectors due to their exquisite specificity and affinity for their antigens, their slow blood clearance is a major disadvantage. From a practical perspective, it means that – in the context of imaging – PET/SPECT scans usually have to be performed 5–7 days after the administration of the radioimmunoconjugate in order to obtain images with satisfactorily high tumor-to-background activity contrast ratios [83–88]. For therapeutic studies (and, to a lesser extent, imaging studies), the protracted biological half-life of directly radiolabeled antibodies also results in a high radiation burden to the patient [89]. Pretargeting represents an alternative approach with the potential to overcome all of these problems.

In its simplest form, pretargeting is performed using a two-step approach (Fig. 9). The first step is the injection of the antibody – the 'primary agent' – which is then permitted sufficient time to accumulate within the target tissue and clear from circulation. This lag interval usually lasts for several days and is followed by the administration of the 'secondary agent', typically a radiolabeled small molecule with a rapid pharmacokinetic profile. Upon encountering one another *in vivo*, the primary and secondary agents rapidly and selectively combine, leading to the accumulation of the radionuclide in the target tissue. Due to the rapid clearance of the secondary agent from the blood, high tumor-to-background contrast ratios can be obtained at much earlier time points compared to directly radiolabeled antibodies. In addition – and just as importantly – pretargeting drastically reduces the overall radiation burden to the patient. Thus, in essence, pretargeting combines the favourable targeting properties of antibodies with the superior pharmacokinetic profiles of small molecules while simultaneously skirting the limitations of both constructs.

It is critical to note that the successful implementation of this approach requires that both the primary and secondary agents are modified with complementary reactive groups which are capable of binding together rapidly and selectively in the complex *in vivo* biological milieu. A variety of approaches have been applied in this endeavour. The original strategy involved the use of bispecific antibodies with the ability to bind both a target antigen and a radiolabeled hapten species (typically, a derivative of ethylenediaminetetraacetic acid [EDTA]). Another popular strategy has exploited the exceptionally high-binding affinity between biotin and (strept)avidin (4×10^{-14} M) [90, 91]. In this case, an antibody conjugated to the protein (strept)avidin is typically employed as the primary agent, and a radiolabeled biotinylated species is used as the secondary agent. Other more recent approaches have involved the use of complementary oligonucleotides [92–101] and enzymatic reactions (*e.g.* HaloTag) [102, 103]. While some of these approaches have yielded promising results in clinical trials, they are often hampered by their inherent limitations, which include difficulties in the production of the (often expensive) primary antibody species, immunogenicity, competing endogenous species (such as biotin), and the metabolism of the secondary agents. As a result of these confounding factors, pretargeting has so far

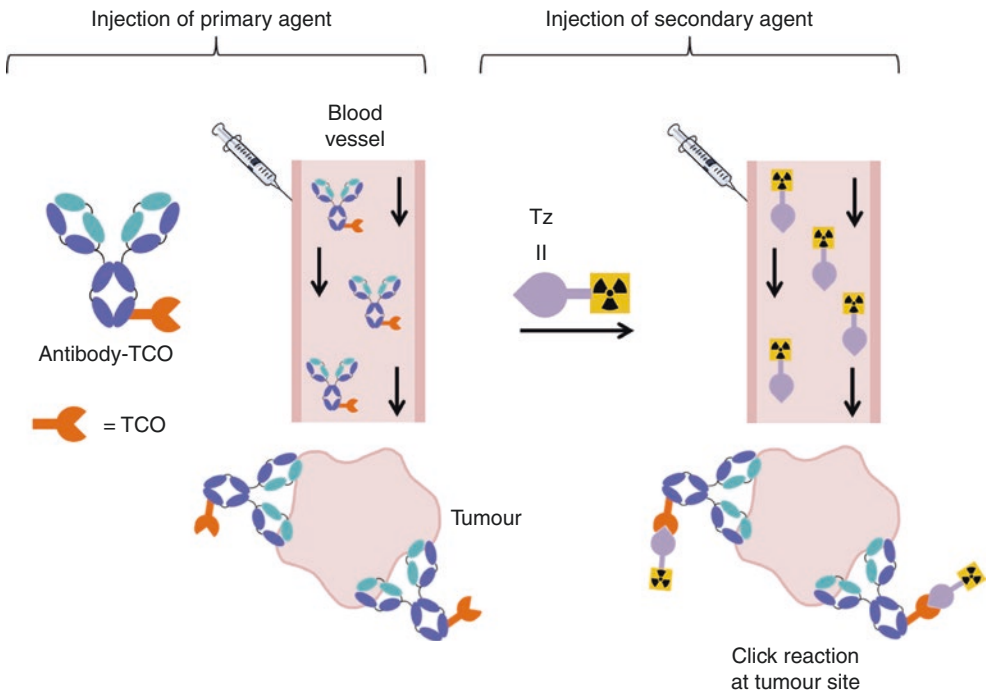

Fig. 9 Simplified schematic of a two-step pretargeting strategy based on IEDDA click chemistry

had a negligible impact on clinical practice despite over 30 years of development.

Click chemistry-mediated pretargeting – specifically pretargeting based on the TCO/tetrazine reaction – is well-placed to overcome the limitations of its predecessors and has yielded highly promising *in vivo* preclinical data in a variety cancer models [71, 80–82]. While even the fastest click chemistry reactions are slower than many biomolecular interactions, the IEDDA ligation offers many advantages in the context of pretargeting, including (*i*) low immunogenicity, (*ii*) high modularity (*i.e.* it can be readily adapted to virtually any combination of antibody and radionuclide), (*iii*) synthetic simplicity (*iv*) bioorthogonality, and (*v*) the availability of commercially available and inexpensive reagents.

First demonstrated in 2010, IEDDA-based pretargeted imaging has now been demonstrated in a variety of preclinical settings with very promising results. The majority of studies have probed cell surface receptors which meet several critical – yet relatively uncommon – criteria, most notably a high level of persistence on the surface of cells. It is also particularly important that the antibody primary agent is not internalized into the cell, as this would prevent its interaction with the secondary agent. So far, only a handful of suitable targets have been identified and used in 'proof-of-principle' studies to validate and optimize this approach to pretargeting. Suitable targets include TAG-72, A33, CEA, and CA19.9. Interestingly, CA19.9 would not appear to strictly abide by these criteria, as it is known to readily shed into circulation; however, IEDDA-based pretargeting has successfully overcome this specific adversity, underscoring the promise of the methodology.

In the vast majority of IEDDA-based pretargeting studies, it is the TCO species rather than the tetrazine which is attached to the antibody. This is mainly due to the superior *in vivo* stability of the TCO compared to tetrazine (these issues are discussed in more detail in the section on 'Early Obstacles and Innovative Solutions' and 'The Future'). Accordingly, the secondary agent is usually a radiolabeled variant of tetrazine. Several secondary agents have been developed in recent years, including constructs containing radionuclides for both imaging (*e.g.* ^{18}F [60, 64], ^{64}Cu [63, 65–67], ^{68}Ga [60], and ^{111}In [69, 104]) and therapy (*e.g.* ^{177}Lu [61, 69, 70, 72, 105]). Many of these reports demonstrate that while tumour uptake values (%ID/g) are invariably lower than what can be achieved using directly radiolabeled antibodies, pretargeting often yields improved activity concentration ratios (such as tumor-to-blood and tumor-to-muscle) at much earlier times after the administration of the radioligand (hours rather than days) [67]. Notably, this strategy has also revealed more favourable dosimetry in mouse models [67].

The promising preclinical data from IEDDA-based pretargeted imaging experiments suggests that both same-day clinical scans and vastly reduced radiation doses to patients are realistic prospects. This reinvigorated imaging strategy is now poised for evaluation in clinical trials and, if successful, has the potential to make a more substantial clinical impact than its predecessors.

Early Obstacles and Innovative Solutions

The recent development of IEDDA-based pretargeting has encountered several early obstacles which, if left unaddressed, would have tempered its successful application. However, as a result of focused investigations, these issues have been identified and have been overcome through innovative, chemistry-based solutions. In this sub-section, we will discuss some of the most important challenges faced by IEDDA-based pretargeting.

Stability of the Tetrazine Reagent Molecular species which are primed with high reactive potential – such as the protagonists of the TCO/tetrazine reaction – are often prone to rapid decomposition. This is undesirable for several (fairly obvious) reasons: First, compounds which will be administered to patients and those which are prepared in accordance with good manufacturing practice (GMP) standards should have a long shelf life. The decomposition of the IEDDA precursor reagents may interfere with the preparation of the primary and secondary agents by reducing reaction yields and producing unwanted side products that would require purification. Second, compounds with short shelf lives would also require more frequent chemical manufacturing at additional expense. And last, the rapid decomposition of these species within the patient would prevent the ligation of the primary and secondary agents, thereby rendering the entire strategy futile.

The stability and reactivity of a wide variety of tetrazine agents have now been evaluated [46]. These data clearly illustrate that the tetrazines with the highest rate constants in reactions with either norbornene or TCO species are often the least stable and therefore do not necessarily represent the best candidates for *in vivo* applications. While a wide array of tetrazines have been evaluated, only two – shown in Fig. 10 – have been widely studied in preclinical pretargeting experiments. These reagents have been selected as they each represent a compromise between stability and reactivity.

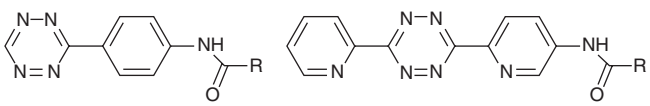

Fig. 10 The two tetrazine species which have been most widely utilized for *in vivo* pretargeting experiments

Stability and Reactivity of the *Trans*-Cyclooctene Reagent As the TCO-modified antibody can require days or weeks to reach its optimal biodistribution *in vivo*, it is crucial that the TCO species is resistant to degradation within this timeframe. Otherwise, of course, its degradation would prevent the ligation with its tetrazine reaction partner. In the first reports of preclinical IEDDA-based pretargeted imaging, the selected TCO species had a suboptimal ability to withstand degradation in mice ($t_{1/2}$~2.6 days). While SPECT images with promising tumour contrast have been obtained, the more protracted circulatory half-life of antibodies in humans necessitates a more stable version of TCO which would allow imaging at much later times.

This issue was addressed in 2013 in an elegant study which identified that this loss of reactivity was caused by the isomerism of TCO to the comparatively unreactive *cis*-cyclooctene (CCO) [73]. Based on the assumption that endogenous metals were responsible, a thorough investigation of several metal-containing proteins led to the discovery that copper-bound proteins were largely to blame. This observation informed rational chemical modifications designed to obstruct this degradation process. Specifically, shortening the PEG linker between the TCO and the antibody leads to an increase in steric hindrance around the TCO which in turn reduces the likelihood of copper-induced isomerization. Another important advancement has been the recognition that the higher energy axial isomer of TCO undergoes a considerably faster reaction with tetrazines compared to its equatorial cousin (k_2 = ~27 × 10^4 versus ~2.7 × 10^4 M^{-1} s^{-1}, respectively). Applying these two improvements in preclinical experiments has enabled the acquisition of exceptional SPECT images following a lag period of 3 days. SPECT images acquired at much later time points – up to 3 days after the injection of the secondary agent – revealed that the radioactivity concentrations within the tumour were not reduced by this added delay, suggesting that the product of the click chemistry ligation is itself resistant to *in vivo* degradation.

Re-routing Excretion Pathways by Chemical Design The lipophilic character of most tetrazine-containing secondary agents promotes excretion *via* the hepatobiliary system. Not surprisingly, this is a problem in cases in which malignant tissue is located within the abdominal region, as sites of interest may be obscured, thus complicating or even preventing the reliable quantification and interpretation of images. This is particularly problematic when considering that the cell surface receptors which represent the most promising candidates for pretargeted imaging and therapy – such as A33 and CEA – are primarily markers of colorectal cancers.

Most of the tetrazine-based secondary agents developed to date have suffered from this shortcoming. However, in recent years, some promising progress has been made in this area. A notable example involving a ^{64}Cu-labeled tetrazine nicely demonstrates the importance of coordination chemistry in determining the overall biodistribution and pharmacokinetic properties of radiometal-containing imaging agents [66]. This study found that when copper-64 was complexed by the macrocyclic chelator NOTA, the overall molecular charge of −1 contributed to the unfavorable excretion of the radioligand through the gut. Yet replacing NOTA with the neutral cryptand chelator SarAr results in an overall electronic charge of +2, which greatly increased the hydrophilicity of the compound and helped to direct its excretion to the renal system. Modifications to the chemical structures of other secondary agents containing non-metal radionuclides such as ^{18}F have also helped re-route the excretion of these radioligands towards renal clearance [75].

The Future

Looking ahead, there are many attractive prospects for click chemistry reactions within radiopharmaceutical chemistry. A particularly exciting area is the development of click chemistry-based prosthetic groups for attaching radionuclides to biomolecular vectors. Existing methods of bioconjugation often rely on the random attachment of radionuclides to functional groups which are prevalent in proteins and peptides (*e.g.* the ε-amino group of lysine residues). This approach – while facile and reliable – invariably leads to a heterogeneous and poorly characterized mixture of products, each with slightly different (and potentially compromised) pharmacokinetic and binding properties. Encouragingly, several bioconjugation methods are being developed which offer considerable improvements over these existing approaches. One such strategy involves the removal of the terminal galactose residues of the heavy chain glycans of the antibody using *β*-1,4-galactosidase and then incorporating azide-modified *N*-acetylgalactosamine monosaccharides into the glycans using a promiscuous galactosyltransferase. These moieties can then be used as handles for the subsequent site-selective SPAAC-mediated attachment of cyclooctyne-modified chelators or prosthetic groups [63, 106, 107]. Other similar chemoenzymatic methods have also shown promise in this area [108]. These site-selective bioconjugation methods will facilitate the highly controlled attachment of a fixed number of cargoes to well-defined and carefully selected sites on antibody-based agents. Given the recent resurgence in antibody-based therapeutics – and their companion diagnostic imaging agents, as well – these site-selective bioconjugation methods will undoubtedly become the preferred option for the synthesis of radioimmunoconjugates.

Given the important advantages offered by pretargeting strategies, it is somewhat surprising that only a small handful

of cancer-associated cell surface receptors have been the subject of investigation in this area. Clearly, these receptors have been selected based on highly restrictive criteria which exclude many of the most clinically relevant antigens (described in the section on 'Rejuvenating an Old Concept: Pretargeted Imaging and Therapy'). Unfortunately, in cases where the antibody has been shown to internalize rapidly – such as the anti-HER2 antibody trastuzumab – these strategies have not been as successful. However, in order to widen the scope of pretargeting strategies beyond this handful of markers, it will be of great importance to identify additional suitable targets which also have high clinical value.

Lastly, the recent development of a new drug delivery strategy referred to as 'click-to-release' is also poised to make an important impact in the coming years [109, 110]. In essence, this approach involves the controlled release of a drug which is initially bound to TCO and is cleaved during the IEDDA reaction with a tetrazine-based secondary agent. From a mechanistic standpoint, the drug is attached at the allylic position of TCO by a carbamate linker and is ejected (with CO_2 as an additional side product) via an electron cascade mechanism when the 1,4-dihydropyridazine intermediate converts to a pyridazine which then subsequently rearranges to an aromatic pyridazine. While there are many alternative (usually enzymatic) systems which allow for the cleavage of drugs bound to targeting vectors, the click-to-release mechanism is advantageous because it does not rely on the assistance of intracellular enzymes and can therefore be targeted against extracellular epitopes and matrix constituents. It is also worth noting that while doxorubicin has been utilized as a model drug in these early investigations, it is easy to envision this approach applied to other chemotherapeutics as well. Another attractive prospect using this chemical technology is the incorporation of a radiolabeled tetrazine into this approach, an alteration which could enable the *in vivo* monitoring of drug release and possibly even facilitate combined chemo- and radiotherapy.

The Bottom Line

Over the last several years, advancements in radiochemistry have yielded an abundance of synthetic methodologies which can now be used to generate radiopharmaceuticals previously considered too complex and time-consuming to synthesize. The incorporation of click chemistry reactions into the radiochemistry toolbox is a particularly notable advancement. Click chemistry offers a mild, rapid, and high-yielding approach for the radiolabeling of heat-sensitive biomacromolecules such as proteins and antibodies. The use of click chemistry to radiolabel smaller vectors such as peptides and small molecules requires more careful consideration, as the comparatively bulky groups created by click chemistry ligations are more likely to affect the ligand-binding properties and *in vivo* behaviour of these constructs. Lastly, the IEDDA cycloaddition is well-placed to facilitate *in vivo* pretargeted imaging and therapy. Continual refinements to the underlying chemistry have resulted in a highly optimized technology which is now poised for evaluation in patients.

References

1. Kolb HC, Finn MG, Sharpless KB. Click chemistry: diverse chemical function from a few good reactions. Angew Chem Int Ed Engl. 2001;40(11):2004–21.
2. Nwe K, Brechbiel MW. Growing applications of "click chemistry" for bioconjugation in contemporary biomedical research. Cancer Biother Radiopharm. 2009;24(3):289–302.
3. Wängler C, Schirrmacher R, Bartenstein P, Wängler B. Click-chemistry reactions in radiopharmaceutical chemistry: fast & easy introduction of radiolabels into biomolecules for in vivo imaging. Curr Med Chem. 2010;17(11):1092–116.
4. Marik J, Sutcliffe JL. Click for PET: rapid preparation of [18F] fluoropeptides using CuI catalyzed 1,3-dipolar cycloaddition. Tetrahedron Lett. 2006;47(37):6681–4.
5. Hausner SH, Marik J, Gagnon MKJ, Sutcliffe JL. In vivo positron emission tomography (PET) imaging with an $\alpha v\beta 6$ specific peptide radiolabeled using 18F-"click" chemistry: evaluation and comparison with the corresponding 4-[18F]fluorobenzoyl- and 2-[18F] fluoropropionyl-peptides. J Med Chem. 2008;51(19):5901–4.
6. Li ZB, Wu Z, Chen K, Chin FT, Chen X. Click chemistry for 18F-labeling of RGD peptides and microPET imaging of tumor integrin $\alpha v\beta 3$ expression. Biconjug Chem. 2007;18(6):1987–94.
7. Richter S, Wuest F. 18F-Labeled Peptides: The future is bright. Molecules. 2014;19(12):20536.
8. Kettenbach K, Schieferstein H, Ross TL. 18F-labeling using click cycloadditions. Biomed Res Int. 2014;2014:16.
9. Jacobson O, Kiesewetter DO, Chen X. Fluorine-18 radiochemistry, labeling strategies and synthetic routes. Biconjug Chem. 2015;26(1):1–18.
10. Miller PW, Long NJ, Vilar R, Gee AD. Synthesis of 11C, 18F, 15O, and 13N radiolabels for positron emission tomography. Angew Chem Int Ed Engl. 2008;47(47):8998–9033.
11. Preshlock S, Tredwell M, Gouverneur V. 18F-labeling of arenes and heteroarenes for applications in positron emission tomography. Chem Rev. 2016;116(2):719–66.
12. Brooks AF, Topczewski JJ, Ichiishi N, Sanford MS, Scott PJH. Late-stage [18F]fluorination: new solutions to old problems. Chem Sci. 2014;5(12):4545–53.
13. Rostovtsev VV, Green LG, Fokin VV, Sharpless KB. A stepwise huisgen cycloaddition process: copper(I)-catalyzed regioselective "ligation" of azides and terminal alkynes. Angew Chem Int Ed Engl. 2002;41(14):2596–9.
14. Huisgen R. 1,3-dipolar cycloadditions. Past and future. Angew Chem Int Ed Engl. 1963;2(10):565–98.
15. Huisgen R. Kinetics and mechanism of 1,3-dipolar cycloadditions. Angew Chem Int Ed Engl. 1963;2(11):633–45.
16. Tornøe CW, Christensen C, Meldal M. Peptidotriazoles on solid phase: [1,2,3]-Triazoles by regiospecific copper(I)-catalyzed 1,3-dipolar cycloadditions of terminal alkynes to azides. J Organ Chem. 2002;67(9):3057–64.
17. Ross TL, Honer M, Lam PYH, Mindt TL, Groehn V, Schibli R, et al. Fluorine-18 click radiosynthesis and preclinical evaluation of a new 18F-labeled folic acid derivative. Biconjug Chem. 2008;19(12):2462–70.

18. Glaser M, Årstad E. "Click labeling" with 2-[18F]fluoroethylazide for positron emission tomography. Biconjug Chem. 2007;18(3):989–93.
19. Glaser M, Goggi J, Smith G, Morrison M, Luthra SK, Robins E, et al. Improved radiosynthesis of the apoptosis marker 18F-ICMT11 including biological evaluation. Bioorg Med Chem Lett. 2011;21(23):6945–9.
20. Ackermann U, O'Keefe G, Lee ST, Rigopoulos A, Cartwright G, Sachinidis JI, et al. Synthesis of a [18F]fluoroethyltriazolylthymidine radiotracer from [18F]2-fluoroethyl azide and 5-ethynyl-2′-deoxyuridine. J Labelled Comp Radiopharm. 2011;54(5):260–6.
21. Smith G, Glaser M, Perumal M, Nguyen QD, Shan B, Årstad E, et al. Design, synthesis, and biological characterization of a caspase 3/7 selective isatin labeled with 2-[18f]fluoroethylazide. J Med Chem. 2008;51(24):8057–67.
22. Zhou D, Chu W, Peng X, McConathy J, Mach RH, Katzenellenbogen JA. Facile purification and click labeling with 2-[18F]fluoroethyl azide using solid phase extraction cartridges. Tetrahedron Lett. 2015;56(7):952–4.
23. Schirrmacher R, Lakhrissi Y, Jolly D, Goodstein J, Lucas P, Schirrmacher E. Rapid in situ synthesis of [11C]methyl azide and its application in 11C click-chemistry. Tetrahedron Lett. 2008;49(33):4824–7.
24. Mindt TL, Müller C, Melis M, De Jong M, Schibli R. "Click-to-chelate": in vitro and in vivo comparison of a 99mTc(CO)3-labeled N(τ)-histidine folate derivative with its isostructural, clicked 1,2,3-triazole analogue. Biconjug Chem. 2008;19(8):1689–95.
25. Agard NJ, Prescher JA, Bertozzi CR. A strain-promoted [3 + 2] azide-alkyne cycloaddition for covalent modification of biomolecules in living systems. J Am Chem Soc. 2004;126(46):15046–7.
26. Dommerholt J, Rutjes FPJT, van Delft FL. Strain-promoted 1,3-dipolar cycloaddition of cycloalkynes and organic azides. Top Curr Chem. 2016;374(2):16.
27. Mbua NE, Guo J, Wolfert MA, Steet R, Boons GJ. Strain-promoted alkyne-azide cycloadditions (SPAAC) reveal new features of glycoconjugate biosynthesis. Chembiochem. 2011;12(12):1912–21.
28. Nikić I, Kang JH, Girona GE, Aramburu IV, Lemke EA. Labeling proteins on live mammalian cells using click chemistry. Nat Protoc. 2015;10:780.
29. Stockmann H, Neves AA, Stairs S, Ireland-Zecchini H, Brindle KM, Leeper FJ. Development and evaluation of new cyclooctynes for cell surface glycan imaging in cancer cells. Chem Sci. 2011;2(5):932–6.
30. Turner RB, Jarrett AD, Goebel P, Mallon BJ. Heats of hydrogenation. IX. Cyclic acetylenes and some miscellaneous olefins. J Am Chem Soc. 1973;95(3):790–2.
31. Jewett JC, Bertozzi CR. Cu-free click cycloaddition reactions in chemical biology. Chem Soc Rev. 2010;39(4):1272–9.
32. Baskin JM, Prescher JA, Laughlin ST, Agard NJ, Chang PV, Miller IA, et al. Copper-free click chemistry for dynamic in vivo imaging. Proc Acad Sci USA. 2007;104(43):16793–7.
33. McKay Craig S, Finn MG. Click chemistry in complex mixtures: bioorthogonal bioconjugation. Chem Biol. 2014;21(9):1075–101.
34. Codelli JA, Baskin JM, Agard NJ, Bertozzi CR. Second-generation difluorinated cyclooctynes for copper-free click chemistry. J Am Chem Soc. 2008;130(34):11486–93.
35. Varga BR, Kállay M, Hegyi K, Béni S, Kele P. A non-fluorinated monobenzocyclooctyne for rapid copper-free click reactions. Chemistry. 2012;18(3):822–8.
36. Ning X, Guo J, Wolfert MA, Boons GJ. Visualizing metabolically labeled glycoconjugates of living cells by copper-free and fast huisgen cycloadditions. Angew Chem Int Ed Engl. 2008;47(12):2253–5.
37. Jewett JC, Sletten EM, Bertozzi CR. Rapid Cu-free click chemistry with readily synthesized biarylazacyclooctynones. J Am Chem Soc. 2010;132(11):3688–90.
38. Dommerholt J, Schmidt S, Temming R, Hendriks LJA, Rutjes FPJT, Van Hest JCM, et al. Readily accessible bicyclononynes for bioorthogonal labeling and three-dimensional imaging of living cells. Angew Chem Int Ed Engl. 2010;49(49):9422–5.
39. Gordon CG, Mackey JL, Jewett JC, Sletten EM, Houk KN, Bertozzi CR. Reactivity of biarylazacyclooctynones in copper-free click chemistry. J Am Chem Soc. 2012;134(22):9199–208.
40. Bouvet V, Wuest M, Wuest F. Copper-free click chemistry with the short-lived positron emitter fluorine-18. Org Biomol Chem. 2011;9(21):7393–9.
41. Hausner SH, Carpenter RD, Bauer N, Sutcliffe JL. Evaluation of an integrin αvβ6-specific peptide labeled with [18F]fluorine by copper-free, strain-promoted click chemistry. Nucl Med Biol. 2013;40(2):233–9.
42. Knall A-C, Slugovc C. Inverse electron demand Diels-Alder (iEDDA)-initiated conjugation: a (high) potential click chemistry scheme. Chem Soc Rev. 2013;42(12):5131–42.
43. Thalhammer F, Wallfahrer U, Sauer J. Reaktivität einfacher offenkettiger und cyclischer dienophile bei Diels-Alder-reaktionen mit inversem elektronenbedarf. Tetrahedron Lett. 1990;31(47):6851–4.
44. Selvaraj R, Fox JM. trans-Cyclooctene—a stable, voracious dienophile for bioorthogonal labeling. Curr Opin Chem Biol. 2013;17(5):753–60.
45. Schoch J, Staudt M, Samanta A, Wiessler M, Jäschke A. Site-specific one-pot dual labeling of DNA by orthogonal cycloaddition chemistry. Biconjug Chem. 2012;23(7):1382–6.
46. Karver MR, Weissleder R, Hilderbrand SA. Synthesis and evaluation of a series of 1,2,4,5-tetrazines for bioorthogonal conjugation. Biconjug Chem. 2011;22(11):2263–70.
47. Lang K, Davis L, Wallace S, Mahesh M, Cox DJ, Blackman ML, et al. Genetic encoding of bicyclononynes and trans-cyclooctenes for site-specific protein labeling in vitro and in live mammalian cells via rapid fluorogenic diels–alder reactions. J Am Chem Soc. 2012;134(25):10317–20.
48. Blackman ML, Royzen M, Fox JM. Tetrazine ligation: fast bioconjugation based on inverse-electron-demand diels−alder reactivity. J Am Chem Soc. 2008;130(41):13518–9.
49. Taylor MT, Blackman ML, Dmitrenko O, Fox JM. Design and synthesis of highly reactive dienophiles for the tetrazine-trans-cyclooctene ligation. J Am Chem Soc. 2011;133(25):9646–9.
50. Liang Y, Mackey JL, Lopez SA, Liu F, Houk KN. Control and design of mutual orthogonality in bioorthogonal cycloadditions. J Am Chem Soc. 2012;134(43):17904–7.
51. Neves AA, Stöckmann H, Wainman YA, Kuo JCH, Fawcett S, Leeper FJ, et al. Imaging cell surface glycosylation in vivo using "double click" chemistry. Biconjug Chem. 2013;24(6):934–41.
52. Li Z, Cai H, Hassink M, Blackman ML, Brown RCD, Conti PS, et al. Tetrazine-trans-cyclooctene ligation for the rapid construction of 18F labeled probes. Chem Commun (Cambridge). 2010;46(42):8043–5.
53. Keliher EJ, Reiner T, Turetsky A, Hilderbrand SA, Weissleder R. High-yielding, two-step 18F labeling strategy for 18F-PARP1 inhibitors. ChemMedChem. 2011;6(3):424–7.
54. Reiner T, Lacy J, Keliher EJ, Yang KS, Ullal A, Kohler RH, et al. Imaging therapeutic PARP inhibition in vivo through bioorthogonally developed companion imaging agents. Neoplasia. 2012;14:169–77.
55. Selvaraj R, Liu S, Hassink M. Huang C-w, Yap L-p, Park R, et al. Tetrazine-trans-cyclooctene ligation for the rapid construction of integrin αvβ3 targeted PET tracer based on a cyclic RGD peptide. Bioorg Med Chem Lett. 2011;21(17):5011–4.
56. Liu S, Hassink M, Selvaraj R, Yap L-P, Park R, Wang H, et al. Efficient ^{18}F labeling of cysteine-containing peptides and proteins using tetrazine-trans-cyclooctene ligation. Mol Imaging. 2013;12(2):121–8.

57. Wu Z, Liu S, Hassink M, Nair I, Park R, Li L, et al. Development and evaluation of 18F-TTCO-Cys40-Exendin-4: A PET probe for imaging transplanted islets. J Nucl Med. 2013;54(2):244–51.
58. Luo H, England CG, Goel S, Graves SA, Ai F, Liu B, et al. ImmunoPET and near-infrared fluorescence imaging of pancreatic cancer with a dual-labeled bispecific antibody fragment. Mol Pharm. 2017;14(5):1646–55.
59. Luo H, Hernandez R, Hong H, Graves SA, Yang Y, England CG, et al. Noninvasive brain cancer imaging with a bispecific antibody fragment, generated via click chemistry. Proc Natl Acad Sci USA. 2015;112(41):12806–11.
60. Meyer JP, Kozlowski P, Jackson J, Cunanan KM, Adumeau P, Dilling TR, et al. Exploring structural parameters for pretargeting radioligand optimization. J Med Chem 2017;60(19):8201–17.
61. Houghton JL, Membreno R, Abdel-Atti D, Cunanan KM, Carlin S, Scholz WW, et al. Establishment of the in vivo efficacy of pretargeted radioimmunotherapy utilizing inverse electron demand diels-alder click chemistry. Mol Cancer Ther. 2017;16(1):124–33.
62. Yazdani A, Bilton H, Vito A, Genady AR, Rathmann SM, Ahmad Z, et al. A Bone-seeking trans-cyclooctene for pretargeting and bioorthogonal chemistry: a proof of concept study using 99mtc- and 177lu-labeled tetrazines. J Med Chem. 2016;59(20):9381–9.
63. Cook BE, Adumeau P, Membreno R, Carnazza KE, Brand C, Reiner T, et al. Pretargeted PET imaging using a site-specifically labeled immunoconjugate. Biconjug Chem. 2016;27(8):1789–95.
64. Meyer JP, Houghton JL, Kozlowski P, Abdel-Atti D, Reiner T, Pillarsetty NVK, et al. 18F-based pretargeted PET imaging based on bioorthogonal Diels-Alder click chemistry. Biconjug Chem. 2016;27(2):298–301.
65. Adumeau P, Carnazza KE, Brand C, Carlin SD, Reiner T, Agnew BJ, et al. A pretargeted approach for the multimodal PET/NIRF imaging of colorectal cancer. Theranostics. 2016;6(12):2267–77.
66. Zeglis BM, Brand C, Abdel-Atti D, Carnazza KE, Cook BE, Carlin S, et al. Optimization of a pretargeted strategy for the PET imaging of colorectal carcinoma via the modulation of radioligand pharmacokinetics. Mol Pharm. 2015;12(10):3575–87.
67. Zeglis BM, Sevak KK, Reiner T, Mohindra P, Carlin SD, Zanzonico P, et al. A pretargeted PET imaging strategy based on bioorthogonal Diels-Alder click chemistry. J Nucl Med. 2013;54(8):1389–96.
68. Altai M, Perols A, Tsourma M, Mitran B, Honarvar H, Robillard M, et al. Feasibility of affibody-based bioorthogonal chemistry-mediated radionuclide pretargeting. J Nucl Med. 2016;57(3):431–6.
69. Van Duijnhoven SMJ, Rossin R, Van Den Bosch SM, Wheatcroft MP, Hudson PJ, Robillard MS. Diabody pretargeting with click chemistry in vivo. J Nucl Med. 2015;56(9):1422–8.
70. Rossin R, Van Duijnhoven SMJ, Läppchen T, Van Den Bosch SM, Robillard MS. Trans-cyclooctene tag with improved properties for tumor pretargeting with the Diels-Alder reaction. Mol Pharm. 2014;11(9):3090–6.
71. Rossin R, Robillard MS. Pretargeted imaging using bioorthogonal chemistry in mice. Curr Opin Chem Biol. 2014;21:161–9.
72. Rossin R, Läppchen T, Van Den Bosch SM, Laforest R, Robillard MS. Diels-alder reaction for tumor pretargeting: in vivo chemistry can boost tumor radiation dose compared with directly labeled antibody. J Nucl Med. 2013;54(11):1989–95.
73. Rossin R, Van Den Bosch SM, Ten Hoeve W, Carvelli M, Versteegen RM, Lub J, et al. Highly reactive trans-cyclooctene tags with improved stability for diels-alder chemistry in living systems. Biconjug Chem. 2013;24(7):1210–7.
74. Rossin R, Verkerk PR, Van Den Bosch SM, Vulders RCM, Verel I, Lub J, et al. In vivo chemistry for pretargeted tumor imaging in live mice. Angew Chem Int Ed Engl. 2010;49(19):3375–8.
75. Keinänen O, Li XG, Chenna NK, Lumen D, Ott J, Molthoff CFM, et al. A new highly reactive and low lipophilicity Fluorine-18 labeled tetrazine derivative for pretargeted PET imaging. ACS Med Chem Lett. 2016;7(1):62–6.
76. Keinänen O, Mäkilä EM, Lindgren R, Virtanen H, Liljenbäck H, Oikonen V, et al. Pretargeted PET imaging of trans-cyclooctene-modified porous silicon nanoparticles. ACS Omega. 2017;2(1):62–9.
77. Knight JC, Richter S, Wuest M, Way JD, Wuest F. Synthesis and evaluation of an 18F-labelled norbornene derivative for copper-free click chemistry reactions. Org Biomol Chem. 2013;11(23):3817–25.
78. Zeglis BM, Mohindra P, Weissmann GI, Divilov V, Hilderbrand SA, Weissleder R, et al. Modular strategy for the construction of radiometalated antibodies for positron emission tomography based on inverse electron demand diels-alder click chemistry. Bioconjug Chem. 2011;22(10):2048–59.
79. Keliher EJ, Reiner T, Thurber GM, Upadhyay R, Weissleder R. Efficient 18F-labeling of synthetic Exendin-4 analogues for imaging beta cells. ChemistryOpen. 2012;1(4):177–83.
80. Altai M, Membreno R, Cook B, Tolmachev V, Zeglis BM. Pretargeted imaging and therapy. J Nucl Med. 2017;58(10):1553–9.
81. van de Watering FC, Rijpkema M, Robillard M, Oyen WJ, Boerman OC. Pretargeted imaging and radioimmunotherapy of cancer using antibodies and bioorthogonal chemistry. Front Med (Lausanne). 2014;1:44.
82. Knight JC, Cornelissen B. Bioorthogonal chemistry: implications for pretargeted nuclear (PET/SPECT) imaging and therapy. Am J Nucl Med Mol Imaging. 2014;4(2):96–113.
83. Börjesson PKE, Jauw YWS, Boellaard R, De Bree R, Comans EFI, Roos JC, et al. Performance of immuno – positron emission tomography with zirconium-89-labeled chimeric monoclonal antibody U36 in the detection of lymph node metastases in head and neck cancer patients. Clin Cancer Res. 2006;12(7 Pt 1):2133–40.
84. Dijkers EC, Oude Munnink TH, Kosterink JG, Brouwers AH, Jager PL, De Jong JR, et al. Biodistribution of 89 Zr-trastuzumab and PET imaging of HER2-positive lesions in patients with metastatic breast cancer. Clin Pharmacol Ther. 2010;87(5):586–92.
85. Rizvi SN, Visser OJ, Vosjan MJ, Van Lingen A, Hoekstra OS, Zijlstra JM, et al. Biodistribution, radiation dosimetry and scouting of 90Y- ibritumomab tiuxetan therapy in patients with relapsed B-cell non-Hodgkin‘s lymphoma using 89Zr-ibritumomab tiuxetan and PET. Eur J Nucl Med Mol Imaging. 2012;39(3):512–20.
86. Gaykema SBM, Brouwers AH, Hooge MNLD, Pleijhuis RG, Timmer-Bosscha H, Pot L, et al. 89Zr-bevacizumab PET imaging in primary breast cancer. J Nucl Med. 2013;54(7):1014–8.
87. Menke-van der Houven van Oordt CW, Gootjes EC, Huisman MC, Vugts DJ, Roth C, Luik AM, et al. 89Zr-cetuximab PET imaging in patients with advanced colorectal cancer. Oncotarget. 2015;6(30):30384–93.
88. Muylle K, Flamen P, Vugts DJ, Guiot T, Ghanem G, Meuleman N, et al. Tumour targeting and radiation dose of radioimmunotherapy with 90Y-rituximab in CD20+ B-cell lymphoma as predicted by 89Zr-rituximab immuno-PET: impact of preloading with unlabelled rituximab. Eur J Nucl Med Mol Imaging. 2015;42(8):1304–14.
89. Laforest R, Lapi SE, Oyama R, Bose R, Tabchy A, Marquez-Nostra BV, et al. [89Zr]Trastuzumab: evaluation of radiation dosimetry, safety, and optimal imaging parameters in women with HER2-positive breast cancer. Mol Imaging Biol. 2016;18(6):952–9.
90. Hnatowich DJ, Virzi F, Rusckowski M. Investigations of avidin and biotin for imaging applications. J Nucl Med. 1987;28(8):1294–302.
91. Green NM. Avidin and streptavidin. Methods Enzymol. 1990;184:51–67.

92. Liu G, Dou S, Liu Y, Wang Y, Rusckowski M, Hnatowich DJ. 90Y labeled phosphorodiamidate morpholino oligomer for pretargeting radiotherapy. Bioconjug Chem. 2011;22(12):2539–45.
93. Liu G, Dou S, Cheng D, Leif J, Rusckowski M, Streeter PR, et al. Human islet cell MORF/cMORF pretargeting in a xenogeneic murine transplant model. Mol Pharm. 2011;8(3):767–73.
94. He J, Wang Y, Dou S, Liu X, Zhang S, Liu G, et al. Affinity enhancement pretargeting: synthesis and testing of a 99mTc-labeled bivalent MORF. Mol Pharm. 2010;7(4):1118–24.
95. Liu G, Liu C, Zhang S, He J, Liu N, Gupta S, et al. Investigations of ^{99m}Tc morpholino pretargeting in mice. Nucl Med Commun. 2003;24(6):697–705.
96. He J, Liu G, Gupta S, Zhang Y, Rusckowski M, Hnatowich DJ. Amplification targeting: a modified pretargeting approach with potential for signal amplification—proof of a concept. J Nucl Med. 2004;45(6):1087–95.
97. Liu G, Cheng D, Dou S, Chen X, Liang M, Pretorius PH, et al. Replacing 99mTc with 111In improves MORF/cMORF pretargeting by reducing intestinal accumulation. Mol Imaging Biol. 2009;11(5):303–7.
98. Liu G, Dou S, Rusckowski M, Hnatowich DJ. An experimental and theoretical evaluation of the influence of pretargeting antibody on the tumor accumulation of effector. Mol Cancer Ther. 2008;7(5):1025–32.
99. Liu G, Dou S, Baker S, Akalin A, Cheng D, Chen L, et al. A preclinical ^{188}Re tumor therapeutic investigation using MORF/cMORF pretargeting and an antiTAG-72 antibody CC49. Cancer Biol Ther. 2010;10(8):767–74.
100. Wang Y, Chang F, Zhang Y, Liu N, Liu G, Gupta S, et al. Pretargeting with amplification using polymeric peptide nucleic acid. Biconjug Chem. 2001;12(5):807–16.
101. He J, Rusckowski M, Wang Y, Dou S, Liu X, Zhang S, et al. Optical pretargeting of tumor with fluorescent MORF oligomers. Mol Imaging Biol. 2007;9(1):17–23.
102. Knight JC, Mosley M, Uyeda HT, Cong M, Fan F, Faulkner S, et al. In vivo pretargeted imaging of HER2 and TAG-72 expression using the halotag enzyme. Mol Pharm. 2017;14(7):2307–13.
103. Knight JC, Mosley M, Stratford MRL, Uyeda HT, Benink HA, Cong M, et al. Development of an enzymatic pretargeting strategy for dual-modality imaging. Chem Commun. 2015;51(19):4055–8.
104. Rossin R, Renart Verkerk P, van den Bosch SM, Vulders RCM, Verel I, Lub J, et al. In vivo chemistry for pretargeted tumor imaging in live mice. Angew Chem. 2010;122(19):3447–50.
105. Läppchen T, Rossin R, van Mourik TR, Gruntz G, Hoeben FJM, Versteegen RM, et al. DOTA-tetrazine probes with modified linkers for tumor pretargeting. Nucl Med Biol. 2017;55:19–26.
106. Zeglis BM, Davis CB, Abdel-Atti D, Carlin SD, Chen A, Aggeler R, et al. Chemoenzymatic strategy for the synthesis of site-specifically labeled immunoconjugates for multimodal PET and optical imaging. Bioconjug Chem. 2014;25(12):2123–8.
107. Zeglis BM, Davis CB, Aggeler R, Kang HC, Chen A, Agnew BJ, et al. Enzyme-mediated methodology for the site-specific radiolabeling of antibodies based on catalyst-free click chemistry. Biconjug Chem. 2013;24(6):1057–67.
108. Dennler P, Chiotellis A, Fischer E, Brégeon D, Belmant C, Gauthier L, et al. Transglutaminase-based chemo-enzymatic conjugation approach yields homogeneous antibody–drug conjugates. Biconjug Chem. 2014;25(3):569–78.
109. Versteegen RM, Rossin R, ten Hoeve W, Janssen HM, Robillard MS. Click to release: instantaneous doxorubicin elimination upon tetrazine ligation. Angew Chem Int Ed Engl. 2013;52(52):14112–6.
110. Rossin R, van Duijnhoven SMJ, ten Hoeve W, Janssen HM, Kleijn LHJ, Hoeben FJM, et al. Triggered drug release from an antibody–drug conjugate using fast "click-to-release" chemistry in mice. Biconjug Chem. 2016;27(7):1697–706.

Equipment and Instrumentation for Radiopharmaceutical Chemistry

Stephen Thompson and Peter J. H. Scott

Fundamentals

The short half-lives of positron-emitting radionuclides – typically minutes to hours – means that positron emission tomography (PET) radiopharmaceuticals need to be synthesized and used on the same day. In light of this, PET Centers are composed of multidisciplinary teams of cyclotron engineers, chemists and radiochemists, quality control chemists, quality assurance specialists, preclinical imaging scientists (responsible for autoradiography, biodistribution, and preclinical PET imaging experiments), couriers (if the offsite distribution of the radiopharmaceutical is planned), study coordinators, PET technologists, medical physicists, nuclear pharmacists, and nuclear medicine physicians/radiologists. PET Centers are also subject to extensive regulatory oversight aimed at ensuring the safe, secure, and effective use of radioactivity from the perspectives of both the workers (*e.g.* Occupational Health and Safety, Nuclear Regulatory Commission) and the patients (*e.g.* US Food and Drug Administration) [1].

Each of these subgroups of team members has at its disposal state-of-the-art equipment that is highly tuned to the needs of PET Center operations from bench-to-bedside (Fig. 1). This equipment includes systems dedicated to the production of radionuclides, the synthesis and quality control analysis of radiopharmaceuticals, preclinical and clinical imaging, and safety monitoring. In this chapter, we review the major equipment used by radiochemists and imaging scientists on a daily basis to take a PET radiopharmaceutical from bench-to-bedside in a manner that is compliant with Current Good Manufacturing Practice (cGMP), radiation safety practices, and other pertinent regulations. We also turn our gaze to the future, imagining what the PET Center of tomorrow will look like when all the equipment is connected through the Internet of Things (IoT) [2].

S. Thompson · P. J. H. Scott (✉)
Department of Radiology, University of Michigan, Ann Arbor, MI, USA
e-mail: pjhscott@umich.edu

Instrumentation Used for the Regulatory Oversight of PET Centers

Dosimeters

Radiation exposure to personnel within the radiochemistry facility is often monitored with personal dosimeters and dosimeter badges. The former is an electronic device that enables the real-time detection of radiation levels in a radioactive materials (RAM) area. Personal dosimeters usually feature programmable alarms with visual, audible, and vibrating alarm indicators that are triggered when programmed radiation limits are exceeded. Dosimeter badges – such as the commonly used Landauer Luxel® + whole body dosimeter and corresponding finger rings (Fig. 2) – measure radiation exposure due to x-ray, gamma, and beta radiation over a given time period (*e.g.* weekly, monthly, or quarterly) using optically stimulated luminescence (OSL).The Luxel® + dosimeter's OSL radiation detector is a thin strip of crystalline aluminum oxide. After the completion of the wear period, the dosimeter badge is returned to the manufacturer for analysis. During analysis, the aluminum oxide strip is stimulated with light, which causes it to luminesce proportionally to both the frequency of the stimulating light and the amount of radiation to which the badge has been exposed. These data are then returned in a report to the radiation worker (and their employer), allowing for the continual monitoring of the radiation exposure to the worker during performance of his or her duties.

Ionization Chambers

Early in the twentieth century, ionization chambers (ion chambers) – simple gas-filled radiation detectors containing two electrodes – were being used for the detection and measurement of radioactivity (Fig. 3, *left*). Ion chambers remain in widespread use today (Fig. 3, *right*) and operate by recording all the charges resulting from direct ionization within the

J. S. Lewis et al. (eds.), *Radiopharmaceutical Chemistry*, https://doi.org/10.1007/978-3-319-98947-1_27

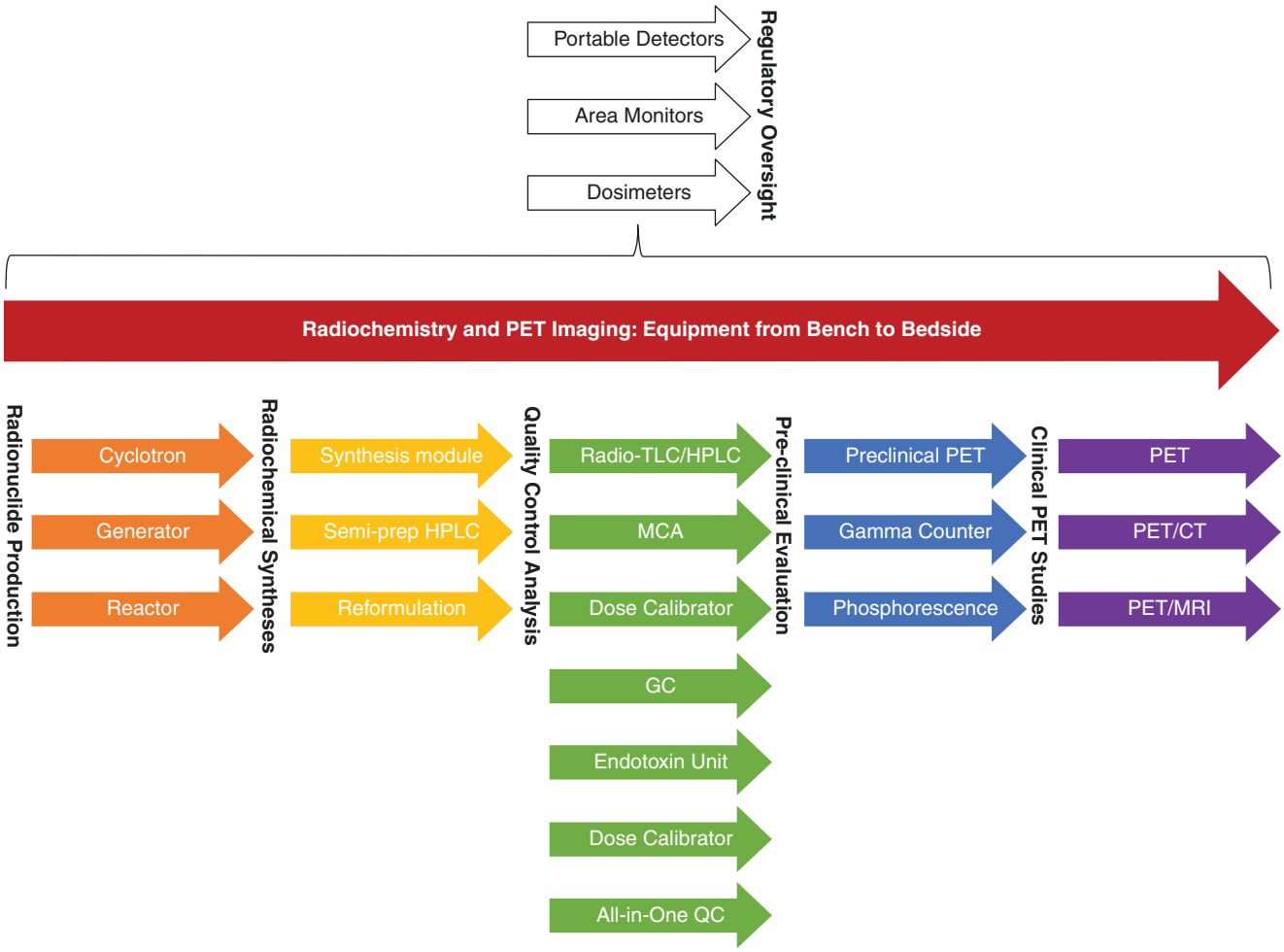

Fig. 1 Equipment in the modern positron emission tomography center

Fig. 2 Badge and ring dosimeters

Fig. 3 *Left:* Ionization chamber made by Pierre Curie, c 1895–1900. (Courtesy of Science Museum London/Science and Society Picture Library and Available under a Creative Commons Attribution Sharealike 2.0 Generic License [CC BY-SA 2.0]); *Right:* Modern ion chamber

gas caused by incidental radiation through the simple application of an electric field. For beta/gamma instruments, there is a sliding window on the bottom that allows discrimination between beta and gamma radiation. The window is closed to exclude beta particles, and such instruments are therefore capable of providing the rate of each radiation type. They are particularly useful in PET Centers for making dose rate measurements in laboratories and in proximity to equipment such as cyclotrons, hot cells, and synthesis modules. Having accurate knowledge of dose rates allows radiation workers to make decisions about when to enter such spaces and/or service the equipment in a safe manner.

Radioactivity Counters

Portable radioactivity counters were developed by a German physicist named Heinz Geiger. Initially, Geiger – working with Ernst Rutherford at the University of Manchester – developed a method of counting the number of α-particles from radioactive substances [3]. Subsequently, he refined this technique with Walther Müller, and, in 1928, they reported the Geiger–Müller (GM) tube that was capable of detecting different types of radioactivity [4]. GM tubes are filled with an inert gas (*e.g.* He, Ne, or Ar), and a high voltage is applied. Incidental radiation makes the gas conductive by ionization, causing the GM tube to conduct electrical charge. This initial ionization event is amplified in the tube due to the Townsend discharge, a gas ionization process in which the free electron liberated by the incident radioactivity is accelerated in the electric field, causing further ionization events by impacting molecules and giving rise to additional electrons [5]. The resulting "avalanche multiplication" leads to electrical conduction through the gas and produces a detection pulse that can be readily measured. GM detectors, equipped with either a GM tube (Fig. 4, *left*) or pancake probe (Fig. 4, *right*), are more sensitive to low levels of radiation than ion chambers,

Fig. 4 Geiger–Müller tubes

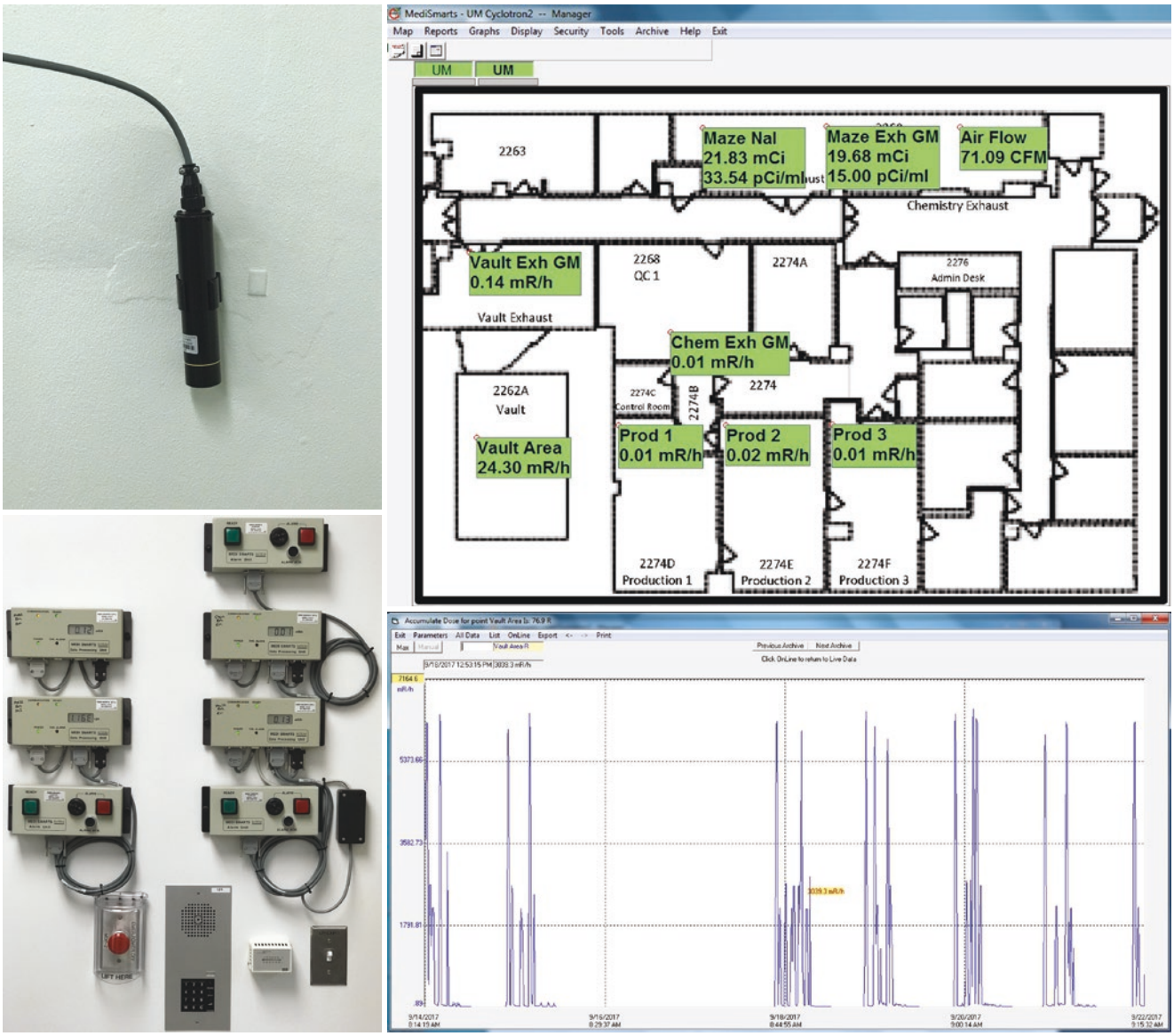

Fig. 5 Positron emission tomography center area monitors

making them ideal for detecting smaller amounts of radioactivity (e.g., identifying contamination to a laboratory or personnel, surveying radioactive trash, *etc*.).

Area Monitors

Comprehensive radiation monitoring systems are an essential part of the safety and regulatory compliance programs in place at any PET Center. For example, Rotem's MediSmarts System (Fig. 5) is a modular system consisting of GM and/or NaI detectors placed at strategic positions in the PET Center, including within cyclotron, production labs, and exhaust system. These detectors provide readouts of radiation levels on both local laboratory displays and a centralized computer. The latter displays data on a map of the laboratory, providing the user with a bird's-eye view of radiological conditions in the PET Center in real time. Both the individual laboratory displays and computer can also be programmed with custom radioactivity alarm levels that will alert workers in the PET Center if these levels are exceeded. The computer also logs all data, allowing for the retrospective analysis (in graph format) of historical readings that, for example, could be useful to estimate doses to workers in the event of a radiological incident.

Equipment for the Production of Radionuclides

Strategies for the production of positron-emitting radionuclides are covered in detail in Chap. 4. Our intent is not to duplicate this information, and as such, this section only

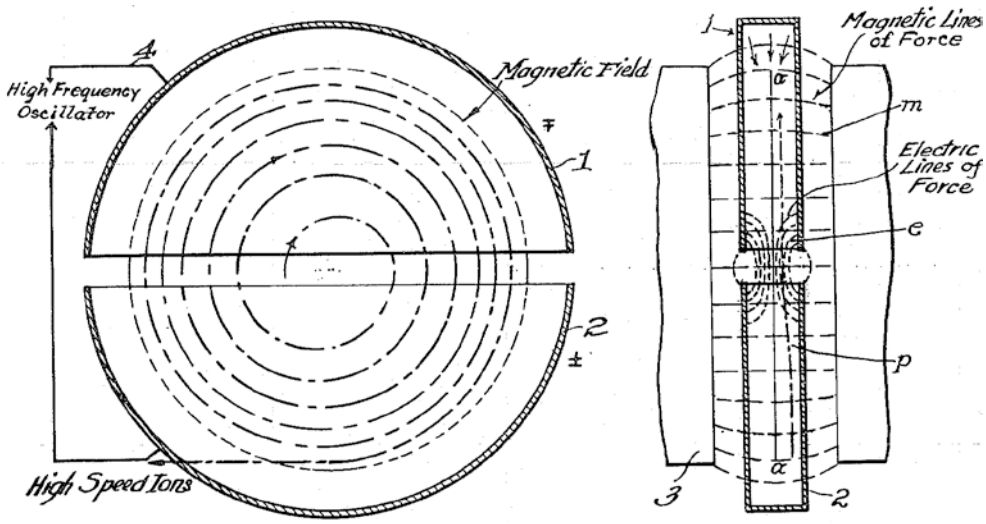

Fig. 6 Illustration of a cyclotron from Lawrence's original patent. (Image in the public domain) [6]

Fig. 7 Cyclotron fitted with multiple targets for the production of different positron emission tomography radionuclides. (Image courtesy of GE Healthcare, Chicago IL, USA). Other manufacturers of cyclotrons include IBA, Siemens, Best Cyclotron Systems, Advanced Cyclotron Systems, and Sumitomo

briefly covers the main pieces of equipment used in the production of radionuclides. Primarily this is accomplished using a cyclotron. Ernest Lawrence invented the cyclotron at the University of California, Berkeley (Fig. 6) [6], and he received the 1939 Nobel Prize in Physics for his efforts. The cyclotron operates by using a static magnetic field and a rapidly varying radiofrequency (RF) field – applied between two hollow metal electrodes (dees) inside a vacuum chamber – to accelerate charged particles. The particles in question accelerate outward from the center of the dees along a spiral path, and when they reach the edge, the beam of particles is focused to hit a remote target.

The cyclotrons used in PET Centers today typically accelerate protons (p) or deuterons (d). The former is used to make, for example, carbon-11, fluorine-18, nitrogen-13, and copper-64, while the latter can be used to produce oxygen-15. The production of radionuclides is achieved through nuclear reactions (Table 27.1) using simple gas or liquid targets specific for the nuclide of choice (Fig. 7). After the particle beam is accelerated, it is focused through an exit valve into a given target where the nuclear reaction occurs to produce the desired radionuclide. For example, to prepare fluorine-18, typically a target filled with ^{18}O-enriched water is bombarded with a proton beam. The proton enters the oxygen nucleus, transforming the element to fluorine, and the resulting unstable intermediate ejects a neutron to generate fluorine-18. Upon completion of this production process (the end of bombardment), the radionuclide is then transferred to the radiochemistry laboratory and used to manufacture the radiopharmaceutical (*vide infra*).

Table 1 Nuclear reactions for production of different PET radionuclides on a small medical cyclotron

Radionuclide	Nuclear reaction for production
^{11}C	$^{14}N(p,\alpha)^{11}C$
^{64}Cu	$^{64}Ni(p,n)^{64}Cu$
^{18}F	$^{18}O(p,n)^{18}F$
^{13}N	$^{16}O(p,\alpha)^{13}N$
^{15}O	$^{14}N(d,n)^{15}O$
^{89}Zr	$^{89}Y(p,n)\ ^{89}Zr$

Cyclotrons dominate the PET radionuclide production landscape. While the standard production of fluorine-18 requires the bombardment of a simple liquid target filled with ^{18}O-enriched water, some of the more exotic radionuclides require the bombardment of solid targets using more specialized equipment. Increasing numbers of PET Centers have the capabilities to irradiate solid targets. However, it is often easier and more cost-effective to produce longer-lived radionuclides (*e.g.* zirconium-89, $t_{1/2}$ = 3.3 days) using dedicated centralized cyclotrons [7] and then ship them to satellite labs.

More exotic PET radionuclides continue to grow in popularity, but many are not (currently) readily accessible using the small medical cyclotrons found in most PET Centers. Depending on the methods used to generate them and their half-life, some may be accessible from commercially available generators. For example, the recent FDA approval of [^{68}Ga]NETSPOT for the localization of somatostatin receptor-positive neuroendocrine tumors (NETs) has created an urgent need for a sustainable nationwide supply of gallium-68. While efforts to develop cyclotron-based production pathways for gallium-68 are underway [8], the vast majority of the current supply comes from $^{68}Ge/^{68}Ga$ generators (Fig. 8) [9]. Generators contain a matrix loaded with the parent radionuclide – germanium-68 ($t_{1/2}$ = 271 days) – which can be produced in proton accelerators. Germanium-68 decays to its daughter radionuclide, gallium-68 ($t_{1/2}$ = 68 min), by electron capture as follows:$^{68}Ge(e^-,\nu)^{68}Ga$. Gallium-68 is eluted from the generator matrix using an appropriate solution (typically HCl to generate $^{68}GaCl_3$) and used to prepare radiopharmaceuticals, often by adding the generator eluent to a kit designed for the synthesis of a given radiopharmaceutical (see Fig. 8).

Fig. 8 Gallium-68 generator and kit for the preparation of [^{68}Ga]NETSPOT. (Image courtesy of Radiomedix, Houston, Texas, USA). Manufacturers of gallium-68 generators include Isotope Technologies Garching GmbH (ITG), Eckert & Ziegler, Institute for Radioelements (IRE), and iThemba Labs

Synthesis Modules and Hot Cells for the Automated Synthesis of Radiopharmaceuticals

Once a PET radionuclide has been delivered to the laboratory (either from the cyclotron or a generator), it needs to be incorporated into a bioactive molecule. The resulting radiopharmaceutical then requires purification and formulation for injection into an animal or patient. To minimize the exposure of workers to radiation, these synthesis, purification, and formulation steps should be as automated as possible. Driven by this need, computer-controlled robotics for carrying out remote-controlled radiopharmaceutical syntheses and purifications have become increasingly integral parts of PET Centers (Fig. 9). Over the years, PET radiopharmaceutical production methods have matured, spurred in the United States by the approval of [^{18}F]fludeoxyglucose ([^{18}F]FDG) by the US FDA and its reimbursement by the Centers for Medicare and Medicaid Services (CMS). As a result, the early homemade remote synthesis apparatuses used in the 1980s [10] were replaced in the 1990s–2000s by more sophisticated, fully automated, commercially supplied radiochemistry synthesis modules to facilitate compliance with FDA regulations (see Fig. 9). These updated synthesis modules offer self-contained systems consisting of modules for receiving radioactivity from the cyclotron (or generator), and there are two main types. The first is the industry standard and consists of vials for the addition of reagents, a reaction vessel, a heater (or microwave) for conducting the radiolabeling reaction, a semi-preparative HPLC purification system, and a module for reformulating the purified radiopharmaceutical into a saline solution suitable for intravenous injection using a solid-phase extraction cartridge. While these systems are widely utilized, there remains room for improvement. To this end, a second type of microfluidic synthesis module that relies on flow chemistry has been developed. The subject has been recently reviewed [11], and microfluidic systems are purported to have advantages over traditional vessel-based systems, including the need to use fewer reagents and greater flexibility in configuration. Additional hardware advantages include a smaller footprint and reliance on fewer valves and connections, which represent potential fail points in traditional synthesis modules.

Synthesis modules are housed in lead-lined fume hoods known as hot cells and are often equipped with robot arms to minimize the need for the manual manipulation of radioactivity. Synthesis modules are then controlled by a computer located outside of the hot cell (Fig. 10). Automation allows

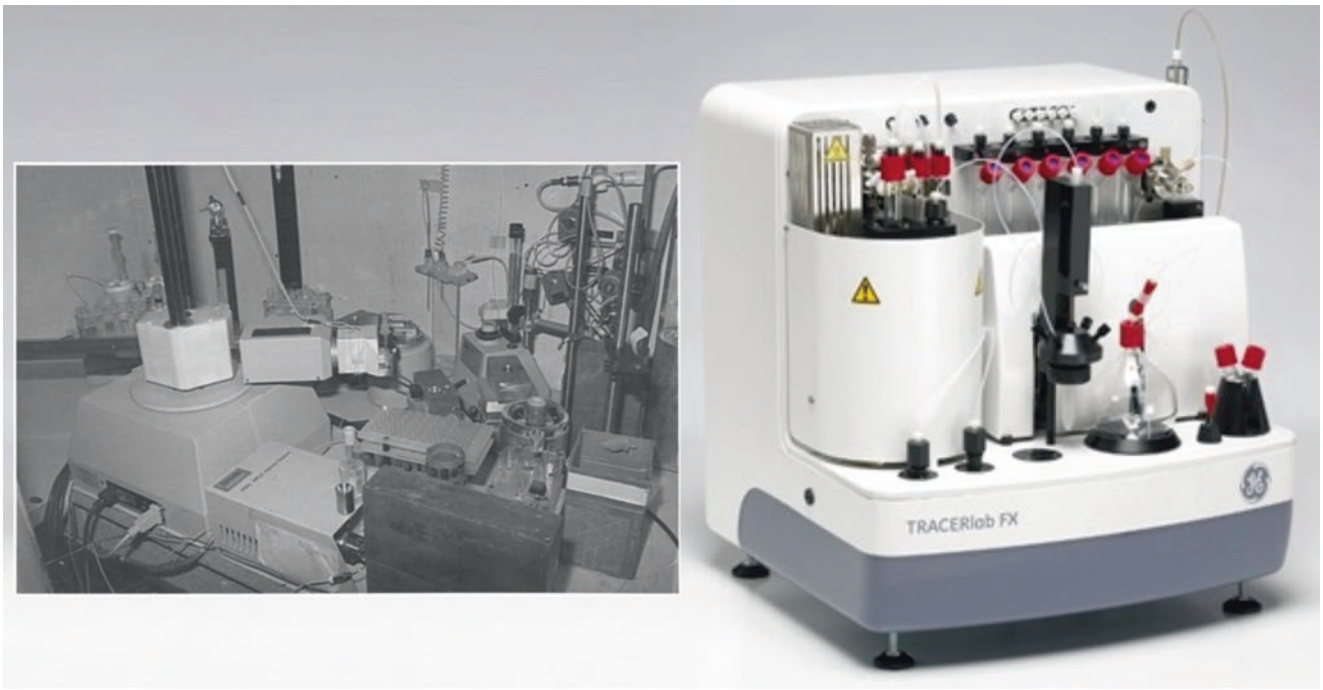

Fig. 9 Radiochemistry synthesis modules – traditional (*left*) (from Brodack *et al*. [10], with permission) and (*right*) self-contained (Image courtesy of GE Healthcare, Chicago IL, USA). Other manufacturers of similar equipment include Synthra GmbH, Siemens, IBA, iPhase Technologies, Optimized Radiochemical Applications (ORA-Neptis), Sofie Biosciences, and Advion

Fig. 10 Hot cells and the computer which controls the synthesis modules inside. Manufacturers of hot cells include Comecer (*shown*), Von Gahlen, Ultraray, Tema, MecMurphil, and Capintec

the radiochemist to set up the synthesis module and seal the hot cell before the delivery of radioactivity from the cyclotron (or generator). A computer program then controls the entire synthesis, purification, and reformulation of the radiopharmaceutical (Fig. 11), as well as the delivery of the final product into a sterile dose vial that can then be removed from the hot cell using the robotic arms.

The next major shift for radiochemists came in 2012, with the mandate that PET radiopharmaceuticals must be prepared for clinical use in accordance with cGMP standards in the United States (while in Europe, this was already required). Much of the regulatory environment surrounding PET radiopharmaceuticals is discussed in Chap. 35 and 36, but, briefly, in the United States, the PET cGMP regulations are described in 21CFR212 and enforced by FDA [1].

The new regulatory environment – and the growth in the clinical utilization of PET – has catalyzed a number of changes in the community. One of the effects of this regulatory flux is that the costs associated with manufacturing PET radiopharmaceuticals have increased considerably, an issue that is further exacerbated by the uncertain environment surrounding healthcare infrastructure and reimbursement in the United States. To cover these increasing costs, PET drug manufacturers aim to maximize uptime at their production facilities (including cyclotrons, synthesis modules, and quality control components), usually striving for >99%. To accomplish this, PET radiochemistry laboratories are invested in improving the reliability of production and minimizing unscheduled downtime caused by equipment failures.

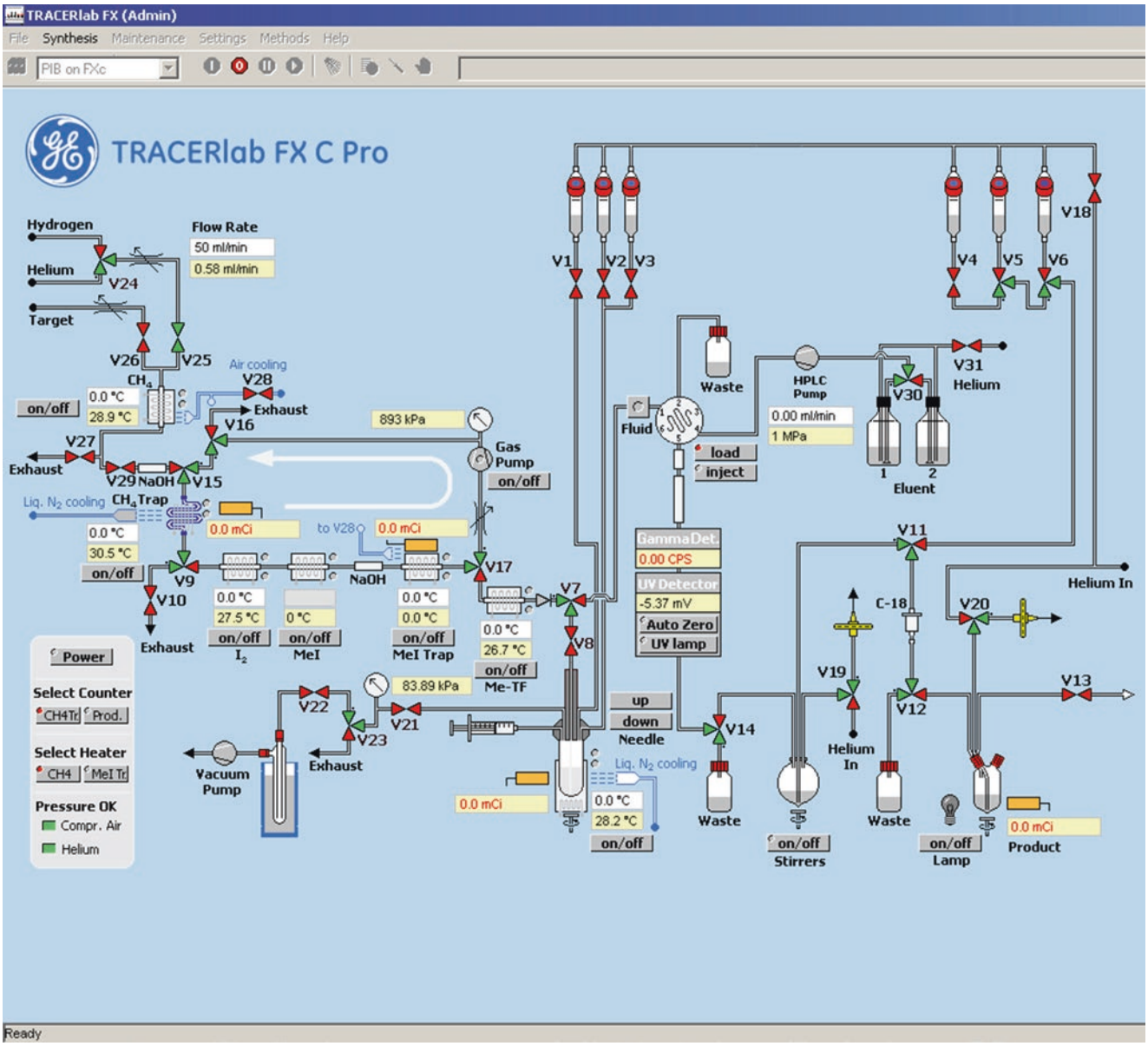

Fig. 11 A typical synthesis module user interface. Manufacturers of radiochemistry synthesis modules include General Electric (*shown*, image courtesy of GE Healthcare, Chicago IL, USA), Synthra GmbH, Siemens, IBA, iPhase Technologies, ORA-Neptis, Sofie Biosciences, and Advion

One approach to improve reliability is to upgrade production facilities to new, fully automated cassette-based synthesis systems for the routine production of radiopharmaceuticals (Fig. 12). Unlike the older automated systems described above (see Fig. 9), this new generation of modules uses cassettes preloaded with both the chemicals and components needed for synthesis and purification. Cassettes are assembled in clean rooms under cGMP conditions, irradiated with gamma radiation so they are sterile, and then finally vacuum packed. The cassette is then attached to the synthesis module, and a barcode on the cassette is read by the module and initiates the corresponding synthesis program for the cassette in question. The use of sterile, disposable cassettes ensures easy handling and increases reliability by reducing errors inherent in the manual setup and operation of older synthesis modules.

Quality Control Instruments for Radiopharmaceuticals

Quality control (QC) requirements for PET radiopharmaceuticals generally require a visual inspection to ensure that doses are clear, colorless, and free of particulate matter. In addition, doses are analyzed to determine radiochemical and chemical purity (by high-performance liquid chromatography [HPLC] or thin-layer chromatography [TLC]), residual solvent levels (by gas chromatography [GC]), pH, osmolal-

Fig. 12 A modern cassette-based synthesis module. (Image courtesy of GE Healthcare, Chicago IL). Other manufacturers of radiochemistry synthesis modules include Synthra GmbH, Siemens, IBA, iPhase Technologies, ORA-Neptis, Sofie Biosciences and Advion

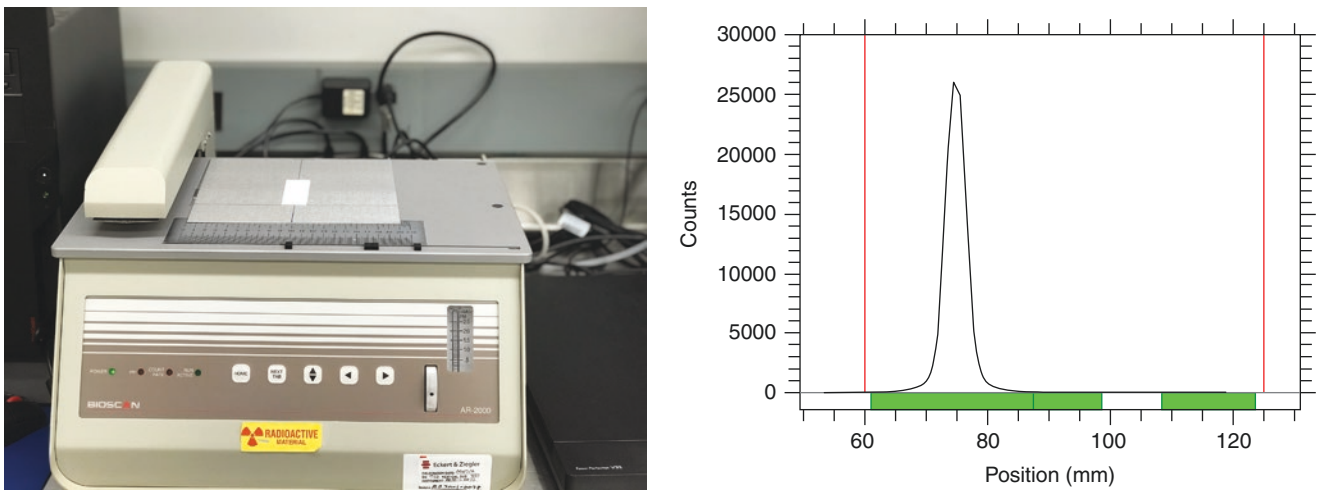

Fig. 13 Radio-thin-layer chromatography (TLC) scanner and a representative radio-TLC analysis. Manufacturers of radio-TLC scanners include Eckert & Ziegler/Bioscan (*shown*), Elysia-Raytest, Capintec, Scannix, Nucare Medical Systems, and LabLogic

ity, radionuclidic identity (by calculating half-life using a dose calibrator) and radionuclidic purity (using a multichannel analyzer), bacterial endotoxin levels, sterile filter integrity, and sterility. A detailed discussion of all of these tests is beyond the scope of this chapter, but the subject of radiopharmaceutical quality control has been covered in other books in recent years [12]. A radiopharmaceutical batch must pass all QC testing (except post-release sterility testing) before it is released to the imaging site for use in a clinical PET study.

Radio-Thin-Layer Chromatography

Analyzing radiolabeled compounds by TLC involves spotting the dose onto a silica-gel TLC plate and developing it in a solvent chamber, just as is the case in traditional organic chemistry. However, because of the low masses involved when preparing no-carrier-added radiopharmaceuticals (typically only a few μg), it is typically to co-spot a sample of unlabeled reference standard that can be visualized using standard methods (UV light, iodine stain, etc.) and then employ a dedicated radio-TLC scanner to analyze the radioactive components. In this way, the radiochemical purity of the sample can be determined using the radio-TLC scanner, while the radiochemical identity of the sample can be confirmed through a comparison of the R_f of the radiochemical peak to that of the unlabeled standard. A number of radio-TLC scanners are commercially available, although the Bioscan/Eckert & Ziegler's AR-2000 radio-TLC Imaging Scanner (Fig. 13) is the industry's gold standard, having been used for decades to analyze the radiochemical purity and identity of radiopharmaceuticals such as [^{18}F]FDG. The TLC plate is placed on the scanning bed, and the detector arm is moved over the plate. The detector arm contains counting gas (9:1 Ar:CH_4) as well as an electrode. Much like

the handheld radioactivity detectors described above, the ionization of the counting gas by interaction with radioactivity is detected, allowing for the rapid and reliable analysis of TLC plates.

Radio-HPLC

Radio-HPLC is the more sophisticated successor to radio-TLC that offers the additional benefit of quantitation. Instead of developing a plate in a TLC solvent chamber, a sample of radiopharmaceutical is injected onto a silica-packed HPLC column and eluted with an appropriate mobile phase that is pumped through the column. The combination of high pressure and carefully packed column scan provides exquisite separation of mixtures of compounds. In radio-HPLC systems, the instrument is equipped with detectors enabling the analysis of both the chemical and radiochemical purities of formulated radiopharmaceutical doses (Fig. 14). Chemical content is typically analyzed with a UV detector or – in the

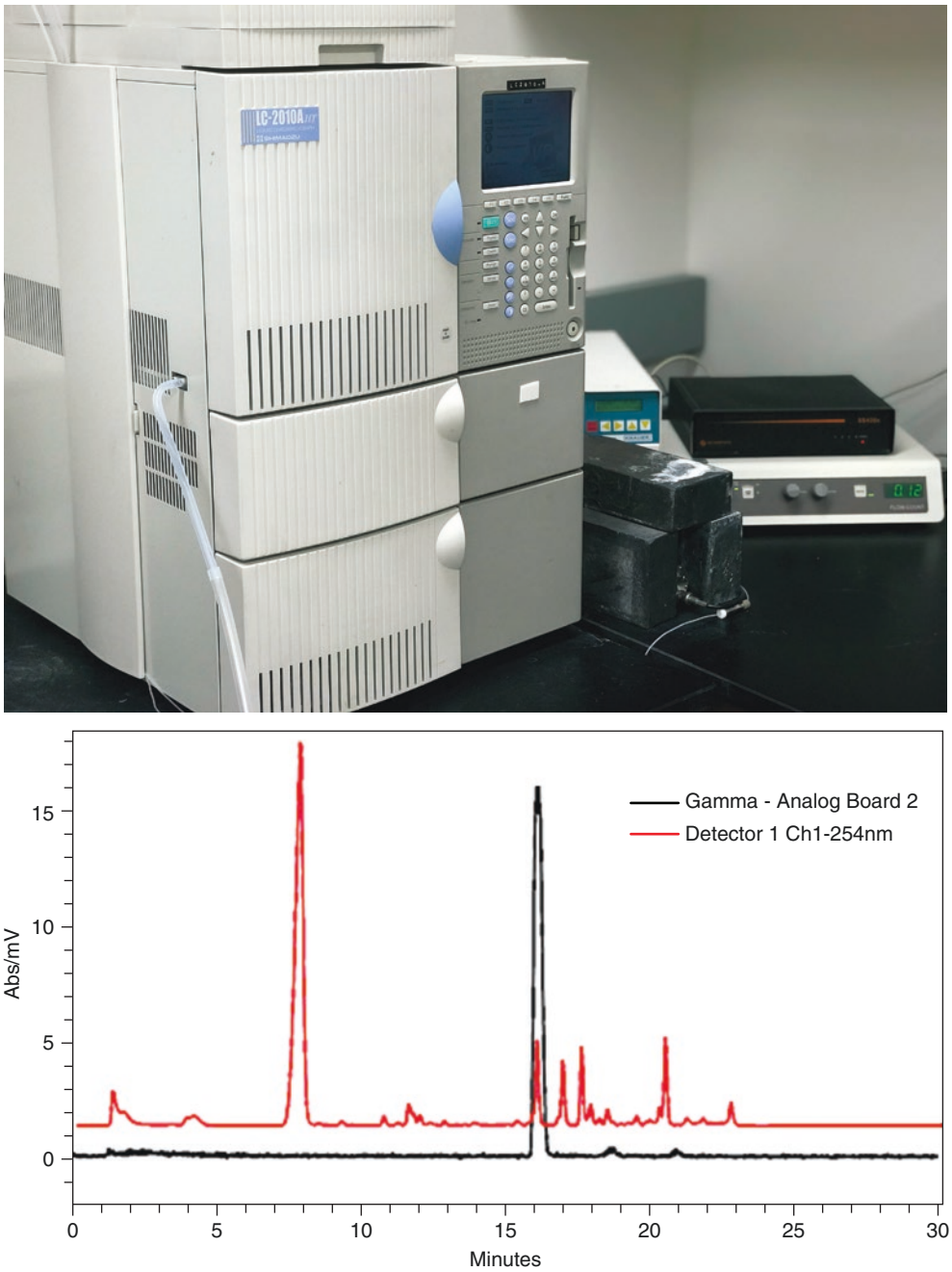

Fig. 14 Radio-high-performance liquid chromatography (HPLC) system and representative HPLC trace. Manufacturers of HPLCs include Shimadzu (*shown*), Agilent, Waters, Dionex, and many others

case of salts – an electrochemical detector. To analyze radiochemical purity, HPLC systems are equipped with photomultipliers and/or PIN diode detectors that are designed to detect positron-emitting radionuclides at both high and low levels of activity.

Dose Calibrators

Dose calibrators are used for a wide variety of PET (as well as nuclear medicine and radioimmunotherapy) applications. Dose calibrators consist of an ionization chamber (*vide supra*) with a well in the center. Radiopharmaceutical samples (*e.g.* vials, syringes) are placed into the well, and the dose calibrator assays how much radioactivity is present in the sample. The ion chamber and well are usually shielded with lead rings to prevent interference from other sources of radioactivity present in the laboratory, and the amount of radioactivity in the sample is displayed on a separate control unit and/or computer (Fig. 15) [13]. With the completion of the quality control on the dose calibrator (constancy, accuracy, and linearity) and the selection of an appropriate predefined calibration factor, dose calibrators can provide accurate measurements of radioactivity in a given sample. These measurements are suitable for calculating the radiochemical yield of a synthesis, establishing radionuclidic identity during quality control testing by taking two activity assays at known time points and determining half-life or dispensing radiopharmaceutical doses for administration to animals or clinical subjects.

Fig. 15 Dose calibrator. (Atomlab 500 Dose Calibrator; Photo courtesy of Biodex Medical Systems, Inc., Shirley, NY). Other manufacturers of dose calibrators include Biodex,Capintec, MED Nuklear-Medizintechnik Dresden, and Comecer

Multichannel Analyzer

Multichannel analyzers (MCAs) coupled with scintillation detectors make it possible to not only measure the radioactivity in a sample but also determine the energy of the radiation particle that was detected. This facilitates the calculation of the radionuclidic purity of a sample by identifying any other radionuclides present beyond the expected PET radionuclide. The sensitive combination of a detector and a MCA is primarily intended to identify the breakthrough of any long-lived radioactive contaminants from the cyclotron targetry or generator matrices. Such breakthrough would be at very low levels and would not be detectable using, for example, a dose calibrator.

Automated QC Testing

The battery of QC tests required before a radiopharmaceutical is released for clinical use has historically required separate pieces of specialized analytical chemistry equipment such as radio-TLC scanners and radio-HPLCs. Such units are expensive to both purchase and maintain and also require trained personnel to operate. To make QC more straightforward and economical and facilitate regulatory compliance, there has been a move to develop miniaturized analytical systems that incorporate all (or most) of these tests into a single automated unit. For example, Tracer-QC (Fig. 16), developed by Trace-Ability, Inc. and commercialized by LabLogic, is fully automated and completes ten QC tests – color, clarity, pH, residual kryptofix, bacterial endotoxins, residual ethanol, residual acetonitrile, radionuclidic identity (half-life), radioactivity concentration (*i.e.* product strength in *e.g.* MBq/mL or mCi/mL), and radiochemical purity – using only an optical plate reader and a pipetting robot.

Equipment for *In Vitro* and *In Vivo* Evaluation of PET Radiopharmaceuticals

The development of novel PET radiopharmaceuticals follows the classical drug development pathway. As a result, this course includes extensive preclinical evaluation studies designed to validate the radiopharmaceutical for a given imaging application prior to undertaking the lengthy (and expensive) process of clinical translation. Numerous strategies are available for confirming the efficacy of a radiopharmaceutical, including autoradiography, biodistribution, and both preclinical and clinical PET imaging.

Fig. 16 A miniaturized and fully automated QC instrument. (Image courtesy of Trace-Ability, Inc., Culver City, California). Other manufacturers of automated QC equipment include QC1

Autoradiography Using a Phosphorescence Imager

Autoradiography is an *ex vivo* technique used to visualize the distribution of a radiopharmaceutical in a biological sample such as a brain slice or tumor section. To this end, the tissue in question is exposed to the radiopharmaceutical and then rinsed to remove any unbound radiopharmaceutical. Historically, the tissue would then be placed on x-ray or photographic film. As the radioactive emissions pass through the film, silver halide crystals are activated and can subsequently be detected during the development of the film. More recently, however, PET Centers have replaced traditional x-ray films with phosphorescence imagers. Phosphorescence imaging uses phosphorimaging plates: thin plates coated with photostimulable crystals. When the plate is exposed to a tissue section containing the radiopharmaceutical, the emitted radiation excites electrons in the crystal which are then trapped in the crystals. Exposing the plate to visible light in the phosphorescence imager triggers release of the trapped electrons and, as the crystal returns to its ground state, the concomitant emission of photons. Detecting these photons enables the accurate quantification of the amount and the location of the radiopharmaceutical in the tissue sample. Following a study, the phosphorimaging plate can be erased and reused.

Biodistribution Studies Using a Gamma Counter

Biodistribution studies offer an accurate *ex vivo* method to track the fate of radiopharmaceuticals following injection into a test animal. Normally, such studies are conducted in rodents. Following the injection of the radiopharmaceutical, groups of animals (*e.g.* n = 5) are euthanized and dissected at different time intervals following injection (*e.g.* 5, 30, 60, 120 min, etc.). Organs of interest as well as blood, urine, *etc*. are then placed into pre-weighed vials that can be counted in a gamma counter.

Gamma counters are instruments that can detect gamma radiation emitted from radionuclides, including the 511 keV gamma photons generated following the annihilation of the positrons emitted from a PET radionuclide. A gamma

counter is (usually) a scintillation counter that automates the counting of multiple tubes on a conveyer belt, making it an ideal instrument for analyzing the large numbers of samples generated during a biodistribution study. The gamma rays have an excitation effect on a scintillator material (*e.g.* NaI crystals), and the resulting photons are converted to an electrical signal by a photomultiplier tube (PMT). These electrical signals are then counted and processed by a computer.

The result of biodistribution studies is a dynamic picture of the distribution of a radiopharmaceutical throughout the animal. After factoring in both the radioactivity in each tube and the weight of the contents, this data is usually presented as an activity concentration in units of percent injected dose per gram of tissue (%ID/g).This data can also be run through software such as OLINDA to perform dosimetry calculations. Taken together, these data can be used to make assessments regarding the potential clinical safety and efficacy of new radiopharmaceuticals.

Fig. 17 Positron emission tomography radiotracer infusion system

PET Scanners

Finally, the *in vivo* imaging properties of a new PET radiopharmaceutical need to be evaluated both preclinically in rodents and/or larger mammals (*e.g.* pigs, nonhuman primates) and, eventually, in a clinical setting. While PET scanners for human imaging have been used since the mid-1970s, the first dedicated large animal PET scanners were not introduced until the early 1990s, and the first small animal scanners appeared toward the end of the same decade. All operate on the same principle, but the animal scanners have higher resolution and a smaller field of view.

When a PET scan takes place, the animal or patient is placed in the scanner and receives an intravenous injection of a radiopharmaceutical. This can either be done using a syringe or, in the case of busy PET Centers dealing with many patients each day, a specialty portable PET infusion system (Fig. 17). When a positron-emitting radionuclide decays, a positron is released and subsequently annihilates with an electron in the body, releasing a pair of 511 keV gamma rays ~180° apart. During the 1950s, early 2D images were obtained by moving opposing NaI crystal detectors by hand. By the 1970s, this technology had developed into rings of detectors surrounding the patient (tomography). Today, PET scanners consist of a ring or rings of gamma ray detectors that are made from scintillation crystals similar to those used in gamma counters. Common crystal choices include sodium iodide doped with thallium, bismuth germinate (BGO), lutetium oxyorthosilicate doped with cerium (LSO), yttrium oxyorthosilicate doped with cerium (YSO), gadolinium oxyorthosilicate doped with cerium (GSO), and barium fluoride. Rings of these scintillation crystals connected to PMTs register the simultaneous arrival of a pair of collinear gamma rays (coincidence event), defining where emission of the positron occurred (Fig. 18). Millions of coincidence events are collected during a PET scan, and, following the scan, all the data is reconstructed to provide 3D images that represent the concentration of the radionuclide throughout the body. This data can then be used to generate tissue time-radioactivity curves for defined regions of interest (ROIs) such as the brain or a tumor.

The quality of the images generated by PET scanners improved throughout the 1990s (Fig. 19) due to the development of better methods for attenuation correction and improved image reconstruction. Yet still, during this period, both clinical and preclinical PET systems remained standalone instruments. However, the late 1990s and early 2000s played witness to the advent of hybrid PET/CT and PET/MRI scanners, which enable the combination of the functional information of PET with the anatomical information of CT or MRI into a single superimposed (*i.e.* co-registered) image (Fig. 20). Clinical PET-CT scanners were the first hybrid scanners available, containing both the PET detector ring and a CT scanner in a single gantry [14], and miniaturized preclinical versions soon followed. The development of PET-MRI scanners was more challenging due to the need for the PET component to function in the presence of a strong magnetic field. Despite this, enormous progress has been made in the last decade, and both clinical and preclinical PET-MRI scanners are also now commercially available. In addition to the incorporation of anatomical imaging to provide high-quality images (see Fig. 20) [15], scanners have also benefited from the introduction of several further performance upgrades in recent years, including (*i*) list mode

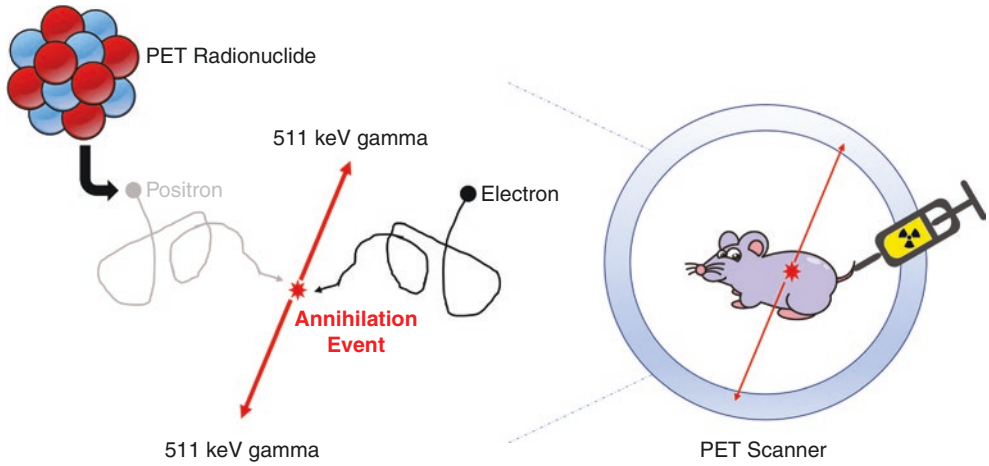

Fig. 18 Principles of a positron emission tomography scanner

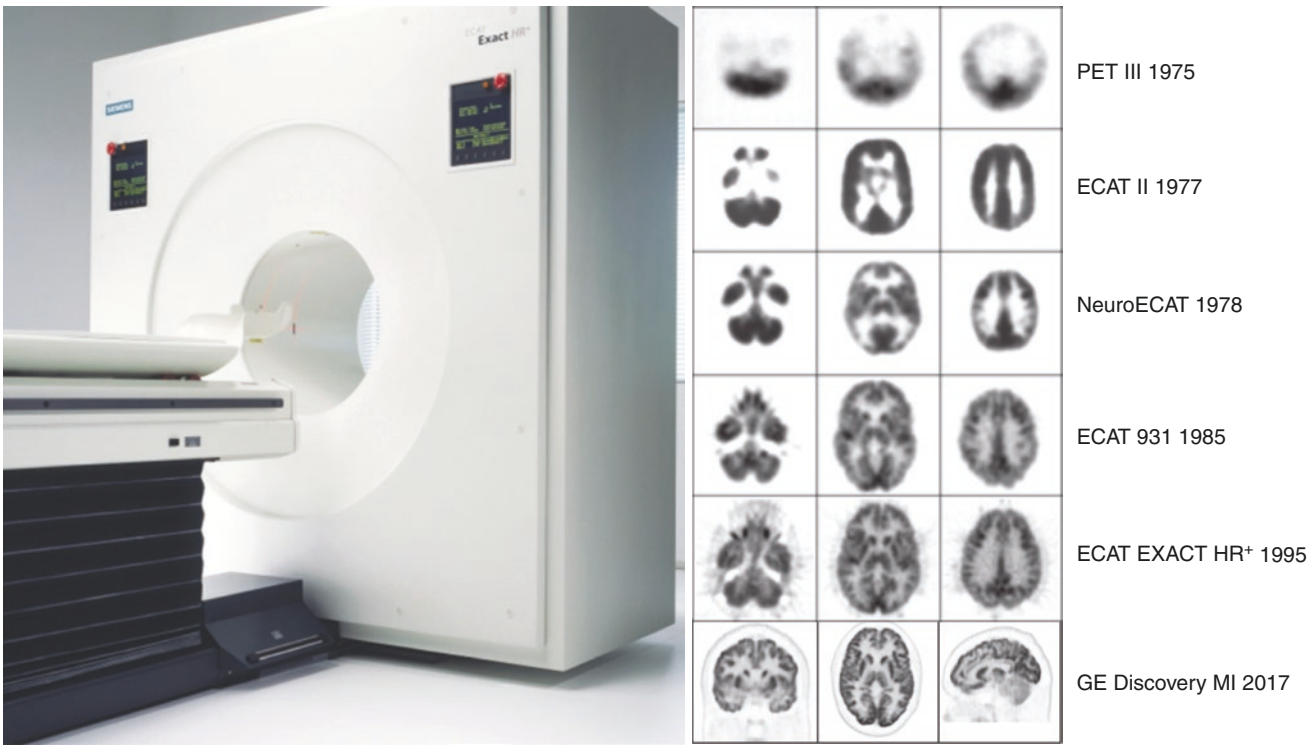

Fig. 19 Siemens ECAT EXACT HR+Positron Emission Tomography (PET) Scanner and representative PET images. (Courtesy of Dr. Michael E. Phelps, David Geffen School of Medicine at UCLA, Los Angeles, California). Other manufactures of PET scanners include General Electric, Philips, Mediso, and Medical Imaging Electronics (MiE)

acquisition, (*ii*) time of flight (TOF), (*iii*) attenuation correction, and (*iv*) gating.

1. **List Mode Data Acquisition.** List mode data acquisition is a scanning mode in which every detected event is recorded (including prompts, randoms, and the line of response [LOR]). Compared to conventional frame mode acquisition, list mode acquisition allows more flexible data analysis since frame rebinning and iterative image reconstruction can be undertaken in a variety of ways after the fact. Real-time motion correction is also possible, leading to further improved image quality.
2. **Time of Flight.** During a PET scan, sophisticated electronics are employed to determine the LOR along which an annihilation has occurred (see Fig. 18). TOF-PET takes this concept further by using the difference in arrival times of the two gamma photons to identify

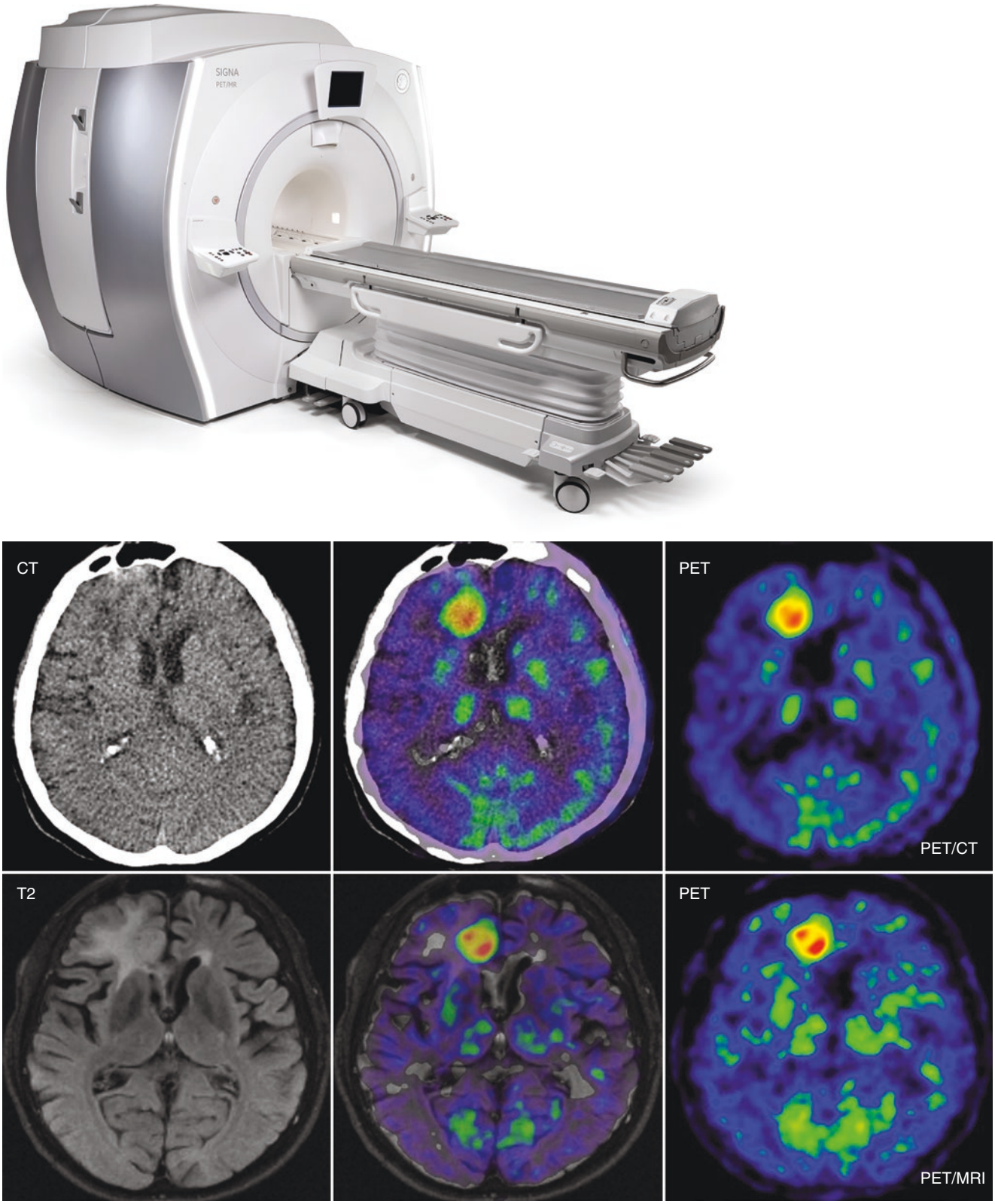

Fig. 20 (*Left*) Clinical positron emission tomography (PET) and magnetic resonance imaging (MRI) scanner (image courtesy of GE Healthcare, Chicago IL). (*Right*) Modern PET/CT and PET/MRI images of patient with glioblastoma demonstrating high diagnostic quality (This research was originally published in JNM. Boss *et al*. [15], with permission. © SNMMI). Other manufactures of PET-MRI scanners include Siemens and Philips

the approximate position along the LOR at which the annihilation event occurred. More accurately pinpointing the location of the annihilation events leads to improved image quality, as it better distinguishes true events from randoms, reduces noise, and increases sensitivity, signal-to-noise ratios, and overall image quality.

3. **Attenuation Correction.** The size of the patient and the amount of tissue between the region of interest and the scanner detectors can lead to attenuation artifacts – typically due to Compton scattering – that have a negative impact on image quality. Attenuation correction is a process for removing such soft tissue artifacts from PET images. Using early PET scanners, attenuation was accomplished using transmission scans acquired with an external photon source before, during, or after the PET scan. The fraction of absorbed radiation in a transmission scan, along the same LOR, is used to correct the PET data. In the age of hybrid scanners, transmission scans have been superseded by the use of CT or MRI data to correct the PET image. In the case of CT, images are acquired as transmission maps and actually represent high-quality images of tissue attenuation. As such, they can form the basis of attenuation correction. In contrast, for PET-MRI systems, attenuation correction is based on the MRI data since the small bore inside the MRI system and the strong magnetic field do not permit the inclusion of a rotating PET transmission source or a CT scanner. Unlike CT measurements, however, MRI signals are not correlated with tissue density. Therefore, other approaches such as the use of templates, atlas information, or direct segmentation of T1-weighted MR are often employed in attenuation correction of the PET data acquired on PET-MRI scanners.
4. **Gating.** Modern scanners are equipped with respiratory and cardiac gating. Gating a PET scan involves dividing the acquired image data into individual time-stamped bins that correlate to the different phases of respiratory and/or cardiac motion by overlaying corresponding time-stamped data. The effect is to improve the quality of the images by reducing motion effects that can lead to the blurring of images and artifacts and enabling the analysis of image data at the same stage of the respiratory and/or cardiac cycles.

Tricks of the Trade

The development, preclinical evaluation, and successful clinical translation of a new PET radiopharmaceutical follow a complex pathway involving a multidisciplinary team of researchers. The PET Centers that do this well are those that are strong in each component of the development pathway. For example, a new radiopharmaceutical needs to be able to be synthesized by radiochemists, allow kinetic modeling by medical physicists, and provide useful information to nuclear medicine physicians managing the patients. If any of these parts is absent, it is unlikely that the new radiopharmaceutical will be translated into the clinic or widely adopted by the PET imaging community.

There are also several practical and logistical aspects of the day-to-day operation of a PET Center that demand attention above and beyond the intellectual challenges inherent to the development of radiopharmaceuticals. Many of these are laid out in the cGMP regulations issued by the FDA (and similar rulings from other regulatory bodies). Thus, ensuring that the PET Center has control over all necessary regulatory oversight is of paramount importance not only to prevent disciplinary action (*e.g.* fines, forced shutdown) but also because, in many ways, the entire workflow stems from the cGMP requirements. By way of example, the cGMP regulations offer stipulations about both staffing and equipment: *"[21CFR212] requires a PET drug production facility to have a sufficient number of personnel with the necessary education, background, training, and experience to enable them to perform their assigned functions correctly. Each center also must provide adequate resources, including equipment and facilities, to enable their personnel to perform their functions.*"

As described in this chapter, radiopharmaceutical production labs and PET imaging suites are equipped with complex and expensive equipment that is often exposed to gigabecquerel–terabecquerel (multi-Curie) levels of positron-emitting radionuclides on a daily basis. As a result, this equipment often needs regular maintenance to ensure peak performance, and providing such maintenance should be considered a facet of cGMP compliance. In light of the risk of disruptions to PET imaging schedules because of unplanned downtime as well as the time sensitivity of making and utilizing short-lived PET radiopharmaceuticals, it is strongly recommended that PET Centers build redundancy into their operating systems (*e.g.* multiple synthesis modules, radio-HPLCs, and radio-TLC scanners). Purchasing manufacturer maintenance contracts on the major equipment used to support clinical PET imaging (cyclotron, synthesis modules, analytical equipment, PET scanners, *etc.*) is also encouraged. Admittedly, such maintenance contracts can be very expensive, but oftentimes they offer the fastest way to bring broken equipment back online. Manufacturer maintenance contracts are frequently also the most affordable and sometimes the only way to access custom parts for the specialized equipment used in PET Centers.

The Future

The development and widespread adoption of the Internet since the 1990s occurred at the same time as PET imaging became routine. The Internet has revolutionized how we generate, collect, store, access, and share data, and PET imaging has not been immune to this revolution. It may be less appreciated, however, how the rise of the Internet has changed the way in which we interact with physical machines and, in the context of this chapter, the laboratory and medical equipment used in PET Centers. The assembly of Internet-connected machines has been broadly termed the "Internet of Things" (IoT) [16]. Recently, interconnected chemical machines, chemical computing devices, and chemical services had been defined as the "Internet of Chemical Things" (IoCT). A similar "Internet of Medical Things" (IoMT) – comprised of medical equipment, devices, and services – also exists. The modern PET Center lies at the interface of medicine and chemistry, and the equipment (or "things") found in a modern PET Center are located at the intersection of the IoCT and IoMT. The use of automated machines for the production of radiopharmaceuticals and automated devices for the collection and logging of data has meant that PET Centers have operated under the paradigms of the IoCT and IoMT, well before these concepts were defined.

The development of networked machines and services in PET Centers has been necessitated by two main factors: the need for the reliable and automated manufacture of PET radiopharmaceuticals (to ensure both patient and worker safety) as well as the requirement of robust systems for the capture and storage of data to ensure that radiopharmaceuticals are manufactured according to cGMP standards. Since the late 1980s, PET Centers have made use of computer-controlled cyclotrons and synthesis and purification modules which are entirely controlled by networked computers (see Fig. 11). As networking, data collection, and archiving as well as the idea of centralized control of the associated systems have permeated the field, all of the equipment commonly found in a PET Center has slowly transitioned online. Along with the newly networked systems in the associated organic chemistry laboratories (electronic notebooks, online inventory and procurement systems, bespoke software, *etc*.) and medical imaging centers (scheduling systems, picture archiving and communication systems [PACS], PET scanners, and PET radiopharmaceutical infusion systems), the modern PET lab lies at the center of its own Internet of Things (Fig. 21). This interconnected network of devices

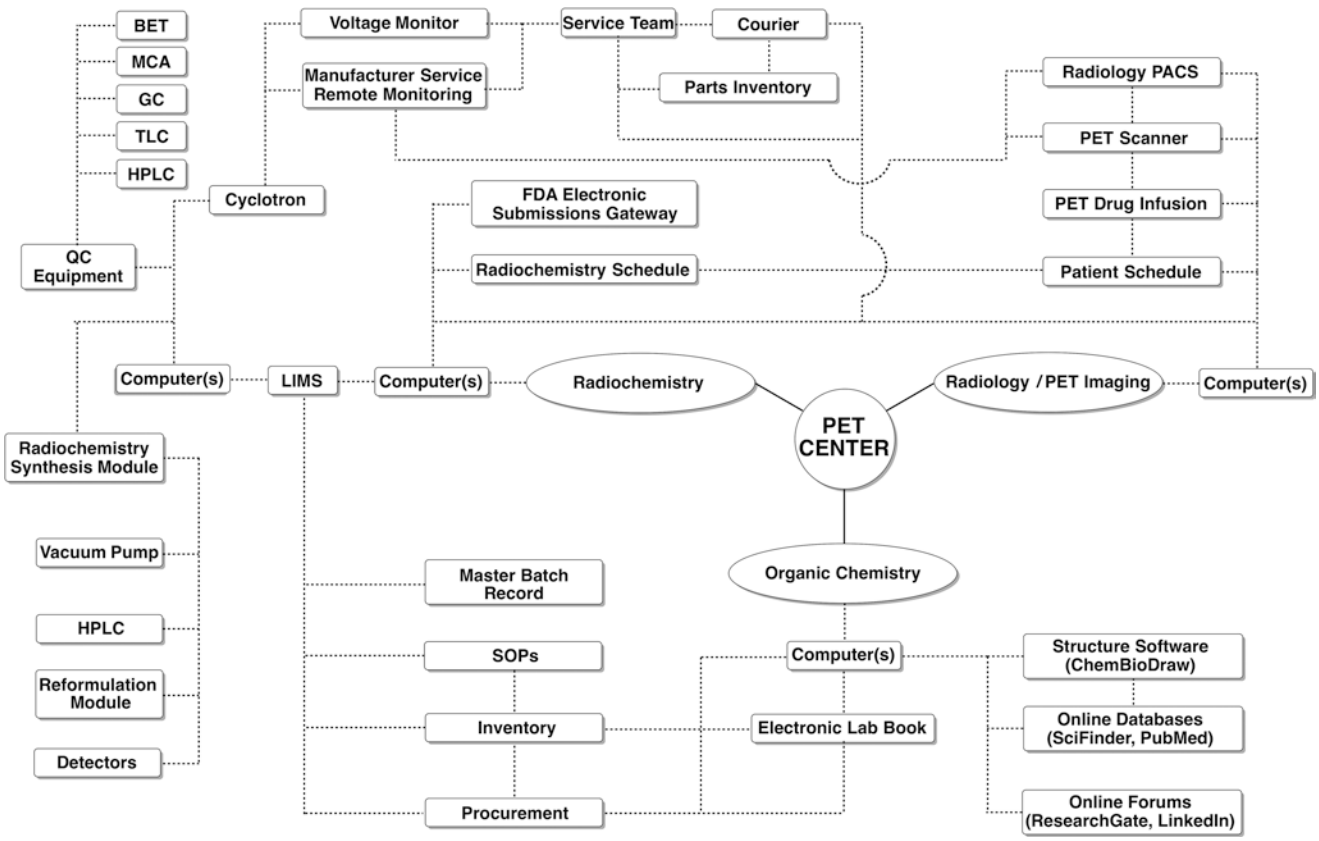

Fig. 21 The Internet of Things in a modern PET Center (From Thompson *et al*. [2], with permission)

represents the ideal setup, in which all the equipment that makes up a PET Center is connected as a single system.

Few PET Centers presently have such complete networks. However, modern regulatory requirements – which mandate extensive recording of components, synthesis reports, quality control, and production releases – are steadily driving PET Centers toward this model. This has led to the development and commercialization of bespoke PET-focused laboratory information management systems (LIMS) to collect, collate, and store the data generated by a PET Center using the IoT. In addition to recording data as it is generated, LIMS coupled to remote monitoring systems are starting to integrate inventory, personnel, and equipment management, thereby streamlining day-to-day operations. The ordering of consumables, maintenance of equipment, and scheduling of production and QC staff can all be automated using such systems. LIMS for PET Centers operating through the IoT can reduce waste, maximize resource efficiency and uptime, and – most importantly – improve patient safety by reducing the probability of errors or oversights which can occasionally occur when such complex systems require constant human interaction. PET Centers in the future will continue to add new devices and equipment to their networks, and this will no doubt have a positive impact on work flow, productivity, and safety.

The networking of devices in a PET Center and their connection to the Internet offers many benefits, but at the same time, this model necessarily creates a plethora of security issues. Devices on the network can become targets for ransomware and cyberattacks if the networks are not adequately protected. As of 2017, there have been numerous cases of ransomware attacks on healthcare providers, during which criminals have ransomed access to the information contained in these systems for monetary gain. The "WannaCry" ransomware attack in May 2017 – which locked users out of their computers unless a ransom was paid – significantly affected the operation of, among others, the National Health Service in the United Kingdom. The ransomware attack affected over 70,000 networked devices (including MRI scanners), placing private data and physical safety in jeopardy [17].

Networked devices commonly found within PET Centers have also been found to be vulnerable to security exploits which may affect their physical operation. In 2015, the Food and Drug Administration issued a recall in 2016 for a network-connected infusion pump after it was found that the device could be hijacked though vulnerabilities in insecure networks, putting patients in danger [18]. In 2017, a major manufacturer of PET and SPECT equipment issued an alert that their scanners were vulnerable to exploitation through the software used to control the devices [19]. PET-CT and SPECT-CT scanners both produce large amounts of ionizing radiation, presenting significant health hazards to both patients and staff if they were to be switched on unexpectedly. In both instances, the choice to connect these devices to the IoT had inadvertently placed patients and operators in danger.

The "WannaCry" ransomware attack and the vulnerabilities of the devices described above highlight the growing need for improved network and device security for systems used in PET Centers and in the healthcare setting more generally. This problem is not isolated to the healthcare industry and presents challenges to the realization of the IoT over a wide range of industries, from space exploration to urban planning and architecture. The transformation of the day-to-day workflow and the streamlining of data collection and analysis across these industries will continue to drive the development of the IoT. This will need to occur alongside the development of protocols to protect users from physical risks and to ensure that the data collected by connected devices remains secure and cannot be accessed, or held ransom, by unauthorized users.

Instrumentation for Other Modalities in Nuclear Medicine

In this chapter,we have used the framework of a modern PET Center to describe many of the pieces of equipment and instrumentation used in preclinical and clinical radiopharmaceutical chemistry. However, PET is not the only modality in present-day nuclear medicine, and both single-photon emission computed tomography (SPECT), and targeted radiotherapy play important roles in the field as well. Many of the pieces of instrumentation that we have discussed are also used for the production and use of radiopharmaceuticals for SPECT and radiotherapy, including Geiger counters, radiation monitoring systems, and quality control equipment. That said, there are other pieces of equipment that are unique to other modalities. For example, while PET radiotracers emit positrons that annihilate to produce two gamma photons that are detected by the PET scanner (*vide supra*), SPECT radiotracers emit single gamma photons that are measured directly. SPECT imaging therefore requires dedicated SPECT (or SPECT-CT) scanners that are compatible with common SPECT radionuclides such as technetium-99 m and iodine-131. Physically, such scanners look similar to PET scanners (Figs. 19 and 20), and while both have somewhat similar modes of operation, there are differences. SPECT scanners consist of gamma cameras that are moved around the patient throughout the scan. The cameras contain crystals, and the luminescence caused when gamma rays strike these crystals is converted to an electrical signal and counted. Historically, they have been sodium iodide crystals activated with thallium, although cadmium–zinc–telluride (CZT) SPECT scanners have also

been introduced recently. Since there is no coincidence event like PET, SPECT scanners rely on detectors divided into pixels and collimators to determine the point of origin of the single gamma photon emitted from the radionuclide. SPECT scanners have continually developed since their introduction, and advances such as attenuation correction and gating have improved the image quality of SPECT scans in a similar fashion to the improvements to PET scans described earlier in the chapter.

The Bottom Line

- PET imaging is a type of functional molecular imaging that is used to enable personalized medicine and support drug discovery.
- A PET Center uses state-of-the-art equipment for the production of radionuclides, the synthesis and quality control of radiopharmaceuticals, preclinical and clinical imaging, and safety monitoring.
- Over the last 30 years, the equipment for the production and quality control testing of PET radiopharmaceuticals has become increasingly miniaturized and automated, in part to facilitate compliance with Current Good Manufacturing Practice (cGMP).
- In the smart PET Center of tomorrow, equipment will be highly interconnected through the Internet of Things (IoT).
- Beyond PET, there are different pieces of equipment that are specific to other nuclear medicine modalities. For example, SPECT imaging relies on SPECT and SPECT-CT scanners that contain collimators and pixelated detectors designed and optimized for detecting the single gamma photons emitted from SPECT radionuclides.

Acknowledgments Financial support of this work from the US DOE (DE-SC0012484) is gratefully acknowledged. The authors declare no competing financial interest.

References

1. Schwarz SW, Dick D, VanBrocklin HF, Hoffman JM. Regulatory Requirements for PETdrug production. J Nucl Med. 2014;55(7):1132–7.
2. Thompson S, Kilbourn MR, Scott PJH. Radiochemistry, PET imaging, and the Internet of Chemical Things. ACS Cent Sci. 2016;24(2):497–505.
3. Rutherford E, Geiger H. An electrical method of counting the number of α -particles from radio-active substances. Proc R SocLond A. 1908;81(546):141–61.
4. Geiger H, Müller W. ElektronenzählrohrzurMessungschwächsterAktivitäten. Naturwissenschaften. 1928;16(31):617–8.
5. Xiao D. Fundamental theory of Townsend discharge. In: Gas discharge and gas insulation. In: Energy and environment research in China, vol. 6. Berlin/Heidelberg: Springer; 2016. p. 47–88.
6. Lawrence, Ernest O. Method and apparatus for the acceleration of ions. US Patent 1,948,384; 1934.
7. Holland JP, Sheh Y, Lewi JS. Standardized methods for the production of high specific-activity zirconium-89. Nucl Med Biol. 2009;36(7):729–39.
8. Pandey MK, Byrne JF, Jiang H, Packard AB, DeGrado TR. Cyclotron production of ^{68}Ga via the ^{68}Zn(p,n)^{68}Ga reaction in aqueous solution. Am J Nucl Med Mol Imaging. 2014;4(4):303–10.
9. Fani M, André JP, Maecke HR. ^{68}Ga-PET: a powerful generator-based alternative to cyclotron-based PET radiopharmaceuticals. Contrast Media Mol Imaging. 2008;3(2):67–77.
10. Brodack JW, Kilbourn MR, Welch MJ, Katzenellenbogen J. Automated production of several positron-emitting radiopharmaceuticals using a single laboratory robot. Int J ApplInstrum A. 1988;39(7):689–98.
11. Pascali G, Watts P, Salvadori PA. Microfluidics in radiopharmaceutical chemistry. Nucl Med Biol. 2013;40(6):776–87.
12. Vallabhajosula S. Quality control of PET radiopharmaceuticals. In: Molecular imaging. Berlin/Heidelberg: Springer; 2009. p. 197–204.
13. Saha GB. Gas-filled detectors. In: Physics and radiobiology of nuclear medicine. 4th ed. New York: Springer; 2013. p. 79–90.
14. Beyer T, Townsend DW, Brun T, Kinahan PE, Charron M, Roddy R, et al. A combined PET/CT tomograph for clinical oncology. J Nucl Med. 2000;41(8):1369–79.
15. Boss A, Bisdas S, Kolb A, Hofmann M, Ernemann U, Claussen CD, Pfannenberg C, Pichler BJ, Reimold M, Stegger L. Hybrid PET/MRI of intercranial masses: Initial experiences and comparison to PET/CT. J Nucl Med. 2010;51(8):1198–205.
16. Ashton K. That 'Internet of Things' thing, 22 Jun 2009. RFID J. http://www.rfidjournal.com/articles/view?4986. Accessed 5 Nov 2017.
17. Ungoed-Thomas J, Henry R, Gadher D. Cyber-attack guides promoted on YouTube. The Sunday Times [Online], 14 May 2017. https://www.thetimes.co.uk/article/cyber-attack-guides-promoted-on-youtube-972s0hh2c. Accessed 5 Nov 2017.
18. U.S. Food and Drug Administration. Vulnerabilities of HospiraLifeCare PCA3 and PCA5 infusion pump systems: FDA safety communication, 13 May 2015. http://wayback.archive-it.org/7993/20170722144742/, https://www.fda.gov/MedicalDevices/Safety/AlertsandNotices/ucm446809.htm. Accessed 5 Nov 2017.
19. Prodhan G. Siemens to update medical scanner software to deal with security bugs. Reuters [Online], 7 Aug 2017. https://www.reuters.com/article/siemens-healthcare-cyber-idUSL1N1KT0WZ. Accessed 14 Jun 2018.

Kinetic Modeling of Radiotracers

Mark Lubberink and Kerstin Heurling

Introduction

The basic assumption underlying the kinetic modeling concepts discussed in this chapter is that a PET tracer is administered in such small amounts that it does not have any pharmacological effects. This is known as the "tracer principle," and it is made possible by the exceptionally high sensitivity of PET combined with the high specific activity of many radiotracers. Furthermore, we must assume that the biological functions that we are studying exist at a steady state, that is, they are not changing during the time of the PET scan. For example, blood flow to tissues should be constant during the measurement of blood flow using [^{15}O]H_2O, plasma glucose concentrations should be constant while doing a PET investigation with [^{18}F]fluorodeoxyglucose (FDG), and the concentrations of receptors and endogenous neurotransmitters should be constant throughout a scan with a neurotransmitter-based tracer. Given these two assumptions, the kinetic models described in this chapter can be used to translate changes in the PET signal over time into insight into the underlying physiological and molecular processes of interest. While simplified quantification methods such as the use of standardized uptake values (SUV) are useful in clinical settings and large cohort studies, precise methods for quantification are necessary for the validation of such methods and are sometimes required in disease monitoring, the assessment of treatment response, and drug development studies [1].

To be able to create these models, we need to measure the distribution of radioactivity in a tissue of interest over time, starting with the injection of the tracer. The length of the scan that is required for an accurate measurement depends on (1) the speed of the kinetics of the tracer and (2) the half-life of the radionuclide used to label the tracer. For example, with ^{11}C ($t_{1/2}$ = 20.4 min), a scan of more than 2 h is largely meaningless since nearly all of the radioactivity has decayed at 2 h after injection. Slower processes require the use of radionuclides with longer half-lives, whereas fast processes—such as measurement of blood flow—can be assessed using tracers labeled with^{15}O or ^{13}N ($t_{1/2}$ = 2 and 9 min, respectively). The technology behind dynamic PET scans will not be further discussed here, as it has been described in depth in Chap. 5. An example of a dynamic PET scan using a ^{11}C-labeled dopamine transporter ligand is shown in Fig. 1.

Tracer kinetic models describe the transport of a tracer between the plasma and different compartments in a volume of interest (VOI) or voxel. The term "compartments" refers not to physical compartments but rather different states of the radiotracer, *e.g.* "free" or "receptor-bound." To be able to use these models, we usually need to know the concentration of the tracer in arterial plasma during the course of the scan as well as the information from the dynamic PET scan as shown in Fig. 1. In the thorax or abdomen, the arterial whole blood TAC—$C_A(t)$—can be obtained using the PET signal in the left ventricle of the heart or in the aorta. In the brain, however, there are no arteries that are large enough relative to the spatial resolution of PET to allow for the accurate measurement of a whole blood TAC. In this case, then, the TAC curve for the blood is usually measured via continuous sampling from a radial artery during the first 10–15 min of a scan followed by the collection of discrete blood samples at set intervals post-injection. The activity in these samples is then determined using detectors that are cross-calibrated to the PET scanner. Even when a large vessel is available in the PET image, blood samples need to be taken to measure plasma tracer concentrations in order to convert the whole blood TAC to a TAC for the plasma alone, since only tracer in plasma is available for transport into tissue. Many PET tracers undergo peripheral metabolism during the course of

M. Lubberink (✉)
Department of Surgical Sciences – Radiology & Nuclear Medicine, Uppsala University and Medical Physics, Uppsala University Hospital, Uppsala, Sweden
e-mail: mark.lubberink@radiol.uu.se

K. Heurling
Wallenberg Centre for Molecular and Translational Medicine and the Institute of Neuroscience and Physiology, University of Gothenburg, Gotenburg, Sweden

J. S. Lewis et al. (eds.), *Radiopharmaceutical Chemistry*, https://doi.org/10.1007/978-3-319-98947-1_28

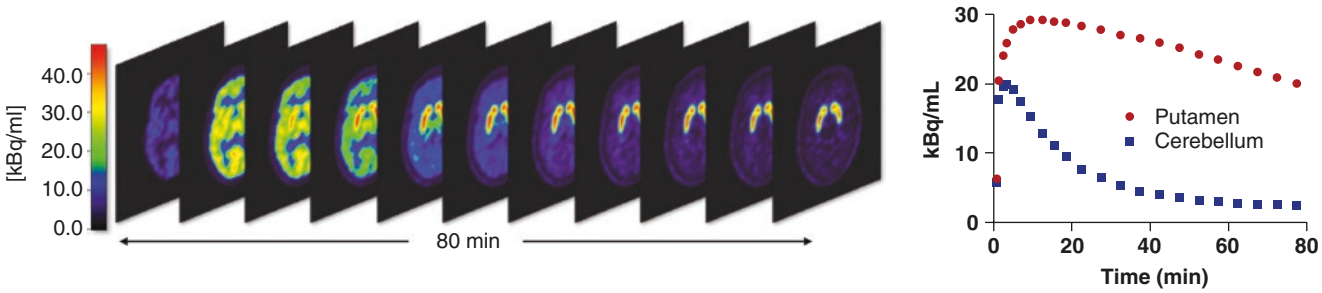

Fig. 1 Dynamic scan showing images of the dopamine transporter ligand [^{11}C]PE2I during 80 min after bolus injection (**a**) as well as the corresponding time-activity curves (TACs) showing the radioactivity concentration over time in the putamen and cerebellum (**b**)

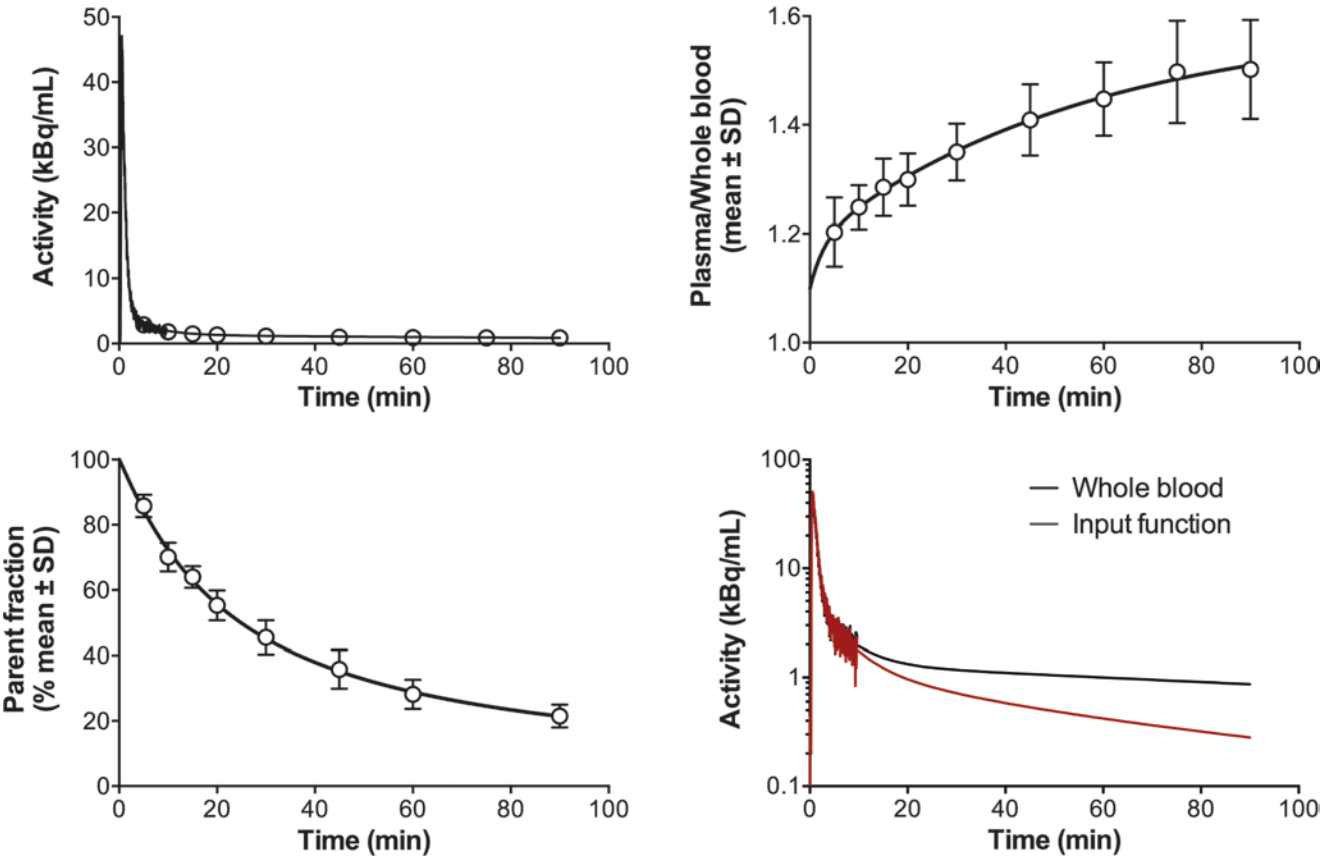

Fig. 2 (**a**) Whole blood TAC of [^{18}F]THK5317 measured using continuous arterial sampling during 10 min followed by discrete samples and interpolation. (**b**) Plasma/whole blood ratio as a function of time (mean ± SD of 9 subjects). (**c**) Fraction of intact tracer in plasma (mean ± SD of 9 subjects). (**d**) Whole blood TAC and resulting mean input curve. The input curve is the product of (**a**–**c**) for each individual subject. Note the logarithmic *y*-axis in (**d**) to stress the difference between whole blood TAC and input curve at later time points. (Adapted from Jonasson *et al.* [2], with permission)

the PET scan, and for those tracers, the fraction of the radioactivity concentration that is due to the intact—or "parent"—tracer needs to be determined by metabolite analysis. The multiplication of the plasma TAC with the fraction of intact parent as a function of time after injection provides the concentration of the tracer in arterial plasma, referred to as the input curve $C_P(t)$. A representative example is provided in Fig. 2 with data from the tau ligand [^{18}F]THK5317 [2]. As seen in Fig. 2c, the parent fraction for this tracer decreases to about 20% of the total activity concentration in plasma over the course of the scan. Needless to say, omitting this correction will lead to erroneous results in tracer kinetic analysis.

Figure 3 schematically describes a single-tissue compartment model for a tracer in which the concentrations in the plasma and whole blood are identical and without metabolism, so $C_A(t)$ can directly be used as the input function.

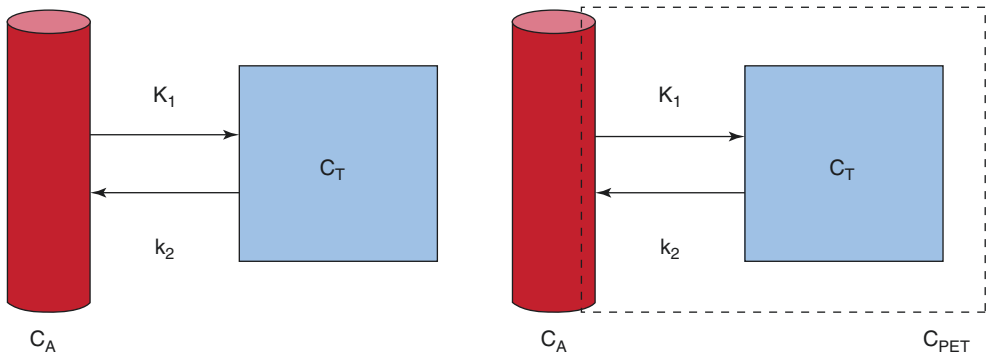

Fig. 3 Single-tissue compartment model. (**a**) K_1 is the transport rate constant from arterial plasma to tissue (in mL·cm^{-3}·min^{-1}), and k_2 is the rate constant describing tracer transport from tissue to blood (in min^{-1}). (**b**) C_{PET} represents the signal measured in the PET scan, which is the sum of the signal in a VOI in the PET image and the signal from blood volume within that VOI

Here, K_1 is the rate constant for the transport of the tracer from arterial plasma to tissue (in mL·cm^{-3}·min^{-1}), while k_2 is the rate constant describing the transport of tracer from tissue to blood (in min^{-1}). The use of capital "K" for K_1—but no other rate constants—highlights the differences in units, stemming from the physiological context of K_1 representing the product of blood flow (F) and tracer extraction from blood to tissue (E).

Compartment models assume that the net rate of transport of a tracer between two compartments is proportional to the difference in the concentrations of the tracer in the two compartments [3]. In light of this assumption, the system can be described mathematically using ordinary differential equations. The compartment model in Fig. 3 can be described by the following differential equation:

$$\frac{dC_T(t)}{dt} = K_1 C_A(t) - k_2 C_T(t) \qquad (1)$$

that is, the change in the concentration of tracer in tissue $C_T(t)$ during a time interval dt equals K_1 multiplied by the arterial plasma tracer concentration at that time $C_A(t)$ minus k_2 multiplied by the tissue concentration. This differential equation can be solved analytically. The derivation is outside the scope of this chapter, but the solution is given here:

$$C_T(t) = K_1 C_A(t) \otimes e^{-k_2 t} \qquad (2)$$

Here, "⊗" is the convolution operation, *i.e.* the mathematical operation whereby the pointwise multiplication of two functions produces a third function. In this case, the radioactivity concentration in the blood as a function of time, convoluted with the tissue response as a function of time, returns the tissue radioactivity concentration as a function of time. This is explained in Fig. 4.

In reality, the signal measured in a voxel or volume of interest in a PET image does not only consist of tracer within the tissue but also tracer in the blood volume present within this voxel or volume (see Fig. 3b). Hence, the total measured signal can be described as:

$$C_{PET}(t) = (1 - V_A) C_T(t) + V_A C_A(t) \qquad (3)$$

where V_A is the partial blood volume within the voxel or volume investigated. By substituting the tissue and arterial plasma curves in Eq. 2, a combination of K_1 and k_2 that best describes the PET data can be found using non-linear regression or weighted non-linear regression in which the different data points are given different weights according to the underlying count statistics of the PET data (Fig. 5).

In addition to the so-called micro-parameters delivery (K_1) and clearance (k_2), an important macro-parameter that can be calculated is the total volume of distribution (V_T) of the tracer:

$$V_T = \frac{K_1}{k_2} \qquad (4)$$

The volume of distribution is equal to the partition coefficient of the tracer, *i.e.* the ratio of the concentrations of the radiotracer in tissue and plasma at equilibrium.

Blood Flow and [^{15}O]H_2O

During the 1940s, Kety and Schmidt [4] presented a model to describe blood flow. This model was founded on the Fick principle that states that for a freely diffusable tracer, the change in the amount of a substance in tissue (in mol) is given by the difference in concentrations of the substance in arterial and venous blood (in mol/mL) multiplied by the physical blood flow (in mL/min) through the tissue:

$$\frac{dq(t)}{dt} = \Phi C_A(t) - \Phi C_V(t) \qquad (5)$$

Dividing both sides of the equation above with the tissue volume and defining that the ratio of the activity concentrations in tissue and venous blood is the distribution volume (V_T) gives:

$$\frac{dC_T(t)}{dt} = F C_A(t) - F \frac{C_T(t)}{V_T} \qquad (6)$$

with F being the tissue perfusion in units of mL per tissue volume per minute. This is the differential equation that

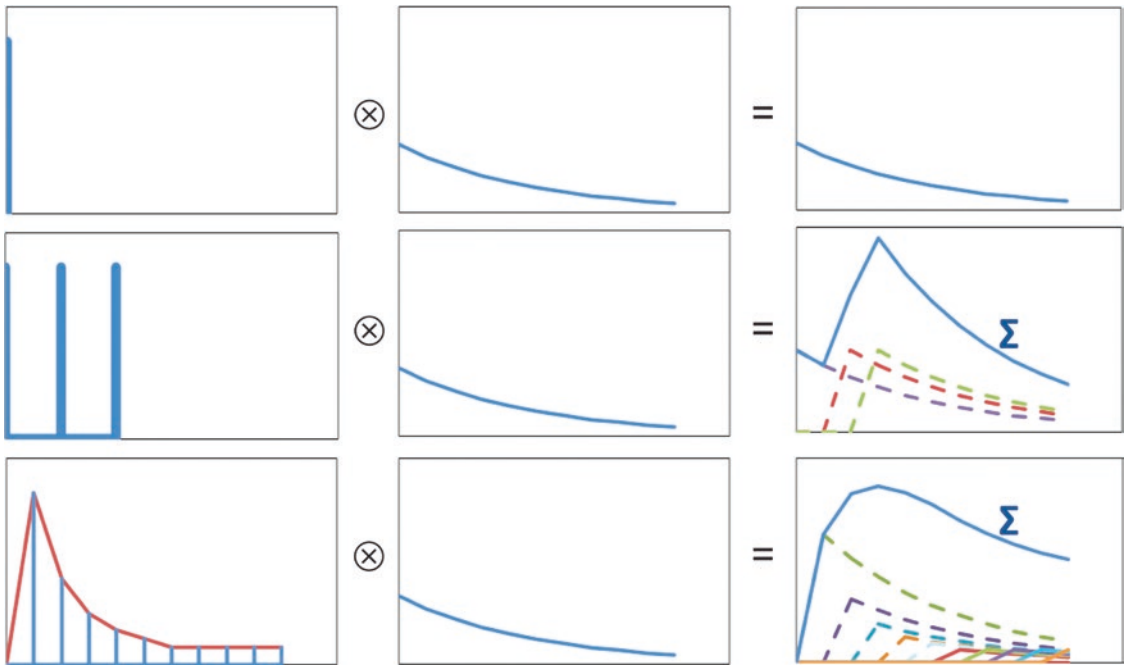

Fig. 4 Convolution. *Left* input function; *center* impulse response function (exponential decay). *Right*: result of convolution. *Top row*: convolution of a delta function with an exponential decay function results in the same exponential decay function. *Middle row*: convolution of three consecutive delta functions. Each delta function gives an exponential response, and the convolution is the sum of the three responses. *Bottom row*: a more realistic example of a plasma input function divided into a large number of delta functions. Again, the result of the convolution is the sum of all individual responses to each delta function

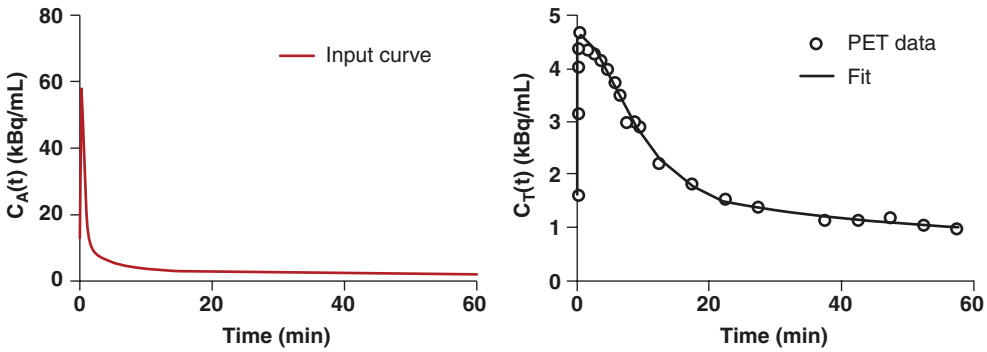

Fig. 5 *Left*: Metabolite-corrected plasma-based arterial input curve (**a**). *Right*: measured PET data (circles) and single-tissue compartment model fit with $K_1 = 0.1$ mL/cm^3/min, $k_2 = 0.2$ mL/cm^3, and $V_A = 5\%$ (**b**)

describes the kinetics of radiolabelled water: [^{15}O]H_2O. The corresponding compartment model representation is given in Fig. 6. The solution of this model is the same as in Eq. 2 but is now written as:

$$C_T(t) = FC_A(t) \otimes e^{-\frac{F}{V_T}t} \qquad (7)$$

Metabolism and Internalization

The compartment model in Fig. 7 can be used to describe the kinetics of tracers that are internalized within cells following their accumulation in a tissue, for example, by metabolic trapping. In this case, there is an additional parameter, k_3, that describes the rate of trapping of the tracer.

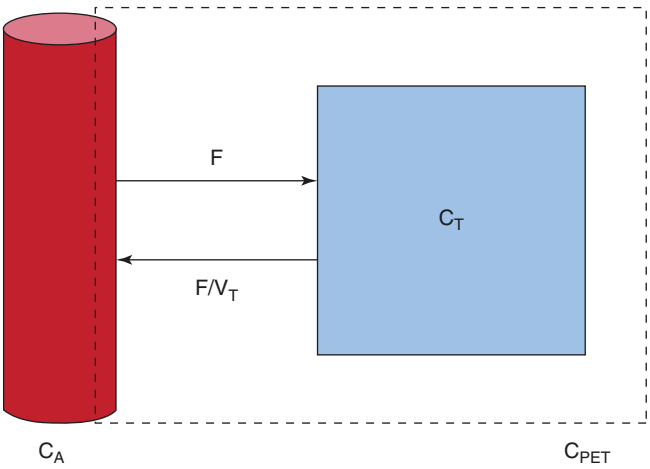

Fig. 6 Blood flow model as used with [^{15}O]H_2O. F, flow; V_T, distribution volume

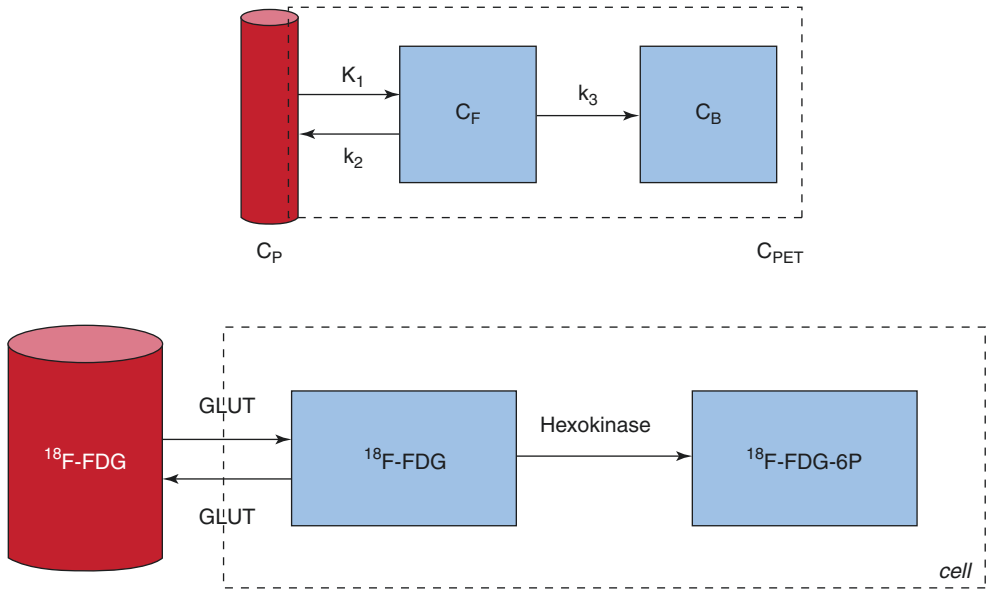

Fig. 7 Irreversible two-tissue model (*top*) (**a**) and its interpretation for (FDG) where GLUT is the glucose transporter membrane protein (*bottom*) (**b**)

The compartment model in Fig. 7 can be described by the following differential equations:

$$\begin{aligned}\frac{dC_F(t)}{dt} &= K_1 C_P(t) - (k_2 + k_3) C_F(t) \\ \frac{dC_B t}{dt} &= k_3 C_F(t)\end{aligned} \tag{8}$$

Here, k_3 is the internalization rate constant describing, for example, the conversion of [^{18}F]FDG into [^{18}F]FDG-phosphate as shown in Fig. 7b. The solution of this model, of course, becomes more complex than that of the single-tissue compartment model discussed above, and deriving it is well outside the scope of this chapter. However, its solution can be written as:

$$\begin{aligned}C_T(t) &= C_{free}(t) + C_{bound}(t) = K_1 e^{-(k_2+k_3)t} \otimes C_P(t) \\ &+ \frac{K_1 k_3}{k_2 + k_3}\left(1 - e^{-(k_2+k_3)t}\right) \otimes C_P(t)\end{aligned} \tag{9}$$

This can be rewritten as:

$$C_T(t) = \frac{K_1 k_2}{k_2 + k_3} e^{-(k_2+k_3)t} \otimes C_P(t) + \frac{K_1 k_3}{k_2 + k_3} \otimes C_P(t) \tag{10}$$

In this equation, the second term on the right side of the equation describes the net influx of the tracer. The macro-parameter that is generally of most interest here is the net influx rate, K_i:

$$K_i = \frac{K_1 k_3}{k_2 + k_3} \tag{11}$$

In case of [^{18}F]FDG, the glucose consumption in the tissue of interest can be calculated as:

$$MR_{glu} = \frac{C_P^{glu} K_i}{LC}, \tag{12}$$

that is, the metabolic rate of glucose is equal to the product of the net influx rate of [^{18}F]FDG and the plasma concentration of glucose at the time of the scan divided by the lumped constant (LC), which accounts for the difference in kinetics between deoxyglucose and glucose itself.

Receptor Binding

For modeling receptor-targeted radiotracers, the compartment model can be expanded further to account for the different possible states of the tracer after it has entered the tissue (Fig. 8). As Figs. 8 and 9 illustrate, a tracer can either be free in the tissue (C_F), bound specifically to the receptor (or transporter, enzyme, *etc.*) of interest (C_S), or bound non-specifically to other receptors or proteins (C_{NS}). Of course, this is still a simplification of the underlying biology, since each separate non-specific binding site will have its own association (k_5) and disassociation (k_6) rate constants. Unfortunately, for the far majority of tracers, however, the model in Fig. 9a contains too many parameters to be robustly determined by PET. Therefore, the model is further simplified by lumping together the free and non-specific compartments, assuming that the non-specific binding fraction is much smaller than the specific binding, and both association to and disassociation from in tissue is so fast that the non-specific binding reaches equilibrium with the free tracer compartment very fast compared to the specific binding compartment (Fig. 9b).

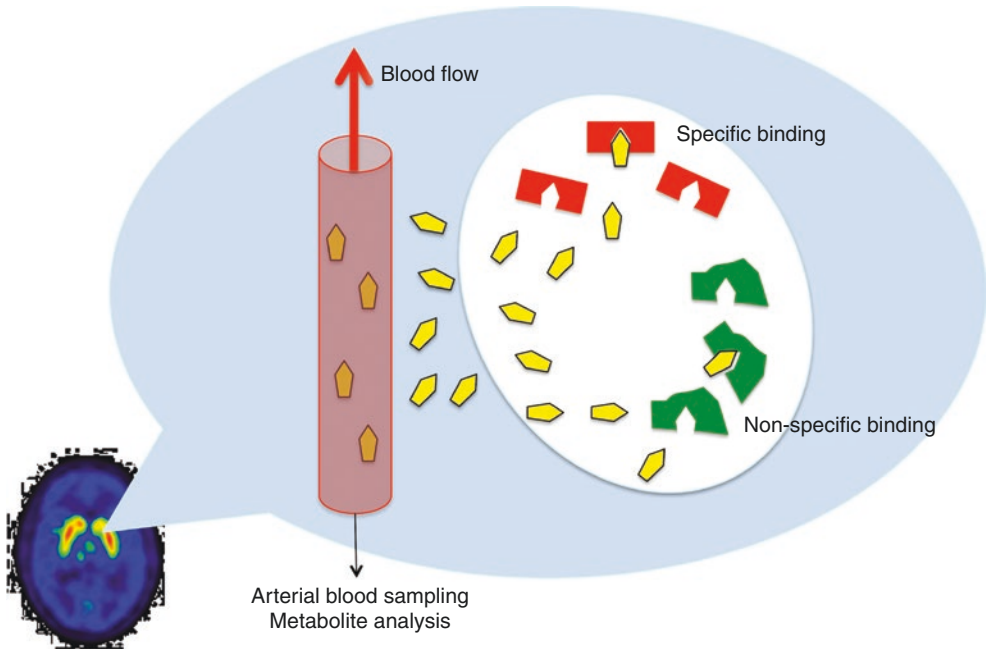

Fig. 8 The binding of a receptor-targeted radiotracer, showing the delivery of the tracer through the capillaries, free tracer in tissue, specific binding to the targeted receptor (*red*), and non-specific binding to other receptors or proteins (*green*)

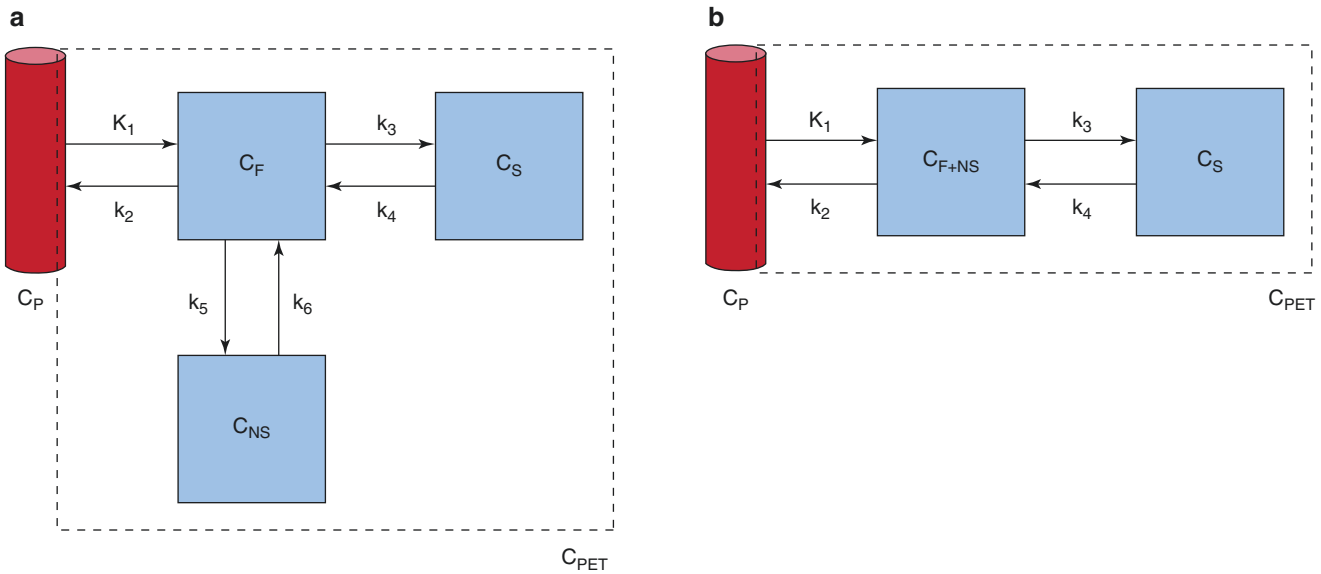

Fig. 9 Models for a receptor-targeted radiotracer: (**a**) Three-compartment model and (**b**) simplified two-compartment model

The differential equations describing the model in Fig. 9b are:

$$\begin{aligned}\frac{dC_{F+NS}(t)}{dt} &= K_1 C_P(t) - (k_2 + k_3) C_{F+NS}(t) + k_4 C_S(t) \\ \frac{dC_S(t)}{dt} &= k_3 C_{F+NS}(t) - k_4 C_S(t)\end{aligned} \tag{13}$$

The equation describing the solution of this model is (of course) more complex than that of the irreversible case, but this model can still be solved analytically. In this case, the outcomes that we are interested in are the total distribution volume V_T:

$$V_T = \frac{K_1}{k_2}\left(1 + \frac{k_3}{k_4}\right) \tag{14}$$

and the binding potential (BP_{ND})

$$BP_{ND} = \frac{k_3}{k_4} \tag{15}$$

The BP_{ND}—the binding potential relative to the non-displaceable compartment—is equal to the product of the receptor density (B_{max}) and the affinity of the tracer for the receptor ($1/K_D$). The term non-displaceable refers to the tracer uptake that is unrelated to the specific binding of the

target, hence not being displaceable by competition from other compounds with known affinity to the same target, *i.e.* $C_{F+NS} = C_{ND}$. BP_{ND} indicates that the estimated binding is related not to plasma tracer concentrations but to non-displaceable uptake. BP_{ND} can only be determined directly if the specifically bound compartment can be clearly distinguished from the free and non-specifically bound compartments. This, unfortunately, is rarely the case. Instead, BP_{ND} can be calculated indirectly by subtracting 1 from the "DVR," the ratio between the volumes of distribution V_T in the target tissue and a reference tissue which does not contain the targeted receptors and hence has no specific binding. This indirect calculation of BP_{ND} equals the direct estimation of BP_{ND} if the non-specific volume of distribution K_1/k_2—also called V_{ND}—is similar between the target and reference tissues:

$$\mathrm{DVR} = \frac{V_T}{V_T'} = \frac{V_{ND}\left(1+\mathrm{BP}_{ND}\right)}{V_{ND}'} = 1+\mathrm{BP}_{ND} \qquad (16)$$

where V_T and V_T' are the volumes of distribution in the target and reference tissues, respectively, and V_{ND} and V_{ND}' are the non-displaceable volumes of distribution in the target and reference tissues, respectively.

Reference Tissue Models

If there is a suitable reference tissue in which the non-displaceable volume of distribution is similar to that in the target tissue (*i.e.* $V_{ND} = V_{ND}'$; Fig. 10a), the differential equations for the reversible two-tissue compartment model can be rearranged so that the signal in the specific compartment can be expressed solely as a function of the signal in the reference tissue, in essence because the tissue response of the reference tissue is assumed to be the same as the part of the target tissue response that is due to non-specific uptake (C_{F+NS}) [5]. These models are primarily used in brain imaging, where the cerebellum can often be used as a reference tissue. Although their use has been attempted in regions outside the brain, the assumptions are often violated, and results should be interpreted with caution. The huge advantage presented by this scenario is that blood sampling is no longer necessary, making the use of quantitative PET much more feasible.

Furthermore, under the circumstances in which the kinetics of the tracer in both the target and reference tissues can both be described by a single-tissue model, that is, the specific and non-displaceable compartments are indistinguishable which is the case where the exchange of tracer between C_{F+NS} and C_S is rapid, the reference tissue model can be reduced even more into the simplified reference tissue model (SRTM; Fig. 10b) [6].

The solution of the SRTM is written as:

$$C_T(t) = R_1 C_{REF}(t) + \left(k_2 - \frac{R_1 k_2}{1+\mathrm{BP}_{ND}}\right) C_{REF}(t) \otimes \mathrm{e}^{-\frac{k_2}{1+\mathrm{BP}_{ND}}t} \qquad (17)$$

The SRTM equation (Eq. 17) also provides an estimate of the target tissue clearance rate k_2 and the parameter R_1, which is the ratio of K_1 in the target tissue to K_1' of the reference tissue. This parameter is also known as the relative delivery R_1 and may be used as a surrogate measure for relative cere-

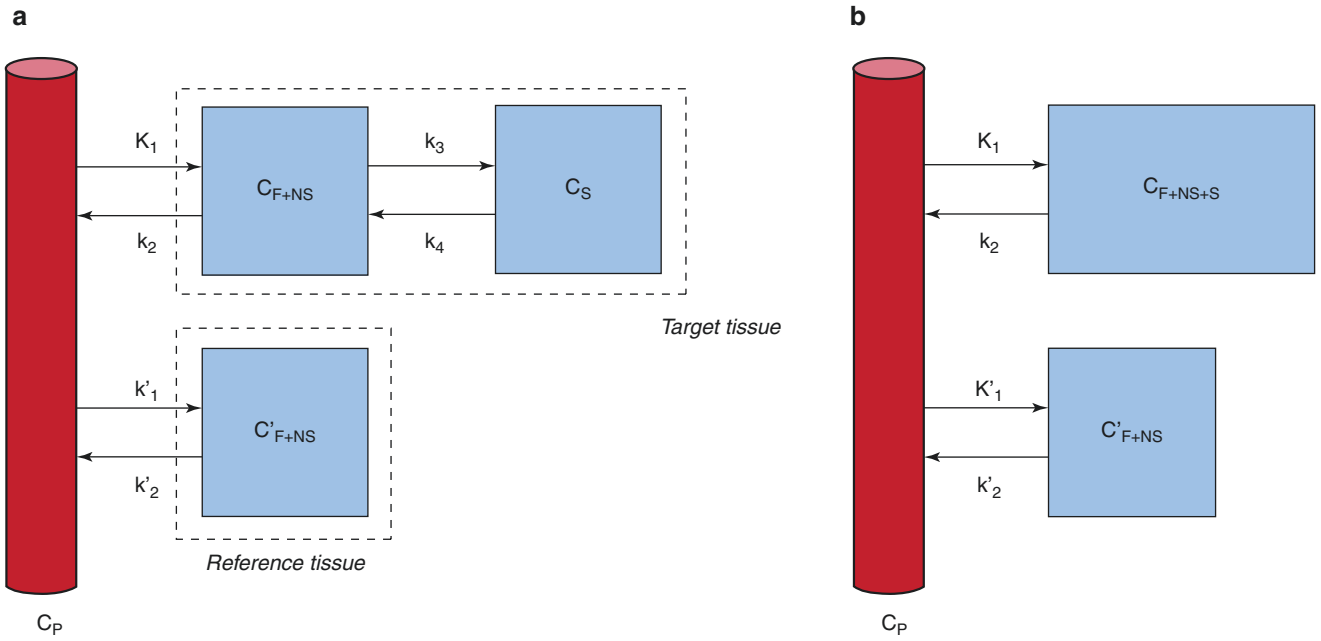

Fig. 10 Full reference tissue model (**a**) and simplified reference tissue model (**b**). The reference tissue contains only one non-specific compartment (C_{F+NS}), and the rate constants for tracer exchange between plasma and reference tissue are often denoted K_1' and k_2'

bral blood flow. This solution does not explicitly show the clearance rate k_2' of the reference tissue, but given the assumption that $V_{ND} = V_{ND}'$, K_1/k_2 also equals K_1'/k_2'. Thus k_2' can be estimated as k_2/R_1. When applying this model to different target regions, an estimate for the reference region k_2' will be acquired for each, but since there is only one reference tissue, $k_2' = k_2/R_1$ should be similar for each target region. A mean k_2' can then be obtained for a small number of regions for which robust fits can be obtained. Subsequently, k_2 can be replaced by $R_1 k_2'$ using this mean k_2' in the equation above, and fitting can be repeated for all regions, determining only two parameters (BP_{ND} and R_1) per TAC. Thus the iterative curve fitting becomes more robust. This is commonly referred to as SRTM2 [7].

Linearizations and Parametric Images

Instead of estimating the parameters of interest—*e.g.* the target density, blood flow, or metabolic rate—for a limited number of VOIs, parametric images can be constructed which display these parameters on a voxel-by-voxel level throughout the entire region scanned (Fig. 11). Parametric images allow for the immediate visual assessment of differences in the parameter of interest across the brain or body. Furthermore, they display this parameter with the spatial resolution of the original PET images, which also allows for the assessment of heterogeneity within tissues. However, the solutions of all of the systems of differential equations describing the compartment models above require nonlinear regression to estimate the individual parameters. Nonlinear regression is an iterative method that requires considerable computation time, which makes it unsuitable to perform calculations on a voxel-by-voxel level. Even if one single fit would take no more than 1/100th of a second on a regular computer, fitting one million voxels in a PET image of the brain would take about 20 min to compute, which is too long for routine use in clinical diagnosis or research. Below, a number of linearizations of the compartment models above will be discussed that allow for the more rapid calculation of parameters at the voxel level.

The Patlak Plot

This method was first described by Gjedde in 1981 [8] and Patlak *et al.* in 1983 and can be used to estimate the net uptake rate of irreversible tracers [9]. As previously stated, the solution of the differential equations describing the irreversible two-tissue compartment model (Eq. 9), shown in Fig. 7, can be written as:

$$C_T(t) = \frac{K_1 k_2}{k_2 + k_3} e^{-(k_2+k_3)t} \otimes C_P(t) + \frac{K_1 k_3}{k_2 + k_3} \otimes C_P(t) \quad (18)$$

When equilibrium between plasma and tissue is reached, the first term on the right-hand side of Eq. 18 becomes a constant multiplied with the plasma tracer concentration, while the second term becomes a constant multiplied with the integral of the plasma tracer concentration:

$$C_T(t) = v_e C_P(t) + K_i \int_t^0 C_P(\tau)\, d\tau \quad (19)$$

Dividing both sides of this equation with the plasma time-activity curve $C_P(t)$ gives:

$$\frac{C_T(t)}{C_P(t)} = v_e + K_i \frac{\int_0^t C_P(\tau)\, d\tau}{C_P(t)} \quad (20)$$

Now, plotting the left-hand side of the equation versus the integral term on the right-hand side, we obtain a graph that becomes linear after equilibrium is reached if tracer kinetics are irreversible, and the slope of which is the net uptake rate K_i. This is illustrated in Fig. 12.

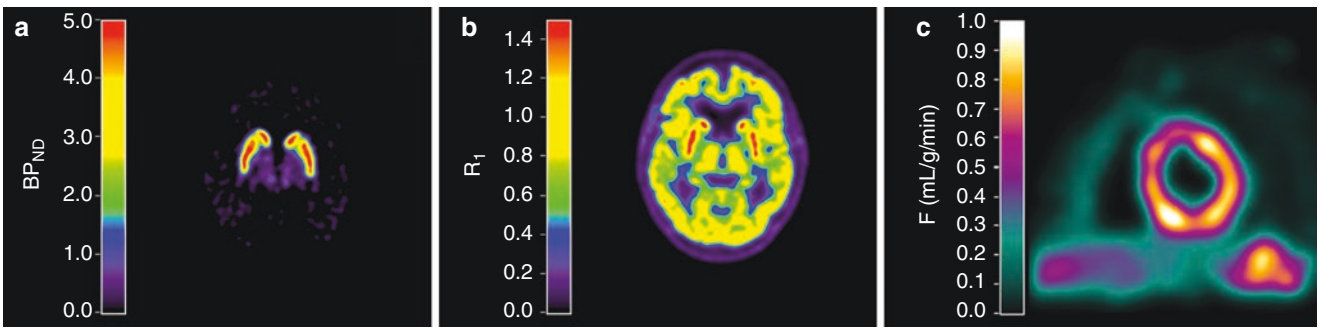

Fig. 11 Parametric BP_{ND} (**a**) and R_1 (**b**) images based on the dynamic [^{11}C]PE2I PET data shown in Fig. 1, showing dopamine transporter availability (**a**) and relative delivery (**b**); and a parametric myocardial blood flow image (MBF) (**c**) based on a 6 min dynamic [^{15}O]H_2O scan, showing MBF in mL/g/min at the voxel level (MBF)

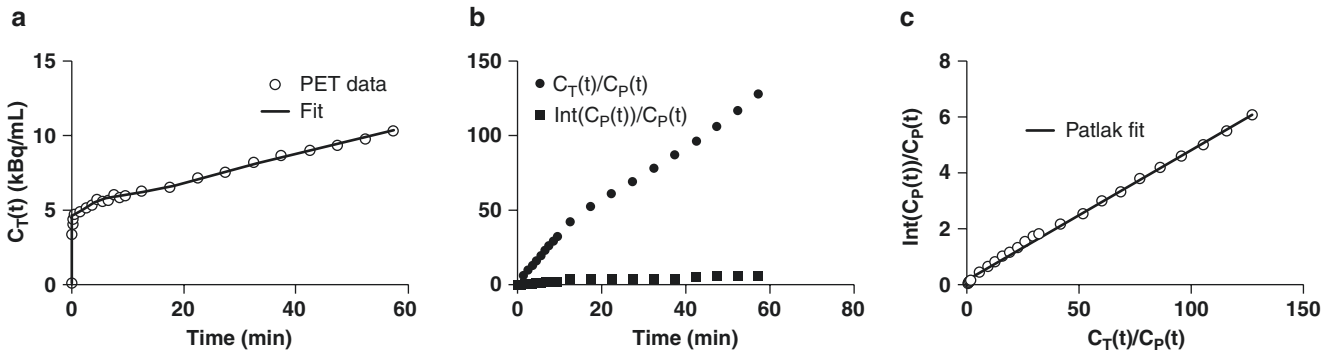

Fig. 12 Simulated PET data of a tracer with irreversible uptake using the same input curve as in Fig. 5 and fit using irreversible two-tissue compartment model (**a**); Patlak *x*- and *y*-axis versus real time (**b**); Patlak plot with linear fit (**c**). The slope of the linear fit equals K_i

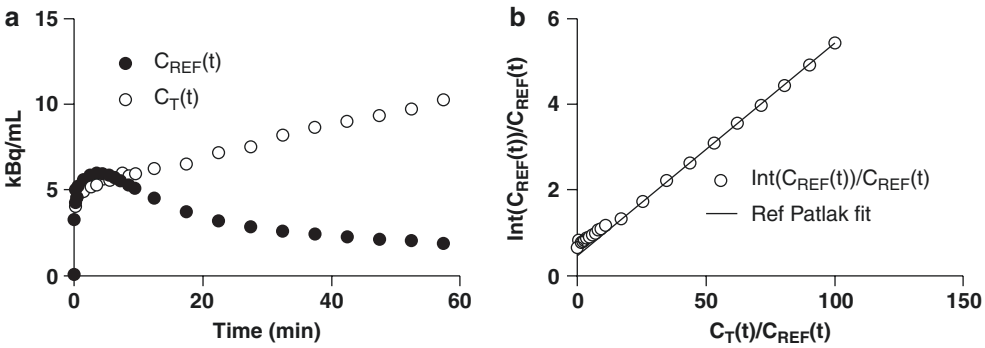

Fig. 13 Simulated PET data of a tracer with irreversible uptake (open symbols) and reference tissue (closed symbols) (**a**) and reference Patlak plot with linear fit (**b**). The slope of the linear fit equals K_i^{REF}

The Patlak method can also be used with a reference tissue approach. In this case, the $C_P(t)$ term in Eq. 20 is replaced by $C_{REF}(t)$, and K_i is replaced by K_i^{REF}, the net influx rate relative to the reference tissue (Fig. 13).

The Logan Plot

The Logan plot was developed for the analysis of PET studies with reversible radioligands [10]. The solution to the reversible two-tissue compartment model (see Eq. 13, Fig. 9) can be written as follows:

$$C_T(t) = \frac{K_1(k_3+k_4-\beta_1)}{\beta_2-\beta_1} e^{-\beta_1 t} \otimes C_P(t) + \frac{K_1(\beta_2-k_3-k_4)}{\beta_2-\beta_1} e^{-\beta_2 t} \otimes C_P(t) \quad (21)$$

where

$$\beta_{1,2} = \frac{k_2+k_3+k_4 \sqrt{(k_2+k_3+k_4)^2-4k_2k_4}}{2} \quad (22)$$

$$\alpha_1 = \frac{K_1(k_3+k_4-\beta_1)}{\beta_2-\beta_1}; \quad \alpha_2 = \frac{K_1(\beta_2-k_3-k_4)}{\beta_2-\beta_1} \quad (23)$$

This can be interpreted as two parallel single-tissue compartment models, and this parallel compartment model is mathematically indistinguishable from the serial two-tissue compartment model (Fig. 14):

$$C_T(t) = \alpha_1 e^{-\beta_1 t} \otimes C_P(t) + \alpha_2 e^{-\beta_2 t} \otimes C_P(t) \quad (24)$$

If the clearance rate from the specifically bound compartment C_S in the serial two-compartment model (see Fig. 14a) is much faster than the overall clearance from tissue ($k_4 >> k_2$), then $\beta_2 >> \beta_1$, α_2 approaches zero, and α_1 approaches K_1. Thus, the second term on the right-hand side quickly becomes very small relative to the first term and can be neglected. So, the total tissue response is essentially C_1, and the system can be treated as a single-tissue compartment model. The differential equation for this single-tissue approximation is then:

$$\frac{dC_T(t)}{dt} = \frac{dC_1(t)}{dt} = \alpha_1 C_P(t) - \beta_1 C_T(t) \quad (25)$$

Integrating both sides of the equation gives:

$$C_T(t) = \alpha_1 \int_t^0 C_P(\tau) d\tau - \beta_1 \int_t^0 C_T(\tau) d\tau \quad (26)$$

And dividing both sides by $C_T(t)/\beta_1$ and rearranging the equation result in:

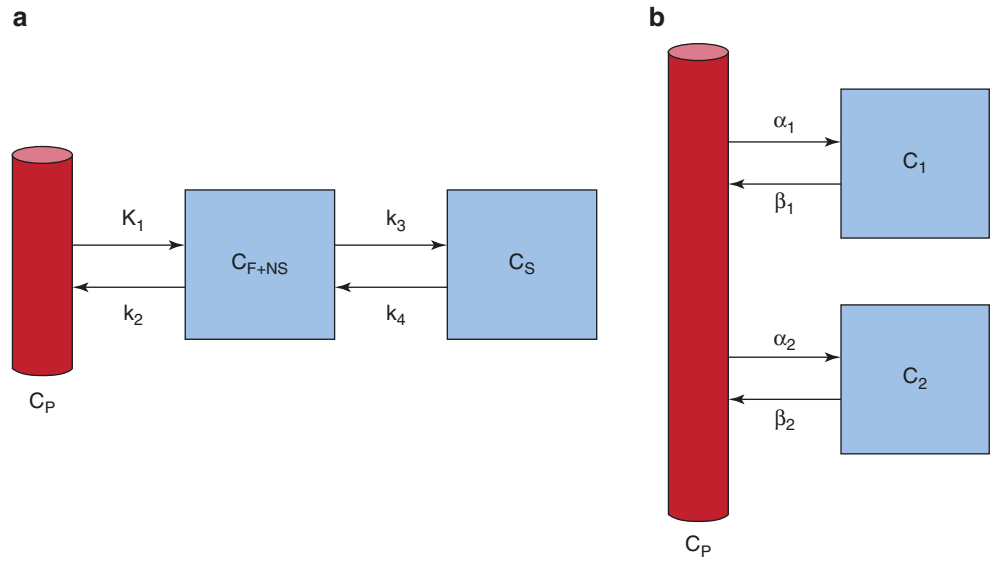

Fig. 14 The regular reversible two-tissue compartment model (**a**) and a set of two parallel single-tissue compartment models (**b**) that are mathematically equivalent to the reversible two-tissue compartment model using the conversions in Eqs. 21 and 22

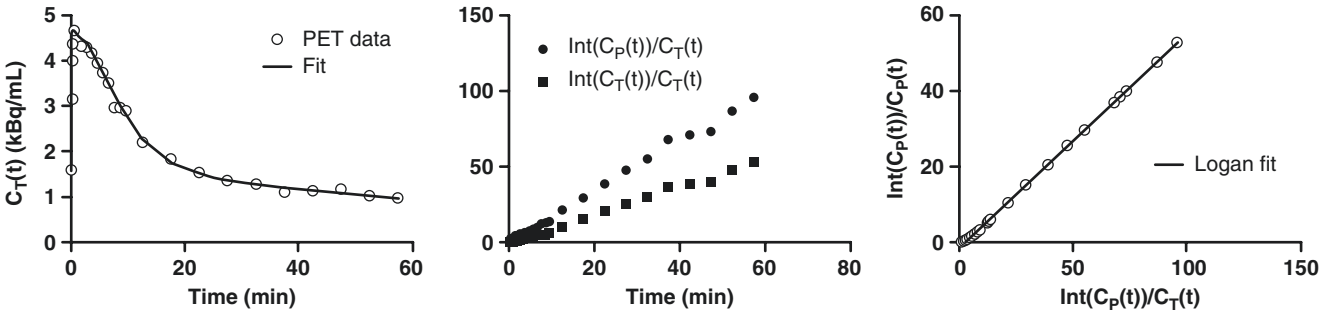

Fig. 15 The Logan plot correlates ratios of measured radioactivity concentrations, resulting in a linear phase in which the slope provides an estimate of the binding. (**a**) Time-activity curve of tissue radioactivity concentration, (**b**) ratios of integrals of plasma radioactivity concentration ($\mathrm{Int}(C_P(t))$ and tissue radioactivity concentration ($\mathrm{Int}(C_P(t))$ over tissue radioactivity concentration ($C_P(t)$) as a function of time and (**c**) ratios plotted against each other providing the Logan plot, where the slope of the linear phase represents V_T

$$\frac{\int_0^t C_T(\tau)d\tau}{C_T(t)} = \frac{\alpha_1}{\beta_1}\frac{\int_0^t C_P(\tau)d\tau}{C_T(t)} - \frac{1}{\beta_1} \qquad (27)$$

This, like the Patlak equation above, is a linear equation $y = ax + b$. Plotting the left-hand side of the equation versus the integral term on the right-hand side gives a graph that becomes linear provided that tracer kinetics are reversible (Fig. 15). The slope of this straight line—α_1/β_1—equals V_T.

The Logan plot can also be implemented as a reference tissue method [11]. In this case, the equation is:

$$\frac{\int_0^t C_T(\tau)d\tau}{C_T(t)} = \mathrm{DVR}\frac{\int_0^t C_{REF}(\tau)d\tau + \frac{C_{REF}(t)}{k_2'}}{C_T(t)} + c \qquad (28)$$

with k_2' the reference tissue clearance rate and the slope representing the distribution volume ratio, DVR, as previously described in Eq. 16.

Basis Function Methods

Both the Patlak and Logan methods have the advantage of being linear, so for individual VOIs, we can even do the calculations in a simple spreadsheet. Another advantage of these approaches is that both methods are computationally fast compared to nonlinear regression methods. Indeed, parametric maps for the whole brain that show K_i or V_T on a voxel-by-voxel level can be calculated in seconds. A disadvantage of these methods, however, is that the individual rate constants, such as K_1 and k_3, can no longer be determined. An alternative linearization method that circumvents this problem makes use of basis functions, as shown in Fig. 16. If we look closer at the solution of the single-tissue compartment model:

$$C_T(t) = K_1 C_P(t) \otimes e^{-k_2 t} \qquad (29)$$

we can construct a library of possible solutions by choosing a suitable range of k_2 values:

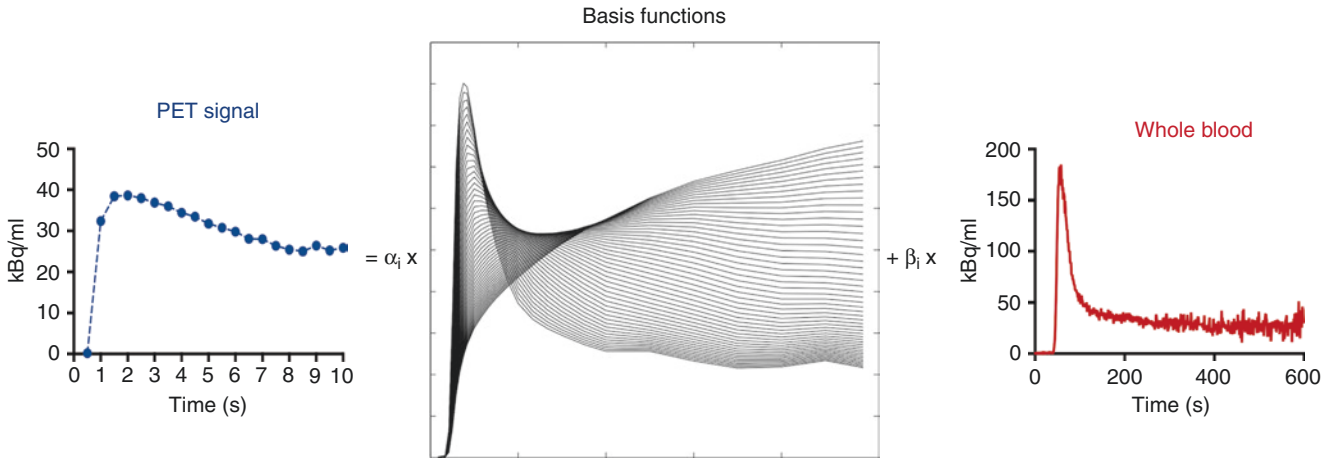

Fig. 16 Identifying the optimal basis function *(center)* to the experimental data (*left*) enables the computation of individual rate constants and facilitates the inclusion of a blood volume component (*right)*

$$BF_i(t) = C_P(t) \otimes e^{-k_2^i t}; k_2^{min} < k_2^i < k_2^{max} \quad (30)$$

The solution can then be written as a linear combination of any single one of these basis functions and, if necessary, a blood volume component:

$$C_T(t) = \alpha_i BF_i(t) + \beta_i C_A(t) \quad (31)$$

This is a linear equation, and by evaluating it for each of the basis functions, the linear combination of a basis function and a blood volume component that results in the best fit can be found. K_1 and V_A are then equal to α and β for that particular basis function, respectively. In addition, k_2 is the k_2 corresponding to that basis function [12, 13]. This process can be implemented very efficiently using matrix equations. Since any common compartment model is mathematically equivalent to a parallel compartment model with the same number of compartments as the original model (see Fig. 14), the basis function method can also be extended to irreversible and reversible two-tissue compartment models. For a two-tissue reversible model, two sets of basis functions are then required, and five parameters are fitted. These parameters can then be translated into their "original" rate constants using, for example, Eqs. 22 and 23 for the two-tissue reversible case.

Although more complicated than the Patlak or Logan methods, the basis function method enables the computation of individual rate constants and facilitates the inclusion of a blood volume component in the calculations. In addition, by limiting the range of clearance rate constants to biologically plausible values and using a limited number of basis functions, the effect of noise on the resulting parametric images can be limited (see Fig. 16).

Given the decreased processing time and lower sensitivity to noise, the basis function method was first suggested in the context of voxel-based receptor parametric mapping (RPM) as a linearization of SRTM [14] to provide parametric images of BP_{ND} and the relative delivery R_1. The images shown in Fig. 11a, b were calculated using RPM, whereas the image shown in Fig. 11c was calculated using a basis function implementation of the single-tissue compartment model for $[^{15}O]H_2O$.

Simplified Methods

Standardized Uptake Value

Standardized uptake values (SUV) are a common means of semiquantitatively describing the uptake of a tracer. SUV is defined as the activity concentration in a tissue at a certain time after injection normalized to the injected amount of radioactivity per body weight W:

$$SUV_W = \frac{C_T}{A_{inj}/W} \quad (32)$$

Instead of normalization to body weight, SUV can also be calculated relative to lean body mass (LBM) or body surface area (BSA) by replacing W with LBM or BSA in Eq. 32. The advantage of using SUV in a clinical setting is that it requires only a single time-point measurement and can easily be used for whole-body scans. Although it has been demonstrated that SUV is very useful in some cases—for example, it correlates very well with glucose consumption in non-small cell lung tumors (Fig. 17) [15] and other cancers—this does not mean that SUV can be used equally well for other applications. The reason that SUV is a good approximation for K_i in certain cases can be explained by looking at the equation describing the irreversible two-tissue compartment model and ignoring the contribution of the reversible component to the signal:

$$C_T(t) = K_i \int_t^0 C_P(\tau) d\tau \quad (33)$$

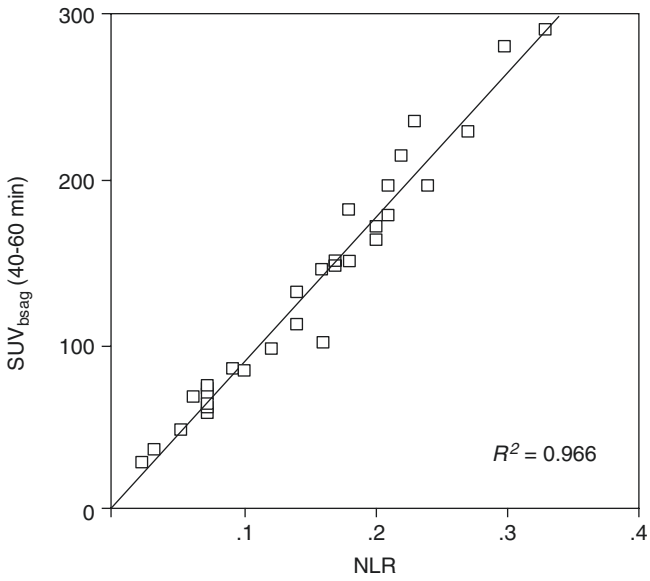

Fig. 17 Standardized uptake value, normalized for body surface area, versus metabolic rate of glucose in non-small cell lung cancer [15] (From Hoekstra *et al.* [15], with permission)

Now, if we don't measure the activity concentration in the blood, we obviously don't know the plasma integral on the right-hand side of the equation. We do, however, know that the plasma integral should probably be somehow related to both the amount of radioactivity that we injected in the patient and the patient's mass. Therefore, we could replace the integral with a constant multiplied by the injected activity per body weight:

$$C_T(t) \approx K_i c \frac{A_{inj}}{W} \tag{34}$$

As a result, SUV at a long enough time after injection can be described by:

$$\mathrm{SUV}(t) = \frac{C_T(t)}{A_{inj}/W} = K_i c \tag{35}$$

Hence, as long as the constant c—which relates the plasma integral to the injected activity per body weight—is similar across subjects or before and after interventions such as chemotherapy, SUV can be used to compare tumor glucose metabolism between patients and to assess the effects of interventions on glucose metabolism. However, if this constant c does vary considerably between patients and interventions, SUV cannot be used reliably. Indeed, its use should be validated against fully quantitative measurements for any new application.

Standardized Uptake Value Ratio

As mentioned above, the volume of distribution (V_T) is defined as the radioactivity concentration ratio between tissue and plasma at equilibrium. Hence, at equilibrium, the distribution volume ratio (DVR) can be approximated by the activity concentration ratio (ACR) in target and reference tissues:

$$\mathrm{DVR} = \frac{V_T}{V_T'} = \frac{C_T / C_P}{C_{REF} / C_P} = \frac{C_T}{C_{REF}} = \mathrm{ACR} = \mathrm{SUVR} \tag{36}$$

Instead of activity concentration ratio, this measure is often referred to as the standardized uptake value ratio (SUVR), which has the same numerical value as the activity concentration ratio, since for SUVR both C_T and C_{REF} are divided by the same injected activity per bodyweight to obtain SUV values from activity concentrations and thus are canceled out. However, since true equilibrium is often not reached during a practically useful time after injection and clearance is slower in target than in reference tissue, C_T/C_P often overestimates V_T, more so in target tissues than in reference tissues. As a result, SUVR will often provide an overestimation of the true BP_{ND} value (*blue symbols* in Fig. 18). Instead of using SUVR at true equilibrium, it can also be estimated at transient equilibrium, *i.e.* at the time when the specific binding curve peaks. At that time, $dC_S(t)/dt$ in Eq. 13 equals zero. Hence:

$$\begin{aligned} &k_3 C_{F+NS} = k_4 C_S \Rightarrow \\ &\frac{k_3}{k_4}\left(= \mathrm{BP_{ND}}\right) = \frac{C_S}{C_{F+NS}} = \frac{C_T - C_{REF}}{C_{REF}} \\ &= \frac{C_T}{C_{REF}} - 1 = \mathrm{SUVR} - 1^{w} \end{aligned} \tag{37}$$

As an example, Fig. 18 shows the relationship between BP_{ND} and SUVR-1 for the tau protein-targeting radiotracer [^{18}F]THK5317 at transient equilibrium—which occurs around 30 min p.i. in the selected regions—and at 80–90 min p.i., at which point true equilibrium is not yet reached for this tracer. A challenge when using early SUVR values corresponding to transient equilibrium is that the time at which transient equilibrium occurs is dependent on the level of binding in the target tissue, which may result in a heterogeneous bias across the brain and/or disease-dependent bias. Late equilibrium SUVR values, on the other hand, tend to show a much more homogeneous bias that is less disease-dependent. Hence, the preference for either early or late values of SUVR—corresponding to DVR rather than BP_{ND} as per Eqs. 16 and 37—is dependent on the research or clinical question at hand.

Model Selection and Simplification

When performing a PET study with a new tracer—or when applying an existing tracer to a different disease or tissue—a number of steps should always be followed in order to determine the optimal method for kinetic analysis. First, it is important to determine which compartment model fits the data best and provides outcome parameters that most accurately describe the biological parameters of interest. This is usually done by fitting single-tissue as well as irreversible

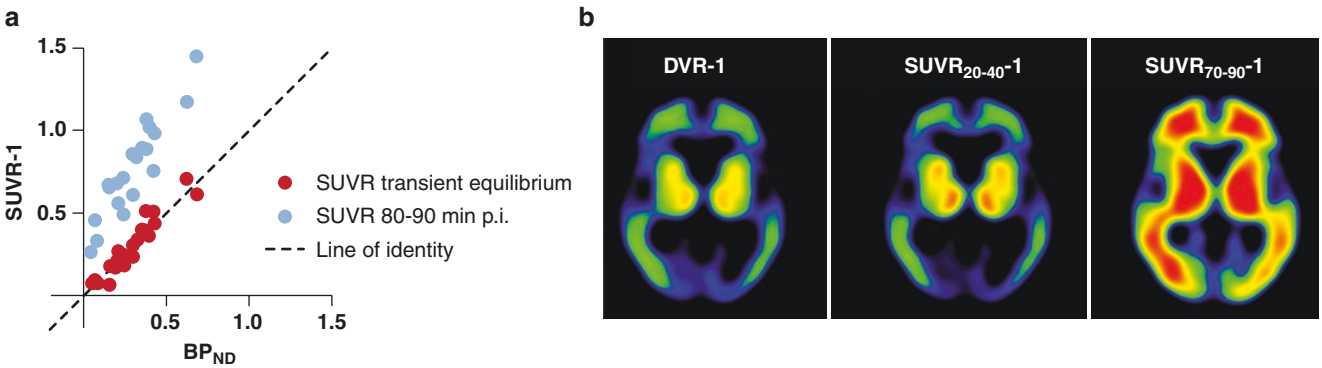

Fig. 18 (**a**) Standardized uptake value ratio versus the binding potential relative to the non-displaceable compartment (BP_{ND}) for the tau ligand [^{18}F]THK5317 in the amygdala, hippocampus, and entorhinal cortex in seven Alzheimer's disease patients at transient equilibrium (red circles) and at 80–90 min p.i. (blue circles). The deviation from the line of identity shows the overestimation bias of $SUVR_{80–90}$-1. (**b**) A parametric DVR-1 image created using the reference Logan method (*left*) and SUVR-1 images at 20–40 and 70–90 min p.i (*center and right*), illustrating how $SUVR_{70–90}$ overestimates DVR, whereas $SUVR_{20–40}$ does not because the 20–40 min interval is roughly the time at which transient equilibrium occurs across most of the brain for this tracer

and reversible compartment models to the measured PET data using a metabolite-corrected plasma input function. The optimal model can be determined based on the quality of the fits using a number of different information criteria (*e.g.* Akaike information criterion, Schwarz information criterion, Bayesian information criterion, *etc.*) which all use the sum of squared residuals penalized for the number of parameters as a goodness of fit criterion. If there is little difference between two models, it is likely that the simpler model will result in more robust parameters and maybe preferred. If a reference tissue is available, its use should be validated against a plasma input compartment model. Further simplifications such as the use of SUVR should always be validated against quantitative kinetic analysis results.

Conclusion

Tracer kinetic analysis can provide us with the underlying biological parameters governing the behavior of a tracer and, as a result, shed light upon pathophysiologic processes. Provided the appropriate tracers are available, numerous functional parameters can be measured, including substrate metabolism, receptor or transporter availability, receptor occupancy, enzyme activity, blood flow, *etc.* The images in Fig. 11 are examples of how we can use tracer kinetic modeling to separate non-specific signal (see Fig. 11a) from specific signal (see Fig. 11b) and how we can use kinetic modeling of data from a freely diffusable tracer (for which uptake images give no useful information by themselves) to compute quantitative images of biological parameters, in this case myocardial blood flow (see Fig. 11c). Oftentimes, simplified methods such as the use of SUVs on static images can be substitutes for parameters based on the tracer kinetic analysis of dynamic scans, but this should always be validated via comparison to the underlying functional parameters based on accurate quantitative methods. Simply put, too much simplification can lead to misleading results. However, precise methods for quantification are necessary for the validation of such strategies and are required for advanced applications of PET such as in precision medicine, disease monitoring, evaluating treatment response, and drug development studies. In recent years, more and more clinical applications have emerged in which quantification outperforms simplified measurements, and novel, automated data processing methods will soon make the routine clinical application of quantification feasible.

Bottom Line

- Tracer kinetic analysis can provide us with the underlying biological parameters governing the behavior of tracers, allowing us to measure regional pathophysiologic processes.
- Precise quantification is necessary in advanced applications of PET, such as in precision medicine, monitoring treatment response, and drug development studies.
- Linearizations of tracer kinetic models allow for the calculation of parametric images, which display quantitative physiological parameters at the voxel level.
- Simplified methods need to be validated against true quantitative measures.

References

1. Lammertsma AA. Forward to the Past: The case for quantitative PET imaging. J Nucl Med. 2017;58(7):1019–24.
2. Jonasson M, Wall A, Chiotis K, Saint-Aubert L, Wilking H, Sprycha M, et al. Tracer kinetic analysis of (S)-18F-THK5117 as a PET tracer for assessing tau pathology. J Nucl Med. 2016;57:574.

3. Kety SS. The theory and applications of the exchange of inert gas at the lungs and tissues. Pharmacol Rev. 1951;3(1):1–41.
4. Kety SS, Schmidt CF. The nitrous oxide method for the quantitative determination of cerebral blood flow in man: theory, procedure and normal values. J Clin Invest. 1948;27(4):476–83.
5. Lammertsma AA, Bench CJ, Hume SP, Osman S, Gunn K, Brooks DJ, et al. Comparison of methods for analysis of clinical [C-11] raclopride studies. J Cereb Blood Flow Metab. 1996;16(1):42–52.
6. Lammertsma AA, Hume SP. Simplified reference tissue model for PET receptor studies. NeuroImage. 1996;4(3Pt 1):153–8.
7. Wu Y, Carson RE. Noise reduction in the simplified reference tissue model for neuroreceptor functional imaging. J Cereb Blood Flow Metab. 2002;22(12):1440–52.
8. Gjedde A. High- and low-affinity transport of D-glucose from blood to brain. J Neurochem. 1981;36(4):1463–71.
9. Patlak CS, Blasberg RG, Fenstermacher JD. Graphical evaluation of blood-to-brain transfer constants from multiple-time uptake data. J Cereb Blood Flow Metab. 1983;3(1):1–7.
10. Logan J, Fowler JS, Volkow ND, Wolf AP, Dewey SL, Schlyer DJ, et al. Graphical analysis of reversible radioligand binding from time-activity measurements applied to [N- 11 C-methyl]-(−)-cocaine PET studies in human subjects. J Cereb Blood Flow Metab. 1990;10(5):740–7.
11. Logan J, Fowler JS, Volkow ND, Wang GJ, Ding YS, Alexoff DL. Distribution volume ratios without blood sampling from graphical analysis of PET data. J Cereb Blood Flow Metab. 1996;16(5):834–40.
12. Watabe H, Jino H, Kawachi N, Teramoto N, Hayashi T, Ohta Y, et al. Parametric imaging of myocardial blood flow with 15O-water and PET using the basis function method. J Nucl Med. 2005;46(7):1219–24.
13. Boellaard R, Knaapen P, Rijbroek A, Luurtsema GJ, Lammertsma AA. Evaluation of basis function and linear least squares methods for generating parametric blood flow images using 15O-water and positron emission tomography. Mol Imaging Biol. 2005;7(4):273–85.
14. Gunn RN, Lammertsma AA, Hume SP, Cunningham VJ. Parametric imaging of ligand-receptor binding in PET using a simplified reference region model. NeuroImage. 1997;6(4):279–87.
15. Hoekstra CJ, Hoekstra OS, Stroobants SG, Vansteenkiste J, Nuyts J, Smit EF, et al. Methods to monitor response to chemotherapy in non-small cell lung cancer with 18F-FDG PET. J Nucl Med. 2002;43(10):1304–9.

An Introduction to Radiation Protection

Brian Serencsits, Brian M. Quinn, and Lawrence T. Dauer

Fundamentals

The rise of nuclear medicine as a critical component of clinical care has prompted a concomitant surge in the importance of radiation protection within radiochemistry laboratories, radiopharmacies, and nuclear medicine facilities [1]. The potential harm of ionizing radiation was recognized not long after it was first implemented into medical applications [2, 3]. Overexposure to radiation was the cause of both deterministic (*e.g.* skin injuries) and stochastic (*e.g.* cancer) health problems for early workers. As such, the development of appropriate radiation safety and protection practices began to be formulated for the safe use of ionizing radiation in both the laboratory and the clinic [4].

Key Organizations in the Field of Radiation Protection

The first recommendations on radiation protection were offered in the late 1920s by an international radiation protection group—"The International X-Ray and Radium Protection Committee"—formed in 1928 during the 2nd International Congress of Radiology in Stockholm to respond to the dramatic increase of injuries to radiologists. In 1950, this committee was renamed the "International Commission on Radiological Protection" (ICRP). Today, the ICRP is an independent registered charity consisting of international experts whose aim is to provide recommendations on appropriate standard human protections and to disseminate this information in reports addressing all aspects of protection against ionizing radiation [4, 7–11]. The ICRP bases many of its recommendations on data produced by the United Nations Scientific Committee on the Effects of Atomic Radiation (UNSCEAR), a committee consisting of scientists from different member nations whose role is to assess and report measurements on the effects of exposure to ionizing radiation [5, 6]. Another important organization in this field is the International Atomic Energy Agency (IAEA). Based within the United Nations, the IAEA is an independent intergovernmental organization that promotes safety in the application of nuclear technologies as well as the protection of human health and the environment against ionizing radiation. The IAEA has developed basic safety standards implementing the guidance in the publications of the ICRP [12–14].

National and local authorities typically have specific regulations governing the use and storage of radioactive materials, including those used by radiochemists. Academic, laboratory, and medical facilities develop specific procedures in order to achieve safety results according to their own local governing structure. The overall objective of all of these organizations is to facilitate the beneficial use of radionuclides and to ensure the safe practice of radiochemistry while simultaneously protecting workers, patients, and the public from the detrimental effects of ionizing radiation.

Fundamental Principles of Radiation Protection

At its core, radiation protection is governed by three principles that can be applied in a variety of settings to determine the actions necessary to ensure the health and safety of staff, patients, and the public:

The principle of justification dictates that any decision that alters the radiation exposure to an individual should do more good than harm. In other words, the benefits to individuals and to society from introducing radiation or continuing exposure to radiation must outweigh the harm created by the exposure to the said radiation [4, 15].

The principle of optimization of protection dictates that the likelihood of incurring exposure, the number of people exposed, and the magnitude of their individual doses should always be kept *a*s *l*ow *a*s *r*easonably *a*chievable (ALARA), considering both economic and societal factors [4, 15].

B. Serencsits · B. M. Quinn · L. T. Dauer (✉)
Department of Medical Physics, Memorial Sloan Kettering Cancer Center, New York, NY, USA
e-mail: dauerl@mskcc.org

J. S. Lewis et al. (eds.), *Radiopharmaceutical Chemistry*, https://doi.org/10.1007/978-3-319-98947-1_29

Table 1 Internationally recommended annual dose limits in "planned exposure" situations

Type of limit	Occupational	Public
Effective dose	20 mSv[a]	1 mSv
Equivalent dose to…		
Lens of the eye	20 mSv[b]	15 mSv
Skin	500 mSv	50 mSv
Hands and feet	500 mSv	–

[a]Averaged over defined periods of 5 years with the further provision that the effective dose should not exceed 50 mSv in any single year. Additional restrictions apply to the occupational exposure of women who have declared a pregnancy.
[b]Some countries have suggested an occupational dose limit of 50 mSv for the lens of the eye.

The principle of dose limits dictates that the total dose to any individual from regulated sources in planned exposure situations should not exceed the limits specified by the applicable regulatory bodies. Fundamental differences between the groups of people exposed (the public, workers, radiochemists, students, apprentices, *etc.*) must be taken into account in order to ensure the most appropriate levels of protection. As such, dose constraints—restrictions on prospective doses to individuals—must be employed as part of the practice of radiopharmaceutical chemistry. Table 1 lists the current internationally recommended dose limits for "planned exposure" situations.

Details

Radiation Interactions with Matter

Broadly speaking, the emissions from radionuclides can be classified into two categories: particles and photons (see Chap. 3 for a far more detailed discussion of radioactive decay and emissions). In the context of radiation protection, the manner in which these emissions interact with matter can have important implications, both in terms of their potential to do damage to tissue as well as the shielding and countermeasures necessary to provide proper protection. The interaction between radiation and matter can often result in ionization events within materials, a process that—not surprisingly—depends on both the source of the radiation and the material being irradiated [2, 16]. The "specific ionization"of radioactive particles or photons of radiation is defined as the number of ion pairs produced by them per unit of path length (number of ion pairs cm^{-1}) as they interact with materials. The average energy required for an ionizing radiation to produce a single ion pair in air is about 33.7 eV, while it is 35 eV in water [17]. The energy lost by the incident particle or photon of radiation is described by the term "linear energy transfer" (LET), which is defined as the average energy imparted per unit of path length ($keV\mu m^{-1}$) [18].

Interactions of Particles Charged particles such as alpha particles, beta particles, and positrons interact with materials in ways that depend heavily on their mass, kinetic energy, and charge [3]. Table 2 provides some basic properties of several alpha- and beta-emitting radionuclides. Alpha particles are high-LET emissions (>100 keV μm^{-1}) and usually possess energies of several MeV. They typically travel in straight lines due to their relatively large mass and momentum and have a high specific ionization due to their large positive charge. They deposit most of their energy as they slow down in materials at the end of their range, a point known as the Bragg peak [2]. In air, this distance corresponds to ~3–4 cm, though it is *much* shorter in tissue: about 10–20 μm. Alpha particles are less of a radiation hazard from external exposures because they cannot penetrate through the outermost layer of dead skin—about 70 μm thick—although several alpha-emitting radionuclides also emit photons that require consideration from a radiation protection standpoint. Figure 1 displays the average range of alpha particles of various energies in water, which is often used as a proxy for the range of the particles in tissue. On the other hand, alpha particles can be a significant concern if introduced internally, where they can directly interact with the cells of the mucosa of the breathing airway, the alveoli in the lung, the lining of the gastrointestinal tract, and the surfaces of the bone [19]. As a result, working with alpha-emitting radionuclides requires careful contamination control along with countermeasures to avoid inhalation or ingestion.

Table 2 Selected physical properties of several alpha- and beta-emitting radionuclides

Radionuclide	Half-life	E_{max} (MeV)	Range in water (mm)
Beta (negatron) emitters			
^{3}H	12.5 years	0.019	<0.1
^{14}C	5730 years	0.157	0.3
^{32}P	14.3 days	1.710	8.0
^{35}S	87 days	0.167	0.3
^{89}Sr	50.5 days	1.491	6.6
^{131}I	8 days	0.606	2.2
^{186}Re	3.8 days	1.077	4.3
^{188}Re	16.8 h	1.965	10.0
^{153}Sm	1.9 days	0.702	2.5
^{177}Lu	6.7 days	0.498	1.5
$^{90}Sr/^{90}Y$	28 years	2.284	12.2
Beta (positron) emitters			
^{18}F	110 min	0.634	2.4
^{11}C	20.4 min	0.960	5.0
^{13}N	10 min	1.199	5.4
^{15}O	2 min	1.732	8.2
^{68}Ga	68 min	1.899	9.1
^{82}Rb	75 s	3.356	15.6
Alpha emitters (and progeny)-alpha only			
^{212}Bi	60.5 min	6.090	0.1
^{225}Ac	10 days	5.800	0.1
^{223}Ra	11.43 days	7.590	0.1
^{224}Ra	3.66 days	8.784	0.1
^{226}Ra	1620 years	7.833	<0.1

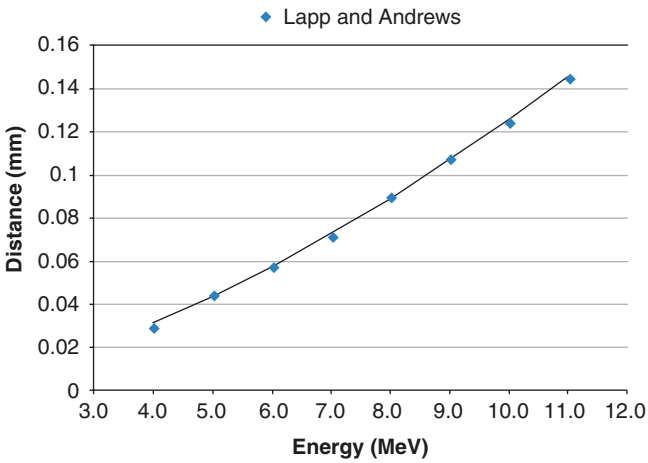

Fig. 1 Range of alpha particles in water ("tissue-equivalent" values)

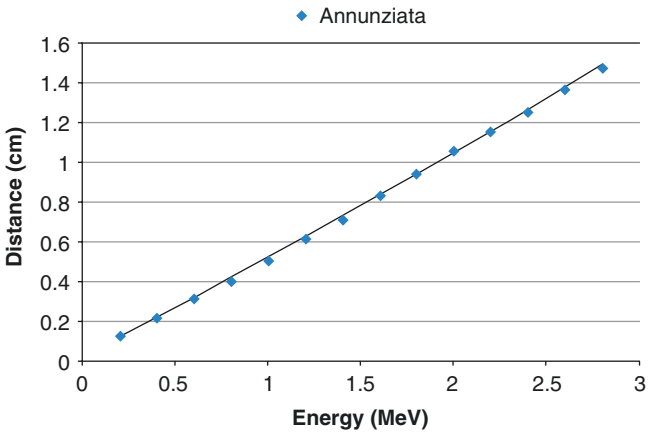

Fig. 2 Range of beta particles in water ("tissue-equivalent" values)

Beta particles and positrons have very low mass and a singular charge. As a result, they are easily deflected during interactions and follow a tortuous trajectory through materials. Beta particles are considered low-LET radiations (<10 keV μm^{-1}) with a much lower specific ionization than alphas. This allows beta particles to travel much greater distances in materials: depending on their energy, a few centimeters to many meters in air and microns to millimeters in soft tissues. Figure 2 displays the average range of beta particles in a tissue-equivalent environment. A deflected (or decelerated) beta particle will also emit a bremsstrahlung photon—typically a low-energy X-ray—that will itself have further interactions in the material. As explained in detail in Chap. 3, when a positron expends all of its energy and comes to a stop, it annihilates with an electron (its antiparticle) and creates two 511 keV photons that travel in opposite directions. These photons also lead to many secondary interactions and therefore require heavy shielding [20, 21]. Depending on their energy, beta particles can represent both an external and an internal radiation exposure hazard.

Interactions of Photons Photons—including gamma rays (from gamma decay, electron capture, or isomeric transition), X-rays (from electron capture), and bremsstrahlung X-rays (from particle interactions)—are electromagnetic radiations. They can cause ionizations as they travel through matter, yet they have no mass and carry no charge. The type of interaction depends heavily on the properties of the material as well as the energy of the photon [2, 3].

At lower photon energies, the photoelectric effect dominates. The photoelectric effect occurs when the photon is completely absorbed, and a tightly bound atomic electron—now called a photoelectron—is ejected with a kinetic energy related to the energy of the incident photon. In addition to this primary ionization, the vacancies in orbital shells are filled immediately, resulting in the emission of additional X-rays and/or Auger electrons. The probability of the photoelectric effect increases with decreasing photon energy and increasing atomic number of the material. The ejected electrons undergo many local ionizing events close to the site of their creation and, therefore, contribute most to the locally absorbed dose.

At medium photon energies, Compton scattering predominates. In Compton scattering, an incident photon transfers some of its energy to—and, as the name suggests, is scattered by—a loosely bound or free electron, the "Compton electron." The scattered photon goes on to create other interactions within the material and can increase the dose rate in the area of the source. The probability of a Compton interaction decreases with energy but is not dependent upon the atomic number of the material. When photons interact with water or soft tissue, the probability for Compton scattering typically predominates. Compton interactions typically result in low-energy absorption and low overall radiation doses to staff.

Internal conversion interactions can occur between a gamma ray emitted from the nucleus of an atom and an orbital electron of that same atom. The gamma ray is completely absorbed, and the orbital electron—the "conversion electron"—is ejected with a kinetic energy that depends upon both the energy of the gamma ray and the binding energy of the electron. As in the photoelectric effect, additional characteristic X-rays and/or Auger electrons can be emitted as the vacancies within various orbitals subsequently refill. These ejected electrons can also undergo many local ionization events close to the site of their creation and, therefore, contribute mostly to the locally absorbed dose. Any deflected or secondary photons carry energy further away from the initial site of interaction and—following subsequent electron-producing interactions—are responsible for the deposition of radiation dose at more distant sites. Higher-energy photons (>1.022 MeV) can also interact with materials by pair production, but the probability of this interaction is rather low and is not a concern in typical radiochemical

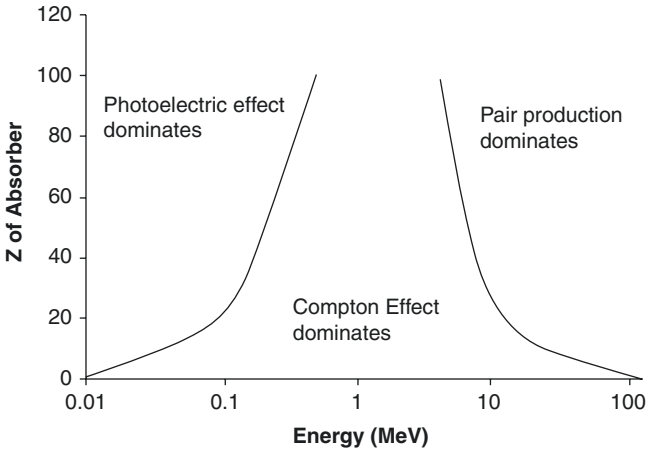

Fig. 3 Major types of interactions between photons and matter at various energy ranges and absorber densities

work. Figure 3 displays an approximation of the energy ranges and types of absorbers for which each of these types of interactions predominate.

Radiation Protection Quantities and Dose Concepts

Exposure Exposure (X) is defined as the sum of all the electrical charges (Q) of one sign produced by photons during primary and secondary ionizations in a given mass (m) of dry air at standard temperature and pressure (STP).

$$X = \frac{Q}{m}$$

The SI unit of exposure is the coulomb per kg (C/kg). The special unit of exposure has historically been called the roentgen (R), defined as 2.58×10^{-4} C kg^{-1} of dry air at STP and only applying to photons less than 3 MeV [17]. The flux of a photon radiation field is defined by the number of photons passing through a cross section of 1 cm^2 at a given distance from the source. In radiochemical applications, the intensity of a photon radiation field is usually represented in terms of the exposure rate (mR h^{-1}) or the effective dose rate (μSv h^{-1}) at a given distance from the source.

Absorbed Dose Absorbed dose (D) is defined as the mean radiation energy imparted to, transferred to, or deposited in a mass of any material.

$$D = \frac{\mathrm{d}\bar{\varepsilon}}{\mathrm{d}m}$$

The unit of absorbed dose was historically called the rad (*r*adiation *a*bsorbed *d*ose), defined as the energy absorption of 100 ergs/g of material (or 0.01 J kg^{-1}). The SI unit of absorbed dose is now the gray (Gy), which corresponds to an absorption of 1 J kg^{-1} [18]. Therefore, 1 Gy = 100 rad. While roentgens are used only for photon exposures, the concept of absorbed dose can be used to measure all types of ionization radiations at all energies. However, one shortcoming of this unit is that it does not take into account the *r*elative *b*iological *e*ffectiveness (RBE) of different types of radiation. The relative amount of biological injury to an irradiated tissue depends on the energy deposited (absorbed dose), the type of radiation (and thus its LET), and the dose rate (*e.g.* acute, fractionated, protracted, or chronic).

Equivalent Dose To account for differing RBEs, the absorbed dose (Gy) can be modified using a radiation-weighting factor (w_R) that depends on the LET distribution of a radiation field. The equivalent dose (H_T) in a tissue is the sum of the product of the absorbed dose in the tissue and the w_R for each of the radiation types [4].

$$H_T = \sum_R w_R D_{T,R}$$

The unit of equivalent dose was historically called the rem (*r*adiation *e*quivalent *m*an). The SI unit is now called the sievert (Sv), and since w_R is dimensionless, the unit for equivalent dose is the same as that for absorbed dose: J kg^{-1}. In water or soft tissue, 1 R is approximately equal to 1 rad and thus about equal to 10 mSv. Newer radiation survey meters often display radiation intensity rate results in terms of μSv h^{-1}. The radiation-weighting factor for photons, gamma rays, X-rays, and beta particles (except those from tritium) is uniform at 1 [4, 22]. The radiation-weighting factor is 2.5 for beta particles emitted from tritium, 2 for protons, and 20 for alpha particles; a range of values can be used for neutrons depending on their energy [4, 22].

Effective Dose The concept of effective dose provides a whole-body equivalent of partial-body exposures and takes organ doses and relative radiation risks into account. The effective dose (E) is the sum of the product of the equivalent dose (H_T) for each organ and the associated tissue-weighting factor (w_T) for that organ [4].

$$E = \sum_T w_T H_T$$

As the tissue-weighting factor is dimensionless as well, the SI unit continues to be the Sv. Table 3 lists the tissue-weighting factors for each organ.

It is often useful to have a sense of the dose rates expected from radioactive sources in order to devise protection schemes or calibrate instruments. The specific gamma constant (Γ) is the dose rate (μSv h^{-1}) from a unit of activity of the source (1 MBq). Table 4 gives the specific gamma con-

Table 3 Tissue-weighting factors (w_T) for each organ

Tissue	w_T
Bone marrow (red), colon, lung, stomach, breast, remainder tissues[a]	0.12
Gonads	0.08
Bladder, esophagus, liver, thyroid	0.04
Bone surface, brain, salivary glands, skin	0.01

[a]Nominal w_T applied to the average dose to 14 "Remainder Tissues": adrenals, extrathoracic region, gall bladder, heart, kidneys, lymphatic nodes, muscle, oral mucosa, pancreas, prostate, small intestine, spleen, thymus, uterus/cervix

Table 4 Specific gamma constants (Γ) and approximate external exposure from 1 MBq of typical radionuclides employed in radiopharmaceutical chemistry

Radionuclide	Gamma constant (Γ) at 1 m (μSv h^{-1} MBq^{-1})	Contact with 5 ml syringe (μSv h^{-1})
^{3}H	N/A	<1
^{11}C	0.1596	2930
^{14}C	N/A	<1
^{13}N	0.1596	2930
^{15}O	0.1596	2930
^{18}F	0.1547	2880
^{32}P	N/A	23,900
^{35}S	N/A	<1
^{51}Cr	0.0049	87
^{57}Co	0.027	275
^{60}Co	0.3475	6500
^{67}Ga	0.019	402
^{68}Ga	0.1789	3500
^{89}Sr	N/A	16,400
^{90}Y	N/A	43,500
^{99m}Tc	0.0211	354
^{82}Rb	0.1647	3100
^{111}In	0.0867	1220
^{123}I	0.044	605
^{125}I	0.041	620
^{131}I	0.0613	1130
^{137}Cs	0.0896	1610
^{153}Sm	0.0124	241
^{177}Lu	0.0076	76
^{201}Tl	0.0124	49
^{223}Ra (and progeny)	0.0534	750

stants (μSv h^{-1} MBq^{-1}) at several distances and typical geometries for many radionuclides used in nuclear medicine [17, 23, 24]. The specific gamma constants are provided for point sources, 5 mL syringes, and 10 mL glass vials. Once the dose rate at some distance from a point gamma-ray source is known, the dose rate at other distances can be calculated. This is because the radiation intensity of a given activity (A) is inversely proportional to the square of the distance (r) from the source. This rapid approximation is accurate within about 1% as long as the distance away from the source is at least three times the longest dimension of the source.

$$\frac{H_T}{t} = \frac{\Gamma A}{r^2}, \left(\mu \mathrm{Sv\,h^{-1}}\right)$$

Biological Effects of Radiation

When particles or photons interact with tissue, ionizations events can disrupt the structure of biomolecules in a manner that can kill cells or induce changes in their genetic makeup that can lead to the development of abnormal cell populations [25]. *In vivo* studies in animals and humans (*e.g.* follow-up of individuals after radiation exposure) have helped our understanding of the effects of radiation organisms. Epidemiologic studies of human populations exposed to high levels of radiation—such as the Japanese survivors of the atomic bombs and the emergency responders to the Chernobyl disaster—have provided critical information on the long-term effects of exposure [25, 26]. In general, risks of cancer have been estimated by extrapolating the dose-response data from these epidemiological studies down to the lower doses received by radiation workers, patients, and the public.

Since the mass of most tissues is about 75% water, water forms the main target for radiation within the body. When a water molecule becomes ionized—a process called water radiolysis—the highly reactive free-radical ion H_2O^+ is formed. Two H_2O^+ molecules can react to form the hydroxyl radical ($OH^\bullet$) which can diffuse short distances and oxidatively damage the primary target of radiation in the cell: DNA. This type of interaction is called the "indirect effect" of radiation. This mechanism stands in contrast to the "direct effect," which occurs when ionizing particles damage DNA directly. The indirect effect is the main cause of radiation damage and accounts for about two thirds of the damage to an exposed cell. Both effects can induce DNA lesions such as base damage, single-strand breaks, and double-strand breaks (DSB). It is estimated that a dose of 1 Gy of gamma radiation will induce >1000 incidents of base damage, about 1000 single-strand breaks, and 20–40 DSB per cell [2].

Radiation-induced DNA damage promotes the formation of "unclean" or "complex" breaks that must be excised before being repaired, a process that holds the potential for the loss of genetic material [2]. It is almost certain that the most important—and most lethal—form of radiation-induced DNA damage is the double-strand break (DSB). About half of radiation-induced DSBs are not repaired correctly, and the complexity of these DSBs increases with the density of ionization. As mentioned earlier, this is the primary reason high-LET emitters have higher RBE than radionuclides with low LET. Cells with damaged but improperly repaired DNA may also survive with modified DNA, a process that may lead to delayed cell death, neoplastic cell transformation, and carcinogenesis. The dose rate of the radiation

exposure represents another important variable for DNA damage. More specifically, protracted—rather than acute—exposure to low-LET radiation has a sparing effect on cells and organisms, as there is time to allow the DNA repair mechanisms of the cell to cope with the lesions created by the radiation [26]. This is referred to as the "dose-rate effect." The dose-rate effect is not typically observed for exposure to high-LET particles, because cells hit by a single high-LET particle experience such a large amount of damage that reducing the dose rate has little sparing effect.

Cells often demonstrate different levels sensitivity to radiation-induced damage. Generally speaking, cells tend to be more radiosensitive if they have high rates of division or are undifferentiated. As a result, erythroblasts, epidermal stem cells, and gastrointestinal stem cells are particularly sensitive, while nerve cells and muscle fiber cells are particularly insensitive. There also appears to be a genetic basis for the vulnerability of cells to ionizing radiation. These trends underscore the importance of tissue-weighting factors when evaluating the radiation risks to individual tissues and organs [4].

Health Effects of Radiation

It is convenient to classify the health effects of radiation into two types: tissue reactions and stochastic effects. Tissue reactions—historically referred to as "deterministic effects"—include the damage done to organs or tissues when a sufficiently high number of cells die [8]. In these situations, the dose threshold is the amount of radiation dose delivered before effects are seen. The severity of tissue reactions shows a clear dose-dependent relationship in which higher doses cause more significant effects. Tissue reactions include skin reactions, cataracts, and other injuries. Tissue reactions are categorized as either "early effect" or "late effect" based on whether the effects occur immediately following exposure or after a time delay (sometimes as long as months or years). Two of the most common tissue effects—erythema (reddening of the skin) and epilation (the loss of hair)—are reversible following doses of only a few Gy but become permanent at doses approaching 10 Gy.

Stochastic effects are probabilistic in nature and originate in cells that survive a dose (or doses) of radiation [5]. Stochastic effects generally occur with longtime delays and include cancer, non-cancer diseases (*e.g.* cardiovascular diseases or cerebrovascular diseases), and hereditary effects. According to current models, stochastic effects can originate from a single, mutated cell. Therefore, stochastic effects do not have a dose threshold, and the severity of the effects does not increase with dose. The most significant risk from low-dose radiation exposure is the latent development of cancer. For adult radiation workers, the ICRP have adopted a linear risk coefficient for cancer of 4.1% Sv^{-1} for radiation protection purposes and whole-body doses [4, 11]. For example, if a population of workers were to receive 250 mSv over the course of their employment, they may have about a 1% increased risk of cancer above the background level of cancer expected in a population of unexposed workers. It should be noted that this risk value is highly uncertain (within approximately a factor of about three), and statistically significant increases in risk have not been demonstrated below 100 mSv. That said, the principles of optimization of protection and application of dose limits ensure that personnel doses are managed well below these doses [27].

Detection and Measurement in Radiation Protection

Radiation measurements are central to radiopharmaceutical chemistry and radiation protection, and the basics of radiation detection are covered in Chap. 27. In this section, we will discuss several specific types of instruments that are utilized in radiation protection. Along these lines, radiation surveys are performed to evaluate external radiation fields and check for the radioactive contamination of areas and personnel. There are two basic types of radiation detectors: dose metersand counters [16, 28–30]. Dose meters are designed with an output that is proportional to a dose-related quantity delivered to the detector (μSv h^{-1} or μGy h^{-1}). In contrast, a counter gives an output as a measure of the number of ionization events occurring within the detector (counts per second, cps). In a radiochemistry lab, several radiation survey meters are utilized alongside specialized probes and detectors.

Gas Detectors Detectors such as Geiger-Müller (GM) counters and ion chambers operate by applying a voltage across a gas-filled cavity. Ionizing radiation induces ionization events in the gas, and the electron-ion pairs are separated by the applied electric field. The movement of these charges within the electric field results in a measureable electric current. Gas detectors operate differently depending on both the applied voltage and the filling gas. Geiger-Müller counters are typically operated at high voltage (about 500–1000 V) and utilize a gas with a high atomic number such as neon or argon. In a GM probe, the movement of charges within the high voltage electric field results in a cascade of secondary ionizations from the freed electrons [30]. This amplification process produces a very large, short-term discharge in the entire chamber that is recorded as an individual "count." This cascade effect allows a large amount of current to be collected for a single event, therefore providing high sensitivity albeit with a short dynamic range. GM counters with thin entrance windows are generally sensitive monitors

for the location and measurement of contamination with beta- and gamma-emitting radionuclides. They are rugged instruments with large signal outputs, making them suitable for use with very basic and inexpensive pulse-counting circuitry. However, they tend to overrespond at low energies (in the range of 40–100 keV) by about a factor of five when calibrated for high-energy radiation (such as >600 keV).

Ion chambers, in contrast, are operated at lower voltages so that the incoming radiation releases electrons and the collected charges produce a small electric current. All of the charges created by the ionization events or radiation interactions are recorded to give a measurement, which can then be related to dose or dose rate (*i.e.* the higher the current, the higher the dose rate). Therefore, ionization chambers are often used for routine dosimetry and generally have a very low variation in their energy response [30].

Solid-State Detectors Solid scintillation detectors are made of materials that produce light when exposed to ionizing radiation. Scintillation materials have a characteristic efficiency with which the incident radiation is converted to light. For radiation protection purposes, a sodium iodide crystal activated with thallium—NaI(Tl)—coupled to a photomultiplier tube (PMT) is a common and useful radiation detector. The PMT converts the incident light pulse created by the detector into a measureable electric current. Scintillation detectors are used widely in photon dose-rate meters and in gamma contamination monitors [30]. Scintillation probes fitted with thin entrance windows are also used for monitoring less penetrating emissions, such as low-energy photons, beta particles, and alpha particles. Portable scintillation survey instruments are generally very sensitive.

Wipe Tests When it is necessary to assess small amounts of activity on contaminated surfaces, wipe or swab tests should be performed as indirect survey methods. Wipe tests are also particularly useful, as they allow the user to check if the contamination is removable. In a wipe test, glass fiber disks, paper disks, or cotton-tipped swabs are usually used to wipe surfaces and are then measured with calibrated counting systems [*e.g.* a NaI(Tl) gamma counter or a beta counter]. Wipe tests allow for surface contamination to be estimated in units of activity per wipe area (dpm cm^{-2} or Bq cm^{-2}) after appropriate calibration factors are applied. These calibration factors are functions of the instrument's efficiency for the specified radionuclide, the area wiped, the duration of counting, and the "removal factor" (typically about 10% or so). The frequency with which wipe tests should be conducted depends on the amount of activity used in a laboratory as well as types of manipulations performed. That said, wipe tests should be performed on a weekly or monthly basis.

Liquid Scintillation Counter A liquid scintillation counter (LSC) is a very common instrument for measuring the results of wipe tests. LSCs use liquid as the counting medium and have a very high counting efficiency due to the mixing of the radioactive samples with the scintillation cocktail. The liquid absorbs the energy from the interaction of the radiation and re-emits this energy as light. The intensity of this pulse of light is directly proportional to the amount of energy deposited in the cocktail. LSCs are especially useful for assessing wipes or swabs containing alpha- or beta- emitting contaminants removed from surfaces and for the evaluation of leakage from radiation sources.

Radiation Dosimetry and Occupation Monitoring

The primary objectives of occupational monitoring are to provide a basis for estimating the actual radiation exposure of workers and to demonstrate compliance with local administrative, legal, regulatory bodies. Radiation monitoring is also useful to test the optimization of operating procedures, to increase the awareness of risk for individuals, and to motivate workers to reduce their own exposure [31]. All workers in radiochemistry must be continuously monitored for whole-body radiation exposure with whole-body dosimeters. In addition, extremity monitoring (with ring or wrist dosimeters) is also needed in cases in which operations could result in significant radiation exposure to the hands or arms, including the elution of generators as well as the preparation, dispensing, and handling of radiopharmaceuticals [23, 24, 32]. In radiopharmaceutical chemistry, external sources are the predominant source of exposure to personnel. Internal exposures can typically be prevented by basic safe-handling practices coupled with proper administrative and engineering controls [23, 24]. From a dosimetry standpoint, gamma radiation is responsible for the majority of the external dose to radiation workers in most cases.

External whole-body monitoring methods include the use of film badges, thermoluminescent dosimetry badges (TLD), pocket dosimeters, electronic dosimeters, optically stimulated luminescence dosimeters (OSL), and solid-state devices. Hand-dose monitoring methods include the use ring or wrist dosimeters with film or TLDs. Some newer electronic detectors also provide a visual readout of both the dose rate and the cumulative dose and are equipped with an audible alarm signal to warn the wearer for radiation levels above a pre-defined threshold. Radiochemists should be provided periodic dosimetry reports and should be made aware of their overall whole-body and hand (or extremity) doses. This enables the ongoing assessment of their radiation dose as well as the opportunity to identify situations that require

improved protection measures. In many situations, extremity monitoring at the base of the index or ring finger of the non-dominant hand is appropriate. However, to determine the best position for the extremity monitoring for a specific individual, the most exposed position on the hand should be determined by individual measurements over a short trial period.

Internal dosimetry techniques are also available in the event of the accidental intake of radioactive materials. In this case, a bioassay is often necessary. The term "bioassay" refers to a procedure for determining the nature and activity of the internal contamination through either *in vivo* measurements or *in vitro* measurements on elimination products (*e.g.* nasal swabs or urine/fecal samples). The route of entry into the body is also an important consideration for determining the means for measurement. Inhalation, ingestion, percutaneous absorption, and wound entry are the most common routes for the intake of radioactive materials. It is common to utilize partial body *in vivo* bioassay counting methods to assess the uptake of radioiodine in the thyroid [i.e., a thyroid counter system using a NaI(Tl) probe detector calibrated to measure the activity of radioiodine in the neck]. "Whole-body" counting—*e.g.* using a gamma camera—is another common method to measure internal contamination in the absence of bodily fluids for testing. Periodic bioassay measurements are typically required when using radioisotopes of iodine or high-activity alpha sources and should be coordinated with radiation protection staff.

Radiation Protection in Radiopharmaceutical Chemistry

Safe Handling of Radioactivity The work performed in radiochemistry labs often involves the use of high amounts of radionuclides, typically up to tens of GBq for short-lived radionuclides. Moreover, procedures require the handling of radiopharmaceuticals very close to the extremities (*e.g.* fingers, hands, and wrists) and the exposure to highly ionizing pure beta emitters and mixed photon/beta emitters. These activities will expose workers to external radiation, the potential for external contamination, and the potential for internal contamination upon accidental intake. It is therefore critically important to ensure the safe handling of radioactivity. The goal of any radiation protection scheme is to optimize protection while facilitating the safe use of radioactive sources and materials. Key considerations in this regard include minimizing the amount of surplus material used in the laboratory, minimizing the time spent by radiation workers near radioactive materials, maximizing the distance between radiation workers and radioactive materials, employing sufficient amounts of shielding, and ensuring careful planning prior to the start of work with radioactive materials.

Time The dose accumulated from external irradiation is directly proportional to the amount of time spent working near the source. Practice and experience are crucial for minimizing the time necessary to perform each step of a radiochemical process. Nonradioactive trial runs are often suggested for gaining practical experience without the possibility of radiation exposure.

Distance One of the most effective strategies in radiation protection is increasing the distance between the worker and the source. With regard to the manual manipulation and handling of radioactive materials, significant reductions in dose can be achieved by using tools with long handles, such as tongs or forceps.

Shielding Although working quickly can reduce radiation exposure, minimizing the time spent manipulating radioactive materials is not sufficient as a lone countermeasure. Indeed, the use of shielding and increasing the distance between the worker and the radioactive source is often more effective than working swiftly. The choice of shielding material depends on the type and energy of the radioactive emission. For gamma rays, a high atomic number material such as lead is very effective for maximum attenuation. Beta radiations are best shielded with low atomic number materials—such as plastic, Plexiglas, or acrylic—that minimize the production of bremsstrahlung X-rays, which are more penetrating than beta particles. When large activities of high-energy beta emitters are used, a mixed shielding strategy using plastic on the inside and lead on the outside is preferred. For gamma radiation, the shielding efficacy of a specific material is expressed by the half-value layer (HVL): the thickness of material needed to reduce the intensity of radiation by a factor of two [29]. Table 5 lists typical HVLs for various shielding materials, and Table 6 includes several commonly used syringe and vial shields.

In general, working behind lead or leaded-glass shields (or in heavily shielded hot cells) and using long-handled tools, shielded vials, and syringe shields can dramatically reduce external exposure during the synthesis, preparation, and formulation of radiopharmaceuticals. Figures 4 and 5 show examples of possible laboratory setups for the proper shielding or beta particles and photons, respectively.

Planning Ahead When synthesizing and manipulating radiopharmaceuticals, it is critical to think about what you are going to do and anticipate possible issues that could pre-

vent the successful completion of the experiment. Some questions that should be considered before beginning an experiment include …What could go wrong? What could distract you during the procedure? Have you reviewed the laboratory protocols for the experiment at hand? Are all the necessary supplies available? Have you checked the relevant instruments and equipment to ensure that they are working correctly? Are your gloves, coat, and shoes properly covering your body? Do you know the location of the closest safety shower and eyewash? Where is your survey meter, and has it been calibrated?

Table 5 Half-value layers (HVL) of lead for selected radionuclides

Radionuclide	Major photon energies (keV)	HVL Pb (mm)
^{11}C, ^{13}N, ^{15}O	511 (200%)	5.5
^{18}F	511 (194%)	5.5
^{67}Ga	93 (38%), 184, (21%), 300 (17%)	0.86
^{82}Rb	511 (192%), 777 (13%)	13.5
^{99m}Tc	140 (89%)	0.23
^{111}In	23 (68%), 171 (91%), 245 (94%)	0.257
^{123}I	27 (71%), 159 (83%)	0.067
^{125}I	~27–35	0.021
^{131}I	364 (81%)	3.0
^{133}Xe	30 (38%), 81 (37%)	0.2
^{201}Tl	71 (47%), 167 (11%)	0.258

Table 6 Examples of typical syringe and vial shields

Radionuclide	Syringe shield	Vial shield
^{99m}Tc	2 mm tungsten	7 mm lead
^{18}F	8 mm tungsten	25 mm lead
^{90}Y	10 mm plastic or 5 mm tungsten (to reduce associated bremsstrahlung)	10 mm plastic or 5 mm tungsten (to reduce associated bremsstrahlung)

Facility Design The physical facilities of a radiochemistry laboratory must ensure an efficient and safe environment for working with radioactive materials. Design factors to be considered include ensuring the safety of sources, optimizing protections for staff and the general public, preventing the uncontrolled spread of contamination, maintaining low background where most needed, and fulfilling national regulatory requirements for radiochemistry or radiopharmaceutical work [12]. The workplace should be classified based on the type of work performed in each area. "Cold" areas are open to the public, clerical staff, and visitors. No radioactivity should be handled in these nonrestricted areas, and the exposure levels should never exceed 20 μSv h^{-1} and 1 mSv y^{-1}. "Lukewarm" areas such as bioassay facilities and counting rooms can be utilized for procedures involving very low levels of radioactivity (kBq), and "warm" areas can be designated for larger levels of radioactivity (MBq). "Hot" areas—in which high levels (GBq) of radioactivity are handled in shielded containers, hot cells, or other enclosures—should not be used except by trained radiation workers. These "hot" spaces include radiochemistry laboratories, radiopharmacies, "hot labs," and "decay-in-storage" areas.

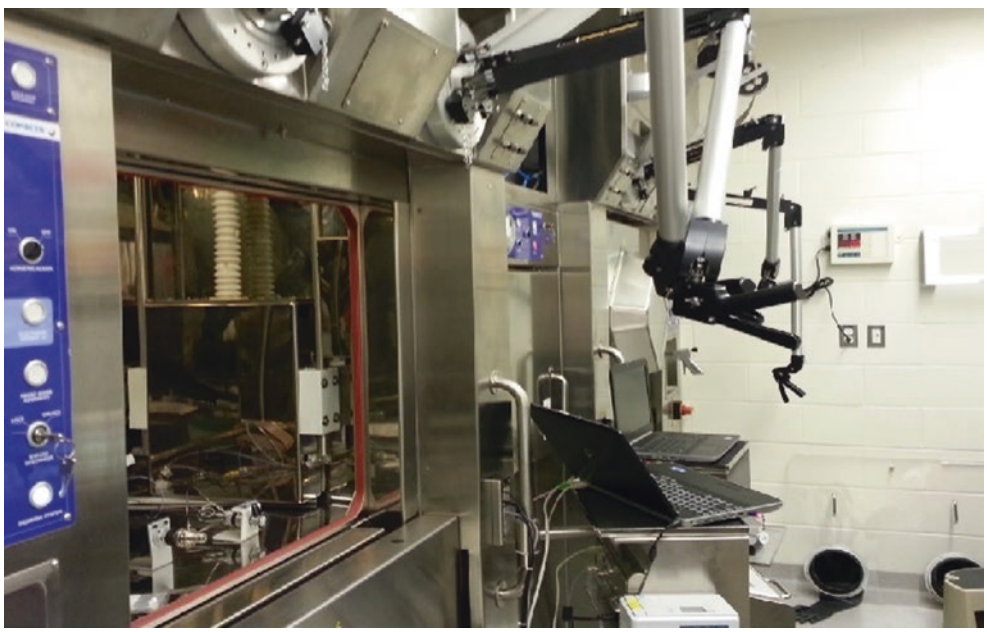

Fig. 4 An example of a standard hot cell and manipulator. This setup is used mainly for high-energy photon emitters such as positron-emitting radionuclides

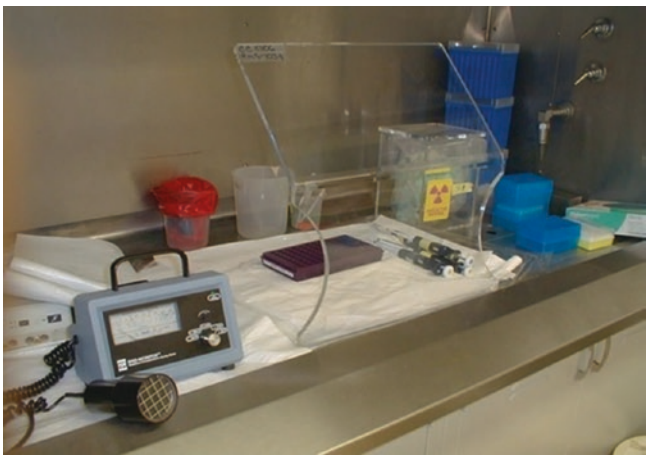

Fig. 5 An acrylic glass setup commonly used for the shielding of beta particles in a laboratory

Control of Radiation Contamination

When working with radioactive materials, it is essential to practice procedures to prevent contamination. Contamination is defined as the presence of radioactive materials in undesirable locations, including surfaces such as countertops and floors as well as body parts such as the skin, hair, face, and hands. In this regard, it is essential to keep areas clean, employ removable and disposable impermeable gloves (two layers can often be helpful), and perform frequent workspace surveys and wipes. The contamination of clothing, skin, or workspace areas should be quickly removed or contained [35]. Table 7 lists beta-emitter dose estimates for the contamination of the skin with various radioactive materials. Please note that these values are for the listed radionuclide only and do not account for equilibria with radioactive daughter products.

Preventing Internal Contamination Small amounts of radioactivity in the body can result in large radiation doses depending on the physical and biological behavior of the radiochemicals. More hazardous internal irradiations arise from radionuclides that emit energetic particles (rather than photons), radioactive substances with longer physical half-lives, and radioactive substances that concentrate in or near radiosensitive tissues (*e.g.* bone marrow, lung, thyroid). The risk of ingesting or inhaling radioactivity is always present during the use of solutions, even if it is low. The main routes through which radionuclides can be internalized are contaminated hands, contaminated skin, accidental wounds incurred during the manipulation of radioactive materials, accidental punctures incurred during the preparation of doses with syringes, and the inhalation of radionuclides vaporized in air [33]. Thankfully, with the exception of liquids containing isotopes of radioiodine [34], the majority of radiopharmaceuticals used in nuclear medicine are non-volatile.

Table 7 Half-life and dose rates for skin exposure of selected medical radionuclides

Radionuclide	Half-life	mGy min^{-1} MBq^{-1} cm^2
^{3}H	12.5 years	<0.1
^{11}C	20 min	38.1
^{14}C	5730 years	5.5
^{13}N	10 min	41.2
^{15}O	2 min	48.2
^{18}F	110 min	34.2
^{32}P	14.3 days	40.0
^{35}S	87 days	5.9
^{51}Cr	27.7 days	0.25
^{57}Co	271 days	1.3
^{60}Co	5.27 years	18.8
^{67}Ga	78.3 h	5.0
^{68}Ga	68 min	36.1
^{89}Sr	50 days	38.1
^{90}Y	2.7 days	40.0
^{99}Mo/^{99m}Tc	6.0 h	31.7
^{111}In	2.81 days	6.3
^{123}I	13.2 h	6.1
^{125}I	60 days	2.5
^{131}I	8.02 days	28.5
^{137}Cs	30.17 years	26.6
^{177}Lu	6.73 days	23.5
^{201}Tl	73 h	4.4
^{223}Ra	11.4 days	10.5
^{226}Ra	1620 years	0.8

Nevertheless, the use of a shielded fume hood (or vented biosafety cabinet) for the manipulation of radiopharmaceuticals is recommended to lower the risk of the inadvertent inhalation of radionuclides.

Radiation Protection in Practice

Radiochemistry facilities typically operate under a radioactive materials license from the local regulatory agency for radiation protection and as such need to implement a detailed documented radiation protection program [13, 23]. A radiation safety officer (RSO) is typically in charge of all aspects of radiation protection. The RSO is usually a health physicist, medical physicist, physician, radiopharmacist, or a nuclear medicine technologist with appropriate credentials based on local legal requirements. A second level of oversight is provided by the radiation safety committee (RSC), a group of individuals from the facility that oversees the operation and implementation of the radiation protection program. The members of this RSC typically include the RSO, administrators, radiochemistry supervision personnel, nurses, physicians, and other "users" (radiochemists, radiopharmacists, nuclear medicine technologists, *etc.*). The RSC meets periodically to review ongoing activities under the program as well as opportunities for improvements. The RSC reviews and approves changes to the radiation protection program, confirms that all new procedures are imple-

Fig. 6 Radiation safety training is crucial for all staff members who use—or come into contact with—radioactive materials

mented safely, investigates and reports radiation safety problems, and ensures the practice of radiation safety and ALARAguidelines.

Radiopharmaceutical chemistry—especially in the context of clinical nuclear medicine—is often performed in accordance with a quality management program (QMP) and under good manufacturing practice (GMP) and good laboratory practice (GLP) protocols. The specifics of these programs should be documented by, taught to, and well understood by each radiochemist. All radiation workers must be formally trained in both radiochemical techniques and radiation protection, including all aspects of regulatory compliance [36, 37]. Such training should be performed upon the hiring of new workers and periodically thereafter as a refresher for even long-serving personnel (Fig. 6).

Safe Practices(Rules) for Radiochemistry Laboratories Radiochemistry laboratories and work areas need to develop standardized laboratory rules for safe practice. We earnestly recommend that these rules include the following suggestions [23, 24, 32]:

- Only individuals who have completed radiation safety training should use radioactive materials.
- The relevant chemical, radiation, and handling hazard precautions and safety protocols should be reviewed prior to any experiment or procedure.
- Only approved radionuclides—and approved quantities of said radionuclides—may be ordered, and receipts should be kept and filed for each order.
- An up-to-date inventory of all radioactive materials should be kept.
- Radioactive materials should be stored to minimize dose rates in work areas. Photon- and high-energy beta emitters should be shielded such that the dose rate at 30 cm is <20 μSv h^{-1} in low-traffic areas and <2 μSv h^{-1} in high traffic areas.
- Radioactive sources must be handled in designated areas, labeled with radioactive warning signs (*e.g.* "Caution: Radioactive Material"), and enclosed in containment vessels with appropriate shielding.
- Secondary containment should be provided in order to limit spills and facilitate their rapid cleanup.
- Food and beverages should not be present in work areas, and refrigerators, hot plates, or ovens that are used for radioactive materials should not be used for food.
- No eating or drinking should be allowed in areas in which radionuclides are used.
- Well-ventilated work areas should be set up in rooms with frequent air changes and negative pressure with respect to the outside. Fume hoods should be used when working with volatile materials (*e.g.* the radioisotopes of iodine, ^{35}S) or alpha-emitting radionuclides.
- Work areas should be kept as clean as possible; plastic-backed absorbent pads or trays should be used to cover work areas and replaced when necessary.
- Pipetting by mouth should be prohibited.
- Long-handled tools should be used whenever practical, and manipulators should be used with high-activity sources.
- Dosimeters—whole body, wrist, and/or ring—should be worn as assigned.
- When practical, syringe and vial shields should be utilized to transfer or manipulate radioactive sources.
- A calibrated survey meter should be kept nearby when using radioactive materials; radiation workers should survey themselves and their workstations frequently.
- A Geiger-Müller counter should be used to detect beta-emitting radionuclides, and a NaI(Tl) counter should be used to detect photon-emitting radionuclides.
- Impervious shoes, a lab coat, and safety glasses should be worn whenever radioactive materials are being handled. Disposable impermeable gloves must be worn and replaced frequently. Generally, common items in the lab such as scissors, tape dispensers, phones, *etc.* should not be handled while wearing gloves that were used with radioactive materials. If these items must be handled with gloves that could be contaminated, they should be designated as "possibly contaminated" and should not be handled with bare hands.
- Reagents should be opened and dispersed behind a splash shield and adequate shielding.
- Capped tubes should be used in centrifuges and agitators to prevent contamination.
- Individual containers should be labeled before placing them in storage.
- Bench covers should be changed between experiments to avoid cross-contamination.
- Glassware, instruments, and central facility appliances should be surveyed frequently and decontaminated before use.

- Waste should be segregated into appropriately shielding containers that are differentiated for short and long half-life radionuclides. All disposals should be logged in a detailed inventory.
- Injuries or personnel contamination should be reported immediately to supervisors and radiation protection staff according to local protocols.
- Work surfaces should be regularly monitored for contamination using radiation survey meters. Whenever unsealed sources are used, wipe or swab tests should be performed to check for contamination.
- At the end of each experiment or procedure, hands, lab clothes, and shoes should be checked for contamination before leaving the work area.

Receipt of Radioactive Packages The receipt of packages containing radioactive materials is regulated by the licensing agency, and local specific regulations must be consulted [38]. Generally, packages must be externally monitored (for dose rate), and an assessment of external contamination levels (dpm cm^{-2} or Bq cm^{-2}) must be performed within 3 h of their arrival. The records of these monitoring procedures and wipe tests must be kept for a minimum of 3 years. Packages that exceed regulator-specified exposure or contamination levels must be reported to both the delivery carrier and the licensing agency. After receipt, radioactive materials need to be appropriately stored and secured to prevent theft or accidental removal.

Radioactive Waste In many cases, waste contaminated with radionuclides with half-lives shorter than 120 days can be allowed to "decay-in-storage" before disposal along with nonradioactive waste (or medical waste as appropriate). Shielded waste containers—such as those in Fig. 7—may be needed for proper containment during decay-in-storage. If radioactive waste cannot be properly stored for decay, it can be disposed of through a licensed waste broker or contractor. Depending on the local license, some small amounts of liquid radioactive waste may be released into the sanitary sewer provided that required monthly average concentrations do not exceed licensing limits. Radiation protection staff should always be consulted on the specifics of handling, storing, and disposing radioactive waste.

Transporting Radioactive Material During the transport of radioactive materials, the risk of accidents, spills, and the loss of material increases. As a result, strict controls are legally enforced during transportation. Most local regulatory requirements include special training and certification for packaging and transporting radioactive materials. The containers used for transport are designed to minimize the risk

Fig. 7 A lead-shielded waste container used for the storage and disposal of photon emitters such as positron-emitting radionuclides

of damage to the source, to contain any spillage of the radioactive material, and to minimize the radiation exposure to any person handling or coming into contact with the container. Each package needs to be adequately labeled (as required by local regulatory agencies) so that it can be identified by anyone who has to handle it. Labels also bring awareness to hazards in the event of an accidental breach of the packaging. Packages should be easily and safely handled, properly secured during transport, capable of withstanding mechanical impacts and vibration, and have surfaces that can be easily decontaminated.

Radiation Emergencies Most accidents involving radioactive materials can be avoided if all laboratory personnel follow the recommended procedures for safe handling. However, radiochemists must be thoroughly familiar with the emergency procedures of the facility as well as the location of all safety devices in the event of an accident [39]. All radioactive materials in the laboratory that are not immediately in use should be stored in a manner that will safeguard against the possible accidental spread of radioactive material in the event of a major disaster (fires, floods, *etc.*). Spills of radioactive materials can often result in unnecessary exposure and therefore should be properly addressed immediately. Minor spills of radioactivity (up to several kBq) can be addressed by warning other workers and decontaminating the area. Major spills of radioactivity (over 100 MBq) should be addressed by

stopping the spill (if possible), warning other radiation workers, preventing access to the area, and calling the radiation protection staff for assistance with cleanup and decontamination.

Decontaminating Personnel In the event of a life threatening or major injury, precedence should be given to health over exposure concerns. If clothing is contaminated, the contaminated items should be removed to reduce the exposure to the skin and minimize the spread of contamination. The contaminated area should be surveyed quickly to assess the initial general area of contamination. The affected area(s) should be washed using only mild soap and water (and perhaps a soft bristled brush) rinsing away from the body. The washing should proceed toward the center of the contamination so as to avoid enlarging the contaminated area. Stiff brushes and other abrasive items should be avoided, and particular attention should be paid to creases in the skin, the fingernails, and the spaces between the fingers and thumbs. The contaminated areas should be resurveyed after washing to check for reductions in contamination levels, and this washing process should be repeated as long as contamination levels are being reduced or until the skin starts to become irritated. The local radiation protection staff members should be notified so that they can assess the level of contamination remaining and decide if further decontamination procedures are required.

Radiation Protection During Pregnancy Studies have shown that the unborn child is sensitive to high doses of ionizing radiation, particularly during the first 3 months of gestation [40]. As a result, additional controls must be implemented in order to protect pregnant staff and their fetuses from the hazards of ionizing radiation. As soon as a pregnant woman informs her employers of her pregnancy, the protection to the conceptus (*i.e.* the embryo during the earliest stage of pregnancy) must be comparable with that provided for members of the public [41]. The conditions of employment of the pregnant woman must subsequently be adjusted such that the dose to the conceptus will be ALARA and that it will be unlikely to exceed 1 mSv during the remainder of the pregnancy [42]. It is not risky for pregnant staff to work in a radiochemistry laboratory as long as practical measures are implemented to avoid accidental high-dose situations, and there is reasonable assurance that the dose to the conceptus is kept below 1 mSv [13]. Often, work practices can be arranged to allow for the continuation of routine work, but certain radiochemistry procedures—*e.g.* work with volatile radioiodinated compounds [34] or work involving a significant risk of bodily contamination—should be reassigned during pregnancy to ensure that the dose to the conceptus remains ALARA [42].

Tricks of the Trade

Rules of Thumb for Radiation Protection

- Practice ALARA in all situations. Minimize time, maximize distance, utilize shielding, and plan ahead.
- Laboratory gloves minimize the skin dose from beta emitters.
- Consider utilizing two layers of gloves.
- Change gloves frequently, and avoid touching "clean" areas or your skin.
- After five hand-washes with water and soap, only about 2% of the initial activity typically remains on the surface of the skin.
- Use protective goggles or glasses.
- For quick radiation protection purposes, the skin dose per activity per unit area can be roughly approximated as 1 mSv h^{-1} per Bq cm^{-2}. More specific factors based on individual radionuclides are listed in Table 7.
- Syringe shields reduce extremity doses by about 50–85% for ^{99m}Tc and about 25% for positron-emitting radionuclides.
- It requires a beta particle of at least 70 keV to penetrate the protective 0.07 mm thick layer of the skin.
- It requires an alpha particle of at least 7.5 MeV to penetrate the protective 0.07 mm thick layer of skin.
- The activity of any radionuclide is reduced to <1% after seven half-lives. For decay-in-storage, waste should be held for a minimum of ten half-lives before surveying for residual activity and disposal.
- In case of a spill of radioactive materials, practice the SWIM principle: *s*urvey, *w*arn, *i*solate, *m*itigate. In case of a major spill, contact radiation protection staff for assistance.
- Surfaces measuring >100 cps above background with a Geiger-Müller probe should be considered contaminated [43].
- Surface wipes measuring >2200 dpm cm^{-2} for beta emitters or >220 dpm cm^{-2} for alpha emitters should be considered contaminated.

Example Laboratory Audit Checklist

Radiochemists should make arrangements for periodic reviews of their protocols and work areas (at least annually) in order to systematically appraise their radiation protection programs [44]. The purpose of such audits is to ensure the optimization of their protection programs and to take corrective actions when and where necessary. The results of any review or audit of radiation protection should be documented, and follow-up actions should be highlighted to

ensure their implementation. A checklist can be helpful for such periodic assessments. Examples of items to be reviewed during an audit could include the following:

- Workers are knowledgeable and properly trained to work with the radioactive materials present. Documentation of their training is available.
- Workers are aware of emergency procedures and proper ways to respond to a spill of radioactive material.
- Radioactive warning signs (*e.g.* "Caution: Radioactive Material") are posted and visible in all locations that contain radioactive materials.
- ALARA principles are adhered to in the laboratory. This may include using items such as long-handled tools, proper shielding, bioassay tests, ventilated hoods, and hot cells.
- Proper radiation detection instrumentation is present to detect and/or quantify radioactive materials in the laboratory. These instruments are fully functional and calibrated properly.
- Regular contamination survey results, inventory and waste logs, and shipment receipts are maintained and easily accessible.
- Workers are wearing dosimeters when working with radioactive materials and are returning them in a timely manner for processing.
- No food or drinks are being stored or consumed in the workplace.

The Bottom Line

- All work performed with radioactive materials must be justified and beneficial, have an optimized approach for ALARA guidelines, and be performed according to all relevant federal, state, and local dose limitations.
- While long-term health effects have not been statistically demonstrated below 100 mSv, it is important to practice ALARA guidelines to limit possible deleterious biological effects.
- Shielding requirements, handling precautions, and survey instrumentation can vary greatly for different radionuclides. Always prepare carefully before working with a new type of radioactive material.
- In the event of personal contamination, quickly locate and clean the source of the contamination on the skin. Make sure not to irritate the affected area, and contact radiation protection staff for assistance.
- Proper surveying, documentation, work practices, and communication when using radioactive materials can help prevent most radiation safety problems.

References

1. Dauer LT. Exposed medical staff: challenges, available tools, and opportunities for improvement. Health Phys. 2014;106(2):217–24.
2. Hall EJ, Giaccia AJ. Radiobiology for the radiologist. 7th ed. Philadelphia: Lippincott Williams & Wilkins; 2012. ix, 546 pp.
3. Johns HE, Cunningham JR. The physics of radiology. 4th ed. Springfield: Charles C. Thomas; 1983. xix, 796 pp.
4. Protection. ICoR. The 2007 recommendations of the international commission on radiological protection. ICRP publication 103. Ann ICRP. 2007;37(2–4):1–332.
5. United Nations. Scientific committee on the effects of atomic radiation. Sources and effects of ionizing radiation : United Nations scientific committee on the effects of atomic radiation : UNSCEAR 2008 report to the general assembly, with scientific annexes. New York: United Nations; 2008.
6. United Nations. Scientific committee on the effects of atomic radiation. Sources and effects of ionizing radiation : United Nations scientific committee on the effects of atomic radiation : UNSCEAR 2012 report to the general assembly, with scientific annexes. New York: United Nations; 2012.
7. Protection ICoR. ICRP publication 116. Conversion coefficients for radiological protection quantities for external radiation exposures. Ann ICRP. 2010;40(2–5):1–257.
8. Protection ICoR. ICRP publication 118: ICRP statement on tissue reactions and early and late effects of radiation in normal tissues and organs--threshold doses for tissue reactions in a radiation protection context. Ann ICRP. 2012;41(1–2):1–322.
9. Protection ICoR. ICRP publication 130: occupational intakes of radionuclides: part 1. Ann ICRP. 2015;44(2):5–188.
10. Protection ICoR. ICRP publication 134: occupational intakes of radionuclides: part 2. Ann ICRP. 2016;45(3–4):7–349.
11. Protection. ICoR. Low-dose extrapolation of radiation-related cancer risk. Ann ICRP. 2005;35(4):1–140.
12. Agency IAE. Applying radiation safety standards in nuclear medicine. Vienna: International Atomic Energy Agency; 2005.
13. Agency IAE. Radiation protection and safety of radiation sources: international basic safety standards, general safety requirements part 3. Vienna/Austria: IAEA; 2014.
14. Bailey DL, Humm J, Todd-Pokropek A, van Aswegen A. Nuclear medicine physics – a handbook for teachers and students. Vienna: IAEA; 2014.
15. National Council on Radiation Protection and Measurements. Limitation of exposure to ionizing radiation : recommendations of the National Council on Radiation Protection and Measurements. Bethesda: The Council; 1993. vi, 88 pp.
16. Gollnick DA. Basic radiation protection technology. 6th ed. Altadena: Pacific Radiation Corp; 2011. xiii, 889 pp.
17. Shleien B, Slaback L, Birky B. Handbook of health physics and radiological health. 3rd ed. Baltimore: Williams & Wilkins; 1998.
18. Measurements ICoRUa. Report 85: fundamental quantities and units for ionizing radiation. J ICRU. 2011;11(1):1–31.
19. National Council on Radiation Protection and Measurements. Alpha-emitting particles in lungs : recommendations of the National Council on Radiation Protection and Measurements. Washington, DC: The Council; 1975. v, 28 pp.
20. Williamson MJ, Dauer LT. Activity thresholds for patient instruction and release for positron emission tomography radionuclides. Health Phys. 2014;106(3):341–52.
21. Zanzonico P, Dauer L, St Germain J. Operational radiation safety for PET-CT, SPECT-CT, and cyclotron facilities. Health Phys. 2008;95(5):554–70.
22. National Council on Radiation Protection and Measurements. The relative biological effectiveness of radiations of different quality:

recommendations of the National Council on Radiation Protection and Measurements. Bethesda: The Council; 1990. viii, 218 pp.
23. Martin CJ, Sutton DG. Practical radiation protection in healthcare. 2nd ed. Oxford: Oxford University Press; 2015. xiii, 536 pp.
24. Mattsson SR, Hoeschen C. Radiation protection in nuclear medicine. Heidelberg/New York: Springer; 2013. viii, 165 pp.
25. National Research Council (U.S.). Committee to assess health risks from exposure to low level of ionizing radiation. Health risks from exposure to low levels of ionizing radiation : BEIR VII phase 2. Washington, D.C.: National Academies Press; 2006. xvi, 406 pp.
26. Dauer LT, Brooks AL, Hoel DG, Morgan WF, Stram D, Tran P. Review and evaluation of updated research on the health effects associated with low-dose ionising radiation. Radiat Prot Dosim. 2010;140(2):103–36.
27. National Council on Radiation Protection and Measurements. Risk estimates for radiation protection. Bethesda: the Council; 1993. viii, 148 pp.
28. National Council on Radiation Protection and Measurements. A Handbook of radioactivity measurements procedures : with nuclear data for some biomedically important radionuclides, reevaluated between August 1983 and April 1984. 2nd ed. Bethesda: National Council on Radiation Protection and Measurements; 1985. xvi, 592 pp.
29. Cember H, Johnson TE. Introduction to health physics. 4th ed. New York: McGraw-Hill Medical; 2009. xi, 843 pp.
30. Knoll GF. Radiation detection and measurement. 4th ed. Hoboken: John Wiley; 2010. xxvi, 830 pp.
31. National Council on Radiation Protection and Measurements. Use of personal monitors to estimate effective dose equivalent and effective dose to workers for external exposure to low-LET radiation : recommendations of the National Council on radiation protection and measurements. Bethesda: The Council; 1995. vi, 64 pp.
32. Medicine EAoN. Best practice in nuclear medicine part 2: a technologist's guide. Vienna: European Association of Nuclear Madicine; 2007.
33. National Council on Radiation Protection and Measurements. Use of bioassay procedures for assessment of internal radionuclide deposition : recommendations of the National Council on Radiation Protection and Measurements. Bethesda: The council; 1987. vi, 82 pp.
34. National Council on Radiation Protection and Measurements. Scientific committee 1–8 on risk to the thyroid from ionizing radiation., National Council on radiation protection and measurements. Risk to the thyroid from ionizing radiation. Bethesda: National Council on Radiation Protection and Measurements; 2009. xv, 544 pp.
35. National Council on Radiation Protection and Measurements. Biological effects and exposure limits for "hot particles" : recommendations of the National Council on Radiation Protection and Measurements. Bethesda: National Council on Radiation Protection and Measurements; 1999. ix, 258 pp.
36. National Council on Radiation Protection and Measurements. Operational radiation safety training : recommendations of the National Council on Radiation Protection and Measurements. Bethesda: National Council on Radiation Protection and Measurements; 2000. vii, 69 pp.
37. Dauer LT, St Germain J. A review of educational philosophies as applied to radiation safety training at medical institutions. Health Phys. 2006;90(5 Suppl):S67–72.
38. Lombardi MH. Radiation safety in nuclear medicine. 2nd ed. Boca Raton: CRC/Taylor & Francis; 2007. 231 pp.
39. National Council on Radiation Protection and Measurements. Scientific committee 46–7 on emergency preparedness. Developing radiation emergency plans for academic, medical, or industrial facilities : recommendations of the National Council on radiation protection and measurements. Bethesda: The Council; 1991. viii, 129 pp.
40. National Council on Radiation Protection and Measurements. Scientific committee 4–4 on the risks of ionizing radiation to the developing embryo fetus and nursing infant., National Council on Radiation Protection and Measurements. In: Preconception and prenatal radiation exposure : health effects and protective guidance : Recommendations of the National Council on Radiation Pretection and Measurements, May 24, 2013. Bethesda: National Council on Radiation Protection and Measurements; 2013. xiii, 371 pp.
41. Dauer LT, Miller DL, Schueler B, Silberzweig J, Balter S, Bartal G, et al. Occupational radiation protection of pregnant or potentially pregnant workers in IR: a joint guideline of the society of interventional radiology and the cardiovascular and interventional radiological society of Europe. J Vasc Interv Radiol. 2015;26(2):171–81.
42. Chu B, Miodownik D, Williamson MJ, Gao Y, St Germain J, Dauer LT. Radiological protection for pregnant women at a large academic medical Cancer center. Phys Med. 2017;43:186–9.
43. Commission NR. NUREG-1507: minimum detectable concentrations with typical radiation survey instrumentation for carious contaminates and field conditions. Washington, DC: Commission NR; 1995.
44. National Council on Radiation Protection and Measurements. Self-assessment of radiation safety programs : recommendations of the National Council on Radiation Protection and Measurements. Bethesda: National Council on Radiation Protection and Measurements; 2010. x, 118 pp.

An Introduction to Biostatistics

Kristen M. Cunanan and Mithat Gönen

The Fundamentals

What is biostatistics? And why does it matter? Biostatistics is a scientific field that deals with the collection, analysis, interpretation, and presentation of biological and/or medical data to answer specific scientific questions. Each of these steps is equally important on its own yet must be considered in the context of the entire process to ensure the statistical validity of the conclusions from an experiment.

Data collection involves the design of a study (*i.e.* how the data are sampled/collected) and the recording and preparation of lab measurements for statistical analysis. The statistical analyses of most of your experiments will likely involve one or more of the following: summarization (*e.g.* the mean, standard deviation, median, range, ratio, or graphical summary of data), hypothesis testing (*e.g.* *t*-tests, significant differences in biodistribution curves), and estimation (*e.g.* quantifying the strength of association between an outcome, such as tumor percent uptake, and a factor, such as plasma half-life). The subsequent interpretation of the results should take into account any changes to the data (such as transformations) or limitations (such as small sample sizes or omitted data observations). Last, the thoughtful presentation of the data is helpful to better understand what we can learn from the experiment and process how it helps in answering the scientific questions being asked.

We realize that scientific inquiry is a continuous and iterative process, but throughout this chapter, we assume that you have clearly identified (i) the scientific questions you are trying to answer, (ii) what measurements or data you will collect to answer said questions, and (iii) how you will analyze the data to answer the questions. The determination of sample size (*i.e.* the number of tissue samples or number of mice) is an important factor as well, and it is an issue not only of statistical importance but logistical and financial significance as well.

The Details

This section provides an introduction for conducting your biostatistical analyses. Throughout this process, it is important to always remember the following question: what are the primary research objectives of your study?

After your data have been collected and stored, you should first take a look at your raw data values. Are all measurements on the same scale and using the same calibrated instrument? Take note of the possible sources of variability (*i.e.* noise), such as if measurements are taken on different days or using a different machine or calibration. Do all of the measurement values make biological sense (*i.e.* are all tumoral uptake values positive)? Are there any recording errors (*i.e.* one measurement value magnitudes larger than all other values)?

If the measured values represent a wide range, a *transformation* should be considered. The goal of transforming data is to reduce the impact of the various skews and outliers. There are many possible transformations, but the logarithmic transformation is easily the most popular. You may apply the transformation to all factors, the outcome of interest, or just a few selected ones. It is also important to note that if you apply a logarithmic transformation to measurements that take on a value of 0, you can replace the "0" with a reasonable surrogate value—such as the lower limit of the measuring device used—and mention this in presenting your conclusions. Finally, after applying a transformation, be sure to note the correct scale in your interpretation of results. It is good data management practice to keep a copy of your intact, original dataset and apply changes/amendments either within software or in a second dataset.

To provide an example, consider an experiment similar to that described in Houghton *et al.* [1]. Figure 1 displays the values for the tumor volume and log tumor volume over

K. M. Cunanan · M. Gönen (✉)
Department of Epidemiology and Biostatistics, Memorial Sloan Kettering Cancer Center, New York, NY, USA
e-mail: gonenm@mskcc.org

J. S. Lewis et al. (eds.), *Radiopharmaceutical Chemistry*, https://doi.org/10.1007/978-3-319-98947-1_30

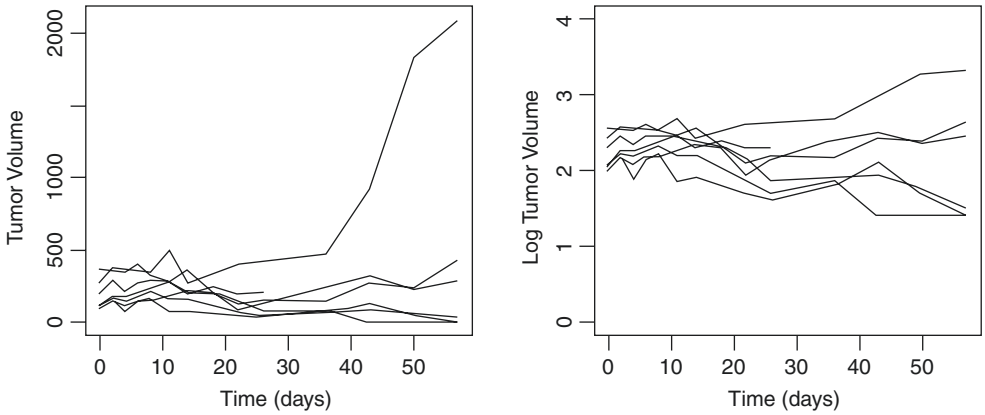

Fig. 1 Tumor growth mouse profiles over time (days) on the original and logarithmic scales

time. On the original scale, we see a relatively large tumor volume after Day 50 for a single mouse; however, after applying a $\log_{10}$ transformation, we see a reasonably symmetric spread of the data over time. Also, in this example, some mice achieve a tumor volume value of 0. However, when applying the transformation, the observed "0"s were replaced with "25"s, the theoretical detectable lower limit of the tumor measurement system. Depending on your intended interpretation, you may want to consider instead using relative tumor volumes given the different tumor volumes in mice at Day 0.

Summary Measures

After examining individual data points, we will consider the data as a whole and/or in groups and look at different statistical summary measures to get an idea of general trends and the spread of the data. The primary statistical summary measures that capture general trends include the *mean*, *median*, and *mode*; the primary statistical summary measures that capture the general spread of the data include the *standard deviation* (variance), *range*, and *quantiles*. These statistical summary measures should always be calculated and evaluated before proceeding to hypothesis testing and/or estimation in order to determine an appropriate method.

The *mean*—or average—captures the central tendency of a set of data values. Formally, the mean is calculated as the sum of a set of individual data values divided by the total number of data values used in that sum. It is the most commonly used summary measure because it is easy to interpret and has many established statistical methods for inference, such as linear regression and *t*-tests (see the section on "Hypothesis Testing and Estimation"). However, this summary measure is sensitive to outliers.

The *median* is the midpoint of a set of values ordered from smallest to largest and thus separates the measurements in two equal-sized groups. If the size of the dataset is an even number, the median is the mean of the two central numbers in the frequency distribution. If the frequency distribution of the dataset is symmetric, the mean and median are equivalent. Briefly, let's consider two toy sets of six values in the table below.

Variable	
x	*y*
8	5
12	37
11	6
12	5
12	7
11	6

Both variables —*x* and *y*—have a mean value of 11. However, the median of *x* is 11.5 (similar to the mean), and the median of *y* is 6. This quick analysis also shows how the mean can misrepresent the center of the distribution in small data sets with outliers and explains why the median is considered a summary statistic robust to outliers.

The *mode* is the value that appears most often in a set of data values; that is, it's the value that is most likely to occur (*i.e.* be sampled/measured). If all values occur only once, then there is no mode. When investigating your data, it is important to inspect and note that the data is unimodal (*i.e.* there's only one maximum in the dataset's frequency distribution). In the previous toy set of values, the second variable (*y*) has two modes: 5 and 6. However, since these are consecutive numbers, this set of values is still unimodal, since there is only one maximum in the dataset's frequency distribution.

The *standard deviation* quantifies the extent to which a set of values deviates (or differs) from the central mean of those values. For example, the standard deviation of the previous variable (*x*) is 1.549 and can be calculated using:

$$\mathrm{sd}_x = \sqrt{\frac{1}{n-1}\sum_{n}^{i=1}\left(x_i - \bar{x}\right)^2} = \sqrt{\frac{1}{5}\sum_{6}^{i=1}\left(x_i - 11\right)^2}$$

A small standard deviation indicates most of the values in the set are close to (or similar in numeric value to) the mean value. In contrast, a large standard deviation indicates

a wide spread of data values. Be cautious drawing conclusions with respect to general trends or central tendencies of data with a large standard deviation. However, a large standard deviation may suggest a larger sample size is needed and that there is heterogeneity of the outcome, both of which are also interesting to note when interpreting your results. The *range* is almost always represented as an interval of the minimum and maximum values in a set of data observations. For example, the range of variable ***y*** is presented as (5, 37). Typically, the mean and standard deviation are provided together, while the median and range are provided together for skewed or small datasets and/or datasets with outliers.

A *quantile* is the value that divides the frequency distribution—or separates the set of ordered values—of a variable into the desired percentage. For example, the 50% percentile (or 2nd quantile) is the median, since it separates the data into two equal parts. There are three quantiles ($Q1$, $Q2$, $Q3$) that separate the data into four equal parts, so that 25, 50, and 75% of the frequency distribution (or ordered data) are in the first, second, and third quantiles, respectively. For example, for variable x, $Q1 = 11$, $Q2 = 11.5$, and $Q3 = 12$. These three summary measures are frequently presented using box plots, where the top and bottom of the box are formed by $Q1$ and $Q3$ and $Q2$ divides the box into two (often "whiskers" are added to represent variability).

The *ratio* represents a relationship between two numbers. For example, consider an *in vivo* biodistribution study—such as that described in Sharma *et al.* [2]—performed to evaluate the uptake of a radiopharmaceutical. Some relevant measurements are the uptake of the radiopharmaceutical in the tumor and muscle of each mouse. To evaluate how well the radiotracer in question binds to the tumor *relative* to other tissues, consider the $\log_2$-ratio of the uptake in the tumor to the uptake in the muscle, so that a value of 0 represents no difference. Working with ratios requires considerable care. Both the tumor and muscle uptake each have their own mean values and standard deviations. Therefore, to properly capture this variability in the ratio of tumor uptake (x) and muscle uptake (y), the *propagated error* of the ratio should be calculated as follows:

$$\frac{\bar{x}}{\bar{y}}\sqrt{\left(\frac{\mathrm{sd}_x}{\bar{x}}\right)^2+\left(\frac{\mathrm{sd}_y}{\bar{y}}\right)^2}$$

in which sd_x and $\bar{x}$ represent the standard deviation and mean of variable x. Note that this calculation assumes independence between x and y. If this is not a reasonable assumption, there will be an additional term involving the correlation between the two variables. Perhaps not surprisingly, this can get even more complicated. In this example, the authors compare the *in vivo* behavior of a non-site-specifically labeled radioimmunoconjugate (NS) and a site-specifically labeled radioimmunoconjugate (S). In this case, a ratio of ratios—$r_{NS} = x_{NS}/y_{NS}$ and $r_S = x_S/y_S$—might be needed. Again, the propagated error should be calculated and presented for the ratio of ratios:

$$\frac{\bar{x}_{NS}\bar{y}_S}{\bar{x}_S\bar{y}_{NS}}\sqrt{\left(\frac{\mathrm{sd}_{xNS}}{\bar{x}_{NS}}\right)^2+\left(\frac{\mathrm{sd}_{yNS}}{\bar{y}_{NS}}\right)^2+\left(\frac{\mathrm{sd}_{xS}}{\bar{x}_S}\right)^2+\left(\frac{\mathrm{sd}_{yS}}{\bar{y}_S}\right)^2}$$

This quantity can be used in hypothesis testing to determine if there is a significant difference in the tumor-to-muscle uptake ratio between non-site-specific and site-specific radiolabeling. Again, note that this calculation assumes independence across all factors.

When looking at the summary measures for interpretation, it is important to consider the sample size that these metrics represent. Thus, in presenting your results, you should provide the sample size along with your summary measures. This will allow readers to objectively interpret your results and should improve the reproducibility of your results in future experiments. This is especially important if you have unequal group sizes, either by design or due to missing data. As a final note, it is important to consider what data you are trying to represent with these summary measures and for what purpose. It is of questionable value to present the mean and standard deviation for a set of three values, as you are using two numbers to summarize three numbers. In this case, it may be more informative to simply provide all three values.

Each of these summary statistics indicates a different characteristic of the distribution of the measurements. It is neither possible nor desirable to report all of them for each variable in an experiment. While the mean and standard deviation are most commonly reported, our recommendation is to report the median and the lower ($Q1$) and upper ($Q3$) quantiles, especially for smaller datasets.

Hypothesis Testing and Estimation

Statistically speaking, a hypothesis is something very specific. It is possible to have a scientific hypothesis but no statistical hypothesis and vice versa. Things usually work best if you can actually translate your scientific hypothesis into a statistical hypothesis. Therefore, at the design stage, it is critical to spend some time on the formulation of statistical hypotheses. This will also facilitate many of the downstream statistical activities, such as power calculations. *Statistical power* quantifies how likely you are to declare a significant finding when a true signal exists, or, more formally, the probability of rejecting the null hypothesis given the null hypothesis is false. *False-positive rate* (*i.e. type 1 error*) is the counterpart of power and quantifies how likely you are to declare a significant finding when a true signal does not

exist, or, more formally, the probability of rejecting the null hypothesis given the null hypothesis is true.

First, let's discuss some common methods of statistical analysis for testing different hypotheses. We note that each method requires different assumptions in order to draw rigorous conclusions from the hypothesis tests. You can informally identify if these assumptions are met by evaluating the appropriate summary statistics of the data before hypothesis testing. Formally, you can test if the data violates the required assumptions before running your research hypothesis tests; however, the most commonly used methods are fairly robust to deviations or violations in these assumptions, and most *in vivo* preclinical experiments are too small for the proper evaluation of these assumptions. Hence, formal tests of assumptions are rarely used in practice.

The most commonly used statistical analysis for hypothesis testing is the *Student's t-test*, named after the pseudonym of its inventor. The *t*-test, as it is often called, can be used to compare the central or average tendencies of the data. For example, to test if the average uptake of a radiopharmaceutical in the tumor tissue is significantly greater than the average uptake of the same radiopharmaceutical in normal tissue (μ_0) at Day 21 of your experiment, one can formulate the corresponding null and alternative hypotheses as $H_0 : \mu_{\%\mathrm{ID}/g} \leq \mu_0$ versus $H_A : \mu_{\%\mathrm{ID}/g} > \mu_0$. Using values of tumor uptake from Day 21, one can apply a one-tailed, one-sample *t*-test. It is a "one-tailed" test because you are only interested in testing if the average tumor uptake is greater than the uptake in normal tissues, which we assume is a given number and not estimated from the same data set. If you replace "≤" with "=" in the null hypothesis (and ">" with "not =" in the alternative hypothesis), you would be performing a "two-tailed" test. To determine the statistical significance of a one-sample *t*-test, calculate the test-statistic, and compare it to a critical value (or quantile) of the student *t*-distribution. The test-statistic is calculated as:

$$\text{test statistic} = \frac{\bar{x} - \mu_0}{\mathrm{sd}_x / \sqrt{n}}$$

where $\bar{x}$ is the sample mean, μ_0 is the specified null value you are testing against, sd_x is the sample standard deviation, and n is the sample size.

The overused and often abused *P value* captures the probability of observing a result as extreme or more extreme than the previously calculated test-statistic, assuming the null hypothesis is true (*e.g.* the true average tumor uptake $\mu_{\%\mathrm{ID}/g} = \mu_0$). This is displayed in Fig. 2 with the *P* value represented by the striped region.

A very small *P* value suggests against (or rejects) the null hypothesis as being the underlying biological truth, whereas a *P* value larger than the desired significance level (say 5%) fails to reject the null hypothesis at that desired significance level. Either conclusion—rejecting or failing to reject the null hypothesis—is informative and should be reported, along with possible limitations and explanations of your results. When declaring significant *in vivo* preclinical findings, it is essential to be cautious when interpreting these findings for small sample sizes. It is possible to observe a significant *P* value arising from a hypothesis test on only three data values, an interpretation which could lead to incorrectly declaring a significant result. Alternatively, a large *P* value may suggest that there is no significant effect on the average biodistribution measurement of interest, or it may suggest a lack of power (hence the importance of a power calculation).

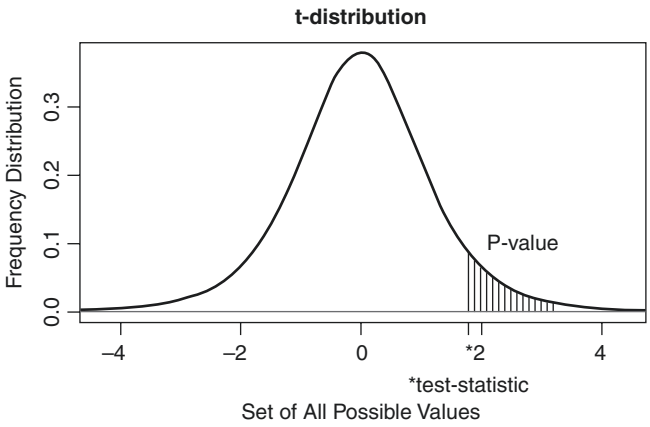

Fig. 2 Hypothetical *P* value (striped region) based on the test-statistic from a *t*-test

An alternative to the *P* value is the 95% *confidence interval*, a more interpretable metric calculated as:

$$\bar{x} \pm t \times \mathrm{sd}_x / \sqrt{n}$$

where t is the critical value for the *t*-distribution corresponding to the 95% percentile/quantile (in other words, if you want a 90% confidence interval, you will have to use a different value of t in this formula). Intuitively, we can interpret this interval as follows: there is a high chance that the true mean value of the biodistribution measurement is contained within this interval. In fact, some would call this an interval estimate of the mean. The formal interpretation of a confidence interval is somewhat awkward and requires imagining, repeating the experiment, and constructing a confidence interval each time: 95% of these intervals will contain the true mean value. One can perform a hypothesis test using a confidence interval as well: if the null hypothesis value—say 0 or μ_0—is within the confidence interval, we fail to reject the hypothesis that the true mean value is different than the null value since it is contained within our confidence interval. Thus, confidence intervals provide not only comparable information to a *P* value with respect to inferential statements using hypothesis tests but also inform

us about the likely location of the mean. Wide confidence intervals reflect a large variability and/or small sample size and consequently should be interpreted with caution; it is important to note that these artifacts are not necessarily reflected in the *P* value. Both *P* values and confidence intervals can be used to declare significance in hypothesis testing. However, confidence intervals contain more information to better qualify this significance, especially with respect to the biodistribution measurement of interest. Currently, this is a greatly underutilized tool in presenting statistical findings in basic sciences, due primarily to the inertia of convention.

If you want to compare biodistribution measures for two different groups, you can apply a *two-sample t-test*. A two-sample *t*-test—sometimes called an independent-sample *t*-test—evaluates a significant difference in means for two sets of values collected from two different groups of mice or samples (*e.g.* experiment versus control). In contrast, a dependent, or "paired", *t*-test evaluates a significant difference in means for two sets of values collected from the same group of mice or samples (*e.g.* repeated measures).

An important requirement for the validity of a *t*-test is that the observations are randomly sampled. This is violated if one of the chosen samples is subsequently excluded from analysis. Unfortunately, it is common practice to do this without understanding the consequences. Another requirement of a *t*-test is that the observations follow a normal distribution, although departures from this assumption are not as consequential as violations of random sampling and might be repaired by using transformations. Typical sample sizes in preclinical work do not lend themselves to formal evaluations of normality, but visual tools such as histograms or the subjective judgment of the closeness of the mean and the median might be sufficient. If the distribution of observations appears to be unimodal and symmetric, the *t*-test is fairly robust for the normality assumption. However, if the distribution appears to be skewed, consider a transformation—such as the log transformation discussed earlier in this chapter—to reduce the skew. Distributions with multiple modes are problematic; they should be presented and discussed as to how the multiple modes might arise. Researchers often approach biostatisticians seeking a threshold of sample size above which anomalies in the distribution of measurements can be ignored. Unfortunately, there is no such "golden threshold"; rather, it is a spectrum. The bigger the sample size, the smaller the problem. Nonparametric tests—such as the Mann-Whitney U or Wilcoxon rank-sum test—don't require assumptions of normality and are thus less sensitive to outliers or skewed data. Consequently, these tests have less power to detect small effect sizes or differences compared to the parametric *t*-test. Nevertheless, they can be good alternatives to the *t*-test if there are strong outliers in a data set.

Many preclinical studies involve collecting measurements over multiple days or weeks (repeated measures), resulting in longitudinal data. You can incorporate the additional information from multiple time points using a linear regression model, $y_i = \beta_o + \beta x_i + e_i$, where time is the independent variable (x), the collected measurement is the dependent variable (y), and e is the random noise. In this model, β_o represents the baseline value for each observation (y_i) at time 0, and β represents the slope or average rate of change in y for a unit increase in x. To account for the repeated measures of an individual mouse, a random effect should be added to the model to capture the additional variability arising from that individual mouse. With this specification, each mouse will have its own random effect. This model can be used for both hypothesis testing and estimation. For example, to evaluate if there is a significant difference in average log tumor volume over time, you might consider evaluating the null hypothesis $H_0 : \beta = 0$ using a so-called Wald test. However, do not expect to apply this model without help from a biostatistician, as it requires specialized software and formal statistical training to fit and interpret. Alternatively, to estimate the half-life of a new radionuclide, you might estimate $\frac{\ln(2)}{\beta}$, where $\hat{\beta}$ is the point estimate of the coefficient β from the regression model. We note that to obtain a 95% confidence interval of the estimated half-life, the standard error can be calculated as $\mathrm{SE}(\hat{\beta})\ln(2)/\hat{\beta}^2$ using the delta method [3], in which $\mathrm{SE}(\hat{\beta})$ is the standard error for the point estimate β obtained from the regression model. Likewise, this kind of analysis is usually feasible only with professional statistical software.

A linear regression model—$y = \beta_0 + \beta x + e$—assumes that the relationship of the observed measurements over an independent variable (x) (such as time or dose level) is linear and that the unobserved error values (e) are independent and identically normally distributed (with mean zero and the same standard deviation). These error values capture noise or variation from factors other than variable x that influence the dependent variable y. The assumption of linearity can be informally assessed by using a scatter plot (plotting x versus y) and looking for a linear trend. To investigate the distribution of the unobserved error variable, you can calculate and evaluate the residual values. The residual for each observation is the difference in the fitted value— $\hat{y}_i = \hat{\beta}_o + \hat{\beta} x_i$, where $\hat{\beta}_o$ and $\hat{\beta}$ are the maximum likelihood model parameter estimates—from the observed data value (y_i). For the model and subsequent inferences to be valid, residuals should be approximately normal, which can be evaluated as before using summary statistics and visuals. The most important assumptions to check when using a regression model are linearity and homoscedasticity (i.e., the variation of observations is more or less the same across all x). Homoscedasticity

can be quickly assessed using a scatter plot of x versus e. This assumption is met if the band or spread of points is constant across all x values. However, if the points appear to be close together at first and then funnel outward as x increases (resembling a megaphone or sideways ice cream cone), then this assumption is violated.

For ethical reasons, sometimes an individual mouse must be sacrificed during *in vivo* studies. If so, it is important to consider how the sacrificed mouse (or mice) might affect your calculated summary measures, hypothesis tests, and linear models. For example, if you are estimating the rate of tumor volume growth over time, sacrificed mice will bias this estimate and (possibly) underestimate the true rate. If too many mice are sacrificed relative to the entire sample size, a regression model is not appropriate. Furthermore, if too many mice are sacrificed early in the experiment, truncating the data to the first time point a mouse is sacrificed may not be useful when answering your questions. In this case, you may still apply the previously mentioned methods, but be sure to be very transparent in your interpretation of this limitation and its potential ramifications. Alternatively, you may have to alter the scientific question you can answer with your data. For example, rather than test for a significant difference in average tumor volumes over time between two groups, you may pursue a slightly more complicated method of comparing the tumor growth profiles of individual mice between the two groups using a two-sample test under dependent right censoring, which compares the area under the tumor growth curves [4]. This is another method that will require a biostatistical collaborator.

Sample Size

How large should my sample size be? This is probably the most commonly asked question of biostatisticians. In clinical studies, one can perform a sample size calculation and use it to guide the design of a study. However, in most *in vivo* and preclinical studies, financial and logistical constraints—such as the cost of manufacturing the radiopharmaceutical or the available cage capacity—usually dictate the sample size. Therefore, a more reasonable approach is to calculate the power afforded by this sample, assuming different true states of nature. For example, let's consider an experiment to compare the log tumor volumes of two groups that have been administered different doses of the same radiopharmaceutical. For this experiment, if the larger dose can significantly reduce the average log tumor volume by one unit compared to the smaller dose, then the larger dose will be used for further investigations of the experimental compound. Figure 3 displays some representative data from Houghton *et al.* [1].

We will examine the expected power (*i.e.* the probability of declaring a significant difference between the two dose levels when a true difference exists) to detect a reduction of one unit in log tumor volume. To estimate the power of an independent, two-sample t-test (one-tailed) for different sample sizes, we must also specify an anticipated level of standard deviation for the difference between the two group averages. To give you some context, the mice-receiving Dose A in Fig. 3 have an average log tumor volume of 5.4 at Day 44, while the mice-receiving Dose B have an average log tumor volume of 4.5. The difference between these two group averages is 0.9. To estimate power, you must have an idea of the amount of variability for this difference in means. This is both difficult and consequential, so we will return to it soon. The best estimates of variability are obtained from using previous pilot data or published literature, although a sensitivity analysis evaluating what your power would be if you were to assume a more or less extreme standard deviation is always useful. For the example in Fig. 3, the pooled variance for the difference in means between the two groups is 1.1. In Fig. 4, we estimate the power for a future study to detect a decrease of one unit in the average log tumor volume for Dose B from Dose A and assume this difference has a standard deviation of 0.5, 1, or 1.5.

In this power analysis (see Fig. 4), we consider sample sizes of 3, 5, 7, 10, 15, and 20 mice for each group. When we assume a standard deviation similar to what we observed in Fig. 3 (sd = 1), we see that for three mice/group, we expect a little over 25% power to detect a one unit decrease in log tumor volume, and for ten mice per group, we expect around 70% power. If we were conservative in our estimate of the

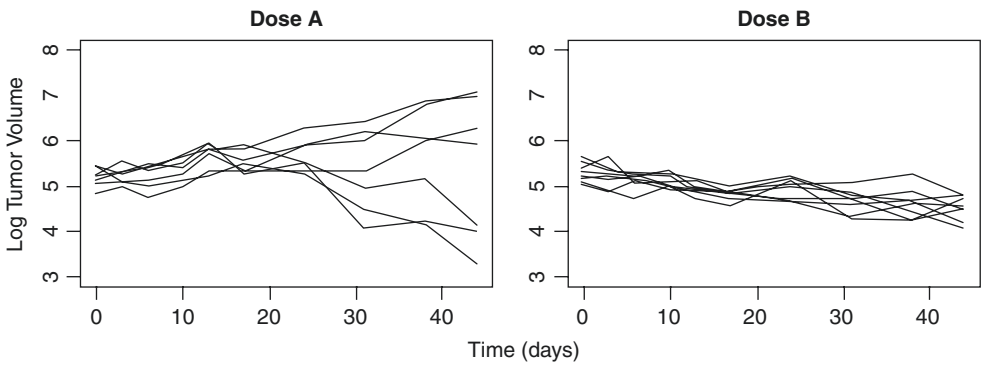

Fig. 3 Log tumor growth mouse profiles over time for two different doses: Dose A (*left*) and Dose B (*right*)

standard deviation (*i.e.* Fig. 3, sd = 1.5), we see that even with 20 mice/group, we can only expect around 65% power. However, if the standard deviation of the difference is half as large as the difference you are trying to detect (Fig. 3, sd = 0.5), then with five mice/group, you can expect over 80% power to detect that difference. In all scenarios, we see an experiment has very little power with only three mice per group. To put this in context, remember that it is for a single *t*-test; if your analysis becomes more complex—for example, regression modeling or simultaneously testing multiple hypotheses—your power can quickly diminish. A good practice is to avoid hypothesis testing when you have poor power.

Interpretation and Presentation

Interpreting your data involves communicating the overall findings of your experiments and their likelihood to be replicated in other experiments. It is essential to provide specific details for the experimental design and statistical analyses. In drawing conclusions, it is important to present the strength of promising signals alongside a fair discussion of the limitations. In many *in vitro* or preclinical studies, one of the primary limitations is small sample sizes (<10). Given this limitation, different presentations of the data can provide differing interpretations of the study.

To this end, the left plot in Fig. 5 displays the log tumor volumes for individual mice over time (in days), with each mouse represented by a different color. The right plot in Fig. 5 displays the average log tumor volumes using all mice at each time point with standard error bars (here, using +1 standard deviation). Clearly, we see how different presentations project different interpretations for the reader. Investigations of your data should begin with the individual plotted data (left plot), which provides more information about the experimental intervention. Furthermore, this can potentially provide more information about data transformations that may be necessary, the presence of any violations in the assumptions for the methods of analysis, or changes in the appropriate statistical analysis that may be necessary if said violations cannot be corrected.

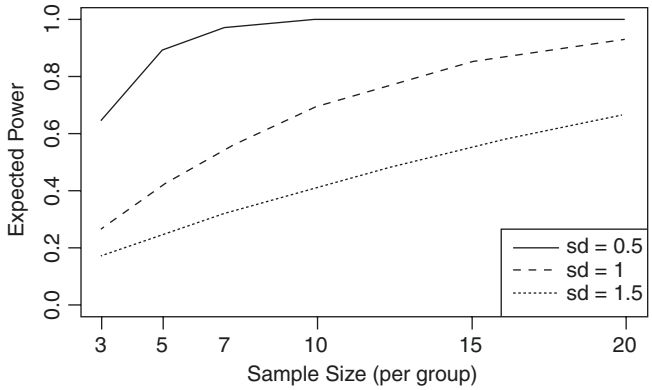

Fig. 4 Power curves for an independent, two-sample *t*-test

Tricks of the Trade

In this section, we provide some tips that will help you when performing your statistical analyses.

For anyone planning to analyze his or her own data, it is essential to acquire practical knowledge of statistical software. Some software packages—such as Prism, a commercial package—are user-friendly but limited, while others are very capable but have a steep learning curve (such as R, an open-source programming language). Familiarity with software will increase your familiarity with your data but needs to be balanced against the dangers of conducting improper or incorrect analyses. It is also helpful to understand the calculations, even though one might never actually have to perform them manually. For example, examining the formula of the two-sample *t*-test leads to the intuitive understanding that it evaluates the difference of means relative to the variability, an insight that cannot be gained from software alone.

There are some easy ways to quickly check one's results. As we mentioned in the previous section, you should visu-

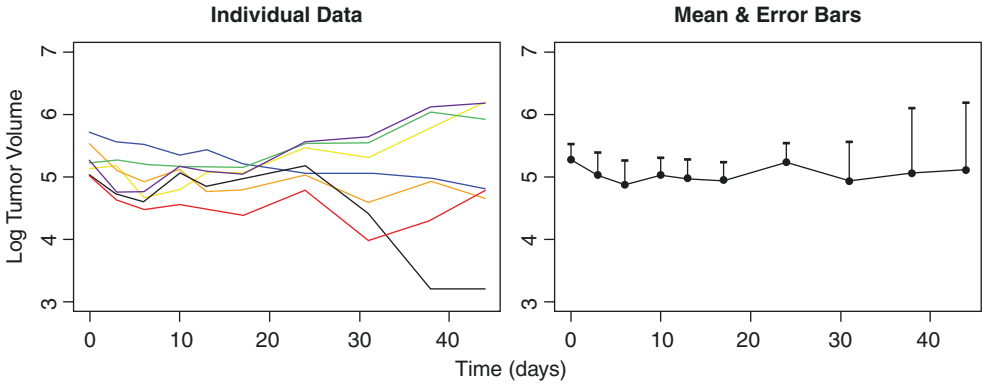

Fig. 5 Plots of log tumor volume versus time in days for (*left*) individual mice data and (*right*) mean and standard error bars for all mice at each time point

ally inspect your data before hypothesis testing. For example, the smaller the *P* value from your analysis, the more separated your error bars should be in visual graphs for the two groups being compared. If the error bars overlap and you found a significant difference between the two groups, then something is wrong: either with the data or the analysis method you are using. When looking at spaghetti plots, if experimental units appear to cross—*i.e.* experimental units that start at smaller values end at larger values, while those that start at larger values end at smaller values—then it is important to consider a regression model. In this case, applying a *t*-test may be inappropriate. For non-linear trends, applying a *t*-test using the first and, say, last time points is inappropriate, as is the use of a linear regression model. In more complicated cases, several alternatives exist, but a biostatistical collaborator will be needed.

Controversial Issues

In this section, we discuss two controversial issues that many biostatisticians still debate over: Should you apply a correction for testing multiple hypotheses on the same data? And should you remove data that you believe to be an outlier?

Correction for Multiple Comparisons

Oftentimes in *in vitro* or preclinical experiments, you will want to compare the biodistribution data of multiple groups. In this case, you are testing multiple hypotheses—one for each dose level or compound—and using the same control data. Many biostatisticians believe when you reuse the same data for multiple tests, you should correct for multiple comparisons. This is because every hypothesis test has a false-positive rate associated with it (commonly 5%). As a result, performing more hypothesis tests using the same data increases the chance of a false-positive result (more than the specified 5%). If you perform 20 tests, you would expect to find one significance purely by chance. Applying a correction for the multiple comparisons will protect and control the false-positive rate of your experiment. On the other hand, other biostatisticians believe that for *in vitro* and preclinical studies, a correction for multiple comparisons is not applicable. This is because the sample sizes are too small and moderate signals could be missed. In this case, reporting that a correction was not implemented due to small sample sizes will suffice.

If you do plan to apply a correction for multiple comparisons, it is important to take this correction into account when performing your power analysis in order to determine the sample size during the design phase. Otherwise, your experiment may be underpowered after the correction for multiple comparisons. The Bonferroni method—which is simple to apply—is not only the most commonly used example but also the most conservative in controlling the false-positive rate (and potentially diluting your power to detect modest signals). To implement this method, first calculate the new statistical significance level by taking your specified significance level (usually 5%) and dividing by the number of hypotheses being tested. For example, if you have five experimental groups that will be compared with a control group, then the adjusted significance level is now 1%. If the *P* value from each hypothesis test is less than or equal to 1%, then you reject the null hypothesis. Alternatively, you can present the adjusted *P* value by multiplying the original *P* value by the number of hypotheses being tested (*i.e.* five in the previous example). There are more powerful methods, but these will require professional input.

Outliers

What should you do with that experimental mouse that showed exponential tumor growth when all of the other mice in that same group showed dramatic tumor shrinkage? Many biostatisticians believe that for *in vitro* or preclinical studies, you should use all the data, even those that appear to be outliers. This is because of the small number of samples (which makes each piece of data precious) and the nature of the experimental units, *i.e.* the mice are genetically engineered to be identical. On the other hand, many statistical methods to detect outliers have been proposed. Many biostatisticians believe that removing experimental units that are found to be outliers by the proposed metrics is valid. In this case, the experimental unit has been shown to be statistically significantly different from the other units in the same experimental group.

Nevertheless, all biostatisticians would agree that outliers that arise from violations of the protocol or errors in the intervention—such as tumor graft failure—should be removed for the analysis. In fact, any such data point, whether it is an outlier or not, should be removed. The critical issue is to make that determination *before* the data is completely observed to avoid any bias. Furthermore, whenever an experimental unit is removed from the analysis, it should be reported in the manuscript.

The Future

The future of biostatistics for *in vitro* and preclinical studies will be centered on methods utilizing more data! Increasingly, researchers will explore more factors in a single study in an effort to more completely characterize a given radiopharmaceutical. Here, both the thoughtful

design of the experiment and the use of appropriate statistical methods are essential for the efficient and powerful interpretation of the data. In response to this growth, the field should evolve to include larger sample sizes (*i.e.* more mice, tissue samples, or replicates) for each study. And for investigations which ask more complicated questions, a biostatistician should be included as a collaborator during the design of the study and the analysis of the data. Finally, the role of biostatistical software is also poised to grow because of the increasing amount of data being collected in any single study.

The Bottom Line

- Before running your experiment, be sure to clearly identify the scientific questions—*i.e.* hypotheses—that are being asked in the study.
- During the design stage of your study, determine the number of experimental units needed to answer the scientific questions.
- During the design stage of your study, preplan the methods you will use for the statistical analysis of your data.
- For more complex studies, be sure to involve a biostatistician as a collaborator during the design of the experiment and the analysis of the data.
- In the presence of known and unknown limitations in the design of the experimental study, be careful and transparent when interpreting and presenting your data.

References

1. Houghton JL, Membreno R, Abdel-Atti D, Cunanan KM, Carlin S, et al. Establishment of the in vivo efficacy of pretargeted radioimmunotherapy utilizing inverse electron demand Diels-Alder click chemistry. Mol Cancer Ther. 2017;16(1):124–33.
2. Sharma SK, Pourat J, Abdel-Atti D, Carlsin SD, Piersigilli A, et al. Noninvasive interrogation of DLL3 expression in metastatic small cell lung cancer. Cancer Res. 2017;77(14):3931–41.
3. Casella G, Berger R. Statistical inference. Pacific Grove: Duxbury; 2002.
4. Vardi Y, Ying Z, Zhang CH. Two-sample tests for growth curves under dependent right censoring. Biometrika. 2001;88(4):949–50.

Choosing a Target for Nuclear Imaging or Targeted Radiotherapy

Andrew M. Scott, Yit Wooi Goh, Sze Ting Lee, and Salvatore U. Berlangieri

Introduction

The investigation of physiology and disease states has been the cornerstone of nuclear medicine since its inception [1–3]. The radiotracer principle has been extended from initial investigations of blood hormone and protein levels to imaging-based studies that have had significant clinical impact across the broad spectrum of human pathologies [3]. As our understanding of the biology of normal and abnormal cells has evolved thanks to a deeper understanding of the metabolic, biochemical, and genomic changes that occur in various diseases, our ability to select targets suitable for nuclear imaging has expanded dramatically [4–7] (Fig. 1). The ability to image physiologic processes with precision at low radiotracer concentrations is a distinguishing feature of nuclear imaging, one that allows for the broad interrogation of a vast array of targets in both model systems and patients [1, 3].

A. M. Scott (✉)
Department of Molecular Imaging and Therapy, Austin Hospital, Heidelberg, VIC, Australia

Tumour Targeting Laboratory, Olivia-Newton John Cancer Research Institute, and La Trobe University, Melbourne, VIC, Australia

University of Melbourne, Melbourne, VIC, Australia
e-mail: andrew.scott@austin.org.au

Y. W. Goh
Tumor Targeting Laboratory, Olivia Newton-John Cancer Research Institute, Melbourne, VIC, Australia

S. T. Lee
Department of Molecular Imaging and Therapy, Austin Hospital, Heidelberg, VIC, Australia

Tumor Targeting Laboratory, Olivia Newton-John Cancer Research Institute, Melbourne, VIC, Australia

S. U. Berlangieri
Department of Molecular Imaging and Therapy, Austin Hospital, Heidelberg, VIC, Australia

Target Properties

The properties of targets suitable for nuclear imaging are dependent on the physiologic process under investigation as well as the phenotype of the cell population targeted by the nuclear medicine scan. The principles for the selection of targets are outlined in Table 1. These apply across the spectrum of disease states—including neurology, cardiology, cancer, musculoskeletal, infection, and organ systems—that require functional imaging data to identify and characterize the cause of abnormal physiology.

Expression

The optimal target for a diagnostic radiopharmaceutical is abundantly expressed in cells or tissues involved in the disease process and allows for dynamic and quantitative information to be obtained from scans. In some instances (*e.g.* blood pool scans for cardiac function or gastrointestinal bleeding studies), the distribution of the target (*e.g.* red blood cells) in normal tissue is relatively constant, and abnormalities in the distribution of the tracer are used for diagnosis. For studies which involve the identification of specific receptors, antigens, or cell populations, the target should be preferentially expressed in diseased tissue compared to normal tissue [8–12]. Low physiologic expression in healthy tissues is particularly important for targets which may be used for both imaging and therapy.

The number of targets per cell required for imaging with radiopharmaceuticals depends on both the type of tracer used and the expression level of the target in normal tissue. For example, the single-photon emission computerized tomography (SPECT) imaging of the bone with [^{99m}Tc]Tc-methylene diphosphonate (MDP) is dependent on the uptake of the radiopharmaceutical by osteoblasts, and the discrimination of abnormalities—*e.g.* fractures, infections, or tumors—requires an increase in the uptake of the tracer in diseased tissue relative to normal bone. Furthermore, the detection of β-amyloid in Alzheimer's disease with positron-emission tomography

J. S. Lewis et al. (eds.), *Radiopharmaceutical Chemistry*, https://doi.org/10.1007/978-3-319-98947-1_31

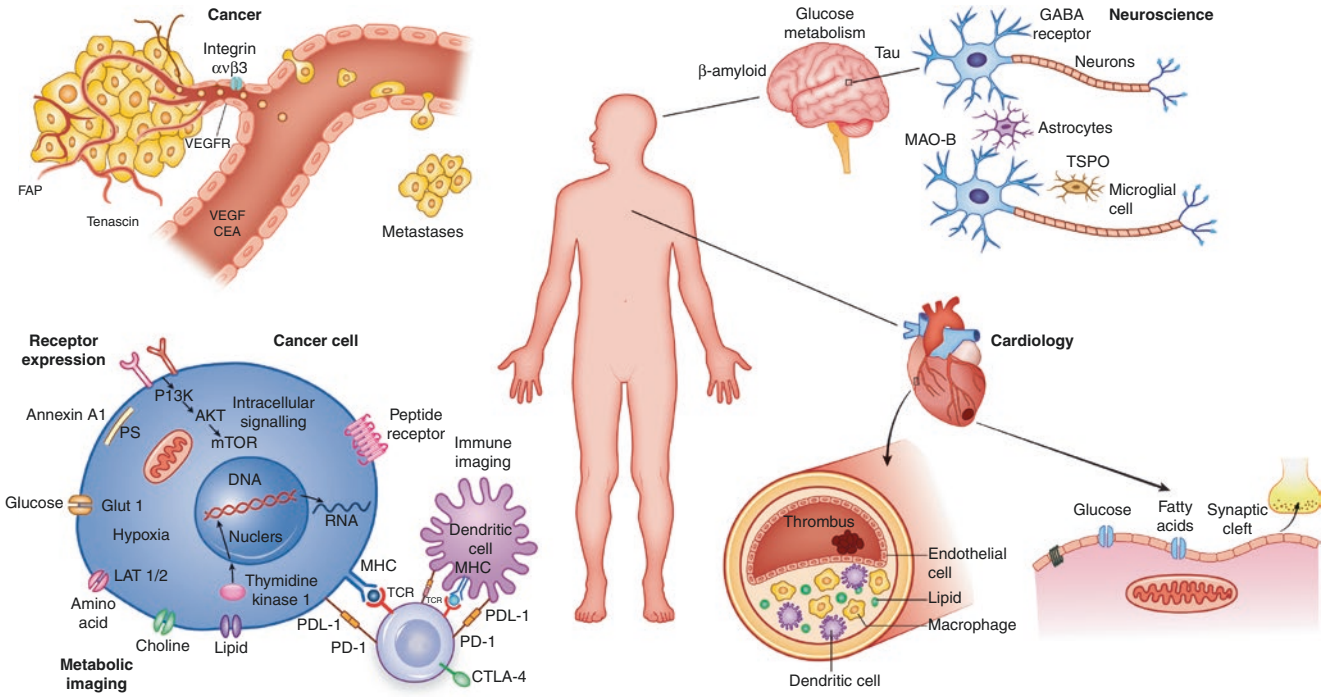

Fig. 1 Targets for nuclear imaging. Radiopharmaceuticals targeting metabolic pathways, physiologic processes, and disease pathways can be used for nuclear imaging and targeted radiotherapy

Table 1 Properties of promising targets for nuclear imaging

Target expression
Abundant in relevant cells or tissues
Accessible to the radiopharmaceutical
Stable
Target function
Clear metabolic pathway or physiologic function
Linked to disease etiology or phenotype
Known internalization mechanism
Specificity of target for disease
Target expression strongly associated with disease activity
Low abundance in normal cells or tissue
Pattern of expression relevant to disease state
Relevance of target for therapy
Expression in target cell population or tissue
High AUC target-to-normal tissue ratio
Target expression linked to therapeutic response

(PET) tracers can be achieved up to 10 years prior to the clinical presentation of the disease, highlighting the predictive accuracy and sensitivity of this technique for detecting threshold levels of protein in diseased areas of the brain [13] (Fig. 2). For peptide and antibody imaging, target levels must typically be greater than 10,000 copies per cell, although the number of peptides or antibodies that bind per cell is usually quite small, at times as low as 5–10 molecules per cell [14–16].

A target must also be accessible to radiopharmaceuticals to ensure adequate uptake. This is particularly important for peptides and large proteins, for which diffusion through the vasculature's interstitial membrane can restrict the delivery of the tracer unless high concentrations are present. The blood-brain barrier may also impact the penetration of both small and large molecules due to their lipophilicity, charge, or size [17, 18]. As a result, the *in vivo* validation of new radiopharmaceuticals demands careful evaluation of the biological distribution and uptake of the tracer in target cell populations or tissues in order to ensure that target engagement is achieved and reproducible.

Moving forward, the stability of targets is essential for reliable imaging as well, and any changes in a target due to phenotypic instability (*e.g.* PSMA or HER2) may have an adverse impact on the sensitivity of the scan [14]. In addition, if the target is impacted by enzymatic activity (*e.g.* biochemical pathways) or metabolic degradation, the temporal pattern of uptake and retention can be markedly variable. This is relevant for a range of commonly used radiopharmaceuticals, including [^{131}I]-NaI. In this case, the high turnover rate of the sodium-iodide symporter can impact scan results as well as therapeutic dosimetry [19]. An additional factor which can have an influence on imaging is the tendency of some targets—for example, CEA and HER2—to shed from the surface of cells, a trait that can cause the rapid clearance of radiopharmaceuticals from the blood and reduce uptake in the target cell population [14].

Function

The metabolic processes of cells are often altered due to genetic, transcriptional, or microenvironment-induced

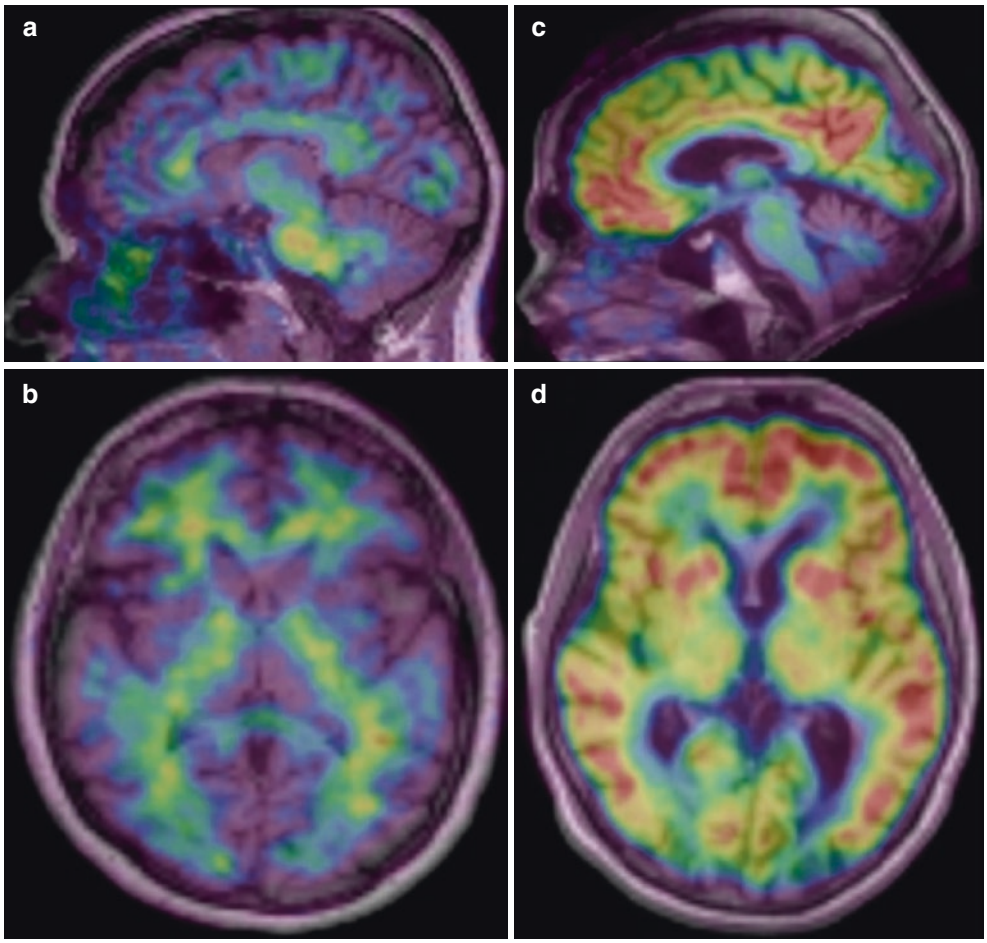

Fig. 2 Imaging of β-amyloid with [^{11}C]PiB PET/CT. A normal subject shows no evidence of cortical amyloid, with tracer distributed to the corpus callosum and pons in (**a**) the sagittal image and—marked white matter pattern in the perithalamic area—(**b**) the axial image. A patient with Alzheimer's disease shows amyloid distribution to the medial orbitofrontal cortex, cingulate gyrus, and precuneus in (**c**) the sagittal image and in the frontal, parietal, lateral temporal, occipital, and striatal cortex in (**d**) the axial image. (Image courtesy of Christopher Rowe MD, Nuclear Medicine and Centre for PET, Austin Health, Heidelberg, Victoria, Australia)

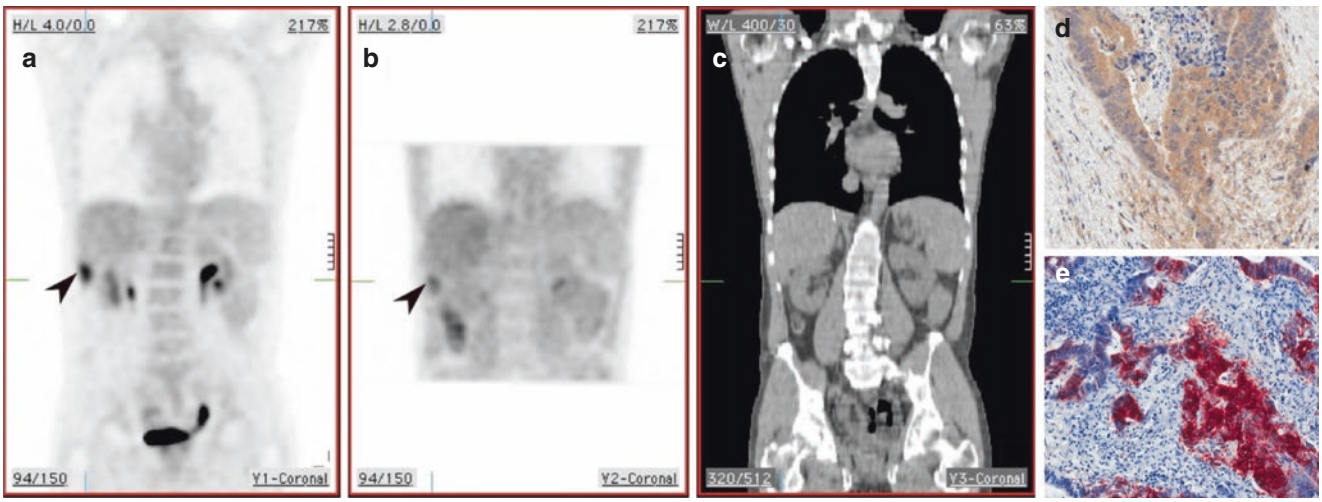

Fig. 3 Metabolic imaging of glucose uptake and hypoxia in colorectal cancer. (**a**) [^{18}F]FDG PET showing metastatic lesion in the colon (*arrow*); (**b**) [^{18}F]FMISO PET showing hypoxic cell fraction of the metastasis (*arrow*); (**c**) CT coronal image of the patient; (**d**) HIF-1α staining of the hypoxic tumor after resection; and (**e**) CAIX staining of the hypoxic tumor after resection

changes associated with disease states. For example, shifts in the metabolism of glucose, amino acids, and lipids as well as physiological alterations such as hypoxia are well-known hallmarks of cancer (Fig. 3). Perhaps not surprisingly, radiopharmaceuticals that can visualize these changes can be instrumental in the diagnosis and management of disease (see Fig. 1). These metabolic changes are often associated with alterations to enzymes or pumps that control the uptake of cellular building blocks as well as shifts in the expression of proteins and receptors linked to metabolic pathways (*e.g.* HIF-1α

and CAIX in hypoxic conditions). In addition, disease states may be associated with genomic changes that result in the overexpression of target proteins or the modification of targets (*e.g.* mutant signaling pathways or receptors) compared to normal cells, alterations that can be exploited for imaging and therapy [4–7]. A detailed understanding of the biology of a disease is critical for the identification of an appropriate target as well as the development of imaging probes that can both assist with the assessment of the disease and aid in the study of the fundamental biochemical and metabolic changes that occur in diseased tissue.

The processing of a target may also impact its suitability for nuclear imaging as well as the choice of the most appropriate radionuclide. Cell surface receptors, for example, are often oligomerized or internalized upon binding ligands, processes which can result in the intracellular sequestration—and subsequent degradation—of the radiopharmaceutical/receptor complex in endosomes and lysosomes [20, 21]. This is not well suited to radiohalides, which can be extruded from the cell rapidly following the degradation of their biomolecular vector; as a result, radiometals are often a more appropriate choice in these cases.

Specificity

Many of the targets that are used in nuclear imaging are expressed in normal tissues, and it is highly unusual for a target to be expressed only in a disease state. However, the overexpression or selective expression of these biomarkers in diseased tissues may provide opportunities for developing imaging probes that can specifically define pathology (Figs. 2, 3, and 4). One example is PSMA, which is overexpressed on prostate cancer cells compared to normal tissue and upregulated in more aggressive disease [22]. Hormone receptors are another example of targets which are selectively overexpressed in disease (*e.g.* cancer) compared to normal tissues.

Relevance of Target for Therapy

In identifying a target suitable for targeted radiotherapy, the specificity and stability of the target as well as its cellular processing are key factors. These factors become less important, of course, when the radiopharmaceutical is administered locally (*e.g.* direct injection or regional

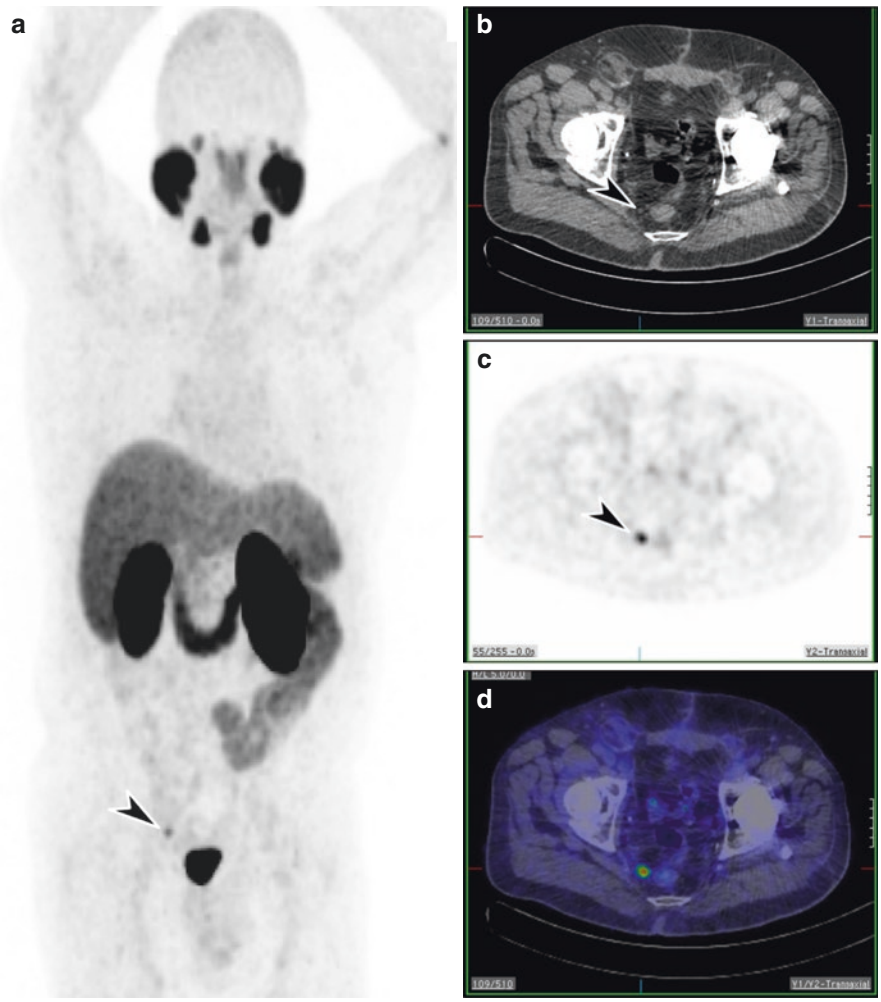

Fig. 4 [^{68}Ga]PSMA PET/CT scan in a patient with a history of prostate cancer and elevated PSA level. (**a**) Normal uptake of [^{68}Ga]PSMA in salivary glands, liver, spleen, and kidneys is evident, and a focus of abnormal uptake (*arrow*) was due to metastatic disease in a normal size lymph node seen on (**b**) CT, (**c**) PET, and (**d**) PET/CT scans

perfusion) (Fig. 5). Due to the selective dosimetric advantage of internalized targets for radiometal-based therapy, the internalization of the radiopharmaceutical is also a key consideration for systemically administered radiotherapeutics. In cases in which the targets are *not* internalized, the use of radiohalides can be highly effective. For example, [^{131}I]-NaI has proven extraordinarily effective for the targeted radiotherapy of hyperthyroidism and well-differentiated thyroid cancer in hundreds of thousands of patients worldwide (Fig. 6) [23]. The validation of therapeutic targets requires the careful preclinical assessment of the biodistribution, therapeutic index, and dosimetry of the

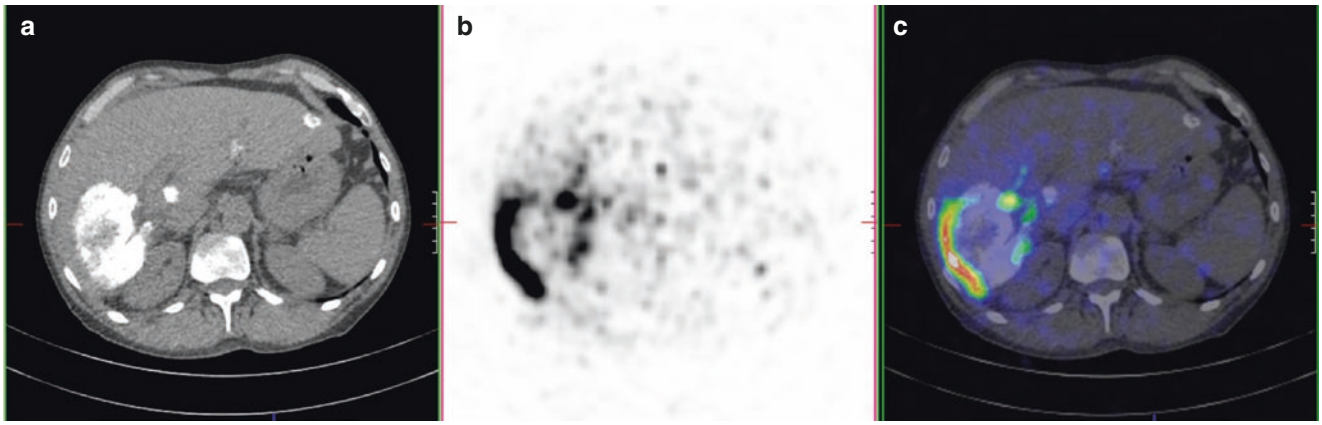

Fig. 5 Treatment of metastatic colorectal cancer to liver with ^{90}Y-labeled microsphere radioembolization. (**a**) CT showing necrotic metastatic lesion in the liver; (**b**) PET imaging of the distribution of the ^{90}Y-labeled microspheres; (**c**) PET/CT merged image showing distribution of ^{90}Y-labeled microspheres in the viable tumor at the edge of the mass

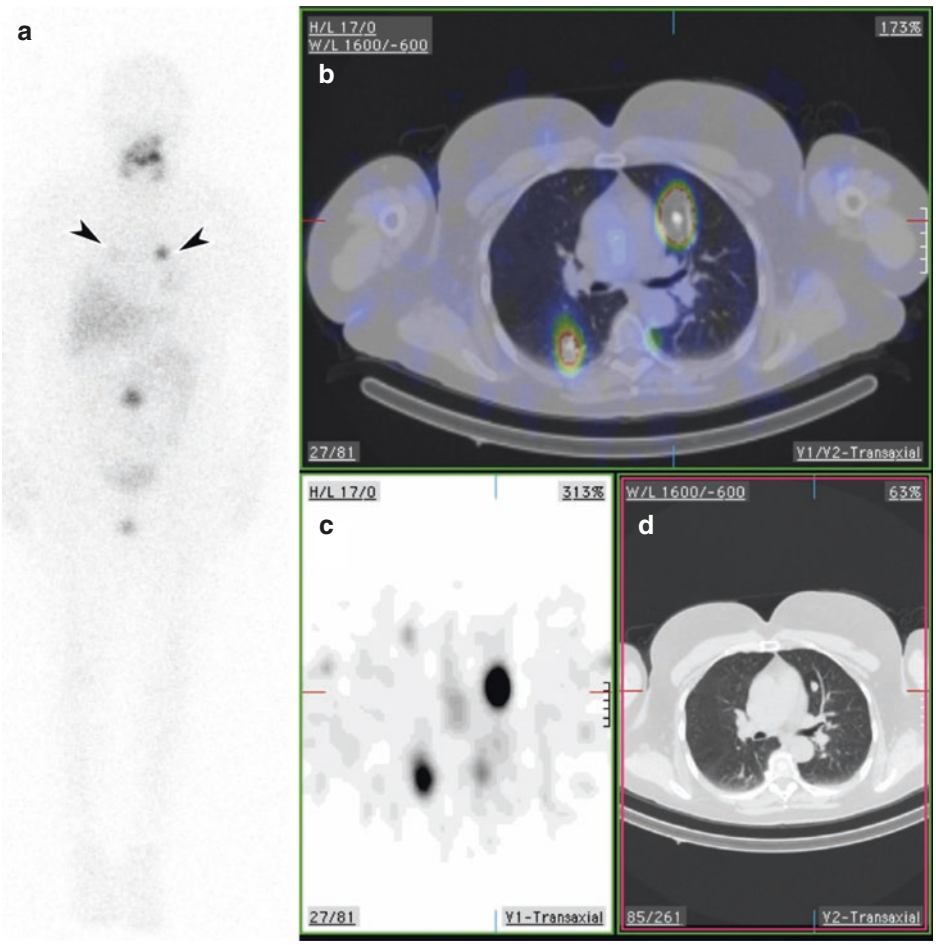

Fig. 6 Metastatic follicular thyroid carcinoma. (**a**) Whole body [^{131}I]NaI scan following treatment with 200 mCi [^{131}I]NaI shows uptake in pulmonary nodules (*arrows*), also seen via (**b**) co-registered SPECT/CT; (**c**) SPECT and (**d**) CT confirm the sites of metastatic disease. The central abdominal uptake of [^{131}I]NaI was due to a further metastatic deposit

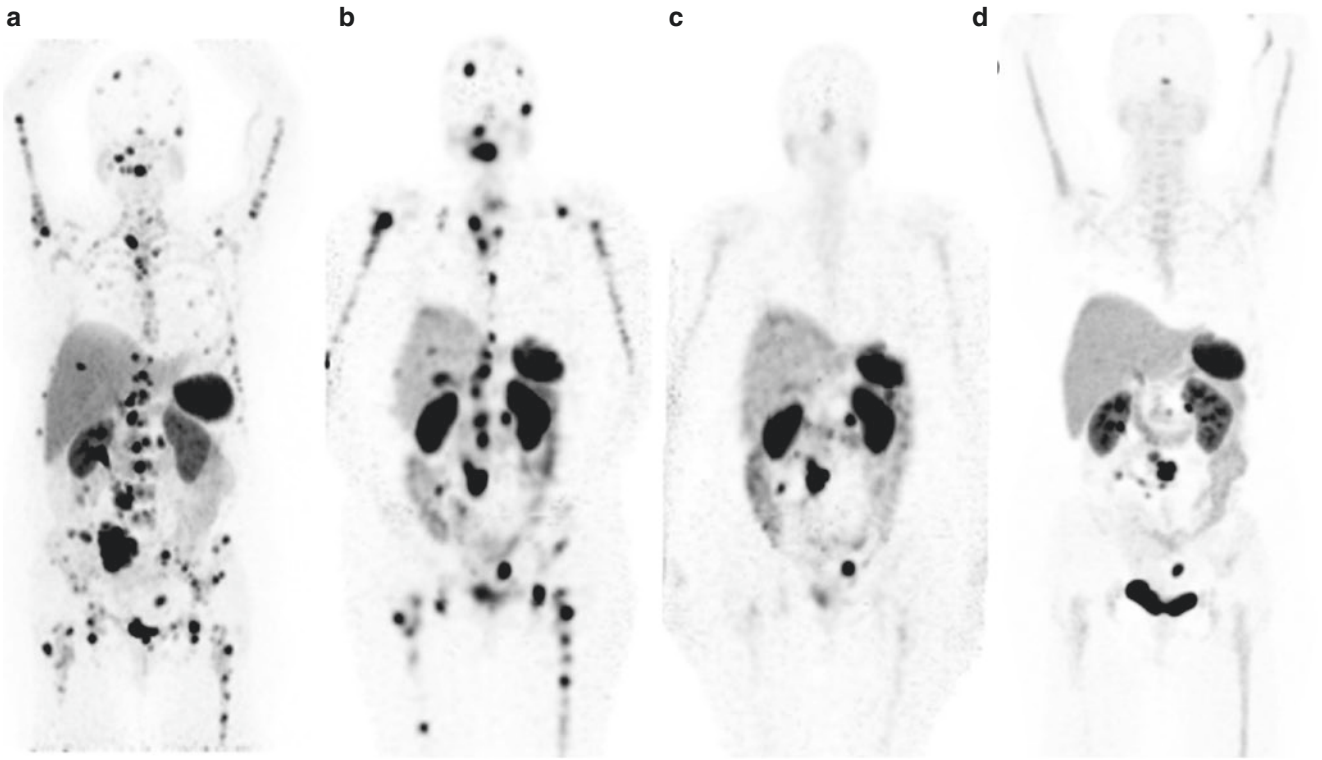

Fig. 7 Somatostatin receptor imaging and targeted therapy in a patient with metastatic midgut neuroendocrine tumor. (**a**) A [^{68}Ga]Ga-DOTATATE PET scan showing widespread metastatic disease; (**b**) [^{177}Lu]Lu-DOTATATE treatment post-therapy scan, showing excellent uptake of [^{177}Lu]Lu-DOTATATE in sites of metastatic disease; (**c**) [^{177}Lu]Lu-DOTATATE scan post second [^{177}Lu]Lu-DOTATATE treatment; (**d**) [^{68}Ga]Ga-DOTATATE PET scan after second [^{177}Lu]Lu-DOTATATE therapy, showing marked reduction in sites of metastatic disease, indicating an excellent response to treatment

proposed radiopharmaceutical, as well as the development of imaging probes that accurately reflect the biodistribution of the therapeutic radiopharmaceutical (see Figs. 6 and 7). The latter also allows for the development of a "theranostic" imaging probe that can be used to select patients and predict likely response. Indeed, the development of theranostic imaging tools has emerged as a powerful approach for the creation of effective new therapeutic radiopharmaceuticals [24, 25].

The Selection of Targets

Small Molecules

An ideal small molecule radiopharmaceutical should have fast plasma clearance, high specificity and affinity for its target, low non-specific and non-selective binding, and low peripheral metabolism. Binding constants in the high picomolar to low nanomolar range are typically required in order to achieve sufficient concentrations for detection and quantitation. In addition, the size, charge, and lipophilicity of the radiopharmaceutical all play important roles in determining its pharmacokinetic profile and uptake by the cell or tissue where the target is expressed [17]. Small molecules are most frequently used as vectors for intracellular targets due to their membrane permeability and the ability to design molecules for specific biochemical targets within the cytoplasm and nucleus. Indeed, the targets best suited to small molecule radiotracers are kinase domains, signaling pathways, and nuclear receptors. The chemical nature of these compounds often lends itself to the creation of ^{18}F- or ^{11}C-labeled PET radiotracers, although recent improvements in ^{99m}Tc chemistry have facilitated the development of small molecule SPECT radiopharmaceuticals as well [26].

Peptides

Peptides have a number of advantages over small molecules, including their exquisite specificity for receptors as well as recent advancements in design and bioconjugation that have opened the door to radiolabeled peptides with enhanced potency and *in vivo* stability [27–29]. Peptides generally display high stability at room temperature and have a greater

ability than larger proteins to penetrate tissues/tumors to allow fast target uptake and blood clearance (see Figs. 4 and 7). In addition, peptides are also less likely to cause immunogenic reactions than proteins or antibodies [30].

Cell surface receptors which are expressed by diseased tissues are ideal targets for radiolabeled peptides. Indeed, the classical receptor targets for peptide-based radiopharmaceuticals are the 7-transmembrane (7TM) proteins, often referred to as G-protein-coupled receptors (GPCRs). Several hundred GPCRs have been identified, and it is estimated that 50% of clinically relevant drugs are acting upon this class of receptors [31]. A large number of these receptors are overexpressed in disease states and are thus being evaluated as targets for nuclear imaging probes. These include somatostatin receptors (SSTR), $\alpha_v\beta_3$integrins, the gastrin-releasing peptide receptor (GRPr), the cholecystokinin 2 receptor (CCK2), the glucagon-like peptide 1 receptor (GLP-1), and the chemokine receptor 4 (CXCR4). Recent reviews have identified a large number of potential new targets for peptide-based radiopharmaceuticals [32].

Proteins

Antibodies are produced *in vivo* by the immune system in response to the expression of an antigen and bind specifically to the antigen to form an antigen-antibody complex. Antibodies are large proteins—IgG1 weigh in at around 150 kDa—and, if administered systemically, can take many days to accumulate within target tissue and clear from the blood [14, 15]. Due to the spatial orientation of the complementarity-determining regions (CDRs) that confer the antibody's ability to bind its target, complex antigens or receptors on the cell membrane and in the tumor microenvironment can be targeted with exquisite specificity and high affinity, and antibodies are ideally suited to these more complex protein targets [14]. The ideal targets for antibodies are uniformly expressed in diseased cells or tissues, have low levels of expression in normal tissues, are genetically stable, and are not shed from tissues into the bloodstream. Smaller fragments of intact antibodies (*e.g.* scFv, minibodies) have been developed that have shorter half-lives are more suited to nuclear imaging. Targets suited to antibodies have been explored clinically for over 20 years, and there are approved antibodies for therapy in cancer, cardiology, and immune disease indications [33]. Furthermore, radiolabeled antibodies and antibody fragments are emerging as powerful tools in drug development, as they can be used to assist in the development of therapeutics through the evaluation of target expression, occupancy, and dose response in early phase clinical trials [34].

Targets and Disease

With thousands of new targets for disease being discovered, a comprehensive review of all of them is beyond the scope of this chapter. The principle clinical areas of nuclear imaging are in neuroscience, cardiology, and oncology (see Fig. 1). Some of the most important clinical targets in these areas will be discussed in the following pages.

Neuroscience

Nuclear imaging is a powerful tool for quantifying brain metabolism, visualizing alterations in regional blood flow, and elucidating and studying complex neurological disorders such as Alzheimer's disease and Parkinson's disease. A wide range of targets and radiotracers have been developed to investigate brain function and disease.

Amyloid Plaques The deposition of amyloid plaques in the brain has been identified as one of the core pathologic features of Alzheimer's disease (AD). Amyloid plaques block cell-to-cell signaling at synapses, a process which is essential for storing memories, processing thoughts and emotions, and planning. PET imaging with small molecule amyloid-targeted radiotracers such as [^{11}C]Pittsburgh compound B (PIB) and other recently FDA-approved, ^{18}F-labeled amyloid-targeted radiotracers has been used to visualize the accumulation of amyloid in the brain before cognitive deficits become clinically evident (Fig. 1). In addition, amyloid radiotracers are used in AD patients to confirm their eligibility for amyloid therapy and to monitor their response to therapy [13].

Intracellular Tau Neurofibrillary Tangle Intracellular tau neurofibrillary tangle (NFT) is another mis-aggregated protein which is found in the brain of patients with Alzheimer's disease. Tau protein is associated with microtubules, specifically promoting their assembly and providing stability. However, in AD, there is dysfunction of the enzymes responsible for phosphorylation of tau, which gives rise to a hyperphosphorylated version that aggregates and forms insoluble NFT [13]. Several small molecule radiotracers with high selectivity for NFT have been recently developed, including [^{18}F]AV1451, [^{18}F]THK523, and [^{11}C]PBB3 [13, 35].

Dopaminergic Pathway Dopaminergic neurotransmission plays an important role in regulating several aspects of basic brain function, including motor skills, behavior, motivation, and working memory [36]. It is also involved in the pathogenesis of a variety of neurological disorders, such as Parkinson's disease, schizophrenia, attention-deficit

hyperactivity disorder, and drug dependence. A number of small molecule PET and SPECT radiotracers have been developed to visualize the activity of dopamine synthesis, reuptake sites, and receptors in a variety of neurological disorders [36, 37]. [^{18}F]FDOPA—an analogue of L-DOPA (L-dihydroxyphenylalanine), an immediate precursor for dopamine—has been used clinically as a small molecule PET radiotracer to trace the dopaminergic pathway and evaluate striatal dopaminergic presynaptic function in patients affected by Parkinson's disease. Parkinson's disease patients with low dopamine formation will have low [^{18}F]FDOPA uptake.

γ-Aminobutyric Acid-Benzodiazepine (GABA-BZD) Receptor Ion channels are membrane proteins which control the flow of ions passing through the cell membrane. Ion channel linked receptors are bound in cell membranes and mediated via the conformational interaction between ion channels and chemical ligands. The γ-aminobutyric acid-benzodiazepine (GABA-BZD) receptor is one of the most studied ion channel linked receptors in the brain [38]. Decreases in GABA-A receptor expression have been observed in many brain disorder such a dystonia, epilepsy, and ischemic stroke in clinical research studies using [^{11}C]flumazenil and [^{18}F]flumazenil PET imaging.

Nicotinic Acetylcholine Receptors Nicotinic acetylcholine receptor (nAChR) is another well-studied ion channel linked receptor, and reductions in the expression of nAChR have been reported in various neurodegenerative diseases, including epilepsy, depression, schizophrenia, and Parkinson's disease [39]. PET imaging with [^{18}F]2-FA has shown promise in the imaging of Alzheimer's disease and Parkinson's disease patients [40].

TSPO Neuroinflammation that causes neuronal damage and death is known to involve the expression of receptors that may be targets for radiopharmaceuticals. For example, the translocator protein 18 kDa (TSPO)—a mitochondrial protein found in the CNS—is an important target for the visualization of activated microglia that mediate the inflammatory process in disorders such as Alzheimer's disease, Parkinson's disease, and multiple sclerosis [41]. The level of TSPO is low in the healthy brain but increases when the inflammatory pathway is activated. Many different TSPO-targeted PET radiotracers have been developed, of which [^{11}C]PK11195 is the most frequently used [42].

Cardiology

In cardiovascular disease, a large number of targets associated with atherosclerotic plaque inflammation, myocardial infarction, impaired myocardial autonomic innervation, cardiac cell apoptosis, and vulnerable plaque rupture-prone lesions have been explored for nuclear imaging [43]. Even though there are many radiopharmaceuticals being developed and evaluated clinically for nuclear imaging in cardiovascular disease, probes for the visualization of myocardial perfusion imaging and myocardial metabolism are the most commonly used in current practice.

Myocardial Perfusion Imaging (MPI) Cardiac SPECT and PET imaging is commonly performed to assess myocardial perfusion and left ventricular function in patients with coronary artery disease (CAD). Myocardial perfusion imaging (MPI) enables the accurate measurement of the passage of blood through the heart, and the combination of MPI and stress testing (exercise or pharmacologic) can facilitate the identification of areas of myocardial damage or impaired blood flow [44]. SPECT tracers such as [^{201}Tl]thallous chloride, [^{99m}Tc]sestamibi, and [^{99m}Tc]tetrofosmin are commonly used for MPI, while imaging with [^{99m}Tc]Tc-red blood cells is used for the assessment of left and right ventricular function and shunts. [^{18}F]FDG and [^{82}Rb]RbCl can also be used for the PET imaging of myocardial viability and blood flow [44].

Norepinephrine Transporter The maintenance of homeostasis in the cardiovascular system by the sympathetic nervous system is mediated in part by catecholamines such as norepinephrine (NE). The stimulation of the adrenergic receptors of the cardiac muscle is caused by NE released from sympathetic neurons. The overexpression of an NE transporter known as hNET—a transmembrane protein that facilitates the reuptake of NE in sympathetic nervous system in the heart—has been correlated with the progression of heart disease as well as increased mortality. To date, the majority of clinical myocardial innervation imaging studies have utilized radiolabeled analogues of norepinephrine, including ^{123}I-labeled metaiodobenzylguanidine ([^{123}I]MIBG) and ^{11}C-labeled meta-hydroxyephinephrine ([^{11}C]mHED) [45].

Integrins and Adhesion Molecules Vulnerable atherosclerotic plaque is known to be responsible for most major cardiovascular events such as acute myocardial infarction and stroke, and the overexpression of integrin $\alpha_v\beta_3$has been associated with plaque rupture. SPECT and PET radiotracers developed from RGD peptides—including [^{99m}Tc]Tc-IDA-D-[c(RGDfK)]2 and [^{18}F]AlF-NOTA-PRGD2—have been reported to bind selectively to integrin $\alpha_v\beta_3$ in atherosclerotic aorta compared to normal aorta which does not express the integrin in question [46]. The expression of surface adhesion molecules such as VCAM-1 and selectins also plays a fundamental role in atherosclerotic plaque progression. These

surface adhesion molecules are responsible for the receptor-mediated recruitment of leukocytes, and VCAM-1 expression contributes to the inflammation after ischemic injury. ^{18}F-labeled nanobodies against VCAM-1 have been shown to have utility in the PET imaging of atherosclerotic plaques in mouse models [47].

Phosphatidylserine Apoptosis is a critical process in cardiology diseases such as chronic heart failure, atherosclerotic vascular disease, and myocardial ischemia. Apoptosis is characterized by cellular biochemical events leading to nuclear fragmentation and cell death. It is carefully regulated in normal cells and when defective can contribute to disease (*e.g.* cancer). The imaging of apoptosis has potential clinical utility in scenarios where cell death is uncertain and may impact clinical management decisions. For example, several clinical trials have shown that radiolabeled annexin V (a 37 kD protein) is capable of detecting apoptosis in ischemia-reperfusion injury and cardiac allograft rejection by targeting phosphatidylserine in a calcium-dependent manner [48].

Interleukin-2 (IL-2) Atherosclerosis is a lipid storage disease, and inflammatory cells are thought to be responsible for the transformation of a stable plaque into a vulnerable one. Lymphocytes constitute at least 20% of infiltrating cells in these vulnerable plaques. Therefore, the IL-2 receptor—which is overexpressed on activated T lymphocytes—is thought to be an attractive target for the visualization plaque vulnerability. Radiotracers developed by radiolabeling IL-2 directly with technetium-99m or iodine-123 have shown high affinity to the IL-2 receptor and are used in the detection of activated T lymphocytes in atherosclerosis [49].

Cancer

There are a broad array of targets for the nuclear imaging of cancer, including the aberrant metabolism of cancer cells, the deregulation of the expression of receptors on the surface of cells, increases in angiogenesis and cell proliferation within tumors, hypoxia, the inactivation of apoptosis pathways, and the evasion of the immune system (see Fig. 1). Metabolic pathways represent the most common oncologic targets for nuclear imaging, although a broad range of new targets are being explored with SPECT and PET imaging.

Cell Metabolism Alteration in the metabolism of cancer cells is one of the classic "hallmarks of cancer" and a trait which has been exploited for nuclear imaging for decades [50]. The staging of tumors with [^{18}F]FDG has been established as a cornerstone of patient management for most types of cancer and has been implemented in most countries as an integral part of oncology practice [51–53] (see Fig. 3). Other metabolic targets—including choline and lipid moieties, fatty acids, and biochemical pathways—have also emerged as potential targets for cancer staging, with the recent approval of [^{11}C]choline PET in prostate cancer standing as a prominent example. The sensitivity and accuracy of [^{18}F]FDG PET in detecting tumors and monitoring response to treatment has meant that other metabolic targets are being explored primarily to assist with the biological and functional characterization of tumors, to aid clinicians with therapeutic decisions, and to provide alternative radiopharmaceuticals in circumstances in which [^{18}F]FDG PET is not useful.

Receptors and Protein Kinases Protein kinases play a pivotal role in signal transduction pathways, and their dysregulation can cause significant alterations in many cellular processes, such as transcription, proliferation, angiogenesis, and the inhibition of apoptosis. Approximately 50% of the known oncogenes encode protein tyrosine kinases (PTKs). Cell surface receptors can activate cellular PTKs, and both can serve as targets for the imaging or therapy of cancer. Cancer cell surface receptors are normally targeted by monoclonal antibodies or peptides, while cellular PTKs and intracellular ATP-binding domain of PTKs receptor are usually targeted by small molecule pharmaceuticals. The broad array of cancer cell receptors have been described in detail elsewhere and form the basis for a large number of therapeutic antibodies and peptides that neutralize receptor activation and inhibit tumor growth [14, 33]. Receptors that are expressed in the tumor microenvironment as well as immune regulatory receptors on cancer cells and immune cells may also be targets for therapy (see Fig. 1). These targets have also been exploited for both nuclear imaging and therapy [14, 54]. Finally, intracellular tyrosine kinase domain targets may also be targets for imaging to evaluate the suitability of tumors for therapy. To this end, radiotracers such as [^{11}C]imatinib, [^{11}C]gefitinib, and [^{11}C]erlotinib have been developed based on FDA-approved small molecule therapeutics [54].

Cell Proliferation Increased cell proliferation is also one of the hallmarks of malignant tumors [50]. The imaging of cell proliferation with probes can assist with staging cancer and assess response to treatment. The uptake of [^{18}F]fluorothymidine—which is trapped in cells during S phase and therefore provides a measure of proliferation—has been shown to be highly correlated with response to treatment in certain tumors [55]. Amino acids enter the cell via the L-type amino acid transporter (LAT1), which is overexpressed in most cancer types compared to normal tissues.

Amino acid imaging has also been used to evaluate the turnover of proteins in cancer cells, and [^{18}F]fluoroethyltyrosine has been shown to accurately identify recurrent tumor from post-therapy changes in a range of tumors including high-grade gliomas [56].

Hypoxia Tissue hypoxia is a physiological effect strongly linked to the aberrant tissue vasculature in many tumors [57]. Hypoxia is characterized by lower levels of oxygen in tissue than would normally be present. The imaging of hypoxia with SPECT and PET radiopharmaceuticals can provide important information on tumor biology and assist in the selection of patients for treatment with hypoxia-targeted drugs (see Fig. 3). A range of radiopharmaceuticals that are trapped within hypoxic tissues have been evaluated in cancer patients, including ^{18}F-labeled fluoromisonidazole ([^{18}F]FMISO) and [^{64}Cu]Cu-ATSM [58].

Targeted Radiotherapy

Targeted radiotherapy is a treatment approach predicated on specifically delivering vectors bearing therapeutic radionuclides to sites of disease in order to inhibit cell proliferation and induce cell death. The therapeutic radiopharmaceutical can be administered locally or systemically. If administered locally, there may not be a specific molecular target for the radiopharmaceutical, and passive diffusion or regional blood flow is relied upon for the delivery of the radiopharmaceutical to the target cells. Localized radiotherapy has been successfully applied in patients with hepatocellular cancer or hepatic metastases of a range of malignancies (mainly colorectal and breast cancer) with ^{90}Y-embedded particles such as SIR-Spheres® and TheraSpheres® (see Fig. 5). These radiopharmaceuticals are typically injected into a hepatic artery and preferentially lodge in the small vessels of liver tumors and internally irradiate the adjacent tumor tissue [59]. In addition, the use of localized radiotherapy of joint arthritis with yttrium-90 colloid (radiosynovectomy) has been long established as an effective treatment approach for individual large joints affected by inflammatory arthritis [60].

Perhaps the most well-known application of systemic radiotherapy with beta-emitting radionuclides has been the treatment of thyroid cancer with [^{131}I]NaI, which targets the NaI symporter protein (see Fig. 6). However, systemic radiotherapy has increasingly been explored using radiolabeled antibodies and peptides that target cancer-specific antigens or receptors. The typical characteristics of targets utilized for therapy were described previously in this chapter. The expression of the target in the tumor as well as the suitability of the patient for treatment are usually confirmed by an imaging study performed using an analogue of the therapeutic radiopharmaceutical labeled with a positron- or gamma-emitting radionuclide (Fig. 8 and see Fig. 7) [61]. The uptake of the therapeutic radiopharmaceutical in normal tissue can stem from the expression of the target in healthy organs (*e.g.* CD20 in the bone marrow and spleen or A33 antigen in the normal bowel) or due to the size of the protein (*e.g.* the preferential uptake of radiolabeled peptides in the kidneys). Dosimetric analyses can also be performed to confirm that the dose delivered by the radiopharmaceutical will be sufficient to achieve a therapeutic effect. A key goal of performing imaging studies prior to target radiotherapy is to determine the expected biodistribution of the therapeutic radiopharmaceutical and thus help avoid toxicity to healthy organs. This "theranostic" approach is exemplified by the use of [^{68}Ga]Ga-DOTATATE and [^{177}Lu]Lu-DOTATATE in patients with neuroendocrine tumors [62]. A large number of new peptide targets are being currently explored in clinical trials, with a radiopharmaceutical targeting PSMA in metastatic prostate cancer showing impressive early clinical results [63].

To date, only two radiolabeled antibodies have been approved for treatment by the FDA: [^{90}Y]Y-ibritumomab tiuxetan and [^{131}I]I-tositumomab for the treatment of non-Hodgkin's lymphoma by targeting the CD20 antigen. However, [^{131}I]I-tositumomab was later removed from the market due to infrequent use. Currently, [^{90}Y]Y-ibritumomab tiuxetan (Zevalin®) is currently the only FDA-approved agent for radioimmunotherapy. A range of other antibodies against receptor and antigen targets in cancer are being developed at present, with approaches such as multistep targeting being explored to enhance blood clearance and improve tumor dose delivery [64]. The recent FDA approval of [^{223}Ra]$RaCl_2$ (Xofigo®) for the treatment of metastatic bone pain has reinvigorated interest in the use of therapeutic radiopharmaceuticals bearing alpha-emitting radionuclides, which offer the promise of high tumor doses and reduced normal tissue bystander doses compared to analogues labeled with beta-emitting radionuclides [65, 66].

Conclusions

At core, the selection of a target for nuclear imaging or targeted radiotherapy is based on the underlying physiologic and biochemical processes of the disease being considered. The emergence of targeted radiotherapy as a highly promising modality across a range of diseases—particularly cancer—has resulted in renewed interest in targets for peptide- and antibody-based approaches. The integration of radiopharmaceuticals for imaging with therapy (known as "theranostics") will undoubtedly be an area of active preclinical and clinical research in the future.

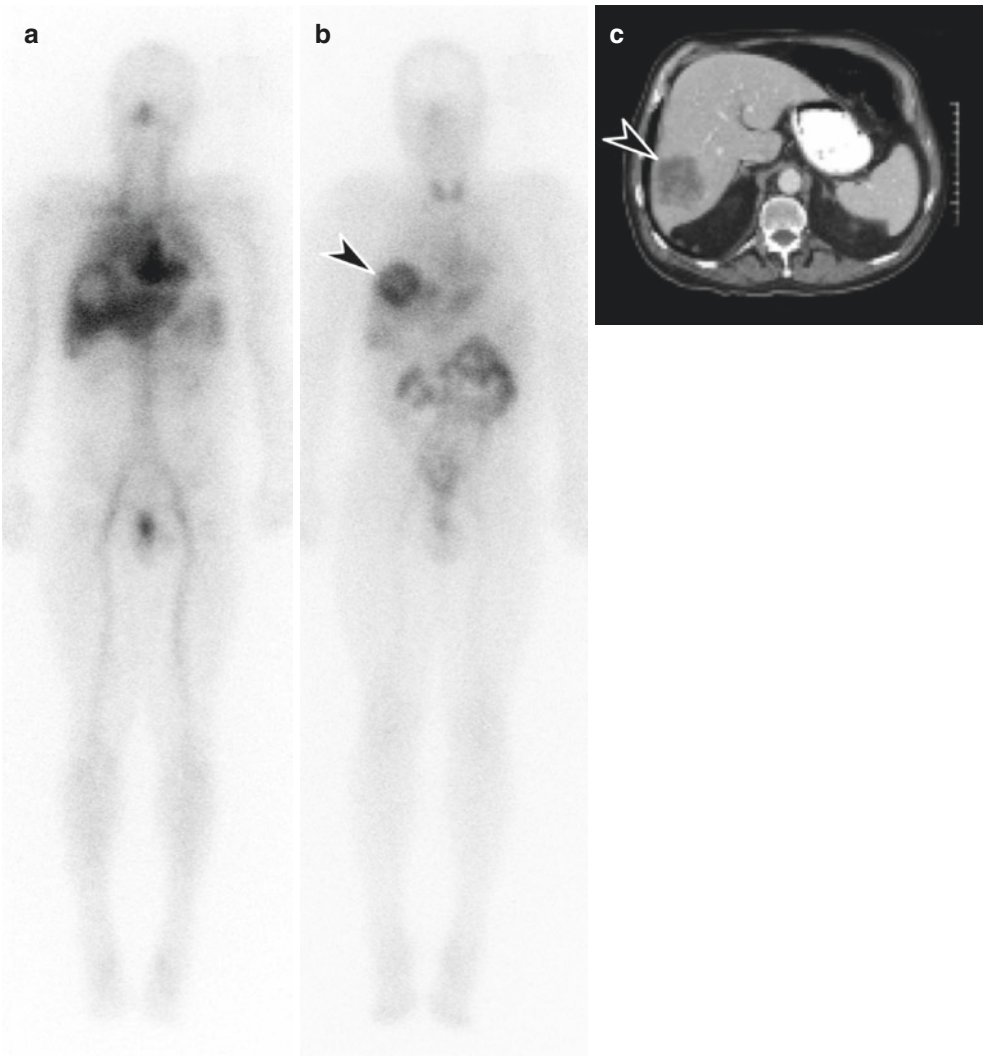

Fig. 8 Antibody targeting of colorectal cancer. Gamma camera images on (**a**) day 0 and (**b**) day 5 following the infusion of [^{131}I]I-huA33 in a 50-year-old patient with metastatic colorectal cancer. High concentrations of [^{131}I]I-huA33 can be seen in a metastatic lesion in the liver (*arrow*) by day 5 as well as some uptake in the normal bowel. (**c**) CT scan of the liver metastatic lesion (*arrow*). (From Chong *et al.* [59], with permission)

Bottom Line

- The selection of a target for nuclear imaging is dependent on both the physiology and biology of the disease in question.
- The specificity of a target for a given disease state is relevant to its clinical utility.
- Stable expression of a target is required for consistent imaging results.
- Therapeutic targets should be specific for the disease in question and have minimal expression in normal tissue.
- Targets that can be used for both nuclear imaging and targeted radiotherapy are increasingly sought after for clinical use.

Acknowledgments The authors acknowledge support from NHMRC (grants 1092788, 1143710, 1084178), Cancer Council Victoria, and Operational Infrastructure from the Victorian Government.

References

1. Edwards CI. Tumor localizing radionuclides in retrospect and prospect. Semin Nucl Med. 1979;3:186–9.
2. Ice RD. History of medical radionuclide production. Health Phys. 1995;69(5):721–7.
3. Ell P, Gambhir S, editors. Nuclear medicine in clinical diagnosis and treatment. 3rd ed. London: Churchill Livingstone; 2004.
4. Thul PJ, Åkesson L, Wiking M, Mahdessian D, Geladaki A, AitBlal H, et al. A subcellular map of the human proteome. Science. 2017;356(6340). pii: eaal3321.
5. Esteller M. Non-coding RNAs in human disease. Nat Rev Genet. 2011;12(12):861–74.
6. Bhullar KS, Lagarón NO, McGowan EM, Parmar I, Jha A, Hubbard BP, Rupasinghe HP. Kinase-target cancer therapies: progress, challenges and future directions. Mol Cancer. 2018;17(1):48.
7. Cardon LR, Harris T. Precision medicine, genomics and drug discovery. Hum Mol Genet. 2016;25(R2):R166–72.
8. Weber J, Haberkorn U, Mier W. Cancer stratification by molecular imaging. Int J Mol Sci. 2015;16(3):4918–46.
9. Kenny LM, Aboagye EO. Clinical translation of molecular imaging agents used in PET studies of cancer. Adv Cancer Res. 2014;124:329–74.

10. Gandal MJ, Leppa V, Won H, Parikshak NN, Geschwind DH. The road to precision psychiatry: translating genetics into disease mechanisms. Nat Neurosci. 2016;19(11):1397–407.
11. Varley J, Brooks DJ, Edison P. Imaging neuroinflammation in Alzheimer's disease and other dementias: recent advances and future directions. Alzheimers Dement. 2015;11(9):1110–20.
12. Osborn EA, Kessinger CW, Tawakol A, Jaffer FA. Metabolic and molecular imaging of atherosclerosis and venous thromboembolism. J Nucl Med. 2017;58(6):871–7.
13. Villemagne VL, Doré V, Bourgeat P, Burnham SC, Laws S, Salvado O, et al. Aβ-amyloid and tau imaging in dementia. Semin Nucl Med. 2017;47(1):75–88.
14. Scott AM, Wolchok JD, Old LJ. Antibody therapy of cancer. Nat Rev Cancer. 2012;12(4):278–87.
15. Orcutt KD, Adams GP, Wu AM, Silva MD, Harwell C, Hoppin J, et al. Molecular simulation of receptor occupancy and tumor penetration of an antibody and smaller scaffolds: application to molecular imaging. Mol Imaging Biol. 2017;19(5):656–64.
16. Ciprotti M, Chong G, Gan HK, Chan A, Murone C, MacGregor D, et al. Quantitative intratumoral microdistribution and kinetics of (131)I-huA33 in patients with colorectal carcinoma. EJNMMI Res. 2014;4:22.
17. Pardridge WM. Drug transport across the blood-brain barrier. J Cereb Blood Flow Metab. 2012;32(11):1959–72.
18. Gan HK, van den Bent M, Lassman AB, Reardon DA, Scott AM. Antibody-drug conjugates in glioblastoma therapy: the right drugs to the right cells. Nat Rev Clin Oncol. 2017;14(11):695–707.
19. van Isselt JW, Gast B-d. The radioiodine turnover rate as a determinant of radioiodine treatment outcome in Grave's disease. Hell J Nucl Med. 2010;13(1):2–5.
20. Goldstein JL, Anderson RGW, Brwon MS. Coated pits, coated vesicles and receptor-mediated endocytosis. Nature. 1979;279:679–85.
21. Sorkin A, von Zastrow M. Endocytosis and signalling: intertwining molecular networks. Nat Rev Mol Cell Biol. 2009;10:609–22.
22. Perner S, Hofer MD, Kim R, Shah RB, Li H, Möller P, et al. Prostate-specific membrane antigen expression as a predictor of prostate cancer progression. Hum Pathol. 2007;38(5):696–701.
23. Luster M, Pfestroff A, Hänscheid H, Verburg FA. Radioiodine therapy. Semin Nucl Med. 2017;47(2):126–34.
24. Puranik AD, Kulkarni HR, Baum RP. Companion diagnostics and molecular imaging. Cancer J. 2015;21(3):213–7.
25. Yordanova A, Eppard E, Kürpig S, Bundschuh RA, Schönberger S, Gonzalez-Carmona M, et al. Theranostics in nuclear medicine practice. Onco Targets Ther. 2017;10:4821–8.
26. Braband H. High-valent technetium chemistry – new opportunities for radiopharmaceutical developments. J Label Compd Radiopharm. 2014;57(4):270–4.
27. SmitDuijzentkunst DA, Kwekkeboom DJ, Bodei L. Somatostatin receptor-2 targeting compounds. J Nucl Med. 2017;58(Suppl 2):10S–6S.
28. Oliveira BL, Caravan P. Peptide-based fibrin-targeting probes for thrombus imaging. Dalton Trans. 2017;46(42):14488–508.
29. Bjornmalm M, Thurecht KJ, Michael M, Scott AM, Caruso F. Bridging bio-nano science and cancer nanomedicine. ACS Nano. 2017;11(10):9594–613.
30. Lee S, Xie J, Chen X. Peptides and peptide hormones for molecular imaging and disease diagnosis. Chem Rev. 2010;110(5):3087–111.
31. Katritch V, Cherezov V, Stevens RC. Structure-function of the G protein-coupled receptor superfamily. Annu Rev Pharmacol Toxicol. 2013;53:531–56.
32. Schottelius M, Wester H-J. Molecular imaging targeting peptide receptors. Methods. 2009;48(2):161–77.
33. Parakh S, Parslow AC, Gan HK, Scott AM. Antibody-mediated delivery of therapeutics for cancer therapy. Expert Opin Drug Deliv. 2016;13(3):401–19.
34. Moek KL, Giesen D, Kok IC, de Groot DJA, Jalving M, Fehrmann RSN, et al. Theranostics using antibodies and antibody-related therapeutics. J Nucl Med. 2017;58(Suppl 2):83S–90S.
35. Goedert M, Yamaguchi Y, Mishra SK, Higuchi M, Sahara N. Tau filaments and the development of positron emission tomography tracers. Front Neurol. 2018;9:70.
36. Suwijn SR, van Boheemen CJ, de Haan RJ, Tissingh G, Booij J, de Bie RM. The diagnostic accuracy of dopamine transporter SPECT imaging to detect nigrostriatal cell loss in patients with Parkinson's disease or clinically uncertain Parkinsonism: a systematic review. EJNMMI Res. 2015;5:12.
37. Elsinga P, Ishiwata K, Hatano K. PET tracers for imaging the dopaminergic system. Med Chem. 2006;13(18):2139–53.
38. Slifstein M. Abi-Dargham. Recent developments in molecular brain imaging of neuropsychiatric disorders. Semin Nucl Med. 2017;47(1):54–63.
39. Kassenbrock A, Vasdev N, Liang SH. Selected PET radioligands for ion channel linked neuroreceptor imaging: focus on GABA, NMDA and nACH receptors. Curr Top Med Chem. 2016;16(16):1830–42.
40. Meyer PM, Tiepolt S, Barthel H, Hesse S, Sabri O. Radioligand imaging of α4α2* nicotinic acetylcholine receptors in Alzheimer's disease and Parkinson's disease. Q J Nucl Med Mol Imaging. 2014;58(4):376–86.
41. Denora N, Natile G. An updated view of the translocator protein (TSPO). Int J Mol Sci. 2017;18(12). pii. E2640.
42. Alam MM, Lee J, Lee SY. Recent progress in the development of TSPO PET ligands for neuroinflammation imaging in neurologic diseases. Nucl Med Mol Imaging. 2017;51(4):283–96.
43. Shaw SY. Molecular imaging in cardiovascular disease: targets and opportunities. Nat Rev Cardiol. 2009;6:567–79.
44. Underwood SR, de Bondt P, Flotats A, Marcasa C, Pinto F, Schaefer W, Verberne HJ. The current and future status of nuclear cardiology: a consensus report. Eur Heart J. 2014;15:949–55.
45. Travin MI. Current clinical applications and next steps for cardiac innervation imaging. Curr Cardiol Rep. 2017;19(1):1.
46. Gaertner FC, Kessler H, Wester HJ, Schwaiger M, Beer AJ. Radiolabelled RGD peptides for imaging and therapy. Eur J Nucl Med Mol Imaging. 2012;39(Suppl 1):S126–38.
47. Bala G, Blykers A, Xavier C, Descamps B, Broisat A, Ghezzi C, et al. Argeting of vascular cell adhesion molecule-1 by 18F-labelled nanobodies for PET/CT imaging of inflamed atherosclerotic plaques. Eur Heart J Cardiovac Imaging. 2016;17(9):1001–8.
48. Laufer EM, Winkens HM, Corsten MF, Reutelingsperger CP, Narula J, Hofstra L. PET and SPECT imaging of apoptosis in vulnerable atherosclerotic plaques with radiolabeled Annexin A5. Q J Nucl Med Mol Imaging. 2009;53(1):26–34.
49. Annovazzi A, Bonanno E, Arca M, D'Alessandria C, Marcoccia A, Spagnoli LG, et al. 99mTc-interleukin-2 scintigraphy for the in vivo detection of vulnerable atherosclerotic plaques. Eur J Nucl Med Mol Imaging. 2006;33(2):117–26.
50. Hanahan D, Weinberg RA. Hallmarks of cancer. Cell. 2011;144(5):646–74.
51. Fletcher JW, Djulbegovic B, Soares HP, Siegel BA, Lowe VJ, Lyman GH, et al. Recommendations on the use of ^{18}F-FDG in oncology. J Nucl Med. 2008;49:480–508.
52. Zhu A, Lee D, Shim H. Metabolic PET imaging in cancer detection and therapy response. Semin Oncol. 2011;38(1):55–69.
53. Jadvar H, Colletti PM, Delgado-Bolton R, Esposito G, Krause BJ, Iagaru AH, et al. Appropriate use criteria for ^{18}F-FDG PET/CT in restaging and treatment response assessment of malignant disease. J Nucl Med. 2017;58(12):2026–37.
54. Van Dongen GA, Poot AJ, Vugts DJ. PET imaging with radiolabeled antibodies and tyrosine kinase inhibitors: immuno-PET and TKI-PET. Tumour Biol. 2012;33(3):607–15.

55. Peck M, Pollack HA, Friesen A, Muzi M, Shoner SC, Shankland EG, et al. Applications of PET imaging with the proliferation marker [18F]-FLT. Q J Nucl Med Mol Imaging. 2015;59(1):95–104.
56. Dunet V, Pomoni A, Hottinger A, Nicod-Lalonde M, Prior JO. Performance of 18F-FET versus 18F-FDG-PET for the diagnosis and grading of brain tumors: systematic review and meta-analysis. Neuro Oncol. 2016;18(3):426–34.
57. Lee ST, Scott AM. Hypoxia imaging with ^{18}F-Fluoromisonidazole. Semin Nucl Med. 2007;37(6):451–61.
58. Fleming IN, Manavaki R, Blower PJ, West C, Williams KJ, Harris AL, et al. Imaging tumour hypoxia with positron emission tomography. Br J Cancer. 2015;112:238–50.
59. Chong G, Lee FT, Hopkins W, Tebbutt N, Cebon JS, Mountain AJ, et al. Phase I trial of 131I-huA33 in patients with advanced colorectal carcinoma. Clin Cancer Res. 2005;11(13):4818–26.
60. Khajornjiraphan N, Thu NA, Chow PKH. Yttrium-90 microspheres: a review of its emerging clinical indications. Liver Cancer. 2015;4(1):6–15.
61. Knut L. Radiosynovectomy in the therapeutic management of arthritis. World J Nucl Med. 2015;14(1):10–5.
62. Strosberg J, El-Haddad G, Wolin E, Hendifar A, Yao J, Chasen B, NETTER-1 Trial Investigators, et al. Phase 3 trial of 177Lu-Dotatate for midgut neuroendocrine tumors. N Engl J Med. 2017;376(2):125–35.
63. Emmett L, Willowson K, Violet J, Shin J, Blanksby A, Lee J. Lutetium 177 PSMA radionuclide therapy for men with prostate cancer: a review of the current literature and discussion of practical aspects of therapy. J Med Radiat Sci. 2017;64(1):52–60.
64. Cheal SM, Fung EK, Patel M, Xu H, Guo HF, Zanzonico PB, et al. Curative multicycleradioimmunotherapy monitored by quantitative SPECT/CT based theranostics, using bispecific antibody pretargeting strategy in colorectal cancer. J Nucl Med. 2017;58(11):1735–42.
65. Florimonte L, Dellavedova L, Maffiolo LS. Radium-223 dichoride in clinical practice: a review. Eur J Nucl Med Mol Imaging. 2016;43(10):1896–909.
66. Marcu L, Bezak E, Allen BJ. Global comparison of targeted alpha vs targeted beta therapy for cancer: in vitro, in vivo and clinical trials. Crit Rev Oncol. 2018;123:7–20.

Target Identification, Lead Discovery, and Optimization

Julien Dimastromatteo and Kimberly A. Kelly

Introduction

The sequencing of the human genome marked the beginning of the age of "-omics." The age of "-omics," in turn, ushered in a new era in the understanding of the biological processes that govern our survival as human beings. In this regard, the new knowledge gained from the "-omics" fields—genomics, metabolomics, proteomics, *etc.*—represents a critical first step in beginning to fulfill the promise of "precision medicine": targeting diseased cells while leaving healthy cells (relatively) unaffected. However, the ultimate clinical success of precision medicine is predicated on the identification and exploitation of molecular targets that distinguish healthy tissue from disease. In this chapter, we will explore the concepts of targets and targeting. More specifically, we will explore the properties of an ideal target as well as the various methods used to identify good targets. From there, we will move on to address the development of ligands, particularly how to find and optimize lead candidates that are suitable for radiopharmaceutical applications. Finally, we will conclude with a brief discussion of target-ligand binding kinetics.

The Ideal Target

Choosing a target is the first step in developing a radiopharmaceutical and is a critically important aspect of the process, as the selection of an inappropriate target can result in a probe that either does not accumulate sufficiently in the desired tissue (making it ineffective) or accumulates at high levels in healthy organs (making it ineffective *and* potentially toxic). There are several factors to consider when choosing a suitable target:

Selectivity

The target should be present only on the cells of interest and not on other cells. Admittedly, however, this "all or nothing" phenotype rarely occurs, and the expression of the target cells other than those desired can result in high background uptake as well as radiation-related toxicity. The acceptable relative difference in the levels of target expression between healthy and diseased cells depends on the application and, for therapies, the sensitivity of the tissue or organ to the drug. Generally speaking, targets for imaging require a larger difference between healthy and diseased cells than targets for therapy.

Target Number per Cell

In general, the higher the number of targets per cell, the better. Both nuclear imaging and therapy rely on the selective delivery of radiopharmaceuticals to cells. In the context of imaging, the higher the number of targets per cell, the greater the signal for that cell and the better the signal-to-noise ratio. In the context of therapy, the greater the number of targets per cell, the greater the activity concentration at the cell the more potent the therapeutic irradiation. The absolute number of targets per cell required to create appropriate signal or to generate therapeutic effect has not been studied, but it is generally accepted that 1×10^4 is in the lower range. Examples of targets where successful drugs and radiopharmaceuticals have been developed are Her2 and the somatostatin receptor (SSTR). Her2 has a high copy number, with levels of over 1×10^6 in tumors that have genetic amplifications of Her2 [1]. Patients with tumors with lower copy numbers — in the 1×10^5 range — still receive therapy, as clinical trials have proven efficacy of the drug (trastuzumab) when its target is expressed to that level. In contrast, tumor cells expressing 10^4 or fewer targets are refractory to treatment. The copy number of SSTRs expressed on tumor cells generally hovers around 1×10^5 [2].

J. Dimastromatteo · K. A. Kelly (✉)
Department of Biomedical Engineering, School of Medicine, University of Virginia, Charlottesville, VA, USA
e-mail: kak3x@virginia.edu

J. S. Lewis et al. (eds.), *Radiopharmaceutical Chemistry*, https://doi.org/10.1007/978-3-319-98947-1_32

Bioavailability of the Target

The target needs to be accessible or bioavailable for ligand binding. This must be considered both on the cellular level as well as on the tissue and systemic levels. At the cellular level, molecules located on the cell membrane are more available for binding than cytoplasmic or nuclear targets. For the latter, a radiopharmaceutical must cross either one barrier (the plasma membrane) or two barriers (the plasma membrane *and* the nuclear envelope) in order to efficiently reach its targets. In general, small molecules can cross the plasma membrane and are able to target moieties in the cytoplasm and the nucleus. Peptides, proteins, and antibodies, however, cannot cross these membranes, making these poor choices if the target is a biomolecule within the cytoplasm or nucleus.

Taking a wider view, organs are organized groups of tissues with a very specific architecture. Tissues are groups of similar cells working together, *i.e.* epithelial cells, stromal cells, extracellular matrix, blood vessels, and immune cells. Any of these cells can be potential targets. The endothelial cells that line blood vessels are the easiest to target, as they encounter the radiopharmaceutical first. However, they are of relatively low abundance in tissues and in diseases such as tumors. In order to reach cells beyond the blood vessels, a ligand or radiopharmaceutical must be able to extravasate out of the bloodstream. In most healthy tissues, molecules larger than 5 nm in diameter are unable to simply extravasate out of the bloodstream into the interstitium. In malignant tissue, however, the blood vessels are disordered and leaky, allowing for the extravasation of molecules 10- to 20-fold larger. In addition, the lymphatics responsible for the drainage of cancerous tissues are impaired as well, resulting in a higher retention of molecules in the tumor. These complementary phenomena are collectively known as the "*e*nhanced *p*ermeability and *r*etention" (EPR) effect. The EPR effect allows molecules such as proteins, antibodies, and nanoparticles to selectively accumulate in tumorsin the absence of a specific molecular target. A consequence of the EPR effect is an increase in the interstitial fluid pressure (IFP) of tumor tissue. This elevated IFP effectively creates a barrier that keeps most molecules perivascular and thus hinders the homogeneous distribution of radiopharmaceuticals throughout the tumor. Understanding EPR and IFP—and specifically how to take advantage of EPR while overcoming IFP—is an active area of research.

In some cases, the blood vessels are designed to form a tight, nearly impermeable barrier. For example, even small molecules have difficulty extravasating through the blood-brain barrier and the blood vessels in the testes. In order to cross these barriers, the blood vessels either have to be disrupted by mechanical means (ultrasound or radiofrequency ablation) or have to use the process of transcytosis, a mechanism by which molecules are shuttled from the luminal side of the blood vessel through the cell and out into the interstitium. Not surprisingly, this is an inefficient process and requires more complicated engineering of the radiopharmaceutical.

After extravasation, agents encounter the interstitium, which consists of cells (*e.g.* fibroblasts and immune cells) as well as extracellular matrix proteins (*e.g.* collagen, fibronectin, and laminin). All these molecules and cells can be targets for radiopharmaceuticals. If, however, the goal is to target an epithelial cell, this mix of cells and proteins are barriers that the agent must overcome in order to bind to its target. Not all interstitial spaces are the same, however, even among cancers; for example, pancreatic cancer has a dense fibrotic stroma with higher levels of hyaluronic acid compared to other tumors.

Finally, the orientation of epithelial cells can also pose a barrier to the delivery of radiopharmaceuticals. A characteristic of epithelial cells in healthy tissues is that they are polar. The epithelial cells adhere to each other through junctions that can be tight and restrictive, controlling the paracellular transport of ions and small molecules, severely limiting the exchange of proteins on the membrane, and creating areas of the cell membrane that are not freely exchanged. Thus, epithelial cells have an apical and a basal side. The apical side faces the lumen or the external environment, while the basal side faces the basement membrane of the tissue. The tight junctions represent a barrier to any ligand being able to reach targets beyond the barrier. Thus, a target that is present on the apical side of an epithelial cell can only be reached by transcytosis or direct application into the lumen and not by simple diffusion or convection after extravasation out of a blood vessel. A hallmark of cancers is that the epithelial cells have lost polarity, so targets that were previously "off limits" can become available for binding.

Finding Targets

Finding targets that exhibit all the requirements mentioned above to be a good target is not trivial. In this section, we will describe the most commonly used methods to identify novel targets for the development of radiopharmaceuticals.

Data Mining

The easiest way to find a good target is to perform a literature and data search. PubMed is an invaluable resource to determine what targets have been identified and whether radiopharmaceuticals have been developed to target them. Other less well-known databases include the Molecular Imaging and Contrast Agent Database (MICAD; http://www.ncbi.nlm.nih.gov/books/NBK5330/), Protein Atlas (http://www.

proteinatlas.org), and a suite of tools from NCBI. MICAD contains a list of radiopharmaceutical contrast agents that are in development, have been used *in vivo*, and have been published in peer-reviewed journals. Chapters of the database are available on PubMed. The database is not disease- or modality-specific: rather, it contains agents for SPECT, PET, ultrasound, optical, and MRI and covers cancer, cardiovascular disease, neural, and inflammation.

Protein Atlas is a great source for determining the selectivity and expression levels of a potential target. Protein Atlas has archived immunohistochemical (IHC) data for the expression of targets in both healthy and diseased tissues and cells. Helpfully, Protein Atlas lists the antibodies used and frequently has data from more than one antibody. This is an important set of information, as antibodies can give widely different results depending on their specificity and also the domain against which they were raised. Using Protein Atlas is fairly intuitive and free. After navigating to the homepage, type in the protein of interest ("plectin" has been used as an example in Fig. 1). After clicking "Search," a description of the protein will be displayed as well as the sub-atlas in which it can be found. The three current sub-atlases are entitled "Tissue," "Cell," and "Pathology." Clicking on any of the three sub-atlases will give a summary of the protein, data regarding its expression in different tissues, data regarding its isoforms and transcripts, and IHC staining (an example of IHC staining for plectin in a cancer specimen is in Fig. 2). The data is well annotated with the sex and age of the patient, the tumor type, the location of protein staining (membranous, cytoplasmic, nuclear, *etc.*), and the amount of protein expression. Clicking on any of the thumbnails will reveal the stained sample alongside information on the patient and staining (Fig. 3). The only drawback to Protein Atlas and MICAD is that the identity of the protein or target must be known; there isn't a way to do an unbiased search to find novel targets. For Protein Atlas, only targets that have antibodies are entered into the database, so it is heavily biased toward proteins with limited lipid and carbohydrate information available. For MICAD, only targets for which agents have been generated and tested *in vivo* are listed, limiting the number of targets that can be searched.

NCBI has a suite of free tools to aid in the process of choosing a target, including Gene Expression Omnibus (GEO) (https://www.ncbi.nlm.nih.gov/geo/). To explain this tool, it is helpful to review cell biology. The central dogma of cell biology is that a cell's genome is first transcribed into mRNA and then translated into protein. This means, of course, that the presence of proteins within a cell is controlled on both the transcriptional and translational levels. Complementary DNA (cDNA) microarray technology was developed in order to study the transcription of genes and profile the mRNA of cells in a high-throughput manner. In a

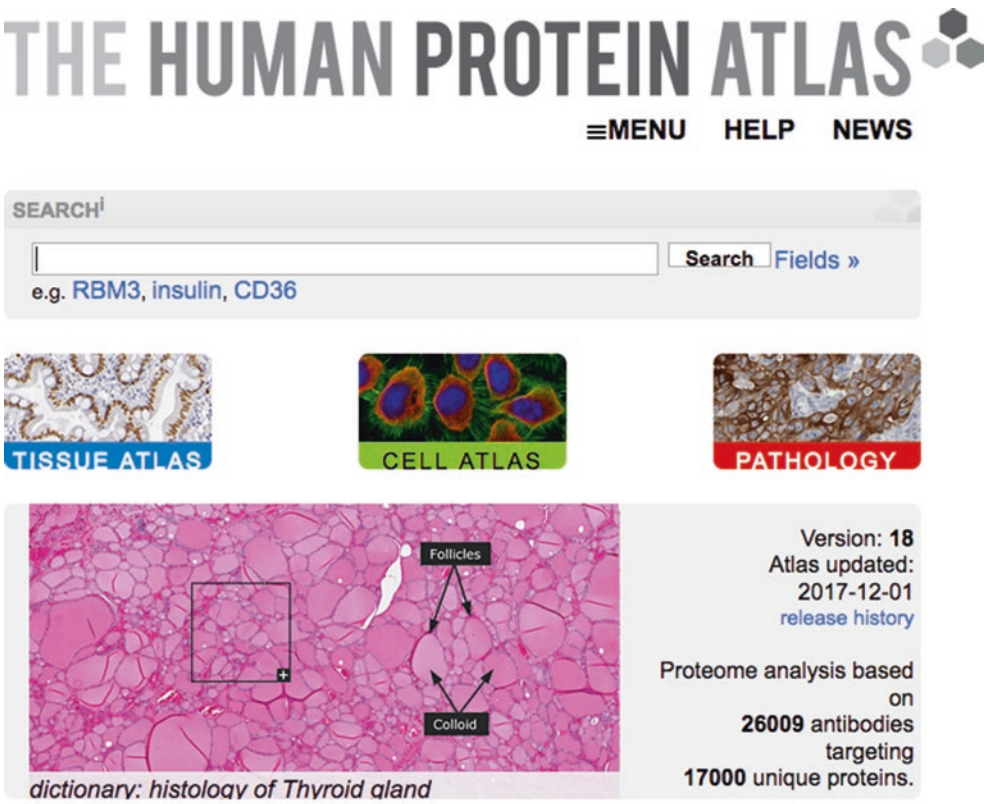

Fig. 1 Home screen of ProteinAtlas.org (https://www.proteinatlas.org/)

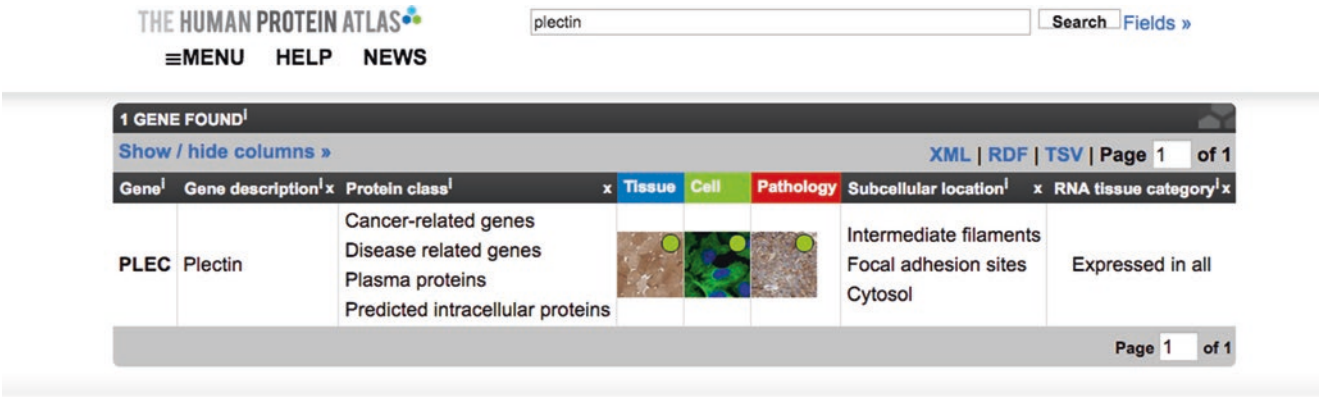

Fig. 2 Screenshot of protein search (https://www.proteinatlas.org/search/plectin)

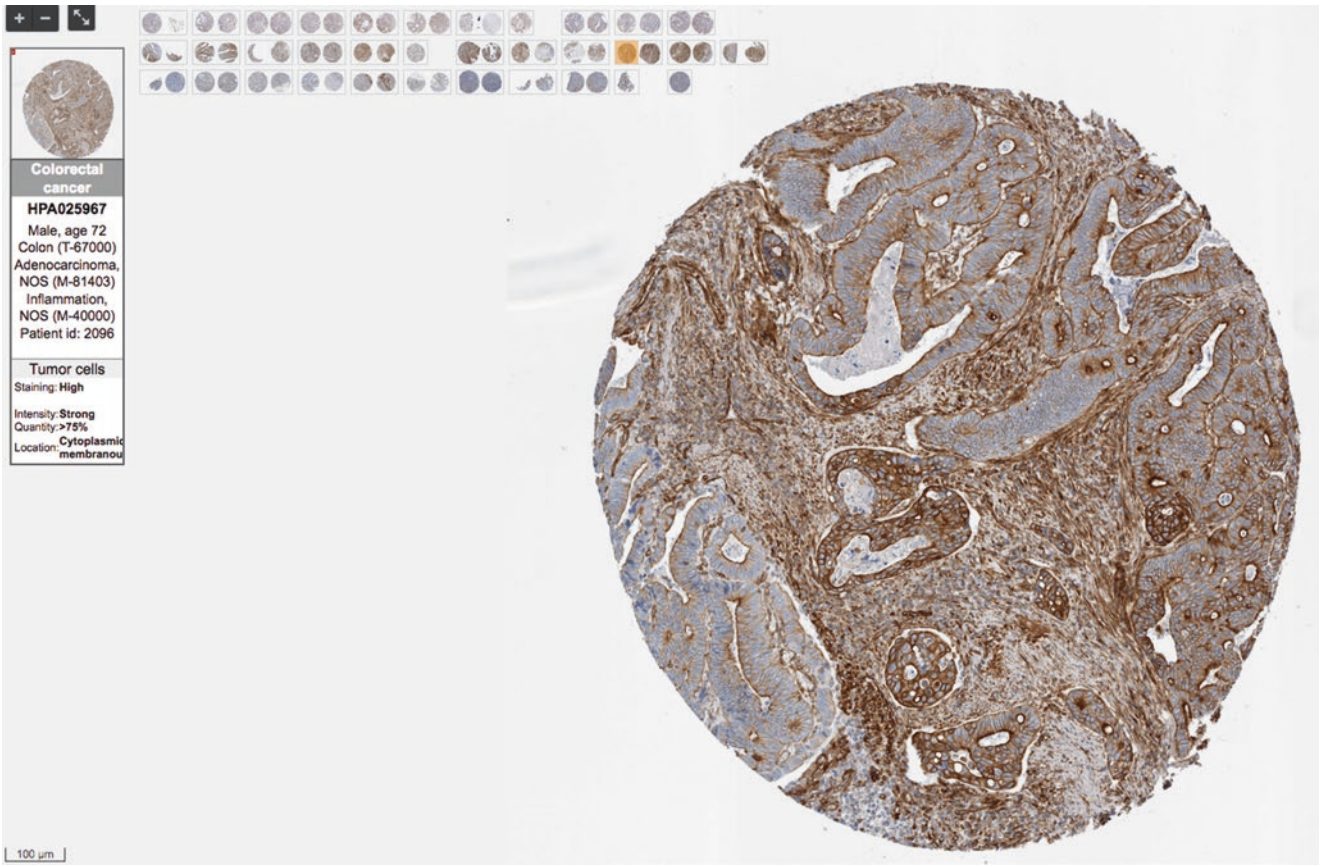

Fig. 3 Screenshot of plectin 1 immunohistochemical staining of colorectal adenocarcinoma (https://www.proteinatlas.org/ENSG00000178209-PLEC/pathology/tissue/colorectal+cancer#img)

cDNA microarray assay, short DNA probes corresponding to all of the known genes in an organism are spotted onto a chip or microarray. The mRNA from cells—typically disease vs. normal or treated vs. non-treated—is extracted and subsequently turned into cDNA. The cDNA from each cell type is labeled with a distinct fluorophore, allowing for its detection. Equal amounts of cDNA from the two cell populations are plated onto the chip, and the DNA is allowed to hybridize with the probes already spotted on the chip. The total amount of cDNA from the cells that bind to each spot can then be quantified. By determining the unique cDNA in each cell population, the investigators have a way to find differences in transcription patterns between the cell populations. This, of course, facilitates the identification of targets. All papers that perform cDNA microarray experiments must upload their findings into GEO, making it an

invaluable resource for researchers looking for new targets or to validate existing targets. There are many different ways to construct queries of the data entered, so it is not feasible to include all of the relevant screenshots in this chapter. Luckily, the GEO homepage has an excellent set of easy-to-follow tutorials.

The data generated from a cDNA microarray or gene expression profiling experiment is unbiased and can be used to identify novel targets. These techniques are not, however, without their flaws. One caveat to cDNA microarray profiling, for example, is that not all mRNA expression levels correlate with protein levels due to the stability or instability of the mRNA transcripts and/or protein degradation and processing. In addition, as we will see with mass spectrometry, this information is also devoid of spatial information. This meaning that if a protein is transcribed similarly in two populations of cells but it is also aberrantly localized in one—for example, a cytoplasmic protein that is displayed on the membrane in diseased cells—it may be overlooked. Oftentimes, the levels of protein expression between disease and healthy cells are not that drastic, but dramatic differences in the spatial or temporal distribution of the protein can nonetheless be exploited to make it a useful target.

Mass Spectrometry-Based Quantitative Proteomics

Mass spectrometry-based quantitative proteomics has provided a unique and powerful strategy for the identification and quantification of proteins in complex biological systems. It has been used to systematically reveal changes in the proteome that have been implicated in many diseases by quantifying protein abundance, protein posttranslational modifications (PTMs), protein complexes, and pathway interactions.

One widely used approach to mass spectrometry-based proteomics is the "shotgun proteomics" or "bottom-up approach," in which proteins are digested and analyzed by tandem mass spectrometry for the identification of peptides and proteins [3–5]. The workflow for a typical experiment involves the preparation of the sample, protein/peptide separation, tandem mass spectrometric analysis, and bioinformatic data analysis [3]. In disease studies, much of the focus is centered upon either identifying proteins that are expressed differentially in disease states or finding post-translational modifications or protein-protein interactions that are implicated in disease. Another advantage of this family of techniques is that mass spectrometry can detect proteins with relatively low abundance. In recent years, quantitative proteomics has evolved and is now able to systematically compare the static state of the proteomes of two or more biological systems as well as identify perturbation-induced changes in the expression of proteins. Such an approach typically involves the comparison of a cancerous tissue with a healthy tissue and provides an—at least—semiquantitative comparison of the abundance of proteins in the disease and control tissues.

All of this said, the use of quantitative proteomics is not easy. The enormous complexity of protein species and the substantial dynamic differences in protein abundance in tissue require a concerted approach drawing from different technologies to accomplish a quantitative proteomic analysis. The reduction of a sample's complexity to enhance analytical sensitivity is accomplished by extracting proteins from tissues or organs and performing orthogonal fractionation and separation prior to mass spectrometric analysis. After tandem mass spectrometric analysis, the MS/MS spectra are processed and searched against established protein databases using algorithms such as SEQUEST [6], MASCOT [7], or X!tandem [8] for the identification of peptides/proteins. This step is followed by the quantification of the peptides/proteins using a suite of bioinformatics software [9]. The end result is a list of proteins and post-translational modifications that can be mined for targets. Because the cells are destroyed to extract the proteins, however, spatial information is lost. As a result—just as in cDNA microarrays—only proteins that are either upregulated or differentially modified will be found using this technique.

Phage Display-Based Functional Proteomics

A more recently developed technique to identify targets is a two-step procedure that (1) uses phage display to identify disease-specific peptides and then (2) uses these peptides as "bait" to identify the target of the peptide. Phage display-based functional proteomics has several advantages. It can be used to screen complex mixtures of cells, but even more notably, it can enable *in vivo* screening in animal models, a technique that ensures that the targets identified are accessible for binding. Furthermore, phage display-based functional proteomics keeps spatial information intact so that it is easy to discern the cell membrane from the cytoplasm, for example.

In order to discuss phage display-based functional proteomics, we must first discuss phage display. Phage or bacteriophages are viruses that are exquisitely selective for bacteria. Almost all bacteria have their own phage that recognize and are propagated only in the host bacterium. Phage display employs a population of bacteriophage genetically modified to display a library on various phage coat proteins. Phage display was first born in the 1980s, when George Smith displayed peptides on the pVIII coat protein of the M13 filamentous phage whose host bacterium is the F pilus

expressing *Escherichia coli*. Now, phage display libraries are commercially available for linear and cyclic peptides of a wide variety of lengths as well as proteins, antibodies, and antibody fragments. Phage display is not limited to M13 either: other bacteriophages—such as T7—have been utilized as well and are especially used for antibody or protein display. In the case of peptides, the library can have a diversity of over 2×10^9 different peptides, making the screening process high throughput and accessible to researchers. In this way, phage display offers a number of important advantages over other techniques, including a rapid and economical biological expansion, a vast diversity of peptides, a rapid and high-throughput screening process, and the availability of many types of phage clones and libraries (for more information, please see [10–12]). Importantly, what makes a phage display screen work quickly is that the genotype of the phage equals the phenotype of the phage, so a clone isolated based on biological properties is easy to identify by sequencing the appropriate portion of its genome. This "genotype equals phenotype" phenomenon enables screening in a single well, thereby reducing the amount of starting material (proteins, cells, tissue, *etc.*) needed for the screen and allowing for the competition of displayed entities against each other.

Screening

While there are many factors to consider when designing a screen for new ligands and targets using phage display, the affinity and specificity of the phage — and thus the affinity and specificity of the peptide sequence for its target — are the two most important parameters. As we will discuss later in this chapter, K_d represents the affinity and is defined by the ratio of association and dissociation rates k_{off}/k_{on} (see Equation 3). Knowing this parameter gives us a way to set up the screening to maximize the affinity of the phage. For example, by allowing the phage library to incubate for shorter periods of time (15–30 mins), one can select for short k_{on} values. Conversely, by eluting with progressively harsher eluents and only retaining the eluted phage from the most stringent elutions, one can screen for the tightest binders. However, these strategies may be too stringent and may not produce any phage clones that bind. It is common, therefore, to do several screens with varying conditions to get the binders with the highest affinity. Screening for specificity will be discussed later.

The simplest phage screen uses purified target material (*e.g.* protein, sugars, DNA) immobilized on a solid support such as immunoplates or beads. The use of purified material has the advantage that the only interactions involved are between the target and the peptides displayed on the phage. In addition, the phage selection binding stringency can be better controlled by vigorous washing, blocking non-specific binding sites, adding stronger detergents to the wash buffer, and plating less of the target material. However, this approach also has several disadvantages, including (1) that screening for receptor-mediated internalization is precluded, (2) that the phage are not in a cellular environment and may thus bind to sections of protein that are not bioavailable in cells or tissues, (3) that the target may need to multimerize in its native environment, and (4) that the density of the target is highly artificial and may not recapitulate what happens in the context of the cellular milieu.

To overcome some of these disadvantages, cells can be found that naturally overexpress the target of interest, or, alternatively, cells can be *engineered* to express the target of interest. Screening on cells allows for the selection for compounds that undergo receptor-mediated internalization and has the added advantage that the target resides in a closer recapitulation of its native environment. For example, transmembrane receptors have hydrophobic domains that allow them to cross the plasma membrane. When taken out of the membrane, the hydrophobic transmembrane domain can change the structural conformation of the protein, exposing surfaces that would not naturally be available for binding in the protein's native, membrane-bound context. Another advantage to cell-based systems is that selectivity for the target can be factored into the screen, since moieties other than the target will be present on the surface of the cells. This can also be a limitation, however, as molecules other than the target molecule will bind phage, making it important to determine whether the peptides bind directly to the desired target or to other molecules on the cell. To alleviate this, peptides can be eluted with the target or the target's naturally occurring ligand, but this technique necessitates purifying or purchasing large quantities of target, which may be prohibitively expensive.

Selectivity

The selectivity of phage for a target has generally been increased via negative selection or subtraction with related targets or cell lines by preincubating the phage display library before using it with disease tissues or cells. A newer technique is the use of next-generation sequencing (NGS) to allow for the *in silico* selection of phage clones. NGS has had a major impact on phage display by deepening the characterization of the enriched phage library. More specifically, millions of phage sequences from each screen can be sequenced and compared to each other to determine the clones with the highest selectivity for the desired tissue or cell. There are many challenges to this type of experiment, however. Phage clones have an amplification bias, so some may appear in a screen due to bias rather than selection. Additionally, NGS has a 10% error rate in sequences. To simplify the procedure, PHASTpep was created: https://github.com/LindseyBrinton/PHASTpep [13]. PHASTpep is freeware and is MATLAB-based with a graphical user interface that guides users

through two phases of analysis. The first part of the software allows the importation of sequences directly from the sequencer, aligns the portion of DNA corresponding to the displayed peptides, translates the sequences into amino acids, and calculates the frequency of each unique peptide. The second part of PHASTpep normalizes each screen to its number of reads as well as the control library that was amplified but not selected. In this way, clones that have an amplification bias can be removed. The software then generates a matrix in which each row is a unique peptide sequence and each column is a positive or negative screen, allowing the user to visually find phage clones that are selective. Using NGS, no information is lost, and, in fact, more information is retained, facilitating the quantitation of phage display screening data as well as the rapid analysis of multiple screens.

Using Phage Display-Based Proteomics to Identify Targets

The examples described above all focus on screening using targets that are already known. Yet screening has also been performed on cells, using tissue samples, and *in vivo* without any *a priori* knowledge of specific targets. This approach has important advantages in systems that are less well characterized biologically. In addition, because the cells and tissues that are screened are intact, phage display-based functional proteomics allows for the identification of proteins that are differentially expressed on the cell membrane or become accessible through differential trafficking to the cell surface. The procedures for screening the validation of binding are the same as above. Once a phage clone or peptide has been validated as specific for a target (see above), the phage clones can then be used as "bait" for functional proteomics. The methodology for identifying the cell surface binding partners of the phage is very similar to immunoprecipitation. The phages are labeled with biotin and sulfo-SAED, a photoactive cross-linker. The labeled phage clones are then incubated with the cells and then subjected to UV light to activate the sulfo-SAED, cross-linking the phage to the protein it has bound. The cells are then lysed, and the phage and protein complex are extracted with streptavidin beads, followed by the cleavage of the cross-linked protein. The eluates are then analyzed via SDS-PAGE, and unique bands are excised, digested with trypsin, and sent for mass spectrometric analysis. From there, a list of potential binding partners is generated. The interaction between the phage clone and the purported binding partner is validated by incubating the phage clone with purified recombinant protein and other negative control proteins. This method has the advantage of generating lead compounds for targeting (peptides) as well as potentially novel proteins. Examples include plectin—a biomarker for pancreatic ductal adenocarcinoma [14]—and hornerin, a novel angiogenic protein not regulated by vascular endothelial growth factor [15]. Plectin is a cytoskeletal protein that is normally expressed in the cytoplasm of cells from the skin and genitourinary tract. In cancer, however, plectin is aberrantly localized to the plasma membrane. This makes it a promising target, as it is not accessible in healthy cells. Hornerin was recently identified from a phage display-based proteomics screen and plays a role in the development of the blood vessels of tumors. The silencing of hornerin resulted in blood vessels that were less tortuous and less leaky and had higher perfusion, making hornerin a potential drug target as well.

Ligands as Vectors for Radiopharmaceuticals

One of the advantages of phage display-based functional proteomics is that in the process of screening, a lead peptide is generated that binds to the target. Yet of course, peptides generated via phage display are not the only ligands that can be used to bind molecular targets. Small molecules, for example, have many advantages as platforms for the creation of radiopharmaceuticals, including their rapid elimination from the body and relatively facile production. They have disadvantages, too, of course, including most notably the bioinformatics and robotic infrastructure needed to screen combinatorial arrays and identify effective small molecule ligands. For many years, libraries of biologically active small molecules were painstakingly assembled via the efforts of medicinal chemists (who synthesized compounds), natural products chemists (who isolated them), and biologists (who tested them). With the advent of combinatorial chemistry and high-throughput screening, much larger libraries can be generated far more easily and screened using robotic instruments. That said, this combinatorial approach generates a tremendous amount of data and necessitates the use of bioinformatics to analyze the data.

Moving from chemistry to biology, antibodies have also been employed with great success as platforms for targeted radiopharmaceuticals. To this end, the immunization of animals using purified a recombinant version of the intended target leads to the development of monoclonal or polyclonal antibodies specific to the target. The immunization of mice, for example, leads to the production of whole antibodies such as immunoglobulin G (IgG). IgG antibodies are 150 kilodaltons (kDa) and typically have blood half-lives on the order of days. This necessitates the use of long-lived radionuclides for nuclear imaging and therapy, though pretargeting—or multistep targeting—approaches have been shown to provide a route to circumvent this requirement [16]. Smaller versions of antibodies—known as antibody fragments—can be created via protein engineering and screened using phage display libraries. Another method for producing molecules with antibody-like affinities and specificities is the generation of nanobodies or camelid antibodies through the inoculation of

targets into sharks or camels [17, 18]. Nanobodies are single monomeric variable antibody domains with molecular weights between 12 and 15 kDa. While they boast affinities similar to those of full-length antibodies, their smaller size results in far more rapid pharmacokinetic profiles.

Radioligand Binding Assays

Once lead binding candidates have been generated for the chosen target, the affinity and specificity of these compounds must be assessed. The binding constant—commonly referred to as K_d—of a molecule to its target is the driver of any procedures for the optimization of lead compounds. Assaying the binding kinetics of a molecule provides important information on how fast the molecule will contact its target (k_{on}), how long it will remain associated with its target (k_{off}), and—finally—the strength of the interaction of the molecule with its target. In general, the lower the K_d, the higher the affinity for the target. The interaction between a ligand and its target is not covalent. Rather, it is a dynamic interaction composed of binding and disassociation. Affinity and binding kinetics are determined experimentally. While "binding kinetic assays" are generally used to determine the optimal time for the ligand-target system to reach equilibrium, "saturation binding assays" are used to describe an experiment aimed at determine the affinity of the ligand to its receptor as well as the receptor density. Finally, "competitive binding assays" are used to determine the specificity of the ligand for its target. Before going into the details of the experiments, we must first understand what happens when a ligand and target are introduced to one another.

Mechanism of Action

The mass action law helps to predict the behavior of molecules that are operating in a dynamic environment. As an example, an antibody binds to its receptor on the surface of a cancer cell. The dynamic equilibrium between a ligand (L) and its receptor (R) is reversible and can be chemically written as follows:

$$L+R \rightleftharpoons LR \tag{1}$$

As the reaction occurs in a dynamic system, the ligand is either binding (on) or in dissociation (off) at specific rates. The association reaction is defined by a second-order rate constant, k_{on}, which is expressed in $M^{-1}.s^{-1}$. The dissociation reaction is defined by a first-order rate constant, k_{off}, which is expressed in $time^{-1}$.

$$L+R \underset{k_{off}}{\overset{k_{on}}{\rightleftharpoons}} LR \tag{2}$$

At equilibrium, these relationships can be converted into the following mathematical equation by applying the mass action law:

$$\frac{k_{off}}{k_{on}} = \frac{[L][R]}{[LR]} = K_d \tag{3}$$

Considering that the concentration of free receptor is equal to the total number of receptor (R_t) minus the number of occupied receptor (LR), Eq. (3) can be rewritten as:

$$\frac{k_{off}}{k_{on}} = \frac{[L][R_t - LR]}{[LR]} = K_d \tag{4}$$

or

$$f = \frac{[LR]}{[R_t]} = \frac{[L]}{[K_d + L]} \tag{5}$$

which is the equation of a hyperbola. When graphed, the y-axis is $[LR]/[R_t]$ and is also referred to as fractional occupancy (f). K_d is equal to the concentration of free ligand $[L]$ that occupies 50% of the receptors ($f = 50\%$; Fig. 4). To calculate K_d, one must make the assumption that the system is at equilibrium.

Kinetic Binding

The time required for a ligand of interest and its receptor to reach the equilibrium state can be determined experimentally. The concept is relatively straightforward. A constant concentration of receptors is incubated with a constant concentration of ligand (usually below the presumed K_d) for variable periods of time. Then, the concentration of bound ligand or fractional occupancy data ($[LR]/[R_t]$, Y-axis) is plotted against time (X-axis) to obtain a hyperbolic curve

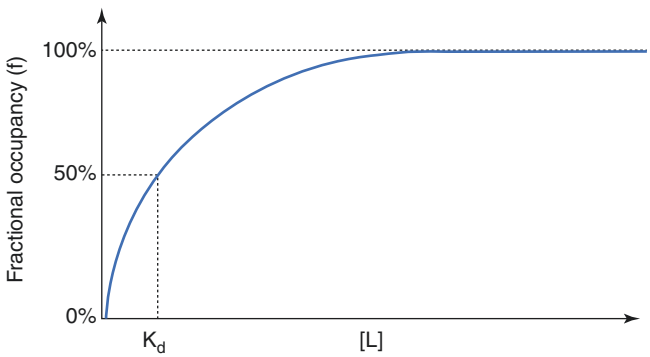

Fig. 4 Hyperbola curve resulting from plotting fractional occupancy against the concentration of ligand. Note that K_d is defined as the concentration of ligand that occupies 50% of the receptors

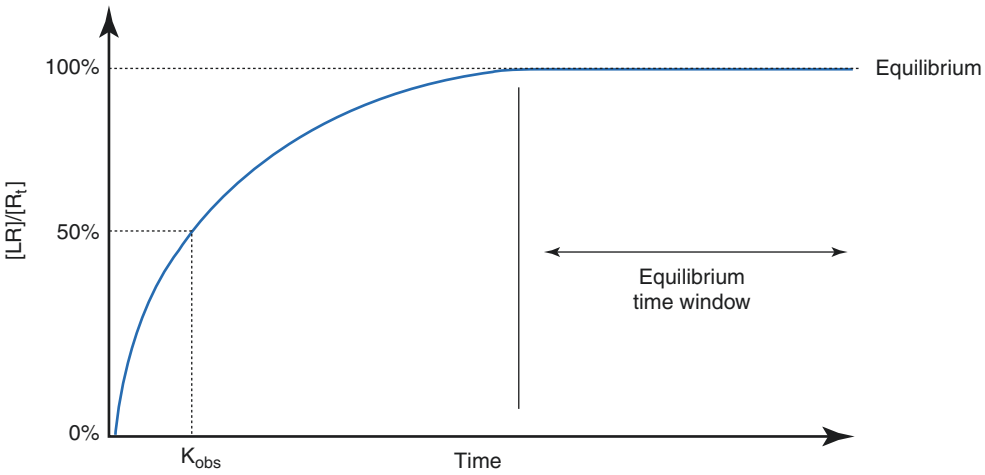

Fig. 5 Hyperbola curve resulting from plotting ligand binding against time

like the one shown in Fig. 5. The association constant k_{on} ($M^{-1}s^{-1}$) can then be determined by repeating the experiment using different concentrations of ligand. For each increased ligand concentration, the K_{obs} (min^{-1}), defined by 50% occupancy, should increase linearly. The slope of the graph K_{obs} (Y-axis) vs. ligand concentrations (X-axis) gives the k_{on}. Note that the time to reach equilibrium is dependent on temperature. At 37 °C, the receptors will be saturated more rapidly than at room temperature, as molecular motion is increased as the temperature increases. The value of k_{on} is mostly driven by the rate of diffusion and usually falls in the range of 10^6–10^8 $M^{-1}s^{-1}$.

The dissociation constant k_{off} can also be determined experimentally as well. Once the system reaches equilibrium, the free ligand in solution is quantitated at regular time intervals until completely depleted. Since k_{off} is tightly linked to K_d, most experiments are designed to maximize k_{off} while forgetting about k_{on}. However, for imaging applications, k_{on} is also critically important, especially for small molecules that are cleared from the bloodstream and tissues far more rapidly than biomolecular vectors.

Saturation Binding

Saturation binding assays are more universally performed and allow for the determination of binding affinities as well as the quantitation of the number of binding sites per cell. In this assay, the number of cells or targets typically remains constant, while the concentration of radiolabeled ligand is varied over 5 log units of concentration. The radiolabeled ligand is incubated for a time *at least* equal to the time to reach equilibrium, and then the amount of bound ligand is quantitated. In general, this assay should be performed under two conditions to demonstrate the accurate determination of specific binding. In the first, the ligand is simply introduced

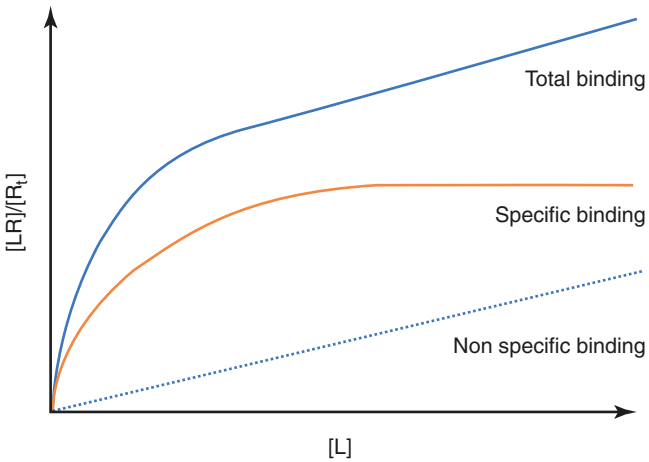

Fig. 6 Consideration of non-specific binding during the design of a saturation binding experiment

to the target. In the second, the ligand is introduced to an already-saturated target or a non-specific target of similar molecular weight. The need for the latter condition is based on the fact that the ligand may bind non-specifically to constituents in the system other than its target, for example, the plastic of the plate or the phospholipid within the cell membrane. During a saturation binding experiment, a step of saturation of non-specific binding sites, also called blocking step, should reduce the bulk of non-specific binding (NSB); however, not all NSB can be eliminated. Therefore, control experiments should be performed to quantify the amount of non-specific binding. Specific binding can then be calculated by subtracting the NSB from the total binding at each ligand concentration, ultimately producing a graph of specific binding (Fig. 6).

$$TB = SB + NSB \tag{6}$$

NSB usually—but not necessarily—appears as a linear relationship between ligand concentration added to the system and its binding.

Generally speaking, it is desirable to minimize non-specific binding during these assays. Several methods to reduce the amount of NSB exist, including the use of detergents or blocking with proteins. Most of the time, the detergents—for example, Tween 20 or Triton X—are used during wash steps at concentrations of 0.005–0.15% to disrupt ionic and hydrophobic bonds. Protein blockers like bovine serum albumin (BSA—1% to 5%), casein, and animal sera can be used to block site of non-specific binding as well. These proteins have a weak affinity for other proteins, so they will not inhibit productive, high-affinity interactions between the ligand and receptor.

By plotting the bound ligand [*LR*] or occupied receptor fraction (*f*) versus total ligand [*L*], the total binding curve should appear smooth with no inflection points (see Fig. 6). If the curve does not plateau, it is because of non-specific binding. Commonly, the bound ligand is plotted in linear scale versus the $\log_{10}$ of the concentration of total ligand. This plot is also called a Klotz plot or semilog plot. The original hyperbola is transformed into a more recognizable sigmoidal curve (Fig. 7). In the sigmoidal plot, the B_{max} value equivalent to $f = 100\%$ allows for the determination of the number of receptors. In the case of in-cell binding, the number of cells in identically plated wells is quantified to give the total number of cells per well. To convert B_{max} to the number of receptors, the relationship between the label and the ligand must be known (*i.e.* is there one label per ligand or two labels per ligand, *etc.*). Once the relationship between the label and the ligand is known, the number of ligands bound can be quantified and then divided by the number of cells to produce the number of receptors per cell. As an example, the following illustrates the calculation of receptors/cell for a ligand radiolabeled with iodine. If the specific activity (*i.e.* the number of molecules radiolabeled per mole of total ligand) post-HPLC purification and fractionation is 2190 Ci/mmol or 4133 cpm/fmol with 90% counting detector efficiency, we can generate Table 1.

This example assumes that the ligand and receptor bind at a ratio of 1:1. This is not always the case, of course, and can be determined by the slope of the plot. If the slope deviates from 1, then there is either cooperative or noncooperative binding, and a Hill plot can be used to determine the relationship between the ligand and receptor. The most commonly cited example of cooperative binding is the binding of dioxygen to hemoglobin, as hemoglobin can bind up to four oxygen molecules. Once the first oxygen binds, the conformation of hemoglobin changes, making the affinity of binding to the second oxygen higher than the affinity for the first oxygen. The third oxygen has an even higher affinity than second or third oxygen.

The third parameter of this sigmoidal plot is the K_d. The K_d, or affinity, is the concentration of ligand needed to occupy 50% of the receptors. The lower the K_d, the higher the affinity. K_d is also known as the equilibrium constant expressed in molar (M). It is equal to k_{off} (in s^{-1}) divided by k_{on} (in $M^{-1}s^{-1}$):

$$\frac{k_{off}}{k_{on}} = K_d \tag{7}$$

K_d is used to describe the affinity of the ligand to its target. It is inversely correlated to the affinity: the lower the K_d value, the higher is the affinity. For instance, ligands with K_d values in the 0–10 nM range are commonly considered "high affin-

Table 1 An example determination of the number of receptors per cell using a radioiodinated radiopharmaceutical

Molecule type	Peptide
Number of binding site	1
Radionuclide	Iodine-125
Specific activity (cpm/fmol)	$4.1.10^3$
Bmax (cpm)	10^4
Labeled ligand bound to target (fmol)	$10^4/4.1.10^3 = 2.4$
Labeled ligand bound to target (molecules)	$6.02 \times 10^{23} \times 2.4 \times 10^{-15} = 1.4.10^9$
Number of cells	10^3
Number of receptors per cell	$1.4.10^9/10^3 = 1.4.10^6$

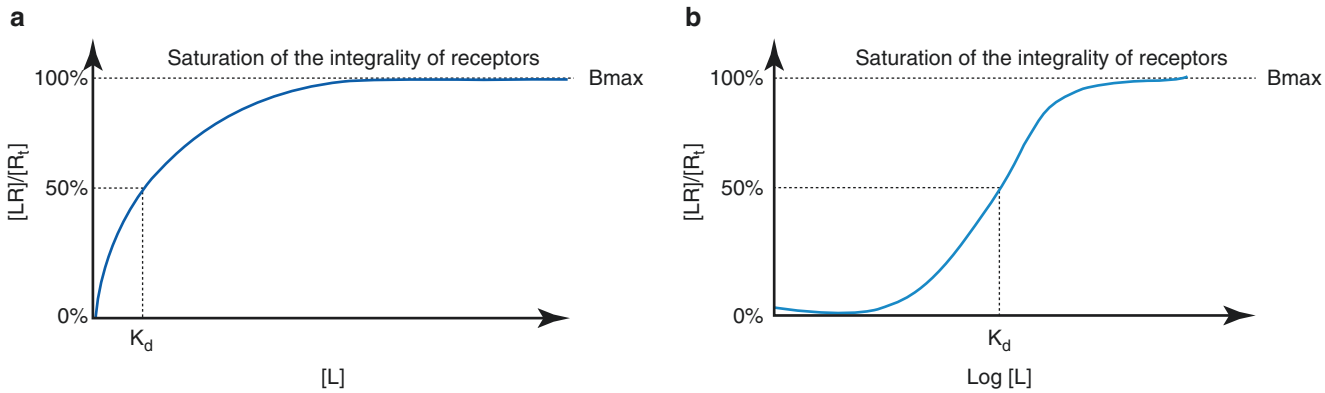

Fig. 7 Saturation function (**a**) and Klotz plot (**b**)

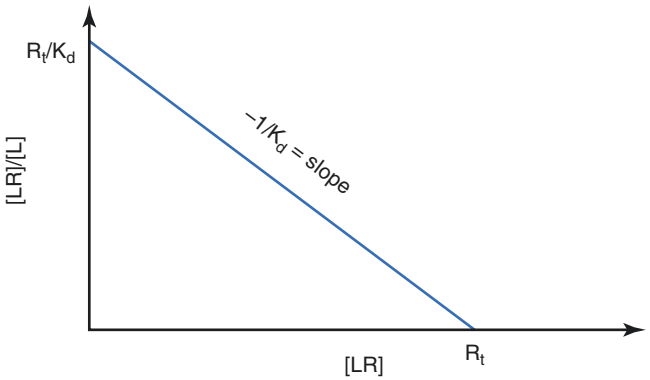

Fig. 8 Representation of binding via a Scatchard plot

ity," whereas ligands with K_d values in the micromolar range are typically considered "low affinity." Importantly, K_d and B_{max} are not related. A ligand can have a high affinity for a target, but the cell can only have a handful of targets. Conversely, a ligand can have a low affinity for a target, but a cell can have a very high number of targets. The fourth and final important parameter in this kind of plot is the bottom, which should be 0. When this deviates, it is typically because of the non-specific binding of the ligand.

The traditional way to analyze all of this binding data before the introduction of sophisticated curve fitting software was the Scatchard plot. This use of the Scatchard plot is predicated on the following rearrangement of Eq. 4:

$$\frac{[LR]}{[L]} = \frac{-[LR]}{K_d} + \frac{[R_t]}{K_d} \tag{8}$$

Equation 7 follows the form of a linear equation $y = mx + b$. By plotting $[LR]/[L]$ vs. $[L]$, the X-intercept is R_t and the Y intercept is $[R_t]/K_d$. An example graph is shown in Fig. 8. A linear representation is very helpful, as it simplifies the math to obtain graphically important value such as B_{max} or K_d. Note that the total amount of saturated receptor R_t is also denoted as B_{max}.

Competitive Binding

Competitive binding assays are used when it is not possible to saturate binding because of the need for μM or mM concentrations of ligand. This is most common in radiopharmaceutical chemistry. These assays are similar to the determination of NSB in that a known ratio and unlabeled and labeled molecule are incubated with the target. These assays are also often performed to ensure that the radiolabeling of the ligand did not affect the affinity of the ligand. In that case, if the K_d of the unlabeled ligand is within an acceptable range of the inhibitor constant (K_i) value, the labeling did not affect the binding capacity of the compound. Finally, competitive binding assays can also be performed to compare several compounds with different affinities for the same target. The data generated from a competitive binding assay is most often reported as the half maximal inhibitory concentration, IC_{50}. The IC_{50} is defined as the concentration of inhibitor necessary to displace the radiolabeled ligand from 50% of the receptor sites. From there, the inhibitor constant K_i is calculated as follows:

$$K_i = \frac{IC_{50}}{1 + L/K_d} \tag{9}$$

and

$$K_d = \frac{EC_{50}}{1 + I/K_i} \tag{10}$$

Therefore, K_d can be derived from K_i via the following mathematical arrangement provided by Nikolovska-Coleska et al. [19]:

$$K_i = \frac{[I]_{50}}{\frac{[L]_{50}}{K_d} + \frac{[R]}{K_d + 1}} \tag{11}$$

This arrangement appears to be very useful when it comes to characterizing several compounds with a limited amount available. It is also important to remember that IC_{50} is not the affinity of a compound, as it will vary depending on the number of receptors present in the dish. If fewer cells or more cells are plated, then different IC_{50} values will result. Only by converting to K_i or K_d can these values be directly compared.

After the affinity, specificity, and number of targets or receptors per cell have been determined, the lead candidate often needs to be optimized. Of course, the number of receptors per cell is dependent on the target and cannot be optimized. The specificity of a ligand can be difficult to optimize as well. Thankfully, the optimization of affinity—known in some circles as "affinity maturation"—can be performed readily and routinely. Here we present several different strategies.

Peptide Maturation

In alanine scanning mutagenesis—also known as an alanine walk or an ala scan—a library of peptides is synthesized in which an amino acid of the sequence has been replaced by an alanine (Fig. 9). One peptide of the library has an alanine in the first position followed by the rest of the original amino acid sequence, a second peptide has an alanine in place of the

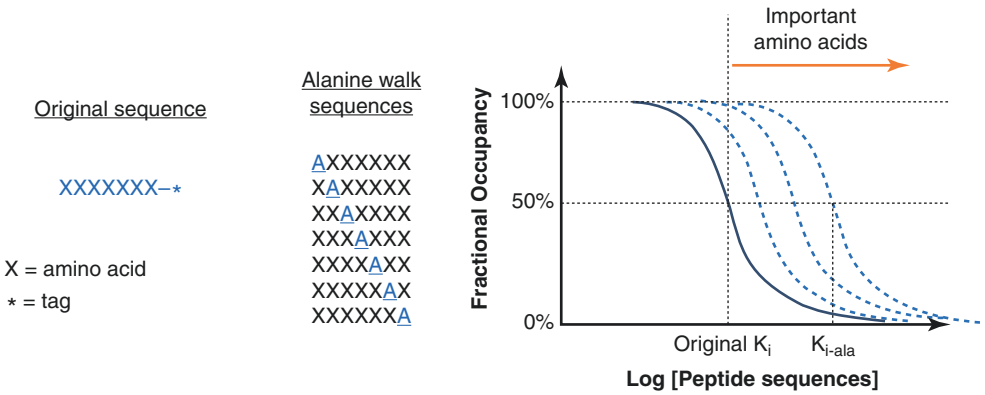

Fig. 9 The "alanine walk" method for peptide maturation is performed by incubating a labeled candidate peptide at a single known concentration with an escalating amount of a modified non-labeled variant of itself. The peptide sequence is modified by the substitution of one amino acid by an alanine. This procedure is repeated inserting alanine at each position in the sequence. The different $K_{i\text{-}ala}$ obtained are compared to the original K_i. If $K_{i\text{-}ala} = K_i$, then the substituted amino acid is considered to have a minimal role in the binding activity. If $K_{i\text{-}ala} > K_i$, then the substituted amino acid is playing an important role in the binding of the candidate peptide to its target

second amino acid, and so on. To perform this experiment, the original peptide is labeled. A mixture of the unlabeled alanine-substituted peptide and the labeled original peptide are incubated with cells or target (exactly as described above in the section on competition binding assays). If the alanine substitution does not change the K_i, then it becomes clear that that amino acid is not important for binding. If, however, the K_i of the alanine-substituted peptide deviates significantly from that of the lead peptide, then that amino acid is essential for binding. Once the essential amino acids are determined, a second phage display library can be constructed in which the essential amino acids are held constant and the other amino acids are randomized. This newly generated phage library can then be screened for ligands with higher affinities for the target.

Another method of affinity maturation, the one-bead-one-compound (OBOC) combinatorial library method, calls for the creation of a library of millions of random peptide sequences each connected to a bead. The beads are mixed with the target of interest, and the beads that can bind the target are physically isolated for further peptide amino acid sequencing using an automatic protein microsequencer. The resultant "second generation" peptide sequences are then evaluated for their binding specificity in an iterative process. While ala scans are a robust technique for determining the most important amino acids of the sequence, the OBOC method directly offers sequences with high binding affinity. Once a lead candidate peptide sequence has been identified, the improvement of the binding affinity can be obtained via multimerization. Making constructs (*e.g.* polymers or dendrimers) which contain multiple copies of a ligand can result in the creation of probes that have apparent affinities two to three log units higher than the corresponding monomeric versions.

Conclusion

The selection of a target is a key first step in the development of a successful radiopharmaceutical. The ideal target should be selectively expressed on disease tissues in high copy number and should be accessible for binding by the radiopharmaceutical. In the era of "omics" technologies, a wide variety of methods—such as database searching, proteomics, and transcriptomics—can be used to validate targets as well as identify new targets. Once the target is identified, the next step in the development of a radiopharmaceutical is the creation of ligands with high affinity and high specificity for the target. In this chapter, we have discussed the characteristics of an ideal target, ways to identify targets, the properties of various ligands, and the binding theory that underpins the thoughtful maturation of lead ligands into optimized, high affinity vectors.

Bottom line

- Target selection is the first step to a successful radiopharmaceutical.
- An ideal target is selectively expressed on diseased cells and accessible to drugs.
- Phage display-based functional proteomics is a robust platform for the discovery of new targets.
- K_d, B_{max}, k_{on}, and k_{off} are important parameters that describe the interactions between ligands and targets.
- Several different methods exist to optimize—or "mature"—the interaction between ligands and targets in order to produce robust, clinically useful radiopharmaceuticals.

References

1. Brand FX, Ravanel N, Gauchez AS, Pasquier D, Payan R, Fagret D, et al. Prospect for anti-HER2 receptor therapy in breast cancer. Anticancer Res. 2006;26(1B):463–70.
2. Fueger BJ, Hamilton G, Raderer M, Pangerl T, Traub T, Angelberger P, et al. Effects of chemotherapeutic agents on expression of somatostatin receptors in pancreatic tumor cells. J Nucl Med. 2001;42(12):1856–62.
3. Aebersold R, Mann M. Mass spectrometry-based proteomics. Nature. 2003;422(6928):198–207.
4. Aebersold R, Goodlett DR. Mass spectrometry in proteomics. Chem Rev. 2001;101(2):269–96.
5. McDonald WH, Yates JR. Shotgun proteomics: integrating technologies to answer biological questions. Curr Opin Mol Ther. 2003;5(3):302–9.
6. Eng JK, McCormack AL, Yates JR. An approach to correlate tandem mass spectral data of peptides with amino acid sequences in a protein database. J Am Soc Mass Spectrom. 1994;5(11):976–89.
7. Perkins DN, Pappin DJ, Creasy DM, Cottrell JS. Probability-based protein identification by searching sequence databases using mass spectrometry data. Electrophoresis. 1999;20(18):3551–67.
8. Craig R, Beavis RC. TANDEM: matching proteins with tandem mass spectra. Bioinformatics. 2004;20(9):1466–7.
9. Mueller LN, Brusniak M-Y, Mani DR, Aebersold R. An assessment of software solutions for the analysis of mass spectrometry based quantitative proteomics data. J Proteome Res. 2008;7(1):51–61.
10. Parmley SF, Smith GP. Filamentous fusion phage cloning vectors for the study of epitopes and design of vaccines. Adv Exp Med Biol. 1989;251:215–8.
11. Willats WGT. Phage display: practicalities and prospects. Plant Mol Biol. 2002;50(6):837–54.
12. Smith GP, Petrenko VA. Phage display. Chem Rev. 1997;97(2):391–410.
13. Brinton LT, Bauknight DK, Dasa SSK, Kelly KA. PHASTpep: analysis software for discovery of cell-selective peptides via phage display and next-generation sequencing. PLoS One. 2016;11(5):e0155244.
14. Kelly KA, Bardeesy N, Anbazhagan R, Gurumurthy S, Berger J, Alencar H, et al. Targeted nanoparticles for imaging incipient pancreatic ductal adenocarcinoma. Gambhir S, editor. PLoS Med. 2008;5(4):e85.
15. Gutknecht MF, Seaman ME, Ning B, Cornejo DA, Mugler E, Antkowiak PF, et al. Identification of the S100 fused-type protein hornerin as a regulator of tumor vascularity. Nat Commun. 2017;8(1):552.
16. Kraeber-Bodéré F, Rousseau C, Bodet-Milin C, Frampas E, Faivre-Chauvet A, Rauscher A, et al. A pretargeting system for tumor PET imaging and radioimmunotherapy. Front Pharmacol. 2015;6:54.
17. Broisat A, Hernot S, Toczek J, De Vos J, Riou LM, Martin S, et al. Nanobodies targeting mouse/human vcam1 for the nuclear imaging of atherosclerotic lesions. Circ Res. 2012;110(7):927–37.
18. Fridy PC, Li Y, Keegan S, Thompson MK, Nudelman I, Scheid JF, et al. A robust pipeline for rapid production of versatile nanobody repertoires. Nat Methods. 2014;11(12):1253–60.
19. Nikolovska-Coleska Z, Wang R, Fang X, Pan H, Tomita Y, Li P, et al. Development and optimization of a binding assay for the XIAP BIR3 domain using fluorescence polarization. Anal Biochem. 2004;332(2):261–73.

Preclinical Experimentation in Oncology

Sridhar Nimmagadda, Sagar Shelake, and Martin G. Pomper

Fundamentals

The advent of gene sequencing and gene knockout technologies has provided unprecedented insight into the expression of various genes and their role in the incidence, growth, and progression of cancer. Furthermore, refinements to high-throughput genomic platforms, the development of next-generation sequencing, and the completion of The Cancer Genome Atlas (TCGA) project have enabled the mapping of genetic aberrations in many cancers, including non-small cell lung cancer (NSCLC), brain tumors, and pancreatic cancers to name a few [1, 2]. These developments have provided unique opportunities for the selective targeting of cancer cells by identifying highly cancer-specific therapeutic targets. Those novel targets include, for example, fusion oncologic proteins that drive signaling cascades, immune checkpoint proteins involved in cloaking cancer cells from detection by the immune system, and deregulators of metabolic pathways.

Choosing a Target

Novel therapeutics that target aberrant protein expression have led to treatments with high efficacy and reduced toxicities that have produced increased overall survival rates in a variety of cancers [3]. Although the scope of molecularly targeted therapeutics in oncology has expanded, there is a considerable need to evaluate the therapeutic effectiveness of these agents with a focus on evaluating their activity at the site of action, *i.e.* at the tumor. Molecular imaging targets, like drug targets, are generally proteins—including antigens, enzymes, receptors, and ion channels—that can be either extra- or intracellular. In this chapter, we will share our experience in harnessing the latest developments in oncology to identity and evaluate novel imaging agents with sufficient rigor and reproducibility to be ready for clinical translation.

For the development of novel imaging agents, our group's approach has been to (i) choose a disease for which imaging will have an impact; (ii) select a biological target that would be most sensitive to the detection, progression, and possibly prognosis of the disease; and (iii) develop a probe that is highly specific for the target. Using this approach, we have been developing agents targeting prostate-specific membrane antigen (PSMA) as theranostics for detecting, treating, and guiding the treatment of prostate cancer therapy [4]. PSMA is highly expressed in prostate cancer, and several PSMA-targeted imaging agents are in clinical trials for the detection and evaluation of disease progression [5–7]. A major opportunity afforded by the aforementioned genomic studies is that PSMA expression can be assessed in a multi-cancer panel, allowing us to identify non-prostate cancer cell lines and tumors with high levels of PSMA expression [8]. Those observations suggest that existing PSMA-based theranostic agents may find use in a small percentage of non-prostate cancers, particularly those with limited therapeutic options. Our laboratory and others have also relied on other means to select targets for cancer-specific imaging whose overexpression has been highly correlated to disease progression or indicative of response to therapy. Such examples include the overexpression of chemokine receptor 4 (which is indicative of metastatic potential of tumors [9]), programmed death ligand-1(PD-L1, which denotes tumor response to immune checkpoint therapy [10]), and delta-like 3 protein (which is highly expressed in small cell lung cancer [11]). One way to identify and validate such highly relevant cancer cell-specific targets is through genomic and proteomic data mining. Several resources that form a compendium of large-scale data sets derived from human cancer cells and tumors are freely available for data mining. Detailed information on these resources is provided in Table 1.

S. Nimmagadda (✉) · S. Shelake · M. G. Pomper (✉)
Russell H. Morgan Department of Radiology and Radiological Science, Johns Hopkins University School of Medicine, Baltimore, MD, USA
e-mail: snimmag1@jhmi.edu; mpomper@jhmi.edu

J. S. Lewis et al. (eds.), *Radiopharmaceutical Chemistry*, https://doi.org/10.1007/978-3-319-98947-1_33

Table 1 Web resources for the validation of targets for imaging

Database	Web address	Application and data types	Search terms and notes
Cancer Cell Line Encyclopedia (CCLE)	https://portals.broadinstitute.org/ccle	A set of resources for the analysis and visualization of the genetic and pharmacologic characterization of human cancer cell lines	Cell line, gene annotation, gene name
The Cancer Genome Atlas (TCGA)	https://cancergenome.nih.gov/	A database that contains the characterization of genetic changes and mutations pertaining to cancers harvested from patients	Tumor types, gene names Gene expression in normal tissue can be identified
cBioPortal	http://www.cbioportal.org/	A portal that provides an interactive visualization of genomic and clinical data	Gene copy number, mutation, mRNA expression, protein level, tumor type, tissue type, signaling pathway
Regulome explorer	http://explorer.cancerregulome.org/	A database that enables exploration of multi-scale associations within the context of genomic coordinates	Tumor type, TCGA ID
OASIS	http://www.oasis-genomics.org/	A tool which provides exploratory and integrative analyses of gene mutations, DNA copy number, and gene expression datasets	Gene name, mutation, tumor type Gene expression in normal tissue can be identified
UCSC cancer genomics browser	http://xena.ucsc.edu/welcome-to-ucsc-xena/	A tool for the functional visualization of genomic data such as SNPs, INDELS, DNA copy number, lncRNA, DNA methylation	Tumor type, study name, gene name, tissue
The Cancer Proteome Atlas (TCGA)	http://tcpaportal.org/tcpa/	A portal with tools for the visualization of functional proteomic data from tumor samples in the TCGA dataset	User-defined selection from four available modules: "summary," "myprotein," "visualization," and "analysis"
Clinical Proteomic Tumor Analysis Consortium (CPTAC)	https://cptac-data-portal.georgetown.edu/	A repository that consists of proteogenomic sequence datasets from TCGA tumor samples	Genomics, proteomics, and imaging assays
LinkedOmics	http://linkedomics.org/	A data portal containing datasets form TCGA and mass spectroscopy-based proteomic CPTAC data	Clinical data, DNA copy number, methylation, proteomics, RNAseq
TCGA GDAC Firehose	http://gdac.broadinstitute.org/	A repository containing standardized TCGA datasets for the comprehensive analysis, available for public use	Clinical correlation analyses, RNAseq, miRNA, mutations, pathway analyses
Cytoscape	http://www.cytoscape.org/	A tool to perform genetic and proteomic exploratory studies and data visualization	Genomic and proteomic interactions, pathway analyses
Cancer Research Institute (CRI) iAtlas	https://www.cri-iatlas.org/	A web-based tool to study the interplay between the tumor microenvironment and the immune system in tumors presently catalogued in the TCGA	Tumor type, gene expression, immune modulator, cytokine profiling, neo-antigen load
Catalogue Of Somatic Mutations In Cancer (COSMIC)	https://cancer.sanger.ac.uk/cosmic	A database containing resources for exploring the effects of somatic mutations in cancer	Gene, tumor type, mutation, methylation, study name

Once a target is identified, the expression of the target within the tumor microenvironment as well as normal tissues can be noninvasively visualized using imaging agents based on antibodies, peptides, and small molecules. A compendium of >6000 imaging agents has been tabulated in the Molecular Imaging and Contrast Agents Database (MICAD). The MICAD provides freely accessible information on radiotracers, contrast agents, and multimodality imaging agents that are currently in preclinical development or clinical evaluation. The summary chapters provided in the MICAD are a unique source of model systems as well as techniques and parameters that may be suitable for the evaluation of a particular imaging agent. While MICAD is now defunct, updates on the development of imaging agents are freely available—thought admittedly harder to find —via PubMed (https://www.ncbi.nlm.nih.gov/pubmed/).

Validating a Target

Once a molecular target of interest has been identified, the information needed for the development of a targeted molecular imaging probe includes the following:

(a) The expression level or concentration of the target (B_{max}) within tissue, particularly relative to potential co-localized, non-specific interactions
(b) The affinity (K_d) of the putative imaging agent for the target, with the knowledge that the lower the B_{max}, the higher the K_d value needed for productive imaging [12]
(c) The pharmacokinetics of the agent, with the added necessity of rapid non-target washout, particularly for radiotracers that employ radionuclides with short physical half-lives

There are many clinically applicable radiosynthetic methods for the radiolabeling small molecule-, peptide-, and antibody-based vectors, though this is an ongoing area of intense research [13]. In the following sections, we will discuss the various methods available to validate the expression of the target and to identify cell lines for the *in vitro* and *in vivo* evaluation of a radiotracer. In addition, we will try to demonstrate these concepts using examples derived from the literature.

Details

The Cancer Cell Line Encyclopedia (CCLE)

The CCLE is a comprehensive compilation of gene expression data detailing the gene copy number, mRNA expression levels, methylation patterns, and mutations of more than 1000 different cancer cell lines [14] (see Table 1). These datasets are open access resources. The CCLE can be used to identify cell lines that express the desired levels of a molecular target, design genomic computational models to stratify and predict the sensitivities of various cancer cell lines to treatment, and, by extension, provide a starting point for treating the corresponding cancers *in vivo*.

Microarray and RNA sequencing data can be used to identify and explore the relationships between common sequence variation and predisposition to disease or response to drug treatment [15]. Such differential gene expression analyses are also referred to as genome-wide association studies or GWAS. GWAS have primarily been focused on single nucleotide polymorphism (SNPs), but other more complex forms of genetic variations—such as copy number variations (CNVs, usually defined as genomic segments of size $\geq$1 kb showing copy number variability among individuals with respect to a reference genome) and mutations—are also employed [15]. To date, the CCLE contains SNP data from the NCI-60 cancer cell line panel, as well as enriched and normalized counts of gene copy number, mutations, and mRNA expression in order to perform GWAS analysis.

The data in the CCLE have been used to characterize the expression of specific proteins in a variety of cancers. One of the earliest examples of using data from the CCLE for the validation of a new molecular target and the development of a corresponding imaging probe was centered on ACKR3, also known as CXCR7 [16]. ACKR3 is an atypical chemokine receptor and modulates the tumor microenvironment by mediating adhesion, angiogenesis, tumorigenesis, and tumor cell survival. ACKR7 also contributes to tumor growth by regulating angiogenic, proliferative, and signaling pathways [17, 18]. A comprehensive analysis of ACKR7 expression in CCLE datasets indicated high expression in breast and non-squamous lung cancer cell lines, which led to the validation of ACKR7 expression in xenograft models of those cancers using a radiolabeled antibody [16].

Another example of employing CCLE data to expand the use for existing imaging agents was the characterization of the expression of PSMA in non-prostate cancers. PSMA expression is elevated and differentially localized to the plasma membrane in prostate adenocarcinoma. Indeed, nearly 95% of prostate cancers are reported to have elevated PSMA expression [19]. PSMA is also expressed on the endothelial cells of tumor-associated neovasculature of most tumor types, but its expression in non-prostatic tumors and cell lines is not well characterized [20]. Remarkably, data mining for PSMA transcript levels in the CCLE showed that nearly 5% of all of the cell lines in the CCLE have PSMA transcript levels above the median value of the prostate cancer cell lines that have the highest PSMA expression (Fig. 1) [8]. The further evaluation of selected non-prostate cell lines and xenografts via quantitative real-time PCR, flow cytometry, and immunoblotting validated the levels of PSMA transcript and protein expression (Fig. 2).

The Cancer Genome Atlas (TCGA)

The Cancer Genome Atlas is a database that contains a comprehensive genomic analysis of human tumors and provides source code for efforts relating individual genomics to enhanced cancer diagnosis and treatment. The TCGA websites provide open access to data and related analytic visualization tools. The curated scientific data and summarized results can be harnessed using user-friendly interactive tools such as cBioPortal and Regulome Explorer (Table 1). This is complemented by "omics" data generated in parallel in large patient cohorts, such as mass spectrometry-based global proteomics data from selected TCGA tumor samples generated by the Clinical Proteomic Tumor Analysis Consortium (CPTAC) [21]. Several web resources that make the data publicly available are described in Table 1. Those resources provide mutation, copy number alteration (CNA), methylation, mRNA expression, miRNA expression, and reverse phase protein array (RPPA) data at the gene level. In addition, mutation data at the site level, CNA data at the region level, RPPA data at the analyte level, and clinical data for the validation of target expression are provided as well [22]. Collectively, these data sets enable a system-level quantitative integration of DNA, RNA, and protein expression data across cancer types.

The availability of sequencing data from a large number of cancer cell lines allows us to profile the transcript levels of a target in various cancers. However, one needs to be cautious in relying too heavily on information derived from cell lines. After all, these cell lines have been cultured for many passages, a process that that may have resulted in clonal

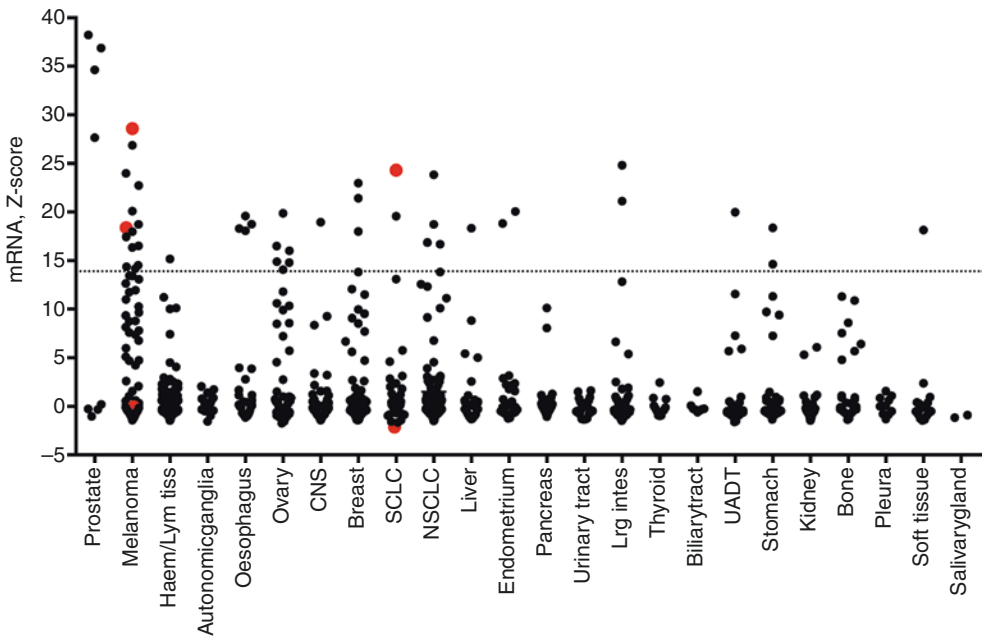

Fig. 1 Prostate-specific membrane antigen gene expression in the CCLE database. mRNA expression in $\log_2$ counts was converted to *z*-score and plotted on the basis of tumor types as a dot plot. Horizontal line represents the median *z*-score value of prostate cancer cell lines. Validated cell lines are shown in red. (From Nimmagadda *et al.* [8], with permission)

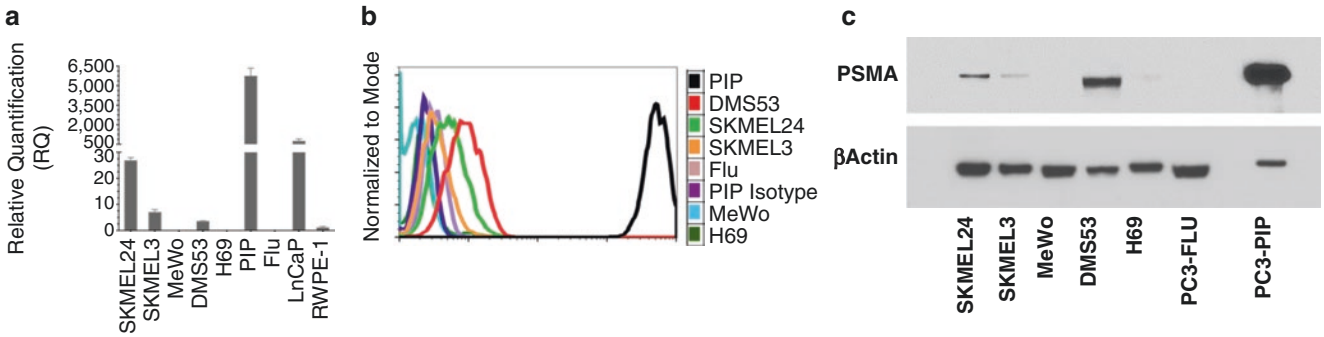

Fig. 2 Prostate-specific membrane antigen (PSMA) expression in non-prostatic human cancer cell lines and the corresponding tumor xenografts in mice. (**a**) PSMA mRNA gene expression as analyzed by RT-qPCR in selected prostate, melanoma, and lung cancer cell lines. (**b**) Flow cytometry histograms of the surface expression of PSMA in PSMA-positive PC3-PIP, PSMA-negative PC3-Flu, and non-prostatic cancer cell lines. PC3-PIP is a prostate cancer cell line stably transfected to overexpress PSMA, whereas PC3-Flu is a PSMA-negative cell line. DMS53, SKMEL24, and SKMEL3 are PSMA-positive cell lines, while MeWo and H69 are PSMA-negative cell lines. (**c**) Western blot analysis of PSMA protein levels in selected prostate, melanoma, and lung cancer xenograft tumors (From Nimmagadda *et al.* [8], with permission)

selection or changes in expression profiles or patterns. As a result, it is important to validate the observations made using the CCLE with human tumor data derived from TCGA. Of course, the analysis of TCGA data could provide novel insights into the expression of a target as well.

In our experience, for example, the PSMA transcript profile from the CCLE database was dissimilar to that derived from the TCGA [8]. Transcript expression data from 21 tumor types in TCGA showed high expression levels of PSMA in prostate cancers, followed by cancers of the kidneys, liver, and urothelium (Fig. 3) [8]. Nearly 97% of prostate cancers exhibited PSMA transcripts, which was anticipated. Surprisingly, however, nearly 10% of cancers of the kidney, liver, and urothelium as well as squamous cell lung and melanoma tumors exhibited PSMA transcript levels similar to—or *above*—that of the first quartile of prostate tumors. Within an individual cancer type, 57% of kidney, 39% of liver, 26% of urothelium, 21% of low-grade glioma, 12% of lung squamous cell carcinoma, and 9% of skin cancers demonstrated PSMA transcript levels in the aforementioned range. These data indicate that PSMA is expressed in a variety of non-prostate tumors, although at lower frequencies than in prostate cancer. Studies using PSMA-targeted PET imaging agents show high radiotracer uptake in non-prostate cancers [23], supporting these observations from the genomic study and further providing

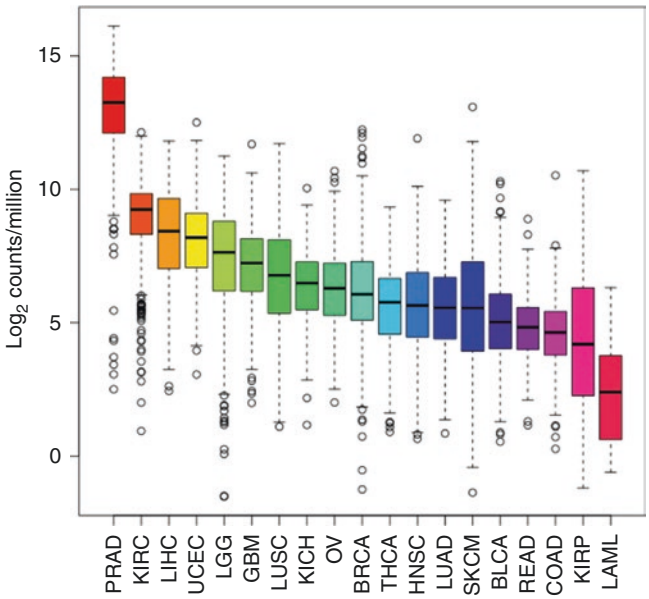

Fig. 3 Prostate-specific membrane antigen (PSMA) expression in different types of tumors from the TCGA RNA-Seq version 2 data. Each box represents 50% of the samples. The horizontal bold lines inside each box represent the median PSMA expression in each disease type. The bars at the top and bottom of each box represent the minimum and maximum expression values of the PSMA gene, respectively, excluding outliers. The dots on the top and bottom of each box represent outliers. *CNS* central nervous system, *NSCLC* non–small cell lung carcinoma, *UADT* upper aerodigestive tract, *PRAD* prostate adenocarcinoma, *KIRC* kidney renal clear cell carcinoma, *LIHC* liver hepatocellular carcinoma, *UCEC* uterine corpus endometrial carcinoma, *LGG* brain lower-grade glioma, *GBM* glioblastoma multiforme, *LUSC* lung squamous cell carcinoma, *KICH* kidney chromophobe, *OV* ovarian carcinoma, *BRCA* breast invasive carcinoma, *THCA* thyroid carcinoma, *HNSC* head and neck squamous cell carcinoma, *LUAD* lung adenocarcinoma, *SKCM* skin cutaneous melanoma, *BLCA* bladder urothelial carcinoma, *READ* rectum adenocarcinoma, *COAD* colon adenocarcinoma, *KIRP* kidney renal papillary cell carcinoma, *LAML* acute myeloid leukemia (From Nimmagadda *et al.* [8], with permission)

support for the integration of genomics with molecular imaging.

Target Expression Levels and Affinity of the Radiotracer

Once a new target for a radiotracer has been identified and appropriate cell lines have been selected from the CCLE or the literature, one of the most significant pieces of information that must be determined is the concentration of the target in the selected cell lines. Along these lines, we have leveraged the extensive range of validated and commercially available antibodies and have relied heavily on flow cytometry as a tool to characterize and select cell lines with graded levels of target expression [24]. Using microspheres bearing known numbers of fluorophores, a properly calibrated fluorescence intensity (FI) scale can be created that allows for the comparison of the FIs of different cell lines and facilitates the assignment of the number of antibodies bound to—and thus the number of receptors or targets expressed on—test cells [25]. Alternatively, one could also use classic radiotracer assays using tissue homogenates and cell cultures to determine the target concentration provided a high-affinity radioligand is available [26, 27]. Occasionally, a molecular target is sufficiently mature that target expression levels as well as high-affinity ligands—which can be derivatized to form imaging agents—have already been reported in the literature.

Radiotracer Characterization and Validation

The rigorous chemical characterization and biological evaluation of a radiotracer are of paramount importance prior to preclinical validation and, eventually, translation to patients. Observations from carefully designed chemical characterization and *in vitro* studies can aid in the progression of the radiotracer toward *in vivo* evaluation; reduce the time, effort, and expense of *in vivo* studies; and provide opportunities for the further optimization of the imaging agent. The most commonly used vectors for radiopharmaceuticals are small molecules, peptides, and antibodies. Once a high-affinity ligand has been identified for a given target, a wide variety of methods can be used to incorporate the desired radionuclide into the molecule (see Chaps. 11, 12, 13, 14, 15, 16, 17, 18, 19, 20, 21, 22, 23, and 24). The efficiency of the incorporation of the radionuclide can be evaluated using a variety of techniques, including radioHPLC, instant thin-layer chromatography, and autoradiography. If the radiotracer contains a chelator, it is important to consider both the number of chelators attached to the vector as well as their charge, as both factors can have a profound effect on the pharmacokinetics of the agent. This is true for small molecules, peptides, and biomolecules such as proteins and antibodies. For small molecules and short peptides, the number of chelators per vector is often one, while for antibodies, the degree of labeling a chelator can vary between one and five.

Once the radiopharmaceutical has been synthesized, the purification of the tracer from both the free radionuclide as well as any unreacted precursor is essential for a variety of reasons: (1) to allow for the determination of the percentage of bound radioactivity in the final product, (2) to facilitate the assessment of the *in vitro* and *in vivo* metabolic stability of the radiotracer, and (3) to enable the isolation of the radiotracer in high specific activity. The third point is particularly important in the context of quantifying target expression. Specific activity is defined as quantity of radioactivity per unit mass (radioactive plus nonradioactive) of an element, molecule, or a compound. The specific activity of an imaging agent will depend on the efficiency of the radiosynthetic

method as well as the physical half-life of the radionuclide, as radiotracers labeled with nuclides with short half-lives—*e.g.* ^{11}C ($t_{1/2}$ = 20 min)—show a rapid loss of specific activity over time. It is especially important for radiopharmaceuticals to have high specific activity when imaging low-density targets, because they can often easily be saturated by excess nonradioactive ligand.

One of the primary physical characters of an imaging agent is its lipophilicity [28]. Unlike drugs—which can bind to a multitude of unintended targets *in vivo*, provided that such binding does not cause an adverse reaction or significant side effect—imaging agents must wash away from non-target sites before the scan is collected, or sufficient contrast for detection will not be generated. The lipophilicity of a radiotracer can shed light on its protein-binding potential and *in vivo* distribution characteristics. More lipophilic compounds tend to have more non-specific binding and, consequently, have suboptimal *in vivo* behavior. At the same time, however, lipophilicity enables target engagement, facilitates crossing of the blood-brain barrier (as needed), and engenders prolonged tissue uptake [29]. As a result, researchers must often walk a fine line with respect to lipophilicity. Many software platforms exist that assist in characterizing lipophilicity (*e.g.* ACDLabs software) and calculating logD (cLogD) and logP (cLogP) values. LogP is defined as the partition coefficient of the neutral molecule in octanol/water and is a measure of the lipophilicity of a neutral compound (*i.e.* when the compound exists in a single form). LogD, on the other hand, is a distribution coefficient that takes into account all of the neutral and charged forms of a molecule and is thus a more suitable descriptor for the lipophilicity of ionizable compounds. While LogP is a constant for a molecule in its neutral form, LogD is pH-dependent and accounts for the differential solubility of the ionized and non-ionized species of a compound in the octanol/water system. Generally, low LogP values indicate that the radiotracer is hydrophilic. Hydrophilic molecules are likely to demonstrate low non-specific binding to the surface of cells, often need specific mechanisms for intracellular accumulation, and may show low non-specific uptake in tissues *in vivo*. In addition, hydrophilic molecules often demonstrate renal clearance and provide high-contrast images within the time frames most suitable for clinical application (*i.e.* within 60–120 min after radiotracer administration). High LogP values, in contrast, indicate that a radiotracer is hydrophobic and is likely to be retained in the lipophilic compartments of the cell such as the cell wall. Generally speaking, hydrophobic radiotracers can passively diffuse into cells, demonstrate high non-specific binding, and display high levels of uptake in non-specific tissues (especially the liver) *in vivo*. As we have alluded to above, agents with LogP values between one and three are often considered suitable for the penetration of the blood-brain barrier and can be useful as imaging agents for tissues and lesions within the central nervous system.

Additional insights into the biodistribution of a radiotracer can be obtained by conducting protein-binding studies. The binding of an imaging agent to proteins can be determined by incubating the radiotracer with mouse or human serum and subsequently evaluating the fraction of radioactivity that is adsorbed on serum proteins. Plasma protein binding can correlate with the half-life of the radiotracer in circulation, as radiotracers with high protein binding generally circulate for longer periods of time and exhibit higher activity concentrations in the blood pool *in vivo*. In certain circumstances, both of these properties can be advantageous [30]. Unfortunately, however, only a small fraction of the radiotracers with high protein binding are available in their free form that can bind to the target. This can result in poor image contrast or blood-brain barrier penetration [29], although exceptions are observed with steroids and some neuroreceptor-binding radiotracers [31].

Once a radiopharmaceutical has been synthesized and chemically characterized, it is critical to ensure that the specificity and activity of the radioligand have remained intact. As a result, the specificity and affinity of radiopharmaceuticals for their targets are often characterized using either recombinant proteins or cell lines. More specifically, the validation of a radiotracer should be performed in cell lines with graded levels of expression of the target using cell binding, cell uptake, internalization, and washout assays [32]. Cell-binding assays—for example, saturation binding experiments and competition binding assays [26, 27]—can be analyzed to infer biophysical parameters such as equilibrium dissociation constants (K_d) or inhibitor constants (K_i). More importantly, results from these cell-binding assays can shed light on the specificity and affinity of the radiotracer compared to its non-radiolabeled parent molecule, which can help predict the success of the radioligand *in vivo*. The uptake and internalization assays quantify the concentrations of the radiotracer taken into and retained within target cells, while washout (*i.e.* clearance kinetics) studies can provide clues as to the radiotracer's *in vivo* tumor residence times. For example, to demonstrate internalization, cells incubated with the radiotracer at 37 °C are collected at predetermined time points, washed, and treated with mildly acidic buffer to remove cell surface-bound radioactivity. The analysis of the activity in the cell pellet gives an indication of the degree and rate of internalization. As controls, cells that do not express the antigen can be used, and/or target-expressing cells can be incubated with the radiotracer at 4 °C to minimize endocytosis [32]. The data obtained in these experiments can be used to calculate endocytosis (k_e) and recycling (k_r) rate constants, assuming the simple two-compartment model described by Koening and Edwardson for G-protein-coupled receptors [33].

In Vivo Model Systems

Animal models play a critical role in determining the *in vivo* selectivity, specificity, biodistribution, and pharmacokinetic profile of a radiotracer. Of course, the animal model used in the evaluation of a radiopharmaceutical must be rationally linked to the scientific query. For example, non-human primates are often used prior to human studies during the development of imaging agents for neurological or psychiatric applications. Because mice are the most widely used model system for the evaluation of imaging agents and therapeutics in oncology, we will place emphasis on describing various murine models (Table 2) as well as the importance of selecting a particular model for the evaluation of a radiotracer.

Table 2 Characteristics of commonly used mouse models in oncology

Mouse strain	Description	Immune system status and tumor engraftment
Nude	The absence of thymus owing to spontaneous Foxn1 mutation	T-cell deficiency Normal B- or other myeloid-derived immune cells Intact innate immunity Tumor engraftment possible
SCID	Carries a CB17-Prkdcscid loss-of-function mutation causing defects in DNA protein kinase, resulting in downstream defects in the rearrangement of antigen-specific receptors on lymphocytes	T- and B-cell deficiency Develops thymic lymphoma Lifespan is less than 12 months Normal myeloid cells Radiosensitive Low level of human cell engraftment Variable level of tumor engraftment
NOD-SCID	Scid mutation on NOD background strain	Reduced NK and myeloid functionality Loss of C5 complement Lifespan is less than 12 months Prone to thymic lymphomas Moderate human immune engraftment Improved tumor engraftment
RAG 1^{null}/ $RAG1^{null}$	RAG1- and RAG2-knockout mice; impaired somatic mutation, resulting in the absence of somatic recombination in TCT and Ig genes	T- and B-cell deficiency Reduced NK cell immunity Radioresistant Variable immune cell engraftment
NSG	NOD.Cg-Prkdc ^{scid} IL2rg ^{tm1Wjl}/SzJ. NODscid mutation combined with IL2rg knockout mutation results complete loss of cytokine binding ability	T- and B-cell deficiency Reduced macrophage and dendritic cell function Lacks complement activity No thymic lymphomas Improved lifespan Very high lymphoid and myeloid cell engraftment Highest tumor engraftment
NOG	NOD.Cg-Prkdc^{scid} IL2rg $^{tm1Sug.}$NODscid mutation combined with IL2rg truncated intracytoplasmic domain; cytokine binding is possible	Similar to NSG mice (see above)
Hu-PBL-SCID	SCID mice transplanted with human PBMCs	Easy and quick T-cell engraftment Very few B or myeloid cells Prone to develop GvHD within few weeks due missing T-cell tolerance Preferred for GvHD studies
Hu-SRC-SCID	SCID mice transplanted with human CD34 + HSC	Reconstituted with multiple components of human immune system Upon transplantation, immune cell development takes place in the bone marrow and thymus of recipient mice Naïve T-cells H-2 restricted
huBLT	Surgical co-engraftment of human thymus and fetal liver in the kidneys as well as the intravenous delivery of autologous HSC	Reconstituted with multiple components of human immune system T-cell maturation on human MHC Repopulated human mucosal immunity Increased risk of GvHD/ wasting syndrome Requires the use of fetal tissue

BLT = bone marrow/liver/thymus, *GvHD* = graft-versus-host disease, *MHC* = major histocompatibility complex, *NOD* = non-obese diabetic, *PBMC* = peripheral blood mononuclear cell, *RAG* = recombination activating gene, *SCID* = severe combined immunodeficient

Cell Line-Derived Xenografts Xenografts generated by injecting human tumor cells into immune-deficient mice—*e.g.* nude or severe combined immunodeficient (SCID) mice—have been the cornerstone model for the validation of imaging and therapeutic agents for cancer for nearly three decades. The popularity of this approach is fueled by its ease of use, the rapid development of tumors, the reproducibility of the model, and the low costs associated with generating tumor-bearing mice. However, the model has notable flaws. A typical human tumor xenograft is generated by subcutaneously injecting 0.5–10 million cells, resulting in the formation of palpable tumor nodules in 4–6 weeks. The NCI-60 cancer cell line panel represents a collection of the best characterized cancer cells from which xenografts have been derived. While these so-called conventional cell lines are derived from human tumors, they have also been adapted to grow indefinitely in artificial culture conditions. As a result, these cell lines have been subjected to irreversible alterations in their biological properties as well as the loss of specific

cell populations or clones due to continued propagation [34]. The tumors developed using these cell lines are essentially a "human-in-mouse system," in which fully established human cancer cells are grown with the support of mouse stroma and vasculature. In addition, these tumors are homogenous and thus lack the genetic diversity seen in human tumors. Furthermore, the oncogenomic profiles of the cell lines we use represent only a limited combination of the wide spectrum of genetic and epigenetic mutations that are present in a given tumor type in the clinic. In practice, this means that one could overestimate the sensitivity of an imaging agent using a tumor model that consists of a homogenous cell population with high target expression, a scenario that most certainly does not reflect what goes on in the clinic. However, a selection of tumor xenografts with graded levels of molecular target expression can mitigate the shortcomings of this model system and thus improve the rigor of the evaluation of a radiotracer.

Patient-Derived Xenografts In recent years, patient-derived xenografts (PDXs) have surged in popularity as an alternative to xenografts derived from conventional cell lines. PDXs are established by directly transplanting a human tumor into immunocompromised mice and propagated for multiple passages in mice [35]. They have become a prominent model system to study cancer, as they faithfully represent the genetic diversity of primary human tumors. Indeed, PDXs allow us to capture the broad genetic diversity of cancers seen in the clinic. These model systems also provide an unprecedented opportunity to study molecularly targeted therapeutics and imaging agents in co-clinical trials, thereby advancing personalized medicine in real time [36]. However, the value of PDXs depends on their faithful representation of human tumors. It was shown recently that PDXs are genomically unstable and that the genetic stability of PDXs changes with passage number. Furthermore, increased copy number alterations were also observed with increasing passage number [37]. These passage-induced copy number alternations alter the genetic diversity of the PDX and can influence the response of the tumor to chemotherapeutics and targeted drugs. Importantly, these changes in target expression could also confound observations made using imaging agents.

Humanized Murine Models The limitations associated with using standard mouse models to study human cancer has led to the development of more elaborate model systems that increasingly recapitulate human disease situation. Along these lines, some components of the mouse immune system are incongruent with those of the humans [38]. That is particularly apparent in investigations related to deciphering the interactions between tumor cells and the immune system, which is critical to evaluating new immunotherapeutics. These concerns led to the development of "humanized" mouse models that can faithfully recapitulate the human immune system. Humanized mice are defined as "mice engrafted with functional human cells or tissues or expressing human transgenes." All humanized mouse models are developed using mouse strains with a severely compromised immune system that facilitates the engraftment of human cells. The three key strains include NOD.Cg-*Prkdc*^{scid}*Il2rg*^{tm1Wjl}(NSG), NODShi.Cg-*Prkdc*^{scid} *Il2rg*^{tm1Sug} (NOG), and 129S4- *Rag2*^{tm1Flv}*Il2rg*^{tm1Flv} (commonly referred to as BALB/c-*Rag2*^{null} *IL2rg*^{null} mice or BRG). Due to the mutations in the IL2 receptor common gamma chain (*IL2rg*^{null}), protein kinase DNA-activated catalytic polypeptide (*Prkdc*^{scid} or *scid*), and recombination activating gene (*Rag*) 1 or 2 (*Rag1*^{null} or *Rag2*^{null}), those mouse strains lack adaptive immunity and exhibit severe deficiencies of innate immunity, including the absence of murine natural killer (NK) cells, providing a unique environment for human cell engraftment. Humanized mice provide an opportunity to study species-specific agents that require human tissues and facilitate the study of the developing human immune response. They are increasingly being used in the evaluation of novel therapeutics that target and activate the immune system to kill cancer cells.

Three approaches are primarily used to engraft elements of the human immune system into immunodeficient *IL2rg*^{null}mice. The first and perhaps simplest model—known as Hu-PBL-SCID—is created by the injection of human peripheral blood leukocytes [39]. This model ensures the rapid engraftment of human T cells within a week. These mice, however, develop graft-versus-host disease within 4–8 weeks, providing only a short window for experimentation. However, the Hu-PBL-SCID model can be used to study the kinetics of imaging agents specific for cells of the human immune system [40]. The second model—known as Hu-SRC-SCID—is created by the intravenous or intra-femoral injection of human CD34+ hematopoietic stem cells (HSCs) derived from bone marrow (BM), umbilical cord blood (UBC), fetal liver, or G-CSF-mobilized peripheral blood. This model supports the engraftment of a complete human immune system and it has been used for studies that involve therapeutic monitoring, although all aspects of human T-cell development are not possible in this model due to the role that the mouse thymus plays in educating the immune system [41]. The third model—known as the bone marrow/liver/thymus (BLT) model—is established by transplanting human fetal liver and thymus under the kidney capsule and intravenously injecting autologous fetal liver HSCs. In this model, as with the Hu-SRC-SCID model, one can observe robust immune responses [42]. This model also has an advantage of T cells educated in an autologous human thymus as well as the delayed incidence of graft-vs-host disease. In the end, both models using HSCs provide a time window of 6–8 months to conduct experiments, and each is suitable

for protracted imaging studies involving the monitoring of immune system function.

An example of the use of humanized mice for the study of pharmacokinetics is provided by the humanized antibody pembrolizumab, which targets the programmed cell death protein 1 (PD-1). PD-1 is an inhibitory receptor that is expressed by activated T cells, regulatory T cells, B cells, natural killer cells, and some myeloid cell populations [43]. PD-1 regulates T-cell effector functions and plays a critical role in the modulation of immune responses within tumors. Two PD-1-targeted antibodies—pembrolizumab and nivolumab—have received approval from the United States Food and Drug Administration (US FDA). Patients receiving pembrolizumab show an overall response rate of 20–30% in a variety of tumor types, with 8–10% of patients reporting deleterious immune-related adverse events [44]. The *in vivo* disposition of these therapeutic agents is poorly understood. As a result, a radiolabeled derivative of pembrolizumab (or nivolumab) could aid in the characterization of the pharmacokinetics, tissue distribution, and intratumoral distribution of the antibody, all of which could be related to the effectiveness of treatment and could help guide therapeutic decisions. To this end, pembrolizumab conjugated with *p*-SCN-desferrioxamine (*p*-SCN-DFO), radiolabeled with the long-lived radionuclide zirconium-89 was evaluated in mouse and rat models [45]. In addition, PET imaging studies were conducted in NSG mice engrafted with human peripheral blood mononuclear cells. Generally speaking, the PET imaging studies showed accumulation of the radioimmunoconjugate in the spleen and kidneys, though the humanized mice also displayed faster elimination of [^{89}Zr]Zr-DFO-pembrolizumab compared to control NSG mice. One reason for the low blood pool activity could be the target-mediated clearance of the antibody that is often observed with anti-PD-1 antibodies [46]. The accumulation of high concentrations of radioactivity in the salivary glands was shown to be specific to PD-1, and the presence of PD-1-positive immune cells was confirmed by immunohistochemistry. Collectively, the results from this study demonstrate how humanized mice models can be indispensible in the evaluation of the *in vivo* behavior of radiolabeled antibodies.

Genetically Engineered Mouse Models (GEMMs) Murine models—one of the most experimentally tractable mammalian systems—have been instrumental in advancing our basic understanding of cancer biology and in promoting drug development [47]. Hundreds of "candidate genes" have been examined for their effects on cancer in mice during the quest to investigate the mechanisms contributing to the development and progression of cancer. GEMMs, which harbor the genetic aberrations of human tumors and phenocopy the human malignancy, have become a powerful resource for the assessment of candidate drugs, as they faithfully mimic the genetic and biological evolution of human malignancies. The candidate genes selected for GEMM models are based on hypotheses generated from our understanding of cancer cell lines and have provided valuable data on cancer incidence, progression, and adaptation to therapy. With the development of multiple genetic engineering strategies—such as CRISPER/Cas9 technology—one can now direct the expression of a gene of interest in a target tissue or throughout the entire mouse [48, 49]. New alleles that encode for the gene of interest can be inserted heritably into the genome of a mouse, or specific portions of the mouse genome can be selectively altered using knockout/knock-in technology. Routinely used GEMMs include (1) engineered models of reduced gene expression (knockdown or knockout), (2) engineered models of mouse gene overexpression (transgenic mice), (3) engineered models of human gene expression, and (4) models of drug treatment. Some examples of GEMMs that have improved our understanding of the onset and progression of disease include one example with Myc expression in the mammary epithelium that predisposed the mice to breast carcinoma as well as another with the expression of *k*-Ras, which predisposed acinar cells of the pancreas to pancreatic neoplasia [50, 51]. GEMMs have also become important tools in the evaluation of drug resistance. For example, several GEMMs have been created that incorporate a number of common mutations identified in NSCLC and used to study acquired resistance to therapy [52].

In combination with molecular imaging techniques, GEMMs could be used to monitor cancer progression, response to therapy, and relapse. However, the use of GEMMs in evaluating molecular imaging agents in cancer has been limited. Some examples include the use of the thymidine analog 3′-deoxy-3′-^{18}F-fluorothymidine ([^{18}F]FLT) for the PET imaging of tumor cell proliferation in a GEMM of high-grade glioma [53]. Another example is the use of the hu-CD20 knock-in mouse for the evaluation of CD20-targeted imaging agents. CD20 is a surface marker antigen that is present in greater than 90% of B-cell lymphomas. Novel CD20-targeted PET imaging agents have been developed and evaluated in huCD20-knock-in mice to gain a better understanding of the distribution of the therapeutic agent, as well as the specificity and distribution of the corresponding imaging agent [54].

In Vivo Validation Studies

It is important to choose the most relevant tumor models and animal species for *in vivo* studies. Among other things, the choice of an animal model has implications for deriving the necessary dosimetry data in support of an investigational new drug (IND) application. In addition, there are differences between species in how agents are metabolized,

which—not surprisingly—have substantial implications for the pharmacokinetic profile of a radiopharmaceutical. As noted by Li *et al.,* "…not a single animal species would behave like a (hu)man," and there is no "perfect" animal model [55].

A good example of interspecies differences is provided by the evaluation of thymidine-based imaging agents used to assess proliferation. Endogenous plasma thymidine levels are 100–300-fold higher in rats and mice compared to humans and dogs, a discrepancy that can dramatically influence the uptake of the radiotracer in the former due to increased competition from natural thymidine for thymidine kinase 1 [56]. As a result, dogs—rather than mice—are a better model system for the evaluation of these agents. In addition, humans show much higher hepatic uptake of the [^{18}F] fluorothymidine (FLT) and 1-(2′-deoxy-2′-fluoro-beta-D-arabinofuranosyl)thymine)(FMAU) than either mice or dogs due to differences in glucuronidation [56]. In order to keep these interspecies differences in perspective, focus should be placed on the application of comparative interspecies data during the design and subsequent analysis of animal experiments.

As discussed above, high target-binding affinity—denoted by a K_d value in the single digit nanomolar or sub-nanomolar range—is important to obtain high bound-to-free (B/F) radiotracer ratios and thus ensure high image contrast. In addition to affinity, a number of other factors can influence the B/F ratios as well, including protein binding, metabolism, and clearance. For all newly synthesized radiotracers, the biodistribution of the agent can be assessed by whole body PET or SPECT imaging. The time and concentration kinetics of the agent can be plotted by measuring the accumulated activity in various tissues using static images acquired at multiple time points after injection. In addition, whole body dynamic PET scans can be used to elucidate the time-activity curves of the radiotracer in different tissues and thus gain insight into the accumulation and clearance of the radiopharmaceutical in tumors and healthy organs (Fig. 4). These imaging data are often validated by *ex vivo* biodistribution studies. Data acquired at a series of time points and plotted in time vs. radioactivity concentration curves can provide insight into both the pharmacokinetic profile and biodistribution of an agent. Generally speaking, these results are expressed in terms of either percentage of injected dose per gram of tissue (%ID/g) or standardized uptake value (SUV).

In vivo studies of binding specificity are also critical to the development of radiopharmaceuticals. Indeed, it is necessary to demonstrate the specificity of a radiotracer *in vivo*, even for imaging agents with proven affinity *in vitro*. This is because *in vitro* affinity studies are often performed using a purified protein or using cell lines

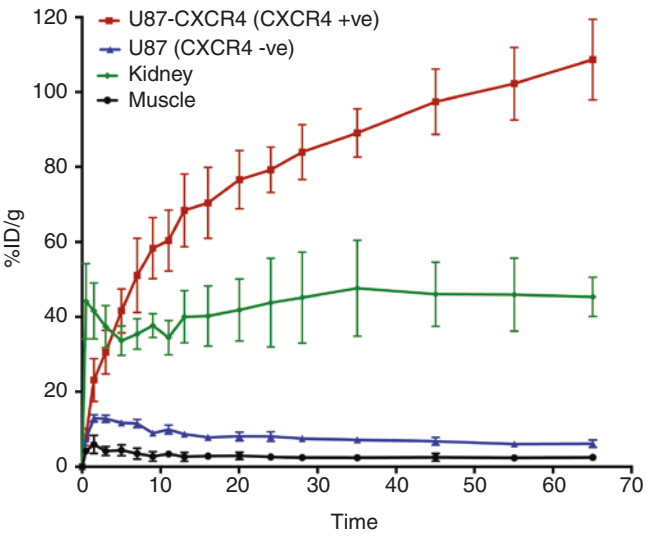

Fig. 4 Time-activity curves of [^{64}Cu]Cu-AMD3465— a CXCR4-specific imaging agent— in mice bearing subcutaneous U87 xenografts with stable CXCR4 expression. NOD/SCID mice bearing U87 and U87-stb-CXCR4 glioblastoma xenografts on the left and right flanks, respectively, were given approximately 9.25 MBq (250 mCi) of [^{64}Cu]Cu-AMD3465 via tail vein injection. Whole-body pseudo dynamic imaging was performed to measure the accumulation of the radiotracer for 70 min using an imaging sequence consisting of 16 frames with variable dwell times (2 × 60 s, 6 × 120 s, 4 × 240 s, and 4 × 600 s), and the resulting images were analyzed by region-of-interest analysis. Time-activity curves for various tissues show the uptake, distribution, and clearance of [^{64}Cu]Cu-AMD3465. Data represent the mean ± SD of 4 mice. (From De Silva *et al.* [32], with permission)

with known high molecular target expression and thus do not fully capture the complexity of the *in vivo* biological milieu. The *in vivo* specificity of a radiotracer is often demonstrated using blocking studies, which involve injecting an increasing amount of competing, nonradioactive ligand before, after, or with the radiopharmaceutical. To this end, a dose of the competing ligand below or at the lower end of the pharmacologically relevant dose should be used to minimize the pharmacological effects of the drug on the accumulation of the radiotracer. The appropriate dose generally lies in the mg/kg range. A significant decrease in the accumulation of the radiotracer (often 50–75% less than the positive control) should be observed during blocking studies to indicate at least a measure of specific binding. While conducting blocking dose studies, caution should be applied when using agonists, as they may prompt the internalization of the target and can lead to biological effects—including changes in blood flow, vascular permeability, and metabolism—that can confound the target-specific accumulation of the radiotracer.

In addition to these blocking studies, radioligands with lower affinity or peptides with scrambled sequences can also be employed as negative controls to help demonstrate

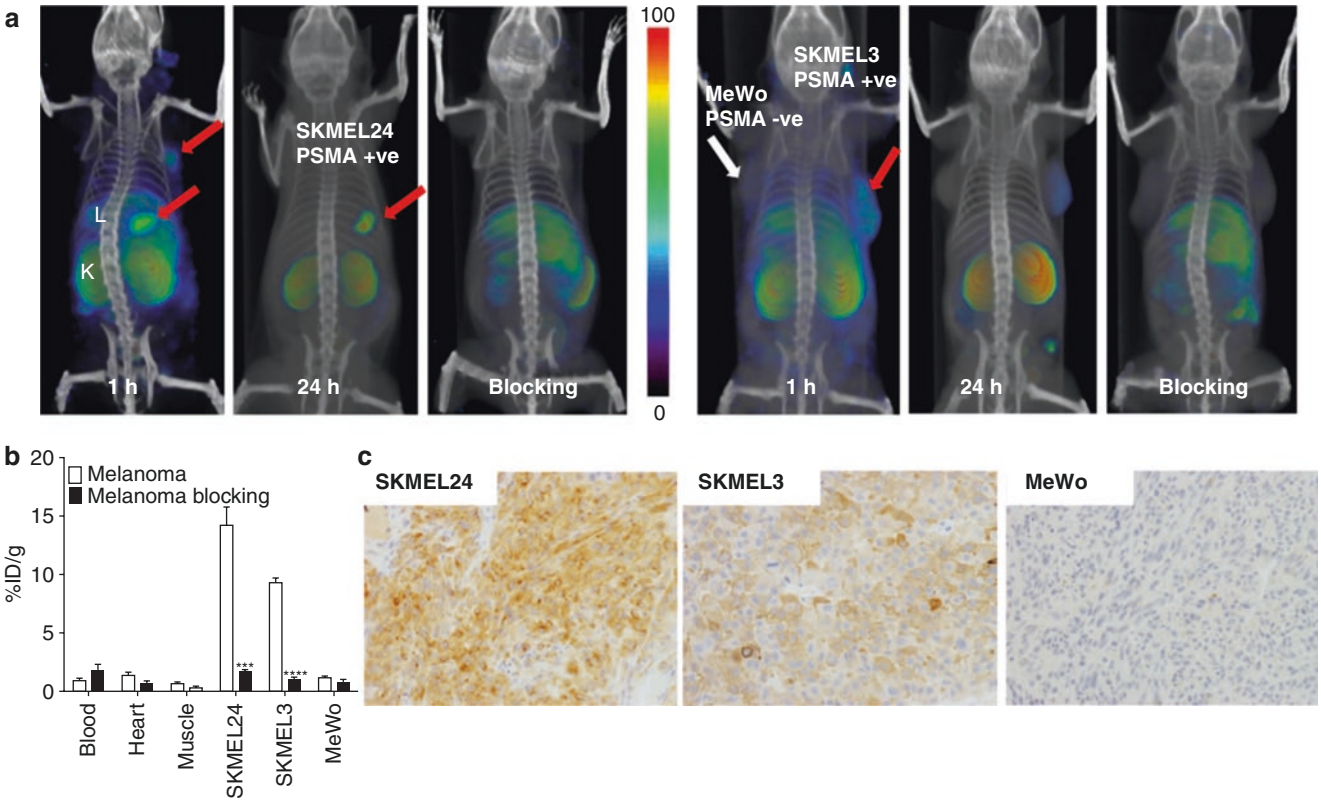

Fig. 5 Prostate-specific membrane antigen (PSMA) imaging in subcutaneous melanoma xenografts with a known PSMA-specific radiotracer, [^{125}I]DCIBzL. (**a**) PSMA-positive SKMEL24, SKMEL3, and PSMSA negative MeWo subcutaneous xenografts were established in male NOD/SCID mice, which were injected with 37 MBq (1 mCi) of [^{125}I]DCIBzL via tail vein. SPECT/CT images were acquired 1 and 24 h later. Arrows denote the tumors, while L = liver and K = kidney. (**b**) Mice bearing SKMEL24 or SKMEL3 and MeWo subcutaneous xenografts were intravenously injected with 74 kBq (20 μCi) of [^{125}I]DCIBzL, and biodistribution studies were performed at 1 h post injection. DCIBzL at 50 mg/kg was injected subcutaneously 30 min prior to the administration of [^{125}I]DCIBzL. The data are represented as the mean ± SEM for 4 mice. Asterisks represent significant differences: *** $P < 0.001$ and **** $P < 0.0001$. (**c**) Representative immunohistochemical staining images for PSMA obtained at 20× magnification from tumor-bearing mice of the same experimental cohort (From Nimmagadda *et al.* [8], with permission)

specificity. For small molecule-based radiotracers, pharmacologically inactive isomers are also a good option. Furthermore, it is often useful to use blocking agents of a different chemical class than the imaging agent to test specificity. However, if a blocking agent other than the identical nonradioactive analog is used, one must assure that both the radiopharmaceutical and the blocking agent have similar pharmacokinetic profiles and have been tested in the same tumor models.

Tumor models with no or low target expression can be used as negative controls as well. In the case of PSMA, for example, we have selected non-prostatic tumor models that are negative or low in PSMA expression as negative controls (Fig. 5). Furthermore, we have complemented those biological controls with blocking studies using a nonradioactive molecule that has the same pharmacokinetic profile as the PSMA imaging agent [8]. Finally, the use of knockout animals is another way to demonstrate the specificity of the radiotracer.

Radiolabeled Antibodies The evaluation of radiotracers based on monoclonal antibodies (mAbs) deserves special mention here. MAbs have many advantages as vectors for radiopharmaceuticals, including their high affinity, longer biological half-life, and low off-target effects. Most antibodies used as imaging agents are derivatives of immunoglobulins that were initially developed as therapeutics. Generally speaking, antibodies can be transformed into imaging agents via the conjugation of bifunctional chelators that bind to radiometals (*e.g.* zirconium-89 or indium-111) and to lysine moieties or via the direct radioiodination of tyrosine residues. However, such non-site-specific modification methods have their risks, as they produce heterogeneous radioimmunoconjugates and can reduce immunoreactivity by altering the antibody's antigen-binding domains [57]. An alternative to this approach lies on site-specific bioconjugation via antibody engineering or the manipulation of the antibody's heavy chain glycans [58].

In spite of their advantages, mAbs pose challenges as imaging agents and require several days to a week of clearance time before producing images with high contrast. The on- and off-rates of mAbs for their antigens are generally slower than those of small molecules, due to their high avidity. Furthermore—unlike small molecules—the interaction of a mAb with its target clearly affects its pharmacokinetic profile. More specifically, the binding of a mAb to its target may change the natural kinetics of the target by inducing its stabilization or internalization [59]. This phenomenon, known as target-mediated drug disposition (TMDD), is generally characterized by higher mAb clearance rates at lower antibody doses [60]. TMDD is common for mAbs directed against proteins expressed on cell membranes, such as the immune checkpoint protein PD-L1. TMDD results in nonlinear kinetics for antibodies at lower doses and linear kinetics at higher doses [61]. When TMDD is involved, the tumoral concentration of mAbs may be two to three orders of magnitude lower than the concentration in the plasma [62, 63]. Without question, this has implications for imaging. To circumvent this nonlinear kinetics phenomenon, it is important to conduct dose-optimization studies and find the optimal protein doses needed to achieve linear kinetics *in vivo*. With PD-L1-targeted antibodies, we have observed that a dose of at least 1 mg/kg protein is needed to achieve optimal image contrast [64].

Cohort Size in Preclinical Experiments The number of animals needed for a statistically viable preclinical study depends on the goal of the investigation. For example, more animals per time point are required to demonstrate target engagement than are needed for *in vivo* quantification of antigen expression. Our strategy has been to conduct pilot studies using at least five mice per cohort and then to use the results from these experiments to consult a biostatistician to deduce the numbers needed for more definitive studies. Generally speaking, we recommend using xenografts of multiple cancer types with variable levels of target expression. Finally, we strongly encourage a through reading of the article by Eckelman *et al.* that addresses the size of animal cohorts in the preclinical validation of imaging agents [65]. The statistical discussion in Chap. 30 of this book should be a valuable resource as well.

The Future

A significant and relatively new development in nuclear medicine is the expansion of the use of radiopharmaceuticals other than ^{18}F-fluorodeoxyglucose ([^{18}F]FDG). This trend is due in part to the plethora of new, clinically relevant imaging targets that have been uncovered through gene and protein arrays, some of which have enabled the subtyping of disease. In addition, there are also several new ways to generate affinity agents as well as more reliable cell lines and more relevant animal models which can be used to validate radiopharmaceuticals. A plethora of advances have also been made in radiosynthetic chemistry that has expanded the range of radiotracers to which researchers and clinicians have access. Finally, clinical PET scanners are becoming more sensitive and are providing images with higher resolution than before. Taken together, all of these developments make it particularly important that researchers both choose their targets wisely and ensure that their radiopharmaceuticals are evaluated in a thorough and rigorous manner using the appropriate techniques, cell lines, and animal models.

The Bottom Line

- Both a target with high levels of expression and a vector with high affinity are needed for the development of a successful radiopharmaceutical.
- High-specific activity is of paramount importance for receptor-binding radiotracers.
- Attention needs to be paid to the protein-binding properties of an imaging agent, as high levels of protein binding can reduce the concentration of free radioligand, even for agents with very high affinity for their target.
- The lipophilicity of a radiotracer can have a significant impact on its *in vivo* behavior.
- A battery of cell-based experiments—including binding, uptake, internalization, and washout assays—can be used to validate the specificity of a radiotracer and shed light on its potential *in vivo* behavior.
- Detailed information on the pharmacokinetic profile of a radiotracer can be obtained using static images collected at several time points, whole body dynamic imaging, or biodistribution studies performed at multiple time points.
- A variety of different murine models are available for the *in vivo* validation of radiopharmaceuticals, including mice bearing xenografts derived from human cell lines, mice bearing patient-derived xenografts, genetically engineered mouse models, and humanized mouse models. Each has its own set of advantages and disadvantages (Table 2).
- Human tumor xenografts of different cancer types and with graded levels of target expression are highly desirable and can improve the rigor of the validation of a radiotracer. These cell lines can be identified using the CCLE database.
- Attention must be paid to biological changes associated with the *in vitro* and *in vivo* passage of cell lines and PDXs.

- The investigation of antibody-based imaging agents should include determining the protein dose required to ensure high image contrast and the optimal accumulation of the radiotracer in the tumor.
- To increase reproducibility, the evaluation of a radiotracer should be performed over 2 or 3 days using the same model system and separate but identical groups of mice, with 5–8 mice per cohort.

Acknowledgments We gratefully acknowledge support from Allegheny Health Network-Johns Hopkins Cancer Research Fund, NIH R01CA166131, NIH R01CA236616, DoD W81XWH-16-1-0323, NIH R01 CA134675, NIH P30 CA006973, and NIH P41EB024495.

References

1. Cancer Genome Atlas Research N. Comprehensive genomic characterization defines human glioblastoma genes and core pathways. Nature. 2008;455(7216):1061–8.
2. Cancer Genome Atlas Research N, Weinstein JN, Collisson EA, Mills GB, Shaw KR, Ozenberger BA, et al. The Cancer Genome Atlas Pan-Cancer analysis project. Nat Genet. 2013;45(10):1113–20.
3. Weinstein IB, Joe AK. Mechanisms of disease: oncogene addiction--a rationale for molecular targeting in cancer therapy. Nat Clin Pract Oncol. 2006;3(8):448–57.
4. Rowe SP, Drzezga A, Neumaier B, Dietlein M, Gorin MA, Zalutsky MR, et al. Prostate-specific membrane antigen-targeted radiohalogenated pet and therapeutic agents for prostate cancer. J Nucl Med. 2016;57(Suppl 3):90S–6S.
5. Eiber M, Fendler WP, Rowe SP, Calais J, Hofman MS, Maurer T, et al. Prostate-specific membrane antigen ligands for imaging and therapy. J Nucl Med. 2017;58(Suppl 2):67S–76S.
6. Wustemann T, Haberkorn U, Babich J, Mier W. Targeting prostate cancer: prostate-specific membrane antigen based diagnosis and therapy. Med Res Rev. 2018 May 17. https://doi.org/10.1002/med.21508. [Epub ahead of print]
7. Rowe SP, Gorin MA, Salas Fragomeni RA, Drzezga A, Pomper MG. Clinical experience with (18)F-labeled small molecule inhibitors of prostate-specific membrane antigen. PET Clin. 2017;12(2):235–41.
8. Nimmagadda S, Pullambhatla M, Chen Y, Parsana P, Lisok A, Chatterjee S, et al. Low-level endogenous PSMA expression in nonprostatic tumor xenografts is sufficient for in vivo tumor targeting and imaging. J Nucl Med. 2018;59(3):486–93.
9. Chatterjee S, Behnam Azad B, Nimmagadda S. The intricate role of CXCR4 in cancer. Adv Cancer Res. 2014;124:31–82.
10. Mansfield AS, Dong H. Implications of programmed cell death 1 ligand 1 heterogeneity in the selection of patients with non-small cell lung cancer to receive immunotherapy. Clin Pharmacol Ther. 2016;100(3):220–2.
11. Sharma SK, Pourat J, Abdel-Atti D, Carlin SD, Piersigilli A, Bankovich AJ, et al. Noninvasive interrogation of DLL3 expression in metastatic small cell lung cancer. Cancer Res. 2017;77(14):3931–41.
12. Eckelman WC, Reba RC, Gibson RE, Rzeszotarski WJ, Vieras F, Mazaitis JK, et al. Receptor-binding radiotracers: a class of potential radiopharmaceuticals. J Nucl Med. 1979;20(4):350–7.
13. Jacobson O, Kiesewetter DO, Chen X. Fluorine-18 radiochemistry, labeling strategies and synthetic routes. Bioconjug Chem. 2015;26(1):1–18.
14. Barretina J, Caponigro G, Stransky N, Venkatesan K, Margolin AA, Kim S, et al. The Cancer Cell Line Encyclopedia enables predictive modelling of anticancer drug sensitivity. Nature. 2012;483(7391):603–7.
15. Sud A, Kinnersley B, Houlston RS. Genome-wide association studies of cancer: current insights and future perspectives. Nat Rev Cancer. 2017;17(11):692–704.
16. Behnam Azad B, Lisok A, Chatterjee S, Poirier JT, Pullambhatla M, Luker GD, et al. Targeted imaging of the atypical chemokine receptor 3 (ACKR3/CXCR7) in human cancer xenografts. J Nucl Med. 2016;57(6):981–8.
17. Burns JM, Summers BC, Wang Y, Melikian A, Berahovich R, Miao Z, et al. A novel chemokine receptor for SDF-1 and I-TAC involved in cell survival, cell adhesion, and tumor development. J Exp Med. 2006;203(9):2201–13.
18. Wani N, Nasser MW, Ahirwar DK, Zhao H, Miao Z, Shilo K, et al. C-X-C motif chemokine 12/C-X-C chemokine receptor type 7 signaling regulates breast cancer growth and metastasis by modulating the tumor microenvironment. Breast Cancer Res. 2014;16(3):R54.
19. Bostwick DG, Pacelli A, Blute M, Roche P, Murphy GP. Prostate specific membrane antigen expression in prostatic intraepithelial neoplasia and adenocarcinoma: a study of 184 cases. Cancer. 1998;82(11):2256–61.
20. Chang SS, O'Keefe DS, Bacich DJ, Reuter VE, Heston WD, Gaudin PB. Prostate-specific membrane antigen is produced in tumor-associated neovasculature. Clin Cancer Res. 1999;5(10):2674–81.
21. Ellis MJ, Gillette M, Carr SA, Paulovich AG, Smith RD, Rodland KK, et al. Connecting genomic alterations to cancer biology with proteomics: the NCI Clinical Proteomic Tumor Analysis Consortium. Cancer Discov. 2013;3(10):1108–12.
22. Vasaikar SV, Straub P, Wang J, Zhang B. LinkedOmics: analyzing multi-omics data within and across 32 cancer types. Nucleic Acids Res. 2018;46(D1):D956–D63.
23. Salas Fragomeni RA, Amir T, Sheikhbahaei S, Harvey SC, Javadi MS, Solnes LB, et al. Imaging of nonprostate cancers using PSMA-targeted radiotracers: rationale, current state of the field, and a call to arms. J Nucl Med. 2018;59(6):871–7.
24. Nimmagadda S, Pullambhatla M, Stone K, Green G, Bhujwalla ZM, Pomper MG. Molecular imaging of CXCR4 receptor expression in human cancer xenografts with [64Cu]AMD3100 positron emission tomography. Cancer Res. 2010;70(10):3935–44.
25. Vasilyev FF, Lopatnikova JA, Sennikov SV. Optimized flow cytometry protocol for analysis of surface expression of interleukin-1 receptor types I and II. Cytotechnology. 2013;65(5):795–802.
26. Hulme EC, Trevethick MA. Ligand binding assays at equilibrium: validation and interpretation. Br J Pharmacol. 2010;161(6):1219–37.
27. Maguire JJ, Kuc RE, Davenport AP. Radioligand binding assays and their analysis. Methods Mol Biol. 2012;897:31–77.
28. Pollastri MP. Overview on the rule of five. Curr Protoc Pharmacol. 2010;Chapter 9:Unit 9.12.
29. Waterhouse RN. Determination of lipophilicity and its use as a predictor of blood-brain barrier penetration of molecular imaging agents. Mol Imaging Biol. 2003;5(6):376–89.
30. Wang Z, Jacobson O, Tian R, Mease RC, Kiesewetter DO, Niu G, et al. Radioligand therapy of prostate cancer with a long-lasting prostate-specific membrane antigen targeting agent (90)Y-DOTA-EB-MCG. Bioconjug Chem. 2018;29(7):2309–15.
31. Pike VW. PET radiotracers: crossing the blood-brain barrier and surviving metabolism. Trends Pharmacol Sci. 2009;30(8):431–40.
32. De Silva RA, Peyre K, Pullambhatla M, Fox JJ, Pomper MG, Nimmagadda S. Imaging CXCR4 expression in human cancer xenografts: evaluation of monocyclam 64Cu-AMD3465. J Nucl Med. 2011;52(6):986–93.
33. Koenig JA, Edwardson JM. Endocytosis and recycling of G protein-coupled receptors. Trends Pharmacol Sci. 1997;18(8):276–87.

34. Gillet JP, Calcagno AM, Varma S, Marino M, Green LJ, Vora MI, et al. Redefining the relevance of established cancer cell lines to the study of mechanisms of clinical anti-cancer drug resistance. Proc Natl Acad Sci U S A. 2011;108(46):18708–13.
35. Aparicio S, Hidalgo M, Kung AL. Examining the utility of patient-derived xenograft mouse models. Nat Rev Cancer. 2015;15(5):311–6.
36. Chen Z, Cheng K, Walton Z, Wang Y, Ebi H, Shimamura T, et al. A murine lung cancer co-clinical trial identifies genetic modifiers of therapeutic response. Nature. 2012;483(7391):613–7.
37. Ben-David U, Ha G, Tseng YY, Greenwald NF, Oh C, Shih J, et al. Patient-derived xenografts undergo mouse-specific tumor evolution. Nat Genet. 2017;49(11):1567–75.
38. Zschaler J, Schlorke D, Arnhold J. Differences in innate immune response between man and mouse. Crit Rev Immunol. 2014;34(5):433–54.
39. Pearson T, Greiner DL, Shultz LD. Creation of "humanized" mice to study human immunity. Curr Protoc Immunol. 2008;Chapter 15:Unit 15 21.
40. England CG, Ehlerding EB, Hernandez R, Rekoske BT, Graves SA, Sun H, et al. Preclinical pharmacokinetics and biodistribution studies of 89Zr-labeled pembrolizumab. J Nucl Med. 2017;58(1):162–68.
41. Wang M, Yao LC, Cheng M, Cai D, Martinek J, Pan CX, et al. Humanized mice in studying efficacy and mechanisms of PD-1-targeted cancer immunotherapy. FASEB J. 2018;32(3):1537–49.
42. Walsh NC, Kenney LL, Jangalwe S, Aryee KE, Greiner DL, Brehm MA, et al. Humanized mouse models of clinical disease. Annu Rev Pathol. 2017;12:187–215.
43. Francisco LM, Sage PT, Sharpe AH. The PD-1 pathway in tolerance and autoimmunity. Immunol Rev. 2010;236:219–42.
44. Sun C, Mezzadra R, Schumacher TN. Regulation and function of the PD-L1 checkpoint. Immunity. 2018;48(3):434–52.
45. England CG, Ehlerding EB, Hernandez R, Rekoske BT, Graves SA, Sun H, et al. Preclinical pharmacokinetics and biodistribution studies of 89Zr-labeled pembrolizumab. J Nucl Med. 2017;58(1):162–8.
46. Ahamadi M, Freshwater T, Prohn M, Li CH, de Alwis DP, de Greef R, et al. Model-based characterization of the pharmacokinetics of pembrolizumab: a humanized Anti-PD-1 monoclonal antibody in advanced solid tumors. CPT Pharmacometrics Syst Pharmacol. 2017;6(1):49–57.
47. Gould SE, Junttila MR, de Sauvage FJ. Translational value of mouse models in oncology drug development. Nat Med. 2015;21(5):431–9.
48. Xue W, Chen S, Yin H, Tammela T, Papagiannakopoulos T, Joshi NS, et al. CRISPR-mediated direct mutation of cancer genes in the mouse liver. Nature. 2014;514(7522):380–4.
49. Heckl D, Kowalczyk MS, Yudovich D, Belizaire R, Puram RV, McConkey ME, et al. Generation of mouse models of myeloid malignancy with combinatorial genetic lesions using CRISPR-Cas9 genome editing. Nat Biotechnol. 2014;32(9):941–6.
50. Stewart TA, Pattengale PK, Leder P. Spontaneous mammary adenocarcinomas in transgenic mice that carry and express MTV/myc fusion genes. Cell. 1984;38(3):627–37.
51. Quaife CJ, Pinkert CA, Ornitz DM, Palmiter RD, Brinster RL. Pancreatic neoplasia induced by ras expression in acinar cells of transgenic mice. Cell. 1987;48(6):1023–34.
52. Rottenberg S, Jonkers J. Modeling therapy resistance in genetically engineered mouse cancer models. Drug Resist Updat. 2008;11(1–2):51–60.
53. Bradbury MS, Hambardzumyan D, Zanzonico PB, Schwartz J, Cai S, Burnazi EM, et al. Dynamic small-animal PET imaging of tumor proliferation with 3′-deoxy-3′-18F-fluorothymidine in a genetically engineered mouse model of high-grade gliomas. J Nucl Med. 2008;49(3):422–9.
54. Natarajan A, Hackel BJ, Gambhir SS. A novel engineered anti-CD20 tracer enables early time PET imaging in a humanized transgenic mouse model of B-cell non-Hodgkin's lymphoma. Clin Cancer Res. 2013;19(24):6820–9.
55. Li AP. Overview: hepatocytes and cryopreservation – a personal historical perspective. Chem Biol Interact. 1999;121(1):1–5.
56. Bading JR, Shields AF. Imaging of cell proliferation: status and prospects. J Nucl Med. 2008;49(Suppl 2):64S–80S.
57. Lindmo T, Boven E, Cuttitta F, Fedorko J, Bunn PA Jr. Determination of the immunoreactive fraction of radiolabeled monoclonal antibodies by linear extrapolation to binding at infinite antigen excess. J Immunol Methods. 1984;72(1):77–89.
58. Houghton JL, Zeglis BM, Abdel-Atti D, Aggeler R, Sawada R, Agnew BJ, et al. Site-specifically labeled CA19.9-targeted immunoconjugates for the PET, NIRF, and multimodal PET/NIRF imaging of pancreatic cancer. Proc Natl Acad Sci U S A. 2015;112(52):15850–5.
59. Liu H, Rajasekaran AK, Moy P, Xia Y, Kim S, Navarro V, et al. Constitutive and antibody-induced internalization of prostate-specific membrane antigen. Cancer Res. 1998;58(18):4055–60.
60. Tabrizi MA, Tseng CM, Roskos LK. Elimination mechanisms of therapeutic monoclonal antibodies. Drug Discov Today. 2006;11(1–2):81–8.
61. Herbst RS, Soria JC, Kowanetz M, Fine GD, Hamid O, Gordon MS, et al. Predictive correlates of response to the anti-PD-L1 antibody MPDL3280A in cancer patients. Nature. 2014;515(7528):563–7.
62. Baxter LT, Zhu H, Mackensen DG, Butler WF, Jain RK. Biodistribution of monoclonal antibodies: scale-up from mouse to human using a physiologically based pharmacokinetic model. Cancer Res. 1995;55(20):4611–22.
63. Deng R, Bumbaca D, Pastuskovas CV, Boswell CA, West D, Cowan KJ, et al. Preclinical pharmacokinetics, pharmacodynamics, tissue distribution, and tumor penetration of anti-PD-L1 monoclonal antibody, an immune checkpoint inhibitor. MAbs. 2016;8(3):593–603.
64. Chatterjee S, Lesniak WG, Gabrielson M, Lisok A, Wharram B, Sysa-Shah P, et al. A humanized antibody for imaging immune checkpoint ligand PD-L1 expression in tumors. Oncotarget. 2016;7(9):10215–27.
65. Eckelman WC, Kilbourn MR, Joyal JL, Labiris R, Valliant JF. Justifying the number of animals for each experiment. Nucl Med Biol. 2007;34(3):229–32.

Preclinical Experimentation in Neurology

Kristina Herfert, Sabina Marciano, Laura Kuebler, Sabrina Buss, Natalie Landeck, Julia G. Mannheim, and Hanna Napieczynska

Fundamentals

Over the past decade, many novel positron emission tomography (PET) tracers for the central nervous system (CNS) have been developed and have contributed valuable insights to our understanding of the function of the brain. The human brain is the most complex organ in the human body, and even today, we know relatively little about how the brain is organized and how it performs its very sophisticated functions. The main cell types of the human brain are neurons and glia cells. Each cell type is responsible for distinct functions, which are mediated in a highly specialized manner by an array of receptors, transporters, ion channels, enzymes, second messengers, and cytokines. PET imaging has contributed immensely to our understanding of the changes in the brain in various diseases. Furthermore, PET studies are frequently used in pharmaceutical science to study the interactions of drugs with receptors and make correlations between the dose of the drug and the resulting response. One limiting factor to this burgeoning area of research, however, has been the limited availability of selective PET tracers for particular brain targets such as receptors, ion channels, glia cells, and enzymes. Recent progress in the development of dedicated small animal PET scanners with high sensitivity and resolution has led to the design and development of many promising CNS PET tracers and contributed tremendously to our understanding of brain functions in neurodegenerative and neuropsychiatric disorders (Fig. 1).

K. Herfert (✉) · S. Marciano · L. Kuebler · S. Buss
J. G. Mannheim
Department of Preclinical Imaging and Radiopharmacy, University of Tübingen, Tübingen, Germany
e-mail: kristina.herfert@med.uni-tuebingen.de

N. Landeck
Department of Experimental Medical Science, Lund University, Lund, Skane, Sweden

H. Napieczynska
Department of Animal Phenotyping, Max Delbrück Center for Molecular Medicine, Berlin, Germany

The development of PET radiotracers is an expensive and long process because many criteria need to be fulfilled before a PET tracer can be translated to the clinic (Table 1). Perhaps the most basic criterion is a chemical structure that allows for the incorporation of short-lived radionuclides such as carbon-11 ($t_{1/2}$ = 20.4 min) or fluorine-18 ($t_{1/2}$ = 109.7 min). In addition, the compound must also have a high affinity for the intended target (typically <1 nM) as well as a high selectivity for the target relative to other, structurally similar biomolecules (ideally >30–100-fold).

The affinity of a radiotracer for its target is typically represented by the reciprocal value—($1/K_d$)—of its equilibrium dissociation constant (K_d), while the number of binding sites in a volume of interest is represented by the B_{max} value. Both of these values can be determined in preliminary *in vitro* assays, which are fast and cost-effective compared to *in vivo* studies or *in vitro* experiments performed on human brain tissue slices or homogenates. The binding affinity required to make a good tracer is dependent on the value of B_{max}. If the number of binding sites for the radiotracer is low, a higher target affinity—and thus a lower K_d value—is needed to ensure a sufficient signal relative to non-specific binding (NSB). Conversely, if the number of binding sites for the radiotracer is high, a lower target affinity is required to produce adequate signal-to-noise ratios (SNR). In addition, it is important to note that if the binding affinity is too high, equilibrium might not be reached on the timescale of *in vivo* imaging, making the reliable quantification difficult. Therefore, a ratio of $B_{max}/K_d \geq 10$ is considered to be a good rule of thumb [1].

A suitable CNS PET tracer must also penetrate the BBB sufficiently to produce good uptake in the brain while clearing from the brain quickly with low non-specific binding. The ability of a tracer to penetrate the BBB is not only dependent on its size and charge but also on its lipophilicity, a trait regularly expressed in terms of log *P* values, where *P* is the *n*-octanol/water partition coefficient of the un-ionized species. High log *P* values indicate high lipophilicity, while low log *P* values indicate low lipophilicity. The correspond-

J. S. Lewis et al. (eds.), *Radiopharmaceutical Chemistry*, https://doi.org/10.1007/978-3-319-98947-1_34

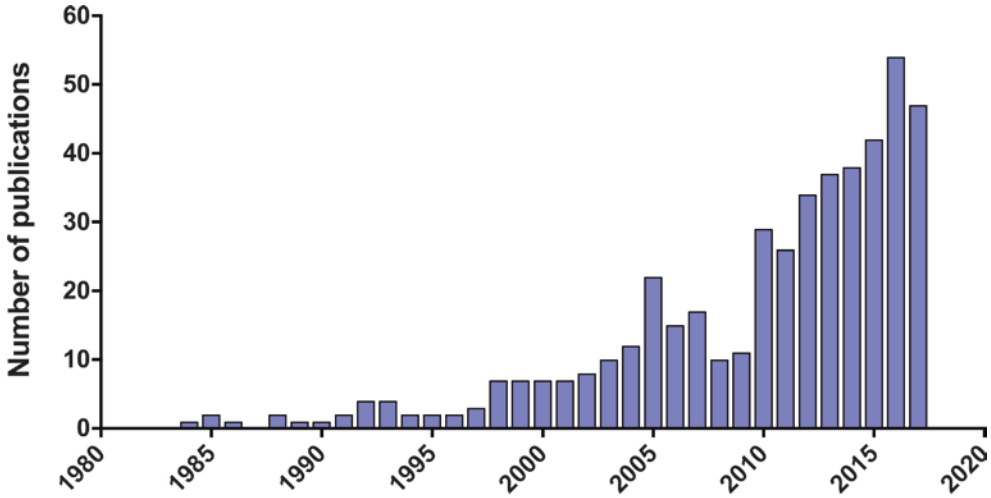

Fig. 1 The number of publications found in PubMed using the search criteria "PET tracer development brain." The graphic shows a steadily increasing number of results over the past 20 years

Table 1 Characteristics needed for an ideal CNS PET tracer

PET tracer characteristics	Criteria	Preclinical experiments
Favorable structure	Chemical structure allows for the incorporation of short-lived PET radionuclides (carbon-11 and fluorine-18)	Predefined by radiochemist
In vitro target specificity	*In vitro* affinity in the single-digit nanomolar range; $B_{max}/K_d \geq 10$	Saturation binding assay; *in vitro* AR
In vitro target selectivity	Low *in vitro* affinity to similar targets (K_d >30–100-fold)	Saturation binding assay; *in vitro* AR
Delivery to the brain	Good BBB penetration (SUV >1.5); low plasma protein binding	Biodistribution and PET experiments in healthy mice or rats
Clearance from the brain	1 < log *P*/log *D* <3; low non-specific binding (NSB)	PET experiments in healthy mice or rats
Metabolites	No brain-permeable radioactive metabolites, signal from parent tracer	Blood sampling after *in vivo* injection into rats and mice
Plasma protein binding	Low plasma protein binding	*In vitro* serum stability testing and *in vivo* blood sampling
In vivo target specificity	Binding to target; high signal-to-noise ratio	PET experiments in animal models of human disease and cross validation with IHC
In vivo target selectivity	No observable binding to similar targets	PET experiments in animal models of human disease and cross validation with IHC

AR autoradiography, *IHC* immunohistochemistry

ing distribution coefficient at physiological *pH* is termed $D_{7.4}$. Generally speaking, compounds with moderate log $D_{7.4}$ values of 2.0–3.5 penetrate the BBB well. Lower lipophilicity can prevent the passive membrane penetration of radiotracers because membranes are made of a lipid bilayer with a hydrophobic core. However, if the log $D_{7.4}$ value of a tracer is too high, the tracer may not be able to cross the BBB due to its non-specific binding to proteins in the blood. Another disadvantage of high lipophilicity is that it can enhance the non-specific binding of the radiotracer to white matter—which is largely composed of the lipid-rich substance myelin surrounding axons and nerve cells—leading to high background signals. Regardless of its log *P* or log $D_{7.4}$, a tracer will be metabolized by enzymes within the liver as part of the elimination process, ultimately transforming it into a more hydrophilic molecule. Along these lines, it is particularly important that the radiolabeled metabolites of a radiotracer cannot penetrate the BBB, because the signal from brain-permeable radio metabolites cannot be distinguished from the signal produced by the parent radiotracer, leading to bias in the quantification of images.

Ultimately, if the battery of *in vitro* tests (*vide infra*) suggest that the radiotracer possesses favorite properties, the delivery, clearance, metabolism, and plasma protein binding of the radiotracer must then be determined *in vivo*. Indeed, after the completion of these basic evaluation experiments, proof-of-principle studies are carried out in carefully selected animal models of human disease. In the following sections, we will describe the basic *in vitro* and *in vivo* experiments needed to validate a brain-targeted nuclear imaging agent.

Basic *In Vitro* Experiments to Validate a Brain-Targeted Nuclear Imaging Agent

The development of a brain-targeted nuclear imaging tracer starts with the creation of a lead compound that is subjected to several possible modifications. Testing each of these

derivatives *in vivo* would be very expensive and time-consuming and involve a high failure rate. Thus, potential compounds are screened *in vitro* for their log *P* or log $D_{7.4}$ values as well as their binding affinity and specificity for their molecular target using variants labeled with long-lived radionuclides such as tritium or iodine-125. Then, the most promising candidates are labeled with the desired positron-emitted radionuclide and subjected to a similar collection of *in vitro* tests.

Binding Assays

The most commonly used *in vitro* binding assays are saturation and competition binding experiments to either determine the affinity of the radiotracer for a target molecule or the affinity of an unlabeled ligand for a target molecule (see below). These experiments can either be performed using filters (filter-binding assays) or scintillator-coated plates (scintillation proximity assays) (Fig. 2). The choice of the assay mainly depends on the available equipment in the lab (since some scintillation counters can either read out plates or filters) and on the target molecule used in the assay. While filters are restricted by a certain pore size, the use of scintillator-coated plates is dependent on the adherence of the target molecule to the plate during incubation and washing. This needs to be tested in advance.

In a scintillation proximity assay, a scintillator-coated plate is incubated with the target molecule (Fig. 2a). To avoid the non-specific binding of the radiotracer to the plate, a non-reactive protein (*e.g.* BSA) is used to block any non-specific binding sites. If the radiotracer specifically binds the target molecule, the vicinity of the β^--emitting isotope to the bottom of the scintillator-coated well results in the emission of light, which is detected by a liquid scintillation counter.

In a filter-binding assay, the radiotracer and the target molecule are incubated together in solution using filter plates (Fig. 2b). Vacuum filtration is applied to separate target-bound radiotracer from free radiotracer, which is washed away through the filter. Subsequent washing steps are performed to reduce the non-specific binding of the radiotracer to the filter. The addition of the scintillator to the dried filter results in the emission of light due to the proximity of the β^--emitting radionuclide. In contrast, β^+-emitters trapped in the filter induce the release of γ-radiation which can be measured in a γ-counter.

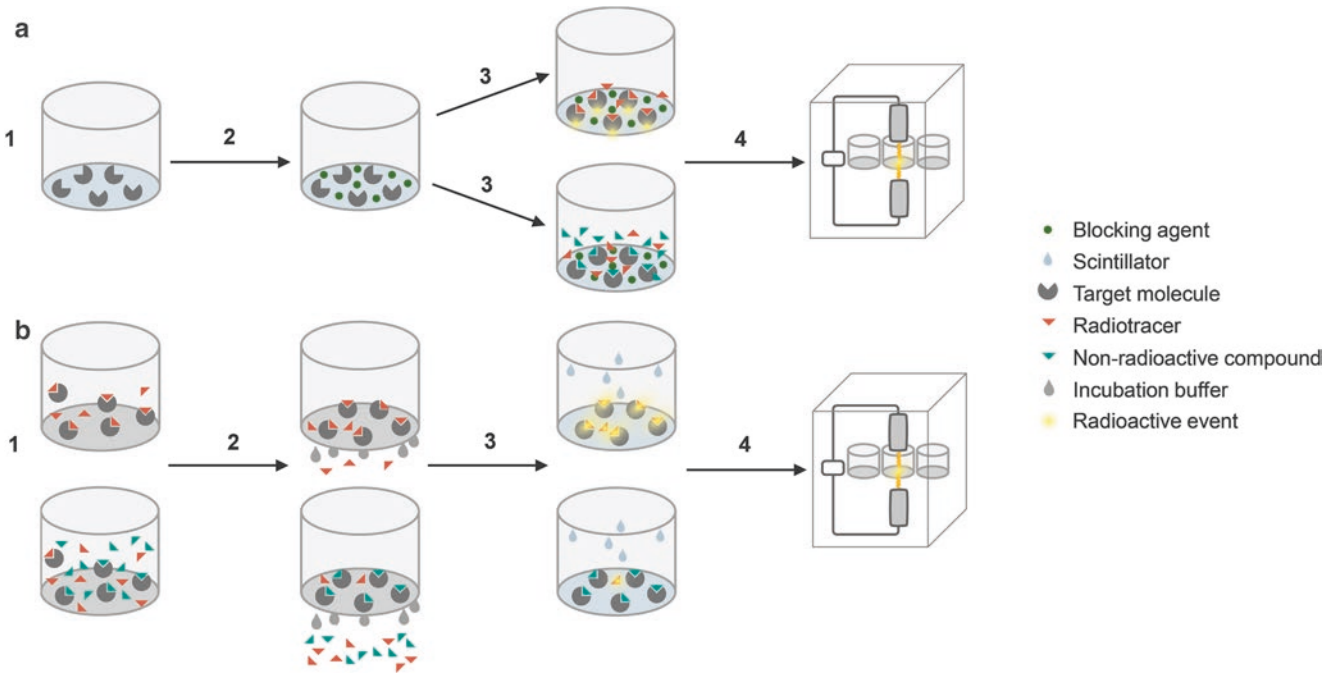

Fig. 2 (**a**) Scintillation proximity assay (SPA): (1) the target protein is incubated on a scintillator-coated plate. (2) A consecutive blocking step reduces the non-specific binding to the plate. (3) For total binding, the radiotracer dissolved in assay buffer is added to the wells. To determine non-specific binding, radiotracer and an excess of the nonradioactive compound are added to a second set of plates. (4) Light—produced by the proximity of the low-energy β^--emitters to the scintillator-coated plate—is detected in a scintillation counter. (**b**) Filter-binding assay (FBA): (1) the radiotracer and target protein are incubated in solution on a filter plate to determine total binding (TB). For the determination of non-specific binding, a nonradioactive compound is added in excess in a second set of filter plates. (2) Subsequently, vacuum filtration is used to separate bound from free radiotracer. Afterwards, several washing steps are applied to remove non-specifically bound radiotracer. (3) The scintillator is added to each well of the filter plate. (4) Light emitted by the scintillator is detected by a scintillation counter

Saturation Binding Assay In a saturation binding experiment, the target density B_{max} and the dissociation rate constant K_d are calculated using increasing concentrations of the radiotracer added to a constant concentration of the target molecule to derive the total binding. The non-specific binding (NSB) is determined in a second set of binding reactions containing an excess of the unlabeled compound. The amount of the radiotracer used in a saturation experiment should vary from 1/10 of the estimated K_d to 10 × K_d, while the concentration of the target molecule and the amount of unlabeled compound (1000 × K_d) are kept constant. From the resulting TB and non-specific binding curves, B_{max} and K_d values can be estimated from nonlinear regression analysis (Fig. 3a). The specific binding (SB) is calculated by subtracting the NSB from the total binding. Since the binding affinity is defined as $1/K_d$, small K_d values represent a high binding affinity. Below, we describe a protocol for a saturation binding assay using a tritium-labeled ligand in a 96-well plate and the filtration assay format:

1. Label glass tubes for total binding ("TB") and non-specific binding ("NSB") and note their respective radiotracer concentration (*e.g.* 12 nM TB, 6 nM TB, etc.; 12 nM NSB, 6 nM NSB, etc.).
2. Prepare the assay buffer (put half of it on ice!).

Assay buffer			
Component	M.W.	Quantity	Mass for 1 liter
Tris	121.14 g/mol	50 mM	6 g

If the radioligand is highly lipophilic, different concentrations of ethanol (5–20%) or BSA (0.1–1%) may be added to the incubation buffer. Adjust each buffer to $pH = 7.4$.

3. When working with tritium, wear two gloves and change them every 10 min! Work carefully to avoid the contamination of surfaces and personnel.
4. Prepare a stock solution of the radiolabeled compound. The volume of tracer needed is dependent on the number of wells used in the experiments. When working in 96-well plates, a volume of 150 µL is used for each well. An example calculation is shown below:

Tracer molar activity (MA)	87 Ci/mmol
Radioactivity concentration	1 mCi/ml
Final concentration of stock	48 nM
Final volume needed	5 ml

$$C_1 = \frac{\text{Activity}}{\text{Tracer volume}} \times \frac{1}{\text{MA}} = 1\left[\frac{\text{mCi}}{\text{ml}}\right] \times \frac{1}{87\left[\frac{\text{Ci}}{\text{nnol}}\right]} \quad (1)$$

$$= 1.15 \times 10^{-5} \frac{\text{mol}}{\text{l}}$$

$$C_2 = 48 \times 10^{-9} \frac{\text{mol}}{\text{l}} \quad (2)$$

$$V_2 = 0.0051 \quad (3)$$

$$V_1 = \left(\frac{C_2 \times V_2}{C_1}\right) = \frac{\left(48 \times 10^{-9} \frac{\text{mol}}{\text{l}} \times 0.0051\right)}{1.15 \times 10^{-5} \frac{\text{mol}}{\text{l}}} = 21\,\mu l \quad (4)$$

5. Prepare a dilution series of the stock solution of the tracer starting from 10 times the estimated K_d (ideally 8–10 dilutions) using the glass tubes labeled with "TB."
6. Divide each dilution in half and add to the second set of tubes labeled "NSB."
7. Add the non-labeled compound in 1000-fold excess to each of the "NSB" tubes.

   Note: Now you should have a dilution series of the radiolabeled compound and a second dilution series of the radiolabeled compound which also contains 1000× *excess of the non-labeled compound.*
8. Add a fixed concentration of the target molecule diluted in PBS (50 µL/well) to a 96-well filter plate; use triplicates for each concentration.
9. Add the solutions of radiotracer to the plate containing the target molecule (150 µL/well) (see Fig. 2b). Keep in mind that final target and tracer concentrations will change.
10. Incubate the plate (200 µL/well) for the chosen time and temperature on a shaker to ensure constant agitation during the radiotracer incubation. The incubation time should be long enough to allow for equilibrium conditions and can be reduced in an incubator at 37 °C.
11. Before using the harvester for vacuum filtration, wash the harvester 2–3 times with 50% ethanol and assay buffer.
12. Position the plate in the harvester and apply vacuum filtration.
13. Wash the filter plate 3× with ice-cold washing buffer to remove any residual, non-specifically bound radiotracer.
14. Let the filters dry completely (*e.g.* with a microwave, a drying cabinet for 1 h at 60 °C, or overnight at room temperature).
15. Add an adequate volume of scintillator to each well and count the filter plate in a scintillation counter.
16. Calculate the mean counts per minute (cpm) values as well as the standard deviations for the triplicates for TB and NSB, and transfer these data to analysis software (*e.g.* GraphPad Prism).
17. For conversion into molar units (cpm/fmoL), convert the cpm values into disintegrations per minute (dpm) by taking both the counter efficiency (e) and the molar activity of the radiotracer into account:

$$\text{dpm} = \frac{\text{cpm}}{\text{efficiency}} \tag{5}$$

$$\frac{\text{cpm}}{\text{fmol}} = \text{molar activity}\left(\frac{\text{Ci}}{\text{mmol}}\right)\times\left(2.22\times10^{12}\,\frac{\text{dpm}}{\text{Ci}}\right)\times e\left(\frac{\text{cpm}}{\text{dpm}}\right) \tag{6}$$

$$1\,\text{mmol} = 10^{12}\ \text{fmol} \tag{7}$$

$$\frac{\text{cpm}}{\text{fmol}} = \text{molar activity}\times 2.22\times e \tag{8}$$

Divide the cpm value by the cpm/fmoL value calculated using Eq. 8 as well as the volume (in L) to obtain fmoL/L:

$$\frac{\text{fmol}}{\text{L}} = \frac{\text{cpm}}{\text{SA}\times 2.22\times e\times V} \tag{9}$$

Calculate the amount of bound radiotracer in fmoL or pmoL per nmoL of added target molecule using the following equation:

$$\frac{\text{bound radiotracer}\left[\text{fM}\right]}{\text{added target molecules}\left[\text{nM}\right]} = \frac{\text{bound radiotracer}\left[\text{fmol}\right]}{\text{added target molecules}\left[\text{nmol}\right]} \tag{10}$$

18. To calculate B_{max} and K_d, plot the radiotracer concentration in nM (x-axis) against the total and non-specific binding in pmoL/nmoL (y-axis), and analyze the resulting curve via nonlinear regression using "One site – Fit Total and Nonspecific Binding" in GraphPad Prism software.

Competition Binding Assay In a competition binding assay, the binding of a single concentration of the radiotracer to a constant concentration of the target molecule is measured in the presence of various concentrations of an unlabeled competitor to indirectly determine the affinity of the competitor for the target. In a competition binding plot (Fig. 3b), radioligand binding is expressed as a function of the added concentration of the competitor. Since these concentrations usually span a large range, they are expressed on a logarithmic scale. Competition binding assays can be divided into homologous and heterologous experiments. In a homologous competition assay, the radiolabeled compound and the competitor are identical. In a heterologous competition assay, the chemical structures are different. Competition binding assays are generally used to determine the affinity of a newly synthesized compound for a specific target. Since radiolabeling is fairly expensive, the K_d value cannot always be measured directly in a saturation experiment. The equilibrium dissociation constant of the unlabeled competitor, K_i, calculated in a competition experiment should be the same as the K_d value of the radiolabeled form of the same drug. To

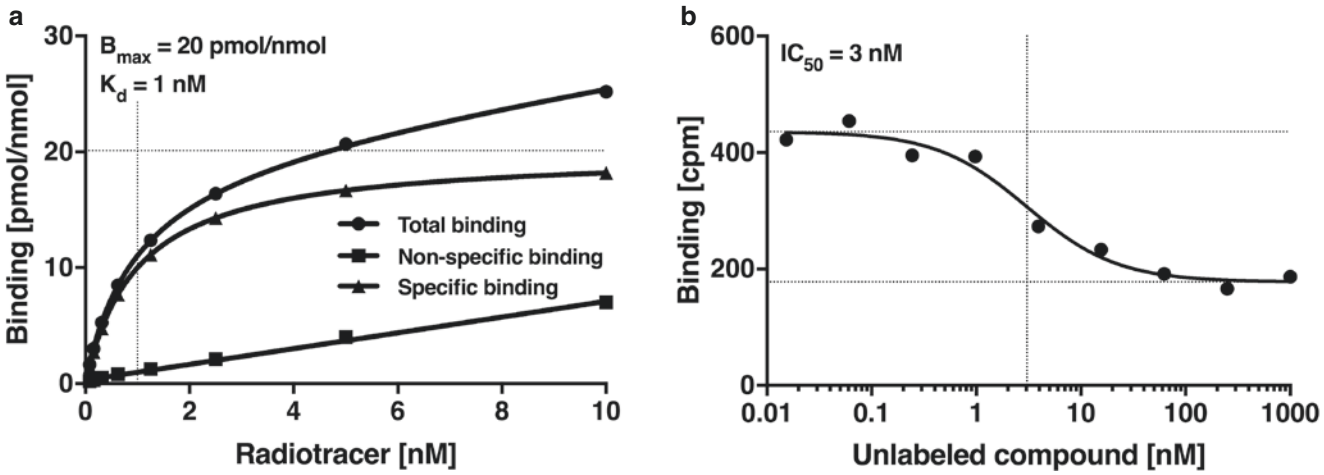

Fig. 3 (**a**) In a saturation binding assay, fixed concentrations of the target molecule are incubated with increasing concentrations of the radiotracer to calculate the total binding. Non-specific binding is achieved in a second set of binding experiments containing an excess of a non-radioactive compound. To obtain the specific binding curve, the non-specific binding curve is subtracted from the total binding curve. B_{max}—the amount of available binding sites per target molecules—is indicated by the horizontal dotted line and approaches the specific binding curve at saturation. The dissociation constant, K_d, is denoted by the vertical dotted line and is defined as the concentration of radiotracer needed to achieve half-maximum binding ($B_{max}/2$). (**b**) In a competition binding experiment, a single radiotracer concentration and increasing concentrations of a non-radioactive compound are used to calculate the specific binding of the radiotracer at equilibrium. The IC_{50}—defined as the concentration of non-radioactive compound that inhibits 50% of the binding of the radiotracer—can be determined graphically by drawing an intersection at the half-maximum (*black vertical line*) of the fit through the competition curve

calculate the K_i value in a competition experiment, the K_d value of the radiotracer needs to be known. The K_i value is calculated from the following equation [2]:

$$K_i = IC_{50} / \left(1 + \frac{[L]}{K_d}\right) \quad (11)$$

in which L is the concentration and K_d is the dissociation constant of the radiotracer, determined from a saturation binding experiment.

The IC_{50} calculated in a competition experiment is defined as the concentration of competitor at which 50% of the radiolabeled compound binding is inhibited. In contrast to the K_i value—which can be compared from data that have not been collected under identical conditions—IC_{50} values depend on the target molecule concentration used. Therefore, IC_{50} values can only be compared if they were obtained under strictly identical conditions, *i.e.* the same source of the target molecule and the same concentration of the same radioligand.

The following general protocol can be used for competition binding assays using the filtration binding assay format:

1. Label tubes with different concentrations of the unlabeled compound (8–12 concentrations) (*e.g.* 1000 nM to 0.1 nM).
2. Prepare the assay buffer as described above (put half of it on ice!).
3. When working with tritium, wear two gloves and change them every 10 min! Work carefully to avoid the contamination of surfaces and personnel.
4. Prepare a solution of the radiolabeled compound. The radiolabeled ligand should have a high affinity for the target molecule, and the concentration should be about 1× the K_d value and should provide sufficient count rates. If higher concentrations are used, higher concentrations of the unlabeled ligand will be needed to compete for half of the radioligand binding sites. The volume of tracer needed is dependent on the number of wells used in the experiments. When working in 96-well plates, a volume of 150 µL can be used for each well.
5. Prepare a dilution series of the non-labeled compound (competitor) starting from 1000 times the estimated K_d of the radiotracer and add these solutions to the fixed concentration of the radiotracer.
6. Add a fixed concentration of the target molecule diluted in PBS (50 µL/well) to a 96-well filter plate, and add the radiotracer/inhibitor solutions to the plates (150 µL/well) as well. Use triplicates for each concentration. Keep in mind that final target and tracer concentrations will change.
7. Incubate the plates (total of 200 µL/well) for the chosen time and temperature on a shaker to ensure constant agitation during the radiotracer incubation. The incubation time should be long enough to allow for equilibrium conditions and can be reduced in an incubator at 37 °C.
8. Before using the harvester for vacuum filtration, wash the harvester 2–3 times with 50% ethanol and assay buffer.
9. Position the plate in the harvester and apply vacuum filtration.
10. Wash the filter 3× with ice-cold washing buffer to remove any residual, non-specifically bound radiotracer.
11. Let the filters dry completely (*e.g.* with a microwave, a drying cabinet for 1 h at 60 °C, or overnight at room temperature).
12. Add an adequate volume of scintillator to each well and count the filter plate in a scintillation counter.
13. Calculate the mean counts per minute (cpm) values as well as the standard deviations for the triplicates, and transfer this data to analysis software (*e.g.* GraphPad Prism).
14. To calculate IC_{50} or K_i values, plot the calculated cpm values (y-axis) against the logarithmic concentration of the competitor (x-axis). Analyze by nonlinear regression using "One site – Fit logIC_{50}" or "One site – Fit K_i" in GraphPad Prism software.

Binding Assays Using Positron-Emitting Radionuclides All of the binding assays described above can be adapted for compounds labeled with positron-emitting radionuclides such as carbon-11 and fluorine-18. In these cases, however, a γ-counter or radio-HPLC must be used as detection method.

The Optimization of Assay Performance

Several different *in vitro* binding assays can be used to screen compounds for potential *in vivo* applications. Depending on the information desired, saturation or competition binding assays are performed as described above. However, if a binding assay is established for a novel radiotracer and target molecule, several factors have to be considered in advance in order to ensure the reliable quantification of the data. In the following section, we will discuss some of the most important practical aspects of implementing radiotracer binding assays.

The Choice of the Concentration of Radiotracer The concentration of radiotracer used in each assay is determined by the amount of available binding sites as well as the K_d value, non-specific binding, and specific activity of the radiotracer. These factors—together with buffer conditions and incubation times—determine the number of counts in the assay. For the reliable quantification of data, this number of

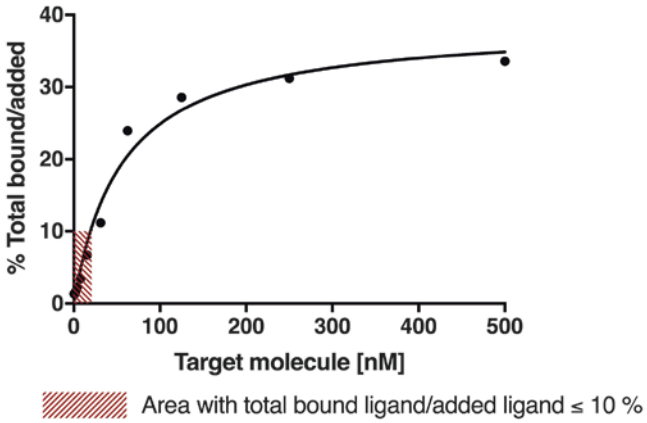

Fig. 4 To determine the optimal concentration of the target molecule for radiotracer binding studies, the radioactivity (% total bound/added ligand) is plotted as a function of the increasing concentration of target. Concentrations at which ≤10% of the radiotracer is bound (hatched area) are optimal and should be used for binding experiments

counts needs to be high enough to clearly differentiate between the total and non-specific binding. As a rule of thumb, the counts measured for the non-specific binding need to be less than 50% of the counts measured for the total binding at the highest concentration of radiotracer that is used ($10 \times K_d$). The amount of non-labeled compound to be added in excess depends on the affinity of the radiolabeled compound toward the target molecule ($1000 \times K_d$) [3, 4].

The Choice of the Concentration of Target Molecule The determination of the concentration of target molecule needed is a critical step in the development of the assay. This is due to the fact that the amount of radiotracer needs to exceed the amount of available binding sites in order to avoid radiotracer depletion. To graphically determine the optimal concentration of the target molecule, the radioactivity (% total bound/added radiolabeled compound) is plotted against the concentration of the target molecule. The concentration at which ≤10% of the added ligand binds to the target molecule (the hatched area in Fig. 4) is considered optimal. Levels of 10–30% are still acceptable but may compromise the reliability of the estimated parameters, while levels of 50% will invalidate the experiment entirely [3, 4].

Incubation Time and Temperature

In order to reliably determine the values of B_{max} and K_d in a saturation binding assay, the binding reaction needs to be at equilibrium. This is dependent on the association and dissociation rates of the radiotracer-target molecule complex. For a detailed description, please refer to Hulme and Trevethick (2010) [4].

Non-specific Binding In a filter binding experiment, the free radiotracer is separated from the bound radiotracer via vacuum filtration through a filter membrane. Non-specifically bound radiotracer can be removed by washing the filter several times with a washing buffer. This low-affinity binding is usually non-saturable, increases linearly with increasing tracer concentrations, and can be subtracted from the total binding curve to calculate the specific binding in a saturation binding experiment. To ensure that the radiotracer-target molecule complex does not dissociate during the washing procedure, it is recommended to use ice-cold washing buffer. The optimal buffer composition is highly dependent on the target molecule and radiotracer in the experimental approach. Therefore, the optimal pH, type and concentration of organic solvent, type of detergent (*e.g.* Triton X-100, Tween 20), and type of buffer (*e.g.* HEPES, Trizma) need to be determined for each experiment. In addition, it is important to remember that under some circumstances, the concentration of radiotracer and non-labeled compound on the filter can approach the molecule's critical aggregation concentration, resulting in the formation of aggregates in the filter that increase the apparent amount of non-specific binding.

In Vitro Autoradiography

In vitro autoradiography is used to determine the binding specificity of a radiolabeled molecule for brain tissue sections. Ideally, human brain sections are used if the tracer is being developed for clinical use. However, since human brain slices are very valuable and difficult to obtain, validation experiments are often performed using brain sections from healthy or diseased animals (depending on the target protein). There are three types of autoradiography: whole-body autoradiography, tissue autoradiography, and micro-autoradiography. Most small animal PET scanners have a maximum spatial resolution of ~1.2–1.5 mm full width at half maximum (FWHM) in the center of the field of view (FOV) as well as a rather small FOV. As a result, whole-body AR is performed to determine the distribution of the tracer in the whole animal with high resolution after its intravenous (*i.v.*) injection. As its name suggests, tissue autoradiography is used with tissue slices of organs of interest. Finally, micro-autoradiography is used to visualize the distribution of radiotracers on a cellular and subcellular level. In this section, we will focus on tissue autoradiography, since it is most commonly used for the development of PET radiotracers.

Binding Experiments with Tritiated Ligands Autoradiography binding experiments are performed using either phosphor screens or X-ray film. The main advantage of phosphor screens compared to X-ray film is the much shorter exposure times needed due to the higher sensitivity. While X-ray film

needs to be exposed to the tissue for several weeks, the phosphor screens only require few days of exposure. In addition, since X-ray film is highly sensitive to light, a dark room and a developer solution are needed. This also requires careful handling and some practical experience. Phosphor screens are less sensitive to light, and the readout is performed using a phosphor imaging device. However, one major limitation of tritium-sensitive phosphor screens has been their reusability. Since ß⁻-emitters have low radiation energy (18.6 keV for tritium), the screens must be placed very close to the tissue in the cassettes. This can result in the contamination of the very expensive screens. Another problem with phosphor screens is their loss of sensitivity over time due to the accumulation of moisture (which leads to increased background noise). Therefore, we recommend correcting for background noise or using plates for no more than 2–3 months. Another important factor to consider is the spatial resolution of each approach. While phosphor screens have an intrinsic spatial resolution of 50 µm, the resolution of X-ray film is <1 µm. For most receptor binding experiments, a spatial resolution of 50 µm is sufficient. However, if small target structures are investigated, X-ray film may be preferred to phosphor imaging plates.

For the accurate quantification of the autoradiography data, reusable tritium tissue standards can be obtained. However, decay correction needs to be considered when using older standards. In addition, X-ray screens have a smaller linear range than phosphor screens, and therefore, standards with maximum activity concentrations up to 20 MBq/g are usually sufficient. Table 2 summarizes the characteristics of film and phosphor screens.

Table 2 Comparison of X-ray film and phosphor screen for autoradiography

	H-3		F-18
Characteristics	X-ray film	Phosphor screen	Phosphor screen
Spatial resolution	<1 µm	~ 50 µm	~ 470 µm [4]
Sensitivity	Low	High (decrease over time)	High
Exposure time	8–12 weeks	1 week	10 half-lives (~ 1 day)
Handling	Difficult (dark room, developer solution)	Simple (phosphor imager)	Simple (phosphor imager)
Costs	Low	High, screens not reusable	Reusable, tracer costs are high
Linear range	Small	High	High

Binding Experiments with PET Tracers Autoradiography-based binding experiments can also be performed with radiotracers labeled with positron-emitting radionuclides. However, due to its low sensitivity, X-ray film would require long exposure times that are incompatible with the short half-lives of many of the most common positron-emitting radionuclides. In contrast, the higher sensitivity of phosphor screens allows for short exposure times (usually on the order of ten half-lives of the radionuclide) and thus the reliable quantification of images. However, there are several factors that need to be taken into account when using PET radiotracers in autoradiography experiments. One major limitation is the loss in the spatial resolution due to the range of the positron. For fluorine-18, for example, a tenfold loss of resolution—to about 500 µm—has been determined [5, 6].

Another factor to consider is that activity standards have to be prepared for each experiment (see below). These can be obtained via the addition of serial dilutions of the tracer—usually in the range of 10–1000 kBq/g tissue—to brain tissue homogenates. This is, however, a time-consuming process and difficult to apply when working with short-living nuclides such as carbon-11. An alternative, easier approach to this problem is the use of thin-layer chromatography (TLC) plates. In this method, 5 µL of serial dilutions of the tracer are applied to the TLC plates and exposed to the phosphor screens together with the tissue slides. It is also important to note that the molar activity of the tracer can vary between syntheses and experiments. Indeed, the amount of tracer (MBq) added to the buffer in order to obtain a certain concentration will vary as a function of the molar activity (GBq/µmol).

The following is a representative protocol for an *in vitro* autoradiography experiment:

I. *Data Acquisition*
   1. The preparation of brain tissue slices for saturation experiments:
      (a) Remove the brain from the animal.
      (b) Add Tissue-Tek® and use ice spray until frozen. Keep the brain at −80 °C until needed.
      (c) Prepare 20-µm-thick cryosections from the part of the brain containing your region of interest.

      Note: Use sequential brain slices to determine total and non-specific binding.
   2. Prepare the incubation and washing buffers (put the washing buffer on ice!).

Preincubation buffer			
Component	M.W.	Quantity	Mass for 1 liter
Tris	121.14	50 mM	6 g
NaCl	58.44	150 mM	8 g

Incubation buffer			
Component	M.W.	Quantity	Mass for 1 liter
Tris	121.14	50 mM	6 g
NaCl	58.44	150 mM	8 g
Ascorbic acid	176.13	0.1%	1 g

Wash buffer			
Component	M.W.	Quantity	Mass for 1 liter
Tris	121.14	50 mM	6 g

3. Prepare the tracer solution (for calculations, see binding assay).
4. Leave the slides outside of the freezer for 15 min so that they can reach room temperature.
5. Put the slides in preincubation buffer for 20 min at room temperature.
6. Incubate the slides for 45–60 min with the appropriate tracer solution. Add 750 µL of the solution of radiotracer to each slide. Make sure that the tissue is fully covered and that the incubation solution does not contain any air bubbles. Alternatively, incubate several slides in a glass dish containing the solution of radiotracer.
7. Wash the slides 3 × 10 min with ice-cold washing buffer.
8. Dip the slides in distilled cold water for 3 s and then wait until they have dried.
9. Put the slides—including the standards slides—in a cassette and expose them to a phosphor plate. The exposure time to the phosphor plate should be about ten half-lives of the PET tracer (3–4 h for C-11, 18–24 h for F-18). If the experiments are performed with tritiated ligands, films or tritium-sensitive phosphor screens can be used. The exposure time to a phosphor screen should be about 1 week. For the same tracer, the exposure time to X-ray film is about 8–12 weeks.
10. For experiments with tritiated ligands, quantify the scintillation counts by adding 100 µL of the tracer stock solution to 10 mL scintillation solution (leave the pipette tip in the tube, as tritium can stick to the tube).
11. Count each vial 3 times in a scintillation counter and calculate the mean value (15,000–30,000 dpm should be reached).
12. Prepare the standards:
    (a) Manually homogenize brain tissue and make 8–10 aliquots.
    (b) Add serial dilutions of the tracer to the homogenized tissue (10–1000 kBq/g tissue) and mix well.
    (c) Freeze the brain tissue containing the tracer and prepare 20-µm-thick cryosections.

If the same experiment is repeated at a different time point and quantitative values need to be compared, the scintillation counts should be similar between the two experiments for a reliable comparison. Therefore, the stock solution of the second experiment should be prepared by adjusting the scintillation counts to values similar to those used in the first experiments using the following steps:

II. *Preparation of stock solution for retest experiments:*
    1. When preparing the stock solution, add the tritium solution in only 2/3 of the incubation buffer (*e.g.* in 17 mL, if 25 mL of stock solution is needed).
    2. Add 100 µL of this solution to 10 mL of the scintillation solution (leave the pipette tip in the tub, as tritium can stick to the tube).
    3. Count each vial 3 times in the counter and calculate mean counts.
    4. Calculate the amount of buffer that needs to be added to the 2/3 stock solution:

    Factor = amount in the counter/amount wanted (*e.g.* ~20,000 counts or as in a previous experiment)

    Factor × 2/3 solution = total

    Total – 2/3 solution = amount of buffer that needs to be added to the 2/3 stock solution

III. *Image analysis* (*ImageJ open-source software*):
    1. Before you start, download the plugin for Fuji format on the ImageJ home page; save ISAC Manager in plugin folder.
    2. Make a standard curve from the standards:
        (a) Draw regions of interest (ROIs) over the standards. Calculate the mean intensity values of your phosphor screen or X-ray film and copy and paste them to a spreadsheet (= y-axis). X-axis = activity concentration of the standard (for tritium standards, it is provided with the standard from the company and needs to be decay-corrected).
        (b) Place one ROI in the background for background noise correction (set the value to a zero concentration or subtract this value from other values).
        (c) Fit the data with nonlinear regression and enable data interpolation in the analysis tab.
    3. To make sure that the maximum intensity value of your brain tissue slices is in the pseudo-linear range of the standard curve, draw ROIs over the whole brain slices. Ensure that you do not include any dirt or other contaminants on the film or phosphor screen, as this will provide a falsely high maximum value.
    4. Draw ROIs over the tissue of interest and in the background of each slice and add the mean intensity value to the standard curve.
    5. Interpolate the activity concentration values from the standard curve and convert to fmol/mg using the following equation:

$$\frac{\text{value interpolated from standard curve}\left[\frac{\text{nCi}}{\text{mg}}\right]}{\text{molar activity}\left[\frac{\text{nCi}}{\text{fmol}}\right]} = \text{value}\left[\frac{\text{fmol}}{\text{mg}}\right] \quad (12)$$

Basic *In Vivo* Experiments to Validate a Brain-Targeted Nuclear Imaging Agent

The Determination of Delivery and Clearance Using PET

Injection Route In neurology, PET imaging can provide insight into the biochemical, neurochemical, and pharmacological processes underlying brain disease. In rodent PET studies, the radiotracer is preferably injected *i.v.*, either by a fast bolus, by a bolus plus a constant infusion or by constant infusion. This ensures the rapid delivery of the radiopharmaceutical to the brain, which is important if kinetic modeling is performed to calculate binding parameters. One disadvantage of the *i.v.* injections is the possibility of paravenous administration, which results in the slow diffusion of the radiopharmaceutical into the blood and therefore the slow delivery of the tracer to the brain. This affects the K_1 value—the tracer delivery constant from plasma to tissue—and therefore, the PET measurement may need to be repeated.

Other routes of administration might be considered according to the study design and radiotracer used. Intraperitoneal injections—validated for [^{18}F]FDG rat and mice brain PET studies [7, 8]—allow for the administration of larger volumes of radiotracer (up to 10 mL/kg) compared to *i.v.* injections (which are commonly restricted to 5 mL/kg according to animal welfare guidelines). This provides a significant advantage for administering painful substances, which often need to be diluted. The disadvantages of this application route include irritation to the surrounding tissue in longitudinal studies with repeated injections and the less efficient delivery of the radiotracer to the brain because of the passage of the compound through the portal system and its biotransformation in the liver. In addition, kinetic modeling cannot be applied due to the slow delivery of the tracer to the brain. Finally, administration through inhalation can be performed for gaseous radiotracers such as [^{15}O]O_2 and [^{15}O]CO_2. Wider input function peaks will result from the inhalation, which can be neglected if the purpose of the experiment is to reach a steady state. If bolus administration is desired, the gaseous tracer can be mixed with blood and injected *i.v.*.

A typical setup for a brain PET imaging procedure in rodents:

I. Preparing the animal for the placement of the *i.v.* catheter:
   A. Place the animal in an anesthesia box saturated with 1.5–2.5% isoflurane vaporized in oxygen gas for about 5 min at a flow rate of 1.0 L/min.
   B. Move the animal to a warming pad with a mask for the inhalation of anesthesia on a plane table to ensure a constant temperature.
   C. Place eye ointment over the animal's eyes to avoid eye desiccation.
   D. Place the tail into a cup filled with warm water to foster vasodilatation and the visualization of the tail veins.
   E. Place the catheter (materials provided in Table 3) into the tail vein as close to the end of the tail as possible in order to facilitate more attempts and to avoid clotting and inflammation. Indeed, multiple perforations may damage the vein, meaning that following injections can only be performed on its proximal part (Fig. 5).
   F. Flush the catheter with heparinized saline to avoid blood coagulation. If the catheter is properly placed, the saline will flush very smoothly.
   G. Apply a thin layer of tape or glue to help secure the catheter in position.

II. Preparing the animal for the *i.v.* injection of the radiotracer on the PET scanner:
   A. Place the animal on a dedicated rat or mouse (brain) bed on the PET scanner and keep the body temperature constant (ideally 36.5 °C) with a rectal temperature probe with a feedback mechanism. Insert stereotactic holders into the ears to avoid head motion during the scan time.
   B. Center the rodent brain in the FOV of the PET scanner.
   C. Start the acquisition of the PET and administer the tracer *i.v.* shortly thereafter.
   D. After the collection of the images, remove the catheter needle and press a swab over the injection site to stop any bleeding and prevent the backflow of the PET tracer.

Table 3 Materials used for intravascular mouse and rat catheters

	Cannula needle	Microtubing	Syringe
Mouse	BD Microlance™ 3, 30G	0.28 × 0.6 mm	BD U40 insulin
Rat	BD Microlance™ 3, 25G	0.40 × 0.8 mm	BD U40 insulin
Rat	24G BD Insyte	None	Injekt® F Braun

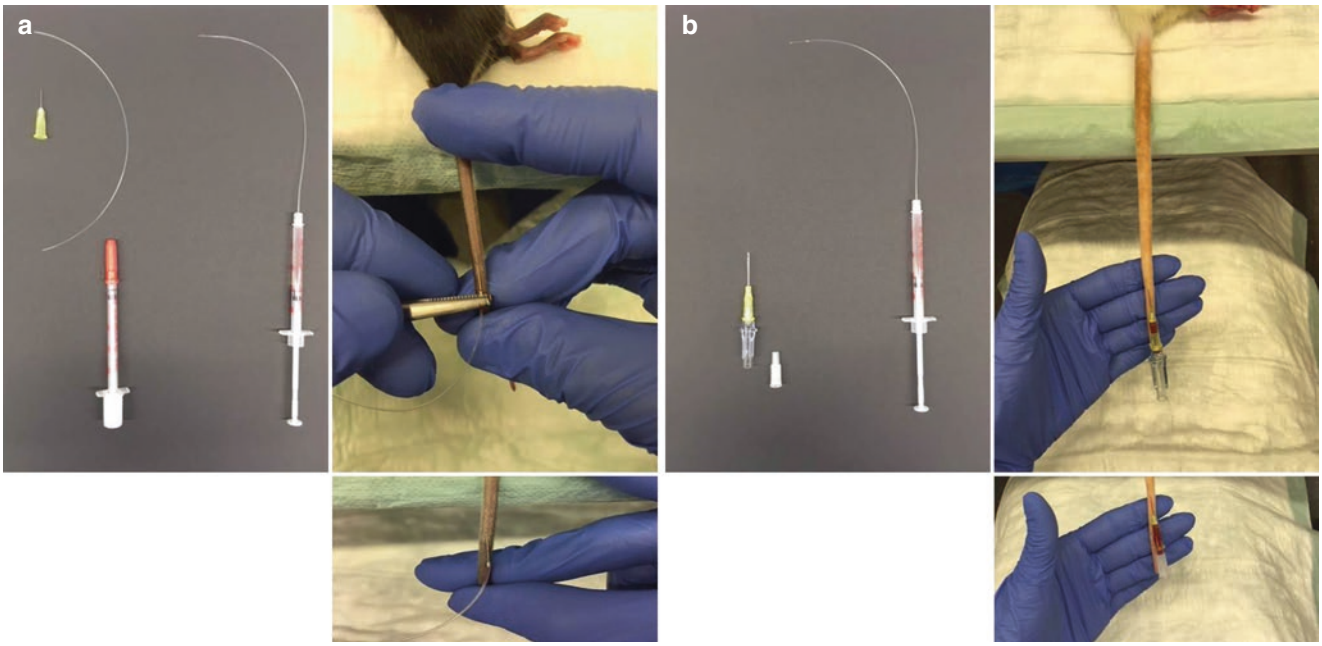

Fig. 5 (**a**) Mouse catheter. A 30G needle is inserted into a flexible tube connected to a syringe filled with heparinized saline. After insertion into the tail vein, the syringe is exchanged with one containing the radiotracer after the start of the PET acquisition. (**b**) Rat catheter. The use of a catheter with a 24–25 G needle is preferable in rats to avoid blood coagulation and reduce the dispersion of radioactivity in the inner walls. The catheter is placed as far as possible from the heart. Blood backflow indicates correct placement, and tape can be used to fix the catheter in position

Anesthesia A few brain PET imaging studies have been carried out in conscious animals using head fixation devices that can minimize motion artifacts [9, 10]. However, rodents need to be extensively trained to get used to this sort of experimental setup, and the immobilization of the head can induce stress and alter physiological processes, obfuscating the interpretation of the data. Therefore, most PET experiments are carried out in anesthetized rodents. Anesthetics such as ketamine and pentobarbital have a very low safety margin and can produce experimental errors due to variability in the depth of induced anesthesia. Thus, volatile anesthetics are preferred due to their hypnotic, analgesic, and relaxant effects. In addition, they are easy to induce and rapidly reversible. Among these, isoflurane is the most commonly used anesthetic because of its low respiratory and cardiovascular depression. Nevertheless, care must be taken when administering isoflurane, because rodents can develop hypothermia (body temperature below 35 °C). The use of heating mats and rectal probes to monitor the temperature of the mouse as well as the administration of the anesthetic according to the animal weight is crucial for the animal survival. Most importantly, the application of anesthetics will impact the delivery and clearance of the radiotracer to and from the brain and will also impact the expression state of some receptors. Of course, these factors must be considered during the interpretation of PET data. Indeed, several PET studies have reported anesthesia-induced changes in the binding of radiotracers to the dopamine receptor and in the regional cerebral blood flow and metabolism of oxygen and glucose [11, 12].

Reconstruction The process of reconstruction translates the raw data of a PET scan into an actual image. However, the algorithms used for reconstruction can influence the quality and quantification accuracy of images. A common algorithm for the reconstruction of brain PET scans is the two-dimensional (2D) filtered back projection (FBP) algorithm due to its fast and robust nature. However, image quality can be affected by low SNR and reduced contrast. This can be improved by integrating oblique lines of response to the reconstruction—from 2D to three-dimensional (3D) image space—or using iterative algorithms like ordered subset expectation maximization (OSEM) instead [13, 14]. OSEM provides images with high quality and signal-to-noise ratios as well as better contrast and spatial resolution. In a pilot study, we determined ~10% higher [^{11}C]raclopride binding values in the rat striatum using the 3D-OSEM algorithm compared to 2D-FBP and ~25% higher using a maximum a posteriori (3D-MAP) algorithm (Fig. 6). In addition, due to the higher sensitivity, OSEM reconstruction outperforms FBP when between-group differences (*e.g.* baseline and blocking) need to be evaluated [15]. The relatively long computing time needed for the 3D-OSEM or MAP algorithms compared to 2D algorithms is their biggest limita-

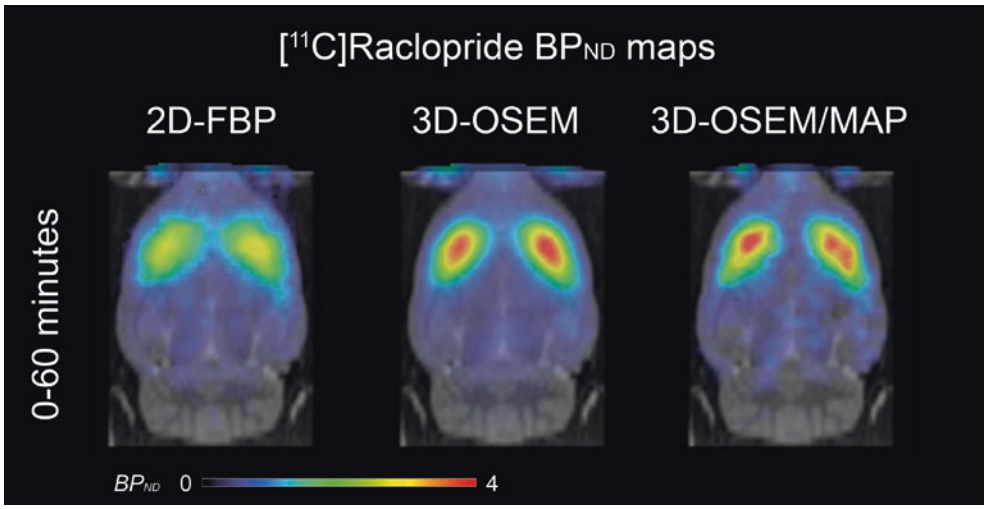

Fig. 6 Comparison of different reconstruction algorithms for a [^{11}C] raclopride brain PET scan of a rat: 2D-FBP, 3D-OSEM, and 3D-OSEM/MAP. The BP_{ND} maps were calculated using pixel-wise modeling and the Logan reference model with the cerebellum (CER) as a reference region. Notably, quantitative values are affected by the reconstruction algorithm

tion, though this can be ameliorated by using dedicated reconstruction clusters. In general, problems with image quality and quantification accuracy are exaggerated when working with PET data with poor statistics, *e.g.* dynamic PET data processed with short frame lengths or having a low count rate. Indeed, [^{11}C]raclopride binding values are underestimated when the PET data are processed with short time frames and reconstructed with OSEM [16]. Hence, reconstruction algorithms should be carefully evaluated for each study and applied to achieve the best trade-off between quantification accuracy, image quality, count statistics, and reconstruction time.

Attenuation Correction During a PET acquisition, the energy of the photons can be attenuated by interactions with the surrounding tissues of the subject or/and the animal bed. This attenuation increases with the density of the tissue. The radial geometry of PET scanners also influences the attenuation effect, as photons released in the center of the PET scanner are likely to be attenuated more than photons released closer to the detectors. Not correcting for attenuation can lead to artifacts in PET images and biases in the quantification of the data, most notably the underestimation of the uptake of the radiotracer. Attenuation effects can be estimated by performing a transmission acquisition using an external radioactive source such as Co-57 (Fig. 7a). To this end, the rodent is placed in the FOV of the PET scanner, and the transmission is started either before or after the emission scan. The external source performs a 360° cycle to estimate the attenuation through both the animal tissue and the PET scanner bed. Afterward, the attenuation is obtained by computing the transmission scan based on a blank acquisition performed without the animal and can be used to correct the emission data. It is important to note that inaccuracies in the co-registration of the transmission and emission acquisitions—when not acquired in the same bed position— might bias the quantification accuracy. Furthermore, since Co-57 decays with a half-life of 271.8 days, the count statistics of the transmission scans change over time and should be adjusted according to the decay (or new blank scans should be acquired to match the decay of the source). Alternatively, the attenuation effect can also be estimated from a CT scan if a PET/CT scanner is available. This is still the gold standard attenuation correction, as it provides a better tissue contrast (Fig. 7b).

Static Versus Dynamic Data Acquisition and Quantification In preclinical as well as clinical PET or SPECT studies, the tracer is usually administered to a subject *i.v.* and reaches the brain within a few seconds. Generally speaking, there are two ways of acquiring imaging data.

First, knowing the kinetics of the tracer, a PET scan may be performed at a certain time after the administration of the tracer when the radiolabeled compound has reached equilibrium between a target and a reference region in tissue. Since the distribution of the tracer does not change over the duration of the measurement, we speak of a "static" acquisition (Fig. 8a). The principal advantage of static measurements is their relatively short acquisition time (*e.g.* 10–15 min). This allows for shorter times under anesthesia for the animals and facilitates the imaging of more animals following the preparation of a tracer. However, the results obtained from static scans cannot be used for kinetic modeling. For analysis of static scans, the standardized uptake value (SUV) is commonly used:

$$\mathrm{SUV} = \frac{C_{\mathrm{img}}}{C_{\mathrm{inj}}} \left[\frac{\frac{\mathrm{MBq}}{\mathrm{mL}}}{\frac{\mathrm{MBq}}{\mathrm{g}}} \right] = \left[\frac{\mathrm{g}}{\mathrm{mL}} \right] \tag{13}$$

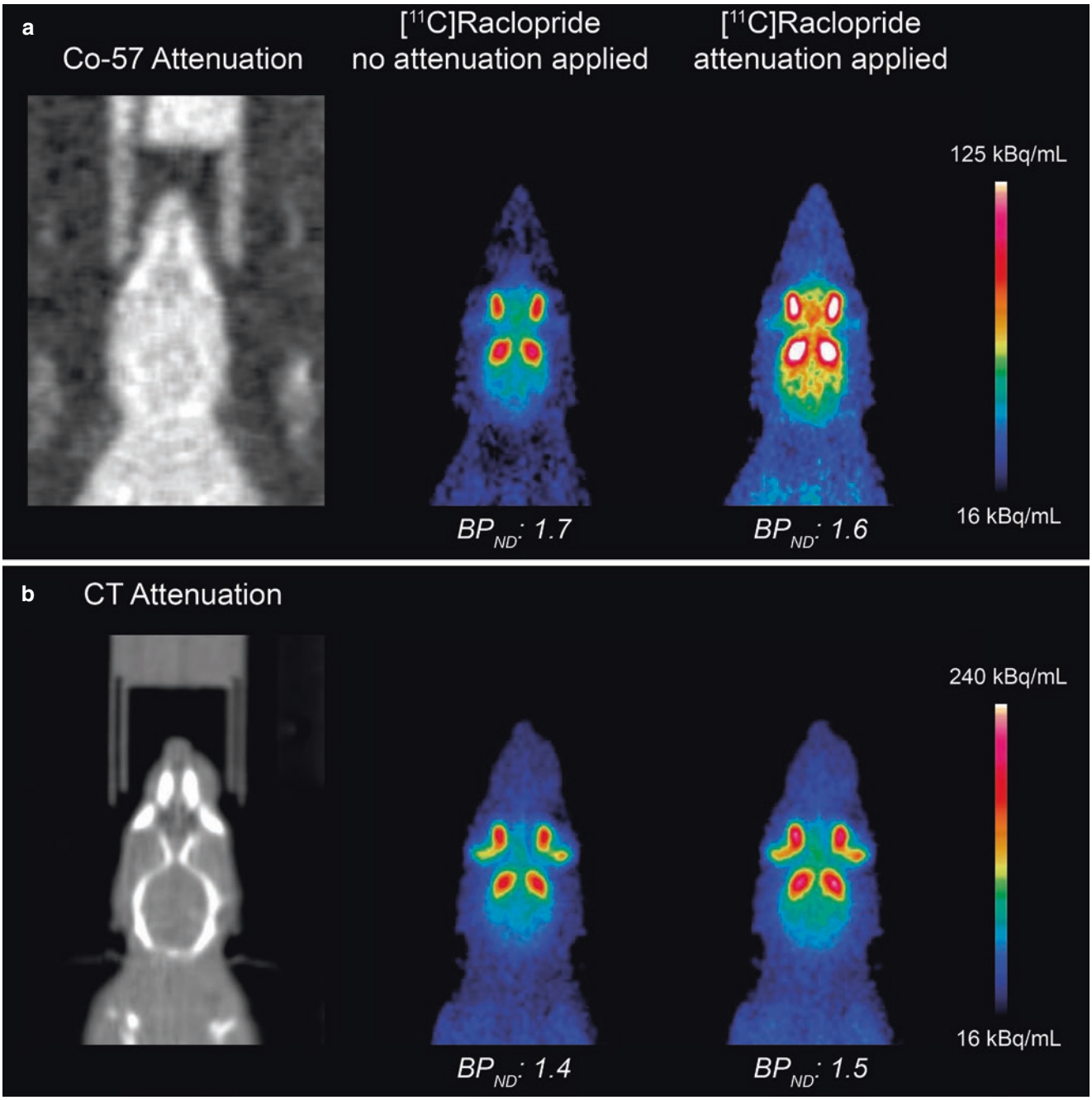

Fig. 7 Comparison of Co-57 attenuation (**a**) and CT attenuation (**b**). [^{11}C]Raclopride PET images of two rat brains reconstructed with 2D-FBP without attenuation (*second column*) and with attenuation (*third column*). Images show how Co-57 and CT attenuation correction influences quantitative PET values. Binding potentials (BP_{ND}) were calculated from the striatum using the Logan graphical approach and the cerebellum as a reference region

In this equation, C_{img} is the image – derived concentration of the tracer, while C_{inj} is the ratio of the injected dose (ID) and the body weight (BW):

$$C_{inj} = \frac{ID}{BW} \tag{14}$$

Since PET is commonly used for the imaging of biological tissues with the approximate density of 1 g/mL, the SUV is sometimes unitless [17].

In the case of a "dynamic scan," both the measurement and the data analysis are more complicated (Fig. 8b). In this case, the tracer is administered immediately after the start of the data acquisition, and the progressive increase in the activity concentration in the brain is recorded. Since it may take 1 h or even longer before a stable concentration of the tracer is achieved, dynamic measurements are more time-consuming—and consequently more expensive—than static ones. However, the data from dynamic scans are necessary to

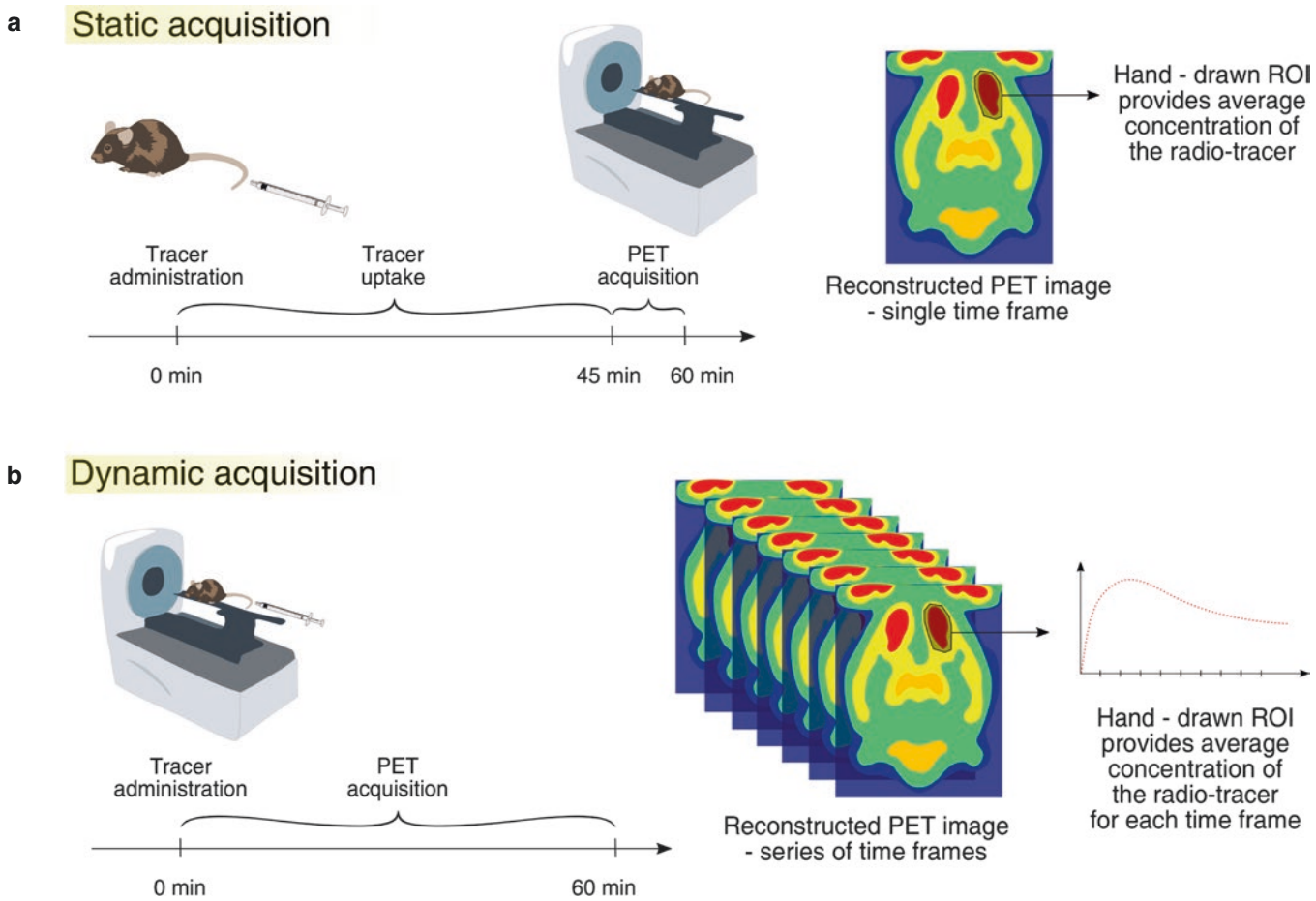

Fig. 8 (**a**) Static versus (**b**) dynamic PET data acquisition

describe *in vivo* kinetics of the radiotracer using kinetic modeling approaches. The main differences between static and dynamic acquisitions are presented in Fig. 8.

An image reconstructed from a dynamic data set can be three- or four-dimensional, and it provides information about the concentration of the tracer over time. This can be derived from the image in the form of a time-activity curve (TAC) and subsequently used for data analysis. The analysis is often performed using kinetic modeling, which relies on the application of mathematical models—which describe the pharmacokinetics of the radiotracer as accurately as possible—in order to obtain the information about the physiological processes of interest (see the Chapter on "Kinetic Modeling of Radiotracers").

Blood Sampling Applying full kinetic models for the analysis of dynamic data requires that the time course of the radioactivity concentration in blood plasma is known. This is called the arterial input function (AIF) and can be obtained from blood samples collected—most commonly via an arterial catheter—during the PET measurement. The catheter should be inserted in the blood vessel prior to the scan and filled with heparinized saline to prevent blood clotting. In contrast to human studies, blood sampling in small animals is challenging due to the limited blood volume of the subject. Since withdrawal of large volumes of blood may affect the physiology of the animal, it is crucial to minimize the total amount of the collected blood. Nevertheless, if the tracer is administered as a bolus, the samples should be taken frequently (~every 5 s) in the beginning to ensure that the time of peak activity is captured accurately. Subsequently, it is sufficient to sample the blood every several minutes, even every 15–20 min in the end of the measurement. Using this approach, approximately 20 samples are collected over 60 min (Figs. 9 and 10). Provided that each sample contains a volume of 50 μL, the total blood loss will be 1 mL. For a 300 g rat with an approximate total blood volume of 20 mL, this is still acceptable, especially because the solution of PET tracer partially replaces the lost volume.

The blood samples should be collected in microcentrifuge tubes coated with an anticoagulant, such as Li-heparin or EDTA. Subsequently, a small volume of whole blood (wb) from each sample should be measured in a γ-counter, while the remaining fraction should be centrifuged to separate the plasma (p). A defined volume of the separated plasma will then also be measured in the γ-counter. While the p-TAC

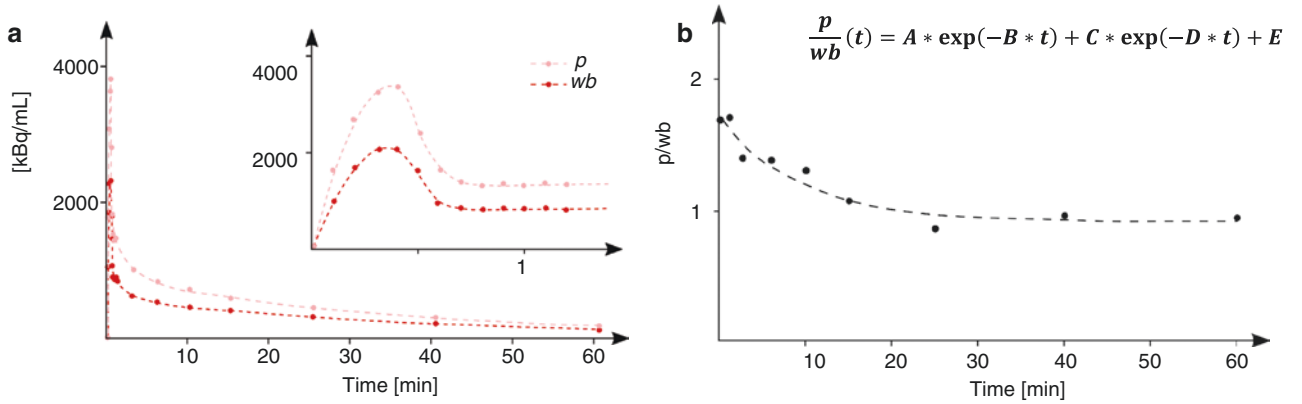

Fig. 9 (**a**) Radioactivity concentration measured in whole blood (wb) and plasma (p) samples collected from a rat after the administration of ~60 MBq of [^{18}F]FDG. (**b**) The values from (**a**) are used to calculate the $\frac{p}{\mathrm{wb}}$ concentration ratio. In this example, a biexponential function with A-E fit coefficients describes the ratio. The dots represent individual data points, while the dashed lines are fits to the data. (Adapted from Napieczynska *et al.* [22], with permission)

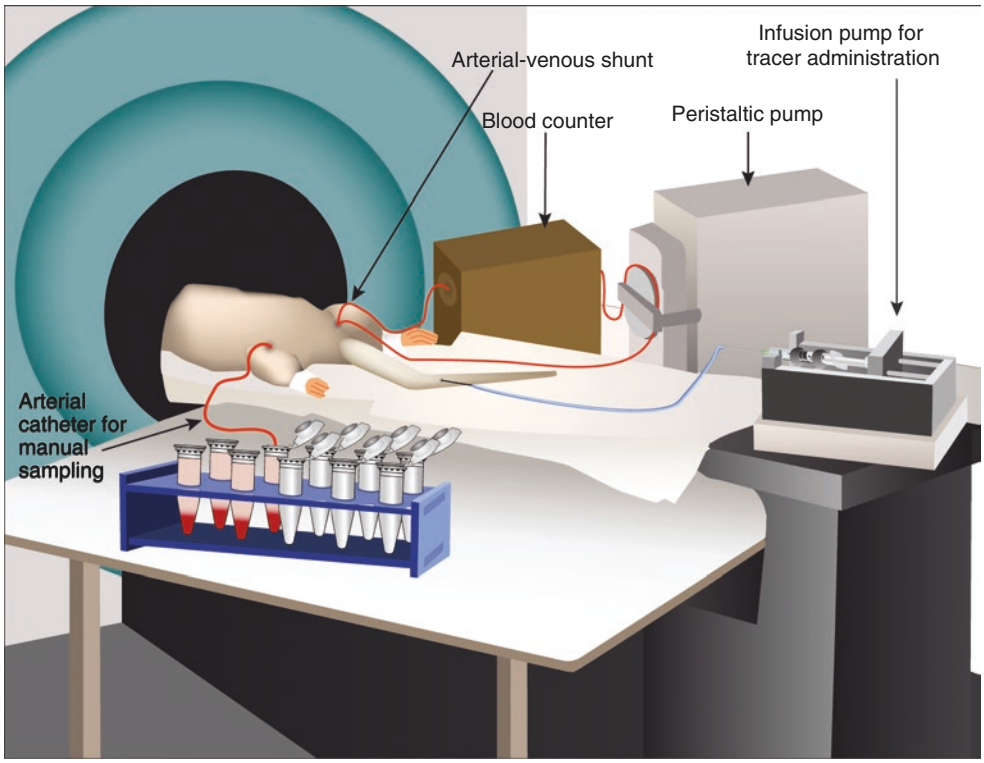

Fig. 10 PET and online blood radioactivity measurements using a blood counter. In small animal studies, the arterial-venous shunt can be inserted in the femoral artery and vein. The blood circulates in this closed system and flows through the blood counter where its radioactivity level is measured. The data are subsequently used for kinetic modeling. In this example, blood samples are also collected manually from the contralateral femoral artery to validate the data obtained with the counter

serves as the AIF in kinetic modeling, the wb-TAC is required to estimate the fraction of PET signal in a ROI which originates from blood capillaries rather than from the brain tissue. Moreover, if the molecules of the radiotracer in the plasma bind to plasma proteins, the precipitation of the proteins may be necessary to define the fraction of free radiotracer.

Plasma Protein Binding The binding of PET tracers to plasma proteins can affect both their bioavailability and pharmacokinetics and therefore their calculated kinetic parameters. Unlike free radiotracer, radiotracer that is bound to plasma proteins is not able to cross capillary membranes and enter tissues. Most available PET tracers show some degree of binding to blood cells; however, the equilibrium of the tracer between bound and free states in plasma is reached rapidly. If a tracer is highly lipophilic, its binding to plasma proteins is enhanced, thereby reducing its availability to enter tissues of interest.

The determination of plasma protein binding *in vitro* is difficult and has been critically reviewed [18], since binding to plasma proteins is highly dependent on pH, temperature, and other parameters which are unknown and may vary significantly between different tissues or regions in the brain. Another way to determine plasma protein binding is the measurement of the plasma radioactivity after the *in vivo* injection of the PET tracer. Here, it should be noted that radiometabolites may influence the calculations [19, 20]. In addition, if small blood samples of only 50 µL are taken, the radioactivity signal may not meet the detection thresholds for ^{11}C-labeled compounds. In this case, larger blood samples must be obtained.

An example protocol for determining the fractional binding of a radiotracer to plasma proteins using ultrafiltration is described below:

1. Inject mice or rats with 12–17 MBq or 25–30 MBq, respectively, of the radiotracer via the tail vein.
2. Take blood samples intraocularly or from an arterial catheter and centrifuge the blood at 1800 g for 5 min at 4 °C.
3. Collect the plasma in a tube and place it on ice immediately.
4. Add the plasma to ultrafiltration tubes.
5. Centrifuge the tubes at high speed to separate the protein-bound radiotracer (trapped in the filter) from the unbound radiotracer (in the filtrate).
6. Measure the radioactivity of the protein-bound radiotracer in the filter and the filtrate using a γ-counter.
7. Use radiotracer dissolved in phosphate-buffered saline—instead of blood plasma—to determine the non-specific binding of the tracer to the filter (if this is >25%, the assay may not produce valid results).
8. Calculate the fraction of the radiotracer bound to plasma proteins using Eq. 15:

$$1-\left(C_{p,f}/C_0\right)\left(1+\mathrm{NSB}\right)\times 100 \tag{15}$$

with

$$\mathrm{NSB}=1-\left(C_{b,f}/C_{b,uf}\right) \tag{16}$$

$C_{b,f}$ is the average concentration in the filtrate;
$C_{b,f}$ is the average concentration in the retentate (unfiltered PBS);
$C_{p,f}$ is the concentration in the filtered matrix;
C_0 is the concentration of the compound.

Radiometabolite Analysis Following the administration of a PET tracer to a subject, radiolabeled metabolites of the parent compound may be gradually formed in plasma. If these metabolites cross the BBB, they contribute to the PET signal in the brain and influence the data quantification. Indeed, the production of brain-permeable radiometabolites is a common criterion for the failure of novel brain PET tracers. However, if these radiometabolites are present in the plasma but not in the brain, a correction can be applied to the AIF to account for the amount of the radiometabolites.

The correction is usually done using a separate group of animals. Following administration of the tracer, a few blood samples are collected over the course of the dynamic PET acquisition. After separating the plasma and precipitating the plasma proteins, the radioactivity level associated with the parent compound and the radioactivity level of the radiometabolites are measured using HPLC to calculate the ratio of the two over time, called the "parent fraction." Depending on the sensitivity of the HPLC system available, withdrawing relatively large blood samples may be necessary to obtain sufficient volumes of serum. Subsequently, the defined parent fraction can be applied to plasma TACs obtained in other studies if strain-, age-, and sex-matched animals are used. Although such a "population-based" correction method may be not perfect, it is often the only way to account for radiometabolites in rodent studies. The blood volume required for determination of the parent fraction in each individual animal would be too high.

An example protocol for determining the presence of radiometabolites in blood plasma and brain tissue is shown below:

1. Inject mice or rats with 30 MBq or 60 MBq, respectively, of the radiotracer via the tail vein.
2. Take blood from an arterial catheter and place it on ice immediately.
3. Centrifuge the blood at 1800 g for 5 min at 4 °C to separate the plasma.
4. Collect the plasma in a tube and place it on ice immediately.
5. Perfuse the animal with ice-cold PBS through the left ventricle using 10 mL for mice and 50 mL for rats of ice-cold PBS.
6. Remove the brain from the animal, homogenize and disperse it for 30 s, and place it on ice immediately.
7. Add an organic solvent such as methanol or acetonitrile to both the homogenized brain tissue sample and the plasma samples (1:1) and centrifuge at 16,000 g for 5 min at 4 °C to precipitate the proteins.
8. Analyze the supernatants of the plasma and brain homogenates using chromatographic methods (*e.g.* radio-high-performance liquid chromatography [radio-HPLC] or radio-thin-layer chromatography [radio-TLC]). Compare the retention times of radiolabeled molecules of the

plasma and brain samples with the parent compound. Additional peaks in the spectrum are radiometabolites which may contribute to the PET signal if present in the brain tissue sample.

An example protocol for determining the plasma parent fraction for kinetic modeling is shown below:

1. Inject mice or rats with 30 MBq or 60 MBq, respectively, of the radiotracer via the tail vein.
2. Take blood samples from an arterial catheter after 1, 5, 10, 15, 20 and 25 min and place them on ice immediately (the fast decay of radioactivity of C-11-labeled tracers limits the number of samples that can be analyzed).
3. Centrifuge the blood at 1800 g for 5 min at 4 °C to separate the plasma.
4. Collect the plasma samples in tubes and place them on ice immediately.
5. Add an organic solvent such as methanol or acetonitrile to the plasma samples (1:1) and centrifuge at 16,000 g for 5 min at 4 °C to precipitate the proteins.
6. Analyze the supernatants of the plasma using radio-HPLC or radio-TLC. Calculate the ratio of the radioactivity level associated with the parent compound and the radioactivity level of the radiometabolites.
7. Fit a mathematical function to the parent fractions in order to extrapolate missing values and to minimize the impact of measurement errors. The function depends largely on the type of tracer; a selection guideline is described in Tonietto *et al.* [21].

Alternative Approaches to Generate an AIF Since blood loss is a serious limitation in preclinical studies involving blood sampling, a number of other procedures have been developed to circumvent this problem. The two principal alternative strategies include (i) recording the blood radioactivity in the vessel or in an arterial-venous shunt with a dedicated device (a blood counter or a β-probe) and (ii) deriving the wb-TAC from a reconstructed image.

Blood counters may be very sensitive, detecting up to 23% of the radioactivity present [22], and they operate with a high sampling rate (2 Hz or higher) which is not possible using manual sampling. However, the use of a blood counter requires inserting an arterial-venous shunt, which is more invasive than inserting an arterial catheter alone. Nevertheless, since the blood circulates in a closed system, blood loss can be completely avoided (Fig. 10). The detectors of the blood counter are similar to those in a PET scanner, and they detect γ-rays from annihilation events occurring in the blood flowing through the shunt.

β-probes work differently, as they directly detect positrons emitted from the radionuclide. β-probes can be similar in size to the γ-detecting counters [23], although in some cases they may be small enough to be inserted directly into an artery [24]. In fact, the main advantage of β-probes is their small size. However, this comes with a price of lower sensitivity. Moreover, some positrons originating in the artery walls or in the surrounding tissue may be recorded by a β-probe, and this background signal has to be later subtracted from the recorded data. Therefore, an additional β-probe should be positioned near the main one to account for the background activity. The sampling rate of a β-probe can be as high as that of a blood counter, and both types of devices prevent the loss of blood. However, a surgical intervention is necessary in both cases.

Alternatively, the wb-TAC can also be obtained from a reconstructed image. In this approach, a VOI is drawn on the left ventricle of the heart. Although the partial-volume and spillover effects substantially degrade the signal in this small volume, techniques have been developed to correct for these phenomena in rats as well as mice [25]. Additionally, deriving the wb-TAC from the image requires a FOV large enough to cover the brain as well as the heart of the animal.

Finally, whether the wb-TAC is derived from a PET image or acquired with an external device, it alone cannot serve as the AIF in kinetic modeling. As explained above, the p-TAC—corrected for the metabolite fraction—is necessary as well. Ideally, plasma metabolites should be determined from each animal individually. However, the individual TACs are often noisy, and taking blood samples from every animal is not applicable, especially for longitudinal studies. Therefore, a population-based $\frac{p}{\mathrm{wb}}$ radioactivity concentration ratio is often used, if the interindividual variation in the rate of metabolism is small. Similarly to the parent fraction correction, the $\frac{p}{\mathrm{wb}}$ radioactivity ratio is first determined in one group of animals using manually collected blood samples (Fig. 10). Subsequently, the p value of an animal under investigation can be calculated from its wb data. For example:

$$p(t)/\mathrm{wb}(t) = A \times \exp(-B \times t) + C \times \exp(-D \times t) + E \quad (17)$$

$$p'(t) = \mathrm{wb}'(t) \times A \times \exp(-B \times t) + C \times \exp(-D \times t) + E \quad (18)$$

where the p(t) and wb(t) are the plasma and whole blood TACs, respectively, determined in the additional group of animals, while the p'(t) and the wb'(t) are the corresponding data of the subject under investigation. When calculating the p radioactivity values in this manner, factors such as age, sex, body weight, health, or dietary conditions should be considered since they may influence the $\frac{p}{\mathrm{wb}}$ ratio.

As it may be concluded based on the above discussion, every procedure of determining the AIF has its limitations. A recently introduced "CD-Well"-based approach [26] seems to be the most optimal currently available solution. With this apparatus, wb samples as small as 23 μL are collected in tiny U-shaped capillaries in which they are subsequently centrifuged. The radioactivity concentration in both separated sections is then measured using autoradiography to obtain the wb-TAC as well as the p-TAC. Thus, PET measurements with blood sampling become feasible also in mice, although an additional cohort of animals is still necessary for the evaluation of metabolites.

Finally, whenever a catheter is used to withdraw blood samples—whether with a blood counter, a β-probe, or a "CD-Well"—it is important to keep in mind the delay and dispersion effects that occur along it. The delay is caused simply by the longer distance the radiotracer needs to be transported to reach the sampling site. The dispersion occurs due to the interaction of the blood with the vessel walls, regardless of whether the vessels are the veins, arteries, or external tubing. Taken together, these effects result in a delayed, widened, and flattened AIF (Fig. 11) [27].

While the "internal" dispersion, which takes place within the body vasculature is usually not corrected for, different correction methods have been developed to account for the dispersion within a catheter. In a classical approach [28], the dispersion (d) is modeled with a monoexponential function:

$$d(t) = \frac{1}{\tau}\exp\left(-\frac{t}{\tau}\right) \tag{19}$$

For example, in a blood counter recording, the recorded data have to be deconvolved with the dispersion function.

Ex Vivo Experiments for the Cross Validation of PET Data

***Ex Vivo* Autoradiography** Along with *in vivo* PET scans, the distribution and kinetics of a radiolabeled molecule can be characterized via *ex vivo* autoradiography. Indeed, autoradiography is a powerful tool for the rapid *ex vivo* analysis of whole-body sections or tissues of interest. In both mice and rats, it allows for the visualization of the distribution of a radiotracer with higher resolution compared to PET (see section on *in vitro* autoradiography). For a direct PET to autoradiography comparison, the ratio between the target and the reference regions can be calculated for both modalities. Furthermore, to estimate the partial-volume effect (PVE) for a particular target region, the uptake values from PET and autoradiography can be directly compared (Fig. 12) [29]. The PVE influences in particular the quantification of small organs or tissues with a size below the spatial resolution of the PET scanner. Thereby, the concentration of the real activity in smaller regions can be underestimated ("spill-out" effect) or overestimated ("spill-in" effect) due to activity spillover from the surrounding tissue.

Ex vivo autoradiography is performed immediately after the PET scan to allow for a direct comparison to the PET data. The logistics of this process are especially important while working with short-lived radionuclides. For example, with ^{11}C-labeled radiotracers, the short half-life of only 20.4 min can lead to noisy images if the specific uptake of the tracer into the brain is low and the slices are exposed to the phosphor plate after more than 2 h. In those cases, *ex vivo* autoradiography is performed after a separate application of the tracer. Here, it is important to know the kinetics of the radiotracer to estimate the time after which equilibrium is reached between the target and reference region. The amount of

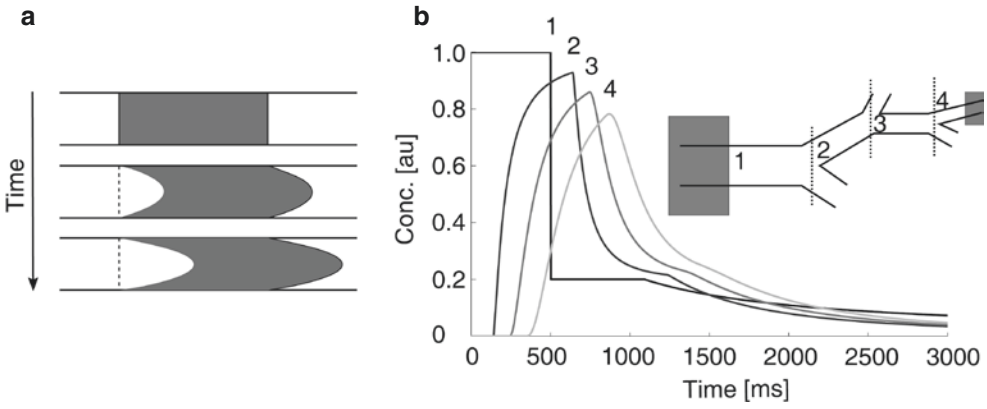

Fig. 11 (**a**) Dispersion of a bolus in a blood vessel. (**b**) The distance the blood travels in a bifurcated vasculature system affects the shape of the arterial input function used in kinetic modeling. (Adapted from Kellner *et al.* [27], with permission)

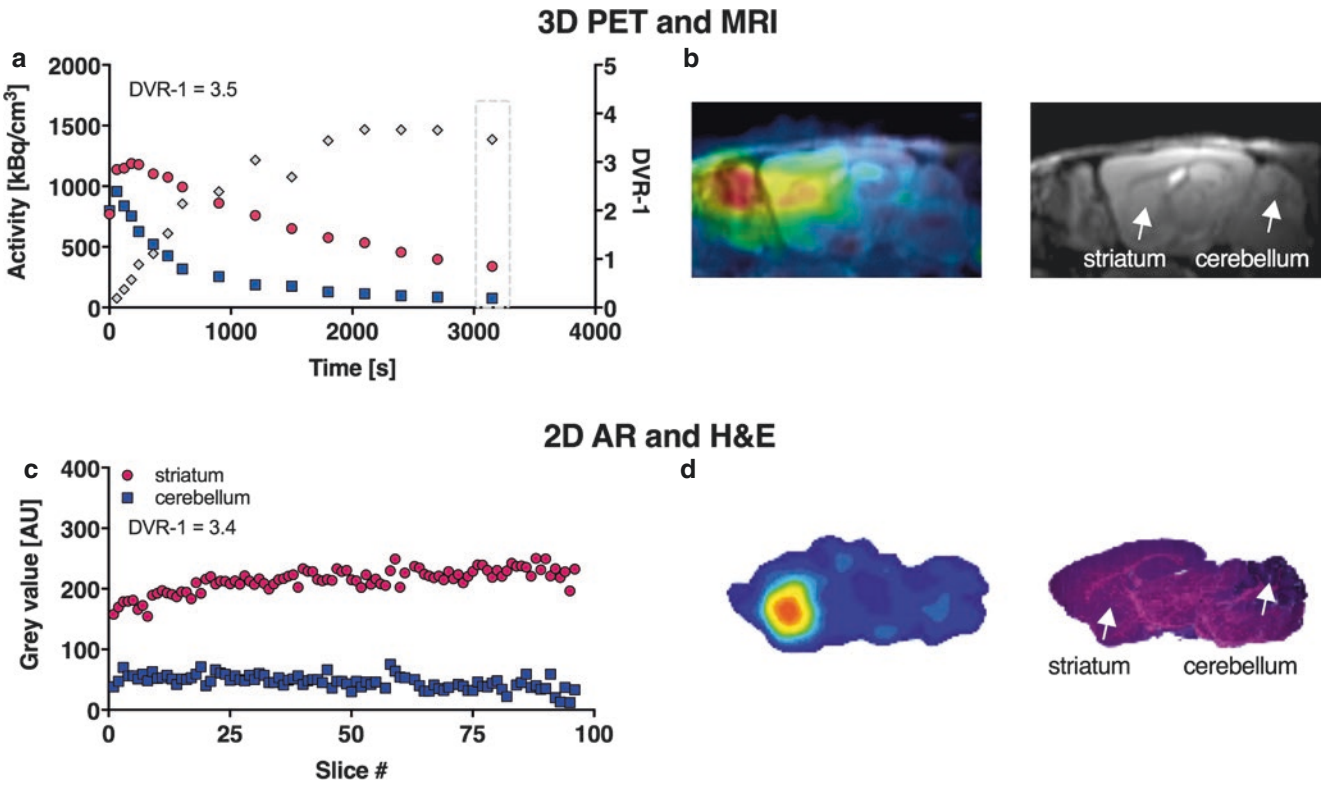

Fig. 12 PET-autoradiography cross validation. (**a**) *In vivo* [^{11}C]raclopride PET time-activity curves of the striatum (red) and cerebellum (blue) and the corresponding distribution volume ratio (striatum/cerebellum)-1 (gray) over time of one representative mouse. The last time frame was selected to calculate the DVR-1 and compared to *ex vivo* autoradiography. (**b**) Sagittal PET image of the last time frame (3150–3600 s) co-registered with the corresponding MR image as an anatomical reference to identify the striatum and cerebellum. (**c**) Autoradiography: counts, calculated from the striatum and cerebellum from medial to lateral. The DVR-1 was calculated from the average counts in the striatum and cerebellum. (**d**) Autoradiography (AR) image of one representative brain slice and the corresponding H&E staining used as an anatomical reference for the placement of the region of interest (ROI). ROIs were selected according to the placement of the volume of interest in PET

radioactivity within the tissue can be quantified as well by exposing a standard to the phosphor screen. For the standard, different radiotracer concentrations are pipetted on a TLC slice, which is then placed next to the sections on the imaging plate (see section on *in vitro* autoradiography).

An example protocol for performing *ex vivo* autoradiography is described below:

1. Inject mice or rats with 12–17 MBq or 25–30 MBq, respectively, of the radiotracer via the tail vein.
2. Sacrifice the animal using CO_2 (cervical dislocation may lead to small blood accumulations in the brain and unspecific signals) either (a) after the acquisition of the PET scan or (b) after radiotracer reaches equilibrium between a target and reference region.
3. Quickly dissect the brain, put it on ice, and embed it into embedding medium.
4. Rapidly freeze the brain to −20 °C and use ice spray to speed up the freezing process.
5. Cut the brain into 20 μm brain slices and mount it on super frosted glass tissue slides.
6. Prepare a standard by pipetting decreasing concentrations of radiotracer on a TLC slide.
7. Place brain sections and the standard into an autoradiography cassette and cover them with plastic wrap to avoid the contamination of the phosphor imaging plates.
8. Expose the brain sections and the standard to the phosphor screens for ten half-lives of the radiotracer (erase the phosphor screens before use via exposure to light).
9. Read out the imaging plates with a phosphor imager.
10. For data analysis and quantification, see the section on *in vitro* autoradiography.

Biodistribution Experiments (γ-Counting) Another method to assess the tissue distribution of a radiotracer is the direct counting of the radioactivity in dissected tissues and organs using a γ-counter. This relatively simple method provides organ level information and estimates the actual radioactivity in the tissue of interest at a single time point, avoiding erroneous quantification due to partial-volume effects (PVE). Therefore, biodistribution studies are commonly used to cross-validate *in vivo* PET data.

In order to validate a brain-targeted radiotracer using *ex vivo* γ-counting, healthy animals are injected *i.v.* with the radiotracer and sacrificed by cervical dislocation at predeter-

mined time points. Organs and tissues such as the heart, blood, liver, kidneys, muscle, lungs, lymph nodes, bone, and brain are excised and then assayed for radioactivity on a γ-counter. It is also feasible to use the same tissue of interest for both γ-counting and immunohistochemical staining. In this case, however, formalin needs to be added into the test tubes. After the measurement, the organ dehydration process can be carried out to facilitate later immunohistochemical staining.

The results of a biodistribution study are typically expressed as the percentage of the injected dose per gram of tissue (%ID/g) (Eq. 21). The measured radioactivity must be corrected for radioactive decay of the radionuclide. To calculate the %ID/g for a given tissue, the following equation is used:

$$\text{activity}(\text{sample}) = \frac{\text{cpm}(\text{sample})}{\text{cpm}(\text{standard})} * \text{activity standard} \quad (20)$$

$$\frac{\%\text{ID}}{g} = \frac{\frac{\text{activiy}(\text{sample})}{\text{activiy}(\text{injection})} * 100}{\text{weight}(\text{sample})} \quad (21)$$

For the standard, the injected activity is diluted in 30 mL (for a mouse) and 50 mL (for a rat) water, representing the body volume of the animal. From this dilution, 3 × 1 ml is used for γ-counting.

A typical experimental setup for a γ-counting assay is described below:

1. Pre-weigh empty test tubes or test tubes containing formalin (if immunohistochemistry [IHC] is to be performed after the experiment).
2. Inject mice or rats with 12–17 MBq or 25–30 MBq, respectively, of the radiotracer via the tail vein.
3. Dissolve the diluted tracer in 30 mL (for mice) or 50 mL (for rats) of water and add 1 ml to three empty, preweighted test tubes.
4. Sacrifice the animal via cervical dislocation under deep anesthesia.
5. Dissect the organs of interest and place them into the preweighed test tubes (if possible, remove any residual blood).
6. Measure the test tubes on the γ-counter.
7. Reweigh the test tubes containing the organs and calculate the weight of each organ.

Advantages and Disadvantages of Different Animal Models of Neurological Disorders

A wide array of different animal models have been developed to study disorders of the nervous system [30]. Ideally, animal models of neurodegeneration in particular should be characterized by the progressive loss of neurons, the accumulation of disease-related proteins, the onset by appropriate symptoms, and the responsiveness to corresponding therapies. Unfortunately, none of the currently available animal models fully satisfy all of these requirements and adequately recapitulate all clinical symptoms and pathologies. Most animal models are based on either toxins that specifically target certain cell populations or genetic factors such as the overexpression, mutation, or knockout of disease-causing proteins. In addition to rats and mice, *Drosophila melanogaster*, *Caenorhabditis elegans*, and nonhuman primate models have been established to gain insight into how various genes can cause neuronal dysfunction and cell death. As each model sheds light on different aspects of the disease, it is important to carefully consider the question being asked in an experiment before choosing which model to use. Here, we will focus on rodent models of Parkinson's disease (PD) as an example for models of neurological disorders.

Toxin-based models for PD mostly focus on the degeneration of dopaminergic neurons to recapitulate one of the hallmarks of this disorder. Both intraperitoneal applications of toxins and the direct, stereotaxic injection of toxins into the brain have been used to reproducibly eradicate a high percent of cells within a small time frame [31, 32]. Most of the toxins used are not able to replicate the mechanistic and pathological features of PD, such as the accumulation of proteins within neurons [33, 34]. However, these models are valuable in order to study behavioral deficits and recovery after treatment, as well as functional changes within brain circuits [35].

Numerous transgenic rodent models have been generated using a variety of promoters driving the (over)expression of disease-causing proteins—such as human alpha-synuclein (asyn)—in the central nervous system. Depending on the promoter used, this expression can be broad or specifically restricted to neurons involved in the disease [36, 37]. Transgenic models have the advantage of ensuring consistent expression from generation to generation as well as within a litter, thereby providing lower animal-to-animal variation. Once a particular transgenic line is successfully created, expanding and crossbreeding a colony are both fairly facile. However, in PD, both the recapitulation of specific neurodegeneration and the particular pathology have been lacking in most transgenic lines [36]. While a form of asyn aggregation can be found in many transgenic models, none of these PD models exhibit the progressive loss of dopaminergic cells. Furthermore, due to the absence of degeneration, robust behavioral phenotypes are lacking [37]. Nevertheless, these models are useful to investigate mechanistic and cellular changes triggered by the overexpression of disease-causing genes *in vivo*.

In contrast to transgenic models, models based on viral vector-mediated overexpression offer a more flexible

approach. In these models, recombinant viral vectors encoding disease-causing genes are used to transduce neurons located in brain areas affected in PD [38–41]. As a result, researchers are able to inject the vector into any area of the brain to induce or cure the disease, choose a specific time of onset, or express different protein levels based on the concentration of the vector in a broad range of animal species, including rodents, pigs, and monkeys. The laborious stereotaxic injection of one or more vectors expressing disease-causing or disease-preventing genes allows for the rapid investigation of hypotheses *in vivo*. Furthermore, by targeting only one hemisphere, the contralateral side can be used as an internal reference. When asyn is overexpressed via viral vectors, cellular and axonal pathology as well as progressive dopaminergic cell loss can be observed and correlated with behavioral deficits. However, differences in targeting lead to a large variation in neurodegeneration between animals, which is responsible for the behavioral variability seen in injected animals [38]. Nonetheless, this approach allows for the fast and versatile generation of various combinations of models.

A recently established model based on the transmission and seeding hypothesis is predicated on the injection of preformed fibrils of recombinant asyn (PFFs) or purified aggregates from brain tissue into the rodent brain [42, 43]. All experiments done so far indicate that the stereotaxic injection of these PFFs or purified aggregates results in a widespread pathology of endogenous asyn in the mouse brain, as well as the loss of dopaminergic neurons [44, 45]. However, this model relies on the ability to consistently produce fibrils of recombinant asyn protein *in vitro*. Many diverse forms of asyn fibrils have been described, and their injection results indistinct seeding and spreading patterns *in vivo* [46]. In addition, a unilateral injection can result in bilateral pathology and, as a result, in a loss of the internal control hemisphere. However, this model has two particularly important advantages: the minimal disruption of the endogenous system as well as the better recapitulation of asyn aggregation *in vivo*. It is therefore a valuable model to study therapeutic interventions in addition to the mechanism and pathology of PD.

All of the models described above have biological and methodical advantages and disadvantages when used for testing new PET radiopharmaceuticals *in vivo*. When choosing an *in vivo* model to assess the specificity and sensitivity of a novel PET tracer, it is important for the preclinical model to present the targeted aspect of the disorder in a manner that recapitulates human disease as closely as possible. Furthermore, the methodological and technical pros and cons of each model have to be carefully considered. Aside from the cost and logistical aspects of the models, the benefits of a unilateral versus transgenic approach, the ability to test tracers before and after the onset of disease, the effect of therapeutic intervention, and the feasibility of longitudinal studies all have to carefully considered prior to *in vivo* validation in order to ensure successful translation to the clinic.

Particular Important Works

Over the past several years, significant progress has been made in the development of radiotracers targeting pathological protein depositions in the brain. The first PET tracer [^{11}C] Pittsburg compound B (PIB) to detect fibrillary ß-amyloid (Aß) in Alzheimer's disease (AD) patients was introduced by Klunk and colleagues 14 years ago [47]. Since then, [^{11}C] PIB has been used in more than 300 preclinical and clinical studies and has become a valuable tool for distinguishing AD patients from those with mild cognitive impairment or healthy controls at early time points. Preclinical evaluation studies to develop [^{11}C]PIB started approximately 10 years earlier and were initiated upon chemical modifications to dyes—such as members of the Congo Red and Chrysamine G families—that were known to interact with Aß plaques but failed to fulfill the requirements of a PET tracer (Table 1) [for a review of this work, see Mathis *et al.* [48]]. In 1999, Mathis and colleagues started to explore neutral derivatives of thioflavin-T and identified a lead compound, [^{11}C]PIB, that met all the requirements of an ideal PET tracer, including high affinity to aggregated $Aß_{(140)}$ and $Aß_{(142)}$ fibrils (K_d of 2.8 and 4.7 nM), good BBB penetration (SUV of ~1.0), and a clearance half-life time of 6 min from the mouse brain [49, 50]. Over the past 10 years, several ^{18}F-labeled derivatives of PIB—for example, [^{18}F]flutemetamol [51], [^{18}F]florbetaben [52], and [^{18}F]florbetapir [53]—have been developed to make the tracer more available for preclinical and clinical research.

Another pathological hallmark of AD is the aggregation of tau into neurofibrillary tangles. In 2005, a screening of small molecules at the Tohoku University in Japan led to the identification of quinoline and benzimidazole derivatives for tau imaging [54]. Six years later, the first PET tracer to quantify tau depositions in the brain—[^{18}F]THK523—was introduced by Fodero-Tavoletti *et al.* [55]. Preclinical *in vitro* investigations using recombinant tau fibrils revealed that the compound has one high-affinity tau-binding site (K_d = 1.67), one low-affinity tau-binding site (K_d = 21.74), and 13-fold selectivity for tau over Aß (K_d = 20.7). Fluorescence and autoradiography analysis indicated that the tracer specifically binds tau tangles but not amyloid plaques. *In vivo* microPET studies in transgenic mice that overexpress tau revealed higher activity concentrations in the brain of the transgenic mice compared to their wild-type littermates. Moreover, low retention of the radiotracer was observed in transgenic mice with Aß pathology. In clinical

studies, however, the tracer showed high retention in white matter, precluding the assessment of tau pathology by visual inspection. Since then, several derivatives of [^{18}F]THK523 were developed and tested in preclinical and clinical studies, including [^{18}F]THK5351, which showed faster kinetics, lower white matter retention, and higher signal-to-noise ratios [56]. Further, several tau-specific radiotracers have been the subject of *in vitro* and *in vivo* screening, such as the pyrido-indole derivative [^{18}F]AV-1451 [57, 58] (also known as T807 and flortaucipir) and the phenyl/pyridinyl-butadienyl-benzothiazole/benzothiazolium derivative [^{11}C] PBB3 [59, 60].

The Future

Today, there is still a major need for novel radiotracers for a wide variety of targets—including G-protein-coupled receptors, ion channels, enzymes, and second messenger systems—both for drug development studies and understanding disease physiology. In addition, significant effort has been dedicated to create radiotracers for neuroinflammatory markers and to distinguish glia cells from neurons. The development of PET radiotracers capable of quantifying protein deposits in neurodegenerative disorders is crucial as well. For example, imaging the aggregation of α-synuclein in the brain of Parkinson's patients will allow for the early and differential diagnosis of different types of synucleinopathies. Indeed, while several compounds have been investigated, none appears to be an ideal candidate for α-synuclein imaging [61–64].

Due to the fact that the development of PET radiotracers for the CNS is time-consuming, expensive, and risky, many pharmaceutical companies have discontinued their research in this field. Therefore, biomathematical models and *in vitro* methods have been introduced to predict the behavior of radiotracers *in vivo*, providing critical tools that can optimize the timeline and success of radiotracer development [65–68]. Furthermore, the creation of novel animal models that better reflect human disease pathology would facilitate preclinical evaluations and improve the translation of radiotracers to the clinic.

The Bottom Line

- *In vitro* saturation and competition binding experiments are useful screening approaches for identifying promising PET tracers.
- Assay conditions—such as target concentration, incubation times, and temperature—must be carefully evaluated before experiments are conducted.
- Autoradiography experiments are a useful tool to explore the specific binding of a lead compound to its target in brain slices and can be performed using a molecule that is tritiated or labeled with a positron-emitting radionuclide.
- When autoradiography experiments are performed, the spatial resolution and sensitivity of phosphor screens and film have to be taken into account.
- Basic *in vivo* experiments include the acquisition of PET data in small animals to determine the delivery and clearance of the radiotracer to and from the brain, blood sampling for the analysis of radiometabolites, and *ex vivo* autoradiography and gamma counting for the cross validation of data.

References

1. Zhang L, Villalobos A, Beck EM, Bocan T, Chappie TA, Chen L, et al. Design and selection parameters to accelerate the discovery of novel central nervous system positron emission tomography (PET) ligands and their application in the development of a novel phosphodiesterase 2A PET ligand. J Med Chem. 2013;56(11):4568–79.
2. Cheng Y, Prusoff WH. Relationship between the inhibition constant (K1) and the concentration of inhibitor which causes 50 per cent inhibition (I50) of an enzymatic reaction. Biochem Pharmacol. 1973;22(23):3099–108.
3. Auld DS, Farmer MW, Kahl SD, Kriauciunas A, McKnight KL, Montrose C, et al. Receptor binding assays for HTS and drug discovery. In: Sittampalam GS, Coussens NP, Brimacombe K, editors. Assay guidance manual. Bethesda: Eli Lilly & Company and the National Center for Advancing Translational Sciences; 2012. p. 1–49.
4. Hulme EC, Trevethick MA. Ligand binding assays at equilibrium: validation and interpretation. Br J Pharmacol. 2010;161:1219–37.
5. Strome EM, Jivan S, Doudet DJ. Quantitative in vitro phosphor imaging using [3H] and [18F] radioligands: the effects of chronic desipramine treatment on serotonin 5-HT2 receptors. J Neurosci Methods. 2005;141(1):143–54.
6. Sihver W, Sihver S, Bergstrom M, Murata T, Matsumura K, Onoe H, et al. Methodological aspects for in vitro characterization of receptor binding using 11C-labeled receptor ligands: a detailed study with the benzodiazepine receptor antagonist [11C]Ro 15-1788. Nucl Med Biol. 1997;24(8):723–31.
7. Marsteller DA, Barbarich-Marsteller NC, Fowler JS, Schiffer WK, Alexoff DL, Rubins DJ, et al. Reproducibility of intraperitoneal 2-deoxy-2-[18F]-fluoro-D-glucose cerebral uptake in rodents through time. Nucl Med Biol. 2006;33(1):71–9.
8. Wong KP, Sha W, Zhang X, Huang SC. Effects of administration route, dietary condition, and blood glucose level on kinetics and uptake of 18F-FDG in mice. J Nucl Med. 2011;52(5):800–7.
9. Mizuma H, Shukuri M, Hayashi T, Watanabe Y, Onoe H. Establishment of in vivo brain imaging method in conscious mice. J Nucl Med. 2010;51(7):1068–75.
10. Hosoi R, Matsumura A, Mizokawa S, Tanaka M, Nakamura F, Kobayashi K, et al. MicroPET detection of enhanced 18F-FDG utilization by PKA inhibitor in awake rat brain. Brain Res. 2005;1039(1–2):199–202.
11. Momosaki S, Hatano K, Kawasumi Y, Kato T, Hosoi R, Kobayashi K, et al. Rat-PET study without anesthesia: anesthetics modify the dopamine D1 receptor binding in rat brain. Synapse. 2004;54(4):207–13.

12. Matsumura A, Mizokawa S, Tanaka M, Wada Y, Nozaki S, Nakamura F, et al. Assessment of microPET performance in analyzing the rat brain under different types of anesthesia: comparison between quantitative data obtained with microPET and ex vivo autoradiography. NeuroImage. 2003;20(4):2040–50.
13. Chatziioannou A, Qi J, Moore A, Annala A, Nguyen K, Leahy R, et al. Comparison of 3-D maximum a posteriori and filtered backprojection algorithms for high-resolution animal imaging with microPET. IEEE Trans Med Imaging. 2000;19(5):507–12.
14. Cheng JC, Shoghi K, Laforest R. Quantitative accuracy of MAP reconstruction for dynamic PET imaging in small animals. Med Phys. 2012;39(2):1029–41.
15. Torrent E, Farre M, Abasolo I, Millan O, Llop J, Gispert JD, et al. Optimization of [(11)C]raclopride positron emission tomographic rat studies: comparison of methods for image quantification. Mol Imaging. 2013;12(4):257–62.
16. Wallsten E, Axelsson J, Karlsson M, Riklund K, Larsson A. A study of dynamic PET frame-binning on the reference Logan binding potential. IEEE Trans Radiat Plasma Med Sci. 2017;1(2):128–35.
17. Tahari AK, Chien D, Azadi JR, Wahl RL. Optimum lean body formulation for correction of standardized uptake value in PET imaging. J Nucl Med. 2014;55(9):1481–4.
18. Hinderling PH, Hartmann D. The pH dependency of the binding of drugs to plasma proteins in man. Ther Drug Monit. 2005;27(1):71–85.
19. Patt M, Becker GA, Grossmann U, Habermann B, Schildan A, Wilke S, et al. Evaluation of metabolism, plasma protein binding and other biological parameters after administration of (-)-[18F] Flubatine in humans. Nucl Med Biol. 2014;41:489–94.
20. Sorger D, Becker GA, Hauber K, Schildan A, Patt M, Birkenmeier G, et al. Binding properties of the cerebral α4β2 nicotinic acetylcholine receptor ligand 2-[18F]fluoro-A-85380 to plasma proteins. Nucl Med Biol. 2006;33:899–906.
21. Tonietto M, Rizzo G, Veronese M, Fujita M, Zoghbi SS, Zanotti-Fregonara P, et al. Plasma radiometabolite correction in dynamic PET studies: insights on the available modeling approaches. J Cereb Blood Flow Metab. 2016;36(2):326–39.
22. Napieczynska H, Kolb A, Katiyar P, Tonietto M, Ud-Dean M, Stumm R, et al. Impact of the Arterial Input Function Recording Method on Kinetic Parameters in Small-Animal PET. J Nucl Med. 2018;59(7):1159–64.
23. Convert L, Morin-Brassard G, Cadorette J, Archambault M, Bentourkia M, Lecomte R. A new tool for molecular imaging: the microvolumetric beta blood counter. J Nucl Med. 2007;48(7):1197–206.
24. Pain F, Laniece P, Mastrippolito R, Gervais P, Hantraye P, Besret L. Arterial input function measurement without blood sampling using a beta-microprobe in rats. J Nucl Med. 2004;45(9):1577–82.
25. Fang YH, Muzic RF Jr. Spillover and partial-volume correction for image-derived input functions for small-animal 18F-FDG PET studies. J Nucl Med. 2008;49(4):606–14.
26. Kimura Y, Seki C, Hashizume N, Yamada T, Wakizaka H, Nishimoto T, et al. Novel system using microliter order sample volume for measuring arterial radioactivity concentrations in whole blood and plasma for mouse PET dynamic study. Phys Med Biol. 2013;58(22):7889–903.
27. Kellner E, Gall P, Gunther M, Reisert M, Mader I, Fleysher R, et al. Blood tracer kinetics in the arterial tree. PLoS One. 2014;9(10):e109230.
28. Iida H, Kanno I, Miura S, Murakami M, Takahashi K, Uemura K. Error analysis of a quantitative cerebral blood flow measurement using H2(15)O autoradiography and positron emission tomography, with respect to the dispersion of the input function. J Cereb Blood Flow Metab. 1986;6(5):536–45.
29. Fischer K, Sossi V, Schmid A, Thunemann M, Maier FC, Judenhofer MS, et al. Noninvasive nuclear imaging enables the in vivo quantification of striatal dopamine receptor expression and raclopride affinity in mice. J Nucl Med. 2011;52(7):1133–41.
30. McGonigle P. Animal models of CNS disorders. Biochem Pharmacol. 2014;87(1):140–9.
31. Vingill S, Connor-Robson N, Wade-Martins R. Are rodent models of Parkinson's disease behaving as they should? Behav Brain Res. 2017;352:133–41.
32. Blesa J, Phani S, Jackson-Lewis V, Przedborski S. Classic and new animal models of Parkinson's disease. J Biomed Biotechnol. 2012;2012:845618.
33. Duty S, Jenner P. Animal models of Parkinson's disease: a source of novel treatments and clues to the cause of the disease. Br J Pharmacol. 2011;164(4):1357–91.
34. Francardo V. Modeling Parkinson's disease and treatment complications in rodents: potentials and pitfalls of the current options. Behav Brain Res. 2017;352:142–50.
35. Tronci E, Francardo V. Animal models of L-DOPA-induced dyskinesia: the 6-OHDA-lesioned rat and mouse. J Neural Transm (Vienna). 2017;125(8):1137–44.
36. Chesselet MF. In vivo alpha-synuclein overexpression in rodents: a useful model of Parkinson's disease? Exp Neurol. 2008;209(1):22–7.
37. Bury A, Pienaar IS. Behavioral testing regimens in genetic-based animal models of Parkinson's disease: cogencies and caveats. Neurosci Biobehav Rev. 2013;37(5):846–59.
38. Kirik D, Rosenblad C, Burger C, Lundberg C, Johansen TE, Muzyczka N, et al. Parkinson-like neurodegeneration induced by targeted overexpression of alpha-synuclein in the nigrostriatal system. J Neurosci. 2002;22(7):2780–91.
39. Lo Bianco C, Ridet JL, Schneider BL, Deglon N, Aebischer P. Alpha -Synucleinopathy and selective dopaminergic neuron loss in a rat lentiviral-based model of Parkinson's disease. Proc Natl Acad Sci U S A. 2002;99(16):10813–8.
40. Klein RL, King MA, Hamby ME, Meyer EM. Dopaminergic cell loss induced by human A30P alpha-synuclein gene transfer to the rat substantia nigra. Hum Gene Ther. 2002;13(5):605–12.
41. Volpicelli-Daley LA, Kirik D, Stoyka LE, Standaert DG, Harms AS. How can rAAV-alpha-synuclein and the fibril alpha-synuclein models advance our understanding of Parkinson's disease? J Neurochem. 2016;139(Suppl 1):131–55.
42. Braak H, Del Tredici K, Rub U, de Vos RA, Jansen Steur EN, Braak E. Staging of brain pathology related to sporadic Parkinson's disease. Neurobiol Aging. 2003;24(2):197–211.
43. Chu Y, Kordower JH. The prion hypothesis of Parkinson's disease. Curr Neurol Neurosci Rep. 2015;15(5):28.
44. Luk KC, Kehm V, Carroll J, Zhang B, O'Brien P, Trojanowski JQ, et al. Pathological alpha-synuclein transmission initiates Parkinson-like neurodegeneration in nontransgenic mice. Science. 2012;338(6109):949–53.
45. Volpicelli-Daley LA, Kirik D, Stoyka LE, Standaert DG, Harms AS. How can rAAV-alpha-synuclein and the fibril alpha-synuclein models advance our understanding of Parkinson disease? J Neurochem. 2016;139(Suppl 1):131–55.
46. Guo JL, Covell DJ, Daniels JP, Iba M, Stieber A, Zhang B, et al. Distinct alpha-synuclein strains differentially promote tau inclusions in neurons. Cell. 2013;154(1):103–17.
47. Klunk WE, Engler H, Nordberg A, Wang Y, Blomqvist G, Holt DP, et al. Imaging brain amyloid in Alzheimer's disease with Pittsburgh Compound-B. Ann Neurol. 2004;55(3):306–19.
48. Mathis CA, Mason NS, Lopresti BJ, Klunk WE. Development of positron emission tomography beta-amyloid plaque imaging agents. Semin Nucl Med. 2012;42(6):423–32.
49. Klunk WE, Wang Y, Huang GF, Debnath ML, Holt DP, Shao L, et al. The binding of 2-(4′-methylaminophenyl)benzothiazole to postmortem brain homogenates is dominated by the amyloid component. J Neurosci. 2003;23(6):2086–92.

50. Mathis CA, Wang Y, Holt DP, Huang GF, Debnath ML, Klunk WE. Synthesis and evaluation of 11C-labeled 6-substituted 2-arylbenzothiazoles as amyloid imaging agents. J Med Chem. 2003;46(13):2740–54.
51. Vandenberghe R, Van Laere K, Ivanoiu A, Salmon E, Bastin C, Triau E, et al. 18F-flutemetamol amyloid imaging in Alzheimer disease and mild cognitive impairment: a phase 2 trial. Ann Neurol. 2010;68(3):319–29.
52. Rowe CC, Ackerman U, Browne W, Mulligan R, Pike KL, O'Keefe G, et al. Imaging of amyloid beta in Alzheimer's disease with 18F-BAY94-9172, a novel PET tracer: proof of mechanism. Lancet Neurol. 2008;7(2):129–35.
53. Wong DF, Rosenberg PB, Zhou Y, Kumar A, Raymont V, Ravert HT, et al. In vivo imaging of amyloid deposition in Alzheimer disease using the radioligand 18F-AV-45 (florbetapir [corrected] F 18). J Nucl Med. 2010;51(6):913–20.
54. Okamura N, Suemoto T, Furumoto S, Suzuki M, Shimadzu H, Akatsu H, et al. Quinoline and benzimidazole derivatives: candidate probes for in vivo imaging of tau pathology in Alzheimer's disease. J Neurosci. 2005;25(47):10857–62.
55. Fodero-Tavoletti MT, Okamura N, Furumoto S, Mulligan RS, Connor AR, McLean CA, et al. 18F-THK523: a novel in vivo tau imaging ligand for Alzheimer's disease. Brain. 2011;134(Pt 4):1089–100.
56. Lockhart SN, Baker SL, Okamura N, Furukawa K, Ishiki A, Furumoto S, et al. Dynamic PET measures of tau accumulation in cognitively normal older adults and Alzheimer's disease patients measured using [18F] THK-5351. PLoS One. 2016;11(6):e0158460.
57. Holt DP, Ravert HT, Dannals RF. Synthesis and quality control of [(18) F]T807 for tau PET imaging. J Labelled Comp Radiopharm. 2016;59(10):411–5.
58. Xia CF, Arteaga J, Chen G, Gangadharmath U, Gomez LF, Kasi D, et al. [(18)F]T807, a novel tau positron emission tomography imaging agent for Alzheimer's disease. Alzheimers Dement. 2013;9(6):666–76.
59. Wang M, Gao M, Xu Z, Zheng QH. Synthesis of a PET tau tracer [(11)C]PBB3 for imaging of Alzheimer's disease. Bioorg Med Chem Lett. 2015;25(20):4587–92.
60. Hashimoto H, Kawamura K, Igarashi N, Takei M, Fujishiro T, Aihara Y, et al. Radiosynthesis, photoisomerization, biodistribution, and metabolite analysis of 11C-PBB3 as a clinically useful PET probe for imaging of tau pathology. J Nucl Med. 2014;55(9):1532–8.
61. Kikuchi A, Takeda A, Okamura N, Tashiro M, Hasegawa T, Furumoto S, et al. In vivo visualization of alpha-synuclein deposition by carbon-11-labelled 2-[2-(2-dimethylaminothiazol-5-yl) ethenyl]-6-[2-(fluoro)ethoxy]benzoxazole positron emission tomography in multiple system atrophy. Brain. 2010;133(Pt 6):1772–8.
62. Bagchi DP, Yu L, Perlmutter JS, Xu J, Mach RH, Tu Z, et al. Binding of the radioligand SIL23 to alpha-synuclein fibrils in Parkinson disease brain tissue establishes feasibility and screening approaches for developing a Parkinson disease imaging agent. PLoS One. 2013;8(2):e55031.
63. Zhang X, Jin H, Padakanti PK, Li J, Yang H, Fan J, et al. Radiosynthesis and in Vivo evaluation of two PET Radioligands for imaging alpha-Synuclein. Appl Sci (Basel). 2014;4(1):66–78.
64. Chu W, Zhou D, Gaba V, Liu J, Li S, Peng X, et al. Design, synthesis, and characterization of 3-(benzylidene)indolin-2-one derivatives as ligands for alpha-synuclein fibrils. J Med Chem. 2015;58(15):6002–17.
65. Guo Q, Brady M, Gunn RN. A biomathematical modeling approach to central nervous system radioligand discovery and development. J Nucl Med. 2009;50(10):1715–23.
66. Guo Q, Owen DR, Rabiner EA, Turkheimer FE, Gunn RN. Identifying improved TSPO PET imaging probes through biomathematics: the impact of multiple TSPO binding sites in vivo. NeuroImage. 2012;60(2):902–10.
67. Jiang Z, Reilly J, Everatt B, Briard E. A rapid vesicle electrokinetic chromatography method for the in vitro prediction of non-specific binding for potential PET ligands. J Pharm Biomed Anal. 2011;54(4):722–9.
68. Friden M, Wennerberg M, Antonsson M, Sandberg-Stall M, Farde L, Schou M. Identification of positron emission tomography (PET) tracer candidates by prediction of the target-bound fraction in the brain. EJNMMI Res. 2014;4(1):50.

The Clinical Translation Process in Europe

Iván Peñuelas and Philip H. Elsinga

Introduction

This chapter describes the process of bringing radiopharmaceuticals from preclinical to first-in-man studies, specifically the first application of a new radiopharmaceutical in an imaging study in humans aiming to demonstrate the potential of the radiotracer to image a specific molecular target. This translational trajectory – often called moving "from bench to bedside" – includes several steps that require attention to specific regulations. As these regulations differ throughout the world, we will focus on the current situation in Europe. This chapter will focus on the philosophy developed in the European Union by European agencies and associations – *e.g.* the European Medicines Agency (EMA) and the European Pharmacopoeia (Ph. Eur.) – as well as societies such as the European Association of Nuclear Medicine (EANM).

As the first-in-man administration of a new radiopharmaceutical may hold safety risks for the volunteer, information derived from preclinical data regarding the toxicity, radiation dosimetry, product quality, and imaging potential of the radiopharmaceutical need to be available before human administration. All of this information is collected in an Investigational Medicinal Product Dossier (IMPD), and each of these topics will be discussed in more detail in this chapter. See Table 1 for references to legal binding documents, guidelines, and recommendations; see Table 2 for definitions of pertinent terms.

I. Peñuelas
Unidad de Radiofarmacia, Clinica Universidad de Navarra, Pamplona, Spain

P. H. Elsinga (✉)
Department of Nuclear Medicine and Molecular Imaging, University Medical Center Groningen, University of Groningen, Groningen, The Netherlands

Faculty of Medical Sciences, University of Groningen, Groningen, The Netherlands
e-mail: p.h.elsinga@umcg.nl

Investigational Medicinal Product Dossier (IMPD)

The European Union (EU) has produced a specific legislative framework for the use of radiopharmaceuticals in clinical trials. The preparation of an Investigational Medicinal Product Dossier (or IMPD) as part of the clinical trial application process is an essential step and is required by Regulation 536/2014 ("The Clinical Trials Regulation"). However, there are situations in which a simplified IMPD will be sufficient. A simplified IMPD may be submitted if information has been assessed previously as part of a marketing authorization in any Member State or a clinical trial under a competent authority (http://www.imp-dossier.eu/). The IMPD should include all the necessary information related to the chemical and pharmaceutical quality of the drug and product substances, as well as non-clinical data related to pharmacology, pharmacokinetics, radiation dosimetry, and toxicology. Of course, both a description of the clinical trial and a risk assessment must be included as well.

The format of the IMPD is described by the European Medicines Agency (EMA) "Guideline on the requirements to the chemical and pharmaceutical quality documentation concerning Investigational Medicinal Product in clinical trials" (Fig. 1). IMPD1 contains two main sections related to the production of the radiopharmaceutical: the "Drug Substance" (the active pharmaceutical ingredient, or API, the S-section) and the "Drug Product" (or finished product, described in the P-section). These parts are further divided into subsections that address more detailed topics, such as chemical information on the new entity, batch production and analysis, analytical methods, release criteria, *etc.* With respect to the documentation required during a marketing authorization application (MAA), information included in the IMPD should particularly focus on the risk aspects of the radiopharmaceutical (such as a justification of its use as well as data on toxicity and radiation dosimetry).

In the case of most PET radiotracers, the drug substance is not isolated and characterized during the preparation of the

J. S. Lewis et al. (eds.), *Radiopharmaceutical Chemistry*, https://doi.org/10.1007/978-3-319-98947-1_35

Table 1 The clinical translation process in Europe: legal binding documents, guidelines, and recommendations

Name	Common name	Official name	Webpage (as per November 2017)
Regulations			
Regulation (EU) 2017/1569	The GMP Regulation for IMPs	Commission Delegated Regulation (EU) 2017/1569 supplementing Regulation (EU) No 536/2014 of the European Parliament and of the Council by specifying principles of and guidelines for good manufacturing practice for investigational medicinal products for human use and arrangements for inspections	https://eur-lex.europa.eu/legal-content/EN/TXT/HTML/?uri=CELEX:32017R1569&from=EN
Regulation 536/2014	The Clinical Trial Regulation	Regulation (EU) No 536/2014 of the European Parliament and of the Council of 16 April 2014 on clinical trials on medicinal products for human use and repealing Directive 2001/20/EC	https://ec.europa.eu/health/sites/health/files/files/eudralex/vol-1/reg_2014_536/reg_2014_536_en.pdf
Regulation 1394/2007	The ATMP Regulation	Regulation (EC) No 1394/2007 of the European Parliament and of the Council of 13 November 2007 on advanced therapy medicinal products and amending Directive 2001/83/EC and Regulation (EC) No 726/2004 (Consolidated version: 02/07/2012)	https://ec.europa.eu/health/sites/health/files/files/eudralex/vol-1/reg_2007_1394/reg_2007_1394_en.pdf
Directives			
Directive (EU) 2017/1572	The New GMP Directive	Commission Directive (EU) 2017/1572 supplementing Directive 2001/83/EC of the European Parliament and of the Council as regards the principles and guidelines of good manufacturing practice for medicinal products for human use	https://eur-lex.europa.eu/legal-content/EN/TXT/HTML/?uri=CELEX:32017L1572&from=EN
Directive 2001/20	The Clinical Trial Directive	"Directive 2001/20/EC of the European Parliament and of the Council of 4 April 2001 on the approximation of the laws, regulations, and administrative provisions of the Member States relating to the implementation of good clinical practice in the conduct of clinical trials on medicinal products for human use"	https://ec.europa.eu/health/sites/health/files/files/eudralex/vol-1/dir_2001_20/dir_2001_20_en.pdf
Directive 2001/83	The Medicinal Products Directive	Directive 2001/83/EC of the European Parliament and of the Council of 6 November 2001 on the community code relating to medicinal products for human use (Consolidated version: 16/11/2012)	https://ec.europa.eu/health/sites/health/files/files/eudralex/vol-1/dir_2001_83_consol_2012/dir_2001_83_cons_2012_en.pdf
Directive 2003/94	The GMP Directive	Commission Directive 2003/94/EC of 8 October 2003 laying down the principles and guidelines of good manufacturing practice in respect of medicinal products for human use and investigational medicinal products for human use	https://ec.europa.eu/health/sites/health/files/files/eudralex/vol-1/dir_2003_94/dir_2003_94_en.pdf
Directive 2001/20	The GCP Directive	Directive 2001/20/EC of the European Parliament and of the Council of 4 April 2001 on the approximation of the laws, regulations, and administrative provisions of the Member States relating to the implementation of good clinical practice in the conduct of clinical trials on medicinal products for human use (Consolidated version : 07/08/2009)	https://ec.europa.eu/health/sites/health/files/files/eudralex/vol-1/dir_2001_20/dir_2001_20_en.pdf
Directive 2010/63		Directive on the protection of animals used for scientific purposes	http://eur-lex.europa.eu/legal-content/EN/TXT/HTML/?uri=CELEX:32010L0063&from=EN
Guidelines and concept papers			
EMA/CHMP/SWP/545959/2016		Concept paper on the development of guidance on the non-clinical evaluation of radiopharmaceuticals	http://www.ema.europa.eu/docs/en_GB/document_library/Scientific_guideline/2017/07/WC500232667.pdf
CHMP/QWP/185401/2004	IMPD guideline (deprecated)	Guideline on the requirements to the chemical and pharmaceutical quality documentation concerning investigational medicinal products in clinical trials	https://ec.europa.eu/health/sites/health/files/files/eudralex/vol-10/18540104en_en.pdf
EMA/CHMP/QWP/834816/2015 (draft)	New IMPD guideline	Guideline on the requirements to the chemical and pharmaceutical quality documentation concerning investigational medicinal products in clinical trials	http://www.ema.europa.eu/docs/en_GB/document_library/Scientific_guideline/2016/04/WC500204674.pdf
CHMP/SWP/28367/07	First-in human guideline	Guideline on strategies to identify and mitigate risks for first-in human clinical trials with investigational medicinal products	http://www.ema.europa.eu/docs/en_GB/document_library/Scientific_guideline/2009/09/WC500002988.pdf
CHMP/BWP/534898/2008		Guideline on the requirements for quality documentation concerning biological investigational medicinal products in clinical trials	http://www.ema.europa.eu/docs/en_GB/document_library/Scientific_guideline/2012/05/WC500127370.pdf

No reference number in document	AxMP recommendations	Auxiliary medicinal products in clinical trials (June 2017)	https://ec.europa.eu/health/sites/health/files/files/eudralex/vol-10/2017_06_28_recommendation_on_axmps.pdf
No reference number in document	Risk proportionate approaches recommendations	Risk proportionate approaches in clinical trials (April 2017)	https://ec.europa.eu/health/sites/health/files/files/eudralex/vol-10/2017_04_25_risk_proportionate_approaches_in_ct.pdf
Guidelines from associations			
	EANM RP IMPD	EANM guideline for the preparation of an Investigational Medicinal Product Dossier (IMPD)	https://link.springer.com/article/10.1007%2Fs00259-014-2866-8
		Guideline to regulations for radiopharmaceuticals in early-phase clinical trials in the EU	https://link.springer.com/article/10.1007/s00259-008-0853-7
	EANM cGRPP guidance	EANM guidance on current good radiopharmacy practice (cGRPP) for the small-scale preparation of radiopharmaceuticals	http://www2.eanm.org/publications/guidelines/5_EJNMMI_Guidance_cGRPPfulltext_05_2010.pdf
	EANM cGRPP guideline	EANM guidelines on current good radiopharmacy practice (cGRPP) in the preparation of radiopharmaceuticals	http://www2.eanm.org/publications/guidelines/gl_radioph_cgrpp.pdf

Table 2 The clinical translation process in Europe: terms and definitions

Term	Definition
Radiopharmaceutical	Any medicinal product which, when ready for use, contains one or more radionuclides included for a medicinal purpose
Phase 0 study	First-in-man study of a medical device or drug in humans to obtain pharmacokinetic/pharmacodynamic information. Group sizes of 10–15 persons are typically used, most often healthy volunteers.
Phase 1 study	A study to assess the safety, adverse reactions, and dosage of a drug. The group size can be up to 100 subjects.
Target	The intended binding or interaction site of a radiopharmaceutical, for example, a receptor, enzyme, and transporter
PK/PD	Pharmacokinetics/pharmacodynamics
IMP	Investigational medicinal product, a medicinal product that is being tested or used as a reference – including as a placebo – in a clinical trial
IMPD	Investigational Medicinal Product Dossier. A document that compiles information on the quality, manufacture, and control of an IMP as well as data from non-clinical studies and its clinical use. The information in an IMPD should be concise; it is preferable to present data in tabular form, accompanied by a brief narrative highlighting the most salient points.
AxMP	Auxiliary medicinal product, a medicinal product used for the needs of a clinical trial as described in the protocol but not as an investigational medicinal product
Clinical trial protocol	A document that describes the objectives, design, methodology, statistical considerations, and organization of a clinical trial
Ethical committee	An independent body constituted of medical professionals and nonmedical members whose responsibility is to ensure the protection of the rights, safety, and well-being of human subjects involved in a trial and to provide public assurance of that protection
EudraCT	A European database that contains all ongoing or completed clinical trials falling within the scope of Directive 2001/20/EC, *i.e.* with at least one investigator site in the EU (including the European Economic Area) and commencing after the implementation of Directive 2001/20/EC by the Member States
Good clinical practice	A set of detailed ethical and scientific quality requirements for designing, conducting, performing, monitoring, auditing, recording, analyzing, and reporting clinical trials that ensures that the rights, safety, and well-being of subjects are protected and that the data generated in clinical trials are reliable and robust

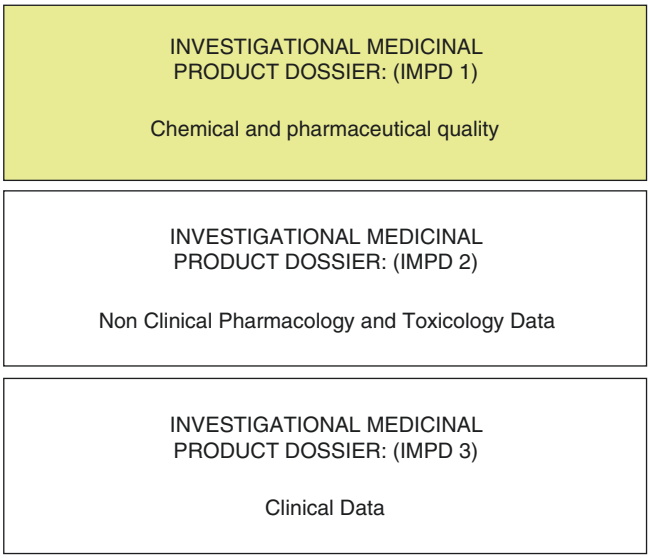

Fig. 1 Schematic template displaying the main sections of an Investigational Medicinal Product Dossier (IMPD)

radiopharmaceutical, especially when the process is continuous and automated. Therefore, in the proposed guidelines, information in various 2.2.1.S subsections is not necessary, and the required details can instead be provided in the corresponding 2.2.1.P subsections [EANM guideline for the preparation of an Investigational Medicinal Product Dossier (IMPD)].

Toxicity Issues/Dosimetry

Information on toxicity as an indicator of the safety of the IMP should be included in the IMPD as part of the non-clinical pharmacology section. As the requirements for toxicity are addressed in a variable way within Europe, a position paper has been published by the Radiopharmacy Committee of the EANM addressing toxicology studies for new diagnostic and therapeutic radiopharmaceuticals [1]. This paper excludes endogenous and ubiquitous substances in human such as radiolabeled amino acids, as they are present in the body anyway and no toxicity studies would therefore be required.

To better understand how to address different points of view regarding toxicity, two distinct scenarios are recognized with respect to the reaction of a radionuclide with a non-radioactive precursor:

Scenario #1

The radiolabeling reaction of the radionuclide with a chemical precursor proceeds quantitatively. Therefore, no purification is required to separate the product and the unreacted radionuclide. In these cases, the precursor is typically used in a large molar excess over the radionuclide (*e.g.* the complexation of a radiometal by a chelator-bearing biomolecule). As a result, all components – including the precursor (or precursor hydrolysis product) and the resulting radiopharmaceutical active ingredient – are injected into the patient. In this case, the precursor or precursor hydrolysis product should be subjected to preclinical toxicity studies.

Scenario #2

The radiolabeling reaction of the radionuclide with a chemical precursor does not proceed quantitatively. In this scenario, purification is required to separate the desired radioactive compound from the reaction mixture, including the unreacted radionuclide and the precursor. In this case, the molecule containing a stable isotope of the intended radioactive nuclide should be used (*e.g.* ^{19}F instead of ^{18}F) for toxicity testing.

Based on the above scenarios and taking into consideration the generally accepted toxicity guidelines, the EANM has described a new approach for the assessment of toxicology based upon three distinct toxicological limits: (1) <1.5 μg, (2) <100 μg, and (3) >100 μg.

Less Than 1.5 μg

The <1.5 μg limit is based on the Threshold of Toxicological Concern (TTC) concept. A TTC value of 1.5 μg/day intake of a genotoxic impurity is considered to be associated with an acceptable risk – excess cancer risk of <1 in 100,000 over a lifetime – for most pharmaceuticals. Based on case-by-case judgments for radiopharmaceuticals applied in amounts of <1.5 μg per dose, it can be considered that no toxicology tests are needed. However, a risk assessment on potential toxicity should be included. This risk assessment of potential toxicity may be performed by in silico screening and (quantitative) structure-activity relationship (Q)SAR. For radiopharmaceuticals, doses of <1.5 μg can be achieved when the radiotracer is produced with high molar activity. For example, in the case of a 250 MBq dose of a radiopharmaceutical with a molecular weight of 300 and a molar activity of 50,000 GBq/mmol, only 1.5 μg of tracer is actually injected. In light of the fact that next-generation cameras are much more sensitive – and therefore require fewer MBq of activity – this dosage of <1.5 μg will be much easier to achieve in the future.

Less Than 100 µg

In this case, we are dealing with the so-called microdosing concept, and the "Note for guidance on non-clinical safety studies for the conduct of human clinical trials and marketing authorization for pharmaceuticals" (CPMP/ICH/286/95) can be applied. Typically, a 100-fold larger dose than the clinical dose is tested in 30 rodents. More specifically, ten animals/sex are examined on the day following the injection, and five animals/sex are examined after 14 days (via hematology, clinical chemistry, necropsy, and histopathology). Subsequently, allometric scaling should be applied to translate from animal to human doses. It is important to note that at present, *in vivo* toxicology tests must be performed in compliance with GLP standards. Alternatively, the 1000-fold scaling is mentioned in the same guideline and may be followed if allometric scaling is not used. Both approaches can be used and may be subject to negotiation with the appropriate authorities.

One major limitation of this microdosing approach is that it does not take into account that pharmacological and toxicological effects are usually not determined by the mass but the molar amount administered. As a result, the toxicological effects of larger molecules such as proteins or peptides can be underestimated. In light of this, in the case of larger molecules such as proteins, the FDA's "Guidance for Industry, Investigators, and Reviewers: Exploratory IND Studies" sets the limit to <30 nmoles.

To reduce time-consuming and costly toxicity studies, biodistribution data (often including imaging) from preclinical studies can be used to assess toxicity as well. These studies give detailed quantitative data on the accumulation of the drug in tissues and its elimination via excretion pathways. Based on these *in vivo* data, extended single dose toxicity studies can be focused primarily on risk organs and tissues. Such arguments must be made on a case-by-case basis, and the rationale for this approach must be described in detail in the application process.

More Than 100 µg

Dosages of more than 100 µg of a substance may be required for imaging with radiolabeled peptides, proteins, or antibodies or for therapeutic applications. Under these circumstances, masses in excess of 100 µg are used because cold peptide/protein has been added to the formulated radiopharmaceutical to modify the biodistribution (*e.g.* to uptake in organs such as the liver). In this case, the "Note for guidance on non-clinical safety studies for the conduct of human clinical trials and marketing authorization for pharmaceuticals" (CPMP/ICH/286/95) can also be applied. An extended single dose toxicity study should be done in both a rodent and non-rodent species, as well as a test for genotoxicity (usually an Ames test). Apart from following the current guidelines, it is also necessary to perform a risk assessment for each compound in order to evaluate which toxicological studies are needed and/or useful. Therefore, a scientific advice meeting with the appropriate authorities can be very helpful before starting expensive toxicity studies.

Radiation Dosimetry

Before conducting a study in humans, an estimate of the radiation dosimetry of the radiotracer is required. The intended radiation dose to a patient should always be justified and is a requirement by the local/national authorities in the application for the clinical trial. Generally speaking, the radiation dose can be estimated from animal biodistribution data using OLINDA software and then later confirmed in humans. This can be performed using imaging in nonhuman primates or via multi-timepoint biodistribution studies in rodents in conjunction with a Medical Internal Radiation Dose (MIRD) system for calculations. A dose equation consisting of biological and physical parameters is proposed by MIRD. The biological parameters are determined by the time that the radioactivity spends in each organ and the physiological effects of the decay of the radiopharmaceutical. Therefore, knowledge of the distribution of the radioactivity within the body is required, data which can be obtained by extrapolation from preclinical experiments, external measurements with a PET or a SPECT camera, and estimations using compartmental models or measurements of excretory fluids. The physical parameters depend on the nature of the radiation, the absorption characteristics, and the anatomical model. The nuclear characteristics of any radionuclide can be found in MIRD radionuclide data as well as decay schemes published by the Society of Nuclear Medicine in 1989. In addition, source/target organ configurations, absorbed fractions, and S-values can be found in MIRD pamphlets.

The guidelines of the International Commission on Radiological Protection (ICRP 62) are adapted to estimate the risks and consequences of radiation doses received by patients. Several risk categories are defined. The radiation dose of all radiopharmaceuticals falls within categories IIb and III. The ICRP has described these categories as follows:

Category IIb: Effective Dose Range 1–10 mSv (Adults)

This category involves risks to the irradiated individual of the order of 1 in 10,000. The degree of benefit to society from studies in this category should be "moderate"; the

benefit would be expected to be "aimed directly at the diagnosis, cure, or prevention of disease."

Category III: Effective Doses Greater Than 10 mSv (Adults)

Here, the risks to the irradiated individual are estimated at greater than one in a thousand. This is a moderate risk for a single exposure but might be considered as verging on the unacceptable for continued or repeated exposures. To justify investigations in this category, the benefit would have to be "substantial and usually directly related to the saving of life or the prevention or mitigation of serious disease." Doses should be kept below the threshold for deterministic effects unless these are necessary for the therapeutic effect.

In practice, the radiation dose to a patient should be kept as low as reasonable achievable (the ALARA principle). The next-generation PET and SPECT cameras are significantly more sensitive than the currently used instruments, so in the future, lower amounts of radioactivity can be administered to humans.

Preclinical Requirements

Data from preclinical studies should be collected in order to assess whether the new radiopharmaceutical performs according to the expectations. The results from these studies need to be summarized in the IMPD. The following preclinical data illustrate that the interaction of the radiopharmaceutical with the intended target is the major driver of uptake and thus contributes to the justification for using a new radiopharmaceutical in humans:

- Plasma and metabolic stability
- Affinity for the target
- *Ex vivo* biodistribution data obtained in appropriate animal models
- Calculations of non-specific and non-saturable binding
- Imaging data obtained in appropriate animal models
- Pharmacokinetic data obtained in appropriate animal models
- Non-clinical pharmacology
- Toxicity (discussed above)
- Radiation dosimetry (discussed above)

With respect to the first item on the list, the stability of a radiopharmaceutical is important because the overly rapid breakdown of the radiotracer can prevent its interaction with the intended target. Furthermore, a fundamental understanding of the metabolic fate of a radiopharmaceutical can be extraordinarily helpful in assessing its *in vivo* performance. For example, it is crucial to know whether the radiolabeled metabolites of the parent tracer have binding affinity for the same target as the intact radiopharmaceutical. In addition, the non-specific uptake of metabolites in the tissue of interest can cause confounding results. Knowledge of the identity of metabolites can also help determine the optimal radiolabeling position in the molecule. Ideally, the radiolabel should be excreted rapidly upon metabolic breakdown. Along these lines, it is advisable to perform metabolite studies with cold reference material in human liver microsomes to assess the metabolic stability of the radiopharmaceutical and the chemical identity of potential metabolites. Information on metabolic stability can be obtained from biodistribution studies.

The affinity of a radiopharmaceutical for its target is also a critical parameter. A radiotracer is often chemically modified after radiolabeling, especially in the case of labeling with ^{18}F or radiometals. As a result, it is important to test the affinity of the new molecular entity for its target. Affinities are usually determined by competition assays for interaction with the target (*e.g.* receptors, transporters, enzymes). Of course, the radiopharmaceutical must have sufficient affinity to ensure contrast with its surrounding tissue. As uptake and contrast are also determined by the expression levels of the target, the ratio between the density of the target and the affinity of the radiotracer should be assessed. In the case of receptor-targeted radiopharmaceuticals, the ratio B_{max}/K_D can be used and should be larger than 4 and preferably >10.

Tissue uptake data obtained either from imaging or biodistribution experiments can provide information on several of the *in vivo* characteristics of the radiopharmaceutical, including its uptake in target-rich tissues (specific binding), uptake in target-negative tissues (non-specific binding), excretion pathways, and pharmacokinetics. Critically, animal welfare legislation should also be followed when obtaining preclinical biodistribution and/or imaging data. This legislation is based on the 3R approach – replacement, reduction, and refinement – and should therefore include a justification for the selected animal model, a justification of the required number of animals for the study, and an evaluation of alternative approaches which could yield comparable information. The European legislation describing the protection of animals with respect to scientific research is Directive 2010/63.

Generally speaking, it is recommended to first use healthy mice or rats to investigate the pharmacokinetic profile, excretion profile, and non-specific uptake of a radiopharmaceutical. To further test the specificity and selectivity of a radiotracer, the following experiments could be employed:

- The use of animal models with increased expression of the target, most commonly disease models such as tumor-bearing animals (though many animal models are

available for cardiovascular, brain, and inflammation research as well)
- The use of knockout mice
- Blockade experiments based on the co-administration of a known competitive ligand or substrate
- Displacement studies based on the administration of a competitive ligand or substrate in the equilibration phase

Relevant Clinical Data

All available clinical information on the radiopharmaceutical and/or its non-radioactive reference counterpart should be collected in the IMPD as it might be useful to assess its safety. This includes information on absorption, distribution, metabolism, and excretion (ADME). Available clinical data and information on the investigated patient groups, related drugs/radiopharmaceuticals, adverse events, and radiation dosimetry in combination with other exposures in the study (*i.e.* CT or other radiopharmaceuticals) should be included as well.

Regulations for the Production of a Radiopharmaceutical

When bringing a novel radiopharmaceutical into the clinic, specific requirements for its production must be considered. According to European regulations, a radiopharmaceutical is "Any medicinal product which, when ready for use, contains one or more radionuclides (radioactive isotopes) included for a medicinal purpose" (Art. 1.6 Directive 2001/83/EC). Since it is a medicinal product, a radiopharmaceutical must comply with all the requirements for such products, though specific considerations exist in relation to radiopharmaceuticals due to their unique traits. Namely, they are radioactive products, and the radiation dose to the patient must hence always be considered. Furthermore, their radioactive nature means that their composition is not constant (due to radioactive decay) and that their preparation process has some peculiarities that we shall discuss in more detail below.

The manufacturing or importation of medicinal products – including investigational medicinal products – is subject to a manufacturing or import authorization. The holder of such an authorization is obliged to comply with the principles and guidelines of good manufacturing practice (GMP) for medicinal products and to use as starting materials only active substances (active pharmaceutical ingredients) that have been manufactured in accordance with GMP. The principles and guidelines of GMP concerning medicinal products for human use and investigational medicinal products are in Commission Directive 2003/94/EC, the so-called GMP Directive. In addition, many detailed GMP guidelines from the European Medicines Agency (EMA) exist as well. Nonetheless, the special nature of radiopharmaceuticals has necessitated special provisions. One such special provision stems from the radioactive nature of radiopharmaceuticals, resulting in the fact that they are subject to both radiation protection legislation (designed for the protection of personnel) and GMP legislation (designed for the protection of the patient).

Good Manufacturing Practices

Good manufacturing practices (GMP) are the basis for ensuring that medicinal products are produced in such a way that it can be guaranteed that they are fit for their intended use, comply with the requirements of the marketing or clinical trial authorizations, and do not place patients at risk due to inadequate safety, quality, or efficacy. To achieve this quality objective reliably, there must be a comprehensively designed and correctly implemented pharmaceutical quality system that incorporates GMP and quality risk management (QRM). The pharmaceutical quality system involves quality management, good manufacturing practice, quality control, product quality review, and quality risk management. Quality management – in which good manufacturing practice is included – is a wide-ranging concept that covers all matters that individually or collectively influence the quality of a product. GMP is concerned with both production and quality control. In a GMP-based system, all processes are defined, systematically reviewed, and shown to be capable of consistently providing medicinal products of the required quality and complying with their specifications. Validation is a crucial part of GMP, meaning that all critical steps of manufacturing processes as well as significant changes to these processes are validated.

The scope of GMP includes the following aspects of the production of a medicinal product: the pharmaceutical quality system, personnel, premises and equipment, documentation, production, quality control, self-inspection, and outsourced activities. Complaints and product recalls must also be taken into account. Each of the aforementioned topics is addressed in a specific chapter of the GMP guidelines (EudraLex Chap. 4). In addition, these guidelines also include several annexes that deal with specific topics related to GMP production. Of these, there are several that are especially important in the context of the production of radiopharmaceuticals for investigational purposes in humans: manufacture of radiopharmaceuticals (Annex 3), manufacture of investigational medicinal products (Annex 13), manufacture of sterile products (Annex 1), computerized systems (Annex 11), qualification and validation (Annex 15), and parametric release (Annex 17). These annexes are especially

relevant because they address some of the unique aspects of the production of radiopharmaceuticals. For example, radiotracers are most often produced using computerized systems to ensure robustness and reproducibility and to provide radiation protection for the operator. Furthermore, in many cases, due to the extremely short life of radiopharmaceuticals, not all of the quality controls of the final MP (*i.e.* sterility) can be finished before the radiopharmaceutical is released for human use. The application of GMP in the production of radiopharmaceuticals is intended to ensure not only that the subjects to whom these radiopharmaceuticals are administered are not placed at risk but also that the results of the clinical trials are not compromised by inadequate safety, quality, or efficacy due to unsatisfactory manufacture. Notwithstanding the production of radiopharmaceuticals under GMP, in many cases – especially in hospitals and academia-based radiopharmacies –radiopharmaceuticals are produced in accordance with an individual prescription for an individual patient or in accordance with a pharmacopoeia monograph. The preparation of such radiopharmaceuticals can be done under the provisions stated in Article 3.1 or 3.2 of Directive 2001/83, that is, magistral or officinal preparations. Such preparations are considered out of the scope of the directive and regulated at the national level. This has led to substantial variations with respect to whether (or not) such an approach can be used for radiopharmaceuticals in different EU countries. In principle, such a radiopharmaceutical could not be used in clinical trials according to the Clinical Trial Directive. However, the new Clinical Trial Regulation has an exception – Article 63.2 Regulation 536/2014 – for diagnostic radiopharmaceuticals used in clinical trials under some circumstances: diagnostic radiopharmaceuticals used as IMPs when the production process is carried out in hospitals and when they are intended to be used exclusively in hospitals. In this case, there is no need for GMP production. This decision follows the spirit of "proportionate risk" in the new regulation and allows that in some specific cases, it should be possible to allow deviations from those rules in order to facilitate the conduct of a clinical trial. Therefore, the applicable rules should allow for some flexibility, provided that subject safety as well as the reliability and robustness of the data in the clinical trial are not compromised.

We have recently seen two new relevant documents related with GMP, albeit both of them will only become applicable once the Clinical Trial regulation is applicable. Such documents are the new Regulation (EU) 2017/1569 specifying principles of and guidelines for good manufacturing practice for investigational medicinal products for human use and the new Directive (EU) 2017/1572 supplementing Directive 2001/83/EC of the European Parliament and of the Council as regards the principles and guidelines of good manufacturing practice for medicinal products for human use.

Needless to say, GMP is not the only way to ensure the adequate quality of a medicinal product: rather, it is just one of the most widely used ways to do it. We should not forget that the implementation of strict GMP for the production of radiopharmaceuticals could (in many cases) introduce so many hurdles that the availability of critical radiotracers for trials is reduced. Yet still, GMP is intended to ensure that there is consistency between batches of the same investigational medicinal product used in the same or different clinical trials and that changes during the development of an investigational medicinal product are adequately documented and justified.

Validation

Validation is the act of proving that any procedure, process, equipment, material, activity, or system actually leads to the expected results, while *qualification* indicates the actions and operations aimed to demonstrate that a system or piece of equipment is properly installed, works correctly, and leads to the expected results. In any case, qualification may be considered a part of validation. General Principles on Validation and Qualification are outlined in Annex 15 of GMP, while the validation of analytical methods are outlined in the Note for Guidance on validation of analytical procedures: text and methodology [ICH Q(2) guideline]. In any case, both documents are very general, though radiopharmaceuticals require specific validation protocols because they are radioactive and their shelf life is often extremely short. When dealing with the production of radiopharmaceuticals, the proper qualification of all equipment involved in production or QC is of the utmost importance. This would be the first step in the overall validation of the processes in which this equipment is used. When qualifying equipment used for the measurement of radioactivity, issues including the range of activity utilized, the energy and type of radiation used, and the efficiency of the detectors under each of these conditions must be considered.

The overall validation activities should be described in a general document – the validation master plan, VMP – that should not only detail a general validation policy with a description of the intended working methodology but also all of the issues related to the overall validation process. All validation activities must be extensively documented. Further information on the overall process can be found in an article by Todde *et al.* [2].

In addition, good laboratory practices (GLP) should be followed whenever possible, especially with respect to non-clinical pharmacology and toxicology data. The principles of GLP promote the quality and validity of data in the testing of chemicals and prevent fraudulent practices. In this way, requirements including organization, personnel, the integrity and traceability of quality management system data, inspections, archiving, the cross-contamination of data and materials, the qualification and validation of equipment and

experimental methods, and the storage of materials must be considered.

EU Regulation Related to Clinical Trials

The regulation of clinical trials in the EU has been ruled by Directive 2001/20/EC (the "Clinical Trial Directive") and was concretized further by Directive 2005/28/EC (the "GCP Directive"), both of which lay down principles and detailed guidelines for good clinical practice (GCP). In addition, the preparation of medicinal products for clinical trials had to follow the principles established in Directive 2003/94/EC (the "GMP Directive"), as we have previously explained. However, because a directive needs transposition to the national legislation corpus of the different states in the EU, substantial differences in its practical implementation have emerged across Europe. Soon after its implementation in the practice of the Clinical Trial Directive, the negative effects that this regulation had on clinical research in Europe became evident. Patients and researchers from academia, foundations, hospitals, research networks, and industry alike criticized the directive mainly for its disproportionately stringent regulatory requirements, the high costs associated with satisfying these regulations, and the lack of harmonization of the applicable rules necessary for multinational clinical trials.

The principal negative attributes of the CT Directive were (1) the legislative differences between different nations; (2) the obstacles to the conduct of clinical trials; (3) the significant expense of the highly demanding regulatory requirements, irrespective of the level of risk of the trial; (4) the sluggish pace of the trial implementation process; and (5) the theoretically similar but practically different ethical and regulatory requirements between countries. Not surprisingly, this has led to a decrease in investigator-driven studies since its implementation.

Regulation 536/2014 ("The Clinical Trials Regulation") was approved in April 2014 and replaced Directive 2001/20. However, the new regulation is not applicable yet. The main characteristics of the new regulation are (1) it repeals the Clinical Trial Directive; (2) as it needs no transposition and is enforceable "as is," it ensures that the rules for conducting clinical trials are identical throughout Europe; (3) the new regulation is focused on patient safety and reasonable and proportionate risk assessment; (4) it facilitates multicenter transnational clinical trials; and (5) it established a streamlined application procedure that greatly simplifies the overall authorization procedures. In summary, the new procedures will ensure patient safety and public health, promote strict scientific and ethical reviews, avoid administrative delays, and encourage prompt answers for applicants.

For the specific case of radiopharmaceuticals, Regulation 536/2014 introduces two very relevant changes that are exceptions to the general rules. First, it establishes that there is no need to hold an authorization for the preparation of radiopharmaceuticals used as diagnostic (not therapeutic) IMPs under specific circumstances. And second, it establishes there is no need for the GMP production of these diagnostic radiopharmaceuticals, as the regulation itself allows for some flexibility provided that subject safety – as well as the reliability and robustness of the data generated in the clinical trial – is not compromised. As previously stated, while GMP are the most common way to ensure the quality of the products, we must emphasize that it is not the only method that can be used to ensure the quality and safety of radiopharmaceuticals provided a sufficiently robust pharmaceutical quality control system is implemented.

As a whole, the new CT Regulation establishes a new framework for clinical research in the EU. It tries to correct all of the problems and drawbacks that the old CT Directive generated and focuses on the protection of subjects involved in CTs using reasonable and proportionate risk assessment as well as the overall simplification of procedures. Regarding radiopharmaceuticals, very relevant changes have been introduced for diagnostic radiotracers that will hopefully make clinical research easier. Hopefully, all the changes introduced by the regulation will help increase and facilitate clinical research in the EU, not only for sponsored CTs but also for investigations promoted in the academia environment.

Specifics for the Preparation and Use of Radiopharmaceuticals for Research Applications in Humans in Different EU Countries

Numerous differences exist among the different EU countries with respect to the use of novel radiopharmaceuticals in humans, mainly due to the fact that the currently available pan-European regulation for clinical trials is the CT Directive until the new CT Regulation becomes applicable (probably by 2018). In addition, the in-house preparation of radiopharmaceuticals can be considered under the umbrella of "pharmacy practice" in some countries, while this is not the case in others. This has led to significant heterogeneity and means that procedures that can be done in some countries cannot be done in the same way in others [3, 4].

Guidelines and Guidance Documents

Apart from the aforementioned legislation, there are a good number of guidelines and guidance documents published by groups such as the European Medicines Agency (EMA) and the European Association of Nuclear Medicine. Guidelines

are not mandatory but rather are recommendations for the effective implementation of legislation; guidances are also recommendations, but in a more specific and detailed form.

Very recently, the Safety Working Party of the CHMP of EMA has recommended the issuing of a guidance on principles for the non-clinical development of radiopharmaceuticals. As a preliminary step, a concept paper – *Concept paper on the development of guidance on the non-clinical evaluation of radiopharmaceuticals* – has been open for public consultation from August till October 2017. In principle, the Safety Working Party suggests that the paper should be based on current guidelines and the scientific review of the different intended uses of both diagnostic and therapeutic radiopharmaceuticals.

The main documents of interest in this respect are:

- CHMP/SWP/28367/07: "Guideline on strategies to identify and mitigate risks for first-in-human clinical trials with investigational medicinal products" that covers non-clinical issues for consideration prior to the first administration in humans as well as the design and conduct of trials in the initial phase of single and ascending doses during clinical development.
- CHMP/QWP/185401/2004: Guideline on the requirements for the chemical and pharmaceutical quality documentation concerning investigational medicinal products in clinical trials. This guideline addresses the documentation of the chemical and pharmaceutical quality of IMPs to be submitted to the competent authority for approval prior to beginning a clinical trial in humans.
- EMA/CHMP/QWP/834816/2015 (draft): Guideline on the requirements for the chemical and pharmaceutical quality documentation concerning investigational medicinal products in clinical trials. This guideline replaces the "Guideline on the requirements for the chemical and pharmaceutical quality documentation concerning investigational medicinal products in clinical trials" (CHMP/QWP/185401/2004 final). This guideline addresses the documentation on the chemical and pharmaceutical quality of IMPs and AxMPs containing chemically defined drug substances, synthetic peptides, synthetic oligonucleotides, herbal substances, herbal preparations, and chemically defined radioactive/radiolabeled substances to be submitted to the competent authority for approval prior to beginning a clinical trial in humans.
- CHMP/BWP/534898/2008: Guideline on the requirements for quality documentation concerning biological investigational medicinal products in clinical trials – this guideline addresses the specific documentation requirements on the biological, chemical, and pharmaceutical quality of IMPs containing biological/biotechnology-derived substances. The guidance outlined in this document applies to proteins and polypeptides, their derivatives, and products of which they are components (*e.g.* conjugates) and thus includes radiolabeled bioconjugates, although they are not even mentioned as such.
- EANM guideline for the preparation of an Investigational Medicinal Product Dossier (IMPD): This guideline aims to take radiopharmaceutical scientists through the practicalities of preparing an IMPD, in particular giving advice where the standard format is not suitable. Examples of generic IMPDs for three classes of radiopharmaceuticals are given: a small molecule, a kit-based diagnostic test, and a therapeutic radiopharmaceutical.
- EANM guideline to regulations for radiopharmaceuticals in early phase clinical trials in the EU. The purpose of this guideline is to help investigators by giving an overview of relevant current EU requirements concerning the quality of starting materials and final drug products (the radiopharmaceuticals) as well as the non-clinical safety studies and dosimetry considerations for designing a human clinical trial that includes the use of radiopharmaceuticals.
- EANM guidance on current good radiopharmacy practice (cGRPP) for the small-scale preparation of radiopharmaceuticals. This guidance is meant as a guidance to Part B of the EANM "Guidelines on Good Radiopharmacy Practice (GRPP)" issued by the Radiopharmacy Committee of the EANM (see www.eanm.org) and covers the small-scale, "in-house" preparation of radiopharmaceuticals which are not kit procedures. The aim is to provide more detailed and practice-oriented guidance to those who are involved in the small-scale preparation of PET, therapeutic, or other radiopharmaceuticals which are not intended for commercial purposes or distribution.
- EANM guidelines on current good radiopharmacy practice (cGRPP) in the preparation of radiopharmaceuticals. The preparation of radiopharmaceuticals for injection involves adherence to regulations on radiation protection as well as to appropriate rules of working under aseptic conditions, which are covered by these guidelines on good radiopharmacy practice (GRPP)

In addition – and to clarify and facilitate the implementation of Regulation (EU) No. 536/2014 – several recommendation documents have recently been published in EudraLex Vol 10:

- Auxiliary medicinal products (AxMP) in clinical trials (June 2017). This is the previously named guidance on investigational medicinal products (IMPs) and "noninvestigational medicinal products" (NIMPs). This document includes as AxMP those PET radiopharmaceuticals administered to assess the effect of a new drug whose effects are the primary end point of a clinical trial.

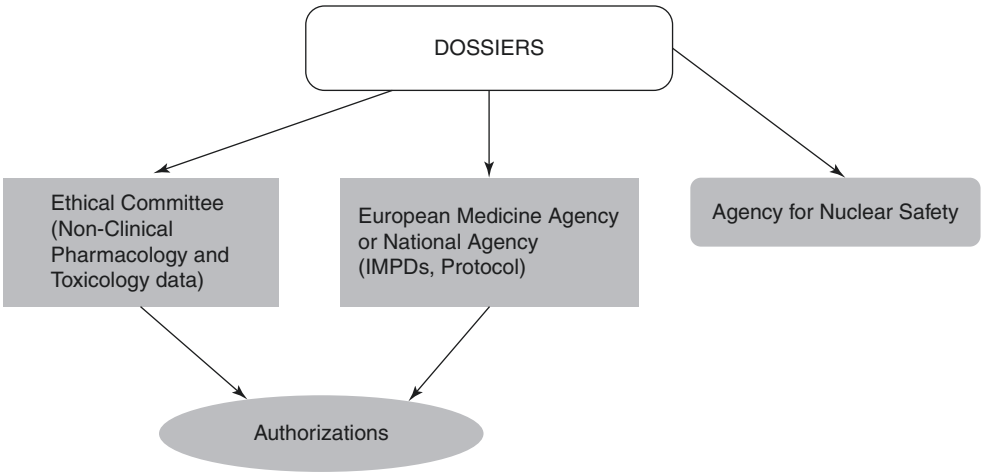

Fig. 2 The authorizations required and parties involved in setting up a clinical trial

- Risk proportionate approaches in clinical trials (April 2017). This document provides further information on how a risk proportionate approach can be implemented and also highlights the areas identified in the regulation that allow such adaptation. The aim of risk control is to determine whether the risk is acceptable and, if not, to reduce the risk to an acceptable level. For this purpose, predefined quality tolerance limits should be established. The main components of risk control are risk mitigation, adaptation, and risk acceptance actions (including accountability).

To perform clinical trials, authorizations are required from the medicine agency, which can be the EMA, as well as national/local agencies. These agencies will ask for the IMPD and the Study Protocol (Fig. 2). In addition, authorization is needed from the Ethics Committee requiring investigator brochures, and investigators will need to follow GCP. GCP is an international ethical and scientific quality standard for the design, conduct, recording, and reporting of clinical trials involving humans. The clinical trial should comply to provide public assurance that the rights, safety, and well-being of trial subjects are protected and that the quality and reliability of the data are secured. The key elements of the quality system include:

- The development, implementation, and maintenance of documented procedures
- The training of sponsor personnel as well as the personnel in affiliates, at partners, and at trial sites
- The validation of computerized systems
- The monitoring of trial sites and technical facilities on-site or by using centralized monitoring techniques
- The establishment of appropriate data management and quality control procedures
- The performance of internal and external audits by independent auditors

Serious adverse events (SAEs) and suspected unexpected serious adverse reactions (SUSARs) must be documented and reported, as they can be the result of the administered radiopharmaceutical. Depending on the local situation, a pharmaco-vigilance document should be kept.

The Future

We foresee the following developments affecting the production of radiopharmaceuticals:

Increased Use of Radiotherapeutic Agents We believe that in the next few years, we will see an increase in the use of radiotherapeutic agents, mainly radiopharmaceuticals labeled with alpha emitters. The use of these agents poses tremendous challenges during the development process due to their intended toxicity and the difficulties they present with respect to the evaluation of their safety. The new guideline on the non-clinical evaluation of radiopharmaceuticals – which will hopefully be published soon by the EMA – will help clarify the complex world that researchers are currently trying to navigate.

More Sensitive Cameras Technological advances in both PET and SPECT cameras will produce increased resolution and augmented sensitivity. This could provide more precise data for *in vivo* pharmacokinetics and biodistribution studies in phase 0 trials.

Trends in Legislation The implementation of the new Clinical Trial Regulation (hopefully during 2018) will likely boost academic research in the field of diagnostic radiopharmaceuticals given that the regulation, for the very first time, includes specific exemptions for diagnostic

radiopharmaceuticals (prepared and used under very specific circumstances).

Risk-Based Approaches to Mitigate Potential Dangers There is a growing trend of applying risk-based approaches rather than strict rules. This has been prompted by several factors, most notably (1) the fact that one-size-fits-all rules are detrimental to advancing the development of radiopharmaceuticals and decrease the number of clinical trials and (2) the increased awareness by authorities of the specifics of the development of radiopharmaceuticals.

The Bottom Line

- For investigational medicinal products (IMPs) used under the new Clinical Trial Regulation, GMP is no longer required.
- Risk assessment must be applied for the evaluation of the toxicity of new radiopharmaceuticals.
- More sensitive PET and SPECT cameras will result in reduced radiation burdens for patients as well as reductions in the amount of compound injected.
- The validation of production and analytical methods is a critical component of the synthesis of radiopharmaceuticals.

References

1. Koziorowski J, Behe M, Decristoforo C, Ballinger J, Elsinga PH, Ferrari V, et al. Position paper on requirements for toxicological studies in the specific case of radiopharmaceuticals. EJNMMI Radiopharm Chem. 2016;1:1.
2. Todde S, Peitl P, Elsinga PH, Koziorowski J, Ferrari V, Ocak EM, et al. Guidance on validation and qualification of processes and operations involving radiopharmaceuticals. EJNMMI Radiopharm Chem. 2017;2:8.
3. Decristoforo C, Penuelas I, Patt M, Todde S. New tracers to the clinic: translational studies. QJNM. 2017;61(2):135–44.
4. Bormans G, Buck A, Chiti A, Cooper M, Croasdale J, Desruet M, et al. Position statement on radiopharmaceutical production for clinical trials. EJNMMI Radiopharm Chem. 2017;2:12.

The Clinical Translation Process in the United States

Sonia Sequeira and Serge K. Lyashchenko

Introduction

Over the last 25 years, the drive to make medicine more precise and personalized has catalyzed the creation of novel agents for nuclear imaging and targeted radionuclide therapy. Following preclinical evaluation and validation, a promising radiopharmaceutical will be tested for safety in a first-in-human clinical study. The road from the laboratory to a first-in-human study is notoriously long and daunting. This chapter reviews available regulatory guidance and provides practical recommendations for planning first-in-human radiopharmaceutical clinical trials in the United States from the perspective of a leading academic, comprehensive cancer care center: Memorial Sloan Kettering Cancer Center (MSK). Both translational scientists and clinicians interested in preparing investigator-initiated investigational new drug applications may find this chapter particularly helpful. Importantly, the previous chapter has covered similar areas from a European perspective.

Planning a First-in-Human Trial

Memorial Sloan Kettering (MSK) has established a strong translational program that supports rapid and efficient first-in-human clinical trials. Through this program, MSK has initiated 35 radio-oncological first-in-human clinical studies in the last 7 years. Our translational strategies and interactions with the US Food and Drug Administration (FDA) have evolved with experience, and some key outcomes are shared here.

S. Sequeira
Research and Technology Management,
Memorial Sloan Kettering Cancer Center, New York, NY, USA

S. K. Lyashchenko (✉)
Department of Radiology, Memorial Sloan Kettering
Cancer Center, New York, NY, USA
e-mail: Lyashchs@mskcc.org

The regulatory requirements for a clinical trial for a novel agent can be challenging to navigate. In order to initiate a clinical study of a novel agent, a regulatory application must be submitted to the regulatory agency for review and approval for the study. In the United States, this application is called the investigational new drug application (IND), and the regulatory agency responsible for review and approval is the FDA. The US federal law titled the Code of Federal Regulations Title 21 (21CFR) establishes the FDA's regulations on drugs, biologics, and devices. Notable sections of 21 CFR relevant to the development of radiopharmaceuticals are Parts 58 (*Good Laboratory Practices (GLP) for Nonclinical Studies)*, 210 (*Good Manufacturing Practices*), and 312 (*Investigational New Drug Application*) [1–3]. The FDA also provides non-binding recommendations to industry sponsors of new diagnostics/therapeutics in the form of guidance documents that are publicly available. These guidance documents include *Guidance for Industry*, *Investigational New Drug Applications Prepared and Submitted by Sponsor Investigators* [4], *Content and Format of Investigational New Drug Applications (INDs for Phase 1 Studies for Drugs, Including Well-Characterized, Therapeutic, Biotechnology-Derived Products* [5], and *Exploratory IND Studies* [6]. Because the resources and objectives of industry sponsors are often critically different from those of academic investigators, a sliding scale with respect to the required manufacturing controls and a phase-dependent safety and quality package are often applicable in academic IND applications. In other words, the minimum necessary controls are required during the preparation of the drug for initial clinical evaluation, but the degree of controls increases as the agent progresses through clinical development. On issues such as these, early consultation with the agency is recommended via a pre-IND meeting.

Another reason for engaging the agency at an early phase—*i.e.* before performing IND-enabling safety studies and designing clinical protocols—is that for certain new classes of agents (such as nanoparticles), guidance that entirely addresses the particular characteristics of the agent

J. S. Lewis et al. (eds.), *Radiopharmaceutical Chemistry*, https://doi.org/10.1007/978-3-319-98947-1_36

may not yet be available. A selection of guidance documents is publicly available on the FDA website and can be easily found in the "Drugs Guidance" section. In general, guidance S9 for the *Nonclinical Evaluation for Anticancer Pharmaceuticals* supersedes other related product guidances given that cancer is a life-threatening disease [7].

The three most pivotal considerations when planning a first-in-human clinical trial are clinically needed, manufacturing quality, and non-clinical safety evaluation.

The ability to fulfill a clinical need greatly contributes to the success of a study by ensuring the sufficient and timely recruitment of subjects, because both physicians and patients are more motivated to participate in a clinical trial that may potentially benefit the patient. Furthermore, the identification of an unmet clinical need may entitle the investigational drug to significant regulatory support from the FDA through an expedited program for serious conditions or an orphan drug designation [8, 9]. Finally, focusing upon the clinical need can help investigators plan with respect to tumor models, dosing and drug schedules, proof-of-concept experiments, and *in vivo* animal safety studies.

In our experience, forming a multidisciplinary team that engages clinicians and regulatory scientists immediately upon the identification of a promising lead compound is critical for the success of the program. The input from regulatory advisors can—and should—include advice on the design and timing of nonclinical studies during the development of the radiotracer, especially with respect to the budget and resources necessary. This contribution is particularly important when evaluating novel radiopharmaceuticals used for diagnostic imaging applications. These agents are generally expected to generate a smaller return on investment than therapeutic radiopharmaceuticals once an authorization for commercial marketing is obtained. As a result, smaller resources are generally available to initiate these studies. Regulatory advisors will also provide guidance on whether the design and size of the clinical study are consistent with the level of risk presented by the available previous human experience, the preclinical and manufacturing information, the objectives of the study, and the target product profile.

Intellectual property specialists, the institutional review board, and committees focusing on clinical operations, compliance, and biostatistics will also be involved throughout the development of a drug. Therefore, a robust internal infrastructure with checks and balances and frequent communication are essential. However, most of these tasks can be outsourced if they are not available in-house. Importantly, for an academic institution testing new agents for which the marketing potential may not be known, institutional commitment with respect to the allocation of dedicated resources may become critical for the success of clinical translation. An example of the various teams involved in the clinical translation process is given in Fig. 1.

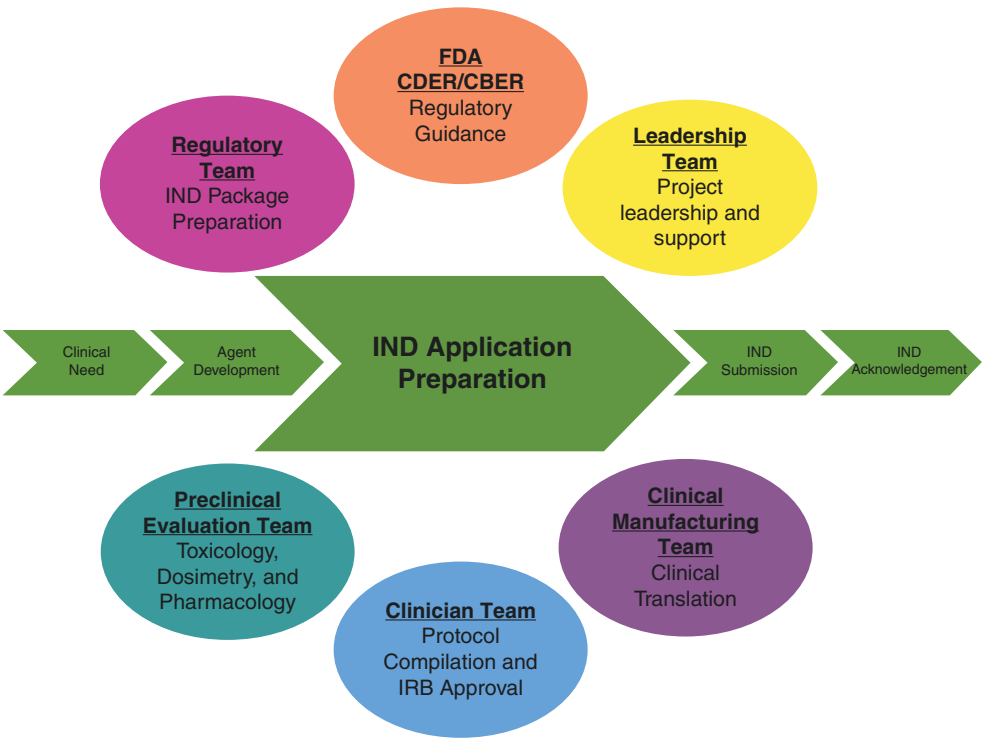

Fig. 1 The multi-team approach to the clinical translation of a radiopharmaceutical

Preclinical Studies

The main supporting elements of an investigational new drug (IND) application are preclinical studies, chemistry, manufacturing and controls, and a well-designed clinical protocol. For radiopharmaceuticals, these preclinical studies typically include proof-of-concept imaging experiments; the evaluation of the effect of the radiopharmaceutical on animal tumor burden or survival; and estimations of the human dosimetry, clearance, and biodistribution of the tracer in relevant *in vivo* models. Data showing the *in vitro* plasma stability and target specificity are also typically provided for conjugated radiopharmaceuticals.

The FDA also requires that a new agent be tested for chemical toxicity in one or two animal species under good laboratory practice (GLP). The agent should be manufactured and formulated as it is intended clinically; however, it is not mandatory that the lot for toxicology be the same as the clinical lot. It is important to note that many radiopharmaceuticals will be effective in humans in minute amounts, designated as microdoses. A microdose corresponds to less than 100 micrograms or less than 30 nanomoles for proteins with molecular weights greater than 100 kDa. Furthermore, a microdose must be at least 100 times lower than the known or predicted pharmacologically active range of the molecule. In this case, since the exposure to a human is low, a toxicology study in a single relevant species—normally a rodent—is considered acceptable. The selected high dose for this type of toxicology study should be at least 100 times the human equivalent dose. Critically, a microdose study or a study for a cancer agent will still require GLP toxicology information unless otherwise agreed with the agency. For radiopharmaceuticals, toxicology studies are conducted with either cold, unlabeled agents (*i.e.* an antibody labeled with non-radioactive zirconium rather than zirconium-89) or naked, non-labeled agents (*i.e.* the unmodified parent antibody of a radioimmunoconjugate), since a very low proportion of the radiotracer is actually radiolabeled. The choice of one over the other depends on whether there is a pharmacological difference between the radiolabeled, cold labeled, and parent compound. Generally speaking, microdose studies are lower risk than studies in the subtherapeutic or therapeutic range of mass and activity, and studies for cancer indications typically allow reasonably more risk than those for non-cancer indications. On this topic, the reader is referred to FDA guidance *S9 Nonclinical Evaluation of Anti-Cancer Pharmaceuticals*, which is harmonized with regulatory requirements in Europe and Japan [7].

The Quality of the Radiopharmaceutical

The question of the exact manufacturing process controls and requirements is a major topic of discussion in any new first-in-human IND application project. From a practical standpoint, the quality of the final product for a clinical trial is defined by a set of product quality acceptance specifications that address the product's identity, strength, quality, purity, and potency. The manufacturer commits not to use the product in human subjects unless product quality control (QC) testing results clearly demonstrate that the characteristics of the product conform to the acceptance criteria. In order to be able to consistently achieve this acceptable drug quality, manufacturers are required to follow certain rules designed to make sure that the manufacturing process is both controlled and traceable. In general, these rules include the implementation of standard operating procedures (SOPs), the execution and recording of production records, staff training, and continuously improving the processes based on recommendations received during various audits.

The concept of adhering to good manufacturing practices (GMP) is central to the discussion of product quality when manufacturing drug. Simply defined, GMP is a set of project-specific documented practices that the manufacturer commits to follow when making the drug in order to ensure that the quality of the manufactured product consistently meets the pre-defined acceptance specifications. This definition is very broad and does not include any specific recommendations on what would make a particular process GMP-compliant. Furthermore, one could reason that the manufacturing processes for both first-in-human investigational agents and FDA-approved agents are both GMP-compliant despite the fact that the actual manufacturing controls required are very different for first-in-human investigational radiopharmaceuticals compared to agents in later stages of clinical development. As a general rule, "the minimum necessary controls" should be in place when manufacturing radiopharmaceuticals for their initial introduction into humans, followed by the addition of extra controls as the agent progresses through development. These "minimum necessary controls" vary and are based on agent-specific scientific reasoning and risk assessment. Factors such as limited patient exposure, limited dose, increased patient monitoring, absence of agent entry into general distribution, and quality control data representing the quality of the entire batch can allow for decreased degrees of manufacturing process control and validation. This approach is critical because it both assures sufficient quality of investigational agent and concurrently avoids the additional time and resources that may be spent on completing unnecessary tasks. The end result is that the process of clinical translation becomes more efficient.

The FDA *Guidance to Industry: CGMP for Phase I Investigational Drugs* [10] provides basic recommendations for manufacturing controls that would be sufficient when manufacturing radiopharmaceuticals for first-in-human clinical trials. Since the content of this guidance is not all-inclusive, the sponsor of the IND will have to propose the

IND-specific tests and procedures that will be used to demonstrate the ability to prepare multiple batches of drug with acceptable quality. These commitments are detailed in the chemistry, manufacturing, and controls (CMC) section of the IND application and are discussed with the agency—either at a pre-IND meeting or during the IND review period—until a consensus is met.

The CMC document is composed of two main sections. The first provides information on the drug substance or the active pharmaceutical ingredient. The second provides a description of the final drug product in its intended formulation, container unit, and final label. For the vast majority of radiopharmaceuticals, the drug substance or the active pharmaceutical ingredient (API) is also the drug product. In other words, the synthesis and formulation of the API occur simultaneously in the same process to the final container. In the CMC section of the IND, the equivalence of the drug substance and the drug product should be stated, and the chemistry, manufacturing, and controls information should be described in full in the drug product section of the CMC.

Formal requests for CMC information during the initial IND review period are common and are related to the safety of the product and the manufacturing process. Questions may be subject to a clinical hold—in which the investigators are not allowed to administer the product to patients until they are resolved—or non-clinical hold issues that require clarification or justification. Due to evolving technologies and agents that fit more than one class of product, more than one division of the FDA may contribute to this discussion. During these interactions, the investigator is given clear direction on what is required for the agency to consider the study safe.

The acceptance specifications for a novel radiopharmaceutical consist of controls for identity, purity, microbiological content, and potency and are based on qualification runs, stability data, the physicochemical and pharmacological characteristics known at the time of development, and the level of risk of the study. Frequently, the acceptance specifications of the product are subject to discussion since they collectively represent the single most important way of defining the product in Phase 1. Products administered into the central nervous system or for pediatric patients are subject to more stringent criteria. As the clinical study progresses, the acceptance criteria will also tighten, and additional manufacturing data, manufacturing process changes, and human patient data will be required. Before implementing these changes, the investigator must notify the FDA by filing a CMC amendment. For small molecule injectable radiopharmaceuticals, the acceptance criteria typically include pre-release confirmation of radiochemical purity and identity, acceptable pH, absence of particulates, acceptable endotoxin content, radionuclidic identity, and sterilizing filter integrity (sterility is typically performed post-release). For radiolabeled macromolecules, the specific acceptance criteria may include additional parameters such as a measure of protein monomer content and the determination of the immunoreactive fraction of the construct.

A key factor in the quality of a drug is the quality of the reagents and materials from which it has been made. For Phase 1 trials for oncology, the basic characterization of reagents and materials may be acceptable. However, at later stages of clinical development, it will be necessary to obtain pharmaceutical grade materials or to perform additional testing on incoming materials. Generally speaking, in the early stages of an agent's clinical development, if the final drug product testing includes the confirmation of identity and purity, an examination of the CoA to confirm material quality compliance with an established specification may be sufficient, and no additional testing is required. However, it is recommended that potential investigators discuss the exact grade of key intermediates—*i.e.* the radionuclide and the precursor—in a pre-IND meeting to ensure sufficient quality for preliminary evaluation in humans.

Clinical Considerations

For a novel agent, demonstrating safety is the primary objective of Phase 1 clinical trials. Safety is determined by the incidence of drug-related adverse events associated with increasing amounts of the agent. For radiopharmaceuticals, the delivered mass may be a microdose and therefore is not expected to contribute toxicity. In this case, the radioactive dose to normal organs is considered by performing dosimetric estimations based on animal biodistribution studies. For short-lived PET agents, the low-linear energy transfer and short radioactive half-life (minutes to hours) of the radionuclides may further reduce potential toxicity caused by radiation, and the human dose range can be based on the quality of the images.

Diagnostic macromolecules administered systemically are associated with long circulation times to localize at the tumor sites (as opposed to minutes to hours required by small molecules), making these compounds subject to liver metabolism. The administration of an insufficient mass of antibody may result in suboptimal tumor localization due to the rapid uptake of the radiopharmaceutical by the liver, a phenomenon that is often termed the "liver sink." To avoid this uptake in the liver, most radiolabeled antibodies are co-administered with non-radiolabeled antibodies that are intended to saturate the body's normal elimination mechanisms for immunoglobulins and thus allow the radiolabeled antibody sufficient time to localize at its target. Since this total administered mass is usually in excess of microdose levels, there is a potential for toxicity resulting from the injected mass. In addition, the use of radionuclides with longer radioactive

half-lives may increase the risk of toxicity associated with radiation exposure.

For therapeutic radiopharmaceuticals—particularly radiolabeled antibodies and peptides—the selection of mass doses that allow for the optimal distribution of the radiopharmaceutical to the target as well as the maximum deposition of energy in the tumor relative to healthy tissues should be explored. For example, increasing the injected mass may result in the saturation of areas where the normal physiological expression of the target occurs (*i.e.* kidneys, salivary glands, or lungs), allowing the radiopharmaceutical to accumulate more at the intended site where the target is overexpressed. Depending on the decay profile of the radionuclide, the evaluation of a radiotherapeutic may be challenging because imaging may be difficult or even impossible. In these cases, the use of a companion—or theranostic pair—radionuclide for imaging may prove very helpful.

Given what we have discussed above, Phase 1 clinical trials are typically dose escalations in which the mass or radioactivity is increased until a maximum tolerated dose is achieved. As a result, the elucidation of the pharmacokinetic profile or the systemic exposure of the agent is often a secondary objective of these studies. For imaging agents, dose de-escalation studies may also be performed to optimize imaging at the lowest dose possible.

Regulatory Mechanisms

The authors of the previous chapter provide a detailed overview of the requirements needed for every section of the investigational agent applications used in Europe. The same requirements apply to traditional IND submissions in the United States. In the traditional IND application, the collected preclinical data and agent characterization are extensive enough to allow the investigators to study safety, efficacy, and metabolism. There are times, however, when the investigators simply want to perform a preliminary clinical evaluation of an agent in order to determine its pharmacodynamics and pharmacokinetics, without the goal of evaluating safety. At other times, the investigators may have several analogues in preclinical development and may want to see which one of the candidates has the best *in vivo* behavior profile so that it could be selected for further development. To facilitate this preliminary evaluation process, the regulators have created an exploratory IND (eIND) application regulatory mechanism. The eIND process allows for the initial clinical evaluation of metabolism using one or even several chemically related agents in order to determine whether the subsequent development of these agents is warranted. The requirements for collecting toxicology and manufacturing quality data are less stringent for eIND studies than traditional IND studies, resulting in the need for fewer resources and a faster submission process. However, eIND limitations designed to reduce patient risk—*i.e.* microdose level dosing, limited number of patients, limited patient exposure—ensure that the study goals are limited to the preliminary evaluation of metabolism.

Interestingly, regulations require the withdrawal of the eIND and a subsequent submission of the traditional IND for the same agent should the investigators decide to study the safety and efficacy of the agent. This requirement makes sense for most traditional pharmaceuticals, because both safety and efficacy will be based on escalating the mass dose. For diagnostic radioactive tracers—in which the injected mass is not expected to increase above microdose levels during subsequent development—the requirement to withdraw the IND is not justified, and the sponsor is encouraged to discuss product development with the FDA in a pre-IND meeting.

A pre-IND meeting with the FDA should also be considered when the nature of the agent does not clearly fall under a single category (*e.g.* biologic radiolabeled with a therapeutic radionuclide or antibody pre-targeting) or is novel with respect to the molecule type or method of production. Other reasons for a pre-IND meeting are a lack of a relevant toxicology model, the unavailability of clinical-grade critical reagents, or the use of novel test methods or processes. Information on the format of a meeting request is available [11]. Furthermore, sponsors are advised to thoroughly plan the meeting package to include questions about preclinical data, CMC, clinical and long-term development and marketing as well as enough supporting information for the agency to provide useful feedback and help plan early clinical development activities. Rather than asking the agency how to move forward, it is important that the sponsor explicitly states how he or she intends to safely implement the clinical trial as well as the scientific and regulatory rationale. The meeting package should resemble the IND application to help both sides envision optimal outcomes and—if necessary—offer alternative approaches to which the FDA is amenable. At a minimum, the contents of this package should include the following:

- A phase-appropriate *in vitro* and *in vivo* preclinical safety plan for the intended dose range, route, and schedule of the drug. As in Europe, this information is normally detailed in the pharmacology, toxicology, and dosimetry sections of the IND.
- A phase-appropriate clinical dose escalation plan, as supported by preclinical or previous human data as well as information regarding sample size for meaningful data collection, monitoring, and reporting according to good clinical practice (GCP). This information is summarized in the general investigational plan and is detailed in the clinical protocol section of the IND.

- A phase-appropriate discussion of the agent quality and manufacturing controls. The investigators of the clinical study must provide sufficient data in the CMC section demonstrating that the investigational agent can be reliably manufactured under a set of process controls that ensure the good quality of the drug.
- Other documentation that is required by law to be included with each IND document package, such as government-issued forms and various statements of compliance.

As of May 2018, the FDA has required that all commercial IND regulatory submissions must be submitted electronically and in a specific standardized format, known as the electronic common technical document (or eCTD) format. The eCTD format relies on a set of standardized document templates that are populated with information and then inserted into the respective standardized sections—or modules—that make up the IND application. The list of modules is provided in Table 1. This standardization of the format, combined with the ease of access to electronic documents, makes the regulatory review process much easier and more efficient for the reviewer. However, the completion of the eCTD templates, the organization of the modules, and the physical submission require the dedication of additional time and resources from the investigators. These resources may not be available at some academic institutions. Recognizing these challenges, the FDA has created an exemption to the electronic submission requirements for noncommercial IND sponsors. Careful consideration regarding the use of the eCTD format should be made for INDs that are likely to be transferred to commercial entities in early stages of clinical development. Additional details on IND applications and electronic submission requirements can be found in 21CFR312 and the FDA Guidance entitled *Providing Regulatory Submissions in Electronic Format – Certain Human Pharmaceutical Product Applications and related Submissions Using the eCTD Specifications* [12].

Table 1 Investigational new drug application eCTD modules

Module	Subject matter
1. Regional administrative information	Contains form FDA1571, table of contents, general investigation plan, investigators brochure (if applicable), and environmental assessment
2. Summaries	Contains the IND introductory statement, CMC introduction, nonclinical summary, previous human experience summary (if applicable), and clinical summary
3. Quality	Contains information on chemistry, manufacturing, and controls (CMC) for the investigational agent
4. Nonclinical study reports	Contains pharmacology and toxicology data and nonclinical reports
5. Clinical study reports	Contains clinical protocol and previous human experience reports (if applicable)

eCTD electronic common technical document; *IND* investigational new drug application

Conclusion

The clinical translation of new radiopharmaceuticals is both challenging and rewarding. In the coming years, both the variety of newly introduced agents and the complexity of conducting first-in-human trials are expected to increase. The clinical introduction of radiobiologics for targeted therapy, antibody pretargeting strategies, and alpha-emitting radiopharmaceuticals will also undoubtedly bring new challenges. Overcoming these obstacles, however, is ultimately one of the key factors that make the entire process deeply satisfying.

The Bottom Line

- The expansion of nuclear imaging and targeted radionuclide therapy has created the need for introducing new radiopharmaceuticals into clinical trials.
- The existing regulations governing drug production provide a general overview of the requirements that must be followed when introducing drugs—including radiopharmaceuticals—into the clinic.
- From a technical standpoint, the unique nature of radiopharmaceuticals often makes it challenging to decide exactly what is required to translate a particular agent to the clinic. For this reason, both a multi-team approach and initial communication with regulators are absolutely essential.
- Critical areas of focus such as clinical trial planning, clinical study design, product quality, and regulatory considerations must be coordinated in order to ensure the successful clinical translation of nuclear imaging agents and therapeutic radiopharmaceuticals for first-in-human trials.

References

1. U.S. Food and Drug Administration. United States Code of Federal Regulations Title 21 – Food and Drugs, Chapter I – Department of Health and Human Services, Subchapter A – General, Part 58 – Good Laboratory Practice for Nonclinical Laboratory Studies. Available from: https://www.accessdata.fda.gov/scripts/cdrh/cfdocs/cfcfr/CFRSearch.cfm?CFRPart=58. Accessed 26 June 2018.
2. U.S. Food and Drug Administration. United States Code of Federal Regulations Title 21 – Food and Drugs, Chapter I – Department of Health and Human Services, Subchapter C – Drugs: General, Part 210 – Current Good Manufacturing Practice in Manufacturing, Processing, Packing, or Holding of Drugs: General. Available

from:https://www.accessdata.fda.gov/scripts/cdrh/cfdocs/cfcfr/CFRSearch.cfm?CFRPart=210. Accessed 26 June 2018.
3. U.S. Food and Drug Administration. United States Code of Federal Regulations Title 21 – Food and Drugs, Chapter I – Department of Health and Human Services, Subchapter D – Drugs for Human Use, Part 312 – Investigational New Drug Application. Available from: https://www.accessdata.fda.gov/scripts/cdrh/cfdocs/cfcfr/CFRsearch.cfm?CFRPart=312. Accessed 18 Mar 2018.
4. U.S. Food and Drug Administration. Guidance for Industry, Investigational New Drug Applications Prepared and Submitted by Sponsor Investigators.U.S. Department of Health and Human Services, Center for Drug Evaluation and Research (CDER), May 2015. Available from: https://www.fda.gov/downloads/Drugs/Guidances/UCM446695.pdf. Accessed 20 Mar2018.
5. U.S. Food and Drug Administration. Guidance for Industry – Content and Format of Investigational New Drug Applications, (IND's) for Phase 1 Studies for Drugs, Including Well-Characterized, Therapeutic, Biotechnology-derived Products. U.S. Department of Health and Human Services, Center for Drug Evaluation and Research (CDER) and Center for Biologics Evaluation and Research (CBER), Nov 1995. Available from: https://www.fda.gov/downloads/drugs/guidancecomplianceregulatoryinformation/guidances/ucm071597.pdf. Accessed 20 Mar 2018.
6. U. S. Food and Drug Administration. Guidance for Industry, Investigators, and Reviewers – Exploratory IND Studies. U.S. Department of Health and Human Services, Center for Drug Evaluation and Research (CDER), Jan 2006. Available from: https://www.fda.gov/downloads/drugs/guidancecomplianceregulatoryinformation/guidances/ucm078933.pdf. Accessed 20 Mar 2018.
7. U.S. Food and Drug Administration. Guidance for Industry, S9 Nonclinical Evaluation for Anticancer Pharmaceuticals. U.S. Department of Health and Human Services, Center for Drug Evaluation and Research (CDER) and Center for Biologics Evaluation and Research (CBER), March 2010. Available from: https://www.fda.gov/downloads/Drugs/Guidances/ucm085389.pdf. Accessed 27 June 2018.
8. U.S. Food and Drug Administration. Draft Guidance for Industry, Clarification of Orphan Designation of Drugs and Biologics for Pediatric Subpopulations of Common Diseases, Dec 2017. U.S. Department of Health and Human Services, Office of Medical Products and Tobacco, Office of Orphan Products Development. https://www.fda.gov/downloads/RegulatoryInformation/Guidances/UCM589710.pdf. Accessed 21 Jun 2018.
9. U.S. Food and Drug Administration. Guidance for Industry Expedited Programs for Serious Conditions – Drugs and Biologics, May 2014. U. S. Department of Health and Human Services, Center for Drug Evaluation and Research (CDER) and Center for Biologics Evaluation and Research (CBER). https://www.fda.gov/downloads/Drugs/Guidances/UCM358301.pdf. Accessed 21 Jun 2018.
10. U.S. Food and Drug Administration. Guidance for Industry: CGMP for Phase I Investigational Drugs. U.S. Department of Health and Human Services, Center for Drug Evaluation and Research (CDER) and Center for Biologics Evaluation and Research (CBER), Office of Regulatory Affairs (ORA), July 2008. Available from: https://www.fda.gov/downloads/drugs/guidances/ucm070273.pdf. Accessed 20 Mar 2018.
11. U.S. Food and Drug Administration. Guidance for Industry, Formal Meetings Between the FDA and the Sponsors or Applicants of PDUFA Products. U.S. Department of Health and Human Services, Center for Drug Evaluation and Research (CDER) and Center for Biologics Evaluation and Research (CBER), Dec 2017. Available from: https://www.fda.gov/downloads/Drugs/GuidanceComplianceRegulatoryInformation/Guidances/UCM590547.pdf. Accessed 20 Mar 2018.
12. U.S. Food and Drug Administration. Guidance for Industry, Providing Regulatory Submissions in Electronic Format – Certain Human Pharmaceutical Product Applications and related Submissions Using the eCTD Specifications. U.S. Department of Health and Human Services, Center for Drug Evaluation and Research (CDER) and Center for Biologics Evaluation and Research (CBER), Apr 2017. Available from: https://www.fda.gov/downloads/drugs/guidancecomplianceregulatoryinformation/guidances/ucm333969.pdf. Accessed 20 Mar 2018.

Setting Up a Successful Radiopharmaceutical Production Facility

Ashley Mishoe and Phillip DeNoble

Introduction

You're finally at the stage where you're ready to move forward in designing a new radiopharmaceutical production facility, but where do you start? What are your next steps in planning the facility in order to ensure success? This chapter will focus on the scientific, clinical, and logistical challenges associated with creating a lab capable of producing both investigational agents and approved radiopharmaceuticals such as [^{18}F]fluorodeoxyglucose. More specifically, in the following pages, we will review the key elements of setting up a successful facility for the production of radiopharmaceuticals, including the design of the facility, equipment validation, training of personnel, and quality assurance management.

Facility Workflow Design

While there are many ways to design the facility, the overall goals remain the same. Regardless of size constraints, the laboratory space should promote efficient and orderly operation, prevent contamination and mix-ups, and consistently produce repeatable results. The facility should be designed with areas for at least four basic functions: storage, aseptic manipulations, production, and analytical testing.

The storage area should be systematically designed to facilitate the segregation of inventory into at least three categories: quarantined, approved, and rejected/expired. As inventory is received and checked in, it will be assigned one of the first two categories based on whether or not the items meet acceptance criteria. Items that do not meet specifications should be quarantined or rejected. Supplies that are commonly used in production can be kept out of the storage area and in the production area in an effort to promote optimal and efficient workflow [1].

Although nearly all radiopharmaceuticals are sterile drugs, they are not always produced in clean rooms. However, all aseptic manipulations should take place in a segregated area away from heavy traffic. Although the laminar flow hood (LFH) or biological safety cabinet (BSC) ideally should be in a segregated room, this is not always possible due to space constraints. In these cases, the use of the room containing this equipment should be minimized during the performance of aseptic processes.

Next, the equipment for production should be considered. The facility will not only need equipment for the production of radiopharmaceuticals – such as hot cells and mini cells – but also equipment for chemical mixing and production. Along these lines, the facility should contain a chemical fume hood at a minimum. In the beginning stages of radiopharmaceutical production, radiosyntheses will likely be performed using manual techniques. However, as the radiopharmaceutical in question moves forward in its development, automated synthesis modules should be incorporated not only to protect the worker from larger amounts of radiation but also to minimize human error and increase batch-to-batch consistency. For the production of commercial PET tracers, the facility should contain mini cells capable of housing multiple automated synthesis units as well as a hot cell with robotic arms for manipulating large amounts of radioactivity. The same synthesis unit will most likely be used for multiple products. Therefore, preventing cross-contamination is critical. This is easily achieved by using disposable supplies or performing a validated cleaning method after every radiosynthesis to ensure there are no residual chemicals or cleaning agents carried from one synthesis to the next. Methods used for cleaning should be validated prior to use and documented when used after every production.

More than likely, the facility will be used to manufacture both FDA-approved drugs and investigational agents.

A. Mishoe (✉)
Department of Radiology and Biomedical Imaging, University of California San Francisco, San Francisco, CA, USA
e-mail: Ashley.Mishoe@ucsf.edu

P. DeNoble
Department of Radiology, Memorial Sloan Kettering Cancer Center, New York, NY, USA

J. S. Lewis et al. (eds.), *Radiopharmaceutical Chemistry*, https://doi.org/10.1007/978-3-319-98947-1_37

Although the regulatory requirements for these are different, it is common to use the same facility and equipment for both. If planning to do so, it is critical to put in place procedures and production controls to prevent contamination and mix-ups [1, 2]. For example, supplies should be segregated during manufacturing so that products are physically separated. Following the production of one drug, clear the work area before starting production of subsequent batches. It is common to include this step at the beginning of the radiopharmaceutical synthesis procedure to ensure operator compliance.

In addition to space requirements, the access of personnel should also be considered. Of course, access to the facility needs to be limited to key personnel only. This can be achieved using anything from a simple locked door to more elaborate mechanisms such as fingerprint readers or retina scanners. The main goal is to ensure that the primary staff have easy access, but the ancillary staff (such as janitors and administrators) are only in the facility while under supervision.

Special Considerations for the Production of Therapeutic Radiopharmaceuticals

Radiopharmaceuticals used in the treatment or mitigation of disease are becoming increasingly important in the field of nuclear medicine. While drugs like Zevalin® and TheraSpheres® have been around for several years, newly approved drugs such as Xofigo® and Lutathera® have resulted in billion-dollar drug company acquisitions. In addition, several other promising therapeutic radiopharmaceuticals are quickly advancing through the development and regulatory approval pathway. While these radiopharmaceuticals have and surely will continue to change the fields of nuclear medicine and molecular imaging, the production of these compounds also has major implications for manufacturing facilities.

Unlike diagnostic radiopharmaceuticals that are governed under United States Pharmacopeia (USP) <823> and/or 21 CFR 212, radiotherapeutic compounds are subject to all USP general chapters and/or 21 CFR 211. In addition to the differing regulatory requirements for these drugs, their modes of decay also have implications for the manufacturing facility. This section will highlight some of these differences and their impact on the production workflow.

Ideally, the decision to work with and develop therapeutic radiopharmaceuticals should be made during the planning stage of building a production facility. This allows for the developer not only to plan for the specific requirements of a 21 CFR 211 facility (if pursuing an NDA or BLA) but also to prepare for the unique radiation safety requirements of therapeutic radionuclides. Therapeutic radiopharmaceuticals – usually labeled with α- or β-emitting radionuclides – require unique shielding due to the nature of their decay and their relatively long half-lives. A good recommendation would be to completely segregate these radiopharmaceuticals from the other radiotracers produced in the facility. This strategy allows for the separation of long-lived radioactive waste from short-lived radioactive waste. It also protects the operator from possible harmful contamination and unnecessary exposure to radiation that – while less penetrating – is potentially more harmful.

Whether designing a new facility or retrofitting an existing one, let us consider exactly what adequate shielding and workspace entails. While alpha and beta radiation can be adequately shielded by several millimeters of plexiglass, therapeutic radionuclides often emit gamma rays as well. For example, lutetium-177 – the centerpiece of [^{177}Lu]Lu-DOTATATE (Lutathera®) – emits gamma rays with energies of 113 and 208 KeV. These gammas require the use of dense metals such as lead or tungsten to provide adequate shielding. The shielding material of choice is usually lead, due to its relatively lower cost and widespread availability. In addition to shielding, protections against accidental contamination should be made as well. High-energy gammas, such as the 511 KeV energy emitted from PET radionuclides, are usually less of a concern with therapeutic radiopharmaceuticals; however, the internalization or ingestion of these nuclides can cause serious harm to the operator due to their alpha or beta components. With this in mind, a glove box is helpful. An example of a commercially available setup is shown below in Fig. 1.

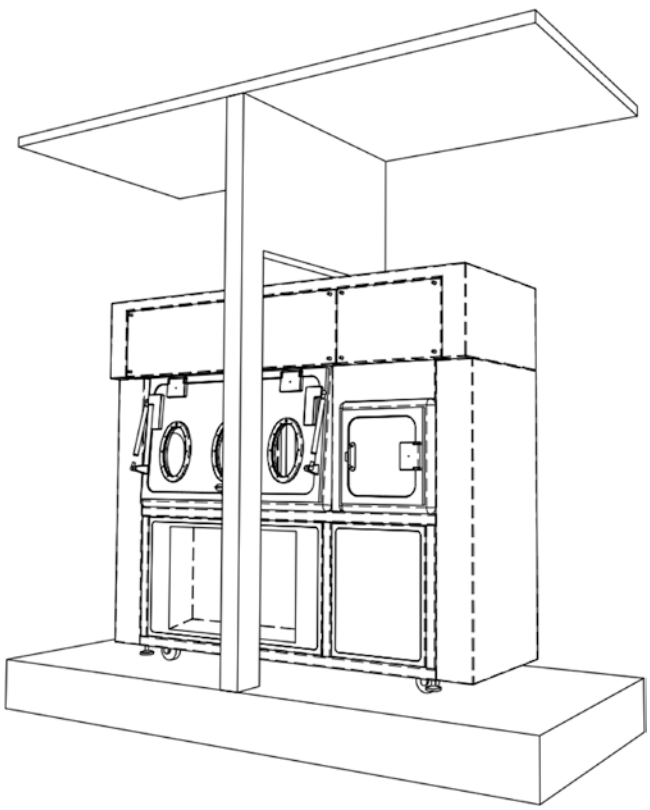

Fig. 1 Example of a commercially available glove box (Courtesy of Tema Sinergie®, with permission)

Next, we will highlight some of the more pertinent regulatory differences between the production of therapeutic radiopharmaceuticals and diagnostic radiopharmaceuticals. The first and probably most critical point to keep in mind is that the USP general chapter <823> *Positron Emission Tomography Drugs for Compounding, Investigational, and Research Uses* and FDA regulation 21 CFR 212 *Current Good Manufacturing Practice For Positron Emission Tomography Drugs* do not provide guidance for the production of therapeutic radiopharmaceuticals. This is simply because therapeutic radiopharmaceuticals are not positron emitters. Hence, several USP <823> exemptions would not necessarily apply. For example, 21 CFR 212.40 exempts PET facilities from inspecting the manufacturer of incoming components and instead allows the facility to rely on the certificate of analysis (COA). Not having this exception means that all incoming components used as ingredients in manufacturing must be certified by inspection of the manufacturer [1, 3].

With regard to personnel, PET facilities are allowed to operate with minimal staffing; both self-verification of production and single-person oversight of production and quality assurance tasks are permitted. However, this is not the case in the production of therapeutic radiopharmaceuticals. Here, the facility must perform dual verification of critical production steps, and a different operator must be responsible for quality control (QC) testing.

For radiopharmaceuticals with a very short half-life (*e.g.* $[^{13}N]NH_3$; $t_{1/2}$ = 9 min), the FDA allows provisions for sub-batching. This means that the facility first manufactures one batch that is solely dedicated to quality control testing, and subsequent batches produced on the same day are only required to undergo minimal testing. But because this concept is only allowed for radiopharmaceuticals containing radionuclides with very short half-lives, no therapeutic radiopharmaceuticals would be eligible to participate in the sub-batch process [1, 2]. Although the above PET exemptions are not explicitly allowed for facilities that produce therapeutic radiopharmaceuticals, it is possible to petition the FDA to waive these requirements if sufficient justifications are offered. If amenable, these concessions should be written into the sponsor's Investigational New Drug (IND) application, Abbreviated New Drug Application (ANDA), New Drug Application (NDA), or Biologics License Application (BLA) application.

Equipment and Process Validation

The concepts of equipment validation and process validation are well known in the drug manufacturing field. Equipment validation is a process to ensure that the equipment being used is capable of producing consistent results for the intended purpose. Similarly, process validation ensures that the manufacturing steps in the procedure are capable of producing consistent, high-quality results. Mentions of "process validation" in the Federal Register can be traced back to 1987, when the FDA first announced the availability of a guidance for process validation [4]. Considerable changes and updates have been made since then. While highlighting all of these requirements is outside of the scope of this chapter, it will nonetheless provide a summary of how these requirements affect the development of a radiopharmaceutical production facility. We will first review equipment validation and then discuss process validation. Finally, we will conclude with a discussion of how these processes are interrelated.

The concept of equipment validation rests upon three basic principles: installation qualification (IQ), operational qualification (OQ), and performance qualification (PQ). Generally, IQ, OQ, and PQ are performed when the customer takes delivery of the equipment. The testing can be performed either by the manufacturer of the equipment or a qualified third-party vendor. Documentation of the testing should be kept by the customer indefinitely [4].

Installation qualification (IQ) is defined in 21 CFR 820 and requires that processing equipment and other systems are installed and used in compliance with manufacturers' recommendations. For example, if installing a biological safety cabinet (BSC), the manufacturer may require for the hood to be 316 grade stainless steel, and you must confirm that the enclosure meets this specification. Other installation considerations include weight requirements for installation, voltage parameters, and temperature/humidity restrictions [5]. Operational qualification (OQ) follows the IQ and determines whether or not the equipment meets its predetermined operating specifications. For example, if the motor of the BSC is required to run at a range of 100–150 RPM, you must confirm that the motor does, in fact, run at this speed. Performance qualification (PQ) is generally the last qualification performed and ensures that the equipment operates as expected during continued use. Continuing with the BSC example, although we verified that the motor runs at a range of 100–150 RPM, we must now test that it still functions in this manner under normal operating conditions. For instance, if we intend to operate the hood with 25 kilograms of material in it, we must verify the RPMs of the motor under this load [4].

Process validation is the qualification of the manufacturing and production processes to confirm they are able to operate at a certain standard during sustained manufacturing. In other words, process validation is a way of demonstrating the robustness of your production and analytical methods. To demonstrate reproducibility, a validation campaign consisting of three or more exhibition batches is performed. The

following principles should be consistently demonstrated in the exhibition batches:

1. Deviations from the master batch record should not be required or be minor in nature.
2. Production yield should be sufficient to cover anticipated demand.
3. Production and analytical equipment should be fit for use.
4. Release specifications must be met.

Once the process validation is complete and approved by the appropriate regulatory body, changes to the process will require a formalized procedure to enact changes. Hence, sufficient research and development should be performed to ensure future change requirements are minimized.

Finally, it's important to note that equipment and process validations are interrelated. Before embarking on a validation campaign for a particular process or manufacturing method, you must ensure your equipment has been properly validated. The use of equipment that has not undergone validated IQ/OQ/PQ will raise questions by the regulatory body governing your facility and could jeopardize the validity of the associated process validations.

Quality Control Methods for Radiopharmaceuticals

Small Molecules

Immediately following synthesis, all manufactured radiopharmaceuticals undergo rigorous testing, all of which must be completed in a short timeframe due to the half-life of the product. At a minimum, these tests (in **bold** below) should include appearance, filter integrity, pH, radiochemical identity and purity, bacterial endotoxins, residual solvents, and sterility. Depending on whether the radionuclide is made in-house or is purchased from an outside vendor, testing for radionuclidic identity and radionuclidic purity may also be required.

After the operator records the end-of-synthesis (EOS) time and final product assay (in MBq), the first test is often a **visual inspection** of the product behind leaded glass. This test ensures that the product is clear, colorless, and free of particulate matter. Failures in this test can result from several factors, including synthesis problems leading to a turbid solution or a cored septum of the final product vial causing particulate matter to appear in the final product vial. Any steps taken to reprocess the final product following appearance failure should be validated and included in the master formula of the drug product [2, 6]. The **radioactive concentration** is determined by dividing the final product assay at EOS by the volume of the final product as recorded in MBq/mL. The volume can be determined several different ways, including weighing the final product vial before and after synthesis or by validating a known delivery volume from the synthesis module. Radioactive concentration is part of the final product label and must be within the range listed on the label. When determining the required range, it is important to consider the production capabilities, the volume of the final product, and activity required for patient injection. For example, let's consider the production of [^{68}Ga]Ga-PSMA11 using a 1850-MBq (50-mCi) generator, a final product volume of 12 mL, and a patient injection of 185 MBq (5 mCi). When the generator is new, the concentration will likely be close to 148 MBq/mL (4 mCi/mL). However, as the germanium-68 decays, the amount of gallium-68 eluted will also decrease, resulting in a lower final product concentration. At the end of the generator's life, the elution activity will likely be less than 444 MBq (12 mCi), resulting in a final product concentration of <37 MBq/mL (<1 mCi/mL) at EOS. Ideally, the label should cover both ends of the spectrum. The injection volume should also be considered. While likely not as big of a concern at higher concentrations, the lower the concentration, the higher the volume administered to the patient becomes. Continuing with our [^{68}Ga]Ga-PSMA11 example, the higher concentration of 148 MBq/mL at EOS would likely result in an injected volume of 2.5 mL. However, at the lower end of the range, the volume of the injection would likely be more than 10 mL. Larger volumes are not as big of a concern in adult patients but should be used with caution in pediatric patients.

The 0.22 μm filter attached to the final product vial serves as a terminal sterilization device for the final product, so this filter must be tested as part of quality control to ensure that the membrane remained intact during the delivery of the final product. The minimum pressure threshold is different for each filter and is listed on the filter's COA. **Membrane filter integrity testing** is most commonly performed by the bubble point test [7]. The Leur-lock of the filter is attached to the outlet of compressed air, and the needle bevel is submerged in a small beaker of water. The operator slowly increases the pressure of the compressed air and watches for a steady stream of bubbles in the beaker. The pressure level that causes the membrane to burst is recorded as the bubble point. Several factors can affect the bubble point and result in a failure. For example, ethanol has a lower surface tension than water or normal saline, so higher levels of ethanol in the product will lower the bubble point. However, this is not a true filter integrity failure. In this case, the filter should be rinsed with water prior to testing to ensure there is no residual ethanol in the filter. Any potential rinsing requirements should also be listed in the procedure.

The **pH** of the final product is also normally listed as a range. Testing can be done with pH paper or with a calibrated pH meter if more precise values are required.

Residual solvents are classified by their relative risks and range from Class 1 (should be avoided) to Class 3 (should be limited) [8]. When these are used in synthesis steps, residual amounts in the final product must be quantified during quality control testing. This is primarily determined by gas chromatography (GC). When planning for quality control testing, first determine if the solvent is truly a residual solvent or if it is part of the final product formulation. For example, ethanol is a Class 3 solvent and is one of the most common solvents tested for in the production of radiopharmaceuticals. However, if it is used in small quantities to elute the drug product from a purification cartridge, it can be considered a part of the final product formulation. In this example, a calculation can be performed to show that the total amount of ethanol in the final product is lower than the Class 3 solvent limit.

Radiochemical identity and purity is usually determined by thin-layer chromatography (TLC) or reverse-phase high-pressure liquid chromatography (HPLC). For radiopharmaceuticals that have been used for long periods of time like [^{18}F]FDG, a TLC method has likely been validated and incorporated into the associated USP monograph [9]. However, for newer agents, HPLC should be used to have better separation and identification of impurity peaks. Due to expense, the chromatography system and columns will likely be used for QC of multiple drugs; however, systems must be in place to ensure that no cross-contamination occurs. For example, ensure that a proper cleaning method is in place for the columns and that they are labeled to prevent mix-ups.

The **bacterial endotoxins test** is a required test to detect the presence of endotoxins. Endotoxins are pyrogen-producing – or fever-producing – components of the outer wall of gram-negative bacteria. Although the drug product may be sterile, endotoxins may be present and must be tested for prior to release. The maximum amount of endotoxin allowed is 175 endotoxin units (EU) per patient injection (in mL) for radiopharmaceuticals [10]. The USP lists three methods for performing this test; however, the chromogenic method is most common [10]. This method is based on a color change after reaction of limulus amebocyte lysate (LAL) with endotoxin. Some commercially available units are able to perform the chromogenic method in under 15 minutes using disposable cartridges. The cartridges are designed to contain known amounts of endotoxin at various sensitivity levels, so a maximum valid dilution calculation should be performed prior to validating the method.

Special Considerations for Macromolecules

Proteins and other macromolecules behave differently than their small molecule counterparts. As a result, the quality control verification of radiolabeled macromolecules requires some unique tests in addition to those discussed above.

Antibodies and antibody fragments typically require a chelator to affix the radionuclide to the macromolecule. For example, desferrioxamine (DFO) is a metal chelator that is often employed in the conjugation and radiosynthesis of ^{89}Zr-labeled antibodies. Intuitively, you can deduce that not having enough DFO chelators affixed to the antibody will result in poor radiochemical yields, while the over-conjugation of DFO can have other deleterious effects on the radioimmunoconjugate. To wit, affixing too many chelators to an antibody can adversely affect its *in vivo* biodistribution. Most literature reports suggest restricting the number of chelators per antibody, but the ideal number of chelators per immunoconjugate is dependent on the identity of the antibody itself. **Radiometric isotopic dilution assays** are often used to assess the number of chelators attached per antibody [11–13].

Immunoreactivity is a measure of how effectively a radioimmunoconjugate binds its cognate antigen after radiolabeling. The physical, chemical, and radiological stress of the radiolabeling process can all take a toll on the antibody. Therefore, it is critical to assess the immunoreactivity of a radioimmunoconjugate at both EOS and at time points at which administration could occur (*e.g.* 24, 48, 72 h post-EOS). This is typically performed using any one of a variety of antigen binding assays.

Methods to determine the chemical and radiochemical purity of macromolecules differ from their small molecule counterparts as well. While the determination of the purity of small molecule radiopharmaceuticals is typically determined using TLC or HPLC, size exclusion chromatography (SEC) is often used for radiolabeled macromolecules such as antibodies. SEC is a method in which molecules in solution are separated based on size, typically molecular weight [14]. For example, when evaluating the purity of a radiolabeled antibody, the user is typically looking to evaluate the percent of the final product that contains the single, intact antibody that retains the chelating group and the radionuclide. While the purity of small molecule radiopharmaceuticals is typically expected to be greater than 90%, the expected purity for antibodies can vary widely.

Staffing and Workflow

As mentioned previously, the FDA has exemptions in place for PET facilities to allow for minimal staffing. Indeed, it is common to have the same person not only verifying production steps but also performing both production and quality control. However, best practice is to separate these two duties when possible. This can prevent human errors from occurring and can ensure that the operation runs smoothly. Most PET facilities employ a combination of cyclotron engineers, radiopharmacists, radiochemists, and

production technicians. While each of these will have special background expertise, cross-training is critical to prevent downtime and ensure success. Depending on the working hours of the facility, the staff will probably be staggered. This will enable the cyclotron engineer to perform necessary maintenance of equipment during non-production hours and will allow production to continue throughout the day without interruption.

The Quality Assurance System

The overall goal of the quality assurance (QA) system is to ensure that minimum quality requirements are consistently met. The QA system encompasses the entire operation, from personnel training and the receipt of materials to production, quality control, and batch review. When comparing QA to quality control, think of QA as the oversight of the entire process, while QC is the release testing of the final product. In this regard, QC is just a small part of the overall QA system.

QA will most likely be performed by on-site personnel, and depending on staffing, this person will also likely participate in production. QA should work with other staff in the development of all of the procedures of the facility. A well-written procedure provides detailed information for staff to complete the task but is not so detailed that importance of key steps is lost in the details. Procedures should be reviewed at least annually to determine if updates are necessary. In addition, staff should be periodically tested on key procedures to ensure compliance. All proposed changes should be reviewed and recorded on the associated procedure. As individual radiopharmaceuticals move from preclinical research to human use, production staff should work closely with the QA team to determine process controls, production methods, appropriate testing methods, and release criteria. Careful consideration during this stage can help prevent mistakes from occurring later.

Following production and QC, QA personnel should review the production record for errors. This may happen immediately following batch release and again after the 14-day sterility period is over. If errors are found, QA will determine whether or not an investigation should take place. If the error is determined to be an acute or minor error, there may not be an appropriate preventive action. However, if a root cause analysis determines that the mistake will likely be repeated, QA should take steps to prevent recurrence. This can include retraining staff, changing workflow, or reevaluating procedural requirements.

Training of staff is an essential part of any successful program and falls under QA oversight. While most of the training will be hands-on, didactic training with tests should be incorporated when possible. New staff will likely undergo a significant amount of training at the beginning of their employment. However, all personnel should complete periodic testing to ensure they are still performing procedures as required. This is especially critical for aseptic manipulations, such as final product preparation or sterility testing.

Additionally, all staff involved in aseptic manipulations will perform initial media fill tests in triplicate to ensure they are capable of preventing contamination. Media fill testing involves personnel completing a process simulation of the intended aseptic process with a microbiological growth medium such as tryptic soy broth (TSB). For example, if during the intended aseptic process the operator is required to assemble a series of five final product vials each containing a sterilizing filter, a vent filter, and a QC-testing syringe, the same process should be completed with a vial of TSB to ensure the process is, in fact, aseptic and that no bacterial contamination occurs as a result of the process. While the full details of media fill testing are outside the scope of this chapter, the reader is encouraged to reference the USP and US FDA guidance documents for more information [15, 16]. In addition to annual media fills, semiannual reviews during normal workflow should be considered as well. This is an easy way for QA to quickly stop any bad habits that have developed and also look for opportunities to improve the facility's processes. No matter the training incorporated, it should always be documented, and the documentation should be kept as long as the employee remains with the facility.

Tricks of the Trade

As discussed throughout this chapter, there are many elements to consider when setting up a facility for the production of radiopharmaceuticals. The purpose of this section is to highlight several key points that can minimize the risk of problems in the future. Documentation is critical in all steps of facility setup, including validation, training, production, quality control, and investigations. An organized and detail-oriented person should be enlisted to serve as QA manager so that any deficiencies or discrepancies are caught early and corrected quickly. If a particular method (quality control, production, *etc.*) is not referenced in USP general chapters or monographs or FDA guidance documents, an alternative method should be validated. This alternative method should be included along with supporting documentation in the original FDA submission or as a supplement/amendment to an existing application. For example, consider a case in which the original submission required HPLC for radiochemical identity and purity testing, but subsequent research and testing proved that a simpler TLC method is equivalent. In this case, the proposed methods and results should be submitted as an amendment to the current application. This is

especially helpful as process improvements occur and will continue to promote an efficient operation.

When approving sources for supplies, multiple vendors should be included even if one is considered primary. For critical supplies such as the final product vials, multiple vendors or vial sizes should be qualified to minimize the risk that backorders will disrupt production.

Employees should be cross-trained as much as possible. For example, the production technician will likely not have the in-depth expertise of cyclotron maintenance, but should be able to operate the cyclotron and diagnose minor problems when the engineer is unavailable. All staff who could likely be needed to perform aseptic manipulations should complete media fill validations annually. Even if certain personnel will not perform aseptic manipulations on a regular basis, having multiple people qualified can prevent crises during staffing shortages. All operators should be routinely observed while performing critical steps not only to ensure that deleterious shortcuts are not applied over time but also to determine if process improvements can be implemented.

The Bottom Line

- Careful planning during the beginning stages of creating a radiopharmaceutical production facility will help maximize your chance of success.
- Although space is often limited, a facility that promotes efficient workflow should be designed. The facility should include areas for at least four basic functions: storage, aseptic manipulations, production, and analytical testing.
- Both equipment validation and process validation are essential in a well-functioning radiopharmaceutical production facility. Equipment validation is the process of ensuring that the equipment being used is capable of producing consistent results for the intended purpose. Process validation is the qualification of the manufacturing and production processes to confirm they are able to operate at a certain standard during sustained manufacturing.
- Immediately following synthesis, all manufactured radiopharmaceuticals undergo rigorous testing. At a minimum, these tests should include appearance, filter integrity, pH, radiochemical identity and purity, bacterial endotoxins, residual solvents, and sterility.
- The overall goal of the quality assurance (QA) system is to ensure that minimum quality requirements are consistently met. When comparing QA to quality control (QC), think of QA as the oversight of the entire process, while QC is the release testing of the final product. In this regard, QC is just a small part of the overall QA system. A thorough QA program can safeguard against excessive human error and prevent redundant investigations.
- It is critical to keep abreast of current regulations to ensure the compliance of the facility.

References

1. National Archives and Records Administration. Office of the Federal Register. Electronic Code of Federal Regulations. Current good manufacturing practice for positron emission tomography drugs. Sect. Part 212. https://catalog.data.gov/dataset/electronic-code-of-federal-regulations.
2. United States Pharmacopeia. Positron emission tomography drugs for compounding, investigational, and research uses. Sect. Chapter 823. USP40-NF35.
3. National Archives and Records Administration. Office of the Federal Register. Electronic Code of Federal Regulations. Current good manufacturing practice in manufacturing, processing, packing, or holding of drugs; General. Sect. Part 210. https://catalog.data.gov/dataset/electronic-code-of-federal-regulations.
4. U.S. Food and Drug Administration. FDA guidance for Industry: Process validation: general principles and practices. 2011.
5. National Archives and Records Administration. Office of the Federal Register. Electronic Code of Federal Regulations. Quality system regulation. Sect. Part 820.
6. United States Pharmacopeia. Positron emission tomography drugs-information. Sect. Chapter 1823. USP40–NF35.
7. U.S. Food and Drug Administration. FDA guidance for industry: Sterile drug products produced by aseptic processing – current good manufacturing practice. 2004.
8. U.S. Food and Drug Administration. Q3C – Tables and list guidance for industry. 2017.
9. United States Pharmacopeia. USP Monographs: Fludeoxyglucose F 18 Injection. Sect. USP40-NF35 p. 4520.
10. United States Pharmacopeia. Bacterial endotoxins test. Sect. Chapter 85. USP40-NF35.
11. Milton MJT, Wielgosz RI. Uncertainty in SI-traceable measurements of amount of substance by isotope dilution mass spectrometry. Metrologia. 2000;37(3):199.
12. Holland JP, Divilov V, Bander NH, Smith-Jones PM, Larson SM, Lewis JS. 89Zr-DFO-J591 for immunoPET of prostate-specific membrane antigen expression in vivo. J Nucl Med. 2010;51(8):1293–300.
13. Anderson CJ, Schwarz SW, Connett JM, Cutler PD, Guo LW, Germain CJ, et al. Preparation, biodistribution and dosimetry of copper-64-labeled anti-colorectal carcinoma monoclonal antibody fragments 1A3-F(ab′)2. J Nucl Med. 1995;36(5):850–8.
14. Paul-Dauphin S, Karaca F, Morgan TJ, Millan-Agorio M, Herod AA, Kandiyoti R. Probing size exclusion mechanisms of complex hydrocarbon mixtures: the effect of altering eluent compositions. Energy Fuel. 2007;21(6):3484–9.
15. U.S. Food and Drug Administration. Center for Drug Evaluation and Research (CDER). FDA guidance for industry: Media fills for validation of aseptic preparations for positron emission tomography (pet) drugs. 2012.
16. USP General Chapter ⟨1823⟩ Positron Emission Tomography Drugs – Information. United States Pharmacopeial Convention; 2017.

Index

A
Absorbed dose, 518
Accelerator targets, 76
  gas targets, 77
  liquid targets, 77
  reactions of charged particles, cross sections for, 78, 79
  solid targets, 77, 78
Actinides, 443
Actinium-225, 419, 443
Active pharmaceutical ingredient (API), 622
Acyclic chelator, 364
Acyclic polydentate chelator, 300
Affinity maturation, 565, 566
Alanine walk, 565
Allowed transitions, 45
Alpha-emitting radionuclides
  bifunctional chelators, 417
  bonding and chelation, 415–422
  carrier molecules bearing, 409
  chelation method, 415, 416
  controversial issues, 422
  decay characteristics, 411
  decay schemes, 413
  incorporation, 409
  monoclonal antibody (mAb), 416
  physical properties, 410
  and potential theranostic radionuclide pairs, 418
  production methods, 413
  production routes, 413, 414
  radiobiological effects, 409–410
  radionuclide decay schemes, 412
  radiopharmaceutical development, 411
  selection of, 411
  terbium-149, 415
  zirconium-89, 420
Alpha-melanocyte stimulating hormone (α-MSH) receptor, 146
Alpha-[^{11}C]methyl-L-tryptophan ([^{11}C]AMT), 227
Alpha-transformation, 46, 47
  energetics, 48
  excited states, 51
  quantum mechanics, 50
  tunnel effect, 50, 51
  velocities, 49
ALSYMPCA phase III trial, 94
Aluminum fluoride, 298
AMBF, 147
Amino acid dehydrogenase, 244
Amino acids (AAs), 137
  A20FMDV2, 139
  bombesin, 139
  enzymatic synthesis of, 243–248
  Fmoc-amino acid, 141
  Fnic-amino acid, 141
  high-purity, 141
  N-protected, 140
  octreotide, 139
Analytic reconstruction methods, 112
Anesthesia, 593
Anger, Hal, 18
Angiogenesis, 165, 168, 191
Annihilation, 59
Annihilation coincidence detection (ACD), 109
Anthropogenic radionuclides, 63
Antibody dependent cell-mediated cytotoxicity (ADCC), 164
Antibody-drug conjugate (ADC), 165, 176
Anti-CD20 antibody, 7
Anti-CD44 antibody, 176
Anti-matter, 36
Arginine-glycine-aspartic acid (RGD) motif, 138
Aromatic amino acid decarboxylase (AADC), 216
Aromatic amino acids, 208
Aromatic nucleophilic substitution (S_NAr), 277
Arsenic, 433
Arterial input function (AIF), 596
As low as reasonably achievable (ALARA), 515, 525, 527
Aspartic acid, 216
Astatine labeling methods, 418
Astatine-211, 434
Ataxia-telangiectasia mutated/checkpoint kinase 2 (ATM/Chk2), 88
Atom, 27
Atomic Energy Act (AEA), 85
Atomic Energy Commission (AEC), 16
Atomic mass unit, 28
Atomic nucleus, 27
Attenuation correction, 496, 594
Auger electron, 57, 86
Auger electron emitter therapy, 270
Automated QC testing, 491
Autoradiography
  binding with PET tracers, 590
  binding with tritiated ligands, 589–590
  data acquisition, 590–592
  film and phosphor screen, 590
  image analysis, 591–592
  stock solution for retest experiments, 589–591
  types, 589
  using phosphorescence imaging, 492
Avalanche photodiodes (APDs), 105

B
Bacterial endotoxins test, 631
Balz-Schiemann and Wallach reactions, 276
B-cell, 163
B-cell lymphoma, 7
Becquerel, Antoine Henri, 11

J. S. Lewis et al. (eds.), *Radiopharmaceutical Chemistry*, https://doi.org/10.1007/978-3-319-98947-1

Benzoate esters, 421
Beta-mercaptoethanol (BME), 377
Beta-phenethylamine, 241
Beta-transformation, 33
  anti-matter, 36
  β^+ and EC processes, 38
  β^+-emission vs. electron capture, 40
  β- process, 38
  electron capture, 40, 41
  elementary particles, 35, 36, 38
  excited states, 45
  isobars to parabolas, 34
  isotopes to isobars, 34
  kinetic energetics, 41
  laws of symmetry, 38
  log(ft)-values, 43
  nuclear spin, 43
  parity, 43, 45
  Q value, 40
  quantum theory, 41, 42
  selection rules, 43
  valley of β-stability, 35
  velocities, 42
Bevacizumab, 175
Bexxar, 7
Bifunctional chelators (BFCs), 150, 152
Binding assays, 585
  competition binding, 587–588
  in vitro autoradiography, 589
  optimization, 588
  saturation binding, 586–587
  using positron-emitting radionuclides, 588–589
Binding energy, 29
Bioavailability, 556
Biocompatibility, 183
Bioconjugation
  carbohydrates and saccharides, 457
  chemical reactions, 453
  chemoselectivity, 451
  controversial issues, 464
  cysteines, 455
  definition, 449
  enzymatic approach, 461
  lysines and N-terminus, 454
  nucleic acids, 458
  orthogonal functionalities, 463
  peptide substrates, 452–453
  peptides and proteins, 452
  phospholipids, 461
  post-labeling approach, 449
  pre-labeling approach, 449
  regioisomers, 451
  selectivity, 453–454
  site-specificity, 451
  tyrosines, 455
Biodistribution studies, 157
Bioorthogonal chemistry, 462
Biostatistics
  correction for multiple comparisons, 538
  data collection, 531
  definition, 531
  false positive rate, 533
  in vitro and preclinical studies, 538–539
  interpretation and presentation, 537
  linear regression model, 535–536
  mean, 532
  median, 532
  mode, 532
  95% confidence interval, 534
  outliers, 538
  P value, 534–535
  propagated error, 533
  quantile, 533
  range, 533
  ratio, 533
  research objectives, 531
  sample size, 531, 536–537
  standard deviation, 532
  statistical power, 533
  student's test, 534
  trade tricks, 537–538
  transformation, 531–532
  two-sample t-test, 535
Bis(thiosemicarbazones) (BTS), 341–346
Bismuth, 433
Bismuth-212/213, 419
Blood brain barrier (BBB), 583–584
Blood flow, 503
Blood sampling, 596
Blood-brain barrier (BBB), 167
Bolton-Hunter reagent, 401, 402
Bombesin (BBN), 138, 139
Bone metastases, 7
Boron group
  gallium-66, 429–431
  indium-110m, 431
  medical applications, 428
  thallium-201, 431
Bosons, 35
Bound state, 27
Brain-targeted nuclear imaging
  binding assays (*see* Binding assays)
  ex vivo autoradiography, 600
  in vitro autoradiography, 589
  using PET (*see* Positron emission tomography (PET))
Bremsstrahlung, 59
Bromine, 434

C
Cadmium selenide, 188
Calibration, 176
Canadian NRU reactor, 82
Cancer
  catecholamine-producing, 7
  detection, 4
  therapy, 91, 190–192
  treatment, 7
The Cancer Cell Line Encyclopedia (CCLE), 571
The Cancer Genome Atlas (TCGA), 571–573
Carbohydrates and saccharides, 456
Carbon
  positron emission tomography (PET), 336
  single photon emission computed tomography (SPECT), 336
Carbon group
  germanium-69, 431–432
  lead-212, 433
  tin-117m, 432
Carbon isotope, 28
Carbon nanomaterials, 187, 188

Carbon nanotubes, 187
Carbon radionuclides, 15, 16
Carbon-11, 15, 193
  alkyl groups, 212
  ammonium cyanide, 212
  carbon dioxide, 210
  carbonylation reactions, 214–215
  cetrozole, 214
  cyanide, 211
  decay characteristics, 208–209
  double isotope labeling, 216–218
  enzymatic catalysis and, 214–216
  gas-phase method, 212
  Grignard reagent, 213
  half-life, 209
  high molar activity, 210
  historic view, 207–208
  in-target produced primary precursors, 211
  isotopic dilution, 209–210
  labeling strategies, 213–218
  methylation of amines, 210
  molar activity, 209
  nitroalkanes, 213
  organoboranes, 214
  organostannanes, 214
  PET tracers, 209
  *p*hosgene, 212
  platinum-catalyzed reaction, 212
  position-specific labeling, 215–217
  positron emission tomography, 209
  production, 211
  radiation dose, 209
  radiochemistry, 210
  radiochemistry with, 208
  secondary precursors, 211
  stannanes, 214
  tracer studies, 209
  transition metal-mediated reactions, 213–214
  umpolung, 212
  wet-chemistry method, 212
Carbon-11 radiochemistry
  acids, 226
  alcohols, 226
  amines, 226
  amino acids, 226
  3-amino-4-(2-dimethylaminomethylphenylsulfanyl) benzonitrile, 229
  carbondisulfide, 235
  carbonylation, 233
  CH_3-moieties, 226
  chemical behavior, 235
  [^{11}C]CH_3I production, 224–226
  choline, 227
  CO_2 fixation chemistry, 230
  3,5-dichloro-N-[[(2S)-1-ethylpyrrolidin-2-yl]methyl]-2-hydroxy-6-methoxy benzamide, 229–230
  dithiocarbamate salts, 235
  equipment and labeling procedures, 221
  formaldehyde, 233
  formulation, 224
  Gas Phase production, 225
  Grignard reactions, 230–231
  harmine, 230
  hydrogen cyanide, 234
  labeled neuroimaging tracers, 227–230
  methyl triflate, 225
  methylserotonin, 233
  moisture sensitivity, 231
  optimizing Possibilities within synthesizer, 224
  PHNO and [*carbonyl*-^{11}C]WAY-100635, 232
  phosgene, 234
  Pittsburgh compound B, 228
  post-target production, 226
  precursors, tracer preparation, 233–235
  preparation, 231
  Purification and separation, 223–224
  reaction vessels vs. in-loop syntheses, 231–232
  reactors and reagent vessels, 222–223
  solvents, 231
  synthesizers setup, 221–222
  technical considerations, 221
  thiocarbonyl-labelled thioureas, 235
  thiols, 226
  wet chemistry method, 225
Carbon-14
  after second world war, 207
  draw-back of, 207
Carbon-germanium bonds, 394
Cardiology
  integrins and adhesion molecules, 548
  interleukin-2 receptor, 549
  myocardial perfusion imaging, 548
  norepinephrine transporter, 548
  phosphatidylserine, 549
Cardiovascular disease, 5
Cassen, Benedict, 18
Cation exchange, 195
Cationic amphiphilic drug-like (CAD), 127
Cell line-derived xenografts, 575
Cell metabolism, 549
Cell proliferation, 549
Cell-based assays, 155, 156
Centers of rotation (CORs), 112
Cetrozole, 215
Chadwick, James, 13
Chain reaction, 71
Chart of Nuclides, 53
Chelated aluminum fluoride, 147, 148
Chelators, 143, 144, 147, 148, 150–153, 176, 178, 194
Chemical reactive probes, 451
Chemistry, manufacturing, and controls (CMC), 622
Chemoselectivity, 451
Cherenkov resonance energy transfer, 188
Chimeric antigen receptor (CAR), 165
Chloranil test, 141
Chlorine-34m, 434
Cholecystokinin B receptor (CCKBR), 90
Chromium-51, 439
Circulating tumor cells (CTC), 85
Click chemistry
  archetypal, 468–469
  chemoenzymatic method, 475
  drug delivery strategy, 476
  excretionpathways by chemical design, 475
  [^{18}F]-labeled prosthetic group, 467
  IEDDA cycloadditionsreaction, 471–472
  PET, 468
  pretargeted imaging and therapy, 472
  SPAAC, 469–470
  tetrazine agent stability, 474
  trans-cyclooctene reagent, 475
Click-to-chelate concept, 326

Clinical need, 620
Clinical translation process
  in Europe (*see* European clinical translation process)
  in United States (*see* U.S. clinical translation process)
CNS PET tracers
  See Brain-targeted nuclear imaging
CO_2 fixation chemistry, 230
Cobalt-55, 440
Compartment models, 503
Competitive binding assays, 565, 587
Complement dependent cytotoxicity (CDC), 164
Complementarity-determining region (CDR), 164
Compton scattering, 101
Computer tomography (CT), 3
Confidence interval, 534
Conversion electron, 54, 56
Copper (II)-mediated [^{18}F]fluorination, 305–307
Copper radionuclides
  bis(thiosemicarbazones) (BTS), 343–345
  chelation chemistry, 341–346
  coordination chemistry, 341–343
  copper-60, 339
  copper-61, 339
  copper-62, 341
  copper-64, 339
  copper-67, 337–339
  historical use, 336
  macrocyclic chelators and chelator-bearing bioconjugates, 346–350
  production, 336–337
  types, 336
Copper radiopharmaceuticals, 336
Copper(I)-catalyzedazide-alkyne cycloaddition (CuAAC), 468
Copper(II)-bis(thiosemicarbazone) (Cu-BTS) complexes, 343
Copper-mediated radioiodination, 396
Cosmogenic radionuclides, 63
COSTER-KRONIG electrons, 58
Coulomb barrier, 70, 78
Crane, Robert, 21
Cross-bridged macrocyclic chelators, 350–351
Curie, Irène, 14
Curie, Marie Sklodowska, 11, 13
Curie, Pierre, 11, 13
Curie (Ci), 11
Current good manufacturing practice (cGMP), 172
Cyclotrons, 14, 63, 74, 485
  acceleration and constraining forces, 75
  equations of the motion of particles, 75
  extraction, 75, 76
  plasma/ion source, 74
Cysteines, 454–455

D
DASB radiotracer, 132
Data collection, 531
d-block radionuclides
  chromium-51, 439
  cobalt-55, 440
  iridium, 440
  iron-52, 439
  manganese, 439
  mercury-197m, 441
  nickel-57, 440
  niobium-90, 438
  platinum-195m, 441
  rhenium, 439
  rhodium, 440
  ruthenium-97, 440
  scandium, 436
  silver-111, 441
  tantalum-178, 438
  technetium-94m, 439
  titanium-45, 436
  yttrium-86, 436
  zinc-65, 441
De Hevesy, George, 14, 15
Deiodination, 403–404
Dendrimer, 190
Deoxyribonucleic acid (DNA), 456
Deprenyl, 218
Depth-of-interaction (DOI), 111
Desferrioxamine (DFO), 178, 379
Desferrioxamine B to antibodies, conjugation of, 375–378
Deterministic effects
  See Tissue reactions
Deuterium, 27
2-Deoxy-2-[18F]fluoro-D-glucose, 21, 22
Dichloromethane (DCM), 142
Dideuteriumdeprenyl, 218
N,N-Dimethylformamide (DMF), 142
Dimethyl sulfoxide (DMSO), 142, 377
Diphosphonates, 3
Direct electrophilic approach, 399
Dithiothreitol (DTT), 377
DNA damage response (DDR) pathways, 88
DNA-dependent protein kinase (DNA-PK), 88
Dopamine, 216
Dopamine D_2 receptors, 121
Dopamine transporter (DAT), 123
Dopaminergic neurotransmission, 547
Dose limits, 516
Dosimeters, 481
Dosimetry, 521–522
DOTA-NHS derivative, 419
Drug delivery, nanoparticles in
  See Nanoparticles
Drug development, 169, 620
Dynamic imaging, 103
  frame-mode studies, 103
  gated imaging, 103
  list-mode data, 103

E
Effective dose, 518
Electron capture, 33, 34, 40
  See also Primary transformation
Electron vacancies, 57
Electronic common technical document (eCTD), 624
Electrophilic substitution, 392
Electrostatic repulsion, 70
Endocrine disorders, 4
Enhanced permeability and retention (EPR) effect, 556
Enzymatic method, 460
Enzyme-linked immunosorbent assay (ELISA), 154, 155
Equipment validation
  definition, 629
  principles, 629
Equivalent dose, 518
Erbium-165, 442
European Association of Nuclear Medicine (EANM), 616
European clinical translation process
  clinical trials, 614–615

good manufacturing practices, 613–614
guidelines, 615–617
human research applications, 615
investigational medicinal product dossier, 607–610
preclinical requirements, 612–613
radiation dosimetry, 611–612
radiotherapeutic agents, 617
regulations for radiopharmaceutical production, 613
relevant clinical data, 612–613
risk-based approaches, 618
sensitive cameras, 617
toxicity, 607–611
trends in legislation, 617
validation, 613–615
European Medicines Agency (EMA), 615
Evans, Robley, 21
Excited nuclear level, 43, 45, 52
Excretion pathways by chemical design, 475
Excretory organs, 5
Exposure, 518
External beam radiation therapy (EBRT), 85
Extracellular matrix (ECM), 192
Extravasation, 182

F
Fab region, 164
Facility design, 523, 627
False positive rate, 533
f-block radionuclides
actinides, 443
actinium-225, 443
erbium-165, 442
holmium-166, 443
lanthanides, 441–443
samarium-153, 442
terbium, 442
Feraheme (FH), 379
Fermi, Enrico, 20
FERMI's golden rule, 41
Fermions, 35
Fermium-255, 420
Fetal bovine serum, 196
Fission, 63, 70, 71, 74, 82
Flight time, 494
N-9-Fluorenylmethyloxycarbonyl (Fmoc), 140
Fluorescence *in situ* hybridization (FISH), 176
[^{18}F]Fluoride, 297
[^{18}F]-Fluoride labeled prosthetic group, 467
Fluorine-18, 22, 360
acyclic polydentate ligands, 300
advantages, 297, 300
[AlF]$^{2+}$ complex, 298
alkylammoniomethyltrifluoroborate ($AMBF_3$), 303
bonds with, 297
copper (II)-mediated, 305
electrophilic radiofluorinations
[^{18}F]radiofluorinations *vs.* [^{18}F]fluorodemetallation reactions, 287–290
building blocks, 286–287
fluorodemetallation, 289
fundamentals, 285–286
homolysis, 290
organocopper(III), 293
oxidizing agents, 290–292
preparation and use, high molar activity, 290–293
radiopharmaceutical selection, 291–292
reductive elimination chemistry, 292–293
secondary labeling precursors, 286–287
selectfluor *bis*(triflate), 287
[^{18}F]FDOPA, 309
[^{18}F]fluoroborates, 300–302
heteroatoms, 298–302
macrocyclic chelator, 298
nucleophilic fluorinations
advantages, 273
aliphatic ^{18}F-substitutions, 275–276
altanserin, 277
aromatic ^{18}F-substitution of heteroarenes via classical S_NAr approach, 278–279
aromatic nucleophilic ^{18}F-substitution (S_NAr), 276–278
decay scheme, 273
fluoro-3,4-dihydoxy-L-phenylalanine, 277
fluoroepibatidine, 279
iodonium ylides, 280
late-stage radiofluorination, 274
onium salts, 279–280
pre-processing steps, 274
prerequisites, 279
production, 274
prosthetic group, 274
rules for performing, 281
steps, 274
tert-BuOH/acetonitrile, 276
palladium and nickel mediated, 303–305
umpolung concept, 290
4-[^{18}F]fluorobenzoic acid ([^{18}F]FBA), 146
[^{18}F]fluorodeoxyglucose ([^{18}F]FDG), 77, 505
2-[^{18}F]fluoroethylazide, 468
Folate receptor alpha (FRα), 91
Forbidden nuclear transitions, 45
Formaldehyde, 233
Full-width half-maximum (FWHM), 102
collimator resolution, 107
intrinsic resolution, 107
septal-penetration resolution, 107
spatial resolution, 107
Fusarinine, 384

G
Gadopentetic acid, 186
Gadoteric acid, 186
Gallium
acyclic chelators, 259–261
Auger electron emitter therapy, 270
bifunctional chelators, 258, 259
biology, 265–266
chloride, 267
citrate, 267
clinical use, 256
coordination chemistry, 256–258
cyclotron-based production, 264–265
^{67}Ga, 255, 256
^{68}Ga, 255
vs. F-18, 269
generator use, 266
gamma emissions, 256
generator concept, 269
generator production, 263–264
GMP issues, 269
imaging prostate specific membrane antigen, 267–268
imaging role, 265–266

Gallium (*cont.*)
instant thin-layer chromatography (ITLC), 266
iron-mimicking properties, 255
macrocyclic chelators, 259–260
metastable chelates, 258–259
molar activity, 269
production, 265
radioactive emissions, 256
radioactivity measurements, 266
radiopharmaceuticals, 268
Gallium-66, 429
Gamma amino butyric acid, 210
Gamma-amino butyric acid-benzodiazapine (GABA) receptor, 548
Gamma camera
basic design of, 107
clinical, 106
collimator, 106
energy rating, 107
FWHM, 107
Gamma counter, 492–493, 601
Gamma radiation, 54
Gas detectors, 520
Gastrin releasing peptide receptor (GRPR), 90, 137, 146
Gated imaging, 103
Gating, 496
Genetically engineered mouse models (GEMMs)
CRISPER/Cas9 technology, 576
in vivo validation studies, 577–578
knockout/knock-in technology, 576
murine models, 576
PET imaging, 577
Geometric distortion, 106
Germanium-69, 431
Gluons, 36
Gold nanoparticles, 184
Good clinical practice (GCP)., 615
Good laboratory practice (GLP), 621
Good manufacturing practices (GMP), 149, 613–614, 621
G-protein-coupled receptors (GPCR), 90
Graves's disease, 7
Greenberg, Joel, 24
Grignard reactions, 231–232
Griseofulvin, 395

H
Halogens
astatine-211, 434–435
bromine, 434–435
chlorine-34m, 434
Haloperidol, 132
Hamacher, Kurt, 22, 25
Helium isotope, 27, 29
Hematological tumors, 168
High performance/pressure liquid chromatography (HPLC), 142, 146, 148, 153, 154, 488
Highly enriched uranium (HEU), 71
HEU reactors and technetium-99m, 82
Hoffman, Edward, 24
Holmium-166, 443
Homologous recombination repair (HRR), 88
Hornerin, 561
Hot-cells, 486
Hot-plus-cold synthesis, 194
Human anti-mouse antibodies (HAMA), 163
Human epidermal growth factor receptor 2 (HER2), 176
Humanized murine models, 575
Hünig's base, 141
Hybrid systems, 113
Hybridoma technology, 163
Hydrazinonicotinamide, 325
Hydrazinonicotinic acid (HYNIC), 318–319
Hydroxamate-based resin systems, 373
Hydroxamate-functionalized cyclams, 386
2-Hydroxyisophthalamide, 387
1,2-Hydroxypyridinone (HOPO), 381
Hyperthyroidism, 7
Hypothesis testing and estimation
false positive rate, 533
linear regression model, 535
95% confidence interval, 534
P value, 534
statistical power, 533
student's test, 534
t-test, 535
Hypoxia, 345–346, 550
imaging, Cu, 345, 346, 352

I
Imaging, 192
computing and analytics, 8
diagnosis, 4
instrumentation, 8, 18, 19
Immunoglobulins, 164
discovery, 163, 164
immunoPET and immunoSPECT, 174–176
mAb, 164
mechanisms of action, 164, 165 (*see also* Radioimmunoconjugates) (*see also* Radioimmunodetection)
target expression and accessibility, 167, 168
ImmunoPET, 371
In vitro autoradiography, 589
Independent-sample t-test
See Two-sample t-test
Indium
availability, 256, 270
bifunctional chelators, 258, 261–263
cell labeling, 267
cell tracking, 262–263
coordination chemistry, 256–258
gamma emissions, 256
metastable chelates, 258–259
problems with sampling, 267
production, 265
radioactive emissions, 256
radioactivity measurements, 266
Indium-110m, 431
Inhibiting concentration IC_{50}, 565
Innovative targetry, 81, 82
Installation qualification (IQ), 629
Instant thin-layer chromatography (iTLC), 173
Institutional review board (IRB), 620
Interleukin-2 (IL-2) receptor, 549
Internal contamination prevention, 524
International Atomic Energy Agency (IAEA), 515
International Commission in Radiological Protection (ICRP), 515
Internet of chemical things (IoCT), 497
Internet of medical things (IoMT), 497
Internet of things (IoT), 497
Intracellular tau neurofibrillary tangle (NFT), 547

Intrinsically radiolabeled nanoparticles, 194
Inverse electron-demand Diels Alder (IEDDA) cycloaddition reaction, 471–472
Inverse electron-demand Diels-Alder (IEDDA) reaction, 148
Investigational medicinal product dossier (IMPD), 607–610
Investigational new drug (IND), 621
Iodine radionuclides, 15
Iodine-131 (^{131}I), 4, 85, 391
Iododeboronation, 394
Iododediazonization, 397
Iododegermylation, 394
Iododemercuration, 394
Iododemetallation reactions, 393
Iododeprotonation, 392
Iododesilylation, 394
Iododestannylation, 393
Iododethallation, 394
Iodonium salt precursors, 397
Ionization detectors, 103–104
Ionizing radiation (IR), 86–88, 515, 516, 520, 527
  autophagy, 88
Iridium, 440
Iron oxide nanoparticles, 186
Iron-52, 439
Irreversible and reversible compartment models, 513
Isobar, 34
Isothiocyanates, 150
Isothiocyanato-*p*-benzyl-desferrioxamine (*p*-NCS-Bn-DFO), 375
Isotopes, 27

J
Joliot-Curie, Frédéric, 14
Justification, 515

K
Kaiser (ninhydrin) test, 141
Kamen, Martin, 16, 17
Ketanserine, 132
Kinetic binding, 562–563
Kinetic energy, 70
Kinetic isotope effect (KIE), 217–218
Krypton-81m, 435

L
L-[*methyl*-^{11}C]methionine, 227
Lanthanide nanoparticles, 186
Lawrence, Ernest O., 14
Lawrence, John, 20
Lead-212, 432
Lead-212/Bi-212, 420–422
Leptons, 36
Ligand affinity, 573
Ligand identification, 561–562
  competitive binding, 565
  kinetic binding, 562
  mechanism of action, 562
  peptide maturation, 565–566
  radioligand binding assays, 562
  saturation binding, 563–565
Lindmo assay, 173
Line of response (LOR), 109, 110
Linear accelerator (linac), 76
Linear energy transfer (LET), 86, 516
Linear regression model, 535
Lipophilicity, 125, 126
Liposomes, 189
Liquid drop model (LDM), 29
Liquid scintillation counter, 521
List mode data acquisition, 494
Livingood, John, 16
Log(ft)-values, 43
Logan plot, 509
Low enriched uranium (LEU), 71
LUTATHERA, 137, 153, 159
Lutetium-177, 186
  bifunctional chelators, 363–364
  bioinorganic chemistry, 362
  gamma rays, 361
  half-life, 361
  myelotoxicity, 361
  nuclear properties, 359–360
  single photon emission computed tomography (SPECT), 361, 362
  solution chemistry, 359
  and yttrium-90, 361
Lysines and N-terminus, 454

M
Macromolecules, quality control method for, 631
Magnetic nanoparticles, 185, 186
Maleimide, 146
Maleimide-based prosthetic group, 300
Manganese, 439
Manhattan Project, 71
Manufacturing quality, 620
Mass, 27–29
Mass defect, 27–29
Mass number, 27, 70
Mass spectrometry-based quantitative proteomics, 559
Matrix metalloproteinases (MMP), 91
Maximum-likelihood expectation maximization (MLEM), 113
Mean, 532
Mean binding energy, 29
Mean free path (MFP), 105
Median, 532
Medical radionuclides
  imaging, 192
  therapy, 192
Medium-energy collimator, 107
Medullary thyroid cancer (MTC), 85, 90
Melanin nanoparticles (MP), 379
Membrane filter integrity testing, 630
Memorial sloan kettering (MSK), 619
Mercury-197m, 441
Mesoporous silica nanoparticles, 187
Metaiodobenzylguanidine (MIBG), 91
Metallic radionuclides, 150
Metastatic castration resistant prostate cancer (mCRPC), 94
Metastatic colorectal cancer (mCRC), 94
[^{11}C]Methyl iodide, 208
Micelles, 190
Microdose, 621
Miniaturized quality control, 491
Mode, 532
Molar activity, 153
Molecular imaging, 4, 101
Molecular imaging and contrast agent database (MICAD), 557, 570
Molecularly targeted therapeutics, 569

Molybdenum, 16
Molybdenum-99, 17
^{99}Mo/^{99m}Tc generator, 311–312
Monoamine oxidase (MAO), 230
Monoamine oxidase type B (MAO-B), 217
Monoclonal antibodies (mAbs), 163
  chimeric, 164
  development and functionalization, 164
  humanized, 164
Mononuclear phagocyte system, 183, 198
Multichannel analyzers (MCAs), 491
Multimodality (hybrid) systems, 113
Myocardial perfusion imaging, 548

N
Nanobodies, 562
Nanoparticles, 250
  advantages, 181, 182
  carbon, 187, 188
  covalent labeling with non-metallic radionuclides, 193, 194
  dendrimers, 190
  drug delivery, 181
  gold nanoparticles, 184
  in vitro studies, 197, 198
  in vivo studies, 198, 199
  lanthanide, 186
  liposomes, 189
  magnetic, 185, 186
  medical radionuclides, 192, 193
  micelles, 190
  quantum dots, 188
  radiometals, 194, 195
  shape effects, 183
  silica, 186, 187
  size effects, 182
  solution-based test
    radiolabeling efficiency and stability, 196, 197
    stability and degradation, 196
  surface modifications and biocompatibility, 183
  target cancer with
    active, 191
    passive, 190, 191
    tumor microenvironment, 192
    vasculature, 191
NCBI, 557
NETSPOT, 153, 159
NETTER phase III trial, 94
Neuroendocrine tumors (NETs), 7, 137
Neurologic and psychiatric diseases, 5
Neuroscience
  amyloid plaques, 547
  dopaminergic neurotransmission, 547
  γ-aminobutyric acid-benzodiazapine receptor, 548
  intracellular tau neurofibrillary tangle, 547
  nicotinic acetylcholine receptor, 548
  translocator protein-18 kDa, 548
Neutral endopeptidase (NEP), 92
Neutrino hypothesis, 38
Neutron, 27
  discovery of, 13, 14
Next generation sequencing (NGS), 560
N-haloamidate, 240
Nickel-57, 440
Nickel mediated fluorination, 303–305
Nicotinic acetylcholine receptor (nAChR), 548
Niobium-90, 438
Nitrogen-13 (^{13}N)
  adenosine, 241
  amine reduction, 241
  amino acids, 243
  ammonia, 238
  aryldiazonium ion, 247
  aryldiazonium salt, 247
  β-phenethylamine, 241
  discovery, 237–238
  glutamic acid dehydrogenase, 245
  N-haloamidate, 240
  in-cyclotron production, 239
  limitation, 247
  lock-and-key model, 243
  mechanistic studies, 249–250
  nanoparticle radiolabeling, 250–252
  nitrite (NO_2^-), 245–248
  nitrogen gas, 240
  nitrosamines, 247
  nitrosothiols, 247
  phenylacetone, 240
  production, 238–240
  properties, 237
  radiochemistry, 240–245
  sodium hypobromite, 241
N-Methyl acetohydroxamic acid (Me-AHA), 373
N-Methylpyrrolidone (NMP), 142
Noble gases
  krypton-81m, 435
  xenon-133, 435
Noddack, Ida, 21
Non-bound nucleons, 27
Non-clinical safety evaluation, 620
Non-commercial sponsors, 624
Non-displaceable binding, 126
Non-Hodgkin's lymphomas (NHL), 91
Non-homologous end joining (NHEJ), 88
Non-metallic radionuclides, 193, 194
Non-selective binding, 121
Non-specific binding (NSB), 563, 589
Norepinephrine transporter (NET), 91, 123, 548
NOTA-based chelators, 299
N-succinimidyl 4-[^{18}F]fluorobenzoate ([^{18}F]SFB), 144–147
Nuclear imaging, 3
  advantages and disadvantages of, 102
  cancer detection, 4, 549–550
  cardiovascular disease, 5, 548–549
  clinical diagnosis, 4
  endocrine disorders identification, 4
  excretory organs, 5
  gamma camera, 106, 107
  interactions of radiation with matter, 101
  multimodality (hybrid) systems, 113
  neurologic and psychiatric diseases, 5
  in neuroscience, 547–548
  PET (*see* Positron emission tomography (PET))
  planar *vs.* tomographic imaging, 102, 103
  radiation detection, basic principles of
    scintillation detectors, 104, 105
    semiconductor-based ionization detectors, 105, 106
  radiopharmaceuticals, 113–115
  selection of targets, 546–547
  SPECT (*see* Single-photon emission computed tomography (SPECT))

static *vs.* dynamic imaging, 103
target expression, 541–542
target function, 542–544
target properties, 541–544
target specificity, 544
targeted radiotherapy, 544, 550
tissue damage identification, 5
whole-body imaging, 103
Nuclear medicine, 9, 101, 105, 106
advantage, 3, 4
post-World War II, 16
Nuclear radiotherapy
advantages, 3
clinical applications, 7
Nuclear reactors, 63
cross sections, 71, 72
fission reactions, 74
fundamentals of, 70
control rods, 71
modern reactor designs, 71
pressurized water reactor core, 70, 71
supercritical fission reaction, 71
uranium-235, 71
(n,p) and (2n,γ[gamma]) reactions, 74
(n,γ[gamma]) reactions and specific activity, 73, 74
neutron capture reactions, 72, 73
target considerations
product burn up, 73
self-shielding, 73
target burn up, 73
Nuclear spin, 43
Nuclear transformation
α-emission, 46–48, 50, 51
anti-matter, 36
for β^+-emission vs. electron capture, 40
β^+ and EC processes, 38
β-particle and electron neutrino, 41
β- process, 38
β-transformation, 33, 34, 38, 40–43, 45, 46
binding energy, 29
electron capture, 40
elementary particles, 35, 36
isobars to parabolas, 34, 35
isotopes to isobars, 34
log(ft)-values, 43
models, 29–31
nuclear spin, 43
parity, 43
post-process, 33, 56–60
primary transformation, 32
quantum theory, 41, 42
secondary transformation, 32, 52–56
spontaneous fission, 52
stable to unstable nuclei, 31
valley of β-stability, 35
velocities, 49
Nucleic acids, 456
Nucleon binding energy, 29–31
Nucleons, 27–29, 31
Nucleophilic substitution, 391, 392, 395
Nucleus, 31

O
OctreoScan, 159
OctreoTher, 159
Octreotide, 158, 159
On the Use of the New Rays (Roentgen's report), 11
Oncologic targets
cell metabolism, 549
cell proliferation, 549
hypoxia, 550
receptors and protein kinases, 549
Oncology
affinity agent generation, 579
The Cancer Cell Line Encyclopedia, 571
The Cancer Genome Atlas, 571–573
cohort size in preclinical experiments, 578
development in nuclear medicine, 579
genetically engineered mouse models, 576–578
humanized murine models, 575–576
molecular imaging and contrast agents database, 570
molecularly targeted therapeutics, 569
prostate-specific membrane antigen, 569
radiotracer (*see* Radiotracer)
targeted molecular imaging, 570
TRT (*see* Targeted radionuclide therapy (TRT))
xenografts, 575
One-bead-one-compound (OBOC) combinatorial library method, 566
One-bead-one-compound (OBOC) library, 139, 140
Operational Qualification (OQ), 629
Opsonization, 182
Ordered-subset expectation maximization (OSEM), 113
Organofluoroborates, 147
Organofluorosilanes, 146, 147
Organotrifluoroborate salts, 301
Overall survival (OS), 94
Oxidizing agents, 392
Oxygen-15 (^{15}O)
discovery, 237–238
production, 248–249
properties, 237
radiochemistry, 249
Oxygen-17, 13

P
P value, 534
Palladium
mediated fluorination, 303–305
palladium(IV)-based electrophilic radiofluorination, 304
Pd(II)-aryl complex, 303
Parabolas, 34, 35
Parallel compartment model, 509
Parity, 43
Parkison's disease (PD)
toxin-based model, 602
transgenic rodent models, 602
Particle accelerators, 63
Particles-radiation interactions, 516
Patient-derived xenografts (PDXs), 157, 575
Patlak plot, 508–509
p-block radionuclides
boron group/triels, 428–431
carbon group/tetragens, 431–433
chalcogens, 434
halogens, 434–435
noble gases, 435
pnictogens, 433–434
Penetrability factor, 51
Peptide receptor radionuclide therapy (PRRT), 90–92, 97, 142, 149, 156, 157, 159, 366

Peptides, 546
clinical imaging, 137
development of, 138
general structure of, 138
goals, 137
GRPRs, 137
identification, 139
combinatorial library approaches, 139
initial sequence, 139
rational design, 139
in vitro and *in vivo* performance of, 137
integrins
$\alpha_v\beta_3$, 138
$\alpha_v\beta_6$, 138
maturation, 565–566
modifications and optimization, 158, 159
NETs, 137
oncological targets, 138
and proteins, 452
radiolabeling of
approaches, 144
cell viability studies, 156
cell-based assays, 155, 156
ELISA, 154, 155
hydrophilicity, 156
in vitro validation, 154
in vivo validation, 157, 158
position of, 142–144
purification, analysis and characterization of, 153, 154
radiofluorination and [^{18}F]fluoride acceptor chemistry, 146–148
radiofluorination and classic prosthetic group chemistry, 144–146
radiofluorination and click chemistry, 148
radioiodination, 149
radiolabeled prosthetic groups, automation of, 148, 149
radiometals, 149, 150, 153
radionuclide selection, 142
serum stability studies, 154
substrates, 452–453
synthesis, 140, 141
activating agent, 141, 142
amino acids, 141
cleavage, 142
colorimetric tests, 140
crude, 140
C-terminus, 140
in-house, 140
Kaiser (ninhydrin) test, 141
N-terminal amine, 140
purification and characterization, 142
resins, 141
solvent, 142
SPPS, 140, 141
Performance Qualification (PQ), 629
Perrin group, 147
Pertechnetate ([^{99m}Tc]TcO_4^-), 316
PET agent, 622
PET Tracer
See Radiotracer
pH, 630
Phage display-based functional proteomics
advantages, 559
genotype, 560
lead peptide, 561
screening, 560
selectivity, 560–561
target identification, 561
Phantom, 361
PHASTpep, 560, 561
Phenethylsuccinamide ester, 421
Phenytoin, 216
Pheochromocytomas/paragangliomas (PHEO/PGL), 91
Phosphatidylinositide 3-kinase (PI3K), 88
Phosphatidylserine, 549
Phospholipids, 459
Phosphoramidon (PA), 92
Phosphorus-32, 433
Photomultiplier tube (PMT), 103, 104
configurations, 105
inner surface of, 104
irregular PMT output signal, 104
two-dimensional array of, 106
Photon emission, 54
Photons-radiation interactions, 517
Photonuclear isotope production, 80
Picrylsulfonic acid (PSA), 141
Pinhole collimators, 106
[^{11}C]Pittsburg compound B (PIB), 603
Planar imaging, 102
Plasma protein binding, 126, 597
Platinum-195m, 441
Plectin, 561
Pnictogens
arsenic, 433
bismuth, 433–434
phosphorus-32, 433
Polonium, 13
Poly ADP-ribose polymerase (PARP), 88
Polyethylene glycol (PEG), 183
Porphyrins, 195
Position-sensitive PMT (PSPMT), 105
Positron, 58
Positron emission tomography (PET), 8, 142, 171, 192, 576, 577
advantages and disadvantages of animal models, 602–603
anesthesia, 593
approach for arterial input function, 599
attenuation correction, 594
autoradiography, 492
binding affinity, 583
biodistribution using gamma counter, 492–493, 601–602
blood sampling, 596–597
centers, 481
central nervous system, 584
comprehensive radiation monitoring systems, 484
data corrections, 111, 112
development, 583, 604
developmental aspects, 496
dosimeters, 481
equipment, 481
ex vivo autoradiography, 600–601
first tracer, 603
future aspects, 604
image reconstruction, 112, 113
in vitro and *in vivo* evaluation, 491
injection route, 592
internet of things, 497
IoCTand IoMT, 497
networked devices, 498
nuclear medicine, 498–499
plasma protein binding, 597–598
quality control instruments (*see* Quality control (QC) instruments)
radioactivity counters, 483–484
radiometabolite analysis, 598–599

radionuclide emitting low-energy, 114
radionuclide production, 484–486
radiotracers, 114
reconstruction, 593–594
scanners
ACD, 109
DOI effect, 111
instrumentation-related determinants, 111
LORs, 109, 110
modern, 109
non-colinearity related blurring, 111
non-TOF, 111
positron-emitting nuclides, 111
ring scanners, 110
single event, 109
singles count rate, 109
spatial resolution of, 111
3D PET, 110
TOF, 110
2D PET, 110
whole-body, 111
static *vs.* dynamic data acquisition and quantification, 594–596
synthesis module, 484–488
transverse images, 102
whole-body PET scan, 103
Positron-emitting radionuclides
incubation time and temperature, 589
non-specific binding, 589
optimization of binding assay, 588
radiotracer concentration, 588–589
target molecule concentration, 589
Post-effects
electromagnetic radiation, 57
electron emissions, 57
mechanisms, 33
positron, 58, 59
vacancies of shell electrons, 56
X-ray, 57
X-ray emission vs. electron emission, 58
Post-labeling approach, 449
Potassium-38, 426
Precision medicine, 555
Pre-formed fibrils of recombinant asyn (PFFs), 603
Pre-labeling approach, 449
Pretargeted imaging and therapy, 472–474
Pretargeted radioimmunotherapy (PRIT), 92, 93
Primary transformation, 32
Primordial radionuclides, 63
Process validation, 629
Product quality control (QC) testing, 621
Production facility
documentation, 632
equipment validation, 629
process validation, 629–630
quality assurance system, 632
treatment (*see* Therapeutic radiopharmaceuticals)
workflow design, 627–628
Progression-free survival (PFS), 91, 94
Projection imaging, 102
Propagated error, 533
Prostate-specific membrane antigen (PSMA), 90, 91, 327, 569
Prosthetic agents, 391, 399
Prosthetic groups, 143, 144, 146
Protein kinases, 549
ProteinAtlas, 557
Proteins, 547
Proton, 27, 36
Proton number, 70
Pseudo-first order kinetics approximation, 210
Pulse-height analyzer, 104

Q
Q value, 40, 70
Quality assurance (QA) system, 632
Quality control (QC) instruments, 488–491
automated QC testing, 491
dose calibrators, 491
multichannel analyzers, 491
radio-HPLC systems, 490
radio-thin layer chromatography, 488–490
Quality control method
membrane filter integrity testing, 630
pH, 630
radioactive concentration, 630
radiochemical identity and purity, 631
residual solvents, 631
visual inspection, 630
Quality of radiopharmaceutical, 621–622
Quantile, 533
Quantitative proteomics, 559
Quantum dots (QDs), 188
Quarks, 36

R
Racemic [^{11}C]alanine, 208
Raclopride, 132
Radiation, 31
Radiation biology, 519–520
Radiation dosimetry, 611–612
See also Dosimetry
Radiation emergencies, 526
Radiation interactions
linear energy transfer, 516
with particles, 516–517
with photons, 517–518
specificionization, 516
Radiation protection
absorbed dose, 518
biological effects, 518–520
contamination control, 522–524
decontaminating personnel, 527
distance, 522
dose limits, 516
dose meters and counters, 520
dosimetry and occupation monitoring, 521–522
during pregnancy, 527
effective dose, 518–519
equivalent dose, 518
exposure, 518
facility design, 523
gas detectors, 520–521
interactions with matter, 516
justification, 515
laboratory audit checklist, 527–528
liquid scintillation counter, 521
optimization of protection, 515
organizations, 515
planning, 523
radiation emergencies, 526–527
radiation safety committee, 524

Radiation protection (*cont.*)
radioactive material transport, 526
radioactive packages, 526
radioactive waste, 526
rules of thumb, 527
safe handling of radioactivity, 522–523
safety, 525–526
shielding, 522–523
solid-state detectors, 521
stochastic effects, 520
time, 522
tissue reactions, 519–520
training, 525
wipe tests, 521
Radiation safety, 525
Radiation, discovery, 11
Radiation-induced cell death, 86
Radioactive concentration, 630
Radioactive emission, 31, 60
Radioactive iodine (RAI), 85
Radioactive material transport, 526
Radioactive packages, 526
Radioactive waste, 526
Radioactivity, 31
artificial, 14
discovery of, 11 (*see also* Nuclear transformation)
Radioactivity counters, 483
Radiochemical identity and purity, 631
Radiochemistry, 28, 147, 148, 153, 159, 425
click chemistry reaction in, 467–468
Radioembolization
See Selective interarterial radiation therapy (SIRT)
Radiofluorination
classic prosthetic group chemistry, 144
^{18}F-labeled prosthetic groups, 145
maleimide prosthetic groups, 146
solid-phase peptide radiolabeling, 144, 146
click chemistry, 148
[^{18}F]fluoride acceptor chemistry, 146
chelated aluminum fluoride, 147, 148
organofluoroborates, 147
organofluorosilanes, 146, 147
Radiohalogenation of peptides
See Peptides
Radio-HPLC systems, 490
Radioimmunoconjugates, 7
approval, 169
current good manufacturing practice, 172
development, 171
immunoglobulin integrity, 172
immunoreactive fraction, 173
in drug development, 169
in vivo biodistribution, 174
inert radiolabeling, 171
LC-MS/MS, 173
performance, 174
PET/SPECT imaging, 171
preparation of, 176
quality control, 172
radiochemical purity, 173
radiolabeling efficiency and purification, 171, 172
radionuclide selection, 168, 169
SDS-PAGE, 173
size exclusion chromatography, 172
stability, 172
theranostics and radioimmunotherapy, 171
Radioimmunodetection
antibody delivery, 175
immunoPET and immunoSPECT, 175
pharmacokinetics and biodistribution, 175
target expression and accessibility, 174, 175
target modulation and monitoring response, 175
target saturation, 175
Radioimmunotherapy (RIT), 7, 91, 171
Radioiodination, 149
click chemistry, 403
by click reactions, 400
deiodination, 403
electrophilic, 393
electrophilic substitution, 392
exchange, 395–397
from triazines, 397
iododeboronation, 394
iododediazonization, 397
iododegermylation, 394
iododemercuration, 394
iododemetallation reactions, 393
iododeprotonation, 392
iododesilylation, 394
iododestannylation, 393–394
iododethallation, 394
iodonium salt precursors, 397–398
kit methods, 398–399
molecular imaging and targeted radiotherapy, 392
by nucleophilic substitution, 395
of low molecular weight organic compounds, 392–398
of peptides and proteins, 399
oxidizing agents, 392
peptide via preconjugation, 401
peptide via tetrazine-*trans* cyclooctene, 401
peptides, 400
preconjugation of precursor moiety, 400
via pre-labeled prosthetic groups, 399
via prosthetic agents, 401
proteins, 400
residualizing labels, 402
supported precursors, 399
tin-based precursors, 398
tricks of trade, 404
Radioiododemetallation, 393
Radioiododeprotonation, 393
Radiolabeled antibodies, 89, 92, 578
Radiolabeled nanoparticles, 182
Radiolabeling approach, 171
post-labeling, 450
pre-labeling, 449
Radiolabeling of peptides
analysis and characterization, 153, 154
approaches, 144
cell viability studies, 156
cell-based assays, 155, 156
chromatographic methods and chromatography-based, *in vitro* testing, 153
ELISA, 154, 155
hydrophilicity, 156
in vitro validation, 154
in vivo validation, 157, 158
position of
functional groups, 143
integrin $\alpha_v\beta_3$-targeting cycloRGD peptides, 143
in vivo stability, 144
lysine residue, 143
non-site-specific radiolabeling, 144

N-terminus, 144
reactive sites, 143
sulfhydryl group of cysteine, 144
ε-NH_2 group of lysine, 144
radiofluorination
classic prosthetic group chemistry, 144–146
click chemistry, 148
[^{18}F]fluoride acceptor chemistry, 146–148
radioiodination, 149
radiometals, 149, 150, 153
radionuclide selection, 142
right HPLC system, SPE, 153
serum stability studies, 154
Radioligand binding assays, 562–566
Radiometabolite analysis, 598
Radiometals, 149, 194–196
bifunctional chelators, 150, 152
chelator pairings, 150, 151
isothiocyanates, conjugation of, 150, 152
PET imaging, 150
SPECT imaging, 150
therapeutic applications, 150
Radiometric isotopic dilution assays, 631
Radionuclides, 183–190, 192
actinides, 443
actinium-225, 443
α-radiotherapy, 444
boron group/triels, 430
carbon group/tetragens, 432
chalcogens, 434
chromium-51, 439
cobalt-55, 440
erbium-165, 442–443
generator, 79
halogens, 434
holmium-166, 443
iridium, 440
iron-52, 439–440
lanthanides, 441–443
manganese, 439
mercury-197m, 441
nickel-57, 440
niobium-90, 438
noble gases, 435
PET/SPECT imaging, 444
platinum-195m, 441
pnictogens, 433–434
potassium-38, 427
production of, 20, 484
PSMA, 444
radiopharmaceuticals application, 444
radiotracers, 443
radium-223, 428
rhenium, 439
rhodium, 440
rubidium-82/82m, 426–427
ruthenium-97, 440
samarium-153, 442
scandium, 436
silver-111, 441
strontium-82/83/89, 426–428
tantalum-178, 438
targeted radiotherapeutic drugs, 445
technetium-94m, 439
terbium, 442
titanium-45, 436–438
yttrium-86, 436
zinc-65, 441
Radionuclide production, in medicine
accelerator targets, 76
gas targets, 77
liquid targets, 77
reactions of charged particles, cross sections for, 78, 79
solid targets, 77, 78
anthropogenic, 63
cosmogenic, 63
cyclotrons, 74
acceleration and constraining forces, 75
equations of the motion of particles, 75
extraction, 75, 76
plasma/ion source, 74
HEU reactors and technetium-99m, 82
linear accelerators, 76
nuclear reactions/reactors
cross sections, 71, 72
energetics of, 69, 70
fission reactions, 74
fundamentals of, 70, 71
neutron capture reactions, 72, 73
(n,p) and (2n,γ[gamma]) reactions, 74
(n,γ[gamma]) reactions and specific activity, 73, 74
secondary particle, 69
stationary target nucleus, 69
target considerations, 73
photonuclear isotope production, 80
practical considerations, 80
innovative targetry, 81, 82
simulation tools, 80, 81
target material, selection of, 81
primordial, 63
radionuclide generators, 79
Radionuclide therapy
See Nuclear radiotherapy
Radioresistance, 87, 88
Radiosynthesis, 125
Radiotherapy, 544
Radio-thin layer chromatography (radioTLC), 196, 489
Radiotracer, 120
affinity, 122–124
applications, 119
basis function methods, 510–511
biodistribution, 574
blood flow and ^{15}O-water, 503–504
chemical characterization and biological evaluation, 573
^{11}C-labelled dopamine transporter ligand, 501
compartment model, 503
concentration, 588
development, 128
dynamic PET scan, 501
in vivo model systems, 575
in vivo tumor, 574
lipophilicity, 574
Logan plot, 509–510
metabolism and internalization, 504–505
model selection and simplification, 512–513
non-linear regression, 503, 508
number of linearizations, 508
parametric images, 508
pathways discovery, 129
Patlak plot, 508–509
plasma protein binding, 126
proteins/cell lines, 574
radiolabeled antibodies, 578

Radiotracer (*cont.*)
radiosynthesis, 125
radiosynthetic method, 573–574
receptor binding, 505–507
reference tissue models, 507–508
selectivity, 124, 125
single tissue model, 507
single-tissue compartement model, 502
standardized uptake values, 511–512
target accessibility and non-displaceable binding, 125–128
target expression and affinity, 573
target selection, 121, 122
test criteria
in vivo pharmacokinetics, 132
i*n vivo* pharmacology, 132
radiolabelled metabolites, 132, 133
signal-to-noise ratio *in vivo*, 130, 131
target sensitivity, 133
tracer kinetic models, 501
tracer principle, 501
translation, 133, 134
Radium, 12
Radium-223, 8, 428
Radium-223/224, 420
Range, 533
Ratio, 533
Reactive oxygen species (ROS), 86
Receptor, 549
Receptor parametric mapping (RPM), 511
Recoil energy, 41
Reduced transition probability, 51
Regioisomers mixture, 451
Region of interest (ROI), 121
Regulatory mechanisms, 623–624
Reivich, Martin, 22
Reliable and automated manufacture requirements, 497
Residual solvents, 631
Residualizing radionuclides, 168
Reticuloendothelial system (RES), 115, 183
Rhenium, 439
Rhodium, 440
Ribonucleic acid (RNA), 456
Richards, Powell, 18
Roentgen, Wilhelm Conrad, 11, 12
Ruben, Samuel, 16, 17
Rubidium-82/82m, 426–427
Ruthenium-97, 440
Rutherford, Ernest, 13

S
Samarium-153 (^{153}Sm), 3, 186, 442
Sample size, 531, 536
SARAH trial, 94
Sarcophagine family of chelators, 349
Saturation binding, 563, 586
s-block radionuclides
potassium-38, 426
radium-223, 428
rubidium-82/82m, 426–427
strontium-82/83/89, 428
Scandium, 436
Scanners, 493–496
attenuation correction, 496
flight time, 494
gating, 496
list mode data acquisition, 494
Scatchard equation, 123
Scintillation detectors
basic design and operation of, 104
practical features of, 105
Seaborg, Glenn, 16
Secondary transformation
conversion electrons, 56
excited nuclear states, 52
Gamma radiation, 54
meta-stable nuclides/nuclear isomers, 53
multipoles of different order, 55
nucleon composition, 32
orbital momentum, 55
pair formation, 56
photon emission, 54
X-rays, 54
Selectfluor®, 287
Selection of targets
peptides, 546–547
proteins, 547
small molecules, 546
Selective interarterial radiation therapy (SIRT), 89, 94, 96, 97
Selenium, 434
Semiconductor-based ionization detectors, 105, 106
Septal penetration, 106
Serotonin transporter (SERT/5-HTT), 123, 129, 229
SERT-5, 131
Shell model, 30, 31
Shielding materials, 522
Shotgun proteomics, 559
Si photomultipliers (SiPMs), 105
Signal transduction, 165
Signaling pathways, 546
Signal-to-noise ratio (SNR), 110
Silica nanoparticles, 186, 187
Silicon photodiode, 105
Silver triflate (AgOTf)-impregnated graphitized carbon, 226
Silver-111, 441
Simplified reference tissue model (SRTM), 507
Simulated bodily fluid, 196
Single-aperture pinhole collimators, 106
Single photon emission computed tomography (SPECT), 142, 171, 192, 498, 577
basic SPECT imaging paradigm, 108
data acquisition, 108
data corrections, 111, 112
γ-rays and x-rays, 113
image reconstruction, 112, 113
and planar imaging, 114
radiotracers, 114
transverse images, 102
Single tissue compartment model, 502, 505
Site-specificity, 451
Size exclusion chromatography (SEC), 172
Small molecules, 546
quality control method for, 630–631
S_N2 mechanisms, 275
Walden inversion, 275
S-nitrosoglutathione, 246
S-nitrosothiols, 245
Sodium dodecyl sulfate polyacrylamide gel electrophoresis (SDS-PAGE), 173
Sokoloff, Louis, 22

Solid phase extraction (SPE), 153
Solid-phase peptide synthesis (SPPS), 140, 141, 146, 150
Solid-state detectors, 521
Sols, Alberto, 21
Somatostatin receptors (SSTR), 90, 137, 139, 146, 147
Somatotropin-release inhibitory factor (SRIF), 139
Sortase A, 462
Spectators, 38
Spontaneous fission, 52
Staffing and workflow, 631–632
Standard deviation, 532
Standard uptake value (SUV), 113, 157, 511–512
Standardized uptake value ratio (SUVR), 512
Stannous chloride ($SnCl_2$), 318
Static imaging, 103
Static *vs.* dynamic data acquisition and quantification, 594
Statistical power, 533
Statistical summary measures
  individual data, 532
  mean, 532
  median, 532
  mode, 532
  propagated error, 533
  quantile, 533
  range, 533
  ratio, 533
  standard deviation, 532
Stille and Suzuki cross-couplings, 214
Stille coupling, 214
Strain-promoted azide-alkyne cycloaddition (SPAAC), 469
Streptavidin (SA), 92
Strontium-82/83/89, 428
Student's test, 534
Styrene maleic acid neocarzinostatin, 190
Sulfhydryl groups, 454–455
Super-allowed transitions, 45
Super paramagnetic iron oxide nanoparticles, 186
Surface plasmon resonance (SPR), 173
Surface-enhanced Raman scattering (SERS) nanoparticles, 184

T
Tantalum-178, 438
Target identification
  bioavailability, 556
  data mining, 556–559
  mass spectrometry-based quantitative proteomics, 559
  molecule concentration, 589
  number per cell, 555
  phage display-based functional proteomics, 559–561
  selectivity, 560
Target nucleus, 70
Targeted alpha therapy, 413, 422
Targeted radionuclide therapy (TRT), 97
  clinical application of, 93, 94, 96
  limitations for, 97
  molecular targets and radiotherapeutics
    CD-20, 91
    folate receptor alpha, 91
    GPCR, 90
    norepinephrine transporter, 91
    PSMA, 90, 91
    radioimmunotherapeutics, 91
    types of targeting, 88–90
  multimodal treatment strategies, 96, 97
  preclinical and clinical research in, 97
  PRIT, 92, 93
  PRRT, developments in, 91, 92
  radiation-induced cell death, 86
  radioresistance, 87, 88
  strategies for, 85
  therapeutic radionuclides
    α-particles, 86
    Auger electrons, 86
    β-particles, 86
    cross-fire effect, 86
    DNA damage, 86, 87
Targeted radiotherapy, 550
Targetry, 81, 82
Technetium, 16
Technetium-94m, 439
Technetium-99m, 3, 17
  angiogenesis target, 327
  bifunctional chelators, 324–326
  biodistribution, 322, 323
  biodistribution studies, 321–322
  bone imaging, 314–315
  characteristics, 312
  chemistry, 312–313
  clinical use, 313–318
  eluting a $^{99}Mo/^{99m}Tc$ generator, 318
  hydrazinonicotinamide (HYNIC), 325
  isotopes, 311
  $K_2[BH_3CO_2]$, 320
  mass determination, 318
  $^{99}Mo/^{99m}Tc$ generator, 311
  neuroendocrine tumours (NETs), 327
  N_xS_y tetradentate chelators, 325
  pertechnetate ($[^{99m}Tc]TcO_4^-$), 316
  preclinical data, 329
  preparation, 318
  production, 311–312
  renal imaging, 315–316
  structure, 312–318
  synthesis, 313–318
  $[^{99m}Tc][Tc(CO)_3]^+$ complexes, 318–321
  Tc(I) chelators, 325–326
  $[^{99m}Tc]$Tc-DISIDA (diisopropryl iminodiacetic acid), 316
  $[^{99m}Tc]$Tc-DMSA (Dimercaptosuccinic acid), 315–316
  $[^{99m}Tc]$Tc-DTPA (diethylenetriaminepentaacetate), 316
  [99mTc]Tc-ECD (ethylene cysteine dimer; NeuroliteTM), 317
  $[^{99m}Tc]$Tc-exametazime (Ceretec™), 316
  $[^{99m}Tc]$Tc-MAG_3 (^{99m}Tc-mercaptoacetyltriglycine), 316
  $[^{99m}Tc]$Tc-Medronate (DraxImage® MDP-25 and TechneScan® MDP), 314
  $[^{99m}Tc]$Tc-Sestamibi (Cardiolite™), 314
  ^{99m}Tc-sulfur colloid, 318
  $[^{99m}Tc]$Tc-Tetrofosmin (Myoview™), 314
Tellurium-132, 17
Terbium, 442
Terbium-149, 415, 420
2,3,5,6-Tetrafluorophenol (TFP), 375
Tetrahydrofuran (THF), 142, 215
Tetrahydroxamate chelators, 383
N,N,N',N'-Tetramethyl-*O*-(*N*-succinimidyl)uronium tetrafluoroborate (TSTU), 141, 146
Tetrazine agent, 474
  stability and reactivity, 474
Thallium-201, 431

Theranostic pair, 623
Theranostic radiopharmaceuticals, 411, 419, 420
Theranostics, 9, 181, 184, 365–366
Therapeutic radionuclides, 85
  α-particles, 86
  Auger electrons, 86
  β-particles, 86
  cross-fire effect, 86
  DNA damage, 86
Therapeutic radiopharmaceuticals
  α and β-emitting radionuclides, 628
  21 CFR 211 facility, 628
  clinical trial, 623
  peptide dose, 623
  PET facilities, 629
  setup, 628
  sub-batch process, 629
  Xofigo® and Lutathera®, 628
Thin layer chromatography (TLC), 488
Thorium, 11
Thorium-226/227, 420
Thyroid cancer, 4, 7
Time-activity curve (TAC), 130, 157
Time-of-flight (TOF) PET, 110
Tin-117m, 432
Tissue reactions, 520
Titanium-45, 436
Tomographic imaging
  advantage of, 102
  basic paradigm of, 102
  emission, 102
  transmission, 102
Toxicity
  IMPD, 610
  less than 1.5 μg limit, 610
  less than 100 μg limit, 610–611
  more than 100 μg limit, 611
  radionuclide with chemical precursor, 610
  radionuclide without chemical precursor, 610
Toxin-based model, 602
Tracer principle, 4, 14
Training of staff, 632
Trans-cyclooctene (TCO), 471
  reagent stability and reactivity, 475
Transferrin-independent pathways, 266
Transgenic rodent models, 602–603
Transglutaminase (TGase), 462
Transient equilibrium, 79
Translocator protein-18 kDa (TSPO), 548
Trastuzumab-based radioimmunoconjugate, 383
Triazene precursor, 397
Triazoles, 248
Tricationic radiometals, 150
Trifluoroacetic acid (TFA), 142
N,N,N-Trimethylammonium triflate precursor, 146, 147
Tripodal tris(hydroxypyridinone), 384
Tris(2-carboxyethyl)phosphine (TCEP), 377
Tritium, 27
Tucker, Walter, 18
Tumor interstitial fluid (TIF), 168
Two-sample t-test, 535
Tyrosines, 455

U
U.S. clinical translation process
  clinical trial, 622–623
  first-in-human clinical trial, 619–621
  IND, 621
  preclinical studies, 621
  radiopharmaceutical quality, 621–622
  regulatory mechanisms, 623–624
U.S. Food and drug administration (FDA), 619
Umpolung concept, 290
United Nations Scientific Committee on the Effects of Atomic Radiation (UNSCEAR), 515
University of Missouri Research Reactor (MURR), 72
Unstable nuclei, 31, 60
Uranium, 11
Uranium-238 (^{238}U), 50
Uronium-based peptide coupling agents, 141

V
Validation campaign, 629
Valley of β-stability, 35
Visual inspection, 630

W
Wagner, Henry, 20
WAY1000635, 217
WAY100635, 134, 217
Weizsäcker equation, 29
Whole-body imaging, 103
Wipe tests, 521
Workshop on Targetry and Target Chemistry (WTTC), 76

X
Xenografts
  cell line, 575
  patient-derived, 575
Xenon-133, 435
Xenon-method, 215
Xofigo®, 94, 96
X-rays, 33, 54, 57
  discovery of, 11

Y
Yttrium, proton-induced reactions, 373
Yttrium-86, 436
  characteristics, 360
  chemical indistinguishability, 366
  positron-emitting radionuclide, 360
  quality of, 368
  radiolabeling protocols, 367
  theranostics, 365
Yttrium-90
  bifunctional chelators, 363–364
  bioinorganic chemistry, 362–363
  characteristics, 360
  crossfire effect, 360
  ibritumomab tiuxetan, 94
  nuclear properties, 359–360

positron emission tomography (PET), 360, 361
radionuclide therapy, 360
solution chemistry, 359
theranostics, 365–366

Z
ZEPHIR trial, 176
Zevalin, 7
Zinc-65, 441
Zirconium
isotopes, 371
radioisotopes, 371
Zirconium-89, 176
aminohexanoic acid spacer, 378
biomedical utility, 371–372
cell labeling, 378
cobalamin vector, 378
coordination chemistry, 372
demetallation, 384
deposition, 379
desferrioxamine B (DFO) characteristics, 374
feraheme, 379
label-free vectors, 378–379
melanin nanoparticles (MP), 379
non-immunoglobulin vectors, 378–379
nuclear properties, 372
oxines, 378
production, 372–374
purification, 372–374
radioimmunoconjugate, 378
radiolabeling, 377
Zr-oxalate, 374–375
Zolmitriptane, 216